

Lecture Notes in Mechanical Engineering

Hari Kumar Voruganti  
K. Kiran Kumar  
P. Vamsi Krishna  
Xiaoliang Jin *Editors*

# Advances in Applied Mechanical Engineering

Select Proceedings of ICAMER 2019

 Springer

# **Lecture Notes in Mechanical Engineering**

**Lecture Notes in Mechanical Engineering (LNME)** publishes the latest developments in Mechanical Engineering - quickly, informally and with high quality. Original research reported in proceedings and post-proceedings represents the core of LNME. Volumes published in LNME embrace all aspects, subfields and new challenges of mechanical engineering. Topics in the series include:

- Engineering Design
- Machinery and Machine Elements
- Mechanical Structures and Stress Analysis
- Automotive Engineering
- Engine Technology
- Aerospace Technology and Astronautics
- Nanotechnology and Microengineering
- Control, Robotics, Mechatronics
- MEMS
- Theoretical and Applied Mechanics
- Dynamical Systems, Control
- Fluid Mechanics
- Engineering Thermodynamics, Heat and Mass Transfer
- Manufacturing
- Precision Engineering, Instrumentation, Measurement
- Materials Engineering
- Tribology and Surface Technology

To submit a proposal or request further information, please contact the Springer Editor in your country:

**China:** Li Shen at [li.shen@springer.com](mailto:li.shen@springer.com)

**India:** Dr. Akash Chakraborty at [akash.chakraborty@springernature.com](mailto:akash.chakraborty@springernature.com)

**Rest of Asia, Australia, New Zealand:** Swati Meherishi at [swati.meherishi@springer.com](mailto:swati.meherishi@springer.com)

**All other countries:** Dr. Leontina Di Cecco at [Leontina.dicecco@springer.com](mailto:Leontina.dicecco@springer.com)

To submit a proposal for a monograph, please check our Springer Tracts in Mechanical Engineering at <http://www.springer.com/series/11693> or contact [Leontina.dicecco@springer.com](mailto:Leontina.dicecco@springer.com)

**Indexed by SCOPUS. The books of the series are submitted for indexing to Web of Science.**

More information about this series at <http://www.springer.com/series/11236>

Hari Kumar Voruganti · K. Kiran Kumar ·  
P. Vamsi Krishna · Xiaoliang Jin  
Editors

# Advances in Applied Mechanical Engineering

Select Proceedings of ICAMER 2019

 Springer

*Editors*

Hari Kumar Voruganti  
National Institute of Technology Warangal  
Warangal, Telangana, India

K. Kiran Kumar  
National Institute of Technology Warangal  
Warangal, Telangana, India

P. Vamsi Krishna  
National Institute of Technology Warangal  
Warangal, Telangana, India

Xiaoliang Jin  
University of British Columbia  
Vancouver, BC, Canada

ISSN 2195-4356

ISSN 2195-4364 (electronic)

Lecture Notes in Mechanical Engineering

ISBN 978-981-15-1200-1

ISBN 978-981-15-1201-8 (eBook)

<https://doi.org/10.1007/978-981-15-1201-8>

© Springer Nature Singapore Pte Ltd. 2020

This work is subject to copyright. All rights are reserved by the Publisher, whether the whole or part of the material is concerned, specifically the rights of translation, reprinting, reuse of illustrations, recitation, broadcasting, reproduction on microfilms or in any other physical way, and transmission or information storage and retrieval, electronic adaptation, computer software, or by similar or dissimilar methodology now known or hereafter developed.

The use of general descriptive names, registered names, trademarks, service marks, etc. in this publication does not imply, even in the absence of a specific statement, that such names are exempt from the relevant protective laws and regulations and therefore free for general use.

The publisher, the authors and the editors are safe to assume that the advice and information in this book are believed to be true and accurate at the date of publication. Neither the publisher nor the authors or the editors give a warranty, expressed or implied, with respect to the material contained herein or for any errors or omissions that may have been made. The publisher remains neutral with regard to jurisdictional claims in published maps and institutional affiliations.

This Springer imprint is published by the registered company Springer Nature Singapore Pte Ltd. The registered company address is: 152 Beach Road, #21-01/04 Gateway East, Singapore 189721, Singapore

# Preface

The main aim of the First International Conference on Applied Mechanical Engineering Research (ICAMER 2019) is to bring together all interested academic researchers, scientists, engineers, and technocrats and provide a platform for continuous improvement of mechanical engineering research.

ICAMER 2019 received an overwhelming response with more than 300 full paper submissions. After due and careful scrutiny, about 160 of them have been selected for oral presentation. The papers submitted have been reviewed by experts from renowned institutions, and subsequently, the authors have revised the papers, duly incorporating the suggestions of the reviewers. This has led to significant improvement in the quality of the contributions.

Springer publications have agreed to publish the selected proceedings of the conference in their book series of Lecture Notes in Mechanical Engineering (LNME). This enables fast dissemination of the papers worldwide and increases the scope of visibility for the research contributions of the authors.

This book comprises three parts, viz. thermal, design and production engineering. Each part consists of relevant full papers in the form of chapters. The thermal part consists of chapters on research related to IC engines, CFD, solar energy, automobiles, etc. The design part consists of chapters on computational mechanics, design of mechanisms, composite materials, tribology, and advanced areas like the isogeometric analysis. The production part consists of chapters on machining, new materials, additive manufacturing, unconventional manufacturing, and industrial engineering areas. This book provides a snapshot of the current research in the field of mechanical engineering and hence will serve as valuable reference material for the research community.

Warangal, India  
Warangal, India  
Warangal, India  
Vancouver, Canada

Dr. Hari Kumar Voruganti  
Dr. K. Kiran Kumar  
Dr. P. Vamsi Krishna  
Dr. Xiaoliang Jin

# Acknowledgements

Our sincere thanks to Springer publications for agreeing to publish the select proceedings of the conference in their book series of Lecture Notes in Mechanical Engineering (LNME). We wish to thank all the authors who submitted quality contributions to this book. A large number of reviewers have contributed to the enhancement of the quality of the papers, providing constructive critical comments, corrections, and suggestions to the authors. Our due gratitude to all of them.

Prof. N. V. Ramana Rao, Director, NIT Warangal, and Prof. P. Bangaru Babu, Head, Department of Mechanical Engineering, have been a constant source of inspiration and support. We deeply acknowledge their contributions. Special thanks to Dr. Vijay Kumar Manupati, Dr. Syed Ismail, and Dr. Karthik Balasubramanian for their prompt efforts in the review process. Contributions by the research scholars from the Department of Mechanical Engineering are praiseworthy.

Thanks to Dr. Akash Chakraborty, Associate Editor, Applied Sciences and Engineering, Springer, for his support and guidance during the publication process.

We express our sincere thanks to all the deans, registrar, head of the departments, and faculty-in-charges of various units of NIT Warangal for their administrative support in making this effort possible.

Dr. Hari Kumar Voruganti  
Dr. K. Kiran Kumar  
Dr. P. Vamsi Krishna  
Dr. Xiaoliang Jin  
Organizing Secretaries  
ICAMER 2019

# Contents

## Thermal Engineering Section

<b>Computational Study of Mixed Convection of Electronic Chips with Surface Radiation</b> . . . . .	3
Arnab Deb and S. K. Mandal	
<b>Combustion Performance of Hybrid Rocket Motor Under the Influence of Cylindrical Protrusion</b> . . . . .	11
Kabaleeswaran Manikandan, K. Lakshmi Das, N. Purushothaman and L. Karthik	
<b>Social and Economic Impact Assessment of Solar Water Pumping System on Farmers in Nagpur District of Maharashtra State of India</b> . . . . .	19
Devidas H. Yadav, Arunedra K. Tiwari and Vilas R. Kalamkar	
<b>Thermally Developing Region of a Parallel Plate Channel Partially Filled with a Porous Material with the Effect of Axial Conduction and Viscous Dissipation: Uniform Wall Heat Flux</b> . . . . .	27
J. Sharath Kumar Reddy and D. Bhargavi	
<b>Experimental Study of Closed-Loop Thermosyphon System Using Different Working Fluids</b> . . . . .	37
Mahasidha R. Birajdar and C. M. Sewatkar	
<b>Identifying Empirically Important Variables in IC Engine Operation Through Redundancy Analysis</b> . . . . .	45
Satishchandra Salam and Tikendra Nath Verma	
<b>Mixed Convective Heat Transfer with Surface Radiation in a Vertical Channel in Presence of Heat Spreader</b> . . . . .	53
S. K. Mandal, Arnab Deb and Dipak Sen	



<b>Experimental Analysis on Thermal Performance of a Solar Air Heater at Different Angular Positions</b> . . . . .	63
Sk. A. Rahaman, T. Eswar, S. J. Reddy and M. Mohan Jagadeesh Kumar	
<b>Surface Pressure Characteristics over Indian Train Engine</b> . . . . .	73
K. Vivek, B. Ashok Kumar, Karthick Dhileep, S. Arunvinthan and S. Nadaraja Pillai	
<b>Exergy Modelling of a Coal-Fired MHD Power Plant</b> . . . . .	81
Prabin Haloi and Tapan Kumar Gogoi	
<b>Design, Development and Analysis of Intake Manifold of Single-Cylinder Diesel Engine</b> . . . . .	91
Nikhil A. Bhave, Mahendra M. Gupta, Sandeep S. Joshi, Mohan G. Trivedi and Neeraj Sunheriya	
<b>Calibration of Reference Velocity and Longitudinal Static Pressure Variation in the Test Section of an Open-Type Subsonic Wind Tunnel</b> . . . . .	107
Neeraj Verma and Beena D. Baloni	
<b>Optimal Selection of Insulating Material for Energy Conservation in Steam Pipe Using Analytical Hierarchy Process</b> . . . . .	115
Mendu Siva Subrahmanyam, Imandi Aparna Devi and Beejapu Jagadeesh	
<b>Heat Transfer Enhancement Using Overlapped Dual Twisted Tape Inserts with Nanofluids</b> . . . . .	123
Rokkala Rudrabhiramu, K. Harish Kumar, K. Kiran Kumar and K. Mallikarjuna Rao	
<b>Flow Characteristic Study of Contraction of Compressor Intermediate S-Shaped Duct Facility</b> . . . . .	131
Manish Sharma and Beena D. Baloni	
<b>Alternate Heating Process in ESP Hoppers of Thermal Power Plant—An Experimental Pilot Investigation</b> . . . . .	143
R. Saravanan and Ramakotaiah Maddumala	
<b>Experimental Study on the Performance of Micro-aerial Vehicle Propeller</b> . . . . .	151
P. S. Premkumar, M. Sureshmohan, K. Siyuly, S. Vasanthakumar, R. Naveen Kumar, S. DenielGrene and S. Sanjaykumar	
<b>Heat Transfer Enhancement of Al<sub>2</sub>O<sub>3</sub>-Based Nanofluid in a Shell and Helical Coil Heat Exchanger</b> . . . . .	159
Prabhakar Zainith and Niraj Kumar Mishra	
<b>Numerical Analysis of the Effect of Fluid–Structure Interaction on Heat Transfer in the Square Cavity Using OpenFOAM</b> . . . . .	167
Nikhil Chitnavis and Trushar B. Gohil	

**Experimental Investigation of the Effect of Particle Concentration and Temperature on Thermophysical Properties of Water-Based Metal-Oxide Nanofluids** ..... 175  
 Ramesh Babu Bejjam, K Kiran Kumar, S Venkata Sai Sudheer and N Praveena Devi

**Pressure Drop in Vertical Pneumatic Conveying: Comparison Between Numerical Predictions with Existing Correlations** ..... 183  
 Pandaba Patro and Debasis Mishra

**CFD Analysis in the Design of Diffuser for Air Cooling of Low-Concentrated Photovoltaic/Thermal (LCPV/T) Solar Collector** ..... 191  
 Rohit Meshram and P. D. Sawarkar

**CFD Analysis of Wind Turbine with Different Flange Angles** ..... 199  
 S. M. Bichitkar, P. P. Buddiyal, S. S. Chavan, A. A. Kulkarni and V. B. Gawande

**Performance and Emission Characteristics of Thermal Barrier Coating on Diesel Engine Fueled with Cottonseed Biodiesel** ..... 205  
 Badal Kudachi, Nitin Satpute, Nilaj N. Deshmukh and Bipin Mashilkar

**Performance and Emission Analysis of Rapeseed Methyl Ester on DI Diesel Engine Using Artificial Neural Network** ..... 215  
 V. Amosu, S. K. Bhatti and S. Jaikumar

**The Analytical Study of Velocity Slip on Two-Phase Flow in an Eccentric Annular Region** ..... 223  
 B. Umadevi, P. A. Dinesh and C. V. Vinay

**Numerical Study on the Effect of Impeller Geometry on Pump Performance** ..... 233  
 Arshdeep Singh, Siga Satya Sekhar, S. Jayavel and Sudhir Varadarajan

**Numerical Study of Hydrogen-Fueled Scramjet Performance with Passive Techniques** ..... 243  
 Obula Reddy Kummitha, K. M. Pandey and Rajat Gupta

**Numerical Simulation of Heat Transfer and Fluid Flow Characteristics of Triangular Corrugated Wavy Channel** ..... 251  
 Meghna Das Chaudhury and Raju

**Emission and Performance Characteristics of CI Engine with Diesel–Butanol Blends Using Intake Pressure Boost** ..... 261  
 Hemant Gowardhan, Amit Karwade and J. G. Suryawanshi

**Thermal Design Methodology for Regenerative Fuel-Cooled Scramjet Engine Walls** ..... 269  
 G. Vijayakumar

<b>Computational Studies of Shock Wave Boundary Layer Interactions in Hypersonic Flow Over Double Cone Geometries</b> .....	279
Siva Vayala and Ravi K. Peetala	
<b>Thermal Design and Testing of External Protuberance of Hypersonic Carrier Vehicle Airframe</b> .....	287
G. Vijayakumar, S. Narendar and J. Justina Geetha	
<b>The Effect of Diesel and Biodiesel Blends on CI Engine Performance and Emission Characteristics</b> .....	297
J. Venkatesu Naik, K. Kiran Kumar, S. Venkata Sai Sudheer and Mahesh Pallikonda	
<b>Numerical Analysis of Fluid–Structure Interaction of Blood Flow Through a Flexible Tube with 90-Degree Bend Using OpenFOAM</b> .....	303
Rishabh N. Jaiswal and Trushar B. Gohil	
<b>Design Engineering Section</b>	
<b>Damage and Failure Analysis of Short Carbon Fiber Reinforced Epoxy Composite Pipe Using FEA</b> .....	313
Anju Verma, Apurba Mandal and Dungali Sreehari	
<b>Dynamic Performance Analysis of a Four-Ton Automobile Chassis</b> .....	321
P. Sowmya, K. Karthik Rajashekar, M. Madhavi and P. A. Sastry	
<b>Experimental Studies on Steel Beam-to-Column Connections Under Elevated Temperature</b> .....	335
A. Cinitha and V. Nandhini	
<b>Investigating the Influence of Higher-Order NURBS Discretization on Contact Force Oscillation for Large Deformation Contact Using Isogeometric Analysis</b> .....	343
Vishal Agrawal and Sachin S. Gautam	
<b>Simple Optimization Algorithm for Design of a Uniform Column</b> . . . .	351
Joji Thomas, Anshuman Kumar Sahu and Siba Sankar Mahapatra	
<b>Unbalance and Dynamic Parameters Estimation in a Rigid Rotor Mounted on Active Magnetic Bearings</b> .....	363
Prabhat Kumar, Vikas Kumar, Kundan Kumar and Lakhan Singh Meena	
<b>Investigating the Influence of Geometrical and Material Parameters on Peeling Behaviour of a Gecko Spatula</b> .....	373
Saipraneeth Gouravaraju and Sachin S. Gautam	

**Quantitative Analysis of Tribological Performance on Al–CSA Composite Using Orthogonal Array** . . . . . 381  
 R. Siva Sankara Raju, B. Venkata Siva and G. Srinivasa Rao

**Pre-strain in Dielectric Elastomer Actuator; Challenges Towards Structure–Property Relationship** . . . . . 389  
 Dhananjay Sahu, Om Prakash Prabhakar, Raj Kumar Sahu and Karali Patra

**Modified Electromechanical Model for Dielectric Elastomer Cylindrical Actuators** . . . . . 397  
 Om Prakash Prabhakar, Dhananjay Sahu and Raj Kumar Sahu

**A Numerical Study to Investigate the Modal Analyses of Cracked Airplane Wing (NACA2415)** . . . . . 405  
 Gaurav Verma, Anshul Sharma and Yogesh K. Prajapati

**Synthesis and Characterization of Nano-grease for Automotive Wheel Bearing Application** . . . . . 413  
 Pankaj S. Ghatage, Abhijeet P. Shah and Dhananjay Kumbhar

**Hamiltonian-Based Solutions of Certain PDE in Plasma Flows** . . . . . 423  
 Vivek S. Sharma, Parag V. Patil and Milan A. Joshi

**Low-Cost Test Rig for Demonstrating Single Plane Balancing Using Vibrations** . . . . . 433  
 N. V. S. Shankar, K. V. Jitendra, H. Ravi Shankar and M. Manikumar

**Nonlinear Dynamic Analysis of Automotive Turbocharger Rotor System** . . . . . 443  
 S. Bala Murugan, Rabindra Kumar Behera and P. K. Parida

**On the Response of a Beam Structure to a Moving Mass Using Green’s Function** . . . . . 455  
 Sudhansu Meher, Suraj Parida and Rabindra Kumar Behera

**A Programmatic Approach for the Prediction of Service Life of Deep Drawing Die Using ANN** . . . . . 465  
 Vishal Naranje and Sachin Salunkhe

**Thermo-Mechanical Analysis of Unidirectional PALF Composites Using Micromechanical Approach** . . . . . 475  
 Anurag Jasti and Sandhyarani Biswas

**Analysis and Selection of Bio-stents Using Finite Element Method** . . . . . 485  
 Jannatul Bashir and K. Jayabal

**Electromechanical Responses of Dielectric Elastomers** . . . . . 495  
 Moumita Tewary and Tarapada Roy

<b>Design, Manufacturing, and Testing of Feeding and Bending Mechanism</b> . . . . .	505
Vijay V. Mehta, Vedant K. Parmar, Nirav P. Maniar and Jasmin P. Bhimani	
<b>Design and Kinematics of a Coal Bunker Scraper Guide-Mechanism</b> . . . . .	513
Bijoy Ramakrishnan, Alex Sherjy Syriac, Chetan Chaudhari, Aditya Shah and S. S. Chiddarwar	
<b>Measurement of Elastic Modulus and Damping Properties of Friction Stir Processed Pure Metals Using Impulse Excitation Technique</b> . . . . .	521
K. Venkateswara Reddy, R. Bheekya Naik, Sandeep Yadav, G. Madhusudhan Reddy and R. Arockia Kumar	
<b>Dynamic Response of FGM Kirchhoff's Plate</b> . . . . .	529
Pratikshya Mohanty and Rabindra Kumar Behera	
<b>Comparative Study of Various Defects in Monolayer Graphene Using Molecular Dynamics Simulation</b> . . . . .	539
Kritesh Kumar Gupta, Aditya Roy and Sudip Dey	
<b>Application of Single-Sided NMR and Acousto-Ultrasonic Methods for NDE of Composite Structures</b> . . . . .	547
S. K. Sahoo, R. N. Rao, Srinivas Kuchipudi and M. K. Buragohain	
<b>Effect of Material Damping on the Vibration Response of Cantilever Beams in Dynamic Environment</b> . . . . .	557
L. Viswanadham, R. N. Rao and Ch. Sri Chaitanya	
<b>Active Vibration Control in Turbocharger Rotor System with the Use of Electromagnetic Actuator</b> . . . . .	563
Rajasekhara Reddy Mutra and J. Srinivas	
<b>Coupled Analysis of Underwater System by Numerical Approach</b> . . . . .	571
V. Rama Krishna, B. Ajay Kumar, O. R. Nandagopan, N. Ravi kumar and U. Urban Kumar	
<b>Design and Analysis on Reinforced Carbon–Basalt Fibres Composite Laminate</b> . . . . .	581
S. Nagarjuna Reddy and M. Trivikrama Sankar	
<b>Optimum Geometry of Steering Mechanism for an Automobile</b> . . . . .	591
R. Venkatachalam and A. Padma Rao	
<b>Influence of Surface Textures by Ink-Jet Print Followed by Chemical Etching Process on the Performance of HSS Cutting Tool</b> . . . . .	603
K. Nagendra Prasad and Ismail Syed	

**Effect of Temperature on the Tribological Performance of MoS<sub>2</sub>-TiO<sub>2</sub> Coating Material** . . . . . 611  
 Avinash V. Borgaonkar and Ismail Syed

**Topology Optimization Using Strain Energy Distribution for 2D Structures** . . . . . 619  
 Srinivasan Bairy, Rafaque Ahmad and Hari K. Voruganti

**Kinematic Analysis for Optimum Manipulability and Trajectory Planning of Human Leg** . . . . . 633  
 Abhijeet Dhoke, V. V. M. J. Satish Chembuly and Hari K. Voruganti

**Structural Topology Optimization: Methods and Applications** . . . . . 643  
 Rafaque Ahmad and Hari K. Voruganti

**A Multi-objective Optimization Method Based on Nelder-Mead Simplex Search Method** . . . . . 655  
 Vivek Kumar Mehta and Bhaskar Dasgupta

**Production and Industrial Engineering Section**

**Performance and Life Cycle Analysis of Soybean Oil-Based Minimum Quantity Lubrication in Machining of Ti6Al4V** . . . . . 671  
 Rukmini Srikant Revuru and Nageswara Rao Posinasetti

**Investigations on Corrosion Behaviour in Micro-Milling of Biomedical Grade Ti-6Al-7Nb Alloy** . . . . . 679  
 S. P. Leo Kumar and D. Avinash

**Optimization of Machining Parameters for Multi-performance Characteristics in Milling of Composite Solid Propellants Using RSM** . . . . . 687  
 Kishore Kumar Katikani, A. Venu Gopal and Venkatesara Rao Vemana

**The Effect of ZrO<sub>2</sub> and TiO<sub>2</sub> Reinforcing Agent on the Microstructure and Mechanical Properties of Hydroxyapatite Nanocomposites** . . . . . 699  
 Vemulapalli Ajay Kumar, Penmetsa Rama Murty Raju, Nallu Ramanaiah and Siriyala Rajesh

**Optimization of Machining Parameters for Vibration-Assisted Turning of Ti6Al4V Alloy Using Analysis of Variance** . . . . . 713  
 D. Venkata Sivareddy, P. Vamsi Krishna and A. Venu Gopal

**Characterisation and Performance Measure Evaluation of Nanofluid Blended Thin-Film Temperature Gauges** . . . . . 725  
 P. Jayesh, Sheikh Afridhi and Abhay Mohan

<b>Base Transesterification of Ineffectual Soybean Oil Using Lab Scale Synthesized CaO Catalyst</b> . . . . .	735
Rakesh Singh Ningthoujam, Ronaldo Singh Naorem, Denin Singh Langpokpam, Thokchom Subhaschandra Singh and Tikendra Nath Verma	
<b>Solid Lubricant Effect on the Microstructure and Hardness of the Functionally Graded Cemented Tungsten Carbide</b> . . . . .	745
Rityuj Singh Parihar, Srinivasu Gangi Setti and Raj Kumar Sahu	
<b>Experimental and Microstructural Analysis of TIG and MIG Welding on Dissimilar Steels</b> . . . . .	753
A. Aravind Reddy and Abu Sufyan Malik	
<b>Thermal Management of Avionic Packages Using Micro-blower</b> . . . . .	763
K. Velmurugan, V. P. Chandramohan, S. Karunanidhi and D. Sai Phaneendra	
<b>Evaluation of Mechanical Properties of Banana and S-glass Fiber-Reinforced Hybrid Nanosilica Composite</b> . . . . .	775
P. Srinivas Manikanta, M. Somaiah Chowdary and M. S. R. Niranjan Kumar	
<b>Tribological Behaviour of Carbon Fibre Polymer Composites Reinforced with Nano-fillers</b> . . . . .	791
Shylesh K. Siddalingappa, Bhaskar Pal, M. R. Haseebuddin and K. Gopalakrishna	
<b>Environment Effect on Impact Strength of Pistachio Shell Filler-Based Epoxy Composites</b> . . . . .	801
Sandeep Gairola, Somit Gairola and Hitesh Sharma	
<b>Performance Improvement of Nanofluid Minimum Quantity Lubrication (Nanofluid MQL) Technique in Surface Grinding by Optimization Using Jaya Algorithm</b> . . . . .	809
Sharad Chaudhari, Rahul Chakule and Poonam Talmale	
<b>Wear Resistance of Structural Steels Having Ultra-Low Carbon to High Carbon Concentration</b> . . . . .	817
Soumya Sourav Sarangi, Lavakumar Avala and D. Narsimhachary	
<b>Experimental Investigation on Laser Beam Welded Joints of Dissimilar Metals and Optimization of Process Parameters Using Firefly Algorithm</b> . . . . .	823
B. Narayana Reddy, P. Hema, Y. Prasanth Reddy and G. Padmanabhan	
<b>Parametric Optimization of Electrical Discharge Grinding on Ti-6Al-4V Alloy Using Response Surface Methodology</b> . . . . .	831
Murahari Kolli and Adepu Kumar	

**Mathematical Modeling of Material Removal Rate Using Buckingham Pi Theorem in Electrical Discharge Machining of Hastelloy C276** ..... 843  
 P. Ravindranatha Reddy, G. Jayachandra Reddy and G. Prasanthi

**Effect of Exfoliated Vermiculite as Thickening and Foaming Agent on the Physical Properties of Aluminium Foam** ..... 853  
 V. V. K. Lakshmi, V. Arun Vikram, K. V. Subbaiah, K. Suresh and B. Surendra Babu

**Multi-response Optimization of Process Parameters in Turn-Milling Processes—An Experimental Approach** ..... 861  
 K. Arun Vikram, C. Ratnam, V. V. K. Lakshmi and R. D. V. Prasad

**On the Role of Amylum Additive-Based Cutting Fluids in Machining—An Experimental Investigation** ..... 873  
 R. Padmini, P. Vamsi Krishna and P. Jeevan Kumar

**Tensile Property of Ultra-High Molecular Weight Polyethylene Fibre and Its Composite Laminate** ..... 881  
 Arun Kumar Singh, Dharmendra Kumar Shukla and N. Esvara Prasad

**Experimental and Numerical Modeling of ECMM on Al 7075 T6 Alloy** ..... 889  
 K. Samson Praveen Kumar and G. Jaya Chandra Reddy

**FEM Modeling of Coated Tools to Study the Influence of Coating Thickness** ..... 899  
 M. Khirod Kumar, Manne Hareesh, P. Vamsi Krishna and S. Sambhu Prasad

**Effect of Graphene Nanofluid on Machining Inconel 718** ..... 913  
 Siva Bevara, M. Amrita, Sanjay Kumar and B. Kamesh

**Mechanical Properties of AA 7075-Nano ZrO<sub>2</sub> Reinforced Matrix Composites** ..... 921  
 B. Prasanna Nagasai, S. Srikanth and J. A. Ranga Babu

**Experimental Investigation on Friction Stir Welding of HDPE Reinforced with SiC and Al and Taguchi-Based Optimization** ..... 929  
 S. Ramesh Babu, S. R. K. Hudgikar and Y. Poornachandra Sekhar

**Design and Simulation of Porous Ti–6Al–4V Alloy Structures for Additive Manufacturing of Bioimplants** ..... 941  
 A. Rudra Kumar, S. Rambabu and K. Sri Harsha

**Effect of Tool Geometry and Heat Treatment on Friction Stir Processing of AA6061** ..... 947  
 Karan Chauhan, M. V. N. V. Satyanarayana and Adepu Kumar



<b>Analysis of Micro-cracks and Micro-hardness in White Layer Formation on Machined Surfaces in EDM Process . . . . .</b>	<b>955</b>
K. Leela Kumar, Ch. Srinivasa Rao, B. Sateesh and M. S. R. Viswanath	
<b>Multi-objective Optimization of Submerged Friction Stir Welding Process Parameters for Improved Mechanical Strength of AA6061 Weld Bead by Using Taguchi-L18-Based Gray Relational Analysis . . .</b>	<b>965</b>
Laxmana Raju Salavaravu and Lingaraju Dumpala	
<b>Investigation on Wear Behaviour of AA5052/SiC/Al<sub>2</sub>O<sub>3</sub> Hybrid Composite Fabricated Using Stir Casting Process . . . . .</b>	<b>975</b>
V. G. Shanmuga Priyan, R. Malayalamurthi and S. Kanmani Subbu	
<b>Numerical Modelling of High Energy Density Beam-Assisted Machining of Hardened Armour Steel . . . . .</b>	<b>983</b>
A. Sahu, A. N. Jinoop, C. P. Paul, Adepu Kumar and K. S. Bindra	
<b>Experimental Investigation of Electro-Discharge Machining on NIMONIC 80A Through Response Surface Methodology . . . . .</b>	<b>991</b>
G. Vishnu Pramod Teja, K. Saraswathamma, P. Murali Krishna and G. Tejeswara Rao	
<b>Optimization of Minimum Quantity Lubrication Parameters . . . . .</b>	<b>1001</b>
M. Amrita, R. R. Srikant and V. S. N. Venkata Ramana	
<b>Experimental Investigation and Mathematical Modeling for Material Removal and Tool Wear in Making of Rectangular Channels by Electric Discharge Machining (EDM) on Aluminum–Boron Carbide Composite Sintered Preform . . . . .</b>	<b>1011</b>
Suresh Gudipudi, Selvaraj Nagamuthu, Kanmani Subbu Subbian and Surya Prakasa Rao Chilakalapalli	
<b>Investigation on the Microstructure and Mechanical Properties of AZ91D Magnesium Alloy Plates Joined by Friction Stir Welding . . . . .</b>	<b>1021</b>
Nagabhushan Kumar Kadigithala and C. Vanitha	
<b>Mechanical Characterization of Unidirectional Banana–Glass Fiber-Reinforced Hybrid Composites . . . . .</b>	<b>1031</b>
Ch. Naveen Reddy, M. Bhargav and Ajay Kumar Kaviti	
<b>Experimental Investigation of Ultrasonic Flaw Defects in Weld Clad Materials Using NDT Technique . . . . .</b>	<b>1039</b>
P. Ravindra Kumar, G. Vijay Kumar, K. Naga Murali and R. B. S. S. Kishore	

**An Effective and Economical Method to Improve Structural Homogeneity and Mechanical Properties of Al-Mg Alloy Processed by ECAE** ..... 1053  
 Ananda Babu Varadala, Swami Naidu Gurugubelli and Sateesh Bandaru

**Characterization of Kenaf/Aloevera Fiber Reinforced PLA-Hybrid Biocomposite** ..... 1061  
 P. Ramesh, B. Durga Prasad and K. L. Narayana

**Performance Analysis of Different Tool Shape in Electric Discharge Machining Process with Vegetable Oil as Dielectric Fluid** ..... 1069  
 B. Singaravel, K. Chandra Shekar, G. Gowtham Reddy and S. Deva Prasad

**Experimental and Finite Element Analysis of Fracture Toughness of Chilled LM13 MMC** ..... 1079  
 H. S. Harshith and Joel Hemanth

**Design and Fabrication of Die Back Door for Manufacturing of Cylinder Liners** ..... 1089  
 T. Vadivelu, C. Vijaya Bhaskar Reddy and G. Prasanthi

**Fabrication and Characterization of Functionally Graded Composites Using Friction Stir Processing** ..... 1103  
 B. Venkatesh, T. Sadasiva Rao and Adepu Kumar

**Multi-Parametric Optimization of Electrical Discharge Machining of Inconel-690 Using RSM-GRA Technique** ..... 1113  
 Bhavani Marturi, Murahari Kolli, Adepu Kumar, Seelam Pichi Reddy and Sai Naresh Dasari

**Effect of Nanoparticles Addition on Microstructural and Mechanical Properties of Friction Stir Welded 2014 Aluminium Alloy** ..... 1127  
 Kethavath Kranthi Kumar, Adepu Kumar and Divya Sachan

**Investigation on Influence of Hybrid Nanofluid/MQL on Surface Roughness in Turning Inconel-718** ..... 1137  
 Mechiri Sandeep Kumar, V. Vasu and A. Venu Gopal

**Fuzzy Logic and Regression Modelling of Machining Parameters in Turning AISI 1040 Steel Using Vegetable-Based Cutting Fluids with Extreme Pressure Additive** ..... 1147  
 B. Satheesh Kumar, Neelam Parimala and P. Vamsi Krishna

**A New Approach in Establishing Stable Machining Parameters Using Frame Statistics and Kurtosis** ..... 1159  
 V. Srinivasa Rohit, A. Venu Gopal and L. Rama Krishna

**Design and Ergonomic Work Posture Evaluation of Garbage Disposal Pushcart** ..... 1169  
P. Jayesh, A. Gopala Krishna, M. Vishal, Abhay Mohan and Sheikh Afridhi

**Redesigning of Electric Plug for Assembly Time Reduction Using DFA** ..... 1179  
V. Naga Malleswari, B. SurendraBabu and Ch. Praneeth

**Analysis and Optimization of Queueing Systems in Airports—Discrete Event Simulation** ..... 1189  
Rishabh Jain, Hrishikesh Bedekar, K. Jayakrishna, K. E. K. Vimal and M. Vijaya Kumar

**An Extensive Study of Multi-level Inventory Lot Sizing Optimization Problem** ..... 1195  
V. V. D. Sahithi, C. S. P. Rao and M. Srinivasa Rao

## About the Editors

**Dr. Hari Kumar Voruganti** is currently an Associate Professor at the Department of Mechanical Engineering, National Institute of Technology Warangal, India. He has obtained his B.Tech (Mechanical) from KITS Warangal, M.E from Osmania University, Hyderabad and Ph.D. from IIT Kanpur. His major research interests include geometric modeling (CAD), structural shape optimization, iso-geometric/finite element analysis (IGA, FEA), and robot path planning and kinematics. He has published several articles in journals and international conferences. He has received the National Doctoral Fellowship and URC Postdoctoral Fellowship. Dr. Voruganti has about 10 years of research and teaching experience. He has also worked in other institutions namely TU Berlin, IIITDM Jabalpur and University of Witwatersrand. He is associated with many professional bodies and is a reviewer for many reputed journals.

**Dr. K. Kiran Kumar** is currently an Associate Professor at the Department of Mechanical Engineering, National Institute of Technology Warangal, India. He obtained his B.Tech (Mechanical) and M.Tech (Thermal Engineering) from JNTU Hyderabad, and his Ph.D. from IIT Kharagpur. He has technical expertise in areas such as refrigeration, air conditioning, nanofluids, electronics cooling and solar thermal systems. He has published 25 journal articles and 15 conference papers. He has more than 10 years of teaching experience. He is also a reviewer of several reputed journals.

**Dr. P. Vamsi Krishna** is currently an Associate Professor at the Department of Mechanical Engineering, National Institute of Technology Warangal, India. He obtained his B.Tech (Mechanical) and M.Tech (Production) from Sri Venkateswara University, Tirupati, and his Ph.D. from Andhra University. His research interests include application of solid lubricants in machining process, application of eco-friendly nano cutting fluids in machining, vibration assisted machining, modeling and simulation of manufacturing processes. He holds a patent on Drill tool assembly. Currently, he is an editorial board member of IJEPE, AJME, NNR, AJN,

JoPRM, Journal of Manufacturing Science and Technology, Horizon Research Publishing Corporation and Amity Journal of Research, Innovation and Commercialization. He has published 55 journal papers and 30 conference papers.

**Dr. Xiaoliang Jin** is an Assistant Professor at the Department of Mechanical Engineering, University of British Columbia, Vancouver. He obtained his B.Sc (Mechanical) and M.A.Sc from Beihang University, China, and Ph.D. from the University of British Columbia. His primary research interests include mechanics and dynamics in machining processes, micro machining, vibration assisted machining, and surface integrity in precision machining process, precision machine and controller design. Dr. Xiaoling Jin received the National Science Foundation CAREER Award in 2016. He was honored with the Outstanding Early Career Researcher at Oklahoma State University in 2016, Outstanding Self-financed Students by China Scholarship Council 2011, Outstanding Graduate Thesis by Beihang University 2004. He also received the UBC Four Year Fellowship from University of British Columbia 2009 – 2012. He has published 17 journal articles and 12 conference papers.

# **Thermal Engineering Section**

# Computational Study of Mixed Convection of Electronic Chips with Surface Radiation



Arnab Deb and S. K. Mandal

**Abstract** In this present study, the effect of heat spreader in a horizontal channel consisting of electronic chips with mixed convection and surface radiation is examined. SIMPLER algorithm with finite volume method is used to solve governing equations using ANSYS 16.2 software. Results show the increase in the performance of heat transfer with an increase in the values of governing parameters like Reynolds number and emissivity of the spreader.

**Keywords** Heat spreader · Mixed convection · Radiation · Electronic chip

## 1 Introduction

The dependability of the basic electronic components of a device has key importance in the overall reliability of the device. Electronic equipment becomes less efficient if it exceeds a specific temperature limit. As the temperature is increased, the failure rate is enhanced exponentially. So, control of the temperature of the electronic parts is a vital issue in the design and operation. A virtuous literature survey suggests that many of the studies are focused on heat transfer augmentation with the utility of various shaped control elements. Various forms of vortex generators can be used to enhance the heat transfer such as protrusions, inclined blocks, wings, fin and ribs, winglets [1, 2] in different geometries like circular, non-circular channel under turbulent flow [3–5] as well as laminar flows [4]. Effect of surface radiation along with mixed convection also improves the heat transfer performance [6, 7]. Electronic chip covered by heat spreader can also be used to enhance the rate of heat transfer. It also avoids direct contact of air with the chips.

---

A. Deb (✉) · S. K. Mandal  
Department of Mechanical Engineering, NIT-Arunachal Pradesh, Yupia, Arunachal Pradesh  
791112, India  
e-mail: [arnabdeb93@gmail.com](mailto:arnabdeb93@gmail.com)

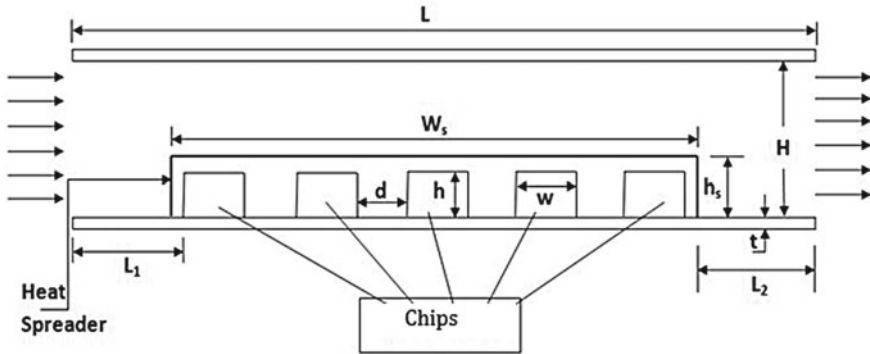


Fig. 1 Schematic diagram of the problem

## 2 Problem Description

The schematic diagram of a rectangular parallel plate channel with five identical electronic chips covered by a rectangular heat spreader is shown in Fig. 1. Electronic chips are located at the bottom wall of the channel maintaining a spacing of ' $d$ ' with successive chip. Channel has a length ' $L$ ' and a width ' $H$ '. Each chip has a width ' $w$ ' and height ' $h$ '. The heat spreader has a width of ' $W_s$ ' and height ' $h_s$ '. Left face of the first chip maintains a distance of ' $L_1$ ' from the inlet and right face of the 5th chip is positioned at a distance of ' $L_2$ ' from the outlet. Walls of the channel has a fixed thickness of ' $t$ '. Each chip with volumetric heat-generating capacity of  $100,000 \text{ W/m}^3$  is chosen in the present case. Fluid properties are supposed to be constant.

## 3 Governing Equations and Boundary Conditions

For a two-dimensional, steady, incompressible, laminar flow the governing equations are given as follows:

$$\frac{\partial U}{\partial X} + \frac{\partial V}{\partial Y} = 0 \quad (1)$$

$$U \frac{\partial U}{\partial X} + V \frac{\partial U}{\partial Y} = -\frac{\partial P}{\partial X} + \frac{1}{Re} \left( \frac{\partial^2 U}{\partial X^2} + \frac{\partial^2 U}{\partial Y^2} \right) \quad (2)$$

$$U \frac{\partial V}{\partial X} + V \frac{\partial V}{\partial Y} = -\frac{\partial P}{\partial Y} + \frac{1}{Re} \left( \frac{\partial^2 V}{\partial X^2} + \frac{\partial^2 V}{\partial Y^2} \right) + \frac{Gr}{Re^2} \theta \quad (3)$$

$$U \frac{\partial \theta}{\partial X} + V \frac{\partial \theta}{\partial Y} = \frac{1}{Re Pr} \left( \frac{\partial^2 \theta}{\partial X^2} + \frac{\partial^2 \theta}{\partial Y^2} \right) \quad (4)$$



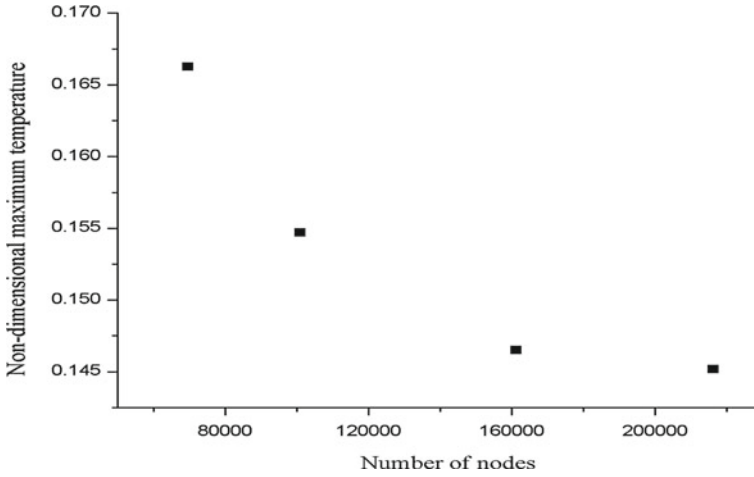


**Fig. 2** Variation of non-dimensional maximum temperature with number of nodes

Surface to surface radiation model is used considering all internal surfaces are grey, opaque and diffuse. Air is a non-participating medium. No-slip boundary conditions are employed at surfaces. Couple boundary conditions are used at wall-to-fluid and wall-to-wall boundaries [7]. At inlet, velocity inlet boundary condition and at outlet, pressure outlet boundary condition is imposed.

## 4 Grid Independence Test

Grid independence study is conducted for  $Re = 250$ . A non-uniform grid is used all through the domain along with very fine grids in front of the chips and spreader. Figure 2 shows that by increasing the total number of nodes from 161,265 to 216,279, a change is only less than 1% on the maximum non-dimensional temperature. Hence, the node of 161,265 is considered in whole study for time limits.

## 5 Results and Discussions

Present study is conducted for diverse Reynolds number ( $Re = 100, 250$  and  $500$ ), various emissivity values of heat spreader ( $\epsilon_s = 0.1, 0.3, 0.5, 0.7$  and  $0.9$ ) by fixing emissivity of substrate at  $0.9$  to create sufficient data for non-dimensional temperature ( $\theta$ ). In this investigation, the dimensionless geometric parameters have been taken as  $L_1 = 2H, L_2 = 8H, d = w$ .

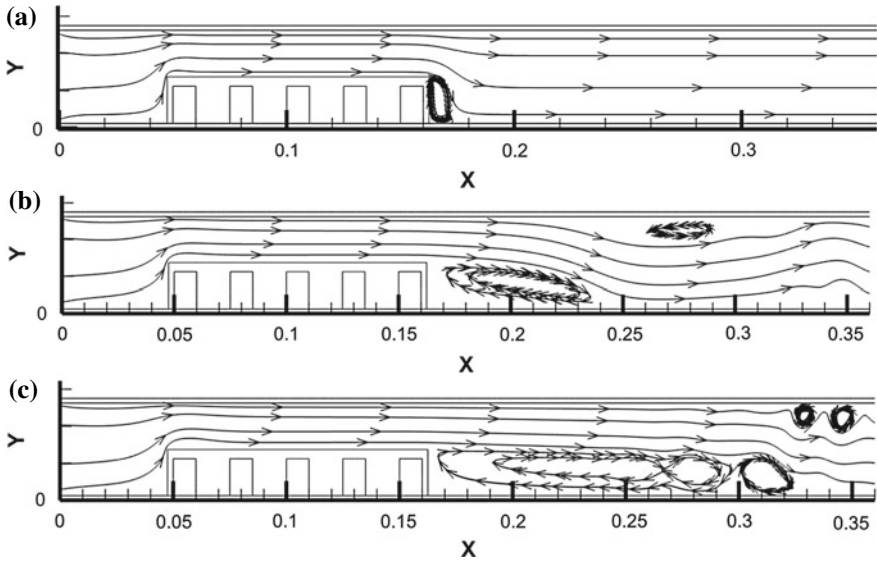


Fig. 3 Streamline for  $\epsilon_s = 0.5$  at **a**  $Re = 100$ , **b**  $Re = 250$  and **c**  $Re = 500$

### 5.1 Influence of Reynolds Number on Heat Transfer

One of the considerable parameters in this present numerical study is Reynolds number. Flow field is characterized by using streamline as shown in Fig. 3. Temperature distribution is shown in Fig. 4.

From Fig. 3, it is observed that with the increase in Reynolds number, recirculation strength behind the spreader increases due to sudden increase in cross-sectional area which leads to backward pressure drop. At higher Reynolds number, a weak flow reversal takes place near the top wall of the channel due to sudden expansion of cross-sectional area. Figure 4 depicts that with the increase in Reynolds number, thermal boundary layer thickness decreases and also temperature of the channel decreases. As, due to radiation, heat is transferred from spreader to top wall of the channel, and thus, thermal boundary layer is also developed at the top wall which decreases with increase in Reynolds number.

### 5.2 Influence of Heat Spreader Emissivity on Heat Transfer

Figure 5a depicts that with the increase in emissivity of heat spreader, non-dimensional temperature decreases. When emissivity changes from 0.1 to 0.9, maximum temperature changes from 347 to 334 K as radiative interaction between spreader and wall increases. Figure 5b depicts the effect of surface radiation on

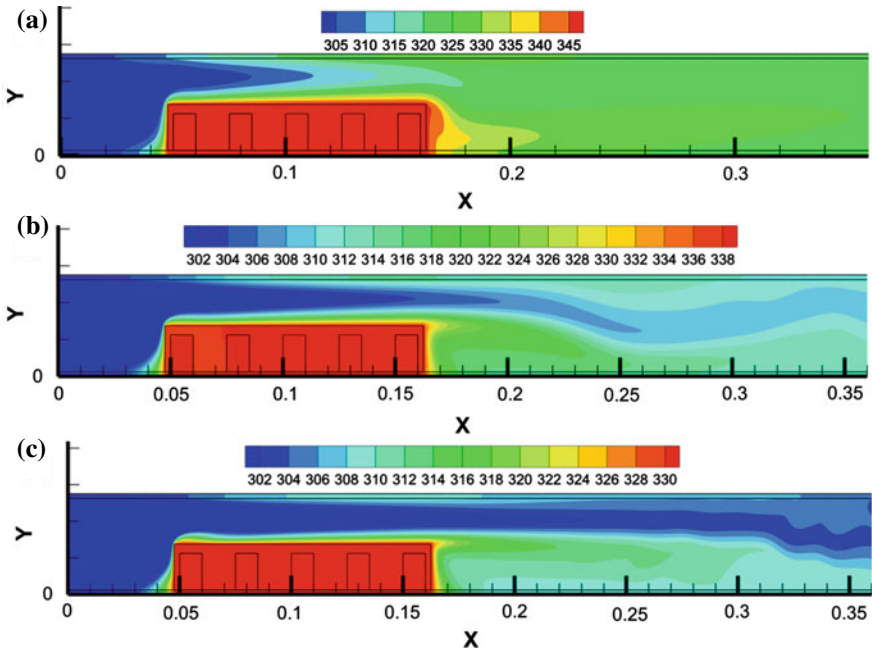


**Fig. 4** Temperature distribution for  $\epsilon_s = 0.5$  at **a**  $Re = 100$ , **b**  $Re = 250$  and **c**  $Re = 500$

total heat transfer. At  $Re = 250$ , when spreader emissivity 0.1, the contribution of radiation is 7.65%, while for emissivity 0.9, it is 31.87%. At higher Reynolds number, the contribution of surface radiation on total heat transfer decreases as mixed convection effect dominates. Temperature distribution for various emissivities of heat spreader is shown in Fig. 6.

## 6 Conclusions

From the above analysis, it is observed that with the increase in Reynolds number, maximum temperature within the channel decreases and also, contribution of radiation decreases. Again, it is observed that with the increase in spreader emissivity, the temperature at the chip surface decreases.

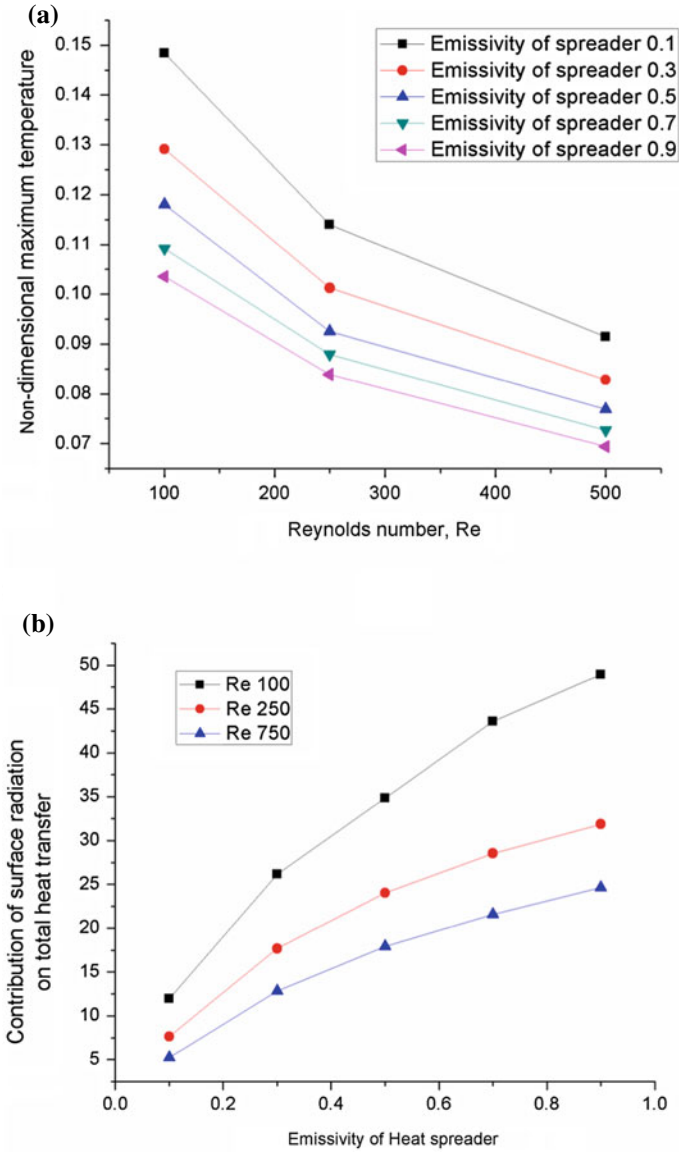


**Fig. 5** Graph **a** variation of non-dimensional temperature with  $Re$  for different emissivity, **b** contribution of radiation on total heat transfer for different  $Re$

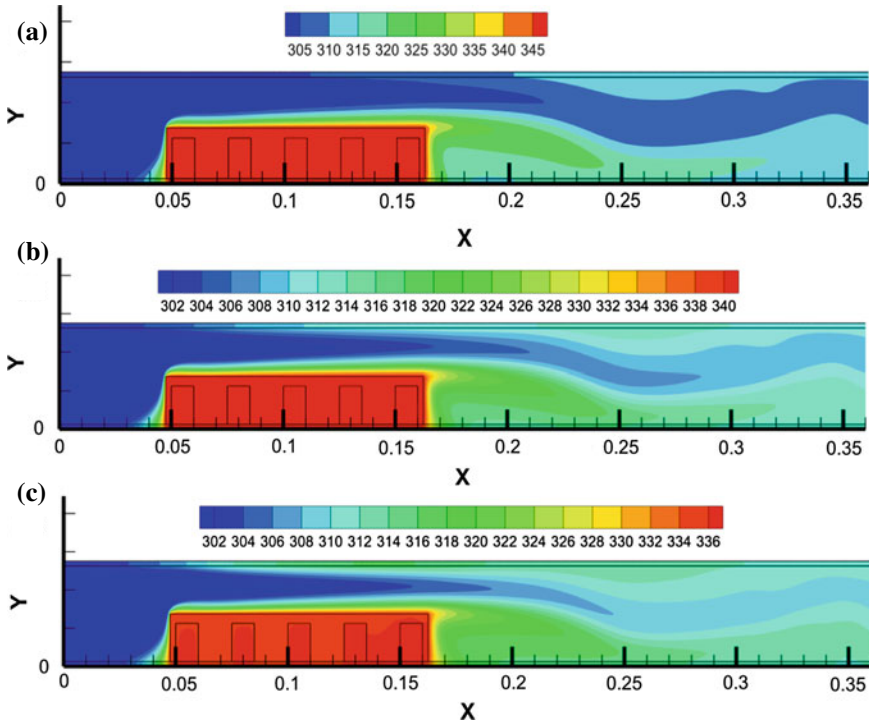


**Fig. 6** Temperature distribution for  $Re = 250$  **a**  $\epsilon_s = 0.1$ , **b**  $\epsilon_s = 0.3$  and **c**  $\epsilon_s = 0.7$

## References

1. Ebrahimi A, Roohi E, Kheradmand S (2015) Numerical study of liquid flow and heat transfer in rectangular microchannel with longitudinal vortex generators. *Appl Therm Eng* 78:576–583
2. Ahmed HE, Mohammed HA, Yusoff MZ (2012) An overview on heat transfer augmentation using vortex generators and nanofluids: approaches and applications. *Renew Sustain Energy Rev* 16(8):5951–5993
3. Min C et al (2010) Experimental study of rectangular channel with modified rectangular longitudinal vortex generators. *Int J Heat Mass Transf* 53(15–16):3023–3029
4. Habchi C et al (2012) Enhancing heat transfer in vortex generator-type multifunctional heat exchangers. *Appl Therm Eng* 38:14–25
5. Kherbeet AS et al (2016) Mixed convection nanofluid flow over microscale forwardfacing step — effect of inclination and step heights. *Int Commun Heat Mass Transfer* 78:145–154
6. Premachandran B, Balaji C (2006) Conjugate mixed convection with surface radiation from a horizontal channel with protruding heat sources. *Int J Heat Mass Transf* 49:3568–3582
7. Sharper B, Saglam M, Aydin O (2018) Experimental and numerical investigation of natural convection in a discretely heated vertical channel: effect of the blockage ratio of the heat Sources. *Int J Heat Mass Transfer* 126:894–910

# Combustion Performance of Hybrid Rocket Motor Under the Influence of Cylindrical Protrusion



Kabaleeswaran Manikandan, K. Lakshmi Das, N. Purushothaman and L. Karthik

**Abstract** The sequence of hybrid rocket motor static firings is performed, with and without cylindrical protrusion, to evaluate the combustion behavior of bee-wax fuel grain. Firing is done for the injection pressures of 2.75 bar, 4.15 bar, and 5.51 bar, respectively, all firings are done for an identical firing duration of 7 seconds. Experimental outcome confirms the addition cylindrical protrusion as vortex generator yield an average of 45% higher regression rate than that of the baseline rocket motor. Among all injection pressures, modest 4.15 bar with cylindrical protrusion shows a significant improvement in the combustion performance by exhibiting the enhanced regression rate as well as mass consumption rate of the fuel grain. Hence, the addition of cylindrical protrusion as a vortex generator to the classical hybrid motor promise to improve the combustion performance of the bee-wax fuel grain.

**Keywords** Hybrid rocket · Regression rate · Vortex generator · Bee-wax fuel grain

## 1 Introduction

Propulsion systems play the major role as a workhorse for the space launch vehicles to accomplish its mission. Different rocket engines are used in the launch vehicles based on their mission requirements. Currently, solid, liquid and cryogenic engines are employed to perform the mission task. Among these engines, solid and liquid engines are widely used in the primary stages of the launch vehicles. Even though, these engines are used primarily both engines has some characteristics, which need to be addressed to optimize the vehicle performance. The hybrid rocket is naturally safer than other rocket engines, where the oxidizer is stored as a liquid and the fuel as a solid. Hybrid rocket motors are less susceptible to chemical explosion than conventional solid and bi-propellant liquid designs [1]. The main shortcoming of

---

K. Manikandan (✉) · K. L. Das · L. Karthik  
SASTRA Deemed to be University, Thanjavur, Tamil Nadu 613401, India  
e-mail: [manikandan@mech.sastra.edu](mailto:manikandan@mech.sastra.edu)

N. Purushothaman  
Hindustan Deemed to be University, Chennai, Tamil Nadu 603103, India

© Springer Nature Singapore Pte Ltd. 2020  
H. K. Voruganti et al. (eds.), *Advances in Applied Mechanical Engineering*,  
Lecture Notes in Mechanical Engineering,  
[https://doi.org/10.1007/978-981-15-1201-8\\_2](https://doi.org/10.1007/978-981-15-1201-8_2)

the hybrid is that the combustion process relies on a relatively slow mechanism for combustion, with a sequence of fuel melting, evaporation, and diffusive mixing. But, in a solid rocket, the flame is much closer to the fuel surface and the regression rate is typically an order of magnitude larger. As a rough comparison, the regression rate in a classical hybrid rocket fuel regression rate is typically one-third of the composite solid rocket propellants [2].

In order to compensate for the low regression rate, the surface area for burning must be increased. This is accomplished through the use of a multi-port fuel grain, but it reduces the volumetric loading as well as the structural integrity of the fuel grain [3]. More attempts are made to increase the regression rate by increasing the heat transfer rate to the fuel surface. Mainly, the performance of a hybrid motor depends critically on the degree of flow mixing attained in the combustion chamber, also the local regression rate of the fuel is quite sensitive to the general turbulence levels of the combustion port gas flow because localized combustion gas eddies or recirculation zone adjacent to the fuel surface act to significantly enhance the regression rate in this area [4]. In this work, novel idea of using blunted objects like cylindrical protrusion is employed to induce the turbulence in the combustion port, where the bee-wax fuel grain is selected to perform combustion analysis.

## 2 Experimental Setup and Research Methodology

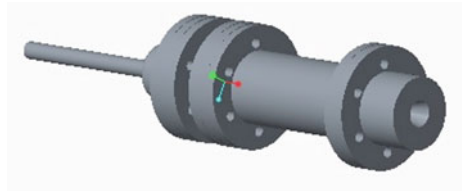
The experimental setup consists of a static firing mount, a rocket motor assembly, solid fuel grain, oxygen supply, ignition setup, recording device, and hand tools. This section gives a detailed description of each and every component and subsystem of the complete setup. The hybrid rocket motor unit consists of the parts like an accumulator, combustion chamber, and nozzle. All the subcomponents are fabricated by stainless steel 304 grade. In general, accumulator consists of an oxidizer settling chamber followed by the showerhead injector plate with six orifices of diameter 1.5 mm, subsequently, the combustion chamber is fabricated for the length to diameter ratio of 3. In case of the nozzle, the simple convergent–divergent cone shape is made from stainless steel with graphite insert for the throat diameter of 6 mm. A schematic of the 3D exploded and assembled views of a hybrid rocket motor is shown in Figs. 1 and 2.

Few sample static firings are done to fix the oxidizer injection pressure range and firing duration so that after every firing there should be enough sliver (i.e., Leftover) in the fuel grain to perform the internal ballistic calculations. Based on the input from the sample firing injection pressure range is fixed between 2.75 and 5.51 bar as well as 7 s as firing duration. The primary aim of this work is to analyze the combustion behavior of bee-wax in the hybrid rocket motor with and without cylindrical protrusions. The first set of firing is carried out without the cylindrical protrusion for injection pressures of 2.75, 4.15, and 5.51 bar, the second set of firing is also completed for the same injection pressures and firing duration with

**Fig. 1** Exploded view of a rocket motor



**Fig. 2** Assembled view of a rocket motor



an attachment of cylindrical protrusion. The injection pressure values are chosen in order to induce additional turbulence of the incoming gaseous oxygen. The blunted object like a cylindrical projection of 8 mm is chosen as a vortex generator because it can generate larger wake region in the downstream, which can provide an additional turbulence fuel grain port [5].

A cylindrical projection is placed with a fixed distance of 50 mm from the injector plate also 25 mm ahead of the fuel grain. A specific CAD model of the vortex generator (i.e., VG) detail is shown in Fig. 3.

**Fig. 3** CAD model vortex generator

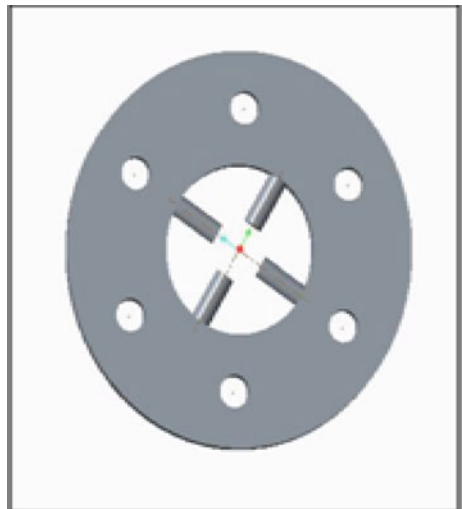






**Fig. 4** Bee-wax fuel grain and wax quadrant

Gaseous oxygen along with the bee-wax is selected as a propellant combination for this experimental analysis. The bee-wax is received in the form of thick cubes, and then it is melted and molded using a cylindrical die to the configuration of single-port cylindrical shape. Once the molding is done the raw fuel grain is machined to give the length of 100 mm, outer diameter 45 mm, an inner diameter of 17 mm, respectively. A basic bee-wax molded fuel grain and wax-quadrant are shown in Fig. 4.

All the subsystems of rocket static firing unit, like oxygen supply, an ignition device, and recording devices are checked twice to ensure the reliability of each component. Similarly, a primitive examination of the parameters like throttling time, ignition pressure, and cut-off timing was also carried out to ensure the safety of rocket firing. Based on the simulated firing inputs, injection pressure is fixed between 2.75 and 6.90 bar. Similarly, firing duration is also fixed as 7 s of its total firing duration in order to keep enough left out of fuel grain to complete combustion performance calculations.

The rocket motor's combustion performance fully depends on the combustion parameters like local (i.e., regression at any location along the fuel grain length) and average regression rate, the mass consumption rate of fuel, etc. Regression rate is generally referred to as the burning surface of a propellant grain recedes in a direction essentially perpendicular to the surface, which is usually expressed in mm/s [6]. For further performance determination, the mass of the fuel grain before and after firing, and fuel grain web thickness before and after firing need to be measured and tabulated. After each firing rocket motor is allowed to cool for some time then the fuel grain is removed and sliced into four pieces as shown in Fig. 4. From the injector end as a reference point length of 100 mm fuel grain is divided into five equal parts, from each location local web thickness is measured using a screw gauge. Each static firing

is recorded as a video with the help of a Nikon DSLR D5100 camera to evaluate the temporal behavior of rocket exhaust plume.

### 3 Result and Discussion

In total, six static firings are performed with and without the cylindrical protrusion, firings are conducted at the varied injection pressures of 2.75, 4.15, and 5.51 bar for the fixed firing duration of 7 seconds. In general, hybrid rocket fuel combustion performance is evaluated through the values of local and average regression rate, as well as mass consumption rate. Each firing is recorded by the Nikon DSLR D5100 camera to measure the firing duration and to understand exhaust plume behavior of the fuel grain. Local regression rate behavior of bee-wax with and without cylindrical protrusions (i.e., vortex generator) is shown in Fig. 5.

From Fig. 5, each local regression rate curves of different injection pressures were distinguished into three regimes (1) high regressive head end, which is present near the injector surface. This end is susceptible to the maximum shear of the oxidizer flow (2) the mid-regressive end which occurs usually between  $(\frac{1}{3} \leq l_c \leq \frac{2}{3})$ , where  $l_c$  is the total length of the cylindrical grain. In this regime, the grain experiences the high to mid-level shearing [7] when axially measured towards the end (3) low regressive tail due to lesser shear than the other portion of the fuel grain, which is the

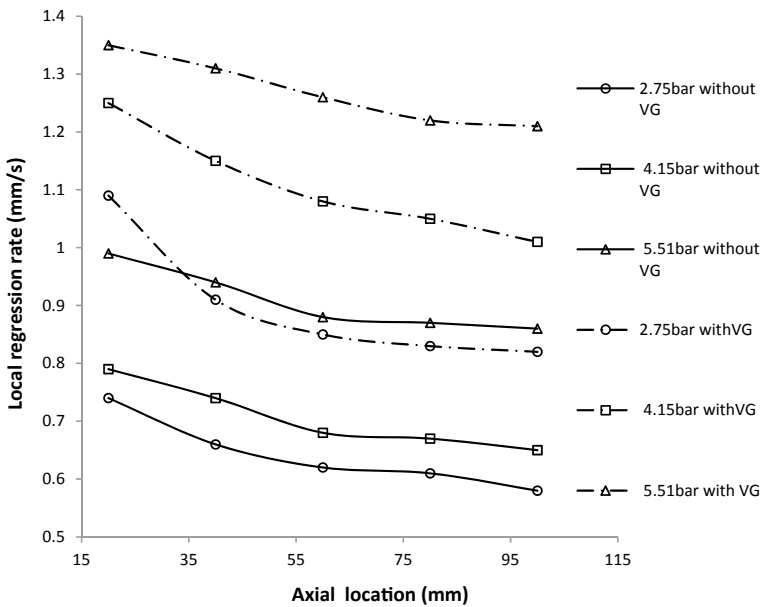


Fig. 5 Local regression rate with and without VG

**Table 1** Average regression rate of fuel grain with and without VG

Pressure (bar)	Average regression rate of fuel grain (mm/s)		Incremental percentage
	Without VG	With VG	
2.75	0.647	0.9856	40.38
4.15	0.709	1.1132	57.00
5.51	0.911	1.26876	39.27
		Average increment	45.55

end portion of the grain beyond which, the nozzle is located. Figure 5, reveals that the regression rate of the fuel grain increases linearly with oxidizer injection pressure, higher injection pressure leads to increasing the amount of an oxidizer flux [1], hence amplified regression all along the fuel grain. Among the other injection pressures, the 5.51 bar of injection shows the higher local regression rate, because of higher injection pressure can get an increased mass flux of oxidizer into the combustion chamber. In case of firings without the VG, local regression value of fuel grain at the injector end varies between 0.75 mm/s and 1 mm/s for the baseline firings (i.e., without cylindrical protrusion) of all injection pressures.

As it can be noticed from Fig. 5, the minimum injection pressure 2.75 bar itself is reaching the local regression of 1.11 mm/s at an injector end, whereas maximum injection pressure of 5.51 bar without VG reaches only 1 mm/s, which is roughly 11% higher. So, it is exceptionally apparent that fuel grain experiences an improved local regression all along fuel grain with the addition of VG. This enhanced regression is due to induced turbulence by the VG to the incoming oxidizer flow, this additional turbulence results in higher mixing and greater residual time [3]. As the injection pressures increase local regression profile attains more linear in nature. Interestingly, 4.15 bar shows superior improvement in the regression. This is mainly due to a higher percent of increment in the average regression rate (i.e., 57%) as well as mass consumption rate (i.e., 71%), as is can be seen from the Tables 1 and 2, respectively. Hence, the introduction cylindrical protrusion as VG seems to favors the moderate injection pressures like 4.15 bar to possess a higher enhancement in the regression

**Table 2** Fuel grain mass consumption rate with and without VG

Pressure (bar)	Fuel grain mass consumption rate(gm/s)		Incremental percentage
	Without VG	With VG	
2.75	3.44	4.75	38.15
4.15	4.46	7.63	71.26
5.51	8.33	10.10	21.20
		Average increment	43.54



**Fig. 6** Exhaust plume of bee-wax with and without VG with the pressure of 4.4 bar at  $t = 3$  sec

rate. Unlike baseline firings, rocket motor with VG gets higher regression values at the injector end ranges between 1.11mm/s to 1.35 mm/s.

Comparison of the average regression rate and mass consumption rate of the grain for all the injection pressures with and without VG are calculated and tabulated. In the case of the average regression rate, fuel grain shows the average increase of 40%, 57%, and 39% for the injection pressures of 2.75 bar, 4.15 bar, and 5.51 bar, respectively. Similarly, fuel grain mass consumption rate also shows the significant improvement exhibiting average percent increase of 38%, 71%, and 21% for the injection pressures of 2.75 bar, 4.15 bar, and 5.51 bar, respectively. Higher local regression rate enhancement with VG at 4.15 bar can be the main reason for this significant performance of the bee-wax fuel grain from the hybrid rocket motor. Finally, exhaust plume images of bee-wax with and without VG are exposed in Fig. 6, which shows a significant reduction in secondary burning area as well as plume length. This is due to effective mixing in the combustion port, because of induced turbulence from the cylindrical protrusion.

## 4 Conclusion

The present study reports the regression behavior of bee-wax fuel grain in a Hybrid Rocket Motor by adding cylindrical protrusion. Three different injection pressures 2.7 bar, 4.15 bar, and 5.51 bar were used for static firing test and the regression rate and mass consumption rate of the fuel were measured. The experimental static firing test results showed an improved regression rate because of introducing the vortex generator. Moreover, bee-wax fuel grain showed a maximum increment value of 57.00% when vortex generator was introduced. Additionally, the mass consumption rate is enhanced to a greater extent of 71.26%. The results showed that the head end regression value is enhanced. With the inclusion of the vortex generator, the study proved that bee-wax can be used as one of the potential candidate as hybrid fuel grain.

## References

1. Sutton GP, Biblarz O (2013) Rocket propulsion elements, 7th edn. Wiley, New Delhi New Delhi
2. Altman D (1991) Hybrid rocket development history. In: AIAA, 91-2515, USA
3. Korting PAOG, Schoyer HFR, Timnat YM (1987) Advanced hybrid rocket motor experiments. *Acta Astronautica* 15(2):97–104
4. Waidmann W (1988) Thrust modulation in hybrid rocket engines. *J Propulsion Power* 4(5):421–427
5. Lerner JC (2012) Bluff body aerodynamics and wake control. In: Applied aerodynamics, Greece. ISBN: 978-953-51-0611-1
6. Smoot LD, Prince CF (1966) Regression rates of metalized hybrid fuel systems. *AIAA J* 4(5):910–915
7. Estey P, Altman D, McFlare J (1991) An evaluation of scaling effects for hybrid rocket motors. In: AIAA, 91-2517, China

# Social and Economic Impact Assessment of Solar Water Pumping System on Farmers in Nagpur District of Maharashtra State of India



Devidas H. Yadav, Arunedra K. Tiwari and Vilas R. Kalamkar

**Abstract** In India, farmers depend on variable rainfall and groundwater for irrigation. Load shedding and high diesel cost are the barriers for regular watering of crops. Solar photovoltaic water pumping system (SPVWPS) is a better sustainable option, but the high capital cost is hindering widespread applications. The Maharashtra state government distributed SPVWPS to marginal farmers (Whose land holding is less than 5 acres) and are grid isolated, providing subsidies as high as 95%. Total, 8959 pumps are distributed till November 2018 in the whole Maharashtra state with 210 in Nagpur district only. Current work assesses the impact of the use of SPVWPS on the livelihoods of farmers, their social and economic condition by conducting a survey. The aim of the study is to evaluate the health, reliability and durability of SPVWPS. An effort has been made to understand the grassroots level insights associated with solar pump use. The field research was carried on by interviewing farmers. Questionnaires were created in order to get useful data required easily. By splitting up the questionnaires into different areas, the results gave a general impression of the farmer's daily challenges and troubles. The authors surveyed total 25 sites from 17 villages of 8 Talukas of Nagpur district. Payback period value of solar pump is calculated with respect to electric and diesel pump using breakeven point analysis and found that shifting from diesel to solar pump have shorter payback period.

**Keywords** Solar photovoltaic water pumping · Survey · Irrigation · Cost-benefit analysis

## 1 Introduction

In a developing country like India whose economy depends on agriculture, and which is rapidly changing into the realm of renewable energy, the future of solar pumps seems brighter than ever [1–3]. Agriculture sector in India employs almost

---

D. H. Yadav (✉) · A. K. Tiwari · V. R. Kalamkar  
Department of Mechanical Engineering, Visvesvaraya National Institute  
of Technology, Nagpur, Maharashtra 440010, India  
e-mail: [dhy.devidas@gmail.com](mailto:dhy.devidas@gmail.com)

© Springer Nature Singapore Pte Ltd. 2020  
H. K. Voruganti et al. (eds.), *Advances in Applied Mechanical Engineering*,  
Lecture Notes in Mechanical Engineering,  
[https://doi.org/10.1007/978-981-15-1201-8\\_3](https://doi.org/10.1007/978-981-15-1201-8_3)

50% of the workforce, and gives 17.32% to India's GDP. Thus, it is important to assure a high return of agricultural crops, by introducing new practices like efficient irrigation techniques. Water pumps have come forth as a reliable mode of irrigation, and the advent of renewable energy has ensured the speedy progress of solar water pumps. At the fore of this breakthrough is The Ministry of New and Renewable Energy (MNRE), which has collaborated with various state governments and started promoting solar water pumps by providing various subsidies to farmers [4].

Solar water pump scheme for farmers in Maharashtra was launched by the State Government of Maharashtra in 2016. Farmers got solar pumps at a highly subsidized rate and beneficiaries paid just 5–10% of the pump's cost. One solar pump costs between 3 and 7.5 lakh depending on the horsepower [5]. To get benefits from this scheme, a farmer has to have a landholding smaller than five acres. Preference is given to the farmers who are grid isolated. Up to date, 8959 pumps are distributed. The main objective of this survey is to assess the socio-economic impact, on-field performance of the system and train the farmers for better uses of system. To get useful data from a survey, the main step is the design of survey.

## 2 Methodology

### 2.1 Survey Design

The Maharashtra state government distributed solar water pumps in 20 districts, including major quantities in the drought-hit districts. In this study, surveys are conducted in 8 talukas covering whole Nagpur district. Nagpur region falls in the "Hot and Dry" zone, all survey sites fall under Hot Zone [6]. A total of 1200 km was covered in remote villages of Nagpur for the study.

The field research was conducted by interviewing farmers and by observing their fields and irrigation systems. Questionnaires were created in order to facilitate the survey. By splitting up the questionnaires into different arenas, the results gave a general picture of cropping pattern, irrigation method, peak water requirement, water head, total cultivated area, and the daily challenges and troubles confronted by farmers. All farmers were questioned at their farm. As a consequence of this, it was more comfortable to watch over their situation and get extra notes if required.

Totally 25 farmers were interviewed from 17 villages of 8 Talukas of Nagpur district. The survey sites are marked in Fig. 1. Inside information of beneficiaries are presented in Table 1. Altogether the 25 farmers interviewed were male, education level among farmers were low; 52% farmers studied up to elementary school.

Before acquiring any system it is important to check its economic feasibility. So in this study, breakeven point analysis is done to find out payback period of solar pump.

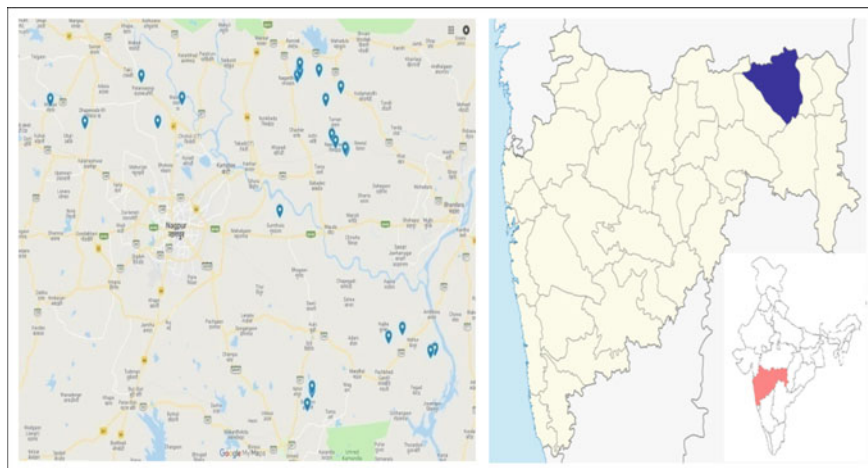


**Fig. 1** Surveyed farmer's location in Nagpur district of Maharashtra

**Table 1** Details of farmers interviewed

Average age of respondents	43.2
<i>Education level</i>	
Primary	13
Secondary	5
Graduation	7

## 2.2 Cost-Benefit Analysis

Cost-benefit analysis (CBA) is a systematic procedure for estimating and comparing benefits and costs of a project, decision or government insurance. This method compares the total anticipated cost of each alternative against the total expected benefits, to examine whether the benefits compensate the costs, and by how much [7].

In this research, diesel-driven pump, electric-driven pump and SPVWPS are analyzed with cost-benefit analysis with different power ratings of 3, 5 hp. The breakeven point is worked out for diesel-driven pump and electric-driven pump against SPVWPS by considering subsidy provided and without subsidy.

$$\text{Total Cost (TC)} = \text{CC} + \text{OC} + \text{MC} \quad (1)$$

where

CC Capital cost

OC Operating cost

MC Maintenance cost.



The cumulative total cost is calculated over the years to find breakeven point or payback period for different scenarios mentioned above. Total cost from second year onwards does not include capital cost.

### 3 Result and Discussion

Most of the farmers had a field size of less than 5 acres. Open well and Borehole was the primary source of water for irrigation, as it was mandatory to have source at farm to obtain the benefit of the system. Rice (Paddy), Wheat, Black Gram, and cotton are the principal crops cultivated in Nagpur district. Most of the farmers used basin irrigation method to irrigate; only 20% used drip irrigation method. 44% system runs against a water head of 10–20 m (Fig. 2).

#### 3.1 Economic Analysis

For an economic analysis of the system, the following factors were considered for better conclusions.

1. The capital cost of the systems in Indian rupees as shown in Table 2.
2. Diesel consumed by 3 hp and 5 hp diesel pump is found to be 1.25 and 1.8 l/h, respectively.
3. Average electric bill per year reported by the farmers during the survey for 3 hp pump is Rs. 12,000 and to 5 hp is Rs. 22,000.
4. A total of 270 sunny days in an year are considered in the calculation.
5. Maintenance cost per year of solar pump, electric pump and diesel pump is considered as Rs. 2500, 3000 and 4000, respectively.
6. Every year 10% increase in bill and fuel prices is taken in calculations. Due to the hike in fuel prices, this assumption is justifiable.

The cost-benefit analysis for switching to solar pump from diesel and electric pumps for capacities 3 and 5 hp is represented in Fig. 3a, b, respectively. From Fig. 3a, it can be seen that for farmers using 3 hp pumps payback period in the case of switching to solar pump from that of diesel is 8 years whereas in the case of switching to solar pump from that of electric pump is 15.1 years. Similarly, from Fig. 3b, it can be seen that for the farmers using 5 hp pumps the payback period for switching to solar pump from that of diesel is 9.2 years and whereas in the case of switching to solar pump from that of electric pump is 14.5 years. hence it is clear that for both 3 and 5hp capacities pumps, farmers using diesel pumps are in more favourable side to switch to solar pumps.

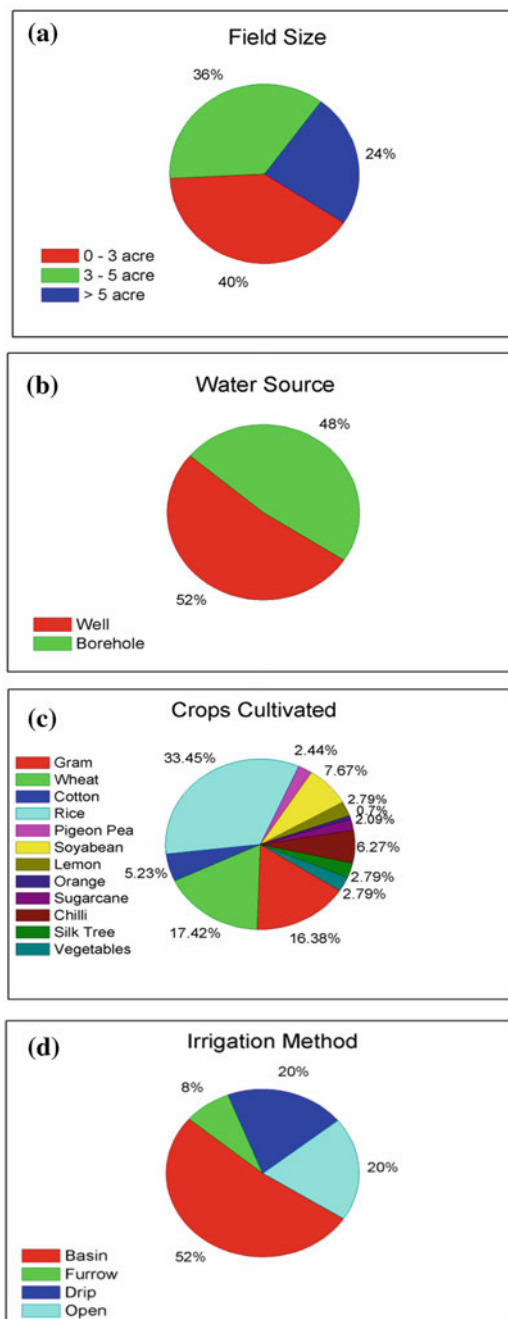


**Fig. 2** Most common **a** field sizes, **b** water source, **c** crops cultivated, **d** irrigation method

**Table 2** The capital cost of systems

Capacity of the pump	Solar pump without subsidy	Solar pump with 90% subsidy	Electric pump	Diesel pump
3 hp	405,000	40,500	13,500	19,000
5 hp	675,000	67,500	17,000	27,000

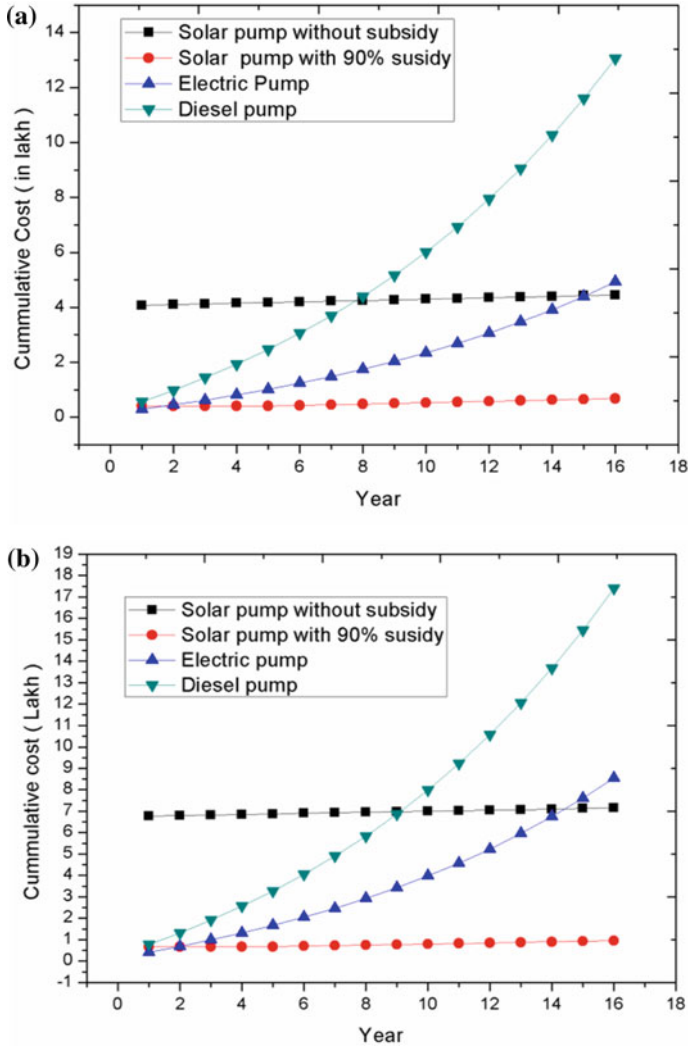


**Fig. 3** Cost-benefit analysis of solar, diesel and electric pump for **a** 3 hp capacity, **b** 5 hp capacity

### 3.2 Findings from Survey

- Around 80% of farmers used daily tracking regularly. Remaining 20% never used daily tracking of the PV module. Not a single farmer used seasonal tracking out of system surveyed.
- Most farmers used DG pumps before opting for the SPVWPS. According to farmers, they used 8–10 L of oil (diesel + kerosene) in the DG pump for irrigation before. Because of SPVWPS, they saved 40–50 thousand rupees per year.
- 20% of farmers have never cleaned the PV module. Remaining 80% said they cleaned the module every 8–10 days.
- It is observed that those who cleaned modules regularly, the first few modules have been cleansed properly, but modules that were stationed at more than 2.5 m above from the ground were not cleaned.
- The length of the wiper given to farmers was only 1.5 m. Proper cleaning tools with appropriate size should be provided to farmers.
- Around 20% of beneficiaries used tricks to get the pump. One beneficiary in Mauda taluka has never used the pump for the farming.
- Farmer growing cotton and wheat told due to the use of solar pump, production of wheat and cotton increased. Wheat production increased by 7 quintals and cotton production increased by 13 quintals per acre.
- In addition, the chili farmers told that significant improvement in production of chili. Previously they used to irrigate chili crops every 10 days and they used to pluck chilies every 20–25 days. After installing SPVWPS, all farmers used drip irrigation and they irrigate chili daily. According to them, they pluck the chilies every 15–20 days. The production of chilies increased by 15–25%.
- DC pumping system has better performance in cloudy and overcast conditions compared to AC. Moreover, DC also requires lesser maintenance.
- The maintenance time for any break down of motor and pump varied from 8 to 12 days as told by farmers and restated by Jain irrigation.
- No formal training has been given to farmers about the operation of SPVWPS. Because of that, initially, the response to the scheme was poor. In this study, it is established that all beneficiaries are comfortable with the operation but with proper training the production from these installations can be amended substantially.

## 4 Conclusion

- Use of SPVWPS provides regular water to crops, which ensued in 15–30% increase in crop production quantity and also saved fuel cost substantially.
- Since no operational cost is required for SPVWPS, habit of overuse pumping system is observed, most farmers operated the system for 9 h daily. This may eventually result in greater rate of decrease in groundwater level.

- 16% less maintenance is required for solar pumping systems compared to electric and 37% less maintenance as diesel pumping system.
- Though the solar pump system is technically complex to understand, it is found that all users considered the solar systems very easy to use.
- Payback period is shorter by 5–7 years when switching from diesel pump to solar pump in comparison to switching from electric pump to solar pump.

## References

1. Tiwari A, Kumar R, Rohan P, Sharma S, Kalamkar V (2017) Effect of forced convection cooling on performance of solar photovoltaic module in rooftop applications. In: 6th international conference on advanced energy resources. Springer Proceedings in Energy, IIT, Mumbai
2. Tiwari AK, Kalamkar VR (2017) Effects of total head and solar radiation on the performance of solar water pumping system. *Renew Energy*. <https://doi.org/10.1016/j.renene.2017.11.004>
3. Tiwari AK, Kalamkar VR (2016) Performance investigations of solar water pumping system using helical pump under the outdoor condition of Nagpur, India. *Renew Energy* 97. <https://doi.org/10.1016/j.renene.2016.06.021>
4. Bora RB, Prasad B, Sastry OS, Kumar A, Bangar M (2017) Optimum sizing and performance modeling of Solar Photovoltaic (SPV) water pumps for different climatic conditions. *Sol Energy* 155:1326–1338. <https://doi.org/10.1016/j.solener.2017.07.058>
5. T.I. EXPRESS, Maharashtra to supply solar pumps to 1 lakh farmers (n.d.). <https://indianexpress.com/article/cities/mumbai/maharashtra-to-supply-solar-pumps-to-1-lakh-farmers-5398292/>
6. Chattopadhyay S, Dubey R, Kuthanazhi V (2016) All-India survey of photovoltaic module reliability. [http://www.ncpre.iitb.ac.in/research/pdf/All\\_India\\_Survey\\_of\\_Photovoltaic\\_Module\\_Reliability\\_2016.pdf](http://www.ncpre.iitb.ac.in/research/pdf/All_India_Survey_of_Photovoltaic_Module_Reliability_2016.pdf)
7. Boardman AE (2008) Cost benefit analysis. Pearson Education. <https://books.google.co.in/books?id=T38UiMX9P9sC>

# Thermally Developing Region of a Parallel Plate Channel Partially Filled with a Porous Material with the Effect of Axial Conduction and Viscous Dissipation: Uniform Wall Heat Flux



J. Sharath Kumar Reddy and D. Bhargavi

**Abstract** The present investigation has been undertaken to assess the effect of axial conduction and viscous dissipation on heat transfer characteristics in the thermally developing region of a parallel plate channel with porous insert attached to both the walls of the channel. Both the walls are kept at uniform heat flux. The fully developed flow field in the porous region corresponds to Darcy–Brinkman equation and the clear fluid region to that of plane Poiseuille flow. The effect of parameters, Brinkman number,  $Br$ , Darcy number,  $Da$ , Peclet number,  $Pe$ , and a porous fraction,  $\gamma_p$  have been studied. The numerical solutions have been obtained for,  $0.005 \leq Da \leq 1.0$ ,  $0 \leq \gamma_p \leq 1.0$  and  $-1.0 \leq Br \leq 1.0$  and  $Pe = 5, 25, 50, 100$  and neglecting axial conduction (designated by  $A_c = 0$ ) by using the numerical scheme successive accelerated replacement (SAR). There is an unbounded swing in the local Nusselt number because of viscous dissipation.

**Keywords** Viscous dissipation · Axial conduction · Parallel plate channel partially filled with a porous material

## 1 Introduction

Present-day applications involving flow through porous media call for including viscous dissipation effects in the conservation of energy equation. Some of them generically are described as internal flows, say, flow through a porous material partially or fully filled, pipes, channels, and in general ducts. In general, if the effective fluid viscosity is high or temperature differences are small or kinetic energy is high that warranted inclusion of Forchheimer terms, viscous dissipation can be expected to be significant. The use of porous media in the cooling of electronic equipment has

---

J. Sharath Kumar Reddy (✉) · D. Bhargavi  
Department of Mathematics, NITW, Warangal, Telangana, India  
e-mail: [jskreddy.amma@gmail.com](mailto:jskreddy.amma@gmail.com)

© Springer Nature Singapore Pte Ltd. 2020  
H. K. Voruganti et al. (eds.), *Advances in Applied Mechanical Engineering*,  
Lecture Notes in Mechanical Engineering,  
[https://doi.org/10.1007/978-981-15-1201-8\\_4](https://doi.org/10.1007/978-981-15-1201-8_4)

been restored interest in the problem of forced convection in a channel filled with a porous medium.

Several studies (Agrawal [1], Hennecke [2], Ramjee and Satyamurty [3], and Jagadeesh Kumar [4]) have shown that the axial conduction term becomes significant in the equation of energy at the low Peclet number in the case of forced convection in the ducts. In particular, Shah and London [5] studied the problem of heat transfer in the entrance region for a viscous incompressible fluid in both two-dimensional channel and circular cylindrical tube taking into consideration axial conduction term. Ramjee and Satyamurty [3] studied local and average heat transfer in the thermally developing region of an asymmetrically heated channel.

Hooman et al. [6] have studied thermally developing forced convection in rectangular ducts subjected to uniform wall temperature. Thermally developing forced convection in a circular duct filled with a porous medium with longitudinal conduction and viscous dissipation effects subjected to uniform wall temperature studied by Kuznetsov et al. [7]. Nield et al. [8] investigated the effects of viscous dissipation, axial conduction with the uniform temperature at the walls, on thermally developing forced convection heat transfer in a parallel plate channel fully filled with a porous medium.

In the present paper, the thermally developing region of a parallel plate channel partially filled with a porous material with the effect of axial conduction and viscous dissipation with wall boundary condition uniform heat flux has been studied. Numerical solutions for the two-dimensional energy equations in both the fluid and porous regions have been obtained using numerical scheme successive accelerated replacement (Ramjee and Satyamurty [3], Satyamurty and Bhargavi [9], and Bhargavi and Sharath Kumar Reddy [10]). The effects of important parameters on the local Nusselt number have been studied.

## 2 Mathematical Formulation

Governing equations and the boundary conditions are non-dimensionalizing by introducing the following non-dimensional variables.

$$\left. \begin{aligned} X &= x/H, Y = y/H, U_f = u_f/u_{\text{ref}}, U_i = u_i/u_{\text{ref}}, \\ U_p &= u_p/u_{\text{ref}}, P = p/\rho u_{\text{ref}}^2, \theta_f = (T_f - T_e)/(qH/k_f), \\ \theta_p &= (T_p - T_e)/(qH/k_f) \end{aligned} \right\} \quad (1)$$

In Eq. (1),  $X$  and  $Y$  are the non-dimensional coordinates.  $U$  and  $P$  are the non-dimensional velocity and pressure. The subscripts f and p refer to fluid and porous regions.  $\theta, \{\theta_f$  in the fluid region and  $\theta_p$  in the porous region $\}$ , is the non-dimensional temperature.  $u_{\text{ref}}$  is the average velocity through the channel (Fig. 1).

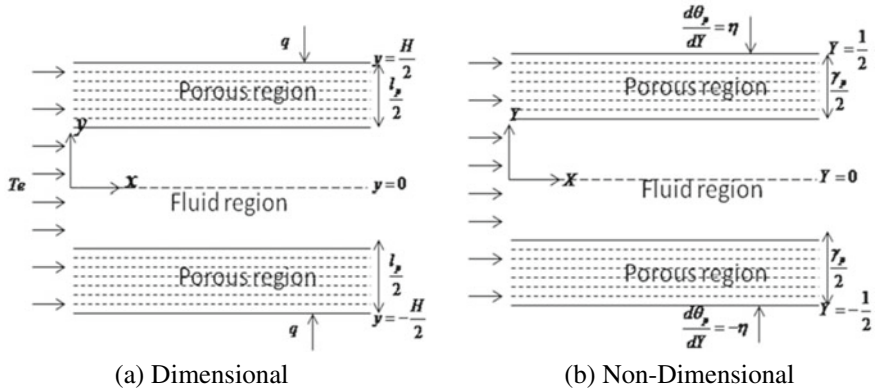


Fig. 1 Geometry of the physical model of the problem

The non-dimensional governing equations and boundary conditions for momentum and energy equations applicable in the fluid and porous regions become [using non-dimensional variables given in Eq. (1)].

**Fluid Region:**

$$\frac{d^2 U_f}{dY^2} = Re \frac{dP}{dX} \quad (2)$$

$$U_f \frac{\partial \theta_f}{\partial X^*} = A_c \frac{1}{Pe^2} \frac{\partial^2 \theta_f}{\partial X^{*2}} + \frac{\partial^2 \theta_f}{\partial Y^2} + Br \left( \frac{dU_f}{dY} \right)^2 \quad (3)$$

In Eq. (2),  $Re$ , the Reynolds number is defined by

$$Re = \rho u_{ref} H / \mu_f \quad (4)$$

In Eq. (3),  $Pe$ , Peclet number and  $Br$ , Brinkman number and  $X^*$  are defined by,

$$Pe = u_{ref} H / \alpha_f, \quad Br = \mu_f u_{ref}^2 / (qH), \quad X^* = X / Pe \quad (5)$$

when  $Br < 0$  represents the fluid is getting heated.  $Br > 0$  represents the fluid is getting cooled.

**Porous Region:**

$$\frac{d^2 U_p}{dY^2} - \frac{\varepsilon}{Da} U_p = \varepsilon Re \frac{dP}{dX} \quad (6)$$

$$U_p \frac{\partial \theta_p}{\partial X^*} = \frac{1}{\eta} \left( A_c \frac{1}{Pe^2} \frac{\partial^2 \theta_p}{\partial X^{*2}} + \frac{\partial^2 \theta_p}{\partial Y^2} \right) + \frac{Br}{Da} U_p^2 \quad (7)$$



In Eqs. (6) and (7),  $Da$ ,  $\varepsilon$ , and  $\eta$  are defined as,

$$Da = K/H^2, \quad \varepsilon = \mu_f/\mu_{\text{eff}} \quad \text{and} \quad \eta = k_f/k_{\text{eff}} \quad (8)$$

When  $A_c = 1$  in Eqs. (3) and (7) means that axial conduction is included, and when  $A_c = 0$ , axial conduction is neglected. When  $A_c = 0$ , the solutions to Eqs. (3) and (7) in terms of  $X^*$  do not depend on  $Pe$ .

**Non-dimensional Boundary Conditions:**

$$\frac{dU_f}{dY} = 0, \quad \frac{\partial\theta_f}{\partial Y} = 0 \quad \text{at} \quad Y = 0 \quad (9)$$

$$U_f = U_p = U_i, \quad \frac{dU_f}{dY} = \frac{1}{\varepsilon} \frac{dU_p}{dY} \quad \text{at} \quad Y = -\frac{1}{2} + \frac{\gamma_p}{2} \quad (10)$$

$$\theta_f = \theta_p = \theta_i, \quad \frac{\partial\theta_f}{\partial Y} = \frac{1}{\eta} \frac{\partial\theta_p}{\partial Y} \quad \text{at} \quad Y = -\frac{1}{2} + \frac{\gamma_p}{2} \quad (11)$$

$$U_p = 0, \quad \frac{\partial\theta_p}{\partial Y} = -\eta \quad \text{at} \quad Y = -1/2 \quad (12)$$

Inlet conditions

$$\theta_p(0, Y) = 0 \quad \text{for} \quad -\frac{1}{2} \leq Y \leq -\frac{1}{2} + \frac{\gamma_p}{2} \quad (13)$$

$$\theta_f(0, Y) = 0 \quad \text{for} \quad -\frac{1}{2} + \frac{\gamma_p}{2} \leq Y \leq 0 \quad (14)$$

$$\frac{\partial\theta_b}{\partial X^*} = 0 \Rightarrow \frac{\partial\theta_{f,p}}{\partial X^*} = \frac{\theta_{f,p}}{\theta^*} \frac{\partial\theta^*}{\partial X^*} \quad \text{at} \quad X^* \geq X_{\text{id}}^* \quad \text{for} \quad -1/2 \leq Y \leq 0 \quad \{\text{downstream condition}\} \quad (15)$$

In Eq. (15),  $\theta_b$  is the non-dimensional temperature based on the bulk mean temperature defined by

$$\theta_b = \frac{T - T_c}{T_b - T_c} = \frac{\theta}{\theta^*} \quad (16)$$

The velocity expressions in fluid and porous regions satisfying the interfacial conditions are available in Bhargavi and Sharath Kumar Reddy [10].

### 3 Numerical Scheme: Successive Accelerated Replacement (SAR)

Numerical solutions to non-dimensional energy Eqs. (3) and (7) along with the non-dimensional boundary conditions on  $\theta$  given in Eqs. (9)–(16) have been obtained using the numerical scheme successive accelerated replacement [3, 9, 10].

#### 3.1 Local Nusselt Number

After non-dimensionalizing (using Eq. (1)),  $Nu_{px}$ , the local Nusselt number at the lower plate  $Y = -1/2$ , is given by

$$Nu_{px} = \frac{h_{px}(2H)}{k_f} = -\frac{2(\partial\theta_p/\partial Y)|_{Y=-1/2}}{\eta[\theta_w - \theta^*(X)]} = \frac{2}{\theta_w - \theta^*(X^*)} \quad (17)$$

## 4 Results and Discussion

Assumed that  $\varepsilon = \mu_f/\mu_{eff} = 1$  and  $\eta = k_f/k_{eff} = 1$ . The channel referred to clear fluid channel when porous fraction,  $\gamma_p = 0$ . The channel referred to fully filled with a porous medium, when porous fraction,  $\gamma_p = 1.0$ . The channel referred to partially filled with a porous medium, when porous fraction,  $0 \leq \gamma_p \leq 1.0$ .

#### 4.1 Local Nusselt Number with the Effect of Viscous Dissipation and Without Axial Conduction

Variation of the local Nusselt number,  $Nu_{px}$  against  $X^*$  for the Darcy number,  $Da = 0.005$  is shown in Fig. 2a, b for  $Br \leq 0$  and  $Br \geq 0$ , respectively, for porous fractions,  $\gamma_p = 0$  when axial conduction is neglected ( $A_c = 0$ ). Similarly, for porous fractions,  $\gamma_p = 0.2, 0.8$  and  $1.0$  are shown in Figs. 3, 4, and 5, respectively. Clearly,  $Nu_{px}$  displays an unbounded swing for  $Br < 0$  at say,  $X_{cc}^*$  in all Figs. 2, 3, and 4. This unbounded swing  $X_{sw}^*$  occurs for  $\gamma_p \leq 0.8$  But when  $Br > 0$ ,  $Nu_{px}$  displays an unbounded swing  $X_{sw}^*$  for  $\gamma_p > 0.8$  see in Fig. 5. The value of  $X_{sw}^*$  (which occurs for  $Br < 0$ ) increases as  $\gamma_p$  increases from 0 to 0.8. The Nusselt number values, as well as the limits, differ if  $Da$  is larger. The local Nusselt number,  $Nu_{px}$  displays an unbounded swing for  $Br < 0$  since the bulk mean temperature reaches wall temperature and exceeds because of viscous dissipation. Beyond  $X_{sw}^*$ ,  $Nu_{px}$  starts decreasing to reach the limiting value.

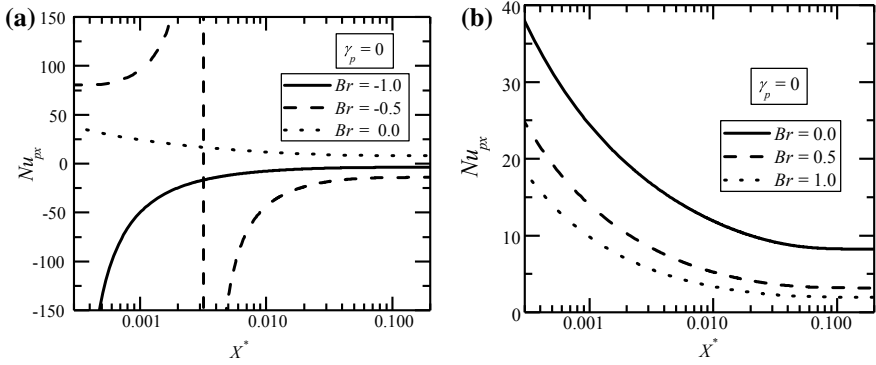


**Fig. 2** Variation of local Nusselt number against  $X^*$  for **a**  $Br \leq 0$  and **b**  $Br \geq 0$  for axial conduction neglected ( $A_c = 0$ ) for  $\gamma_p = 0$

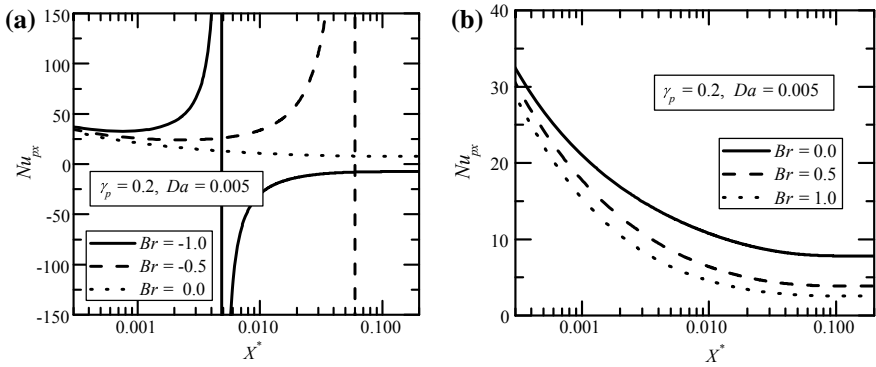


**Fig. 3** Variation of local Nusselt number against  $X^*$  for **a**  $Br \leq 0$  and **b**  $Br \geq 0$  for axial conduction neglected ( $A_c = 0$ ) for  $\gamma_p = 0.2$

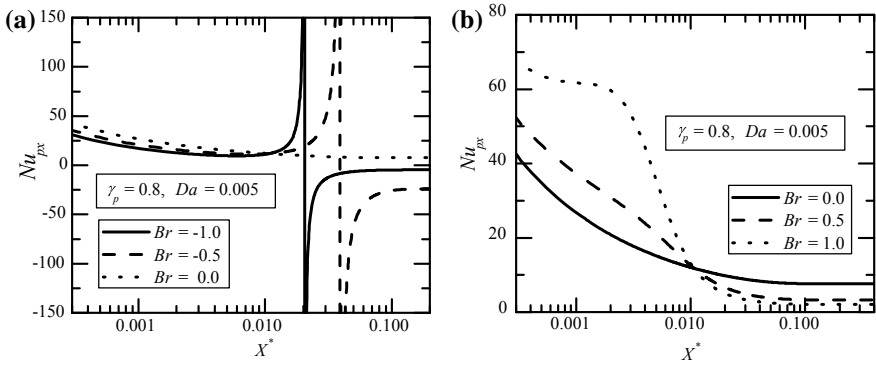


**Fig. 4** Variation of local Nusselt number against  $X^*$  for **a**  $Br \leq 0$  and **b**  $Br \geq 0$  for axial conduction neglected ( $A_c = 0$ ) for  $\gamma_p = 0.8$

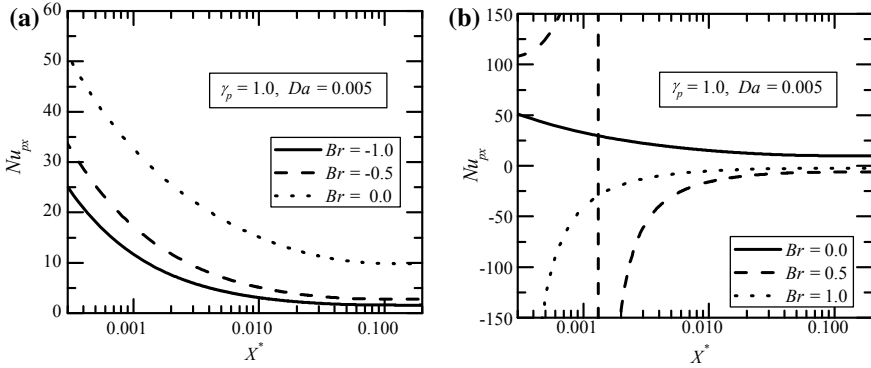


**Fig. 5** Variation of local Nusselt number against  $X^*$  for **a**  $Br \leq 0$  and **b**  $Br \geq 0$  for axial conduction neglected ( $A_c = 0$ ) for  $\gamma_p = 1.0$

### 4.2 Local Nusselt Number with the Effect of Viscous Dissipation and Axial Conduction

Variation of local Nusselt number,  $Nu_{px}$  against  $X^*$  for the Darcy number,  $Da = 0.005$  and at Brinkman numbers, (a)  $Br = -0.5$  and (b)  $Br = 0.5$  for different Peclet numbers,  $Pe = 5$  and  $25$ , respectively, are shown in Figs. 6, 7, 8, and 9 for porous fractions,  $\gamma_p = 0, 0.2, 0.8$ , and  $1.0$ , respectively. In parallel plate channel partially filled with a porous medium also,  $Nu_{px}$  displays an unbounded swing,  $X_{sw}^*$  for  $Br < 0$  in all Figs. 6, 7, and 8. This unbounded swing depends on porous fractions,  $\gamma_p$ . At low Peclet number, the value of the  $X_{sw}^*$  is more for all porous fractions. This unbounded swing  $X_{sw}^*$  occurs for  $\gamma_p \leq 0.8$ . But when  $Br > 0$ ,  $Nu_{px}$  displays an unbounded swing  $X_{sw}^*$  for  $\gamma_p > 0.8$  see in Fig. 9. As Darcy number increases, there is no unbounded swing in the local Nusselt number for all porous fractions. The qualitative behavior

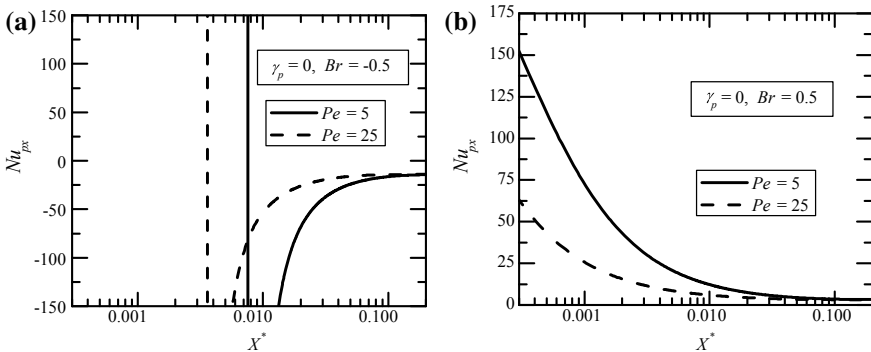


**Fig. 6** Variation of local Nusselt number against  $X^*$  for different Peclet numbers,  $Pe$  for **a**  $Br = -0.5$  and **b**  $Br = 0.5$  for  $\gamma_p = 0$

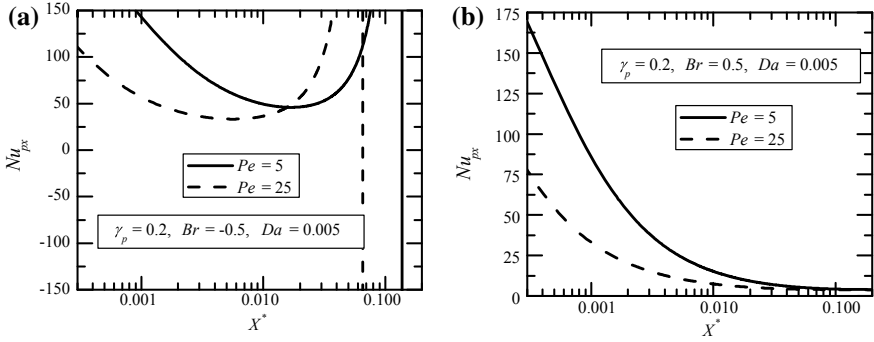


**Fig. 7** Variation of local Nusselt number against  $X^*$  for different Peclet numbers,  $Pe$  for **a**  $Br = -0.5$  and **b**  $Br = 0.5$  for  $\gamma_p = 0.2$

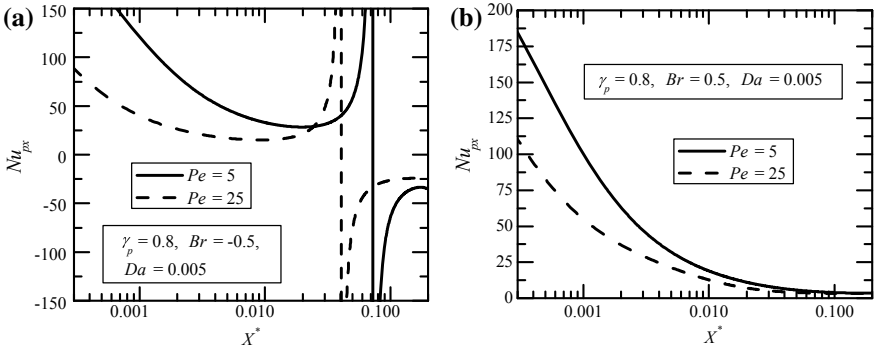


**Fig. 8** Variation of local Nusselt number against  $X^*$  for different Peclet numbers,  $Pe$  for **a**  $Br = -0.5$  and **b**  $Br = 0.5$  for  $\gamma_p = 0.8$

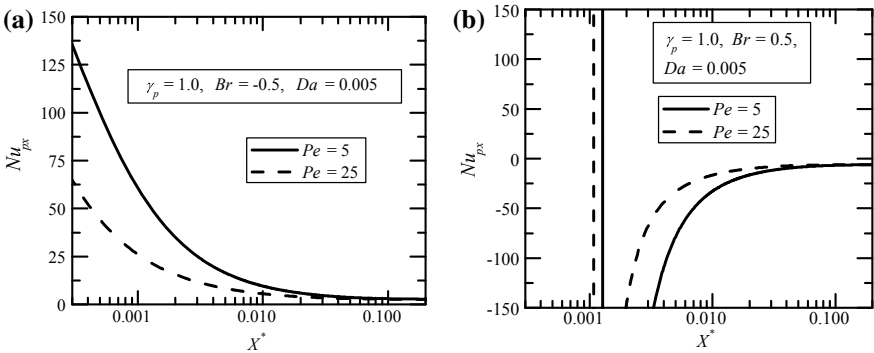


**Fig. 9** Variation of local Nusselt number against  $X^*$  for different Peclet numbers,  $Pe$  for **a**  $Br = -0.5$  and **b**  $Br = 0.5$  for  $\gamma_p = 1.0$

of the present local Nusselt number values with the Jagadeesh Kumar [4] and Ramjee and Satyamurty [11] are in good agreement for the clear fluid channel ( $\gamma_p = 0$ ).

## 5 Conclusions

Numerical solutions have been obtained for  $0 \leq \gamma_p \leq 1.0$ ,  $5 \leq Pe \leq 100$ ,  $-1.0 \leq Br \leq 1.0$  and  $Da = 0.005, 0.01$ , and  $0.1$ , using the SAR [3, 9, 10] numerical scheme. There is an unbounded swing in the local Nusselt number since the bulk mean temperature reaches wall temperature and exceeds because of viscous dissipation,  $Br < 0$  for the porous fraction,  $\gamma_p \leq 0.8$ . In the case of porous fraction,  $\gamma_p > 0.8$ , unbounded swing occurs at  $Br > 0$ . As, Darcy number increases, there is no unbounded swing in the local Nusselt number.

## References

1. Agrawal HC (1960) Heat transfer in laminar flow between parallel plates at small Peclet Numbers. *Appl Sci Res* 9:177–189
2. Hennecke DK (1968) Heat transfer by Hagen-Poiseuille flow in the thermal development region with axial conduction. *Warme- und Stoffubertragung* 1:177–184
3. Ramjee R, Satyamurty VV (2010) Local and average heat transfer in the thermally developing region of an asymmetrically heated channel. *Int J Heat Mass Trans* 53:1654–1665
4. Jagadeesh Kumar M (2016) Effect of axial conduction and viscous dissipation on heat transfer for laminar flow through a circular pipe. *Perspect Sci* 8:61–65
5. Shah RK, London AL (1978) Laminar flow forced convection in ducts. *Advances in heat transfer, supplement 1*. Academic Press, New York
6. Hooman K, Haji-sheik A, Nield DA (2007) Thermally developing Brinkman-Brinkman forced convection in rectangular ducts with isothermal walls. *Int J Heat Mass Trans* 50:3521–3533
7. Kuznetsov AV, Xiong M, Nield DA (2003) Thermally developing forced convection in a porous medium: circular duct with walls at constant temperature, with longitudinal conduction and viscous dissipation effects. *Transp Porous Media* 53:331–345
8. Nield DA, Kuznetsov AV, Xiong M (2003) Thermally developing forced convection in a porous medium: parallel plate channel with walls at uniform temperature, with axial conduction and viscous dissipation effects. *Int J Heat Mass Trans* 46:643–651
9. Satyamurty VV, Bhargavi D (2010) Forced convection in thermally developing region of a channel partially filled with a porous material and optimal porous fraction. *Int J Therm Sci* 49:319–332
10. Bhargavi D, Sharath Kumar Reddy J (2018) Effect of heat transfer in the thermally developing region of the channel partially filled with a porous medium: constant wall heat flux. *Int J Therm Sci* 130:484–495
11. Ramjee R, Satyamurty VV (2013) Effect of viscous dissipation on forced convection heat transfer in parallel plate channels with asymmetric boundary conditions. In: *Proceedings of the ASME, International Mechanical Engineering Congress and Exposition (IMECE 2013)*, San Diego, California, USA, 15–21 Nov 2013

# Experimental Study of Closed-Loop Thermosyphon System Using Different Working Fluids



Mahasidha R. Birajdar and C. M. Sewatkar

**Abstract** Thermosyphon is a heat transferring device which transfers heat over long distance and where the liquid is returned to the evaporator by gravitational force. The closed-loop thermosyphon (CLT) transfers heat with phase change phenomenon. A large amount of heat is transferred from evaporator section to condenser section with a relatively small temperature difference. The thermal performance of closed-loop thermosyphon (CLT) is influenced by the governing parameters like filling ratio, heat input, adiabatic length, working fluids, etc. This paper investigates the effects of these parameters on thermal performance of closed-loop thermosyphon system for different working fluids. In this work the filling ratio (FR) is varied in the range of 30–80% in the step of 10% at various heat inputs of 0.5–2 kW with a step of 0.5 kW for each evaporator and adiabatic length (vapor line length) is taken as 200 mm. The working fluid used as methanol, ethanol, acetone, and distilled water. The performance plots of the performance parameters like thermal resistance, evaporative heat transfer coefficient (HTC), and condenser heat transfer coefficient for these different working fluids, heat inputs, and filling ratios are plotted and results are analyzed. From the result, it is found that acetone has comparatively lowest thermal resistance. Water has comparatively highest evaporative heat transfer coefficient as well as condenser heat transfer coefficient.

**Keywords** Closed-loop thermosyphon · Thermal performance · Working fluid

## 1 Introduction

Closed-loop thermosyphon (CLT) transfers huge amounts of heat from evaporator region to condenser region with a relatively small temperature difference. Heat applied at evaporative section converts liquid into vapor and the vapor then condenses after passing through the condenser section. During this process, heat is transferred from evaporator to condenser through latent heat of evaporation, therefore this method is very efficient than conventional heat exchange method. In this process of

---

M. R. Birajdar (✉) · C. M. Sewatkar  
College of Engineering, Pune, Maharashtra, India

© Springer Nature Singapore Pte Ltd. 2020  
H. K. Voruganti et al. (eds.), *Advances in Applied Mechanical Engineering*,  
Lecture Notes in Mechanical Engineering,  
[https://doi.org/10.1007/978-981-15-1201-8\\_5](https://doi.org/10.1007/978-981-15-1201-8_5)

heat transfer, there is no requirement of power or pump for transferring heat from one location to another. Therefore, this method of heat exchange is known as passive heat exchange method [1–3]. Analysis of closed-loop thermosyphon (CLT) is carried out by different researchers using different working fluids. Pal et al. analyzed two-phase compact thermosyphon which is applied to the cooling process of computers. The thermosyphon experimented using the working fluids like PF5060 (dielectric liquid) and deionized water at different heat inputs such as 20–90 W. They noticed that performance of thermosyphon is affected by the working fluids and found that water is better working fluid than PF5060 [4]. Ersoz and Yıldız reported the effect of working fluids such as distilled water, methanol, and petroleum ether on thermoeconomic analysis of two-phase closed thermosyphon (TPCT). For all input conditions, the maximum energy efficiency and exergy efficiency are obtained for methanol whereas the minimum energy and exergy efficiency is obtained for petroleum ether. Also, they conclude that distilled water is more effective working fluid than methanol and petroleum ether in terms of cost [5]. Jouhara and Robinson carried out an experimental study of two-phase closed thermosyphon (TPCT) with working fluids such as distilled water and dielectric heat transfer fluids such as FC-77, FC-3283, and FC-84. They noticed that the distilled water filled thermosyphon shows better thermal performance than other working fluids [6]. Karthikeyan et al. carried out experiments on the two-phase closed thermosyphon (TPCT) charged with distilled water and *n*-butanol solution. The thermal performance of an aqueous solution of *n*-butanol charged TPCT was better than the distilled water [7]. Tong et al. reported the thermal performance of two-phase closed-loop thermosyphon charged with R744 and R22. They noticed that R744 filled two-phase closed-loop thermosyphon may work with a very small temperature difference of 5 °C. Also, they conclude that the thermal performance of working fluid R744 is better than the fluid R22 [8].

From the literature review, it is noticed that at the lower operating temperatures, working fluid water shows less satisfactory thermal performance compared to the low saturation temperature fluids. Also, at lower heat input water has its limited application. Therefore, in the present study, comparative performance of closed loop thermosyphon (CLT) using different working fluids such as ethanol, methanol, acetone, and water is reported as a function of different governing parameters such as heat input, filling ratio, and adiabatic length (vapor line length) [9].

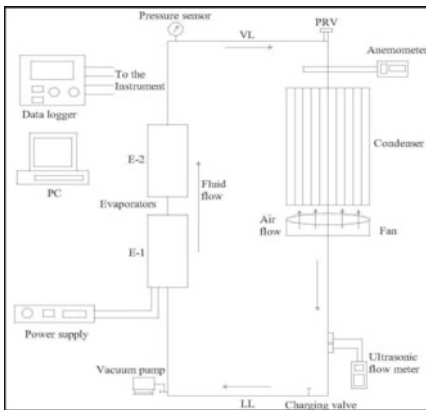
## 2 Experimental Setup and Procedure

The thermosyphon test rig consists of a closed-loop with two evaporators with two heaters, a plate-type condenser, a cooling (fan) section, a liquid reservoir for charging, a vacuum pump, data acquisition (logger) system, and measuring instruments like ultrasonic flow meter, anemometer, pressure transmitter, and thermocouples. The lower portion of closed loop thermosyphon (CLT) is having a vacuum seal valve for the connection of thermosyphon to vacuum pump and a charging valve for the connection of the working fluid to the thermosyphon tube. The mechanical vacuum



pump is used for evacuation of closed-loop and also for removal of non-condensable gases from the thermosyphon. The closed loop thermosyphon (CLT) is a long carbon steel pipe with an inner diameter of 32 mm and outer diameter of 42 mm. The insulation is wrapped around the evaporator for preventing thermal losses. Heat flux is given to evaporator through plate type heater using a power supply. Amount of input heat flux is controlled with the help of a controller on the control panel. The heat removal section (condenser) of the thermosyphon consists of an enclosure surrounding a plate type heat exchanger. The fan is used for the heat removal from the condenser section through forced air convection. There is a pressure transmitter to measure the loop pressure and 20 thermocouples to measure temperatures at 20 different locations. All these thermocouples are connected to the data acquisition system which is then connected to a personal computer for displaying the data. All experimental data are recorded and stored in computer system till the steady-state condition is achieved. Figure 1a shows a schematic diagram of the experimental setup and Fig. 1b shows the actual set up picture. The abbreviations mentioned in the Fig. 1 are: PRV: Pressure relief valve, VL: Vapor line length, LL: Liquid line length, E-1: Evaporator 1 and E-2: Evaporator 2, PC: Personal computer.

Before charging the thermosyphon, gases and air present in a loop are removed by the vacuum pump to ensure the perfect operation of the thermosyphon. Vacuuming is down to 0.09 bar (abs). After vacuuming no leakages in the system are ensured. After evacuation, the loop is charged with working fluid as per the required filling ratio. After charging, all the valves are closed tightly. The power supply is given to heat the evaporator section. The heat input is raised gradually to particular heating load. Fans are started. The evaporator surface temperatures are measured at ten different locations by thermocouples. The system pressure is measured by using pressure transmitters at the top portion of the loop. The input and output temperatures of the air flowing over the condenser plates are measured. The flow rate of the working



(a) Schematic diagram



(b) Actual set up

Fig. 1 Experimental setup

fluid is measured by the ultrasonic flow meter. The air velocity is measured after it passes over the condenser plates. Temperatures of incoming and outgoing fluid are measured in the evaporator section as well as in the condenser section for per second, time interval until the system reaches thermal steady-state condition. The stored data from PC is used for further analysis. In the calculation of performance parameters, the steady-state values of temperatures are considered. The data reduction and result discussions are carried out in the next sections [10, 11].

### 3 Data Reduction

The data reduction of the experimental data is carried out by calculating performance parameters like thermal resistance, evaporative heat transfer coefficient, and condenser heat transfer coefficient.

The system thermal resistance (k/W) of the thermosyphon is calculated using the equation:

$$R_{\text{sys}} = \frac{(T_e - T_c)}{Q_e} \quad (1)$$

Here, evaporator temperature  $T_e$  is taken as the average of all surface temperatures of evaporator ( $T_1$  to  $T_{10}$ ), and condenser temperature  $T_c$  is taken as average of surface temperatures at condenser inlet and outlet ( $T_{16}$  and  $T_{17}$ ).

The heat transfer capacity of an evaporator section for closed-loop thermosyphon is determined by the heat transfer coefficient ( $h_e$ ) [7].

$$h_e = \frac{Q_{\text{avg}}}{A_e \times (T_e - T_v)} \quad (2)$$

Here,  $T_v$  is average adiabatic temperature ( $T_{15}$  and  $T_{16}$ ), i.e., vapor temperature between evaporator and condenser.  $A_e$  is the surface area the evaporator.

The heat transfer capacity of the condenser section for closed-loop thermosyphon is determined by the heat transfer coefficient ( $h_c$ ) which is obtained as [7]:

$$h_c = \frac{Q_{\text{avg}}}{A_c \times (T_v - T_c)} \quad (3)$$

The surface area of the condenser ( $A_c$ ) is calculated by from the surface area of the ten condenser plates.

## 4 Results and Discussions

Analysis of the closed-loop thermosyphon (CLT) system is carried out to understand the thermal behavior of the thermosyphon system and to calculate performance parameters such as thermal resistance, evaporative heat transfer coefficient (HTC), and condenser HTC for different working fluids. In the present work, the closed-loop thermosyphon (CLT) system is designed and developed to explore its possible application in the cooling of huge computational clusters. Assuming that the amount of heat to be removed is in the range of 0.5–4.00 kW, the system is designed with basic components such as evaporator, condenser as shown in Fig. 1. The experimentation is carried out by filling ratio (FR) in the range of 30–80% in the step of 10% at various heat inputs of 0.5–2 kW with a step of 0.5 kW for each evaporator and adiabatic length (vapor line length) of 200 mm. The working fluids used for the experiments are distilled water, acetone, methanol, and ethanol. The comparative study of these different working fluids is reported in this section. The plots drawn in this section are representative of the result. Filling ratio 30% and heat input ranging from 0.5 to 2 kW is taken as representative of the results, similar trends may be obtained from the other configuration.

### 4.1 Thermal Resistance

Thermal resistance is a function of temperature difference between evaporator and condenser section and heat input. Variation of thermal resistance with heat input is plotted for different working fluids at the filling ratio (FR) = 0.3 (30%) and at the adiabatic length of 200 mm as shown in Fig. 2. It is noticed that for all the working fluids thermal resistance decreases with an increase in heat input. At smaller heat input thermal resistance is higher as large number liquid molecules in the evaporator section become obstruction for transfer of heat. It is further noticed that thermal resistance is higher for the methanol at all the heat inputs and it is lower for acetone for all heat input except at 2 kW. Thus, acetone is better fluid comparatively as its thermal resistance is lower within this range of heat input. The thermo-physical characteristics of methanol are more heat resistive than others whereas thermo-physical characteristics of acetones are more heat conductive than other working fluids.

### 4.2 Evaporative Heat Transfer Coefficient ( $H_e$ )

Evaporative heat transfer coefficient's (HTC) variation with heat input at FR = 0.3 and at the adiabatic length of 200 mm is shown in Fig. 3. Water shows several orders of magnitude greater evaporative heat transfer coefficient than other working fluids

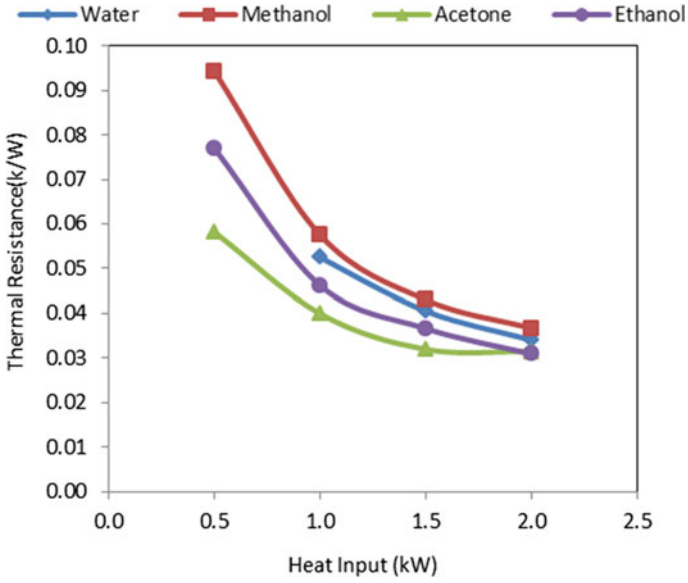


Fig. 2 Thermal resistance (k/W) variation with heat input (kW) at FR = 0.3

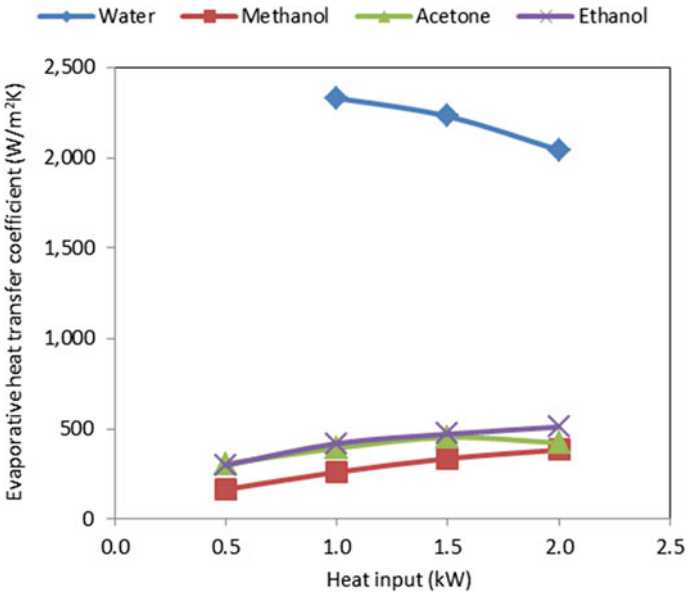


Fig. 3 Evaporative HTC (W/m<sup>2</sup>K) variation with heat input (kW) at FR = 0.3

and its trend is different than remaining other three fluids. For distilled water, with the increase in heat input, evaporative heat transfer coefficient decreases slightly, whereas with the increase in heat input evaporative heat transfer coefficient (HTC) of acetone, methanol, and ethanol increases. The heat-carrying capacity of water is higher than other fluids, therefore, water having higher evaporative heat transfer coefficient than another and also its heat carrying capacity decreases slightly with an increase in heat input. The saturation point of water is higher; therefore it is having a higher heat transfer coefficient and also its specific heat decreases with the increase in heat input. Therefore, its evaporative heat transfer coefficient decreases with the increase in heat input. The specific heat of low saturation point fluid is lower than water therefore there heat transfer coefficient is significantly lower than other fluids.

### 4.3 Condenser Heat Transfer Coefficient ( $H_c$ )

Condenser heat transfer coefficient as a function of heat input at  $FR = 0.3$  is shown in Fig. 4. Water shows a much higher condenser heat transfer coefficient (HTC) than other working fluids. With the increase in heat input the condenser heat transfer coefficient increases for all the fluids used in this analysis. Comparatively higher condenser heat transfer coefficient of the water should allow maximum heat transfer rate from the condenser than other fluids. Also, it is noticed that condenser heat

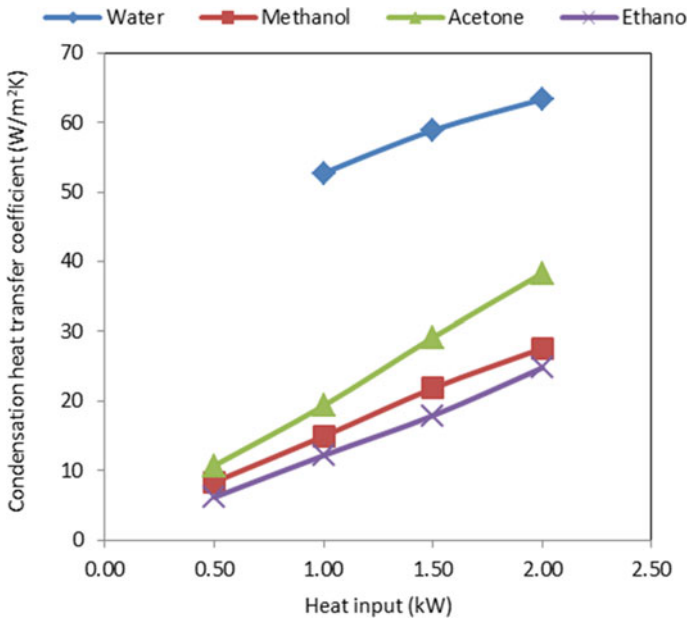


Fig. 4 Condenser HTC ( $W/m^2K$ ) variation with heat input (kW) at  $FR = 0.3$

transfer coefficient is lower than evaporative heat transfer coefficient because film-wise condensation start from the adiabatic section which leads to decrease in the rate of heat transfer which further reduces condenser heat transfer coefficient.

## 5 Conclusions

The effect of different working fluids on the performance of the closed-loop thermosyphon (CLT) system is investigated experimentally. It is noticed that the thermal resistance decreases with an increase in heat input for all the working fluids used in this experiment. Its value is minimum for acetone and maximum for methanol. Evaporative heat transfer coefficient (HTC) decreases with the increase in heat input for distilled water as a working fluid, but for methanol and ethanol evaporative heat transfer coefficient (HTC) increases with the increase in heat input. The distilled water shows much higher evaporative heat transfer coefficient than other working fluids because it has a higher heat carrying capacity. Condenser HTC increases with the increase in heat input for all the working fluids. Its value for distilled water is much higher than other working fluids, whereas ethanol shows comparatively lower condenser HTC. Also, the condenser heat transfer coefficients are lower than evaporative heat transfer coefficients; this is because of film-wise condensation start in the adiabatic section which leads to decrease in the heat transfer rate.

## References

1. Reay D, Kew P (2006) Heat pipes, 5th edn. Butterworth-Heinemann, Oxford
2. Franco A, Filippeschi S (2012) Closed loop two-phase thermosyphon of small dimensions: a review of the experimental results. *Microgravity Sci Technol*
3. Patel A, Yarasu R (2012) Factors affecting the thermal performance of two phase closed thermosyphon: a review. *Int J Emerg Technol Adv Eng* 2(9)
4. Pal A, Joshi Y, Beitelmal M, Patel C, Wenger T (2002) Design and performance evaluation of a compact thermosyphon. *IEEE Trans Compon Packag Manuf Technol* 25(4):601–607
5. Ersoz M, Yıldız A (2016) Thermoeconomic analysis of thermosyphon heat pipes. *Renew Sustain Energy Rev* 58:666–673
6. Jouhara H, Robinson A (2010) Experimental investigation of small diameter two-phase closed thermosyphons charged with water, FC-84, FC-77 and FC-3283. *Appl Thermal Eng* 30
7. Karthikeyan M, Vaidyanathan S, Sivaraman B (2013) Heat transfer analysis of two phase closed thermosyphon using aqueous solution of n-butanol. *Int J Eng Technol* 3(6)
8. Tong Z, Ding T, Li Z, Liu X (2015) An experimental investigation of an R744 two-phase thermosyphon loop used to cool the data center. *Appl Thermal Eng* 90:362–365
9. Mousa M (2011) Thermal performance of thermosyphon charged by nanofluid for cooling electronic component. *Int J Sci Eng Res* 2(6)
10. Naresh Y, Balaji C (2017) Experimental investigations of heat transfer from an internally finned two phase closed thermosyphon. *Appl Therm Eng* 112:1658–1666
11. Noie S (2005) Heat transfer characteristics of a two-phase closed thermosyphon. *Appl Therm Eng* 25:495–506

# Identifying Empirically Important Variables in IC Engine Operation Through Redundancy Analysis



Satishchandra Salam and Tikendra Nath Verma

**Abstract** Computational studies incur engineering costs. While direct numerical simulations can provide detailed solutions, they cannot deliver quick and convenient solutions which are pragmatic for industry applications such as fault detection and diagnosis. But in the study of internal combustion engines, there are no such unified models that can completely capture the engine operation and hence, computational methods still are of great value. In this pursuit, an attempt had been made in this study to evaluate the empirical redundancy amongst the engine variables. Using Pearson correlation coefficient to quantify the linear dependencies among a set of variables, a representation score was developed to measure how effectively various variables can represent other variables. With the suggested methodology, those empirically important variables can be identified and they can be used to develop empirically reduced models for its possible employment in further computational studies.

**Keywords** Correlation matrix · Redundancy analysis · Empirical modelling · IC engine

## 1 Introduction

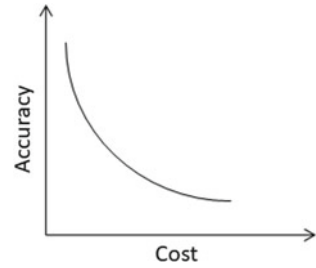
Even after almost 150 years of its introduction, the pursuit for engineering solutions of internal combustion engine (ICE) still continues. Essentially, a heat engine that converts the chemical energy of the fuel to mechanical energy, it fundamentally involves controlled combustion of fuel inside the combustion chamber. Therefore, the process is influenced even by small length and time scales. And as ICE research evolves, the paradigm has shifted from the fundamental analytical modelling to phenomenological modelling, and in the last few decades to computational modelling [5].

---

S. Salam (✉) · T. N. Verma  
Department of Mechanical Engineering, National Institute of Technology  
Manipur, Langol, Imphal 795004, India  
e-mail: [satisji@gmail.com](mailto:satisji@gmail.com)

© Springer Nature Singapore Pte Ltd. 2020  
H. K. Voruganti et al. (eds.), *Advances in Applied Mechanical Engineering*,  
Lecture Notes in Mechanical Engineering,  
[https://doi.org/10.1007/978-981-15-1201-8\\_6](https://doi.org/10.1007/978-981-15-1201-8_6)

**Fig. 1** Illustration of cost-accuracy trade-off



The success with computational modelling has been largely achieved with improved computational fluid dynamics (CFD) based methods which can deliver detailed direct numerical solutions (DNS). By decomposing large real-life systems into smaller subsystems, analytical models are implemented at the sub-system level to evaluate the phenomenon associated with the whole system. This has delivered solutions which are of extreme value, and are even sometimes left as the only feasible method.

But despite how CFD can deliver those DNS, it incurs large engineering resources including time and capital. There is a significant trade-off between the cost of the method and the accuracy of solution it can deliver (Fig. 1). For instance, when all the combinatorics of all operating conditions are to be considered for the full-scale simulation of studying technical feasibility of various biofuels as alternative fuel, CFD-based methods racks up large computational cost which are not feasible for industry applications. This (therefore) calls for alternative methods which can deliver quick and convenient industry feasible solutions for diagnosis and fault detection.

One such possible alternative method could be delivered by what has been popularly known as ‘data reduction’ in the emerging applications of data science [1, 3]. In this mathematically black-box modelling method, the objective is to identify the empirical pattern embedded in the observation regardless of what mechanistic explanation the model can offer. Mathematically, when the number of variables is greater than the number of equations, multiple sets of solutions can exist. These various solutions are superfluous and are alternative to one another. While each solution is unique, the involved variables can accommodate variability amongst a set of the involved variables. This redundancy when perceived from empirical perspective for the purpose of black-box modelling is hereby referred to as empirical redundancy. This can be achieved by sequestering redundancy from the dataset whose detailed methodology in the case of ICE operation will be discussed in the following sections.



## 2 Methods

Salam and Verma [4] have reported empirical redundancy in the engine responses. The correlation matrix reported in this study suggested methods to harness the redundancy in the system. Here, using the correlation matrix reported in Salam and Verma [4] as sample correlation matrix, the following methodology is proposed to evaluate those reported redundancy. The study used inputs of loading, blending and fuel injection pressure to characterise for performance with specific fuel consumption (SFC), brake thermal efficiency (BTE), indicated efficiency (IE) and scavenging efficiency (SE); combustion with exhaust gas temperature (EGT), cylinder peak pressure (CPP), cylinder peak temperature (CPT), maximum rate of pressure rise (MRPR), outer mean diameter of injected droplet (Dout) and ignition delay (ID); and emission with Hartridge smoke unit (HSU), smoke, specific particulate matter (SPM), carbon dioxide (CO<sub>2</sub>), oxides of nitrogen (NO<sub>x</sub>), summary of emission (SoE) and nitrous oxide (NO<sub>2</sub>).

### 2.1 Correlation Matrix

Correlation indicates how strongly a variable is related to another variable. Of different indicators of correlation, Pearson correlation coefficient ( $\rho$ ) is one such indicator which can quantify the monotonic dependencies among the set of variables. Mathematically, for two matrixes  $X(a)$  and  $Y(b)$  with means  $\bar{X}_a$  and  $\bar{Y}_b$ , respectively, it is defined as (1):

$$\rho(a, b) = \frac{\sum(X_{a,i} - \bar{X}_a)(Y_{b,i} - \bar{Y}_b)}{\left\{ \sum(X_{a,i} - \bar{X}_a)^2 \sum(Y_{b,j} - \bar{Y}_b)^2 \right\}^{1/2}} \quad (1)$$

For the empirical analysis of the engine variables, this was performed using the 'corr' function available in MATLAB 2016a. These correlation coefficients across all the variables were presented in Fig. 2. It can be noted that the diagonal cells had a value of unity since they represent self-correlation.

### 2.2 Cumulative Histogram

A histogram was prepared for the correlation coefficients with a bin size of 20(= $\sqrt{20} \times 20$ , [6]). Since we are interested only in those strongly correlated variables regardless of the directionality, the histogram was computed for absolute of the correlation coefficients. As it was evident from Fig. 3, the correlation coefficients were sparsely distributed over [0,1] with significant counts towards correlation coefficient of 1. This

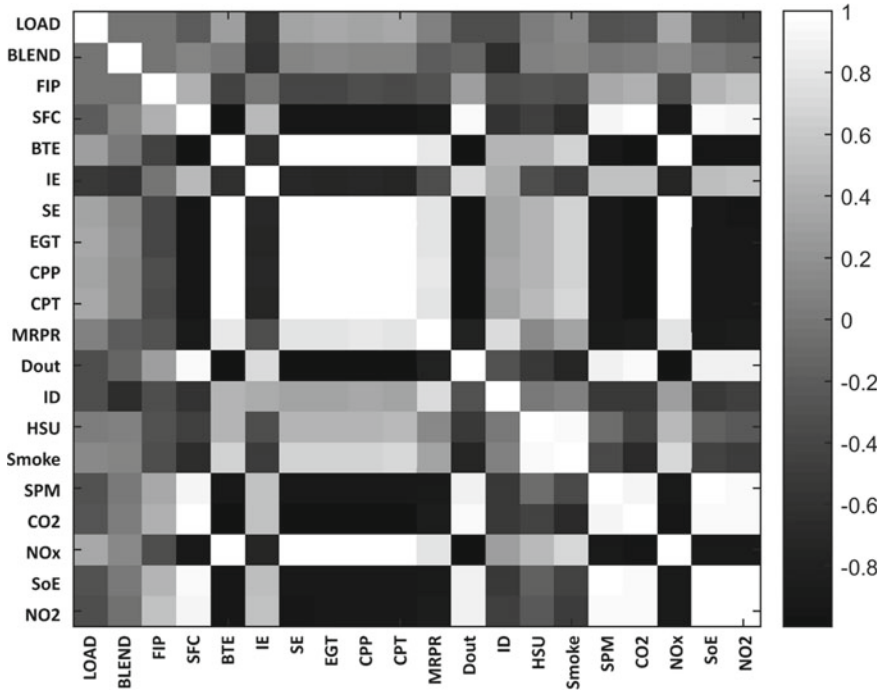


Fig. 2 Correlation matrix of the engine variables

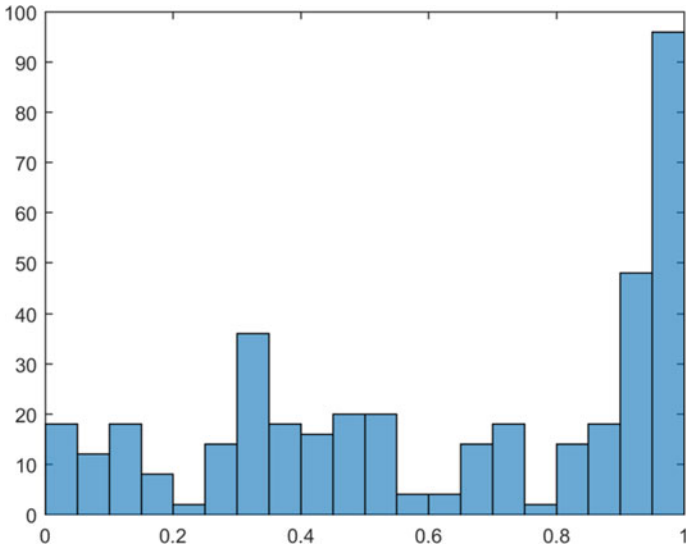


Fig. 3 Histogram of absolute of Pearson correlation coefficients

was indicative of how several variables were strongly related to each other empirically. It is to be noted that it had not yet been discussed about how these empirical dependencies actually manifest into functional mechanistic dependencies.

### 2.3 Representation Score

To quantify how efficient a variable is in representing a set of redundant variables, an index hereby referred to as representation score was introduced (2):

$$\text{Representation score of } i\text{th variable} = \frac{1}{n} \sum (\text{correlation coefficient with } i\text{th variable}) \tag{2}$$

By averaging the correlation coefficients for a variable with all other variables, representation score provided a basis for comparing how a variable (as compared with other variables) can effectively represent other variables. Larger the representation score is, more efficient it is in representing the whole set of variables. Thus, variables with higher representation score are the more suitable variables to empirically represent the whole system. For this set of variables, the sorted variables in order of decreasing representation score were presented in Fig. 4.

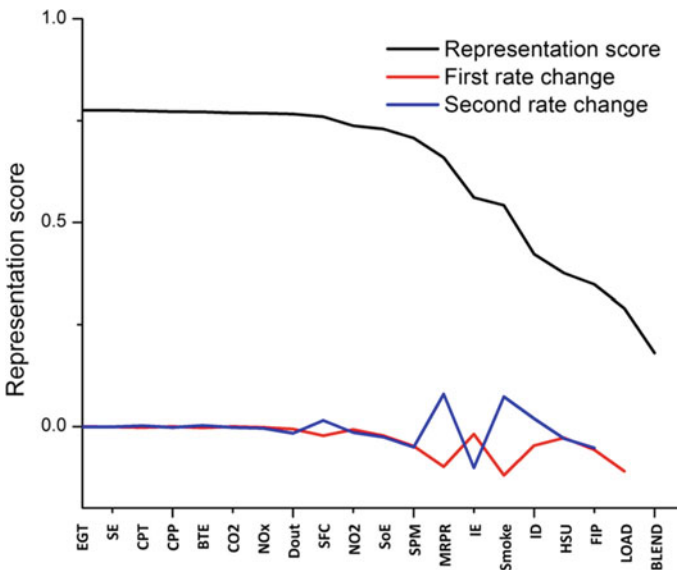


Fig. 4 Engine variables sorted by representation scores

## 2.4 Thresholding

To decide on exactly how many variables should be picked as representative variables to substitute for the whole system, this thresholding section is added only to assist the designer in the decision-making process. While there is the obvious upper limit of 100% reconstruction accuracy when all the variables are chosen, it entirely rests on the designer to select a lesser number of variables under the constraint of cost-accuracy trade-off as discussed earlier.

An alternative here is to maximise the ratio of accuracy to number of variables, i.e. to get the maximum accuracy out of least number of variables. This can be mathematically achieved by taking the first derivative of profile of the representation score ranking as in Fig. 4. A second rate change will help decide the local extremas of the profile (i.e. either local maxima or minima).

## 3 Results and Discussion

Figure 4 shows all the engine associated variables sorted in order of empirical importance. The superficial interpretation would be that variables having highest representation score would be the most important variables from empirical perspective. These variables have the highest linear dependencies with all other variables as well as amongst all other variables. Consequently, they are the best candidates to empirically represent other variables.

As discussed on thresholding, the reconstruction accuracy will be affected by the number of variables chosen for data reconstruction. And as it is unlikely for the reconstruction accuracy to be directly proportional to the number of variables, the ‘best’ number of choice under the constraint of cost-accuracy trade-off can be decided by picking the threshold value which can be decided by the designer.

In closure, while this study analysed the empirical dependencies, incorporating the functional mechanistic relations amongst the variables was out of scope of the study. It had not commented on how these empirically identified ‘important’ variables are influencing the actual ICE operation. This lack of explanation was inherently because of why ‘correlation is not causality’ [2], and on how black-box models cannot explain the cause and effect relationships. Therefore, enough emphasis should be given to dataset-specific interpretation with domain knowledge for the proper implementation of the presented methodology.

## 4 Conclusion

The study had presented a systematic methodology to empirically reduce a set of variables associated with ICE operation. After employing Pearson correlation coefficient to quantify the monotonic dependencies among the engine variables, an index called representation score had been used to compare how efficiently a variable can represent the whole system. Such models will help derive quick and convenient solutions for a large class of industry applications.

## References

1. Bevington PR et al (1993) Data reduction and error analysis for the physical sciences. *Comput Phys* 7(4):415–416
2. Harford T (2014) Big data: a big mistake? *Significance* 11(5):14–19
3. Hinton GE, Salakhutdinov RR (2006) Reducing the dimensionality of data with neural networks. *Science* 313(5786):504–507
4. Salam S, Verma TN (2019) Appending empirical modelling to numerical solution for behaviour characterisation of microalgae biodiesel. *Energy Convers Manage* 180:496–510
5. Shi Y, Ge HW, Reitz RD (2011) *Computational optimisation of internal combustion engines*. Springer Science and Business Media, Berlin
6. Shimazaki H, Shinomoto S (2007) A method for selecting the bin size of a time histogram. *Neural Comput* 19(6):1503–1527

# Mixed Convective Heat Transfer with Surface Radiation in a Vertical Channel in Presence of Heat Spreader



S. K. Mandal, Arnab Deb and Dipak Sen

**Abstract** Numerical analysis of mixed convection with surface radiation on a vertical channel is conducted. Five protruding heat sources are mounted on the left wall of the channel, and copper heat spreader is attached upon each heat source. Governing equations are solved using SIMPLER algorithm in ANSYS 16.2 software. Results are presented to depict the effects of parameters like heat spreader width ( $W_s = W - 2W$ ), emissivity of heat spreader ( $\varepsilon_{sp} = 0.1-0.9$ ) and Reynolds number ( $Re$  250–750) on the rate of heat transfer by fixing emissivity of heat source and substrate. It is found that with increasing spreader width and emissivity, heat transfer performance increases.

**Keywords** Mixed convection · Surface radiation · Heat spreader

## Nomenclature

$K$	Thermal conductivity
$\varepsilon$	Emissivity
$F_{jk}$	View factor from $j$ th element to the $k$ th element of an enclosure
$J_k$	Radiosity of surface $k$
$J_j$	Radiosity of surface $j$
$E_k$	Emissive power of surface $k$
	Non-dimensional temperature
$\theta = \frac{T-T_0}{\Delta T_{ref}}$	
$\Delta T_{ref}$	Reference temperature difference,
$\Delta T_{ref} = \frac{q''_{wh}}{k}$	

---

S. K. Mandal (✉) · A. Deb · D. Sen  
Department of Mechanical Engineering, NIT-Arunachal Pradesh, Yupia, Arunachal Pradesh  
791112, India  
e-mail: [sandip@nitap.ac.in](mailto:sandip@nitap.ac.in)

© Springer Nature Singapore Pte Ltd. 2020  
H. K. Voruganti et al. (eds.), *Advances in Applied Mechanical Engineering*,  
Lecture Notes in Mechanical Engineering,  
[https://doi.org/10.1007/978-981-15-1201-8\\_7](https://doi.org/10.1007/978-981-15-1201-8_7)

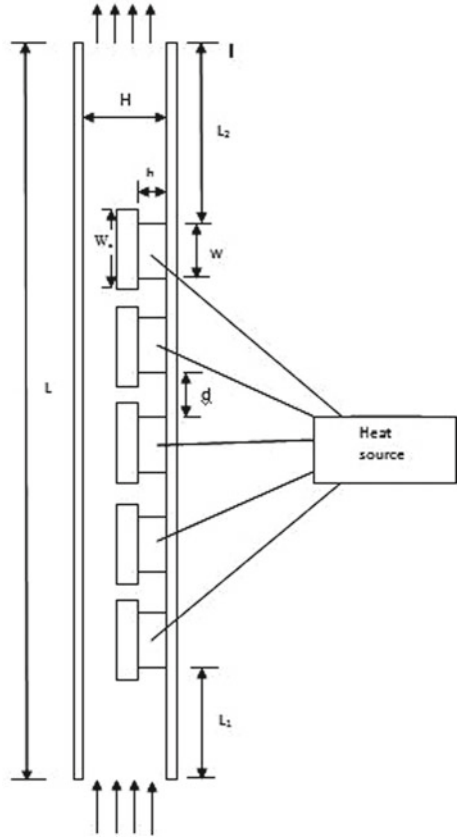
## 1 Introduction

In enhancing the reliability and to prevent the permanent failure of electronic devices, thermal management plays an important role. Improved heat generation together with different levels of electronic packaging creates a great challenge for the researcher. Each electronic package has heat source with different aspect ratio, which creates some vortex in the flow field. The rate of heat transfer by convection and radiation changes with changing the area of heat transfer surface. So, for efficient cooling, appropriate flow and mechanism of heat transfer must be analyzed, and accordingly, design must be made. As the present work is mixed convection with surface radiation, the significant literature briefly reviewed here. Smith et al. [1] numerically studied the effect of surface radiation with conjugate free convection considering diverse sizes of heat-generating component mounted on a printed circuit board. An analytical study carried out on a vertical cavity by Balaji and Venkateshan [2] on surface radiation with conjugate free convection considering conducting walls and isothermal bottom, whereas Bahlaoui et al. studied in a horizontal cavity on mixed convection with surface radiation. Premachandran and Balaji [3, 4] investigated surface radiation with combined free-forced convection from vertical and also in horizontal channel considering four numbers of protruding heat sources. Fahad et al. [5] analytically investigated the influence of surface radiation of a transparent gas between two asymmetrically heated vertical plates. Flow is considered to be laminar mixed convective and developing. Siddiqa et al. [6] numerically investigated on free convection in a vertically heated wavy surface. Investigation on natural convection with surface radiation in a vertical channel with copper heat source array which simulating electronic package performed both analytically and experimentally by Sarper et al. in 2018 [7]. Heat spreader also can be used to enhance the heat transfer from electronic devices. It also provides mechanical support to the devices to prevent physical damage during testing and handling.

## 2 Problem Description

The schematic diagram of a rectangular vertical channel with five identical protruding heat sources and rectangular heat spreader pasted upon each heat source is shown in Fig. 1. Five protruding heat sources are located at the right wall of the channel maintaining spacing ' $d$ ' with successive heat source. Channel has a length ' $L$ ' and a width ' $H$ .' Every heat source has a width ' $w$ ' and height ' $h$ .' Each heat spreader has a width ' $W_s$ .' Left face of the first heat source maintains a distance ' $L_1$ ' from the entrance plane. Right face of the 5th heat source is positioned at a distance ' $L_2$ ' before the outlet plane. The inlet fluid (air) temperature is assumed to be at 27 °C and non-participating media. Each heat source with volumetric heat generating capacity of 100,000 W/m<sup>3</sup> is chosen in the present case. Fluid properties are supposed to be constant.

**Fig. 1** Schematic diagram of the problem



### 3 Governing Equations and Boundary Conditions

The governing equations for a 2D, steady, incompressible, laminar flow are given as follows:

$$U \frac{\partial U}{\partial X} + V \frac{\partial U}{\partial Y} = -\frac{\partial P}{\partial X} + \frac{1}{Re} \left( \frac{\partial^2 U}{\partial X^2} + \frac{\partial^2 U}{\partial Y^2} \right) \quad (1)$$

$$U \frac{\partial V}{\partial X} + V \frac{\partial V}{\partial Y} = -\frac{\partial P}{\partial Y} + \frac{1}{Re} \left( \frac{\partial^2 V}{\partial X^2} + \frac{\partial^2 V}{\partial Y^2} \right) + \frac{Gr}{Re^2} \theta \quad (2)$$

$$U \frac{\partial \theta}{\partial X} + V \frac{\partial \theta}{\partial Y} = \frac{1}{Re Pr} \left( \frac{\partial^2 \theta}{\partial X^2} + \frac{\partial^2 \theta}{\partial Y^2} \right) \quad (3)$$

$$U \frac{\partial \theta}{\partial X} + V \frac{\partial \theta}{\partial Y} = \frac{1}{Re Pr} \left( \frac{\partial^2 \theta}{\partial X^2} + \frac{\partial^2 \theta}{\partial Y^2} \right) \quad (4)$$



Pressure outlet and velocity inlet boundary conditions are applied at the channel entrance and channel exit, respectively. No-slip boundary conditions are used at all surfaces. Surface-to-surface radiation model used assuming all interior surfaces are to be diffuse, opaque and gray. The surface-to-surface radiation model equations are given below

$$J_k = E_k + \rho k \sum_{j=1}^n F_{kj} J_j \quad (5)$$

Coupled boundary condition was used at wall-to-wall and wall-to-fluid boundaries. Emissivity of channel walls considered 0.9. Copper heat spreader emissivity varied from 0.1 to 0.9.

## 4 Grid Independence Test and Validation

The grid independency test is performed for  $Re = 250$ , heat generation rate ( $q_v$ ) equal to  $1 \times 10^5 \text{ W/m}^3$  considering nonuniform grid throughout the domain. Result of grid independence test is shown in Table no. 1. It is found that the change in non-dimensional maximum temperature is less than 1% when number of nodes changes from 1,36,880 to 1,87,671. So, for present study, 136880 nodes are used.

In order to authenticate the present work, it was compared with the work of Premachandran and Balaji [4] maintaining identical test field and parameter used by them. The difference in result lies in less than 2% which has shown in Table no. 2. The present results show a good agreement with the literature.

**Table 1** Grid independence test

S. no.	Nodes	Maximum non-dimensional temperature	Percentage of change (%)
1	69,687	0.16627	–
2	100,941	0.15468	6.9
3	161,265	0.14648	5.3
4	216,279	0.14517	0.89

**Table 2** Validation

Emissivity	Reynolds number	$\theta_{\max}$ as per Premachandra and Balaji [4]	$\theta_{\max}$ as per present work
$\varepsilon_p = 0.3, \varepsilon_s = 0.55$	250	0.11373	0.11355
	500	0.09612	0.094886
	750	0.085512	0.08434

## 5 Results and Discussions

The study has been carried out for various heat spreader width ( $W$ , 1.5 W and 2 W), emissivity (0.1 to 0.9) in the channel with respect to various Reynolds number ( $Re = 250, 500$  and  $750$ ) to create sufficient data of non-dimensional temperature ( $\theta$ ). An isotropic conduction was considered in channel walls and heat spreader.

### 5.1 Streamline and Temperature Contour

The flow field configuration is characterized by using streamline with uniform profile of temperature and uniform velocity of the fluid thrust within the channel. Temperature contour and streamline are shown in Figs. 2 and 3, respectively. Figure 2 shows that temperature of the first heat source is much lower than other as because cold air first came in contact with the first heat source. Maximum temperature arises at penultimate heat source as large circulation beyond last heat source carries away

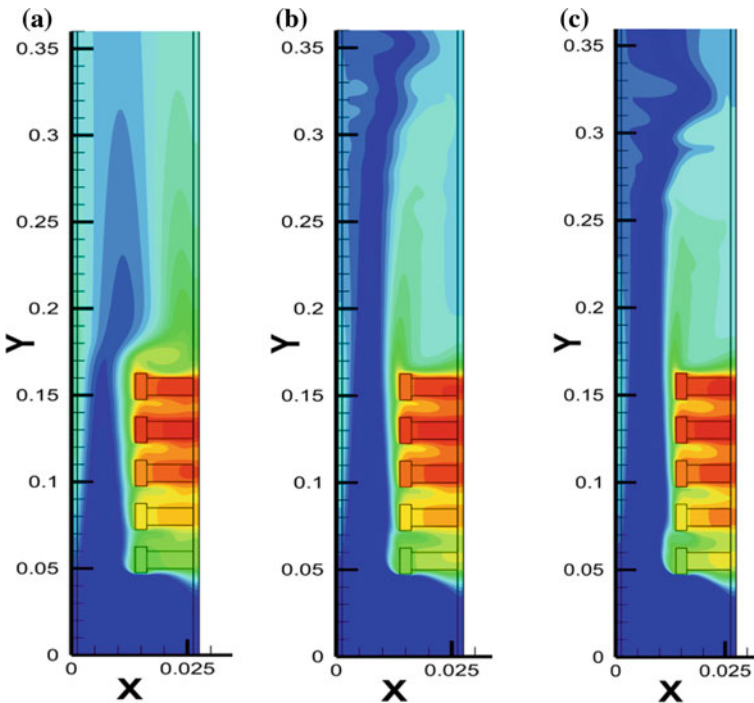


**Fig. 2** Temperature contour for  $W_s = 1.5$  W,  $\varepsilon_c = 0.5$ ,  $\varepsilon_{sp} = 0.5$ . **a**  $Re = 250$ , **b**  $Re = 500$  and **c**  $Re = 750$

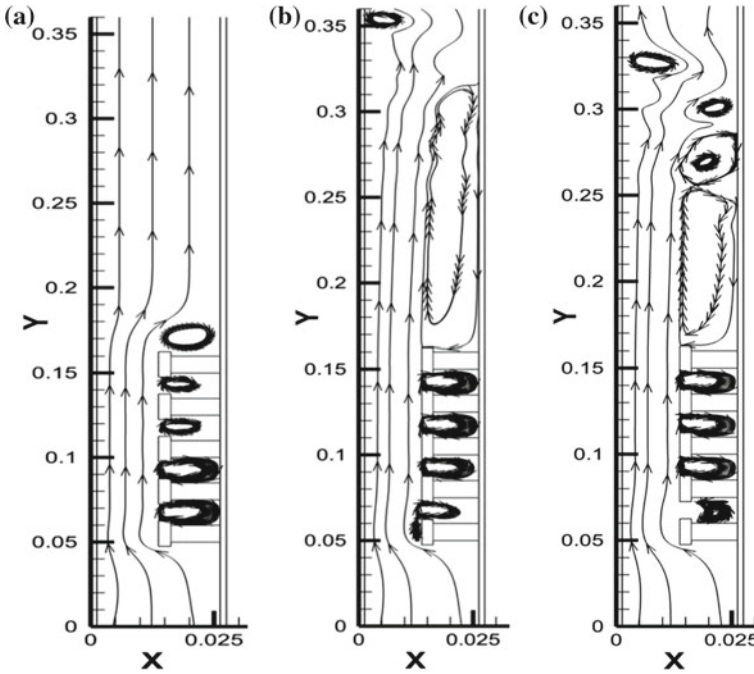


**Fig. 3** Streamline for  $W_s = 1.5 W$ ,  $\varepsilon_c = 0.5$ ,  $\varepsilon_{sp} = 0.5$ . **a**  $Re = 250$ , **b**  $Re = 500$  and **c**  $Re = 750$

heat to the core flow as shown in Fig. 3. As Reynolds number increases, circulation strength also increases. As the first heat source temperature is lowest compared to other, radiative heat transfer is insignificant compared to the rest. Heat source mounted on right wall substrate which carries heat by conduction, and its temperature increases which again involved in radiation. Left wall substrate temperature increases due to the radiative interaction with heat source and right wall substrate. A thermal boundary layer was developed over left wall substrate due to radiation. With increasing Reynolds number, thickness of that layer decreases.

## 5.2 Influence of Heat Spreader

Heat spreader creates an additional heat surface area like extended surface. Whenever heat spreader attached with heat source, heat transfer takes place from heat source to heat spreader by conduction, and temperature of heat source decreases. So, it is important to check the influence of heat spreader on overall heat transfer within the channel. Figure 4a shows that, after introducing heat spreader over the heat source, non-dimensional maximum temperature ( $\theta_m$ ) within the channel decreases.

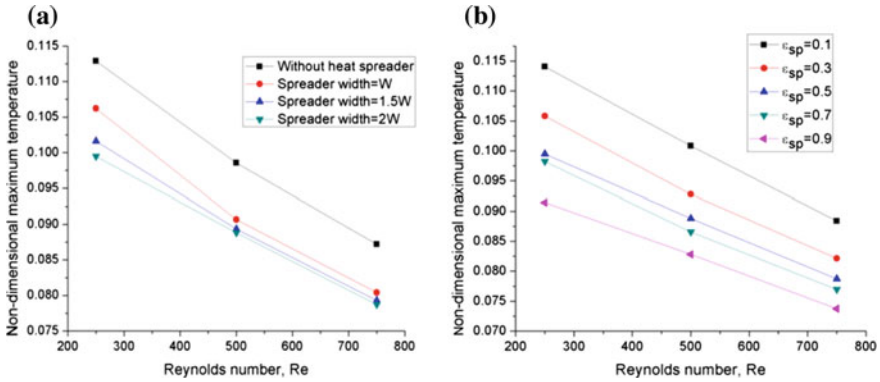


**Fig. 4** Graphs **a** variation of non-dimensional maximum temperature with  $Re$  for different spreader width at  $\epsilon_c = 0.5, \epsilon_{sp} = 0.5$ , **b** variation of non-dimensional maximum temperature with  $Re$  for different spreader emissivity at  $\epsilon_c = 0.5$

For spreader width of  $W, 1.5 W$  and  $2 W$ ,  $\theta_m$  decreases by 6%, 9% and 12%, respectively, at  $Re$  250 with comparison to without spreader. Temperature distribution for different spreader width at  $Re$  250 is shown in Fig. 5. Figure 4b depicts that when

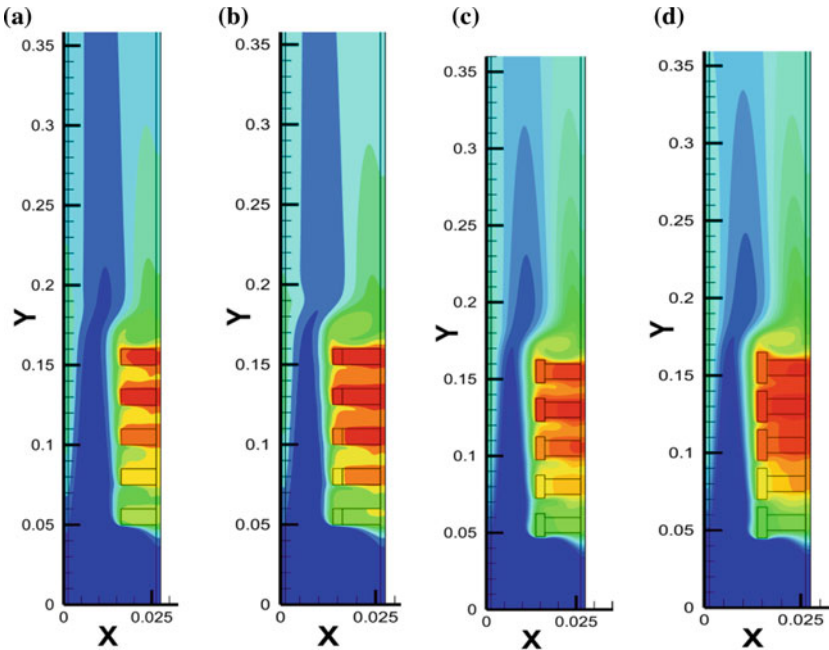


**Fig. 5** Temperature distribution at  $Re = 250$  for **a** without spreader, **b**  $W_s = W$ , **c**  $W_s = 1.5 W$ , **d**  $W_s = 2 W$

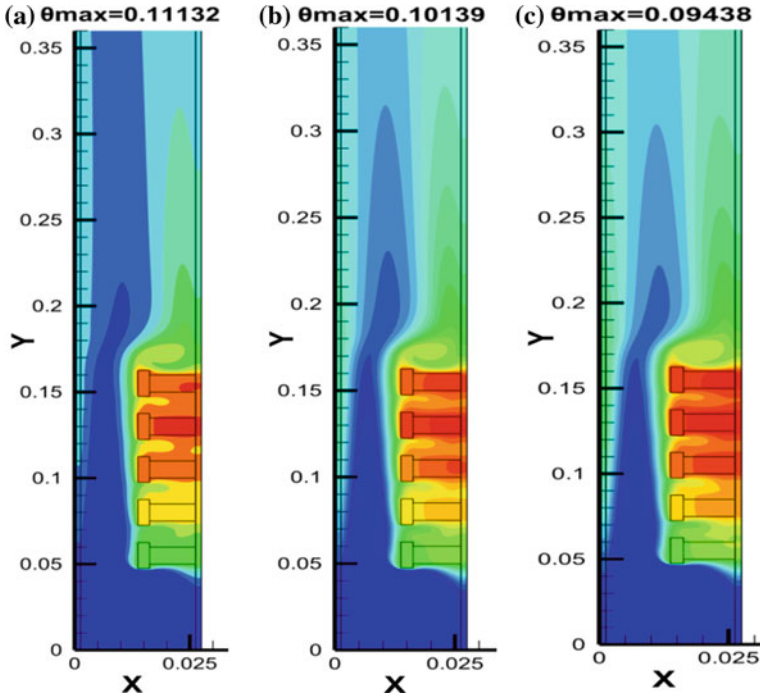


**Fig. 6** Temperature distribution for  $Re = 250$ . **a**  $\varepsilon_{sp} = 0.1$ , **b**  $\varepsilon = 0.5$  and **c**  $\varepsilon_{sp} = 0$

heat spreader emissivity,  $\varepsilon_{sp}$ , varies from 0.1 to 0.9, non-dimensional maximum temperature decreases by 20, 18 and 16.5% at  $Re = 250$ , 500 and 750, respectively, and as with increasing emissivity, radiative interaction between surfaces increases. Temperature distribution for different emissivity is shown in Fig. 6.

## 6 Conclusions

Based on numerical study in a vertical channel, the following conclusions are found

- With increasing Reynolds number, maximum non-dimensional temperature decreases, and radiation heat transfer decreases.
- As heat spreader width increases from  $W$  to  $2W$ , non-dimensional maximum temperature decreases by 6–12% in comparison with the value obtained without spreader.
- As the emissivity of the heat spreader increases from 0.1 to 0.9, maximum non-dimensional temperature decreases by 20% at  $Re = 250$ .

## References

1. Smith TF, Beckermnn C, Weber SW (1991) Combined conduction, natural convection, and radiation heat transfer in an electronic chassis. *ASME J Electron Packag* 113:382–391
2. Balaji C, Venkateshan SP (1995) Combined conduction, convection and radiation in a slot, cavity. *Int J Heat Fluid Flow* 14:260–267
3. Premachandran B, Balaji C (2011) Conjugate mixed convection with surface radiation from a vertical channel with protruding heat sources. *Numer Heat Transfer Part A Appl Int J Comput Methodol* 60(2):171–196
4. Premachandran B, Balaji C (2006) ‘Conjugate mixed convection with surface radiation from a horizontal channel with protruding heat sources. *Int J Heat Mass Transf* 49:3568–3582
5. Al-Amri FG, El-Shaarawi MAI (2012) Mixed convection with surface radiation between two asymmetrically heated vertical parallel plates. *Int J Thermal Sci* 58:70–78
6. Siddiqa S, Hossain MA, Saha SC (2013) Natural convection flow with surface radiation along a vertical wavy surface. *Numer Heat Transfer Part A* 64:400–415
7. Sharper B, Saglam M, Aydin O (2018) Experimental and numerical investigation of natural convection in a discretely heated vertical channel: effect of the blockage ratio of the heat sources. *Int J Heat Mass Transfer* 126:894–910

# Experimental Analysis on Thermal Performance of a Solar Air Heater at Different Angular Positions



Sk. A. Rahaman, T. Eswar, S. J. Reddy and M. Mohan Jagadeesh Kumar

**Abstract** Heat transfer enhancement and hence performance of solar air heaters can be improved by absorbing maximum amount of solar insolation. Absorption rate in solar air heater is increased when it is oriented all the time in perpendicular direction to solar insolation. Hence, inclination of solar air heater along with other geometrical and operating parameters plays an important role to decide its thermal performance. In the present work, a double-pass packed bed solar air heater is experimentally tested to know the effect of its inclination to solar insolation on its thermal performance. Experiments are conducted at different mass flow rate of air in the range of 0.038–0.0508 kg/s and at different inclination of solar air heater in the range of 5°–25° to the horizontal surface. It was found that efficiency of solar air heater is lower at 5° and 10° inclinations for all mass flow rates of air. Efficiency increased and reaches to its maximum value for 15° and 20° inclinations of the solar air heater, and it decreases with further increase in inclination to 25° at all mass flow rates of air.

**Keywords** Solar air heater · Heat transfer · Thermal performance · Convection

## 1 Introduction

Solar air heaters (SAHs) can be integrated with many industrial applications like preheaters in boiler furnaces, moisture removal from agricultural products, paper and pulp, space heating and cooling, supply process heat in sugar industries, etc. Solar air heater is a heat exchanger which converts solar energy into heat and transfers the same to air passing over its absorber plate. Thermal performance of SAHs can be improved passively by providing artificial ribs on its absorber plate Rajaseenivasan et al. [1], Mahmood et al. [2], Lakshmi et al. [3], Varun et al. [4], Varshney and Saini [5], packed beds Mahmood et al. [2], Lakshmi et al. [3], Mittal and Varshney [6], Prasad and Saini [7], Lalji et al. [8], Naphon [9], Lal Singh et al. [10], Dhiman et al.

---

Sk. A. Rahaman · T. Eswar · S. J. Reddy · M. Mohan Jagadeesh Kumar (✉)  
Gayatri Vidhya Parishad College of Engineering (A), Kommadi, Visakhapatnam, Andhra Pradesh  
530048, India  
e-mail: [mohan\\_mandapati@gvpce.ac.in](mailto:mohan_mandapati@gvpce.ac.in)

© Springer Nature Singapore Pte Ltd. 2020  
H. K. Voruganti et al. (eds.), *Advances in Applied Mechanical Engineering*,  
Lecture Notes in Mechanical Engineering,  
[https://doi.org/10.1007/978-981-15-1201-8\\_8](https://doi.org/10.1007/978-981-15-1201-8_8)

[11], Verma and Varshney [12], Sopian et al. [13], Thakur et al. [14], Paul et al. [15], Ho et al. [16] and attaching thermal storage units either with sensible or latent heat storage materials Lakshmi et al. [3], Fath [17], Enibe [18], Aboul-Enein et al. [19], Alkilani et al. [20]. Comprehensive review on performance analysis of SAHs with thermal energy storage units is given in Jose and Philip [21] and Kinga and Krzysztof [22].

Rajaseenivasan et al. [1] conducted experiments for  $Re$  in the range of 6000–12,000 to study the nature of SAH with circular and V-type turbulators attached on absorber plate. Experiment results revealed that the SAH efficiency increases with Reynolds number and number of turbulators in absorber plate. Mahmood et al. [2] investigated single and double-pass SAHs with transverse fins and a packed wire mesh. The results indicated that thermal efficiency increases with increase in air flow rate. Lakshmi et al. [3] conducted experiments on a trapezoidal corrugated SAH with gravel placed below the absorber plate sensible as heat storage material. The average daily thermal efficiency of flat plate SAH is improved from 8.5 to 12.2% when trapezoidal corrugations are provided on its absorber plate. It improved to 36.6% when sensible heat storage material is used in SAH. Varun et al. [4] conducted experiments on SAH with inclined as well as transverse ribs on its absorber plate for  $Re$  in the range of 2000–14,000, relative roughness pitch between 3 and 8 and relative roughness height equal to 0.030. Best performance of the SAH was observed for absorber plate having ribs with relative roughness pitch of 8. Varshney and Saini [5] carried experimental investigations on SAH for fully developed turbulent flow conditions. Absorber plate was provided with protrusion wires of small in diameter. It was observed that due to increase in the roughness pitch, there is decrease in the rate of heat transfer and friction factor as well. It was also found that the increase in relative roughness height decreases the rate of heat transfer enhancement. Mittal and Varshney [6], Prasad and Saini [7] analytically investigated thermo-hydraulic performance of a wire mesh-packed SAH with a mathematic model. Thermal performance of SAH is governed by the porosity of the bed and is also a function of the geometrical parameters of the matrix. Lalji et al. [8] have done experimental and thermal exergy evaluation of packed bed SAH. It was concluded from their results that packed bed SAH with lower porosity performs better than packed bed SAH with higher porosity due to greater turbulence. Naphon [9] developed a mathematical model to predict effect of porosity and thermal conductivity of packed bed on thermal performance of the double-pass flat plate SAH. Lal Singh et al. [10] performed experimental analysis to know the thermal performance of the packed bed solar heat storage system under varying solar and ambient conditions in different months. The study indicated that temperature gain in the packed bed was significantly affected with the input solar insolation. Dhiman et al. [11] investigated the effect of air mass flow rates and bed porosity on the thermal and thermo-hydraulic efficiencies of counter and parallel flow packed bed SAHs. The results showed that the thermal efficiency of the counter flow packed bed SAH is 11–17% more compared to the parallel flow packed bed SAH. Verma and Varshney [12], Sopian et al. [13] have performed investigations on wire screen matrix packed SAH. Comparative study between SAHs with high and low porosity matrices indicates that the efficiency of SAH improves by 26%



with highly porous packed bed compared to packed bed with lower porosity. Thakur et al. [14] conducted experiments on a low porosity packed bed SAH covering a wide range of geometrical parameters of wire screen diameter 0.795–1.40 mm, pitch 2.50–3.19 mm and number of layers from 5 to 12. Paul et al. [15] conducted theoretical analysis and developed a programming code in C to optimize parameters of packed bed used in SAHs. Ho et al. [16] have performed experiment on wire mesh-packed double-pass SAH with external recycle. It was found that double-pass SAH with external recycle gives better heat transfer rates and thermal efficiency. Hassan [17] conducted experiments on a plane SAH with built-in thermal energy storage system. Use of sand as storage material improved daily average efficiency of SAH to 59%. Absorber plate with corrugated set of tubes filled with a PCM increased SAH daily average efficiency to 63.35% with an air outlet temperature 5 °C above its corresponding inlet value. Enibe [18] experimentally tested a single-glazed flat plate SAH with natural convection of air under daytime no-load conditions at Nigeria, over an ambient temperature range of 19–41 °C and a daily global irradiation range of 4.9–19.9 MJ/m<sup>2</sup>. Paraffin wax equally spaced on the absorber plate in modules is used as a storage material. It was found that the maximum predicted cumulative useful and overall efficiencies of SAH are within the ranges 2.5–13% and 7.5–18%, respectively. Aboul-Enein et al. [19] developed a mathematical model to study the effect of geometrical dimensions of collector and spacing between absorber plate and glass cover on temperature rise across SAH. Mahmud Alkilani et al. [20] presented complete literature on recent advances in SAHs with thermal storage units. Murali and Mohan [23] numerically investigated the effect of artificial ribs on the performance of SAH. It is found that modified-arc ribs improved the performance of SAH. Lakshmit and Mohan [24] suggested that SAHs could be used in jaggery making units by providing hot air to preheat the sugarcane juice.

It is found from the literature that studies on the effect of inclination of SAH on its thermal performance are limited. Hence, in the present work, experiments are conducted on SAH with different mass flow rates of air in a range of 0.038–0.0501 kg/s and at different inclinations of the solar air heater in a range of 5°–25° towards solar insolation.

## 2 Experimental Setup and Procedure

A double-pass packed bed SAH present at the rooftop of mechanical engineering department, GVP College of Engineering (A), Vizag, is used to conduct the experiments. Experimental setup used in the present work is shown in Fig. 1. Dimensions of SAH are given in Table 1, and various equipments used in experiment along with their specifications are given in Table 2. Experiments are conducted for twenty continuous days between 11 am to 1 pm every day. SAH is fixed at different inclinations in the range of 5°–25° to the horizontal, and variable speed blower is operated to supply air at different mass flow rates in the range of 0.038–0.0508 kg/s. On first day of the experiment, SAH is fixed at 15° inclination, and blower is operated to

**Fig. 1** Experimental setup

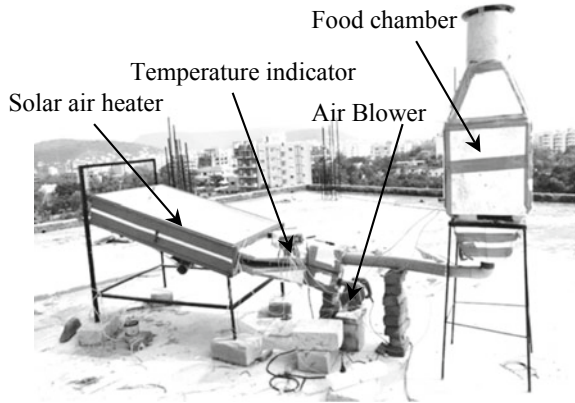


**Table 1** Dimensions of solar air heater

Part	Specification
Upper channel	120 cm × 80 cm × 10 cm
Aspect ratio	8 as per ASHRAE standards
Glass	Thickness 0.5 cm 9600 cm <sup>2</sup> surface area
Packed bed	3 cm thick Mild Steel chips
Absorber plate	GI sheet of 0.4 cm thickness
Insulation	2 cm thick polystyrene
Absorber coating	Blackboard paint

**Table 2** Equipement used for the experiment with specifications

Equipment	Specification
Air blower	Variable speed motor with 0.74 hp
Temperature indicator	Digiquel 12 channel
Thermocouples	J-type (10 in number)
Solar power metre	WACO TM-206 model

supply air at a mass flow rate of 0.038 kg/s. Thermocouples are attached at various locations in the experimental setup, and temperatures are observed at regular time interval between 11 am and 1 pm. Temperature of air at SAH inlet ( $T_1$ ), packed bed ( $T_2, T_3$ ), absorber plate ( $T_4, T_5$ ), upper glass ( $T_6$ ) and air at SAH exit ( $T_7$ ) is manually recorded. Solar insolation ( $I$ ) is measured with solar metre by placing it perpendicular to the upper glass. Experiment is repeated on 2nd, 3rd and 4th day of the experiment with same inclination of SAH and mass flow rate of air equal to 0.041 kg/s, 0.047 kg/s and 0.0508 kg/s, respectively. After that, experiments are repeated at 10°, 15°, 20° and 25° inclinations of SAH and at different mass flow rates of air in the range of 0.038–0.0508 kg/s.

## 2.1 Mathematic Modelling

Thermal efficiency of SAH ( $\eta$ ) is defined as the ratio of useful amount of heat absorbed by air ( $Q_u$ ) to total amount of radiation incident on SAH ( $Q_i$ ). Average values of air temperature at SAH exit and inlet are used to find  $Q_u$ . Similarly, average value of solar radiation incident within a time period between 11 am and 1 pm is used to calculate  $Q_i$ . Expressions for  $Q_u$  and  $Q_i$  are given in Eqs. (1) and (2).

$$Q_u = mC_p(T_7 - T_1) \quad (1)$$

$$Q_i = IA \quad (2)$$

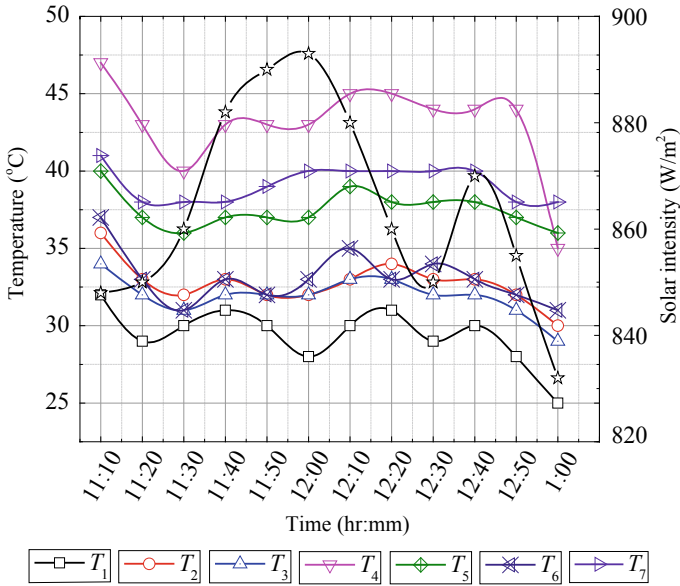
$$\eta = \frac{Q_u}{Q_i} = \frac{mC_p(T_7 - T_1)}{IA} \quad (3)$$

In Eqs. (1)–(3),  $m$  is the mass flow rate of air in kg/s,  $C_p$  is the specific heat of air in J/kg K, and  $A$  is the collector surface area in  $m^2$ .

## 3 Results and Discussion

Values of  $Q_u$ ,  $Q_i$  and  $\eta$  are calculated using Eqs. (1)–(3). At  $15^\circ$  inclination of SAH and mass flow rate of air equal to 0.041 kg/s, variation of temperatures at various locations in SAH and solar intensity with time is shown in Fig. 2. As absorber plate is coated with black paint and placed almost perpendicular to the direction of insolation, it absorbs maximum solar radiation and converts it into heat. As a result, its temperature is higher compared to any location in the experimental setup. Out of total heat available at the absorber plate, a fraction is transferred by convection to the air moving over its top and bottom surfaces, a fraction is lost by conduction through walls, a fraction is lost by convection to the lower glass, and remaining is stored in the packed bed. Hence, at any given instant of time, temperatures of packed bed and glass are higher than air temperature at SAH inlet. Air absorbs heat from packed bed and absorber plate and leaves SAH at temperature higher than its value at SAH inlet but lower than the absorber plate temperature. Similar trends of temperatures with time are observed for other mass flow rates of air and inclinations of SAH.

It is observed that solar intensity gradually increases between 11 am and 12 noon reaches to a maximum value at 12 noon and thereafter decreases up to 1 pm. Average values of air temperature at SAH exit ( $T_7$ ) are calculated from the observations, and its variation with inclination of SAH for different mass flow rates of air is shown in Fig. 3. Thereafter, it decreases with increase in inclination of SAH for all mass flow rates of air. In SAHs, heat transfer conversion rates are maximum when the solar radiation incident at perpendicular, i.e.  $90^\circ$  to the absorber plate. Solar radiation is perpendicular to the absorber plate throughout the day when SAH is inclined at



$T_1$ : Temperature of air SAH inlet,  $T_{2,3}$ : Temperatures of packed bed,  $T_{4,5}$ : Temperature of absorber plate,  $T_6$ : Temperature of upper glass,  $T_7$ : Temperature of air SAH exit.

**Fig. 2** Variation of temperatures and solar intensity with time

**Fig. 3** Variation of air temperature at SAH exit with inclination of SAH

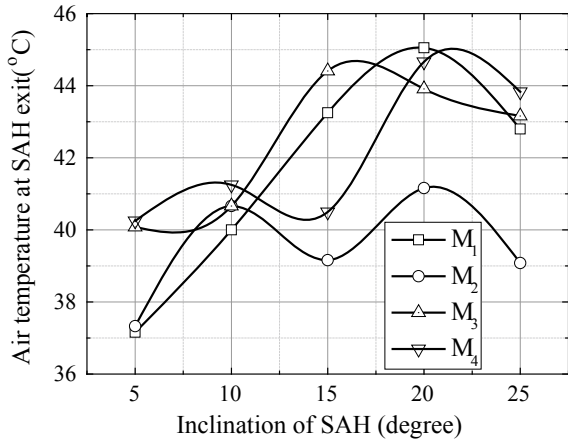
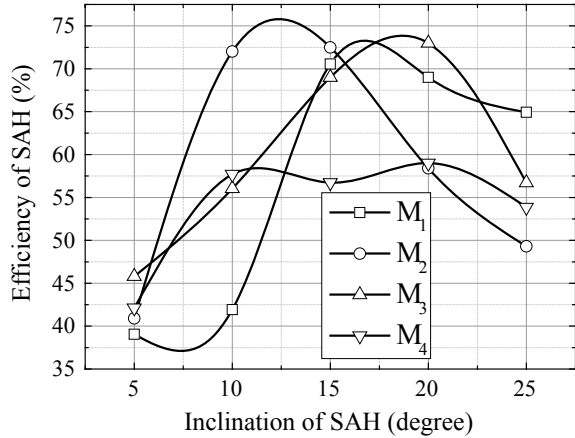


**Fig. 4** Variation of efficiency of SAH with inclination of SAH



15° to 20° to the horizontal. Hence, it is observed from Fig. 3 that  $T_7$  is small at lower inclinations of SAH at all mass flow rates of air. It increases with increase in inclination of SAH and reaches maximum for inclinations in between 15° and 20°. Efficiency of SAH is calculated with average values of air temperature at SAH inlet and exit, and its variation with SAH inclination for different mass flow rates of air is shown in Fig. 4. In Figs. 3 and 4,  $M_1$ ,  $M_2$ ,  $M_3$  and  $M_4$  correspond to mass flow of air equal to 0.038 kg/s, 0.041 kg/s, 0.047 kg/s and 0.0508 kg/s, respectively.

It is observed that variation in efficiency of SAH with inclination of SAH at different mass flow rates of air shows similar trends as air temperature at SAH exit in Fig. 3. Efficiency of SAH is higher at lower mass flow rates of air for lower inclination of SAH with horizontal. Efficiency increases with increase in SAH inclination and mass flow rate of air. Higher mass flow rates up to a limit of  $M_3 = 0.047$  kg/s efficiency increase due to increase in heat transfer coefficients by convection. Further increase in mass flow rates reduces the contact period of air with the absorber plate, and hence, heat transfer coefficients decrease resulting in reduction in SAH efficiency.

## 4 Conclusion

Experiments are conducted to know the effect of inclination of double-pass packed bed solar air heater (SAH) on its thermal performance at different values of mass flow rate of air. It is found that air temperature at SAH exit and efficiency of SAH is strong function of inclination of SAH. Efficiency and air exit temperature are lower for small inclination of SAH. They increase with increase in inclination and reach maximum values when the inclination is in between 15° and 20°. Thereafter, these values are observed to be decreasing with further increase in inclination of SAH.




## References

1. Rajaseenivasan T, Srinivasan S, Srithar K (2015) Comprehensive study on solar air heater with circular and V-type turbulators attached on absorber plate. *Energy* 88:863–873
2. Mahmood AJ, Aldabbagh LY, Egelioglu F (2015) Investigation of single and double pass solar air heater with transverse fins and a package wire mesh layer. *Energy Convers Manage* 89:599–607
3. Lakshmi DVN, Layek A, Muthu Kumar P (2017) Performance analysis of trapezoidal corrugated solar air heater with sensible heat storage material. *Energy Procedia* 109:463–470
4. Varun, Saini RP, Singal SK (2008) Investigation of thermal performance of solar air heater having roughness elements as a combination of inclined and transverse ribs on the absorber plate. *Renew Energy* 33:1398–1405
5. Varshney L, Saini (1998) Heat transfer and friction factor correlations for rectangular solar air heater duct packed with wire mesh screen matrices. *Sol Energy* 62(4):255–262
6. Mittal MK, Varshney L (2006) Optimal thermos-hydraulic performance of a wire mesh packed solar air heater. *Sol Energy* 80:1112–1120
7. Prasad BN, Saini JS (1988) Effect of artificial roughness on heat transfer and friction factor in a solar air heater. *Sol Energy* 41(6):555–560
8. Lalji MK, Sarviya RM, Bhagoria JL (2012) Exergy evaluation of packed bed solar air heater. *Renew Sustain Energy Rev* 16:6262–6267
9. Naphon P (2005) Effect of porous media on the performance of the double-pass flat plate solar air heater. *Int Commun Heat Mass Transfer* 32:140–150
10. Lal Singh P, Deshpandey SD, Jena PC (2015) Thermal performance of packed bed heat storage system for solar air heaters. *Energy Sustain Develop* 29:112–117
11. Dhiman P, Thakur NS., Chauhan SR (2012) Thermal and thermos-hydraulic performance of counter and parallel flow packed bed solar air heaters. *Renew Energy* 46:259–268
12. Verma P, Varshney L (2015) Parametric investigation on thermo-hydraulic performance of wire screen matrix packed solar air heater. *Sustain Energy Technol Assess* 10:40–52, (2015)
13. Sopian K, Alghoul MA, Alfegi EM, Sulaiman MY, Musa EA (2009) Evaluation of thermal efficiency of double pass solar collector with and without porous media. *Renew Energy* 34(3):640–645
14. Thakur NS, Saini JS, Solanki SC (2003) Heat transfer and friction factor correlations for packed bed solar air heater for a low porosity system. *Sol Energy* 74:319–329
15. Paul B, Saini JS (2004) Optimization of bed parameters for packed bed solar energy collection system. *Renew Energy* 29:1863–1876
16. Ho C-D, Lin C-S, Chuang Y-C, Chao C-C (2013) Performance improvement of wire mesh packed double-pass solar air heaters with external recycle. *Renew Energy* 57:479–489
17. Fath HES (1995) Thermal performance of a simple design solar air heater with built in thermal energy storage system. *Renew Energy* 6:1033–1039
18. Enibe SO (2003) Thermal analysis of a natural circulation solar air heater with phase change material energy storage. *Renewable Energy* 28(14):2269–2299
19. Aboul-Enein S, El-Sebaii AA, Ramadan MRI, El-Gohary HG (2000) Parametric study of a solar air heater with and without thermal storage for solar drying applications. *Renewable energy* 21(3–4):505–522
20. Alkilani MM, Sopian K, Alghoul MA, Sohif M, Ruslan MH (2011) Review of solar air collectors with thermal storage units. *Renew Sustain Energy Rev* 15(3):1476–1490
21. da Cunha JP, Eames P (2016) Thermal energy storage for low and medium temperature applications using phase change materials—a review. *Appl Energy* 177:227–238

22. Pielichowska K, Pielichowski K (2014) Phase change materials for thermal energy storage. *Prog Mater Sci* 65:67–123
23. Murali TSVV, Mohan MJK (2019) Thermal performance analysis of artificially roughened solar air heater with ribs: a CFD analysis. *Int. J. Recent Technol Eng (Scopus Indexed with IF 0.03)* 7(6S4):33–38
24. Jakkamputi LP, Mandapati MJK (2016) Improving the performance of jaggery making unit using solar energy. *Perspect Sci (Indexed by Directory of Open Access Journals, DOAJ)* 8:146–150

# Surface Pressure Characteristics over Indian Train Engine



K. Vivek, B. Ashok Kumar, Karthick Dhileep , S. Arunvinthan   
and S. Nadaraja Pillai 

**Abstract** In the present study, the surface pressure distribution of an Indian train engine was experimentally investigated. A scaled model of the engine was tested at different Reynolds numbers ranging from  $3.22 \times 10^4$  to  $14.49 \times 10^4$ . The variation of aerodynamic drag and pressure distribution with Reynolds number were studied. The results show that the pressure distribution is not significantly affected with the Reynolds number and a maximum coefficient of drag of 0.6005 is obtained at a Reynolds number of  $6.44 \times 10^4$ . The mean drag was also calculated for further understanding of drag characteristic of the engine model.

**Keywords** Surface pressure characteristics · Indian train · Drag characteristics

## 1 Introduction

Trains are the most preferred mode of transport in India ferrying about 23.07 million passengers per day with around 12,617 trains per day [1]. This accounts for around 2% of the total population taking the train every day to commute. Improved railway network and accessibility have increased the patronage for trains over the years. To accommodate the surge in rail passengers, it is, therefore, deemed necessary to increase railway services to meet the demand. This, in turn, increases the energy demand for traction of these trains. Hence, it is of prime importance to reduce energy demands to avert the energy crisis prevalent in developing countries. The drag force experienced by a train significantly contributes to its total energy expenditure. With the increase in speed of high-speed trains, the aerodynamic drag force increases thus leading to higher energy consumption [2]. Drag reduction of heavy vehicles is an important area of research as it varies monotonically with the fuel consumption of the vehicle [3]. The effect of the Reynolds number on the aerodynamic forces and pressure distribution of trains were investigated experimentally by Niu et al [4]. It

---

K. Vivek · B. Ashok Kumar · K. Dhileep · S. Arunvinthan · S. Nadaraja Pillai (✉)  
Turbulence and Flow Control Laboratory, SASTRA Deemed University, Thanjavur,  
Tamil Nadu 613401, India  
e-mail: [nadarajapillai@mech.sastra.edu](mailto:nadarajapillai@mech.sastra.edu)

© Springer Nature Singapore Pte Ltd. 2020  
H. K. Voruganti et al. (eds.), *Advances in Applied Mechanical Engineering*,  
Lecture Notes in Mechanical Engineering,  
[https://doi.org/10.1007/978-981-15-1201-8\\_9](https://doi.org/10.1007/978-981-15-1201-8_9)



was found that there was a significant effect of Reynolds number on the pressure coefficient. An experimental study by Choi & Kim [5] investigated the influence of the frontal shape of a train and it was established that a drag reduction of up to 50% can be achieved by altering its shape. The unsteady aerodynamics of high-speed trains has been an important area of interest for a long time. Experiments have confirmed that small-scale experimental techniques provide reliable drag characteristics of high-speed trains [6].

India is projected to have the largest railway network, but studies on the Indian trains are found to be limited. With extensive efforts being taken to reduce the travel time of trains by increasing the speed of the train, it is of utmost importance to study the aerodynamic characteristics of Indian trains to put forth possible design modification for an energy efficient train. The careful optimization of the nose and tail design can possibly reduce the effect of the pressure drag [7]. The aim of this research is to study the surface pressure distribution of the Indian train engine and associated aerodynamic drag.

## 2 Experimental Methodology

### 2.1 Wind Tunnel

The experimental investigation was carried out in a low-speed subsonic wind tunnel (Fig. 1) at the Aerodynamics Laboratory of SASTRA Deemed University. The cross section of the open-circuit suction type wind tunnel is  $300 \times 300$  mm and spans a length of 1500 mm. The flow speed in the test section can vary up to a maximum of 60 m/s and the free-stream turbulence intensity is nearly 0.51%.

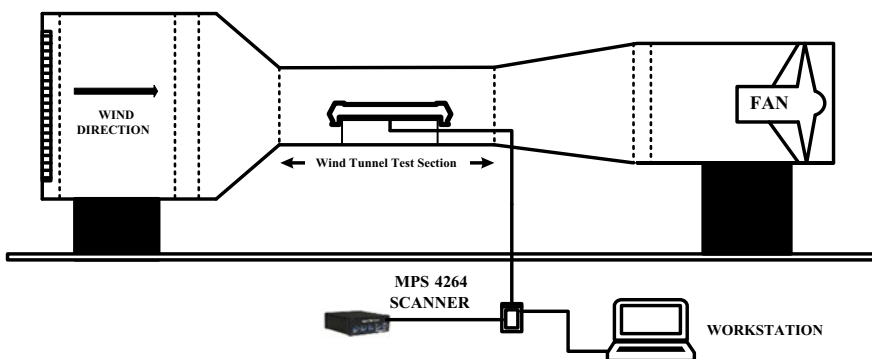


**Fig. 1** Low-speed subsonic wind tunnel

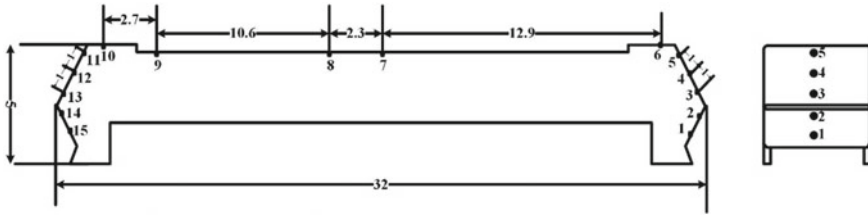


Fig. 2 The engine model and the location of pressure ports (distance between ports in cm)

### 2.2 Model and Instrument

WAP-7 engine was the chosen model for the tests. The schematic diagram of the model is shown in Fig. 2. A 1:60 scale model was designed and was fabricated by 3-D printing using polylactic acid with a resolution of 100 μ. A total of 42 pressure ports were made on the test model out of which only 15 were utilized for the current test. Since the test focuses on measuring the pressure drag, 12 of the pressure ports were arranged on the front and rear part of the model each at a distance of 1 cm from the previous one as shown in Fig. 2. The pressure ports were pneumatically connected to a simultaneous pressure scanner to obtain the surface pressure over the test model.

The model was mounted in the test section of the wind tunnel by a clamp in such a way that it does not hinder the airflow. A 64-channel miniature pressure scanner (MPS 4264) (Fig. 1) of Scanivalve make was used to obtain the simultaneous surface pressure measurements from the model. The sampling frequency had been set at 700 Hz. The number of pressure data collected at each channel was 10,000.

### 2.3 Calculation

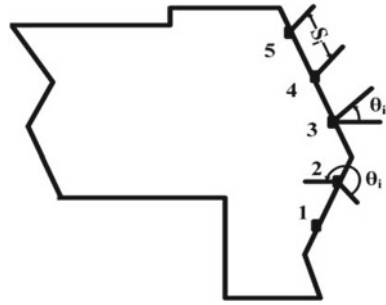
The pressure distribution over the test model is understood by calculating the corresponding values of the coefficient of pressure at each pressure port which is calculated as given in Eq. (1). Drag over the test model is quantified in terms of coefficient of drag as given in Eq. (2).

$$C_p = \frac{P_i - P_\infty}{0.5 \rho v^2} \tag{1}$$

$$C_d = \sum_{i=1}^n C_{pi} s_i \cos \theta_i \tag{2}$$

where ‘C<sub>p</sub>’ is the coefficient of pressure, ‘v’ is the free-stream velocity, ‘C<sub>d</sub>’ is the drag coefficient, ‘s<sub>i</sub>’ is the distance between two pressure ports, ‘θ<sub>i</sub>’ is the angle of

**Fig. 3** Schematic representation of pressure ports



the ports (Fig. 3) , ' $\rho$ ' is the density of free-stream air, and  $(P_1 - P_\infty)$  is the pressure difference measured by the pressure scanner. The Reynolds number is calculated by considering the height of the model as the characteristic length.

### 3 Results and Discussion

#### 3.1 Pressure Distribution

The surface pressure distribution of the WAP-7 test engine model at different Reynolds number is as shown in Fig. 4. The pressure distribution in the front part of the model (port numbers 1–5) is seen to be relatively higher with pressure coefficients ( $C_p$ ) in the range of 0.2–0.8. This range of pressure coefficients is higher than that observed at the rear part of the model. This effect is due to the fact that the frontal region obstructs and slows down the incoming flow, resulting in a high-pressure region [8].

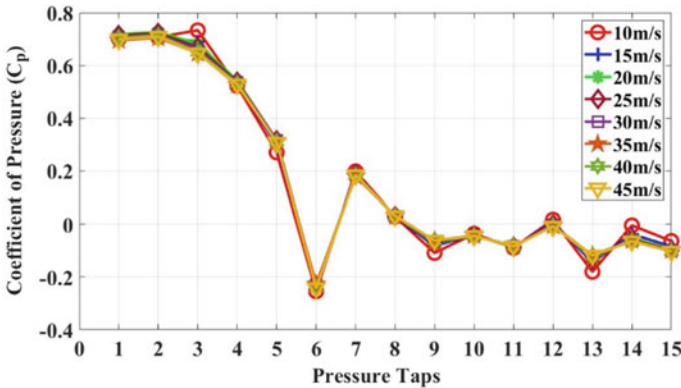


**Fig. 4** Surface pressure distribution of the WAP-7 engine model at various Reynolds numbers

A sharp change in the value of pressure coefficient is observed from port 5 to port 6 where pressure coefficient drops from  $C_p = 0.3075$  to  $C_p = -0.2423$ . Pressure port 6 exhibits the highest negative pressure coefficient which can be attributed to the sharp change in the geometry at the top of the frontal part of the test model. A sharp change in the geometry leads to a sudden drop in the value of pressure coefficient [3] and this drop is attributed to flow separation [9]. Hence, the change in geometry in the frontal region of the engine results in the onset of an adverse pressure gradient causing the flow to separate.

The trend observed in  $C_p$  plot after the pressure port 6 is possibly due to the flow reattachment on the flat upper surface of the test model. As a result, the pressure at ports 7 and 8 gradually approaches the ambient free-stream pressure. A step-like geometry on the rear side of the upper surface is responsible for the significant surge in pressure observed at port 9.

The ports 11–15 are present on the rear side of the train model. The lower pressure on the rear side is indicative of a wake region. The pressure coefficients observed at the rear part of the train show that the flow again separates in close proximity to the port 13 [9].  $C_p$  in the rear part is found to be in the range of  $[-0.0836, -0.133]$ . On observation of the  $C_p$  distribution on the front and the rear part of the model, it is understood that there is an overall pressure difference between them. The differential pressure between the front and rear part of the model is responsible for the development of pressure drag on the model.

The pressure distribution of 15 ports at a velocity of 25 m/s along with the maximum and minimum pressure coefficient values (Max  $C_p$  and Min  $C_p$ ) is as shown in Fig. 5. The figure conveys that there has not been any abrupt fluctuation in the  $C_p$  values encountered during the experiment.

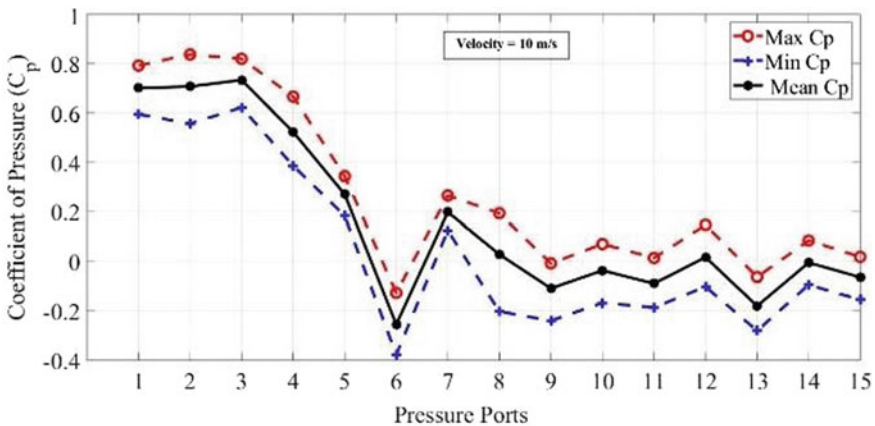


**Fig. 5** Maximum, minimum, and mean pressure coefficient across the length of the model at  $Re = 6.44 \times 10^4$

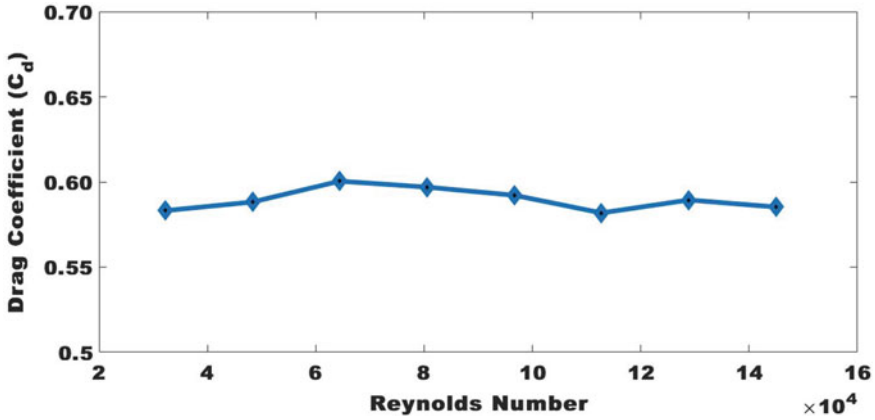


Fig. 6 Variation of  $C_d$  with respect to Reynolds number

### 3.2 Drag Coefficient

The present study is limited to aerodynamic drag characteristics that arise due to pressure distribution over the engine. The pressure drag is the most dominant of the total drag observed for a bluff body [10]. Figure 6 shows the variation of the drag coefficient as a function of Reynolds number. From the figure, it can be inferred that there is no significant change in the coefficient of drag ( $C_d$ ) with the increase in the Reynolds number. The mean drag over the range of Reynolds numbers was found out to be 0.5897. Initially, the WAP-7 test engine configuration had a drag coefficient of 0.5832 at a Reynolds number of  $3.22 \times 10^4$  and 0.5882 at Reynolds number of  $4.83 \times 10^4$ . At Reynolds number =  $6.44 \times 10^4$ , the drag coefficient reaches the maximum value of  $C_d = 0.6005$  which is nearly 1.83% greater than the mean. Following that, the drag coefficient starts reducing until Reynolds number =  $11.27 \times 10^4$ . At Reynolds number =  $12.88 \times 10^4$ , the drag coefficient ( $C_d$ ) undergoes a small increase and then settles down invariably. The drag coefficient ( $C_d$ ) was found to vary negligibly in the range of Reynolds number  $11.27 \times 10^4$  to  $14.49 \times 10^4$ . From these results, it has been identified that the variation of drag coefficient ( $C_d$ ) with respect to Reynolds number ( $Re$ ) is almost consistent with a maximum deviation of 1.83% from the mean drag obtained at Reynolds number =  $6.44 \times 10^4$ .

The reasons for the independence of the drag coefficient with Reynolds number has to be analyzed by further investigation of the flow field over the test model.

## 4 Conclusion

Experimental wind tunnel tests were conducted on a model of an Indian railway engine of WAP-7 type. The primary objective of this experimental investigation was

to analyze surface pressure distribution and drag characteristics of the Indian train engine. The following conclusions are arrived at from the series of tests performed at eight different Reynolds number ranging from  $3.22 \times 10^4$  to  $14.49 \times 10^4$ .

1. The surface pressure distribution on the test model of WAP 7 engine is found to have minimal variations with a change in Reynolds number.
2. The highest value of the coefficient of pressure drag is  $C_d = 0.6005$  which is observed at an air velocity of 20 m/s ( $Re = 6.44 \times 10^4$ ).
3. The overall variation of pressure drag with respect to Reynolds number is found to be minimal. The maximum deviation of 1.83% from the mean pressure drag is reported at a velocity of 20 m/s ( $Re = 6.44 \times 10^4$ ).
4. The mean drag coefficient is observed to be  $C_d = 0.5897$  over the range of Reynolds numbers in which the experiment had been conducted.

The underlying flow phenomenon is to be further examined to arrive at a comprehensive understanding of the drag mechanism. The  $C_d$  could be further reduced by optimizing the geometry of the nose of the engine.

## References

1. Indian Railways Year Book, Ministry of Railways, Govt. of India (2012–2013)
2. Li Z, Yang M, Huang S, Liang X (2017) A new method to measure the aerodynamic drag of high-speed trains passing through tunnel. *J Wind Eng Ind Aerodynam* 171:110–120
3. Kim JJ, Lee S, Kim M, You D, Lee SJ (2017) Salient drag reduction of a heavy vehicle using modified cab-roof fairings. *J Wind Eng Ind Aerodynam* 164:138–151
4. Niu J, Liang X, Zhou D (2016) Experimental study on the effect of Reynolds number on aerodynamic performance of high-speed train with and without yaw angle. *J Wind Eng Ind Aerodynam* 157:36–46
5. Choi J-K, Kim K-H (2014) Effects of nose shape and tunnel cross-sectional area on aerodynamic drag of train travelling in tunnels. *Tunn Undergr Sp Tech* 41:62–73
6. Brockie NJW, Baker CJ (1990) The aerodynamic drag of high speed trains. *J Wind Eng Ind Aerodynam* 34:273–290
7. Baker C (2010) The flow around high speed trains. *J Wind Eng Ind Aerodynam* 277–298
8. Rocchi D, Tomasini G, Schito P, Somaschini C (2018) Wind effects induced by high speed train pass-by in open air. *J Wind Eng Ind Aerodynam* 173:279–288
9. Niu J, Wang Y, Zhang L, Yuan Y (2018) Numerical analysis of aerodynamic characteristics of high-speed train with different train nose lengths. *Int J Heat Mass Transf* 127:188–199
10. Niu J, Zhou D, Liang X (2017) Experimental research on the aerodynamic characteristics of a high-speed train under different turbulent conditions. *Exp Therm Fluid Sci* 80:117–125

# Exergy Modelling of a Coal-Fired MHD Power Plant



Prabin Haloi and Tapan Kumar Gogoi

**Abstract** Energy quality can be best measured through the application of the proven method of exergy analysis. Exergy analysis of thermal systems provides a better way to determine the deficient sub-components and also estimate the amount of losses that occurred in such components. The present work models a coal-fired open-cycle Magneto-hydrodynamics (MHD) power generation system in terms of exergy analysis. The exergy analysis is carried out side-to-side energy analysis in order to determine the components with major energy losses and exergy destruction in the modelled plant. It is observed that the nozzle has the maximum energy losses as well as exergy destruction followed by the generator. Energy losses for the compressor, combustor, air preheater, seed recovery unit, sulphur removal unit and the stack showed a higher value of energy losses in comparison to that of exergy destruction values in these components. From the exergy point, it has been found that the components that require most improvement are the nozzle and the generator.

**Keywords** Magneto-hydrodynamics · Energy loss · Exergy · Exergy destruction

## Nomenclature

$\xi^{0, ch}$	Chemical exergy of dry coal (kJ/kg)
NCV	Net calorific value (kJ/kg)
$\emptyset_{dry}$	Ratio of chemical exergy to NCV (dimensionless)
HHV	Higher heating value (MJ/kg)
$T(K)$	Temperature (K)
$\dot{m}$	Mass flow rate (kg/s)
p	Pressure (bar)

---

P. Haloi (✉) · T. K. Gogoi  
Department of Mechanical Engineering, Tezpur University, Tezpur, Assam 784028, India  
e-mail: [haloi\\_p@tezu.ernet.in](mailto:haloi_p@tezu.ernet.in)

T. K. Gogoi  
e-mail: [tapan\\_g@tezu.ernet.in](mailto:tapan_g@tezu.ernet.in)

© Springer Nature Singapore Pte Ltd. 2020  
H. K. Voruganti et al. (eds.), *Advances in Applied Mechanical Engineering*,  
Lecture Notes in Mechanical Engineering,  
[https://doi.org/10.1007/978-981-15-1201-8\\_10](https://doi.org/10.1007/978-981-15-1201-8_10)

$\dot{Q}_{cv}$	Heat input to control volume (kJ/kg)
$\dot{W}_{cv}$	Work done (kJ/kg)
$\dot{Q}_z$	Instantaneous heat (kJ/kg)
$\dot{\epsilon}$	Specific exergy rate (kJ/kg)
$\dot{\xi}_w$	Exergy rate of work (MW)
$\dot{E}_{loss}$	Energy loss rate (MW)
$R$	Universal gas constant (kJ/kmol K)
$\bar{s}$	Absolute entropy (kJ/kmol K)
$\bar{s}_k^0$	Standard entropy of formation of the $k$ -th element (kJ/kmol K)

## 1 Introduction

Thermal system analysis is one of the crucial parts in estimating the overall performance of a thermal plant. In any thermal system, various losses may incur leading to a less efficient system with a low output. It is thereby necessitated to undertake certain analysis in order to estimate the cause and location of such losses and consider suitable preventive measures to minimize the deficiencies. Analysis based on the first law of thermodynamics also called the energy analysis alone if carried out fails to rightly predict the correct scenario of energy utilization as have been mentioned in various literature on thermodynamics [9, 14]. On the other hand, the exergy analysis as reported by different authors is a better approach to find the quality of energy by rightly pointing to the amount, causes and location of losses within a system or in system components. Going beyond exergy, there are other major contributions that are found towards more advanced method for exergy analysis through splitting of exergy destruction [11, 13] and exergo-economic analysis which also takes into account the related cost. Contributions in understanding the basics of exergy and exergy analysis of thermal systems [8, 12, 14] have been lucidly described. Exergy or availability is the maximum theoretical work that can be extracted from an energy system when a system or its components are brought to equilibrium with its environment while considering only heat transfer as the mode of interaction with the environment. Exergy analysis measures both the physical and chemical components of exergy taking into account the restricted dead state and the dead state [14] and accordingly termed them as thermo-mechanical and chemical exergies. While considering exergy, the chemical exergy of elements and the effects of preheating [8, 10] are well illustrated. Though there are innumerable contributions towards the exergy and advanced exergy analysis of thermal systems, the same for an MHD-based plant has not been elaborated. For MHD plant analysis, works on varied aspects have been reported in the literature and a number of published contributions can be found.

Performance analysis of MHD-based integrated systems has achieved a higher efficiency [1] when syngas is used instead of direct coal combustion. Supersonic inlet has been considered to obtain optimum power extraction [2] where the critical interaction parameters remain passive at the exit of MHD generator. MHD power



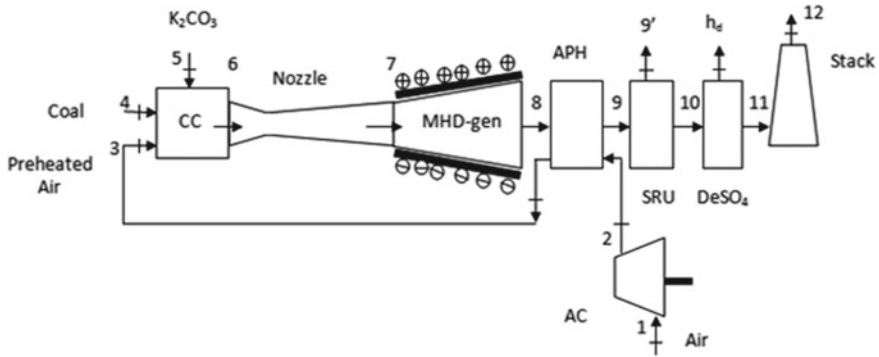


**Fig. 1** Schematic of the MHD power generation system

system has been analysed, and the processes involved in MHD power generation were discussed [3]. Enhancement in power generation using MHD system [4] has been reported. Performance analysis of MHD power cycles at maximum power density increases MHD cycle efficiency [5]. Performance and stability of MHD generator under the effect of ionized seed plasma [6] have been studied considering varied seed fractions. The nozzle efficiency is found to be almost independent of either the area ratio or Mach number at nozzle exit. The maximum voltage and power increase with the increase in area ratio [7]. Analysis of the preheating of combustion reactants reduces chemical energy uses and improves scope for increasing lean fuel in gaseous fuel mixture [8]. Although a large number of contributions towards the development of MHD power generation system are available, the exergy approach to MHD is still underdeveloped.

The present work considers an MHD power generation system using the exergy method of analysis. A Magneto-hydrodynamics power generation system works on the principle of Faraday’s laws of electro-magnetic induction. An MHD system has the advantages of direct conversion of heat to electricity with the added advantages of absence of rotational parts, higher temperature ranges, low emission of  $SO_x$ ,  $NO_x$ , higher conversion efficiency and moreover the conventional and other non-conventional power generation systems. An MHD power system operates in either an open-cycle or a closed-cycle mode. In an open-cycle system, the combustion of fossil fuels in the presence of seed at a very high temperature results in ionized product which is then fed at a high velocity to the generator subjected to a strong magnetic field applied transversely. A closed-cycle MHD uses a compressed seeded noble gas which is recirculated.

## 2 Combustion Analysis

The fuel for analysis is coal from coal fields of Assam with average (% wt): C—75.59, H—5.8, S—2.825, O—14.89, N—1.47, A—6.8, M = 6.0, VM = 47% on an as-received basis. With air molar analysis (%) [14]: N<sub>2</sub> = 77.48, O<sub>2</sub> = 20.59, CO<sub>2</sub> = 0.03, H<sub>2</sub>O = 1.9, the combustion reaction equation of coal with air is given as

$$f(aC + bH + cO + dN + eS) + (0.7748N_2 + 0.2059O_2 + 0.0003CO_2 + 0.019H_2O) \rightarrow (1 + f)[x_1N_2 + x_2O_2 + x_3CO_2 + x_4H_2O + x_5SO_2] \quad (1)$$

where  $x_1, x_2, x_3, x_4, x_5$  are the mole fractions of nitrogen, oxygen, carbon dioxide, water and sulphur dioxide in gas phase, respectively, obtained accordingly from balancing the elements and  $f, a, b, c, d, e$  are the fuel-to-air ratio and the mass fractions of coal composition. The chemical exergy of dry coal and the heating values of coal are estimated from Eqs. (2)–(5) using [9, 15] correlations.

$$\xi^{0, ch} = [NCV + wh_{fg}] \times \emptyset + 9417s \left( \frac{\text{kJ}}{\text{kg}} \right) \quad (2)$$

$$\emptyset_{dry} = 1.0437 + \frac{0.1882h + 0.0610(o) + 0.0404n}{c} \quad (3)$$

where  $w$  and  $h_{fg}$  are the mass fraction of moisture in fuel and enthalpy of evaporation of water at standard temperature (Table 1).

$$HHV = 0.3491C + 1.1783H + 0.1005S - 0.1034O - 0.0211A - 0.015N \quad (4)$$

and

$$LHV = HHV - 2.442m_w \quad (5)$$

Considering the reference environment at 298.15 K and 1 bar, the constant-pressure adiabatic flame temperature has been computed. Assuming compressor pressure ratio of 10.0, an air preheat temperature of 1900 K and pressure drops for air and gases with isentropic flow for nozzle and generator, the pressure and temperature are suitably estimated at all state points. Mass flow rate of fuel is evaluated using computed overall conversion efficiency of 0.295, heating value and heat rate. Subsequently, the mass flow rates of air and combustion products are determined.

**Table 1** Determination of fuel-air ratio, heating values and chemical exergy of dry coal

f	HHV (MJ/kg)	LHV (MJ/kg)	$\xi^{ch}$ (MJ/kg)	$\emptyset_{dry}$
0.07181	31.8026	24.7208	26.897	1.07092

**Table 2** Determination of  $T$ ,  $p$  and  $\dot{m}$ 

Variables	State points						
	1	2	3	4	5	6	7
$\dot{m}$ (kg/s)	50.61	50.61	50.61	3.634	0.5424	54.2364	54.2364
$T$ (K)	298.15	621	1900	298.15	298.15	5000	3147
$p$ (bar)	1	10.0	9.5	1.0	2.0	20	2.6134
Variables	State points						
	8	9	9'	10	$h_d$	11	12
$\dot{m}$ (kg/s)	54.2364	54.2364	0.5424	54.2364	54.2364	54.2364	54.2364
$T$ (K)	1967	1011	1011	991	991	971	874.2
$p$ (bar)	2.5088	2.4085	2.4085	2.36034	2.36034	2.3131	2.1975

**Table 3** Energy–exergy balance equations of MHD components

Components	Energy balance	Exergy balance
Air compressor	$-\dot{w}_{AC} = \dot{m}_1(h_1 - h_2)$	$-\dot{w}_{cv} = (\dot{\xi}_1 - \dot{\xi}_2)$
Combustor	$\dot{m}_6 h_6 - \dot{m}_3 h_3 - \dot{m}_4 h_4 - \dot{m}_5 h_5 = \dot{Q}_{CC,MHD}$	$\dot{\xi}_6 - \dot{\xi}_3 - \dot{\xi}_4 - \dot{\xi}_5 = \dot{\xi}_D$
Nozzle	$\dot{m}_6(h_6 - h_7) = \dot{m}_6 \frac{v_7^2}{2}$	$(\dot{\xi}_6 - \dot{\xi}_7) - \dot{\xi}_D = 0$
Generator	$\dot{w}_e = \dot{m}_7(h_7 - h_8)$	$\dot{w}_e = (\dot{\xi}_7 - \dot{\xi}_8) - \dot{\xi}_D$
Air preheater	$\dot{m}_8(h_8 - h_9) - \dot{m}_2(h_3 - h_2) = 0$	$(\dot{\xi}_8 - \dot{\xi}_9) - (\dot{\xi}_3 - \dot{\xi}_2) = \dot{\xi}_D$
Seed recovery unit (SRU)	$\dot{Q}_{SRU} - [\dot{m}_9 h_9 - \dot{m}_9 h_{9'} - \dot{m}_{10} h_{10}] = 0$	$\dot{\xi}_9 - \dot{\xi}_{9'} - \dot{\xi}_{10} = \dot{\xi}_D$
Desulphurization unit (DeSO <sub>4</sub> )	$\dot{Q}_{DeSO_4} = [\dot{m}_{10} h_{10} - \dot{m}_{h_d} h_{h_d} - \dot{m}_{11} h_{11}]$	$\dot{\xi}_{10} - \dot{\xi}_{11} - \dot{\xi}_{h_d} = \dot{\xi}_D$
Stack	$\dot{m}_{11}(h_{11} - h_{12}) = \dot{m}_{11} \frac{v_{11}^2}{2}$	$\dot{\xi}_{11} - \dot{\xi}_{12} - \frac{v_{11}^2}{2} = \dot{\xi}_D$

Table 2 illustrates the evaluated values for mass flow rates, pressure and temperatures at various state points.

In Table 2, states 1, 2 and 3 denote values for air, 4 and 5 are the values for fuel and seed and from 6 to 12 are those for the combustion exhaust.

## 2.1 Absolute Enthalpy and Entropy of Air, Combustion Products and Fuel at Various States

The absolute enthalpies and entropies at the reference states for calculating the thermo-mechanical exergies at the states 1, 2, 3, 4..., 12 are calculated using relations

as depicted [14]. The molar enthalpies for air at states 1, 2, 3 and for the combustion products at states 6–12 can be determined using the relations Eqs. (6) and (7).

$$\bar{h}_{\text{air}} = 0.7748\bar{h}_{\text{N}_2}(T) + 0.2059\bar{h}_{\text{N}_2}(T) + 0.0003\bar{h}_{\text{CO}_2}(T) + 0.019\bar{h}_{\text{H}_2\text{O}}(T) \quad (6)$$

$$\bar{h}_{\text{product}} = 0.7234\bar{h}_{\text{N}_2}^0 + 0.1971\bar{h}_{\text{O}_2}^0 + 0.051\bar{h}_{\text{CO}_2}^0 + 0.031867\bar{h}_{\text{H}_2\text{O}}^0 + 0.001867\bar{h}_{\text{SO}_2}^0 \quad (7)$$

For coal at state 4, the enthalpy is calculated as

$$\bar{h}_{\text{coal}} = 0.7559\bar{h}_{f,C}^0 + 0.058\bar{h}_{f,H}^0 + 0.1489\bar{h}_{f,O}^0 + 0.0147\bar{h}_{f,N}^0 + 0.02825\bar{h}_{f,S}^0 \quad (8)$$

The absolute entropy for any state can be obtained from

$$\bar{s}_i = \sum_k x_k \bar{s}_k \quad (9)$$

where ‘ $k$ ’ denotes the component in the given mixture or coal and ‘ $i$ ’ is the state point, and

$$\bar{s}_k = \bar{s}_k^0 - R \ln \frac{P_k}{P_0} \quad (10)$$

### 3 Exergy Modelling of the MHD Plant

The exergy model for the MHD plant constitutes both energy and exergy balances for the sub-components.

For a steady-state steady flow process, the mass and energy balances are given by

$$\sum_{\text{in}} \dot{m}_{\text{in}} = \sum_{\text{out}} \dot{m}_{\text{out}} \quad (11)$$

$$\dot{Q}_{\text{cv}} + \sum_{\text{in}} \dot{m}_{\text{in}} h_{\text{in}} = \dot{W}_{\text{cv}} + \sum_{\text{out}} \dot{m}_{\text{out}} h_{\text{out}} \quad (12)$$

The exergy for similar SSSF process for the control volume is given as

$$\sum_z \left(1 - \frac{T_0}{T_z}\right) \dot{Q}_z + \sum_{\text{in}} \dot{m}_{\text{in}} \dot{e}_{\text{in}} = \dot{\xi}_w + \sum_{\text{out}} \dot{m}_{\text{out}} \dot{e}_{\text{out}} + \dot{\xi}_D \quad (13)$$

where  $z$  is the instantaneous value and ‘ $\dot{\xi}_D$ ’ denotes the exergy destruction rate.

### 3.1 Energetic–Exergetic Equations for the MHD System Components

The components of the MHD plant are analysed using energy and exergy balance equations as follows.

## 4 Results

The total exergy rate at all state points is determined after evaluating the thermo-mechanical and chemical exergies of flow streams. The values of total exergy rate at each state of the flow stream in Table 4 are used to determine the exergy destruction and energy losses in components using the equations illustrated in Table 3. The component-wise energy losses and exergy destruction are shown in Table 5.

From the data in Table 5, it is observed that the nozzle has the maximum amount of energy losses and exergy destruction followed by the generator. The air preheater, combustor, air compressor and the seed recovery unit are in the same sequence in terms of energy losses or exergy destruction. The difference is observed in case of

**Table 4** Calculation of total exergy rates

State	$\dot{\xi}_i^t$ (MW)	State	$\dot{\xi}_i^t$ (MW)
1	0.000	8	85.6605
2	14.621	9	28.2605
3	69.048	9'	0.2158
4	115.5287	10	26.7764
5	0.34625	$h_d$	0.9063
6	252.5945	11	24.3004
7	134.4566	12	23.0898

**Table 5** Evaluation of energy losses and exergy destruction rates

Component	$\dot{E}_{loss}$ (MW)	$\dot{\xi}_D$ (MW)
Air compressor	16.576	1.93511
Combustor	17.662	47.899
Nozzle	118.410	117.46
MHD generator	43.706	48.7961
Air preheater	20.216	2.973
Seed recovery unit(SRU)	4.8148	1.2683
Desulphurization unit	34.4181	1.5697
Stack	4.93926	1.2106

the sulphur removal unit which is the third most energy loss component, whereas it is the second to last component in terms of exergy destruction value.

## 5 Conclusion

The exergy analysis of a coal-fired MHD power generation depicts the nozzle with maximum losses. The generator of the MHD plant is the next component where further improvement is sought based on the results obtained in terms of energy loss and exergy destruction. Further analysis combining MHD with other systems will be able to provide a better picture on the use of MHD and its real potential as a power generation system. Both the energy and exergy analyses have shown a similar trend in losses except the desulphurization unit. Though the trend of losses stands on similarity, there are differences in values for a given component. The combustor, compressor, seed recovery unit, the sulphur minimizer and the stack have a lower exergetic destruction values when compared to the corresponding energy losses.

**Acknowledgements** The authors of this present work are thankful to all the authors and contributors whose contributions towards the development of Magneto-hydrodynamics have been a source of inspiration to get ourselves involved in this area of work. We, the authors of this work are indebted to the creators of this vast area of Magneto-hydrodynamics.

## References

1. Cicconardi PS, Perna A (2014) Performance analysis of integrated systems based on MHD generators. *Energy Procedia* 45:1305–1314
2. Aithal SM (2009) Characteristics of optimum power extraction in a MHD generator with subsonic and supersonic inlets. *Energy Convers Manage* 50:765–771
3. Krishnan RA, Jinshah BS (2013) Magneto-hydrodynamic power generation. *Int J Sci Res Publ* 3(6):1–11
4. Poonthamil R, Prakash S, Varma AK (2016) Enhancement of power generation in thermal power plant using MHD system. *IOSR J Mech Civil Eng.* 13:142–146
5. Sahin B, Ali K, Hasbi Y (1996) A performance analysis for MHD power cycles operating at maximum power density. *J Phys D Appl Phys* 29:1473–1475
6. Murakami T, Nakata Y, Okuno Y, Yamasaki H (2003) An analytical study of the plasma conditions and performance of an MHD generator. *Electr Eng Japan* 144(2):9–15
7. Haloi P, Gogoi TK (2018) Performance analysis of a coal-fired open cycle MHD plant at constant subsonic inlet nozzle mach number with variation in nozzle area-ratio. In: *Proceedings of the international conference on recent innovations and developments in mechanical engineering*, NIT Meghalaya, Shillong
8. Szargut J (1988) Energy and exergy analysis of the preheating of combustion reactants. *Int J Energy Res* 12:45–58
9. Kotas TJ (2012) *The exergy method of thermal plant analysis*. Exergon Publishing Company UK Ltd., London
10. Szargut J (1989) Chemical exergies of the elements. *J Appl Energy* 32:269–286

11. Tsatsaronis G, Morosuk T (2012) Advanced thermodynamic (exergetic) analysis. In: 6th European thermal sciences conference (Eurotherm 2012). Journal of Physics: Conference Series, vol 395, pp 12–16. <https://doi.org/10.1088/1742-6596/395/1/012160>
12. Bejan A (2002) Fundamentals of exergy analysis, entropy generation minimization, and the generation of flow architecture. *Int J Energy Res* 26:545–565. <https://doi.org/10.1002/er.804>
13. Tsatsaronis G, Morosuk T (2009) Advanced exergetic analysis: approaches for splitting the exergy destruction into endogenous and exogenous parts. *Energy* 34:384–391. <https://doi.org/10.1016/j.energy.2008.12.007>
14. Bejan A, Tsatsaronis G, Moran M (1996) *Thermal design and optimization*. Wiley, New York
15. Channiwala SA, Parikh PP (2002) A Unified Correlation for estimating HHV of solid, liquid and gaseous fuels. *Fuel* 81:1051–1063. [https://doi.org/10.1016/S0016-2361\(01\)00131-4](https://doi.org/10.1016/S0016-2361(01)00131-4)

# Design, Development and Analysis of Intake Manifold of Single-Cylinder Diesel Engine



Nikhil A. Bhave, Mahendra M. Gupta, Sandeep S. Joshi, Mohan G. Trivedi and Neeraj Sunheriya

**Abstract** Engines are one of the greatest Mechanical Engineering application developed in 90s. Compression ignition engines are very robust, durable and efficient. The volumetric efficiency of CI engine is higher because of absence of throttle losses in comparison to SI engine. The flow of air through the intake manifold considerably affects the power and volumetric efficiency of CI engines. In present investigation, existing intake manifold of CI engine is modified and manufactured by additive manufacturing technique. The optimized design was finalized by undergoing computational fluid dynamic analysis. The new intake manifold is fitted to the engine intake and performance tests were performed. For all load conditions, the volumetric efficiency, brake power and brake thermal efficiency were considerably improved. The brake specific fuel consumption was also reduced.

**Keywords** Intake manifold · CI engine · CFD analysis

## 1 Introduction

The air flow through the engine intake system greatly affects the performance of CI engine. The components involved in the gas exchange process are intake valve opening and closing area, dimensions of the intake and exhaust valves, number of valves per cylinder, location of fuel injector, intake and exhaust port geometry and intake and exhaust manifold design. Small variations in any one of the above parameters can significantly affect the performance of engine. In the present investigation, the design of intake manifold is being considered [1]. The single-cylinder diesel engines have been focused upon to increase the thermal efficiency by various researchers all over the world. But the work related to increase in volumetric efficiency of CI engine has been rarely reported. Wentsch et al. [2] investigated factors influencing the

---

N. A. Bhave (✉) · M. M. Gupta · S. S. Joshi · M. G. Trivedi  
Shri Ramdeobaba College of Engineering and Management, Nagpur 440013, India  
e-mail: [bhavena1@rknc.edu](mailto:bhavena1@rknc.edu)

N. Sunheriya  
National Institute of Technology, Raipur 492013, India

© Springer Nature Singapore Pte Ltd. 2020  
H. K. Voruganti et al. (eds.), *Advances in Applied Mechanical Engineering*,  
Lecture Notes in Mechanical Engineering,  
[https://doi.org/10.1007/978-981-15-1201-8\\_11](https://doi.org/10.1007/978-981-15-1201-8_11)



hollow cone jet propagation, fuel distribution and therewith directly associated back flow into the intake manifolds. Guo et al. performed reverse engineering approach to optimize the design of intake manifold of multi-cylinder engine. It was found in his investigation that reverse technology is reasonable for the intake manifold design through the theory and simulation analysis; it can ensure sufficient air intake and reduce the resistance in intake, the energy loss of the air was also reduced and it resulted in improved air intake uniformity [3].

## 2 Experimental Setup Details and Methodology

In the present investigation, a stationary, single cylinder, four-stroke, 5 BHP/1500 rpm, water cooled, direct injection (DI) comet diesel engine was used. The engine is coupled with a rope brake dynamometer. The brake drum can be loaded by maximum of 12 kg and spring balance is attached to the other end. A calorimeter is installed to the exhaust manifold which is a concentric tube heat exchanger. The exhaust gases are cooled by cooling water through the heat exchanger. The dynamometer is continuously cooled by supply of cold water. Cooling water is circulated through the jackets to cool the engine. An air box fitted with an orifice plate is installed at the inlet air side to measure the air flow rate, while the calibrated buret is present for fuel measurement.

The engine is also equipped with power transducer for load measurement, piezo sensor and amplifier for pressure measurement, a crank angle encoder, water flow meter, RPM indicator and fuel flow sensor. Thermocouples are attached at intake and exhaust port, calorimeter inlet and outlet of water and exhaust gas and ambient cooling water inlet and outlet. A high-speed data acquisition system collects the data signal and sends it to a computer equipped with an INTEL i7 core to duo processor. A powerful software for studying different performance parameters of the engines such as BP, BSFC, A:F, BSEC and so on is also installed in the computer.

The design of existing engine manifold is as shown in Fig. 5. Previously, the overall length of the manifold was 160 mm. It was having a 90° bend in the middle section. The bend is responsible for energy loss. Loss in energy results in decrease in air flow through the intake manifold. This results in lesser volumetric efficiency and power. The aim of this research work is to design an intake manifold which will increase the power and efficiency of the engine. The design was to be optimised based on the overall length and the angle of bend. Thus, ANSYS 14 FLUENT, was used to perform CFD simulation of fluid flow through the pipe. Firstly, the bend was considered with angles 90°, 60°, 30°, 15° and 0°. Secondly, the further consideration was made to create a converging–diverging nozzle which will accelerate the flow at the outlet of manifold. Thirdly, the manifold was manufactured by additive manufacturing technique as shown in Fig. 8. The experimentation was performed on Kirloskar AV1 direct injection CI engine. The air flow rate, fuel flow rate, engine RPM and brake power were measured by flow anemometer, buret method, shaft encoder and rope brake dynamometer, respectively.

### 3 Results and Discussions

The flow through the pipe has Mach number less than 0.3. Therefore, the flow is considered to be incompressible. The roughness of the pipe was considered negligible and flow condition is considered as inviscid. The value of velocity was selected corresponding to mass flow rate calculated experimentally. At inlet to the manifold, the constant velocity of 7 m/s was considered for all cases of calculations Tables 1 and 2 present the details of grid formation and boundary conditions, respectively.

In the first case, the pressure drop went on decreasing with the increase in angle as seen in Figs. 1, 2, 3, 4 and 5. If the Bernoulli’s equation is applied to the pipe flow, the head loss due to friction is very small. However, the head loss due to velocity component in bend is higher. The  $k$  value for  $[k(0.45 \text{ to } 4.5)V^2/2g]$  was selected based on the bend angle. The calculation of pressure drop is in the range of 0–10 Pa. The simulations results are close to analytical results performed. The value of pressure drop seems to be very small since the length is small. The details have been presented in Table 3.

It was inferred that a straight pipe will definitely increase the volumetric efficiency of the engine [4]. The acceleration of the charge can further enhance the efficiency of the engine. So another consideration was performed to model a nozzle with same

**Table 1** Details of mesh formation

<i>Sizing</i>	
Use advanced size function	On: curvature
Relevance center	Fine
Initial size seed	Active assembly
Smoothing	Medium
Curvature normal angle	Default (18.0°)
Min size	Default (5.0764e−004 m)
Max face size	Default (5.0764e−002 m)
Max size	Default (0.101530 m)
Growth rate	Default (1.20)
Minimum edge length	0.6350 m
<i>Inflation</i>	
Use automatic inflation	None
Inflation option	Smooth transition
Transition ratio	0.272
Maximum layers	5
Growth rate	1.2
<i>Statistics</i>	
Nodes	25,737
Elements	23,664

**Table 2** Details of boundary conditions adopted

Fluent setup input parameters	
Solver type	Density based
Model	Energy equation, viscous Inviscid
Material	Air-real gas Redlich–Kwong
Cell zone—operating pressure	40 Pa
Boundary conditions	Velocity inlet: 7 m/s Pressure outlet: 0 Pa
Current number	06
Solution initialization	Standard from inlet
Solution method	Second-order upwind

**Fig. 1** Pressure and velocity profile for 0° bend

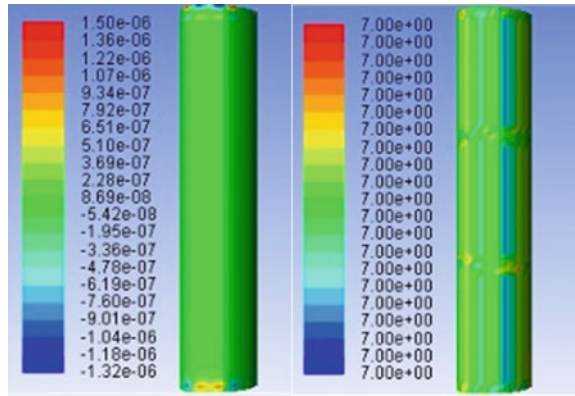


**Fig. 2** Pressure and velocity profile for 15° Bend

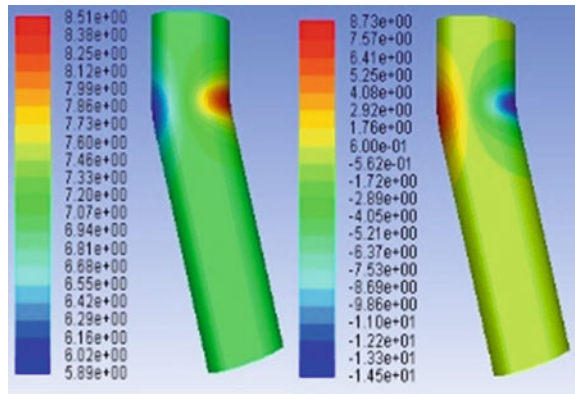


**Fig. 3** Pressure and velocity profile for 30° bend

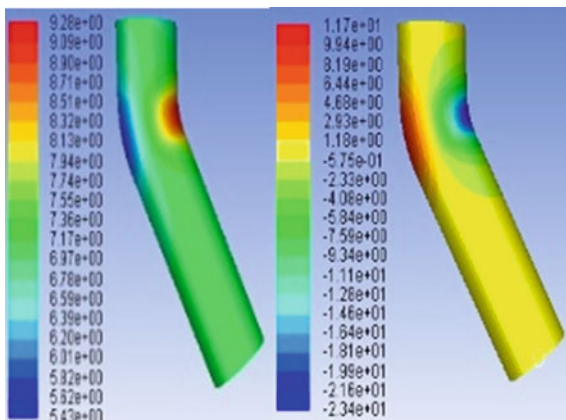


**Fig. 4** Pressure and velocity profile for 60° bend

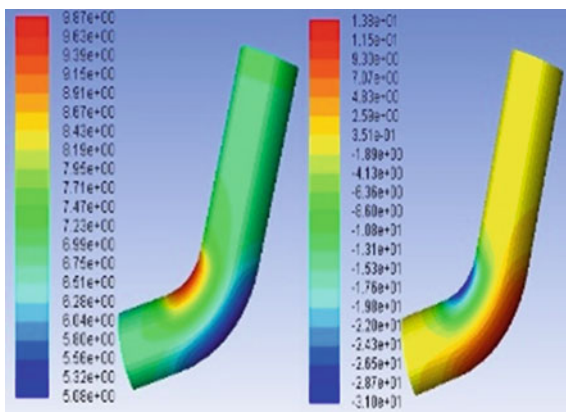


**Fig. 5** Pressure and velocity profile for 90° bend

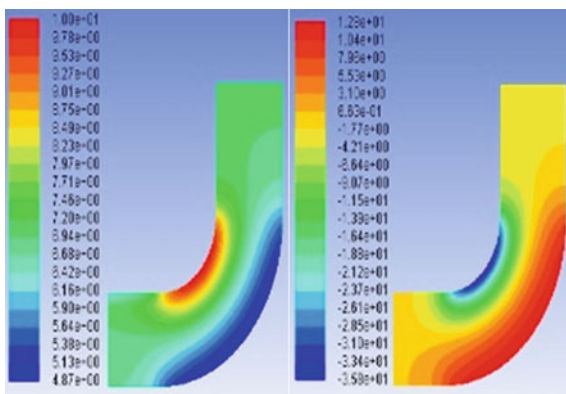


**Table 3** Variation of pressure drop and velocity with angle of bend

Angle of bend	Pressure drop (pascal)	Exit velocity (m/s)
90	5.975	6.93
60	2.239	6.99
30	0.605	7.17
15	0.001	7.07
0	0.000001	6.999999

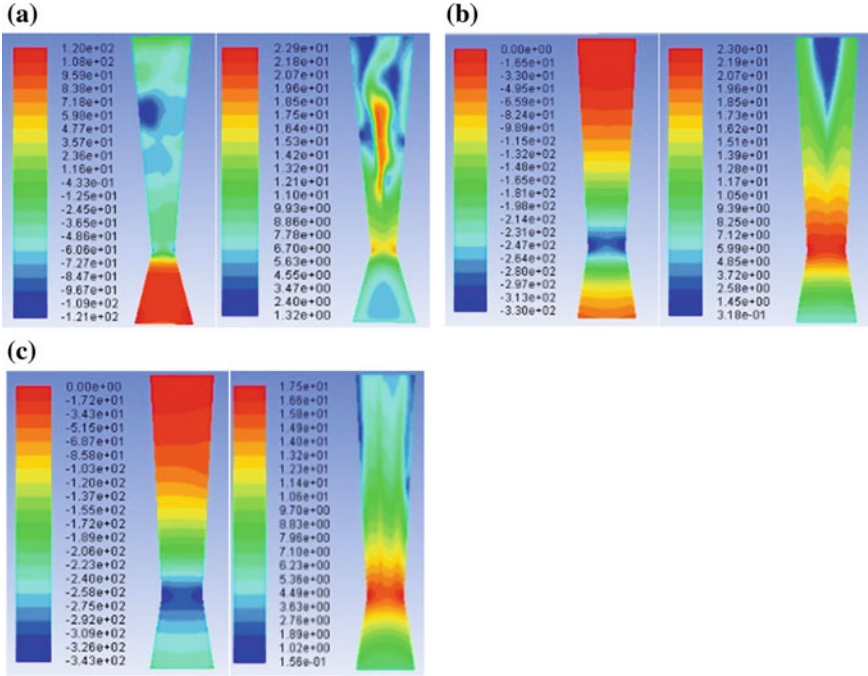


**Fig. 6** a Pressure and velocity profile for 40-12, b pressure and velocity profile for 40-16, c pressure and velocity profile for 40-20

length of pipe. Various design of converging–diverging nozzle was done by varying the convergence length and throat diameter. The convergence length was varied from 40 to 75 mm, while the throat diameter was varied from 12 to 20 mm such what the nozzle angle does not exceed 6°. Simulations were performed and results for pressure drop and exit velocity is presented in Table 4. Note that the names of figures are given in terms of “Converging length–Diameter of Throat i.e. 40–12, 40–16 etc.”. Figure 6 shows the variation of pressure and velocity in 40 mm diameter pipe with throat diameter of 12 mm, 16 mm and 20 mm, respectively. The same logic of figure nomenclature applies to Figs. 7, 8, 9, 10 and 11.

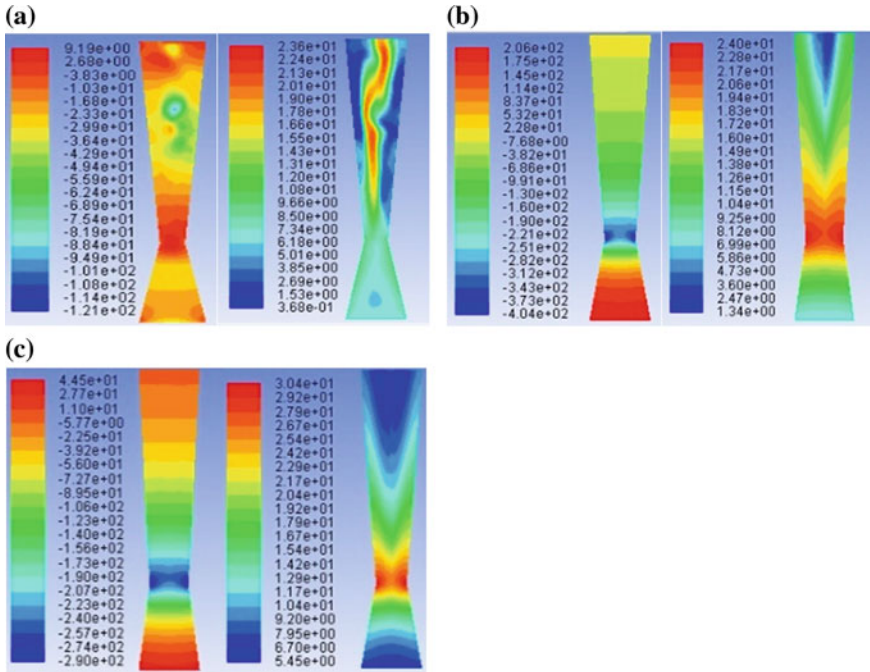


**Fig. 7** a Pressure and velocity profile for 45-12, b pressure and velocity profile for 45-16, c pressure and velocity profile for 45-20

Following are the observations from the above CFD simulation (Figs. 12 and 13).

- (1) As the converging length is varied keeping the throat diameter 12 mm, it was found that the least pressure was obtained at throat with higher converging lengths. Thus, no turbulent eddies are found at the nozzle exit and the flow is fairly uniform with increase in converging length.
- (2) A triangular vortexial motion at the exit was seen with C–D nozzle when throat diameter was 16 mm, which further died down with increase in converging length. The lesser converging length facilitates greater turbulence at the exit side. The pressure drop was found to be lesser compared to all cases when the throat diameter was 20 mm.
- (3) For all cases of the converging nozzle flow, the velocity was found to be higher with the expense of the pressure drop. Maximum average velocity was found

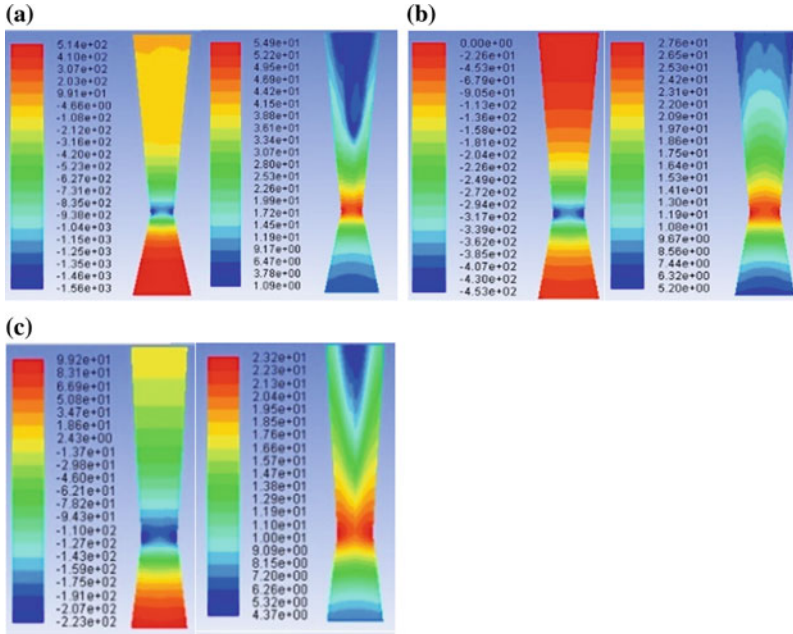


**Fig. 8** a Pressure and velocity profile for 50-12, **b** pressure and velocity profile for 50-16, **c** pressure and velocity profile for 50-20

to be in 50-32 converging nozzle. The pressure drop was also in the range of 100 Pa.

- (4) Instead of converging–diverging nozzle, only a converging nozzle can be the most appropriate solution for the present case. The 50-32 nozzle gives exit velocity of 17 m/s by analytical and CFD simulation.

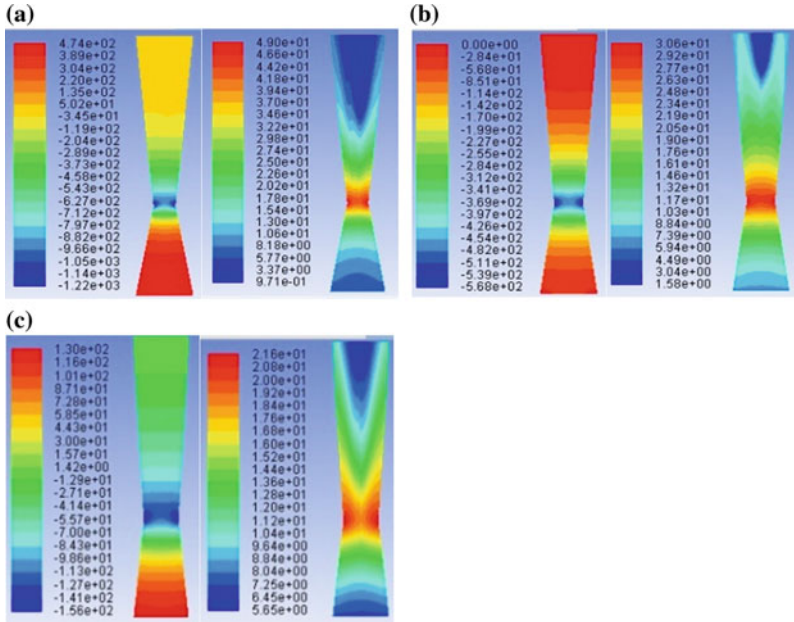


**Fig. 9** a Pressure and velocity profile for 55-12, b pressure and velocity profile for 55-16, c pressure and velocity profile for 55-20

The nozzle (50–32) was manufactured by using additive manufacturing technique and fitted to the engine and the performance test was conducted before and after the use of modified manifold. The variation of volumetric efficiency, brake specific fuel consumption and brake thermal efficiency are plotted and presented as shown in Figs. 14, 15 and 16. The details of experimental setup are available in Fig. 17.

## 4 Conclusions

- (1) A small change in shape and size of intake manifold can bring about huge change in the performance of the engine.
- (2) Not much work is available on the co-relations for prediction of nozzle performance based on converging length, diverging length, throat diameter and exit



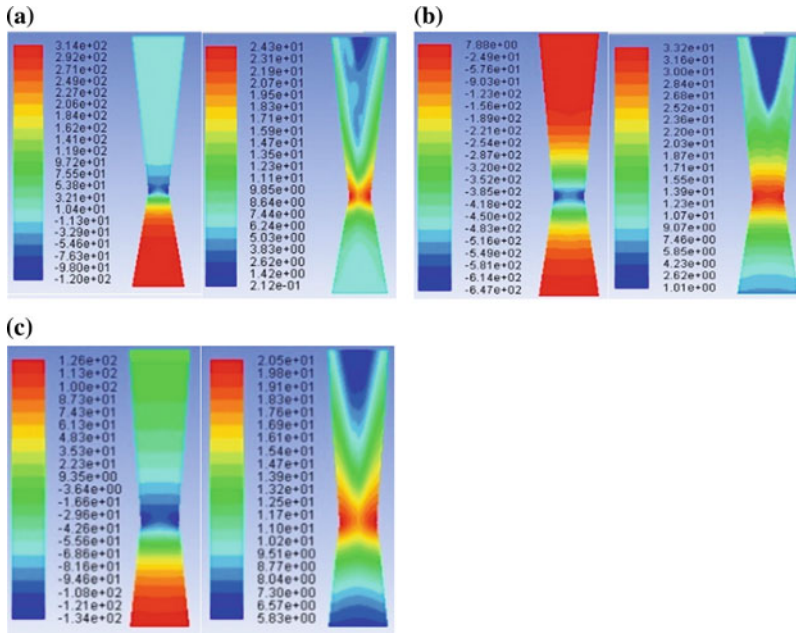


**Fig. 10** a Pressure and velocity profile for 60-12, b pressure and velocity profile for 60-16, c pressure and velocity profile for 60-20

diameter. CFD analysis is accurate to predict the pressure and velocity variations accurately.

- (3) The intake manifold modified into 50-32 nozzle resulted in considerable increase in volumetric and thermal efficiency by approx. 65.38 and 57.92% for full load. The fuel consumption was greatly reduced due to better combustion.

**Table 4** Variation of pressure drop and velocity with different geometry

Length of converging section	Diameter of pipe in mm (D1)	Diameter of throat in mm (D2)	Divergence angle	Pressure drop in pascal	Velocity at exit in m/s
40	32	12	4.764	72	1.31–15.31
	32	16	3.814	–65.94	0.31–9.38
	32	20	2.862	–240.35	1.89–5.36
45	32	12	4.97	–40.18	8.49–9.66
	32	16	3.979	183.28	5.44–6.96
	32	20	2.987	21.94	1.34–12.64
50	32	12	5.194	406.27	3.78–9.16
	32	16	4.16	–67.88	7.43–8.55
	32	20	3.122	79.31	5.31–6.36
55	32	12	5.44	354.42	0.971–10.57
	32	16	4.357	–85.12	3.05–10.51
	32	20	3.27	102.81	7.24–8.04
60	32	12	5.711	281.15	0.21–7.43
	32	16	4.574	0.059	1.012–12.29
	32	20	3.434	106.93	6.56–11.71
70	32	12	6.34	295.98	0.375–7.37
75	32	12	6.72	–333.77	3.56–21.74
162	45	32	–	80	13.47–14.30
162	50	32	–	135	16.37–17.50

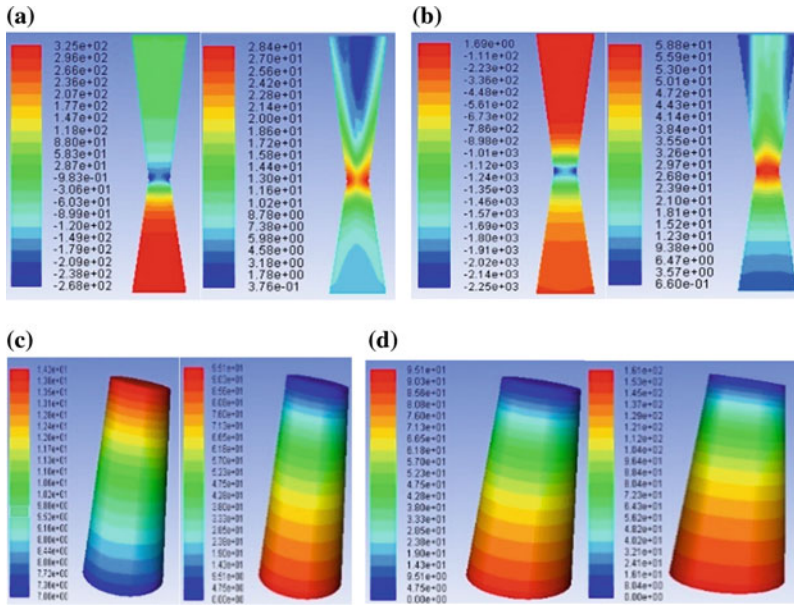


**Fig. 11** a Pressure and velocity profile for 70-12, b pressure and velocity profile for 75-12, c pressure and velocity profile for 45-32, d pressure and velocity profile for 50-32

**Fig. 12** GUI for additive manufacturing

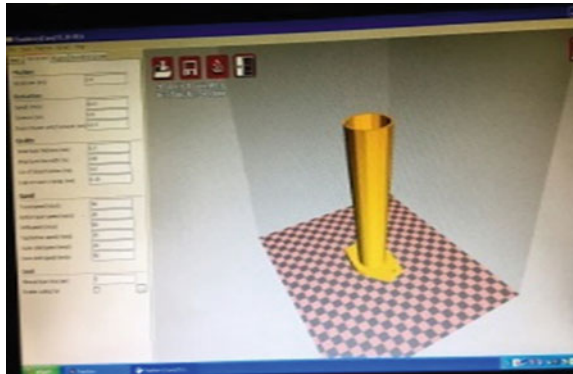


**Fig. 13** 3D printing machine

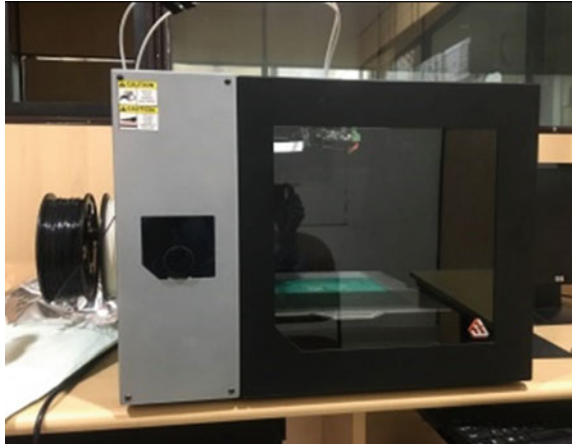


**Fig. 14** Volumetric efficiency versus load

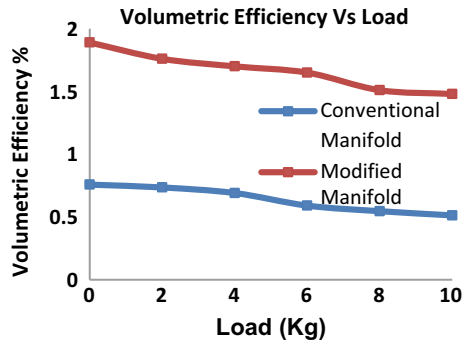


**Fig. 15** Thermal efficiency versus load

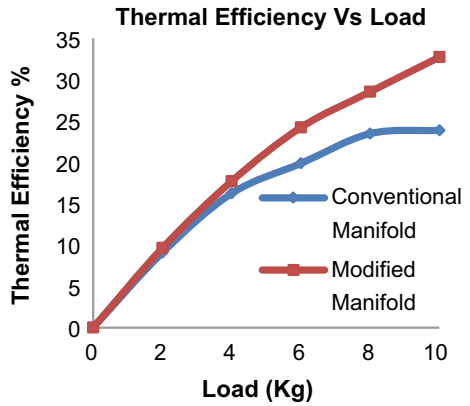


Fig. 16 BSFC versus load

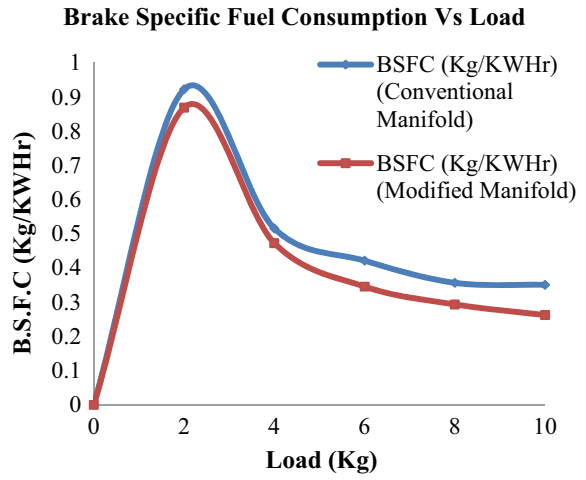


Fig. 17 Experimental setup



## References

1. Heywood JB (2017) Internal combustion engines fundamentals, 2nd edn. McGraw Hill Publishers, New Delhi
2. Wentsch M, Chiodi M, Bargende M, Seboldt D, Lejsek D (2016) 3D-CFD analysis on scavenging and mixture formation for CNG direct injection with an outward-opening nozzle. In: Bargende M, Reuss HC, Wiedemann J (eds) Internationales Stuttgarter symposium. Springer, Wiesbaden
3. Guo S, Huang S, Chi M (2018) J Image Video Proc 2018:70. <https://doi.org/10.1186/s13640-018-0304-8>
4. Hushim MF, Alimin AJ, Razali MA, Mohammed AN, Sapit A, Carvajal JCM. ARPN J Eng Appl Sci 10

# Calibration of Reference Velocity and Longitudinal Static Pressure Variation in the Test Section of an Open-Type Subsonic Wind Tunnel



Neeraj Verma and Beena D. Baloni

**Abstract** The reference wind velocity inside the test section of an open-type subsonic wind tunnel is established from the measurements of dynamic pressure and the average static wall pressure difference between stations at upstream of the test section and at the settling chamber. A wind tunnel calibration factor was obtained which relates the dynamic pressure and thus the wind velocity inside the test section with the average static wall pressure difference at a station near upstream of the test section and at the settling chamber. An average wind tunnel calibration factor was found to be 0.8189. The longitudinal variation of static pressure inside the test section is also obtained using the pitot-static tube.

**Keywords** Wind tunnel · Calibration factor  $K$  · Longitudinal static pressure variation

## 1 Introduction

During an aerodynamic experiment, actively using any flow-measuring device (pitot tube or anemometers) to determine the flow conditions in the test section is not advisable. The presence of induced flow by the test object may alter the actual flow conditions inside the test section, and hence, a flow-measuring device will not measure the actual flow conditions [1]. So, prior to any aerodynamic experiment in a wind tunnel, it is essential to assess the flow condition with an empty test section. This prior assessment of the flow condition inside the test section is carried out during the calibration process. A complete calibration process involves the determination of velocity variation in the plane of the model supports, longitudinal static pressure variation, flow angularity, turbulence, and deviation of large scale fluctuations [2, 3].

In the present work, calibration of reference velocity, alongside measurements for longitudinal static pressure variation in the test section of an open-type subsonic wind tunnel, has been carried out.

---

N. Verma (✉) · B. D. Baloni  
Sardar Vallabhbhai National Institute of Technology, Surat, Gujarat 395007, India  
e-mail: [turbo.neeraj@gmail.com](mailto:turbo.neeraj@gmail.com)

© Springer Nature Singapore Pte Ltd. 2020  
H. K. Voruganti et al. (eds.), *Advances in Applied Mechanical Engineering*,  
Lecture Notes in Mechanical Engineering,  
[https://doi.org/10.1007/978-981-15-1201-8\\_12](https://doi.org/10.1007/978-981-15-1201-8_12)

## 2 Calibration Process

The dynamic pressure and consequently the reference velocity inside the test section can be obtained by utilizing the measurements of the static pressure drop between the rings of static orifices at the settling chamber and just upstream of the test section [4–6]. Figure 1 shows the typical measurement stations at the settling chamber and test section of the wind tunnel.

Referring to Fig. 1, applying the energy equation between stations  $A$  and  $B$  gives,

$$P_A + \frac{1}{2}\rho V_A^2 = P_B + \frac{1}{2}\rho V_B^2 + K_1 \frac{1}{2}\rho V_B^2 \quad (1)$$

where  $P$  is the static pressure,  $V$  is the velocity,  $\rho$  is the density of air, and  $K_1$  is the coefficient of pressure loss between stations  $A$  and  $B$  due to tunnel contraction geometry and flow irregularities. Subscripts  $A$  and  $B$  denote the stations at settling chamber and upstream of the test section, respectively. Considering incompressible flow, the continuity equation gives,

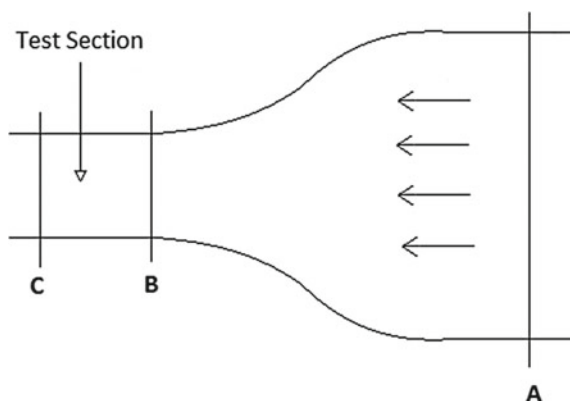
$$A_A V_A = A_B V_B = A_C V_C \quad (2)$$

where  $A$  is the cross-sectional area at the respective station and subscript  $C$  denotes the station in the test section. The station  $C$  in the test section is mobile in nature so that it can cover the maximum extent of the test section. The positions of the station  $C$  occupied in the test section are shown in Fig. 3.

Using Eq. (2), the energy equation can be reduced to Eq. (3) which can further be simplified to Eq. (4) or (5).

$$P_A - P_B = \frac{1}{2}\rho V_C^2 \left[ \left( \frac{A_C}{A_B} \right)^2 (1 + K_1) - \left( \frac{A_C}{A_A} \right)^2 \right] \quad (3)$$

**Fig. 1** Typical measurement station for wind tunnel





$$\frac{1}{2}\rho V_C^2 = K(P_A - P_B) \quad (4)$$

$$q_C = K(P_A - P_B) \quad (5)$$

where  $K$  is the tunnel calibration factor and  $q_C$  is dynamic pressure at station  $C$ . The dynamic pressure inside the test section can be directly measured by a pitot-static tube.

An independent measurement of stagnation pressure and static pressure by pitot-static tube can provide the local static pressure in the test section [1, 7]. Thus, by traversing the pitot-static tube in the test section, static pressure variation inside the test section can be obtained.

### 3 Experimental Setup

The experimental setup mainly comprised of wind tunnel facility, pitot-static tube, and pressure transducers. The wind tunnel facility under consideration is an open-type subsonic wind tunnel with a contraction ratio of 9 and a test section of  $60 \times 60 \times 120 \text{ cm}^3$ . The wind tunnel is powered by a 15 hp a.c. motor. Figure 2 shows the wind tunnel facility.

To measure the dynamic pressure, a calibrated, Dwyer make pitot-static tube of 750 mm length is used. Average static pressure at the upstream of the test section was measured through a ring of orifice containing pressure tapings on each wall of the periphery of the test section. However, at the settling chamber, due to the large dimension of the settling chamber, only one pressure taping was provided. Pressure readings were recorded by silicon microstructure-incorporated make differential pressure transducer with a range of 0.3 psi (vacuum).

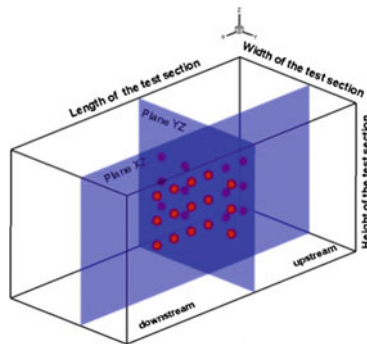


**Fig. 2** Wind tunnel facility

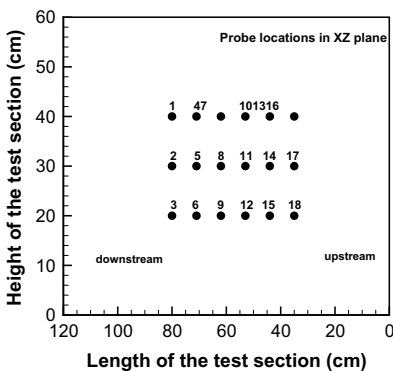
### 4 Test Procedure

The test was carried out at five different wind speeds, corresponding to which the variable frequency drive (VFD) settings for each fan speed were 10, 15, 20, 25, and 30 Hz. A total of 27 probe locations inside the test section were selected. The probe locations were grouped into two vertical planes (planes XZ and YZ), which were perpendicular to each other, as shown in Fig. 3a. Figure 3 shows the schematic of the test section with probe locations.

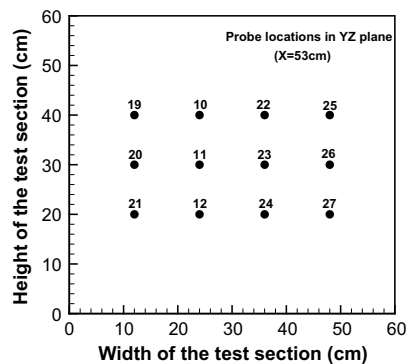
At each probe location, stagnation pressure and static pressure were measured independently with the help of a pitot-static tube. By independently measuring the static pressure from the pitot-static tube at each probe location, a longitudinal variation of static pressure was obtained. Dynamic pressure is obtained by simply subtracting the stagnation pressure with the static pressure. The average static wall pressure was also measured at the settling chamber (referring to Fig. 1, station A) and at



(a) Test section with pitot-static probe locations



(b) Side view of the test section (XZ plane, Y=24cm)



(c) Front view of the test section (YZ plane, X=53cm)

Fig. 3 Schematic view of the test section with probe locations

upstream of the test section (referring to Fig. 1, station *B*). All the 27 probe locations represent the different locations for station *C* in Fig. 1.

A linear regression fit of pressure data obtained from station *A* and *B* (static pressure) and from the pitot-static tube (dynamic pressure) at each probe location provides the required range of calibration factor *K*.

### 5 Results and Discussion

Calibration was carried out with five different wind speeds. Figure 4 shows the longitudinal variation of static pressure at all speed ranges along the longitudinal plane passing through the center of the test section.

From Fig. 4, it can be observed that at each wind speed, the variation of static pressure along the length of the test section at different probe heights remains more or less the same. At low wind speed, the maximum deviation of static pressure variation along different probe heights is 3.3% of average pressure, whereas, at high speed, it is limited to 1.9% of average pressure at different probe heights. This indicates uniformity in the flow along the traverse plane (cross section).

However, at any given probe height, the deviation of the static pressure variations along the length of the test section is noticeable. At lower pressure range (low wind velocity), the deviation indicates a relatively higher range of pressure variation (4.38 Pa, i.e., 17.6% of average pressure), whereas, at higher pressure ranges (high wind velocity), it is relatively low (13.16 Pa, i.e., 4.03% of the average pressure).

The implication of this variation in the deviation of pressure range can also be seen in the velocity variation along the length of the test section, as shown in Fig. 5. At higher range of deviation in the pressure variation, i.e., at low wind velocity, the

**Fig. 4** Longitudinal variation of static pressure in the test section at different velocities

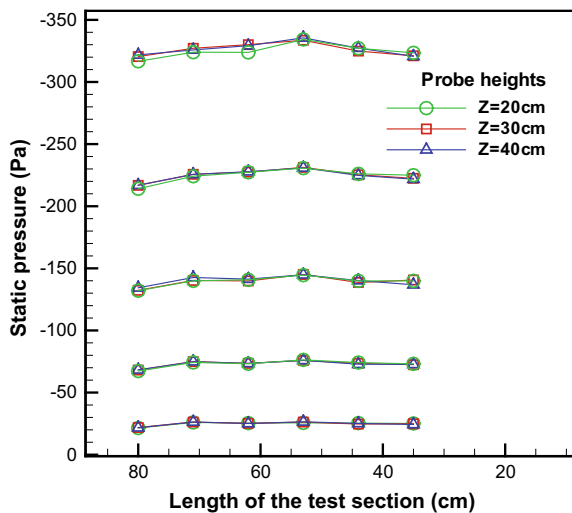
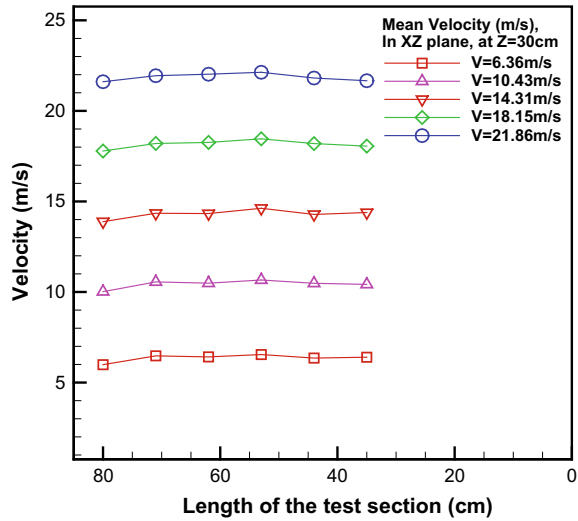


**Fig. 5** Variation of wind velocity along the length of the test section at different fan speeds



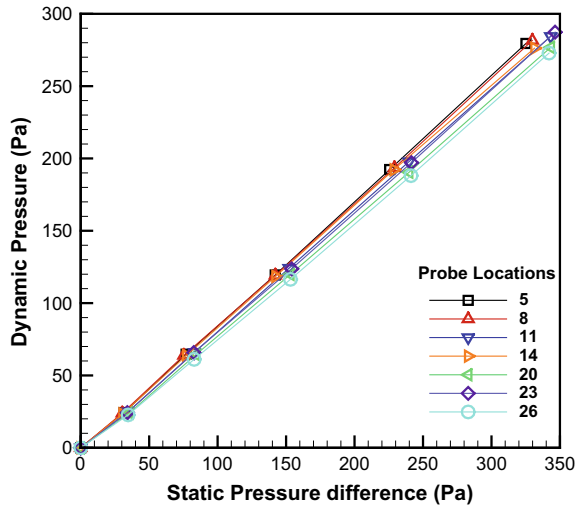
corresponding deviation in the velocity variation along the length of the test section is 0.55 m/s (8.5% of average velocity). However, at a lower range of deviation (at high wind speed), the deviation in the velocity variation is 0.52 m/s (2.3% of average velocity). This implies that at lower speed range the flow lacks uniformity along the longitudinal plane. However, as the wind speed increases, flow achieves more uniformity along the longitudinal plane.

Generally, during an aerodynamic test, the test model is mounted at the center plane of the tunnel ( $Z = 30$  cm). Referring to Fig. 3, probe locations 2, 5, 8, 11, 14, 17, 20, 23, and 26 sufficiently cover the center plane of the test section. Therefore, the measurements of wind velocity at the designated probe locations, i.e., 2, 5, 8, 11, 14, 17, 23, and 26 are sufficient for calibration of the reference velocity.

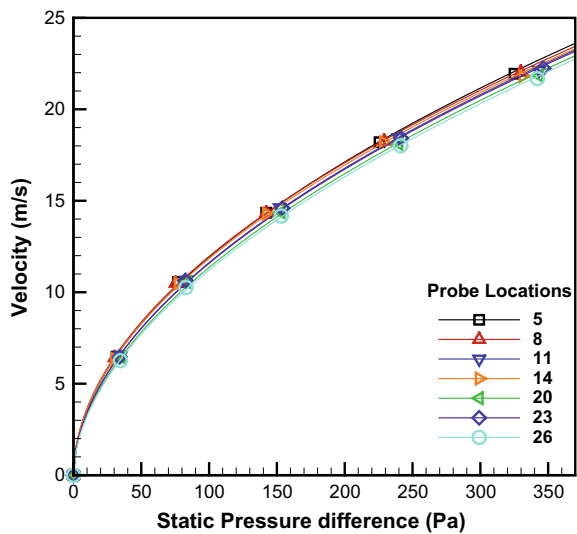
Figure 6 shows the variation of the dynamic pressure at designated probe locations with the average static pressure difference between stations *A* and *B*, whereas Fig. 7 shows the variation of derived wind velocity from the dynamic pressure measurements with the average static pressure difference between stations *A* and *B*. The slope of the regression fits in Fig. 6 provides the local wind tunnel calibration factor (*K*) at the designated probe locations.

Figure 8 provides the variation of local wind tunnel calibration factor at the designated probe locations along the longitudinal (*XZ* plane) and cross-sectional (*YZ* plane). It can be observed from Fig. 6 that, at any given wind tunnel fan speed, the static pressure difference and dynamic pressure at any designated probe locations are dispersed. This follows that, although the stations *A* and *B* are fixed, the static pressure difference between the stations is not the same even at the same wind tunnel fan speed. Also, the dynamic pressure changes for various probe locations even at the same fan speed. This indicates of irregularities in the flow inside the test section.

**Fig. 6** Variation of dynamic pressure (at various probe locations) with respect to static pressure difference at stations *A* and *B*



**Fig. 7** Variation of wind velocity with respect to the static pressure difference between stations *A* and *B*



The flow irregularities can be accounted by a single wind tunnel calibration factor based on the average of local calibration factors at probe locations covering the center plane of the test section. Thus, the average of the local calibration factor at the designated probe locations on the center plane is found to be  $K = 0.8189$ . However, placement of the model inside the test section along the longitudinal direction should be preferred in a way such that the local wind tunnel calibration factors encompassing the model remain more or less the same.

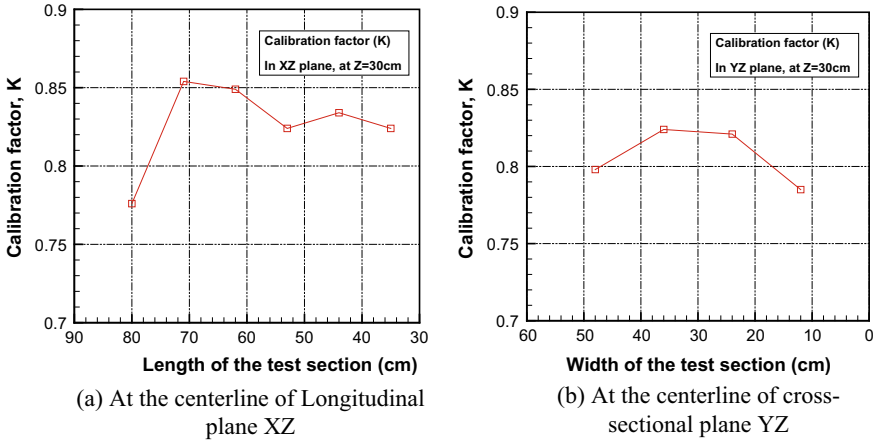


Fig. 8 Variation of wind tunnel calibration factor ( $K$ ) in different planes

## 6 Conclusion

Calibration of an open-type subsonic wind tunnel was carried out. The static and dynamic pressure variations along the length of the test section reveal that the flow achieves uniformity at higher wind speeds. A calibration factor was established to measure the reference velocity inside the test section of the wind tunnel. Calibration factor along with static pressure difference at the test section and the settling chamber provides the dynamic pressure and thus the mean wind velocity inside the test section. A single wind tunnel calibration factor of the wind tunnel was found to be 0.8189. The mean reference velocity at different fan speeds was found to be 6.36, 10.43, 14.31, 18.15, and 21.86 m/s.

## References

1. Barlow JB, Rae WH Jr, Pope A (2015) Low speed wind tunnel testing. INCAS Bull 7(1):133
2. Pope A (1961) Wind-tunnel calibration techniques. Advisory Group for Aeronautical Research and Development, Paris
3. Rathakrishnan E (2007) Instrumentation, measurements, and experiments in fluids, 1st edn. CRC Press, Boca Raton
4. Swanson RS, Gillis CL (1944) Wind-tunnel calibration and correction procedures for three-dimensional models. National Advisory Committee for Aeronautics, Washington
5. Edwards CD (2000) Calibration of the reference velocity in the test section of the low speed wind tunnel at the Aeronautical and Maritime Research Laboratory (No. DSTO-TN-0248). Defence Science and Technology Organisation, Canberra (2000)
6. Gorlin SM, Slezinger II (1966) Wind tunnels and their instrumentation (No. 346). Israel Program for Scientific Translations Ltd., Jerusalem
7. Matheson N (1983) Static pressure and axial velocity distributions near the centre of the working section of the ARL 2.7 m  $\times$  2.1 m Wind Tunnel (No. ARL/AERO-TM-346). Aeronautical Research Labs, Melbourne

# Optimal Selection of Insulating Material for Energy Conservation in Steam Pipe Using Analytical Hierarchy Process



Mendu Siva Subrahmanyam, Imandi Aparna Devi and Beejapu Jagadeesh

**Abstract** During past decade, there has been an increasing trend to save the amount of heat energy lost from the steam while carried through pipes. Improper selection of the pipe insulation material leads to the loss of energy and reduces the amount of energy content at the usage point which in turn increases the fuel cost. Hence, there is a need to conserve energy by choosing suitable insulating material. The present paper deals with optimal selection of insulating material based on multi-criteria decision-making analysis using Analytical Hierarchy Process (AHP). Five different criteria (insulating materials) and five alternatives, namely cost, thermal conductivity, flammability, toxicity, and noise are considered for the analysis of decision making in order to choose best insulating material for energy conservation. Ranks are given to the alternatives based on their criteria weights using AHP pairwise comparison matrices. The results indicate that rock wool is the suitable insulating material for the conservation of energy in the steam pipe.

**Keywords** Insulation · Multi-criteria decision · Analytical Hierarchy Process · Steam pipe

## 1 Introduction

Steam pipes find applications in process industries, power plants, domestic house heating, etc. A lot of energy is being lost from steam pipes to surroundings due to the improper selection of insulating materials. To retain the required thermal energy content, pressure at the user end and energy conservation are needed; which could be possibly achieved by selecting suitable insulating material. Selecting the best insulating material among different insulating materials is a challenging task to the energy planners due to the complexity in considering various facts of technical, economic,

---

M. Siva Subrahmanyam (✉) · I. Aparna Devi  
Mechanical Engineering, MVGR College of Engineering (A), Vizianagaram, AP 535005, India  
e-mail: [m.sivasubrahmanyam@mvgrce.edu.in](mailto:m.sivasubrahmanyam@mvgrce.edu.in)

B. Jagadeesh  
Industrial Engineering, GITAM, Visakhapatnam, AP 530045, India

© Springer Nature Singapore Pte Ltd. 2020  
H. K. Voruganti et al. (eds.), *Advances in Applied Mechanical Engineering*,  
Lecture Notes in Mechanical Engineering,  
[https://doi.org/10.1007/978-981-15-1201-8\\_13](https://doi.org/10.1007/978-981-15-1201-8_13)

social, and environmental aspects. Among the various decision-making techniques in vogue, Analytical Hierarchy Process has received high consideration in making decisions for selecting the best alternative in energy planning. The detailed literature on the implementation of AHP in the energy sector is provided as below. Saaty [1] introduced the Analytic Hierarchy Process (AHP), as an effective tool for dealing with complex decision making, by reducing complex decisions to a series of pairwise comparisons and then synthesizing the results. Akash et al. [2] conducted a study on multi-criteria selection of electric power plants using Analytical Hierarchy Process wherein a comparison among the different electricity power production options was considered. Meixner [3] in his evaluation of energy sources using fuzzy used AHP group decision analysis for evaluation of the energy crisis based on the energy sources. Al-Hawari et al. [4] conducted Analytic Hierarchy Process for selection of temperature measurement sensors. Chinese et al. [5] conducted a study on the multi-criteria analysis for the selection of space heating systems in an industrial building. Lanjewar et al. [6] conducted a study on multi-criteria evaluation of natural gas energy systems using graph theory and Analytical Hierarchy Process. Klein [7] conducted a study on cost estimation for materials and installation of hot water piping insulation. Zhang et al. [8] conducted fire risk assessment of fire retardant polyurethane thermal insulation materials for exterior walls of buildings based on Analytical Hierarchy Process. Paunescu et al. [9] conducted fuzzy AHP to study on pollution produced by electrical generators and the quantity of noxious substances electrically generated when thermal redundancy factors were applied. Abu Taha and Diam [10] conducted an assessment on renewable energy—concluding that AHP is the most used methodology of all multi-criteria decision-making (MCDM) methods. Mohammed et al. [11] conducted a study using the MCDM on the energy supply configuration of autonomous desalination. Socaciu and Unguresan [12] conducted AHP process to select phase change material (PCM) in order to prioritize and select the proper PCMs for comfort application in buildings. Siadati and Shahhosseini [13] compared the modern structural systems using the fuzzy AHP where of AHP was deployed to rank the best structural systems such as light steel frames. Gholami Rostama and Mahdavinejada [14] operated AHP for selection of utilizing of nano-insulating materials in building industry. After detail literature study, it is seen that AHP-based multi-criteria decision-making analysis can be applied for steam carrying pipes. The present paper is centered around implementation of AHP methodology to evaluate the best insulating material among the available alternatives, i.e., polystyrene, polyurethane, calcium silicate, glass wool, and rock wool against the criteria being-cost, thermal conductivity, flammability, toxicity, and noise.



## 2 Solution Methodology

The methodology of AHP can be explained in the following steps:

Step 1: Initially, the structure of hierarchy (see in Fig. 1) consisting of goal, criteria, and alternatives is developed. Data are collected from the literature and information from the suppliers corresponding to the hierarchy structure, in a pairwise comparison of alternatives on a qualitative Saaty’s scale as shown in Table 1.

Step 2: The comparisons are made for each criterion and converted into quantitative numbers based on the scale.

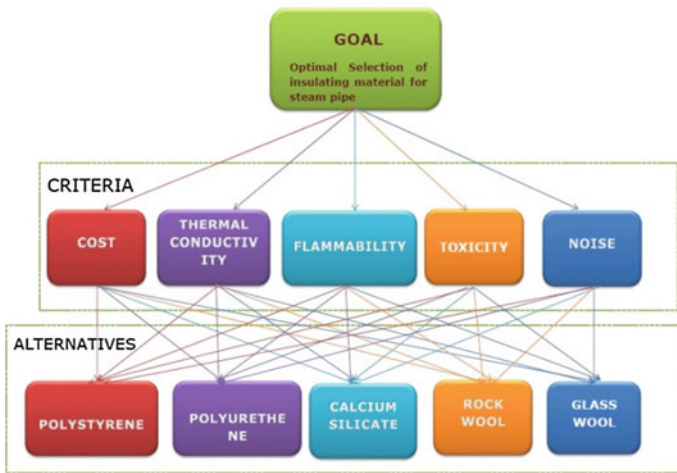


Fig. 1 Hierarchy structure of the present problem

Table 1 Saaty’s scale of AHP

Intensity of importance	Definition
1	Equal importance
2	Weak or slight
3	Moderate importance
4	Moderate plus
5	Strong importance
6	Strong plus
7	Very strong
8	Very, very strong
9	Extreme importance
Reciprocals of above	If activity $i$ has one of the above non-zero numbers assigned to it when compared with activity $j$ , then $j$ has the reciprocal value when compared with $i$

Step 3: The pairwise comparisons of various criteria generated are reorganized into a square matrix. The diagonal elements of the matrix are one. The criterion in the  $i$ th row is better than criterion in the  $j$ th column if the value of element  $(i, j)$  is more than 1; otherwise the criterion in the  $j$ th column is better than that in the  $i$ th row. The  $(j, i)$  element of the matrix is the reciprocal of the  $(i, j)$  element.

Step 4: Two criteria are evaluated at a time in terms of their relative importance, and index values of 1–9 are used. The weights of the individual criteria are calculated.

Step 5: A normalized comparison matrix is created. Each value in the matrix is divided by the sum of its column. To get the weights of the individual criteria, the mean of each row of this second matrix is determined. Priority vector or criterion weight can be calculated using mean of row method.

Step 6: Arithmetic mean is calculated for the row for obtaining the priority vector.

Step 7: On a parallel note, different criteria weights are obtained. Depending on each criterion, same process has to be repeated for the alternatives.

Step 8: Final rating table is generated using criteria's weights wherein the entire weights related to the different alternatives are entered.

Step 9: The transpose of the final rating matrix is done. After the transpose, each element of the row is multiplied with the original criteria weights. The final priorities are obtained according to the criterion weights.

Step 10: The obtained priorities are ranked according to decreasing order, and the one which obtained the highest priority is selected as the best alternatives among various alternatives.

### 3 Results and Discussion

In order to select the most accurate insulation material for steam pipe, by considering polystyrene, polyurethane, calcium silicate, glass wool, and rock wool as materials, computations have been carried out for different alternatives with thermal conductivity, cost, toxicity, flammability, and noise as its criteria based on the comprehensive analysis of the literature survey done as discussed in earlier sections. When objects of differing temperatures are placed in contact with each other, heat flow is inevitable. Insulation material would then come into action by restraining the heat flow. Such insulating capability of a material is generally measured in terms of its thermal conductivity. Lower the thermal conductivity higher is the insulating capability. The cost factor here represents price of insulation material hinting in which insulation material is cheaper than the other. In case of commercial businesses, the manufacturer is likely to settle for: the best insulation material at a cheaper cost so as to reduce the initial investment, material with least toxic factor which represents the intensity of health hazard caused to humans as the insulation materials which are used in the industries should not cause any health hazardous to the workers. Manufacturers also look for insulation materials that have the ability to absorb the high frequency sounds coming from the machinery represents the level of echo caused by the insulation material.

Aspect of flammability representing the ease with which a material can be set to fire is also considered to avoid any fire hazardous in the plant. The industries prefer the above type of materials has so as to be more cautious and give more importance to fire and safety factors in the plant.

Considering the above facts pertaining to various listed criteria, computations are carried out using AHP methodology as described in the Sect. 2. Pairwise and normalized comparisons of criteria are made by following the stepwise procedure as mentioned in the earlier section, and results are tabulated as shown in Table 2. The criteria weights were obtained by performing average operation to each row. Depending on the criteria weight, ranks have been given to the evaluated criteria. The alternative with highest weight has been given rank one, and the subsequent criteria were given subsequent ranks in descending order of their weights.

Pairwise comparison of each alternative has been carried out in order to find out the criteria weight further which normalization was carried for ranking the alternatives. For better understanding, the results are presented in Table 3 with the highest rank awarded on basis of highest weight criteria. From the table, it is found that rock wool is the best material in terms of cost, flammability, toxicity, and noise criteria, whereas polyurethane could be the best alternative when looked by thermal conductivity as the deciding criteria.

The final rating matrix is obtained from the normalization of the five criteria. The transpose of the final rating matrix was prepared, and each element of the row was

**Table 2** Normalization of matrix for criteria

	Cost	Thermal conductivity	Flammable	Toxicity	Noise	Criteria weight
Cost	0.692	0.867	0.332	0.494	0.25	0.60
Thermal conductivity	0.077	0.096	0.295	0.439	0.222	0.227
Flammable	0.077	0.012	0.037	0.006	0.250	0.033
Toxicity	0.077	0.012	0.332	0.055	0.250	0.119
Noise	0.077	0.012	0.004	0.006	0.028	0.025
Sum	1.000	1.000	1.000	1.000	1.000	

**Table 3** Weight criteria for alternatives based on different criteria

Alternatives	Criteria weight				
	Cost	Thermal conductivity	Flammability	Toxicity	Noise
Polystyrene	0.123	0.247	0.046	0.036	0.046
Polyurethane	0.072	0.531	0.046	0.036	0.037
Calcium silicate	0.027	0.066	0.046	0.138	0.092
Glass wool	0.237	0.027	0.292	0.271	0.260
Rock wool	0.540	0.129	0.570	0.519	0.565

**Table 4** Final rating matrix

Alternative	Weight	Rank
Polystyrene	0.081162	4
Polyurethane	0.062717	5
Calcium silicate	0.164322	3
Glass wool	0.222741	2
Rock wool	0.474722	1

multiplied with the criteria weight obtained in Table 2 so as to find the final priority. The final priority obtained for various alternatives as shown in Table 4 reveals rock wool to be the best insulating material among the existing alternatives.

## 4 Conclusion

The results in the present work are obtained by the application of multi-criteria decision-making-based Analytical Hierarchy Process to the various alternatives of insulation materials (polystyrene, polyurethane, calcium silicate, glass wool, and rock wool) so as to select the best alternative with: cost, heat load, flammability, toxicity, and noise as the main criteria. After the pairwise comparison of alternatives corresponding to each criterion, normalization was carried out and ranks are obtained for alternatives corresponding to criteria to which criteria's weights are entered to generate final rating table. From the above study, it is found that, of the various alternatives present, rock wool got the highest weight (0.474722), followed by glass wool (0.222741), calcium silicate (0.164322), polystyrene (0.081162), and polyurethane (0.062717). The results obtained from the present study could be useful for decision makers in implementing energy conservation strategies for steam distribution networks.

## References

1. Saaty TL (1990) How to make a decision: the analytic hierarchy process. *Eur J Oper Res* 48:9
2. Akash BA (1999) Multi-criteria selection of electric power plants using analytical hierarchy process. *Electr Power Syst Res* 52:29
3. Meixner O (2010) Fuzzy AHP group decision analysis and its application for the evaluation of energy sources. 1(1)
4. Al-Hawari T, Al-Bo'ola S, Momani A (2011) Selection of temperature measuring sensors using the analytic hierarchy process. *Jordan J Mech Ind Eng* 5:451
5. Chinese D (2011) Multi-criteria analysis for the selection of space heating systems in an industrial building. *Energy* 36:556
6. Lanjewar PB, Rao RV, Kale AV (2011) Multi-criteria evaluation of natural gas energy systems using graph theory and analytic hierarchy process methods. *Int J Adv Therm Sci Eng* 5:237

7. Klein G (2012) Cost estimation for materials and installation of hot water piping insulation. Prepared for Pacific Northwest National Laboratory, 180902, 1
8. Li LJ, Li F, Zhang ZJ (2013) Fire risk assessment of fire retardant polyurethane thermal insulation materials for exterior walls of buildings based on analytical hierarchy process. *Adv Mater Res* 785:191
9. Paunescu MV, Potra LF, Tarnovan IG (2013) Fuzzy AHP study on the pollution produced by electrical generators. *Acta Electrotehnica* 54:151
10. Taha RA, Daim T (2013) Multi-criteria applications in renewable energy analysis, a literature review. *Res Technol Manage Electr Ind* 17 (2013)
11. Mohammed ES, Georgiou D, Rozakis S (2013) Multi-criteria decision making on the energy supply configuration of autonomous desalination units. *AUA Working Paper* 75:459 (2013)
12. Socaciu LG, Unguresan PV (2014) Using the analytic hierarchy process to prioritize and select phase change materials for comfort application in buildings. *Math Model Civil Eng* 10:21
13. Siadati S, Shahhosseini V (2015) Comparison of modern structural systems based on a fuzzy analytical hierarchy process. *Ind J Sci Technol* 8:1
14. Gholami Rostama N, Mahdavinejada MJ (2015) Commercializing usage of nano-insulating materials in building industry and future architecture. In: 5th international biennial conference on ultrafine grained and nanostructured materials, vol 11, p 644

# Heat Transfer Enhancement Using Overlapped Dual Twisted Tape Inserts with Nanofluids



Rokkala Rudrabhiramu, K. Harish Kumar, K. Kiran Kumar and K. Mallikarjuna Rao

**Abstract** The thermal performance of a heat exchanger can be improved by various techniques. It is a major concern when coming to industries as the heat losses play a major role in efficiency of the overall plant. The present work is carried out to enhance the heat transfer rate of a tubular heat exchanger by incorporating overlapped dual twisted tapes (ODTTs) or inserts into a tube and carrying out the numerical simulation for different twisting ratios of ODTTs. In addition to this,  $\text{Al}_2\text{O}_3$  nanoparticles are used as additives to increase the value of heat transfer coefficient ( $h$ ), thereby improving the Nusselt number ( $Nu$ ) and overall thermal performance. The addition of ODTTs resulted in improved residence time, more contact surface area and improved fluid mixing and swirling for effective heat transfer to take place. The numerical simulation is repeated for nanofluid concentrations of 1% and 2% and also for varying twisting ratios of  $Y_o/Y = 1.5, 2$  and  $2.5$ . The tube with 1% nanofluid concentration and twisting ratio  $Y_o/Y = 2$  yielded better results in comparison with all other combinations.

**Keywords** Overlapped dual twisted tapes (ODTTs) ·  $\text{Al}_2\text{O}_3$  nanoparticles · Nanofluids

## Nomenclature

$W$  Width of the tape insert, m  
 $\varphi$  Nanofluid concentration, % by volume  
 $C_{p(\text{np})}$  Specific heat of nanoparticles, J/kg K

---

R. Rudrabhiramu (✉) · K. Harish Kumar  
Vignan's Institute of Information Technology, Visakhapatnam, Andhra Pradesh, India  
e-mail: [ramumittuusha@gmail.com](mailto:ramumittuusha@gmail.com)

K. Kiran Kumar  
National Institute of Technology, Warangal, Warangal, Telangana, India

K. Mallikarjuna Rao  
Jawaharlal Nehru Technological University, Kakinada, Andhra Pradesh, India

© Springer Nature Singapore Pte Ltd. 2020  
H. K. Voruganti et al. (eds.), *Advances in Applied Mechanical Engineering*,  
Lecture Notes in Mechanical Engineering,  
[https://doi.org/10.1007/978-981-15-1201-8\\_14](https://doi.org/10.1007/978-981-15-1201-8_14)

$\rho_{np}$	Density of nanoparticles, kg/m <sup>3</sup>
$\rho_w$	Density of water, kg/m <sup>3</sup>
$A$	Heat transfer surface area, m <sup>2</sup>
$D$	Diameter of the pipe
$k$	Thermal conductivity of nanofluid, W/mK
$m$	Mass of nanofluid, kg/s
$C_p$	Specific heat of nanofluid, J/kg K
$T_i$	Temperature at inlet, °C
$T_o$	Temperature at outlet, °C
$T_w$	Wall temperature, °C
$T_b$	Average bulk fluid temperature, °C
$Y_o$	Overlapped pitch length of the tape insert, m
$Y$	Pitch of the twisted tape insert, m
$Y_o/Y$	Overlapped twist ratio
$U$	Average velocity, m/s
$\mu$	Dynamic viscosity, kg/s m

## 1 Introduction

There is a huge demand for heat transfer enhancement techniques that can be employed in various engineering applications such as power plants, cooling systems used in automobiles, refrigeration systems, chemical and nuclear reactors. The heat transfer rate can be greatly enhanced by various passive techniques one of which is a turbulence promoter. The turbulence intensity can be enhanced by incorporating swirlers, propellers, spiral fins or twisted tapes which in turn enhances the heat transfer coefficient. In addition to this, if fluid is circulated along with nano-additives, it showed even better results which are discussed here.

A lot of research is going on in order to improve the heat transfer rate which is chosen as the core criteria to carry out this work. Majority of the chemical processing plants and oil and gas industries are looking for augmented heat transfer techniques which can enhance their plant efficiency, thus reducing the maintenance cost. One of the passive methods is chosen where twisted tapes are inserted into tubes for improved heat transfer along with nanoparticle additives.

The generation of secondary recirculation by incorporating swirlers resulted in enhanced radial and tangential fluctuations in the intensity of turbulence which lead to reduction in boundary layer thickness and greater fluid mixing inside the tubes of a heat exchanger. Twisted tapes have been chosen as inserts to create swirl in the flow which also demanded additional input power for pumping the fluid through the heat exchanger tubes. The inserts block the fluid partially that provides enough time for fluid with nano-additives to absorb heat resulting in heat transfer enhancement. Hence, economic factor has to be taken into consideration while using heat exchangers with twisted inserts.

Whitham et al. [1] have worked extensively in this area incorporating twisted inserts and reported improved results in most of the heat exchangers. Rahim et al. [2] showed heat transfer enhancement by carrying out numerical study incorporating notch twisted tapes and jagged perforated modified forms. Sivashanmugam et al. [3, 4] proved right–left helical form of screw inserts showed extraordinary heat transfer improvement over screw inserts of straight format. He also gave an empirical relation between Reynolds number, Nusselt number, twist ratio and right–left distance. Nagarajan et al. [4, 5] concluded that left–right-sided geometries have a great impact on thermal performance, friction factor and heat transfer enhancement. Eiamsa-ard et al. [6] gave a fitting conclusion stating the heat transfer improvement alongside friction factor for varying twist angles, i.e. 30°, 60° and 90°, for varying twist ratios. Chang et al. [7] investigated the pressure drop and heat enhancement characteristics in the Reynolds range varying from 3000 to 14,000 where he observed reduced fanning factors for increased Reynolds number. He also observed a significant heat transfer enhancement. Eiamsa-ard et al. [8] studied the behaviour of pressure changes and heat transfer rates by varying three different space ratios which exhibited better characteristics at instances. Zhang et al. [9] have shown a significant rise in Nusselt number by almost 171% and 182% for heat exchangers with triple and quadruple inserts, respectively.

Nanotechnology has been a focused area where nanoscale particles such as  $\text{Al}_2\text{O}_3$ ,  $\text{CuO}$  and  $\text{TiO}_2$  are preferred especially for the applications where heat enhancement plays a vital role. The nanoscale particles listed here usually exhibit better thermal performance characteristics as they usually possess higher thermal conductivities when compared with those of base fluids. Various experiments conducted revealed that nanofluids with greater particle loading exhibited higher friction factor and heat transfer rates whereas few nanofluids exhibited different trends. A suitable or proper particle loading depending upon the type of application yielded better heat enhancement characteristics which emerged as a promising approach to carry out this work.

## 2 Modelling and Analysis

Overlapped dual twisted tapes were incorporated in a 19-mm diameter pipe as shown in Fig. 1. The tube with overlapped dual twisted tapes (ODTTs) is then subjected to multiple flow circulations with water as a standard heat transfer medium and then adding 1 and 2% of  $\text{Al}_2\text{O}_3$  nanoparticles by volume.

The geometry or tube with overlapped dual twisted tapes (ODTTs) is imported and meshed using CFX pre-processor. The mesh domain with type of elements used is shown in Fig. 2. Tetra mesh is chosen for better results where a total of 16,415 nodes and 80,033 elements are taken with a growth rate of 1.2. The average aspect ratio is 1.89.

The domain is then set up with boundary conditions in CFX solver. Some of the assumptions while assigning boundary conditions include smooth and no-slip wall



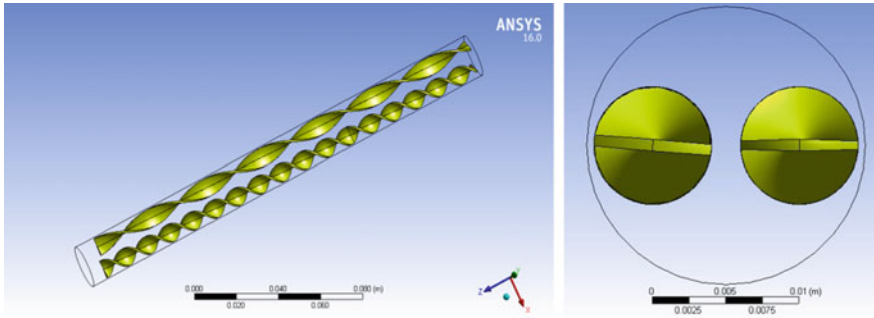


**Fig. 1** Tube with overlapped dual twisted tapes (ODTTs)

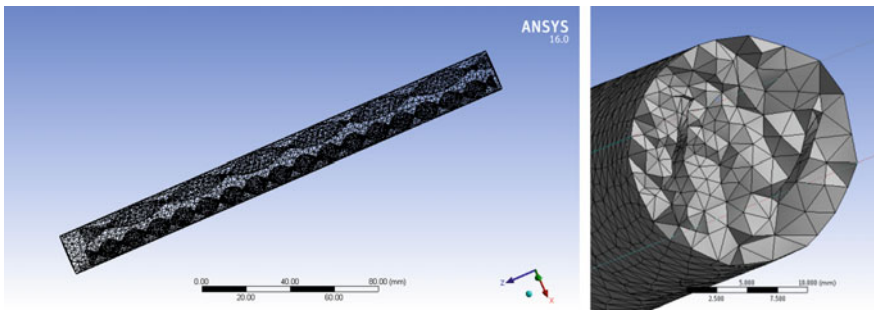


**Fig. 2** Meshed domain and cut section showing tetra elements

along with negligible backpressure. The inlet velocity is varied starting from 0.15 m/s accounting for change in Reynolds number ( $Re$ ).

Domain settings	
Fluid definition	Material library ( $Al_2O_3$ )
Morphology	Continuous fluid
Buoyancy model	Non-buoyant
Domain motion	Stationary
Reference pressure	1 atm
Heat transfer model	Total energy
Turbulence model	$k$ epsilon
Turbulent wall function	Scalable

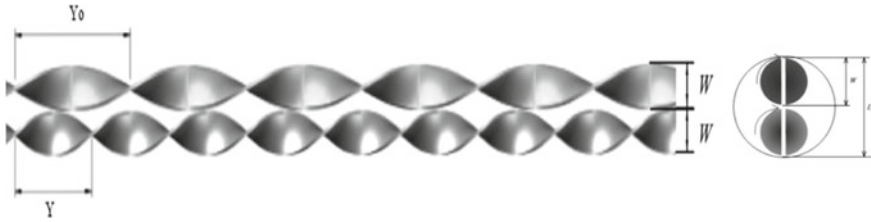


**Fig. 3** Overlapped dual twisted tapes (ODTTs) and its nomenclature

The thermodynamic properties of  $\text{Al}_2\text{O}_3$  considered include a molar mass of 1 kg/kmol, density of  $1007.4 \text{ kg/m}^3$  and specific heat capacity of  $4154.7 \text{ J/kg K}$ .

### 3 Methodology

A numerical simulation is carried out for different  $Y_0/Y$  twisting ratios of ODTTs. The ODTT twisting ratios ( $Y_0/Y$ ) considered are 1.5, 2.0 and 2.5 based on the literature studies [10] (Fig. 3).

The details of the inputs and experimental conditions are mentioned below.

(a) Inner diameter of the tube ( $D$ )	19 mm
(b) Length of the tube ( $L$ )	1000 mm
(c) Temperature at inlet ( $T_i$ )	26 °C
(d) Base fluid	Water
(e) Reynolds no.	5400–15,200
(f) Nanoparticles	$\text{Al}_2\text{O}_3$
(g) Concentration of nanoparticles	1 and 2% by volume
(h) Density of nanoparticles	$1007.4 \text{ kg/m}^3$
(i) Specific heat of nanoparticles	$4154.7 \text{ J/kg K}$
(j) Dynamic viscosity	$0.000612 \text{ kg/ms}$
(k) Thermal conductivity	$0.661 \text{ W/m K}$

The equations used to carry out theoretical calculations are discussed here.

Density of nanofluid	$\rho_{nf} = (1 - \varphi)\rho_w + \varphi\rho_{np}$
Specific heat of nanofluid	$C_{p(nf)} = \frac{\varphi\rho_{np}C_{p(np)} + (1-\varphi)\rho_w C_{pw}}{\rho_{nf}}$
Heat transfer rate of working nanofluid	$Q_f = mc_p(T_o - T_i)$
Average heat transfer coefficient	$h = mc_p(T_o - T_i)/A(T_w - T_b)$
Nusselt number	$Nu = hD/k$
Reynolds number	$Re = \rho U D/\mu$

Reynolds number is varied in the range of 5400–15,200 by changing the flow velocity  $U$ , other parameters being constant.

For a flow velocity of 0.25 m/s, the Reynolds number is calculated as follows.

$$Re = (1007.4 \times 0.25 \times 0.019)/0.000612 = 7819$$

## 4 Results and Discussion

CFD analysis is carried out using water and then adding 1 and 2% of nanoparticles to fluid by volume. Again, the experiment is repeated for different  $Y_o/Y$  twisting ratios of ODTTs incorporated in the tube. The results so obtained for different twisting ratios with different fluid concentrations are discussed in Fig. 5 (Fig. 4).

Figure 5 shows the variation of heat transfer coefficient ( $h$ ), Nusselt number ( $Nu$ ) and pressure drop ( $p$ ) for varying Reynolds numbers ( $Re$ ) in the range of 5400 to

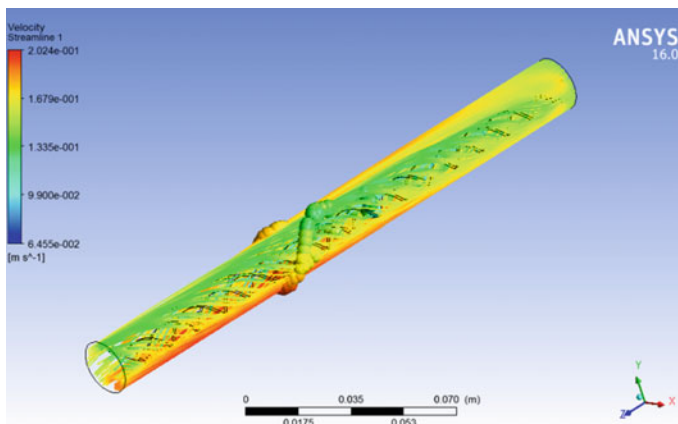


**Fig. 4** Velocity streamlines showing the effect of ODTT inserts in test tube

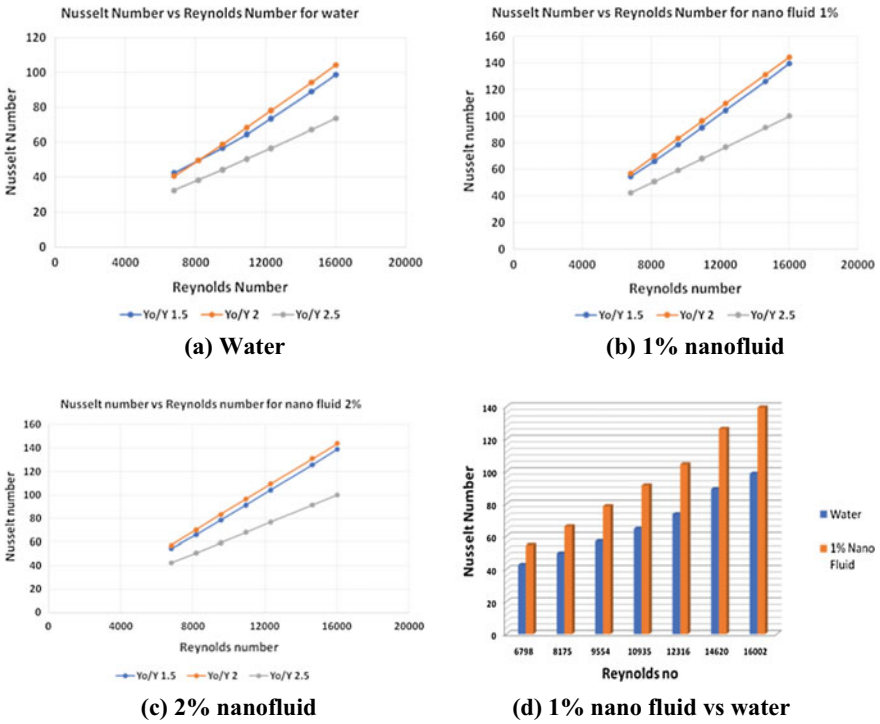


**Fig. 5** Nusselt number versus Reynolds number for varying twisting ratios

15,200. A comparison has been made by varying twisting ratios and concentration of nanofluid which are discussed in subsequent section.

From the plots shown in Fig. 5, it is observed that among all the twisting ratios,  $Y_o/Y = 2$  yielded better results and further raise in twisting ratio resulted in drop of thermal performance of the tube. In addition to that, the Nusselt number has increased resulting in better performance for increase in nanofluid concentration up to 1%. Further raise in concentration resulted in performance decline. It is also observed that the thermal performance when tested for water exhibited better performance in the absence of nanoparticles at low Reynolds numbers ranging in between 6000 and 8500. For all the other twisting ratios and concentrations, the nanofluid with 1% concentration and twisting ratio of  $Y_o/Y = 2$  gave best results.

## 5 Conclusion

The effect of twisted tape inserts (ODTTs) and  $Al_2O_3$  nanoparticles in water are addressed in this study where significant improvement in heat transfer is observed. Some of the conclusions drawn from the study are described below.

1. Nusselt number has increased significantly as the number of tapes increased.
2. The addition of  $\text{Al}_2\text{O}_3$  nanoparticles in water resulted in improved thermal performance.
3. Nusselt number in tubes with 1% nanofluid is found to be higher than that of plain tube when tested over the Reynolds number range of 5400–15,200. Further increase in concentration resulted in performance decline.
4. The twisting ratio of  $Y_o/Y = 2$  yielded better results in comparison with 1 and 1.5.

## References

1. Whithman JM (1896) The effects of retarders in fire tubes of steam boilers. *Railw J* 12:374
2. Rahim M, Shabaniyan SR, Alsairafi AA (2009) Experimental and CFD studies on heat transfer and friction factor characteristics of a tube equipped with modified twisted tape inserts. *Chem Eng Process Process Intensif* 48:762–770
3. Sivashanmugam P, Nagarajan PK (2007) studies on heat transfer and friction factor characteristics of laminar flow through a circular tube fitted with right and left helical screw-tape inserts. *Exp Therm Fluid Sci* 32:192–197
4. Sivashanmugam P, Nagarajan PK, Suresh S (2008) Experimental studies on heat transfer and friction factor characteristics in turbulent flow through a circular tube fitted with right-left helical screw-tape inserts. *Chem Eng Commun* 195:977–987
5. Nagarajan PK, Mukkamala Y, Sivashanmugam P (2010) Studies on heat transfer and friction factor characteristics of turbulent flow through a micro finned tube fitted with left-right inserts. *Appl Therm Eng* 30:1666–1672
6. Eiamsa-ard S, Nanan K, Thianpong C, Eiamsa-ard P (2013) Thermal performance evaluation of heat exchanger tubes equipped with coupling twisted-tapes. *Exp Heat Transfer* 26:413–430
7. Chang SW, Yu KW, Lu MH (2005) Heat transfer in tubes fitted with single, twin and triple twisted tapes. *Exp Heat Transfer* 18:279–294
8. Eiamsa-ard S, Thianpong C, Eiamsa-ard P, Promvong P (2010) Thermal characteristics in a heat exchanger tube fitted dual twisted tape elements in tandem. *Int Commun Heat Mass Transfer* 37:39–46
9. Zhang X, Liu Z, Liu W (2012) Numerical studies on heat transfer and flow characteristics for laminar flow in a tube with multiple regularly spaced twisted tapes. *Int J Therm Sci* 58:157–167
10. Eiamsa-ard S, Kiatkittipong K, Jedsadaratanachai W (2015) Heat transfer enhancement of  $\text{TiO}_2$ /water nanofluid in a heat exchanger tube equipped with overlapped dual twisted-tapes. *Eng Sci Technol Int J*

# Flow Characteristic Study of Contraction of Compressor Intermediate S-Shaped Duct Facility



Manish Sharma and Beena D. Baloni

**Abstract** This paper presents the influence of wall contours on a circular cross-section contraction nozzle of compressor intermediate S-shaped duct facility. Flow uniformity and boundary layer development under different wall contours are examined by using numerical simulations. Effect of wall shape on the pressure loss within the contraction is examined, and the maximum difference of pressure loss between the two wall shapes is about 84 Pa. Higher-order equation encounters higher pressure loss due to secondary flow generation and thicker boundary layer development. CT#4 (marched cubic case) shows the minimum value of  $U_n$  and standard deviation at the outlet of contraction which indicates the lowest non-uniformity among all cases.

**Keywords** S-shaped duct · Contraction wall shape · CFD

## 1 Introduction

Commercial aircraft engines demand lower noise and less specific fuel consumption. Turbofan engine meets these requirements through bypassing some portion of the total air flow from the compressor, combustion chamber, turbine and finally nozzle. Long-range civilian engines like GE90, GP7000 and Rolls-Royce Trent 1000 are operated at high bypass ratio of 8-11 to lower the specific fuel consumption (SFC). This SFC also helps to improve engine fuel efficiency [1]. Flow has to be directed from low-pressure system to high-pressure system and vice versa through annular ducts with a particular radial offset, hence higher the bypass ratio, larger the radial offset and disk bore diameter [2]. In a twin-spool arrangement, interconnecting ducts are used to make flow continuity between the turbo-machinery passages. Besides the compressors, application of the interconnecting ducts can be found in-between various components of the gas turbine. Duct connecting the low- to the high-pressure compressor is designed with virtually negligible diffusion rate. Hence, it ceases

---

M. Sharma (✉) · B. D. Baloni  
Mechanical Engineering Department, Sardar Vallabhbhai National Institute of Technology,  
Surat, Gujarat 395007, India  
e-mail: [sharma.manish726@gmail.com](mailto:sharma.manish726@gmail.com)

© Springer Nature Singapore Pte Ltd. 2020  
H. K. Voruganti et al. (eds.), *Advances in Applied Mechanical Engineering*,  
Lecture Notes in Mechanical Engineering,  
[https://doi.org/10.1007/978-981-15-1201-8\\_15](https://doi.org/10.1007/978-981-15-1201-8_15)

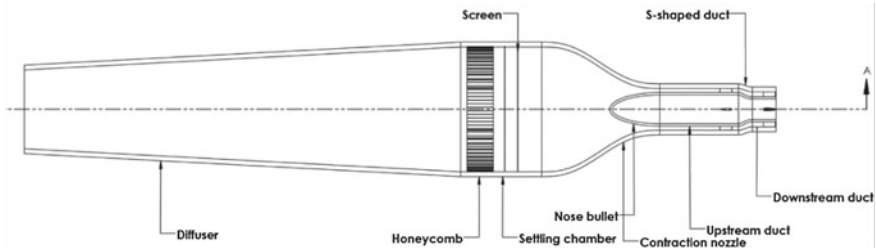


**Fig. 1** Schematic layout of experimental components

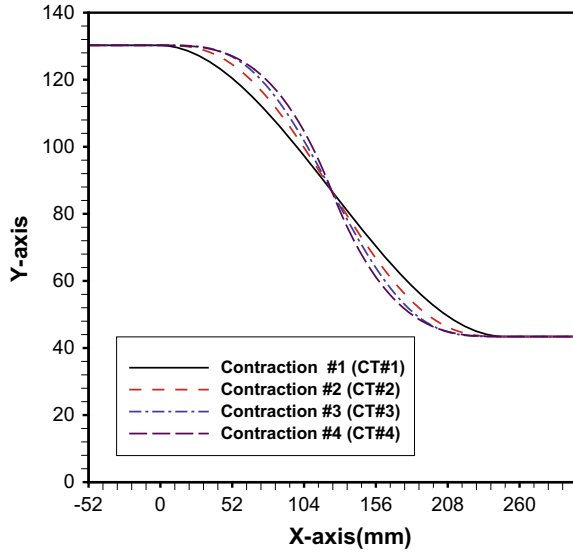
to constant area ratio (AR) whereas inter-stage turbine duct shows area variation throughout the passages, so a significant amount of diffusion is taken place [3].

Moreover, optimization and weight penalties dictate that the duct must be as short as possible, and hence it is designed as an S-shaped. This curved S-shape passage gives the secondary and three-dimensionally effects on the flow. Therefore, a low-speed large-scale experimental rig is designed for studying the flow within the intermediate compressor duct. Schematic layout of the experimental facility is shown in Fig. 1.

It consists of a wide-angle diffuser, settling chamber, honeycomb, screens, and contraction nozzle with a bullet, upstream and downstream straight duct and S-shaped annular duct. Compressed air at the required pressure ratio from the screw compressor is supplied to the facility. S-shaped duct plays a vital role to supply the high-quality air to the downstream high-pressure compressor; hence S-shaped duct itself must be supplied with a highly uniform air from the upstream components. The contraction nozzle placed upstream to the S-shaped duct has taken this responsibility. As soon as the compressed air approaches the contraction nozzle, its mean velocity gets increased which allows putting the honeycomb and screens into a low-speed region that helps to reduce the pressure losses. Moreover, it also mitigates both mean and fluctuating velocity variations to a smaller fraction of the average velocity.

The design of the contraction is significantly affected by the contraction ratio, contraction length, and contraction wall contour [4]. The optimum value of the contraction ratio and length is always desired to minimize the boundary layer thickness, overall cost, and to avoid flow separation. Contraction ratio in between 6 and 9 is generally supposed to produce an acceptable flow quality [5], and for the present case, the contraction ratio of '9' is selected. Moreover, the contraction wall shape also affects the performance of the contraction in terms of pressure drop and boundary layer evolution; hence several researchers had been focusing toward the same especially since the last two decades [6, 7]. The aim of the present work is to carry out numerical simulations using 'ANSYS FLUENT' to analyze the performance of the circular contraction nozzle in terms of pressure drop, exit flow uniformity and boundary layer thickness for four different wall contour shapes.

**Fig. 2** Four investigated contraction wall shapes



## 2 Problem Formulation

### 2.1 Contraction Dimensions

In the present work, the contraction's exit dimensions are based on the S-shaped annular duct. With a contraction ratio of 9, hydraulic diameters of the entrance and the exit are 260.514 mm and 86.838 mm, respectively. As per Bell and Mehta [8], optimum length to height ratio of 0.95 is selected which results in a total length of the computational domain of 352 mm ( $-52 \leq x \leq 300$ ) including upstream ( $-52 \leq x \leq 0$ ) and downstream ( $300 \leq x \leq 352$ ) straight portion of 52 mm each as shown in Fig. 2. In order to design and fabricate compressor intermediate S-shaped duct facility, contraction with an optimum wall contour needs to be designed. It has already been discussed that apart from the contraction ratio and length, contraction wall contour also has a significant impact on the performance of the contraction and finally, after reviewing the existing literature on contraction design, to obtain an optimum design, four contraction wall contours (see Table 1) have been selected.

### 2.2 Computational Fluid Dynamics Modeling

In order to simulate the flow field, it is assumed that flow is steady, three-dimensional, incompressible and turbulent. The computational domain is designed into ANSYS design modeler and meshed in ICEM CFD. Numerical simulation is carried out via



**Table 1** Equations of four investigated contraction (CT) wall contour

Contraction case	Original equation	Adopted equation
CT#1[8]	$Y(x) = H_i - (H_i - H_e) \left[ -2\left(\frac{x}{L}\right)^3 + 3\left(\frac{x}{L}\right)^2 \right]$	$Y = 130.257 - (130.257 - 43.419) \left[ -2\left(\frac{x}{248}\right)^3 + 3\left(\frac{x}{248}\right)^2 \right]$
CT#2[8]	$Y(x) = H_i - (H_i - H_e) \left[ 6\left(\frac{x}{L}\right)^5 - 15\left(\frac{x}{L}\right)^4 + 10\left(\frac{x}{L}\right)^3 \right]$	$Y = 130.257 - (130.257 - 43.419) \left[ 6\left(\frac{x}{248}\right)^5 - 15\left(\frac{x}{248}\right)^4 + 10\left(\frac{x}{248}\right)^3 \right]$
CT#3[8]	$Y(x) = H_i - (H_i - H_e) \left[ -20\left(\frac{x}{L}\right)^7 + 70\left(\frac{x}{L}\right)^6 - 84\left(\frac{x}{L}\right)^5 + 35\left(\frac{x}{L}\right)^4 \right]$	$Y = 130.257 - (130.257 - 43.419) \left[ -20\left(\frac{x}{248}\right)^7 + 70\left(\frac{x}{248}\right)^6 - 84\left(\frac{x}{248}\right)^5 + 35\left(\frac{x}{248}\right)^4 \right]$
CT#4[8]	$Y(x) = H_e + (H_i - H_e) \left[ 1 - \frac{1}{x_m^2} \left(\frac{x}{L}\right)^3, x < x_m \right]$ $Y(x) = H_e + \left[ \frac{(H_i - H_e)}{(1 - x_m)} \left( 1 - \frac{x}{L} \right)^3, x > x_m \right]$	$Y = 43.419 + (130.257 - 43.419) \left[ 1 - \frac{1}{0.5^2} \left(\frac{x}{248}\right)^3, x < 124 \right]$ $Y = 43.419 + \left[ \frac{(130.257 - 43.419)}{(1 - 0.5)} (1 - 248)^3, x > 124 \right]$

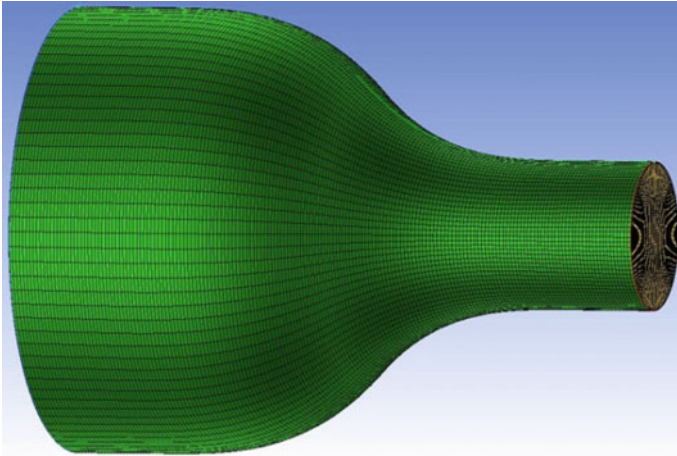


**Fig. 3** Hexahedral mesh of CT#1 case

FLUENT 15.0 by adopting shear stress transportation (SST)  $k-\omega$  turbulence model. This model has more strength to predict the flow in the vicinity of the wall more accurately [8]. Pressure-velocity coupling correction is done by the ‘SIMPLE’ algorithm, and the second-order upwind scheme is imposed for the momentum, turbulent kinetic energy, and specific dissipation rate. Since S-shaped duct was designed as per the exit condition of the low-pressure compressor, hence in order to meet the same, at the inlet of the contraction a uniform velocity profile of 7.5 m/s is selected as the inlet boundary condition and 2.94 bar of pressure is imposed on the outlet whereas the no-slip condition is applied to the contraction walls.

In the present case, the structured hexahedral mesh of  $5.32 \times 10^5$  cells are used for all the cases while maintaining the wall distances ( $y^+$ ) within the boundary layer region below to 1 ( $y^+ \leq 1$ ) and an example of mesh obtained for the case with CT#1 is shown in Fig. 3. To select an optimum mesh size, a grid independent test has been carried out for the case with CT#1. For this, three different mesh sizes are selected and velocity and pressure profiles along the centerline of the contraction are evaluated. Figures 4 and 5 depict that the predicted velocity and pressure profiles are exactly overlapping to each other for all cases hence mesh size of  $5.32 \times 10^5$  is chosen as the optimum size for the remaining cases.

### 3 Results and Discussions

This section will emphasize the effect of contraction wall shape on the axisymmetric circular cross-sections contractions. Figure 6 shows the static pressure variation along the contraction wall for the case of CT#1. Static pressure is the highest at the inlet due to its maximum area, and it is gradually decreasing to achieve the minimum value at

**Fig. 4** Velocity profiles along centerline for different mesh size

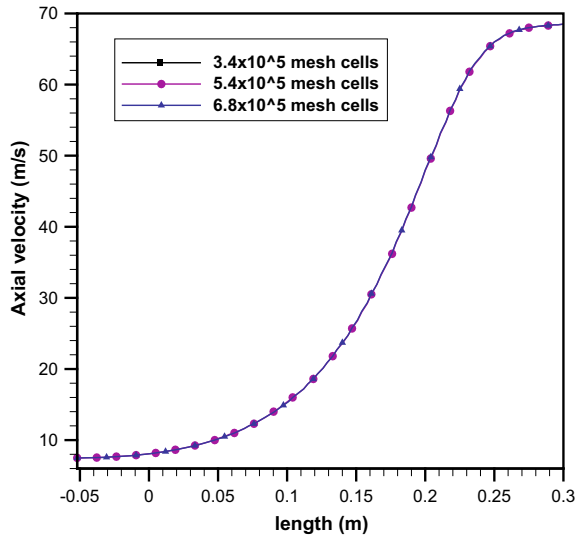
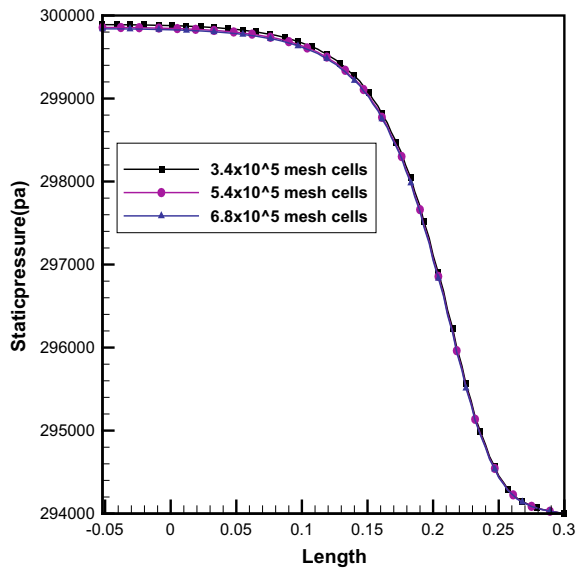


**Fig. 5** Pressure profiles along centerline for different mesh size



the outlet. In fact, static pressure contours for all cases are almost in identical nature but have a marginal difference in magnitude. However, CT#3 requires a higher static upstream pressure to accelerate the flow up to 68 m/s at the contraction exit, and consequently, it encounters pressure loss of 245.84 Pa which is maximum among all cases as shown in Table 2. In addition to it, the minimum pressure loss is observed as 162.05 Pa for the case CT#4. In the last case, because the generation of secondary

**Fig. 6** Static pressures contour for CT#1

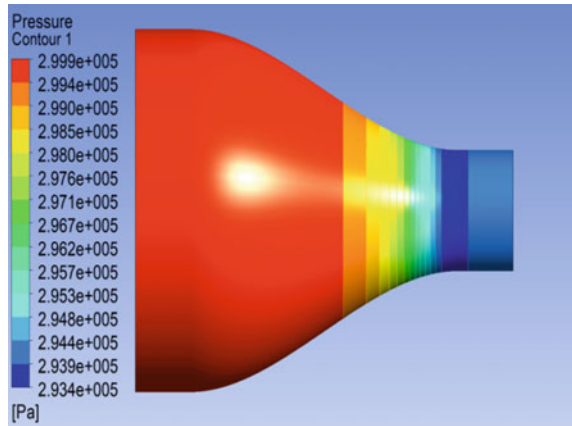


**Table 2** Pressure drops along investigated contractions

Case	Inlet total pressure	Outlet total pressure	Loss	% Loss
CT#1	299,936.41	299,724.28	212.13	0.071
CT#2	299,955.41	299,725.78	229.63	0.077
CT#3	299,972.56	299,726.72	245.84	0.082
CT#4	299,889.22	299,727.16	162.05	0.054

and vortex flow is lowest as compared to other cases and as the consequence of it, CT#4 is subjected to the lowest pressure loss. In other words, it could be concluded that the higher pressure loss might be causing higher operating cost.

The velocity profiles at the contraction exits are shown in Fig. 7. The velocity profile of case CT#1 depicts a thinner boundary layer at the outlet whereas for case CT#4, it is thicker. Higher-order equations show thicker boundary layer generation and hence have more chance of flow blockage.

The core regions of the contraction outlet do not affect the boundary layer development. At the vicinity of the wall, the boundary layer is developed and gradually increases toward the core region. Even though flow through all cases is still attached, all cases show distinct variations of non-uniformity. Figure 8 shows a comparison of the predicted cross-sectional velocity non-uniformity ( $U_n$ ) variations among all cases. Here,  $U_n$  is the ratio of maximum velocity deviation to the local cross-sectional mean velocity. It is observed that at the inlet of the contraction  $U_n$  has the smallest value and starts to increase gradually along the contraction length just because of change in radius of curvature. Moreover, its maximum value for all cases is found between  $x/L = 0.2-0.4$  that is near to the matched point of wall contour. Since the wall contour of contraction consists of concave followed by the convex curvature and because of this, at the matching point, contraction is encountered with a sudden change of slope (see Fig. 2) which eventually increases the non-uniformity. Because CT#3 (cubic match wall contour) is subjected to maximum change in

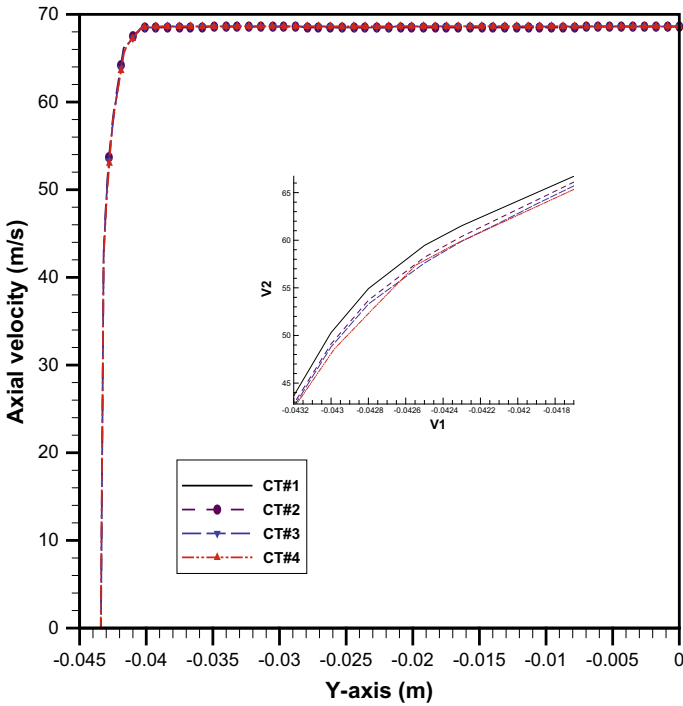
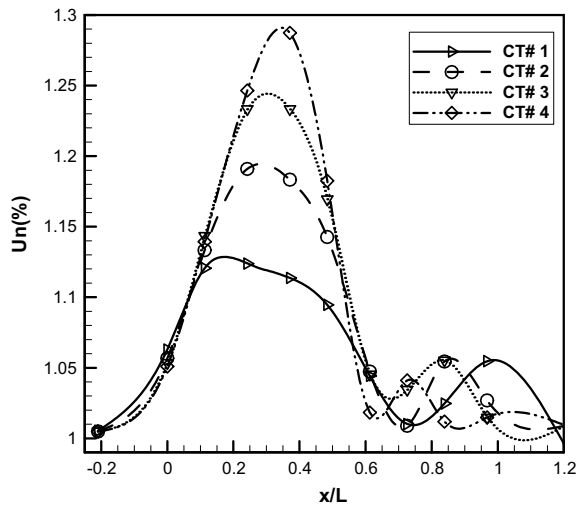


Fig. 7 Axial velocity profiles at exit

Fig. 8 Variations of velocity non-uniformity



**Table 3** Axial velocity standard deviations at the outlet

Case	Standard deviation
CT#1	0.08241
CT#2	0.08818
CT#3	0.08941
CT#4	0.07667

radius of curvature at the matching point (see Fig. 2), it depicts the highest value of  $U_n$  whereas CT#1(third-order polynomial) shows the lowest peak. Even though the CT#3 shows the highest peak of  $U_n$ , it shows the minimum value at the outlet of the contraction which indicates the lowest non-uniformity.

Similarly, the standard deviation is also another way to quantify the non-uniformity. The deterioration in uniformity of the flow at the outlet can be expressed in terms of standard deviation in axial velocity at the outlet. The axial velocity standard deviations at the outlet of the contractions are listed in Table 3. The maximum standard deviation is observed for CT#3 whereas it is the minimum for the CT#4 case.

Since CT#4 has shown lowest non-uniformity at the outlet, mean velocity profiles at the selected cross-sections are demonstrated here (see Fig. 9) only for CT#4 case ( $R$  is the local radius of the section). Figure 9 concludes that maximum velocity for all sections is found at the center regions and this velocity is gradually decreasing toward the wall to satisfy the no-slip conditions. In other words, it can be understood that a large traverse velocity gradients are obtained at the vicinity of the wall due to the existence of boundary layers.

## 4 Conclusions

In the present work, computational simulations of contraction of compressor intermediate S-shaped duct facility have been carried out. In order to make a proper understanding of the flow physics of a contraction, four different wall shapes are selected. The primary outcomes are highlighted as follows:

- Different contraction wall shapes result in pressure loss within the contraction, and the maximum difference between them is about 84 Pa. Therefore, the wall shape has a significant role.
- Higher-order equation of wall shape encounters thicker boundary layer as well as higher standard deviation at the outlet of the contraction whereas lower-order equation results minimum pressure loss.
- In the contraction domain, the highest peak of  $U_n$  is shown by the CT#4 among all cases.
- CT#4 shows the minimum value of  $U_n$  and standard deviation at the outlet of contraction which indicates the lowest non-uniformity among all cases.

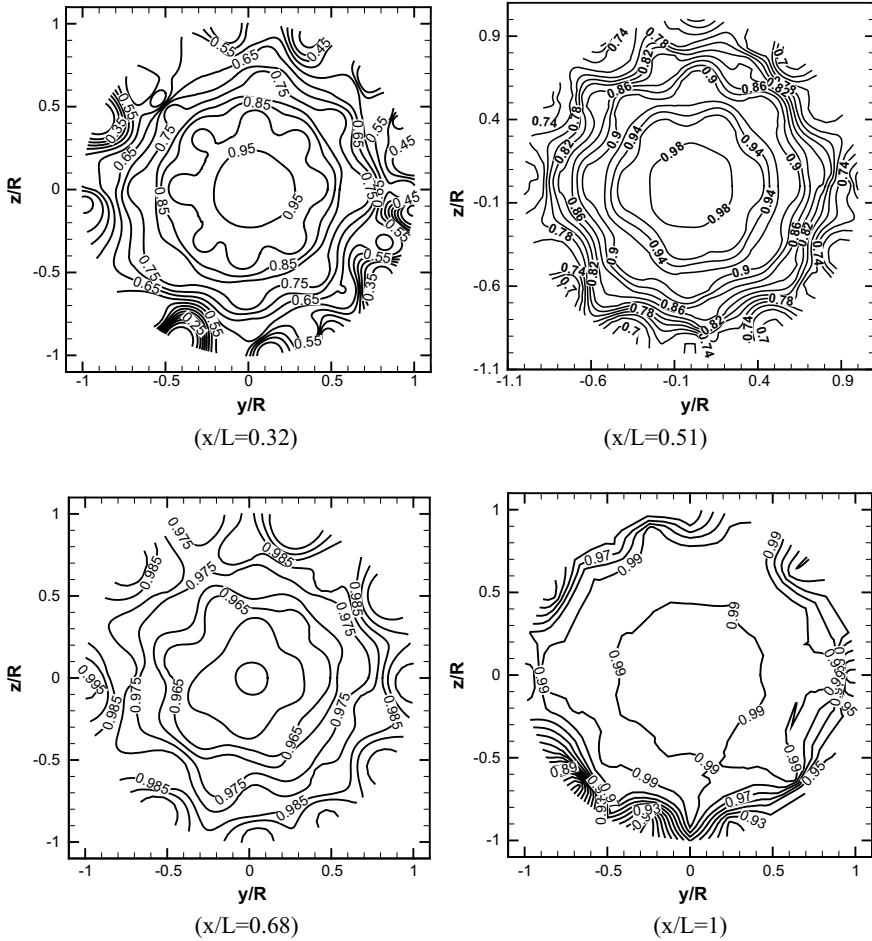


**Fig. 9** Sectional velocity profiles

- Large traverse velocity gradients are obtained at the vicinity of the wall due to the existence of boundary layers.

## References

1. Saravanamuttoo HIH, Rogers GFC, Henry C (2001) Gas turbine theory, 5th edn. Pearson Education Ltd.
2. Joachim K (2009) Fundamental differences between conventional and geared turbfans. In: ASME turbo expo 2009 Power Land, Sea Air, Orlando, Florida, USA, pp 1–9
3. Norris G, Dominy RG (1998) Flow through s-shaped annular, inter-turbine diffusers. University of Durham, Ph.D. thesis

4. Fang F-M (2005) A design method for contractions with square end sections. *J Fluids Eng* 119(2):454–458. <https://doi.org/10.1115/1.2819156>
5. Mehta RD, Bradshaw P (1979) Design for small low speed wind tunnels. *Aeronaut J R Aeronaut Soc* 7:443–453
6. Ahmed NA (2013) Wind tunnel designs and their diverse engineering applications. InTech Ltd.
7. Su Y (1991) Flow analysis and design of three-dimensional wind tunnel contractions. *AIAA J* 29(11):1912–1920
8. Bell JH, Mehta RD (1988) Contraction design for small low-speed wind tunnels. Technical report, NASA



# Alternate Heating Process in ESP Hoppers of Thermal Power Plant—An Experimental Pilot Investigation



R. Saravanan and Ramakotaiah Maddumala

**Abstract** The researchers focus on eco-friendly and economy of power generation in the thermal power plants. The system-wise analysis will help to find the way to economic power generation. This research focuses the hopper heating concern. Usually, the electric heating is employed to maintaining the hopper as warm to avoid distraction in the flow of ash. The research argues the feasibility of steam heating in the view of waste heat recovery. A new kind of hopper was designed, and its prototype was fabricated, tested and analysed. The qualitative and quantitative benefits of proposed system were discussed. The proposed system, irrespective of climatic changes, works well.

**Keywords** ESP hopper · Steam heating · Energy · Pilot investigation

## 1 Introduction

In the thermal power plant, the hopper heating is done by electric heater for avoiding the condensation fly ash. The condensed fly ash causes the big trouble in the ash collecting system [1]. Even though the ESP is a wonderful method for collecting the fly ash [2], [3] insisted that the need for improving the system with economic and environmental pollution concern. Hence, different aspects of improving ESP have been reported in the literature. Reference [4] characterized the fly ash collected in the hopper based on the combustion of various coal grades. Reference [5] discussed the guidelines for making a right choice of material used for duct like stainless steel, aluminium and copper for ESP hopper. Reference [6] validated the ESP performances with the emission norm of the Tamil Nadu state government, [7] reported that the use of alkali content coals as well as non-coking low sulphur coal increase feed of the fuel as far as rapid loading of ash on ESP. Reference [8] discussed the density of fly ash with respect to climate changes and prerequisites for avoiding those issues.

---

R. Saravanan (✉) · R. Maddumala  
Ellenki College of Engineering and Technology, Hyderabad, Telangana 502319, India  
e-mail: [dr.saravanan@gmail.com](mailto:dr.saravanan@gmail.com)

© Springer Nature Singapore Pte Ltd. 2020  
H. K. Voruganti et al. (eds.), *Advances in Applied Mechanical Engineering*,  
Lecture Notes in Mechanical Engineering,  
[https://doi.org/10.1007/978-981-15-1201-8\\_16](https://doi.org/10.1007/978-981-15-1201-8_16)

But in this paper focuses the alternate hopper heating system based on waste heat recovery strategy.

## 2 Materials and Methods

In general, the net power output can be increased by reduction consumption of power by its own accessories such as boiler feed pump, forced draught fan, induced draught fan, DM water pump, APH drive motor, soot blower motor, pulveriser drive motor, emitting electrode, PA fan motor and ESP hopper coil. According to the observed statistics, the ESP hopper coil consumes high energy. So this research focuses on energy conservation on ESP hopper heating. At present, electric heating is employed for heating the hoppers. This paper addresses the feasibility of adopting the steam heating for the same. The source of such steam was identified. The option 1 (refer Fig. 1) is by tapping hot air from wind box section in the boiler, i.e. such air pre-heater (APH). The option 2 (refer Fig. 2) is by taking the flash steam which is sent to the atmosphere after condensing the boiler feed water. This high-pressure and high-temperature water gets vaporized due to sudden expansion if it is released to the atmosphere. Hence, that source can be used for ESP hopper coil.

The conventional hopper and its principal parts are depicted in Fig. 3. Averagely, the ESP hopper coils consume 6 kW of energy. The methodology is primarily some feasibility studies to be carried out like steam flow specification to replace those heating coils. The distance considered from wind box to hopper is 40 m (the actual distance is 30–35 m apart) for estimating heat transfer and heat loss. The fabrication

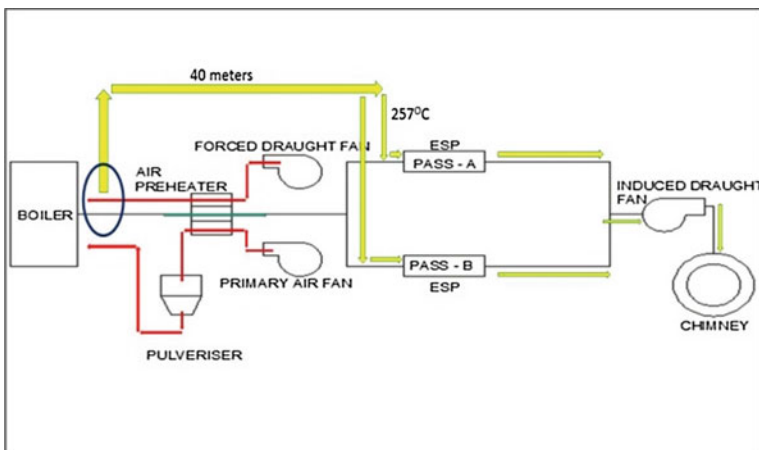


**Fig. 1** Proposed heat sources: before air pre-heater

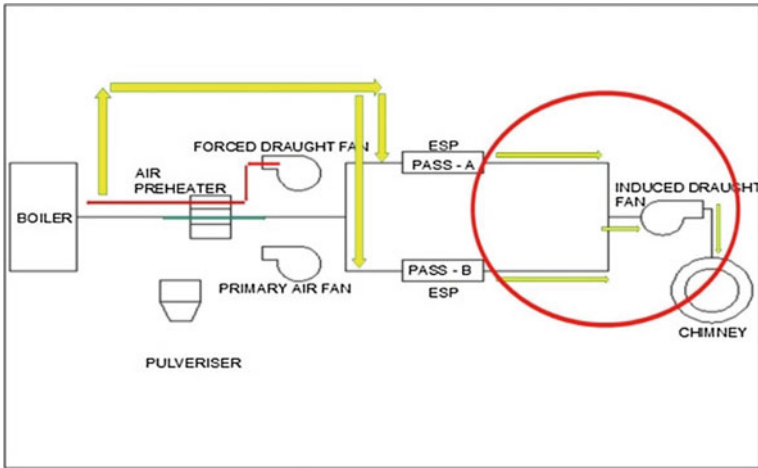


Fig. 2 Proposed heat source at disposal of hot air

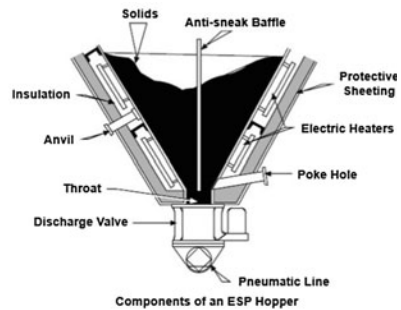


Fig. 3 Conventional ESP hopper (left) and components of ESP hopper (Right) (1)

of the model, testing and analysis is to be carried out. The theoretical and actual performances are to be compared.

### 3 Design

The heating chamber is to be designed to replace the hopper coil. It has to provide power source to maintain fly ash at a temperature range to avoid sticking of them in the inside walls of hopper while collection. Estimation of total mass flow rate required for specified power and velocity of hot air can be estimated by fusing following data. The minimum relative temperature required is 120–130 °C. The ambient air temperature or heating chamber temperature ( $T_s$ ) without heater is 35 °C. The available heat source, i.e. hot air temperature, is 300 °C. The measured mass

flow rate in the duct is 4.688 T/h the required power ( $Q$ ) is 6 kW. The specific heat of air ( $C_p$ ) at 300 °C is 1.049 kJ/Kg K. The required mass flow rate ( $m$ ) out of 464 t/h is  $Q/(C_p \Delta T)$ , i.e. 0.0390 kg/s per hopper. There are 24 hoppers connected; hence, overall mass flow rate is 0.936 kg/s or 3.32 tonne per h. The available square duct is 0.1-m-long slant surface. The leaving air temperature at the distance of 30 m is 257.7 °C or 496 F (in let temperature of the hopper heating ( $T_i$ )). The density of the air  $\approx 257.7$  °C is 0.616 kg/m<sup>3</sup>. Hence, volume flow rate is 1.51 m<sup>3</sup>/s. The area of cross section is 0.01 m<sup>2</sup>, and then flow velocity is 151 m/s. The usual notations were used for properties of air for calculated temperature. The hydraulic diameter ( $D_h$ ) is the cross-sectional area ( $A_c$ ) in which the entry of air is made.  $D_h = (4A_c^2/4A_c) = A_c = 0.0125$  m. The velocity of air flows through the cross-sectional area or velocity of the medium ( $v_m$ ) is equal to  $(V/A_c) = (0.052/0.0125) = 4.16$  m/s. The Reynolds number ( $R_e$ ) is equal to  $[(v_m * D_h)/\nu] = (4.16 * 0.0125)/30.09 * 10^{-6} = 1395.08 < 2300$ , i.e. the flow is laminar. For laminar flow, Pr is 0.682. Hence, the Nusselt number  $Nu = 0.023R_e^{0.8} Pr^{0.3} = 6.722$ . The thermal conductivity ( $k$ ) is 0.03469. Therefore, the value of  $h$  obtained from the relation of  $Nu = (h * D_h)/k$  is 19.5748 W/m<sup>2</sup> K. The exit temperature ( $T_e$ ) of hot air from the hopper heating system can be computed by using the mathematical relation of  $T_e = T_s - (T_s - T_i) * e^{-h.A_c/(mC_p)}$  and equal to 152.13 °C. The logarithmic mean temperature difference (LMTD) can be computed as 137.018 °C =  $\nabla T_{ln}$ . Hence, the overall heat transfer coefficient ( $Q$ ) =  $hA\nabla T_{ln} = 6.2$  kW. The requited heating is 6 kW. Hence, the design is safe.

## 4 Prototyping

As the hopper is taper, the heating system to be fabricated is shown in the proposed model. The serpentine tubes are fixed by welding on outside surfaces of the inner shell of hopper, i.e. the steam should pass through a continuous small tube and spread the tube on the surface as shown in left in Fig. 4; at the same time, it must be ensured that all the four slant surfaces of heating chamber are maintained at same temperature. Probably, the steam inlet is to be at bottom where more heating is required. The fabricated model is shown in the middle of Fig. 4. The hopper heat testing set-up is



**Fig. 4** Design (Left) fabricated prototype (middle) and testing set-up (right)

shown in the right side of Fig. 4. The exhaust of Kirloskar four-stroke twin cylinder diesel engine is employed as heat source. The exhaust passes in the hopper prototype, and the heating performance is evaluated. The *K*-type thermocouple thermometers were used for temperature measurement. The observations are obtained at various temperatures with respect to time for evaluating the workability of proposed hopper heating and heating response time. The heating performances were observed by passing the exhaust into the inlet of the hopper prototype at slant surface 1 as inlet and the slant surface 4 as outlet i.e., the tube's end of neighbor side was considered as output. Similarly, it was tested and observed for remaining three possibilities. The observations were obtained from five different places of the slant surfaces, and their rounded-off average value is recorded and furnished in Table 1. The procedure is repeated until all four slant surfaces as input as their neighbour slant surface as outlet. Those observations furnished in Tables 2, 3 and Table 4 for slant surface 2 as inlet slant surface 1 as outlet case, slant surface 3 as inlet slant surface 2 as outlet case and slant surface 4 as inlet slant surface 1 as outlet case respectively.

**Table 1** Results of case I (slant surface 1 as inlet and slant surface 4 as outlet)

Sl. no	Time (min)	Temperature (°C)			
		Slant surface 1	Slant surface 2	Slant surface 3	Slant surface 4
1	1–5	35	33	30	31
2	5–15	46	45	41	40
3	15–25	55	55	50	53
4	25–35	59	58	54	57
5	35–45	61	61	57	60
6	45–55	62	62	59	61

**Table 2** Results of case II (slant surface 2 as inlet and slant surface 1 as outlet)

Sl. no.	Time (min)	Temperature (°C)			
		Slant surface 1	Slant surface 2	Slant surface 3	Slant surface 4
1	1–5	32	34	31	31
2	5–15	44	46	42	43
3	15–25	54	55	52	54
4	25–35	58	58	54	56
5	35–45	61	61	58	60
6	45–55	62	62	59	61

**Table 3** Results of case III (slant surface 3 as inlet and slant surface 2 as outlet)

Sl. no.	Time (min)	Temperature (°C)			
		Slant surface 1	Slant surface 2	Slant surface 3	Slant surface 4
1	1–5	33	33	31	34
2	5–15	45	45	42	45
3	15–25	54	53	49	53
4	25–35	59	58	54	58
5	35–45	60	60	57	61
6	45–55	61	61	59	62

**Table 4** Results of case IV (slant surface 4 as inlet and slant surface 3 as outlet)

Sl. no.	Time (min)	Temperature (°C)			
		Slant surface 1	Slant surface 2	Slant surface 3	Slant surface 4
1	1–5	35	36	32	36
2	5–15	49	49	45	49
3	15–25	56	55	52	59
4	25–35	59	59	55	60
5	35–45	61	60	57	61
6	45–55	63	62	59	63

## 5 Result and Discussions

The specially designed and fabricated a prototype of hot gas/steam heating hopper was tested with exhaust gases of IC engine for replacing the conventional electric heating. The test results of prototype of the proposed system are shown in the graphical form in Figs. 4 and 5. Figure 4 illustrates case-wise comparison on each slant surface. Figure 5 depicts the slant surface-wise comparison with respect to the cases considered. From Fig. 4, it is understood that the rise of temperature in each slant surface is found almost as uniform for irrespective of case. The negligence variation was observed. From Fig. 5, it is clear that with respect to input slant surface, the variation of temperature raise with respect time is not significant. Only the slant surface 3 picks up the temperature little slow controversy the rise of temperature of slant surface 4 is fast a little due to some fabrication finish issues. Hence, it is suggested that the thermal insulation to be provided with external surfaces and any slant surface can be preferred for inlet, and its previous will be exit of hot steam (Figs. 5 and 6).

The cost of power supply for industry varies globally based on many factors. The average groups of thermal power plants near coal mine are 100–150 hoppers. The cost of heating is almost free by the use of proposed system. If the thermal power plant operates 24 h per day for a month, the power required varies from 600 kW to 900 kW per h and for a month, 32,000 kWh per month to 648,000 kWh per month.

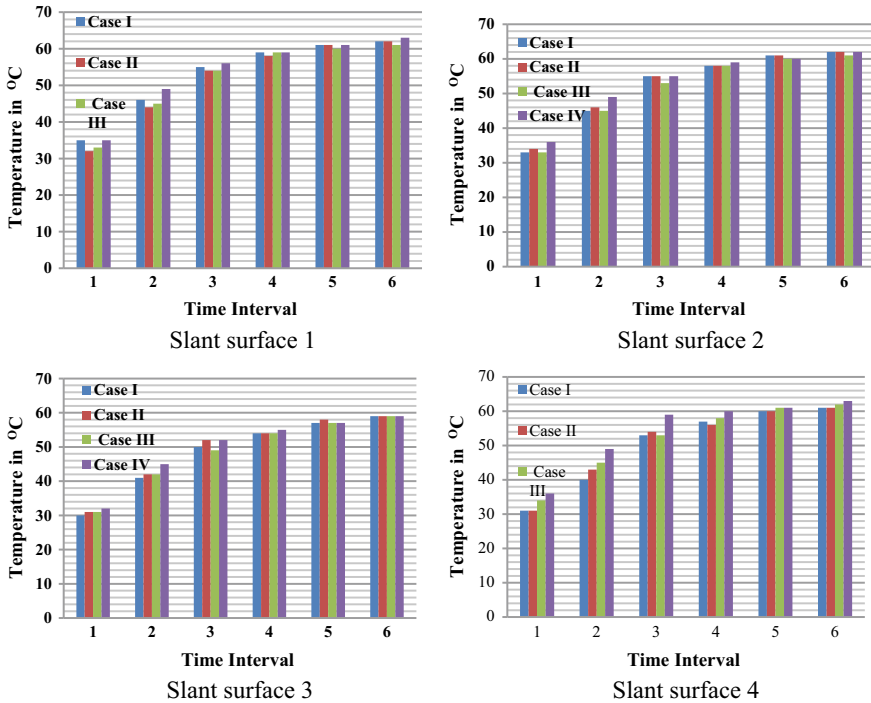


Fig. 5 Case-wise comparison on each slant surface

The reader may be calculating the exact savings based on exact numbers of hopper available and hours of plant running.

## 6 Conclusion

The alternate heating system for ash collecting hopper for thermal power plant is discussed in this paper. The designed and fabricated prototype for hot gas/steam heating system in hopper is tested. This proposal is based on recovery of waste heat from the boiler. As it is continuous operation at stated operating pressure, the supply of steam for the hopper heating system will not affect. Hence, the operating cost is absolutely free. In the proposed system, the steam passes through the small tubes, so noncorrosive tube material is recommended. The proposed system may be used as primary heating of the ash collecting hoppers for higher savings from 432,000 kWh per month to 648,000 kWh per month for the thermal plants having hoppers from 100 to 150 nos. According to poka-yoke concept, as the thermal power plant operating continuously, it is suggested that the electric heating source is secondary for ensuring mistake proof operation. So the proposed system is to be implemented on the existing hopper set-up.

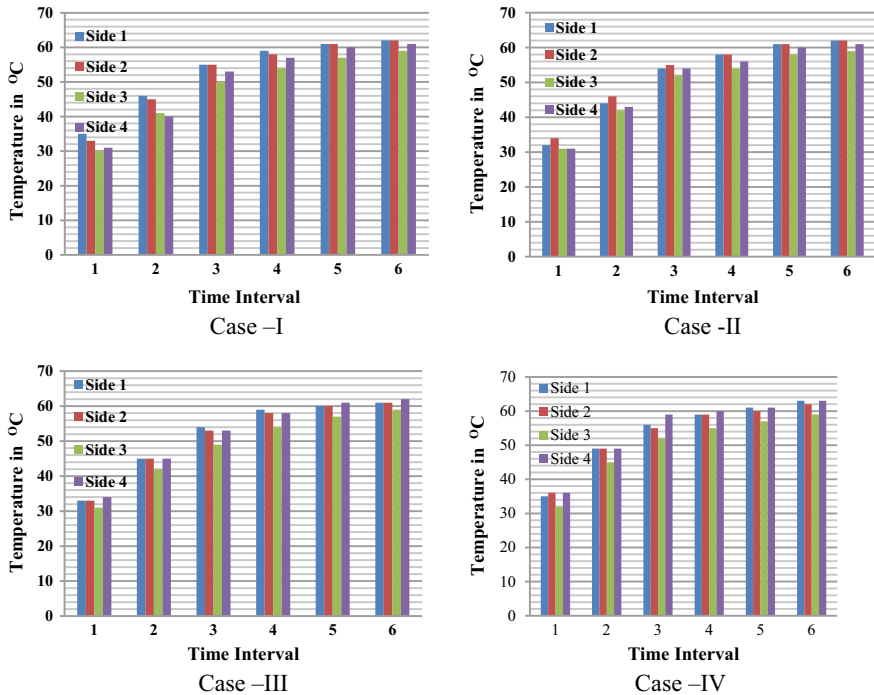


Fig. 6 Slant surface-wise comparison for each case

## References

1. Saravanan R, Raju R (2007) Design of pressurized dense fly ash conveying system (PDFACS) for thermal power plant. In: Proceeding of emerging challenges in design and manufacturing technologies, vol 1. Sathyabama University, Chennai, and COMBAT Vehicles Research and Development Establishment, DRDO, Chennai, pp 1–10
2. Gupta TN (2003) Holistic performance of fly ash in construction technologies. In: 3rd international conference of fly ash utilization and disposal at New Delhi, vol 1, pp 27–34
3. Parker KR (1997) Why an electrostatic precipitator? Appl Electrostat Precipit, 1–10, <https://link.springer.com/book/10.1007/978-94-009-1553-4>
4. Valentine B, Guedes A, Flores D, Ward CR, Hower JC (2009) Variation in fly ash composition with sampling location: case study from a Portuguese power plant. Coal Combust Gas Prod 1:14–24
5. Stratton JH (2000) Metal duct selection and application. ASHRAE J 42(6):24–29
6. Sindhuja S (2018) Emission norms for electrostatic precipitators in Tamil Nadu thermal power plants. J Pure Appl Math 118(20):785–789
7. Mandal PK, Kumar T (2006) Electrostatic precipitator performance in Indian pulverized coal based thermal power stations. In: Problems and solutions, ICESP X, paper 3A1, pp 1–13
8. Chaudhary SK (2014) Fly-ash and climate change. J Env Sci Sustain 2(1):31–35



# Experimental Study on the Performance of Micro-aerial Vehicle Propeller



P. S. Premkumar, M. Sureshmohan, K. Siyuly, S. Vasanthakumar, R. Naveen Kumar, S. DenielaGrene and S. Sanjaykumar

**Abstract** Aircraft propeller performance study is one of the most challenging areas in the aeronautical research field. This paper compares the experimental and theoretical thrust results for various propellers and also provides a methodology for a portable static experimental setup. This will pave the way for propeller design by comparing the thrust values. These data will give more clarity to researchers comparing the experimental and theoretical thrust values of micro-aerial vehicle (MAV) propeller.

**Keywords** Propeller · Micro-aerial vehicle (MAV)

## 1 Introduction

Currently, the aircraft industries test nearly 4,000 propellers to choose the best among them. A two-bladed prop is the most efficient one and hence been widely used. Constant pitch propeller whose blade angle is fixed with respect to the hub is suitable for the low-speed airplane. The propellers have a magnificent role in the aviation field and also several other fields. This research addresses the combined work of experimental and theoretical study that gives a wider conclusion on the selection of best propellers and flow field characteristics around the propeller. The analytical study is done using the 'blade element theory' to determine the thrust and torque of the propeller [1]. The product of thrust developed and airspeed of the aircraft gives the propulsive power. The ratio of propulsive power to the brake horsepower gives the propulsive efficiency. The propeller tip vortices create rotational energy loss. During the rotation of the propeller, velocity components are considered. For each blade, there is always an equal and opposite lift force component being generated

---

P. S. Premkumar (✉) · K. Siyuly · S. Vasanthakumar · R. Naveen Kumar · S. DenielaGrene · S. Sanjaykumar

Department of Aeronautical Engineering, Kumaraguru College of Technology, Coimbatore, India  
e-mail: [premkumar.ps.aeu@kct.ac.in](mailto:premkumar.ps.aeu@kct.ac.in)

M. Sureshmohan  
Altran Technologies, Coimbatore, India

by the diametrically opposed blade. The potential influence and wake effects play a major role [2]. The total efficiency mainly depends on stator performance. The selection of airfoil also plays a vital role. The results are determined by carrying out the experiments using portable setups to measure the propeller characteristics such as thrust. The same process is carried out for various propellers which satisfies the core objective of this paper. This data obtained from this research will be useful for selecting the propeller for miniature aerial vehicle (MAV) based on its operation and requirement.

## 2 Experimental Setup

An experimental setup has been built to find out the static thrust produced by a propeller in different RPM. Keeping in mind the diameter of the propeller chosen, the frame is designed. The height of the frame is 120 cm, width is 60 cm and the length is 25 cm. It is built using a steel rod of thickness 1 and 1/2 inches. The setup takes the shape of a truncated prism. The diameter of the propeller is taken into consideration, so as to reduce the risk of tip flow disturbances. The setup is built to be a strong one to withstand the load produced by the propeller rotation. The setup is designed in such a way that the airflow direction is upward and the thrust direction is toward the ground [3]. The components are chosen to take into account the power required to conduct the experiment at different RPM. It is shown in Table 1.

The weighing scale is the base of the setup. Since the weighing scale value is taken as the thrust value also, the frame is mounted on top of our weighing scale, and the value is tarred. The frame is 6.4 kg approximately. On top of the frame, the motor is mounted upside down. The propeller is screwed to the motor. The rotation of the motor is anti-clockwise. The motor is connected to the electronic speed controller. The ESC is in turn connected to the receiver and the power controller [4]. The power controller is connected to the switched-mode power supply (SMPS). The power controller controls the flow of current to the motor and saves the motor from burning

**Table 1** Experimental setup—component details

Component	Description
Brushless motor	Avionic C2830/12 KV1000 brushless motor
ESC	Wolf pack 30 Amp ESC SKU: RZ04410
Transmitter/receiver	Fly Sky FS-T6 2.4 GHz digital proportional 6 channel transmitter and receiver
Propeller	13 × 8 (inches), Two-bladed propeller
Tachometer	Portable digital laser tachometer non-contact rotate speed detector LCD tachometer (RPM meter range 2.5–99999 RPM)

out. The receiver obtains the signals from the transmitter and delivers it to the motor. Figures 1, 2 and 3 show the proposed experimental setup with components and propellers tested.

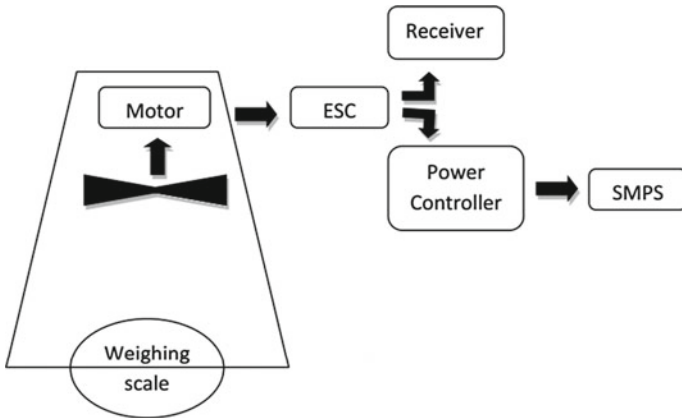


Fig. 1 Line diagram of the experimental setup

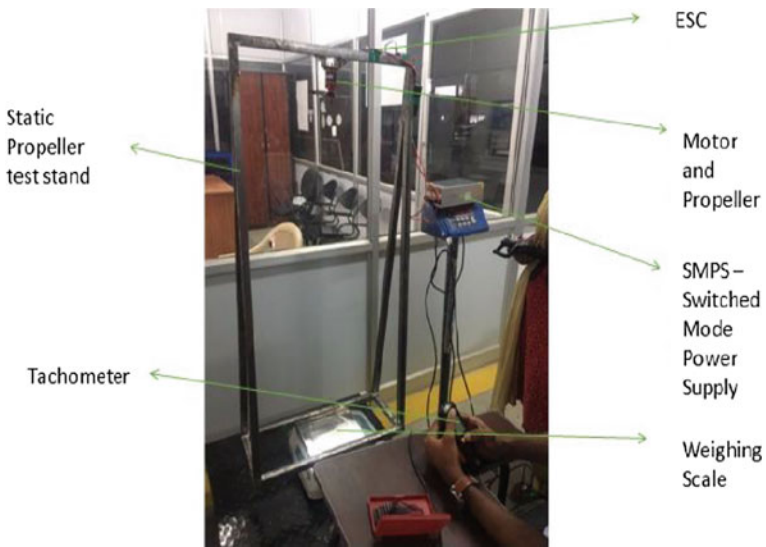
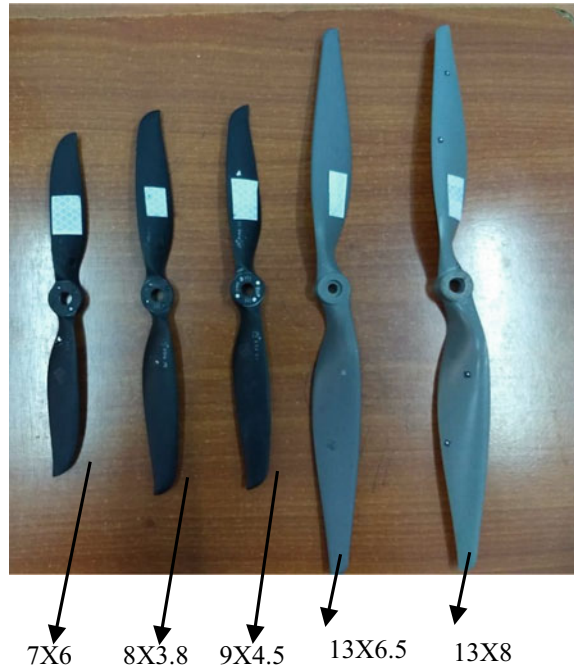


Fig. 2 Experimental setup

**Fig. 3** Various propeller configurations



### 3 Results and Discussion

#### 3.1 Experimental Results

Different RPM was chosen for the test. The experiment was conducted for different specifications of propellers. The thrust value which is equivalent to the weighing scale value is noted down and compared with the theoretical results [4].

From Fig. 4 it is observed that for lower RPM, the thrust value difference (33%) is high between experimental and theoretical values. In the higher RPM, around 10% of differences are observed between the experimental and theoretical values for the  $7 \times 6$  propeller.

From Fig. 5, it is observed that for lower RPM, the thrust value difference (39%) is high between experimental and theoretical values. In the higher RPM, around 28% of differences are observed between the experimental and theoretical values for the  $13 \times 8$  propeller.

From Fig. 6, it is observed that for lower RPM, the thrust value difference (37%) is high between experimental and theoretical values. In the higher RPM, around 14% of differences are observed between the experimental and theoretical values for the  $9 \times 4.5$  propeller.

From Fig. 7, it is observed that for lower RPM, the thrust value difference (39%) is high between experimental and theoretical values. In the higher RPM, around 21%

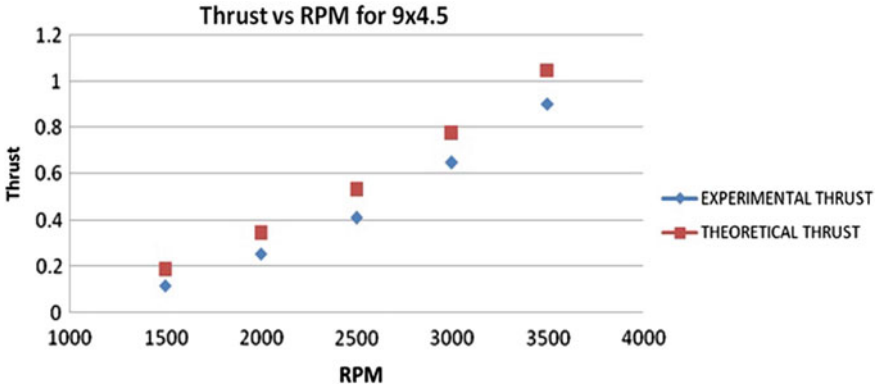


Fig. 4 Thrust vs propeller speed (RPM) for 7 × 6 propeller

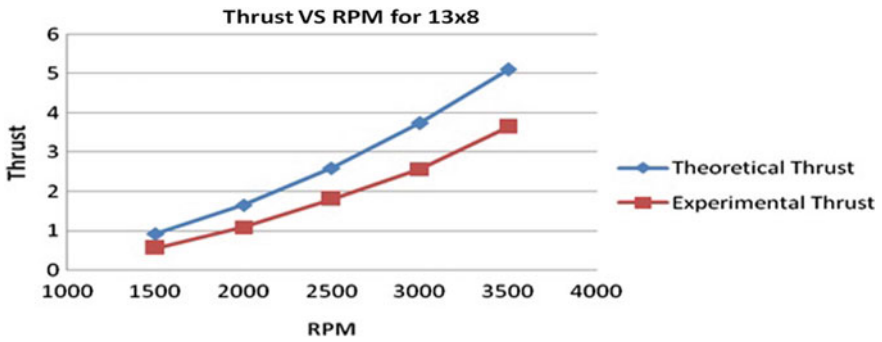


Fig. 5 Thrust vs propeller speed (RPM) for 13 × 8 propeller

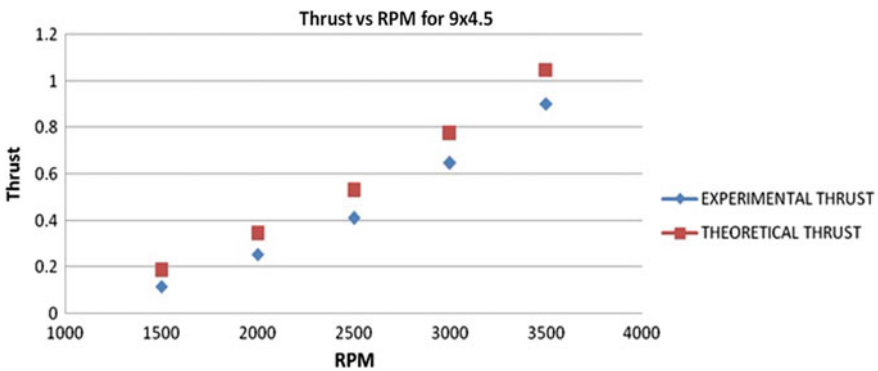


Fig. 6 Thrust vs propeller speed (RPM) for 9 × 4.5 propeller

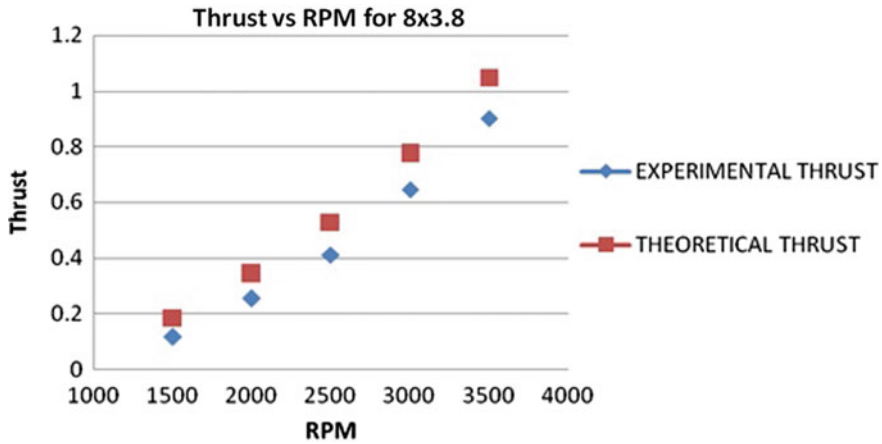


Fig. 7 Thrust vs propeller speed (RPM) for 8 × 3.8 propeller

of differences are observed between the experimental and theoretical values for the 8 × 3.8 propeller.

From Fig. 8, it is observed that for lower RPM, the thrust value difference (42%) is high between experimental and theoretical values. In the higher RPM, around 34% of differences are observed between the experimental and theoretical values for the 13 × 6.5 propeller.

Figure 9 gives the comparison between experimental and theoretical thrust values for the four different RPM with difference 32%. Along with the comparison between numerical and theoretical thrust values for four different RPM with difference of 41% is observed between experimental and numerical simulation results for the 13 × 8

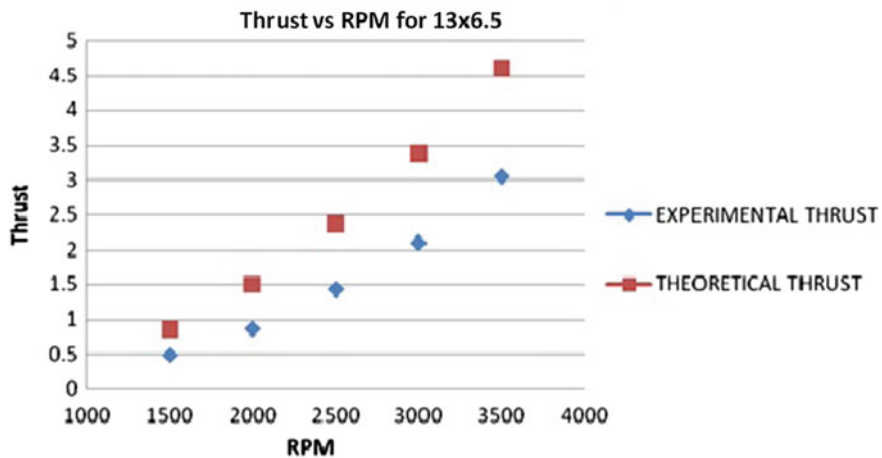


Fig. 8 Thrust vs propeller speed (RPM) for 13 × 6.5 propeller

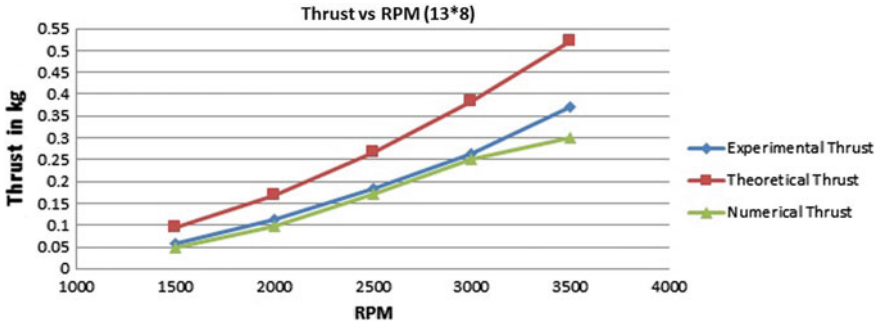


Fig. 9 Thrust vs propeller speed (RPM) for 13 × 8 propeller

propeller. (As a case study, we have done numerical simulation for 13 × 8 propeller in ANSYS CFX) [5].

### 3.2 Theoretical Results

Thrust values of 7 × 6 propellers are validated with theoretical values. The experimental thrust values of each propeller are verified with theoretical thrust values.

Theoretical thrust value of the propeller is calculated as follows:

$F = \text{thrust (N)}$ ,  $d = \text{prop diam. (in.)}$ ,  $\text{RPM} = \text{prop revolution/min.}$ ,  $\text{pitch} = \text{prop pitch (in.)}$ ,  $V_0 = \text{prop forward airspeed (m/s)}$ , for the static thrust  $V_0 = 0$ .

$$F = 4.392399 \times 10^{-8} \cdot \text{RPM} \frac{d^{3.5}}{\sqrt{\text{pitch}}} (4.23333 \times 10^{-4} \cdot \text{RPM} \cdot \text{pitch} - V_0) \quad (1)$$

The propeller diameter and pitch are 7 in. and 6 in., respectively, and five different RPM are 1500, 2000, 2500, 3000 and 3500, respectively. If these values are applied in Eq. (1), the thrust ( $F$ ) as 0.08829 kg, 0.15696 kg, 0.25506 kg, 0.36297 kg and 0.50031 kg respectively are achieved.

## 4 Conclusion

After analyzing the results, it is evident that in the propellers with greater diameters, the variation of experimental thrust from the theoretical thrust is greater for higher RPM. For smaller diameter propellers, the variation in the thrust is comparing well with the theoretical results. The main reason for the variation is because, for higher diameters, the flow is being disturbed at the propeller tip. This is due to the frame size that was chosen at the initial stages. Due to the propeller vibration, the graphs

vary slowly with increasing RPM for bigger diameter propellers (for  $13 \times 8$  and  $13 \times 6.5$  propeller). The results which are obtained from this paper will help the MAV researchers to choose propellers for their application in the better way.

## References

1. Wald QR (2006) The aerodynamics of propellers. *Progr Aerosp Sci* 42(2):85–128
2. Brandt JB et al (2011) Propeller performance data at Low Reynolds Numbers. AIAA, p 1255
3. Moens F (2001) Numerical simulation of the propeller/wing interactions for transport aircraft. AIAA, p 2404
4. Tripathi RK et al (2015) Development of propeller test rig and evaluation of propeller performance. *IJRET* 02(08)
5. Premkumar PS, Senthilkumar C, Elangovan S, ChakravarthyBaskar S (2013) Optimization oil-cooler duct position for a pusher type turboprop aircraft. AIAA, p 4331



# Heat Transfer Enhancement of Al<sub>2</sub>O<sub>3</sub>-Based Nanofluid in a Shell and Helical Coil Heat Exchanger



Prabhakar Zainith and Niraj Kumar Mishra

**Abstract** Active and passive techniques are generally used by the researchers for the heat transfer augmentation of fluids. Conventional fluids like water, ethylene glycol, and oils have not enough heat transfer capabilities to fulfill current requirements of high heat transfer rates of heat exchangers. Nanofluids are the new-generation fluids that have better heat transfer capabilities over traditional heat transfer fluids. The current study examines heat transfer analysis in a shell and helical tube heat exchanger using Al<sub>2</sub>O<sub>3</sub> nanoparticles in aqueous solution. The analysis was carried out to determine the enhanced heat transfer rate as compared to the base fluid (water) in a vertical shell and helical coil geometry. Four different nanoparticle concentrations—1–4% by volume along with four different mass flow rates vary from 0.03 to 0.113 kg/s—were used to simulate the results. Results showed that the heat transfer rate of nanofluids was enhanced at higher mass flow rates, concentrations, and coil-side inlet temperatures.

**Keywords** Heat transfer · Nanofluids · Helical coil

## 1 Introduction

Enhancement in the thermal conductivity of heat transfer fluids through the addition of solid particles has attracted the interest of researchers in this diverse field. These fluids are known as nanofluids and have been considered to have a prominent potential in energy and heat transfer applications for the development of sustainable energy devices and systems [1]. Helical coils are widely used in many industrial applications, like food and dairy processes, nuclear reactors, chemical and refrigeration, and air-conditioning appliances. In the last ten years, the area of research on curved tubes is quite demanding because of their compact structure and high heat transfer coefficients. Earlier helical coiled tubes were studied by Dean [2, 3] and found that symmetrical circular zones were formed over the cross section of coils due to the

---

P. Zainith · N. K. Mishra (✉)

National Institute of Technology, Srinagar, Garhwal, Uttarakhand 246174, India  
e-mail: [nkm.iitg@gmail.com](mailto:nkm.iitg@gmail.com)

© Springer Nature Singapore Pte Ltd. 2020

H. K. Voruganti et al. (eds.), *Advances in Applied Mechanical Engineering*,

Lecture Notes in Mechanical Engineering,

[https://doi.org/10.1007/978-981-15-1201-8\\_18](https://doi.org/10.1007/978-981-15-1201-8_18)

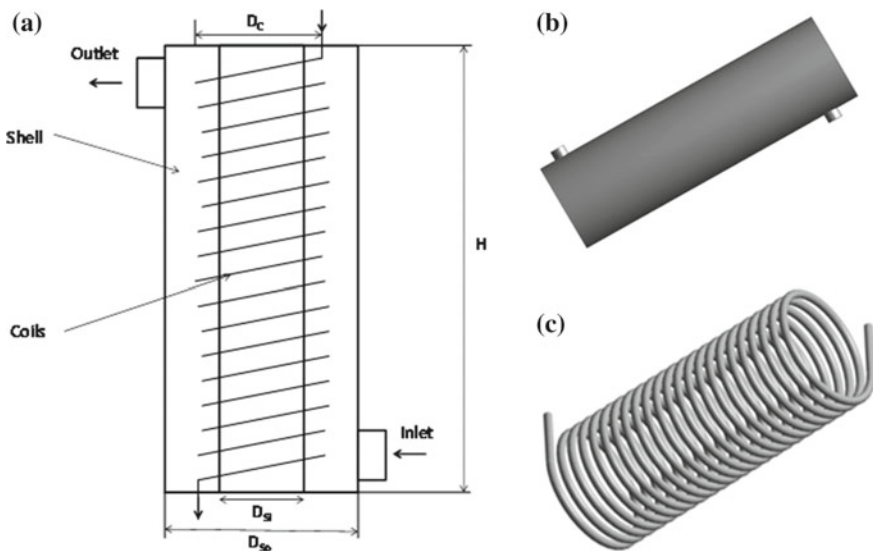
induced centrifugal force. Pourhedayat et al. [4] developed a correlation for exergy losses of Newtonian fluids for a helical tube. They investigated exergy extracted by hot fluid, exergy taken by cold fluid, total exergy loss, NTU, and non-dimensional exergy loss. Finally, a correlation was developed for total non-dimensional exergy loss with respect to number of thermal units (NTU).

From the literature, it is concluded that only few investigations were found in the past for the heat transfer analysis of nanofluids in a shell and helical coil geometry. The objective of present simulated work is to investigate the effect of nanofluids in a shell and helical coil geometry on the thermal aspects.

## 2 Numerical Model

### 2.1 Geometry

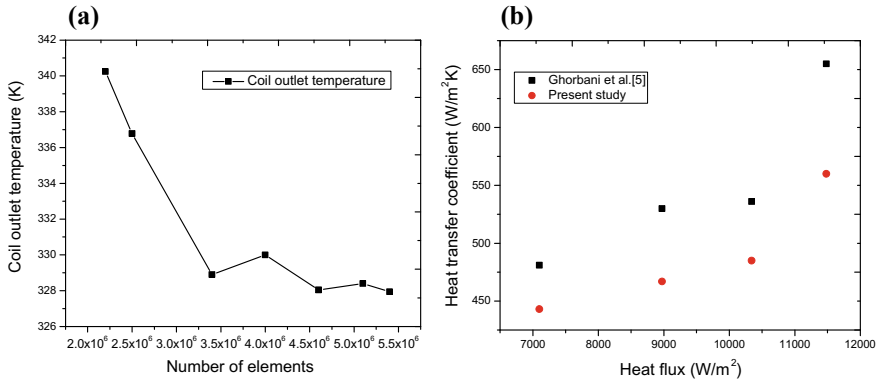
The design module consists of two sections, shell and helical coil, as shown in Fig. 1a. The view of computation fluid domain is shown in Fig. 1b, c. Water was used as the hot fluid in the coil side, and  $\text{Al}_2\text{O}_3$  nanofluid was used in the shell side as working fluid with four different concentrations 1, 2, 3, and 4% by volume. The present study was carried out under laminar flow conditions at the mass flow rates 0.03, 0.05, 0.09, and 0.113 kg/s, for both shell and coil sides. The specifications of physical model are given in Table 1.



**Fig. 1** a Schematic diagram of computational fluid domain, b solid model of shell, and c helical coils

**Table 1** Physical specifications of computational fluid domain

No.	$D_{S,o}$ (mm)	$D_{S,i}$ (mm)	$D_c$ (mm)	$N$	$H$	$t$ (mm)
1	160	90	125	22.5	360	0.86

**Fig. 2** a Grid-independent test and b validation of present study with Ghorbani et al. [5]

## 2.2 Grid Testing and Validation

To verify the results of mesh, a mesh independence test was conducted by increasing the number of elements till the nearly constant results were found as shown in Fig. 2a. In the given mesh independent test, seven different element sizes of mesh were numerically investigated for coil outlet temperature. In the seven different element sizes, only three ( $46 \times 10^5$ ,  $51 \times 10^5$ , and  $54 \times 10^5$ ) sizes give similar results. Thus, the size of  $46 \times 10^5$  is selected for present simulations. Validation of the numerical results compared to the experimental measurements was given in a similar study performed by Ghorbani et al. [5]. The results' measure for heat transfer coefficient of shell side with heat flux per unit area is shown in Fig. 2b. The validation was done for water at both the sides of shell and helical coil.

## 2.3 Thermophysical Properties of Nanofluid

Generally, two methods, single-phase and two-phase models, are used to analyze the thermal performance of nanofluids. Albojamal and Vafai [6] compared the results of single- and two-phase models with experimental data, and they found that lower concentrations of nanoparticles give similar results as compared with the multiphase and experimental studies. As in the current study, the particle concentration is low, so the simulations were performed using single-phase model.

The density of nanofluid was found out by using the general formula for the mixture:

$$\rho_{nf} = \phi\rho_{np} + (1 - \phi)\rho_{bf} \quad (1)$$

The specific heat of the nanofluid was evaluated from:

$$C_{P_{nf}} = \frac{\phi\rho_{np}C_{P_{np}} + (1 - \phi)\rho_{bf}C_{P_{bf}}}{\rho_{nf}} \quad (2)$$

These above equations have given significant results for nanofluids on comparing with experimental results by Pak and Cho [7] and Xuan and Roetzel [8].

The Maxwell model [9] was used to find out the thermal conductivity:

$$\frac{k_{nf}}{k_{bf}} = \frac{k_{np} + 2k_{bf} + 2\phi(k_{np} - k_{bf})}{k_{np} + 2k_{bf} - \phi(k_{np} - k_{bf})} \quad (3)$$

Einstein's equation was used to find out the effective viscosity of nanofluids for the concentrations less than 5% by volume [10]:

$$\mu_{nf} = \mu_{bf}(1 + 2.5\phi) \quad (4)$$

## 2.4 Governing Equations

CFD code FLUENT 18 is used for the numerical solution. Finite volume technique is used to solve the mass, momentum, and energy equations of conservation. A steady-state condition is modeled for heat transfer between the hot fluid in the helical coil tube and the nanofluid in the shell. The convergence criterion chosen for energy equation is  $1.0e-6$ .

The basic governing equations, which are used for heat transfer and flow analysis, are given below:

$$\nabla \cdot (\rho \vec{V}) = 0 \quad (5)$$

$$\rho(\vec{V} \cdot \nabla \vec{V}) = -\nabla p + \nabla \cdot \left[ \frac{\mu(\nabla \vec{V} + \nabla^T \vec{V})}{2} \right] \quad (6)$$

$$\rho C_P(\vec{V} \cdot \nabla T) = K_f \nabla^2 T \quad (7)$$

Average heat flux and convective heat transfer coefficient were calculated as follows

$$q'' = \frac{C_{p,s}(T_{s,o} - T_{s,i})}{A_{\text{coil}}} \quad (8)$$

and

$$\bar{h} = \frac{q''}{(T_{\text{min},cs} - T_{\text{min},s})} \quad (9)$$

Overall heat transfer coefficient

$$U = \frac{q''}{A_o(\Delta T_{\text{LMTD}})} \quad (10)$$

where  $A_o$  is the surface area of coil and  $\Delta T_{\text{LMTD}}$  is the log mean temperature differences.  $\Delta T_{\text{LMTD}}$  can be calculated as per following equation.

$$\text{LMTD} = \frac{(T_{\text{Hi}} - T_{\text{Co}}) - (T_{\text{Ho}} - T_{\text{Ci}})}{\ln\left(\frac{(T_{\text{Hi}} - T_{\text{Co}})}{(T_{\text{Ho}} - T_{\text{Ci}})}\right)} \quad (11)$$

where  $T_H$  and  $T_C$  are the temperature of hot and cold fluids at inlet and outlet sections.

### 3 Result and Discussion

In the present work, laminar heat transfer and fluid flow for Al<sub>2</sub>O<sub>3</sub>-based nanofluids in a three-dimensional fluid domain through a shell and helical coil heat exchanger are numerically investigated for counterflow. The simulations were done for four different values of particle concentrations in the range  $1\% \leq \phi \leq 4\%$  and four different mass flow rates 0.03, 0.05, 0.09, and 0.113 kg/s. Al<sub>2</sub>O<sub>3</sub> nanofluids are used in the shell-side region with a constant inlet temperature of 293 K, and pure water is used in the coil side with different inlet temperatures from 323 to 353 K. The temperature contours of fluid domain for pure water with 2% and 4% particle concentration in counter flow are shown in Fig. 3, respectively. From the temperature contours, it is found that the coil temperature goes down from inlet to outlet and shell temperature rises from inlet to outlet. The whole phenomenon satisfied the general heat balance equation.

#### 3.1 Heat Transfer Analysis

The effects on heat transfer coefficient of shell side with the aluminum oxide particle concentration variation from 1 to 4% by volume for different inlet temperature of coil side from 50 to 80 °C are shown in Fig. 4. From the figure, it is found that

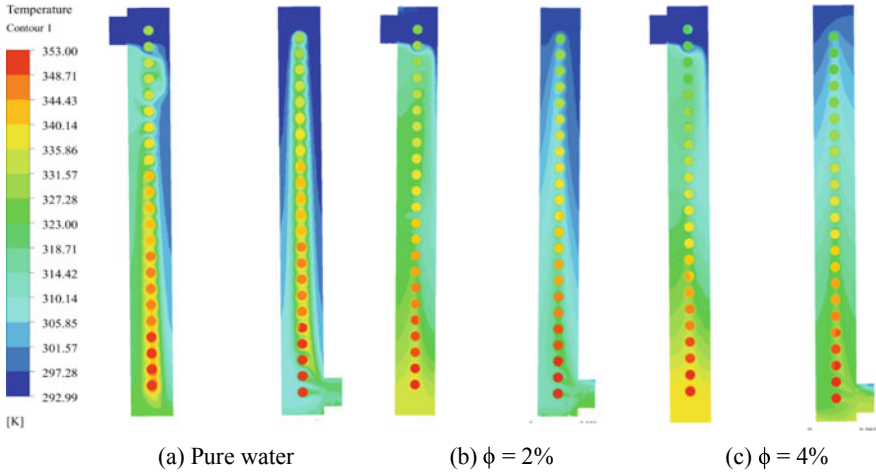
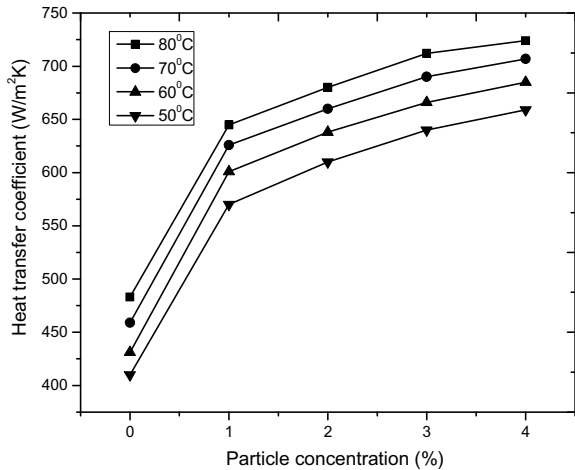


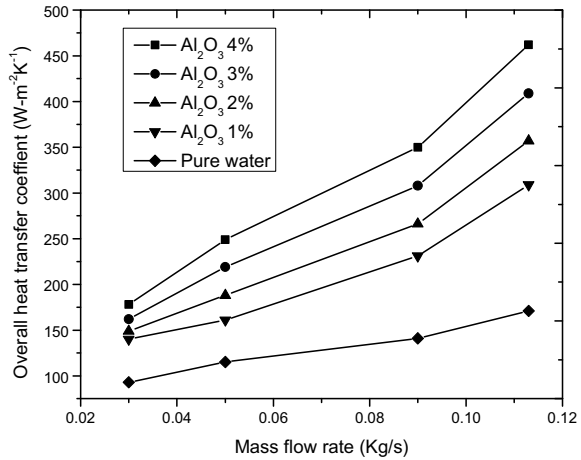
**Fig. 3** Temperature contours of fluid domain in  $x$ - $y$  plane for **a** pure water, **b**  $\phi = 2\%$ , and **c**  $\phi = 4\%$  at inlet coil temperature of 353 K

**Fig. 4** Variation in heat transfer coefficient with particle concentration at different inlet temperatures of coil section



by increasing particle concentration, the heat transfer coefficient increases with the increase in coil inlet temperature. The reason of this enhancement is addition of nanoparticles changes the thermophysical properties of base fluid like density, specific heat, thermal conductivity and viscosity. The maximum heat transfer coefficient was found  $723 \text{ W/m}^2$  at 4% of particle concentration for 353 K inlet temperature of coil. Moreover, overall heat transfer coefficient at a particular mass flow rate increases with the increase in nanoparticle concentration as shown in Fig. 5. This is due to the increase in the average surface area of metallic particles in the base fluid, which is responsible for better heat transfer rate. Another reason for enhanced heat

**Fig. 5** Variation in overall heat transfer coefficient with mass flow rates at different particle concentration



transfer rate is Brownian motion of particles. Brownian motion is taking place due to random movement of nanoparticles caused by the impact of fluid molecules in the surrounding. Thus, as the concentration of nano-sized metallic particles increases, more augmentation of heat transfer occurs. The maximum overall heat transfer coefficient was found 460 W/m<sup>2</sup>K for Al<sub>2</sub>O<sub>3</sub>/water nanofluids. The above discussion suggests that the random movement of aluminum oxide nanoparticles improves the thermal dispersion.

## 4 Conclusions

The present study covers numerical investigation of convective flow heat transfer in a three-dimensional shell and helical coil heat exchanger. Al<sub>2</sub>O<sub>3</sub> nanoparticle is used with four different particle concentrations with water as a working fluid. From the above study, following conclusions are summarized:

1. The results concluded that the heat transfer rate is enhanced by the use of nanofluids. It is also concluded that by increasing the mass flow rate and inlet temperature of coil side leads to increase in the value of heat transfer coefficient.
2. The Al<sub>2</sub>O<sub>3</sub> nanofluids with 4% particle concentration give 176% better heat transfer coefficient with respect to pure water. While the overall heat transfer coefficient found is 380% better at a mass flow rate of 0.113 kg/s with 4% particle concentration as compare to pure water.
3. The implementation of helical coils over circular concentric type accompanied in enhanced heat transfer rate because of aggrandizes mixing of fluids and covers more surface area for convection.

## References

1. Shahsavani E, Afrand M, Kalbasi R (2018) Experimental study on rheological behavior of water–ethylene glycol mixture in the presence of functionalized multi-walled carbon nanotubes. *J Therm Anal Calorim* 131(2):1177–1185
2. Dean WRXVI (1927) Note on the motion of fluid in a curved pipe. *Lond Edinb Dublin Philos Mag J Sci* 4(20):208–223
3. Dean WR (1928) LXXII. The stream-line motion of fluid in a curved pipe (second paper). *Lond Edinb Dublin Philos Mag J Sci* 5(30):673–695
4. Pourhedayat S, Dizaji HS, Jafarmadar S, Khalilarya S (2018) An empirical correlation for exergy destruction of fluid flow through helical tubes. *Appl Therm Eng* 140:679–685
5. Ghorbani N, Taherian H, Gorji M, Mirgolbabaie H (2010) Experimental study of mixed convection heat transfer in vertical helically coiled tube heat exchangers. *Exp Thermal Fluid Sci* 34(7):900–905
6. Albojamal A, Vafai K (2017) Analysis of single phase, discrete and mixture models, in predicting nanofluid transport. *Int J Heat Mass Transf* 114:225–237
7. Pak BC, Cho YI (1998) Hydrodynamic and heat transfer study of dispersed fluids with submicron metallic oxide particles. *Exp Heat Transfer Int J* 11(2):151–170
8. Xuan Y, Roetzel W (2000) Conceptions for heat transfer correlation of nanofluids. *Int J Heat Mass Transf* 43(19):3701–3707
9. Chon CH, Kihm KD, Lee SP, Choi SU (2005) Empirical correlation finding the role of temperature and particle size for nanofluid ( $\text{Al}_2\text{O}_3$ ) thermal conductivity enhancement. *Appl Phys Lett* 87(15):153107
10. Einstein A (1906) Eineneuebestimmung der moleküldimensionen. *Ann Phys* 324(2):289–306



# Numerical Analysis of the Effect of Fluid–Structure Interaction on Heat Transfer in the Square Cavity Using OpenFOAM



Nikhil Chitnavis and Trushar B. Gohil

**Abstract** The present study discusses the effect of fluid–structure interaction (FSI) in a square cavity with a top wall oscillating, i.e., sinusoidal variation of the velocity of the top wall. Due to this varying motion of the top plate, fin (flexible plate) starts oscillating in the transverse direction of the fin length. Due to flexible plate motion, fluid motion also gets disturbed, and because of this it can increase or decrease the heat transfer rate of the hot wall. For checking the effect of fin, flexible plate is set on the left, right and bottom wall. It is observed that incorporation of flexible flap on any wall decreases the heat transfer rate.

**Keywords** FSI · Sinusoidal · Flexible flap

## 1 Introduction

In a lid-driven cavity, heat transfer is mainly due to air circulation by moving wall. To increase the heat transfer rate of the heated wall is a matter of concern, and also it has some engineering application, i.e., cooling of microelectronic devices, flat plate solar collectors, and cooling of the electrical component. Al-Amiri et al. [1] studied the fluid–structure interaction of mixed convection heat transfer with flexible bottom in a lid-driven cavity. It is observed that with respect to bottom rigid wall, flexible bottom is having a higher heat transfer rate.

Flow-induced deformation of a flexible thin structure as a demonstration of an increase in heat transfer is investigated by Soti et al. [2]. Authors concluded that cylinder with a flexible flap having the highest heat transfer rate as compared to a cylinder with no flap and cylinder with a rigid flap is having least heat transfer because it reduces the vortex shedding. Ali et al. [3] investigated the heat transfer and mixing enhancement by free elastic flap oscillation and found that flow through a channel with rigid flap is having less heat transfer rate with respect to flexible flap.

---

N. Chitnavis · T. B. Gohil (✉)

Department of Mechanical Engineering, Visvesvaraya National Institute of Technology,  
Nagpur, Maharashtra 440010, India  
e-mail: [trushar.gohil@gmail.com](mailto:trushar.gohil@gmail.com)

© Springer Nature Singapore Pte Ltd. 2020

H. K. Voruganti et al. (eds.), *Advances in Applied Mechanical Engineering*,

Lecture Notes in Mechanical Engineering,

[https://doi.org/10.1007/978-981-15-1201-8\\_19](https://doi.org/10.1007/978-981-15-1201-8_19)

This study motivates the current research, where square cavity with flexible flaps is installed on various walls to check the heat transfer rate.

## 2 Methodology

For numerical simulation, author used C++-based open-source CFD toolkit OpenFOAM as a platform. Finite volume method-based fsiFoam solver is modified to simulate the present test case. Unsteady incompressible form of Navier–Stokes equation governs is considered. An arbitrary Lagrangian–Eulerian approach (ALE) is used to solve the governing equation as follows:

Continuity equation:

$$\nabla \cdot u_f = 0 \quad (1)$$

Momentum equation:

$$\frac{\partial u_f}{\partial t} + (u_f - u_{m,f}) \cdot \nabla u_f = -\frac{\nabla P}{\rho_f} + \vartheta_f \nabla^2 u_f \quad (2)$$

Energy equation:

$$\frac{\partial T_f}{\partial t} + (u_f - u_{m,f}) \cdot \nabla T_f = \alpha \nabla^2 T_f \quad (3)$$

Here,  $u_f$  = velocity of fluid,  $u_{m,f}$  = mesh motion velocity in fluid domain,  $\alpha$  = thermal diffusivity,  $\vartheta_f$  = kinematic viscosity of fluid, and  $T_f$  = temperature of fluid.

The equation of motion for an elastic adiabatic solid structure can be described from a Lagrangian viewpoint as follows:

$$\rho_s \frac{\partial^2 d_s}{\partial t^2} = F_\vartheta + \nabla \sigma \quad (4)$$

$\rho_s$  = density of solid structure,  $d_s$  = displacement of solid structure, and  $F_\vartheta$  = resultant body force.

### 2.1 Simulation Detail

Figure 1(left) shows the geometrical and boundary condition details of the considered case. The length of the fin is 15 percent the domain length ( $a = 1$ ). The oscillating velocity ( $U = 1 - \cos(\frac{2\pi t}{7})$ ) is applied on the top wall of the cavity having temperature of 300 K.

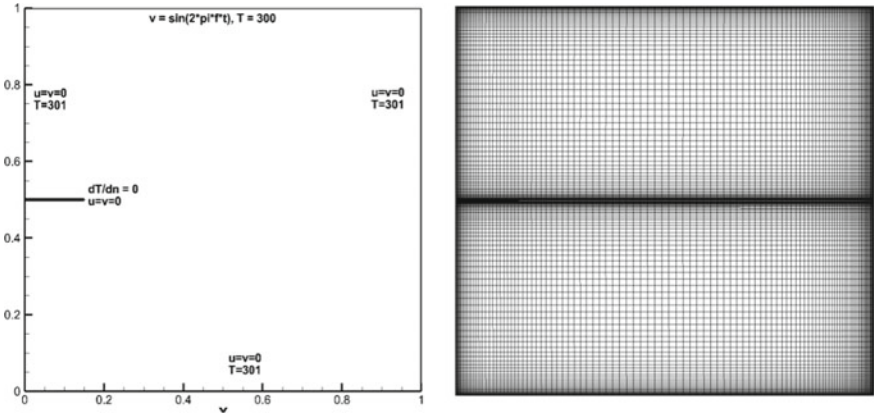


**Fig. 1** Boundary condition and mesh of the test case for simulation

All other boundaries are fixed wall having fixed temperature of 301 K. To finalized grid distribution within computational domain, various grid of size  $100 \times 100$ ,  $120 \times 120$ , and  $140 \times 140$  are considered, and after comparing the Nu of left wall it is observed that grid size of  $120 \times 120$  (Fig. 1(right)) gives satisfactory results. The selected mesh has 0.001 element size near to all the walls and that gives better quantification of heat transfer. All the simulations are performed for a fixed Reynolds number of 250.

### 2.2 Validation

As a validation study, a square cavity with a flexible bottom and the oscillating top wall is considered. All the geometric detail and boundary condition have taken from Habchi et al. [4]. Figure 2 shows the mid-point displacement of the flexible bottom wall with respect to time. Present result shows good agreement with the data of Hubchi et al. [4], Kassiotis et al. [5], and Vazquez [6].

### 3 Results and Discussion

The effects of the fin (flexible plate) placement on the increase or decrease of heat transfer of all hot wall are discussed below with respect to test case in Fig. 1.

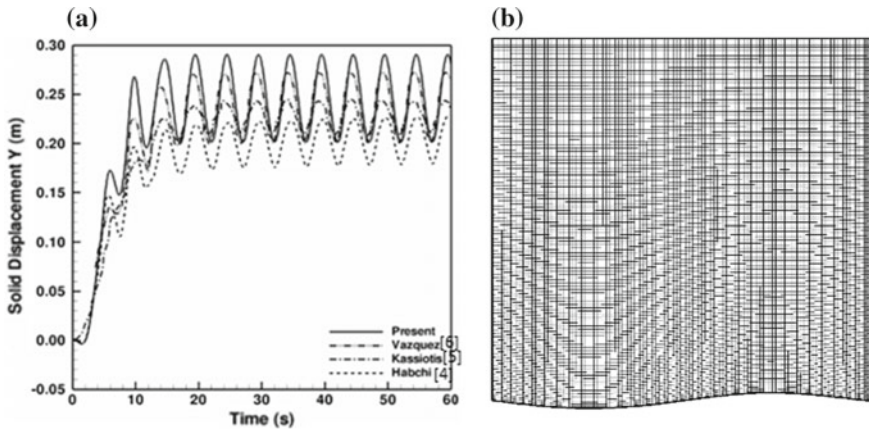


Fig. 2 **a** Displacement of the mid-point on the flexible bottom wall w.r.t. time, **b** mesh diagram of the geometry

### 3.1 Effect of Flexible Plate

In the square cavity, the top wall is at a lower temperature, and the other three walls have isothermally heated with higher equal temperature and stationary. Due to the oscillation of top wall, the fluid inside the cavity starts circulating in the enclosure in the clockwise and anticlockwise direction depending upon the direction of velocity.

Figures 3 and 4 illustrate the effect of placement of flexible flaps on the Nusselt number. In Fig. 3(left) and (right), flap is on the left and right wall, respectively, and

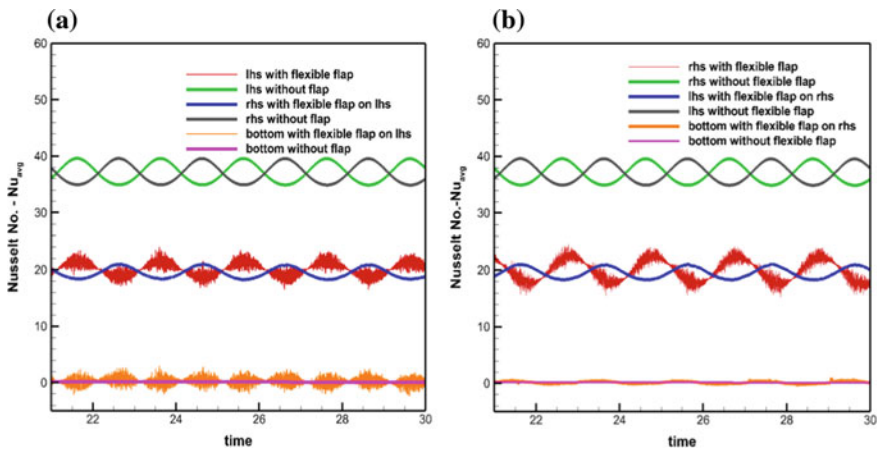
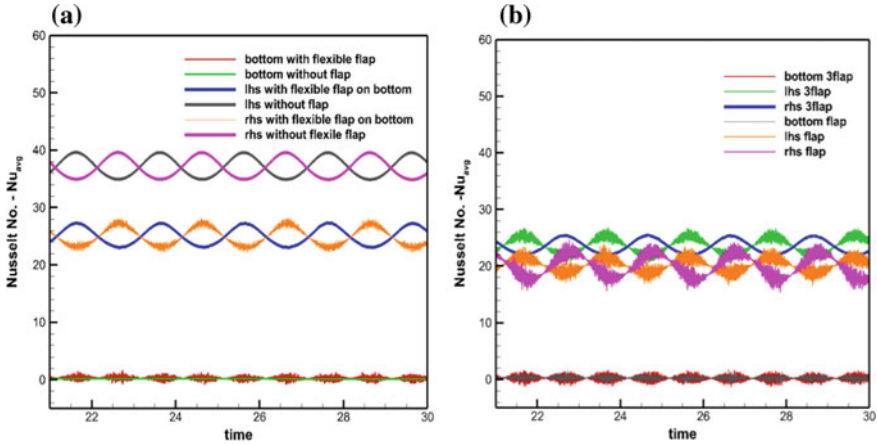


Fig. 3 Variation of average Nusselt number for left, right, and a bottom wall with time (left) flap on the left wall (a), (right) flap on the right wall (b), and comparison with square cavity without a flap



**Fig. 4** a Variation of Nusselt number for the flap on the bottom wall w.r.t. square cavity with no flexible plate. b Variation of Nusselt number with three flaps on the left, right, and bottom wall of the cavity compared with the cases of a single flap on an individual wall

compared the Nusselt number with/without any flap case. Nusselt number of left and right wall with flexible flap is less as compared to the case of without flap. In square enclosure without any flap, the oscillating movement of top wall disturbs the formation of the boundary layer over the stationary wall, and subsequently Nusselt number increases in turn which increases the heat transfer. However, with flap either on left of the right wall, motion of it obstructing the fluid movement within cavity and the heat transfer decreases. However, the oscillation of the top wall does not have that much effect on bottom wall, and therefore, the Nusselt number of the bottom wall is least.

There is not much variation in the Nusselt number of bottom wall with the flap as observed in Fig. 4(left). In Fig. 4b, three flaps are attached inside the square enclosure on the left, right, and the bottom walls. The result has compared with the moving flap on an individual wall of different cases. With the three flaps, heat transfer increases for left and right wall; however, still its Nusselt number is lesser than the case of the square cavity without a flap. Figure 5 shows the flap movement due to the top wall oscillation. It is observed that, as the top wall oscillates in the horizontal direction, the flexible flap starts oscillation in the vertical direction and changes the fluid movement within the cavity.

## 4 Conclusion

In the present study, FSI analysis is performed for square cavity with oscillation top wall and a flexible flap attached to all other three walls. The open-source CFD toolkit OpenFOAM is considered as a platform to simulate the proposed test case. It

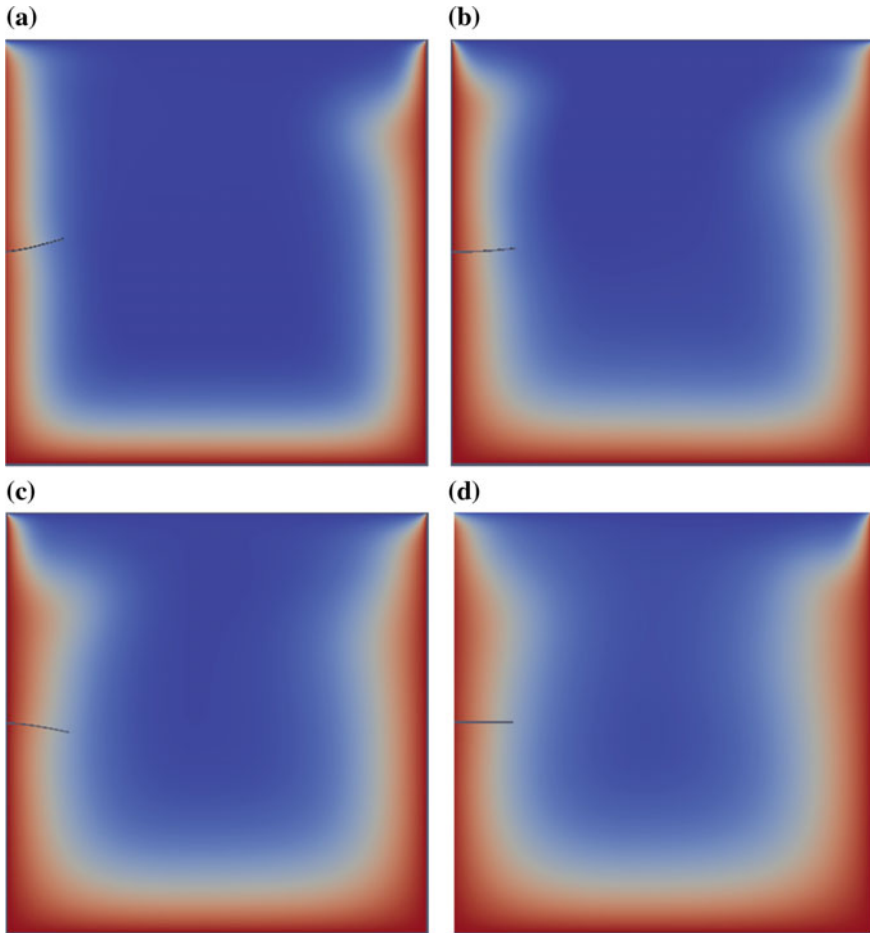


**Fig. 5** Flapping motion of the flexible fin due to oscillation of the top wall

is observed that Nusselt number distributions over left, bottom, and right walls are lower for wall with flexible flap as compared to the cavity wall without and flexible flap. However, the fluid motion considerably alters due to the presence of the flexible flap.

## References

1. Al-Amiri A, Khanafer K (2011) Fluid-structure interaction analysis of mixed convection heat transfer in a lid-driven cavity with a flexible bottom wall. *Int J Heat Mass Transf* 54(17–18):3826–3836

2. Soti AK, Bhardwaj R, Sheridan J (2015) Flow-induced deformation of a flexible thin structure as manifestation of heat transfer enhancement. *Int J Heat Mass Transf* 84:1070–1081
3. Ali S, Habchi C, Menanteau S, Lemenand T, Harion J-L (2015) Heat transfer and mixing enhancement by free elastic flaps oscillation. *Int J Heat Mass Transf* 85:250–264
4. Habchi C, Russeil S, Bougeard D, Harion J-L, Menanteau S, El Hage H, El Marakbi A, Peerhossaini H (2013) Numerical simulation of the interaction between fluid flow and elastic flaps oscillation. FEDSM 2013-16352, V01BT13A002; 9 pages. <https://doi.org/10.1115/FEDSM2013-16352>
5. Kassiotis C, Ibrahimbegovic A, Niekamp R, Matthies H (2011) Nonlinear fluid-structure interaction problem. Part i: implicit partitioned algorithm, nonlinear stability proof and validation examples. *Comput Mech* 47:305–323
6. Vazquez J-G-V (2007) Nonlinear analysis of orthotropic membrane and shell structures including fluid-structure interaction. Ph.D. thesis. Escola Tecnica Superior d'Enginyers de Camins, Universitat Politecnica de Catalunya, Barcelone, Espagne

# Experimental Investigation of the Effect of Particle Concentration and Temperature on Thermophysical Properties of Water-Based Metal-Oxide Nanofluids



Ramesh Babu Bejjam, K Kiran Kumar, S Venkata Sai Sudheer and N Praveena Devi

**Abstract** The dimensionless heat transfer parameters such as Nusselt number, Reynolds number and Prandtl number are function of thermophysical properties of the nanofluids and these numbers strongly influence the convective heat transfer coefficient. In thermal systems, the heat transfer coefficient quantifies the rate of heat transfer. The thermophysical properties of the nanofluid vary with particle concentration and temperature. In the present study, experimental analysis has been performed to evaluate the influences of particle concentration and temperature on thermophysical properties of various metal oxide nanofluids. For this study, aluminium oxide ( $\text{Al}_2\text{O}_3$ ), copper oxide ( $\text{CuO}$ ), titanium dioxide ( $\text{TiO}_2$ ) and silicon dioxide ( $\text{SiO}_2$ ) nanoparticles with de-ionized water are chosen and all the experimental results are compared with pure water. The experimentally measured thermophysical properties of the various nanofluids with the empirical correlations are compared. A considerable deviation is observed between the measured results and the empirical solutions. Finally, from the results it can be concluded that, nanofluids have enhanced thermophysical properties, and they may be considered as a suitable fluid for various heat transfer applications.

**Keywords** Nanofluid · Particle concentration · Temperature · Thermophysical properties

---

R. B. Bejjam (✉)

Sasi Institute of Technology & Engineering, Tadepalligudem, West Godavari, Andhra Pradesh 534101, India  
e-mail: [rameshbabubejjam@gmail.com](mailto:rameshbabubejjam@gmail.com)

K. Kiran Kumar · S. Venkata Sai Sudheer  
National Institute of Technology Warangal, Warangal, Telangana 506 004, India

N. Praveena Devi  
S R Engineering College, Warangal, Telangana 506 004, India

© Springer Nature Singapore Pte Ltd. 2020  
H. K. Voruganti et al. (eds.), *Advances in Applied Mechanical Engineering*,  
Lecture Notes in Mechanical Engineering,  
[https://doi.org/10.1007/978-981-15-1201-8\\_20](https://doi.org/10.1007/978-981-15-1201-8_20)



## Nomenclature

Symbol	Name (Unit)
$C_p$	Specific heat ( $\text{J kg}^{-1} \text{K}^{-1}$ )
$k$	Thermal conductivity ( $\text{W m}^{-1} \text{K}^{-1}$ )
$T$	Temperature (K)
bf	Base fluid
nf	Nanofluid
np	Nanoparticle
$\rho$	Density ( $\text{kg m}^{-3}$ )
$\phi$	Particle volume concentration
$\mu$	Viscosity ( $\text{N-S m}^{-2}$ )

## 1 Introduction

Advancements in nanotechnology open a gateway to a new generation of fluids for heat transfer applications. Suspending the nanoparticles in the working fluid at low concentrations significantly alters the thermal conductivity and consequently heat transfer properties. In the past several years, nanofluids have found as widespread applications in various industrial and commercial applications such as in refrigerators, cooling electronic devices, solar collectors, different heat exchangers, nuclear reactor core cooling, liquid fuels and lubricants.

Nanofluids are a relatively new class of heat transfer fluids spread over all fields of technology and engineering due to their prevalent properties. Higher thermal conductivity of nanofluids attracts and encourages researchers to use them in many technological applications. The other pivotal thermophysical property is viscosity, which defines the hydrodynamic behaviour of a fluid. Both thermal conductivity and viscosity increase with that particle concentration. Along with particle concentration, another considerable parameters that influence the thermophysical properties of nanofluid are temperature, size of particle, properties of base fluid, etc. Suspension of solid particles in fluids to promote their thermal properties is not a new idea. Maxwell et al. [1] dispersed solid particles in liquid medium to enhance the thermal conductivity of the working fluid and developed a correlation to estimate the thermal conductivity of particle-suspended fluid. Hamilton et al. [2] extended the Maxwell research and modified Maxwell thermal conductivity correlation for more precise prediction. But both researchers [1, 2] suspended micro-size particles in flowing fluids.

The capability to produce nanosized solid particle with the advanced material technology creates a new platform for a new class of innovative heat transfer fluids. For the first time Choi and Eastman [3] addressed the phenomenon of suspending nanosized solid particles in a base fluid to augment its thermal and flow properties and labelled such fluid as nanofluids.

## 2 Nanofluid Preparation

For the current research, all the nanoparticles ( $\text{Al}_2\text{O}_3$ ,  $\text{CuO}$ ,  $\text{TiO}_2$  and  $\text{SiO}_2$ ) with sizes of 30–50 nm are purchased from SISCO Research Laboratory (SRL) Pvt. Ltd., Mumbai, India. The size of particles is assumed to be the same as quoted by the supplier. Distilled water was taken as the base fluid for nanofluid preparation as well as for conducting experiments for comparison of NCL performance. Nanofluids were prepared by the two-step method. Nanoparticles were dispersed in the base fluid using an ultra sonicator—(supplied by Electrostatic Industries, India) to break the agglomerated particles and to obtain a stable and homogeneous suspension. The fluid was subjected to continuous sonication for 2 h and the sonicator produced ultrasonic waves at 180 W. C-TAB was used as a surfactant to increase the dispersion stability of nanoparticles in base fluid. Both sonication and surfactant were used to control the agglomeration while preparing stable nanofluid. All the nanofluids were prepared at 0.5, 1.0, 1.5, 2, 2.5 and 3% particle concentrations, which are the suitable particle concentration for heat transfer applications. It is noticed that all the nanofluids have been stable for 72 h at least without forming any sediment or agglomerating.

## 3 Estimation of Thermophysical Properties of the Nanofluids

Several researchers from the past decades proposed many correlations to precisely evaluate the effective thermophysical properties of nanofluids by considering different constraints such as particle size, base fluid properties and operating temperature, and these correlations are match with experimental results. Most of the existing correlations for nanofluid possess good agreement with the experimental outcomes. Thermophysical properties such as density, dynamic viscosity, specific heat, thermal expansion coefficient and thermal conductivity of various nanofluids were estimated using empirical correlations which have close approximations with experimental results.

Among all the thermophysical properties, thermal conductivity and viscosity are key properties, which govern the heat transfer and flow behaviour of a nanofluid. Many engineering applications demand a trade-off between dynamic viscosity and thermal conductivity of a nanofluid. Enhanced thermal transport properties along with minimal augment of viscosity are favourable for better thermal performance of an NCL. Both viscosity and thermal conductivity of water and all nanofluids have been experimentally measured. Experiments were conducted at different particle concentrations from 0.5 to 3% over 20–70 °C temperature range.

In the current research,  $\text{Al}_2\text{O}_3$ ,  $\text{CuO}$ ,  $\text{TiO}_2$  and  $\text{SiO}_2$  nanoparticles with an average particle size of 30–50 nm were considered for the analysis. The particle concentrations for this analysis 0.5, 1.0, 1.5, 2, 2.5 and 3% were chosen to precisely predict

**Table 1** Thermophysical properties of water and various nanoparticles

Material	Thermal conductivity (W/mK)	Density (kg/m <sup>3</sup> )	Specific heat (J/kg K)
Water	0.6	997	4181.3
SiO <sub>2</sub>	1.4	2648	692
TiO <sub>2</sub>	8.9	4250	686
Al <sub>2</sub> O <sub>3</sub>	40	3900	785.2
CuO	69	6350	502.8

the thermophysical properties. The properties of water and various nanoparticles are presented in Table 1.

## 4 Results and Discussion

### 4.1 Viscosity

#### Analytical method

Einstein [4] developed a correlation to estimate the effective viscosity of solution having spherical solid particles in the base fluid using hydrodynamic equations and it is given in Eq. (1). Brinkman [5] modified Einstein's correlation for use in particle concentrations of 4% and it is shown in Eq. (2). Batchelor [6] further modified Einstein's correlation by considering the effect of Brownian motion as given in Eq. (3).

$$\mu_{nf} = (1 + 2.5\phi)\mu_{bf} \quad (1)$$

$$\mu_{nf} = (1 - \phi)^{2.5}\mu_{bf} \quad (2)$$

$$\mu_{nf} = (1 + 2.5\phi + 6.2\phi^2)\mu_{bf} \quad (3)$$

#### Experimental Method

The dynamic viscosity of water and nanofluids at different particle concentrations and temperatures was measured using a Rheolab QC rotational rheometer (Anton Paar supplier, India). The viscosity of a CuO–water nanofluid at different particle concentrations is experimentally measured and compared with several existing empirical correlations. Figure 1 shows the variation of empirically estimated and experimentally measured viscosity of a CuO/water nanofluid as a function of particle concentration. It can be observed from the experimental results that viscosity

of a nanofluid increases with particle concentration and this increment is relatively more at higher concentrations. The increasing particle concentration amplifies the entanglement and resistance between adjacent layers and leads to an increase in the viscosity of a nanofluid. Many other factors related to intermolecular interactions at the microscopic level also play an indirect role in the enhancement of dynamic viscosity of a nanofluid.

The variation in dynamic viscosity of distilled water and various nanofluids (CuO–water, Al<sub>2</sub>O<sub>3</sub>–water, TiO<sub>2</sub>–water and SiO<sub>2</sub>–water) with the temperature at 1% particle concentration is presented in Fig. 2. The viscosity of all nanofluids is decreasing with

**Fig. 1** Comparison of empirical and experimentally measured viscosity of CuO/water nanofluid

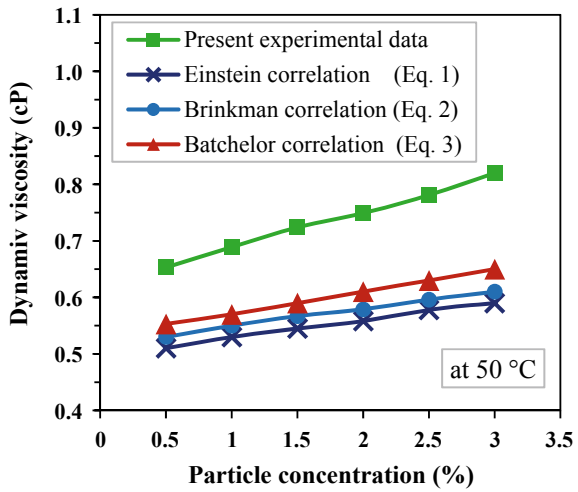
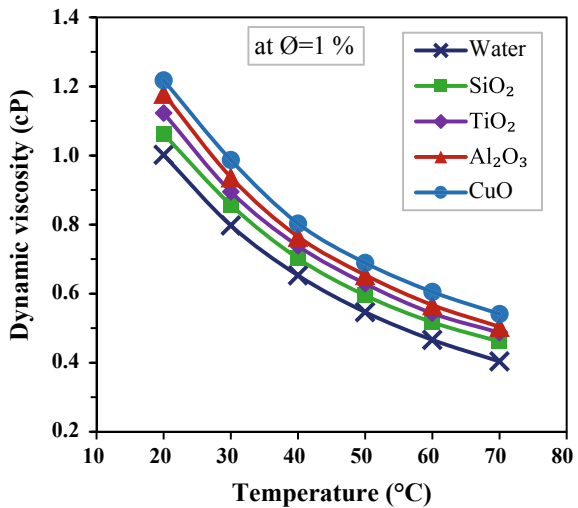


**Fig. 2** Experimentally measured viscosity of water and different nanofluids as a function of temperature



an increase in temperature and this decrement is relatively more at high temperatures. As the temperature of nanofluid increases, Van der Waals forces of attractions gradually cease and lead to a reduction in the viscosity of a nanofluid.

## 4.2 Thermal Conductivity

### Analytical method

Maxwell [1] is the pioneer in this area who proposed a theoretical model to determine the effective thermal conductivity of solid particle suspensions in liquids, which is given in Eq. (4). Bruggeman [7] proposed a correlation for spherical nanoparticles by considering the influence of nano clusters on thermal conductivity of nanofluid, and it is given in Eq. (5). Koo and Kleinstreuer [8] introduced a new correlation to precisely predict the thermal conductivity of nanofluid by considering both the effects of static and dynamic motion of nanoparticles and it is given in Eq. (6).

$$k_{nf} = k_{bf} \left\{ \frac{[k_{np} + 2k_{bf} - 2\phi(k_{bf} - k_{np})]}{[k_{np} + 2k_{bf} + \phi(k_{bf} - k_{np})]} \right\} \quad (4)$$

$$k_{nf} = \frac{1}{4}(3\phi - 1)k_{np} + [(2 - 3\phi)k_{bf}] + \frac{k_{bf}}{4}\sqrt{\Delta} \quad (5)$$

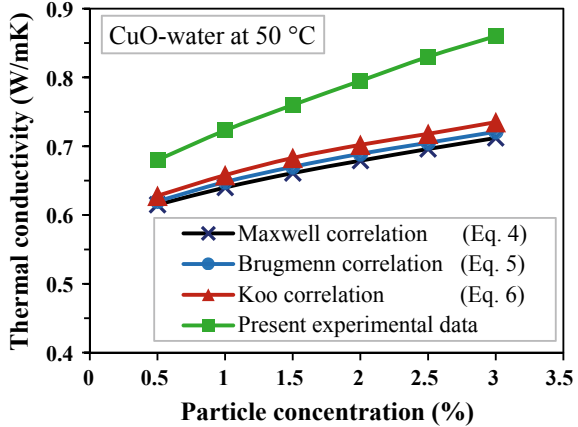
$$k_{nf} = k_{bf} \left\{ \frac{k_{np} + 2k_{bf} + 2\phi(k_{np} - k_{bf})}{k_{np} + 2k_{bf} - \phi(k_{np} - k_{bf})} \right\} + 5 \times 10^4 \beta \phi \rho_{bf} C_{p,bf} \sqrt{\frac{k_p T}{\rho_{np} d_{np}}} f \quad (6)$$

### Experimental method

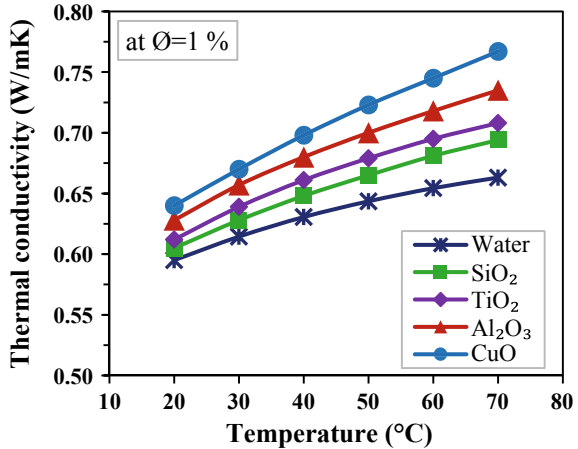
Thermal conductivity of all working fluids (water and nanofluids) considered in the current work were experimentally measured using thermal conductivity analyser (TPS 500S, Thermtest Inc., Fredericton, Canada). Thermal conductivity of CuO/water nanofluid at different particle concentrations was experimentally measured and the results were compared with the empirical correlations available in the literature as shown in Fig. 3. It can be observed from Fig. 3 that the thermal conductivity of CuO/water nanofluid is progressively increasing with the particle concentration and it is amplifying at higher concentrations. As the particle concentration increases, the mean free path of the nanoparticles is decreased, and this leads to lattice vibrations which are commonly known as percolation effect [9]; that may also be one of the root causes for the consequential enrichment of nanofluid thermal conductivity. The maximum deviation between experimental and empirical correlations of Maxwell, i.e. Eq. (4), Bruggeman, i.e. Eq. (5), and Koo, i.e. Eq. (6) is 15%, 12% and 8%, respectively.

Figure 4 shows the enhancement of thermal conductivity of nanofluids with the temperature at 1% particle concentration. It is clearly observed from Fig. 4 that the

**Fig. 3** Variation of thermal conductivity of CuO/water nanofluid with concentration



**Fig. 4** Thermal conductivity of various nanofluids as a function of temperature



thermal conductivity of any fluid increases with temperature. This is because the inter particle cohesive forces and corresponding viscosity are diminished with a rise in temperature which causes Brownian motion. The increased random movement of nanoparticles promotes micro convection between nanoparticle and base fluid and leads to enhancement of the thermal conductivity of nanofluid.

### 5 Conclusions

- Thermal conductivity of nanofluids is estimated from the existing empirical correlations and results are compared with the experimental results. It is found to be less than 10% variation between the empirical and measured readings.

- The thermal conductivity of CuO/water nanofluid is enhanced by 15.67% at 1.0% particle concentration and 70 °C temperature when compared with water.
- In case of viscosity, the results from the existing empirical correlations have a substantial deviation from experimental outcomes. For example, 18.58% deviation is noticed at 1.0% particle concentration of CuO/water nanofluid.
- Since nanofluids have enhanced thermophysical properties, they may be considered as a suitable fluid in natural convection loops for solar and nuclear heat transfer applications.

## References

1. Maxwell JCA (1873) A treatise on electricity and magnetism. Clarendon Press, Oxford
2. Hamilton RL, Crosser OK (1962) Thermal conductivity of heterogeneous two-component systems. *Ind Eng Chem Fundam* 1(3):187–191
3. Choi SU, Eastman JA (1995) Enhancing thermal conductivity of fluids with nanoparticles (No. ANL/MSD/CP-84938; CONF-951135-29). Argonne National Lab, IL (United States)
4. Einstein A (1906) Eine neue Bestimmung der molekul dimensionen. *Ann Phys* 14:229–247
5. Brinkman HC (1952) The viscosity of concentrated suspensions and solutions. *J Chem Phys* 571:1–2
6. Batchelor GK (1977) Effect of Brownian-motion on bulk stress in a suspension of spherical-particles. *J Fluid Mech* 83(Nov):97–117
7. Bruggeman DAG (1935) Berechnung verschiedener physikalischer Konstanten von heterogenen Substanzen. I. Die elastischen Konstanten der quasiisotropen Mischkörper aus isotropen Substanzen. *Ann Phys* 24(5):636–664
8. Koo J, Kleinstreuer C (2004) A new thermal conductivity model for nanofluids. *J Nanopart Res* 6(6):577–588
9. Kumar PM, Kumar J, Tamilarasan R, Sendhilnathan S, Suresh S (2015) Review on nanofluids theoretical thermal conductivity models. *Eng J*. 19(1):67–83

# Pressure Drop in Vertical Pneumatic Conveying: Comparison Between Numerical Predictions with Existing Correlations



Pandaba Patro and Debasis Mishra

**Abstract** Numerical simulations using Euler-Euler model (also known as two-fluid model) were used to predict pressure drop in pneumatic conveying (i.e., gas-solid flows) in vertical pipes. Standard  $k - \varepsilon$  turbulence model has been used for gas phase, and kinetic theory of granular flows (KTGF) was used to close solid phase stresses and solid pressure aroused due to inter-particle collisions. The model was validated by comparison with the available experimental data and good agreement was found for pressure drop prediction. The effect of important flow parameters like gas phase Reynolds number, solid loading ratio and particle density on pressure drop was investigated. It was observed that pressured drop increased with gas velocity and solid loading ratio. Finally, computed results for pressure drop are compared with the existing correlations. Present predictions showed good agreement with the correlations of (Reddy and Pei in *Ind Eng Chem Fundam* 8:490–497, 1969 [1], Capes and Nakamura in *Can J Chem Eng* 51:31–38, 1973 [2]) data.

**Keywords** Pneumatic conveying · Pressure drop · Eulerian modeling · Solids loading ratio

## 1 Introduction

There are many industrial applications of pneumatic conveying of solid particles or gas-solid flows such as pneumatic transporters, fluidized beds, pulverized coal combustion, spray drying, spray cooling, jet impingement cooling and many more. Presence of solids in gas flow gives rise to interaction terms between the two phases and makes the flow complicated for the numerical modeling of these interactions. There are two approaches for numerical modeling of such flows i.e., Lagrangian and Eulerian models. Lagrangian model imposes a restriction on the number of particles (i.e., solids loading ratio or SLR, which is defined as the ratio of mass flow rate of solid phase and mass flow rate of gas phase). So, this model is not suitable for many

---

P. Patro (✉) · D. Mishra  
Veer Surendra Sai University of Technology, Burla, Odisha, India  
e-mail: [ppatro\\_me@vssut.ac.in](mailto:ppatro_me@vssut.ac.in)

© Springer Nature Singapore Pte Ltd. 2020  
H. K. Voruganti et al. (eds.), *Advances in Applied Mechanical Engineering*,  
Lecture Notes in Mechanical Engineering,  
[https://doi.org/10.1007/978-981-15-1201-8\\_21](https://doi.org/10.1007/978-981-15-1201-8_21)



industrial-size problems, where solid loading ratio is relatively high (solid volume fraction in the range 1–10%). However, the Eulerian model can be used for any solid loading ratio. This model treats the solid phase as continuum like gas phase and hence, means equations are solved for both gas phase and solid phase. This model has been used by many researchers [3–5] to investigate the hydrodynamics of gas-solid flows.

For the design of piping layout in pneumatic conveying, it is very important to predict pressure drop to find the pumping power requirement for solids transportation. A number of researchers [6–9] predicted pressure drop in pneumatic conveying experimentally. It is very much complicated to get the pressure drop data under various operating conditions experimentally. With the development of high-speed computers, researchers in industries have extensively been using commercial computer codes to solve two-phase flow problems. But, unfortunately, only very few research publications are available in open literature, which investigated the capabilities of commercially available CFD codes (like ANSYS Fluent) as pressure drop prediction tool in relatively high solids loading (solid volume fraction in the range 0.01–0.1). Patro and Dash [10, 11] investigated gas-solid flows in horizontal and vertical pipes and predicted pressure drop numerically using ANSYS Fluent. It was clear that the commercial CFD computer code ANSYS Fluent can be used successfully to predict pressure drop in gas-solid flow with acceptable level of accuracy.

In the present work, numerical simulations were performed using the Eulerian approach for gas-solid flows in vertical pipes. An extensive study was performed to see the effect of gas Reynolds number, solid loading ratio (SLR) and particle density on pressure drop. The predicted data for pressure drop are also compared with the existing correlations developed from experimental data by many researchers.

## 2 Numerical Procedure

In Euler-Euler model, both gas and solid phases are treated as continuum. So, Navier–Stokes equations are solved for both the phases. The Reynolds stress (generated due to Reynolds Averaging of Navier–Stokes equations) for gas phase employs the Boussinesq hypothesis [3]. It is used to write Reynolds stresses in terms of mean velocity gradients in turbulent flows. Standard  $k - \varepsilon$  model was used for the gas phase turbulence. Particle-particle collisions give rise to solids pressure and stresses, which are closed by incorporating kinetic theory of granular flows (KTGF). Detail mathematical modeling and closure equations are described by Patro and Dash [10, 11]. Space limitation did not permit us to explain these details in the present paper.

Finite volume method has been used to discretize the governing equations in terms of algebraic equations, which are solved along with the initial condition and boundary conditions. For pressure-velocity coupling, phase-coupled SIMPLE algorithm (PC-SIMPLE), which is an extension of SIMPLE algorithm in two-phase flows, has been used. Figure 1 shows the computational domain and the cross-sectional meshing. The computational domain is 30 mm in diameter and 3 m long. Three different grids

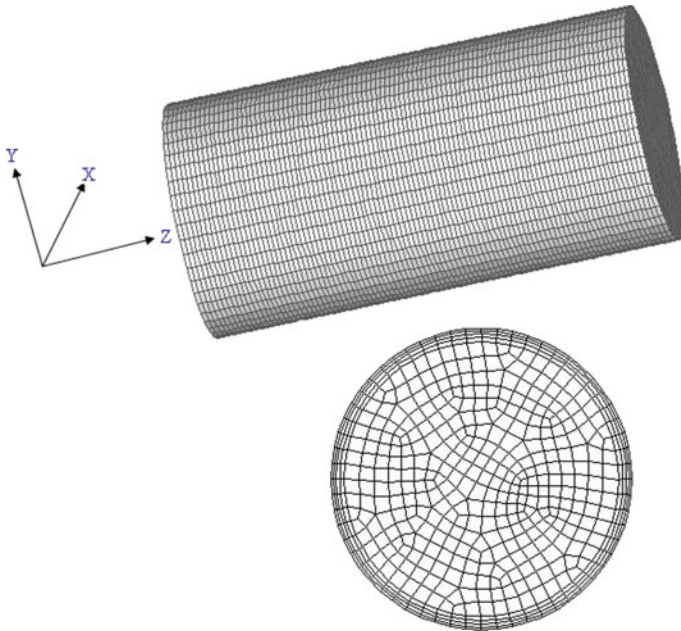


**Fig. 1** Computational domain

of mesh sizes 21,800, 32,700 and 70,600 cells are used for grid independence study. Grid independent solution was observed for the second mesh with 32,700 cells by checking that an increase in number of cells had a negligible effect on the computed velocity profiles and pressure drop.

Velocity inlet boundary conditions are used at the inlet of the pipe. Fully developed velocity profiles are defined for both phases at inlet along with the volume fraction of the solid phase.

$$\frac{U}{U_c} = \left(1 - \frac{r}{R}\right)^{1/7} \tag{1}$$

where  $U_c$  the center line velocity and  $R$  is the radius of the pipe.

The turbulence intensity ( $I_g$ ) at the inlet boundary is specified as 2% based on previous research experience of authors [10, 11] in this field. At the outlet, fully developed flow conditions are used for both phases. For gas phase, no-slip wall condition is valid even in two-phase flows. For the solid phase, no-slip boundary condition is not valid. Solid particle get rebounded or slide along the wall after hitting it. A value of 0.9 is set for coefficient of restitution for particle-particle collision and particle-wall collisions.

### 3 Results and Discussion

Experimental findings for pressure drop of Tsuji et al. [12] have been used for comparing our numerical results and validating the numerical model for the prediction of pressure drop. The experiments are carried out at particle diameter of  $200\ \mu$  and density  $1020\ \text{kg/m}^3$ . Gas phase velocity was varied from 6 to 20 m/s. Numerical simulations were performed for the same operating conditions to validate the numerical modeling.

The numerical parameter known as specular coefficient plays important role in pressure drop prediction while other parameters such as restitution coefficients and drag and lift coefficients are insensitive. The specular coefficient is a measure of the fraction of particle-wall collisions which transfer momentum to the wall. Its value ranges between zero and unity. When the numerical results are compared with experimental data, satisfactory agreement was reported for specular coefficient equal to 0.1 for vertical flows (Fig. 2). So, this value was used for the rest of the simulations.

The main objective of the present research work is to predict pressure drop using available correlations in pneumatic conveying and make a quantitative comparison. Pressure drop from present predictions showed good agreement at low loading (dilute phase pneumatic conveying when volume fraction of solid phase is less than 1%). The most disadvantages of the existing correlations are the inability to predict the pressure drop in pneumatic conveying with relatively high solids loading (solid volume fraction in the range 1–10%). On the other hand, operating parameters of the present work are comparable to industrial applications. There are many correlations [13] available in literature for the pressure drop in pneumatic conveying in vertical pipes. The present computations for two-phase pressure drop are compared with the existing correlations and also the effect of important flow parameters like solids loading ratio (SLR), gas phase Reynolds number ( $Re_g$ ) and solid phase density on pressure drop were investigated. In gas-solid flows, the overall pressure drop consists

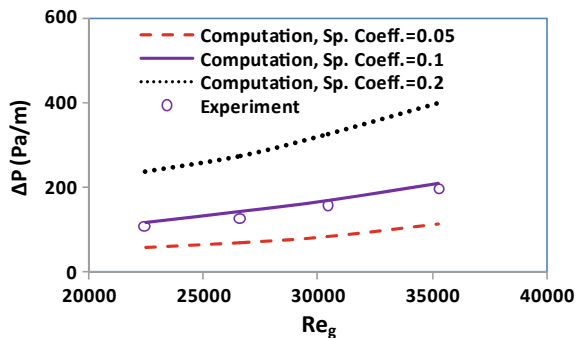


Fig. 2 Comparison of pressure drop predictions in vertical flow with the experimental data at  $SLR = 1$ ,  $d_p = 200\ \mu$

of static and frictional components.

$$\Delta P = \Delta P_{\text{static}} + \Delta P_{\text{frictional}} \quad (2)$$

$$\Delta P_{\text{static}} = \alpha \rho_s g L + (1 - \alpha) \rho_g g L \quad (3)$$

$$\Delta P_{\text{frictional}} = \Delta P_{f_g} + \Delta P_{f_s} \quad (4)$$

$$\Delta p_{f_g} = \frac{f_g \rho_g U_g^2 (1 - \alpha) L}{2D} \quad (5)$$

Here,  $\alpha$  is the solid volume fraction,  $\rho$  is the density,  $L$  is the length of pipe,  $D$  is the diameter of pipe,  $U$  is the velocity. Subscripts  $s$  and  $g$  are used for solid phase and gas phase, respectively.

The gas friction factor ( $f_g$ ) can be calculated using Blasius equation for dilute phase flows.

$$f_g = \frac{0.316}{\text{Re}_g^{0.25}} \quad (6)$$

The solids contribution to the friction pressure loss is normally given as:

$$\Delta p_{f_s} = \frac{f_p \rho_s U_s^2 \alpha L}{2D} \quad (7)$$

For vertical flows, many researchers like Pfeffer et al. [13], Reddy and Pei [1], Konno and Saito [14], Capes and Nakamura [2], Yang [15] etc. developed correlations for solid friction factor ( $f_{ps}$ ). In the present work, predicted pressure drop was compared with the pressure drop calculated from different correlations (Figs. 3, 4 and 5). We observed that solids loading ratio and gas velocity are the dominant factors for pressure drop in pneumatic conveying. Pressure drop increases sharply with increase in solid loading ratio and gas velocity. There is some disagreement in the pressure drop prediction between the existing correlations. The data from Pfeffer et al. [13] over predicts all the data. Our numerical predictions are in good agreement with the pressure drop data by Reddy and Pei [1] and Capes and Nakamura [2].

## 4 Conclusions

Computations using Euler-Euler approach for gas-solid flows were performed in vertical pipes to study the effect of gas inlet velocity (in the range 10–25 m/s), solids loading ratio (in the range 1–10) and particle density (in the range 1000–2500 kg/m<sup>3</sup>) on pressure drop predictions. It was found that pressure drop increases with solids

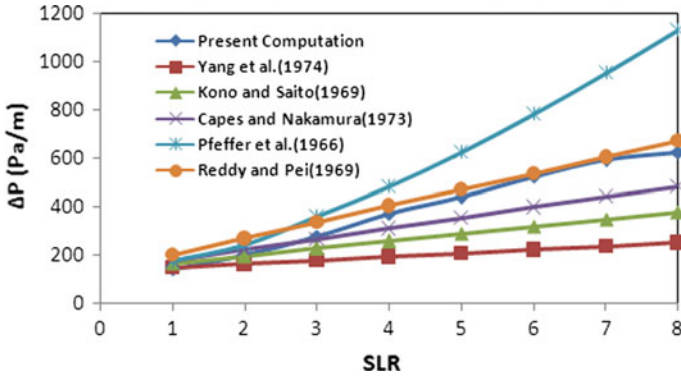


**Fig. 3** Pressure drop comparison at different loading ratios for  $D = 30$  mm,  $dp = 200 \mu$ ,  $U_g = 15$  m/s, particle density =  $2500 \text{ kg/m}^3$

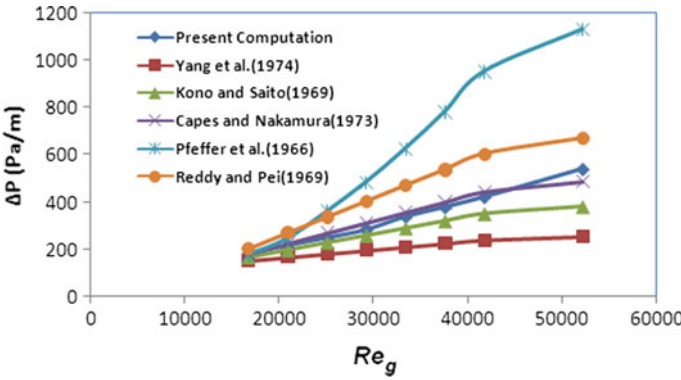


**Fig. 4** Pressure drop comparison at different gas Reynolds number for  $D = 30$  mm,  $dp = 100 \mu$ , SLR = 5, particle density =  $1500 \text{ kg/m}^3$

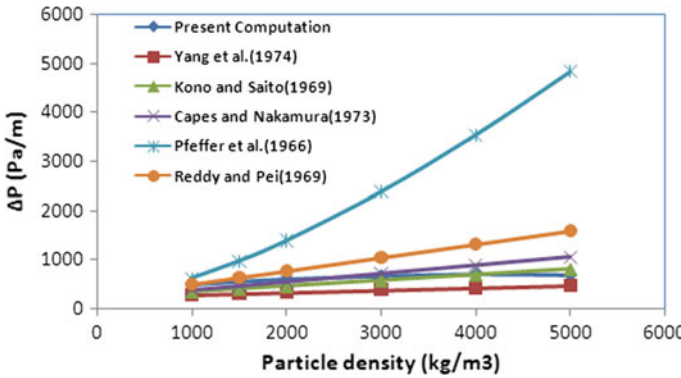


**Fig. 5** Pressure drop comparison at different particle densities for  $D = 30$  mm,  $dp = 150 \mu$ , SLR = 8,  $U_g = 20$  m/s

loading ratio (linearly) and gas phase Reynolds number. There is no significant rise of pressure drop with increase in particle density. Computed results for pressure drop are also compared with the existing correlations in vertical flow. The correlations by Reddy and Pei [1] and Capes and Nakamura [2] show better agreement with our numerical data.

## References

1. Reddy KVS, Pei DCT (1969) Particle dynamics in solids-gas flow in a vertical pipe. *Ind Eng Chem Fundam* 8:490–497
2. Capes CE, Nakamura K (1973) Vertical pneumatic conveying: an experimental study with particles in the intermediate and turbulent flow regimes. *Can J Chem Eng* 51:31–38
3. Lun CKK, Liu HS (1997) Numerical simulation of dilute turbulent gas-solid flows in horizontal channels. *Int J Multiphase Flow* 23(3):575–605
4. Masson C, Baliga BR (1998) Simulation of gas-solid particle flows over a wide range of concentration. *Int J Num Methods Fluids* 28:1441–1479
5. Issa RI, Oliveira PJ (2003) Numerical aspects of an algorithm for the Eulerian simulation of two-phase flows. *Int J Num Methods Fluids* 43:1177–1198
6. Rose HE, Duckworth RA (1969) Transport of solid particles in liquids and gases. *Engineer* 227:478–483
7. Yang WC (1977) A unified theory on dilute phase pneumatic transport. *J Powder Bulk Solids Technol* 1:89–95
8. Yang WC (1974) Correlations of solid friction factors in vertical and horizontal pneumatic conveying. *AIChE J* 20(3):605–607
9. Klinzing GE, Rohatgi ND, Zaltash A, Myler CA (1987) Pneumatic transport—a review (generalized phase diagram approach to pneumatic transport). *Powder Technol* 51(2):135–149
10. Patro P, Dash SK (2014) Numerical simulation for hydrodynamic analysis and pressure drop prediction in horizontal gas-solid flows. *Part Sci Technol* 32(1):94–103
11. Patro P, Dash SK (2014) Two-fluid modeling of turbulent particle–gas suspensions in vertical pipe. *Powder Technol* 264:320–331
12. Tsuji Y, Morikawa Y, Shiomi H (1984) LDV measurements of an air-solid two phase flow in a vertical pipe. *J Fluid Mech* 139:417–434
13. Pfeffer R, Rossetti S, Licklein S (1966) Analysis and correlation of heat transfer coefficient and heat transfer data for dilute gas-solid suspensions. Report NASA, TN-D 360
14. Konno H, Saito S (1969) Pneumatic conveying of solid through straight pipe. *J Chem Eng Jpn* 2(2):211–217
15. Yang WC (1978) A correlation for solid friction factor in vertical pneumatic conveying lines. *AICM J* 24:548–551

# CFD Analysis in the Design of Diffuser for Air Cooling of Low-Concentrated Photovoltaic/Thermal (LCPV/T) Solar Collector



Rohit Meshram and P. D. Sawarkar

**Abstract** The CFD analysis for design of diffuser for air cooling of low-concentrated photovoltaic (PV) solar collector is carried out. PV panel is made up of silicon, a semiconductor, which have the capacity to convert dispersed as well as concentrated solar radiation into electricity directly. The problem encountered with silicon PV panel is overheating due to excessive solar radiation and high ambient temperature. Overheating drastically lowers the efficiency of solar panel. The proper cooling system is required to remove excessive heat and to increase the efficiency of PV panel. One method of cooling PV panel is the supply of uniformly distributed air along the panel. The diffuser is used for uniform distribution of air. Different shapes of diffusers with and without deflector plates are analysed for uniform distribution of air using commercial software ANSYS FLUENT. The CFD analysis revealed that the diffuser with curved sidewalls and deflector plates distribute the air more uniformly than the diffuser with straight sidewalls.

**Keywords** Photovoltaic (PV) · Diffuser · Deflector · Distribution of air

## 1 Introduction

In the world of climate change, importance of renewable energy is crucial. Solar energy is one of the promising ways to tackle this problem. Solar photovoltaic panel is the device which converts the solar energy into electrical energy. However, the use of PV cells is limited due to high cost. Scientists have been doing research on this for two decades and is still going on. Earlier research was carried on PV panels or thermal systems alone, but now the emphasis is on PV/T systems [1]. The temperature of PV cells affects the power output of photovoltaic/thermal systems. The research focused on optimal thermal and electrical configuration of photovoltaic/thermal systems [2]. The various performance improvement techniques have been studied by

---

R. Meshram (✉) · P. D. Sawarkar  
Department of Mechanical Engineering, Visvesvaraya National Institute of Technology, Nagpur,  
Maharashtra 440010, India  
e-mail: [rohit.meshram444@gmail.com](mailto:rohit.meshram444@gmail.com)

© Springer Nature Singapore Pte Ltd. 2020  
H. K. Voruganti et al. (eds.), *Advances in Applied Mechanical Engineering*,  
Lecture Notes in Mechanical Engineering,  
[https://doi.org/10.1007/978-981-15-1201-8\\_22](https://doi.org/10.1007/978-981-15-1201-8_22)

some researchers such as geometrical modification of absorber plate, solar selective coatings and the use of nanofluids [3]. The waste heat of solar PV cells can be utilized in integration with thermo electric generator for enhanced power output [4]. Based on various models it is found that PV panels yield higher output when the cooling of PV panel, starts when the panels reaches a maximum allowable temperature (MAT), that is  $45^{\circ}$ . The MAT is the average temperature between the energy output and the cooling temperature required [5]. The innovative solution proposed to overcome the problem of overheating of PV panels is based on natural convection in which holes are drilled in PV panels to increase the natural convection which increases the heat transfer. This result in a better cooling of panels [6].

One way of improving efficiency of PV panel is the uniform distribution of air velocity along the panel. Diffusers are used for uniform distribution of air. In the present work, various shapes of diffuser and their effect on the air velocity distribution is studied. The deflector plates are also used for uniform distribution of air. The various geometrical modifications of diffuser with and without deflector plates are simulated using commercial software ANSYS FLUENT16.0.

## 2 Experimental Set-up

Figure 1 shows the experimental set-up for studying the air cooling of the PV/T system. The solar collector has a duct through which air is supplied. The fan of suitable capacity is used to supply air flow through the duct. The PV module used to be single crystalline with standard electrical characteristics. The set-up consists of diffuser placed at the bottom side of the collector. For measuring temperature, thermocouple is used with digital temperature indicator.

**Fig. 1** Experimental set-up with PV/T collector





**Fig. 2** Computational domain of diffuser

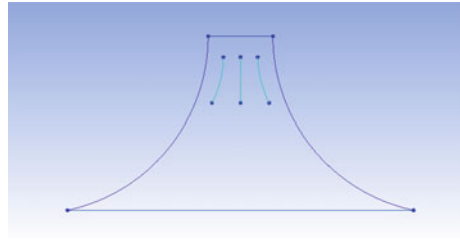


**Table 1** Dimensions of computational domain

Parameters	Dimensions
Panel dimension (m)	0.655 × 0.455
Height of diffuser (m)	0.2275
Radii of side walls (m)	0.275
Diffuser outlet (m)	0.455
Number of air deflectors	3, 4

### 2.1 Geometrical Modelling

Two-dimensional geometrical model of diffuser is created to study the distribution of air velocity. Figure 2 shows one of the sketches of computational domain considered using ICEM CFD (circular side wall with three deflector plates). The dimensions of computational domain for the case considered are given in Table 1. The diffuser dimensions are varied to obtain uniform distribution of air.

### 2.2 Mesh Generation

The computational domain has been discretized. The meshing of computational domain has been done using unstructured grids. Figure 3 shows unstructured mesh generated using ICEM CFD 16.0

**Fig. 3** Unstructured mesh generated for diffuser

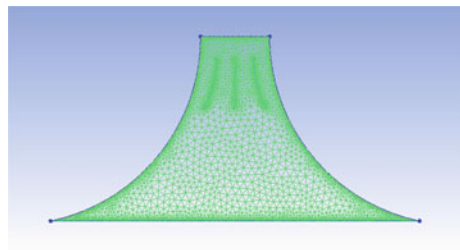


**Table 2** Number of elements for different cases

Case	Number of elements
A	2377
B	4005
C	129,380

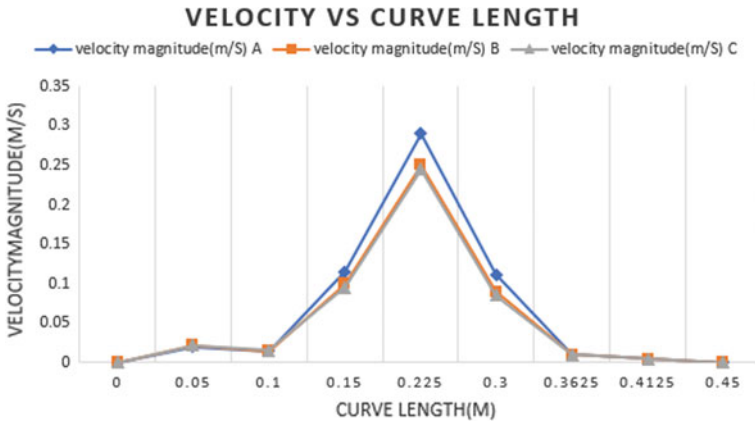


**Fig. 4** Graph of velocity vs. curve length for grid independence

### 2.3 Grid Independence

The grid independence was done by using three different mesh sizes. The case B was chosen to be the optimum mesh size as there is negligible difference between C and B cases. Analysis was done by using case B mesh size. Quality of mesh was found out to be 0.56 min and 0.99 maximum. Convergence criteria were maintained to be  $10^{-6}$  (Table 2; Fig. 4).

## 3 Result and Discussion

Numerical analysis is carried out to study how the predicted flow field varies with the changes in the side walls of diffuser, height of diffuser and incorporating the deflector plates in the flow field.

The analysis is carried out under the assumption of laminar flow. Equations that are used in the analysis are continuity, energy and Navier–Stokes equations. The variation of fluid density was estimated by Boussinesq approximation. The inlet velocity of air is 0.5 m/s. Limited cases of diffusers are simulated computationally using the commercial software ANSYS FLUENT 16.0.

Figure 5 shows simple diffuser cases with the straight sidewalls and changes in the height of diffuser. This geometry does not distribute air velocity uniformly. The effect of deflector plates on trapezoidal geometry is done and observed that with deflector plate's distribution of air is a little bit better. When straight sidewalls of diffuser are replaced by curved sidewalls, air velocity get distributed to some extent. With the increase in radius of curvature of sidewalls, the air velocities tend to distribute more uniformly (Figs. 6 and 7). Figure 8 shows the distribution of air velocity with curved sidewalls. Figure 9 shows effect of use of deflector plates on distribution of air velocity. With three deflector plates, the air reaches to the corner of diffuser, but the centre of diffuser remains unaffected, but if the curve of deflector plates is made little straight the air goes into the centre region. Then, the numbers of deflector plates are increased from 3 to 4 (Fig. 10). But it is observed from Fig. 11 that diffuser with three deflector plates is giving the better distribution of air velocity compared to the diffuser with four deflector plates. Figure 11 shows the effect of curved sidewalls with four deflector plates on distribution of air velocity.

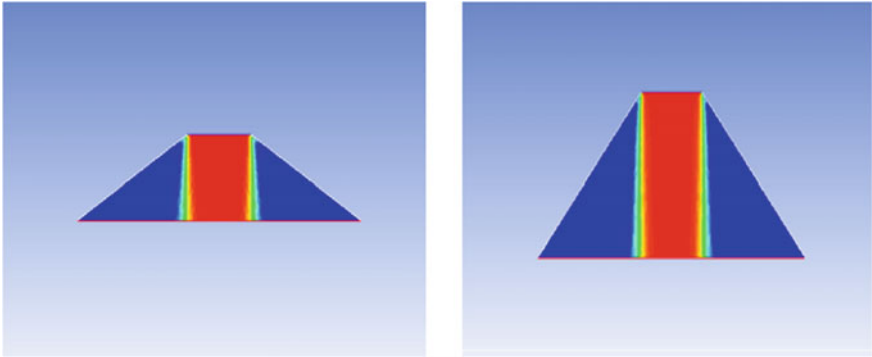


**Fig. 5** Effect of straight side walls and height of diffuser on distribution of air velocity

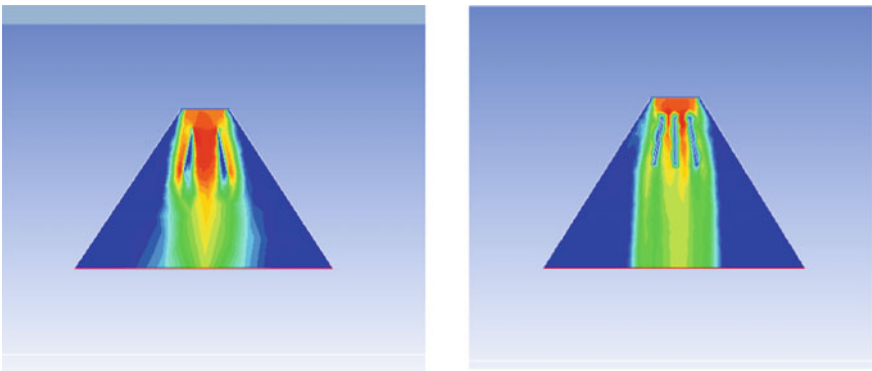


**Fig. 6** Effect of two and three deflector plates on trapezoidal-type of geometry

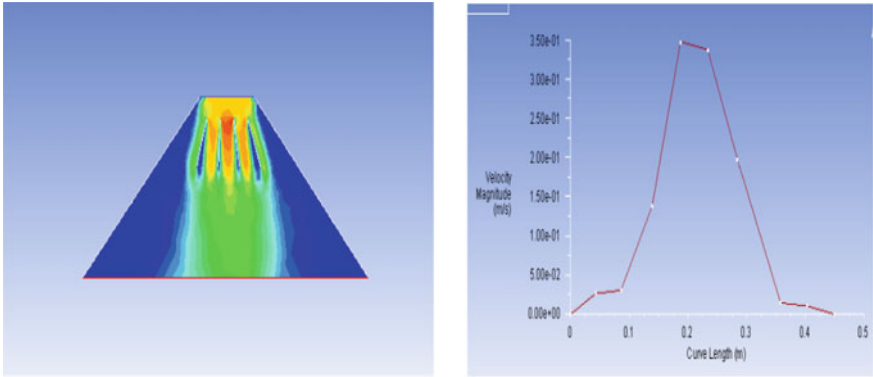


**Fig. 7** Effect of four deflector plates on trapezoidal-type of geometry

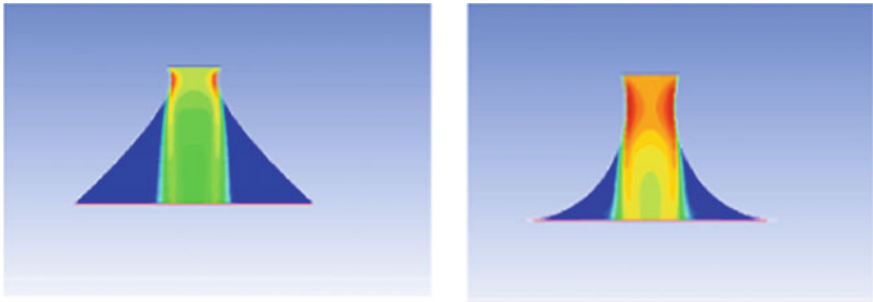


**Fig. 8** Effect of curved side walls of diffuser on distribution of air velocity

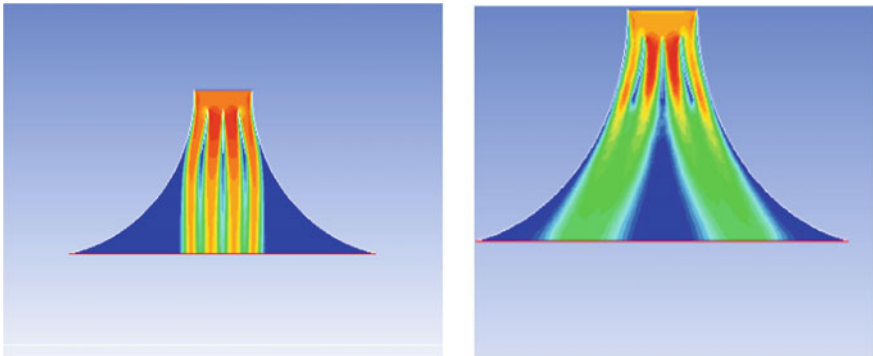


**Fig. 9** Effect of curved deflector plates on distribution of air velocity

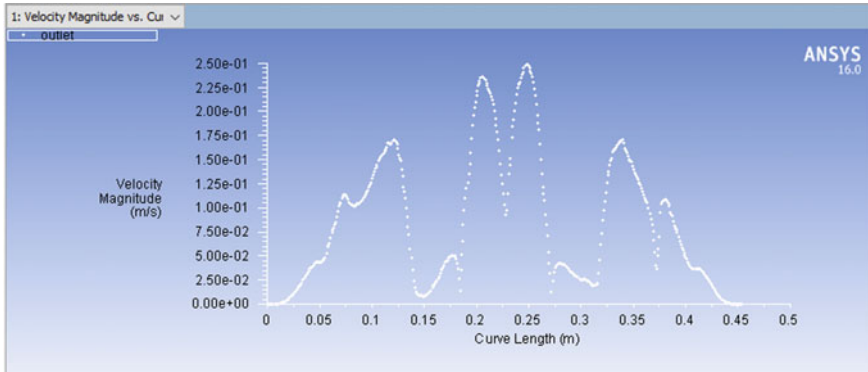


**Fig. 10** Graph for velocity vs. curve length for three deflector plate case

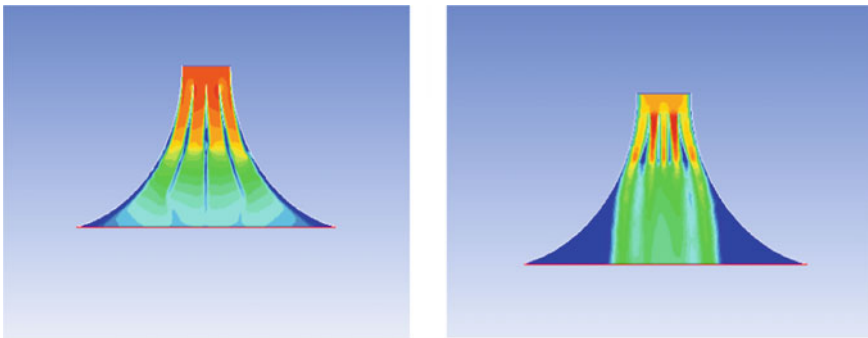


**Fig. 11** Effect of three and four deflector plates on air distribution for curved side walls

## 4 Conclusions

For designing a suitable diffuser for uniform distribution of air velocity, different geometries of diffuser are simulated. The result of simulation shows that among all the geometries, diffuser with curved sidewalls and three deflector plates is the best geometry to be considered for uniform distribution of air velocity. It is also suggested that deflector plates should be close to the inlet of diffuser for uniform distribution of air velocity. It is also observed that height of diffuser has negligible effect on distribution of air velocity. The curvature of side walls and position of deflector plate significantly affects distribution of air velocity.

## References

1. Al-Waelia AHA, Sopiana K, Kazemb HA, Chaichanc MT (2017) Photovoltaic/thermal (PV/T) systems: status and future prospects. *Renew Sustain Energy Rev* 77:109–130
2. Astea N, Del Peroa C, Leonfortea F (2012) Thermal-electrical optimization of the configuration a liquid PVT collector. *Energy Proc* 30:1–7
3. Suman S, Khann MK, Pathak M (2015) Performance enhancement of solar collectors—a review. *Renew Sustain Energy Rev* 49:192–210
4. Makki A, Omer S, Su Y, Sabir H (2016) Numerical investigation of heat pipe-based photovoltaic–thermoelectric generator (HP-PV/TEG) hybrid system. *Energy Convers Manag* 112:274–287
5. Moharram KA, Abd-Elhady MS, Kandil HA, El-Sherif H (2013) Enhancing the performance of photovoltaic panels by water cooling. *Ain Shams Eng J* 4:869–877
6. Abd-Elhadya MS, Seragb Z, Kandilc HA (2018) An innovative solution to the overheating problem of PV panels. *Energy Convers Manag* 157:452–459
7. Amanlou Y, Hashjin TT, Ghobadian B, Najafi G (2017) Air cooling low concentrated photovoltaic/thermal (LCPV/T) solar collector to approach uniform temperature distribution on the PV plate. *Appl Therm Eng* 17:413–421

# CFD Analysis of Wind Turbine with Different Flange Angles



S. M. Bichitkar, P. P. Buddiyal, S. S. Chavan, A. A. Kulkarni  
and V. B. Gawande

**Abstract** Computational fluid dynamics (CFD) analysis of circular diffuser with flange is carried in present analysis using ANSYS CFD tool. A wind turbine with circular diffuser and flange attached over the periphery of the diffuser is simulated for various flange angle range of  $0^{\circ}$ – $25^{\circ}$ . Provision of diffuser has demonstrated significant augmentation in power and speed of the turbine. The study also shows that the variation of flange angle creates strong vortices behind the flange, resulting in sudden decrease in static pressure in the exit of the diffuser. This will increase the velocity through entrance of the wind turbine and is responsible for power augmentation in the wind turbine. Contour plots show an increase in velocity up to optimum flange angle of  $15^{\circ}$ , and then it decreases gradually afterwards. The results obtained in the present analysis are in good agreement with the previous published experimental work.

**Keywords** Wind lens turbine · Circular diffuser · Flange angles · CFD

---

S. M. Bichitkar · P. P. Buddiyal · S. S. Chavan · A. A. Kulkarni · V. B. Gawande (✉)  
V.P.'s Kamalnayan Bajaj Institute of Engineering and Technology, Baramati 413133, India  
e-mail: [vipin.gawande@vpkbiot.org](mailto:vipin.gawande@vpkbiot.org)

S. M. Bichitkar  
e-mail: [sachinbichitkar35@gmail.com](mailto:sachinbichitkar35@gmail.com)

P. P. Buddiyal  
e-mail: [prasadbuddiyal@gmail.com](mailto:prasadbuddiyal@gmail.com)

S. S. Chavan  
e-mail: [sidchavan005@gmail.com](mailto:sidchavan005@gmail.com)

A. A. Kulkarni  
e-mail: [ajinkyakulkarni9498@gmail.com](mailto:ajinkyakulkarni9498@gmail.com)

© Springer Nature Singapore Pte Ltd. 2020  
H. K. Voruganti et al. (eds.), *Advances in Applied Mechanical Engineering*,  
Lecture Notes in Mechanical Engineering,  
[https://doi.org/10.1007/978-981-15-1201-8\\_23](https://doi.org/10.1007/978-981-15-1201-8_23)

## 1 Introduction

Harnessing the wind is one of the cleanest, most sustainable ways to generate electricity. Wind power produces no toxic emissions and none of the heat-trapping emissions contribute to global warming. This, and the fact that wind power is one of the most abundant and increasingly cost-competitive energy resources, makes it a viable alternative to the fossil fuels that harm our health and threaten the environment. Small wind turbines are electric generators in which the energy of the wind is converted into clean, emissions-free energy for individual homes, farms, and small businesses. Efficiency of the wind turbine is affected by the design of wind turbine assembly. The speed of the wind turbine blades could be increased by providing wind lens, which in turn enhances in overall efficiency of the conventional wind turbine. Ohya et al. [1] and his colleagues have developed a wind turbine system that consists of a diffuser shroud with a broad-ring flange at the exit periphery and a wind turbine inside it. This arrangement shows an increase in power and wind speed by a factor of about 4.5 compared to the standard wind turbine. Ohya and Karasudani [2] have experimentally investigated a diffuser shroud with a broad-ring brim at the exit periphery and noted a power augmentation by a factor of about 2–5 compared with a bare wind turbine. Toshimitsu et al. [3] and his colleagues have experimentally investigated the performance of wind turbine with flanged-diffuser shroud in sinusoidally oscillating and fluctuating velocity flows. Kosasih and Tondelli [4] presented the effect of diffuser shape on the performance of wind turbine. Bontempo and Manna [5] have investigated a CFD model for aerodynamic performance of ducted wind turbines. Jafari and Kosasih [6] have carried out experimental and CFD analysis of diffuser-shrouded horizontal axis wind turbine. Their study proposed a method to design effective frustum diffuser geometries for a small wind turbine. A CFD analysis of wind turbine with a shroud and lobed ejector is carried out by Han [7] and his colleagues. El-Zahaby et al. [8] and his colleagues have carried out CFD analysis of flow fields for shrouded wind turbine's diffuser model with different flange angles. Heikal et al. [9] and his colleagues have investigated the effects of diffuser flange inclination angle and the diffuser flange depth inside the exit of the diffuser on the wind lens turbine system performance.

Literature review shows that the overall performance of a small wind turbine could be enhanced with an addition of wind lens in the assembly. In the present study, CFD analysis of a small turbine is carried out using Ohya's circular diffuser model [1] and flow simulation effects are investigated by varying flange angle ( $\theta$ ).

## 2 CFD Analysis

In present work, a computational domain of a wind turbine [1] with circular diffuser ( $D_1 = 40$  mm and  $D_2 = 48$  mm,  $L/D_1 = 1.5$ ) and a flange with a height of  $h =$



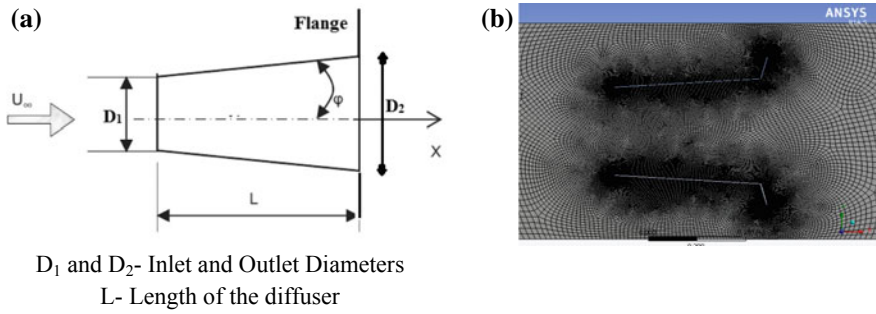


**Fig. 1** a Computational domain of circular-diffuser model with flange and b unstructured meshing around diffuser

10 cm ( $h/D_1 = 0.25$ ) is attached to the outer periphery of the diffuser exit as shown in Fig. 1a.

The area ratio ( $\mu = \text{outlet area/inlet area}$ ) used is 1.44. The angle of inclination ( $\phi$ ) is  $3.7^\circ$  and wind velocity ( $U_\infty$ ) used is in the range of 2–8 m/s. The Reynolds number is defined as  $Re = D U_\infty / \nu$ , where  $D$  is the diameter of the wind turbine rotor and  $\nu$  is the dynamic viscosity. ANSYS 14.5 CFD tool is used for pre- and post-processing. Unstructured mesh (Fig. 1b) is created on computational domain with 65,000 nodes. SIMPLE algorithm is used along with  $k - \epsilon$  turbulence model in FLUENT solver.

### 3 Results and Discussion

Present computational model is verified with the experimental results, carried out by Ohya et al. [1], and is shown in Fig. 2.

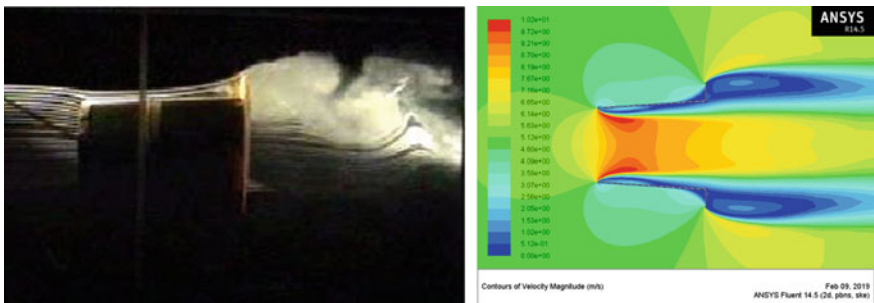


**Fig. 2** Comparison of flow around a circular-diffuser experimental model of Ohya et al. [1] with a brim and CFD analysis result

To predict the performance of a wind turbine, flange angle is varied from  $\theta = 0^\circ$  to  $\theta = 25^\circ$  for the specified set of geometrical and operating parameters. Velocity contour plots for flange angle range ( $0^\circ$ – $25^\circ$ ) are shown in Fig. 3. Based on the CFD results, comparison of velocity increase at diffuser entrance at various flange angles is plotted in Fig. 4. The basic principle adopted for the increase in velocity at the upstream of diffuser is vortex formation in the downstream of the flange. A series of vortices are visible in the contour plots along the length of the diffuser. These

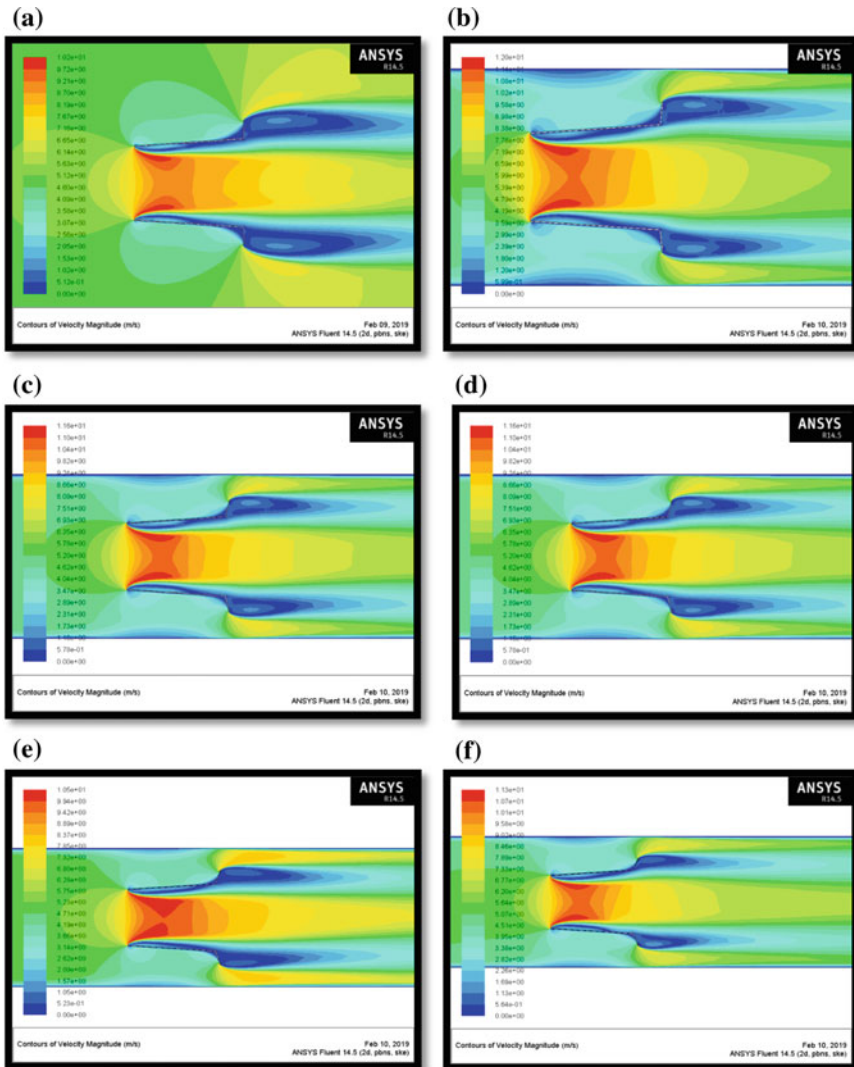


**Fig. 3** Velocity contour plots of flow fields at flange angle of **a**  $0^\circ$  **b**  $5^\circ$  **c**  $10^\circ$  **d**  $15^\circ$  **e**  $20^\circ$  and **f**  $25^\circ$  for  $U_\infty = 5$  m/s

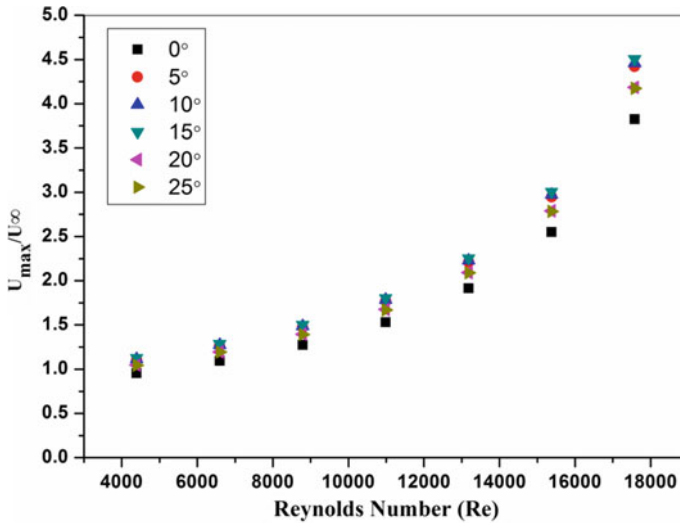


**Fig. 4** Comparison of velocity increase at diffuser entrance at various flange angles for Reynolds number

vortices are responsible for reducing the static pressure in the exit area of the diffuser. Reduction in pressure coefficient in the downstream of diffuser is responsible for increase in velocity at the entry of diffuser. Higher velocity is responsible for power enhancement compared to conventional wind turbine. From Fig. 4, it is concluded that the optimum flange angle is 15°, at which there is maximum entrance velocity increase for inlet wind velocity values. The figure shows, there is a gradual increase in entrance velocity from 0° to 15° for increase in Reynolds number. The velocity contour plots obtained from CFD analysis also confirmed this increase. After flange angle of 15°, there is a gradual drop in the velocity due to reduction in vortices and hence the entrance velocity decreases.

## 4 Conclusions

Present study is carried out using ANSYS CFD tool for simulation of flow characteristics in circular diffuser with varying flange angles. Following outcomes could be derived from the present analysis.

- (1) Insertion of flange results in the formation of strong vortices on the downstream of flange, which in turn results in the increase velocity through the entrance of the wind turbine.
- (2) Maximum entrance velocity is recorded for flange angle of 15° for increase in Reynolds number.

- (3) After flange angle of  $15^\circ$ , the static pressure in the exit area of the diffuser decreases gradually due to reduction in vortices and hence the entrance velocity decreases.
- (4) Present study shows that the speed of the wind turbine blades could be increased by providing wind lens, which in turn enhances in overall efficiency of the conventional wind turbine.

## References

1. Ohya Y, Karasudani T, Sakurai A, Abe K, Inoue M (2008) Development of a shrouded wind turbine with a flanged diffuser. *J Wind Eng Ind Aerodyn* 96:524–539. <https://doi.org/10.1016/j.jweia.2008.01.006>
2. Ohya Y, Karasudani T (2010) A shrouded wind turbine generating high output power with wind-lens technology. *Energies* 3:634–649. <https://doi.org/10.3390/en3040634>
3. Toshimitsu K, Kikugawa H, Sato K, Sato T (2012) Experimental investigation of performance of the wind turbine with the flanged-diffuser shroud in sinusoidally oscillating and fluctuating velocity flows. *Open J Fluid Dyn* 2:215–221. <https://doi.org/10.4236/ojfd.2012.224024>
4. Kosasih B, Tondelli A (2012) Experimental study of shrouded micro-wind turbine. In: *Evolving energy-IEF international energy congress (IEF-IEC 2012)*. Proc Eng 49:92–98. <https://doi.org/10.1016/j.proeng.2012.10.116>
5. Bontempo R, Manna M (2014) Performance analysis of open and ducted wind turbines. *Appl Energy* 136:405–416. <http://dx.doi.org/10.1016/j.apenergy.2014.09.036>
6. Jafari SAH, Kosasih B (2014) Flow analysis of shrouded small wind turbine with a simple frustum diffuser with computational fluid dynamics simulations. *J Wind Eng Ind Aerodyn* 125:102–110. <https://doi.org/10.1016/j.jweia.2013.12.001>
7. Han W, Yan P, Han W, He Y (2015) Design of wind turbines with shroud and lobed ejectors for efficient utilization of low-grade wind energy. *Energy* 89:687–701. <https://doi.org/10.1016/j.energy.2015.06.024>
8. El-Zahaby AM, Kabeel AE, Elsayed SS, Obiaa MF (2017) CFD analysis of flow fields for shrouded wind turbine's diffuser model with different flange angles. *Alex Eng J* 56:171–179. <http://dx.doi.org/10.1016/j.aej.2016.08.036>
9. Heikal HA, Abu-Elyazeed OSM, Nawar MAA, Attai YA, Mohamed MMS (2018) On the actual power coefficient by theoretical developing of the diffuser flange of wind-lens turbine. *Renew Energy* (in press). <https://doi.org/10.1016/j.renene.2018.02.100>

# Performance and Emission Characteristics of Thermal Barrier Coating on Diesel Engine Fueled with Cottonseed Biodiesel



Badal Kudachi, Nitin Satpute, Nilaj N. Deshmukh and Bipin Mashilkar

**Abstract** There is an urgent need to explore the substitute for conventional fossil fuel in light of environmental sustainability. Attempts were made to improve engine efficiency and to reduce greenhouse gasses by certain modification in the use of biofuel. In the present work, experiments have been performed on a single cylinder, four-strokes, direct injection, diesel engine with cottonseed biofuel and its blends. In order to ensure complete combustion of the fuel, cylinder head and piston crown have been coated with yttria partially stabilized zirconia (YPSZ) for a thickness of 0.2 mm. The plasma spray technique has been used for coating engine components. Combustion properties of the cottonseed oil have been improved with the transesterification process. The experimental results showed significant improvement in performance and reduction in emission characteristics of a coated engine. The biodiesel blend B10 and B25 showed good results compared to diesel in an uncoated and coated engine, respectively.

**Keywords** Diesel engine · Thermal barrier coating · Plasma spray technique

---

B. Kudachi (✉) · N. N. Deshmukh · B. Mashilkar  
Department of Mechanical Engineering, Fr. C. Rodrigues Institute of Technology, University of Mumbai, Vashi, Navi Mumbai, Maharashtra 400703, India  
e-mail: [badalkudachi@gmail.com](mailto:badalkudachi@gmail.com)

N. N. Deshmukh  
e-mail: [nilaj.deshmukh@fcrit.ac.in](mailto:nilaj.deshmukh@fcrit.ac.in)

B. Mashilkar  
e-mail: [bipinmashilkar@gmail.com](mailto:bipinmashilkar@gmail.com)

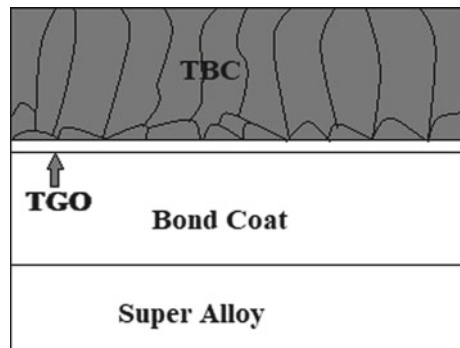
N. Satpute  
Department of Mechanical Engineering, Faculty of Science and Technology, Vishwakarma University, Pune, Maharashtra 411037, India  
e-mail: [nitinsatpute123@gmail.com](mailto:nitinsatpute123@gmail.com)

## 1 Introduction

Fossil fuels play a major role in fulfilling the world energy requirement. Fossil fuels are exhaustible energy sources, and their ability to supply the energy demands continuously is limited to a few decades [1]. The combustion of fossil fuels emits pollutant gasses which cause a major impact on the environment. The global warming problem is caused by greenhouse gas carbon dioxide ( $\text{CO}_2$ ) which traps the heat in the atmosphere [2]. The dependency on fossil fuel has increased enormously due to the growth in the population of the world. The oil crisis in 1973 and the subsequent increase in the cost of fuel urge to enhance the performance of the IC engine and look for alternative fuels [3]. Increasing efforts are being made to enhance the performance of IC engines and the use of alternative fuels in the view of depleting fossil fuels. An attempt has been made in the present study to increase the efficiency of the engine by the modification of engine parts and using alternative fuel. The thermal efficiency of an engine is about 33% with the major heat loss occurred by cooling and exhaust system. These losses can be minimized by coating certain parts of the engine with the ceramic material which acts as a thermal barrier to the heat produced inside the cylinder, which is also known as thermal barrier coating (TBC) material. Initially, TBC was tested for aircraft engine performance. Furthermore; studies have exhibited and analyzed for the effect of inside cylinder thermal insulation. Application of the TBC on the IC engine in addition to the reduction in heat loss increases gas temperature and combustion wall temperature [4].

The typical TBC system consists of super alloy/metals, bond coat (BC), thermally grown oxides (TGO), and thermal barrier coating (TBC) as illustrated in Fig. 1. The upper layer is TBC, which is also called as top coat, is the porous ceramic structure which exhibits low thermal conductivity and coefficient of thermal expansion. The TBC reduces transfer of heat from the combustion gasses to the components of the system. The BC acts as a bond/mediator between the supper alloy/metal and TBC. The function of BC is to protect the supper alloy/metal from the oxidation and to improve adhesion property between the TBC and metal. The TGO forms between the

**Fig. 1** TBC system [5]



TBC and BC at high-temperature exposure. The TGO due to its good adherence and low oxygen diffusivity characteristics prevents the underlying material from heat.

### 1.1 Plasma Spray Technique

The schematic diagram of the plasma spray is shown in Fig. 2. It is a high-frequency arc method, which ignites between the tungsten cathode and an anode. The gas which flows between the anode and cathode electrodes ( $H_2$ , He,  $N_2$ , or mixtures) ionized in a way that plasma plume several centimeters in length develops. The powder zirconia material is fed into the plasma plume where it gets melted and propelled toward the workpiece at a high speed. They form splats by spreading, cooling, and solidifying [6]. The TBC porosity by plasma spray technique is in the range of 3–20% [7]. The porosity of TBC material is desirable since it decreases the thermal conductivity.

The standard piston crown and cylinder head of diesel engine (Kirloskar made Type TV 1) were machined to remove material equal to the desired thickness of coating in order to maintain the engine compression ratio after the assembly of same on the engine. The optimum thickness of coating varies between 0.2 and 0.5 mm. The thinner coatings applied to the engine result in better performance [9]. Hence, the coating of a thickness of 0.2 mm was applied to the engine parts for this study (Fig. 3).

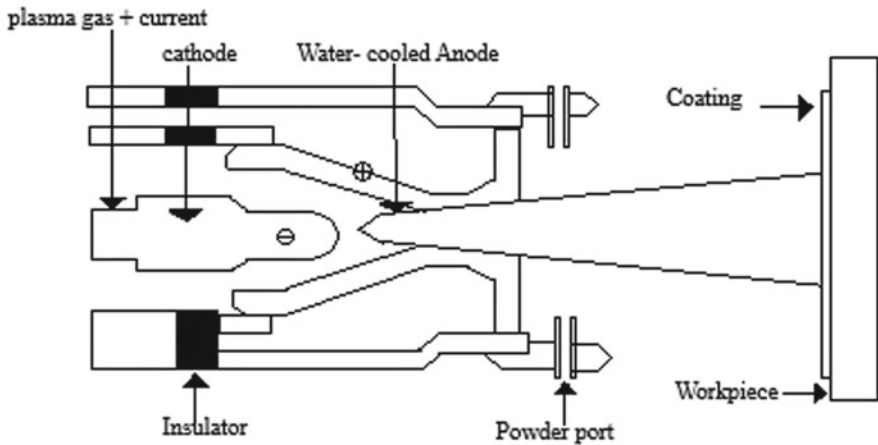
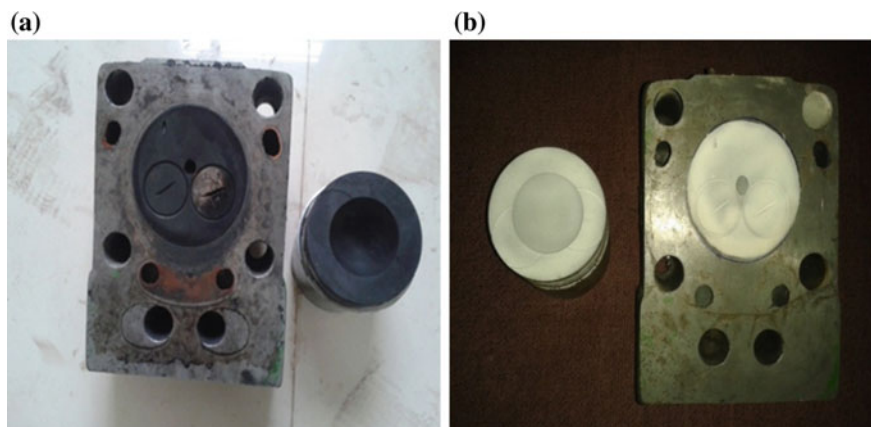


Fig. 2 Schematic diagram of plasma spray technique [8]



**Fig. 3** **a** Uncoated engine parts cylinder head and piston crown. **b** Coated engine parts cylinder head and piston crown

## 1.2 Biodiesel

The cottonseed biofuel is converted into biodiesel by the transesterification process. Figure 4 shows the experimental setup of transesterification. The sodium hydroxide (catalyst) is dissolved in the methanol (alcohol) using a standard agitator. The cottonseed oil is added to the mixture of catalyst and alcohol. The two major products glycerin and biodiesel are formed after the complete reaction. The mixture is then transferred to the separating funnel. Since the glycerin is much denser than biodiesel, it settles at the bottom of the vessel and is taken off. The excess alcohol from both the phases was distilled off under vacuum. The glycerin neutralized with an acid can be stored as crude glycerin. The biodiesel in the upper phase separated from glycerin

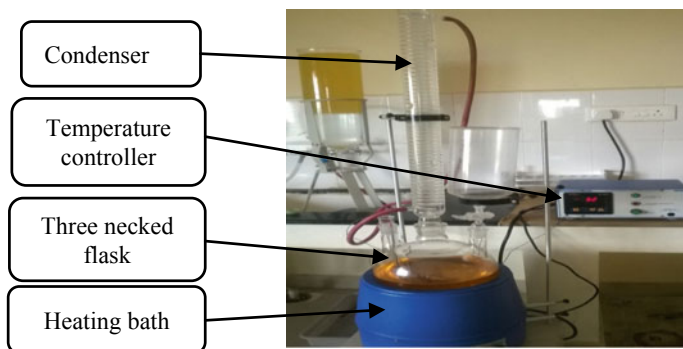


**Fig. 4** Experimental setup of transesterification



**Table 1** Properties of diesel and cottonseed oil

S.no.	Property	Diesel	Cotton seed
1	Calorific value (kJ/kg)	42,500	34936.4
2	Flash point (°C)	44	192
3	Fire point (°C)	49	234
4	Viscosity (cst)	3.07	4.6
5	Density (kg/m <sup>3</sup> )	840	875

was purified by washing gently with warm water to remove the traces of unreacted catalysts, soaps, and glycerin formed during the transesterification process.

The biodiesel blends were prepared with different proportions like B100 (100% biodiesel), B10 (10% biodiesel, 90% diesel), B15, B20, and B25 for the testing. The calorific value of the fuel is the measure of heat or energy produced. The higher calorific value results in higher energy produced inside the cylinder. The calorific value of biodiesel is found to be less than diesel. The viscosity is the important characteristics of the fuel, and higher viscous oil results in poor atomization. The biodiesel is viscous than the diesel, and it increases with the concentration of biodiesel in the mixture. The density values are helpful for quantity calculation and assuming ignition quality. The density of biodiesel increases with the increase in the concentration of the biodiesel in the mixture. The properties of diesel and cottonseed biodiesel are given in Table 1.

## 2 Experimental Setup for Engine Performance Test

The experiment was conducted in the laboratory of PDA College of Engineering, Gulbarga, Karnataka, on the single cylinder, four-strokes, water cooled diesel engine. The specification of the engine is given in Table 2.

The test is conducted by varying the load and keeping constant speed of 1500 RPM, the pressure at 180 bar on the normal standard uncoated engine and coated engine.

**Table 2** Specification of engine

Parameters	Specification
Engine make	Kirloskar made TV 1
Rated power	5.2 kW
Speed	1500 rpm
Injection timing	23° bTDC
Compression ratio	16.5:1
Bore	80 mm
Stroke length	110 mm

### 3 Results and Discussions

#### 3.1 Performance Characteristics

**Brake Power (BP):** The experimental values of BP with different loads are shown in Fig. 5a and b for uncoated and coated engine, respectively. The maximum BP was found 5.42 kW for B10 at maximum load in an uncoated engine, and it was 0.33 kW (6.4%) higher than that of diesel. The maximum brake power was found 5.49 kW for B25 at maximum load in a coated engine, and it was 0.44 kW (8.7%) higher than that of diesel. Increase in the brake power was attained by the ceramic applied to the engine parts which prevents heat loss to the cooling and other medium [10].

**Brake Thermal Efficiency (BTE):** The results obtained pertaining to the BTE are shown with the help of graphs in Fig. 6a and b for uncoated and coated engine, respectively. The maximum BTE was found 29.61% for B10 in an uncoated engine, and it was higher compared to diesel at maximum load. The maximum thermal efficiency was found 33.63% for B100 in a coated engine which was higher than that of diesel at maximum load. The efficiency is improved because of the increase in available power and reduction in heat loss [11].

**Brake-Specific Fuel Consumption (BSFC):** The experimental values for BSFC are shown with the help of graph in Fig. 7a and b for uncoated and coated engine, respectively. The energy content of biodiesel and its blends were lower than that of diesel; therefore, the BSFC of diesel and its blends are nearly the same as that of diesel [12]. The minimum BSFC 0.291 kg/kWh was observed for B10 in an uncoated engine at maximum load. In case of a coated engine, minimum BSFC 0.278 kg/kWh was observed for B25, and it was lower than other biodiesel blends and diesel at maximum load. Subsequent paragraphs, however, are indented.

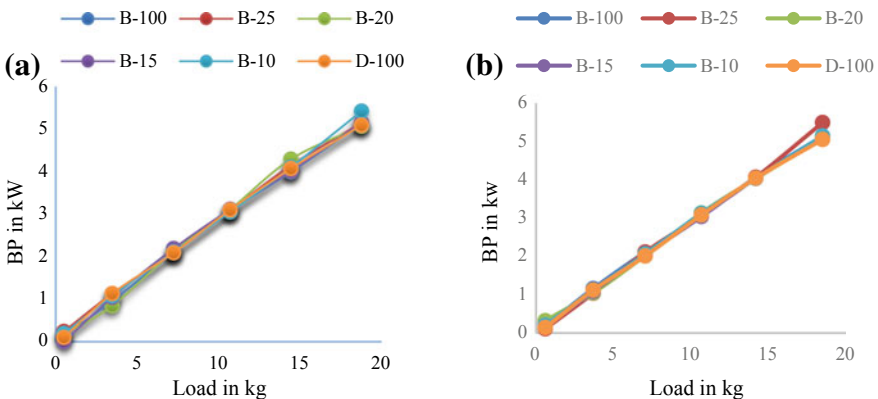


Fig. 5 a Uncoated engine. b Coated engine

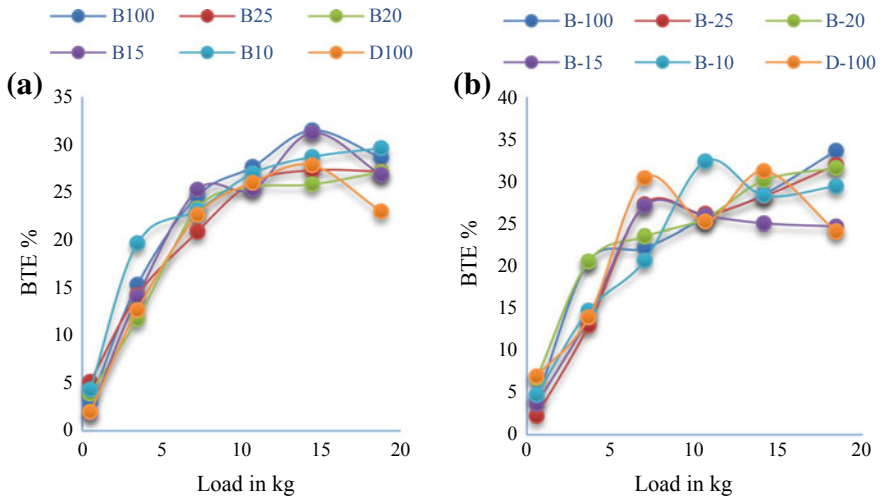


Fig. 6 a Uncoated engine. b Coated engine

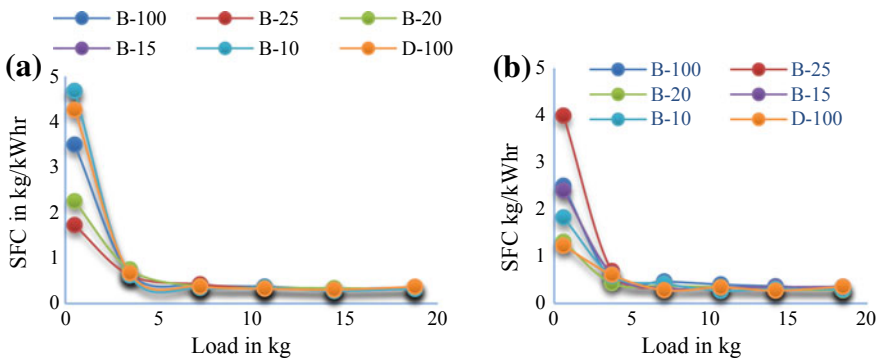


Fig. 7 a Uncoated engine. b Coated engine

### 3.2 Emission Characteristics

**Hydro Carbon (HC) Emission:** In case of uncoated engine, the minimum HC emission was observed for B100 and B25 by 68, 58% compared to diesel at the maximum load. On the other hand, the minimum HC was found for B100 and B25 by 84.31 and 80.4% at the maximum load in a coated engine, which may be attributed to the better combustion efficiency (Fig. 8).

**Nitrogen Oxide (NO<sub>x</sub>) Emission:** The NO<sub>x</sub> emissions in CI engines are formed based on two factors, the cylinder gas temperature and the availability of oxygen for combustion [13]. The NO<sub>x</sub> emissions of uncoated and coated engine are shown in

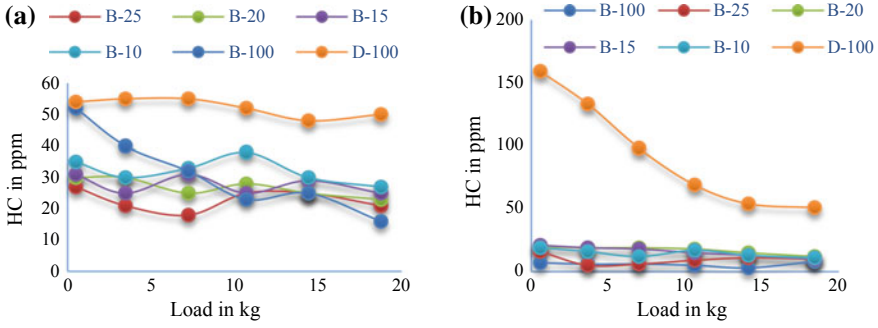


Fig. 8 a Uncoated engine. b Coated engine

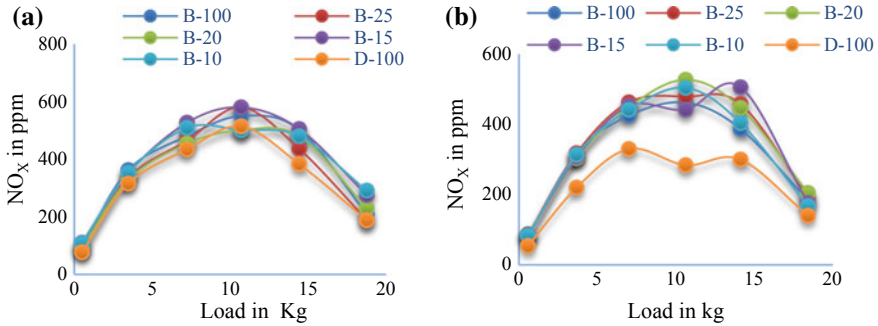


Fig. 9 a Uncoated engine. b Coated engine

Fig. 9a and b, respectively. The NO<sub>x</sub> emission found to be higher for all the biodiesel blends when compared to diesel for both uncoated and coated engines.

### 4 Conclusion

The biodiesel blend B10 shows good results compared to diesel in an uncoated engine. The BP, BTE, and BSFC for B10 were observed to be 5.42 kW, 29.61%, and 0.291 kg/kWh, respectively. These results were compared with diesel, and there was increase in 0.33 kW (6.4%) of BP, 6.6% of BTE, decrease in 0.078 kg/kWh (21.13%) of SFC. In case of coated engine, B25 showed good results compared to diesel. The results showed that BP, BTE, and BSFC for B25 were 5.49 kW of BP, 31.94 of BTE, and 0.278 kg/kWh of SFC, respectively. There was increase in 0.44 kW (8.7%) of BP, 32.75% of BTE, and reduction in 0.074 kg/kWh (21%) SFC compared to diesel. The B25 shows minimum HC emission of 80.4 and 84.31% compared to diesel at maximum load. The NO<sub>x</sub> emissions of all the biodiesel blends were found to be higher than diesel at all the load for both uncoated and coated engines.

## References

1. Shafiee S, Topal E (2009) When will fossil fuel reserves be diminished? *Energy Policy* 37(1):181–189
2. Bose BK (2010) Global warming: Energy, environmental pollution, and the impact of power electronics. *IEEE Ind Electron Mag* 4(1):6–17
3. Roeder John L (2005) What we learned from the oil crisis of 1973: a 30-year retrospective. *Bull Sci Technol Soc* 25(2):166–169
4. Guruprakash V, Harivignesh N, Karthick G, Bose N (2016) Thermal barrier coating on IC engine cylinder liner. *Arch Mater Sci* 38:38
5. Soare A, Csaki I, Sohaciu M, Oprea C, Soare S, Costina I, Petrescu MI (2017) New bond coat materials for thermal barrier coating systems processed via different routes. In: IOP conference series: materials science and engineering, vol 209, No 1. IOP Publishing (2017, June), p 012045
6. Saini AK, Das D, Pathak MK (2012) Thermal barrier coatings-applications, stability and longevity aspects. *Procedia Eng* 38:3173–3179
7. Chen D, Gell M, Jordan EH, Cao E, Ma X (2007) Thermal stability of air plasma spray and solution precursor plasma spray thermal barrier coatings. *J Am Ceram Soc* 90(10):3160–3166
8. Assanis DN, Wiese K, Schwarz E, Bryzik W (1991) The effects of ceramic coatings on diesel engine performance and exhaust emissions. SAE technical paper, no. 910460
9. Badal K, Krishnamurthy KN Experimental evaluation of Ytria partially stabilized Zirconia thermal barrier coating by plasma sprayed technique on I.C engine. In: Proceedings of IC-FEAST, vol 01, NIT, Tiruchirappalli, Tamil Nadu, India, pp 167–172, Apr 27–28
10. Cinviz M, Salman MS, Canlı E, Köse H, Solmaz Ö (2012) Ceramic coating applications and research fields for internal combustion engines. In: Ceramic coatings-applications in engineering. IntechOpen
11. Palaniswamy E, Manoharan N (2008) Ceramic coated combustion chamber for improving IC engine performance. *Int J Des Manuf Technol* 2(1):22
12. Mittal N, Athony RL, Bansal R, Kumar CR (2013) Study of performance and emission characteristics of a partially coated LHR SI engine blended with n-butanol and gasoline. *Alexandria Eng J* 52(3):285–293
13. Ganesan V (2008) Internal combustion engines. In: 3rd Edn. Tata McGraw-Hill Publishing Company Limited, New Delhi, India

# Performance and Emission Analysis of Rapeseed Methyl Ester on DI Diesel Engine Using Artificial Neural Network



V. Amosu, S. K. Bhatti and S. Jaikumar

**Abstract** In the present work, experiments were carried out on four-stroke, single cylinder, water cooled, constant speed, variable compression ratio (VCR) diesel engine. Experiments are done with the engine being fuelled with DI diesel fuel followed by fuel blends of RME20 (20% rapeseed methyl ester and 80% diesel), RME40 (40% rapeseed methyl ester and 60% diesel) and RME100 (pure rapeseed methyl ester) on volume basis. Performance and emission characteristics of diesel and rapeseed methyl ester (RME) with diesel blends are examined. The engine speed is maintained constant at 1500 rpm at different loads and at compression ratios of 16:1, 17:1 and 18:1. The performance parameters like brake thermal efficiency (BTE), brake-specific fuel consumption (BSFC) and exhaust gas temperatures are measured, and the results are recorded. The emission parameters like carbon monoxide (CO), carbon dioxide (CO<sub>2</sub>), unburnt hydrocarbons (UHC), nitrogen oxides (NO<sub>x</sub>) and smoke are measured. The correctness of experimental results is analysed with artificial neural network (ANN). Artificial neural network is a tool to efficiently predict the combustion, performance and emission characteristics by using measured data. Artificial neural network toolbox in MATLAB software is used for simulation of engine parameters. The coefficient of determination  $R^2$  values is in the range of 0.942–0.990.

**Keywords** Rapeseed methyl ester · Performance · Emissions · ANN

---

V. Amosu (✉)

Department of Mechanical Engineering, Andhra University, Visakhapatnam, Andhra Pradesh 530003, India

e-mail: [amosuvadde@gmail.com](mailto:amosuvadde@gmail.com)

S. K. Bhatti

Department of Mechanical Engineering, College of Engineering for Women, Andhra University, Visakhapatnam, Andhra Pradesh 530003, India

S. Jaikumar

Mechanical Engineering Department, GITAM University, Visakhapatnam, Andhra Pradesh 530045, India

© Springer Nature Singapore Pte Ltd. 2020

H. K. Voruganti et al. (eds.), *Advances in Applied Mechanical Engineering*,

Lecture Notes in Mechanical Engineering,

[https://doi.org/10.1007/978-981-15-1201-8\\_25](https://doi.org/10.1007/978-981-15-1201-8_25)

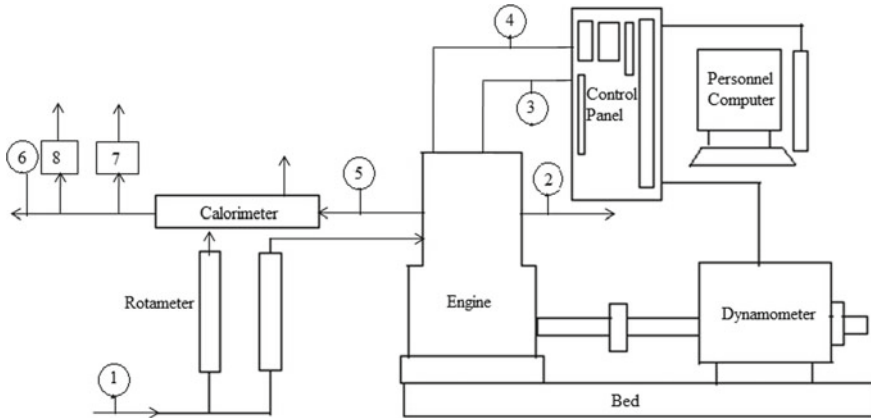
## 1 Introduction

The world is challenging with the new alternate fuel sources as a substitute or direct replacement of petro fuels due to scarcity of energy sources. Also, the pollution levels in the environment are increasing day by day due to increase in vehicles running with petroleum-based fuels. Hence, the edible and non-edible oils are chosen as alternative fuel sources. Biodiesel is the better alternative fuel to conventional diesel on account of having lower emissions of CO, HC and smoke. The combustion, performance and emission characteristics need to be assessed to know the efficiency of the engine. Artificial neural network is greatly useful for the prediction of different output responses using various set of input parameters. Compared to conventional mathematical simulations, ANN is the faster prediction tool for number of variables [1]. In recent years, ANN models are used in internal combustions engines application. The ANN approach is used to predict the performance and emission of the diesel engines [2, 3], equivalence ratio and specific fuel consumption [4]. The effect of turbulence of SI engines due to valve timing variations and fuel economy was studied using ANN [5]. In ANN modelling, the inputs from various sources are received by biological neurons and combine in one way or the other, and the final output responses were envisaged after performing a nonlinear operation. Artificial neural network consists of three layers such as input layer, hidden layer and output layer [6, 7]. Based on the existing literature, the present study focuses on the prediction of experimental performance and emission results using a powerful ANN tool. For this analysis, the rapeseed methyl ester blends were considered as test fuel and operated at different compression ratios and engine loads.

## 2 Experimental Set-up

In this study, experiments were conducted on a single cylinder variable compression ratio four-stroke diesel engine to determine the performance, emissions and combustion characteristics at various loads and at different compression ratios. The inlet side of the engine is connected with biodiesel and diesel tanks separately and air box through the sensors. Similarly, the exhaust side of the engine was connected to INDUS smoke metre and INDUS 5 gas analyser to measure the emissions from the engine. The exhaust temperature indicator is provided at the exhaust side of the engine to measure the exhaust gas temperature. The schematic diagram of the VCR diesel engine set-up is shown in Fig. 1. The detailed technical specification of the VCR diesel engine is shown in Table 1.

The RME blends were prepared with the proportions of 20, 40 and 100% biodiesel with standard diesel. The test fuels considered in this study were diesel, RME20, RME40 and RME100 (pure biodiesel). The experiments are conducted at a constant speed of 1500 rpm. The engine is cooled using circulating water and then started at no load condition using decompression lever for sufficient warm-up and stabilization



- 1. Cooling water inlet
- 2. Cooling water outlet
- 3. Airflow
- 4. Fuel flow
- 5. Exhaust gas out
- 6. Exhaust gas outlet
- 7. Five gas analyzer
- 8. INDUS smoke meter

**Fig. 1** Schematic diagram of VCR diesel engine

**Table 1** Technical specification of the engine

Make	Kirloskar
Number of cylinders	01
Number strikes	04
Power	5.20 kW
Bore X Stroke	87.5 mm × 110 mm
Swept volume	661 cc
Dynamometer	Mechanical loading
Orifice diameter	20 mm
Compression ratio	18:1
Rated speed	1500 rpm

before taking the readings. The experiments were conducted at three different compression ratios of 16, 17 and 18. The fuel injector opening pressure is maintained at 220 bar. VCR diesel engine performance parameters like brake power, torque, brake-specific fuel consumption, brake thermal efficiency and exhaust gas temperature were calculated. Fuel flow is measured by using burette and stopwatch. The time required for 10 cubic centimetre of the fuel flow in the burette is measured by using stopwatch, which gives the flow rate of fuels like diesel, RME20, RME40 and RME100. Exhaust gas temperatures were measured at each load by resistance temperature detectors, whose sensors are placed after the exhaust valve in exhaust pipe.



**Table 2** Uncertainties of parameters

Parameter	% Uncertainty
BTE	$\pm 3.4$
BSFC	$\pm 4.3$
CO	$\pm 0.7$
CO <sub>2</sub>	$\pm 0.5$
UHC	$\pm 3.0$
NO <sub>x</sub>	$\pm 0.1$

Experimental uncertainties for BTE, BSFC, CO, CO<sub>2</sub>, UHC and NO<sub>x</sub> are indicated shown in Table 2.

### 3 Artificial Neural Networks

Neural network toolbox in MATLAB was used in this study for developing the ANN models. ANN model contains seven separate models like ANN1, ANN2, ANN3, ANN4, ANN5, ANN6, and ANN7 for the seven output parameters such as brake thermal efficiency (BTE), brake-specific fuel consumption (BSFC), unburnt hydrocarbons (UHC), carbon monoxide (CO), carbon dioxide (CO<sub>2</sub>), nitrogen oxides (NO<sub>x</sub>) and INDUS smoke number (Smoke), respectively. Input layer consists of three neurons (brake power, fuel blend, and compression ratio) and the output layer consists of corresponding output parameter for each ANN model.

The hidden layer consists of ten neurons, and the output layer consists of one neuron for each separate ANN models. In the present study, the experimental output results at various fuel blends, loads and compression ratios are used to develop ANN models. In the present analysis of ANN, the number of data points was considered as 48, and out of which 70%, 15% and 15% were taken for training, testing and validation, respectively. In ANN database, the values for training, validation and testing subsets were chosen randomly. The ANNs structure is shown in Fig. 2. Selection of number of hidden layers and number of neurons in the ANN model depends upon the experimental data set and difficulty of problem. The standard feed forward back propagation algorithm and target values from training set were used to train the ANN model. In the hidden layer, the activation function is taken as tangent sigmoid (tansig) while in the output layer, pure linear (purelin) function was chosen in the present ANN models. The error was calculated by using target values and ANN output values. The same error was minimized by adjusting the weights in the iteration process. Training the data will be stopped if the validation error surpasses the training error or after reaching the performance goal.

Lavenberg–Marquardt (Trainlm) is the training function, which is faster than the other training functions like trainrp, traingdx and trainscg. The trianlm transfer function will take less number of iterations during the convergence process. In the present

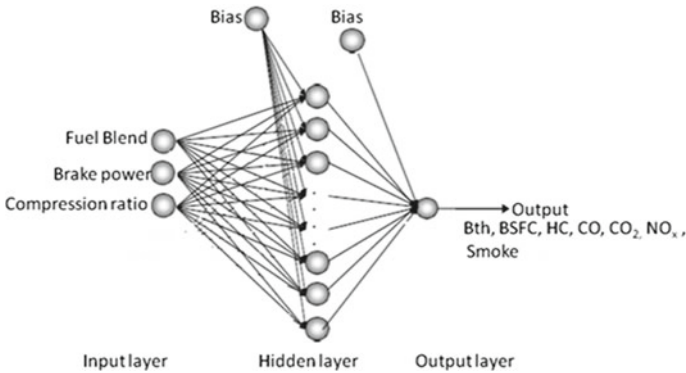


**Fig. 2** Architecture of ANN model

ANN model, the data training was done by using trainlm algorithm. ANN performance measurement and training the data using back propagation algorithm were developed with the neural network toolbox in MATLAB environment [8]. During the learning process of back propagation algorithm, the weights are varied, and these variations are stored as knowledge. One of the approximations of Newton's method is in fact basically LM method [9]. For obtaining the improved convergence, the LM algorithm is used for the second-order derivatives of the constant function. The errors are indicated in terms of root mean square error (RMSE) and absolute fraction of variance ( $R^2$ ).

## 4 Results and Discussion

Root mean square error (RMSE) and regression analysis were calculated for all the ANN models. Statistical values for all the output data are shown in Table 3.

Absolute fraction of variance ( $R^2$ ) values for BTE and BSFC are 0.990 and 0.974, respectively, which are near to unity represents the experimental results, and ANN predicted results have correlated well with each other. Root mean square error values for performance parameters such as BTE and BSFC are 0.441 and 0.031, respectively.

The  $R^2$  values for emission parameters such as UHC, CO, CO<sub>2</sub>, NO<sub>x</sub> and INDUS smoke number are 0.967, 0.968, 0.959, 0.990 and 0.942, respectively. Root mean square error values for emission parameters are 0.720, 0.002, 0.346, 29.477 and 0.015, respectively, which are within acceptable limits. Regression plots of performance and emission characteristics for experimental results and ANN predicted results are shown in Figs. 3a–g. It is observed that the variations between them are very small. Experimental values are predicted by using ANN tool with minimum error and more precision.

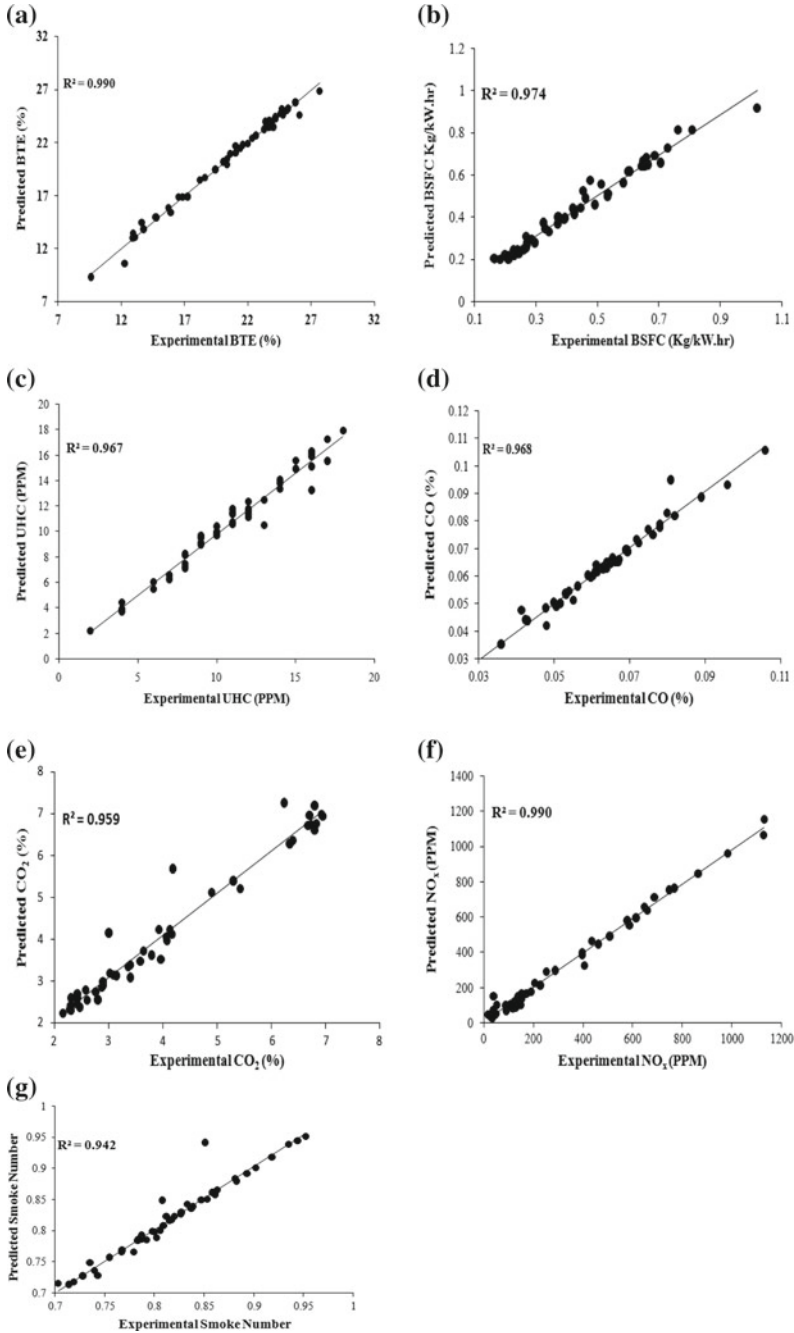


**Fig. 3** Relation between experimental and ANN predicted values for **a** BTE **b** BSFC **c** UHC **d** CO **e** CO<sub>2</sub> **f** NO<sub>x</sub> **g** Smoke

**Table 3**  $R^2$  and RMSE values for ANN models

ANN	Particulars	$R^2$	RMSE
ANN1	BTE	0.990	0.441
ANN2	BSFC	0.974	0.031
ANN3	UHC	0.967	0.720
ANN4	CO	0.968	0.002
ANN5	CO <sub>2</sub>	0.959	0.346
ANN6	NO <sub>x</sub>	0.990	29.477
ANN7	Smoke	0.942	0.015

## 5 Conclusion

In this study, experiments are conducted with diesel fuel and its mixtures with RME blends in various percentages without any modifications in the engine. The performance and emissions characteristics of RME blends are tested at different loads and three different compression ratios. It is concluded that experimental and ANN models predicted results are in good agreement with each other. The coefficient of determination of  $R^2$  values for output parameters is in the range of 0.942–0.990 which represents that the ANN models predicted results are very near to experimental results. For nonlinear problems like IC engine performance applications, artificial neural network tool is an efficient tool for prediction of performance parameters with less cost, shorter duration, reliability, high accuracy and precision.

## References

1. Rao KP, Babu TV, Anuradha G, Appa Rao BV (2017) IDI diesel engine performance and exhaust emission analysis using biodiesel with an artificial neural network (ANN). *Egypt J Petrol* 26:593–600
2. Canakci M, Erdil A, Arcaklioglu E (2006) Performance and exhaust emissions of a biodiesel engine. *Appl Energy* 83:594–605
3. Arcaklioglu E, Celikten IA (2005) Diesel engine's performance and exhaust emissions. *Appl Energy* 80:11–22
4. Celik V, Arcaklioglu E (2005) Performance maps of a diesel engine. *Appl Energy* 81:247–259
5. Golcu M, Sekmen Y, Erduranli P, Salman S (2005) Artificial neural network based modeling of variable valve-timing in a spark ignition engine. *Appl Energy* 81:187–197
6. Haykin S (1994) *Neural networks: a comprehensive foundation*. Mac-millan, New York
7. Chouai A, Laugier S, Richon D (2002) Modeling of thermodynamic properties using neural networks. *Appl Refrig Fluid Phase Equilib* 49:1–10
8. Shivakumar P, Srinivasa P, Shrinivasa Rao BR (2011) Artificial neural network based prediction of performance and emission characteristics of a variable compression ratio CI engine using WCO as a biodiesel at different injection timings. *Appl Energy* 88:2344–2354
9. Marquardt D (1963) An algorithm for least squares estimation of non-linear parameters. *J Soc Ind Appl Math*, pp 431–441

# The Analytical Study of Velocity Slip on Two-Phase Flow in an Eccentric Annular Region



B. Umadevi, P. A. Dinesh and C. V. Vinay

**Abstract** A mathematical model has been developed to study the synchronized effects of particle drag and slip parameter on velocity and rate of flow in an annular cross-sectional region bounded by two eccentric cylinders. In physiological flows, this phenomenon can be seen in blood flow in an eccentric catheterized artery in which the inner cylinder (Catheter) wall is impermeable and the outer cylinder (Artery) wall is permeable. Blood is a combination of plasma in fluid stage and suspended cells as well as proteins in particulate stage. Arterial wall gets damaged due to aging, and lipid molecules get deposited between damaged tissue cells. Blood flow increases toward the damaged tissues in the artery. In this investigation, blood is shown as a two-phase fluid as one is a fluid stage and the other is particulate stage. By using conformal mapping, the eccentric annulus will be transformed as concentric annulus to predict the velocity of the fluid phase and the rate of flow. Modeled governing equations will be solved analytically for the velocity and rate of flow. The examination is taken by changing the eccentricity parameter, slip parameter, and drag parameter. The increase of slip parameter indicates loss of fluid, and then, the velocity and rate of flow will be reduced. As particulate drag parameter increases, then the velocity and rate flow will be reduced. Eccentricity facilitates transfer of more fluid; then, the velocity and rate of flow also increases.

**Keywords** Catheter · Slip parameter · Drag parameter · Eccentricity

## 1 Introduction

Blood vessel narrowing/stenosis is related to noteworthy changes in blood stream, pressure distribution, and resistance to flow. This will cause the blood vessel wall to damage, and it increases the permeability of solvent at the walls. One of the medical

---

B. Umadevi (✉) · C. V. Vinay  
Department of Mathematics, JSS Academy of Technical Education, Bangalore 560060, India  
e-mail: [umadevi.gh@gmail.com](mailto:umadevi.gh@gmail.com)

P. A. Dinesh  
Department of Mathematics, M. S. Ramaiah Institute of Technology, Bangalore 560054, India

© Springer Nature Singapore Pte Ltd. 2020  
H. K. Voruganti et al. (eds.), *Advances in Applied Mechanical Engineering*,  
Lecture Notes in Mechanical Engineering,  
[https://doi.org/10.1007/978-981-15-1201-8\\_26](https://doi.org/10.1007/978-981-15-1201-8_26)

procedures to take care of atherosclerosis is balloon angioplasty that involves the inclusion of a catheter with a minor inflatable balloon toward the end. The insertion of catheter will further increase the frictional resistance to flow and will alter pressure distribution. The placing of catheter also creates an annular region. As the dynamics of flow between circular cylinders can be customized appreciable by dislocation of axis, it is essential to consider eccentric annular region bounded by two circular cylinders. With all the above-said reasons, flow of Newtonian fluid between eccentric cylinders with permeable wall involves conformal mapping of doubly connected region bounded by eccentric circles into concentric circles.

Daripa and Dash [1] have used Fourier series and numerical methods to study the pulsatile flow in eccentric catheterized arteries. Shivakumar and Ji [2] have calculated the transport of Newtonian fluid flowing in an annulus domain  $D$ , in the  $x - y$  plane surrounded by two eccentric circles. Indira et al. [3] have examined the effect of couple stress on the flow in a doubly connected region. The technique is to map the eccentric circles to concentric circles such that the boundary condition on the eccentric annulus is satisfied. In the current investigation, the effect of drag particulate on the flow of a Newtonian fluid is considered. A mathematical model has been framed to examine the synchronized effects of particulate drag and slip parameters on velocity besides the rate of flow in an eccentric catheterized artery. Blood is considered as a two-phase fluid in which liquid phase consists of plasma with a particulate phase of suspended red cells, white cells, platelets, and proteins. It is required to know the consequence of drag presented by these particles on the flow. In the present investigation, the impact of drag of particulate issue on the stream of a Newtonian liquid with the Beavers and Joseph limit slip condition is contemplated.

## 2 Mathematical Formulation

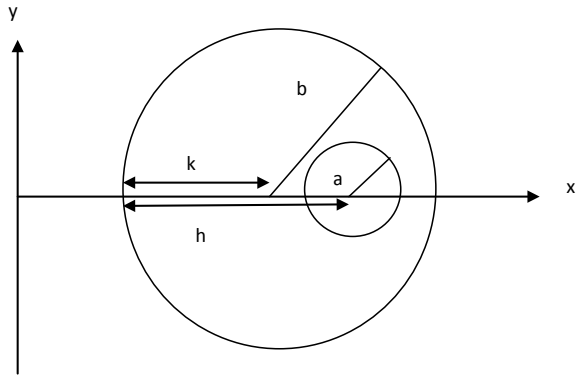
The particulate drag is similar to the resistance offered by dust on the fluid in a two-phase fluid. Saffman [4] has formulated the basic equations for the flow of dusty viscous fluid. The basic governing equations in vector notation for a dusty viscous fluid is given by

$$\left[ \frac{\partial \vec{q}}{\partial t} + (\vec{q} \cdot \nabla) \vec{q} \right] = -\nabla p + \mu \nabla^2 \vec{q} + NK(\vec{v} - \vec{q}) \quad (1)$$

$$Nm \frac{\partial \vec{v}}{\partial t} = NK(\vec{q} - \vec{v}) \quad (2)$$

where  $\vec{q}$ ,  $\vec{v}$  are velocities of fluid phase and particle phase, respectively,  $\rho$  is the density of the fluid,  $\mu$  is the viscosity of the fluid, and  $N$  is the number of density

Fig. 1 Substantial model



of particles.  $K(= 3\mu\pi d)$  is the Stokes resistance coefficient.  $p$  is the pressure,  $m$  is the mass of the particles,  $d$  is diameter of the dusty spherical particle, and  $t$  is the time. Two-phase flow of a Newtonian fluid with particulate matter flowing in an eccentric annulus domain  $D$ , in the  $x - y$  plane bounded internally by  $C_1$  and externally by  $C_2$ , is considered specified in a schematic diagram shown in Fig. 1. The initial flow velocity is assumed as  $(0, 0, w(x, y))$ . The basic governing equations for the specified physical assumptions from Eqs. (1) and (2) are given by

$$\rho \frac{\partial w}{\partial t} = -\frac{\partial p}{\partial z} + \mu \left( \frac{\partial^2 w}{\partial x^2} + \frac{\partial^2 w}{\partial y^2} \right) + KN(v - w) \tag{3}$$

$$Nm \frac{\partial v}{\partial t} = KN(w - v) \tag{4}$$

$$\frac{\partial p}{\partial x} = \frac{\partial p}{\partial y} = 0 \tag{5}$$

where  $w$  is the fluid velocity and  $v$  is the suspended particles velocity.

To solve the above governing equations, we consider the following assumptions for pressure, velocity of fluid, and dusty particles in the form of

$$\frac{\partial p}{\partial z} = -P e^{-nt}, w = W e^{-nt}, v = V e^{-nt}.$$

Implementing the above expressions in the Eqs. (3) and (4) and expressing in terms of complex variables with  $z = x + iy, \bar{z} = x - iy$  by means of variable separable method. The pressure gradient is assumed as constant; then, the set of equations reduces to

$$\frac{\partial^2 W}{\partial z \partial \bar{z}} + \omega^2 W = -\frac{P}{4\mu} \tag{6}$$

$$V = \frac{1}{1 - n\tau} W, \tau = \frac{m}{K} \tag{7}$$

where  $\tau$  is the relaxation time,  $\omega$  is the drag parameter,  $W$  is the velocity of the fluid in non-dimensional form in the direction of the axis of the annulus whose cross section  $D$  is bounded by the annulus region,  $V$  is velocity of particles in non-dimensional form, and  $Q$  be the rate of flow.

We consider the homogeneous boundary value problem for the velocity of the fluid as

$$W = f(z\bar{z}) + g(z \pm \bar{z}) \tag{8}$$

Make use of the series solution in terms of Bessel functions of first and second kinds in the closed-form solution of Eq. (6), then the velocity of the fluid phase is agreed as

$$W = -\frac{P}{4\omega^2} \left[ AJ_0(\omega\sqrt{z\bar{z}}) + BY_0(\omega\sqrt{z\bar{z}}) + Ce^{z+\bar{z}} + De^{z-\bar{z}} + 1 \right] \tag{9}$$

### 3 Eccentric Annulus

By using conformal transformation given by

$$z = \frac{c}{1 - \zeta} \tag{10}$$

where  $z = x + iy$  and  $\zeta = \xi + i\eta$ , the annulus region enclosed by two eccentric circles is transformed as the annulus region bounded by two concentric circles with radii  $|\zeta| = \rho_1$ , and  $\rho_2$ , where

$$C_1 : (x - h)^2 + y^2 = a^2, C_2 : (x - k)^2 + y^2 = b^2, a < b, h > k$$

$\rho_1 = \frac{a}{h}, \rho_2 = \frac{b}{k}$  and  $c = h - \frac{a^2}{h} = k - \frac{b^2}{k}$ ,  $h$  and  $k$  should satisfy the condition  $k - h = \frac{a^2}{h} - \frac{b^2}{k}$ ,

where  $a$  is the catheter radius,  $b$  is the artery radius, and  $\varepsilon$  is the eccentric parameter.

The conditions for the boundary value problem as homogeneous no-slip velocity on  $C_1$  and non-homogeneous BJ-slip condition on  $C_2$ .

$$\text{i.e. } W = 0 \text{ on } C_1 \text{ and } \frac{\partial W}{\partial n} = \eta W \text{ on } C_2 \tag{11}$$

Using the conformal mapping given by Eq. (10), the above boundary conditions become



$$W = 0 \text{ at } \rho = \rho_1 \text{ and } \frac{\partial W}{\partial \rho} = \eta W \text{ at } \rho = \rho_2 \tag{12}$$

Transforming the expression of the velocity of the fluid phase given in Eq. (9) with conformal transformation specified in Eq. (10) and implementing the boundary conditions given in Eq. (12), the velocity of the fluid phase is obtained as

$$W = -\frac{P}{4\omega^2} \left[ A\chi_1(\zeta\bar{\zeta}) + B\chi_2(\zeta\bar{\zeta}) + C\chi_3(\zeta\bar{\zeta}) + D\chi_4(\zeta\bar{\zeta}) + 1 \right] \tag{13}$$

$\chi_1(\zeta\bar{\zeta}), \chi_2(\zeta\bar{\zeta}), \chi_3(\zeta\bar{\zeta}), \chi_4(\zeta\bar{\zeta})$  are specified in the Appendix.

### 4 Rate of Flow

By means of Green’s theorem in Complex form

$$\iint \frac{\partial F}{\partial \bar{z}} dS = \frac{1}{2i} \int_{C_2-C_1} F dz \tag{14}$$

rate of flow is obtained as

$$Q = \iint_{\Omega} W dS$$

$$\text{i.e. } Q = \frac{1}{2i} \frac{P}{4\mu\omega^2} \int \left[ \begin{aligned} &A \frac{2}{\omega} \sqrt{\frac{\bar{z}}{z}} J_1(\omega\sqrt{z\bar{z}}) \\ &+ B \frac{2}{\omega} \sqrt{\frac{\bar{z}}{z}} Y_1(\omega\sqrt{z\bar{z}}) \\ &+ C e^{z+\bar{z}} - D e^{-(z+\bar{z})} - \bar{z} \end{aligned} \right] \tag{15}$$

Using the conformal transformation specified in Eq. (10) on Eq. (15) and computing the integration as well as simplifying, then the rate of flow is agreed as

$$Q = \frac{P\pi c^2}{4\mu\omega^2} [A\Gamma_1 + B\Gamma_2 + C\Gamma_3 + D\Gamma_4 - \Gamma_5] \tag{16}$$

$\Gamma_1, \Gamma_2, \Gamma_3, \Gamma_4, \Gamma_5$  given in the Appendix.

### 5 Results

The investigation reveals that the effect of drag particulate in the eccentric annulus circular region. By using conformal transformation, the eccentric annulus region is transformed into concentric annulus with the assumptions. The results have been obtained by solving analytically and computationally by using Mathematica software. The velocity and rate flow are ruled by three parameters—drag parameter, eccentricity parameter, and slip parameter. The velocity of fluid phase is specified by Eq. (13) that is computed and graphically depicted as shown in Fig. 2a and b for different values of drag parameter  $\omega$ , eccentricity parameter  $\epsilon$ , and slip parameter  $\eta$ .

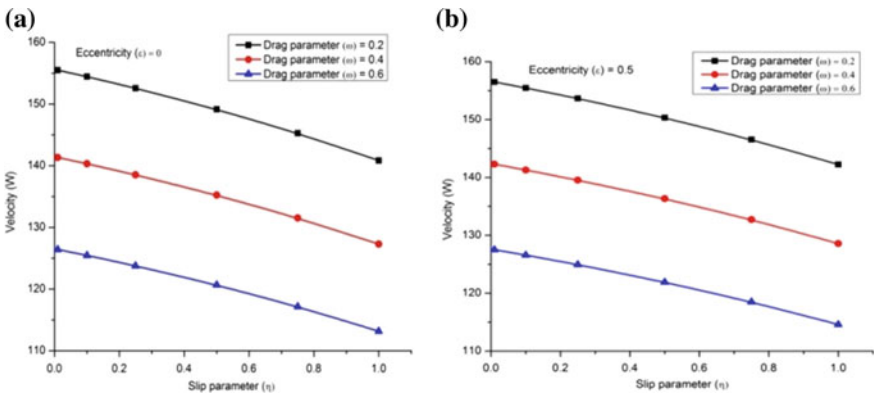


Fig. 2 a, b Velocity profile versus slip parameter for various values of drag parameter, eccentricity parameter  $\epsilon = 0$  and  $\epsilon = 0.5$

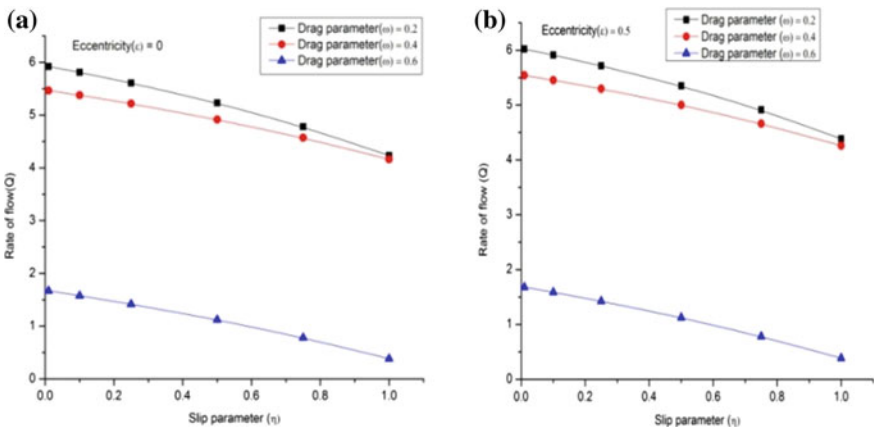


Fig. 3 a, b Rate of flow versus slip parameter for various values of drag parameter, eccentricity parameter  $\epsilon = 0$  and  $\epsilon = 0.5$

**Table 1** Rate of flow  $Q$  for eccentricity, slip, and drag parameters

$\eta$ Slip parameter	Eccentricity ( $\epsilon$ )	Drag parameter ( $\delta$ )	Rate of flow ( $Q$ )
0.01	0	0.2	5.92072
0.5	0	0.2	5.2317
1	0	0.2	4.23465
0.01	0	0.6	1.66859
0.5	0	0.6	1.12225
1	0	0.6	0.384941
0.01	0.3	0.2	5.99123
0.5	0.3	0.2	5.31582
1	0.3	0.2	4.34065
0.01	0.3	0.6	1.67638
0.5	0.3	0.6	1.1252
1	0.3	0.6	0.385691
0.01	0.5	0.2	6.01916
0.5	0.5	0.2	5.34915
1	0.5	0.2	4.38263
0.01	0.5	0.6	1.67941
0.5	0.5	0.6	1.12636

The rate of flow is given by Eq. (16) that is computed and graphically depicted in Fig. 3a and b for different values of drag parameter, cross-sectional area, eccentricity parameter, and slip parameter. Also, the rate of flow for different values of drag parameter, eccentricity parameter, and slip parameter is tabulated in Table 1.

## 6 Discussions

The present investigation makes clear that as drag particulate matter is present, then it influences the flow. The composition of blood varies individually from person to person. If it is more of LDL (low-density lipoproteins), red cells, etc., than requirement, it causes relentless problem for blood circulation and for oxygen supply. Gradually, it leads to blockages in the arteries and also heart problems. To treat this, in many clinical procedures, the insertion of catheter is necessary. The increase in eccentricity results in the increase of cross-sectional area, thereby facilitating flow of more fluid, resulting in increase of velocity. The velocity will be decreased as the drag parameter and slip parameter increased. Enhancement of slip parameter signifies loss of fluid,

thereby declining of velocity and rate of flow. Rate of flow increases with enhancement in eccentricity and decreases with the extension of drag parameter and slip parameters.

### 7 Conclusions

The eccentricity of annulus facilitates transport of more fluid than concentric annulus. As eccentricity parameter  $\varepsilon \rightarrow 0$  gives the results for concentric cylinders. As drag parameter increases, the velocity and rate of flow will be reduced. The present study gives insight into the variations of pressure gradients in pressure of catheter and also the effects of loss of fluid due to permeability of the wall.

**Acknowledgements** The support and encouragement from the managements of JSS Academy of Technical Education, Bangalore, and M. S. Ramaiah Institute of Technology, Bangalore, acknowledged by the authors.

### Appendix

$$\rho_1 = \frac{a}{h}, \rho_2 = \frac{b}{k}, c = h - \frac{a^2}{h},$$

$$\psi(k + 1) = -0.577215666 + \sum_{m=2}^k \frac{1}{m-1}, \alpha_k = \frac{(-1)^k \left(\frac{\omega}{2}\right)^{2k} c^{2k}}{(k!)^2} \gamma_k = \frac{c^{n+2k}}{k!n + k!}$$

$$s_k = \psi(k + 1) - \log\left(\frac{\omega c}{2}\right),$$

$$\beta(k - 1, p) = \frac{(k-1+p)!}{(k-1)!p!}, \beta(n, k - 1, p) = \frac{(n+k-1+p)!}{(n+k-1)!p!},$$

$$\beta_1(k - 1, p, m) = \beta(k - 1, p)\beta(k - 1, m),$$

$$\beta_2(n, k - 1, p) = \beta(n, k - 1, p)\beta(k - 1, p),$$

$$\beta_3(n, k - 1, p, m) = \beta(n, k - 1, p)\beta(k - 1, m) + \beta(n, k - 1, m)\beta(k - 1, p),$$

$$\chi_1(\zeta\bar{\zeta}) = \sum_{k=0}^{\infty} \alpha_k \left(1 + \sum_{m=0}^{\infty} \sum_{p=0}^{\infty} \beta_1(k - 1, p, m)\rho^{2p} \left[\zeta^m + \frac{\rho^{2m}}{\zeta^m}\right]\right);$$

$$\chi_2(\zeta\bar{\zeta}) = \sum_{k=0}^{\infty} \alpha_k \left(1 + \sum_{m=0}^{\infty} \sum_{p=0}^{\infty} \beta_1(k - 1, p, m)\rho^{2p} \left[\zeta^m + \frac{\rho^{2m}}{\zeta^m}\right]\right) \left(s_k + \frac{1}{2} \sum_{n=1}^{\infty} \frac{1}{n} \left[\zeta^n + \frac{\rho^{2n}}{\zeta^n}\right]\right);$$

$$\chi_3(\zeta\bar{\zeta}) = \sum_{k=0}^{\infty} \sum_{n=0}^{\infty} \gamma_k \left(2 \sum_{p=0}^{\infty} \beta_2(n, k - 1, p)\rho^{2p} + \sum_{p=0}^{\infty} \sum_{m=0}^{\infty} \beta_3(n, k - 1, m, p)\rho^{2p} \left[\zeta^m + \frac{\rho^{2m}}{\zeta^m}\right]\right);$$

$$\chi_4(\zeta\bar{\zeta}) = \sum_{k=0}^{\infty} \sum_{n=0}^{\infty} (-1)^n \gamma_k \left(2 \sum_{p=0}^{\infty} \beta_2(n, k - 1, p)\rho^{2p} + \sum_{p=0}^{\infty} \sum_{m=0}^{\infty} \beta_3(n, k - 1, m, p)\rho^{2p} \left[\zeta^m + \frac{\rho^{2m}}{\zeta^m}\right]\right);$$

$$\begin{aligned} \Gamma_1 &= \sum_{k,p,m=0}^{\infty} \phi(k) \left[ \left( 1 + 2\beta_1(k-1, p, 0) (\rho_2^{2p} - \rho_1^{2p}) g_0 \right) + \beta_1(k-1, p, m) g_{pm} \right]; \\ \Gamma_2 &= \prod_{k,p,m=0}^{\infty} \phi(k) \left[ \left( 1 + 2\beta_1(k-1, p, 0) (\rho_2^{2p} - \rho_1^{2p}) \left\{ \left( T_k - \frac{4}{c\omega^2} \right) g_0 + \frac{4}{c\omega^2} h_0 + g_2 \right\} \right) \right. \\ &\quad \left. + \beta_1(k-1, p, m) (\rho_2^{2p} - \rho_1^{2p}) (m+1) \left\{ \left( T_k - \frac{4}{c\omega^2} \right) g_1 + \frac{4}{c\omega^2} h_1 + \frac{1}{m} h_2 \right\} \right]; \\ \Gamma_3 &= \sum_{n,k,p,m=0}^{\infty} m \frac{c^{n+2k+1}}{k!n+k!} \beta_3(n, k-1, p, m) (\rho_2^{2p+2m} - \rho_1^{2p+2m}); \\ \Gamma_4 &= \sum_{n,k,p,m=0}^{\infty} (-1)^{n+1} m \frac{c^{n+2k+1}}{k!n+k!} \beta_3(n, k-1, p, m) (\rho_2^{2p+2m} - \rho_1^{2p+2m}); \\ \Gamma_5 &= c^2 p^2 \left( \frac{1}{(1-\rho_2^2)^2} - \frac{1}{(1-\rho_1^2)^2} \right); \\ \phi(k) &= \sum_{k=0}^{\infty} \frac{(-1)^k c^{2k+2} \left(\frac{\omega}{2}\right)^{2k}}{k!k+1!}; \\ T_k &= \log\left(\frac{\omega c}{2}\right) - \frac{1}{2}(\psi(k+1) + \psi(k+2)); \\ g_0 &= \left( \frac{\rho_2^2}{(1-\rho_2^2)^2} - \frac{\rho_1^2}{(1-\rho_1^2)^2} \right); g_1 = \left( \frac{\rho_2^2}{(1-\rho_2^2)^3} - \frac{\rho_1^2}{(1-\rho_1^2)^3} \right); \\ g_2 &= \left( \frac{\rho_2^2}{(1-\rho_2^2)^4} - \frac{\rho_1^2}{(1-\rho_1^2)^4} \right); g_{pm} = \left( \frac{\rho_2^{2p+2m}}{(1-\rho_2^2)^3} - \frac{\rho_1^{2p+2m}}{(1-\rho_1^2)^3} \right); \\ h_0 &= \left( \frac{\rho_2^4}{(1-\rho_2^2)^2} - \frac{\rho_1^4}{(1-\rho_1^2)^2} \right); h_1 = \left( \frac{\rho_2^4}{(1-\rho_2^2)^3} - \frac{\rho_1^4}{(1-\rho_1^2)^3} \right); \\ h_2 &= \left( \frac{\rho_2^4}{(1-\rho_2^2)^4} - \frac{\rho_1^4}{(1-\rho_1^2)^4} \right); \end{aligned}$$

## References

1. Daripa Dash A (2002) Numerical study of pulsatile blood flow in an eccentric catheterized artery using fast algorithm. *J Eng Math* 42:1-2
2. Shivakumar PN, Ji (1993) On the Poisson's equation for doubly connected regions. *Canadian Appl Math*
3. Indira R, Venkatachalappa M, Siddeshwar PG (2008) Flow of couple-stress fluid Between two eccentric cylinders. *Int J Math Sci Eng App (IJMSEA)* No IV, pp 253-261
4. Saffman PG (1962) On the stability of laminar flow of dusty gas. *J Fluid Mech* 13:120

# Numerical Study on the Effect of Impeller Geometry on Pump Performance



Arshdeep Singh, Siga Satya Sekhar, S. Jayavel and Sudhir Varadarajan

**Abstract** Blade thickness and blade height are the most influencing parameters on the performance of pump. The fluid flow passage can be optimised by the blade thickness. Energy consumption by pump is reduced by employing appropriate blade height. The objective of the present study is to optimise the blade geometry, viz. thickness and height. The duty parameters considered in the present study are flow rate ( $Q$ ) 5000 LPH, Head ( $H$ ) 28–26 m and speed 6000 rpm. Numerical simulations are carried out to study the pump performance. Three-dimensional, steady-state flow equations are solved in ANSYS CFX along with Reynolds-averaged Navier–Stokes (RANS) equations with standard shear stress transport (SST) turbulence models. The results showed that energy consumption decreases with blade height.

**Keywords** Submersible pump · Blade thickness · Blade height · CFD

## Nomenclature

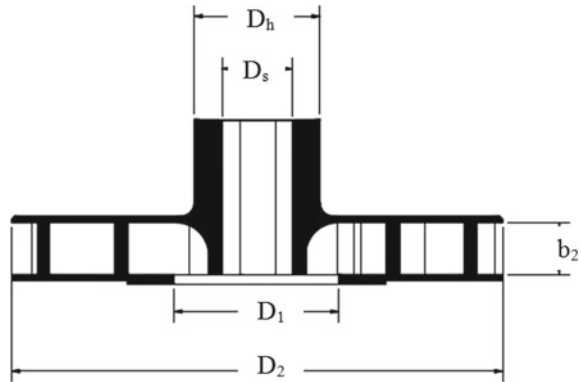
$b$	Blade height
$D_1$	Outer diameter
$D_2$	Eye diameter
$D_s$	Shaft diameter
$H$	Head
$Q$	Flow rate
$Q_d$	Design Flow rate
RPM	Revolution per minute
$t$	Blade thickness
$\beta_1$	Blade inlet angle
$\beta_2$	Blade outlet angle

---

A. Singh (✉) · S. S. Sekhar · S. Jayavel · S. Varadarajan  
Mechanical Department, Indian Institute of Information Technology, Design and Manufacturing,  
Kancheepuram, Chennai, Tamilnadu 600127, India  
e-mail: [mds17m003@iiitdm.ac.in](mailto:mds17m003@iiitdm.ac.in)

© Springer Nature Singapore Pte Ltd. 2020  
H. K. Voruganti et al. (eds.), *Advances in Applied Mechanical Engineering*,  
Lecture Notes in Mechanical Engineering,  
[https://doi.org/10.1007/978-981-15-1201-8\\_27](https://doi.org/10.1007/978-981-15-1201-8_27)

**Fig. 1** Sectional view of a closed radial impeller with geometric parameters



## 1 Introduction

To achieve the best performance and the efficiency, list out the main geometric parameter like the impeller outlet diameter ( $D_2$ ), impeller blade height, impeller blade outlet angle ( $\beta_2$ ) and impeller blade thickness ( $e$ ) as shown in Fig. 2. The minimum and uniform thickness required to achieve good casting qualities must be observed in casting of impellers; it depends on the casting process and is 3–5 mm [1]. High head and small flow rate are the characteristics of the low specific speed centrifugal pump. The speed is completely concerned with inlet diameter ( $D_1$ ) and outlet diameter ( $D_2$ ) of the pump impeller as shown in Fig. 1. Pump inlet diameter is related to the flow, and outlet diameter is related to the head. Generally,  $D_2/D_1$  value is larger. Due to which impeller flow channel diffusion is larger and at internal flow passage flow separation occurs, which decreases the efficiency of low specific speed centrifugal pump. So by controlling the blade thickness and blade height,  $D_2/D_1$  ratio can be reduced [2]. The paper analyses the influence of the inlet and outlet angles on the geometry of the impeller of centrifugal pump and the hydraulic efficiency, and it gives the data that outlet blade angle is in between the range of ( $15^\circ$ – $45^\circ$ ) and inlet blade angle is in between ( $15^\circ$ – $30^\circ$ ) [3]. The passage volume is volume between two blades. If the passage volume increases than input shaft power also increase. To reduce the input shaft power, passage volume has to be reduce and it will be done by controlling the blade height [2].

## 2 CAD Model

Different impeller designs are modelled by using bladegen of the vista CPD for blade thickness and Autodesk Inventor for blade height.

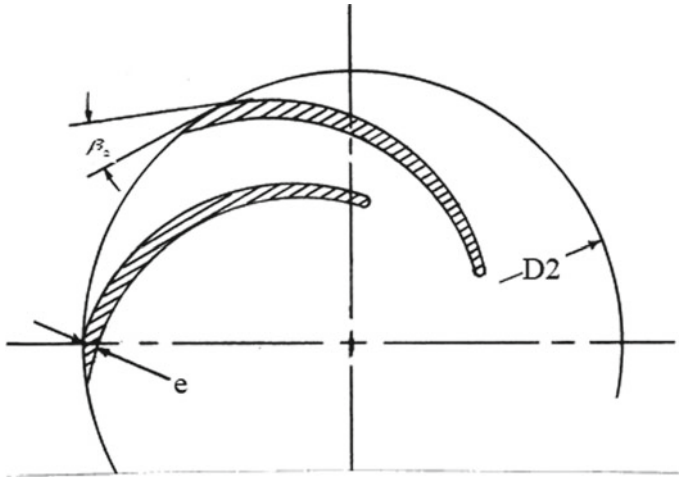


**Fig. 2** Blade thickness and blade outlet angle

### 2.1 Blade Thickness

Four different impeller designs with blade height 8mm and with different varying blade thickness form leading edge to trailing edge. Four different blade Thickness are: (2,2,2,2), (2,2,2,2.5), (2,2,2,3), and (2,2,2.5,2.5). According to the law of thickening of blade, i.e. increasing blade thickness from the middle to outlet of the blade can achieve the effect of build up the channel. Inlet and outlet area ratio is not too small and reduces the flow separation [4], Fig. 3.

### 2.2 Blade Height

Blade height controls the passage volume if the passage volume is more than the input power is also more. Impellers with different blade heights reduce input shaft power and increase efficiency [2]. The four different impellers have same blade thickness value (2, 2, 2, 3), and blade thickness value is optimum one (Fig. 4).

## 3 Meshing

The fluid domain of the impeller was divided into the sub-domains or into discrete elements of the same element size, i.e. 0.90 mm. Mainly, tetrahedron mesh type is used for mesh the fluid domain and for complex shapes (Fig. 5; Table 1).



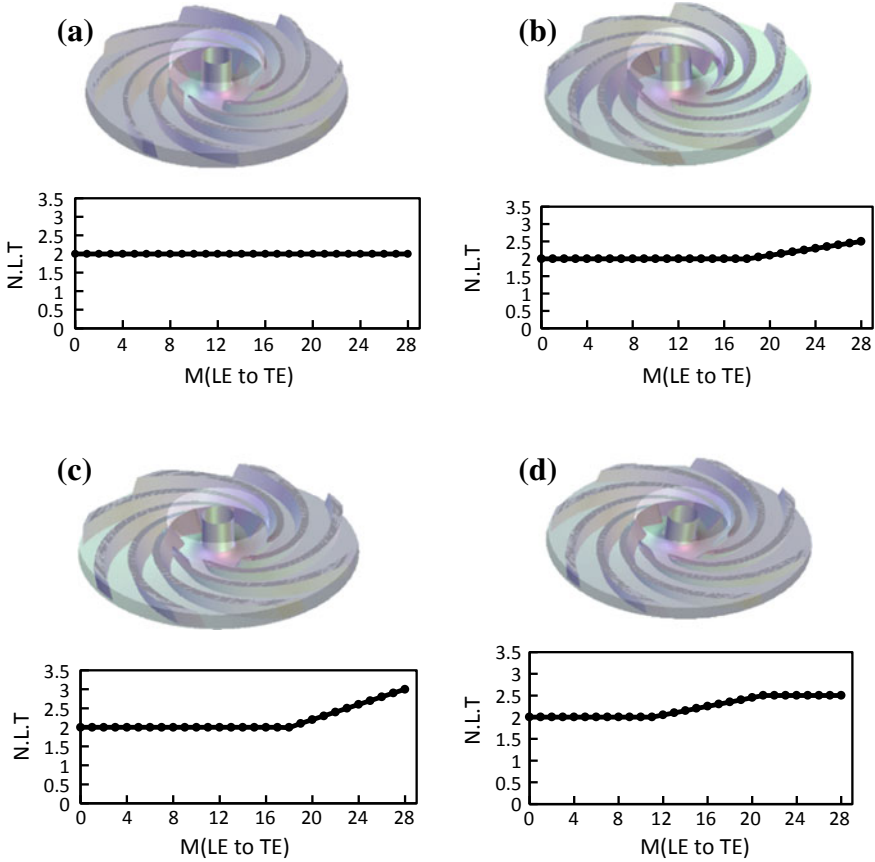


**Fig. 3** Design of different impellers with blade height 8 mm and different blade thicknesses. **a** Blade thickness (2, 2, 2, 2). **b** Blade thickness (2, 2, 2, 2.5). **c** Blade thickness (2, 2, 2, 3). **d** Blade thickness (2, 2, 2.5, 2.5). Modelled in bladegen Vista CPD

### 3.1 Grid Independence

The grid independence study gives optimum mesh size for the computation. Variation of the output results with varying mesh element size is shown in Fig. 7. Impeller used for gird independence has blade height 8 mm and blade thickness (2, 2, 2, 3) (Fig. 6).

## 4 Numerical Simulation

Computations are performed using ANSYS software with appropriate boundary conditions. Present computational results are validated using the results from Jin [2]. The

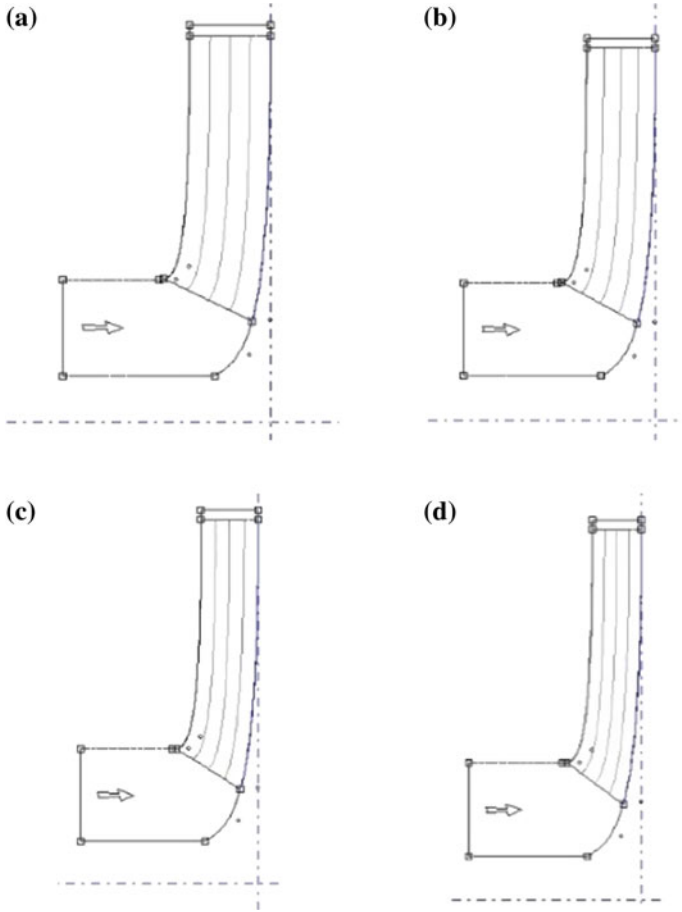


**Fig. 4** Impeller meridional with different blade heights. **a** Blade height 8 mm, **b** Blade height 7 mm, **c** Blade height 6 mm, **d** Blade height 5 mm

present results are found to satisfactorily match with the results of Jin [2]. The results are shown in Fig. 7.

All the calculations have been performed with CFX solver software package of ANSYS Workbench 15.0 that utilises the finite volume method for the three-dimensional (3D) steady-state Reynolds-averaged Navier–Stokes (RANS), Shear stress transport (SST) turbulence models and employing frozen-rotor technique.

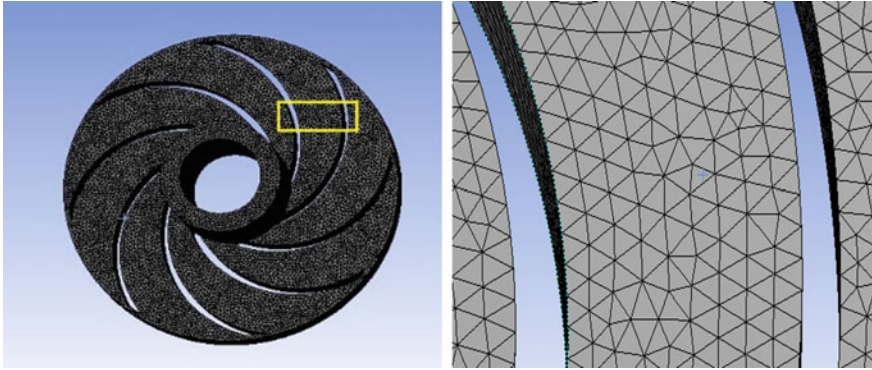
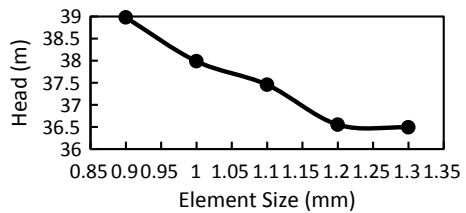


Fig. 5 Tetrahedron meshing of impeller fluid domain

Table 1 Meshing detail

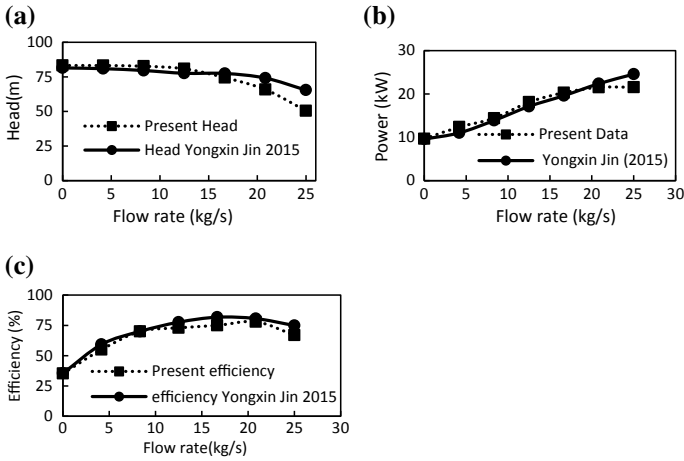
Element size	No. of nodes	No. of elements	Head	Deviation (%)
0.9	651,296	449,180	38.9793	–
1	460,852	314,310	37.9877	2.543
1.1	349,018	235,520	37.4568	1.397
1.2	272,388	182,419	36.5531	2.41
1.3	217,357	144,112	36.492	0.00167

Fig. 6 Effect of mesh element size on the output result (head)



### 4.1 Boundary Condition

For the simulation, the static pressure at inlet is zero (in Pa) and mass flow rate at the outlet (in kg/s) is according to flow rate condition used as the boundary condition. And simulate on the design RPM, i.e. 6000 RPM.



**Fig. 7** Comparison of the present simulated data and the data from “Yongxin jin 2015”. **a** Effect of flow rate on the head. **b** Effect of flow rate on the input shaft power. **c** Effect of flow rate on the efficiency

## 5 Results and Discussion

Computations are performed using ANSYS software with appropriate boundary conditions.

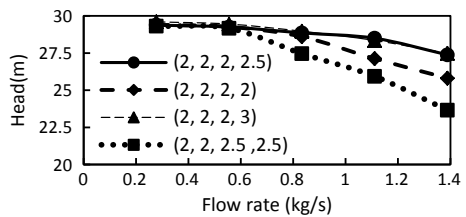
### 5.1 Results of Blade Thickness

For blade thickness simulation the complete single stage of submersible pump was simulated, i.e. impeller, casing and return guide vane. Results are shown in Fig. 8.

Head for impeller having blade thickness (2, 2, 2, 2) and (2, 2, 2.5, 2.5) is less than other two impellers with blade thickness (2, 2, 2, 2.5) and (2, 2, 2, 3) shown in Fig. 8. Head for blade thickness (2, 2, 2, 2.5) and (2, 2, 2, 3) has same head approximately.

Flow in impeller passage is shown in Fig. 9. Four channel flows are compared here to find which is more efficient. When operated under off-design condition,

**Fig. 8** Head for different blade thickness values w.r.t flow rate condition



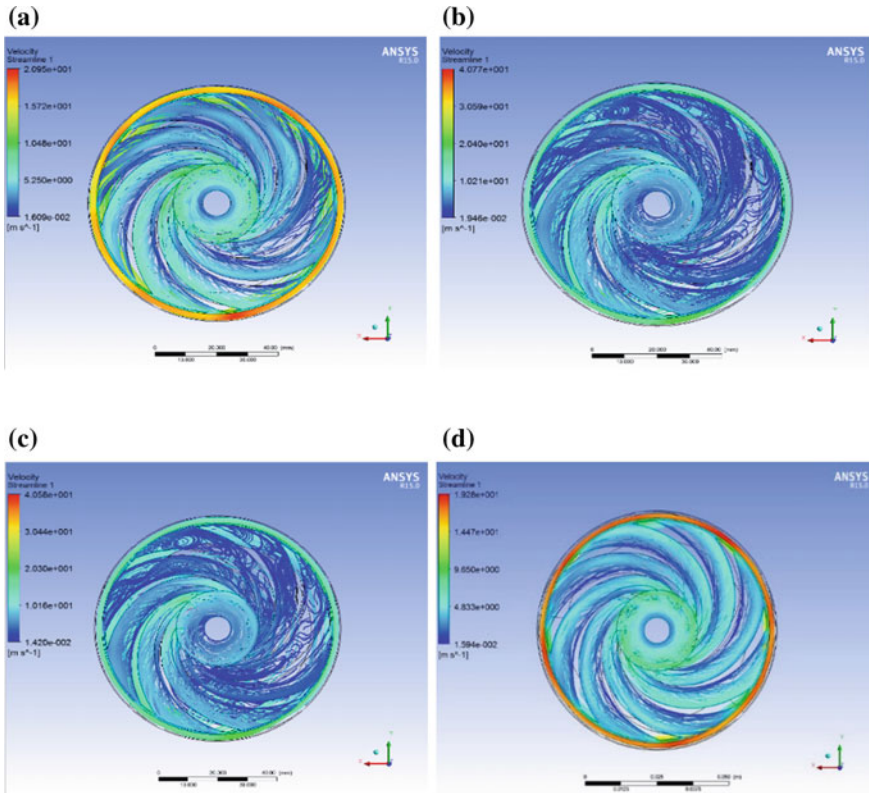


**Fig. 9** Streamline contour of four different blade thicknesses. **a** Blade thickness (2, 2, 2, 2.5). **b** Blade thickness (2, 2, 2, 2). **c** Blade thickness (2, 2, 2.5, 2.5). **d** Blade thickness (2, 2, 2, 3)

flow separation and flow recirculation affect the performance. Flow separation is mostly observed near to the leading edge due to non-tangential inflow. If excessive deceleration of the flow occurs (pressure increase) or if there is a sudden change in the direction of the profile of blade, the flow outside the boundary layer will no longer follow the direction of the wall, but it will separate or leave the surface of the blade. Flow separation leads to flow losses. Suction recirculation can be seen in centrifugal pump at low flow.

### 5.2 Results of Blade Heights

The aim of reducing the blade height is to reduce the energy consumption or input shaft power, but as blade height decreases, head also decreases but the head should be in the range of 39–35 m at impeller. The results are shown in Fig. 10.

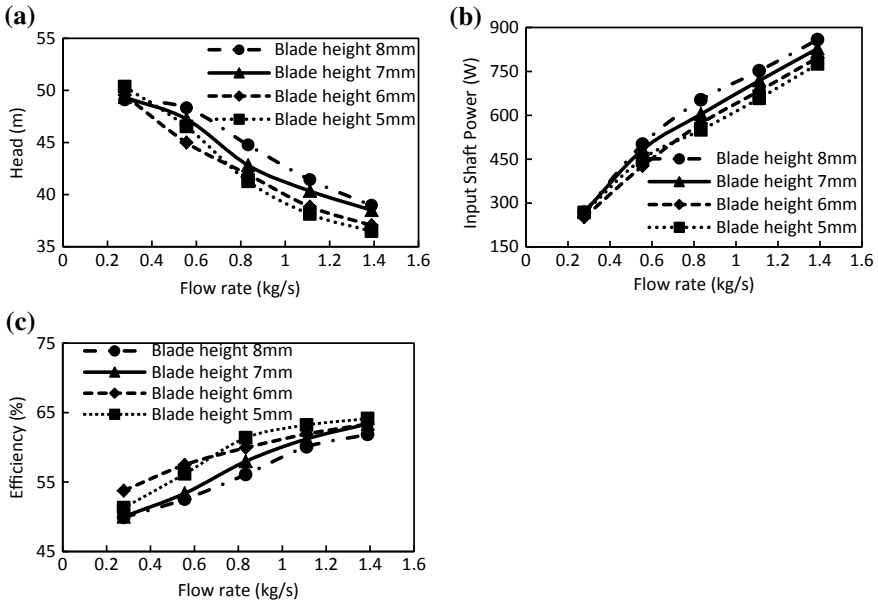


**Fig. 10** Comparison of head, input shaft power and efficiency of the impellers with different blade heights. **a** Effect of flow rate on the head corresponds to different blade heights. **b** Effect of flow rate on the input shaft power corresponds to different blade heights. **c** Effect of flow rate on the efficiency corresponds to different blade heights

Head for impeller with blade height 8 mm is 38.9593 m, but input shaft power and efficiency are 858.4 W and 61.8382%, respectively. But the head for impeller with blade height 5 mm is 36.481 m which is in the range of 39–35 m, and input shaft power and efficiency are 775.1 W and 64.127%, respectively. Impeller with 5 mm blade height consumes less energy and having more efficiency than 8 mm impeller.

## 6 Conclusion

Numerical study has been carried out by varying the impeller parameters such as blade passage width, blade thickness, blade height and flow rate of modified design of the impeller. Conclusions from the present numerical study are as follows: the blade thickness of the impeller should be (2, 2, 2, 3) because it gives more head and has negligible flow separation and flow recirculation. Shaft input power decreases with blade height. Efficiency increases with decreasing blade height. Four different design impellers are studied. Among these impellers, the impeller with 5 mm blade height and blade thickness (2, 2, 2, 3) is more efficient.

## References

1. Gulich JF (2010) Centrifugal pumps, 2nd edn. Springer, Villeneuve, Switzerland
2. Jin Yongxin, Song Wenwu, Jie Fu (2015) A study on the effects of blade thickness on the performance of low specific speed centrifugal pump. *Adv Mater Res* 1070–1072:1957–1962
3. Budea S (2016) Optimization of the impeller geometry and its coating with PTFE to improve the hydraulic performances. *Revista de Chimie–Bucharest* 67(7)
4. Ji P, Yuan S, Li X, Yuan J (2014) Numerical prediction of 3-D periodic flow unsteadiness in a centrifugal pump under part load condition. *J Hydrodyn* 26(2):257–263
5. Muttli RS, Agrawal S, Warudkar H (2014) CFD simulation of centrifugal pump using ANSYS-CFX. *Int J Innov Res Sci Eng Technol* 3(8):15553
6. Zhang Qing (2014) Analysis of effects of impeller inlet width on the performance of centrifugal pump. *J Chem Pharm Res* 6(5):2078–2081
7. Srinivasan KM (2008) Rotodynamic pumps (centrifugal and axial). Newage international (p) limited

# Numerical Study of Hydrogen-Fueled Scramjet Performance with Passive Techniques



Obula Reddy Kummitha, K. M. Pandey and Rajat Gupta

**Abstract** Mixing and combustion efficiencies are two important parameters to visualize the performance of scramjet. The rate of combustion strongly depends on the rate of mixing of fuel and air; hence, the mixing efficiency of fuel and supersonic airstream is the major parameter to optimize the performance of scramjet combustor. In this research paper, the numerical investigation has been carried out to enhance the mixing efficiency of fuel and supersonic air by using passive techniques. The passive techniques are implemented to DLR scramjet by creating the wall attached fuel injectors at various locations and developed different computational geometries. Computational fluid dynamics tool ANSYS Fluent 15.0 has been used to solve the fluid flow governing equations and reaction mechanism of fuel and air along with finite rate/eddy dissipation reaction model. Shear stress transport  $k-\omega$  turbulence model is used for turbulence modeling. Validation of results has been performed with the DLR experimental results available in the open literature and identified a good matching of numerical and experimental results. From the analysis and comparison of numerical results for different passive techniques, it has been noticed that more recirculation regions, oblique and expansion shock waves are developed with the wall attached fuel injectors along with strut injector. These are very much helpful to penetrate into fuel stream and increasing the fuel carrying capacity, which can increase the mixing of fuel and supersonic air.

**Keywords** Scramjet · Strut · Mixing efficiency · Combustion efficiency

---

O. R. Kummitha (✉)  
BVRIT, Narsapur, Telangana 502313, India  
e-mail: [obulareddy.bec10@gmail.com](mailto:obulareddy.bec10@gmail.com)

K. M. Pandey · R. Gupta  
NIT Silchar, Silchar, Assam 788010, India

© Springer Nature Singapore Pte Ltd. 2020  
H. K. Voruganti et al. (eds.), *Advances in Applied Mechanical Engineering*,  
Lecture Notes in Mechanical Engineering,  
[https://doi.org/10.1007/978-981-15-1201-8\\_28](https://doi.org/10.1007/978-981-15-1201-8_28)



## 1 Introduction

Scramjet technology is the most interesting and latest research topic in aerospace technology. A scramjet is the advanced version of ramjet engine with supersonic combustion. The working of scramjet and its performance is strongly influenced by the individual performance of its components. Basically, the scramjet engine consists of three components which are defined as the inlet section, combustor, and diffusion section. All three components play a major role in the overall performance of the scramjet engine. Worldwide a great research is ongoing in scramjet technology by evaluating the performance of its individual components. The combustor is the major part to be considered as a research component due to its complex combustion process. In the scramjet engine combustion chamber, the presence of air is very less, around a tenth of milliseconds and it is not sufficient for the commencement of ignition of fuel and supersonic air. Combustion process strongly depends upon the mixing of fuel and air. Enhancement of the rate of mixing of fuel and air at supersonic speed is a great challenging task.

Raul et al. [1] executed both numerical and experimental investigations on mixing enhancement of supersonic air and fuel in scramjet combustor with turbulent Navier–Stokes fluid flow governing equations. In this study, a sinusoidal shape was considered, which was attached to the walls of scramjet combustor to make a configuration of supersonic air-fuel mixing enhancement technique with spatial forcing. For this geometrical configuration, they have conducted a numerical study with a varying amplitude of sinusoidal wave (wavy wall structure). From the predicted numerical results, they found that the Mach number contours are very helpful for prediction of boundary layer separation over wavy wall and walls of the scramjet combustor.

Hongbo et al. [2] studied numerical combustion of scramjet combustor using a passive scalar method. Flow governing equations were solved by using computational fluid dynamics tool. In this research paper, they have investigated the amount of mass transfer entry into and leaving out of the wall attached cavity of the scramjet combustion chamber. They also explored the effect of cavity flow on residence time under reacting flow condition. Reynolds-averaged Navier–Stokes equations along with large eddy simulation combination were the best simulation method to predict the flow structure of complex problems like combustion and adverse pressure gradient development flows [3–6]. It is a difficult task to sustain the flame at supersonic speed in scramjet combustor. For this, various cavity and fuel injection techniques were established and investigated as follows: strut [7–11]—generation of oblique shocks, cavities [12–15]—development of recirculation regions, and the combinations [16–20] with the principle of vortices generation in the vicinity of combustion chamber walls.

In supersonic flows, the intermixing of fuel with supersonic air stream greatly depends on the residence time of air in the combustion chamber. In scramjet engines, the time available for completion of both intermixing and combustion process is the only a tenth of a millisecond. At this residence time, the chance for mixing augmentation of fuel and supersonic air is a great challenge. Mingle of fuel with airstream at

supersonic speed can be escalated by creating more number of recirculation regions, streamline vortices, and shock waves along the flow field of the combustion chamber. In this exploration paper, the passive technique has been executed by creating the wall attached fuel injectors at different locations of the scramjet combustor. DLR scramjet combustor is considered as a reference or basic model to which wall attached fuel injectors are implemented.

## 2 Computational Domain Modeling

The computational domains of three different scramjet combustors are modeled with the pre-processor tool of ANSYS Fluent 15. DLR scramjet model [19] is considered as a basic or reference model for the development of another two models with wall attached and strut fuel injectors. The first model consists of the only wall attached strut fuel injectors, and the second model consists of axial strut injector (in-line strut) along with wall attached strut fuel injectors. Computational domains of three scramjet combustors are shown in Fig. 1.

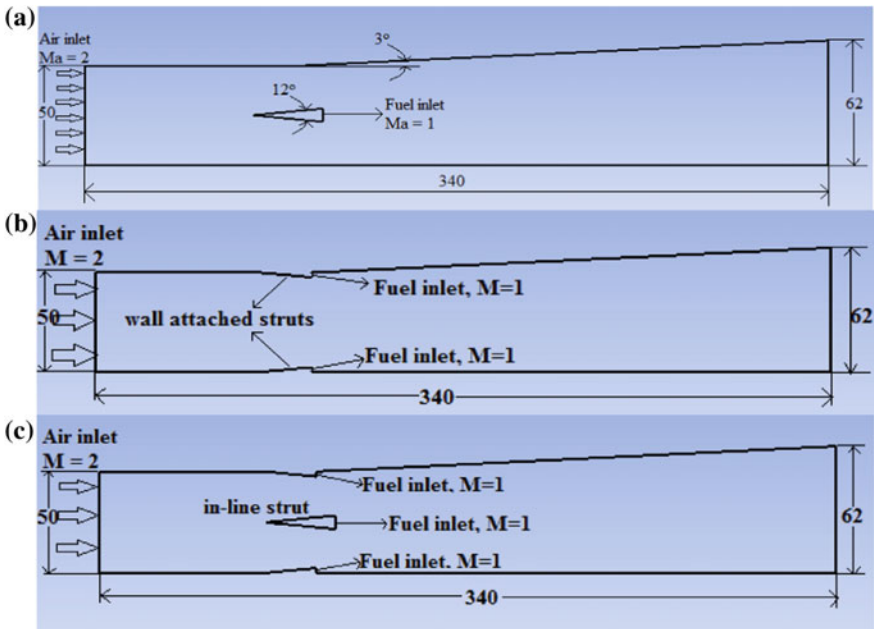


Fig. 1 Computational domains of scramjet: a Basic (or) reference model. b First model (middle). c Second model (bottom) (all dimensions are in mm)

### 3 Numerical Modeling

Two-dimensional numerical analysis has been carried out for all the computational domains. All the flow properties are visualized by solving the Reynolds-averaged Navier–Stokes (RANS) governing equations. Turbulence is modeled with shear stress transport (SST)  $k - \omega$  turbulence and finite rate/eddy dissipation chemistry turbulence model. Finite volume second-order upwind discretization scheme is used for solving all the flow governing equations. Stability of the iterative technique is controlled by maintaining the under-relaxation factors less than one ( $<1$ ). Combustion of hydrogen fuel and air has been modeled with a one-step reaction mechanism [20]. The flow governing equations of continuity, momentum, and energy are defined as follows [20–22]:

$$\frac{\partial \rho}{\partial t} + \frac{\partial}{\partial x_i}(\rho u_i) = 0 \quad (1)$$

$$\frac{\partial}{\partial t}(\rho u_i) + \frac{\partial}{\partial x_i}(\rho u_i u_j) = -\frac{\partial P}{\partial x_i} + \frac{\partial}{\partial x_i}(\tau_{ij}) \quad (2)$$

$$\frac{\partial}{\partial t}(\rho e_t) + \frac{\partial}{\partial x_i}(\rho h_t u_j) = \frac{\partial}{\partial x_i}(\tau_{ij} u_i - q_i) \quad (3)$$

The variables  $\rho$ ,  $\tau$ ,  $P$ ,  $u$ ,  $e_t$ ,  $q$ , and  $h$  are described as density, Reynolds stress, pressure, velocity, total energy, specific heat flux, and specific enthalpy, respectively.

### 4 Results and Discussion

Scramjet combustor internal fluid flow properties have been evaluated by performing the numerical simulations. Mixing of fuel and air at a supersonic speed greatly depends on the rate of creation and its interaction of shock waves, vortices, and shear mixing layer. The passive technique with different types of fuel injection has been executed to enhance the intermixing of fuel and air reactants. Internal flow physics of scramjet combustor are evaluated by predicting the variation of density, which plays a major role in the development of shock waves and recirculation regions.

From Fig. 2, it is observed that both oblique and expansion shock waves are produced from the leading and trailing point of struts, respectively. Both the oblique and expansion shock waves are undergone to multiple reflections in between the combustion chamber wall and wake region of the strut. This causes the interaction of supersonic airstream and fuel stream and thereby enhances the tendency of fuel carrying with multiple reflection shock waves. By analyzing the density flow field of three combustors, it is identified that both the basic and first model has less interaction of shock waves with fuel stream as compared to the last model. The second model consists of both in-line strut and wall attached strut, which are causes for more shock

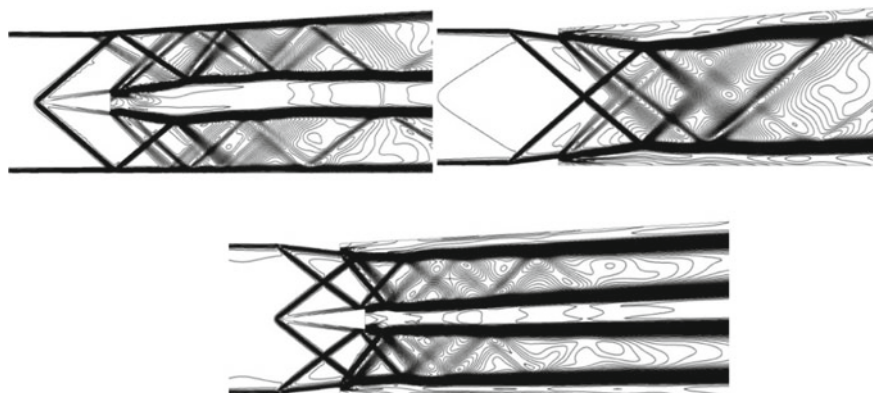


**Fig. 2** Density flow field of scramjet combustors: basic model (DLR-top), first model (middle), second model (bottom)

waves development and increases the interaction of shock waves with fuel stream and enhances the intermixing of fuel and air.

To visualize more about the internal flow dynamics and complex combustion process, the temperature parameter has been considered and studied at different locations of the combustor and the same shown in Fig. 3. From the visualization of temperature variation profiles for different scramjet combustors, it is identified that the combustion phenomenon has been intensified in the downstream of the strut and the same observed with enlargement of temperature along the length of the combustor. Basic model consists of only in-line strut injector, and it causes pressure losses and thereby reduces the performance of scramjet combustor. To diminish these pressure losses, first model is introduced with the only wall attached strut injectors. From the analysis of density flow field and temperature profile of the first model, it is observed that the first model has less performance than that of the basic model because of its fewer shocks and weak combustion. The combination of inclined and parallel fuel injection is the best technique to intensify the intermixing of fuel and air. The second model is the combination of parallel and inclined fuel injection with in-line strut and wall attached strut, respectively. From the analysis of both density flow field (Fig. 2) and temperature profiles (Fig. 3) of the second model, it is recognized that the development of oblique, expansion shock waves and recirculation regions are higher as compared to the other models.

## 5 Conclusion

Numerical analysis of scramjet combustor with in-line strut and wall attached strut fuel injector has been investigated and analyzed to visualize the internal fluid flow properties of the scramjet engine. From the analysis of both density flow field and

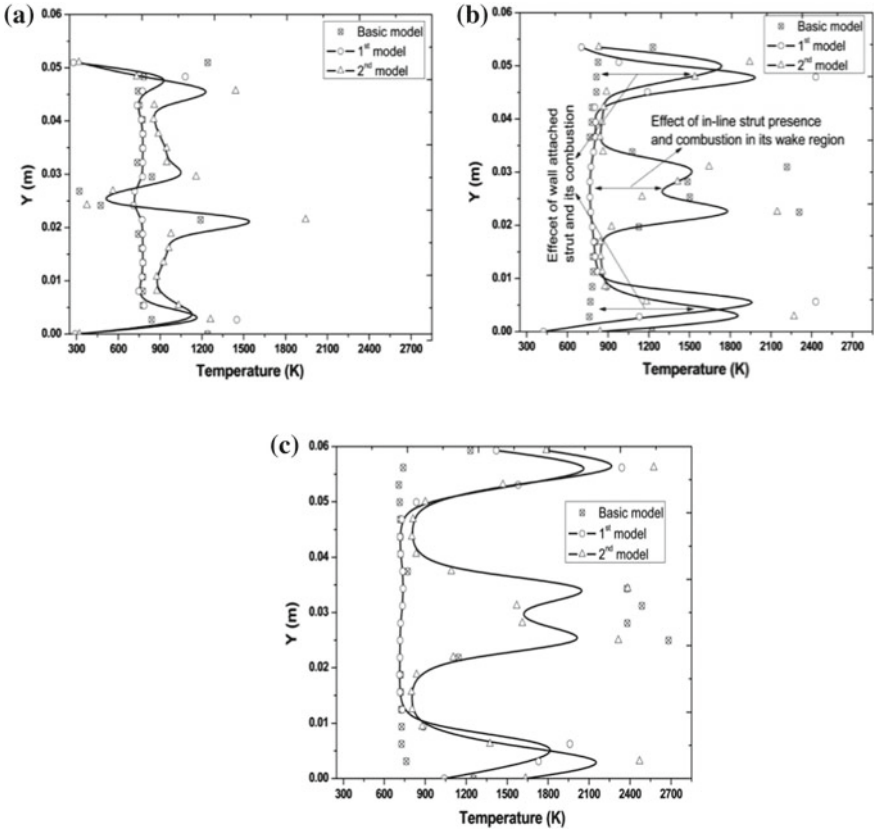


**Fig. 3** Temperature profiles of scramjet combustors at various locations: **a**  $x = 108$  mm, **b**  $x = 167$  mm, and **c**  $x = 275$  mm

temperature profiles for different scramjet combustors, it is identified that location of strut and fuel injection angle with respect to the mainstream plays an important role to enhance the performance of scramjet combustor. In this research paper, both the parallel and inclined strut fuel injection has been investigated. From the investigation of all three models, it is observed that the scramjet combustor with wall and in-line strut fuel injector has better performance as compared to the other two models, due to its more oblique and expansion shock waves and the amalgamation of both parallel and inclined fuel injection technique.

## References

1. Raul R, Gilreath H, Sullins G (1992) Numerical and experimental investigation of mixing enhancement in Scramjets, AIAA-92-5063. In: AIAA fourth international aerospace planes

- conference, Orlando, 1–4 Dec 1992
2. Wang Hongbo, Sun Mingbo, Yang Yixin, Qin Ning (2015) A passive scalar-based method for numerical combustion. *Int J Hydrogen Energy* 40:10658–10661
  3. Sadiki A, Maltsev A, Wegner B, Flemming F, Kempf A, Janicka J (2006) Unsteady methods (URANS and LES) for simulation of combustion systems. *Int J Therm Sci* 45:760–773
  4. Pitsch H (2006) Large eddy simulation of turbulent combustion. *Ann Rev Fluid Mech* 38:453–482
  5. Gicquel LYM, Staffelbach G, Poinso T (2012) Large eddy simulations of gaseous flames in gas turbine combustion chambers. *Prog Energy Combust* 38:782–817
  6. Li J, Song W, Han X, Fu Q, Junniu, Xue W (2015) Design and experiments of the fuel control method for the scramjet engine, *Sadhana* vol 40, Part 1, pp 155–171, Feb 2015
  7. Gerlinger Peter, Stoll Peter, Kindler Markus, Schneider Fernando, Aigner Manfred (2008) Numerical investigation of mixing and combustion enhancement in supersonic combustors by strut induced stream-wise vorticity. *Aerosp Sci Technol* 12:159–168
  8. Zou J, Zheng Y, Liu OJ (2007) Simulation of turbulent combustion in DLR scramjet. *J Zhejiang Univ-Sc A* 8(7):1053–1058
  9. Oevermann Michael (2000) Numerical investigation of turbulent hydrogen combustion in a scramjet 585 using flamelet modeling. *Aerosp Sci Technol* 4(7):463–480
  10. Kumaran K, Behera PR, Babu V (2010) Numerical investigation of the supersonic combustion of kerosene in a strut-based combustor. *J Propul Power* 26(5):1084–1091
  11. Gnani F, Menon S (2010) Simulation of turbulent mixing behind a strut injector in supersonic flow. *AIAA J* 48(3):526–539
  12. Huang W, Luo S, Liu J, Wang Z (2010) Effect of cavity flame holder configuration on combustion flow field performance of integrated hypersonic vehicle. *Sci China Technol Sci* 53(10):2725–2733
  13. Huang W, Luo S, Pourkashanian M, Ma L, Ingham DB, Liu J, Wang Z (2010) Numerical simulations of typical hydrogen-fueled scramjet combustor with a cavity flame holder. In: *International conference of mechanical engineering*, London, UK
  14. Gu H, Chen L, Chang X (2009) Experimental investigation on the cavity-based scramjet model. *Chin Sci Bull* 54(16):2794–2799
  15. Kim KM, Baek SW, Han CY (2004) Numerical study on supersonic combustion with cavity-based fuel injection. *Int J Heat Mass Trans* 47(2):271–286
  16. Zhao Z, Song WY, Xiao YL, Le JL (2009) An experimental investigation of the cold flow field in a model scramjet combustor. *PI Mech Eng G-J Aer* 223(4):425–431
  17. Hsu K-Y, Carter CD, Gruber MR, Barhorst T, Smith S (2010) Experimental study of cavity strut combustion in supersonic flow. *J Propul Power* 26(6):1237–1246
  18. Huang W, Wang Z, Luo S, Liu J, Xia Z, Lei J, Wang Z, Mohamed P, Ma L, Ingham DB (2011) Overview of fuel injection techniques for scramjet engines. In: *Proceedings of ASME turbo expo*, Vancouver, Canada, pp 17–24
  19. Waidmann W, Brummund U, Nuding J (1996) Experimental investigation of supersonic ramjet combustion (scramjet). In: *8th international symposium on transport phenomena in combustion*, Taylor and Francis, Boca Raton
  20. Kumaran K, Babu V (2009) Investigation of the effect of chemistry models on the numerical predictions of the supersonic combustion of hydrogen. *Combust Flame* 156:826–841
  21. Kummitha OR, Pandey KM, Gupta R (2018) CFD analysis of a scramjet combustor with cavity based flame holders. *Acta Astron* 144:244–253
  22. Obula Reddy Kummitha (2017) Numerical analysis of hydrogen fuel scramjet combustor with turbulence development inserts and with different turbulence models. *Int J Hydrogen Energy* 42(9):6360–6368

# Numerical Simulation of Heat Transfer and Fluid Flow Characteristics of Triangular Corrugated Wavy Channel



Meghna Das Chaudhury and Raju

**Abstract** The present numerical simulation was performed with the objective to study the fluid flow and heat transfer characteristics of a corrugated wavy channel and compare its thermal performance with that of a straight channel with the same geometrical parameters. Both the considered channel had rectangular cross section, and one of them had triangular corrugations with a corrugation angle of  $21.8^\circ$ . The flow was assumed to be laminar through the channel with Reynolds number ( $Re$ ) varying from 500 to 1500, and the analysis was performed under steady state and constant heat flux ( $10 \text{ kW/m}^2$ ) conditions. For quantitatively analyzing the heat transfer enhancement rate, Nusselt number ( $Nu$ ) was estimated along the top front corrugated line (TFCL) and it was found that  $Nu$  values increased with increasing  $Re$ . Also, the triangular corrugated channel was found to outperform the straight rectangular channel with regard to its comparatively high  $Nu$  values which increased by 47.8%. The increased  $Nu$  values upon incorporation of corrugations were thought to be due to the formation of recirculation zones and high-intensity swirl flow near the vicinity of corrugations. The only analyzed disadvantage of such a channel was found to be its rise in pressure loss value with increasing  $Re$ .

**Keywords** Corrugated wavy channel · Laminar flow · Nusselt number · Recirculation flow

## 1 Introduction

The increasing need for compact, effective, and efficient heat exchangers for several industrial applications has aggravated the demand for the development of advanced heat transfer enhancement techniques. To realize enhancement in heat transfer rate,

---

M. Das Chaudhury (✉) · Raju  
Department of Mechanical Engineering, National Institute of Technology,  
Rourkela 769008, Odisha, India  
e-mail: [meghc2007@gmail.com](mailto:meghc2007@gmail.com)

Raju  
e-mail: [r.bhatia2194@gmail.com](mailto:r.bhatia2194@gmail.com)

© Springer Nature Singapore Pte Ltd. 2020  
H. K. Voruganti et al. (eds.), *Advances in Applied Mechanical Engineering*,  
Lecture Notes in Mechanical Engineering,  
[https://doi.org/10.1007/978-981-15-1201-8\\_29](https://doi.org/10.1007/978-981-15-1201-8_29)

several methods are incorporated [1] and among those various methods, corrugated surfaces are being extensively researched. It has the capability to promote the formation of recirculation zones, increase the effective fluid flow path [2], etc. and is widely used for electronic cooling, in solar collectors, electrochemical and catalytic reactors [3], etc.

In order to gain a comprehensive insight into the various heat transfer enhancement techniques, this domain has been extensively studied and investigated. Analytically and numerically, the heat transfer enhancement mechanism in both two-dimensional and three-dimensional sinusoidal channels was examined which was subjected to different temperature conditions on the lower and upper wall. The flow was predominantly steady and laminar. The presence of stagnation points and asymmetry of flow was found to be the reason behind heat transfer enhancement in the case of 2D corrugations. Though the primary mechanism behind heat transfer enhancement was essentially the same in case of 3D corrugations as well, advection due to transverse flow was also attributed as one of the additional causes [4]. The use of corrugation also leads to a complex flow pattern which promotes better momentum transfer, swirling, and recirculation of the flow resulting in enhanced heat transfer rate [5]. Additionally, it leads to a significant pressure drop due to friction in the channel which is higher in comparison with the conventional straight channels [6, 7]. The heat transfer rate between a plain channel and three different types of corrugated channel of two different heights (5 and 10 mm) was experimentally examined, and the channel with the maximum corrugation angle ( $50^\circ$ ), minimum pitch (10 mm), and height (5 mm) was found to outperform the other channels as it exhibited the highest  $Nu$  values at  $Re$  ranging from 2000 to 5000 [8]. Heat transfer enhancement is generally quantified by estimating the value of  $Nu$ , and it has been noticed that the value of  $Nu$  increases with an increase in the value of  $Re$  and it strongly depends upon the corrugation angle and height of the channel [9]. Quite recently, numerical simulation was performed on a triangular, sinusoidal, and trapezoidal corrugation channels with inlet  $Re$  varying between 400 and 1400. The flow through the channel was assumed to be laminar, incompressible, steady, and 2D. The effect of  $Re$  and corrugation on viscous entropy generation, pressure drop, and  $Nu$  was studied, and it was concluded that the thermal performance of the sinusoidal channel was superior as compared to the other two [10].

In this present numerical work, the objective was to study the heat transfer characteristics of a triangular corrugated channel (corrugation angle =  $21.8^\circ$ ,  $H_{\max} = 32$  mm and  $H_{\min} = 20$  mm with Pitch = 30 mm) and compare its performance with that of a straight channel, both subjected to a constant heat flux of  $10 \text{ kW/m}^2$  with water as the considered working fluid. For this present problem,  $Re$  was varied between 500 and 1500, and since in this mentioned  $Re$  range, for a straight channel, a viscous laminar model is demanded; hence, in order to draw an appropriate comparison, the same model was considered for the triangular corrugated channel as well. By conducting an extensive literature review, to the best of our knowledge we found that none of the paper till date has worked with the aforementioned geometrical parameters that we had selected for our simulation.



## 2 Numerical Analysis

### 2.1 Geometry (Computational Domain)

In the present problem, the considered geometry as shown in Fig. 1 is a rectangular channel with triangular corrugation profiles with corrugation angle approximately  $21.8^\circ$ . The length, width, and height of the total channel are 300 mm, 130 mm, and 35 mm, respectively, whereas the maximum ( $H_{\max}$ ) and the minimum height ( $H_{\min}$ ) of the triangular corrugations employed are 32 mm and 20 mm, respectively. There are a total of 10 corrugation cycles in the channel, and the length of the pitch ( $\lambda$ ) is 30 mm.

### 2.2 Mesh Generation

The partial differential equations that govern any fluid flow and heat transfer problems are analytically unsolvable except for a very few simple cases. Therefore, in order to analyze such problems, the computational domain is split into smaller subdomains (made up of geometric primitives like hexahedral and tetrahedral shapes in 3D and quadrilaterals and triangles in 2D). The governing equations are then discretized and solved inside each of these subdomains. These subdomains are created by the ‘mesh’ option in ANSYS Fluent. The mesh of the computational domain in the present problem was generated using the edge sizing method with finer mesh near the solid–fluid interface and coarser mesh near the center to reduce the total computational time. Figure 2 a and b depicts the mesh employed in one corrugation section and in the sidewalls of the channel, respectively.

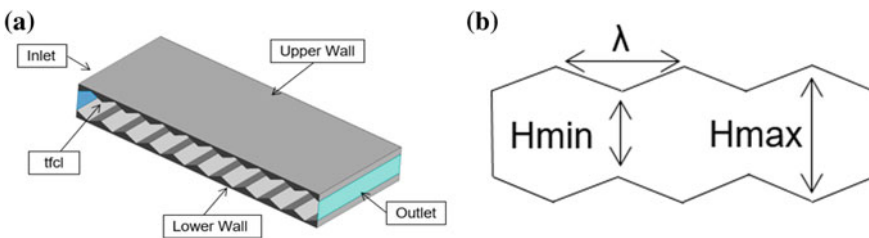


**Fig. 1** a Geometry of the channel and b schematic of a portion of the corrugation

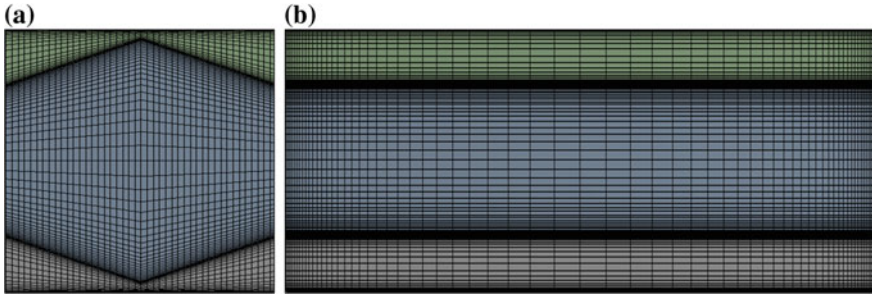


**Fig. 2** **a** Mesh pattern employed in the corrugation and **b** in the sidewall of the channel

### 2.3 Simulation Methodology and Governing Equations Solved

In order to understand and examine the fluid flow and heat transfer characteristics of both the channels, the commercial code, Fluent, was used. The considered  $Re$  was varied from 500 to 1,500, and the flow was assumed to be steady throughout the channel. For simulating the same, viscous laminar model was chosen with water as the working fluid and pipe material as aluminum. During simulation, the following governing equations were solved:

1. Mass conservation equation

$$\frac{\partial \rho}{\partial t} + \nabla \cdot (\rho \vec{v}) = 0 \quad (1)$$

2. Momentum conservation equation

$$\frac{\partial}{\partial t} (\rho \vec{v}) + \nabla \cdot (\rho \vec{v} \vec{v}) = -\nabla p + \nabla \cdot (\vec{\tau}) + \rho \vec{g} + \vec{F} \quad (2)$$

3. Energy conservation equation

$$\frac{\partial}{\partial t} (\rho E) + \nabla \cdot (\vec{v} (\rho E + p)) = \nabla \cdot (k \nabla T + (\vec{\tau} \cdot \vec{v})) \quad (3)$$

where  $\rho$  = density,  $\vec{v}$  = velocity,  $p$  = static pressure,  $k$  = thermal conductivity,  $T$  = temperature, and  $\vec{\tau}$  = stress tensor. Here,  $\rho \vec{g}$  and  $\vec{F}$  are the gravitational body force and external body forces, respectively. The first term in the right-hand side of Eq. (3) represents energy transfer due to conduction, and the second term represents energy transfer due to viscous dissipation. The term ' $E$ ' used in Eq. (3) (total energy) can be expressed as:

**Table 1** Boundary conditions

Domain	Boundary conditions
Inlet	Velocity inlet ( <i>Re</i> dependent)
Upper wall	Constant heat flux (10 kW/m <sup>2</sup> )
Lower wall	Constant heat flux (10 kW/m <sup>2</sup> )
Outlet	Pressure outlet (Atmospheric)
Rest of the walls	At adiabatic conditions

$$E = h - \frac{p}{\rho} + \frac{v^2}{2} \tag{4}$$

Here, ‘*h*’ represents enthalpy.

In order to simulate the flow characteristics and thermal behavior of the channel, it was subjected to specific boundary conditions as illustrated in Table 1. On the basis of the considered *Re*, the inlet velocity was calculated by using the following formulae:

$$Re = \frac{\rho v D_h}{\mu} \tag{5}$$

where

*P* density of the working fluid which is water (kg/m<sup>3</sup>).

*V* the flow velocity at inlet (m/s).

*μ* dynamic viscosity of the flow (kg/ms).

*D<sub>h</sub>* hydraulic diameter (m) of the channel which was calculated as follows:

$$D_h = \frac{4A}{P} \tag{6}$$

where *A* = cross-sectional area of the channel (m<sup>2</sup>), i.e., width × *H<sub>avg</sub>*

*P* = perimeter of the channel (m), i.e., 2 (width + *H<sub>avg</sub>*)

As the channel had both converging and diverging sections, therefore, the average channel height (*H<sub>avg</sub>*) was calculated by taking the mean of both *H<sub>max</sub>* and *H<sub>min</sub>*, where the magnitude of *H<sub>max</sub>* and *H<sub>min</sub>* was 32 mm and 20 mm, respectively.

$$H_{avg} = \frac{H_{max} + H_{min}}{2} \tag{7}$$

From the above calculation, the value of *H<sub>avg</sub>* was found to be 26 mm and width of the channel is 130 mm. Subsequently, inlet velocity was calculated from Eq. (5).

For the purpose of solving the pressure–velocity coupled equation, the SIMPLE scheme was adopted, and for the spatial discretization of pressure, momentum, and energy, second-order upwind interpolation scheme was employed. To ensure convergence in the continuity and momentum equations, the scaled residuals were set to 10e–08, whereas for energy, it was set to 10e–09.

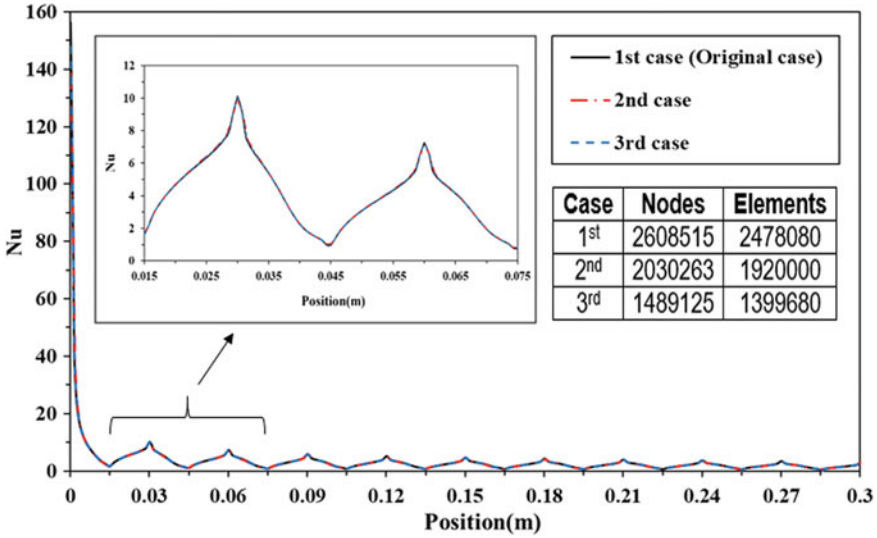


Fig. 3 Mesh independent test graph between  $Nu$  and position (m) at  $Re = 500$

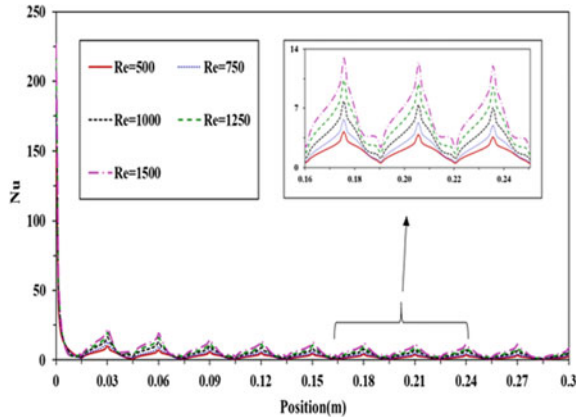
### 2.4 Grid Independence Test

The results obtained from the numerical simulation were mesh independent as shown in Fig. 3. Two different cases were made for  $Re$  500, viz. case 2 and case 3 with around 22 and 27% decrease in the number of mesh elements, and the results were compared with the original case (case 1). The results were found to vary approximately by around 5% (average).

### 2.5 Results and Discussions

To examine the heat transfer characteristics,  $Nu$  values were estimated along the TFCL of the rectangular channel for five different values of Reynolds number ( $Re = 500, 750, 1000, 1250, 1500$ ) as shown in Fig. 4. By carefully analyzing the obtained graph, it was concluded that the value of  $Nu$  increased with the increase in the value of  $Re$ , which can be attributed to the formation of recirculation zones and enhanced swirl flow intensity near the corrugations. But its intensity is not same everywhere inside the corrugation troughs. The intensity is generally maximum near the vertex angle (upper region) of the triangular corrugations as compared to the region near the base angle (lower region), and hence, the convective heat transfer near the upper region is maximum as compared to the lower region. Due to this enhanced convective heat transfer rate near the upper portion,  $Nu$  value along the corrugation lines in that region increased comparatively more than the  $Nu$  values along the corrugation lines

**Fig. 4** Graph of  $Nu$  versus position (m) at  $Re = 1500$  comparing channel behavior



present near the lower portion of the triangular corrugation. This led to its fluctuating nature as shown in Fig. 4 along with the channel position. Taking into consideration this fluctuating nature of  $Nu$  values with position, it was estimated that the overall enhancement in its value, between two consecutive  $Re$ , varied between 1% to 57%. That is, for example, at  $Re$  750,  $Nu$  values increased by 1 to 57% as compared to  $Nu$  values at  $Re$  500.

Since  $Nu$  increased near the upper region, the augmentation of heat transfer rate took place. From the numerical simulation, we observed that  $Nu$  values of the TFCL in case of triangular corrugated channel as compared to straight channel increased drastically at some specific points (such as at  $x = 0, 0.03, 0.06, 0.09, 0.12,$  and  $0.15$  m) along the axial length as shown in Fig. 5. At those points where  $Nu$  value increased, the increment varied between 70 and 200%. At certain other points (such as at  $x = 0.035, 0.066, 0.096,$  and  $0.1275$  m) as shown in the figure, the  $Nu$  value of both the channels seemed to be comparable, and at some other points (such as at  $x = 0.015,$

**Fig. 5** Graph of  $Nu$  versus position (m) long the TFCL at five different  $Re$

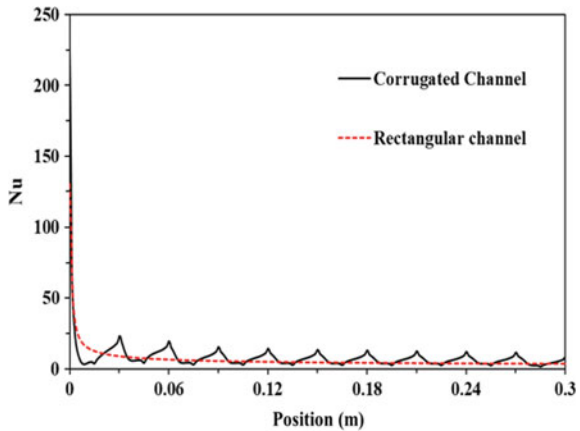
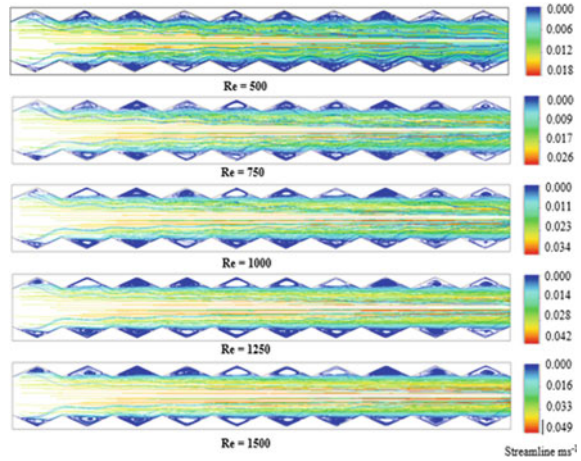


**Fig. 6** Streamlines at different  $Re$  showing zones



0.075, 0.135, and 0.2775 m),  $Nu$  values of the corrugated channel reduced by 50%. But from our estimation, we found that comparatively there were more numbers of points at which the  $Nu$  value increased leading to a net percentage increment in its value. Enhanced  $Nu$  values augmented the heat transfer rate of the corrugated channel as compared to the straight channel, and the average overall percentage enhancement in Nusselt number of the corrugated channel was 47.8%.

Also by observing Fig. 6, it was found that the streamlines obtained at different  $Re$  values were indicating towards the formation of substantial recirculation zones and swirl flow near the triangular corrugations as shown by the dark-blue regions.

The pressure drop across any converging and diverging portion was more prominently observed in case of  $Re$  1500 as compared to  $Re$  500, 750, 1000, and 1250. While a maximum pressure drop of 88.34% was observed in case of  $Re$  1500, for  $Re$  500 the maximum pressure drop was estimated to be 43.68%.

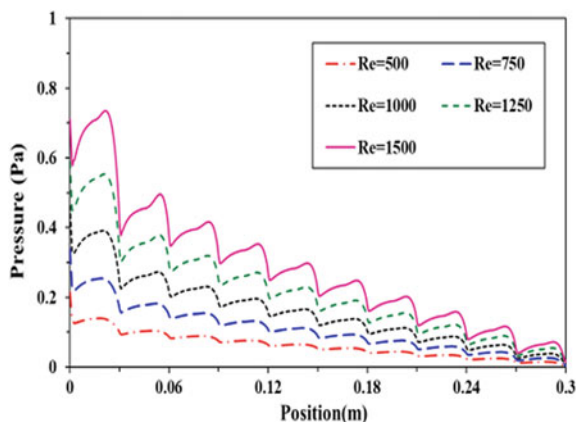
Also, a maximum pressure drop of 78.6%, 68.6%, and 56.57% was calculated for  $Re$  1250, 1000, and 750, respectively. The pressure drop along the TFCL at different  $Re$  values was observed as shown in Fig. 7.

### 3 Conclusions

In the present study, an attempt was made to numerically study the fluid flow and heat transfer characteristics of a triangular corrugated channel by using the finite volume method by employing the commercial numerical code ANSYS Fluent. By varying the  $Re$  values, the subsequent effect in  $Nu$ , pressure drop, and streamlines were analyzed which were as follows:

- The value of  $Nu$  was found to increase with the increase in the value of  $Re$ .  $Nu$  values increased by 1 to 57% at  $Re$  750 as compared to  $Re$  500. Similar nature of

**Fig. 7** Graph of pressure ( $Pa$ ) versus position (m) the formation of recirculation along at TFCL at five different  $Re$



$Nu$  values with position was observed between the other  $Re$  values, i.e. between  $Re$  1000 and  $Re$  750,  $Re$  1250 and  $Re$  1000,  $Re$  1500 and  $Re$  1250.

- On the contrary, with an increase in  $Re$ , rise in pressure drop was noticed and was maximum in case of  $Re$  1500. The maximum pressure drop in case of  $Re$  1500 was 88.34%.
- With the rise in  $Re$  values, the occurrence of flow recirculation and swirling near the corrugations were found to increase substantially and it was thought to be the reason behind enhancement in  $Nu$  values.
- Enhanced  $Nu$  values augmented the heat transfer rate of the corrugated channel as compared to the straight channel by 47.8%.

## References

1. Siddique M, Khaled ARA, Abdulhafiz NI, Boukhary AY (2010) Recent advances in heat transfer enhancements. *Int J Chem Eng* 2010:1–28. <https://doi.org/10.1155/2010/106461>
2. Elshafei EAM, Awad MM, El-Negiry E, Ali AG (2010) Heat transfer and pressure drop in corrugated channels. *Energy* 35:101–110. <https://doi.org/10.1016/j.energy.2009.08.031>
3. Hassan I, Nirdosh I, Sedahmed G (2009) Free convective mass transfer at corrugated surfaces in relation to catalytic and electrochemical reactor design. *Chem Eng Proc: Proc Intens* 48:1341–1345. <https://doi.org/10.1016/j.ccep.2009.06.006>
4. Sawyers DR, Sen M, Chang HC (1998) Heat transfer enhancement in three-dimensional corrugated channel flow. *Int J Heat Mass Transf* 41:3559–3573. [https://doi.org/10.1016/S0017-9310\(98\)00029-5](https://doi.org/10.1016/S0017-9310(98)00029-5)
5. Zhang LZ (2005) Numerical study of periodically fully developed flow and heat transfer in cross-corrugated triangular channels in transitional flow regime. *Num Heat Trans Part A: Appl Int J Comput Methodol* 48:387–405. <https://doi.org/10.1080/10407780590957314>
6. Hwang SD, Jang IH, Cho HH (2006) Experimental study on flow and local heat/mass transfer characteristics inside corrugated duct. *Int J Heat Fluid Flow* 27:21–32. <https://doi.org/10.1016/j.ijheatfluidflow.2005.07.001>

7. Naphon P (2007) Heat transfer characteristics and pressure drop in channel with V corrugated upper and lower plates. *Energy Convers Manag* 48:1516–1524. <https://doi.org/10.1016/j.enconman.2006.11.020>
8. Pehlivan H, Taymaz I, Islamoglu Y (2013) Experimental study of forced convective heat transfer in a different arranged corrugated channel. *Int Commun Heat Mass Trans* (46):106–111. <http://dx.doi.org/10.1016/j.icheatmasstransfer.2013.05.016>
9. Taymaz I, Koc I, Islamoglu Y (2008) Experimental study on forced convection heat transfer characteristics in a converging diverging heat exchanger channel. *Heat Mass Transfer* 44:1257–1262. <https://doi.org/10.1007/s00231-007-0366-0>
10. Akbarzadeh M, Rashidi S, Esfahani JA (2017) Influences of corrugation profiles on entropy generation, heat transfer, pressure drop, and performance in a wavy channel. *Appl Therm Eng* 116:278–291. <https://doi.org/10.1016/j.applthermaleng.2017.01.076>



# Emission and Performance Characteristics of CI Engine with Diesel–Butanol Blends Using Intake Pressure Boost



Hemant Gowardhan, Amit Karwade and J. G. Suryawanshi

**Abstract** Biofuels like ethanol, biodiesel and butanol have attracted attention of people worldwide and found to be the successful alternates of petroleum products. Slight reduction in emissions is observed when biofuels are used in place of Diesel [1]. In the present work, the emission characteristics of CI engine with diesel–butanol blends using intake pressure boost are shown. For improving the performance of any engine, either we have to go with fuel properties or we have to use advanced technologies. In this study, we are doing both by using diesel–butanol blends and by using an intake pressure boost by varying its intake pressure to cylinder. The investigation results showed that the emission and performance parameters of the engine with intake pressure boost were improved in comparison with naturally aspirated engine.

**Keywords** Diesel–butanol blends · Intake pressure boost · Emissions

## 1 Introduction

Use of biofuels potentially reduces the burden on fossil fuels and fulfils the growing energy need of the world, while conserving the nature. The compression ignition mode of combustion promotes the use of diesel–butanol blends in the aim of achieving high performance with improved emissions. Still,  $\text{NO}_x$  emissions are major issues with diffusion combustion. Several engine modifications were done to increase the efficiency and make percentage of butanol suitable for butanol–diesel blends in CI engine.

In SI engines, the air–fuel mixture at stoichiometric ratio provides clean combustion and negligible smoke emissions, due to lower sizes and lower compression ratio. With lower compression ratio, mixture burns at a lower temperature, reducing the  $\text{NO}_x$  emissions. It, however, has lower part-load and fuel efficiency on account of lower compression ratio and throttling losses.

---

H. Gowardhan · A. Karwade · J. G. Suryawanshi (✉)  
Department of Mechanical Engineering, Visvesvaraya National Institute  
of Technology, Nagpur, Maharashtra 440010, India

© Springer Nature Singapore Pte Ltd. 2020  
H. K. Voruganti et al. (eds.), *Advances in Applied Mechanical Engineering*,  
Lecture Notes in Mechanical Engineering,  
[https://doi.org/10.1007/978-981-15-1201-8\\_30](https://doi.org/10.1007/978-981-15-1201-8_30)

The CI engines are regarded as the most fuel-efficient engines for automotive transportation due to its lean operation, high compression ratio and better part-load efficiency. In CI engines, fuel is directly injected into the engine cylinder at the end compression stroke, where auto-ignition of heterogeneous air–fuel mixture causes diffusion combustion at high temperature. As a result, the CI engine emits high  $\text{NO}_x$  and soot emissions. Oxygenated nature biofuels that are derived from the agricultural products offer the benefits of reducing the dangerous diesel engine emissions up to certain levels [2–5].

Here, we have taken the blends on the basis of percent volume in proportion B10, B20, B30, at different BMEP with pressure boost and without pressure boost and observed its behaviour on the basis of emission parameters.

## 2 Experimental Setup

Naturally aspirated, water-cooled, single-cylinder, DI diesel engine was used during this study. The engine specifications of diesel engine are given in Table 1.

The experiments were carried out on a single-cylinder, four-stroke, naturally aspirated, water-cooled, direct-injection diesel engine. The engine specifications are shown in Table 1. Several modifications in the diesel engine pump sets have been done to achieve variable DI timings, intake temperature and intake pressure adjustment shown in Fig. 1. The mechanical fuel injection component was developed to inject the fuel during the early compression stroke of the engine cycle. Camshaft motion was transmitted to the fuel injection pump pulley in 1:1 ratio. The pump pulley connected with fuel injection component which has a capability to change injection timing. Fuel injection timing was set by adjusting timer pulley with respect to end of injection (EOI) mark on fuel injection component and with TDC marker on

**Table 1** Specification of experimental setup

Engine	Original CI engine
Bore	80 mm
Stroke	110 mm
Volume	553 CC
Piston bowl diameter	52 mm
Compression ratio	16.5
No. of valves	02
No of cylinder	01
Engine cooling system	Water-cooled
Fuel injector	Multi-hole
Fuel pressure	20 MPa
Fuel system	Direct injection
Engine speed (RPM)	1350

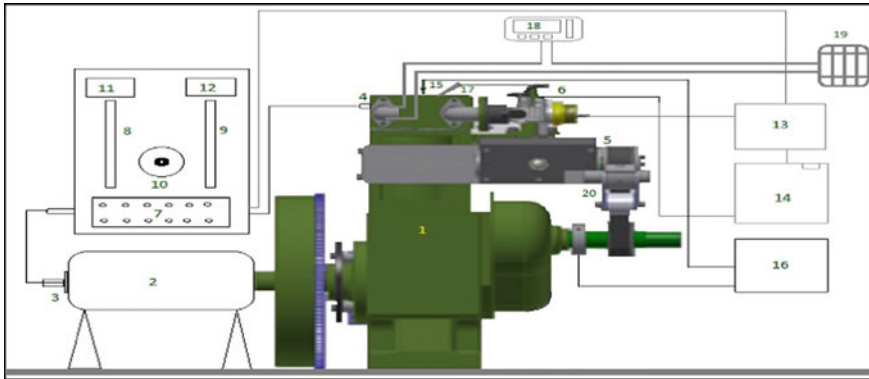


**Fig. 1** Schematic layout of experimental setup 1. Engine, 2. Eddy current dynamometer, 3. Shaft encoder, 4. Pressure transducer, 5. Variable fuel injection timing component, 6. Intake air heater, 7. Data acquisition system, 8. Air manometer, 9. Fuel manometer, 10. Load Regulator, 11. rpm display, 12. Temperature display, 13. Air tank, 14. Fuel tank, 15. Spark plug, 16. Electronic spark ignition system, 17. Fuel injector, 18. Gas analyzer

engine. Ball-type governor was used to maintain 1350 RPM engine speed by controlling fuel supply to the engine. Fuel was injected early in the compression stroke directly inside the cylinder to form homogeneous mixture in high load condition. Late injection required to get more fuel economy during part-load condition.

The experimental setup shows an eddy current dynamometer which is directly coupled to the engine output shaft to measure engine torque. Fuel consumption was measured in terms of the volume of diesel–butanol blend consumed during a specified period of time. In-cylinder pressure was measured using M111A22 quartz crystal dynamic pressure transducer with built-in amplifier having 1 mV/psi sensitivity. The crankshaft position was obtained using an encoder with 1° resolution to determine the in-cylinder pressure as a function of crank angle. All temperatures were measured with K-type thermocouples. The exhaust emissions were measured with AVL DiTEST GMBH A-8020 Graz exhaust gas analyzer. The detection limits of NO<sub>x</sub>, HC and CO are 1 ppm, 1 ppm and 0.01%, respectively

### 3 Results and Discussion

**3.1 The Experiments Was Performed with Taking the Diesel–Butanol Blends for B10, B20, B30 but the Blend of B20 Using the Intake Pressure Boost of Pressure 1.5 Bar, Showed Improved Emissions. Following Are the Obtained Results**

See Figs. 2, 3, 4, 5.

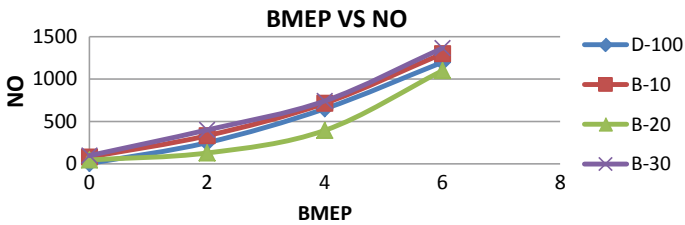


Fig. 2 Variation of BMEP with NO with diesel B10, B20, B30

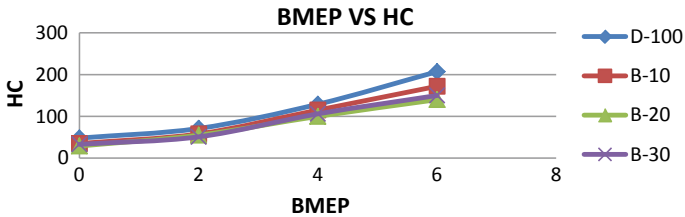


Fig. 3 Variation of BMEP with HC with diesel B10, B20, B30

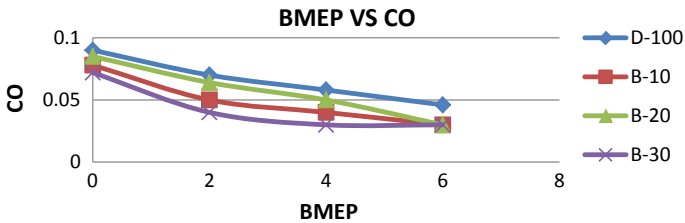


Fig. 4 Variation of BMEP with CO with diesel B10, B20, B30

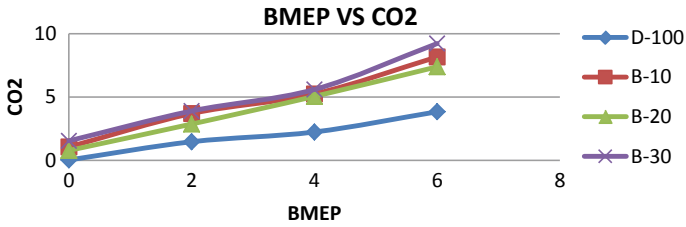


Fig. 5 Variation of BMEP with CO<sub>2</sub> with diesel B10, B20, B30

### 3.2 Following Are Be Performance Parameters When Compared Pure Diesel with Various Diesel–Butanol Blend

See Figs. 6, 7, 8, 9.

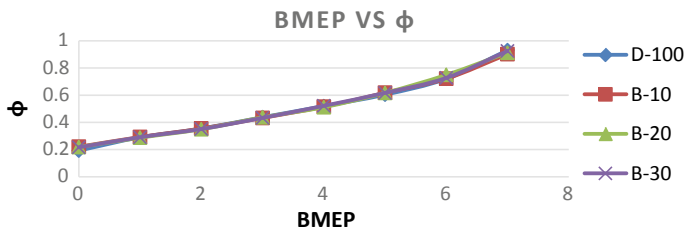


Fig. 6 Variation of BMEP with  $\phi$  with diesel B10, B20, B30

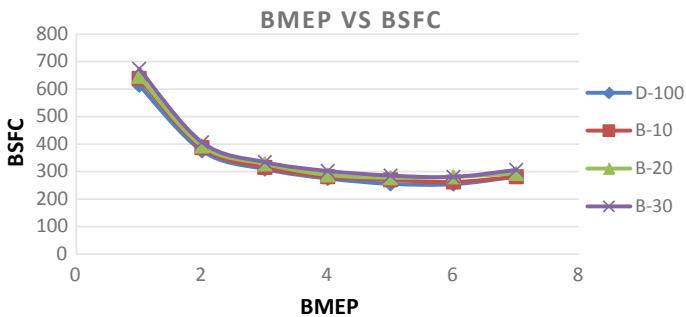


Fig. 7 Variation of BMEP with BSFC with diesel B10, B20, B30

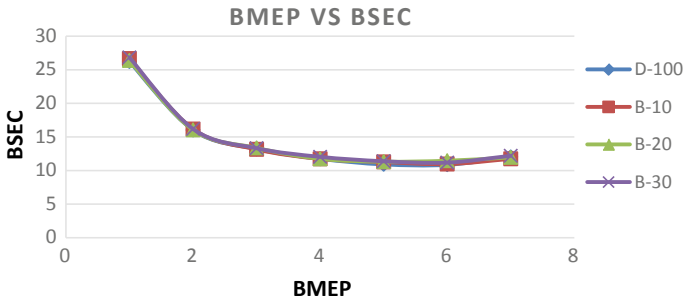


Fig. 8 Variation of BMEP with BSEC with diesel B10, B20, B30

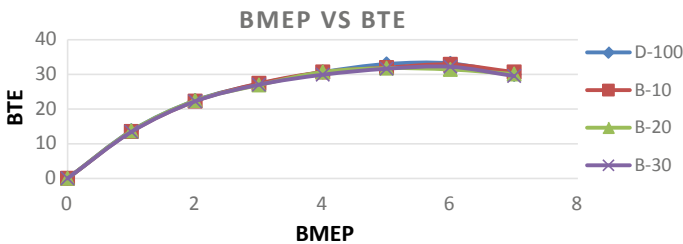


Fig. 9 Variation of BMEP with BTE with diesel B10, B20, B30

## 4 Observation and Conclusion

- NO values are lowered with diesel–butanol blends, when compared with pure diesel operation and with using intake pressure boost, NO formation is little increased.
- But when used B-20, it showed improved and better readings than pure diesel, B-10 and B-30.
- Unburned HC and CO emissions seem to decrease as the extra air is sent to the engine cylinder.
- Performance parameters did not show much variation when compared to diesel.

## References

1. Jagadish D, Kumar PR, Murthy KM (2011) The effect of supercharging on performance and emission characteristics of compression ignition engine with diesel-ethanol-ester blends. *Therm Sci* 15(4)
2. Al-Hasan MI, Al-Momany M (2008) The effect of iso-butanol-diesel blends on engine performance. *Transport* 23(4):306–310

3. Vinod Babu M, Madhu Murthy K, Amba Prasad Rao G (2017) Butanol and pentanol: the promising biofuels for CI engines – a review. *Renew Sustain Energy Rev* 78:1068–1088
4. Zhukov V, Simmie J, Curran H, Black G, Pichon S (2007) Autoignition of biobutanol. In 21st Int. Conf. Dyn. Exp. Reactive Sys. (ICDERS), pp. 23–27
5. Yilmaz N, Ileri E, Atmanli A, Vigil FM Emission characteristics of a diesel engine fueled with diesel-1-pentanol blends

# Thermal Design Methodology for Regenerative Fuel-Cooled Scramjet Engine Walls



G. Vijayakumar

**Abstract** Thermal protection of scramjet engine combustor wall for long-duration operation is one of the major challenges. Regenerative cooling of the combustor walls using hydrocarbon fuel as a coolant is one of the best solutions to withstand high heat transfer rates for the long duration application. In such a case, before embarking on materials development and fabrication, it would be most beneficial to have a procedure that simultaneously selects the preferred material and design. Thermal design methodology of regenerative cooling system for hydrocarbon fueled air-breathing engine walls is presented in this paper. The main ingredient is three-dimensional heat transfer analysis coupled with fluid flow based on FEM that can be used for the thermal management study of regenerative cooled panel configurations and selection of materials including Thermal Barrier Coatings (TBCs). The procedure is applied for the thermal design of fuel-cooled scramjet combustor walls exploiting physical heat sink of hydrocarbon fuel. High-temperature materials, viz., Cb-752, C-103, and C-SiC are considered as the candidate materials along with TBC. Results of the analysis carried out for several combinations of material of construction, TBC with suitable bond coat material, wall thickness, and channel location are presented. It is inferred that TBC along with regenerative cooling is playing a major role in reducing the engine wall temperature thereby maintaining the fuel temperature inside the channels within desirable limit. The Cb-752 material coated with  $Y_2O_3$  TBC remains viable solution for thermal management of scramjet engine walls for the long-duration application.

**Keywords** Thermal design · Scramjet engine · Regenerative cooling

## 1 Introduction

Supersonic combustion ramjet (Scramjet) propulsion [1] is the option for hypersonic air-breathing flight regime. Passive cooling of the engine as a heat sink results in high temperature and exceeds the allowable limit of the materials within short duration,

---

G. Vijayakumar (✉)

Defence Research and Development Laboratory, 500058 Hyderabad, India

© Springer Nature Singapore Pte Ltd. 2020

H. K. Voruganti et al. (eds.), *Advances in Applied Mechanical Engineering*,

Lecture Notes in Mechanical Engineering,

[https://doi.org/10.1007/978-981-15-1201-8\\_31](https://doi.org/10.1007/978-981-15-1201-8_31)



thereby limits the flight duration of hypersonic vehicle. High heat transfer rate due to high-temperature combustion products flowing with supersonic speed inside the engine reveals the need for active cooling system.

In recent years, most studies of active thermal protection for hydrocarbon fueled scramjet engine mainly focus on regenerative cooling [2–5]. The study of regenerative cooling can be concluded into two aspects, the first aspect is the fundamental study of flow and heat transfer in regenerative cooling channels and the second aspect is the design and utilization of the regenerative cooling system. Many researchers put their efforts into studying the basic heat transfer characteristics, the cracking reaction of hydrocarbon fuel and its effects on the heat transfer inside the cooling channel using both experimental and numerical tools. Based on the fundamental results, some researchers built one-dimensional models to better design the regenerative cooling system. Although there are intensive studies about the regenerative cooling for scramjet engine, the studies considering physical heat sink of the fuel combined with effect of TBC are limited, especially for the hydrocarbon fueled scramjet engine. The purpose of this article is to describe the thermal design methodology of regenerative cooling of scramjet engine walls using physical heat sink of the fuel and material selection for long-duration applications.

Generic schematic diagram of regenerative cooling of the scramjet engine is shown in Fig. 1. In regenerative cooling system, the fuel is first pumped into cooling channels to cool the thermal structure as a coolant and then the hot fuel is injected into the combustor as a propellant to generate the thrust. Furthermore, the fuel gets pre-heated after regeneration in the cooling channels can improve the combustion performance.

The engine intake is subjected to air flowing with high velocity which gets compressed in the region. The scramjet combustor is subjected to high heat transfer rate due to high temperature and high-speed combustion products flowing through the engine. Heat flux distribution of the scramjet combustor is shown in Fig. 2.

**Fig. 1** Schematic diagram of regenerative cooling system for scramjet engine walls

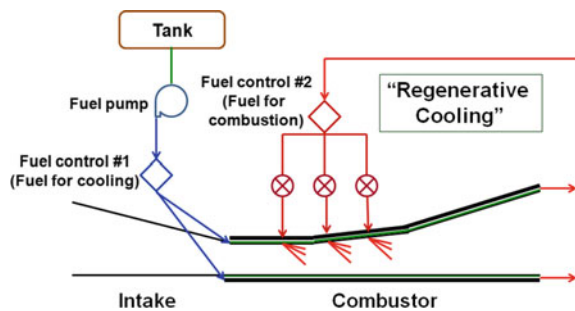
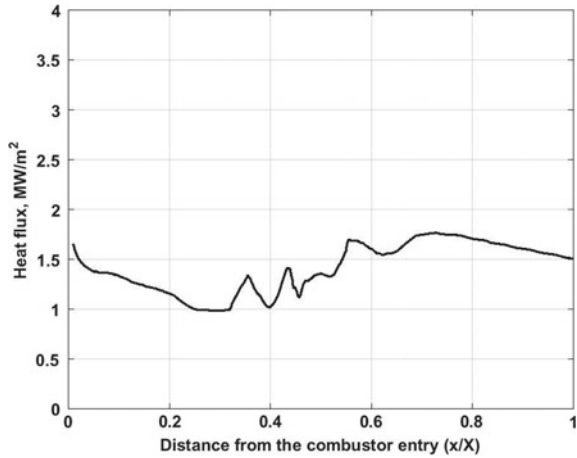


**Fig. 2** Heat flux distribution along the length of the combustor wall



## 2 Scramjet Combustor Walls

Schematic diagram of two-module scramjet combustor with jacket of cooling channels on the walls and cross-section detail of a channel with combustor wall having periodic symmetry is shown in Fig. 3.  $L$  and  $H$  are length and height of the hypersonic vehicle. The present study focuses on rectangular channels. Extension to other periodic shapes is elementary and is not expected to modify the main conclusions. The ratio  $a/b$  and  $Ch_w/b$  is 1.5 and 1, respectively. The TBC along with suitable bond coat has also been considered on inner surface of the combustor wall.

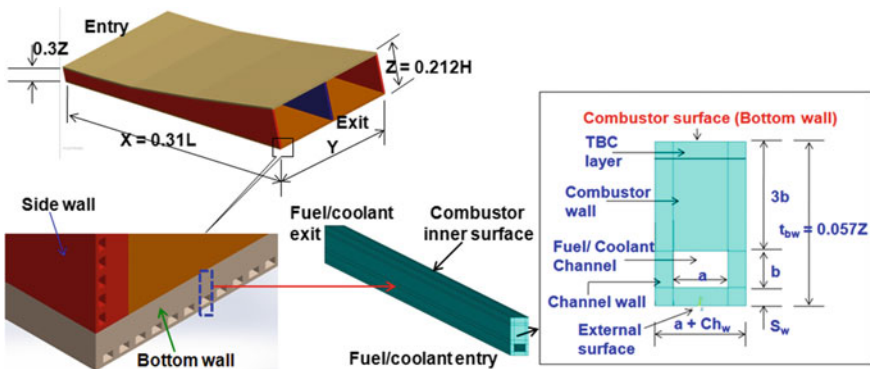


**Fig. 3** Scramjet combustor wall with jacket of cooling channels and cross-section detail of a channel with combustor wall

### 3 Heat Transfer Rate in the Coolant Channel

The coolant mass flow rate per channel is estimated from total fuel mass flow rate required for the combustion, rate of heat to be removed and number of coolant channels. The number of channels depend on geometry of the combustor wall and the channel size. A typical fuel flow rate of 0.325 kg/s per combustor module for the flight regime of Mach 6–7 is considered in the present study. Based on experience of earlier static tests as well as CFD simulations, it is assumed that amount of heat to be removed from the bottom wall is 30% of total amount of heat transfer to the combustor walls. The mass flow rate of coolant per channel in the bottom wall is 0.001741 kg/s. Convection heat transfer coefficient between coolant channel and regenerative coolant has been evaluated using classical engineering method for fully developed turbulent flow through smooth pipes. Petukhov's expression [6] is used for the calculation of heat transfer coefficient considering various isothermal wall conditions.

$$\text{Nu}_d = \frac{(f/8)\text{Re}_d \text{Pr}}{1.07 + 12.7(f/8)^{1/2}(\text{Pr}^{2/3} - 1)} \left( \frac{\mu_b}{\mu_w} \right)^n \quad (1)$$

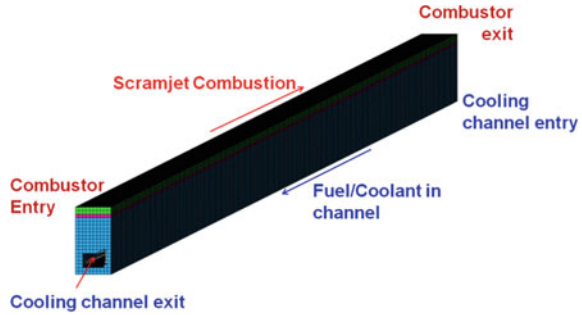
where  $f = (1.82 \log_{10} \text{Re}_d - 1.64)^{-2}$  and  $n = 0.11$ ,  $\text{Nu}_d$  is Nusselt number,  $\text{Re}$  is Reynolds number and  $\text{Pr}$  is Prandtl number. The  $\mu_b$  and  $\mu_w$  are dynamic viscosity of the coolant corresponds to bulk temperature and wall temperature, respectively.

JP-7 is chosen as fuel in the present case due to its better thermal stability and availability. Supercritical pressure condition of 50 bar is considered inside the channels. The heat transfer coefficient is of the order of 1900 W/m<sup>2</sup> K for average fuel temperature of 650 K. Thermo-physical and transport properties of the JP-7 fuel, obtained from NIST database, as a function of temperature and pressure are used in the analysis. Thermal conductivity, specific heat capacity, density, and dynamic viscosity of the JP-7 fuel at 300 K are 0.134 W/m K, 1980 J/kg K, 763 kg/m<sup>3</sup>, and  $9.0525 \times 10^{-4}$  N s/m<sup>2</sup>, respectively.

### 4 Heat Transfer Analysis Coupled with Fluid Flow

Three-dimensional steady-state heat transfer analysis coupled with fluid flow based on Finite element method (FEM) has been carried out for the regenerative fuel-cooled combustor wall. The analysis was carried out for a domain of combustor bottom wall having periodic symmetry using ANSYS software [7]. The finite element grid of coolant and combustor wall along with channel in the heat transfer analysis domain has been modeled using FLUID116 elements and SOLID90 element, respectively. Surface effect element, SURF152, with film coefficients has been used in between the coolant and channel wall to couple the convective heat transfer loads. The finite element mesh for heat transfer analysis domain is shown in Fig. 4. Grid independence

**Fig. 4** Finite element grid for heat transfer analysis domain of the regenerative fuel-cooled scramjet combustor wall



study has been carried out to arrive at a correct mesh size for the analysis domain. As a result, the combustor wall mesh consists of 143,986 nodes and 130,480 elements. Heat flux distribution of the scramjet combustor inner surface was obtained from N-S CFD simulation. The heat flux distribution along the length at bottom wall (at  $y = 0.25Y$ ) of the scramjet combustor corresponds to an isothermal wall condition of 300 K (Fig. 2) is in the range of 1–1.75 MW/m<sup>2</sup>. The convective heat transfer boundary conditions are applied on the inner surface of the combustor wall and inner surface of the coolant channel. The remainder of the cell perimeter is thermally insulated. Fuel temperature at inlet is 300 K. Advantage of this methodology is faster as compare to conjugate heat transfer analysis using CFD software. Temperature-dependent thermo-physical properties of the JP-7 fuel and combustor wall materials are used in the present analysis. Thermal conductivity of Cb-752, C-SiC, C-103, YS Zirconia, and Y<sub>2</sub>O<sub>3</sub> materials at room temperature condition is 37.5 W/m K, 15 W/m K, 37.4 W/m K, 1.04 W/m K, and 0.3 W/m K, respectively.

## 5 Thermal Design of Regenerative Fuel-Cooled Wall

In order to select the suitable materials of construction for regenerative fuel-cooled scramjet combustor wall, heat transfer analysis coupled with fluid flow was carried out considering the various combinations of materials of construction, wall thickness, location of the cooling channel, TBC, and bond coat material. Ten cases were analyzed. The counter flow between coolant inside the channels and hot gases of the combustor was considered for effective heat transfer. The hydrocarbon fuel undergoes cracking [8] when the temperature reaches to 773 K at the supercritical pressure condition. The cracking reaction alters the fuel properties which results drastic change in overall heat transfer coefficient and put in more complexity for thermal management. Hence, the major constraint of the thermal design is to maintain the fuel temperature within a limit of thermal stability of the fuel without undergoing any change in chemical composition during the channel flow.

The coolant channel is located away from the combustor wall inner surface for all the configuration of the combustor wall except case-1 and case-2. The TBC along

with the bond coat is considered on the inner surface of the combustor wall for the cases 5–10. In case-4, TBC along with bond coat is introduced between the combustor wall made of C-SiC material and coolant duct made up of Cb-752 material. The layer of  $Y_2O_3$  TBC is considered in addition to YSZ in case-6 while  $Y_2O_3$  is the TBC for the combustor wall from case-7 to case-10. In case-8,  $NbSi_2$  is considered as bond coat material in place of NiCoCrAlY because of its good compatibility between Niobium alloy (Cb-752 and C-103) and  $Y_2O_3$  TBC. The C-103 alloy is material of construction for combustor wall in the case-9 and case-10.

## 6 Results and Discussion

Result summary of heat transfer analysis of the regenerative fuel-cooled scramjet combustor wall for all the cases is given in Table 1. Due to the location of coolant channel away from inner surface of the combustor wall as shown in

**Table 1** Result summary of heat transfer analysis of the regenerative fuel-cooled Scramjet engine wall

Case	Combustor wall		TBC		Bond coat		Max. $T_f$ , K
	Material (thickness)	Max. $T_w$ , K	Material (thickness)	Max. $T_w$ , K	Material	Max. $T_w$ , K	
1	Cb-752 (3b)	1387	–	–	–	–	1291
2	C-SiC (3b)	1402	–	–	–	–	1249
3	Cb-752 (3b)	1398	–	–	–	–	1258
4	C-SiC (2b), Cb-752 (b)	1744, 1142	YSZ (0.5 mm)	1454	NiCoCrAlY	1151	1059
5	Cb-752 (2b)	1027	YSZ (1.5 mm)	2072	NiCoCrAlY	1034	933
6	Cb-752 (2b)	895	$Y_2O_3$ (0.5 mm) + YSZ (1.0 mm)	2376, 1454	NiCoCrAlY	902	817
7	Cb-752 (2b)	849	$Y_2O_3$ (1.0 mm)	2481	NiCoCrAlY	855	775
8	Cb-752 (2b)	850	$Y_2O_3$ (1.0 mm)	2478	$NbSi_2$	853	776
9	C-103 (1.5b)	851	$Y_2O_3$ (1.0 mm)	2478	$NbSi_2$	854	776
10	C-103 (1.5b)	1025	$Y_2O_3$ (0.5 mm)	2089	$NbSi_2$	1029	929

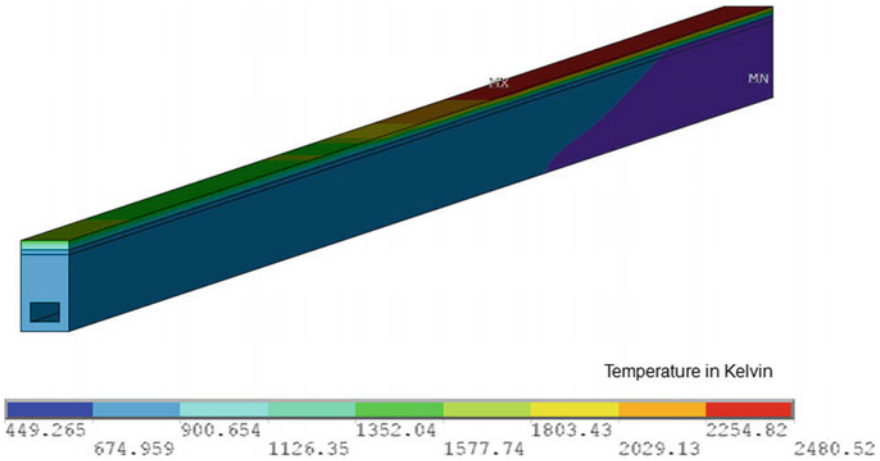


**Fig. 5** Wall temperature distribution of the combustor wall (case-8)

case-3, the coolant attains the temperature lesser than the configuration of case-1. Good reduction in the fuel temperature is observed due to presence of YSZ TBC between the combustor wall and coolant channel (case-4). In all the cases where TBC considered at inner surface of the combustor, temperature attained by the fuel as well as the combustor wall is lesser than that of case-4. The effectiveness of the YSZ TBC was improved by addition of  $Y_2O_3$  layer on its external surface and the fuel attains the temperature of the order of 817 K.

The wall temperature distribution of the combustor bottom wall for case-8 is shown in Fig. 5. The low thermal conductivity of the  $Y_2O_3$  results in significant reduction of wall temperature in the case-7, case-8, and case-9. And temperature attained by the coolant at exit of the channel for these cases is of the order of 776 K which is close to the thermal stability limit of hydrocarbon fuel (~773 K). The temperature distribution of the fuel and at various locations across the channel along with combustor wall for case-8 is shown in Fig. 6. Since thermal conductivity of Cb-752 and C-103 alloy is almost same, not much change in results of the analysis for case-8 and case-9. The temperature distribution of Cb-752 material portion of the combustor wall at cross-section  $x = 0.75X$  for case-8 is shown in Fig. 7. As layer thickness of  $Y_2O_3$  TBC decreased by half of the value in case-10 compared to that of case-9, significant rise in the combustor wall temperature as well as fuel temperature is observed. It is observed from the analysis that TBC along with regenerative cooling is playing a major role in reducing the engine wall temperature thereby the fuel temperature inside the channels. The scramjet engine wall configuration of case-8 and case-9 having Cb752/C-103 material and 1.0 mm thick  $Y_2O_3$  TBC along with compatible bond coat of  $NbSi_2$  is the feasible solution for long-duration flight.

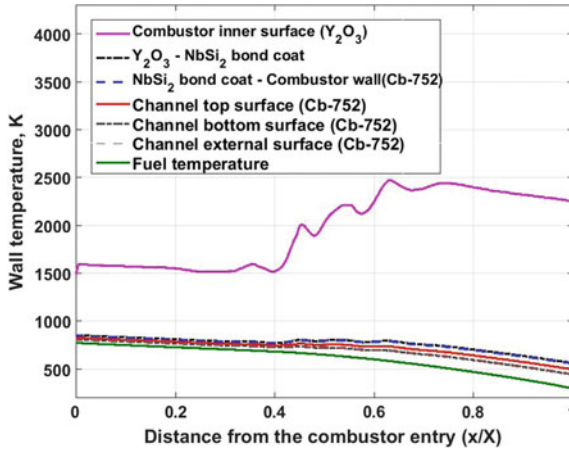


Fig. 6 Temperature distribution at various locations across the combustor wall

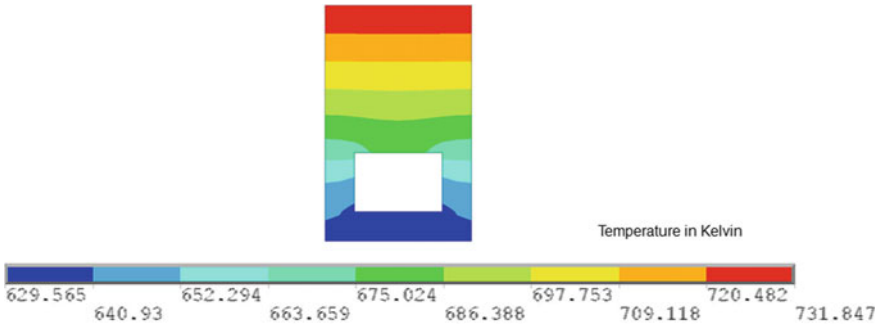


Fig. 7 Wall temperature distribution of the combustor wall (Cb-752 material) at cross-section  $x = 0.75X$  (case-8)

### 7 Conclusion

Thermal design methodology for regenerative cooled engine walls considering physical heat sink of the hydrocarbon fuel has been presented. The procedure encompasses a three-dimensional transfer analysis coupled with fluid flow based on FEM for thermal response study of regeneration cooled combustor wall configuration and selection of materials of construction. The methodology has been applied to the scramjet engine combustor walls with constraint to maintain coolant temperature within the thermal stability limit. The thermal load corresponds to the realistic operating condition of the engine for a cruise flight has been considered in the analysis. All the materials considered in the study present feasible thermal design of combustor wall. Due to high thermal resistance, TBC along with regenerative cooling is playing a major role in reducing the wall temperature thereby the fuel temperature inside the

channels. In the present application, Cb752/C-103 material with 1 mm thick  $Y_2O_3$  TBC having compatible bond coat of  $NbSi_2$  remains viable solution for the regenerative fuel-cooled scramjet engine walls. Finalized configuration of combustor wall is being pursued for the fabrication and testing.

## References

1. Heiser WH, Pratt DT (1994) Hypersonic airbreathing propulsion. AIAA Education Series, Washington, DC
2. Zhang S (2016) *J Propuls Power* 32(1)
3. Valdevit L (2008) *J Appl Mech* 75:061022
4. Qin J (2012) *J Thermophys Heat Transf* 26(4)
5. Zhang D (2016) *J Propuls Power* 32(3)
6. Holman JP (2008) Heat transfer, 10th edn. McGraw-Hill Book Co.
7. ANSYS FLUENT User's Manual (2017) Thermal analysis guide. ANSYS, USA
8. Wickham DT (2005) In: 41st AIAA/ASME/SAE/ASEE joint propulsion conference & exhibit, AIAA 2005-3916, Arizona, pp 1–13



# Computational Studies of Shock Wave Boundary Layer Interactions in Hypersonic Flow Over Double Cone Geometries



Siva Vayala and Ravi K. Peetala

**Abstract** Shock wave boundary layer interactions in the flows over high speed vehicles are considered to be challenging and essential to analyze. Importance of analyzing these for the design of thermal protection system brought it under the active research in the field of compressible flows. In this scenario, an attempt has been made to study the laminar shock wave boundary layer interactions in hypersonic flows over double cone geometry numerically to obtain thermal load variations as well as surface pressure variations on the surface of the vehicle. An open-source CFD tool OpenFOAM based on the finite volume method is used for the current study. The numerical solution captures all important features of the flow accurately and the obtained results are following the corresponding trend and matching with experimental results. Since slope limiters are capable of causing significant changes in the solution, two different slope limiters—vanLeer and superbee—have been used to check the influence on the solution. It is found that the superbee limiter is more accurate than vanLeer but inducing spurious spatial oscillations.

**Keywords** Hypersonic flows · Double cone configurations · OpenFOAM

## 1 Introduction

The future possibilities of hypersonic flow applications in civilian transport, defense sector as well as in space technology kept researchers carrying their work in the field of compressible flows. Hypersonic flows with the speed five times more than the sound speed has its own significance in the compressible flows from supersonic, transonic, and subsonic flows. It involves numerous complex phenomena that made it as a special category of supersonic flows. These include shock–shock interactions, shock wave boundary layer interactions (SWBLI), and high-temperature effects such

---

S. Vayala · R. K. Peetala (✉)

Department of Mechanical Engineering, Visvesvaraya National Institute of Technology, Nagpur, Maharashtra 440010, India

e-mail: [rkpeetala@mec.vnit.ac.in](mailto:rkpeetala@mec.vnit.ac.in)

© Springer Nature Singapore Pte Ltd. 2020

H. K. Voruganti et al. (eds.), *Advances in Applied Mechanical Engineering*,

Lecture Notes in Mechanical Engineering,

[https://doi.org/10.1007/978-981-15-1201-8\\_32](https://doi.org/10.1007/978-981-15-1201-8_32)

as vibrational excitation, dissociation, and ionization. The presence of these phenomena in numerous applications of external as well internal flows gives a lot of importance to hypersonic flows. Out of many complex processes that hypersonic flows involved, shock–shock interactions and shock wave–boundary layer interactions grabbing the attention of researchers. Presence of these processes may induce massive thermal as well as mechanical loads on the surface of the space vehicles. The inevitable presence of boundary layer and shocks in hypersonic flows give chances to SWBLI which induces adverse pressure gradient inside the boundary layer. These results separated flows in the boundary layer accompanied by two or more additional shocks. Separation starts with separation shock and ends with reattachment shock. Flow passes through the reattachment shock will experience a large rise in temperature, which gives large thermal loads to the vehicle surface. A conscious study has to be carried out to understand and analyze these phenomena in the design of the thermal protection system of the space vehicles.

Many researchers have done experimental and computational studies on the SWBLI over many canonical geometries. Out of those, double cone configuration got importance due to its sensitivity to hypersonic flows and its ability to produce most of the possible complexities which are useful for the design aspects of space vehicles. Olejniczak et al. [1] have studied different shock interactions—type IV, V, V and a new interaction on double-wedge geometries computationally and stated that very fine mesh is required to capture these interactions accurately. Holden and Wadhams [2] and Candler et al. [3] have conducted experimental studies of hypersonic flows over double cone configurations to provide the benchmark dataset and to mitigate the preexisting differences between experimental and computational results. Gaitonde and Canupp [4] carried out numerical studies on the double cone hypersonic flows and concluded small changes in flow parameters, and numerical aspects give moderate changes in the flow properties. Later Candler et al. [5] extended his studies through computational works in which he stated possible reasons for the discrepancies between experimental and computational results. In this study, it is concluded that providing the incorrect free stream conditions is the main reason for these deviations of computational results from experimental results. Druguet et al. [6] analyzed a steady hypersonic flow over double cone configurations numerically and provided the insight of different numerical schemes and slope limiters that can be used for compressible flow simulations. It is concluded that less dissipation schemes and limiters provide an accurate solution and it is also shown that solution with very fine mesh will be independent of the changes in the numeric.

The present study focuses on the validation aspects of shock wave–boundary layer interactions over a sharp edge 25–55° double cone geometry at Mach number 11.30 using OpenFOAM.

## 2 Numerical Methodology

An open-source C++ based CFD toolbox OpenFOAM is used for numerical studies based on the finite volume method (FVM). A density-based solver named “*rhoCentralFoam*” based on central-upwind schemes of Kurganov and Tadmor for flux calculations at cell faces has been used for the current study. This solver solves fundamental governing equations in two steps—predictor and corrector. In prediction step, inviscid and convective terms of the conservative variables ( $\rho$ ,  $\rho u$ ,  $\rho e$ ) are treated explicitly from which primitive variables ( $\rho$ ,  $u$ ,  $T$ ) are calculated. In corrector step, earlier predicted primitive variables are corrected implicitly by adding viscous and diffusion terms. Courant number is chosen 0.5 and the time step is chosen according to the stability criteria.

The governing equations are given below.

Conservation of mass:

$$\left(\frac{\partial \rho}{\partial t}\right) + \nabla \cdot (u\rho) = 0 \quad (1)$$

Conservation of momentum:

$$\left(\frac{\partial(\rho u)}{\partial t}\right) + \nabla \cdot [u(\rho u)] + \nabla p + \nabla \cdot T = 0 \quad (2)$$

Conservation of total energy:

$$\left(\frac{\partial(\rho E)}{\partial t}\right) + \nabla \cdot [u(\rho E)] + \nabla \cdot [u p] + \nabla \cdot (T \cdot u) + \nabla \cdot j = 0 \quad (3)$$

where the total energy density  $E = e + \frac{1}{2}U^2$ , specific internal energy  $e = c_v T$ , diffusive heat flux  $j = -k\nabla T$  (Fourier’s law of heat conduction), and  $T$  is the viscous stress tensor, assumed positive in compression. The detailed algorithm is provided by Greenshields et al. [7].

## 3 Results and Discussion

### 3.1 Validation Studies

The present study focuses on the shock wave–boundary layer interactions in hypersonic flows over a 25–55° sharp edge double cone configuration. The geometrical details are same as that of Candler [3] and corresponding geometry with the sample mesh structure used for simulation is shown in Fig. 1. The axisymmetric boundary condition is applied to the axis of the cone to facilitate 2D simulation of the double

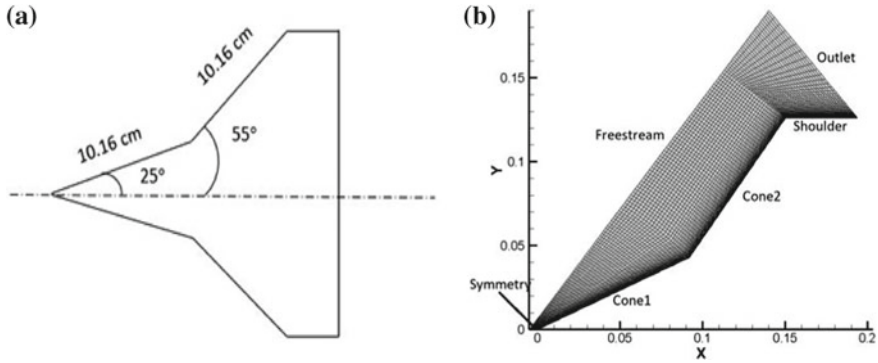


**Fig. 1** Schematic of **a** geometrical configuration; **b** sample structured mesh

cone. Nitrogen is used as test gas with free stream Mach number of 11.30 and free stream temperature of 138.9 K with wall temperature of 296 K is same as that of Druguet et al. [6]. Kurganov–Tadmor flux scheme with superbee interpolation has been used for the simulations. Separation bubble size is taken as a parameter for the validation due to its sensitivity to the changes in the flow. This separation region can be measured from the variations of surface properties like surface pressure, surface heat flux, skin friction coefficient, etc., due to its strong influence on the surface properties. In surface pressure variation, sudden rise on first cone and peak value on the second cone represents starting and endings of the separation zone. The numerical results of present studies are validated with well-established experimental results of Holden and Wadhams [2]. The simulation results shown in Fig. 2 are following the corresponding trend and well in agreement with experimental results.

### 3.2 Effect of Slope Limiter

From the earlier studies, it is concluded that the selection of limiter has a significant effect on the accuracy of the solution. vanLeer limiter is recommended for all kinds of compressible flow simulations due to its less dissipation characteristics. Despite being more accurate than vanLeer limiter, superbee is not used as much as vanLeer due to its nature of inducing spatial oscillations in the flow properties. The present study investigated the ability of both the limiters vanLeer and superbee in providing an accurate solution for the same grid. It is found that for sufficiently fine mesh  $512 \times 256$  with  $5 \times 10^{-7}$  m near wall spacing, superbee is significantly more accurate than vanLeer with negligible oscillations in surface properties which are shown in Fig. 3. It is also observed that superbee oscillations are grid-dependent and diminishes with grid refinement. To investigate the dependency of superbee limiter on the grid in producing oscillations, three different meshes  $128 \times 64$ ,  $256 \times 128$ , and  $512 \times 256$  with appropriate near wall spacings have been considered. Out of three meshes

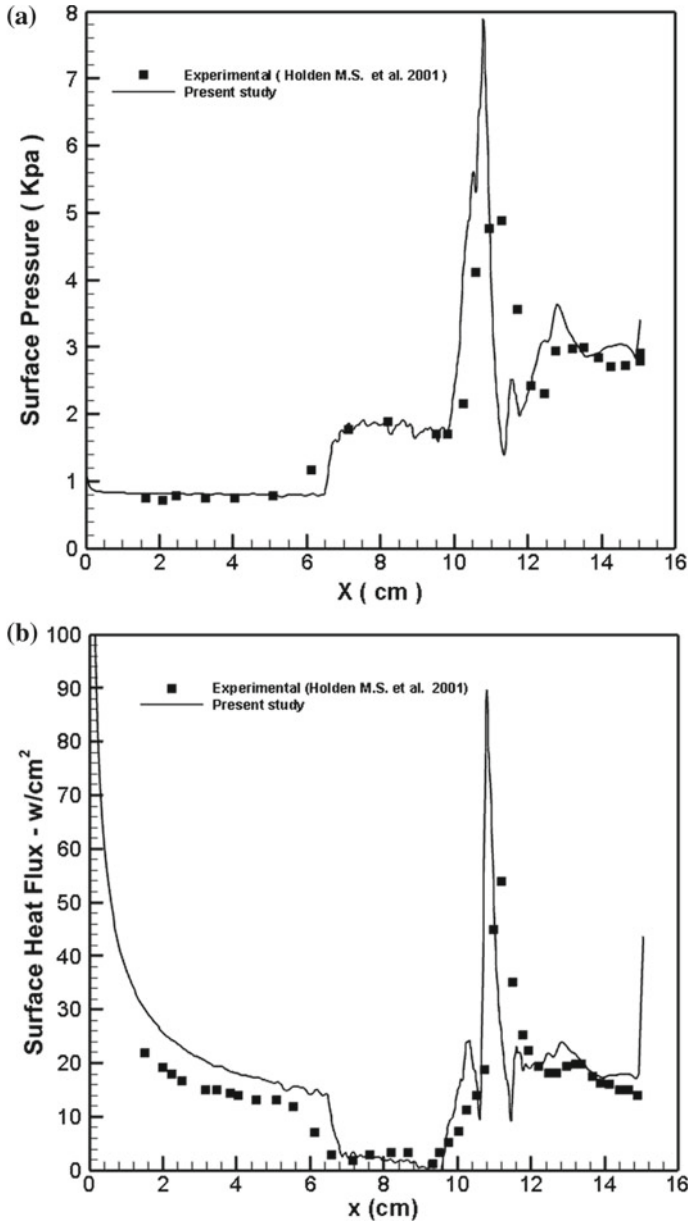


Fig. 2 Variation of surface properties along the streamwise direction a surface pressure; b surface heat flux

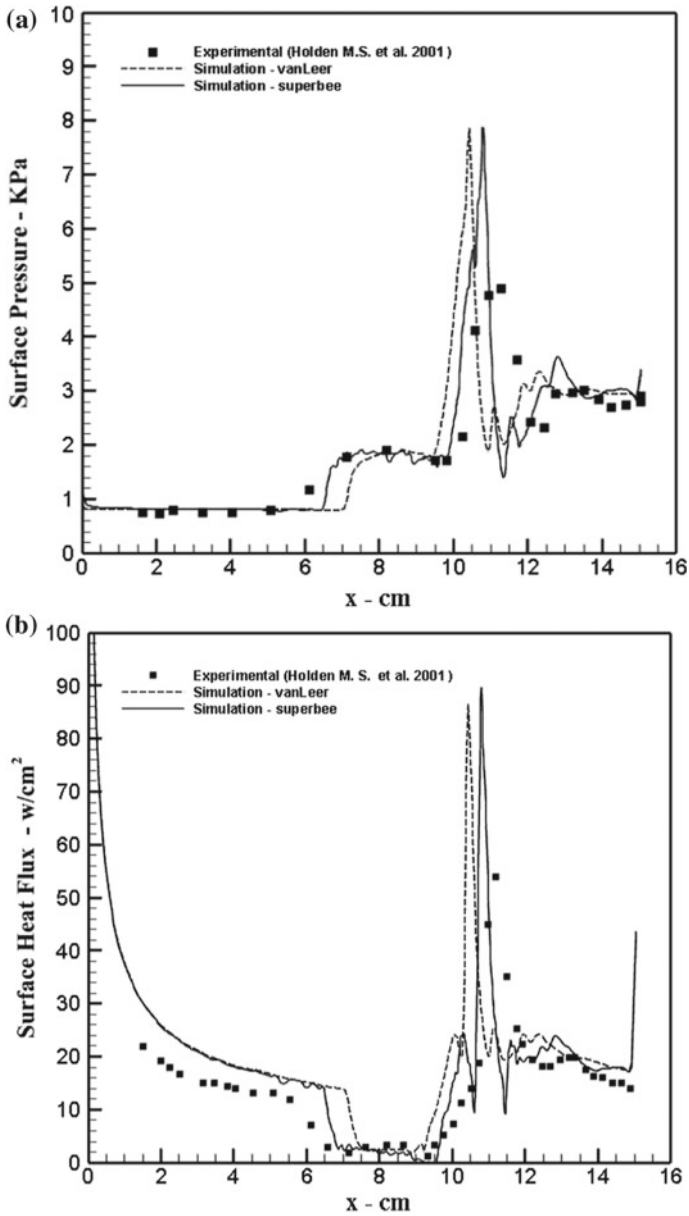
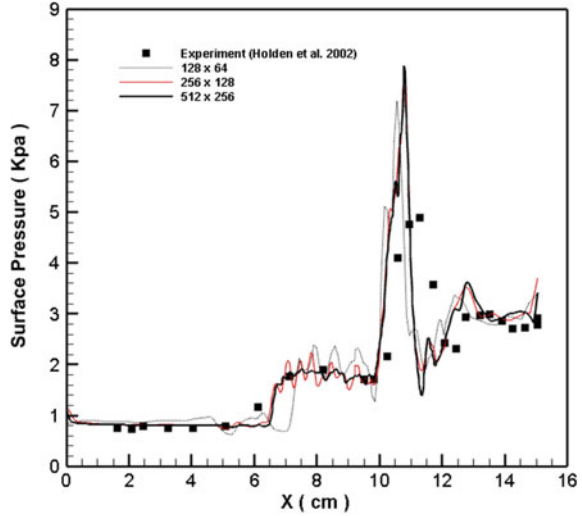


Fig. 3 Effect of slope limiter on surface properties a surface pressure; b surface heat flux

**Fig. 4** Grid independence studies of superbee limiter



**Table 1** Grid refinement details at important sections

S. No.	Mesh	Min. element near the wall $\Delta y_{min}$	Min. element near leading edge $\Delta x_{min,le}$	Min. element at cone-cone junction $\Delta x_{min,junc}$
1	128 × 64	$5 \times 10^{-5}$	$5 \times 10^{-4}$	$4 \times 10^{-4}$
2	256 × 128	$5 \times 10^{-6}$	$5 \times 10^{-5}$	$4 \times 10^{-5}$
3	512 × 256	$5 \times 10^{-7}$	$5 \times 10^{-6}$	$4 \times 10^{-6}$

chosen, 256 × 128 and 512 × 256 are showing the same separation size and similar trends of surface properties. But oscillations with 512 × 256 mesh are in negligible magnitude than 256 × 128 mesh. So, 512 × 256 mesh is chosen as an optimum mesh from grid-independent studies and used for further studies. Grid-independent study results are shown in Fig. 4. Corresponding grid refinement details at important sections like leading edge, cone-cone junction, near wall region, etc., are provided in Table 1.

## 4 Conclusion

The numerical analysis of laminar shock wave-boundary layer interactions over a double cone configuration has been carried out using OpenFOAM. The results obtained from the computational studies are sharing the corresponding trend and are in good agreement with the experimental results. Effect of slope limiters also studied to check the accuracy of superbee and vanLeer limiters in providing an

accurate solution and found that for same grid structure, superbee is considerably more accurate than the vanLeer. It is also observed superbee limiter's ability to produce spurious oscillations is strongly dependent on the grid and diminishes with grid refinement.

## References

1. Olejniczak J, Wright MJ, Candler GV (1996) Numerical study of shock interactions on double wedge geometries. AIAA Paper
2. Holden MS, Wadhams T (2001) Code validation study of laminar shock/boundary layer and shock/shock interactions in hypersonic flow. Part A: experimental measurements. AIAA Paper 2001-1031A
3. Candler GV, Nompelis I, Holden MS (2000) Computational analysis of hypersonic laminar viscous–inviscid interactions. In: 38th AIAA aerospace sciences meeting and exhibit, 10–13 Jan 2000
4. Gaitonde DV, Canupp PW (2002) Heat transfer predictions in a laminar hypersonic viscous/inviscid interaction. *J Thermophys Heat Transf* 16(4)
5. Candler GV, Nompelis I, Druguet M-C, Holden MS, Wadhams TP, Boyd ID, Wang W-L (2002) CFD validation for hypersonic flight: hypersonic double-cone flow simulations. In: 40th AIAA aerospace sciences meeting and exhibit, 14–17 Jan 2002
6. Druguet M-C, Candler GV, Nompelis I (2005) Effect of numerics on Navier–Stokes computations of hypersonic double-cone flows. *AIAA J* 43(3)
7. Greenshields CJ, Weller HG, Gasparini L, Reese JM (2010) Implementation of semi-discrete, non-staggered central schemes in a collocated, polyhedral, finite volume framework, for high-speed viscous flows. *Int J Numer Methods Fluids* 63(1):1–21



# Thermal Design and Testing of External Protuberance of Hypersonic Carrier Vehicle Airframe



G. Vijayakumar, S. Narendar and J. Justina Geetha

**Abstract** Hypersonic carrier vehicle airframe experiences high rate of heat transfer caused by aerodynamic heating due to very high-speed flow during flight. A wire tunnel over the carrier vehicle is used to accommodate the communication and electric cables routed along the external surface of rocket motor casing from electronics packages section to rear part of the carrier vehicle. The wire tunnel leading edge forms an external protuberance. The protuberances are subjected to severe heating during the flight, especially at hypersonic speed. Thermal design of the protuberance structure is imperative to ensure safe operation in the severe thermal environment experienced during flight. This paper describes the thermal design of wire tunnel protuberance. Further, the design of wire tunnel assembly is ascertained by thermal test conducted in the infrared heating facility for aerodynamic heating condition corresponding to the flight trajectory.

**Keywords** Hypersonic vehicle · Wire tunnel · Aerodynamic heating and thermal design

## 1 Introduction

A flying vehicle like missile airframe experiences aerodynamic heating caused by very high-speed flow during launch phase, especially at hypersonic speed [1, 2]. This effect is dominant at protuberances due to the effect of wedge compression. The wire tunnel assembly on missile forms the external protuberance that must survive in severe aerodynamic heating environment. The leading edge attached to the front segment of the wire tunnel experiences severe rate of heat transfer due to three-dimensional wedge compression flow and flow disturbances on the flat region due to protrusion wedge angle.

---

G. Vijayakumar (✉) · S. Narendar · J. Justina Geetha  
Defence Research and Development Laboratory, Hyderabad 500058, India

S. Narendar  
e-mail: [narendar@drdl.drdo.in](mailto:narendar@drdl.drdo.in)

© Springer Nature Singapore Pte Ltd. 2020  
H. K. Voruganti et al. (eds.), *Advances in Applied Mechanical Engineering*,  
Lecture Notes in Mechanical Engineering,  
[https://doi.org/10.1007/978-981-15-1201-8\\_33](https://doi.org/10.1007/978-981-15-1201-8_33)

This paper depicts the thermal design of wire tunnel assembly. The thermal design is involved in the estimation of heat flux distribution over the wire tunnel leading-edge protrusion and selection of suitable material of construction along with wall thickness by considering thermal response analysis of wire tunnel assembly. The aerodynamic heating analysis is used for the prediction of augmented heat flux distribution over the protuberance. Wall temperature prediction is required to verify whether proper material is used in the construction so that it retains its strength at elevated temperatures. Parametric study has been carried out considering various parameters such as protrusion leading-edge angle, geometry, wall thickness, and material of construction. Based on the thermal design and analysis, front segment of the wire tunnel configuration with variable wall thickness has been finalized. The methodology for the evaluation of heat flux distribution, prediction of wall temperature distribution, and selection of wall thickness based on the parametric study is discussed in this paper.

## 2 System Description

Typical hypersonic carrier vehicle configuration and location of the wire tunnel are shown in Fig. 1. The missile is considered to fly in atmosphere at a Mach number as high as 6–8. The missile experiences severe aerodynamic heating due to high acceleration during propulsion system operation.

The enlarged view of front segment of the wire tunnel assembly mounted on the airframe is shown in Fig. 2. Communication and electric cables are routed along the external surface of rocket motor casing from electronics packages section to rear part of the carrier vehicle. The cables are housed inside the wire tunnel. The wire tunnels are provided to protect the cables from high-speed flow and aerodynamic heating during flight. The wire tunnel protuberance forms three-dimensional compression corner for the high-speed flow and its half-wedge angle is  $30^\circ$ . Material of construction is mild steel. The design criteria of the wire tunnel are based on the strength and stiffness requirements, with the objective of minimum weight.

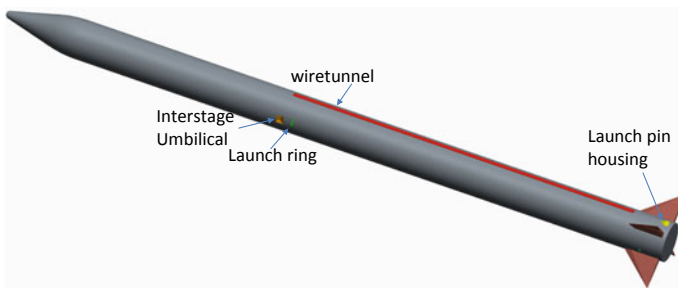


**Fig. 1** Typical hypersonic carrier vehicle configuration

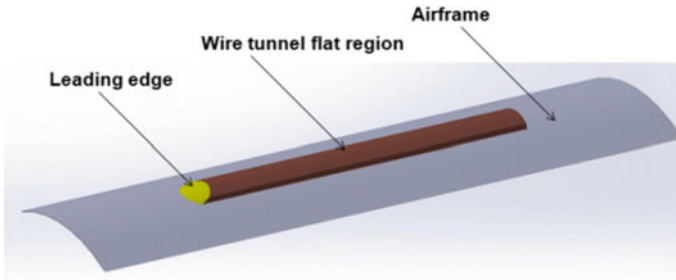


Fig. 2 Front segment of the wire tunnel assembly mounted on airframe

### 3 Methodology of Heat Transfer Analysis

A computer code [3, 4] developed in-house has been used for the estimation of heat flux distribution due to aerodynamic heating over the wire tunnel assembly. It is a versatile code based on the classical engineering methods using well-established correlations. The code estimates the distribution of local flow properties over the airframe surface including protrusion, which is explained in the following sections.

#### 3.1 Local Flow Properties

For the estimation of heat transfer rate on the external protuberance of hypersonic carrier vehicle, the leading edge has been considered as an inclined plane with the wedge angle. At hypersonic speeds, thermal boundary layer over the external protuberance becomes very thin, and leads to higher pressure which results in higher rate of heating [2]. During flight, the hypersonic carrier vehicle experiences various combinations of flight parameters like altitude, velocity, and angle of attack. It results in time-varying local flow parameters distribution over the airframe surface. The local pressure distribution on the airframe with respect to missile attitude has been computed using modified Newtonian theory. The local pressure ( $P_L$ ) on the external protuberance is calculated from the pressure coefficient using Eq. (1),

$$C_P = \frac{P_L - P_\infty}{P_{dyn}} = C_{Pmax} \cos^2(90 - (\alpha + \theta_w)) \tag{1}$$

The  $P_\infty$ ,  $\alpha$ , and  $\theta_w$  are free-stream static pressure, angle of attack, and wedge angle, respectively. The  $C_{Pmax}$  is the maximum pressure coefficient corresponding to the stagnation pressure.  $P_{dyn}$  is the dynamic pressure. From the estimated local pressure distribution, the other local flow parameters are calculated using isentropic relations.

### 3.2 Heat Flux Estimation

Heat flux distribution over the external surface of the protrusion has been estimated using Eckert's reference enthalpy method [5]. The heat flux is estimated using Eckert's relation

$$\dot{q}_w = St^* \rho^* V_e (h_{aw} - h_w) \quad (2)$$

Reference Stanton number  $St^*$  has been calculated using the relation corresponding to turbulent flow conditions.

The  $h_{aw}$  and  $h_w$  are specific enthalpy corresponding to adiabatic wall temperature and updated wall temperature, respectively. The  $V_e$  is the velocity at the edge of the boundary layer, and air density  $\rho^*$  is calculated from the perfect gas law. The air properties used in the calculation of heat flux have been considered as a function of temperature and pressure, taking into account of real gas effect as well [5]. Indian Standard Atmosphere Data is used in the heat flux estimation.

### 3.3 Heat Conduction Analysis

Transient three-dimensional heat conduction analysis has been carried out using convective heat flux boundary condition [6]. Temperature-dependent thermo-physical properties of the materials are considered in the present analysis. The finite element mesh of the wire tunnel front segment including leading edge is shown in Fig. 3.

**Fig. 3** Finite element mesh of wire tunnel segment-1



### 4 Thermal Design and Analysis

The thermal design of the wire tunnel has been carried out in following steps. The heat transfer analysis of aerodynamic configuration of the wire tunnel front segment was carried out as a design check considering specified wall thickness of  $0.039 h$ . In order to reduce the heat flux as well as the wall temperature, a parametric study on protrusion ramp angle was carried out considering  $30^\circ$ ,  $21.75^\circ$ , and  $15^\circ$ . The comparison of heat flux profiles, correspond to isothermal wall condition of  $300\text{ K}$ , for specified ramp angles of the wire tunnel is shown in Fig. 4. The heat flux at the leading-edge protuberance for the ramp angles of  $30^\circ$ ,  $21.75^\circ$ , and  $15^\circ$  is of the order of  $2.09\text{ MW/m}^2$ ,  $1.56\text{ MW/m}^2$  and  $1.07\text{ MW/m}^2$ , respectively. The aerodynamic configuration of the wire tunnel leading edge with  $30^\circ$  protrusion angle is shown in Fig. 5a. As the heat flux decreases with decrease in ramp angle, minimum possible

**Fig. 4** Comparison of heat flux versus time for various ramp angles

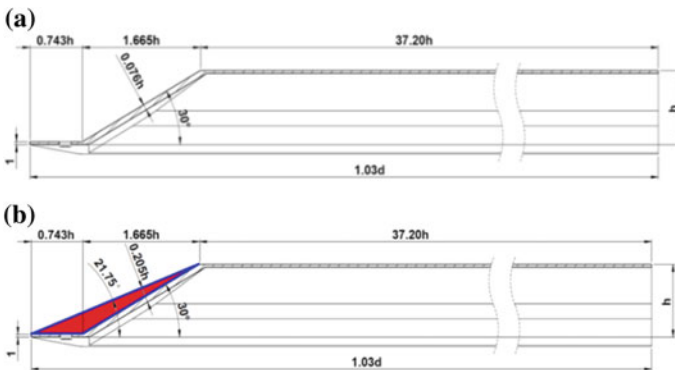
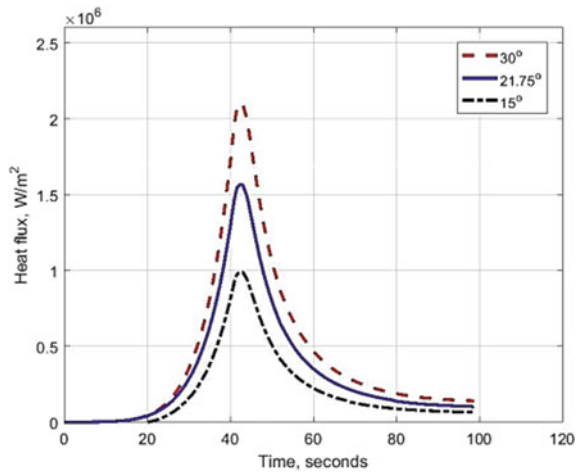


**Fig. 5** a aerodynamic configuration and b modified configuration of the wire tunnel

ramp angle of  $21.75^\circ$  has been arrived out based on the constraint of wire tunnel height, space available ahead of ramp region, and mounting scheme. An additional block of material is considered at the leading-edge region of the wire tunnel to increase the heat capacity as well as to form a minimum possible protrusion ramp angle as shown in Fig. 5b.

Further, the transient heat transfer analysis of modified wire tunnel assembly was carried out by applying heat flux boundary condition for the flight duration of 101 s. The heat flux distribution over flat portion of the wire tunnel assembly for various isothermal wall conditions has been obtained from N-S CFD analysis. The stiffeners inside the wire tunnel was also considered in the analysis. Based on the analysis, wall thickness varying from  $0.039 h$  to  $0.23 h$  is chosen over a length of  $2.88 h$  for flat region of the wire tunnel leading edge. Final configuration of the wire tunnel assembly and materials of construction are shown in Fig. 6. The wall temperature distribution and wall temperature time history at various locations of the wire tunnel assembly are shown in Fig. 7 and Fig. 8, respectively. The predicted linear deformation due to thermal expansion is 2 mm and is shown in Fig. 9.

**Fig. 6** Final configuration of the wire tunnel and its materials of construction

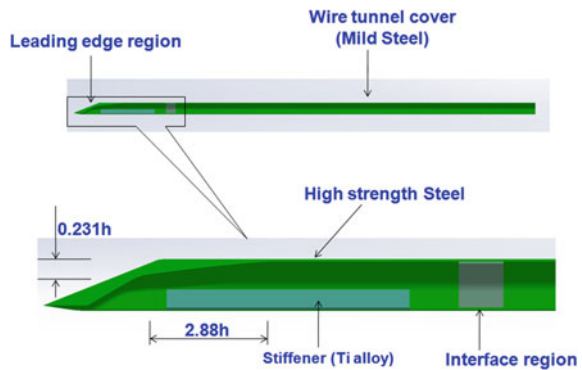


**Fig. 7** Wall temperature distribution of the wire tunnel assembly at 101 s

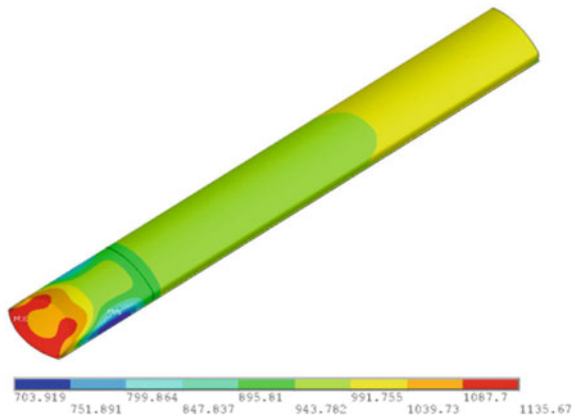


**Fig. 8** Wall temperature versus time profiles at various locations of the wire tunnel

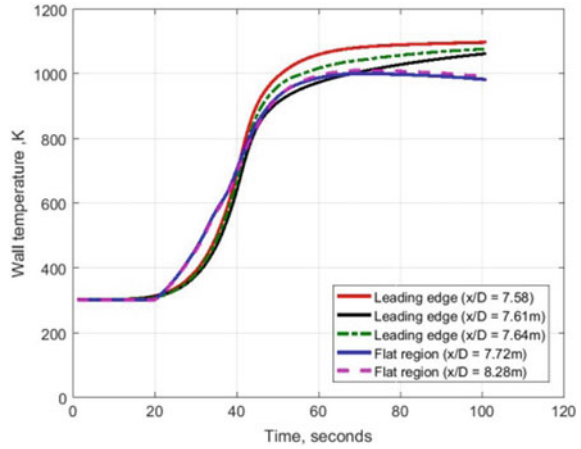
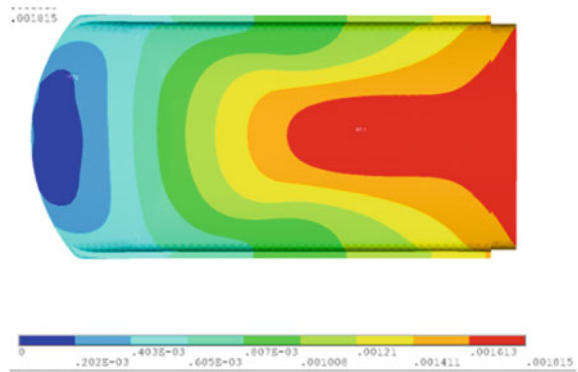


**Fig. 9** Linear expansion distribution over leading edge of the wire tunnel



## 5 Thermal Test

Thermal test of the wire tunnel was carried out in IR heating facility using closed-loop temperature control. The control system of the facility is embedded with industrial form of the three-term (PID) controller. Two thermocouples bonded on leading-edge portion and three thermocouples bonded on the surface of the wire tunnel were used for the purpose of temperature control. By using the thermocouple sensor output as the feedback for the PID controller, the heat intensity of the IR lamp was controlled as per specified input temperature profile.

The wire tunnel assembly was placed in horizontal position during the test. The IR heaters were positioned in front of the wire tunnel assembly at a distance of 0.0307 h. Two sets of cables were routed through the wire tunnel assembly as in the case of flight hardware assembly. The cables were connected to the data acquisition system and protected by thermal insulation as per flight configuration. The additional length of the cable that extended from the wire tunnel assembly was also thermally

protected. The opened exit of the wire tunnel was also covered with silica cloth to avoid direct heating of inner surfaces. The functionality of the cables has also been ensured during the thermal test.

The wire tunnel assembly withstood the thermal loads without any visual observations. The feed-back controlled temperature profile on the wire tunnel surface is shown in Fig. 10. The controlled temperature profile is in very good agreement with the input. The maximum temperature measured on the thermal insulation cloth of cables is 748 K. All the measured temperatures are within the specified limits with respect to the predicted temperature profiles. The deformation measured at the end of the wire tunnel is plotted in Fig. 11. The maximum deformation measured is 2.639 mm at the end of 100 s and is in good agreement with the prediction. The snapshot of the wire tunnel assembly after the thermal test is shown in Fig. 12. The

**Fig. 10** Controlled temperature profile at external surface of leading-edge portion

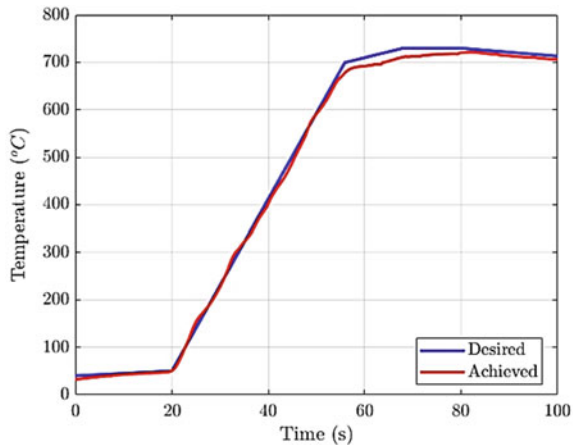


**Fig. 11** Measured deformation during wire tunnel thermal test

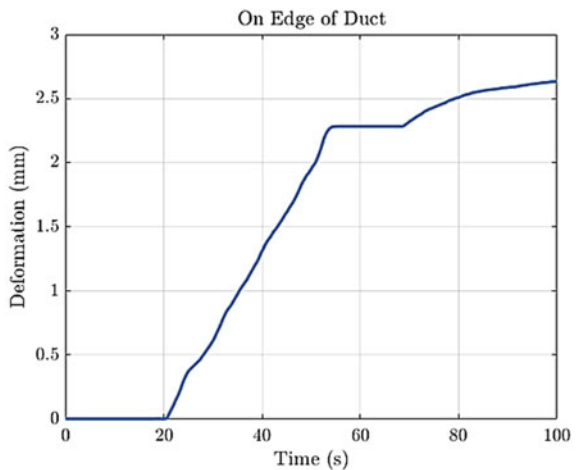




**Fig. 12** Wire tunnel assembly after thermal test



structural integrity of the wire tunnel assembly has been ensured from the thermal load point of view for intended application.

## 6 Conclusions

The thermal design of wire tunnel protuberance has been presented considering rate of heat transfer arising out of the carrier vehicle flying at hypersonic speed. The wall temperature of wire tunnel leading-edge region is brought down to acceptable strength limit by the design of variable wall thickness along the length. An extensive parametric study carried out has made it possible to finalize the configuration of wire tunnel front segment. The design has been validated through thermal test of the wire tunnel assembly in IR heating test facility.

## References

1. Anderson JD (1989) Hypersonic and high temperature gas dynamics. McGraw-Hill Inc., New York
2. Bertin JJ (1994) Hypersonic aerothermodynamics. AIAA Education Series, Washington, DC
3. Heiser WH, Pratt DT (1994) Hypersonic airbreathing propulsion. AIAA Education Series, Washington, DC
4. Vijayakumar G (2007) A report on methodology for kinetic heating analysis. Internal Technical Report, DRDL/DOP/HTD/2007-190
5. Holman JP (1997) Heat transfer, 8th edn. McGraw-Hill Book Co.
6. ANSYS User's Manual (2017) Thermal analysis guide. ANSYS, USA

# The Effect of Diesel and Biodiesel Blends on CI Engine Performance and Emission Characteristics



J. Venkatesu Naik, K. Kiran Kumar, S. Venkata Sai Sudheer  
and Mahesh Pallikonda

**Abstract** The present work aims to present the suitability of pure jatropha biodiesel and its blends as diesel engine fuel. The jatropha biodiesel is prepared by the alkaline-catalysed transesterification process. The biodiesel blends are prepared in the proportions of 20, 40, 60 and 80%. Experiments are conducted on a single-cylinder water-cooled diesel engine at various loads. The performance characteristics are analysed in terms of brake thermal efficiency and brake specific fuel consumption. The brake thermal efficiency of the engine decreases with increasing proportion of jatropha biodiesel. The exhaust emissions such as HC and CO are reduced as compared with neat diesel. However, NO<sub>x</sub> emissions are increased. Overall the 20% jatropha biodiesel blend is suitable alternate fuel for a diesel engine without any modifications.

**Keywords** Jatropha biodiesel · Diesel engines · Combustion · Emissions

## 1 Introduction

The development in science and technology in the diverse engineering sectors results in an improvement in the living standards of the human beings. Among those diverse engineering sectors, the automobile industry is one of crucial importance because it majorly serves in transportation and agricultural field. The latest development in automobile field gives fruit full benefits to mankind, however, on the other side it causes depletion of fossil fuels which results in increase in fuel cost and it also increases global warming due to the exhaust emissions of the engines. So, the scientific community is focusing on alternative sources of energy which can give the same amount of mechanical energy produced by fossil fuels with low emissions.

---

J. Venkatesu Naik (✉)  
SoET, SPMVV, Tirupati, Andhra Pradesh 517502, India  
e-mail: [jatrothurahul@gmail.com](mailto:jatrothurahul@gmail.com)

K. Kiran Kumar · S. Venkata Sai Sudheer · M. Pallikonda  
National Institute of Technology, Warangal, Warangal, Telangana 506004, India

© Springer Nature Singapore Pte Ltd. 2020  
H. K. Voruganti et al. (eds.), *Advances in Applied Mechanical Engineering*,  
Lecture Notes in Mechanical Engineering,  
[https://doi.org/10.1007/978-981-15-1201-8\\_34](https://doi.org/10.1007/978-981-15-1201-8_34)

In order to full fill above requirements, biodiesel is a lucrative option. Biodiesel can be made from non-consumable vegetable product oil such as the Pongamia, Karanja, Neem, etc. [1]. Usages of biodiesel as fuel in internal combustion engines, the emissions are greatly reduced. However, there is a penalty in the performance characteristics such as brake power, brake thermally efficiency (BTE) and brake specific fuel consumption (bsfc) as compared with neat diesel.

There are numbers of scientists conducted experiments using biodiesel to study the engine performance and exhaust emissions characteristics. For example, Mallikappa et al. [2] conducted experiments on a double cylinder compression ignition engine with cardanol biodiesel. They conducted experiments on the biodiesel blends of 10%, 15%, 20% and 25%, respectively. From their results, they observed that the 20% biodiesel blend fuel has higher BTE with low emissions. However, it also observed that CO emissions are increased with increase of biodiesel proportions more than 20%. Raj et al. [3] conducted tests on a single cylinder four-stroke diesel engine at a constant speed of 1500 rpm. They used cottonseed biodiesel blends (BD10 and BD20) with isobutanol of 5 and 10%. From the experimental results, they concluded that the use of cottonseed oil with and without isobutanol has a similar influence on engine performance. However, the HC emissions are increasing with the increase of isobutanol. They proposed B20 + 10% isobutanol fuel is a better alternative to the pure diesel. Özener et al. [4] studied the performance and emission characteristics of soybean biodiesel blends (BD10, BD20 and BD30). Due to the low heating value, soybean biodiesel blends have an average of 1–4% lower torque with an increase in bsfc 2–9%. However, emissions are greatly reduced. The CO emissions are reduced by 28–46% and unburnt HC emissions decreases by 20–40%, whereas the CO<sub>2</sub> and NO<sub>x</sub> emissions are slightly increased. Similarly, Suryawanshi and Deshpande [5], Roy et al. [6] and Nair et al. [7] experimentally investigated the suitability of the biodiesel without any design modifications of the current compression ignition engines.

In the present work, experimentally studied the suitability of pure jatropha biodiesel and it blends as compression ignition diesel engine fuel. The jatropha biodiesel is prepared by alkaline-catalysed transesterification process. The detailed step by step process is explained by Ghimire et al. [8]. Biodiesel blends are prepared in the proportion of 20%, 40% 60%, 80% and 100% and they termed as J20, J40, J 60, J80 and J100, respectively. Experiments are conducted on a single-cylinder water-cooled diesel engine at different loads. The performance characteristics evaluated in terms of BTE and bsfc.

## 2 Experimental Set Up

The test conducted on single-cylinder water-cooled naturally aspirated diesel engine which is commonly used in automobile sector shown in Fig. 1. This engine connected to an eddy current dynamometer with a suitable propeller shaft. The volumetric fuel metering system and airbox are incorporated in the setup to measure the flow rate of

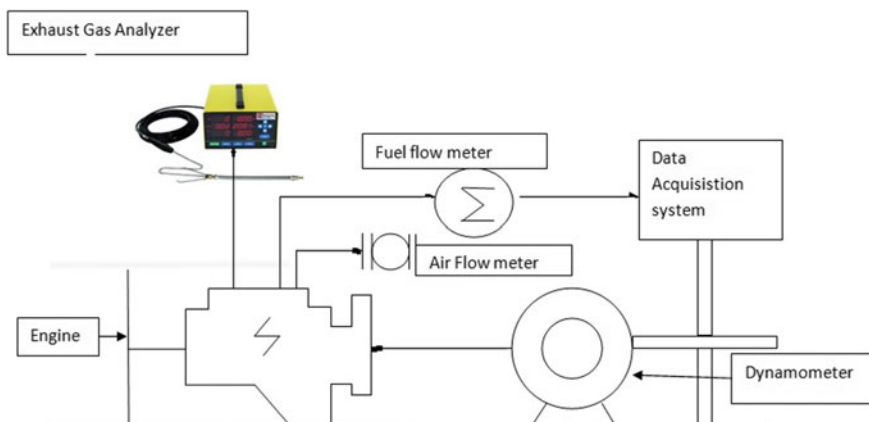


Fig. 1 Schematic diagram of the experimental setup

fuel and flow rate of inlet air respectively. Furthermore, the exhaust gas analyser is used to measure the exhaust gas emission like Hydrocarbon, Carbon monoxide, and oxide of nitrogen emissions.

### 3 Result and Discussions

#### 3.1 Performance Characteristics

Brake thermal efficiency and bsfc are measured as engine performance parameters. Figure 2a and 2b shows the variation of BTE and bsfc with respect to power of diesel, pure jatropha biodiesel and its blends. As power increases BTE increases up to a peak value then it starts to decrease. The pure jatropha biodiesel and its blends follow the same behaviour. The BTE decreases with increase of jatropha biodiesel proportions in the diesel and pure jatropha biodiesel has less BTE. This is because of pure jatropha oil have lower calorific value and high viscosity and poor air–fuel mixture formation. It is observed from Fig. 2a that the BTE of biodiesel blends is bounded in the limits diesel and pure jatropha biodiesel BTEs. Overall, the blends, the J20 biodiesel blend have maximum BTE of 24.25% at full load condition which is 43% more than pure jatropha biodiesel. In the J20 biodiesel fuel, the fine spray particles promote proper mixing of air in the cylinder and attain good combustion results increase in BTE.

Figure 2b depicts the bsfc variation with respect to power of diesel, pure jatropha biodiesel and its blends. The biodiesels have more BSFC as compared with diesel. This is due to less calorific value and higher explicit gravity. The calorific value of the pure jatropha biodiesel is about 7% less than that of diesel fuel. The maximum

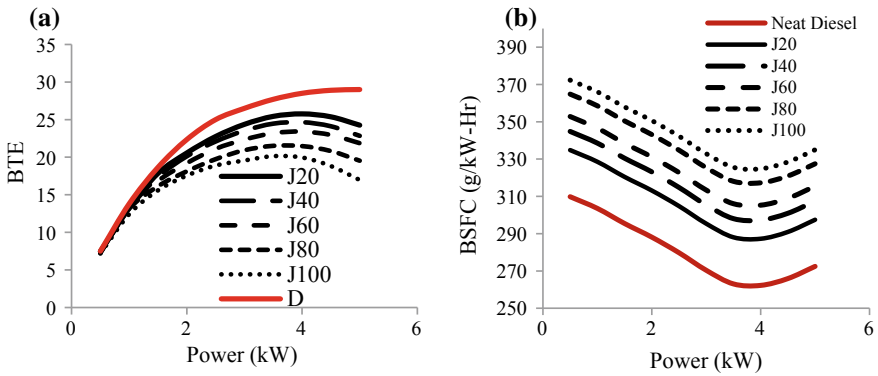


**Fig. 2** a Brake thermal efficiency versus power, b brake specific fuel consumption versus power for diesel, pure jatropha biodiesel and it blends

increase of bsfc is 22.30% of pure jatropha oil. Among all the blends J20 has less bsfc.

### 3.2 Emission Characteristics

Figure 3a, 3b and 3c depicts the exhaust emissions (HC, CO and  $\text{NO}_x$ ) of diesel engine fueled with diesel, pure jatropha biodiesel and it blends. It is observed from Fig. 3a and 3b, the HC and CO emissions are decreased for pure jatropha biodiesel and it blends, whereas  $\text{NO}_x$  emissions are increased. The biodiesels have more oxygen molecules. Thus, in the combustion process, the extra oxygen molecules participate and complete combustion takes place in the cylinder which results decrease in HC and CO emissions. This is because of the extra oxygen molecules progress the combustion process and increases the adiabatic flame temperature. The increased temperature and availability of oxygen molecules in the cylinder result increase in  $\text{NO}_x$  emissions that can be observed in Fig. 3c.

The maximum reduction in HC and CO emissions is 24.43% and 10.03% for pure jatropha biodiesel. The J20 biodiesel blend has decreases HC and CO emissions are by 9.18% and 7.9%. Similarly, the  $\text{NO}_x$  emissions for pure jatropha biodiesel and J20 biodiesel blends are increases by 37.30% and 12.24%, respectively.

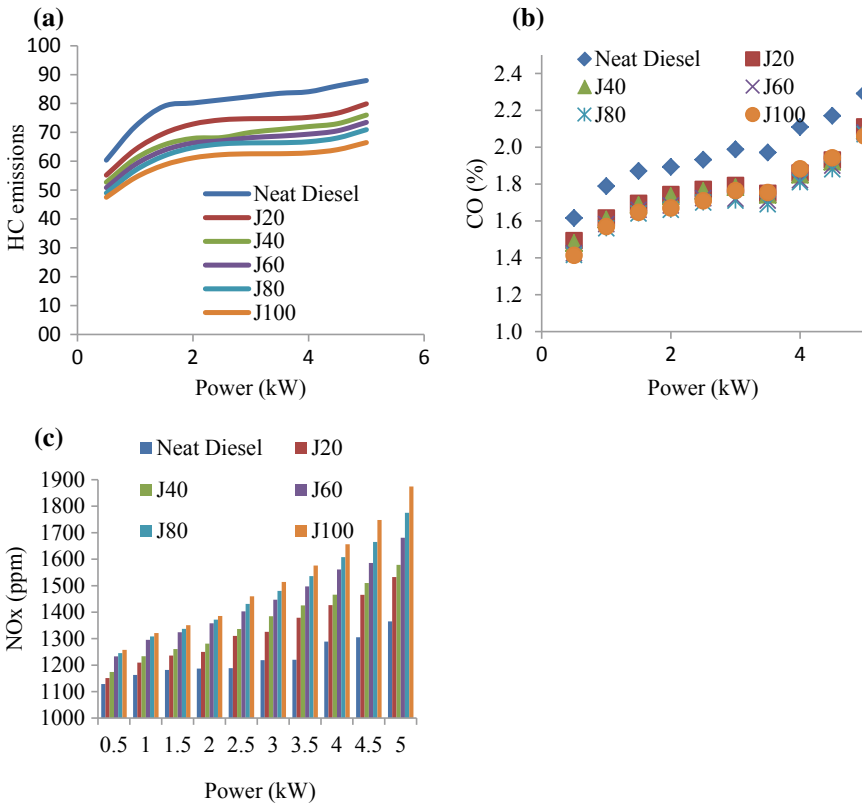


Fig. 3 a Hydrocarbon emissions, b carbon monoxide emissions, c NO<sub>x</sub> emissions for diesel, pure jatropha biodiesel and it blends

### 4 Conclusions

The major findings of this experimental study are as follows:

- The increase of jatropha proportions in diesel decreases the BTE and increases the bsfc. Compared to all biodiesel blends, J20 biodiesel blend has a higher brake thermal efficiency of 24.25% and less bsfc of 297.563 g/kW h.
- Exhaust emissions of HC (hydrocarbon), CO (carbon monoxide) have lower values for all biodiesel blends with increase in NO<sub>x</sub> (nitrogen of oxide) emissions as compared to diesel.
- Out of all blends, the J20 blend shows higher brake thermal efficiency and lower NO<sub>x</sub>. So, the J20 blend is used as alternate fuel without any modifications of the diesel engine.

## References

1. Bhuiya MMK, Rasul MG, Khan MMK, Ashwath N, Azad AK (2014) Second generation biodiesel: potential alternative to-edible oil-derived biodiesel. *Energy Procedia* 61:1969–1972. <https://doi.org/10.1016/j.egypro.2014.12.054>
2. Mallikappa DN, Pratap R, Murthy CSN (2012) Performance and emission characteristics of double cylinder CI engine operated with cardanol bio fuel blends. *Renew Energy* 38:150–154. <https://doi.org/10.1016/j.renene.2011.07.012>
3. Raj VM, Subramanian LRG, Manikandaraja G (2018) Experimental study of effect of isobutanol in performance, combustion and emission characteristics of CI engine fuelled with cotton seed oil blended diesel. *Alexandria Eng J* 57:1369–1378. <https://doi.org/10.1016/j.aej.2017.06.007>
4. Özener O, Yüksek L, Ergenç AT, Özkan M (2014) Effects of soybean biodiesel on a DI diesel engine performance, emission and combustion characteristics. *Fuel* 115:875–883. <https://doi.org/10.1016/j.fuel.2012.10.081>
5. Suryawanshi JG, Deshpande NV (2005) Effect of injection timing retard on emissions and performance of a pongamia oil methyl ester fuelled CI engine. *SAE Tech. Pap.*, SAE International. <https://doi.org/10.4271/2005-01-3677>
6. Roy MM, Wang W, Alawi M (2014) Performance and emissions of a diesel engine fueled by biodiesel–diesel, biodiesel–diesel-additive and kerosene–biodiesel blends. *Energy Convers Manag* 84:164–173. <https://doi.org/10.1016/j.enconman.2014.04.033>
7. Nair JN, Kaviti AK, Daram AK (2017) Analysis of performance and emission on compression ignition engine fuelled with blends of Neem biodiesel. *Egypt J Pet* 26:927–931. <https://doi.org/10.1016/j.ejpe.2016.09.005>
8. Ghimire JR, Shrestha K, Gewali M (2014) Biodiesel production from *Jatropha curcas* (L.) oil by optimized alkali catalysed transesterification process. Outline of presentation Introduction Research objective Materials and Methods Results and discussions Conclusions Acknowledgements Queries

# Numerical Analysis of Fluid–Structure Interaction of Blood Flow Through a Flexible Tube with 90-Degree Bend Using OpenFOAM



Rishabh N. Jaiswal and Trushar B. Gohil

**Abstract** In this study, the fluid–structure interaction of blood flow through a flexible tube with 90° has been analyzed. The numerical investigations are done using open-source CFD toolkit OpenFOAM. The variation of the time rate of change of volume and pressure wave in the case of a flexible tube with the 90-degree bend is evaluated and compared with that of flexible straight tube. It is found that the flexible tube with the 90-degree bend has undergone more rate of change of volume compared to that of flexible straight tube.

**Keywords** Fluid–structure interaction · Wave propagation · OpenFOAM

## 1 Introduction

Fluid–structure interaction (FSI) is the phenomenon where the fluid exerts pressure on the solid which causes the deformation of solid, and in turn, the solid deformation causes a change in fluid flow according to Newton’s third law of motion [1]. These fluid and solid interactions are observed in the blood flow through arteries. Fernandez and Moubachir [2] evaluated the flow behavior of the blood under the pressure pulse through a flexible straight tube. Degroote [3] extended the work to evaluate the rate of volume change for the blood through bifurcating passages. The geometry of the arteries varies in different parts of the human body; the current studies are extended to other geometries such as bend passages to obtain more details about the blood flow in the arteries.

However, very limited work has been done to evaluate the blood flow through the flexible tubes with a 90-degree bend. Therefore, the current study bridges the above gap by conducting a study to evaluate the variation of pressure and volume change rate for the blood flow through a flexible tube with a 90-degree bend. Also, it tries

---

R. N. Jaiswal · T. B. Gohil (✉)

Department of Mechanical Engineering, Visvesvaraya National Institute of Technology,  
Nagpur, Maharashtra 440010, India  
e-mail: [trushar.gohil@gmail.com](mailto:trushar.gohil@gmail.com)

© Springer Nature Singapore Pte Ltd. 2020

H. K. Voruganti et al. (eds.), *Advances in Applied Mechanical Engineering*,

Lecture Notes in Mechanical Engineering,

[https://doi.org/10.1007/978-981-15-1201-8\\_35](https://doi.org/10.1007/978-981-15-1201-8_35)



to establish a strong validation test case for FSI solver in the field of computational fluid dynamics (CFD) for blood flow applications.

## 2 Governing Equations

The fluid considered for this study is assumed to be incompressible and Newtonian. The governing equations for the fluid domain in the integral foam are as follows.

Conservation of mass is given by

$$\rho \frac{d}{dt} \int_V dV + \rho \oint_S n \cdot (v) dS = 0 \quad (1)$$

Conservation of momentum is given by

$$\rho \frac{d}{dt} \int_V dV + \rho \oint_S n \cdot (v) v dS = \oint_S n \cdot \sigma dS + \rho \int_V f_b dV \quad (2)$$

where  $\rho$  is the density,  $v$  is the velocity of a fluid,  $\sigma$  is stress tensor,  $n$  is a normal unit vector to surface  $S$ , and  $f_b$  is body force.

The stress tensor for incompressible Newtonian fluids is given by

$$\sigma = -pI + 2\mu\varepsilon$$

where  $p$  is pressure,  $\mu$  is the dynamic viscosity of the fluid, and  $\varepsilon$  is the strain rate tensor. The solid governing equations are formulated in the Lagrangian approach.

Momentum equation in Lagrangian formulation is given by

$$\rho \frac{D}{Dt} \int_V v dV = \oint_S n \cdot \sigma dS + \rho \int_V f_b dV \quad (3)$$

## 3 Coupling Algorithm

The conditions at the interface to be satisfied are the balance of forces and the no-slip condition [4]. These are given by

$$\begin{aligned} \sigma_{i/f}^f \cdot n &= \sigma_{i/f}^s \cdot n \\ V_{i/f}^f &= V_{i/f}^s \end{aligned}$$

The first condition is the balance of normal stresses on the interface. Also, the velocity of the fluid on the solid surface should be the same as the velocity of the solid surface. To simulate the governing equations, second-order central difference discretization for pressure and second-order upwind scheme for advection terms of momentum equation is considered. The temporal term is discretized using first-order implicit scheme.

## 4 Formulation of Model

### 4.1 Problem Specification and Boundary Condition

In this, the author models the fluid–structure interaction of laminar blood flow in an artery that is linearly flexible, and the blood is assumed to be incompressible. The morphological parameter is considered from Fernandez and Moubachir [2] of a flexible bend tube with a length of 0.050 m and a diameter of 0.01 m and a solid wall thickness of 0.001 m. The solid with  $0.3 \times 10^6 \text{ N/m}^2$  Young modulus and 0.3 Poisson ratio and  $1200 \text{ kg/m}^3$  density. The fluid viscosity is  $0.003 \text{ Pa s}$ , and the density is  $1000 \text{ kg/m}^3$ . A pressure of  $1333.2 \text{ Pa}$  is applied for a duration of  $0.003 \text{ s}$  at the inlet of both straight and bend tubes, and for the remaining time, it is  $0 \text{ Pa}$  up to  $0.01 \text{ s}$ . A fixed pressure of  $0 \text{ Pa}$  is considered at the outlet. No-slip boundary condition is applied to the fluid and solid domain interface. Illustrate the grid distribution and boundary conditions for straight and bend tubes (Fig. 1).

Four grid sizes of 23, 57, 93, and 121 K having  $0.0005$  near wall spacing is considered for grid independence testing, and the variation of volume change rate over time is compared. It is observed that 93 K grid size is sufficient to capture flexible tube physics.

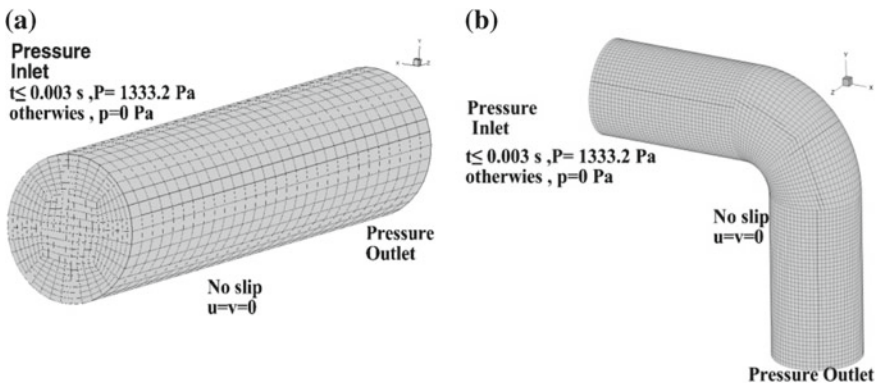
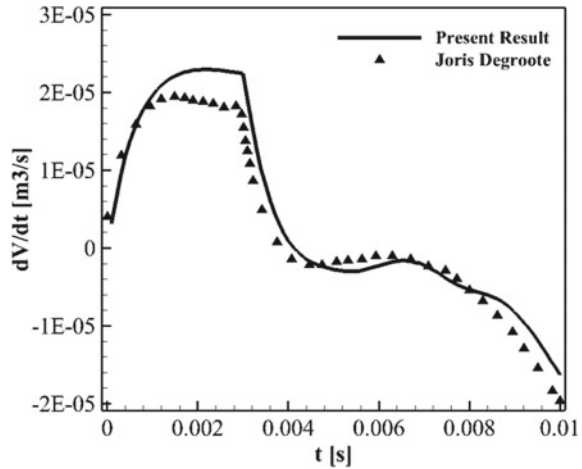


Fig. 1 Mesh diagrams for a **a** straight flexible tube and **b** bend flexible tube with the boundary condition

**Fig. 2** Rate of change of volume of straight tube over a time for the wave propagation in the computational domain



## 4.2 Validation

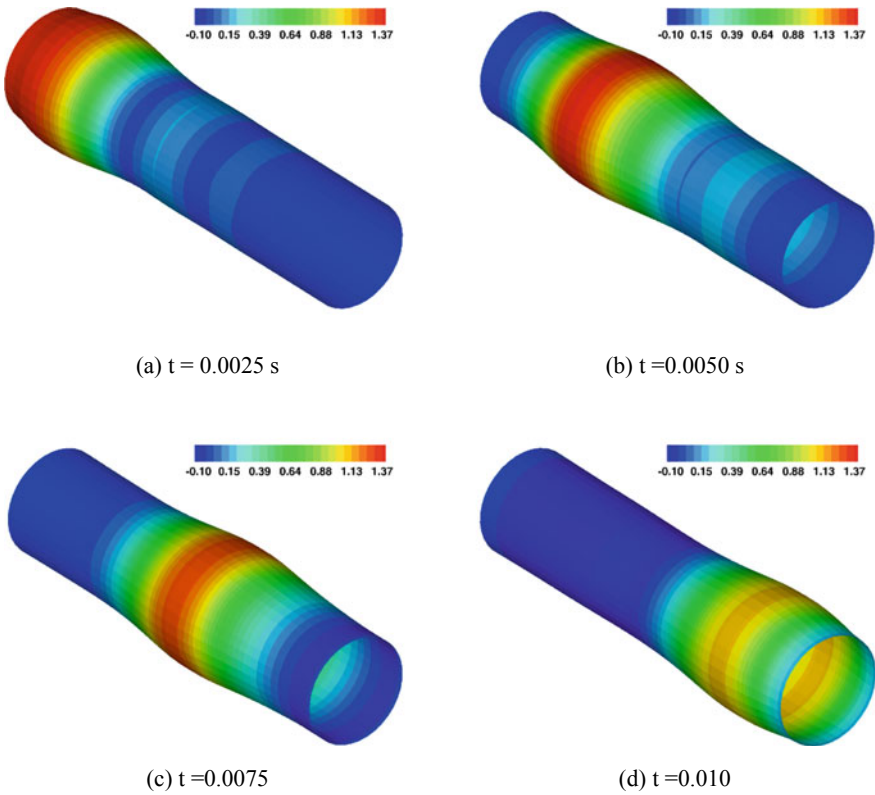
As a validation case, straight flexible tube is considered. All the required boundary condition and geometrical parameters are adapted from Degroote [3]. Figure 2 shows the variation of rate of change of volume of tube over a time and it is compared with the results of Degroote [3]. It is observed that the present result shows good agreement with the reference.

To further compare the present results, pressure distribution at various time steps is reported for various instants of time in Fig. 3. The present results show good comparison with the data of Degroote [3] (which is not shown here). It shows where the pressure reaches a maximum value from the pressure contour. At that instant, the deformation is also maximum. As soon as the pressure reaches its maximum value, it starts to decrease as the wave propagates for the rest of the time. Because of this rate of deformation, it starts to decrease after reaching its maximum value.

## 5 Result

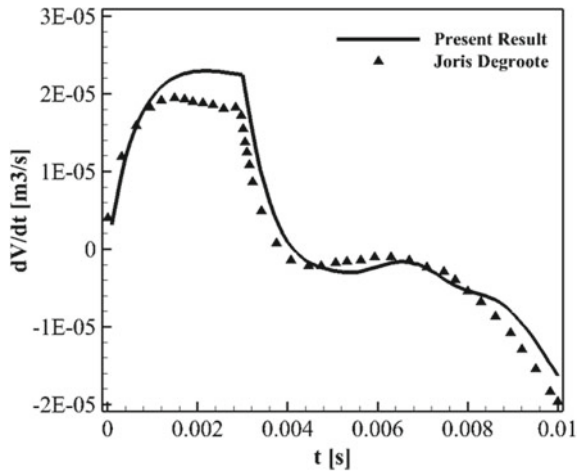
### 5.1 Rate of Change Volume for Bend Flexible Tube

Figure 4 shows the rate of change of volume over a time. It follows the same trend up to 0.001 s as observed for straight tube. However, the rate of deformation is slightly higher than straight tube at 0.0029 s, and the maximum deviation is  $0.29\text{E}-05 \text{ m}^3/\text{s}$ . Then the rate of deformation follows a similar trend as of straight tube up to 0.006 s. It is observed over a range of 0.006–0.001 s. The rate of change of deformation is



**Fig. 3** Pressure contours (in kPa) over a surface of straight flexible tube at various instants of time. The deformations have been magnified by factor 10

**Fig. 4** Comparison of variation of rate of change of the volume over time for bend tube and a straight tube



lower than a straight tube, and the maximum reduction is  $1.083E-05$ ; at the end of pulse, it comes closer again.

### 5.2 Pressure Variation in Bend Flexible Tube

Figure 5 shows variations in pressure over the surface of the bend tube. Initially, the pressure begins to rise and reaches a maximum value of 1.37 kPa, and then, the pressure starts to decrease as soon as it crosses the bend. Compared to the straight

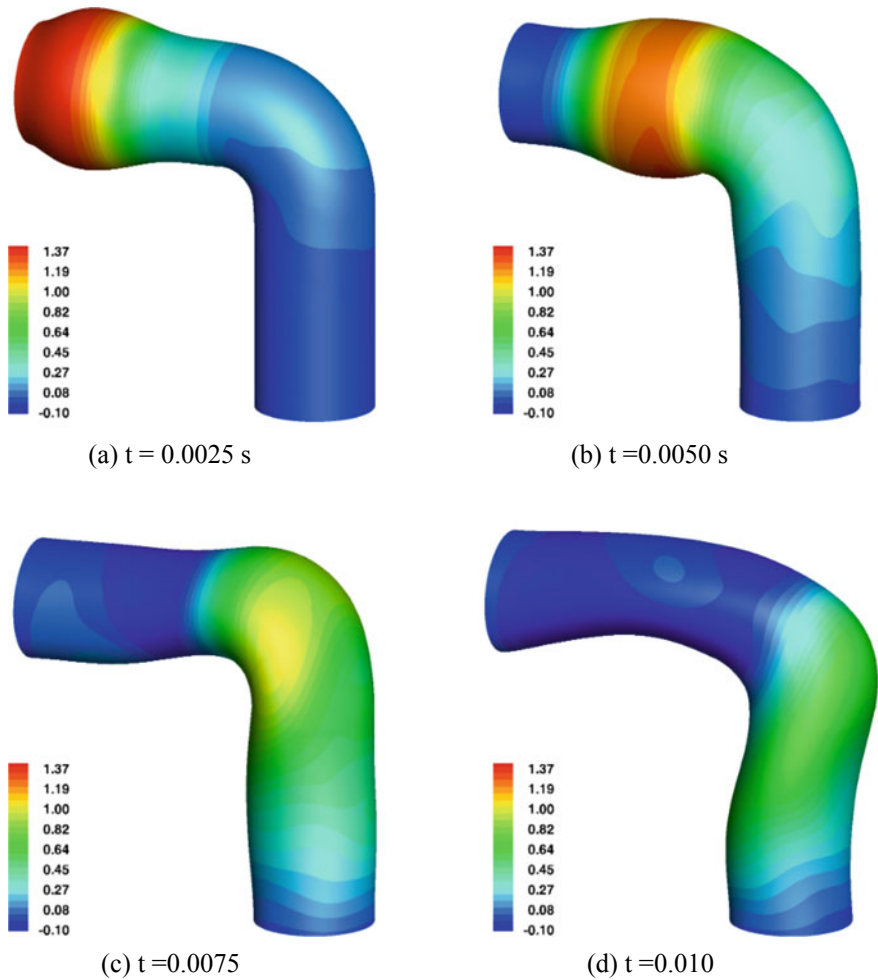


**Fig. 5** Pressure contours (in kPa) over a surface of bend flexible tube at various instants of time. The deformations have been magnified by factor 10

tube, the pressure of the bend tube is slightly increased. The bend causes a sudden drop in the entrance area, which creates negative pressure at the inlet of the tube and attempts to contract the tube. As shown in the pressure contours, this results in changes in the transverse area and the flow within the tube at an instant of 0.0075 and 0.010 s.

## 6 Conclusion

In the present study, to quantify the effect of tube deformation, the blood flow through the straight and 90-degree bend flexible tube is simulated. The open-source CFD toolkit OpenFOAM is used to mimic the FSI analysis. The present study also proposes a strong validation test case for biomedical application. Bend tube has a significant role in the study of blood flow through an artery. As the wave propagates through bend tube, it increases the rate of deformation in that region. Pressure contour shows the location of maximum pressure, and it is in line with maximum deformation. As the pressure wave crosses the bend region behind, it is contracted due to the negative pressure. This study helps to understand the behavior of the blood flow through bending in the patient-specific artery.

## References

1. Hou G (2012) Numerical methods for Fluid–Structure Interaction—a review. *Commun Comput Phys* 12:337–377
2. Fernandez M, Moubachir M (2005) A Newton method using exact Jacobians for solving fluid–structure coupling. *Comput Struct* 83:127–142
3. Degroote J (2010) Simulation of fluid–structure interaction with the interface artificial compressibility method. *Int J Numer Methods Biomed Eng* 26:276–289
4. Kuttler (2010) Coupling strategies for biomedical Fluid–Structure Interaction problem. *Int J Numer Methods Biomed Eng* 26:305–321

# **Design Engineering Section**

# Damage and Failure Analysis of Short Carbon Fiber Reinforced Epoxy Composite Pipe Using FEA



Anju Verma, Apurba Mandal and Dungali Sreehari

**Abstract** Composite pipes are extensively used in various automobile and aeronautical applications due to their high strength to weight ratio. The aim of this work is to numerically analyze the damage and failure of short carbon fiber composite pipe with short carbon fiber as reinforcement and epoxy as matrix. A finite element model was developed in ANSYS workbench 19. A method is discussed to generate short fibers randomly oriented in the volume of composite pipe and the material properties were given to the fibers and matrix. A method is developed to model a composite pipe having anisotropic properties which means young's modulus change with direction along the object as the fiber is of carbon and matrix is epoxy. Hydrostatic pressure was applied on inner and outer surface of the composite pipe. The results were compared with the laminated composite pipe and neat epoxy composite pipe. It was observed that under the same loading conditions the strength of the short carbon fiber composite was comparable with the laminated composite pipe. Short carbon fiber composite pipe which is less costly having good strength can be a good replacement for the costly filament winding pipe.

**Keywords** Carbon fiber (CF) · Finite element analysis (FEA) · Hydrostatic pressure test (HPT)

## 1 Introduction

In various fields, use of lightweight structures is being involved to increase the energy efficiencies in automobiles, aerospace and marine industries. Fiber-reinforced composite has various applications due to its high specific strength and high stiffness [1] also they have high thermal expansion and corrosion resistance [2].

Composite material composed of a material system with two or more macro constituents that differ in form and chemical composition and are insoluble in each other. There is considerable attention over the years to understand the behavior of

---

A. Verma (✉) · A. Mandal · D. Sreehari  
National Institute of Technology, Uttarakhand, Srinagar, Garhwal 246174, India  
e-mail: [vermaanju899@gmail.com](mailto:vermaanju899@gmail.com)

© Springer Nature Singapore Pte Ltd. 2020  
H. K. Voruganti et al. (eds.), *Advances in Applied Mechanical Engineering*,  
Lecture Notes in Mechanical Engineering,  
[https://doi.org/10.1007/978-981-15-1201-8\\_36](https://doi.org/10.1007/978-981-15-1201-8_36)



hollow composite rods due to many applications. Application ranges from power drive shafts, aerospace design like wings, satellite truss structures, robot arms [3]. Filament winding is the conventional method and most effective method of manufacturing any composite vessel and composite pipe. This method is mainly used due to its high accuracy in fiber positioning, high fiber volume fraction, and process automation [4]. There are many factors that influence the strength of the composite tube-like winding tension, sequence of stacking, gradient of winding tension, winding time between layers, cut versus uncut helices [5].

On the other hand, manufacturing of randomly reinforced fiber composite is controlled by less factors like mixing method, mould preparation, resin fiber transfer method. Ozsoy et al. worked on finding the tensile, bending, impact, hardness properties of the chopped carbon fiber epoxy composite. Results were based on the (0, 6, 8, 10%) weight fraction of reinforcement in the epoxy composite. It was observed that the tensile, bending and impact performance increase up to 8% of the reinforcement after which only the hardness increase by increasing the weight fraction of the chopped carbon fiber [6]. Harper et al. worked on effect of fiber length on random carbon fiber composite. Shorter fiber shows good mechanical properties as compared to the longer carbon fiber composite. Strength of the composite follows decreasing power-law relationship with the increasing length. 3 mm is the critical length at which good properties of the composites are observed [7].

In the present work, a method is discussed to model the pipe having randomly distributed short carbon fiber as the reinforcement and epoxy as the matrix in ANSYS 19. As the cost of traditional fabrication of composite by laminates is very high, random short fiber composite pipe can be a good alternative with lightweight structures at low cost. Numerical analysis of the pipe based on short carbon fiber composite pipe which can be made by casting method. The parameters are compared with the laminated composite pipe and neat epoxy pipe under the same loading condition.

## 2 Modeling and Simulation

### 2.1 Generation of Randomly Distributed Chopped Fiber

Generation of random fiber was done using a program in the MS Excel sheet. Six columns of random function to generate the six random numbers that describe the  $x$ ,  $y$ ,  $z$  position of one end of the fiber and  $dx$ ,  $dy$ ,  $dz$  offsets to other end of the fiber. Using the Rand command the randomly distributed fibers are generated which could lie along the length of the pipe and through the thickness of the pipe. The spreadsheet creates a required number of straight fibers and length of fibers as 3 mm which can vary as per the requirement. There are many parameters which affect the material parameters like fiber volume fraction, fiber length, fiber tow size. Of all the parameters, fiber length is the critical parameter which determines the specific energy absorption then longer fiber possibly because of increased concentration of

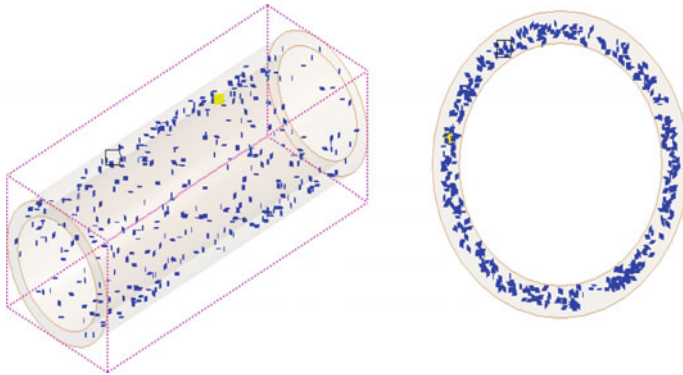


**Fig. 1** Pipe with random carbon fiber reinforcement

stress rises in short fiber specimen. Also if the length of the fiber is more, bad interface is observed between the matrix and fiber. Then the specific text file format is imported as 3D curves in the design modeler of ANSYS. Figure 1 shows the representative volume with reinforcement as carbon fiber in pipe along the length of pipe and within the thickness of the pipe.

## 2.2 Model Development

Composite pipe was developed in ANSYS Workbench 19 software tool using HP workstation, processor of Intel Core i7, 16 GB RAM, 1 TB ROM and Windows 8.1Pro. The dimensions of the composite tube are taken in accordance with the model of Humberto et al. [4]. Length of the pipe was taken as 381 mm and internal radius of 60 mm with wall thickness of 3 mm. The cross-section is assigned to the generated fiber with diameter of 0.1 mm. The properties of carbon fiber are shown in Table 1 [8]. Properties of epoxy are taken from the library of ANSYS as tabulated in Table 1. Pure epoxy resin pipe is shown in Fig. 2 and the composite pipe with reinforced carbon fiber is shown in Fig. 3.

**Table 1** Properties of carbon fiber and epoxy

Material	Tensile strength (MPa)	Young's modulus (GPa)	Density (g/cm <sup>3</sup> )
Carbon fiber	3950	238	1.77
Epoxy resin	–	3.78	1.16

**Fig. 2** Neat epoxy pipe

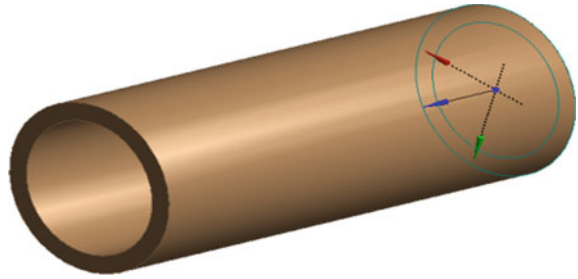
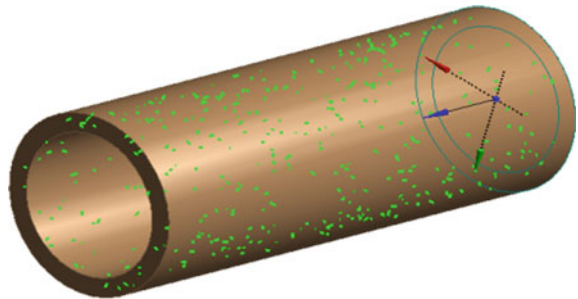


**Fig. 3** CF epoxy composite pipe



### 2.3 Meshed Model

In meshed model, quadrilateral element was used over whole domain as shown in Fig. 4. This element is chosen according to the Humberto et al. [4] model. Meshing was done under user-controlled mesh in which ‘extra fine’ element size given to pipe and fibers. The complete mesh consists of 6816 elements and number of nodes 13,752.

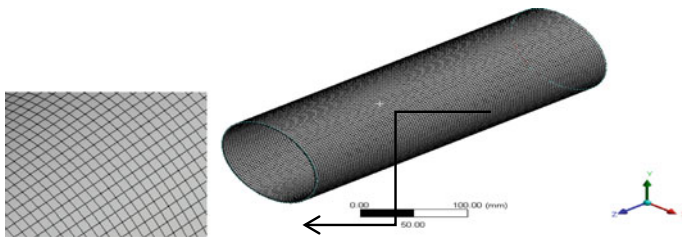


**Fig. 4** Meshed model of the composite pipe

### 3 Numerical Results

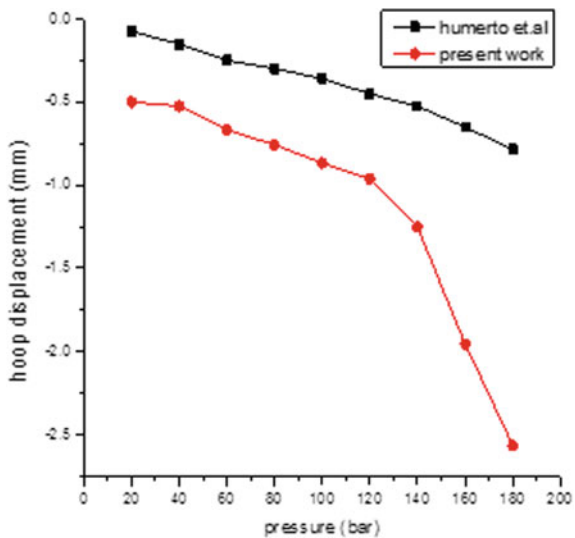
#### 3.1 Hoop Displacement and Total Deformation Under External Pressure

The axial displacement along the z-direction of both the end was restricted and hydrostatic pressure was applied on the external surface of the pipe. The results were compared with the filament winding model,  $[90/\pm 55_8/90]$  as proposed by Humberto et al. [4] and short carbon fiber epoxy pipe of present study with vol. fraction of 5% CF. It was observed that the hoop displacement of the CF composite shows approximately same trend as of the filament winding pipe up to certain level of pressure, about 120 bar as shown in Fig. 5. As the filament winding is a very costly therefore for low to medium pressure application it can be replaced with the short fiber composite.

For the same loading conditions that is under the HPT the variation of total deformation and contours for deformation at 20 bar is represented in Fig. 6.

From Fig. 6, it can be seen that the less deformation taking place in case of higher vol. fraction CF composite as a function of applied pressure. As vol. fraction of composite is increased, the deformation in composites are reduced in every level of applied pressure. In composites, the load applied to the structure is basically carried by the reinforcement and then transfer to the matrix medium; therefore by adding more and more the reinforcement the properties of the composites get enhanced.

**Fig. 5** Depicting the variation of hoop displacement as a function of applied pressure



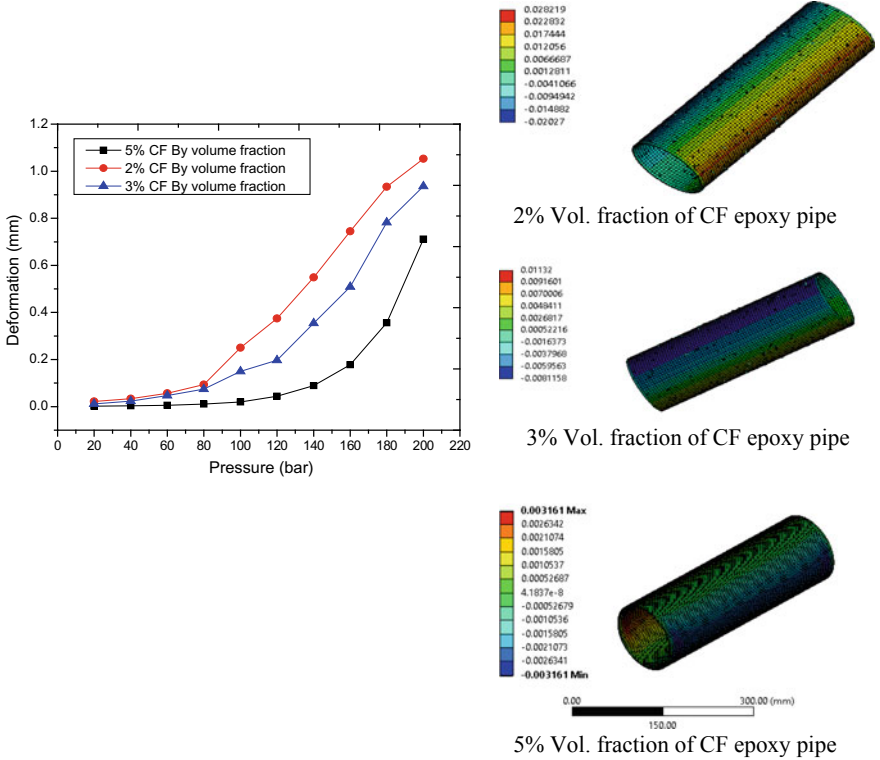


Fig. 6 The variation of total deformation with external pressure for CF epoxy composite

### 3.2 Comparison of Different Structures of CF Epoxy Composite Pipe

Three pipe models with varying vol. fraction of reinforcement were subjected to same loading conditions. Pipe was fixed from both the ends and hydrostatic pressure was applied on the inside surface of the pipe. Stress level at different pressure was found and plotted in Fig. 7. The variation of the stress is represented by the four models for different applied pressures.

Figure 7 depicts that the stress level in the neat epoxy pipe is very high as compared to the other model of CF composites pipe. It is also clear from the plot that the value of Von mises stresses are decreasing as the vol. fraction of CF is increased. Therefore, the chances of failure for in case of composites with higher vol. fraction will be less.

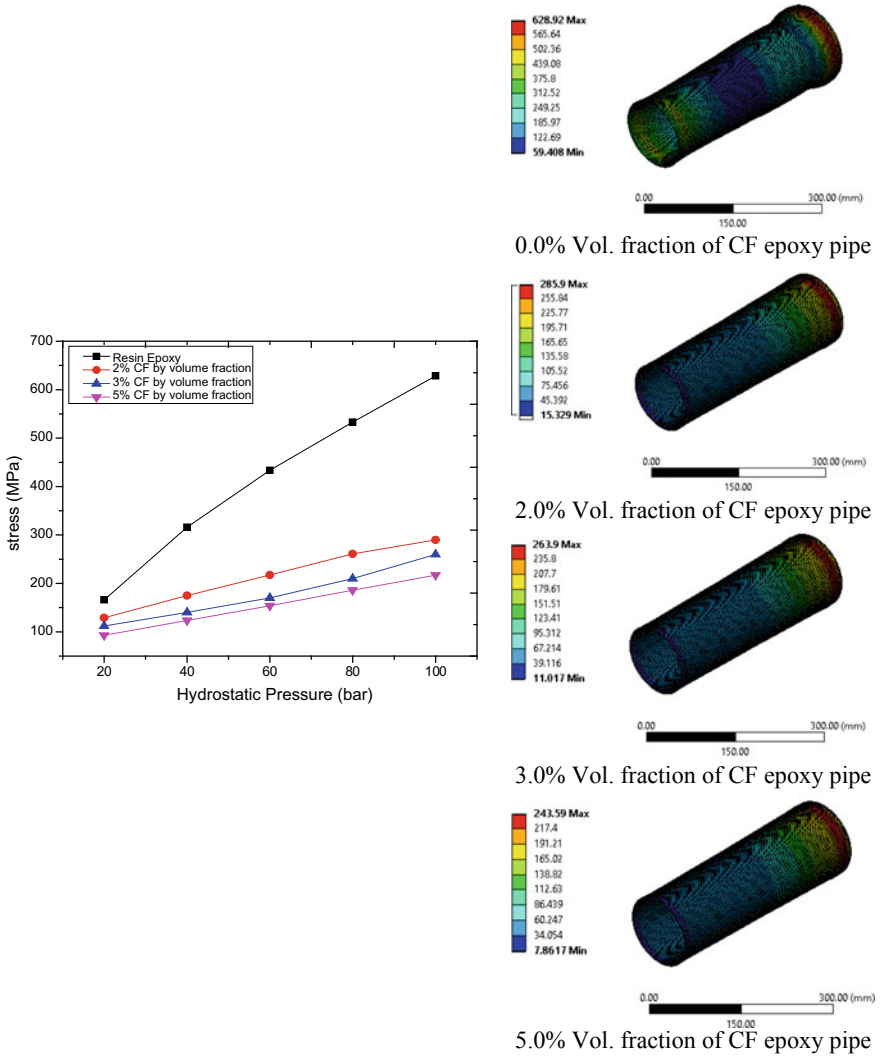


Fig. 7 Depicting the variation of the Von Mises stress in hydrostatic pressure test

### 4 Conclusion

Mechanical performance of short carbon fiber reinforced epoxy composites is investigated numerically with FEA simulation. A novel method is discussed to model the pipe with randomly oriented short carbon fibers. The results show that reinforcement of short carbon fiber has significant effects on the performance of composite under hydrostatic pressure testing conditions. It has been found that in case of low to medium pressure application as well as some structural applications, the costly

filament winding pipe can be replaced with less costly CF reinforced composite pipe. The hoop displacement up to 120 bar of pressure is almost linearly proportional to filament winding pipe. The chances of failure for composites of higher vol. fraction is less as both the total deformation and Von mises stress levels are low.

## References

1. Pan Y, Iorga L, Pelegri AA (2008) Numerical generation of a random chopped fiber composite RVE and its elastic properties. *Compos Sci Technol* 68(13):2792–2798
2. Fleischer J, Teti R, Lanza G, Mativenga P, Möhring HC, Caggiano A (2018) Composite materials parts manufacturing. *CIRP Ann* 67(2):603–626
3. Kim C, White SR (1996) Analysis of thick hollow composite beams under general loadings. *Compos Struct* 34(3):263–277
4. Almeida JHS Jr, Ribeiro ML, Tita V, Amico SC (2016) Damage and failure in carbon/epoxy filament wound composite tubes under external pressure: experimental and numerical approaches. *Mater Des* 96:431–438
5. Cohen D (1997) Influence of filament winding parameters on composite vessel quality and strength. *Compos A Appl Sci Manuf* 28(12):1035–1047
6. Ozsoy N, Ozsoy M, Mimaroglu A (2016) Mechanical properties of chopped carbon fiber reinforced epoxy composites. *Acta Phys Pol A* 130(1):297–299
7. Harper LT, Turner TA, Warrior NA, Dahl JS, Rudd CD (2006) Characterisation of random carbon fibre composites from a directed fibre preforming process: analysis of microstructural parameters. *Compos A Appl Sci Manuf* 37(11):2136–2147
8. Fu SY, Lauke B, Mäder E, Yue CY, Hu X (2000) Tensile properties of short-glass-fiber-and short-carbon-fiber-reinforced polypropylene composites. *Compos A Appl Sci Manuf* 31(10):1117–1125

# Dynamic Performance Analysis of a Four-Ton Automobile Chassis



P. Sowmya, K. Karthik Rajashekar, M. Madhavi and P. A. Sastry

**Abstract** In the present work, an effort is made to investigate the Dynamic performance analysis of a four-ton Automobile chassis due to road undulations. The effects of forcing frequencies due to engine as well as road condition are significant at high speeds of an engine. Numerical analysis is employed on the original dimensions of the chassis of heavy truck made of structural steel. The analysis is extended to fiber-reinforced composites and a combination of structural steel and composite. A new mathematical model is proposed as a 2D beam element with consistent mass matrix solved for mode shapes using determinant-based method. However, the natural frequencies for composites are obtained from the effective stiffness value derived from lamination theory. The study involves the change in dimensions, the addition of cross members to the chassis at maximum deflection, and change of materials of the chassis. Further, under the conditions of base excitation, applying engine harmonic load on the cross members, rolling and pitching conditions, the dynamic response of the chassis are determined. The results show that fiber-reinforced composites have low natural frequencies with 80% weight reduction in comparison with structural steel resulting in increase in payload, life of wheels, and other mounting elements on chassis.

**Keywords** Chassis · Layered beam element · Base excitation · Harmonic engine load

## 1 Introduction

The chassis of an automobile acts as a skeleton on which the engine, wheels, axle assemblies, brakes, suspensions, etc., are mounted. The chassis receives the reaction forces of the wheels during acceleration and braking and absorbs aerodynamic wind forces and road shocks through suspension. All real physical structures, when subjected to loads or displacements, behave dynamically. The additional inertia forces,

---

P. Sowmya · K. Karthik Rajashekar · M. Madhavi (✉) · P. A. Sastry  
Mechanical Engineering, MVSR Engineering College, Hyderabad, Telangana 501510, India  
e-mail: [madhavimatlapudi72@gmail.com](mailto:madhavimatlapudi72@gmail.com)

© Springer Nature Singapore Pte Ltd. 2020  
H. K. Voruganti et al. (eds.), *Advances in Applied Mechanical Engineering*,  
Lecture Notes in Mechanical Engineering,  
[https://doi.org/10.1007/978-981-15-1201-8\\_37](https://doi.org/10.1007/978-981-15-1201-8_37)



according to Newton’s second law, are equal to the mass times of the acceleration [1]. If the loads and displacements are applied very slowly, then the inertia forces can be neglected, and a static load analysis can be justified. However, dynamic loads due to high speeds of engine can also be significant. It is also important to study the effects of forcing frequencies due to engine as well as road condition. Hence, an effort is made to investigate the dynamic response of truck chassis due to road undulations [2].

## 2 Theoretical Background

Chassis is an important part of automobile, it serves as a frame for supporting the body, and different units of automobile like engine, suspension, gearbox, braking system, steering, propeller shaft, differential, axle assemblies, etc., are welded or bolted as shown in Fig. 1. Ladder chassis and body on frame are the terms used when the body of a vehicle is mounted to a separate frame or chassis. This frame is like a ladder in design as two long pieces of steel (approximately the length of the vehicle) are held parallel to each other by shorter pieces running across. This type of chassis is better suited for commercial and heavy-duty work [3].

### 2.1 Layout of Chassis

In the present work, a four-ton heavy-loaded structural steel ladder-type chassis as shown in Fig. 1 is modeled and analyzed for dynamic performance. The frame considered has ‘C’-type cross section for both long and cross members with the specifications mentioned in Table 1.

The analysis involves different cross sections and different materials of long and short members of chassis (Table 2).

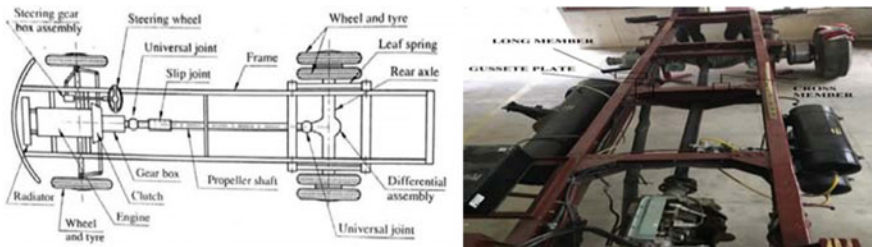


Fig. 1 Layout of chassis

**Table 1** Specification of Four-ton heavy vehicle truck chassis frame

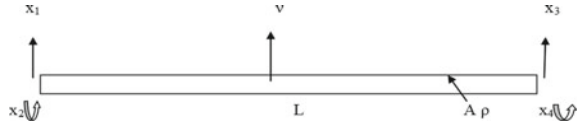
S. No.	Parameters	Value	S. No.	Parameters	Value
1	Total length of the chassis	6775 mm	9	Load acting on single frame	34,335 N/beam
2	Width of the chassis	860 mm	10	Uniformly distributed load	5.08 N/mm
3	Wheel base	6405 mm	11	Reaction at point C $R_c$	16,954.221 N
4	Front overhang	90 mm	12	Reaction at point D $R_d$	17,462.779 N
5	Rear overhang	280 mm	13	Moment of inertia about $x-x$ axis $I_{xx}$	21,979,040.25 mm <sup>4</sup>
6	Capacity	4 ton	14	Deflection of chassis	4.96 mm
7	Capacity of truck	39,240 N	15	Load acting on single frame	34,335 N/beam
8	Load acting on the chassis	68,670 N			

**Table 2** Material specifications for the analysis

S No.	Material	Young’s modulus (N/mm <sup>2</sup> )	Poisson’s ratio	Density (kg/m <sup>3</sup> )	Shear modulus (N/mm <sup>2</sup> )
1	Structural steel	$E = 2.1 \times 10^5$	0.3	7798	$G = 79.3 \times 10^3$
2	Carbon/epoxy	$E_x = 1.21 \times 10^5$ $E_y = 8.6 \times 10^3$ $E_z = 8.6 \times 10^3$	$\nu_{xy} = 0.27$ $\nu_{yz} = 0.4$ $\nu_{zx} = 0.4$	1600	$G_{xy} = 4.7 \times 10^3$ $G_{yz} = 3.1 \times 10^3$ $G_{zx} = 4.7 \times 10^3$

**Mathematical Modeling of Composite Layered Beam Element.** The basic calculation for chassis frame is based on uniformly distributed load of 5.08 N/mm on an overhanging simply supported beam with span length 6405 mm between supports. The closed-form solutions to determine eigenvalues and eigenvectors are used for problems with simple material geometry, loading, and boundary conditions. The analysis of fiber-reinforced composite structures requires a specialized tool to predict the natural frequencies and mode shapes. In reality, fiber-reinforced composite beam structure is a beam comprising of different layers with varying thickness and fiber orientations. There are no solutions to this practical beam structure either in closed form or in numerical technique. In the current study, a **layered beam element (LBE)** theoretical model is developed based on classical lamination theory. The 2D beam with two noded elements consists of two degrees of freedom at each node viz. one

**Fig. 2** Finite element of beam



translation and one rotation along with options to number of layers, thicknesses, and fiber orientations at each layer.

**Finite Element for Beam Element** as shown in Fig. 2.

Element stiffness matrix is given by [4]

$$k^e = \frac{(Efx)I}{l_e^3} \begin{bmatrix} 12 & 6l_e & -12 & 6l_e \\ 6l_e & 4l_e^2 & -6l_e & 2l_e^2 \\ -12 & -6l_e & 12 & -6l_e \\ 6l_e & 2l_e^2 & -6l_e & 4l_e^2 \end{bmatrix} \tag{1}$$

**Mass Matrix of a 2D beam element** [4]:

$$m^e = \frac{\rho A_e l_e}{420} \begin{bmatrix} 156 & 22l_e & 54 & -13l_e \\ 22l_e & 4l_e^2 & 13l_e & -3l_e^2 \\ 13l_e & 3l_e^2 & 156 & -22l_e \\ -22l_e & -54 & -13l_e & 4l_e^2 \end{bmatrix} \tag{2}$$

### 3 Simulation Study

The chassis frame is modeled in high-end analysis software for the given dimensions and discretization is done with 2D beam elements with two nodes, having two degrees of freedom at each node. The necessary boundary and loading conditions are imposed on the model to obtain the static and dynamic performance of the four-ton automobile chassis [5]. Considering the limitations of the utility of 2D beam element on fiber-reinforced composites, algorithms are developed for free vibrations in MATLAB for the theoretical model of layered beam model. The long and short members are considered to be analogues to beam structures and are discretized into the number of beam elements [6]. Under the given loading and boundary conditions, static and dynamic parameters are derived. The study is performed under five cases viz. analysis on original dimensions of C-type section of long member of structural steel material, analysis on reduced dimensions of C-type section of long member of structural steel material, analysis on additional cross member at maximum deflecting area on reduced dimensions of C-type section of long member of structural steel material, analysis on original dimensions of C-type section of long member of carbon/epoxy material,

and analysis on original dimensions of C-type section of long member of structural steel material for long members and carbon/Epoxy material for cross members.

Static analysis is performed to derive maximum deformation and von Mises stresses on the chassis, and dynamic analysis includes modal and harmonic analysis [7]. Modal analysis helps us to find the natural frequencies and the nature of mode for the behavior of the chassis under different conditions [8]. In harmonic analysis, four other conditions are included which are as follows:

Condition 1: In base excitation, the four base points are given amplitude of 100 mm each and a uniformly distributed load of 5.08 N/mm is applied on the chassis frame as shown in Fig. 3.

Condition 2: Engine harmonic load, an engine harmonic load of  $2000 \sin(\omega t)$ ,  $N$  on second cross member, uniformly distributed load of 5.08 N/mm along the chassis frame and the base key points are fixed as shown in Fig. 4.

Condition 3: In pitch condition, a displacement of 100 mm is applied on rear wheels and no displacements on front wheels, an engine harmonic load of  $2000 \sin(\omega t)$ ,  $N$  on second cross member, uniformly distributed load of 5.08 N/mm

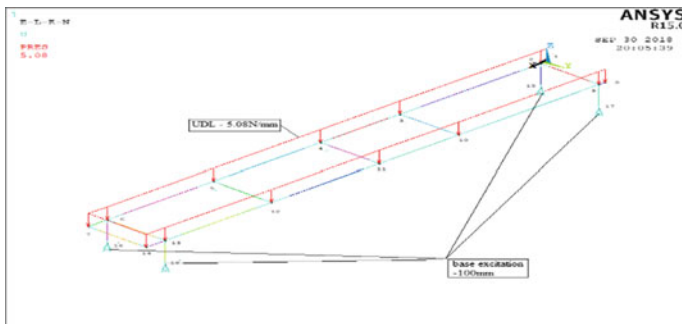


Fig. 3 Base excitation condition

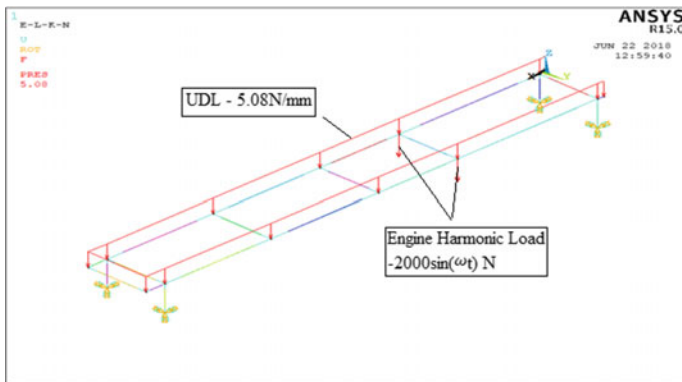
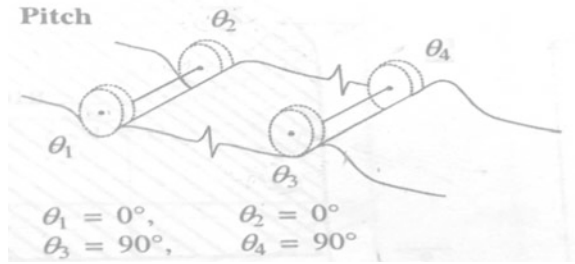
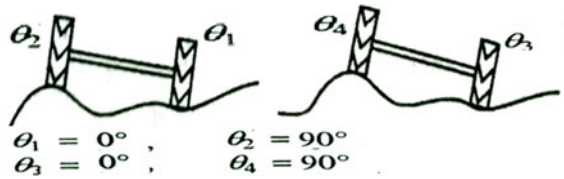


Fig. 4 Engine harmonic load condition

**Fig. 5** Engine harmonic load condition



**Fig. 6** Roll condition on wheels



along the chassis frame and the base key points are fixed as shown in Fig. 5. The displacements can be approximated to  $A \sin(\omega t + \theta_i)$  where  $i = 1-4$ .

Condition 4: In roll condition, a displacement of 100 mm is applied on right side of the vehicle and no displacements on the left side of the vehicle, an engine harmonic load of  $2000 \sin(\omega t) N$  on second cross member, uniformly distributed load of 5.08 N/mm along the chassis frame and the base key points are fixed as shown in Fig. 6.

### 3.1 Results of Structural Steel of 'C' (230.7 mm x 77.5 mm x 8 mm)

See Figures 7, 8 and 9.

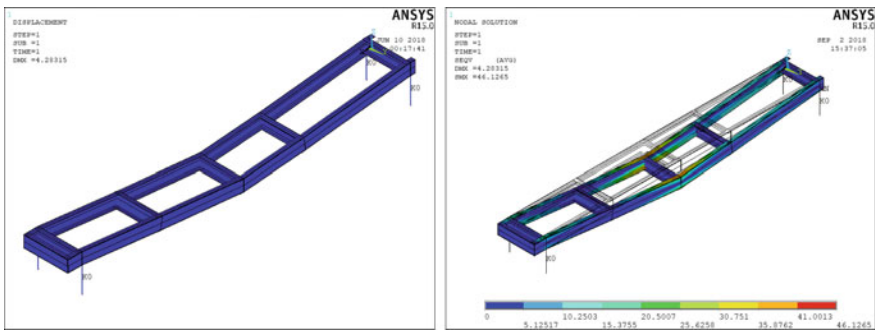


**Fig. 7** Static analysis and von Mises stress of structural steel

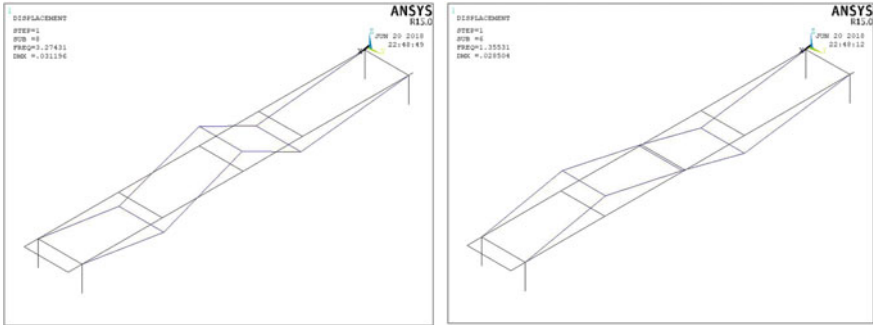


Fig. 8 Modal analysis of structural steel

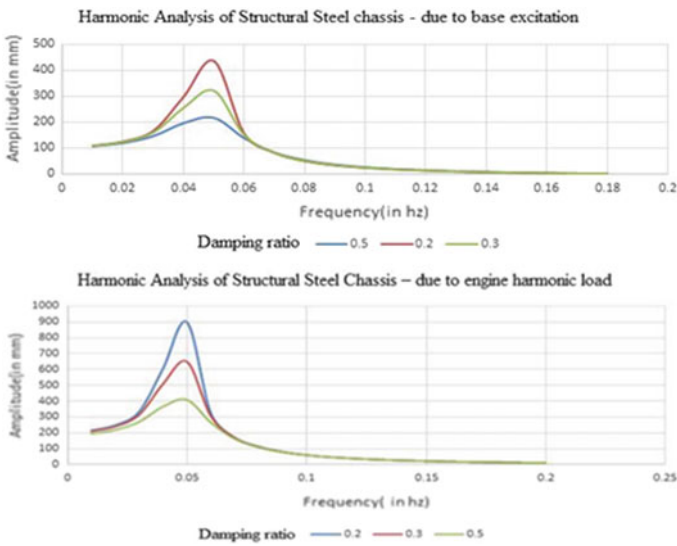


Fig. 9 Harmonic analysis of structural steel chassis

### 3.2 Effect on Composite Material on C-Type Channels (230.7 mm × 7.5 mm × 8.0 mm)

See Figs. 10, 11 and 12.

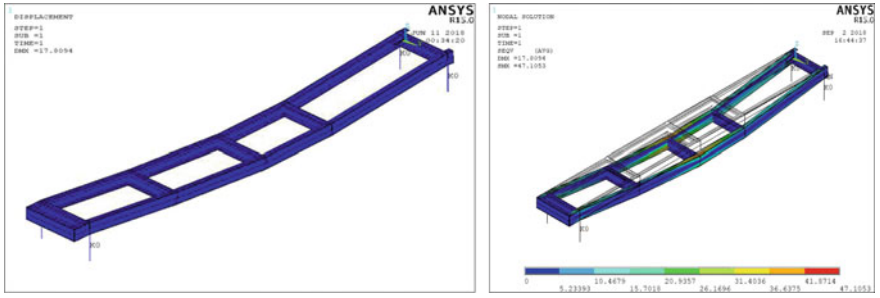


Fig. 10 Static analysis and von Mises stress of carbon/epoxy chassis

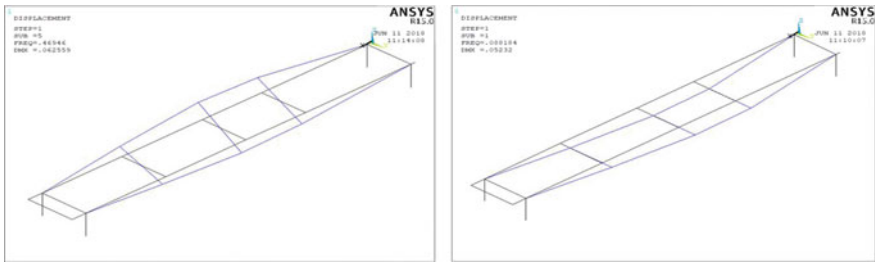


Fig. 11 Static analysis and von Mises stress of carbon/epoxy chassis

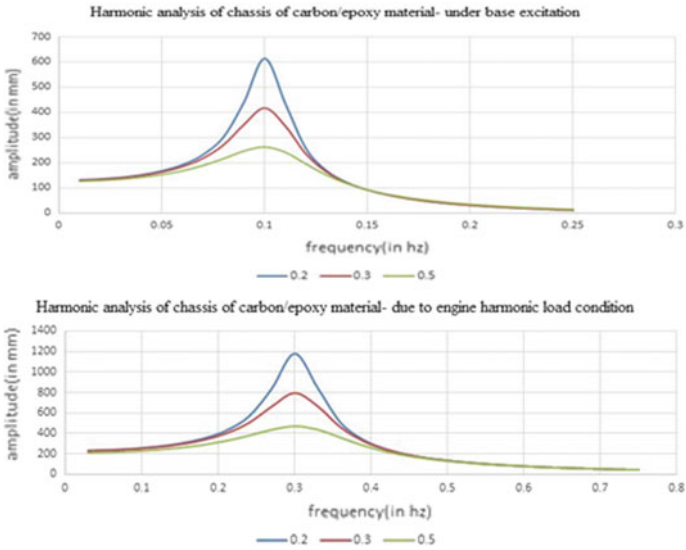


Fig. 12 Harmonic analysis of carbon/epoxy chassis

### 3.3 Results of Layered Beam Model

Deformations and natural frequencies of chassis frame are obtained using layered beam model as shown in Table 3. The results are compared with numerical technique results developed through ANSYS software. Deformations and natural frequencies of structural steel obtained through layered beam model are observed to be very close to analysis software. Considering the validation of the procedure, the simulation is preceded for fiber-reinforced composites and obtained the corresponding deformations and natural frequencies.

**Table 3** Comparison between layer beam model and ANSYS results

Mode shape	Natural frequencies (Hz) structural steel chassis		Nature of mode	Natural frequencies (Hz) Carbon/epoxy		Nature of mode
	LBM	ANSYS		LBM	ANSYS	
1	<b>0.082</b>	0.151	Bending	<b>0.079</b>	0.088	Bending
2	<b>0.295</b>	0.388	Bending	<b>0.205</b>	0.221	Bending
3	<b>0.317</b>	0.392	Bending	<b>0.395</b>	0.404	Bending
4	<b>0.399</b>	0.452	Bending	<b>0.377</b>	0.416	Bending
5	<b>0.731</b>	0.755	Bending	<b>0.401</b>	0.469	Twisting
6	<b>1.298</b>	1.355	Bending	<b>1.051</b>	1.002	Bending
7	<b>1.469</b>	1.598	Twisting	<b>1.093</b>	1.179	Twisting
8	<b>3.157</b>	3.274	Bending	<b>1.802</b>	1.884	Bending
9	<b>3.063</b>	3.633	Transverse	<b>2.011</b>	2.059	Bending
10	<b>3.179</b>	3.865	Bending	<b>2.142</b>	2.059	Bending

*Note* A layered beam element (LBE), theoretical model is developed based on Classical Lamination theory. The 2D beam with two noded elements consists of two degrees of freedom at each node viz., one translation and one rotation. The results obtained by using this theory is indicated in bold color



### 3.4 Results and Discussions. Static Analysis

Parameters	Structural steel (230.7 mm × 77.5 mm × 8 mm)	Structural steel (200 mm × 75 mm × 6.2 mm)	Additional cross member (200 mm × 75 mm × 6.2 mm)	Carbon/epoxy (230.7 mm × 77.5 mm × 8 mm)	Combination (230.7 mm × 77.5 mm × 8 mm)
Deformation (mm)	4.218	7.744	7.844	17.795	4.28
von Mises stresses (N/mm <sup>2</sup> )	6.127	72.373	75.393	47.105	46.127
Weight (ton)	3.574	2.741	2.184	0.7427	3.2

### 3.5 Modal Analysis

Parameters	Structural steel (230.7 mm × 77.5 mm × 8 mm)	Structural steel (200 mm × 75 mm × 6.2 mm)	Additional cross member (200 mm × 75 mm × 6.2 mm)	Carbon/epoxy (230.7 mm × 77.5 mm × 8 mm)	Combination (230.7 mm × 77.5 mm × 8 mm)
Natural frequencies (in Hz)	0.1515	0.1593	0.1610	0.0881	0.1161
	0.3886	0.3435	0.3170	0.2214	0.3600
	0.3929	0.4031	0.3821	0.4041	0.4345
	0.4526	0.4133	0.4293	0.4169	0.4748
	0.7552	0.7953	1.0000	0.4692	0.8339
	1.3553	1.2017	1.0397	1.0028	1.5392
	1.5981	1.4285	1.2424	1.1791	1.6874
	3.2743	2.9249	1.5557	1.8843	3.8656
	3.6332	3.6335	2.6278	2.0596	3.9167
	3.8652	3.6359	3.2646	2.0595	4.0535

## 4 Conclusion

- (i) Natural frequencies and associated mode shapes are obtained through theoretical approach using classical lamination theory and finite element techniques.
- (ii) For all the five design cases considered, maximum amplitude occurs at the fundamental frequency. This frequency varies from 0.05 to 0.27 Hz. Due to engine harmonics, which are 20 Hz and above, the amplitude of oscillation is negligible. Due to road undulations, at speed in the range of 15–40 kmph, and occurring in spacing of 2–0.4 m, the frequency varies from 1 to 25 Hz. In all such cases, the amplitude of vibration of the structure is less than 10 mm. Hence, the chassis is quite safe.
- (iii) The effect of damping ratio considered i.e. 0.2–0.5 is found to be negligible at frequencies beyond 0.3 Hz in all cases of design, and for all dynamic conditions considered.
- (iv). When structural steel chassis is replaced by carbon/epoxy material, static deflection increased from 4.2 to 17.795 mm which is acceptable, while stress is the same. However, the weight of the chassis is reduced by nearly 80%.
- (v) Replacing cross members of steel by carbon/epoxy has not affected the static or dynamic parameters.
- (vi) When the long channel section is reduced from 230.7 mm  $\times$  77.5 mm  $\times$  8 mm to 200 mm  $\times$  75 mm  $\times$  6.2 mm while the weight of the chassis is reduced by 20%, there is a small change in the natural frequencies. The dynamic parameters are not affected much. The static deflection increased from 4.218 to 7.744 mm, and stress is increased from 46.127 to 72.373 N/mm<sup>2</sup>. However, the changes in deflection and stress are both in acceptable limits.
- (vii) Effect of increasing the cross members for the small C section in steel for long members, resulted in insignificant changes in static and dynamic parameters.

# Appendix

## Results of harmonic analysis

Parameters	Structural steel (230.7 mm × 77.5 mm × 8 mm)			Structural steel (200 mm × 75 mm × 6.2 mm)			Additional cross member (200 mm × 75 mm × 6.2 mm)		
	0.2	0.3	0.5	0.2	0.3	0.5	0.2	0.3	0.5
Damping ratio									
Base excitation	435.7 mm at 0.05 Hz	322.3 mm at 0.05 Hz	217.1 mm at 0.05 Hz	448.9 mm at 0.05 Hz	347.5 mm at 0.05 Hz	239.1 mm at 0.05 Hz	498.2 mm at (0.05 Hz)	367 mm at (0.05 Hz)	243.7 mm at (0.05 Hz)
Engine harmonic load (2000 sin( $\omega t$ )/N)	896.9 mm at 0.05 Hz	648.3 mm at 0.05 Hz	408.2 mm at 0.05 Hz	873.3 mm at 0.05 Hz	664.1 mm at 0.05 Hz	433.5 mm at 0.05 Hz	968.1 mm at (0.05 Hz)	700.6 mm at (0.05 Hz)	441.3 mm at (0.05 Hz)
Pitch condition	2067 mm at 0.16 Hz	142.9 mm at 0.16 Hz	94.9 mm at 0.16 Hz	118.6 mm at 0.14 Hz	85.9 mm at 0.14 Hz	66.9 mm at 0.15 Hz	104.3 mm at (0.14 Hz)	80 mm at (0.14 Hz)	60.5 mm at (0.14 Hz)
Roll condition	348 mm at 0.16 Hz	294.2 mm at 0.19 Hz	215.1 mm at 0.18 Hz	316.4 mm at 0.18 Hz	250.3 mm at 0.18 Hz	189.3 mm at 0.15 Hz	340.7 mm (0.16 Hz)	253.5 mm at (0.16 Hz)	183.3 mm at (0.16 Hz)
Parameters	Carbon/epoxy (230.7 mm × 77.5 mm × 8 mm)			Combination (230.7 mm × 77.5 mm × 8 mm)					
Damping ratio	0.2	0.3	0.5	0.2	0.3	0.5	0.2	0.3	0.5
Base excitation	613.4 mm at 0.1 Hz	416.8 mm at 0.1 Hz	262.9 mm at 0.1 Hz	473.5 mm at 0.05 Hz	337.2 mm at 0.05 Hz	221.8 mm at 0.05 Hz	673.2 mm at 0.05 Hz	414.1 mm at 0.05 Hz	
Engine harmonic load (2000 sin( $\omega t$ )/N)	1180.1 mm at 0.1 Hz	789.4 mm at 0.1 Hz	474.7 mm at 0.1 Hz	967.1 mm at 0.05 Hz	673.2 mm at 0.05 Hz	414.1 mm at 0.05 Hz			
Pitch condition	81.2 mm at 0.24 Hz	66.1 mm at 0.24 Hz	56.7 mm at 0.24 Hz	211.3 mm at 0.18 Hz	146.1 mm at 0.18 Hz	96.7 mm at 0.18 Hz			
Roll condition	353.8 mm at 0.27 Hz	265.4 mm at 0.27 Hz	188 mm at 0.27 Hz	447.5 mm at 0.2 Hz	334 mm at 0.2 Hz	230.2 mm at 0.2 Hz			

## References

1. Hari Kumar A, Deepanjali A (2016) Design and analysis of automobile chassis. *Int J Eng Sci Innov Technol (IJESIT)* 5(1). ISSN: 2319-5967
2. Patel RL, Morabiya DB, Rathour AN (2014) Weight optimization of chassis frame using Pro-Mechanica. *SSRG Int J Mech Eng (SSRG-IJME)* 1(8):4–9. ISSN: 2348-8360
3. Gaikwade AV, Ghawade PS (2014) Finite element analysis of ladder chassis frame. *Int J Eng Technol Manag Appl Sci* 2(6). ISSN 2349-4476
4. Murali G, Subramanyam B, Naveen D (2013) Design improvement of a truck chassis based on thickness. In: *Altair technology conference, Sigma Consultancy Service, India*, pp 1–6
5. NK Giri (1998) *Automobile mechanics*, 8th edn. Khanna Publishers, New Delhi
6. Patel VV, Patel RI (2012) Structural analysis of ladder chassis frame. Mechanical Department, Government Engineering College, Gujarat. ISSN 2231-2581
7. Agarwal MS et al (2013) Finite element analysis of truck chassis. *Int J Eng Sci Res.* ISSN: 2277-9655
8. Vijaykumar P et al (2012) Structural analysis of ladder chassis frame and design modification for weight reduction. *Int J Eng Res Technol* 1(3). ISSN: 2278-0181

# Experimental Studies on Steel Beam-to-Column Connections Under Elevated Temperature



A. Cinitha and V. Nandhini

**Abstract** The connection behaviour of square hollow section as column welded with I-section as beam (SHCWIB) is commonly used in the construction of modern steel buildings. The behaviour of such connections under elevated temperature or fire load is limited. In this paper, the experimental studies on the behaviour of SHCWIB connection, subjected to an elevated temperature (of 600 °C) and mechanical load, are presented. The beam-to-column connection is initially exposed to the elevated temperature and then cooled to the room temperature. Pre-thermally damaged connection is subjected to an increasing monotonic load while the column member is subjected to a constant axial compression. It is observed that the connection failed at lower loads due to the combination of P-delta effect and pre-thermal damage.

**Keywords** Square hollow section · Moment connection · Elevated temperature · Monotonic loading

## 1 Introduction

The welded beam-to-column connections are widely adopted in steel-framed structures due to easiness in construction and economy. The fire-resistant design of steel-framed structures demands strength to resist thermal and service loads, during such events to prevent sudden failures. The members are designed to possess adequate strength at specified elevated temperature for a period of time. The effect of thermal forces in beams and columns is determined by the type of the beam-to-column connections, such as rigid, semi-rigid, and flexible [1–4]. The connection member's

---

A. Cinitha (✉)  
CSIR-Structural Engineering Research Centre, Chennai,  
Tamil Nadu 600113, India  
e-mail: [cinitha@serc.res.in](mailto:cinitha@serc.res.in)

V. Nandhini  
Department of Civil Engineering, Nandha Engineering College, Erode,  
Tamil Nadu 638052, India

© Springer Nature Singapore Pte Ltd. 2020  
H. K. Voruganti et al. (eds.), *Advances in Applied Mechanical Engineering*,  
Lecture Notes in Mechanical Engineering,  
[https://doi.org/10.1007/978-981-15-1201-8\\_38](https://doi.org/10.1007/978-981-15-1201-8_38)

335

response to fire has been examined by Lawson [5] under varied moment. Three typical connections were studied, an extended end plate, double-sided web cleat and a flush end plate, and demonstrated that significant moments could be sustained during fire event. Al-Jabri et al. [2, 6] conducted a series of elevated temperature connection tests to study the response under fire by varying parameters such as member size, thickness composite slab characteristics and end plate type. However, there is limited information on the connection behaviour of SHS column and I-section as beam. Hence at CSIR-SERC, efforts have been put forward to understand the behaviour of pre-thermally damaged SHCWIB connection subjected to incremental mechanical load till collapse.

## 2 Problem Definition

An experimental investigation is conducted to assess the performance of pre-thermally affected steel beam-to-column connection under mechanical loading. Towards this, a welded steel I-beam-to hollow-column connection has been fabricated. The connection consists of square hollow section (SHS) column of  $220 \times 220 \times 6$  mm of height 1500 mm and ISMB200 beam of length 2500 mm. The connection is established by welding I-beam-to-SHS-column member with mig weld of size 6 mm. An equal angle of IS 80  $\times$  6 is used as seat and cleat connection, which is welded between I-beam and SHS column with 6-mm fillet weld. The beam-to-column connection with regions exposed to elevated temperature is shown in Fig. 1.

The three zones considered in the study are 350 mm on either side from the face of the connection in member (i.e. Zone 1 (Z1), downward along the column, Zone 2 (Z2) upward in column from the connection region) and Zone 3 (Z3), is on I-beam from the face of the connection. K-type thermocouples are used to trace the heating profile. The thermocouples #0 and #3 are attached to the centre of Z1 and Z2. And thermocouples #4 and #5 are attached to the respective centre of top and bottom

**Fig. 1** Beam-to-column welded connection

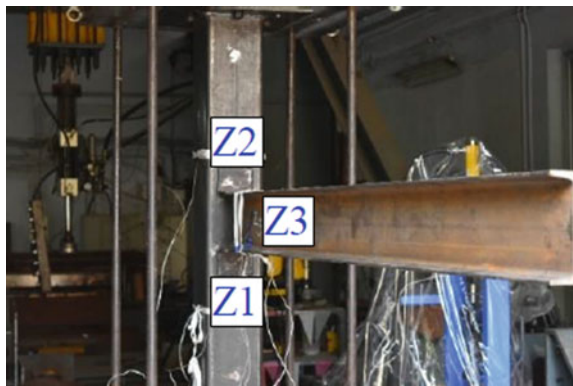
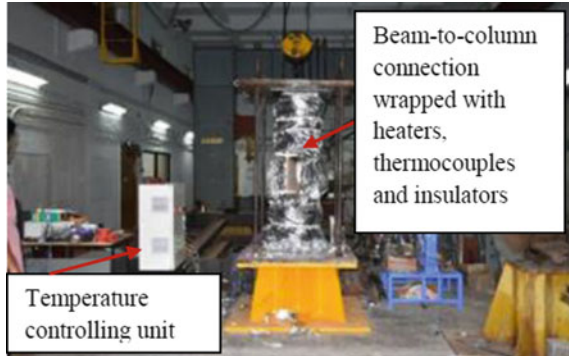


**Fig. 2** Experimental set-up to induce elevated temperature on SHCWIB



flanges of I-beam. Thermocouples #6 and #7 are attached to either face of the web of the beam within Z3. The temperature distribution in regions exposed to the heating up to 600 °C for 240 min (i.e. equivalent to 4 h of low category fire). Mild colour change is observed on the exposed surface with no significant visual deformation in any of the structural member after exposing to elevated temperature.

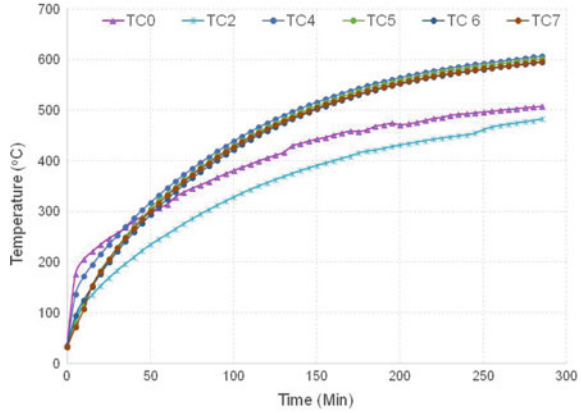
### 3 Experimental Set-Up for Inducing Elevated Temperature Effect

In order to induce elevated temperature effect on the connection from ambient to 600 °C, specially fabricated radiation heaters were used. The flexible heaters were wrapped over the three regions exposed to elevated temperature effect [7]. Insulators capable to withstand more than 1200 °C were used to prevent dissipation of heat to the atmosphere and to the other regions of the structure. The heat conducted to the other part of the structure is measured with adequate numbers of thermocouples. The experimental set-up is as shown in Fig. 2. Figure 3 shows the measured temperature distribution across the joint zone.

### 4 Experimental Set-Up for Mechanical Loading

To examine the response of pre-heated SHCWIB moment connection is subjected to incremental monotonic load till failure. The column member is axially restrained and loaded with a constant load. To understand the P-delta effect, an axial load of 0.6 Py is applied to the column. The I-beam is subjected to incremental load with 25-ton actuator (in monotonic manner) till failure takes place. The strain rate adopted during the experiment is 0.5 mm/min. Linear variable differential transducers (LVDTs) and strain gauges were used to monitor the deformation and strain values

**Fig. 3** Measured temperature distribution across connection. *Note* TC—thermocouple



*Note: TC- Thermocouple*

**Fig. 4** Experimental set-up for mechanical loading to SHCWIB connection

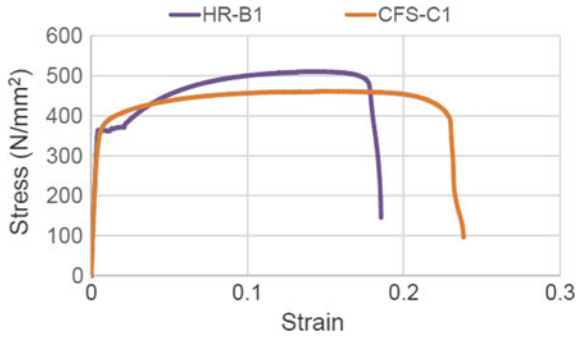


of the specimen at identified regions during the test. The test set-up is shown in Fig. 4. The typical stress versus strain behaviour of coupons extracted from beam and column members at ambient temperature is shown in Fig. 5. Figure 6 shows load versus strain behaviour observed at various regions of beam-to-column connection while subjected to mechanical loading (i.e., S1–S4 are the measurements of strain gauges glued to the column member, S5–S16 are the strain gauges glued to the beam member, and R11–R13 are the rosette strain gauges glued to the web of the beam member nearer to the connection region).

## 5 Results and Discussions

The temperature distribution across the connection region shows uniform distribution in beam and column members. Mild colour change is observed on the exposed





Note: HR-B1 Coupons extracted from beam member  
CFS-C1 Coupons extracted from column member

Fig. 5 Typical stress versus strain behaviour of coupons at ambient temperature

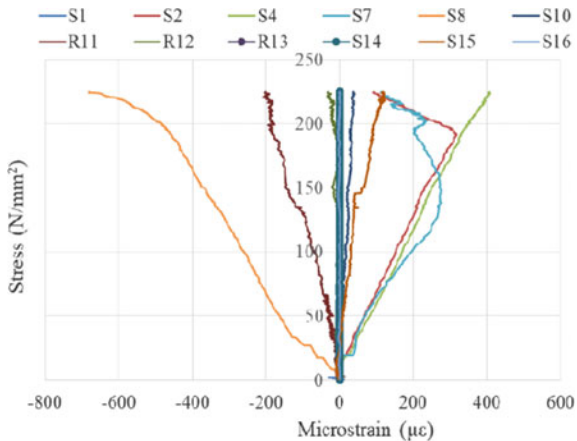
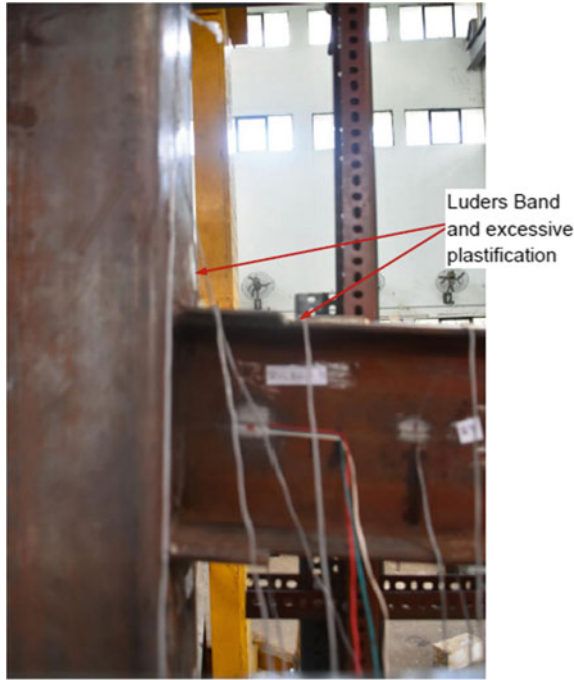


Fig. 6 Stress versus strain behaviour of beam-to-column connections

surface with no significant visual deformation in any of the structural member after exposing to elevated temperature. The deterioration in the strength and stiffness at elevated temperature are important characteristics of steel beam-to-column moment connection [8]. The load versus deflection behaviour of pre-thermally damaged beam-to-column connection subjected to mechanical load is studied. The beam has undergone a deflection of 80 mm at failure. The damage in connection region was less, and no cracks were found in welded regions. The beam member has undergone plastic deformation which was evident from the formation of Lüder's band observed at pre-thermally affected region (Fig. 7) and strain values measured at various locations.



**Fig. 7** Formation of Lüder's band and excessive plastification

The inelastic connection behaviour in terms of moment rotation is required for the prediction of failure in steel structures. The moment-resisting frames have large number of dissipative zones, located near the beam-to-column connections, and it is complex to compute the ultimate load analytically. The experimentally observed load versus deflection and moment versus rotation behaviours are shown in Figs. 8 and 9, respectively.

**Fig. 8** Load versus deflection behaviour

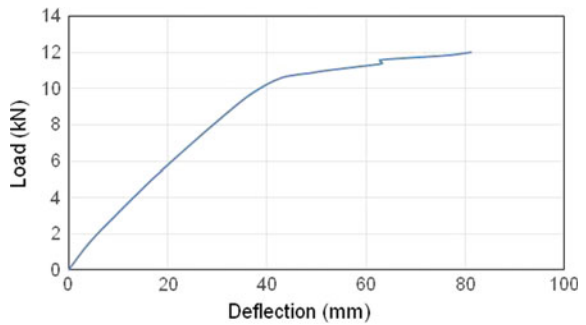
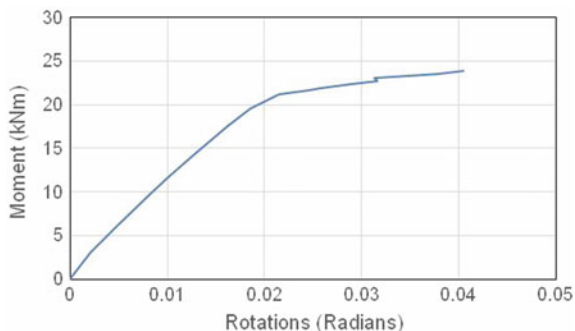


**Fig. 9** Moment versus rotation behaviour



## 6 Conclusion

The behaviour of pre-thermally damaged SHCWIB-type moment connection subjected to mechanical load is experimentally studied and presented. It is found that the connection region had no visible cracks or any other significant damages. The results demonstrate that the moment capacity of the connection decreases by exposure to elevated temperatures. This insight is further emphasised with the load versus strain behaviour of beam-to-column connections under mechanical load (the strain at ultimate load ranges from 100 to 650 microstrain). While subjected to mechanical load, the pre-thermally damaged connection has undergone comparatively lesser strain value than the ambient condition. It is also noticed that axial restraint, i.e. (P-delta effect) force, has a significant effect on moment capacity of steel beam-to-column connection, viz. the connection failed at lower loads.

**Acknowledgements** This work has been supported by CSIR-SERC as part of an in-house R&D work. The technical assistance rendered by the technical staffs, Mr. M. Kumarappan and Mrs. S. Vimala and Ms. M. Nandhini Project Assistant of Steel Structures Laboratory, is greatly acknowledged.

## References

1. Sun Kim US, Lee JS, Kwon YB (1994) Behaviour of connections between SHS columns and W-section beams. In: International speciality conference, Missouri University of Science and Technology
2. Al-Jabri KS, Davison JB, Burgees IW (2008) Performance of beam-to-column joints in fire – a review. *Fire Saf J* 43:50–62
3. Yang K-C, Chen S-J, Ho M-C (2009) Behaviour of beam-to-column moment connection under fire load. *J Constr Steel Res* 65:1520–1527
4. Al-Jabri KS (2011) Modelling and simulation of beam-to-column joints at elevated temperature: a review. *J Franklin Inst* 348:1695–1716
5. Lawson RM (1990) Behaviour of steel beam-to-column connections in fire. *J Struct Eng* 68:262–271

6. Al-Jabri KS, Lennon T, Plank RJ (1987) Behaviour of steel and composite beam-column connections. *J Constr Steel Res* 18:17–54
7. Cinitha A, Umesha PK, Palani GS, Sampath V (2018) Compression behaviour of steel tubular member under simulated corrosion and elevated temperature. *Int J Steel Struct* 18:139–152
8. Eurocode 3 (1995) Design of steel structures—Part 1.2: general rules-structural fire design. European Community for Standardisation, Brussels

# Investigating the Influence of Higher-Order NURBS Discretization on Contact Force Oscillation for Large Deformation Contact Using Isogeometric Analysis



Vishal Agrawal and Sachin S. Gautam

**Abstract** The present work studies the influence of the higher-order non-uniform rational B-spline (NURBS)-based discretizations on the oscillations of contact reaction forces for the large deformation and large relative tangential sliding contact problem. The segment-to-segment-based Gauss-point-to-surface isogeometric contact formulation is used to express the contact contribution to the discretized weak form. The penalty method is adopted for the regularization of the impenetrability contact constraint. The frictionless sliding contact problem involving two deformable bodies is considered for examining the variation in the distribution of contact reaction force on varying the interpolation order of the NURBS-discretized geometry. The solution with a very fine mesh is used as a reference. The study shows that the accuracy of the contact solution improves on increasing the interpolation order of the NURBS. Compared to a very fine mesh, higher-order NURBS with a coarser mesh can achieve the nearly same result at a much lower number of degrees of freedom.

**Keywords** Isogeometric analysis · Computational contact mechanics · Large deformation · NURBS

## 1 Introduction and Motivation

Isogeometric analysis (IGA) uses the computer-aided design (CAD) polynomials as a basis for the modelling of complex geometry exactly and approximation of unknown solution fields [1]. The key purpose of isogeometric analysis technique is to circumvent the computationally expensive mesh generation process by merging the CAD modelling and finite element analysis (FEA) processes into a unified framework. Apart from fulfilling its original purpose, IGA delivers superior results

---

V. Agrawal · S. S. Gautam (✉)

Department of Mechanical Engineering, Indian Institute of Technology Guwahati, Guwahati 781039, India  
e-mail: [ssg@iitg.ac.in](mailto:ssg@iitg.ac.in)

V. Agrawal

e-mail: [v.agrawal@iitg.ac.in](mailto:v.agrawal@iitg.ac.in)

© Springer Nature Singapore Pte Ltd. 2020

H. K. Voruganti et al. (eds.), *Advances in Applied Mechanical Engineering*,

Lecture Notes in Mechanical Engineering,

[https://doi.org/10.1007/978-981-15-1201-8\\_39](https://doi.org/10.1007/978-981-15-1201-8_39)

per degree of freedom over its counterpart FEA due to its inherent features, i.e. the capability to represent the complex shape geometry exactly even with a coarse mesh, tailorable inter-element continuity, and non-negativeness of the underlying basis functions. For the detailed description, the reader is referred to [1] and a monograph by Cottrell et al. [2]. Due to its unique intrinsic properties, isogeometric analysis has emerged as an advantageous computational technology for the treatment of a wide range of contact problems, especially for large deformation ones. In contrast to traditional  $C^0$  continuous Lagrange finite element (FE)-based description, the NURBS-discretized structure inherently provides the smooth representation of the contact interface. Thus, a unique normal vector field across the boundaries of the contact elements is obtained. Attributed to the higher inter-element continuity, the NURBS-based discretization eliminates the need for additional surface smoothing strategies that are often required in the context of traditional FE-based approaches. In the past few years, a considerable amount of research efforts have been devoted to the treatment of large deformation contact problems with or without considering friction within the framework of isogeometric analysis [3–5]. A comprehensive overview of the recent growth of isogeometric analysis and its advantages with respect to traditional finite element-based approaches in the field of contact mechanics is presented by De Lorenzis et al. [6].

Based on the available literature on the treatment of contact using IGA, it has been observed that although superior results are obtained as compared to FEA, a very fine mesh is still needed to get the accurate results [3–6]. With this, a considerable amount of computational efforts is associated which is numerically undesirable. Therefore, an alternative solution approach, which sidesteps the necessity of a very fine mesh and accurately resolves the contact quantities across the contact surface, is required. To address this issue, the present work explores the application of higher-order NURBS discretizations for isogeometric contact analysis. To the best of authors' knowledge, to this date, no such study that makes use of more than quartic interpolation order of NURBS for the treatment of contact is carried out. For the purpose of comparison, the contact solution with a very fine mesh is used as a reference. In the current work, the Gauss-point-to-surface contact algorithm of Dimitri et al. [7] is used to model the contact between two deformable bodies. The impenetrability contact constraint is directly enforced at the Gauss points of the slave body. For the regularization of the impenetrability constraint, the penalty method is adopted. For the determination of an active contact point, an active set strategy is utilized. An in-house code written in the MATLAB environment that incorporates the NURBS toolbox [8] is developed for the simulation of considered large deformation contact problem. For the detailed description of the implementation of isogeometric analysis technology, a tutorial paper by Agrawal and Gautam [9] can also be referred.

## 2 Variational Formulation

In this section, the computational formulation for two-dimensional contact between two hyperelastic bodies without friction is briefly described. To model the contact between the bodies, the full-pass contact algorithm is considered. In this, one body is taken as the slave,  $\mathcal{B}^s$ , while the other as the master,  $\mathcal{B}^m$ . The current configuration of a generic point  $\mathbf{x}^r$  of the body  $\mathcal{B}^r$ , where  $r = \{s, m\}$ , is given by:  $\mathbf{x}^r = \mathbf{X}^r + \mathbf{u}^r$ , where  $\mathbf{X}^r$  and  $\mathbf{u}^r$  denote the reference configuration and displacement field, respectively. In the current configuration, the contact interface for the slave and the master bodies is described as:  $\Gamma_c := \Gamma_c^s = \Gamma_c^m$  (assuming perfect contact). In the case of active contact, the contribution of the contact traction to virtual work is non zero and is given by [10]

$$\delta W_c = \int_{\Gamma_c^s} t_N \delta g_N \, d\Gamma \tag{1}$$

In order to solve the above equation using the Newton–Raphson iterative solution method, the linearization of the contact virtual work  $\delta W_c$  is carried out that leads to [10]

$$\Delta \delta W_c = \int_{\Gamma_c^s} (\Delta t_N \delta g_N + t_N \Delta \delta g_N) \, d\Gamma \tag{2}$$

Here,  $g_N = (\mathbf{x}^s - \bar{\mathbf{x}}^m) \cdot \mathbf{n}$  denotes the normal gap between the given slave point  $\mathbf{x}^s \in \Gamma_c^s$  on the contact surface of the slave body and  $\bar{\mathbf{x}}^m \in \Gamma_c^m$  is a corresponding contact point on the contact surface of  $\mathcal{B}^m$ . The corresponding contact point  $\bar{\mathbf{x}}^m$  on master surface  $\Gamma_c^m$  is determined by drawing a line that passes through the given slave point  $\mathbf{x}^s$  in the direction of normal  $\mathbf{n}$  to  $\Gamma_c^m$ . The penalty-based regularization of normal traction yields  $t_N = \epsilon_N \langle g_N \rangle$ .

Within the context of isogeometric analysis, the parametrization for the contact boundary layer is inherently imported from the description of the bulk domain. We refer to monograph by Piegl and Tiller [11] for the theory on NURBS polynomials. Using the isoparametric concept, the displacement field  $\mathbf{u}^e$ , its variation  $\delta \mathbf{u}^e$ , and the coordinates of the discretized form of the contact surface within its current configuration  $\mathbf{x}^e$  are given by [7, 10]

$$\mathbf{u}^e = \sum_{k=1}^{n_p^e} R_k \mathbf{u}_k, \quad \delta \mathbf{u}^e = \sum_{k=1}^{n_p^e} R_k \delta \mathbf{u}_k, \quad \text{and} \quad \mathbf{x}^e = \sum_{k=1}^{n_p^e} R_k \mathbf{x}_k \tag{3}$$

where  $n_p^e = 1 + p$  represents the total number of control points within an element ‘e’. In the Gauss-point-to-surface-based contact algorithm, the impenetrability constraint is directly enforced at the Gauss quadrature points on the slave body contact surface

$\Gamma_c^s$ . The virtual work is numerically computed on  $\Gamma_c^s$  as [7, 11, 12]

$$\delta W_c = \delta u^T \int_{\Gamma_c^s} \epsilon_N g_N \mathbf{N} d\Gamma = \delta u^T \mathbf{R}_c \tag{4}$$

where  $\mathbf{R}_c$  denotes the contact contribution to the residual vector. It is computed over the active points using the Gauss–Legendre quadrature rule as [7, 11, 12]

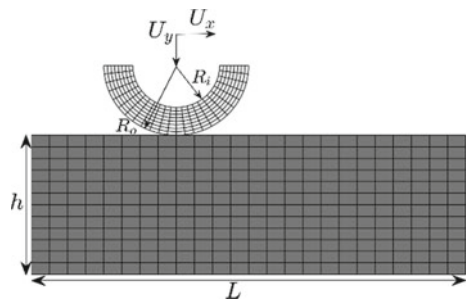
$$\mathbf{R}_c = \epsilon_N \sum_{gp.act}^{n_{gp}^c} g_{N_{gp}} \mathbf{N}_{gp} J_{gp} w_{gp} \tag{5}$$

Here,  $n_{gp}^c$  denotes the total number of Gauss points, and  $w_{gp}$  and  $J_{gp}$  are the weight and the determinant of the Jacobian matrix associated with an active Gauss quadrature point indicated with ‘gp’. The Gauss point is considered active if  $g_N < 0$ . The consistent contact stiffness matrix and other contact matrices can be directly followed from reference [7, 10].

### 3 Numerical Example, Results, and Discussion

In this section, a two-dimensional large deformation and large relative tangential sliding contact problem is considered to study the variation in the distribution of contact reaction force on varying the interpolation order of the NURBS. The geometrical setup along with the considered coarse mesh for the die and slab is illustrated in Fig. 1, where  $R_o = 0.5$  mm,  $R_i = 0.3$  mm,  $L = 3.0$  mm, and  $h = 1$  mm. The bottom surface of the slab is constrained along both the vertical and the horizontal directions. The geometric details, e.g. the control points and knot vectors along each parametric direction for both the die and the slab are obtained from Ref. [2]. A commercial CAD modelling software, viz. Rhino ([www.rhino3d.com](http://www.rhino3d.com)), can also be utilized for their construction. The considered problem is simulated in two steps.

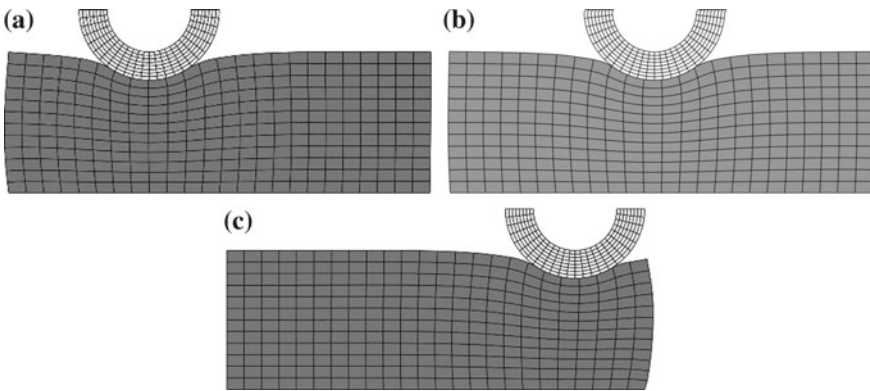
**Fig. 1** Geometrical set-up of the sliding problem. The meshes for the die and the slab are  $24 \times 8$  and  $24 \times 12$ , respectively





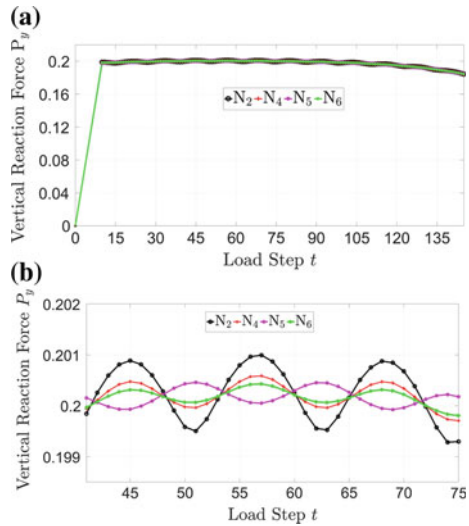
In the first, the top surface of the die is subjected to downward vertical displacement  $U_y = -0.2$  mm in 10 time steps and then moved horizontally along the slab by  $U_x = 1.5$  mm in next 140 time steps. The corresponding deformed configurations of the set-up for the quadratic  $N_2$  order of NURBS discretization at different time steps are shown in Figs. 2a–c. A Neo-Hookean hyperelastic material model with  $E_{\text{die}} = 1000$  GPa and  $E_{\text{slab}} = 1$  GPa, and  $\nu_{\text{die}} = \nu_{\text{slab}} = 0.3$  under the plane strain conditions is considered for modelling the large deformation. The default value of the penalty parameter is  $\epsilon_N = 100$ . For the evaluation of the contact integrals,  $n_{\text{gp}} = p + 1$  number of equidistant Gauss quadrature points for  $N_p$  order of NURBS discretization are used per contact element.

Figure 3a illustrates the variation of vertical global contact reaction force  $P_y$  over the time step  $t$  for  $N_2$  and  $N_4$  order of NURBS discretizations. The resultant contact reaction force for each case of discretizations is evaluated at the top line of the die and is accounted at the end of each time step. It can be observed that during the first step of the simulation, when the die is pressed against the slab, the magnitude of the vertical contact reaction force  $P_y$  increases linearly. After that, during the second step, when the die is horizontally slid across the slab,  $P_y$  continues to oscillates around a mean line; see Fig. 3b. According to theory, no such oscillations should be present during sliding. The commonly employed solution approach to alleviate such non-physical oscillation of the contact responses is to use a very fine mesh that may accurately capture the variation of contact quantities across the contact interface [13]. However, a large amount of computational efforts is associated, which is undesirable. Thus, in the present work, as an alternative to fine meshes which are obtained through the knot insertion or  $h$ -refinement strategy in IGA, the higher-order NURBS are used. In particular, the fifth and sixth orders of NURBS, denoted by  $N_5$  and  $N_6$ , are employed for the discretization of the overall bulk domain of the two bodies including their contact surface. The corresponding plots for both these discretizations are also shown in Fig. 3a. The enlargement of  $P_y$  for  $N_5$  and  $N_6$  is shown in Fig. 3b. It can be observed that on increasing the order of NURBS from  $p = 4$  to  $p = 6$ , the amplitude



**Fig. 2** Deformed configurations: **a** at load step  $t = 11$ , **b** at  $t = 46$ , and **c** at  $t = 141$

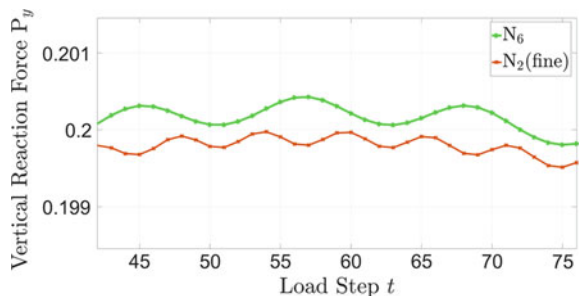
**Fig. 3** **a** Resultant vertical contact reaction force  $P_y$  for the overall simulation process and **b** zoomed view of  $P_y$  for different orders of NURBS discretizations



of the oscillation error in  $P_y$  reduces. This is due to employing higher-order NURBS interpolations for the evaluation of the contact integrals. This, as a result, improves the approximation of contact quantities at coarse mesh compared to quadratic order of NURBS discretization.

Next, the performance of the most accurate  $N_6$  discretization is compared with that of  $N_2$  order of NURBS at a fine mesh level. Figure 4 illustrates the results for  $N_6$  order of NURBS with a coarse mesh shown in Fig. 1 and for  $N_2$  order of NURBS with a fine mesh arrangement, i.e.  $48 \times 16$  for the die and  $48 \times 24$  the slab. The associated total number of degrees of freedom for the two discretization arrangements are 1410 and 4243, respectively. From Fig. 4, it can be seen that compared to  $N_2$  that is with a fine mesh,  $N_6$  order of NURBS that is with a coarser mesh achieves the nearly same result in terms of accuracy as the amplitude of the oscillation with both the discretization arrangements is nearly identical. On the other hand, as compared to  $N_2$ ,  $N_6$  utilizes at least 65% lesser number of degrees of freedom to obtain the similar result, which is appreciable. It is also noted that the small shift in the reaction curve for  $N_2$  is due

**Fig. 4** Resultant vertical contact reaction force  $P_y$  for  $N_6$  with a coarse mesh arrangement shown in Fig. 1 and for  $N_2$  with a fine mesh arrangements



to introduction of a very large number of control points with  $h$  refinement operation with respect to  $N_6$  discretization.

Based on the obtained result, it is clear that higher-order NURBS discretization is a strategy that attains accurate result with a coarser mesh arrangement compared to lower-order based NURBS discretization using a very fine mesh arrangement. However, employing the higher-order NURBS in the vast majority of the bulk domain that does not come into the contact may not be computationally favourable since the accuracy of the contact solution is mainly dependent on the interaction across the contact interface. Therefore, it becomes desirable to develop a contact element enrichment strategy that avoids the employment of higher-order NURBS in the bulk domain. Probably, similar to those presented by Sauer [14], and Corbett and Sauer [15], but in the context of isogeometric analysis.

## 4 Conclusion

This paper studies the higher-order NURBS-based isogeometric analysis for large deformation contact involving two deformable bodies. It is observed that the accuracy of the vertical contact reaction force improves on increasing the order of NURBS discretization. In particular,  $N_6$  order of NURBS-based discretization delivers the most accurate results among all tested cases. Further, as compared to  $N_2$  order of NURBS with the fine mesh arrangement,  $N_6$  order of NURBS utilizes at least 65% lesser number of degrees of freedom to obtain the similar result. The future objective is to modify the existing NURBS discretization procedure in a way that the interpolation order of the NURBS is varied only for the contact surface. A segmentation-free mortar contact formulation by Duong et al. [16] for isogeometric contact analysis can also be incorporated in future work.

**Acknowledgements** The authors are grateful to the SERB, DST, for supporting this research under project SR/FTP/ETA-0008/2014.

## References

1. Hughes TJR, Cottrell JA, Bazilevs Y (2005) Isogeometric analysis: CAD, finite elements, NURBS, exact geometry and mesh refinement. *Comput Methods Appl Mech Eng* 194(39–41):4135–4195
2. Cottrell JA, Hughes TJR, Bazilevs Y (2009) *Isogeometric analysis: toward integration of CAD and FEA*. Wiley
3. Temizer I, Wriggers P, Hughes TJR (2011) Contact treatment in isogeometric analysis with NURBS. *Comput Methods Appl Mech Eng* 200(9–12):1100–1112
4. De Lorenzis L, Temizer I, Wriggers P, Zavarise G (2011) A large deformation frictional contact formulation using NURBS-based isogeometric analysis. *Int J Numer Methods Eng* 87(13):1278–1300

5. Temizer I, Wriggers P, Hughes TJR (2012) Three-dimensional mortar-based frictional contact treatment in Isogeometric analysis with NURBS. *Comput Methods Appl Mech Eng* 209–212:115–128
6. De Lorenzis L, Wriggers P, Hughes TJR (2014) Isogeometric contact: a review. *GAMM-Mitt.* 37(1):85–123
7. Dimitri R, De Lorenzis Scott MA, Wriggers P, Taylor RL, Zavarise G (2014) Isogeometric large deformation frictionless contact using T-splines. *Comput Methods Appl Mech Eng* 269:394–414
8. De Falco C, Reali A, Vázquez R (2011) GeoPDEs: a research tool for isogeometric analysis of PDEs. *Adv Eng Softw* 42(12):1020–1034
9. Agrawal V, Gautam SS (2019) IGA: a simplified introduction and implementation details for finite element users. *J Inst Eng (India): Ser C.* <https://doi.org/10.1007/s40032-018-0462-6>
10. Wriggers P (2006) *Computational contact mechanics*, 2nd edn. Springer, Berlin
11. Piegl L, Tiller W (2012) *The NURBS book*. Monographs in visual communication. Springer, Berlin Heidelberg
12. Agrawal V, Gautam SS (2019) Investigation of contact pressure oscillations with different segment-to-segment based isogeometric contact formulations. In: Abdel Wahab M (ed) *Proceedings of the 1st international conference on numerical modelling in engineering, NME 2018*. Lecture notes in mechanical engineering. Springer, Singapore. [https://doi.org/10.1007/978-981-13-2273-0\\_8](https://doi.org/10.1007/978-981-13-2273-0_8)
13. Franke D, Düster A, Nübel V, Rank E (2010) A comparison of the h-, p-, hp-, and rp-version of the FEM for the solution of the 2D Hertzian contact problem. *Comput Mech* 45(5):513–522
14. Sauer RA (2011) Enriched contact finite elements for stable peeling computations. *Int J Numer Methods Eng* 87(6):593–616
15. Corbett CJ, Sauer RA (2014) NURBS-enriched contact finite elements. *Comput Methods Appl Mech Eng* 275:55–75
16. Duong TX, De Lorenzis L, Sauer RA (2019) A segmentation-free isogeometric extended mortar contact method. *Comput Mech* 63(2):383–407

# Simple Optimization Algorithm for Design of a Uniform Column



Joji Thomas, Anshuman Kumar Sahu and Siba Sankar Mahapatra

**Abstract** Traditional methods for solving constrained optimization problems are not robust enough to get the solution in reasonable computational time. They have drawback of getting stuck in local optima. To overcome these problems meta-heuristic techniques are now widely used. This paper introduces simple optimization algorithm (SOPT), a meta-heuristic technique for solving constrained optimization problems. To handle the constraints, a constraint fitness priority-based ranking method is included in the algorithm. SOPT algorithm for constraint optimization is coded in MATLAB and applied to design a uniform column for minimum design cost. Result obtained is compared with the result obtained by another important meta-heuristic algorithm called cuckoo search (CS) algorithm.

**Keywords** Simple optimization · Cuckoo search · Constraint handling · Design optimization

## 1 Introduction

Engineering design attempts to formulate a plan which results in the creation of some real physical thing which having qualities of proper functionality, reliability, usability, manufacturability and marketability. A generalized process of design is outlined in the Fig. 1 [1]. The process begins with recognizing the need and ends with presenting the plans. Several iterations are made in between to reach the final plans for satisfying the need. One of the important phases in the design process is analysis and optimization. This phase requires constructing or devising abstract models of the system which are called mathematical models. These models are created in the hope that they will simulate the real physical system very well. Modelling of an

---

J. Thomas (✉)

Department of Mechanical Engineering, Saveetha Engineering College, Chennai, Tamilnadu, India

e-mail: [joji.siji@gmail.com](mailto:joji.siji@gmail.com)

A. K. Sahu · S. S. Mahapatra

Department of Mechanical Engineering, National Institute of Technology, Rourkela, Odisha, India

© Springer Nature Singapore Pte Ltd. 2020

351

H. K. Voruganti et al. (eds.), *Advances in Applied Mechanical Engineering*,

Lecture Notes in Mechanical Engineering,

[https://doi.org/10.1007/978-981-15-1201-8\\_40](https://doi.org/10.1007/978-981-15-1201-8_40)

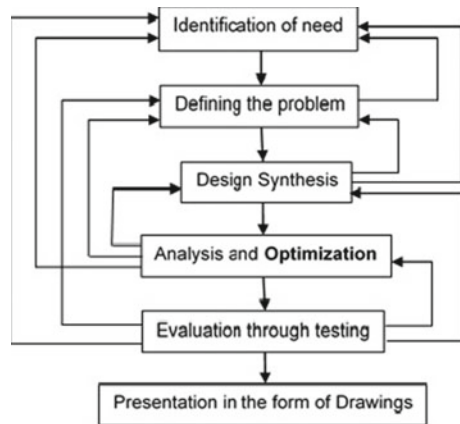
entire mechanical system may result in complex mathematical equations with large number of variables. To overcome the difficulty of analysis and optimization of such large system, it is wise to design individual elements of a system. For example, in an automobile power transmission system, design of a gearbox is computationally and mathematically simpler than the design of complete system.

Once the mathematical model is formed, it should be solved for optimizing the criterion selected. Optimization is the process of finding a solution to a problem in which a single or set of objective functions are to be maximized or minimized within a domain that contains suitable values of variables with restrictions or constraints to be satisfied. Those sets of variables which satisfy the given restrictions or constraint in the domain are feasible solutions.

The best among all the feasible solutions is known as optimum solution of the problem. Models formed are mostly non-linear in nature for engineering design problems. A non-linear problem can be represented as maximize or minimize  $y = f(\vec{x})$  where  $\vec{x}$  is a column vector of  $n$  design variables, i.e.  $\vec{x} = [x_1, x_2, x_3, \dots, x_n]^T$  Subjected to the  $m$  inequality and  $p$  equality constraints, i.e.  $g_i(\vec{x}) \leq 0, i = 1, 2, \dots, m, h_j(\vec{x}) = 0, j = 1, 2, \dots, p$  with variable bounds  $x_k^{(L)} \leq x_k \leq x_k^{(U)}, k = 1, 2, \dots, n$   $x_k^{(L)}$  and  $x_k^{(U)}$  are the upper and lower limit of values which are permissible in the variables.

There are large numbers of techniques available for solving optimization problems. These are basically divided into two groups such as (1) Traditional methods, (2) Non-traditional methods. Two distinct types of algorithms are used in traditional approach. Direct search methods use only objective function values to locate the optimum point. Indirect search or gradient-based methods use the first and/or the second-order derivatives of the objective function to locate the optimum point. There is another class of optimization techniques that is based on the stochastic search and does not require the objective function to be continuous or differentiable. These algorithms are general-purpose algorithms and can be applied to solve a wide variety of optimization problems. Another reason for using such types of algorithms

**Fig. 1** Iterative phases in a design process



lies in ability to get global solutions while traditional methods get stuck to the local optimum solution many times.

Constrained optimization is the process of optimizing an objective function with respect to some variables in the presence of constraints. Coello [2] has discussed constraint handling techniques adopted in popular evolutionary algorithms. The constraint handling techniques are well suited for all types of constraints (linear, non-linear, equality, non-equality) mostly used in engineering applications. Wang and Fang [3] have used an effective shuffled frog-leaping algorithm (SFLA) for solving multi-modal resource-constrained project scheduling problem. Few benchmark problems have been solved by SFLA and compared with existing algorithms like simulated annealing, genetic algorithm, hybrid scatter search, hybrid rank-based evolutionary algorithm, truncated branch and bound and differential evolution (DE) algorithm. Coello and Montes [4] have proposed a dominance-based selection process for constrained handling in genetic algorithm for global optimization. This approach has been compared with several evolutionary optimization algorithms and traditional mathematical programming for problems like welded beam design, design of a 10-bar plane truss, design of a pressure vessel, disjoint feasible region, minimization of the weight of a tension/compression string. The method performs well in several test problems both in form of the number of fitness function evaluations required and in terms of the quality of the solution obtained. Michalewicz [5] has reviewed the methods for handling constraints in genetic algorithm for numerical optimization problems and test them on selected problems highlighting the strength and weaknesses of each method.

## 2 Simple Optimization (SOPT) Algorithm

A meta-heuristic algorithm is essentially a heuristic that can be applied for different varieties of problems. Simple Optimization (SOPT) is one such algorithm, the first step of this algorithm is to generate a random set of solutions. These solutions are then sorted based on the objective function values. The best solution occupies topmost position. Thereafter multiple iterations are performed on these solutions. In each iteration, two new solutions are generated according to Eqs. 1 and 2. In these two equations  $x_{i,new}$  is the  $i$ th parameter of new solution,  $x_{i,best}$  is the  $i$ th parameter of first solution of the set, which is the best solution till that iteration and  $R_i$  is a random number normally distributed around zero with a standard deviation of  $\sigma_i$ . The calculation of the standard deviation for the normal distribution is shown in Fig. 2. Here,  $N$  is population size and  $M$  is number of optimization parameters. Two constants  $c_1$  and  $c_2$  are controlling parameters. To reduce the dependency of algorithm on controlling parameters,  $c_2$  is taken half of the value of  $c_1$ . From the experiments it has been found that value of  $c_1$  taken between 1 and 2 gives better results in fewer computations.

	variable 1	variable 2	variable 3	...	variable M
Candidate solution 1	X11	X12	X13	...	X1M
Candidate solution 2	X21	X22	X23	...	X2M
Candidate solution 3	X31	X32	X33	...	X3M
...	...	...	...	...	...
Candidate solution N	XN1	XN2	XN3	...	XNM

$\sigma_1$   $\sigma_M$

**Fig. 2** Schematic representation of calculating standard deviation

$$x_{i,new} = x_{i,best} + c_1 \times R_i \tag{1}$$

$$x_{i,new} = x_{i,best} + c_2 \times R_i \tag{2}$$

The generated new solution is compared with the latest worst solution and will replace it if better in objective function value. The flow chart of the algorithm is presented in Fig. 3. Iterations will be continued till the termination criterion is not reached which may be the best solution achieved or maximum number of iterations is reached.

For handling constraints, SOPT algorithm incorporated a constraint priority-based ranking method. This method consists of calculating constraint fitness function  $F_i(\vec{x})$  as given by Eqs. 3 and 4. Equation 3 is used for  $m$  number of inequality constraints  $g_i(\vec{x}) \leq 0$ .

$$F_i(\vec{x}) = \begin{cases} 1, & g_i(\vec{x}) \leq 0 \\ 1 - \frac{g_i(\vec{x})}{g_{\max}(\vec{x})}, & g_i(\vec{x}) > 0 \end{cases} \tag{3}$$

where  $g_{\max}(\vec{x}) = \max g_i(\vec{x})$ ,  $i = 1, 2, \dots, m$ . For  $p$  number of equality constraints  $h_i(\vec{x}) = 0$  Eq. (4) is used

$$F_i(\vec{x}) = \begin{cases} 1, & h_i(\vec{x}) = 0 \\ 1 - \frac{|h_i(\vec{x})|}{h_{\max}(\vec{x})}, & h_i(\vec{x}) \neq 0 \end{cases} \tag{4}$$

where  $h_{\max}(\vec{x}) = \max\{h_i(\vec{x})\}$ ,  $i = m + 1, m + 2, \dots, m + p$ .

Thereafter, a total constraint fitness function  $F_{\text{con}}(\vec{x})$  is calculated using Eq. (5)

$$F_{\text{con}}(\vec{x}) = \sum_{i=1}^{m+p} w_i F_i(\vec{x}) \tag{5}$$



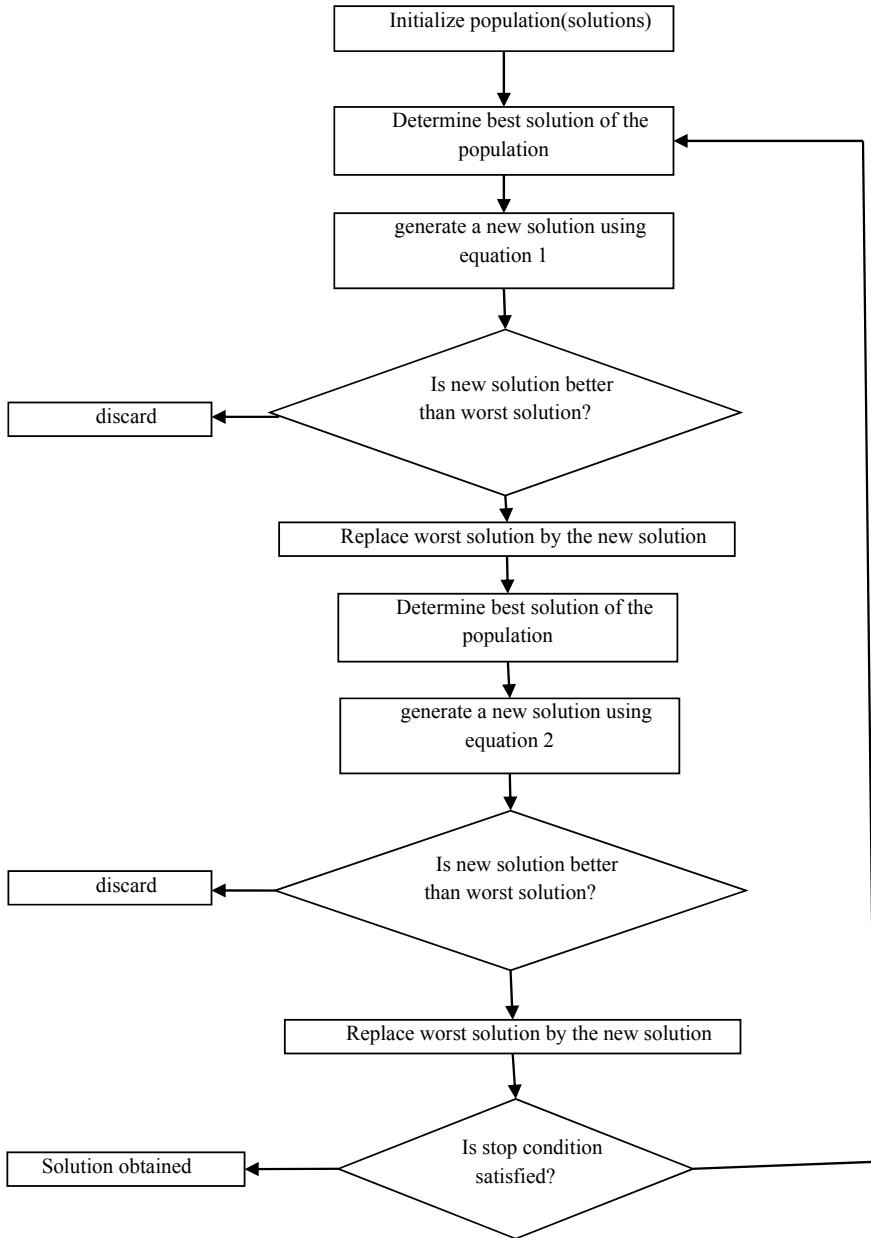


Fig. 3 Flow chart of SOPT algorithm

Weight associated with constraint maintains the diversity of the solutions. Value of  $F_{\text{con}}(\vec{x})$  varies between 0 and 1. When no constraint is violated by a solution, the value of  $F_{\text{con}}(\vec{x})$  will be 1 and if all constraints are violated by the solution then its value will be 0. To rank the solutions from best solution to worst solution, they are sorted on the basis of decreasing value of  $F_{\text{con}}(\vec{x})$ . For same values of  $F_{\text{con}}(\vec{x})$ , the solutions should be sorted in ascending order of objective function values.

## 2.1 SOPT Algorithm for Constrained Optimization

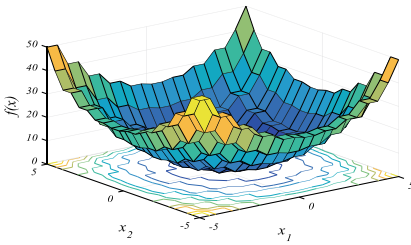
The various steps involved in the proposed SOPT algorithm for constrained problems are as below:

1. Initialize population.
2. Calculate fitness function of the population.
3. Calculate constraint fitness function of the population as explained in Sect. 2.
4. Repeat.
5. Sort population in decreasing order of constraint fitness function and increasing order of fitness value, giving priority to constraint fitness function.
6. Generate new solutions by equation  $x_{i,\text{new}} = x_{i,\text{best}} + c_1 \times R_i$ .
7. Compare the worst solution of population with new one and replace it if new solution is better.
8. Generate new solutions by equation  $x_{i,\text{new}} = x_{i,\text{best}} + c_1 \times R_i$ .
9. Compare worst solution of population with new one and replace it if new solution is better.
10. Store best solution found so far.
11. Replace best solution of the population, if it remains best for limiting number of iterations (replacement counter).
12. Until maximum number of iterations is not reached.

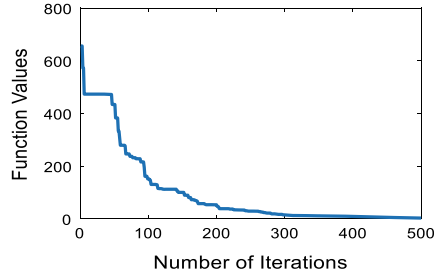
In this method, all solutions are ranked based on the constraint fitness function and the solution with highest constraint fitness value will be in first position. If two different solutions have the same value of constraint fitness, then the one with lower value of objective function is prioritized over others. The advantage of this method is that feasible solutions, which always have constraint fitness value higher than the infeasible solutions will get higher ranking in the list. Therefore, during the iterations, best feasible optimal solution is obtained by maintaining both feasible solutions as well as better infeasible solutions.

## 3 Testing of SOPT on Standard Test Function

It is tested with four standard functions out of which two are unconstrained functions and two are constrained.



(a) Surface plot of test function 1



(b) Convergence curve for test function 1

**Fig. 4** Surface plot and convergence curve for test function 1

### 3.1 Test Function 1 (Step Function)

It is a unimodal separable function which can be represented by Eq. (6). Number of variables in this test is taken as 30 in the range  $[-100, 100]$ . Surface of such a function with two variables is shown in Fig. 4. Minimum value of this function is  $f(\vec{x}) = 0$ .

$$f(\vec{x}) = \sum_{i=1}^D [(x_i + 0.5)^2] \tag{6}$$

### 3.2 Test Function 2 (Camel Back Function)

This is a multi-modal, non-separable function having six local minima; two of which are global. It is a function with two variables in the range  $[-5, 5]$  and represented by Eq. (7). Function is having global minimum value of  $-1.0316$ . Surface plot of the function is shown in Fig. 5.

$$f(\vec{x}) = 4x_1^2 + 2.1x_1^4 + \frac{1}{3}x_1^6 + x_1x_2 + 4x_2^2 + 4x_2^4 \tag{7}$$

### 3.3 Test Function 3 (Himmelblau’s Function)

It is a constrained function of minimization type in the range  $[0, 6]$  which is defined as

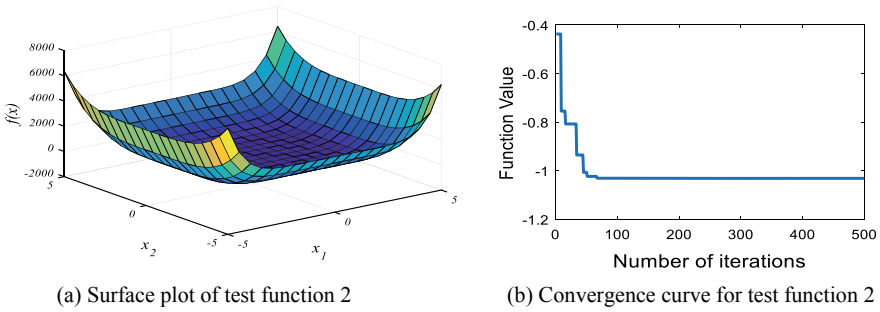


**Fig. 5** Surface plot and convergence curve for test function 2

$$\text{Minimize } f(\vec{x}) = (x_1^2 + x_2 - 11)^2 + (x_1 + x_2^2 - 7)^2 \tag{8}$$

$$\text{Subjected to: } g_1(\vec{x}) = 4.84 - (x_1 - 0.05)^2 - (x_2 - 2.5)^2 \geq 0$$

$$g_2(\vec{x}) = x_1^2 + (x_2 - 2.5)^2 - 4.84 \geq 0 \text{ and } 0 \leq x_1, x_2 \leq 6$$

The problem consists of two constraints. These two constraints cause a very thin feasible region between the two constraint dashed curves shown in Fig. 6a, which are drawn along with contour plot of the test function.

The solution of the problem  $x_1 = 2.2468257$ ,  $x_2 = 2.381866$  with function value of 13.59085 is obtained in less than 500 iterations as shown in Fig. 6b in which the best value of objective function found so far in each iteration is plotted. In the plot, the initial red segment indicates that the best solution is infeasible up to the end of this segment.

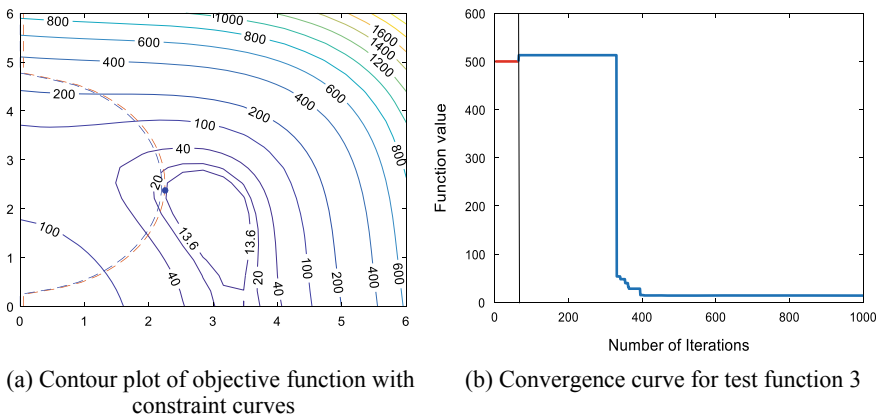


**Fig. 6** Contour plot and convergence curve for test function 3

In every iteration, only two function evaluation is made in the algorithm, therefore, the solution is obtained by evaluating the function about 1000 times.

### 3.4 Test Function 4

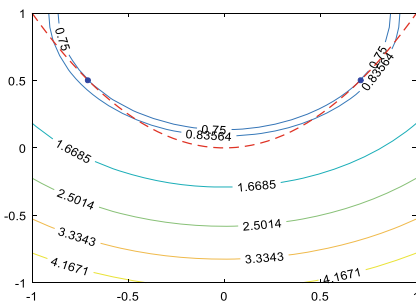
It is defined as

$$\text{Minimize } f(\vec{x}) = x_1^2 + (x_2 - 1)^2 \tag{9}$$

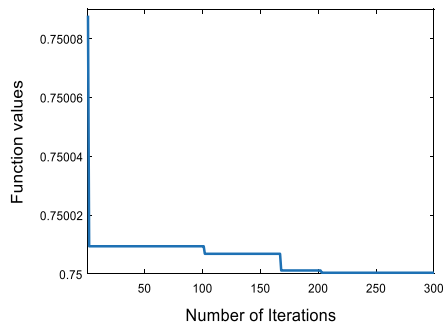
Subject to:  $h(\vec{x}) = x_2 - x_1^2 = 0$  and  $-1 \leq x_1, x_2 \leq 1$ .

This problem is minimization type with two decision variables and consists of an equality constraint. Handling constraints of equality type is normally difficult, therefore such type of constraints are divided into two inequality constraints, e.g.  $h(\vec{x}) = x_2 - x_1^2 = 0$  can be converted to two inequality constraints as  $x_2 - x_1^2 \leq 0.0001$  and  $x_2 - x_1^2 \geq -0.0001$ ; Therefore, solution shall lie in a thin strip of width 0.0002 rather over the exact line. In any real problem, one should try to eliminate equality constraints by eliminating decision variables from the constraint and objective function. In the present case,  $x_2$  can be eliminated from the objective function because of equality constraint.

Figure 7a shows the contour plot of the objective function along with the equality constraint shown in red-dashed curve. From Fig. 7b, it is clear that there are two solutions as shown by two blue dots having function value of 0.75. Figure 7b shows the convergence curve which indicates that solution is obtained in less than 300 iterations. It is the advantage of such type of algorithm that multiple solutions can be obtained simultaneously. In this method, the best function value of 0.75 is obtained for two sets of values at (0.707107, 0.5) and (-0.707107, 0.5).



(a) Contour plot for test function 4



(b) Convergence curve for test function 4

Fig. 7 Contour plot and convergence curve for test function 4

## 4 Design of a Uniform Column for Minimum Cost

To analyze the SOPT algorithm for its application in solving non-linear optimization problems, it was coded in MATLAB 8.5(R2015a) and is used to optimize design of a uniform column for minimum cost.

It is an example of designing a uniform column of tubular section hinge supported at both ends (Fig. 8), for minimum cost [6] the problem is defined as:

Compressive load to be carried by the column  $F = 2500$  kgf

Yield stress of the column material  $\sigma_y = 500$  kgf/cm<sup>2</sup>

Modulus of elasticity of the column material  $E = 0.85 \times 10^6$  kgf/cm<sup>2</sup>

Weight density of material  $\rho = 0.0025$  kgf/cm<sup>3</sup>

Length of column  $l = 250$  cm

Range of mean diameter of column  $d$  in cm = [2, 14]

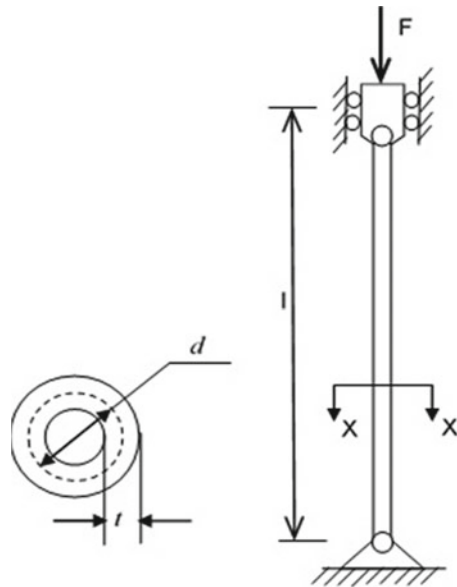
Range of available column thickness  $t$  in cm = [0.2, 0.8].

The purpose is to design the column which should be able to withstand the load so that induced stress is less than yield stress of the material (constraint  $g_1(\vec{x})$ ) and less than the Euler's buckling stress for the given configuration (constraint  $g_2(\vec{x})$ ), with minimum cost. The cost of the column consists of weight and construction cost and in the example, it is taken as  $5 \times$  (weight of the column) +  $2 \times$  (mean diameter of the column).

The objective function is to minimize the cost given by [7]

$$f(\vec{x}) = 5W + 2d = 5\rho l\pi dt + 2d = 9.82dt + 2d \quad (10)$$

**Fig. 8** Tubular column hinged at both ends under compression



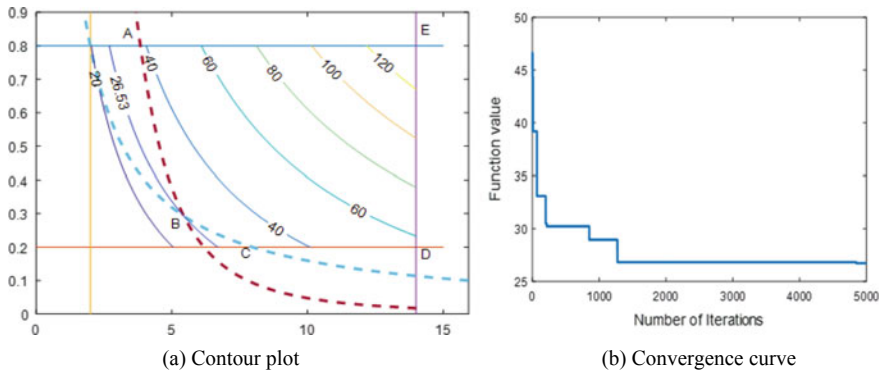


**Fig. 9** Contour plot and convergence curve for the column design problem

where  $\vec{x} = \frac{d}{t}$ .

Objective function has two decision variables mean diameter of column and thickness of the column.

Subject to the constraint  $g_1(\vec{x}) = \frac{2500}{\pi dt} \leq 500$  that is stress-induced  $\leq$  yield stress and  $g_2(\vec{x}) = \frac{2500}{\pi dt} \leq \frac{\pi^2(0.85 \times 10^6)(d^2 + t^2)}{8(250^2)}$  that is stress-induced  $\leq$  Euler’s buckling stress.

## 5 Result and Discussion

Contour curves with constant objective function values along with constraints curves are shown in Fig. 9a. This problem is solved by Gandomi et al. [8] using cuckoo search algorithm the best result obtained is 26.5317 in 15,000 function evaluations and in 2.56919 s. While SOPT algorithm is able to give better result of 26.52751 at (5.442073, 0.292721) in less than 10,000 function (Fig. 9b) evaluations and in 2.37915 s.

## 6 Conclusion

In this work, a simple and efficient SOPT algorithm to solve constrained optimization problems is proposed. To handle the constraint, a constraint fitness priority-based ranking method is used.

SOPT algorithm consists of two simple equations with only two function evaluations in one iteration. To check the effectiveness of SOPT to get optimum solution it is coded in MATLAB and applied to solve a mechanical engineering design problem. The result of optimization is compared with another important non-traditional algorithm cuckoo search and result is observed better in SOPT algorithm in reaching

better optimized value in less computational time. This makes SOPT algorithm a good choice to attempt solving engineering optimization problems.

## References

1. Arora J (2004) Introduction to optimum design. Academic Press
2. Coello CAC (2002) Theoretical and numerical constraint-handling techniques used with evolutionary algorithms: a survey of the state of the art. *Comput Methods Appl Mech Eng* 191:1245–1287
3. Wang L, Fang C (2011) An effective shuffled frog-leaping algorithm for multi-mode resource-constrained project scheduling problem. *Inf Sci* 181:4804–4822
4. Coello CAC, Montes EM (2002) Constraint-handling in genetic algorithms through the use of dominance-based tournament selection. *Adv Eng Inform* 16:193–203
5. Michalewicz Z (1995) Genetic algorithms, numerical optimization, and constraints. In: Proceedings of the sixth international conference on genetic algorithms. Polish Academy of Sciences, Poland
6. Hasançebi O, Azad SK (2012) An efficient metaheuristic algorithm for engineering optimization: SOPT. *Int J Optim Civil Eng* 2:479–487
7. Rao SS, Rao SS (2009) Engineering optimization: theory and practice. Wiley, New Jersey
8. Gandomi HX, Yang S, Alavi AH (2013) Cuckoo search algorithm: a metaheuristic approach to solve structural optimization problems. *Eng Comput* 29:17–35



# Unbalance and Dynamic Parameters Estimation in a Rigid Rotor Mounted on Active Magnetic Bearings



Prabhat Kumar, Vikas Kumar, Kundan Kumar and Lakhan Singh Meena

**Abstract** Online estimation of most severe unbalance fault in a high-speed rotating machinery system such as pumps, gas turbines, etc. is very essential for their smooth functioning. In the present paper, an estimation methodology has been developed to obtain the unbalance parameters such as magnitude and phase of unbalance as well as AMB dynamic parameters such as force–displacement stiffness and force-current stiffness constants in a rigid rotor system mounted on active magnetic bearings. These dynamic constants of AMB play a vital role in the rotordynamic vibrational analysis, which includes improving the stability of the system and control performances. A mathematical model consisting of a rigid rotor with a disc at the middle position supported on two active magnetic bearings are developed for this estimation purpose. Equations of motion of the rotor system are derived and simulated numerically to generate displacement and current responses of the rotor system in the time domain. A fast Fourier Transform technique is utilized to convert the time domain response into frequency domain signal, which has been further used in the developing methodology to estimate the unbalance fault parameters as well as AMB's constants. The results estimated were found showing high stability and good accuracy.

**Keywords** Active magnetic bearing · Fast Fourier transform · Unbalance

## 1 Introduction

Rotating elements are quite common in our use nowadays. Usually, the rotating machines such as centrifugal pumps, gas turbines, aircraft engines, etc. have bearings to provide support to the rotor through physical contact, but the recent trend is to use Active Magnetic Bearings (AMBs) that levitate the rotor system in the air using an electromagnetic force. Thus, the rotor does not feel any frictional resistance or wear while in the rotation. This system is quite advantageous as there is no requirement

---

P. Kumar (✉) · V. Kumar · K. Kumar · L. S. Meena  
Department of Mechanical Engineering, NIT Manipur, Imphal West, Manipur 795004, India  
e-mail: [ysprabhat.pamho@gmail.com](mailto:ysprabhat.pamho@gmail.com)

© Springer Nature Singapore Pte Ltd. 2020  
H. K. Voruganti et al. (eds.), *Advances in Applied Mechanical Engineering*,  
Lecture Notes in Mechanical Engineering,  
[https://doi.org/10.1007/978-981-15-1201-8\\_41](https://doi.org/10.1007/978-981-15-1201-8_41)

of lubrication, high precision and long-lifetime system monitoring and there is cost-down in maintenance also, but above all, it also facilitates smooth functioning at ultra-high speed. These AMBs find application where lubrication may be prohibitive, as in vacuum pumps as well as medical appliances [1]. In the course of gaining this high speed, often the rotating machines come through a phase when the rotor starts vibrating severely with large amplitude and sometimes it even fails. The speed at which this phenomenon occurs is called critical speed. The culprit here is most of the time, the unbalance. A rotating system with unbalance is often noisy, unsafe and short-lasting and requires more maintenance. Rotating unbalance is mainly caused by uneven distribution of mass around an axis of rotation. Mathematically, it is the product of the rotor mass and its eccentricity (the distance of the centre of gravity of the rotor from its centre of rotation) [2]. This unbalance is monstrous during high-speed rotation. So the slightest unbalance can be potential of high impact. Nordmann and Aenis [3] have used AMBs as sensor elements to measure both outputs and inputs and as actuator elements to excite the rotor system for detection and diagnosis of faults in centrifugal pumps. Sinha [4] and Edwards et al. [5] have given an overview of vibration-based condition monitoring of rotating machine. De Queiroz [6] developed a new method for identification of the unknown unbalance parameters of a simple Jeffcott like rotor by exploiting a dynamic robust control mechanism. He used unbalance disturbance forces by an active feedback control mechanism to identify the unbalance-related parameters. Markert et al. [7] and Platz et al. [8] presented a model to generate a dynamic behaviour of an unbalance rotor system utilizing a least-squares fitting approach in the time domain. Sudhakar and Sekhar [9] presented three different approaches based on least-squares fitting technique to identify the unbalance fault in a rotor system supported by two conventional ball bearings. More significant information such as locality and severity of fault can be provided by model-based diagnostic techniques. Zhou and Shi [10] have given a very comprehensive idea of active unbalance control systems. Yao et al. [11] proposed a novel technique which is a combination of both the modal expansion and optimization algorithm to identify the unbalance in a single disk-rotor-conventional bearing system. The technique was found to very effective and valid when compared with the experimental results. Recently, Shrivastava and Mohanty [12] performed both the experimental and numerical investigation for identification of unbalance force in a rigid rotor system supported on conventional bearings utilizing a joint-input state estimation technique.

Although many research works have been previously presented on system diagnosis and unbalance fault identification in a rotor system supported by conventional bearings, the investigation upon AMB-rotor systems, however, has not been addressed adequately, leave aside the quantitative assessment. Conventional bearings have several disadvantages such as low reliability and low efficiency and can be operated only at low speeds. An AMB system offers various advantages over conventional bearings such as rotor can be operated at high spin speeds, can reduce vibration through active and adjustable damping and stiffness coefficients employing a controller, etc. This paper focuses on developing a mathematical model consisting

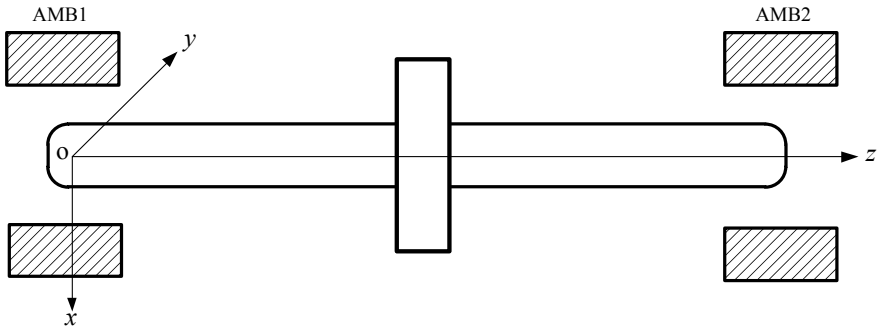


**Fig. 1** A rigid rotor system with a heavy disc at the middle mounted on two active magnetic bearings

of a rigid rotor with a disc at middle position mounted on two active magnetic bearings for the quantitative estimation of unbalance parameters such as eccentricity and phase of unbalance and AMB constants such as force–displacement stiffness and force-current stiffness.

## 2 System Model Configuration

The rotor system used for the purpose is depicted in Fig. 1. It is an unbalanced rigid rotor with a heavy disc at the middle position mounted on two AMBs. The shaft has been assumed to be rigid and massless based on lumped mass parameter model. AMBs with proportional-derivative (PD) control strategy are placed close to the rotor at both the ends. The translational degrees of freedom are considered to be in vertical (*x*-axis) and horizontal (*y*-axis) directions.

## 3 Unbalance Force Model

Unbalance fault in the rotor gives sinusoidal force. Force due to unbalance can be written in *x* and *y* directions as

$$f_{unbx} = me\omega^2 \cos(\omega t + \beta), \quad f_{unby} = me\omega^2 \sin(\omega t + \beta) \quad (1)$$

where *m* is disc mass, *e* is disc eccentricity,  $\omega$  is the spin speed of the rotor,  $\beta$  is the phase of unbalance.

## 4 Force Model Due to Active Magnetic Bearings

The force due to AMBs is also bidirectional, the  $x$  and  $y$  components can be written as

$$f_{\text{AMB}x} = -k_s x + k_i i_x, \quad f_{\text{AMB}y} = -k_s y + k_i i_y \quad (2)$$

where  $k_s$  and  $k_i$  are the force–displacement and force-current stiffness parameters of both AMBs.  $i_x$  and  $i_y$  are the controlling current outputs from the PD controller, these can also be expressed as

$$i_{cx} = k_p x + k_D \dot{x}, \quad i_{cy} = k_p y + k_D \dot{y} \quad (3)$$

where  $k_p$  and  $k_D$  are proportional and derivative gains of PD controllers.

## 5 Equations of Motion of the Rotor System

The equation of motion of the rigid rotor system with consideration of inertia forces, forces due to unbalance and both AMBs in  $x$  and  $y$  directions can be expressed as

$$m\ddot{x} = f_{\text{unb}x} - 2f_{\text{AMB}x}, \quad m\ddot{y} = f_{\text{unb}y} - 2f_{\text{AMB}y} \quad (4)$$

Equation (4) can be written in complex form as

$$m\ddot{r} = me\omega^2 e^{j(\omega t + \beta)} - 2f_{\text{AMB}}^c \quad (5)$$

where complex displacement and complex controlling current are

$$r = x + jy, \quad i_c^c = i_x + ji_y \quad (6)$$

where  $j = \sqrt{-1}$  is a complex number. The complex displacement response and AMB current response are utilized for the purpose of estimating unbalance parameters such as eccentricity of unbalance ( $e$ ) and phase of unbalance ( $\beta$ ) as well as AMB's constants such as force–displacement stiffness parameter ( $k_s$ ) and force-current stiffness parameter ( $k_i$ ). Displacement response of rotor at disc position  $R(t)$  and current response at AMB position  $I(t)$  can be assumed to be  $R(\omega)e^{j\omega t}$  and  $I(\omega)e^{j\omega t}$ , respectively in a harmonic form. So, the second derivative of displacement response in harmonics form can be expressed as

$$R(t) = R(\omega)e^{j\omega t}, \quad \ddot{R}(t) = -\omega^2 R(\omega)e^{j\omega t} \quad (7)$$

FFT function of MATLAB™ is applied to convert the complex system response in time domain signal into a frequency-domain signal.

## 6 Procedure for Estimation of Unbalance and AMB’s Dynamic Parameters

Now, a complex form of unbalance can be written as

$$m\omega^2 e^{j(\omega t + \beta)} = m\omega^2 e^{j\omega t} (e \cos \beta + j e \sin \beta) = m\omega^2 e^{j\omega t} (e_{Re} + j e_{Im}) \quad (8)$$

On substituting Eqs. (7) and (8) and into Eq. (5), and then writing the real and imaginary part of the equations in matrix form such that unknown parameters ( $e_{Re}$ ,  $e_{Im}$ ,  $k_s$  and  $k_i$ ) are on the left side of equations and known parameter ( $m$ ) on the right side, we get

$$\begin{bmatrix} -m\omega^2 & 0 & -2R_{Re}(\omega) & 2I_{Re}(\omega) \\ 0 & -m\omega^2 & -2R_{Im}(\omega) & 2I_{Im}(\omega) \end{bmatrix} \begin{Bmatrix} e_{Re} \\ e_{Im} \\ k_s \\ k_i \end{Bmatrix} = \begin{Bmatrix} m\omega^2 R_{Re}(\omega) \\ m\omega^2 R_{Im}(\omega) \end{Bmatrix} \text{ or } \mathbf{A}_1(\omega)\mathbf{x} = \mathbf{b}_1(\omega) \quad (9)$$

Equation (9) is an underdetermined system with two equations and four unknowns, so it is extremely difficult to get a solution. Thus, the rotor is operated with two spin speeds ( $\omega_1$  and  $\omega_2$ ). Then, the modified matrix equation for two speeds will be written as

$$\mathbf{A}_2(\omega)\mathbf{x} = \mathbf{b}_2(\omega) \quad (10)$$

with

$$\mathbf{A}_2(\omega) = \begin{bmatrix} \mathbf{A}_1(\omega_1) \\ \mathbf{A}_1(\omega_2) \end{bmatrix}; \quad \mathbf{b}_2(\omega) = \begin{bmatrix} \mathbf{b}_1(\omega_1) \\ \mathbf{b}_1(\omega_2) \end{bmatrix}$$

Now, there are four equations and four unknowns, so it is easy to solve this Eq. (10) to estimate the identifiable parameters vector as

$$\mathbf{x} = \{ e_{Re} \ e_{Im} \ k_s \ k_i \}^T \quad (11)$$

## 7 Response Generation and Estimation of Unbalance and AMB Parameters

The SIMULINK™ model shown in Fig. 2 has been used to generate the response of the rotor system such as displacement and current responses in  $x$  and  $y$ -direction in the time domain using Eq. (5).

The simulation for the rigid rotor system was run for 5 s using Table 1 parameters. Responses in the time domain from 4 to 5 s was considered for further analysis. A fourth-order Runge–Kutta solver with a fixed step size of 0.0001 s is used for generating system responses. Responses in the time domain for the unbalanced rigid-AMB rotor system at a spin speed of 106.8 rad/s is represented in Fig. 3. FFT analyzed signal for displacement and current responses with magnitude and phase at the same spin speed is presented in Fig. 4.

It is observed from Fig. 4 that the maximum amplitude of the displacement and controlling current responses are  $4.347 \times 10^{-5}$  m and 0.2613 A at an angular frequency of 17 Hz (or 106.8 rad/s). The real and imaginary part of responses is obtained using magnitude and phase of FFT analyzed response signal at two different speeds, i.e. (106.8 and 188.5 rad/s) which is further used in Eq. (10) to estimate the required parameters.

Table 2 summarizes the estimated values of the unbalance and AMB’s parameters and their error percentage with respect to assumed ones. It can be observed the error

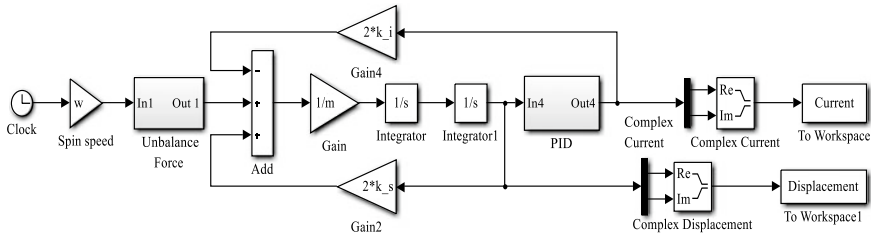
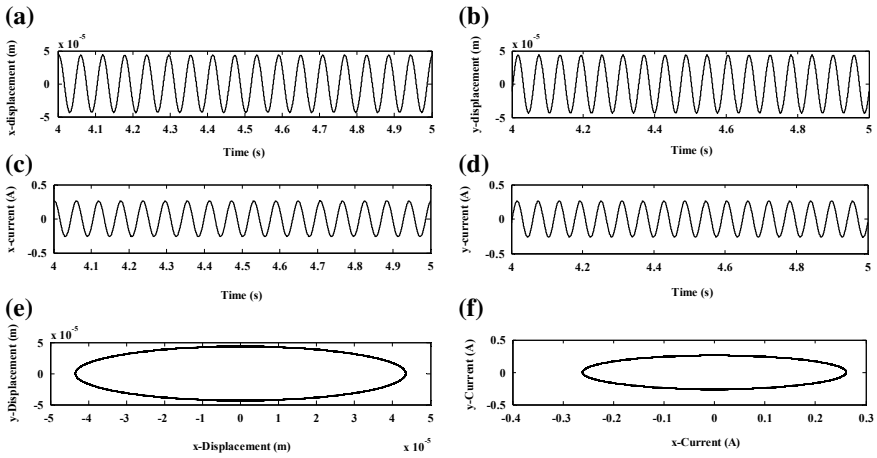


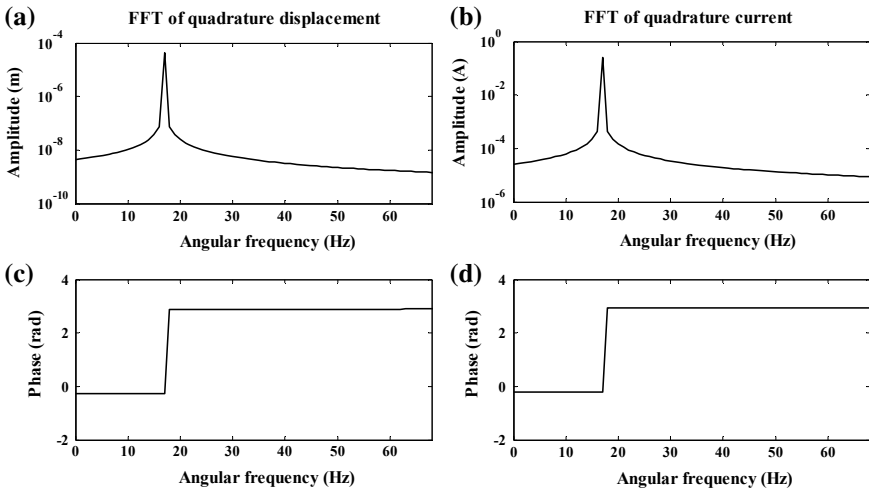
Fig. 2 SIMULINK model of the problem

Table 1 Rotor-AMB system parameters for simulation purpose

Rotor parameters	Assumed values	AMB parameters	Assumed values
Disc mass ( $m$ )	2 kg	AMB force displacement constant ( $k_s$ )	175,440 N/m
Disc eccentricity ( $e$ )	100 $\mu$ m	AMB force displacement constant ( $k_1$ )	35.09 N/A
Unbalance phase ( $\beta$ )	10°	Proportional constant of PD controller ( $k_P$ )	6000 N/m
		The derivative constant of PD controller ( $k_D$ )	3 Ns/m



**Fig. 3** Responses of rigid rotor system: **a** *x*-direction displacement; **b** *y*-direction displacement; **c** *x*-direction current; **d** *y*-direction current; **e** displacement orbit; **f** current orbit



**Fig. 4** FFT analyzed responses: **a** amplitude of displacement; **b** amplitude of current; **c** phase of displacement; **d** phase of current response

percentage is very less for all parameters. Unbalance parameters such as eccentricity ( $e$ ) and phase ( $\beta$ ) are found to be very much accurate and stable using the developed estimation methodology.

**Table 2** Assumed and estimated values of parameters related to unbalance fault and AMBs

Parameters	Symbol	Assumed values	Estimated values	Error %
Unbalance magnitude	$e$ ( $\mu\text{m}$ )	100.00	99.83	-0.17
Unbalance phase	$\beta$ ( $^\circ$ )	10.00	10.04	0.40
Force-displacement constant of AMBs	$k_s$ (N/m)	175,440	172,265	-1.81
Force-current constant of AMBs	$k_i$ (N/A)	35.09	34.24	-2.42

## 8 Conclusions

This paper concludes with the development of an estimation methodology for estimation of unbalance and AMB's parameters in a rigid rotor system mounted on two active magnetic bearings. For accomplishing this purpose, a mathematical model is presented. Equations of motion of the considered rotor system are derived and simulated numerically to obtain displacement and current responses of the system. FFT analyzed response in the frequency domain was used for online estimation of the parameters. Estimation results show that the developed methodology is robust and effective providing good accuracy and stable estimated values.

## References

1. Kasarda M (2000) An overview of active magnetic bearing technology and applications. *Shock Vib Dig* 32(2):91-99
2. Tiwari R (2017) *Rotor systems: analysis and identification*. CRC Press, Boca Raton
3. Nordmann R, Aenis M (2004) Fault diagnosis in a centrifugal pump using active magnetic bearings. *Int J Rotating Mach* 10(3):183-191
4. Sinha JK (2002) *Health monitoring techniques for rotating machinery*. University of Wales, Swansea
5. Edwards S, Lees AW, Friswell MI (2000) Estimating rotor unbalance from a single run-down. In: *Proceedings of the 7th international conference on vibrations in rotating machinery*. IMech, UK, pp 323-334
6. De Queiroz MS (2009) An active identification method of rotor unbalance parameters. *J Vib Control* 15(9):1365-1374
7. Markert R, Platz R, Seidler M (2001) Model based fault identification in rotor systems by least squares fitting. *Int J Rotating Mach* 7(5):311-321
8. Platz R, Markert R, Seidler M (2000) Validation of online diagnostics of malfunctions in rotor systems. In: *Proceedings of the 7th international conference on vibrations in rotating machinery*. IMech, UK, pp 581-590
9. Sudhakar GN, Sekhar AS (2011) Identification of unbalance in a rotor bearing system. *J Sound Vib* 330(10):2299-2313
10. Zhou S, Shi J (2001) Active balancing and vibration control of rotating machinery: a survey. *Shock Vib Dig* 33(5):361-371



11. Yao J, Liu L, Yang F, Scarpa F, Gao J (2018) Identification and optimization of unbalance parameters in rotor-bearing systems. *J Sound Vib* 431:54–69
12. Shrivastava A, Mohanty AR (2019) Identification of unbalance in a rotor system using a joint input-state estimation technique. *J Sound Vib* 442:414–427

# Investigating the Influence of Geometrical and Material Parameters on Peeling Behaviour of a Gecko Spatula



Saipraneeth Gouravaraju and Sachin S. Gautam

**Abstract** Geckos can generate strong attachment forces and at the same time detach swiftly from any surface by employing the hierarchical fibrillar structures on their toe pads. In this paper, a coupled adhesion-friction model in the framework of nonlinear finite element analysis is used to analyse the peeling behaviour of gecko spatulae. It has been found that the material stiffness, adhesion strength, size of the spatula, and adhesion range greatly influence the spatula stresses, pull-off forces, and deformation behaviour.

**Keywords** Gecko adhesion · Dry friction · Nonlinear finite element method · Peeling

## 1 Introduction

Geckos make use of the hierarchical fibrillar structures on their toe pads to adhere to rough as well as smooth substrata [1]. The underside of each digit on the gecko toes has expanded digital scales called scansors, which have rows of lamellae that contain thousands of micro-fibrils called setae. Each seta is about 30–100  $\mu\text{m}$  long and 5  $\mu\text{m}$  in diameters. These setae branch into 100–1000 nanoscale structures called spatulae. Each spatula adheres to the substrate by exploiting the weak van der Waals forces acting between them [2, 3]. Autumn et al. [2] have shown that a single seta can produce a friction force as high as  $\approx 200 \mu\text{N}$ .

There have been many studies, analytical, experimental, as well as numerical to understand the characteristics and design principles of gecko adhesion system [4–6]. Experiments of Huber et al. [7] revealed that when the spatulae are pulled vertically, the maximum pull-off force for a single spatula is close to 10 nN. By employing a

---

S. Gouravaraju · S. S. Gautam (✉)  
Department of Mechanical Engineering, Indian Institute of Technology  
Guwahati, Guwahati 781039, India  
e-mail: [ssg@iitg.ac.in](mailto:ssg@iitg.ac.in)

S. Gouravaraju  
e-mail: [saipraneeth@iitg.ac.in](mailto:saipraneeth@iitg.ac.in)

© Springer Nature Singapore Pte Ltd. 2020  
H. K. Voruganti et al. (eds.), *Advances in Applied Mechanical Engineering*,  
Lecture Notes in Mechanical Engineering,  
[https://doi.org/10.1007/978-981-15-1201-8\\_42](https://doi.org/10.1007/978-981-15-1201-8_42)

tape-peeling model, Tian et al. [8] computed the frictional and adhesive force between a spatula and a rigid substrate. Chen et al. [9] used Kendall's peeling model to study the effect of pre-tension on the peeling force. Sauer and Li [10] proposed a multiscale contact model, called the coarse-grained contact model (CGCM), for analysing the deformation of nanoscale solids due to interatomic interactions. Sauer and Holl [11] proposed a three-dimensional parametric model that accurately captures the spatula geometry. Then, using CGCM of [10], the authors studied the influence of the spatula shape, stiffness and strength and range of adhesion on the adhesion behaviour of gecko spatula and a rigid substrate. Gautam and Sauer [12] analysed gecko spatula adhesion using their newly proposed time integration scheme. In order to model dry friction even under tensile loads, Mergel et al. [13] proposed two new continuum-based adhesive friction models. The authors define a sliding threshold, above which the interacting surfaces start to slide with respect to each other. In their first model ("Model DI"), this sliding threshold is a constant, whereas in the second model ("Model EA"), it is a function of normal distance and normal traction.

The gecko adhesive system has evolved over centuries for optimum attachment and detachment on different surfaces in nature. In order to understand the design principles of gecko's fibrillar structure, it is essential to study the smallest element in the hierarchy, i.e. spatula. In the present work, the influence of material and geometrical parameters on the spatula peeling behaviour is investigated. The current work extends the work done by the authors by including the effect of friction due to adhesion that has not been considered in [14]. For this purpose, in this contribution, the spatula is modelled as a thin strip and is analysed using a combination of CGCM of [10] and "Model EA" of [13] within the nonlinear finite element setting.

## 2 Contact Formulation

In this section, the formulation of contact tractions due to the interatomic interactions between the spatula and the rigid substrate is briefly discussed. The total contact traction ( $\mathbf{T}_c$ ) is obtained by adding the contact contributions due to adhesion ( $\mathbf{T}_{adh}$ ) and friction ( $\mathbf{T}_{fric}$ ) which in the current study arises due to adhesion [13], i.e.

$$\mathbf{T}_c = \mathbf{T}_{adh} + \mathbf{T}_{fric} \quad (1)$$

The mechanism of adhesion of the spatula itself is from the van der Waals interactions between the molecules of the spatula and substrate. In this study, the van der Waals adhesion between any two molecules is described by the Lennard–Jones potential, which is then integrated over the entire spatula to get the adhesion potential. Then, variation of this adhesion potential gives the adhesive traction as (see [15] for the derivation).

$$\mathbf{T}_c(d_s) = \frac{A}{2\pi d_0^3} \left[ \frac{1}{45} \left( \frac{d_0}{d_s} \right)^9 - \frac{1}{3} \left( \frac{d_0}{d_s} \right)^3 \right] \mathbf{n}_p, \quad (2)$$

where  $A$ ,  $d_0$ , and  $d_s$  denote the Hamaker's constant, the atomic equilibrium distance, and the minimum distance between contacting bodies, respectively. Here,  $\mathbf{n}_p$  represents the normal to the substrate and is constant for flat surfaces.

According to "Model EA" of Mergel et al. [13], the magnitude of the frictional traction ( $\|\mathbf{T}_{\text{fric}}\|$ ) is less than or equal to the sliding threshold ( $T_{\text{sl}}$ ) if the interacting surfaces are sticking or sliding with respect to each other, respectively. The sliding threshold is a function of the minimum distance between the spatula and the substrate and is defined as

$$T_{\text{sl}}(d_s) = \begin{cases} \mu[T_a(d_s) - T_a(d_{\text{cut}})], & d_s < d_{\text{cut}} \\ 0, & d_s \geq d_{\text{cut}} \end{cases} \quad (3)$$

where  $T_a = \|\mathbf{T}_a\|$  is the magnitude of the adhesive traction,  $\mu$  is the friction coefficient, and  $d_{\text{cut}}$  is the cut-off distance up to which friction is active (see [13] for more details).

In the coarse-grained contact formulation, the model is characterized by the following two material parameters [10]

$$\gamma_W = \frac{E}{\left(\frac{A}{2\pi^2 d_0^3}\right)}, \quad \gamma_L = \frac{D_0}{d_0}, \quad (4)$$

where  $E$  represents the Young's modulus and  $R_0$  is the global length scale.

The material parameter  $\gamma_W$  thus represents the ration of energy densities due to elastic deformation and due to adhesion. The denominator in the equation for  $\gamma_W$  then denotes the strength of adhesion. On the other hand,  $\gamma_L$  is the ratio between the macroscopic and microscopic length scales and represents the size of the problem.

### 3 Spatula Model

For numerical simulations, the three-dimensional gecko spatula is represented as a two-dimensional strip in plane strain following many other works in the literature [8, 9]. Henceforth, the words "spatula" and "strip" are considered to represent the same entity and are referred interchangeably.

The strip has the dimensions  $L = 200 D_0$  and  $h = 10 D_0$  with  $D_0 = 1$  nm introduced for normalization (see Fig. 1). It is considered that only the bottom 75% of the strip ("AE" in Fig. 1) experiences the adhesive forces. The strip is considered to be isotropic Neo-Hookean material with Young's modulus  $E = 2$  GPa and Poisson's ratio  $\nu = 0.2$ . The atomic equilibrium distance and Hamaker's constant are taken as  $d_0 = 0.4$  nm and  $A = 10^{-19}$  J, respectively. These values result in  $\gamma_W = 25.266$

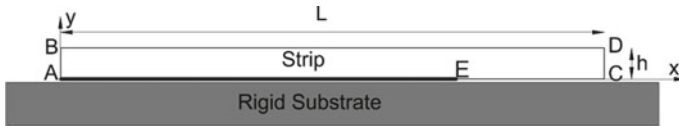


Fig. 1 A deformable strip on a flat rigid substrate



Fig. 2 Peeling by applied displacement

and  $\gamma_L = 2.50$ . In agreement with the experiments of gecko/gecko setae on a glass surface, the friction coefficient is assumed to be  $\mu = 0.3$  [2]. A finite element mesh of  $240 \times 12$  elements along the  $x$  and  $y$  directions, respectively, is used. Plain strain conditions are considered.

Peeling off of the spatula is carried out in two steps. In the first step, an external rotation  $\theta$  is applied on the right end (CD). After achieving a desired angle of rotation of the right end  $\theta = \theta_{sh}$ , the spatula is pulled at an angle by applying a displacement  $\bar{u}$  on the right end (CD) at an angle called as peeling angle  $\theta_p$  (see Fig. 2).

### 4 Results and Discussions

The peeling behaviour of the spatula is characterized by material parameters  $\gamma_W$  and  $\gamma_L$  as described in Sect. 2. From their definitions in Eq. (4), it is clear that by varying these material parameters, the influence of different parameters, viz. spatula size, stiffness, adhesion strength, and adhesion range on the spatula peeling behaviour can be investigated. These material parameters are varied here by a factor of 1.5 similar to the study of Sauer and Holl [11]. The pull-off forces, deformations, and stresses are calculated by varying the parameter  $\gamma_W$  while keeping  $\gamma_L$  constant and vice versa.

Figure 3 depicts the deformation of the spatula for a pre-rotated configuration with  $\theta_{sh} = 90^\circ$  and  $\bar{u} = 0$  nm and different values of  $\gamma_W$  and  $\gamma_L$ . It can be observed that for an increase in  $\gamma_W$  and a decrease in  $\gamma_L$ , the stresses in the spatula decrease. In Fig. 4a, the variation of the resultant pull-off force  $F_{res}$  with peeling angle  $\theta$  is shown for  $\gamma_W = 16.867, 25.266,$  and  $37.95$  with constant  $\gamma_L = 2.50$ . It can be seen that, as  $\gamma_W$  decreases, the pull-off force increases. This is due to the fact that a decrease in  $\gamma_W$  results in an increase in the strength of adhesion. In terms of the material stiffness,

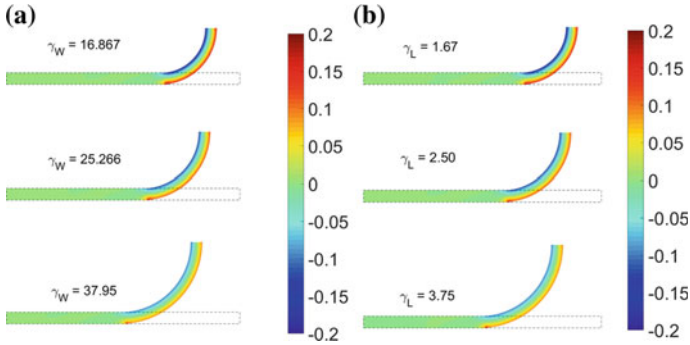


**Fig. 3** Deformation and stress for different  $\gamma_W$  and  $\gamma_L$  for initial pre-rotated configuration with  $\theta_{sh} = 90^\circ$  and  $\bar{u} = 0$  nm. The colour bar shows the normalized stresses  $I_1/E = \text{tr}(\sigma)/E$

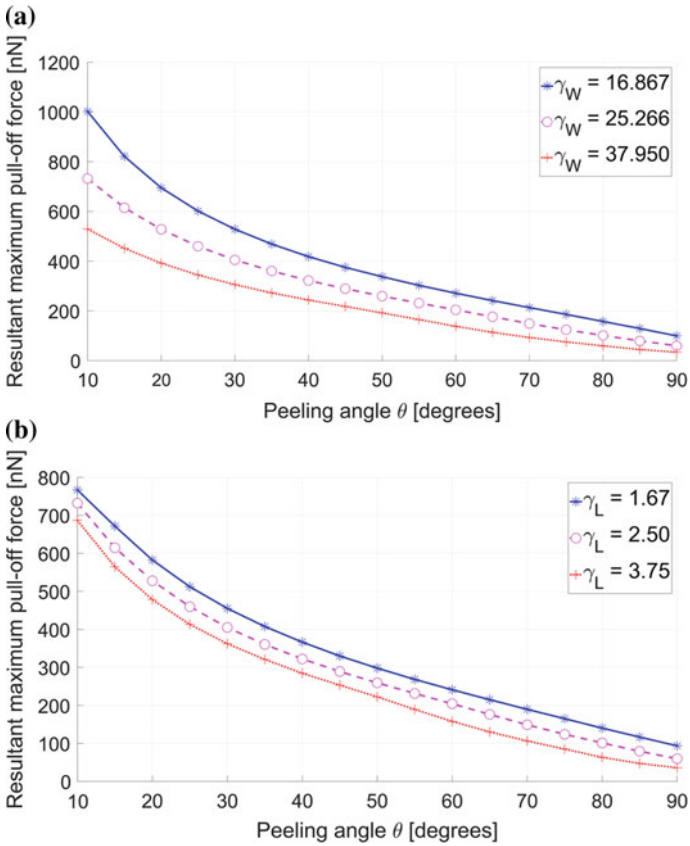


**Fig. 4** Evolution of the resultant maximum pull-off force with peeling angle  $\theta$  for different values of  $\gamma_W$  and  $\gamma_L$

this increase in pull-off force results from the fact that as  $\gamma_W$  decreases, the material stiffness decreases due to which the material becomes more compliant and readily adheres to the rigid substrate. As a result, the force required to detach the spatula from the substrate increases. This can also be observed from the deformed spatula configurations shown in Fig. 3a where the pad area of the spatula still-in-contact increases with decrease in  $\gamma_W$ .

The variation of the resultant pull-off force with the peeling angle  $\theta$  for  $\gamma_L = 1.67, 2.50, \text{ and } 3.75$  with constant  $\gamma_W = 25.266$  is shown in Fig. 4b. It can be observed that as the material parameter  $\gamma_L$  increases, the range of adhesion decreases (see Eq. (4)), and as a result, less force is required to separate the spatula from the substrate. Conversely, if  $\gamma_L$  decreases, the stress inside the spatula increases as shown in Fig. 3b, which is not desirable.

The results discussed here show that  $\gamma_L$  and  $\gamma_W$ , which represent material and geometrical properties, greatly influence the peeling response of the spatula. Studying the effect of these parameters aids in understanding the underlying principles of gecko adhesive system and in choosing appropriate materials, shapes, and size of the micro/nanofibres while designing synthetic adhesives that work in different environments. To illustrate, by choosing a very large spatula size or a very stiff material for the synthetic fibres—although the pull-off force to detach at  $\theta = 90^\circ$  is reduced—it comes at the expense of the friction forces that are generated at low angles during attachment. The influence of various other parameters has been discussed in another work by the authors in [16].

## 5 Conclusions

The influence of stiffness, adhesion range, strength, and spatula size has been analysed by varying the material parameters  $\gamma_W$  and  $\gamma_L$ . It is shown that the pull-off forces increase as  $\gamma_L$  and  $\gamma_W$  decrease, due to either a decrease in the spatula size (or material stiffness) or an increase in the range of adhesion (or strength).

**Acknowledgements** Authors are grateful to the SERB, DST for supporting this research under project SR/FTP/ETA-0008/2014. Authors would also like to thank Prof. Roger A. Sauer at AICES, RWTH Aachen University for his valuable comments.

## References

1. Ruibal R, Ernst V (1965) The structure of the digital setae of lizards. *J Morphol* 117:271–293
2. Autumn K, Liang YA, Hsieh ST, Zesch W, Chan WP, Kenny TW, Fearing R, Full RJ (2000) Adhesive force of a single gecko foot-hair. *Nature* 405:681–684
3. Autumn K, Sitti M, Liang YA, Peattie AM, Hansen WR, Sponberg S, Kenny TW, Fearing R, Israelachvili JN, Full RJ (2002) Evidence for van der Waals adhesion in gecko setae. *Proc Natl Acad Sci* 99:12252–12256

4. Jagota A, Hui CY (2011) Adhesion, friction, and compliance of biomimetic and bio-inspired structured interfaces. *Mater Sci Eng: R: Rep* 72:253–292
5. Hu S, Lopez S, Niewiarowski PH, Xia Z (2012) Dynamic self-cleaning in gecko setae via digital hyperextension. *J Royal Soc Interf* 9:2781–2790
6. Kasar AK, Ramachandran R, Menezes PL (2018) Natural adhesion system leads to synthetic adhesives. *J Bio Tribo-Corr* 4:1–17
7. Huber G, Gorb SN, Spolenak R, Arzt E (2005) Resolving the nanoscale adhesion of individual gecko spatulae by atomic force microscopy. *Biol Lett* 1:2–4
8. Tian Y, Pesika N, Zeng H, Rosenberg K, Zhao B, McGuiggan P, Autumn K, Israelachvili J (2006) Adhesion and friction in gecko toe attachment and detachment. *Proc Nat Acad Sci* 103:19320–19325
9. Chen B, Wu P, Gao H (2009) Pre-tension generates strongly reversible adhesion of a spatula pad on substrate. *J Royal Soc Interf* 6:529–537
10. Sauer RA, Li S (2007) A contact mechanics model for quasi-continua. *J Numer Methods Eng* 71:931–962
11. Sauer RA, Holl M (2013) A detailed 3D finite element analysis of the peeling behaviour of a gecko spatula. *Comput Methods Biomech Biomed Eng* 16:577–591
12. Gautam SS, Sauer RA (2014) A composite time integration scheme for dynamic adhesion and its application to gecko spatula peeling. *Int J Comput Methods* 11:1350104
13. Mergel JC, Sahli R, Scheibert J, Sauer RA (2018) Continuum contact models for coupled adhesion and friction. *J Adhes* 00:1–33
14. Sauer RA, Wriggers P (2009) Formulation and analysis of a three-dimensional finite element implementation for adhesive contact at the nanoscale. *Comput Methods Appl Mech Eng* 198:3871–3883
15. Gouravaraju S, Gautam SS (2019) Nonlinear finite element analysis of a gecko spatula adhesion on a rigid substrate. In: *Advances in Interdisciplinary Engineering*. Springer, pp 471–479
16. Gouravaraju S, Sauer RA, Gautam SS (2019) Investigating the normal and tangential peeling behaviour of gecko spatulae using a coupled adhesion-friction model. <https://arxiv.org/abs/1901.11505v3>



# Quantitative Analysis of Tribological Performance on Al-CSA Composite Using Orthogonal Array



R. Siva Sankara Raju, B. Venkata Siva and G. Srinivasa Rao

**Abstract** This study is described on the optimization of tribological characteristics of Al-coconut shell ash (CSA) reinforced composite prepared with stir casting route. In this study, three operating variables (i.e. load, sliding speed, and % of CSA) and two response [i.e. wear rates (WR in  $\text{mm}^3/\text{m}$ )] and coefficient of friction (CF) are considered. The list of experiments was intended using  $L_{27}$  orthogonal array (full factorial design). The influence of each parameter on the response is established using response tables and response graphs. Based on experimental data, the model equations for each response were developed with multiple linear regressions. The models give the factor effects of individual parameters. Interaction effects provide additional information to understand the detailed behaviour of parameters. It revealed that load is the most influencing effect on wear behavioural responses.

**Keywords** AMCs · Coconut shell ash · Wear rate · ANOVA

## 1 Introduction

Aluminium matrix composites (AMCs) are gained extensive concentration owing to a better specific strength, and exceptional tribological and machinability properties in excess of the unitary alloys [4, 9, 10, 14]. However, AMCs have better-quality properties but unable to expose due to intricacy in fabrication and characterization. In general, stir casting technique is the cheapest and widely used in mass production for automobile industries. Particulate reinforced alloy matrix composites have

---

R. Siva Sankara Raju (✉)

Department Mechanical Engineering, AITAM, Tekkali, A.P 532201, India  
e-mail: [sivaraju80@gmail.com](mailto:sivaraju80@gmail.com)

B. Venkata Siva

Department Mechanical Engineering, NEC, Narasaraopeta, A.P 522601, India

G. Srinivasa Rao

Department Mechanical Engineering, RVR&JC, Guntur, A.P 522019, India

started economic value in many forms, and they can be built by traditional refining approaches [4, 18, 20]. Wear is a linear dimensional loss in the material that occurred due to abrasion. Extensive studies on the tribological performance of AMC are considering with the effect of variables such as particulate size, shape, volume, of reinforcements, and load/pressure, velocity, sliding distance and other extensive operating conditions. Similarly, the tribological behaviour of composite has also been enhanced due to the distribution of reinforcement in matrix which influences the effect of interfacial bonding between matrix and reinforcement [2–4, 7, 8]. Sahin [10] studied the wear mechanism of Al–SiC–MMCs and identified size as well as volume of particles was played a key role in the abrasion mechanism. Kk and zdin [4] studied the tribological performance of Al–2024–Al<sub>2</sub>O<sub>3</sub> composite. Bello et al. [1] studied on Al–CSA (2–10 wt%) and fabricated with compo-casting technique. The strength of composite has increased due to the distribution of fillers within the matrix and their recovery. Wear rate of Al6061/SiC (5–40 wt%) composite decreased with increasing SiC volume [5].

The present work is aimed to determine the optimal condition of tribological performance of Al–1100–CSA composites. ANOVA has been performed to investigate the significant parameters using response table and response graphs, the effect on tribological performance of CSA composite.

## 2 Experimental Procedures

Coconut is one of the most important by-products with various utilities in several manners. Coconut shell of filler contains high lignin, which have prevented as weather resistant. Therefore, coconut shell is considered as reinforcement.

### 2.1 Preparation and Testing of CSA Composites

Al–CSA composites has been fabricated by stir casting route varying amount of CSA volume, the procedures sequences for preparation of reinforced particulates (i.e., CSA) and composite preparation are detailed in elsewhere [6, 12, 14–17]. The tensile properties of Al–CSA have been tested with Hounsfield tensometer (Model: ETM-ER3/772/12). Pin-on-Disc tester (Model: DUCOM 201 LE-PHM-400) has been used for the identification of dry sliding wear behaviour of cast Al–CSA composites. The in situ cast composites were slide against a steel counterface (EN-31, 62 HRC) with constant track of 50 mm. Prior to wear testing, it has polished all the test pin surfaces up to 600-grade emery papers and obtained surface roughness 0.1  $R_a$ . Standard techniques have been used to determine wear rate and coefficient of friction [6, 12, 14]. Coefficient of friction is measured as frictional forces per unit normal load [11, 13, 16].

**Table 1** Parameters and their levels

Factor (units)	Symbol	-1	0	+1
Load (N)	<i>L</i>	10	30	50
% of CSAp (% of vol.)	<i>R</i>	5	10	15
Sliding distance (m)	<i>D</i>	1000	2000	3000

## 2.2 Experimental Layout Using Taguchi Orthogonal Array

In this work, the experiments are carried out based on full factorial design which consists of 27 experimental runs for three factors at three levels. The three operating variables such as load (*L*), % of coconut shell ash (*R*) and sliding distance (*D*) at three different levels are shown in Table 1. Experiments were carried out in arbitrary way in order to evade discrimination. Table 2 shows the tribological performances such as wear rate [WR ((mm<sup>3</sup>/m) × 10<sup>-3</sup>)] and coefficient of friction (CF).

## 3 Results and Discussion

### 3.1 Characterization and Mechanical Properties of Al-CSA-MMC

Table 3 notices hardness and tensile strength of composites that are increased with increasing volume of CSA, while density and elongation decreased. This is owing to the proper segregation of ceramic particles in the composite and strain hardened. CSA particles are harder and capable to reduce movement of inter-spacing particle. Figure 1 reveals that grain size decreased with increasing volume of CSA, due to crystal growth enhances the strength and drops the ductility. Likewise, two phases noted that one bright state matrix and the next one darkened state CSA.

### 3.2 Analysis of the Process Parameters and Interactions

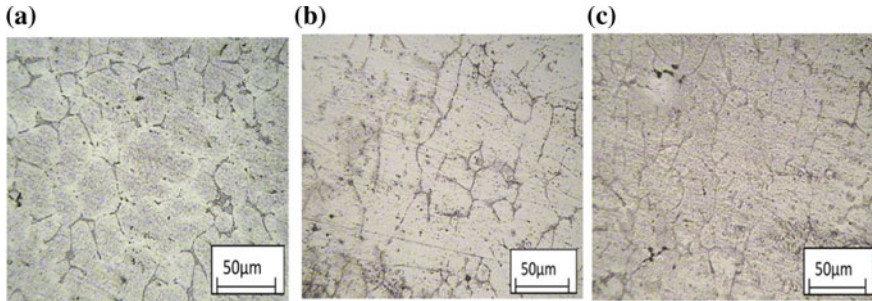
Design of experiments is aiming to obtain the relation between operating variables and tribological performances. This study mainly concerning the determination of the effect of variables on individual tribological response and combined response affect on tribological behaviour of CSA composites. From the full factorial experimental design, mean of a level is computed and shown in Table 2. The influence of each variable parameter (i.e. *L*, *R* and *D*) on the tribological performances (i.e. WR and CF) is carried out using level mean analysis.

Table 2 Experimental layout with responses

Run	L	R	D	WR	CF	Run	L	R	D	WR	CF
1	-1	-1	-1	5.556	0.265	14	0	0	0	3.115	0.263
2	-1	-1	0	2.815	0.201	15	0	0	1	2.436	0.226
3	-1	-1	1	2.173	0.188	16	0	1	-1	5.808	0.355
4	-1	0	-1	5	0.224	17	0	1	0	3.115	0.292
5	-1	0	0	2.423	0.185	18	0	1	1	2.321	0.28
6	-1	0	1	2.159	0.197	19	1	-1	-1	7.111	0.663
7	-1	1	-1	3.462	0.249	20	1	-1	0	4.167	0.501
8	-1	1	0	2.327	0.234	21	1	-1	1	4.012	0.391
9	-1	1	1	1.936	0.271	22	1	0	-1	6.923	0.582
10	0	-1	-1	6.333	0.412	23	1	0	0	3.962	0.445
11	0	-1	0	3.222	0.299	24	1	0	1	2.846	0.359
12	0	-1	1	2.704	0.238	25	1	1	-1	6.615	0.565
13	0	0	-1	6.5	0.351	26	1	1	0	3.654	0.453
						27	1	1	1	2.641	0.392

**Table 3** Properties of Al-CSA-MMC

% of CSA	0	5	10	15
VHN	58.26	62.026	79.4	83.073
Density (g/cc)	2.71	2.66	2.61	2.55
UTS (N/mm <sup>2</sup> )	90.8	101.6	127	143
Elongation (mm)	29.7	23.3	18.3	16



**Fig. 1** Microstructures of **a** Al-5% CSA, **b** Al-10% CSA, **c** Al-15% CSA-MMC

ANOVA Table 4 shows that sliding distance is the highest influencing parameter on wear rate of Al-CSA composites with 75.33% of contribution. Load is the second influencing factor with 45.25 Fisher value. The overall contribution is 98.4% on wear rate of Al-CSA composites. Similarly, ANOVA (Table 5) revealed, load (76.25%) is the most influence parameter followed by sliding distance (15.11%). The combined effect of load and sliding distance is one of the influencing factors with 21.71 Fisher value. The contributions of overall factors are performed 97.9% of the total variance in coefficient of friction.

A level mean is the average value of response at a specific level. The response graphs are representing the effect of process parameters with individual tribological

**Table 4** ANOVA of wear rate

Source	DF	SS	Adj SS	MS	F	P	% Cont.
L	2	61.309	61.309	30.655	45.25	0	18.05
R	2	11.745	11.745	5.873	8.67	0.01	3.46
D	2	255.793	255.793	127.896	188.8	0	75.33
L * R	4	1.979	1.979	0.495	0.73	0.596	0.58
L * D	4	1.27	1.27	0.317	0.47	0.758	0.37
R * D	4	2.058	2.058	0.514	0.76	0.58	0.61
Error	8	5.419	5.419	0.677			
Total	26	339.573					

**Table 5** ANOVA of coefficient of friction

Source	DF	SS	Adj SS	MS	F	P	% Cont.
L	2	200.041	200.041	100.021	1120.53	0	76.25
R	2	5.357	5.357	2.679	30.01	0	2.04
D	2	39.638	39.638	19.819	222.03	0	15.11
L * R	4	3.703	3.703	0.926	10.37	0.003	1.41
L * D	4	7.751	7.751	1.938	21.71	0	2.95
R * D	4	5.15	5.15	1.288	14.42	0.001	1.96
Error	8	0.714	0.714	0.089			
Total	26	262.355					

performance. The slope indicates the effect variation at each level with corresponding response. The interactions of input parameters are also having a significant effect on responses. The influence of process parameters (i.e. *L*, *R* and *D*) on the tribological performance [wear rate (WR) and coefficient of friction (CF)] is observed, which is shown in Fig. 2. From response graphs, it is identified that, *L* is the dominating factor on the response, i.e. wear rate, whereas *D* is dominating parameter on CF. The tribological performances (i.e. WR and CF) increase with increasing load. While the load increases, the composite loses its ability to carry the load due to fracture of reinforced particles and the formation of debris, which causes the loss of material vis-a-vis ploughing, delamination and plastic deformation [14, 19].

At a higher load, the frictional force increases with greater dissipation of energy leading to a higher temperature at contact surface which results in a higher of CF. Wear increasing with increase of sliding distance and decrease of addition of reinforcement (CSA) due to hard ceramic compounds present in CSA which leads to greater bonding of the matrix. The addition of CSA particles having minor effect on CF, and better value is observed at 10% of CSA, whereas more the value of the sliding distance, lesser the value of CF. The optimal conditions for WR and CF are L1R3D3 and L1R2D3, respectively. The input data to SPSS software is provided in coded form of factors, i.e. -1 to +1. From regression equation, the interaction between CF with *LR*, *LD* and *RD* is identified.

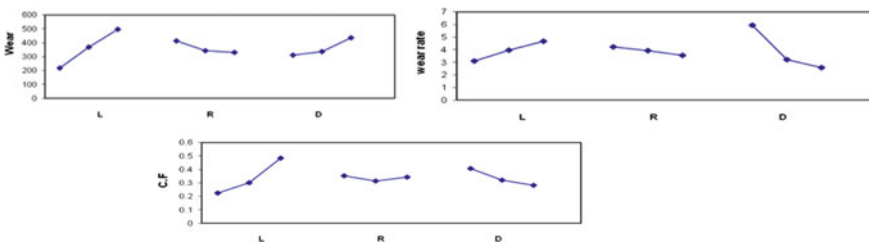


**Fig. 2** Response graphs

$$\begin{aligned} \text{WR} = & 3.2 + 0.782 * L - 0.345 * R - 1.671 * D \\ & + 1.052 * D^2 - 0.283 * LD (R^2 = 0.965) \end{aligned} \quad (1)$$

$$\begin{aligned} \text{CF} = & 0.263 + 0.13 * L - 0.004 * R - 0.062 * D + 0.052 * L^2 \\ & + 0.033 * R^2 + 0.026 * D^2 - 0.020 * LR - 0.049 * LD \\ & + 0.025 * RD (R^2 = 1.00) \end{aligned} \quad (2)$$

## 4 Conclusions

- Aluminium 1100 alloy CSA composites (i.e. 5, 10, 15% CSA) are prepared indigenously with a laboratory scale by stir casting process.
- Full factorial experiments for three process parameters at three levels were conducted to examine the tribological performance (i.e. wear, WR and CF) on CSA composites.
- The resistance to wear of CSA composites increased with increase in volume and decreased with increase in load.
- Load is the dominating factor on the responses such as wear and wear rate, whereas sliding distance is dominating parameter on the coefficient of friction.
- Optimum parameters were predicted through genetic algorithm technique, i.e. load = 10 N, percentage of coconut shell ash = 13.61 and sliding speed = 1795 m to achieve the best responses.

## References

1. Bello SA et al (2017) Study of tensile properties, fractography and morphology of aluminium (1xxx)/coconut shell micro particle composites. *J King Saud Univ Eng Sci* 2(3):269–277. <https://doi.org/10.1016/j.jksues.2015.10.001>
2. Hatch JE (1984) Aluminum properties and physical metallurgy. ASM International, Ohio, pp 1–24. <https://doi.org/10.1361/appm1984p001>
3. Kato K (2000) Wear in relation to friction—a review. *Wear* 241:151–157. [https://doi.org/10.1016/s0043-1648\(00\)00382-3](https://doi.org/10.1016/s0043-1648(00)00382-3)
4. Kök M, Özdin K (2007) Wear resistance of aluminium alloy and its composites reinforced by Al<sub>2</sub>O<sub>3</sub> particles. *J Mater Proc Technol* 183(2–3):301–309. <https://doi.org/10.1016/j.jmatprotec.2006.10.021>
5. Mishra AK, Srivastava RK (2016) Wear behaviour of Al-6061/SiC metal matrix composites. *J Inst Eng Ser C* 1–7. <https://doi.org/10.1007/s40032-016-0284-3>
6. Rallabandi SR, Srinivasa Rao G (2019) Assessment of tribological performance of Al-Coconut shell ash particulate-MMCs using grey-fuzzy approach. *J Inst Eng Ser C* 100(1):13–22. <https://doi.org/10.1007/s40032-017-0388-4>

7. Rodopoulos CA, James KW (2004) Metal matrix composites. In: Wessel JK (ed) Handbook of advanced materials: enabling new designs. Wiley Online Library, pp 99–117. <https://doi.org/10.1002/0471465186.ch6>
8. Rohatgi PK (1993) Metal-matrix composites. *Def Sci J* 43(4):323–349. <https://doi.org/10.14429/dsj.43.4336>
9. Rohatgi PK, Schultz B (2007) Lightweight metal matrix nanocomposites—stretching the boundaries of metals. *Mater Matters* 2(4):1–6
10. Sahin Y (2010) Abrasive wear behaviour of SiC/2014 aluminium composite. *Tribol Int* 43:939–943. <https://doi.org/10.1016/j.triboint.2009.12.056>
11. Siva Sankara Raju R et al (2017) Estimation of tribological performance of Al-MMC reinforced with a novel In-Situ ternary mixture using grey relational analysis. *Ind J Sci Technol* 10(15):1–9. <https://doi.org/10.17485/ijst/2017/v10i15/113825>
12. Siva Sankara Raju R, Srinivasa Rao G (2017) Assessment of tribological performance of coconut shell ash particle reinforced Al-Si-Fe composites using grey-fuzzy approach. *Tribol Ind* 39(3):364–377. <https://doi.org/10.24874/ti.2017.39.03.12>
13. Siva Sankara Raju R, Srinivasa Rao G (2017) Assessments of desirability wear behaviour on Al-Coconut shell ash–metal matrix composite using grey–fuzzy reasoning grade. *Ind J Sci Technol* 10(15):1–11. <https://doi.org/10.17485/ijst/2017/v10i15/113826>
14. Siva Sankara Raju R et al (2017) Investigation of tribological behavior of a novel hybrid composite prepared with Al-Coconut shell ash mixed with graphite. *Metall Mater Trans A*. 48(8):3892–3903. <https://doi.org/10.1007/s11661-017-4139-1>
15. Siva Sankara Raju R et al (2018) Experimental studies of mechanical properties and tribological behaviour of aluminium composite reinforced with coconut shell ash particulates. *Int J Mater Eng Innov* 9(2):140–157. <https://doi.org/10.1504/IJMATEL.2018.093812>
16. Siva Sankara Raju R et al (2018) Optimization of tribological behaviour on Al-coconut shell ash composite at elevated temperature. *IOP Conf Ser Mater Sci Eng* 314:012009. <https://doi.org/10.1088/1757-899X/314/1/012009>
17. Siva Sankara Raju R et al (2019) Tribological behaviour of Al-1100-coconut shell ash (CSA) composite at elevated temperature. *Tribol Int* 129:55–66. <https://doi.org/10.1016/j.triboint.2018.08.011>
18. Venkata Siva B et al (2013) Machinability of aluminum metal matrix composite reinforced with in-situ ceramic composite developed from mines waste colliery shale. *Mater Manuf Proc* 28(10):1082–1089. <https://doi.org/10.1080/10426914.2013.811734>
19. Venkata Siva B et al (2013) Preparation of aluminum metal matrix composite with novel In situ ceramic composite particulates, developed from waste colliery shale material. *Metall Mater Trans B* 44(4):800–808. <https://doi.org/10.1007/s11663-013-9832-x>
20. Venkata Siva B et al (2015) Quantitative studies on wear behavior of Al-(Al<sub>2</sub>O<sub>3</sub>-SiC-C) composite prepared with in situ ceramic composite developed from colliery waste. *J Eng Tribol* 229(7):823–834. <https://doi.org/10.1177/1350650115570696>



# Pre-strain in Dielectric Elastomer Actuator; Challenges Towards Structure–Property Relationship



Dhananjay Sahu, Om Prakash Prabhakar, Raj Kumar Sahu and Karali Patra

**Abstract** Since the last two decades, pre-strain remained proficient techniques to enhance actuation performance of dielectric elastomer actuators (DEAs). However, the influences of pre-strain on properties of elastomer are widely explored. But their co-relation with (macro)molecular structures is lacking in the literature, which give a path to control the properties of dielectric elastomer. Here, the attributions to pre-strain imposed change in electromechanical properties of VHB 4910 elastomer are discussed well and the modification in molecular structure is also shown. A significant change in infrared spectra is observed, and the emergence of new bonds is co-related well with the physical phenomenon of strain hardening. The result may be helpful to transform the structural integrity and to improve material properties for highly efficient electromechanical actuation.

**Keywords** (Macro)molecular structure · Strain hardening · VHB 4910 · Soft actuators

## 1 Introduction

Dielectric elastomers (DEs) are acknowledged as futuristic material towards the design and development of electromechanical soft actuators. The feasibility of soft electromechanical devices is due to their durable softness, high flexibility, ease in handling, high power-to-weight ratio, self-healing competence, biocompatibility, etc. [1–4]. Some prototypes made up of dielectric elastomer in actuator configurations includes force sensors, artificial muscles, tunable lenses, energy harvesting micro-electromechanical systems, micro-pumps, etc. [5, 6].

An ideal DEA comprises a pre-strained elastomer film mounted in rigid frame and surfaces coated with a compliant electrode. When a high voltage is applied across

---

D. Sahu · O. P. Prabhakar · R. K. Sahu (✉)

Department of Mechanical Engineering, National Institute of Technology, Raipur 492010, India  
e-mail: [raj.mit.mech@gmail.com](mailto:raj.mit.mech@gmail.com)

K. Patra

Department of Mechanical Engineering, Indian Institute of Technology, Patna, India

© Springer Nature Singapore Pte Ltd. 2020

H. K. Voruganti et al. (eds.), *Advances in Applied Mechanical Engineering*,

Lecture Notes in Mechanical Engineering,

[https://doi.org/10.1007/978-981-15-1201-8\\_44](https://doi.org/10.1007/978-981-15-1201-8_44)

the electrodes, opposite charges on surfaces attract each other results in actuation strain [7]. The magnitude of voltage-induced deformation depends on electrostatic pressure that can be improved by increasing dielectric permittivity and (or) reducing elastic modulus, as represented in Eqs. (1) and (2) [8].

$$p = \varepsilon\varepsilon_0 E^2 = \varepsilon\varepsilon_0(V/d)^2 \quad (1)$$

$$S_z = -p/Y = -\varepsilon\varepsilon_0 E^2/Y \quad (2)$$

where  $p$  is electrostatic pressure,  $V$  is applied voltage,  $\varepsilon$  is dielectric permittivity of elastomer,  $\varepsilon_0$  is permittivity of free space,  $E$  is the electric field (volts per metre),  $d$  is film thickness,  $S_z$  is field-induced actuation strain in the thickness direction, and  $Y$  is elastic modulus.

Interestingly, the applied pre-strain in actuator configuration decreases the dielectric permittivity to a certain extent. Simultaneously, the actuation strain improves with decreasing thickness that results in reduction of elastic modulus. Specifically, the pre-strain-induced changes in electromechanical properties depend on various other parameters that complicate the material behaviour. Depending on the geometry of the actuator and its application, the regimes of pre-strain can be any of; uniaxial, biaxial, pure shear and radial deformation [9, 10]. Also, the change in properties is associated with material constituent, strain rate, stretch ratio, type of loading, etc. [10].

It is recognized that the dielectric permittivity of VHB 4910 elastomer decreases from 4.4 to 2.4 under equi-biaxial pre-stretch ratio 5. This is attributed to entanglement in the macromolecular chain network that affects the polarizing competence of dipoles by distressing their intrinsic arrangement [11]. Similarly, undesired viscoelastic behaviour of VHB 4910 elastomer is due to the intermolecular linkage or strength of covalent bond within the macromolecules [12]. Control over chain entanglement can be achieved by filling the vacant space in macromolecular network, i.e. by improving crosslink density. The dependency of elastic modulus and dielectric permittivity on crosslink density of elastomer is represented in Eqs. (3) and (4), respectively [13, 14]. This indicates that the increase in crosslink density improves dielectric permittivity as well as elastic modulus [15].

$$Y = 3\rho kT \quad (3)$$

$$\varepsilon = 0.57\rho^2 - 1.22\rho + 1.92 \quad (4)$$

where  $\rho$  is the crosslink density,  $k$  is Boltzmann constant, and  $T$  is the absolute temperature.

As the structure plays a crucial role in physical properties of elastomeric material [9], performance-influencing parameters like loss tangent, electric breakdown strength, dissipation energy, tensile strength, hysteresis, creep, etc., may probably

depend on the (macro)molecular parameters like covalent bond, molecular weight, and crosslink density. However, such co-relations are lacking in available literature.

The present article precisely comprises the attributions revealed to the effect of pre-strain on electromechanical properties of VHB 4910 elastomer. The phenomenon of pre-strain-induced chain entanglement is correlated well with the modification in molecular structure. Elastomer chains under tensile strain are found to be stiff, which leads to carry hardening effect. Comparative infrared absorbance spectra are used to identify hard segment. This contributes a few information towards (macro)molecular structure and their influences on properties of dielectric elastomer. Moreover, it may motivate the readers to concentrate on structure–property relationship to completely understand the electromechanical behaviour of dielectric elastomer.

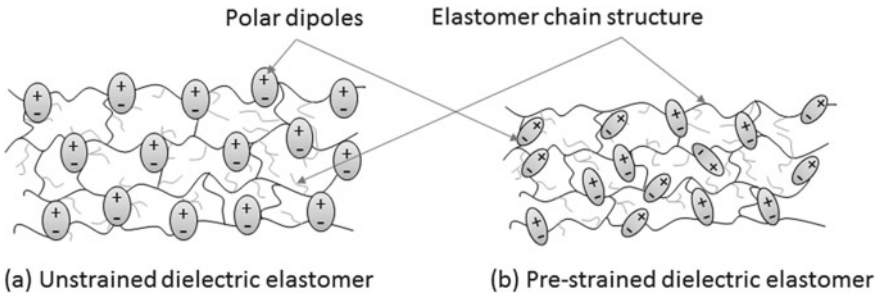
## 2 How Pre-strain Regulate Electromechanical Properties

Pre-strain is appreciated as an effective technique to improve the electromechanical performance of VHB 4910 dielectric elastomers in actuator configuration, as it;

- (a) Reduces thickness of the elastomer which in turn lowers the desired voltage and enhances dielectric breakdown strength [16].
- (b) Reduces elastic modulus that improves energy density and response time [17].
- (c) Guides preferential expansion through strain hardening [18].
- (d) Prevents pull-in instability or the negative effect of inactive boundary material on strain response [19].

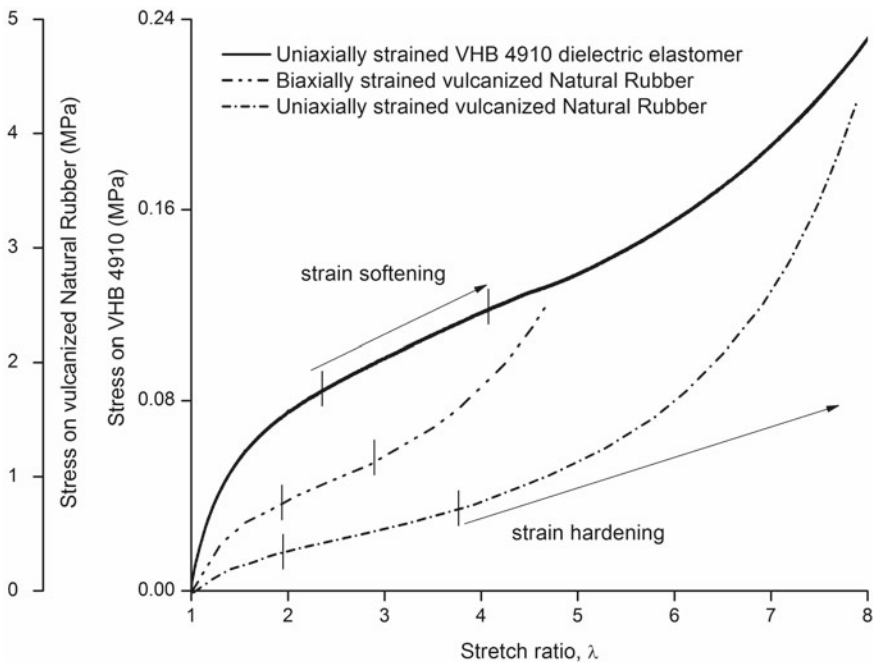
Moreover, to justify how it regulates the electromechanical properties of DEs, most of the literatures referred to the chain entanglement competence of elastomer matrix. The chain matrix is generally termed as long skeleton structure of macromolecules. The long macromolecular chain results in low elastic modulus and macromolecules with low molecular weight integrate high dielectric permittivity [20]. Accordingly, pre-strain-induced changes in properties are possible due to modification in macromolecular structural parameters like strength of covalent bonds, molecular/monomers, lattice structure, molecular weight and crosslink density.

Figure 1 shows a schematic diagram of macromolecular chain with aligned dipoles in unstrained state and the distressed dipoles of elastomer under the pre-strained condition. The adverse effect of pre-strain on dielectric permittivity is one of the reasons to decrease electric polarization, causing distressed dipoles in the chain structure [21–23]. This is also attributed to strain-induced crystallization, change in the glass transition phase, material morphology, homogeneity, etc. [21]. Recently, the stiff macromolecular chains of nano-composite are shown to inhibit chain orientation, results in high dielectric permittivity [24]. Similarly, the hardening competence of the VHB 4910 elastomer under equi-biaxial pre-strain is observed to reduce viscoelastic behaviour [25]. Further, it is shown that the small deformation (stretch ratio,  $\lambda = 1.8$ ) in VHB 4910 elastomer is insufficient to attain strain-hardening effect [26].



**Fig. 1** Schematic illustration for a macromolecular chain with **a** aligned dipoles in unstrained and **b** distressed dipoles under the pre-stretched condition

Figure 2 represents the stress–strain curve of vulcanized natural rubber deducing strain softening and hardening [27]. The tensile behaviour of VHB 4910 elastomer (deformed at 100 mm/min [28]) is merged to optimize the stretch ratio when softening and hardening occur. It is shown that the initial linear behaviour of the stress–strain curve is indicative parameter for strain softening followed by nonlinearity due to strain hardening. The softening features in biaxial strain exist for very short range



**Fig. 2** Distinctive stress–strain plot of vulcanized natural rubber [27] compared with the tensile behaviour of VHB 4910 dielectric elastomer

as compared to uniaxial strain. Hence, the hardening of VHB elastomer is found to occur beyond  $\lambda = \sim 4.0$  in uniaxial state and perceived to start at  $\lambda = 3$  under biaxial condition. This is hardening behaviour perhaps an appropriate reason behind improved actuation strain of 300% biaxially pre-strained VHB 4910 elastomer, as shown in the previous experiment [29]. Further to ensure the strain hardening in terms of the modification in molecular structure, infrared absorbance spectra of biaxially are discussed in the following section.

### 3 Comparative Infrared Spectroscopy of Biaxially Pre-strained VHB 4910 Elastomer

Infrared spectroscopy is widely used to collect the information about phase separation in elastomeric materials. It typically probes the complexation and(or) interaction between the hard and soft segments in chain matrix [30]. The change in molecular structure is usually assessed by comparing band intensity, bandwidth, peak position, peak splitting, etc. Infrared absorbance spectra obtained of an unstrained and 300% biaxially pre-strained VHB 4910 dielectric elastomer are shown in Fig. 3.

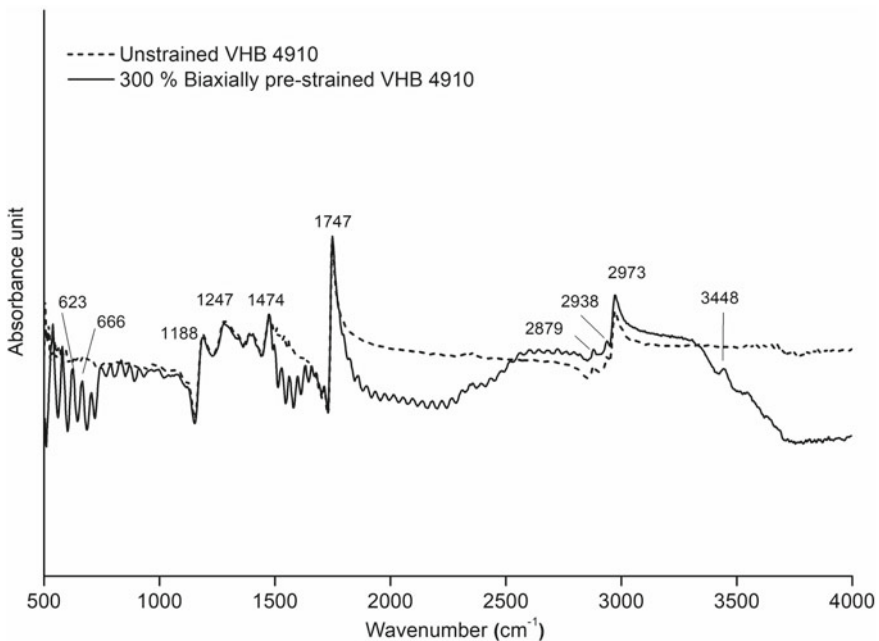


**Fig. 3** Comparative infrared absorbance spectra of 300% biaxially strained VHB 4910 dielectric elastomer

Bruker Alpha TM model ATR-FTIR analyser is used to recorded absorbance spectra in the wavenumber range of 500–4000  $\text{cm}^{-1}$  with a resolution of 4  $\text{cm}^{-1}$ . Here, the effect of pre-strain on various peaks (i.e. at 1188, 1247, 1474, 1747  $\text{cm}^{-1}$ ) is found to be ineffective. However, pre-strain results in the emergence of a novel absorbance peak at 3448  $\text{cm}^{-1}$  assigned to strongest carbonyl bond [31]. Also, absorbance peaks emerged between 630 and 690  $\text{cm}^{-1}$  are found to relate aliphatic bond in VHB 4910 elastomer. The presence of aliphatic bonds indicates hard segments in elastomer network and comprises weak molecular interaction [31–34]. This discussion exemplifies the applied pre-strain in construction of DEA significantly modifies the molecular structure of dielectric elastomers. Hence, the effect of pre-strain on electromechanical behaviour is possibly because of lamellae formation (or strain-induced crystallization), change in glass transition phase, morphology, etc.

## 4 Conclusion

The effects of pre-strain on dielectric permittivity and viscoelastic behaviour of VHB 4910 elastomer are discussed in context with (macro)molecular parameters. The theory of chain entanglement for pre-strain is found to lead stiff matrix, related with the phenomenon of strain hardening. The hardening effect of stiff chains is found to decrease viscoelastic behaviour, and the existence of hard segment is confirmed by the peaks for aliphatic bond. These results mark the importance of structure–property relationship towards complete understanding of dielectric elastomers for actuator applications. The study of pre-strain-induced changes in electromechanical properties and their co-relation with the modification in (macro) molecular structure under dynamic deformation is directed towards future work.

**Acknowledgements** Authors acknowledge the help rendered by the Department of Science and Technology, Government of India, New Delhi, for funding this research through grant file no. ECR/2016/000581.

## References

1. Shankar R, Ghosh TK, Spontak RJ (2007) Elastomers as next-generation polymeric actuators. *Soft Matter* 3:1116–1129
2. Keplinger C, Kaltenbrunner M, Arnold N, Bauer S (2010) Rontgen's electrode-free elastomer actuators without electromechanical pull-in instability. *Proc Natl Acad Sci* 107:4505–4510
3. Yu L, Madsen FB, Skov AL (2017) Degradation patterns of silicone-based dielectric elastomers in electrical fields. *Int J Smart Nano Mater* 1–16
4. Jiang L et al (2018) Electromechanical instability in silicone—and acrylate-based dielectric elastomers. *J Appl Polym Sci* 45733:6–11
5. Michel S, Zhang XQ, Wissler M, Löwe C, Kovacs G (2010) A comparison between silicone and acrylic elastomers as dielectric materials in electroactive polymer actuators. *Polym Int* 59:391–399

6. Wu F et al (2018) Bioinspired universal flexible elastomer-based microchannels. *Small* 1702170:1–7
7. Deng L, He Z, Li E, Chen S (2018) Maximum actuation strain for dissipative dielectric elastomers with simultaneous effect of prestretch and temperature. *J Appl Polym Sci* 1–16
8. Pelrine R, Kornbluh R, Pei Q, Joseph J (2000) High-speed electrically actuated elastomers with strain greater than 100%. *Science* 80(287):836–840
9. Kussmaul B et al (2011) Enhancement of dielectric permittivity and electromechanical response in silicone elastomers: molecular grafting of organic dipoles to the macromolecular network. *Adv Funct Mater* 21(23):4589–4594
10. Kumar A, Ahmad D, Patra K (2018) Dependence of actuation strain of dielectric elastomer on equi-biaxial, pure shear and uniaxial modes of pre-stretching. *IOP Conf Ser Mater Sci Eng* 310:1–9
11. Qiang J, Chen H, Li B (2012) Experimental study on the dielectric properties of polyacrylate dielectric elastomer. *Smart Mater Struct* 21(025006):1–9
12. Fan F, Szpunar J (2015) Characterization of viscoelasticity and self-healing ability of VHB 4910. *Macromol Mater Eng* 300(1):99–106
13. Yang D et al (2012) New polyester dielectric elastomer with large actuated strain at low electric field. *Mater Lett* 76:229–232
14. Chua J, Tu Q (2018) A molecular dynamics study of crosslinked phthalonitrile polymers: the effect of crosslink density on thermomechanical and dielectric properties. *Polymers* 4:1–11
15. Sahu D, Sahu RK, Patra K (2019) Effects of crosslink density on the behavior of VHB 4910 dielectric elastomer. *J Macromol Sci Part A Pure Appl Chem* 56:821–829. <https://doi.org/10.1080/10601325.2019.1610329>
16. Shian S, Diebold RM, Clarke DR, Link C (2012) The thickness and stretch dependence of the electrical breakdown strength of an acrylic dielectric elastomer. *Appl Phys Lett* 101:122905
17. Huang J, Shian S, Suo Z, Clarke DR (2013) Maximizing the energy density of dielectric elastomer generators using equi-biaxial loading. *Adv Funct Mater* 23(40):5056–5061
18. Biddiss E, Chau T (2008) Dielectric elastomers as actuators for upper limb prosthetics: challenges and opportunities. *Med Eng Phys* 30(4):403–418
19. Akbari S, Rosset S, Shea HR (2013) Improved electromechanical behavior in castable dielectric elastomer actuators. *Appl Phys Lett* 10(071906):1–5
20. Zhang QP et al (2017) Tailoring chain length and cross-link density in dielectric elastomer toward enhanced actuation strain. *Appl Phys Lett* 111:1–4
21. Vu-Cong T, Ngyen-Thi N, Jean-Mistral C, Sylvestre A (2014) How does static stretching decrease the dielectric constant of VHB 4910 elastomer? In: *Electroactive polymer actuators and devices (EAPAD)*, SPIE, pp 1–9
22. Jean-Mistral C, Sylvestre A, Basrou S, Chaillout JJ (2010) Dielectric properties of polyacrylate thick films used in sensors and actuators. *Smart Mater Struct* 19:1–9
23. Sahu RK, Yadu S, Singh V, Raja S, Patra K (2017) The effect of micro molecular parameters on the actuation performance of electro active polymers. *Int Mech Eng Congr Expo ASME*, 2017, 71272:1–6. <https://doi.org/10.1115/IMECE2017-71272>
24. Javadi S, Panahi-Sarmad M, Razzaghi-Kashani M (2018) Interfacial and dielectric behavior of polymer nanocomposites: effects of chain stiffness and cohesive energy density. *Polymers (United Kingdom)* 145:31–40
25. Tran DQ, Li J, Xuan F, Xiao T (2018) Viscoelastic effects on the actuation performance of a dielectric elastomer actuator under different equal, un-equal biaxial pre-stretches. *Mater Res Express* 5:1–12
26. Helal A, Doumit M, Shaheen R (2018) Biaxial experimental and analytical characterization of a dielectric elastomer. *Appl Phys A* 124:1–11
27. Davidson JD, Goulbourne NC (2013) A nonaffine network model for elastomers undergoing finite deformations. *J Mech Phys Solids* 61:1784–1797
28. Sahu RK, Patra K (2016) Rate-dependent mechanical behavior of VHB 4910 elastomer. *Mech Adv Mater Struct* 23:170–179. <https://doi.org/10.1080/15376494.2014.949923>

29. Sahu RK, Sudarshan, K, Patra K, Bhaumik S (2014) Evaluation of area strain response of dielectric elastomer actuator using image processing technique. In: *Electroactive polymer actuators and devices (EAPAD)*, vol 9056, pp 11–16
30. Cakić SM, Ristić IS, Marinović-Cincović M, Špirková M (2013) The effects of the structure and molecular weight of the macrodiol on the properties polyurethane anionic adhesives. *Int J Adhes Adhes* 41:132–139
31. Yvon HJ (2017) Raman spectroscopy for analysis and monitoring. Horiba Jobin Yvon, Raman Application Note 1–2
32. Mishra A, Aswal VK, Maiti P (2010) Nanostructure to microstructure self-assembly of aliphatic polyurethanes: the effect on mechanical properties. *J Phys Chem B* 114:5292–5300
33. Jiang L, Ren Z, Zhao W, Liu W (2018) Synthesis and structure/properties characterizations of four polyurethane model hard segments. *R Soc Open Sci* 5:1–11
34. Sahu D, Sahu RK, Patra K (2019) Effects of uniaxial and biaxial strain on molecular structure of VHB 4910 dielectric elastomer. In *Advances in polymer composites: mechanics, characterization and applications 020032*, pp 1–7



# Modified Electromechanical Model for Dielectric Elastomer Cylindrical Actuators



Om Prakash Prabhakar, Dhananjay Sahu and Raj Kumar Sahu

**Abstract** Dielectric elastomers (DEs)-based electromechanical cylindrical actuators are applicable in the field of biomimetic, robotics, microfluidic pumps and similar instrumental devices. However, to achieve efficient actuation performance, significant attention is requisite towards influences of pre-strain on electromechanical properties. This study shows the effect of pre-strain-induced variation in dielectric permittivity to improve the performance of the existing model for a cylindrical actuator. Modified electromechanical model is proposed for a thin-walled actuator configuration. The hypothesis of linear elasticity for small deformation is used to derive the novel model for voltage-induced axial strain. The analytical results shows improved axial actuation strain with relatively less errors and the values are found in good agreement with experimental results. This may encourage future researchers to identify crucial parameters on the way to design and optimization of soft actuators.

**Keywords** Electromechanical · Thin-walled actuator · Axial strain · Soft actuator

## 1 Introduction

Dielectric elastomers belongs to the family of electroactive smart material, which illustrate high elastic deformation under the stimulation of electric field. Due to the tunable features like high flexibility, low cost, ease in production and inherent softness, DEs are acknowledged as feasible material towards fabrication of soft actuators, sensors and energy harvester electromechanical system [1]. The electromechanical performance of DE devices is based on the principle of Maxwell stress which governs the electrostatic pressure ( $P$ ) that induces actuation strain ( $S_z$ ). The expression of Maxwell stress and subsequent field-induced strain as shown in Eqs. (1) and (2), respectively [2], reveals the actuation performance depends on dielectric permittivity ( $\epsilon$ ), the film thickness ( $t$ ) and the elastic modulus ( $E$ ) of the elastomers.

---

O. P. Prabhakar · D. Sahu · R. K. Sahu (✉)

Department of Mechanical Engineering, National Institute of Technology, Raipur 492010, India  
e-mail: [raj.mit.mech@gmail.com](mailto:raj.mit.mech@gmail.com)

© Springer Nature Singapore Pte Ltd. 2020

H. K. Voruganti et al. (eds.), *Advances in Applied Mechanical Engineering*,

Lecture Notes in Mechanical Engineering,

[https://doi.org/10.1007/978-981-15-1201-8\\_45](https://doi.org/10.1007/978-981-15-1201-8_45)

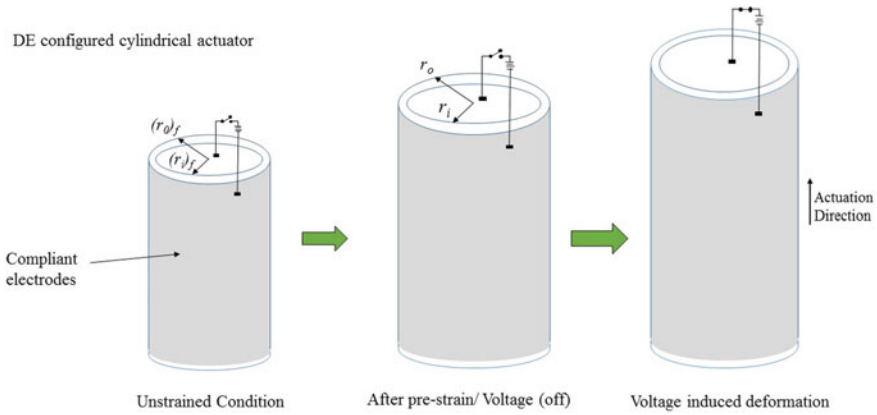


**Fig. 1** Schematic diagram for dielectric elastomer cylindrical actuator configuration

$$P = \varepsilon \varepsilon_0 \left( \frac{V}{t} \right)^2 \quad (1)$$

$$S_z = -P/E = -\varepsilon \varepsilon_0 E^2/E \quad (2)$$

The DE cylindrical actuators are applicable in soft biomimetic instrumentation and robotic arms owing to the competence of bending and rotational motion [3]. As shown in Fig. 1, the cylindrical configuration comprises a rolled elastomer film that supposed to deform in the axial direction. Further, it is noteworthy that the lateral pre-strain is essential to achieve considerable electromechanical actuation strain [4]. The applied pre-strain prevents electromechanical pull-in instability and is known to improve actuation performance by regulating dielectric and mechanical properties [5, 6].

Earlier, the electromechanical model proposed for DE cylindrical actuator assumed dielectric permittivity as constant (i.e. not vary either with strain or with voltage) and underlined the influences of voltage per unit thickness on axial actuation strain [7]. Unfortunately, the extension of this work is yet not found in the available literature, although it is well recognized that applied pre-strain significantly influences the dielectric permittivity of the dielectric elastomers.

This analytical work proposes the modification of an existing model in context with the effects of pre-strain on dielectric permittivity of DE for the cylindrical actuator. The results are observed in good agreement with the available set of experimental data, and comparatively reduced error ensures the reliability of the improved model for high actuation strain.

## 2 Analytical Modelling

Analytical study of DE actuators is the process to realize practical actuation performance in the computational platform. MATLAB is used to modify the existing electromechanical model of DE-based cylindrical actuator. Electrostatic pressures generated across the elastomer surface are considered to be constant; whereas, dielectric permittivity varies with pre-strain. Further, the consideration of a pure electrical analysis enables to define a geometrical parameter ( $\Gamma$ ) in expressions of electrostatic pressure [7]. Hence, for cylindrical configuration with  $r_i$  and  $r_o$  inner and outer radii, respectively, the induced pressure is

$$P_i = \frac{\epsilon V^2}{r_i} \Gamma \tag{3}$$

$$P_o = \frac{\epsilon V^2}{r_o} \Gamma \tag{4}$$

For small strain, material is assumed to be linearly elastic, homogeneous and isotropic. Thus, the mechanical analysis is performed to establish the relationship between stresses and respective pressure-induced actuation strain on the surfaces of the cylindrical actuator. Pressure-induced strains of the actuator can be obtained after the identification of the displacements. To evaluate the displacement in the absence of body forces in the static condition, Navier’s equation [8] for cylindrical actuators in  $r, \theta$  and  $z$ -direction is

$$\begin{aligned}
 &(\lambda + \mu) \frac{\partial}{\partial r} \left( \frac{1}{r} \frac{\partial(r u_r)}{\partial r} + \frac{1}{r} \frac{\partial u_\theta}{\partial \theta} + \frac{\partial u_z}{\partial z} \right) \\
 &+ \mu \left( \frac{\partial^2 u_r}{\partial r^2} + \frac{1}{r} \frac{\partial u_r}{\partial r} + \frac{1}{r^2} \frac{\partial^2 u_r}{\partial \theta^2} + \frac{\partial^2 u_r}{\partial z^2} - \frac{u_r}{r^2} - \frac{2}{r^2} \frac{\partial u_\theta}{\partial \theta} \right) = 0 \tag{5}
 \end{aligned}$$

$$\begin{aligned}
 &(\lambda + \mu) \frac{\partial}{\partial \theta} \left( \frac{1}{r} \frac{\partial(r u_r)}{\partial r} + \frac{1}{r} \frac{\partial u_\theta}{\partial \theta} + \frac{\partial u_z}{\partial z} \right) \\
 &+ \mu \left( \frac{\partial^2 u_\theta}{\partial r^2} + \frac{1}{r} \frac{\partial u_\theta}{\partial r} + \frac{1}{r^2} \frac{\partial^2 u_\theta}{\partial \theta^2} + \frac{\partial^2 u_\theta}{\partial z^2} - \frac{u_\theta}{r^2} + \frac{2}{r^2} \frac{\partial u_z}{\partial z} \right) = 0 \tag{6}
 \end{aligned}$$

$$\begin{aligned}
 &(\lambda + \mu) \frac{\partial}{\partial z} \left( \frac{1}{r} \frac{\partial(r u_r)}{\partial r} + \frac{1}{r} \frac{\partial u_\theta}{\partial \theta} + \frac{\partial u_z}{\partial z} \right) \\
 &+ \mu \left( \frac{\partial^2 u_z}{\partial r^2} + \frac{1}{r} \frac{\partial u_z}{\partial r} + \frac{1}{r^2} \frac{\partial^2 u_z}{\partial \theta^2} + \frac{\partial^2 u_r}{\partial z^2} \right) = 0 \tag{7}
 \end{aligned}$$

where  $\lambda$  and  $\mu$  are the Lamé’s constant, defined as follows:

$$\lambda = \frac{\nu E}{(1 + \nu)(1 - 2\nu)} \tag{8}$$

$$\mu = \frac{E}{2(1 + \nu)} \quad (9)$$

Assuming actuator constrained for deformation only in the axial and radial direction, the displacements dependency on the  $r$  and  $z$  coordinates is

$$u_\theta = 0 \quad (10)$$

$$u_r = u_r(r) \quad (11)$$

$$u_z = u_z(r) \quad (12)$$

On incorporating the constrain (10)–(12) in the Navier's displacement equations (5)–(7), the displacement in  $\theta$  direction (Eq. 6) becomes null, and expression for  $r$  and  $z$ -direction is

$$\frac{d}{dr} \left( \frac{1}{r} \frac{d(ru_r)}{dr} \right) = 0 \quad (13)$$

$$\frac{d^2 u_z}{dz^2} = 0 \quad (14)$$

After writing the stress equations in terms of  $C_1$ ,  $C_2$  and  $C_3$  and applying boundary condition i.e.  $(\sigma_{rr})_{r=r_i} = -P_i$ ,  $(\sigma_{rr})_{r=r_o} = -P_o$  and  $\sigma_{zz} = 0$ , the expression for the constants is:

$$C_1 = \frac{\lambda + 2\mu}{3\lambda\mu + 2\mu^2} \frac{P_o r_o^2 - P_i r_i^2}{r_i^2 - r_o^2} \quad (15)$$

$$C_2 = \frac{(P_o - P_i)r_i^2 r_o^2}{2\mu(r_i^2 - r_o^2)} \quad (16)$$

$$C_3 = \frac{-\lambda}{3\mu\lambda + 2\mu^2} \frac{P_o r_o^2 - P_i r_i^2}{r_i^2 - r_o^2} \quad (17)$$

Further in relation to constitutive equations, the stresses ( $\sigma_{rr}$ ,  $\sigma_{\theta\theta}$  and  $\sigma_{zz}$ ) and strains ( $\varepsilon_{rr}$ ,  $\varepsilon_{\theta\theta}$  and  $\varepsilon_{zz}$ ) are related and represented by the Hooke's law in terms of the Lamé's constants as follows:

$$\sigma_{rr} = \frac{P_o r_o^2 - P_i r_i^2}{r_i^2 - r_o^2} - \frac{(P_o - P_i)r_i^2 r_o^2}{r_i^2 - r_o^2} \frac{1}{r^2} \quad (18)$$

$$\sigma_{\theta\theta} = \frac{P_o r_o^2 - P_i r_i^2}{r_i^2 - r_o^2} + \frac{(P_o - P_i)r_i^2 r_o^2}{r_i^2 - r_o^2} \frac{1}{r^2} \quad (19)$$

$$\sigma_{zz} = 0 \quad (20)$$

Strain in terms of stress Eqs. (18)–(20) by using Hooke's law:

$$\varepsilon_{rr} = \frac{1}{E} \left[ (1 - \nu) \frac{P_o r_o^2 - P_i r_i^2}{r_i^2 - r_o^2} - (1 + \nu) \frac{(P_o - P_i) r_i^2 r_o^2}{r_i^2 - r_o^2} \frac{1}{r^2} \right] \quad (21)$$

$$\varepsilon_{\theta\theta} = \frac{1}{E} \left[ (1 - \nu) \frac{P_o r_o^2 - P_i r_i^2}{r_i^2 - r_o^2} + (1 + \nu) \frac{(P_o - P_i) r_i^2 r_o^2}{r_i^2 - r_o^2} \frac{1}{r^2} \right] \quad (22)$$

$$\varepsilon_{zz} = \frac{2\nu}{E} \left( \frac{P_o r_o^2 - P_i r_i^2}{r_o^2 - r_i^2} \right) \quad (23)$$

Intended to derive expressions for deformation behaviour in axial and radial direction (inner and outer radii) of the actuator. Equations (21)–(23) are used to obtain the desired parameters of interest.

$$\frac{\Delta L}{L} = \frac{1}{L} \int_0^L \varepsilon_{zz} dz \quad (24)$$

$$\frac{\Delta r_i}{r_i} = \frac{1}{2\pi} \int_0^{2\pi} \varepsilon_{\theta\theta}(r_i) d\theta \quad (25)$$

$$\frac{\Delta r_o}{r_o} = \frac{1}{2\pi} \int_0^{2\pi} \varepsilon_{\theta\theta}(r_o) d\theta \quad (26)$$

On substituting the values and simplifying Eqs. (24)–(26) and using the property of incompressibility of material ( $\nu = 0.5$ ) equations yield to

$$\frac{\Delta L}{L} = \frac{P_o r_o^2 - P_i r_i^2}{E(r_o^2 - r_i^2)} \quad (27)$$

$$\frac{\Delta r_i}{r_i} = \frac{1}{E(r_o^2 - r_i^2)} \left[ P_i \frac{r_i^2 + 3r_o^2}{2} - 2P_o r_o^2 \right] \quad (28)$$

$$\frac{\Delta r_o}{r_o} = \frac{1}{E(r_o^2 - r_i^2)} \left[ -P_i \frac{r_i^2 + 3r_o^2}{2} + 2P_o r_o^2 \right] \quad (29)$$

In practical application, voltage-induced actuation strain varies with the changes in relative permittivity and consequently affects the pressure in the inner and outer wall.

Hence, to show the effect of pre-strain on dielectric permittivity, so, on performance of VHB 4910 elastomer based cylindrical actuator, experimental value for change in permittivity at a frequency of 1 MHz is referred to previous work [5].

And following expression is used to evaluate the relative permittivity as a function of strain:

$$\epsilon_r = 3.52479(1 + x)^{-0.01185} \tag{30}$$

where  $x$  represents the induced strain in the system on the application of the voltage across the electrodes.

### 3 Result and Discussion

A purely electrical analytical analysis of a 50-mm-long cylindrical actuator is carried out. The actuator having an initial inner radius,  $r_i = 0.8$  mm and outer radius,  $r_o = 1$  mm is pre-strained for 5% elongation along the axial direction. Due to symmetry, the respective decrease in inner and outer is presumed to be equal, and the resultant change is calculated based on constant volume condition as follows:

$$\frac{(r_o)_f - r_o}{r_o} = \frac{(r_i)_f - r_i}{r_i} = -1 + \frac{1}{\left(1 + \frac{L_f - L}{L}\right)} \tag{31}$$

where  $(r_o)_f$ ,  $(r_i)_f$  and  $L_f$  are unstrained outer, inner radii and length of electrode, respectively. Table 1 represents the parameters used with respect to similar testing condition as used for experimental validation of existing model [7].

MATLAB computational work is performed by using model of solid mechanics for small strain in isotropic material [as in Eq. (27)]. Influences of the pre-strain-induced variation in dielectric permittivity on the performance of modified model for cylindrical actuator are shown in Fig. 2. Voltage-induced deformation behaviour is verified and compared with existing model, and the actuation performance in axial direction is found to fitted well with experimental results. The possible reason for this change is distressed polarizing dipoles of the elastomer under pre-strain

**Table 1** Actuator parameters

<i>Initial parameters</i>	
Inner radius	0.8 mm
Outer radius	1 mm
Pre-strain	5%
Length	50 mm
Poisson's ratio	0.5
Young's modulus	5 MPa
<i>After pre-strain</i>	
Inner radius	0.781 mm
Outer radius	0.976 mm

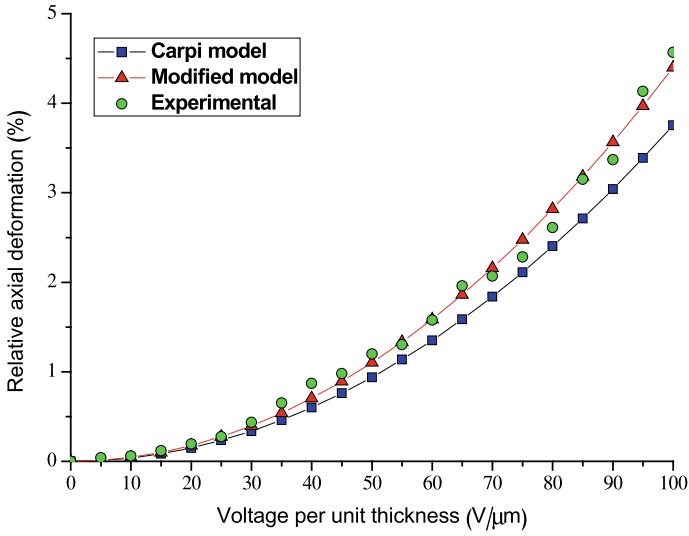


Fig. 2 Relative axial deformation with voltage per unit thickness

(strain) which affects relative permittivity [5]. Further, the comparative absolute error is shown in Fig. 3. The root mean square error also observed to decrease from 31.59 to 10.56% as compared to Carpi model, and this ensures the reliability of modified electromechanical model in prediction of actuation performance for DE-based cylindrical actuator.

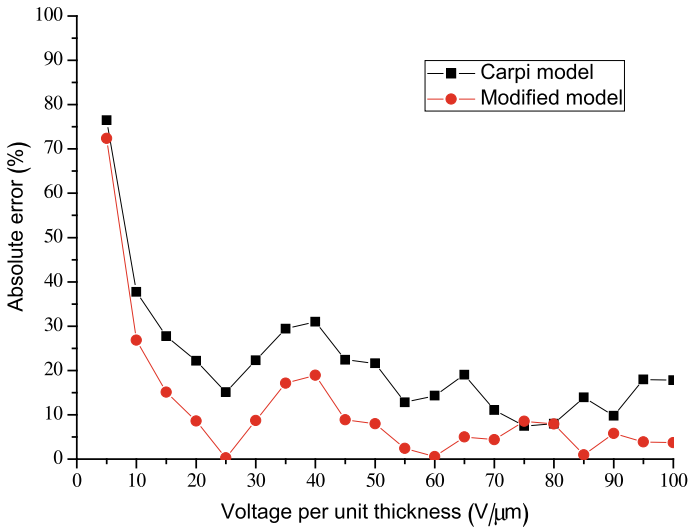


Fig. 3 Absolute error as compared to the existing experimental data

## 4 Conclusion

Electromechanical model for DE cylindrical actuator is modified to improve its efficiency towards electromechanical actuation. Similar to the existing model, the electrostatic pressure across the cylindrical thin wall is assumed to be constant, and the changes in dielectric permittivity with pre-strain are the key consideration in the modified model. The actuation behaviour is validated well with the experimental data, and a relative decrease in root mean square error from 31.59 to 10.56 % is attained. The results show even a small pre-strain can significantly influence the material properties and performances of DE actuator. Control over electromechanical behaviour of the thin-walled actuator in the radial direction will be assessed in the extension of present work.

**Acknowledgements** Authors acknowledge the Department of Science and Technology, Govt. of India, New Delhi, for funding this research through grant file no. ECR/2016/000581.

## References

1. Shankar R, Ghosh TK, Spontak RJ (2007) Elastomers as next-generation polymeric actuators. *Soft Matter* 3:1116–1129
2. Pelrine R, Kornbluh R, Joseph J, Heydt R, Pei Q, Chiba S (2000) High-field deformation of elastomeric dielectrics for actuators. *Mater Sci Eng C* 11:89–100
3. Carpi F, Kornbluh R, Sommer-Larsen P, Alici G (2011) Electroactive polymer actuators as artificial muscles: are they ready for bioinspired applications? *Bioinspiration Biomim* 6
4. Carpi F, Chiarelli P, Mazzoldi A, De Rossi D (2003) Electromechanical characterisation of dielectric elastomer planar actuators: comparative evaluation of different electrode materials and different counterloads. *Sens Actuators A* 107:85–95
5. Sahu RK, Pramanik B, Patra K, Pandey, AK, Setua DK (2012) Experimental study on permittivity of acrylic dielectric elastomer. In: 2012 IEEE 10th international conference on the properties and applications of dielectric materials, Bangalore, India, pp 1–4
6. Jiménez SMA, Mcmeeking RM (2013) Deformation dependent dielectric permittivity and its effect on actuator performance and stability. *Int J Non Linear Mech* 1–8
7. Carpi F, De Rossi D (2004) Dielectric elastomer cylindrical actuators: electromechanical modelling and experimental evaluation. *Mater Sci Eng C* 24:555–562
8. Heinbockel JH (2001) Introduction to tensor calculus and continuum mechanics. Trafford Publishers



# A Numerical Study to Investigate the Modal Analyses of Cracked Airplane Wing (NACA2415)



Gaurav Verma, Anshul Sharma and Yogesh K. Prajapati

**Abstract** One of the major concerns for the structural failure of an airplane wing is due to the initiation of crack and its propagation. The literature survey on aircraft failure indicates that the main source of failure is due to fatigue cracks, which propagate from the wing root region. The modal analyses is one of the important tool used to determine the dynamics behaviour of airplane wing structure including natural frequencies and modes shapes. In the present study, an attempt has been made to perform the modal analyses of aircraft wing structure without cracked airplane wing structure and with cracked airplane wing structure (NACA2415). The results of modal analyses for uncracked wing structure are compared with the results reported in the literature. The main objective of the present study to do the comparative study of modal analyses for with or without crack in aircraft wing and analyses the results which show that natural frequency is affected in presence of crack. The effect of the crack length, depth of the crack and location of the crack on natural frequency is also investigated.

**Keywords** Cracked airplane wing structure · Finite element analysis · Triangular crack

## 1 Introduction

The necessary lift to make an airplane fly can be provided by the wings of the airplane. The structure of the wing consists of outer skin, spar webs and ribs. The spar webs are the most important load carrying member of the wing structure which is extended from fuselage to the tip of the wing structure [1]. The most of the load of the wing structure is carried by the spars so that the spars are designed to have high bending strength [1].

---

G. Verma · A. Sharma (✉) · Y. K. Prajapati  
Department of Mechanical Engineering, National Institute of Technology,  
Uttarakhand, Srinagar, Uttarakhand 246174, India  
e-mail: [anshul@nituk.ac.in](mailto:anshul@nituk.ac.in)

© Springer Nature Singapore Pte Ltd. 2020  
H. K. Voruganti et al. (eds.), *Advances in Applied Mechanical Engineering*,  
Lecture Notes in Mechanical Engineering,  
[https://doi.org/10.1007/978-981-15-1201-8\\_46](https://doi.org/10.1007/978-981-15-1201-8_46)

It is important to study the dynamic behaviour of the aircraft wing structures determined by the modal analyses. By using the modal analyses, one can improve the overall performance of the system in certain operating conditions. It helps to find the reasons of undesired vibrations that may cause damage to the integrated system components resulting in failure of any structure.

Carrera et al. [1] have investigated refined and component wise models, comparison of result done on commercial finite element software. The author performed modal analyses on the two different aircraft wing structures for different degree of freedom. Ostachowicz et al. [2] have investigated the effect of the two open cracks present on the single side or double side of the cantilever beam, on the natural frequency of the cantilever beam. Khalkar et al. [3] have investigated the effect of rectangular shape and V-shape edge cracks on the natural frequency and static deflection of the spring steel cantilever beam. Wang et al. [4] have investigated a simple support point at which if we applied the minimum stiffness support that increases the natural frequency of the beam for the different boundary condition. Sawant and Chauchan et al. [5] have performed modal analyses on healthy beam and cracked beam and investigate the effect of crack on natural frequency at different location and different crack depth. Satpute et al. [6] have investigated behaviour of healthy and cracked beam and conclude the natural frequency to detect the crack in cantilever shaft. Taylan Das et al. [7] studied numerical and experimental modal analyses of curved composite wing with cracks of different depths and different location and different boundary condition like fixed-fixed and fixed-free. Jha et al. have investigated plastic zone length for a straight edge crack with extended finite element method which eliminate the re-meshing process [8].

In the present study, a numerical modal analysis is carried out to investigate the effect of crack length, depth and crack location on the aircraft wing structure. Both uncracked and cracked aircraft wing structure are modelled and analysis is performed using finite element-based software platform ANSYS. The numerical results are validated with the results reported in literature.

## 2 Modelling and Simulation of Aircraft Wing

The modelling of the aircraft wing is done corresponding to the geometrical dimensions reported in literature [1]. The cross-section of the wing with dimensions is illustrated in Fig. 1. The NACA2415 airfoil is used to create the wing with two spar webs, and four spar caps are add-on. The chord length(C) of the airfoil is 1mt. The length (L) along the span direction is equal to 6mt. The thickness of the spar webs of the aircraft wing is  $5 \times 10^{-3}$  mt. The dimensions of the spars flanges are illustrated in Fig. 1. The isotropic material is used for the whole structure, and the material properties are listed in Table 1. Figure 2 shows the aircraft wing structure without crack.

Figure 3 illustrates the aircraft wing structure with triangular surface crack having same geometrical dimensions. The single triangular cracks are introduced at differed

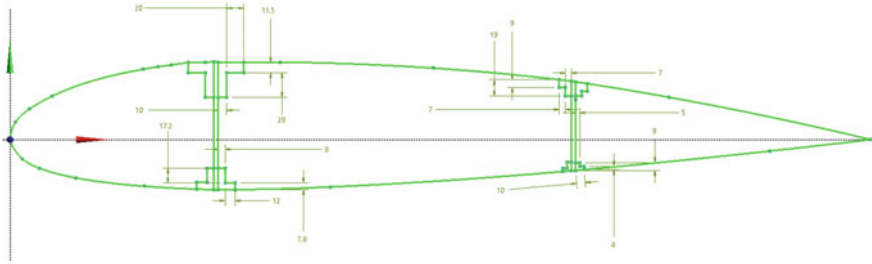


**Fig. 1** Cross-section of the wing with dimensions (mm) [1]

**Table 1** Material properties of the aircraft wings structure [1]

Material properties	Value
Modulus of elasticity (E)	75 GPa
Bulk modulus (K)	73.529 GPa
Modulus of rigidity (G)	28.195 GPa
Density ( $\rho$ )	2700 kg/m <sup>3</sup>
Poisson's ratio ( $\nu_{xy}$ )	0.33

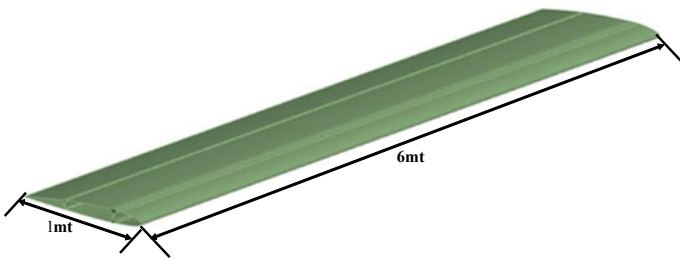


**Fig. 2** Aircraft wing structure without crack

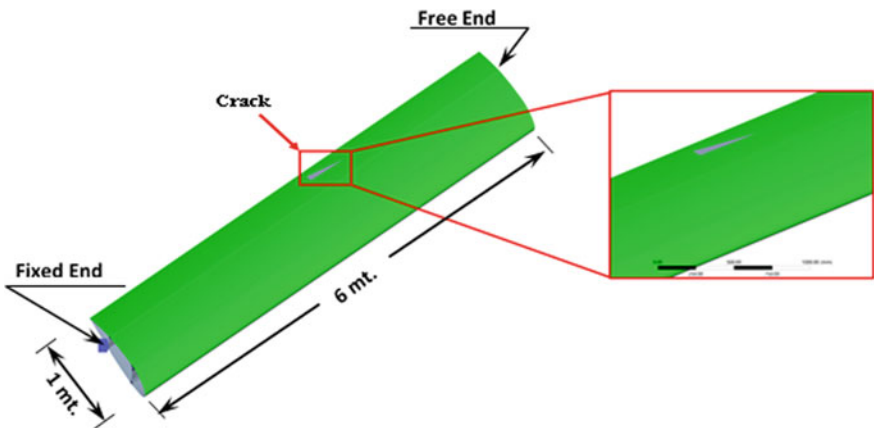


**Fig. 3** Aircraft wing structure with triangular surface crack

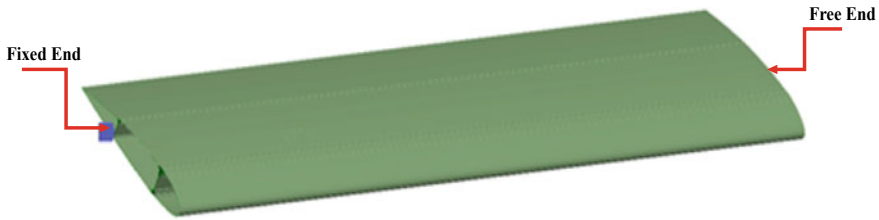


**Fig. 4** Illustration of boundary condition as fixed support applied at the root of the wing

locations (i.e. 866.47, 3269.78, 150.33), of different depth (1.8, 1.5, 1.0, 0.5 and 0.2 mm) and with constant crack length of 0.507 mt in order to perform the parametric dynamic analysis of cracked aircraft wing structure. Moreover, the parametric analysis is also performed with different crack length (0.6, 0.65, 0.7, 0.73 mt) keeping depth of crack constant to 1.8 mm.

The aircraft wing structure was assigned the material properties same as listed in Table 1. The left face of the wing structure is fixed in order to maintain the realistic cantilever boundary conditions while the rest of the structure is kept free. At fixed edge, all the degree of freedoms are fixed. It is to be noted that the geometric properties, material properties and boundary conditions are kept same for both cracked and uncracked aircraft wing structure (Fig. 4).

Thereafter, the finite element analysis is performed on both cracked and uncracked aircraft wing structure using commercially available software package ANSYS versus 19.0. For the discretization of the structure, four-node tetrahedral element is used. The uncracked aircraft wing structure is having 83,700 no. of element while the cracked aircraft wing structure is having 77,169 no. of elements. Figure 5 illustrates the discretized modal of both cracked and uncracked aircraft wing structure.

### 3 Result and Discussion

In order to check the reliability, firstly a validation study is performed and the results of the present analysis are compared with the results reported by Carrera et al. [1]. The same geometric properties, material properties and boundary conditions are adopted. The validation results of the present study with Carrera et al. [1] are listed in Table 2. The results of present study are in good agreement with reported results.

Thereafter, an investigation on the effect of natural frequencies and mode shape are carried out by introducing triangular crack at a location 3269.78 mm away from the fixed end keeping constant crack length of 0.507 mt, and the crack depth is varied as 1.8 mm, 1.5 mm, 1.0 mm, 0.5 mm and 0.2 mm, respectively. It is observed from the numerical results that the frequencies of aircraft wing structure keeps on decreasing with increase in the depth of the crack as listed in Table 3. Presence of crack may reduce the local stiffness of the airplane wing structure at crack location

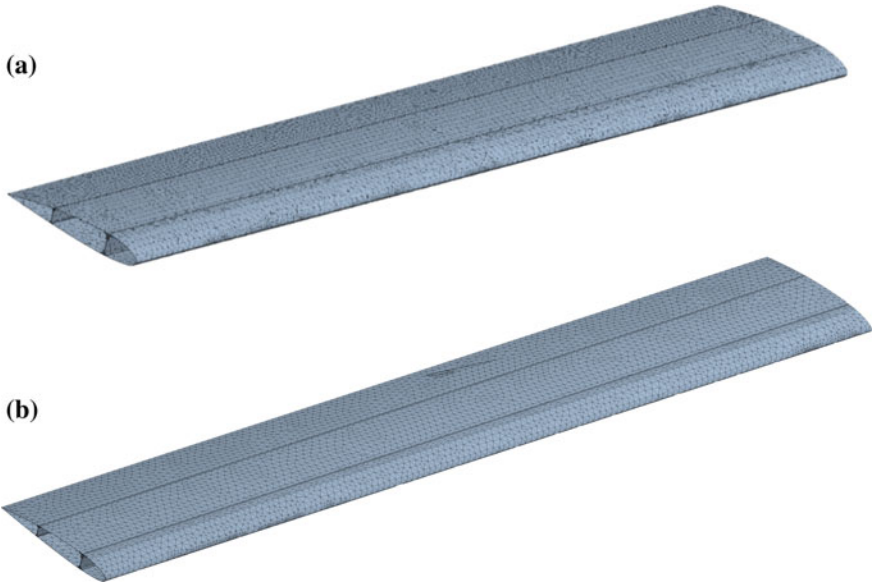


**Fig. 5** Discretized model of aircraft wing structure: **a** Uncracked and **b** Cracked

**Table 2** Comparison of frequency values obtained from present study and Carrera et al. [1]

Mode shapes	Carrera et al. [1]	Present study	Error (%)
I Bending <sup>x</sup>	4.21	4.2814	1.69
I Bending <sup>z</sup>	21.69	21.632	0.26
II Bending <sup>x</sup>	24.78	26.083	5.25
Torsion	29.18	30.39	4.14
III Bending <sup>x</sup>	56.12	59.97	6.86

'x' represents bending and x-direction

'z' represents bending and z-direction

**Table 3** Effect of depth of crack on natural frequency of cracked aircraft wing structure

Depth of crack (mm)	Crack length (mm)	Frequency, $f_n$ (Hz)		
		First	Second	Third
0	0	4.2814	21.632	26.083
0.2	507	4.2757	21.068	26.044
0.5	507	4.2628	20.974	25.978
1.0	507	4.2466	20.921	25.937
1.5	507	4.2398	20.920	25.928
1.8	507	4.2397	20.897	25.925

**Table 4** Effect of crack length on natural frequency of cracked aircraft wing structure

Crack length (mm)	Depth of crack (mm)	Frequency, $f_n$ (Hz)
0	0	4.2814
570	1.8	4.2397
600	1.8	4.2395
650	1.8	4.2379
700	1.8	4.2370
730	1.8	4.2160

which is calculated from the stiffness matrix. Moment of inertia of the airplane wing is reduced in presence of crack and further reduced with increasing of crack depth results in natural frequency is decreased.

An another investigation on frequency is carried out with triangular crack at same location with different crack length such as 0.6, 0.65, 0.7, 0.73 m and constant depth of crack 1.8 mm. The results show that first natural frequency is a function of crack length. First natural frequency is decreasing with increasing crack length (Table 4).

Thereafter, the effect of the crack length on the natural frequency of cracked aircraft wing structure is investigated with triangular crack incorporated numerically at different locations (i.e. 492.15, 3457.89, 214.44) having different crack depths of 1.8, 1.5, 1.0, 0.5 and 0.2 mm with constant crack length of 0.507 m. The width of the crack is assumed as 0.078 m. The numerical simulations shown in Table 5 indicate the natural frequencies of the cracked structure are function of crack location also. First three natural frequencies are decreasing with increasing crack depth at that location.

**Table 5** Effect of depth of crack on natural frequency of cracked aircraft wing structure

Depth of crack (mm)	Crack length (mm)	Frequency, $f_n$ (Hz)		
		First	Second	Third
0	0	4.2814	21.632	26.083
0.2	507	4.2550	20.984	25.959
0.5	507	4.2541	20.973	25.953
1.0	507	4.2522	20.954	25.949
1.5	507	4.2494	20.938	25.943
1.8	507	4.2332	20.875	25.933

## 4 Conclusion

In the present study, a numerical modal analysis is carried out to investigate the effect of crack length, depth and crack location on the aircraft wing structure. Both uncracked and cracked aircraft wing structure are modelled and analysis is performed using finite element-based software platform. The natural frequency for the uncracked aircraft wing model is obtained from numerical analysis which are validated with the results reported in literature. The comparative result shows that the numerical modal analysis procedure for the aircraft wing is correct. Following the same procedure and investigate the numerical model analysis of aircraft wing at different crack length and different depth of crack. It is concluded that the frequency is a function of crack length and depth of crack. An investigation on frequency is carried out with triangular crack at different location with same crack geometry. The results show that frequency is changing when the crack location is changed. The natural frequencies of the cracked wing are decreasing with increase in the crack length and crack depth.

## References

1. Carrera E, Pagani A, Petrolo M (2013) Component-wise method applied to vibration of wing structures. *J Appl Mech* 80:041012
2. Ostachowicz WM, Krawczuk M (1991) Analysis of the effect of cracks on the natural frequencies of a cantilever beam. *J Sound Vib* 150:191–201
3. Khalkar V, Ramachandran S (2018) Analysis of the effect of V-shape and rectangular shape cracks on the natural frequencies of a spring steel cantilever beam. *Mater Today- Proc* 5:855–862
4. Wang D, Friswell MI, Lei Y (2016) Maximizing the natural frequency of a beam with an intermediate elastic support. *J Sound Vib* 291:1229–1238
5. Sawant SU, Chauhan SJ, Deshmukh NN (2017) Effect of crack on natural frequency for beam type of structures. In: AIP conference proceedings. AIP Publishing, pp 020056
6. Satpute D, Baviskar P, Gandhi P, Chavanke M, Aher T (2017) Crack detection in cantilever shaft beam using natural frequency. *Mater Today- Proc* 4:1366–1374
7. Das MT, Yilmaz A (2018) Experimental modal analysis of curved composite beam with transverse open crack. *J Sound Vib* 436:155–164
8. Jha A, Kukshal V, Sharma A, Sharma K (2018) Numerical prediction of plastic zone length in straight edge cracked plate using XFEM. In: AIP conference proceedings. AIP Publishing, pp 030003

# Synthesis and Characterization of Nano-grease for Automotive Wheel Bearing Application



Pankaj S. Ghatage, Abhijeet P. Shah and Dhananjay Kumbhar

**Abstract** The maintenance of various automotive systems has been increased due to improper road conditions in developing countries which results in shorter lifespan of the automotive components like wheel bearing and also discomfort ride of a vehicle which further increases the maintenance and running cost. The problem with friction and wear of various automotive systems like bearing with their noisy operation is becoming more prominent. Therefore, there is need of lubricating greases which decreases friction, wear and noisy operation while maintaining the vehicle. Grease is an important element in the automotive wheel bearing lubrication. Considering emerging need for high load-carrying capacity and viscosity, a new kind of bearing lubricants is required. Nano-grease has the potential to fulfil the emerging needs of lubrication. Now days, there is scope and also challenge to develop new grease for specific application. In this paper, samples of nano-grease are synthesized and characterized for thermal, tribological and rheological properties. The characterization results of nano-grease are compared with conventional greases and suitable nano-grease has been suggested for automotive wheel bearing application.

**Keywords** Nano-grease ·  $\text{CaCO}_3$  nanoparticles ·  $\text{Fe}_2\text{O}_3$  nanoparticles · Nano-tribology

## 1 Introduction

Lubrication is one of the oldest and most useful technologies. A solid or semisolid lubricant consisting of a thickening agent (soap or other additives) in a fluid lubricant is called grease. Grease is a semi-fluid to a solid mixture of a fluid lubricant,

---

P. S. Ghatage (✉) · D. Kumbhar  
Automobile Engineering Department, Rajarambapu Institute of Technology, Islampur, India  
e-mail: [pankaj.ghatage@ritindia.edu](mailto:pankaj.ghatage@ritindia.edu)

P. S. Ghatage · A. P. Shah · D. Kumbhar  
Affiliated to Shivaji University, Kolhapur, Maharashtra, India

A. P. Shah  
Mechanical Engineering Department, Rajarambapu Institute of Technology, Islampur, India

© Springer Nature Singapore Pte Ltd. 2020  
H. K. Voruganti et al. (eds.), *Advances in Applied Mechanical Engineering*,  
Lecture Notes in Mechanical Engineering,  
[https://doi.org/10.1007/978-981-15-1201-8\\_47](https://doi.org/10.1007/978-981-15-1201-8_47)



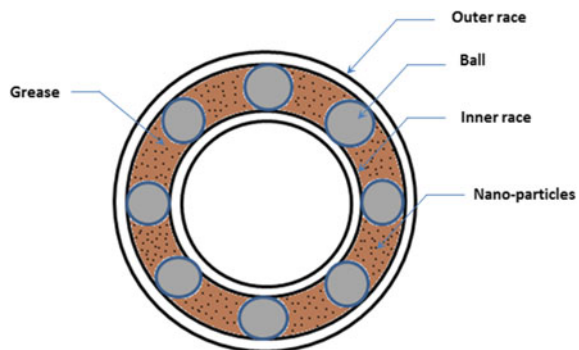
a thickener and an additive. In general, greases contain 70–95% base oil, 5–20% thickening agent and 0–10% additives [1]. Greases are most often used instead of fluids, where a lubricant is required to maintain its original position in a mechanism, especially where opportunities for frequent re-lubrication may be limited or economically unjustifiable. The first modern grease was calcium soaps which are not much used anymore. Later, aluminium and sodium soaps were developed that could cope with higher temperature. Today, the widest greases are based on lithium which was developed in 1940. The 2012 National Lubricating Grease Institute (NLGI) survey shows that today about 70% of the total grease volume consists of lithium thickened soap grease [2]. This illustrates that there is no great development in lubricating grease.

Due to improper road conditions in developing countries, the problem with friction and wear of various automotive systems like bearing with their noisy operation are becoming more prominent. Consequently, improved understanding and optimization of grease frictional performance can offer an important way of reducing power losses in wheel bearings. At present, the literature is missing a comprehensive investigation on the influence of grease composition on friction under condition pertinent to the wheel bearing. It results in a short life of a system and discomfort ride of a vehicle which further makes more maintenance and running cost. So, there is a need to focus on it and improve the lubrication properties of grease.

Today, the trend is to develop grease for the specific application [1], Pena-Paras et al. developed nano-grease for metal mechanics application [3]. The vast majority of automobiles are equipped with disc brakes. Although disc brakes provide better braking performance, their use puts tremendous stress on the wheel bearing grease. Higher temperatures are generated with disc brakes than those with conventional drum brakes. So, it creates a wheel bearing leakage problem. This application is most demanding for a new type of grease. Nano-grease is a new type of grease which is nothing but the addition of nanoparticles in conventional grease. Nano-grease has been rise in the recent years as a way to solve thermal rheological and tribological issues and needs. Figure 1 illustrates the concept of nano-grease.

Many researchers have contributed for the development of general nano-grease, Pena-Paras et al. investigated that the effect of incorporating nanoparticles ( $\text{TiO}_2$ ,

**Fig. 1** Concept of Nano-grease



$\text{Al}_2\text{O}_3$ ,  $\text{CuO}$ ) and multi-walled carbon nanotubes (MWNTs) within base greases like Mobilgrease 28 and Uniflor 8623B on their thermal transport as well as tribological properties and tribological performance [3]. Kamel et al. investigated microstructure of calcium grease, which prepared using multi-walled carbon nanotubes also they presented rheological behaviour nano-grease [4]. Xiangyu et al. synthesized nano-greases using titanium oxide ( $\text{TiO}_2$ ) and silicon oxide ( $\text{SiO}_2$ ) nanoparticles and examined tribological properties and claimed that grease with  $\text{TiO}_2$  particles exhibits good tribological characteristics and the greases prepared using  $\text{SiO}_2$  nanoparticles show good friction-reducing characteristic [5]. Chang et al. improved the lubricating performance of grease by letting tin (Sn) nanoparticles dispersed in lithium grease [6]. Authors have concluded that then 'Sn' nanoparticles can enhance the tribological properties of lithium grease, and iron (Fe) nanoparticles can more effectively enhance wear resistance. Zhao et al. evaluated the friction and wear behaviour of the nano calcium borate (NCB) an additive in lithium grease [7]. Authors have found that the addition of NCB additives in lithium grease results decrease in friction coefficient and significantly improved the anti-wear properties and load-carrying capacities of the lithium grease. Xianbing et al. have found that grease with calcium carbonate ( $\text{CaCO}_3$ ) nanoparticles exhibits properties like anti-wear, friction-reduction, load-carrying capacity and extreme pressure. Also, they have suggested an optimum concentration of nanoparticles in grease is 5% wt. [8]. Shen et al. developed effective nano-grease specifically for extreme operational applications [9]. Lee et al. developed nano-grease using graphite nanoparticles and evaluated tribological characteristics [10]. Authors concluded that the addition of nanoparticles decreases wear and resulted in a relatively smooth surface with fewer scars and significantly reduced metal contact.

The available literature clears that the use of nano-grease is having more advantages over conventional greases. Today's trend is to develop nano-grease for a specific application; however, the nano-grease is developed only for metal mechanics application. So in this research work, the different samples of nano-grease with varying concentrations of calcium carbonate ( $\text{CaCO}_3$ ) and iron oxide ( $\text{Fe}_2\text{O}_3$ ) nanoparticles have been synthesized by keeping a view on the requirement of grease for automotive wheel bearing application and characterized for thermal, tribological and rheological properties. The results of characterization have been compared with conventional greases, and best suitable nano-grease has been suggested for automotive wheel bearing application.

## 2 Materials Selection

In general, greases contain 70–95% of base oils, 5–20% of thickening agent and 0–10% of additives or nanoparticles [1]. Desirable properties of grease improve the not only performance of bearing but also increase the life of bearing. Stability at high temperature, anti-wear performance, resists wheel bearing leakage at high temperature, high dropping point, high water resistance and excellent cold temperature flow

properties are desirable properties of grease for wheel bearing applications. Table 1 shows the desirable properties of grease for automotive wheel bearing application. By keeping a view on desirable properties of grease, the material is selected for the synthesis of nano-grease. While manufacturing the automotive application greases, the major materials need to be considered are base oil, type of nanoparticles, and type of thickener.

The grease contains 70–95% base oil so that base oil plays an important role for making nano-grease for a particular application. In this work, paraffin mineral oil is selected due to its good dynamic viscosity, maximum limits of impurities and having good boiling point also this oil tend to chemically mix better with soaps as well as additives and form stronger structures than naphthenic oils. Paraffinic oil has good thermal and oxidative stability also has good high-temperature viscosity characteristics as compared to naphthenic oil. Table 2 shows the specifications of the selected oil.

Nanoparticles play several roles in lubricating grease. These primarily include enhancing the existing desirable properties, suppressing the existing undesirable properties and imparting new properties. So far, TiO<sub>2</sub>, SiO<sub>2</sub>, CuO, CNT (carbon nanotube) nanoparticles have been used in the different base greases by researchers but in this work calcium carbonate and iron oxide nanoparticles have been used due to its excellent thermophysical properties like, they can greatly improve anti-wear capability, reduce friction coefficient and increases load-carrying capacity. Also, these nanoparticles are chemically stable, safe for human handling and low cost compare to other nanoparticles. Table 3 shows the specifications of the selected nanoparticles.

**Table 1** Desirable properties with their required values of wheel bearing grease [11]

Properties	Required values
Temperature range	–10 to +170 °C
Drop point	180–220 °C
Base oil viscosity	150 CSt
Load-carrying capacity	250–340 kg
Penetration no.	265–295

**Table 2** Specifications of paraffin oil

Parameters	Value
Boiling point	300 °C at 1000 hPa
Dynamic viscosity (20 °C)	>150 MPa.s
Kinematic viscosity (40 °C)	>34.5 CSt

**Table 3** Specifications of nanoparticles

Parameter	Specifications of nanoparticles	
Name of manufacturer	Iron oxide nanoparticles	Calcium carbonate nanoparticles
	Sigma Aldrich Research Laboratories Pvt. Ltd., India	Sisco Research Laboratories Pvt. Ltd., India
Molecular formula	Fe <sub>2</sub> O <sub>3</sub>	CaCO <sub>3</sub>
Molecular Wt.	159.69	100.9
Assay (purity)	Min. 98%	Min. 98%
Nanoparticles size	50 nm	80 nm
Morphology	Cubic	Cubic
pH	8.5–9.5	8.5–9.5

### 3 Synthesis and Characterization of Nano-grease

The manufacturing procedure for lithium soap-based nano-grease can be split into five stages. In the first stage, the soap was formed by adding mineral oil stearic acid into lithium hydroxide solution; hence, this stage is referred to as saponification. After that dehydration was carried out for removal of water. Then mineral oil was added to this mixture to a particular temperature. After completion of this stage, nanoparticles were added to this mixture with compensative mineral oil. Next, the grease was milled. This stage is very important because it will produce a uniform crystal and gel structure. The whole procedure is shown in Fig. 2.

The different samples of nano-grease with different weight percentage have been prepared using this procedure, and some pilot characterization tests have been taken, with the help of these results and requirements of wheel bearing grease the weight percentage of nanoparticles have been decided. The nano-grease samples with 3, 4, 5, 6 and 7% weight of nanoparticles have been selected for further study.

The synthesized samples of nano-grease were characterized for thermal, tribological and rheological properties. Viscosity plays an important role while estimating performance of nanofluids [12]. So that the dynamic viscosity of nano-grease was measured with the help of rotational viscometer. The drop point test measures the dropping point of the lubricating greases, the dropping point is the temperature at which the greases pass from semisolid to the liquid state under the test conditions, so it provides a practical limit of temperature above which grease cannot be used as a lubricant in the semisolid state. So that in order to ensure the temperature limit the drop point test was conducted for the prepared grease samples. As per National Lubricating Grease Institute (NLGI) standards, penetration number gives an appearance of grease through which it is clear that whether grease is soft or hard. Hence, penetration test was conducted. In order to ensure load-carrying capacity of grease, load-carrying capacity test was carried out using four-ball EP tester machine at Central Institute of Road Transport (CIRT), Pune.

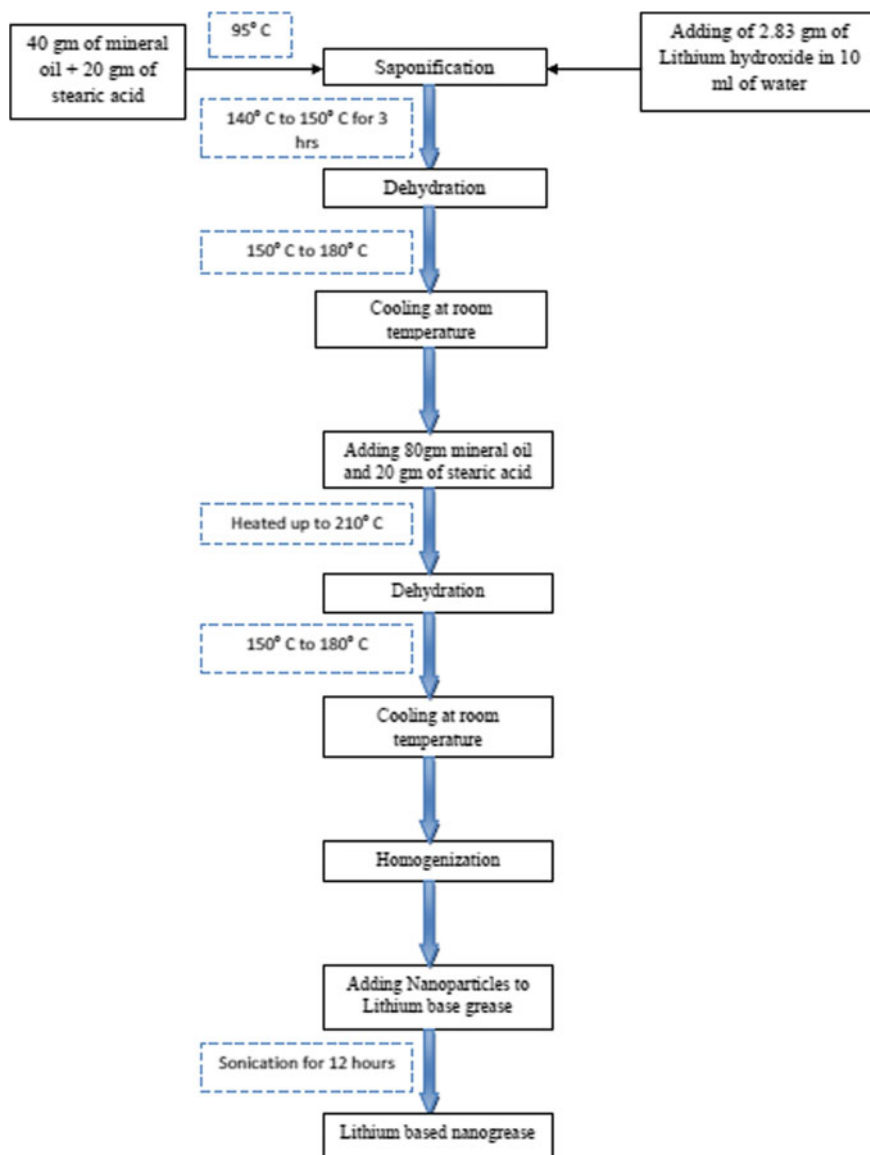


Fig. 2 Procedure for the synthesis of Nano-grease [7]

## 4 Results and Discussions

The results carried out through different tests are analysed and plotted in order to suggest suitable grease for the automotive wheel bearing application. Figure 3 shows the drop points of nano-grease samples with 3–7 weight percent of nanoparticles ( $\text{CaCO}_3$  and  $\text{Fe}_2\text{O}_3$ ).

For wheel bearing application, the drop point temperature limit is required from 180 to 280 °C. The drop point value of lithium base grease is 170 °C. From Fig. 3 it is clear that, as % weight of  $\text{CaCO}_3$  and  $\text{Fe}_2\text{O}_3$  nanoparticles increases in grease, the dropping point also increases exponentially and can be achieved up to the required range. The grease with a  $\text{Fe}_2\text{O}_3$  nanoparticles additive shows better drop point performance than the  $\text{CaCO}_3$  nanoparticles.

Figure 4 shows the penetration number of nano-grease samples with 3–7% weight of nanoparticles ( $\text{CaCO}_3$  and  $\text{Fe}_2\text{O}_3$ ). As lower the penetration number, the grease is harder. This means that the pumping of grease is difficult and the coefficient of friction is more. However, the grease can better withstand higher loads at lower speeds. A higher penetration number means softer grease which is having lower resistance to flow, increased pump ability but unable to withstand higher loads and more attention will have to be paid to prevent leakage. From Fig. 4 the penetration number of  $\text{Fe}_2\text{O}_3$  lithium grease with 7% weight and  $\text{CaCO}_3$  lithium grease with 7% weight is 255 and 265, respectively. The penetration number or the depth of penetration was reduced to 15 and 11% for  $\text{Fe}_2\text{O}_3$  nanoparticles and  $\text{CaCO}_3$  nanoparticles, respectively, if it is compared with lithium base grease which is having penetration number 350.

The load-carrying capacity of lithium based grease in 170 kg. which will be failed for wheel bearing application as it is required 250–340 kg. Figure 5 shows the

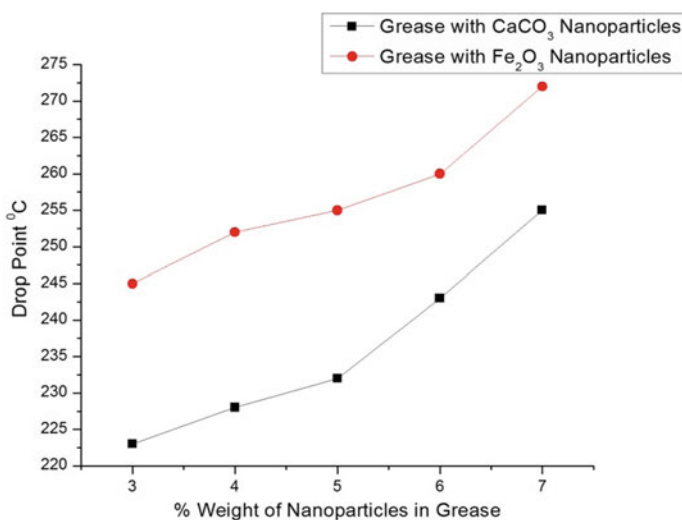
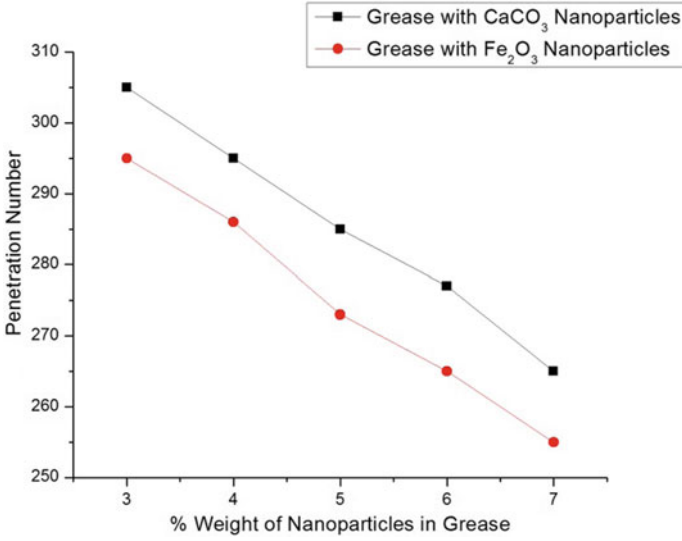
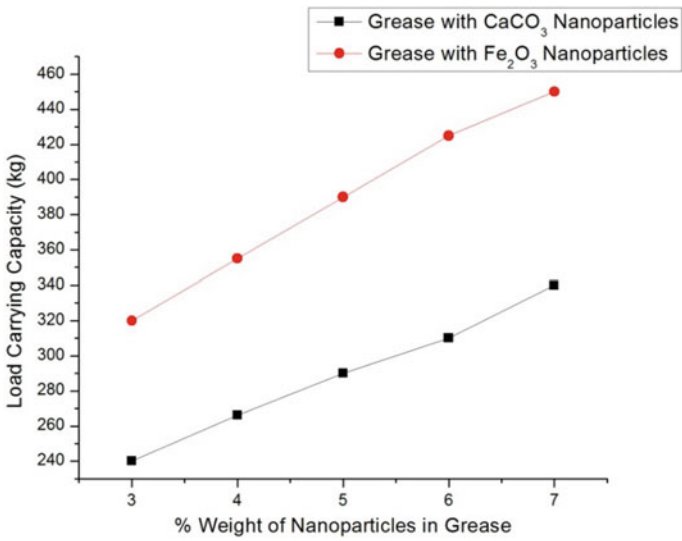


Fig. 3 Drop point of nano-grease with different percentage of nanoparticles ( $\text{CaCO}_3$  and  $\text{Fe}_2\text{O}_3$ )



**Fig. 4** Penetration number of nano-grease with different percentage of nanoparticles (CaCO<sub>3</sub> and Fe<sub>2</sub>O<sub>3</sub>)



**Fig. 5** Load-carrying capacity of nano-grease with different percentage of nanoparticles (CaCO<sub>3</sub> and Fe<sub>2</sub>O<sub>3</sub>)

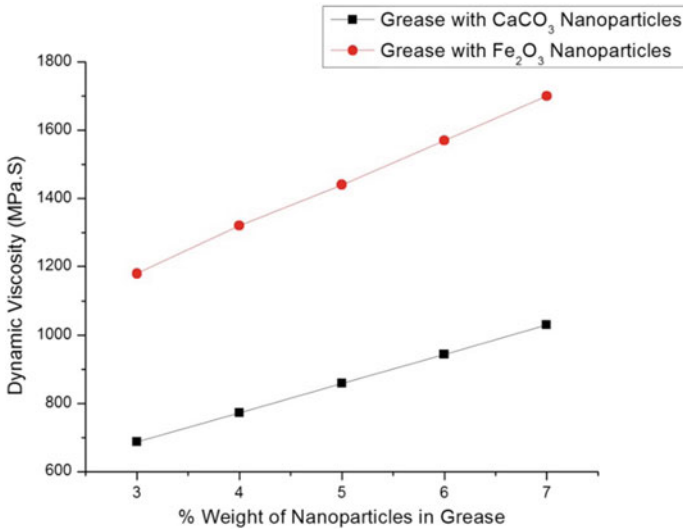


**Fig. 6** Dynamic viscosity of nano-grease with different percentage of nanoparticles (CaCO<sub>3</sub> and Fe<sub>2</sub>O<sub>3</sub>)

grease samples with 7% weight of CaCO<sub>3</sub> and Fe<sub>2</sub>O<sub>3</sub> exhibited better load-carrying performance and could work smoothly to 340 kg and 450 kg, respectively.

Figure 6 shows that the dynamic viscosity increases with an increase in nanoparticle percentage into base grease. The grease with iron oxide particles has higher dynamic viscosity than grease with calcium carbonate nanoparticles.

## 5 Conclusions

In this research work, the different samples of nano-grease with varying concentrations of CaCO<sub>3</sub> and Fe<sub>2</sub>O<sub>3</sub> (with 3, 4, 5, 6 and 7% of weight) nanoparticles have been synthesized by keeping view on requirement of grease for automotive wheel bearing application and characterized for thermal, tribological and rheological properties like drop point, viscosity, load-carrying capacity and penetration number. Experimental results showed that Fe<sub>2</sub>O<sub>3</sub> and CaCO<sub>3</sub> nanoparticles can enhance the tribological and rheological properties of grease compare to base grease. Amongst these Fe<sub>2</sub>O<sub>3</sub> nanoparticles can exert more excellent tribological properties as compared to CaCO<sub>3</sub> nanoparticles. Nano-grease with 7% weight concentration can significantly increase the drop point, load-carrying capacity and reduce the penetration number. The sample of Fe<sub>2</sub>O<sub>3</sub> nanoparticles with 7% weight increase the dropping point in drop point test by approximately 39% than the expected value. So, it is seen that in drop point test Fe<sub>2</sub>O<sub>3</sub> nanoparticles shows a better result than CaCO<sub>3</sub> nanoparticles. In load-carrying capacity test, Fe<sub>2</sub>O<sub>3</sub> nanoparticles grease sample shows 80% increment and



36% increment for grease sample with  $\text{CaCO}_3$  nanoparticles. In a penetration test, the penetration number or the depth of penetration was reduced to 15% and 11% for  $\text{Fe}_2\text{O}_3$  nanoparticles and  $\text{CaCO}_3$  nanoparticles, respectively.

Grease with  $\text{Fe}_2\text{O}_3$  nanoparticles has given better results than  $\text{CaCO}_3$  nanoparticles, but the grease samples of 7% weight with  $\text{Fe}_2\text{O}_3$  and  $\text{CaCO}_3$  nanoparticles exhibit desired properties for automotive wheel bearing application. So both the samples are suitable for this application; however, the cost of  $\text{CaCO}_3$  nanoparticles are less compared to  $\text{Fe}_2\text{O}_3$ , hence grease sample with  $\text{CaCO}_3$  7% weight can more suitable than grease sample with  $\text{Fe}_2\text{O}_3$  nanoparticles. After using these samples to actual wheel bearing one can predict more insights about the performance of grease.

**Acknowledgements** The author would like to acknowledge efforts and support provided from Rajarambapu Institute of Technology, Islampur, Sangli, Maharashtra. Also, we would like to thank Mr. V. D. Chavan, CIRT, Pune (India) and Dr. Kapil Joshi, Anton-Paar Pvt. Ltd., Thane (India) for their valuable support.

## References

1. Lugt PM (2016) Modern advancements in lubricating grease technology. *Tribol Int* 97:467–477
2. Akhtar K, Khalid H, UI Haq I, Malik A (2016) Improvement in tribological properties of lubricating grease with quartz-enriched rice husk ash. *Tribol Int* 93:58–62
3. Peña-Parásn L, Taha-Tijerina J, García A, Maldonado D, ájera A, Cantú P, Ortiz D (2015) Thermal transport and tribological properties of nano-greases for metal-mechanic applications. *Wear*, 1322–1326
4. Kamel BM, Mohamed A, EI Sherbiny M, Abed KA (2016) Rheology and thermal conductivity of calcium grease containing multi-walled carbon nanotubes. *Fuller, Nanotub, Carbon Nanostruct* 24:260–265
5. Ge X, Xia Y, Cao Z (2015) Tribological properties and insulation effect of nano meter  $\text{TiO}_2$  and nanometer  $\text{SiO}_2$  as Tribology. *Tribol Int* 92:454–461
6. Chang H, Kao M, Luo J-D, Lan C-W (2015) Synthesis and effect of nano-grease on tribological properties 1311
7. Zhao G, Zhao Q, Li W (2013) Tribological properties of nano-calcium borate as lithium grease additives. *Lubr Sci*
8. Ji X, Chen Y, Zhao G (2011) Tribological properties of  $\text{CaCO}_3$  nanoparticles as an additive in lithium grease. *Tribol J Impact Factor* 41:113–119
9. Shen T, Wang D, Yun J, Liu Q, Liu X, Peng Z (2016) Tribological properties and tribochemical analysis of nano-cerium oxide and sulfurized isobutene in titanium complex grease. *Tribol Int* 93:332–346
10. Lee C-G, Hwang Y-J, Choi Y-M, Lee J-K, Cheol C, Oh J-M (2009) A study on the tribological characteristics of graphite nano lubricants. *Int J Precis Eng Manuf* 10(1)
11. <https://www.penriteoil.com.au/grease-guide>. Last accessed on 1st Jan 2018
12. Nield DA, Kuznetsov AV (2013) A note on the variation of nano fluid viscosity with temperature. *Int Commun Heat Mass Transf* 41:17–18

# Hamiltonian-Based Solutions of Certain PDE in Plasma Flows



Vivek S. Sharma, Parag V. Patil and Milan A. Joshi

**Abstract** The evolution nonlinear partial differential equations give an insight into the physical, mechanical, thermal, electrical and electro-mechanical behaviour of a nonlinear system. The study of these evolution equations and their solutions, especially in plasma transport through magnetic field lines, is essential to understand important principles applicable for transportation of plasma, such as magnetized plasma diffusion. It also has application to the sources of plasma which work at low temperature and pressure. One such PDE is the modified Kdv–Zakharov–Kuznetsov equation. These equations have solutions that are best described by solitons, kinks and periodic wave-type travelling wave solutions. The Hamiltonian- and the rational trigonometric method-based travelling wave solutions of these evolution equations are obtained. These solutions are also comparable with semi-analytical approaches such as tanh method, exp-function method, Jacobi elliptic function method, Jacobi theta function method, and numerical approaches such as Petrov–Galerkien method and radial basis function method. The solutions obtained here are compared with the recent work by extended mapping method and Jacobi elliptic method and  $\frac{G'}{G}$  method.

**Keywords** Solitons · Hamiltonians · mKdv–Zakharov–Kuznetsov equations · Petrov–Galerkien method

## 1 Introduction

The solitons are one of the most useful structures that widely occur in nature. They have a very unique characteristic of shape preserving. Due to this characteristic, they have potentially useful applications in different domains such as nonlinear optics, plasmas, fluid mechanics, condensed matter, electro-magnetics and many more. Recently, a rich pool of exact and numerical methods has been developed to

---

V. S. Sharma (✉) · M. A. Joshi  
MPSTME, NMIMS, Shirpur, Maharashtra 425405, India  
e-mail: [vivek.sharma@nmims.edu](mailto:vivek.sharma@nmims.edu)

P. V. Patil  
Independent Mathematician, Jalgaon, Maharashtra 425001, India

© Springer Nature Singapore Pte Ltd. 2020  
H. K. Voruganti et al. (eds.), *Advances in Applied Mechanical Engineering*,  
Lecture Notes in Mechanical Engineering,  
[https://doi.org/10.1007/978-981-15-1201-8\\_48](https://doi.org/10.1007/978-981-15-1201-8_48)

study PDEs, with the methods discussed in [1–5] being some of them. Two such methods are the Hamiltonian-based method to find soliton solutions suggested by Zhang et al. [1] and the rational trigonometric expansion method given by Darvishi et al., [2], where, he used it to find exact solutions to some variants of Boussinesq equations. These two methods are used here to find travelling wave solutions to  $(3 + 1)$ -dimensionally modified Kdv–Zakharov–Kuznetsov equations. The solutions obtained are compared with the solutions obtained by Zia-Yun Zhang [3] and Seadawy et al. [6] recent work using extended mapping method.

They are also graphically compared with Islam et al. [7] and Baleanu et al. [8].

## 2 The Hamiltonian-Based Solutions to mKdv–ZK Equations

The preserving of Hamiltonian indicates that given any truncated fluid flow, whether it can be modelled effectively using numerical methods or not. Hence, Hamiltonian in itself, becomes an essential tool for studying fluid flows.

Let us consider a generalized nonlinear partial differential equation given by

$$U(u, u_t, u_x, u_{tt}, u_{xx}, u_{tx}, \dots) = 0 \quad (1)$$

Let the flow of three-dimensional ion-acoustic solitary waves and shocks in homogenous magnetized electron–positron plasma be modelled by a nonlinear partial differential equation of type (1). Assume the flow to contain equal amount of cool and hot species. The governing equations for the fluid flows that describes the dynamics of the species are the Navier–Stokes equations as discussed by Seadawy [5]. If  $u$  is the electrostatic potential, then Seadawy [5] derived the modified Kdv–Zakharov–Kuznetsov equations describing these plasma flows using singular perturbation method as

$$u_t + \beta u^2 u_x + u_{xxx} + u_{xyy} + u_{xzz} = 0 \quad (2)$$

The perturbation methods in themselves are only applicable to nonlinear evolution equations having small parameters. These small parameters are wave variables for nonlinear solitary waves which can give approximate solutions to any nonlinear differential equations of the form (1), if chosen properly.

Considering  $u(-ct + kz + x + y) = U(\vartheta)$  with  $x, y, z$  and  $c$  being constants and  $\vartheta$  as wave variable, the above Eq. (2) can be re-written as

$$(2 + k)U''' + \beta U^2 U' - CU' = 0 \quad (3)$$

Integrating the above Eq. (3) with respect to  $\vartheta$  gives

$$(2 + k)U'' + \beta \frac{U^3}{3} - CU' = \text{Constant} = \vartheta_0 \tag{4}$$

This Eq. (4) is a nonlinear differential equation reduction of the mKdv-ZK Eq. (2). Equation (4) is now solved using Hamiltonian method suggested by Zhang et al. [1], where they studied the Hamiltonian and the bifurcations induced by a generalized nonlinear evolution equations of the form (5), whereas we study the particular reduction (4) (Fig. 1).

$$Q'' = a_3Q^3 + a_2Q^2 + a_1Q + a_0 \tag{5}$$

Equation (4) can be thought of in terms of the generalized system (5) with  $a_3 = \frac{-\beta}{3(2+k)}$ ,  $a_2 = 0$ ,  $a_1 = \frac{C}{(2+k)}$  and  $a_0 = \frac{\vartheta_0}{(2+k)}$ .

If we change the parameters groups of  $P, R$  and  $S$ , we can derive different phase portraits for Eq. (6) below, along with the condition  $S \neq 0$ . Some phase diagrams for two special conditions, namely Fig. 2a and b with  $P = R = S = -1$  and Fig. 3a and b with  $P = R = S = 1$  are plotted to show that the first condition gives periodic solutions and the second condition gives unbounded solutions, respectively. In this context, a recent work of Wang et al. [7] show that bifurcation and phase portrait

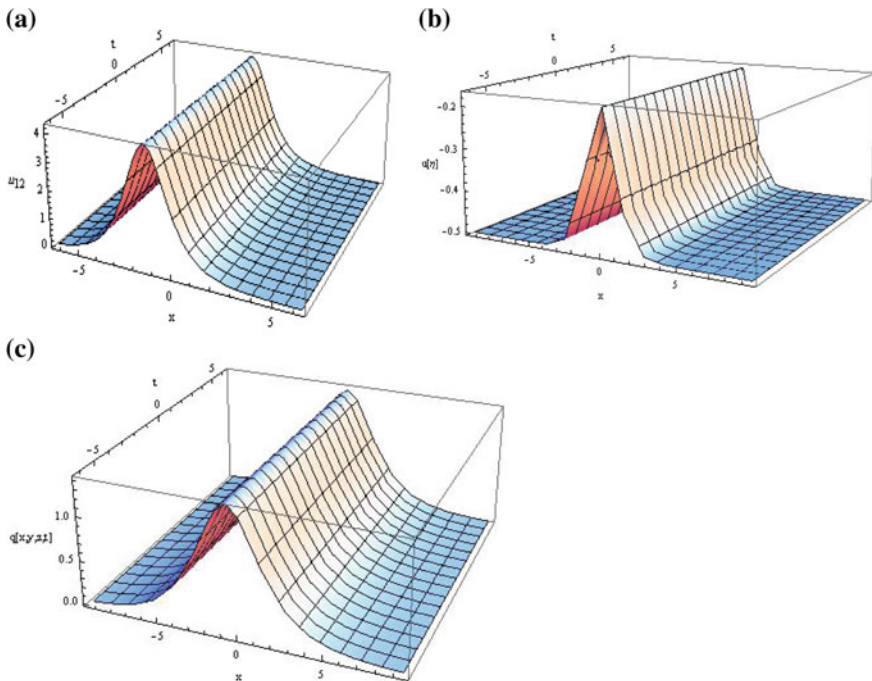


**Fig. 1** a Soliton solution by Islam et al. b Soliton solution from Eq. (17). c Bell soliton solution by Baleanu et al.

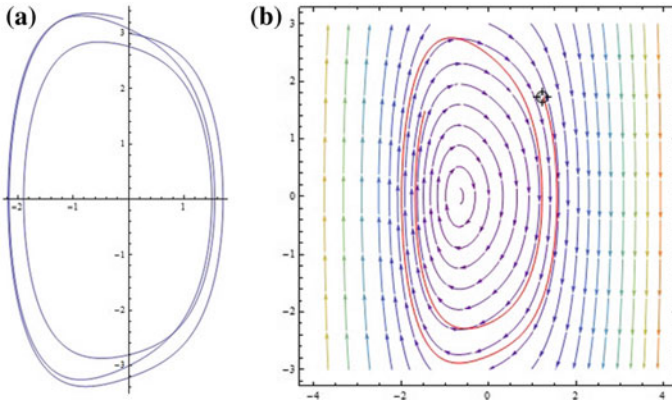


Fig. 2 a and b depict periodic orbits for  $P = R = S = -1$

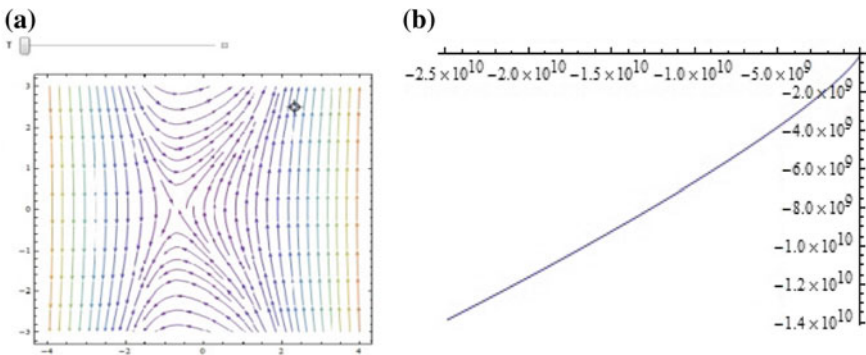


Fig. 3 a and b depict unbounded solutions for  $P = R = S = 1$

study give a whole lot of solutions, whereas Zhang et al. [1], have provided with detailed exposition on the conditions of classification and bifurcation of some class of ODEs of the form given in (6). If  $(2 + k) \neq 0$ , the system (4) can be re-written in a modified form as

$$U'' - (P U^3 + R U + S) = 0 \tag{6}$$

with  $P = \frac{-\beta}{3(2+k)}$ ,  $R = \frac{C}{(2+k)}$  and  $S = \frac{\vartheta_0}{(2+k)}$ .

The Hamiltonian for following two-dimensional system of differential equations obtained from (6) is given by (7) and (8) as

$$\frac{dU}{d\vartheta} = V, \quad \frac{dV}{d\vartheta} = (P U^3 + R U + S) \tag{7}$$

$$H(U, V) = \frac{V^2}{2} - \frac{P U^4}{4} - \frac{R U^2}{2} \tag{8}$$

We, thus, obtain two cases for which phase portraits can be plotted and studied

Case i. When  $S \neq 0$  Case ii. When  $S = 0$ .

### 2.1 Case I. When $S \neq 0$

We take the right-hand side of second equation in the system (7) as zero and obtain

$$U = \frac{\frac{2}{3}R}{G} + \frac{G}{2^{\frac{1}{3}}3^{\frac{2}{3}}}, \quad U = \frac{(1+i\sqrt{3})R}{G2^{\frac{1}{3}}3^{\frac{2}{3}}} - \frac{(1-i\sqrt{3})G}{2^{\frac{1}{3}}3^{\frac{2}{3}}2P}, \quad U = \frac{(1-i\sqrt{3})R}{G2^{\frac{1}{3}}3^{\frac{2}{3}}} - \frac{(1+i\sqrt{3})G}{2^{\frac{1}{3}}3^{\frac{2}{3}}2P} \tag{9}$$

Where,  $G^3 = -9RP^2 + \sqrt{3}\sqrt{4R^3P^3 + 27S^2R^4}$ . If  $R = 0$ . The system (9) reduces to

$$U = \frac{G}{2^{\frac{1}{3}}3^{\frac{2}{3}}}, \quad U = \frac{(-1+i\sqrt{3})G}{2^{\frac{1}{3}}3^{\frac{2}{3}}2P}, \quad U = -\frac{(1+i\sqrt{3})G}{2^{\frac{1}{3}}3^{\frac{2}{3}}2P} \tag{10}$$

Equations (9) and (10) indicate that the system (7) does not have unique equilibrium point; hence, the real roots of the equation  $f(U) = PU^3 + RU + S = 0$  is the abscissa of the equilibrium points. The only equilibrium point of (7) is  $S_1 = \left[ \frac{\frac{2}{3}R}{G} + \frac{G}{2^{\frac{1}{3}}3^{\frac{2}{3}}}, 0 \right]$ , which is a saddle, indicating unbounded solution.

If we change the parameters groups of  $P, R$  and  $S$ , we can derive different phase portraits for (7) along with the condition  $S \neq 0$ .

Some phase diagrams for  $P = R = S = -1$  and  $P = R = S = 1$  are plotted to show that the first condition gives periodic solutions and the second condition gives unbounded solutions, respectively.

In this context, a recent work of Wang et al. [7] have shown that bifurcation and phase portrait study give a whole lot of solutions, where as Zhang et al. [1] have provided with detailed exposition on the conditions of classification and bifurcation of some class of ODEs of the form

$$U'' - (P U^3 + Q U^2 + R U + S) = 0 \tag{11}$$

It is also clear from Zhang et al. [1] work that, the subclasses of solutions applicable for (7) are the following: (Table 1)

The condition 2, for bounded solutions can have following subcategories of solutions. i.  $R < 0$ , ii.  $0 < R < \frac{2}{9}$ , iii.  $R = \frac{2}{9}$  and iv.  $\frac{2}{9} < R < \frac{1}{4}$ .

The details of the solutions for each condition can be obtained if we put  $S = 0$  in (11). In the next section, we study the case of  $S = 0$ .

**Table 1** Subclasses of solutions

S. No.	Conditions satisfied	Type of solutions
1	$P = 1$ and $R = 1$	Unbounded solutions
2	$P = 1, R = \text{any value}$	Bounded solutions
3	$P = 1$ and $R = -1$	Heteroclinic and periodic orbits
4	$P = -1$ and $R = -1$	Periodic orbits
5	$P = -1$ and $R = 1$	Homoclinic orbits and bounded periodic solutions
6	$P = 1$ and $R = 0$	No bounded solutions, one equilibrium point (Saddle)
7	$P = -1$ and $R = 0$	Bounded periodic solutions corresponding to periodic orbits

### 2.2 When $S = 0$

The solutions for the system (6) and hence (3) when  $S = 0$  in (11) are

1. When  $P = 1$  and  $R = \text{any arbitrary value}$ , gives bounded solutions with four subcategories:

- i. When  $R < 0$  gives following bounded solutions:

$$U(\vartheta) = L - \frac{6L(2L + 1)}{2 + 6L + \sqrt{4 + 6L} \cosh[L(2L + 1)](\vartheta - \vartheta_0)} \tag{12}$$

with  $L = \frac{\sqrt{-1+4R}}{2}$  corresponding to homoclinic orbit.

- ii. When  $0 < R < 2/9$ , the bounded solution for homoclinic orbit is

$$U(\vartheta) = \frac{-6R}{2 + \sqrt{4 - 18R} \cosh[\sqrt{R}](\vartheta - \vartheta_0)} \tag{13}$$

- iii. When  $R = 2/9$ ,

$$U(\vartheta) = \frac{1}{3} \tanh\left[\frac{\sqrt{2}}{6}(\vartheta - \vartheta_0)\right] - \frac{1}{3} \text{ and } P(\vartheta) = -\frac{1}{3} \tanh\left[\frac{\sqrt{2}}{6}(\vartheta - \vartheta_0)\right] - \frac{1}{3} \tag{14}$$

are the solutions.

- iv. When  $\frac{2}{9} < R < \frac{1}{4}$ , gives family of periodic solutions as discussed in [1].
2. When  $P = 1$  and  $R = -1$  gives heteroclinic and periodic orbits.

The bounded solutions of the two heteroclinic orbits are

$$U(\vartheta) = \tanh\left[\frac{\sqrt{2}}{2}(\vartheta - \vartheta_0)\right] \text{ and } P(\vartheta) = -\tanh\left[\frac{\sqrt{2}}{2}(\vartheta - \vartheta_0)\right] \tag{15}$$

and the bounded periodic solutions for the periodic orbits are

$$U(\vartheta) = -\sqrt{2 - P_0^2} + \frac{\sqrt{2 - 2P_0^2}}{P_0 + \sqrt{2 - P_0^2 - 2P_0sn^2[\tau(\vartheta - \vartheta_0), p]}} \tag{16}$$

where,  $\tau = \frac{\sqrt{2}}{4} \left[ P_0 + \sqrt{2 - P_0^2} \right]$  and  $p = \frac{2\sqrt{P_0\sqrt{2 - P_0^2}}}{P_0 + \sqrt{2 - P_0^2}}$  for any arbitrary  $0 < P_0 < 1$ .

- 3. When  $P = -1$  and  $R = -1$ , gives periodic orbits and the bounded solutions for these orbits are

$$U(\vartheta) = \frac{2P_0}{1 + [ns[\tau(\vartheta - \vartheta_0), l] + cs[\tau(\vartheta - \vartheta_0), l]]^2} - P_0 \tag{17}$$

Where  $\tau = \sqrt{1 + P_0^2}$ ,  $l = \frac{P_0}{\sqrt{1 + P_0^2}}$ , for arbitrary  $P_0$  with  $ns = \frac{1}{sn}$  and  $cs = \frac{sn}{cn}$  are usual Jacobi elliptic functions.

- 4. When  $P = -1$  and  $R = 1$ , this case may be referred to in [1].
- 5. When  $P = -1$  and  $R = 0$ , this case may also be referred to in [1].

The solutions obtained by us are improvement over those obtain by Zia-yun Zhang [3], where he has used Jacobi elliptic functions to find exact solutions to modified Kdv-ZK equation. The solutions obtained by him, form a particular case of those obtained by us when  $S = 0$ . Also, Islam et al. [7], Baleanu et al. [8] and recently Seadawy et al. [6] have also found solutions to mKdv-ZK equations. Our solution is comparable with all of them.

Figure 1a, b and c show comparison between soliton solution obtained by Islam et al. [7] using  $\frac{G'}{G}$  method, the Bell soliton solutions obtained by Baleanu et al. [8] by the first-integral method and by us, using Hamiltonian method from Eq. (17) with modulus  $\rightarrow 1$  and with  $P_0 = \frac{1}{2}$ . As can be seen, these solutions are comparable, differing by constants of integration, which are responsible for just shift in wave profiles.

In the next section, we explore another method recently introduced by Darvishi et al. [2] to find exact solutions to Boussinesq equations and their variants.

### 3 The Rational Trigonometric Expansion Method Solutions to mKdv-ZK Equations

Darvishi et al. [2] have suggested an extended rational trigonometric expansion method for obtaining travelling waves solutions for Boussinesq equations and its variants. Similarly, we obtain certain travelling wave solutions to the modified Kdv-ZK equations given by (2) and (4). We consider  $u(-ct + kz + x + y) = U(\vartheta)$  with  $x, y, z$  and  $c$  being constants and  $\vartheta$  as wave variable as the solution of (2). Following the work of Darvishi et al. [2], the general form of solutions of (2) as travelling waves



can be represented as following four extended rational trigonometric types

$$\begin{aligned}
 \text{i. } u(\vartheta) &= \frac{a_0 \sin[\mu \vartheta]}{[a_2 + a_1 \cos[\mu \vartheta]]}, \text{ ii. } u(\vartheta) = \frac{a_0 \cos[\mu \vartheta]}{[a_2 + a_1 \sin[\mu \vartheta]]}, \\
 &\text{with } \cos[\mu \vartheta] \neq -\frac{a_2}{a_1} \text{ with } \sin[\mu \vartheta] \neq -\frac{a_2}{a_1} \tag{18} \\
 \text{iii. } u(\vartheta) &= \frac{a_0 \sinh[\mu \vartheta]}{[a_2 + a_1 \cosh[\mu \vartheta]]} \text{ and iv. } u(\vartheta) = \frac{a_0 \cosh[\mu \vartheta]}{[a_2 + a_1 \sinh[\mu \vartheta]]} \\
 &\text{with } \cosh[\mu \vartheta] \neq -a_2/a_1 \text{ with } \sinh[\mu \vartheta] \neq -a_2/a_1
 \end{aligned}$$

Solving Eq. (4) using the rational sine–cosine form of Eq. (18) and proceeding in the similar way as Darvishi et al. [2] also using Mathematica-9 software, and writing  $\vartheta = -ct + kz + x + y$ ,  $\sqrt{6c + 3a_1c} = \sqrt{d}$  and  $\frac{\sqrt{2c}}{\sqrt{k}} = \sqrt{f}$  we obtain following 8 travelling wave solutions to (2).

$$u_{1j}(\vartheta) = \frac{\sin[\pm\sqrt{f}\vartheta]}{\sqrt{\beta}\left[\pm\frac{2}{\sqrt{d}} \pm \frac{1}{\sqrt{3c}}\text{Cos}[\pm\sqrt{f}\vartheta]\right]}, j = 1, 2, 3, \dots, 8 \tag{19}$$

Similarly, Eq. (4) can be solved by rational cosine–sine form of Eq. (18) we obtain following eight more travelling wave solutions to (2).

$$u_{2j}(\vartheta) = \frac{\text{Cos}[\pm\sqrt{f}\vartheta]}{\sqrt{\beta}\left[\pm\frac{2}{\sqrt{d}} \pm \frac{1}{\sqrt{3c}}[\sin \pm\sqrt{f}\vartheta]\right]}, j = 1, 2, 3, \dots, 8 \tag{20}$$

In terms of unknown parameters, we have obtained 16 solution profiles according to the positive and negative values of  $\mu$  in Eq. (18). Similarly, these calculations can also be extended to rational hyperbolic sine–cosine and cosine–sine approximations as discussed in (18). These solutions obtained by us are comparable to the solutions in terms of Tan and Cot functions to those obtained by Islam et al. [9], only differing by a constant multiple.

*Remark* The solutions obtained in Eqs. (19) and (20) are checked using Maple by back substitution and were found to be correct.

### 4 Conclusion

The Hamiltonian-based approach to solve nonlinear partial differential equations is based on understanding of their dynamical behaviour and is highly non trivial. Whereas, the extended rational trigonometric expansion method is a semi-analytical

method for the same. Both methods are applied to modified Kdv–Zakharov–Kuznetsov equations which model plasma flows at high and low pressure. The results obtained are compared to the already established analytical approaches such as first-integral method, Jacobi elliptic function method, the  $\frac{G'}{G}$  method and the extended mapping method. Some new elementary function solutions and new choices of parameters are proposed to obtain soliton solutions. Also the comparison of Hamiltonian-based approach and different mesh-free numerical approaches such as radial basis function method (RBF) and finite element methods such as Galerkin and Petrov–Galerkin can also be thought of as further extension which may be of interest to Engineers and Physicists alike who are working on soliton theory or its applications.

**Acknowledgements** The support from the working institute “MPSTME, NMIMS SHIRPUR” of the first and third author is highly acknowledged.

## References

1. Zhang L, Masood C (2018) Classification and bifurcation of a class of second–order ODEs, and its application to nonlinear pdes. *Disc Cont Dyn Sys Series 11*
2. Darvishi MT, Najafi M, Wazwaz AM (2018) New extended rational trigonometric methods and applications. *Waves in Random Complex Media*, Taylor Francis. <https://doi.org/10.1080/17355030.2018.1478166>
3. Zhang ZY (2014) Jacobi elliptic function expansion method for the modified Korteweg–de Vries–Zakharov–Kuznetsov and the Hirota equations. *Rom J Phys* 60(9–10):1384–1394 Bucharest
4. Raslan KR, Abu Shaeer ZF (2017) A new solution for MKDV equation using Galerkin finite element method. *J Comput Theor Nano Sci* 14(1):800–806 (7)
5. Seadawy AR (2017) Solitary wave solutions of two-dimensional nonlinear Kadomtsev–Petviashvili dynamic equations in dust-acoustic plasmas. *Indian Acad Sci Pramana J Phys* 89:49. <https://doi.org/10.1007/s12043-017-1446-4>
6. Seadawy AR, Wang J (2018) Modified Kdv–Zakharov–Kuznetsov dynamical equation in a homogenous magnetized electron–positron–ion plasma and its dispersive solitary wave solutions. *Indian Acad Sci Pramana J Phys* 91:26. <https://doi.org/10.1007/s12043-018-1595-0>
7. Wang H, Zheng S, Chen L, Hong X (2016) Bifurcation and new exact travelling wave solutions for the bidirectional wave equations. *Pramana- J Phys* 87:77
8. Baleanu D, Kilic B, Ugurlu Y, Inc M (2015) The First Integral Method for the (3+1)-dimensional modified Korteweg–de–vries–Zakharov–Kuznetsov and Hirota equation. *Rom J Phys* 60(1–2):111–125 bukarest
9. Islam MH, Khan K, Akbar MA, Salam K (2014) Exact travelling wave solutions of Modified Kdv–Zakharov–Kuznetsov equation and viscous burgers equation. *SpringerPlus* 3:105

# Low-Cost Test Rig for Demonstrating Single Plane Balancing Using Vibrations



N. V. S. Shankar, K. V. Jitendra, H. Ravi Shankar and M. Manikumar

**Abstract** Rotary unbalance is the main cause of vibrations in high-speed rotating machines. Thus, a test rig is required for training personnel relating to this area. The existing balancing test rigs are costly. Availability of low-cost sensors and development boards like Arduino Uno helps in fabricating the test rigs at low cost. The rig contains four masses mounted on a disc such that radial position can be varied. Vibrations are measured when the disc is rotating. For measuring vibrations, pre-calibrated ADXL335 accelerometer, which is available off the shelf, is used. This is interfaced to PC using Arduino. The measured unbalance is found to be in good agreement with that of theoretically calculated value. This test rig helps in bringing an insight into students as to how unbalance can be estimated and corrected as well as use of various commercially available vibration measurement sensors.

**Keywords** Rotary mass balancing · Accelerometer · Arduino · Vibration

## 1 Introduction

Unbalance existing in rotary masses leads to vibrations due to unbalanced centrifugal force (Fig. 1). These vibrations lead to the failure of machinery. Thus, it is important to balance the unbalance existing in rotary masses of machinery. A lot of work happened in this field. A detailed literature survey regarding field balancing is presented in [1, 2]. The terminology involved and overview field balancing are given in detail in [3, 4]. The mathematical background relating to static and dynamic balancing as well

---

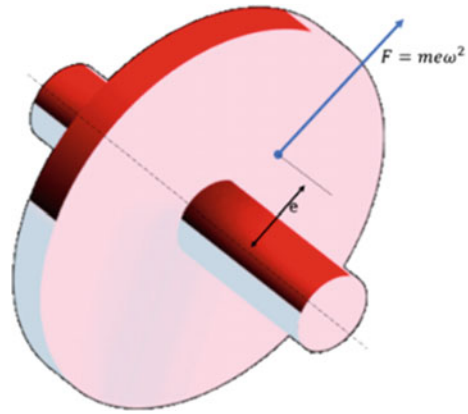
N. V. S. Shankar (✉) · K. V. Jitendra · M. Manikumar  
Department of Mechanical Engineering, Swarnandhra College of Engineering and Technology,  
Seetharampuram 534280, India  
e-mail: [Shankar.publications@gmail.com](mailto:Shankar.publications@gmail.com)

K. V. Jitendra  
e-mail: [viswajitendra5@gmail.com](mailto:viswajitendra5@gmail.com)

H. Ravi Shankar  
Department of Mechanical Engineering, GITAM University, Visakhapatnam 530045, India  
e-mail: [ravigitam.hota@gmail.com](mailto:ravigitam.hota@gmail.com)

© Springer Nature Singapore Pte Ltd. 2020  
H. K. Voruganti et al. (eds.), *Advances in Applied Mechanical Engineering*,  
Lecture Notes in Mechanical Engineering,  
[https://doi.org/10.1007/978-981-15-1201-8\\_49](https://doi.org/10.1007/978-981-15-1201-8_49)

**Fig. 1** Unbalance in rotary mass



as field balancing is given in [5–8]. Vibrations are the primary effects of unbalance in rotors. The use of vibrations during field balancing of wind turbines is discussed in [9]. These vibrations can thus be used in estimating unbalance. This is illustrated in [10–16]. For example, Ehrich [12] discussed the experimental in situ balancing of high-speed machinery. The use of vibrations for field balancing is also discussed in [17]. Howes and Long [18] summarized the field balancing of steam engines. Shannon [19] discussed the causes and identification of imbalance, as well as methods of compensating the same. Various instruments for vibration measurement during field balancing are discussed in [20–22]. In situ balancing is generally done for high-speed machinery. Multi-plane balancing of various turbines is summarized in [23, 24]. Precautions to be followed during this process of in situ balancing are described in [25].

## 2 Laboratory Experiment

Practical teaching of balancing of rotary masses is very much necessary because balancing finds a lot of applications in daily life. Nisbett [26] summarized an experimental set-up for the same. Basic schematic of experimental set-up for studying balancing is given in [27]. Multi-resonance TQ Educational and Training Division [28] detailed their equipment demonstrating multi-plane balancing. Mechatronic laboratory set-up (MMLS) by measuring vibrations for experimentally studying the balancing of rotating masses is described in [29]. Laboratory experimental procedure of two plane balancing is given in [30].

### 3 Motivation

Most of the test rigs used for demonstrating balancing of masses are quite costly [31]. Low-cost instrumentation is now available online which helps instrumenting the test rigs in such a way that they can be interfaced with a computer. This motivated the fabrication of this low-cost test rig which costed around Rs. 5000/- with all the instrumentation.

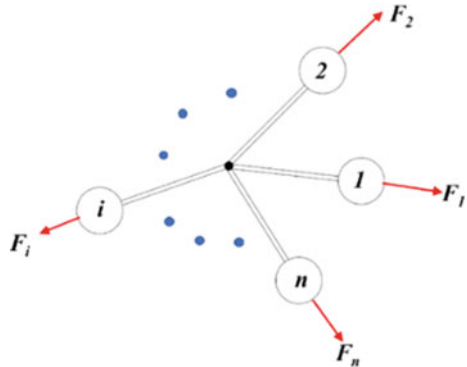
### 4 Balancing of Rotating Masses

Consider  $n$  masses connected at same point to a shaft rotating at angular velocity  $\omega$  and are in a single plane as shown in Fig. 2 such that  $i$ th mass is connected at  $r_i$  radius and at  $\theta_i$  angle. Each mass is subjected to the centrifugal force acting outwards. The magnitude of these forces is given by Eq. (1). The resultant unbalance is the vectorial sum of these forces. This unbalance results in vibrations whose frequency is equal to the angular velocity of the shaft.

$$\left. \begin{aligned} F_{ix} &= m_i r_i \omega^2 \cos \theta_i \\ F_{iy} &= m_i r_i \omega^2 \sin \theta_i \end{aligned} \right\} \tag{1}$$

$$F = \sqrt{\sum F_{ix}^2 + \sum F_{iy}^2} \tag{2}$$

Fig. 2 Masses rotating in the same plane



### 5 Test Rig

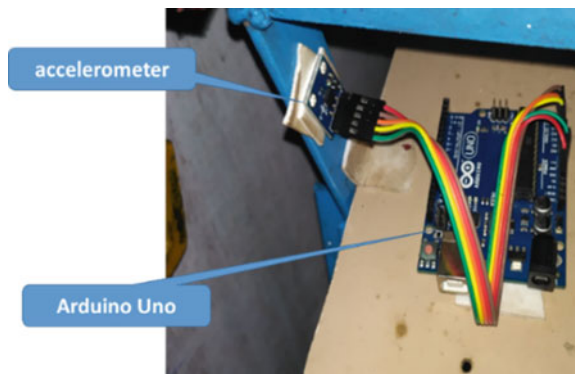
The above principle is demonstrated using a test rig comprising of a disc with four weights attached to it. This rig is shown in Fig. 3. The position of the weights can be adjusted radially along the slots on the disc. The disc with weights is attached to the disc, and the disc is rotated at a predefined rpm. The vibrations resulting from unbalance are measured using accelerometer which is interfaced to the computer using Arduino Uno. Instrumentation is shown in Fig. 4. The accelerometer that is used is ADXL335 which can measure g-force of  $\pm 3.5$  g with an accuracy of  $\pm 0.1$  g. Accelerometer is mounted in such a way that the z-axis is along the shaft axis. The sensor output is obtained in the serial monitor of Arduino which can be copied, and excel can then be used for further data analysis. It can be noted here that each mass added is 1.12 kgs, and mass of total rig is 12 kg. Fabrication of rig costed Rs. 5000.00 only.

Consider  $n$  masses connected at same point to a shaft rotating at angular velocity  $\omega$  and are in a single plane as shown in Fig. 2 such that  $i$ th mass is connected at  $r_i$

**Fig. 3** Test rig for simulating rotary mass balancing



**Fig. 4** Accelerometer and Arduino mounted



radius and at  $\theta_i$  angle. Each mass is subjected to the centrifugal force acting outwards. The magnitude of these forces is given by Eq. (1). The resultant unbalance is the vectorial sum of these forces. This unbalance results in vibrations whose frequency is equal to the angular velocity of the shaft.

## 6 Working

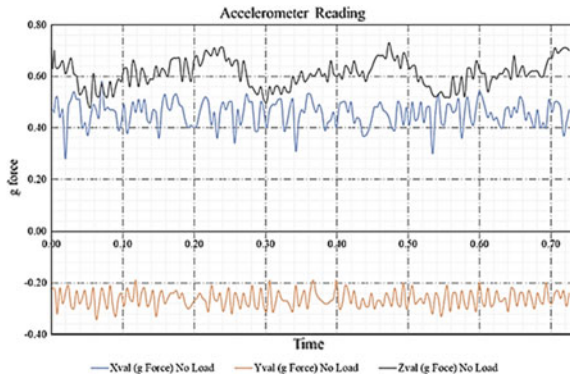
Experimentation is done in two steps:

1. Measuring vibrations under no load.
2. Measuring vibrations under load.

### 6.1 Measuring Vibrations Under No Load

Initially, all the loads are dismantled and the disc is rotated at full speed. The angular velocity, in this case, was found to be 247 rpm. Once the speed of the disc is stabilized, vibrations for 30 s are recorded using accelerometer, and data is transferred to excel for further analysis. Figure 5 shows the g-force variations in  $x$ ,  $y$  and  $z$  directions for two revolutions in this case. Based on the plot, a clear periodicity can be observed along  $z$ -axis. This indicates that there is a wobbling in the disc.

**Fig. 5** Accelerometer reading with no load



### 6.2 Measuring Vibrations Under Load

In the second step, loads are added to the disc. The position of each load is recorded. It may be noted that the radial position of the discs can be adjusted as desired to create the unbalance disc which is rotated at 244 rpm.

The response is recorded using accelerometer for 30 s. Plot in Fig. 6 shows this response. As indicated earlier, periodicity in *z*-axis is due to wobbling. The difference in max and min of *g*-force reading either in *x* or *y* axis is the net unbalance *g*-force. This unbalanced *g*-force multiplied by the weight of the rig will give the unbalance in Newtons. This unbalance is in complete agreement with those computed theoretically. Theoretical calculations are presented in Table 1. The results and computations show that the predicted unbalance is in good agreement with that of measured unbalance.

**Fig. 6** Accelerometer reading with load

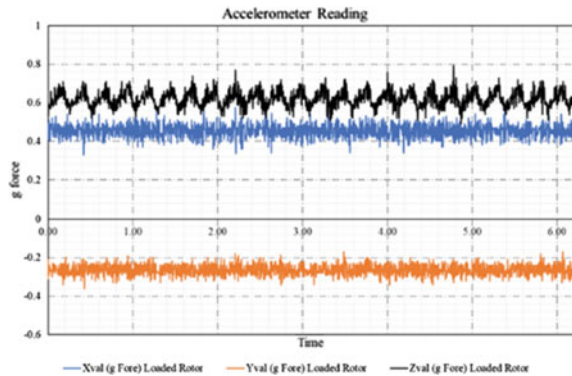


**Table 1** Calculation in excel

<i>i</i>	<i>m<sub>i</sub></i> (kg)	<i>r<sub>i</sub></i> (cm)	<i>θ<sub>i</sub></i>	<i>m<sub>i</sub></i> * <i>r<sub>i</sub></i> *cos( <i>θ<sub>i</sub></i> )	<i>m<sub>i</sub></i> * <i>r<sub>i</sub></i> *sin( <i>θ<sub>i</sub></i> )
1	1.12	12	0	0.134	0.000
2	1.12	12	90	0.000	0.134
3	1.12	12	180	-0.134	0.000
4	1.12	16	270	0.000	-0.179
				0.000	-0.045
Angular velocity (rpm)					242.000
Angular velocity (rad/s)					25.342
Net unbalance force (N)					28.772
Net X <i>g</i> -force					0.260
Net unbalance measured (N)					30.607 = (0.26*9.81*12)



**Table 2** Cost comparison of various test rigs

S. No.	Description	Cost
1	Tech-Ed static and dynamic balancing test apparatus [31]	Rs. 35,000/-
2	EEE static and dynamic balancing apparatus [31]	Rs. 65,000/-
3	Mechmatics static and dynamic balancing apparatus [31]	Rs. 25,500/-
4	Sigma static and dynamic balancing apparatus [31]	Rs. 78,500/-
5	Proposed test rig in the paper	Rs. 5000/-

## 7 Accuracy, Repeatability and Cost

The test rig is designed so as to develop a low-cost class room demonstrator. The availability of low-cost sensors like accelerometers ADXL345 (range  $\pm 3.5$  g), ADXL345 (range  $\pm 2$  g to  $\pm 16$  g) and gyro sensors like MPU6050 as well as development boards like Arduino motivated the development of this test rig. The cost comparison of some test rigs is given in Table 2. The comparison shows to how much extent the cost of the equipment is reduced. The aim of this paper is to demonstrate how these test rigs can be built and made to work. Calibration of various accelerometers can be done following the method described in [32].

The accuracy of the test rig largely depends on the accuracy of the sensor that is positioned to read the data as well as the baud rate that is used to read the data using Arduino. 115,200 baud rate is suggested so that we can match the sensor data acquisition rate. Also, some time lag will be there as data is being printed to serial monitor. But this time lag should not affect the accuracy if no delay is used thus making the experiment highly repeatable.

## 8 Conclusion

The balancing of rotating bodies is important to avoid vibration. In heavy industrial machines such as gas turbines and other high-speed rotary machinery, vibration can cause failure of machines, as well as noise and discomfort. Rotary mass balancing is thus an important concept which must be given a practical exposure. In this work, a test rig which gives insight into balancing of forces, as well as filed balancing, has been fabricated. The unbalance is measured using accelerometer. The measured value is in good agreement with that of theoretically computed.

## References

1. Zhou S, Shi J (2001) Active balancing and vibration control of rotating machinery: a survey. *Shock Vib Dig* 33:361–371
2. Foiles W, Allaire P, Gunter E (1998) Review: rotor balancing. *Shock Vib* 5:325–336
3. Kelm RD (2008) Advanced field balancing. In: Vibration institute annual training seminar. Kelm Engineering, LLC, Houston
4. Pryor WT (2012) Field balancing of rotating machinery. In: Piedmont chapter vibration institute training symposium (2012)
5. Antoni J, Daniere J, Guillet F (2002) Effective vibration analysis of IC engines using cyclostationarity. Part I—A methodology for condition monitoring. *J Sound Vib* 257:815–837
6. Antoni J, Daniere J, Guillet F (2002) Effective vibration analysis of IC engines using cyclostationarity. Part I—new results on the reconstruction of the cylinder pressures. *J Sound Vib* 257:839–856
7. Temple D (1998) Field balancing of large rotating machinery. In: Facilities instructions, standards, and techniques, vol 2–2
8. Prüftechnik (2010) An engineer's guide to shaft alignment, vibration analysis, dynamic balancing and wear debris analysis. Prüftechnik Ltd.
9. Becker E Field balancing of rotor blades. [https://www.pruftechnik.com/fileadmin/pt/Press-News/Telediagnose.com-Servicemagazin/Magazine/English/telediagnose12\\_en.pdf](https://www.pruftechnik.com/fileadmin/pt/Press-News/Telediagnose.com-Servicemagazin/Magazine/English/telediagnose12_en.pdf)
10. Tiwari R (2010) Vibration based condition monitoring in rotating machineries. In: Analysis and identification in rotor bearing systems, pp 1007–1053
11. Thearle EL, Schenectady NY (1934) Dynamic balancing of rotating machinery in the field. *Trans Am Soc Mech Eng J Appl Mech* 56:745–753
12. Ehrich R (1980) High speed balance procedure. In: Proceedings of 9th turbomachinery symposium. Texas, pp 25–32
13. Fang J, Wang Y, Han B, Zheng S (2013) Field balancing of magnetically levitated rotors without trial weights. *Sensors* 13:16000–16022 (Switzerland)
14. Xu X, Chen S (2015) Field balancing and harmonic vibration suppression in rigid AMB-rotor systems with rotor imbalances and sensor runout. *Sensors* 15:21876–21897 (Switzerland)
15. Fox RL (1981) A practical guide to in-plane balancing. In: Proceedings of 10th turbomachinery symposium. Texas, pp 113–130
16. Gruwell DR, Zeidan FY (1980) Vibration and eccentricity measurements combined with rotor dynamic analyses on a six bearing turbine generator. In: Proceedings of 27th turbomachinery symposium. Texas, pp 85–92
17. Chen XQ, Jia YJ, Cheng GZ (2012) Research on field balancing of rotor. *Appl Mech Mater* 201–202, 83–86
18. Howes B, Long B Field balancing experiences. [http://www.betamachinery.com/assets/pdfs/Technical\\_Articles/Field\\_Balancing\\_Experiences.pdf](http://www.betamachinery.com/assets/pdfs/Technical_Articles/Field_Balancing_Experiences.pdf)
19. Shannon RA (2008) Vibration measurement systems and guidelines for centrifugal fans—a filed perspective. In: AMCA international engineering conference. Las Vegas, NV, USA
20. Balance, Vibration, and Vibration Analysis (2001). <http://www.pittsburghairsystems.com/PDF/FanApplications/Balance,Vibration,andVibrationAnalysis.pdf>
21. Kumar PM, Kumar J, Tamilarasan R, Sendhilnathan S, Suresh S (2015) Review on nanofluids theoretical thermal conductivity models. *Eng J* 19:67–83
22. SmartBalancer—the intelligent way to field balancing: simple—fast—accurate, <http://www.smartbalancer.com/fileadmin/smartbalancer/downloads/smartbalancer-E-26.4.16.rz-WEB.pdf>
23. Gunter EJ (1986) Field balancing 70 MW gas turbine generators. In: International conference on rotordynamics, Tokyo, pp 135–143
24. Gunter EJ, Humphris RR Dynamic analysis and field balancing of 70 MW gas-turbine generators. [https://dyrobes.com/wp-content/uploads/2015/09/Dynamic-Analysis-and-Field-Balancing-of-70-MW-Gas-Turbine-Generators1985\\_linked.pdf](https://dyrobes.com/wp-content/uploads/2015/09/Dynamic-Analysis-and-Field-Balancing-of-70-MW-Gas-Turbine-Generators1985_linked.pdf)

25. Precautions and safeguards during in-situ balancing. <https://www.mainttech.se/wp-content/uploads/KNOWLEDGE-OF-BALANCING-AND-VIBRATION-MEASUREMENT.pdf>
26. Nisbett K (1996) Dynamic balancing of rotating machinery experiment. <http://web.mst.edu/~stutts/ME242/LABMANUAL/DynamicBalancingExp.pdf>
27. Ozoegwu CC, Nwangwu CC, Uzoh CF, Ogunoh AV (2012) zPure analytical approach to rotational balancing. *J Saf Eng* 1:50–56
28. Static and Dynamic Balancing (2000) [http://www.dcu.ie/sites/default/files/mechanical\\_engineering/pdfs/manuals/StaticandDynamicBalancing\(a\).pdf](http://www.dcu.ie/sites/default/files/mechanical_engineering/pdfs/manuals/StaticandDynamicBalancing(a).pdf)
29. Boikov VI, Andrievsky B, Shiegin VV (2016) Experimental study of unbalanced rotors synchronization of the mechatronic vibration setup. *Cybern Phys* 5:5–11
30. Two Plane Balancing Example with DAQmx. <http://www.ni.com/example/12500/en/%0ATwo>
31. Static and dynamic balancing experimental setups. <https://dir.indiamart.com/search.mp?ss=static+and+dynamic+balancing&src=as-rcnt>
32. TheDarkSaint: ADXL345 Hookup Guide. <https://learn.sparkfun.com/tutorials/adx1345-hookup-guide/all>

# Nonlinear Dynamic Analysis of Automotive Turbocharger Rotor System



S. Bala Murugan, Rabindra Kumar Behera and P. K. Parida

**Abstract** The present development on the automotive engines on reducing size and increasing greater fuel efficiency, and less emissions took the researchers to several challenges in turbocharger rotor system. However, the challenge towards the evolution of high-efficiency bearing systems with reliability is still over the top. The paper shows the system with dynamic analysis of nonlinear turbocharger rotor system to interpret the unstable positions during running condition. The proposed model of turbocharger in this study is examined as a uniform shaft in nature with varying lengths between two bearings which actually held between compressor end and the turbine disc. The two discs are having force unbalance and the compressor impeller exists with the seal forces. The rotor considered here is supported by bearings with the nonlinear time-varying forces as reactions at the supports. The approach in this paper is allowed to solve the transient conditions, suchlike nonlinear effects due to seal forces, time histories, and Campbell diagram. The computational models are solved with analytical equations using finite element modelling (FEM) and the obtained results are verified with ANSYS® simulations. The impacts of different operating conditions at two different speeds are studied by phase-plane diagrams to understand the stability of the system.

**Keywords** Dual disc rotor · Ball bearing · Seal force · FEM · Stability analysis

---

S. Bala Murugan (✉) · R. K. Behera  
National Institute of Technology, Rourkela, Odisha 769008, India  
e-mail: [balamurugan8202@gmail.com](mailto:balamurugan8202@gmail.com)

P. K. Parida  
College of Engineering and Technology, Bhubaneswar, Odisha 751003, India

© Springer Nature Singapore Pte Ltd. 2020  
H. K. Voruganti et al. (eds.), *Advances in Applied Mechanical Engineering*,  
Lecture Notes in Mechanical Engineering,  
[https://doi.org/10.1007/978-981-15-1201-8\\_50](https://doi.org/10.1007/978-981-15-1201-8_50)

## 1 Introduction

In much kind of machineries, nonlinear vibrations play an important phenomenon in technical applications. Most of the practical cases, the system always dominated through the nonlinear effects. The system examined here in this study, called turbocharger rotor system supported by two bearings with the nonlinear time-varying forces.

In rocket engine, generally the turbocharger is considered as a major part and it supplies the propellants with low temperature to the combustion chamber which operating at extreme high pressures. Turbochargers are regularly operated at very high speeds due to its size. The high speed of turbocharger will lead the system to a pressure drop region which below the vapour pressure causing the liquid propellant to cavitate the compressor blades. In general, the speed of the oxidizer is high due to the greater density than the fuel. The main disadvantage of this provision is making the engine further complex and less reliable.

Several researchers made their extensive contribution of analysing the turbocharger rotor-bearing system. However, past one decade, experimental and theoretical studies were carried on turbochargers and reported the analysis. Bai et al. [1] examined the consequences of nonlinear dynamic characteristics of a flexible support stiffness and system stability by using a dynamic modelling. The induced forces due to nonlinearity by seals and internal damping of rotor also included in the analysis. Son et al. [2] describe the theoretical design of a gas generator of liquid rocket engine. The produced gases by the gas generator, drives the turbopumps through turbine. An analysis based on chemical non-equilibrium and droplet vapourization was given to estimate the properties. Hu et al. [3] studied the methods for detection and health monitoring and a turbopump fault diagnosis with vector machines. Hong et al. [4] carried the test on hydraulic performance of a liquid rocket engine. Wang and Sun [5] extended the analysis of turbopump rotor with gyroscopic effects with one-dimensional finite element model. Smolik et al. [6] studied the dynamic response of the turbocharger rotor for the effects of radial clearances on bearings. Novotny et al. [7] presented an efficient and numerically stable calculation model of plain floating ring bearing.

The present study shows the dynamic stability of a rotor dynamic model of turbocharger system. The rotor system included the ball bearing with Hertzian contact forces, disc mass unbalances and forces of seal which is dynamic in nature based on the Muszynska relations. The equations which are dynamic in nature are solved using implicit scheme of Houbolt's time integration. Finally, the stability of the system with different speeds of operation is carried using frequency response and phase-plane plots.

## 2 Dynamic Model of Turbocharger Unit

Turbochargers are principal parts of rocket engine unit. A schematic view of turbocharger is shown in Fig. 1. The turbopump rotor is supported on two bearings and exist liquid seals at pump disc. Turbopump is considered as a simple single disc in the present task, and has an inducer and diffuser in it. The turbine produces power, and it is kept at the farthest end to drive the turbocharger system.

### 2.1 Dynamic Formulations of System

By using Timoshenko beam theory, a simplified rotor model of the system is considered with finite elements. The shaft elements are divided by four and five nodes thoroughly. Every node of the shaft element has the degrees of freedom (DOF) four, which includes rotational ( $\theta_y, \theta_z$ ) and translational displacements ( $v, w$ ).

For the near in-depth to the dynamic effects of the system the turbocharger parts are taken as rigid bodies which lies at two nodes 3 and 5, respectively. The nodes 2 and 4 represent the ball bearings. The hydrodynamic effect at the seals produces a force which has an extremely nonlinear in nature. The seals are placed at the discharge side of the impeller and inlet end which is equal to the element forces concerned at node 3. Moreover, the component force of mass unbalance and the forces due to gravity are considered at turbine and pump discs. Now, the kinetic and the potential energy of spinning shaft elements can be written by with the effects of bending and shearing effects as:

$$T_s = \frac{1}{2} \int_0^\ell \rho \{ A(\dot{v}^2 + \dot{w}^2) + I_D(\dot{\theta}_y^2 + \dot{\theta}_z^2) + I_P[\Omega^2 + \Omega(\dot{\theta}_z\theta_y - \dot{\theta}_y\theta_z)] \} ds \quad (1)$$

$$U_s = \frac{1}{2} \int_0^\ell \{ EI(\theta_y'^2 + \theta_z'^2) + kGA[(\theta_y - w')^2 + (\theta_z + v')^2] \} ds \quad (2)$$

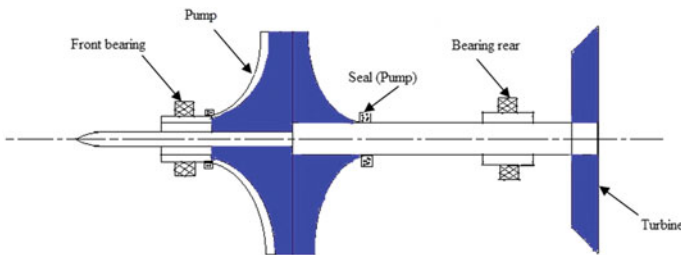


Fig. 1 Turbocharger schematic diagram

The disc kinetic energy can be given as:

$$T_d = \frac{1}{2}m_d(\dot{v}^2 + \dot{w}^2) + \frac{1}{2}J_d(\dot{\theta}_y^2 + \dot{\theta}_z^2) + \frac{1}{2}J_p[\Omega^2 + \Omega(\dot{\theta}_z\theta_y - \dot{\theta}_y\theta_z)] \quad (3)$$

The mass eccentricity of the disc taken as:

$$W_d = m_d r_d \Omega^2 (w \cos \Omega t + v \sin \Omega t) \quad (4)$$

The translation ( $v, w$ ) and rotational displacements ( $\theta_y, \theta_z$ ) of the shaft element can be approximated by finite element method as:

$$\begin{Bmatrix} v \\ w \end{Bmatrix} = [N_t(s)]\{q\}; \begin{Bmatrix} \theta_y \\ \theta_z \end{Bmatrix} = [N_r(s)]\{q\} \quad (5)$$

where  $[N_t(s)]$  and  $[N_r(s)]$  are translation and rotational shape functions. By substituting the above expressions into Eqs. (1) and (2) and integrating over the length of the element with Hamilton’s principle, the following equation of motion for the shaft and disc units are originated:

$$[M_s]\{\ddot{q}_s\} + \Omega[G_s]\{\dot{q}_s\} + [K_s]\{q_s\} = \{F_s\} \quad (6)$$

$$[M_d]\{\ddot{q}_d\} + \Omega[G_d]\{\dot{q}_d\} = \{F_d\} \quad (7 \ \& \ 8)$$

$$[M_s] = \int_0^\ell \rho A [N_t]^T [N_t] ds + \int_0^\ell \rho I_d [N_r]^T [N_r] ds; [G_s] = \int_0^\ell \rho I_p [N_r]^T \begin{bmatrix} 0 & 1 \\ -1 & 0 \end{bmatrix} [N_r] ds$$

$$[K_s] = \int_0^\ell EI [N_r']^T [N_r'] ds + \kappa GA \int_0^\ell \left\{ \begin{array}{l} [N_t]^T [N_t] + [N_r]^T [N_r] \\ + 2[N_t]^T \begin{bmatrix} 0 & -1 \\ 1 & 0 \end{bmatrix} [N_r] \end{array} \right\} ds \quad (9)$$

By including the effects of damping, the system the equation of motion can be given as [8]

$$[M]\{\ddot{q}\} + [[C] + \Omega[G]]\{\dot{q}\} + [K]\{q\} = \{F\} \quad (10)$$

Here,  $F_{py} = m_p e_p \Omega^2 \sin \Omega t - m_p g$  and  $F_{pz} = m_p e_p \Omega^2 \cos \Omega t$  are unbalance and gravity forces at the pump,  $F_{ty} = m_t e_t \Omega^2 \sin \Omega t - m_t g$  and  $F_{tz} = m_t e_t \Omega^2 \cos \Omega t$  are the those at turbine node, while  $F_{sy}$  and  $F_{sz}$  are component seal forces at the pump along  $y$  and  $z$  directions, respectively. Here,  $p$ -pump,  $t$ -turbine,  $b$ -bearing, and  $s$ -seal forces.

### 2.2 Seal Force (Nonlinear)

The force expression of the seal model can be given as follows:

$$\begin{aligned} \begin{Bmatrix} F_{sz} \\ F_{sy} \end{Bmatrix} = & - \begin{bmatrix} K_g - m_g \tau_g^2 \Omega^2 & \tau_g \Omega D_g \\ -\tau_g \Omega D_g & K_g - m_g \tau_g^2 \Omega^2 \end{bmatrix} \begin{Bmatrix} w \\ v \end{Bmatrix} \\ & - \begin{bmatrix} D_g & 2\tau_g \Omega m_g \\ -2\tau_g \Omega m_g & D_g \end{bmatrix} \begin{Bmatrix} \dot{w} \\ \dot{v} \end{Bmatrix} - \begin{bmatrix} m_g & 0 \\ 0 & m_g \end{bmatrix} \begin{Bmatrix} \ddot{w} \\ \ddot{v} \end{Bmatrix} \end{aligned} \tag{11}$$

where,  $K_g$ ,  $m_g$ ,  $D_g$ , and  $\tau_g$  are equivalent stiffness, mass, damping, and the ratios of fluid circumferential velocity, respectively. The all nonlinear functions of the radial displacement of the rotor are follows:

$$K_g = K_0(1 - e^2)^{-n}$$

where,

$$D_g = D_0(1 - e^2)^{-n}(n = 0.5 - 3); \tau_g = \tau_0(1 - e)^b(0 < b < 1); m_g = \mu_2 \mu_3 T_g^2; e = \frac{\sqrt{v^2 + w^2}}{c_g}$$

is the relative eccentricity, and it is ratio between the rotor radial displacement to the seal clearance  $c_g$ ; the coefficients  $n$ ,  $b$ , and  $\tau_0$  varies for different kind of seals; in this work, the variables are taken as:  $n = 2.5$ ,  $b = 0.5$ , and  $\tau_0 = 0.49$ . The characteristic factors  $K_0$ , and  $D_0$  can be calculated from Childs equation [9] as follows: (refer Appendix)

$$K_0 = \mu_3 \mu_0, D_0 = \mu_1 \mu_3 T_g \tag{12}$$

where,

$$\begin{aligned} \mu_0 = & \left( \frac{2\sigma^2}{1 + \xi + 2\sigma} \right) E_g(1 - m_0); \mu_1 = \left( \frac{2\sigma^2}{1 + \xi + 2\sigma} \right) \left( \frac{E_g}{\sigma} + \frac{B}{2} \left( \frac{1}{6} + E_g \right) \right); \\ \mu_2 = & \left( \frac{\sigma}{1 + \xi + 2\sigma} \right) \left( \frac{1}{6} + E_g \right); \mu_3 = \left( \frac{\pi R_g \Delta p}{\lambda} \right); T_g = \frac{\ell_g}{v_a} \end{aligned} \tag{13}$$

Here,  $\xi = 0.1$ ,  $n_0 = 0.079$ , and  $m_0 = -0.25$  and the viscous coefficient of air  $\mu = 1.5 \times 10^{-5}$  Pas. The other constants are follows: seal length  $\ell_g$ , seal pressure margin  $\Delta p$ , radius of seal  $R_g$ , and axial speed of fluid  $v_a = \omega R_g$ .



### 2.3 Bearing Forces

The turbopump rotor system is held on ball bearings. The reaction forces at the bearing nodes are in the nature of Hertzian nonlinear radial contact force. The Hertzian contact theory due to nonlinear says that, due to the rolling contact, the force of contact between ball and race is given in terms of Hertzian contact stiffness  $C_b$  as:

$$F_{zb} = \sum_{j=1}^{N_b} (-C_b(w \cos \theta_j + v \sin \theta_j - r_0)^{3/2} H) \cos \theta_j \quad (14)$$

$$F_{yb} = \sum_{j=1}^{N_b} (-C_b(w \cos \theta_j + v \sin \theta_j - r_0)^{3/2} H) \sin \theta_j \quad (15)$$

where,  $H$  can be defined as,

$$H = \begin{cases} 1, & \text{if } (w \cos \theta_j + v \sin \theta_j - r_0) > 0 \\ 0, & \text{if } (w \cos \theta_j + v \sin \theta_j - r_0) \leq 0 \end{cases} \quad (16)$$

where,  $w = w_b + (R - r_0) \cos q_j$  and  $v = v_b + (R - r_0) \sin q_j$ ,  $\theta_j$  is the angular position of the  $j$ th ball, which is having the expressions as,

$$\theta_j = \omega_{\text{cage}} \times t + \frac{2\pi}{N_b} (j - 1), \quad j = 1, 2, \dots, N_b \quad (17)$$

## 3 Numerical Simulation and Discussion

Finite element equations are solved by an interactive method in MATLAB. The physical and mechanical properties of rotor-bearing systems with the dynamic data are listed in Table 1.

The simulated frequencies are found for the system with prompt code as 8.3756, 36.249, 52.887, and 89.683 Hz. Then, the above results are simulated with ANSYS® program and compared with the frequencies from numerical solutions by taking into the effect of rotary inertia (Rayleigh's beam), and listed in Table 2.

The finite element-coupled nonlinear differential equations are solved with Houbolt's implicit time-integration scheme. This method carries last two time steps to calculate the present displacement. To solve the time steps in the equations, central difference method was employed. The second module of numerical simulation was achieved in the program for obtaining frequency response and phase-plane diagrams. Further, convergence study was carried to validate the present numerical codes.

**Table 1** Parameters considered for the rotor system

Properties	Values	Properties	Values
Density of shaft material (kg/m <sup>3</sup> )	7810	MOI of disc, (kg-mm <sup>2</sup> )	41,750 & 168,100 ( $I_{yy} = I_{zz}$ )
Young's modulus, E (GPa)	197		83,500 and 336,200 ( $I_{xx}$ )
Shear modulus, G (GPa)	80	Bearing, $r_i$ (m)	0.031
Radius of shaft (m)	0.012	Bearing, $R$ (m)	0.049
Length of shaft (m)	0.600	Bearing clear. (micr.)	20
Radius of disc (m)	0.15	Bearing stiffness coefficients (N/m)	$4 \times 10^7$ ( $k_{zz} = k_{yy}$ )
Thickness of disc (m)	20		$1 \times 10^8$ ( $k_{zz} = k_{yy}$ )
No. of balls, $N_b$	8	Bearing damp. (N/m)	$13.34 \times 10^9$ ( $C_b$ )

**Table 2** Frequencies for first three modes from numerical and ANSYS® simulation

Frequency modes		Numerical (Hz)	ANSYS (Hz)	Variation (%)
First	Forward	8.3761	8.4952	1.422
	Backward	8.3756	8.4207	0.538
Second	Forward	36.285	37.322	2.858
	Backward	36.249	37.302	2.905
Third	Forward	53.217	54.105	1.669
	Backward	52.882	53.647	1.447

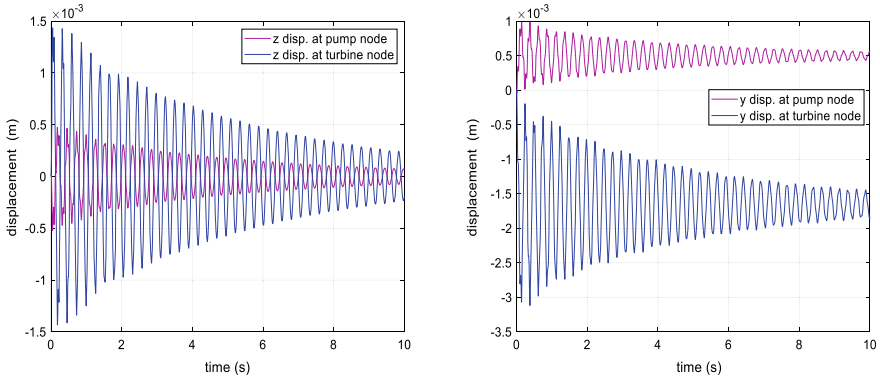
The summary of results for different set of elements from convergence study is listed in Table 3. The investigation reveals that the frequencies are converges.

Figure 2 shows the time histories of pump and turbine nodes for  $z$  displacements (left) and  $y$  displacements (right) for the angular velocity of,  $\Omega = 1000$  rpm for the time period of 10 s. The displacement curves shows that the amplitude is getting reduced due to the nonlinear effects from the seals at both the bearing housings.

*Remarks 1* Boundary conditions follow with the initial assumptions of the system with the disc unbalance,  $e = 0.001$  m, and gravity as well as the viscoelastic force components are treated as external forces. The reaction forces at the bearing nodes are in the nature of Hertzian nonlinear radial contact force. Based on the parameters given in Table 1, the dynamic response of the rotor systems are plotted in Figs. 2 and 3.

**Table 3** Convergence study for numerical simulation

Freq.	Whirl modes (Hz)	Number of elements		Freq.	Whirl modes (Hz)	Number of elements	
		4	8			4	8
1st	Forward	8.3761	8.3752	2nd	Backward	36.249	36.242
	Backward	8.3756	8.3748		Forward	53.217	53.211
2nd	Forward	36.285	36.274	Backward	52.882	52.874	52.865



**Fig. 2** Time histories of pump and turbine nodes for the angular velocity of,  $\Omega = 1000$  rpm

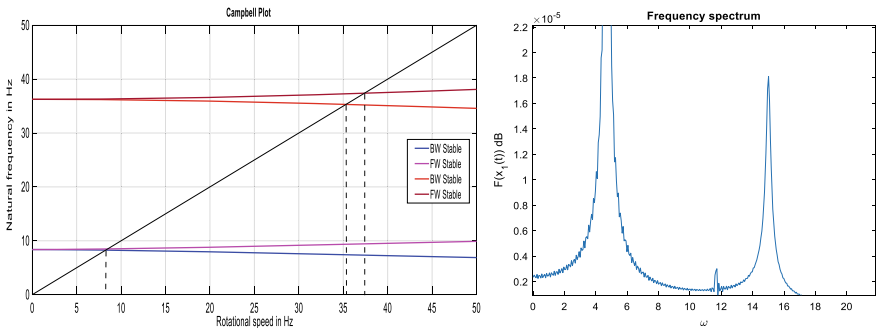


**Fig. 3** Campbell plot for  $\Omega = 3000$  rpm and frequency spectrum of rotor at  $\Omega = 1000$  rpm

### 4 Conclusions

Simulated vibrations of automotive turbocharger rotor supported in bearings were studied and presented with nonlinear hydrodynamic seal forces. The system modelled with Timoshenko beam theory and analysis was carried by using finite element method. At the bearing supports which mounted on the base is experiencing the excitation and the same is transferred to the rotor. The systems include the force due to imbalance, gyroscopic, bearing reactions and the effect of gravity also into account for the specific operational speed level in the dynamic study and have been presented. The results are shown in Figs. 2, 3 and 4. The simulated numerical solutions are compared with the frequencies with ANSYS® program which are listed in Table 2. Furthermore, convergence study was carried to validate the present numerical codes for three set of elements and listed in Table 3. In theoretical analysis, for the large whirling amplitudes can be accounted and studied through the impact of external/nonlinear seal force analysis in the same approach. The system becomes stable (periodic) after 15,000 rpm, and from the results, it is obvious that, due to the

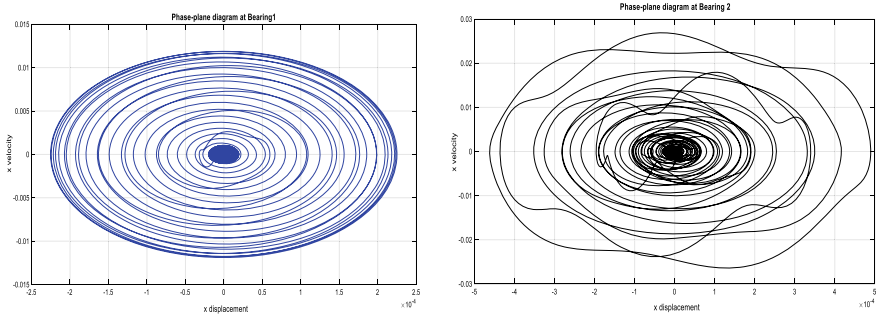


**Fig. 4** Phase-plane diagrams of bearing1 (left) and 2 (right) with  $\Omega = 1000$  rpm

nonlinear dynamic forces of turbopump rotor system, the sub-synchronous motion is observed.

### Appendix

$$\lambda = n_0(R_a)^{m_0} \left[ 1 + \left( \frac{R_v}{R_a} \right)^2 \right]^{(1+m_0)/2}; \sigma = \frac{\lambda \ell_g}{c_g}; E_g = \frac{1 + \xi}{2(1 + \xi + 2\sigma)}; B = 2 - \frac{(R_v/R_a)^2 - m_0}{(R_v/R_a)^2 + 1};$$

$$R_v = \frac{R_g \omega c_g}{\mu}; R_a = \frac{2v_a c_g}{\mu}$$

### References

1. Bai C, Xu Q, Wang J (2011) Effects of flexible support stiffness on the nonlinear dynamic characteristics and stability of a turbopump rotor system. *Nonlinear Dyn* 64:237–252. <https://doi.org/10.1007/s11071-010-9858-4>
2. Son M, Koo J, Cho WK, Lee ES (2012) Conceptual design for a kerosene fuel-rich gas-generator of a turbopump-fed liquid rocket engine. *J Therm Sci* 21:428–434. <https://doi.org/10.1007/s11630-012-0564-z>
3. Hu L, Hu N, Fan B, Gu F (2012) Application of novelty detection methods to health monitoring and typical fault diagnosis of a turbopump. *J Phys Conf Ser* 364. <https://doi.org/10.1088/1742-6596/364/1/012128>
4. Hong SS, Kim DJ, Kim JS et al (2013) Study on inducer and impeller of a centrifugal pump for a rocket engine turbopump. *Proc Inst Mech Eng Part C J Mech Eng Sci* 227:311–319. <https://doi.org/10.1177/0954406212449939>
5. Wang JF, Sun K (2012) The calculation of the rotor critical speed of turbopump. *Adv Mater Res* 529:220–223. <https://doi.org/10.4028/www.scientific.net/amr.529.220>
6. Smolik L, Hajzman M, Byrtus M (2017) Investigation of bearing clearance effects in dynamics of turbochargers. *Int J Mech Sci* 127:62–72. <https://doi.org/10.1016/j.ijmecsci.2016.07.013>

7. Novotný P, Škara P, Hliník J (2018) The effective computational model of the hydrodynamics journal floating ring bearing for simulations of long transient regimes of turbocharger rotor dynamics. *Int J Mech Sci* 148:611–619. <https://doi.org/10.1016/j.ijmecsci.2018.09.025>
8. Nelson HD (2010) A finite rotating shaft element using timoshenko beam theory. *J Mech Des* 102:793. <https://doi.org/10.1115/1.3254824>
9. Childs DW (2009) Dynamic analysis of turbulent annular seals based on hirs' lubrication equation. *J Lubr Technol* 105:429. <https://doi.org/10.1115/1.3254633>

# On the Response of a Beam Structure to a Moving Mass Using Green's Function



Sudhansu Meher, Suraj Parida and Rabindra Kumar Behera

**Abstract** The dynamic responses of a beam structure acted upon by a moving mass or moving load have been of great importance in the design and study of bridges, railway tracks, etc. It also plays a vital role for studying many applications in the field of transportation, overhead cranes, cableways, roadways, pipelines, tunnels, bridges, guideways, etc. All the above-mentioned structures are designed to support moving loads. The structures while supporting the moving loads face the inertial effect of the moving mass which cannot be ignored comparing with the gravitational effect of the moving load. The equation of motion of an Euler–Bernoulli beam acted upon by a concentrated mass moving at a uniform speed is formulated in matrix form. The solutions of the above problems for cantilever beams are evaluated by using dynamic Green's function approach. The present work focuses on the effect of the mass of the moving load and its speed on the response of a cantilever-type beam. The cantilever beam is divided into twenty divisions, and the deflection of beam at the free end is measured, while the mass moves with uniform velocity over the beam through different stations. The deflection results so obtained are plotted in the form of graphs for different velocities of mass.

**Keywords** Euler beam · Moving mass · Green's function

## 1 Introduction

The moving loads over beam-like structures are encountered frequently in the study of structures. The response of structures subjected to moving masses is of great practical significance. The hazards produced by the moving masses on structures are a prime area of study for engineers for many several years. The response of highway bridges and railway bridges under the effect of moving loads has been studied with

---

S. Meher (✉)

Government College of Engineering, Keonjhar 758002, India

e-mail: [mehercetb@gmail.com](mailto:mehercetb@gmail.com)

S. Parida · R. K. Behera

National Institute of Technology, Rourkela, Odisha 769008, India

© Springer Nature Singapore Pte Ltd. 2020

H. K. Voruganti et al. (eds.), *Advances in Applied Mechanical Engineering*,

Lecture Notes in Mechanical Engineering,

[https://doi.org/10.1007/978-981-15-1201-8\\_51](https://doi.org/10.1007/978-981-15-1201-8_51)

great depth during the last few decades. When the Chester Rail Bridge of England collapsed in 1897, many researchers faced the challenge to design structures which support moving load [1]. Structural elements such as beams are widely used in the branches of mechanical, aerospace and civil engineering. Different types of problems related with loads moving over beam are studied by Fryba [2]. Also, the importance of moving loads in the field of transportation, railway and highway bridges, suspension bridges, crane runways, cableways, tunnels and pipelines cannot be denied as these structures are designed to support moving masses. Also, many members can be assumed as beams acted upon by moving loads in the design of machining processes. A. S. Mohamed studied and constructed tables of Green's functions that are used for determining mode shapes and natural frequencies of beams with various boundary conditions and intermediate attachments in the beam [3]. The intermediate attachments in the beam may include rotational or elastic attachments. Lueschen et al. in his paper [4] found a closed-form solution of individual elements of the beam structure using Green's function. A closed-form solution using Green's functions for an Euler–Bernoulli beam and Timoshenko beam without and with axial loads is found out. Mehri et al. in their study found out the dynamic response of an Euler–Bernoulli beam with different boundary conditions [5] acted upon by moving loads using Green's function method and showed the effects of velocity of moving load. Parhi et al. studied in their article [6] a computational work followed by experiments to study the response of a cracked beam acted upon by a moving mass. The cracks are situated at different locations on the beam with different crack depths. Runge–Kutta method is used here to find the response of the cracked beam. Jena et al. in the research article [7] found the dynamic responses of a cracked-type simply supported beam. The response of the simply supported structure is found using Duhamel integral method and validated with the result obtained through ANSYS 2015 along with experimental results. Moving loads effects greatly on structures over which it travels. The effects include intense vibration of the structure, mainly at high velocities of the moving masses. The specialities of moving loads are they are not constant. They are subjected to change in both space and time. During modern era, the means of transport are going faster and heavier, while the structures which support them are going more slender and lighter. This causes the moving loads to produce higher dynamic stresses which are larger by multiple times than the static ones. Among all engineering structures, majority are subjected to loads which vary with respect to time and space. The effects of moving loads are substantial on the dynamic behavior of the engineering structures.

## 2 Response of a Beam Subjected to a Moving Mass

The dynamic response of a cantilever beam subjected to a moving mass under various conditions has been studied in the present work. The differential equation of a beam, which is assumed as an Euler–Bernoulli beam subjected to a concentrated force, is given by Foda and Abduljabbar [8]



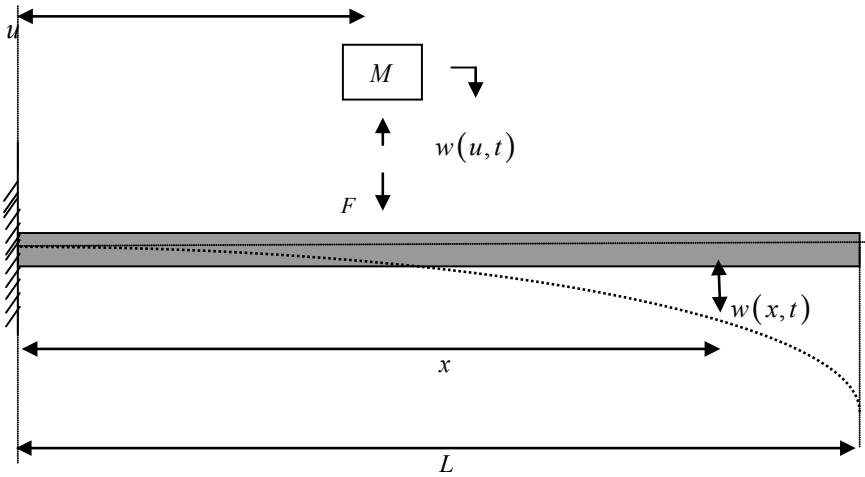


**Fig. 1** A mass moving over a cantilever beam with uniform velocity

$$EI \frac{\partial^4 w(x, t)}{\partial x^4} + m \frac{\partial^2 w(x, t)}{\partial t^2} = F \delta(x - u) \tag{1}$$

where  $E$  is Young’s modulus of the beam,  $I$  is area moment of inertia of the beam cross section,  $m$  is the mass per unit length of the beam,  $x$  is the coordinate along the axis,  $t$  is the time, and  $w(x, t)$  is the transverse displacement of the beam at a distance  $x$  and time  $t$ .  $F$  is the concentrated force applied, and  $\delta(x - u)$  is the Dirac delta function (Fig. 1).

From the above figure [9], we can see,  $F$  is the reaction force of the mass  $M$  on the beam. When Newton’s second law is applied to the mass  $M$ , we can find that

$$F = M \left( g - \frac{\partial^2 \beta}{\partial t^2} \right) \tag{2}$$

Here,  $\beta$  is the displacement of the mass along transverse direction, and  $g$  is the acceleration due to gravity. Hereinafter, we will use the notation

$$\beta(t) = w(x, t)_{x=u}. \tag{3}$$

The solution of the differential Eq. (1) is obtained using dynamic Green’s function. If  $G(x, u)$  is the dynamic Green’s function [10], the solution of the differential Eq. (1) is given in the form of

$$w(x, t) = G(x, u)F \tag{4}$$

Here,  $G(x, u)$  is the solution of the differential equation given by

$$\frac{\partial^4 w(x)}{\partial x^4} - q^4 w(x) = \delta(x - u), \tag{5}$$

where  $q$  is known as the frequency parameter and is given as

$$q^4 = \frac{\omega^2 m}{EI} \tag{6}$$

where  $\omega$  is the frequency that explains the motion of the mass and is equal to  $\frac{\pi v}{L}$ .

Equation (5) has the solution in the form of

$$G(x, u) = \begin{cases} A_1 \cos(qx) + A_2 \sin(qx) + A_3 \cosh(qx) + A_4 \sinh(qx) & 0 \leq x \leq u \\ B_1 \cos(qx) + B_2 \sin(qx) + B_3 \cosh(qx) + B_4 \sinh(qx) & u \leq x \leq L \end{cases} \tag{7}$$

With proper boundary conditions, the Green’s function calculated for the cantilever beam is given by [8]

$$G(x, u) = \frac{1}{2EIq^3 \Delta} \begin{cases} g(x, u) & 0 \leq x \leq u \\ g(u, x) & u \leq x \leq L \end{cases} \tag{8}$$

where

$$g(x, u) = D_1(\cos qx - \cosh qx) + D_2(\sin qx - \sinh qx) \tag{9}$$

Here

$$\Delta = 2(1 + \cos qL \cosh qL)$$

$$D_1 = (\cos qL + \cosh qL)(\sin z + \sinh z) - (\sin qL + \sinh qL)(\cos z + \cosh z)$$

$$D_2 = (\sin qL - \sinh qL)(\sin z + \sinh z) + (\cos qL + \cosh qL)(\cos z + \cosh z)$$

And  $g(u, x)$  is obtained by changing  $x$  and  $u$  in  $g(x, u)$  and  $z = q(L - u)$ .

If we eliminate  $F$  from Eq. (4), it becomes

$$w(x, u) = G(x, u)M \left[ g - v^2 \frac{d^2 \beta}{du^2} \right] \tag{10}$$

Equation (10) above gives the deflection of the beam at a position  $x$  caused by the moving load which is at position  $u$ .

The solution of Eq. (10) is found out by replacing the derivatives by their finite difference approximation. If we divided the beam into  $(N - 1)$  intervals and each interval is of length  $h$ , the Eq. (10) in discretized form is given by

$$w(x_i, u) = G(x_i, u)M \left[ g - v^2 \frac{d^2 \beta}{du^2} \right] \tag{11}$$

The subscript  $i$  in the above equation signifies any one of the  $N$  discrete points also called station. The Houbolt method [11] is used as  $u$  is equivalent to the time variable  $f(u)$  which is approximated as

$$\frac{d^2 f}{du^2} = \frac{1}{h^2} \sum_{k=0}^3 a_k f(u_{j-k}) + O(h^2) \tag{12}$$

Here,  $u_j$  signifies that the moving mass is at the  $j$ th station. The coefficient  $a_k$  is taken to be  $a_0 = 2, a_1 = -5, a_2 = 4, a_3 = -1$ . Substituting Eq. (12) in Eq. (11) gives the results in the form of the following set of equations:

$$h^2 w(x_i, u_j) = G(x_i, u_j)M \left[ h^2 g - v^2 \sum_{k=0}^3 a_k w(x_{j-k}, u_j) \right], i, j = 1, 2, \dots, N \tag{13}$$

Equation (13) can be exhibited in matrix form [8]:

$$[h^2[I] + a_0 v^2[G]M[P_{ij}]]\{w_{u_j}\} = M[G] \left[ h^2 g \{\Delta_{u_j}\} - v^2 \sum_{k=0}^3 a_k [P_{j,j-k}] \{w_{u_{j-k}}\} \right] \tag{14}$$

Equation (14) gives the displacement of the beam in the transverse direction when the mass is at any station  $j$ . The initial conditions signify that the mass is at the initial station point where  $j = 0$ . For this initial station, Eq. (14) will require a value of  $\{w_{u_j}\}$ , such that  $k \leq 0$ , and these values can be taken as zero.

The speed ratio  $\alpha$  is defined as

$$\alpha = \frac{vL}{\pi} \sqrt{\frac{M}{EI}} \tag{15}$$

And the critical speed  $v_{cr}$  is defined as

$$v_{cr} = \frac{2L}{T} = \frac{\pi}{L} \sqrt{\frac{EI}{m}} \tag{16}$$

The ratio  $\frac{v}{v_{cr}} = 1$  signifies resonance with the fundamental mode when the load is a constant load.

### 3 Numerical Analysis

The displacement of the beam at any time can be obtained from Eq. (14). The values of the dynamic response have been calculated for cantilever beams. The materials considered are steel, which are mostly used in the construction of the bridges. For these beams, the displacements at the end or middle points on the beam are found for different values of mass and its speed. In Eq. (14), in order to evaluate approximate response of beams, the derivatives are replaced by finite difference approximation (Fig. 2).

Here, the beam is divided into 20 intervals of length 2.5 m for the total span of 50 m. So, the number of discrete station points located on the beam is 21 stations, and therefore, displacement of the beams can be found at 21 points, while mass is moving on the span [9] (Figs. 3, 4, 5, 6, 7 and 8).

1. Beam type: Cantilever Beam.
  2. Material: Steel ( $E = 200$  GPa).
  3. Weight of the moving mass: 25,000 kg.
- 
1. Beam type: Cantilever Beam.
  2. Material: Steel ( $E = 200$  GPa).
  3. Weight of the moving mass: 50,000 kg.

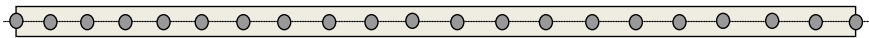


Fig. 2 A beam with 21 stations

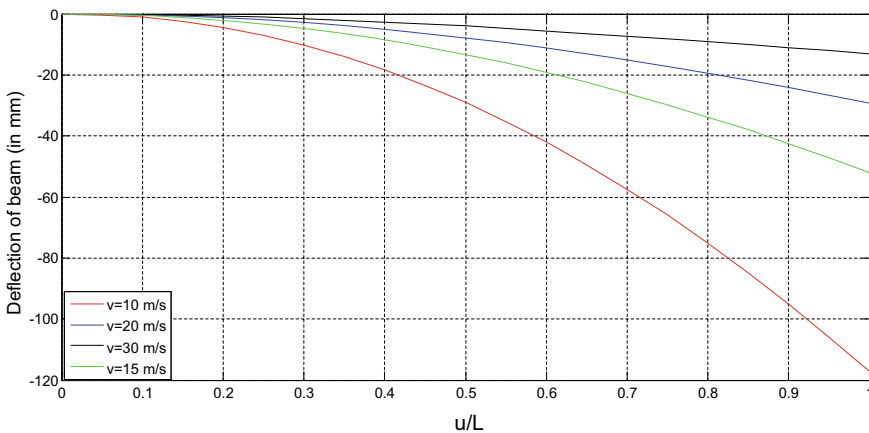


Fig. 3 Deflections of cantilever beam at the end point for different velocities as shown

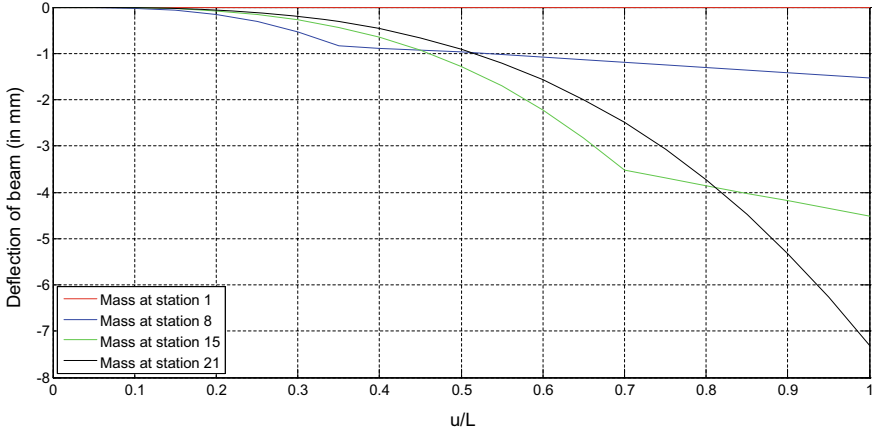


Fig. 4 Shape of the beam when the mass is moving through different stations at velocity of 30 m/s

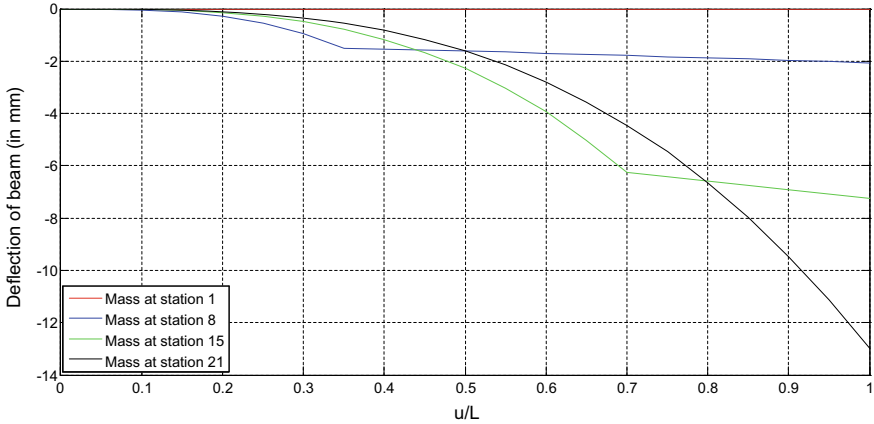


Fig. 5 Shape of the beam when the mass is moving through different stations at velocity of 40 m/s

### 4 Conclusion

As numerical results are obtained the dynamic response of cantilever beam acted upon by a moving mass, they are plotted for deflection of the beam versus position of the moving mass. The following conclusions may be made from the plots and numerical analysis:

1. It can be seen that the deflection at the free end of the cantilever beam decreases as the velocity of the moving mass increases. This happens because of higher velocity of the moving mass. The lower modes of the cantilever beam are not excited as the mass moves with higher velocities over it. The lower modes of

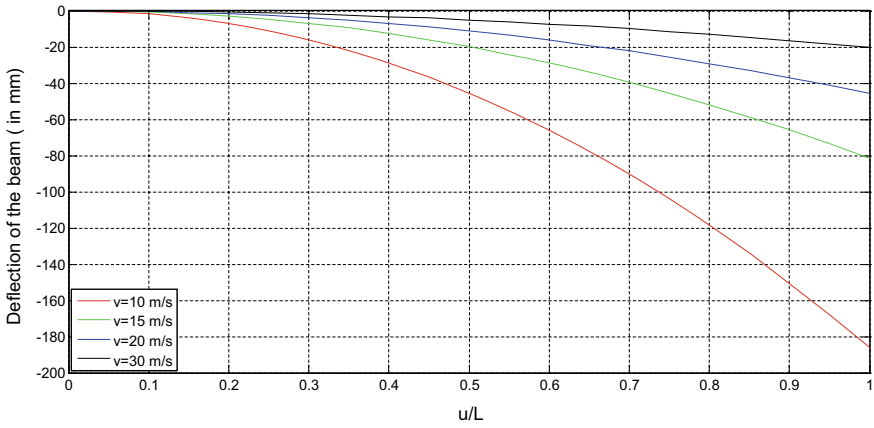


Fig. 6 Deflections of cantilever beam at the end point for different velocities as shown

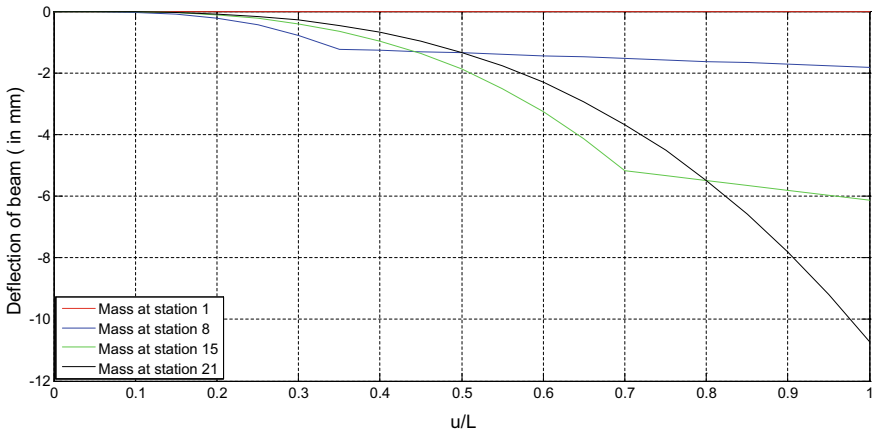


Fig. 7 Shape of the beam when the mass is moving through different stations at velocity of 30 m/s

vibration of the beam contribute mainly for larger deflection as compared to that of higher modes of vibration of the beam, so dynamic deflection of the beam decreases.

2. It can also be seen that, for a cantilever beam subjected to a moving mass over it, the free end deflection increases, as the mass of the moving body increases. This happens due to increase in inertia of the moving mass.

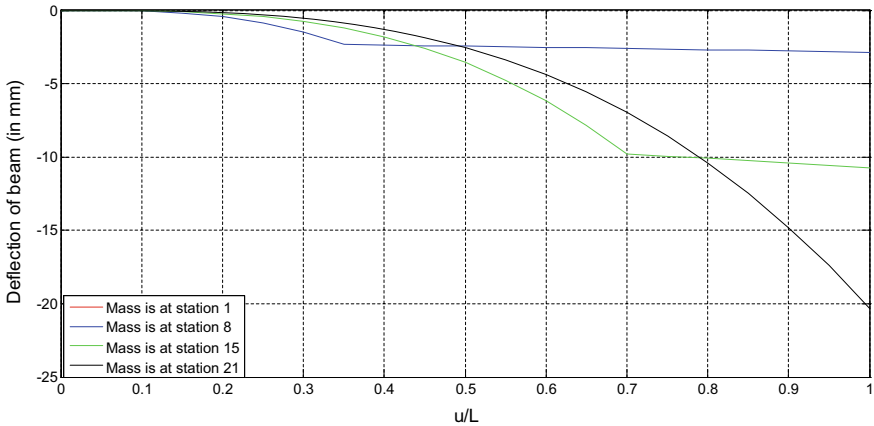


Fig. 8 Shape of the beam when the mass is moving through different stations at velocity of 40 m/s

## References

- Willis R (1849) Report of the Commissioners Appointed to Inquire into the Application of Iron to Railway Structures. Stationary Office, London
- Fryba L (1972) Vibration of solids and structures under moving loads. Noordhoff International, Groningen
- Mohamed AS (1994) Tables of Green's function for the theory of beam vibrations with general intermediate appendages. *Int J Solids Struct* 31(23):257–268
- Lueschen GGG, Bergman LA, Macfarland DM (1996) Green's functions for uniform Timoshenko beams. *J Sound Vib* 194(1):93–102
- Mehri B, Davar A, Rahmani O (2009) Dynamic Green function solution of beams under a moving load with different boundary conditions. *Scientia Iranica* 16(3):273–279
- Parhi DR, Jena SP (2017) Dynamic and experimental analysis on response of multi-cracked structures carrying transit mass. *Proc Inst Mech Eng, Part O: J Risk Reliab* 231(1):25–35
- Jena SP, Parhi DR, Subbaratnam BB (2017) Parametric evaluation on the response of damaged simple supported structure under transit mass. *ASME. Gas Turbine India Conference* 2:V002T05A003
- Foda MA, Abduljabbar Z (1997) A dynamic Green function formulation for the response of beam structures to a moving mass. *J Sound Vib* 230(3):295–306
- Meher S (2012) Dynamic response of a beam structure to a moving mass using Green's function. National institute of technology, Rourkela
- Roach G F (1981) Green's Functions. Cambridge University Press, Cambridge
- Bert CW, Stricklin JD (1988) Comparative evaluation of six different numerical integration methods for non-linear dynamic systems. *J Sound Vib* 127(2):221–229

# A Programmatic Approach for the Prediction of Service Life of Deep Drawing Die Using ANN



Vishal Naranje and Sachin Salunkhe

**Abstract** The present work is concerned with fatigue life prediction of active components of deep drawing dies. Finite element analysis is performed, and S-N approach is used to evaluate the number of cycles of deep drawing die. Based on the available evaluated data (from FE analysis) and mathematical formulae, the ANN program is developed in the MATLAB, which is used to predict the fatigue life of active components of deep drawing dies. The developed ANN program achieved satisfactory results and verified based on a demonstration of an industrial component.

**Keywords** Deep drawing die · FE analysis · S-N approach · Artificial neural network · MATLAB

## 1 Introduction

Press tool is widely used to manufacture the sheet metal parts for various industrial and domestic applications. These sheet metal parts are used in automobile, aerospace, electronics, kitchen utensils, etc. Design of press tool is very time consuming and experienced-based task. The quality of parts, produced by press tool, reflects the service life of die. A well-trained and experienced-based die designer can accurately predict the service life of dies used in press tool. Since most of the sheet metal industries fall in category of small- and medium-scale industries, these industries do not have experienced die designer to predict accurately service life of die. Another way of prediction of die service life is through experimentation, which is time consuming and tedious task. Due to the work pressure, industry people do not have much time to conduct experimentation to find the accurate service life of die. It results in poor quality of produced sheet metal parts and in some cases failure of complete assembly

---

V. Naranje (✉)

Department of Mechanical Engineering, Amity University, 345019 Dubai, UAE

e-mail: [vnaranje@amityuniversity.ae](mailto:vnaranje@amityuniversity.ae)

S. Salunkhe

Department of Mechanical Engineering, Vel Tech Rangarajan Dr. Sagunthala R&D Institute of Science and Technology, Avadi, Chennai, Tamil Nadu 600062, India

© Springer Nature Singapore Pte Ltd. 2020

H. K. Voruganti et al. (eds.), *Advances in Applied Mechanical Engineering*,

Lecture Notes in Mechanical Engineering,

[https://doi.org/10.1007/978-981-15-1201-8\\_52](https://doi.org/10.1007/978-981-15-1201-8_52)



due to these poor quality parts. Hence, there is a need to develop an automated system which will help the die designer to predict the service life of die.

Worldwide research community widely uses artificial neural network (ANN) as an intelligent tool to address the limitations of commercial software and experimental studies. In the proposed work, MATLAB programme has been developed using ANN algorithm to predict service life of deep drawing dies. In the present work, ANN is used to predict the life of deep drawing die. Initially, through analytical method, the number of service cycles of deep drawing die has been calculated. A FEA software is used for the determination of stresses occurred at different stages of deep drawing process. The output of FE analysis (maximum and minimum principal stress) is the inputs of ANN programme. Recently, various researchers are used ANN model for prediction of the performance of various manufacturing processes. Very few researchers have been used ANN tool for prediction of life of press tool components. A few attempts have made like Lange et al. [1], Ahn et al. [2], Hambli et al. [3], Kashid and Kumar [4–6], Salunkhe et al. [7–9], etc. Some other researchers used ANN to predict the fatigue life of the parts by other manufacturing processes, such as welding, Pan et al. [10], Keller et al. [11], Patel et al. [12]. From the reviewed literature, it is observed that some researchers have developed a system using ANN to predict the fatigue life of specific manufacturing areas. There are only a few research efforts are reported in the literature for prediction of fatigue life of deep drawing die. Therefore, there is a need to develop system which can help the die designer for prediction of tool life.

## **2 Methodology for Die Fatigue Life Prediction and Assessment**

The procedure used for the prediction of die life is given as below. The first step is the development of CAD model of active and passive die components. The active die components such as punch and die have the major chance of failure during the working life if press tool. Hence, for analysis, the active die components are selected (as punch). The next step is to carry out finite element analysis using suitable FE software. Static structural analysis is performed on the active components of deep drawing dies. The boundary conditions for the analysis are the total force required to draw the components at each drawing stages. Here, we consider the deep drawing operation having the four stages of draw. For each stage, a separate CAD model is prepared and set the boundary conditions for each stage. The maximum draw force is determined by addition of punch force and blank holder force. The maximum and minimum principal stresses are obtained from FE analysis software. Based on obtained stresses values, the number of cycles is evaluated [13].

### 3 ANN Module for Prediction of Life of Deep Drawing Die

The ANN module is developed using MATLAB 2014R. In this study, the feed forward network and fit net function are used to perform the prediction function. The log-sigmoid transfer function is chosen as an activation function, which is given as below.

$$\text{Output}(a) = \log \text{sig}(\text{input}) = \frac{1}{1 + e^{-n}}$$

The input selected to ANN is the results generated from FE analysis. As a thumb rule, the two-third data are selected for training, and one-third data are selected for testing. The input for ANN is the maximum and minimum principal stress and the ultimate tensile strength of press tool material. Initially, the four-hidden layer ANN architecture is constructed, and afterwards, the hidden layers are increased progressively. After every design of ANN network, the error variation in FEM and output generated by ANN is checked. The network gives the small disparity between FEM and ANN that architecture has been selected. Levenberg–Marquardt Back Propagation training function has been used to supervise the training of the network. The train the network, a learning rate is set as 0.5 and the maximum epoch are set to 2000. These settings help to perform more iterations, and therefore, it results more accurate prediction from ANN.

### 4 Validation of the Proposed System

The proposed model has been tested by considering the problem of fatigue life prediction of die components and die assembly of deep drawing die for a real industrial deep drawn part. 3D CAD models of punch (Fig. 2a–c) for each draw stage were created from the 2D design data obtained from industry M/s Vishwadeep Enterprises, Pune, India, for an example, deep drawn part as shown in Fig. 1. The material selected for FE analysis of punch is CALMAX, and its mechanical properties are given in Table 1.

A hex dominant elements are used to mesh the punches geometry is shown Fig. 3. Total force acting on the punch is obtained by addition of maximum punch force and blankholder force. For stage 1, total force acting on the punch is  $348.3408 \times 10^3$  N. Similarly, total force acting on punch in stage 2 and 3 is  $152.6685 \times 10^3$  N and  $68.1657 \times 10^3$  N, respectively. Outputs of FE the analysis of these punches are shown in Fig. 4, and results are summarized in Table 2. The number of cycles is calculated using S-N curve also mentioned in Table 2 [7]. From the FE analysis results, it has found the critical region which is shown by red contours in Fig. 4. Also, there are some stress concentration occurs in the regions where sudden change in geometry is present.

**Fig. 1** Example component

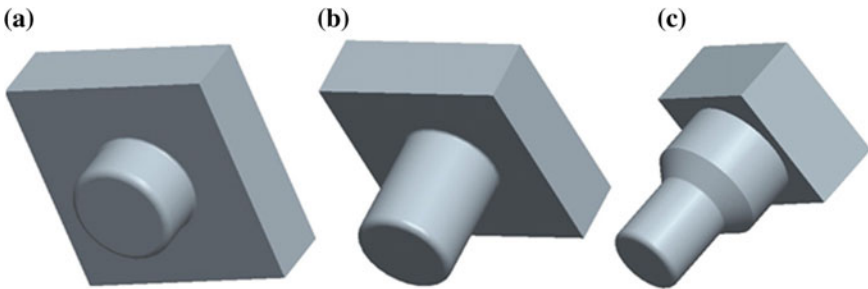
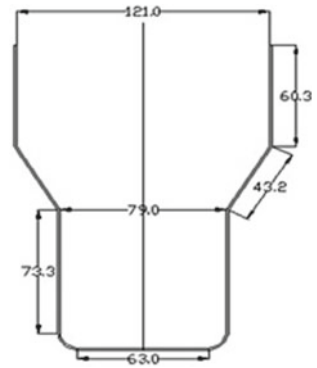


**Fig. 2** Drawing punch for stage 1, stage 2, stage 3

**Table 1** Material properties of punch material

Material properties	Values
Young’s modulus ( $E$ )	210 GPa
Poisson’s ratio ( $\nu$ )	0.29
Tensile yield stress ( $\sigma_{yt}$ )	1400 MPa
Ultimate tensile strength	2100 MPa
Compressive strength	2300 MPa
Density ( $\rho$ )	7770 kg/m <sup>3</sup>
Modulus of rigidity	80 GPa

Figures 5 and 6 show the performance plot error histogram for stage 1. Figure 7 shows scatter diagram with ANN prediction versus experimental weld parameters for test data.

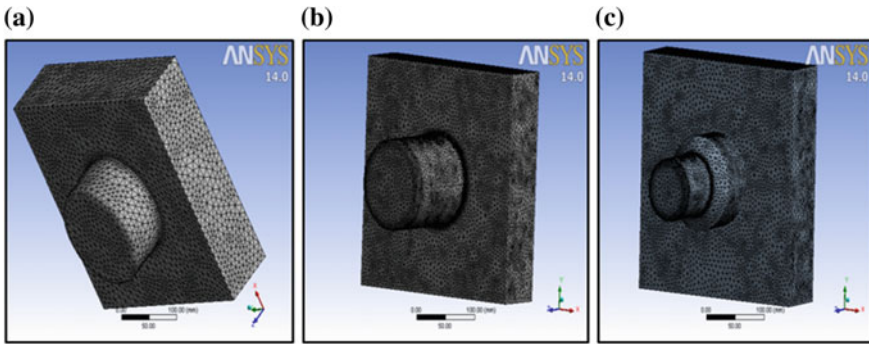


Fig. 3 Meshing punches geometry for each stage

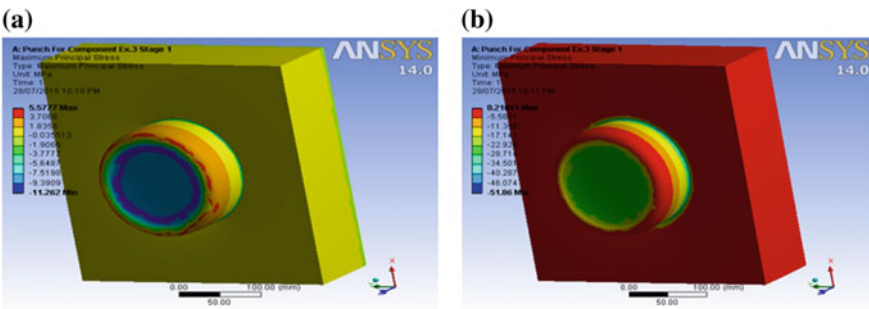


Fig. 4 a Maximum b Minimum principal stress of punch for stage 1

## 5 Conclusions

In this study, ANN approach has been used conjunction FEM analysis to predict life of deep drawing die. This approach reduces the time required for complete FEA analysis and final prediction of die life. Furthermore, a detailed analysis shows the influencing factors responsible for die life. It also proved that ANN predicts the die life near to actual results, and hence, it is an effective tool to improve productivity, reduce manufacturing cost and decrease defective item during production. A sample run on typical deep drawing die punch for each stage demonstrated the usefulness of the developed program. The similar approach can also be used to predict life of blanking, bending, extrusion, compound, progressive die, etc.

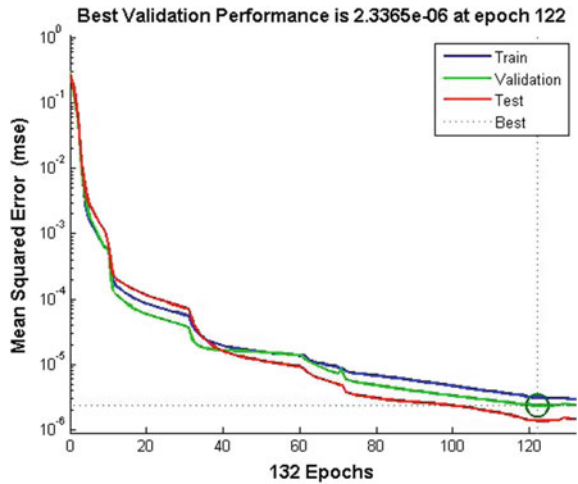
## 6 Sample of Code

```
File_Name = input('n\nSpecify the Excel Workbook Sheet Name = ','s');
```

**Table 2** Sample output of FE analysis, analytical results and ANN results for punch at stage 3

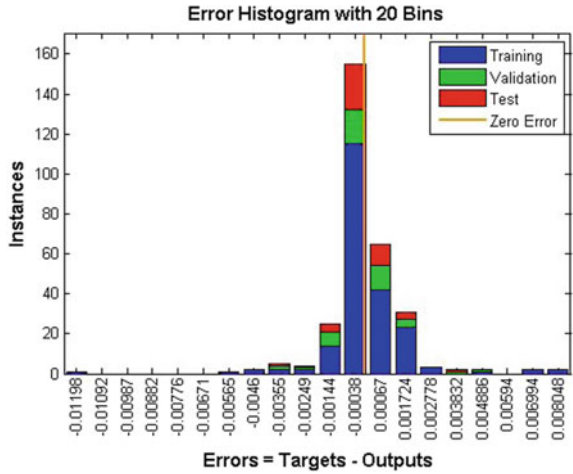
Max. principal stress (MPa)	Min. principal stress (MPa)	Analytical results (Number of cycles)	ANN predicted result
-11.274	-39.145	981,108	981,192
-11.036	-38.74	981,371	981,373
-11.021	-38.658	981,417	981,417
-10.988	-38.623	981,443	981,442
-10.965	-38.586	981,467	981,467
-10.954	-38.577	981,474	981,474
-10.927	-38.534	981,502	981,502
-10.925	-38.481	981,530	981,530
-10.919	-38.48	981,532	981,532
-10.902	-38.431	981,561	981,562
-10.899	-38.424	981,566	981,566
-10.898	-38.347	981,606	981,606
-10.887	-38.333	981,616	981,615
-10.873	-38.32	981,625	981,625
-10.871	-38.318	981,627	981,627

**Fig. 5** Performance plot for stage 1



```
Data_Inputs = xlsread(File_Name);
Read_Data = input('\nEnter the Number of Data Points to be Read for Analysis
from Excel Workbook Sheet = ');
UTS = input('\nEnter the Value of Ultimate Tensile Strength of Tool
Material = ');
EL = 0.5*UTS;
```

**Fig. 6** Error histogram plot for stage 1



```

Input_1st = Data_Inputs(1:Read_Data,1);
Input_2nd = Data_Inputs(1:Read_Data,2);
-----
-----
    Fatigue_Strength(i) = (Amplitude_Stress(i)/(1-(Mean_Stress(i)/UTS)));
end
Z = zeros (1,ND);
W = zeros (1,ND);
Constant_b = zeros (1,ND);
for i = 1:ND
    Z(i) = (Amplitude_Stress(i)/EL);
    W(i) = (log10(Z(i)));
    Constant_b(i) = -(W(i))/3;
end.
    
```

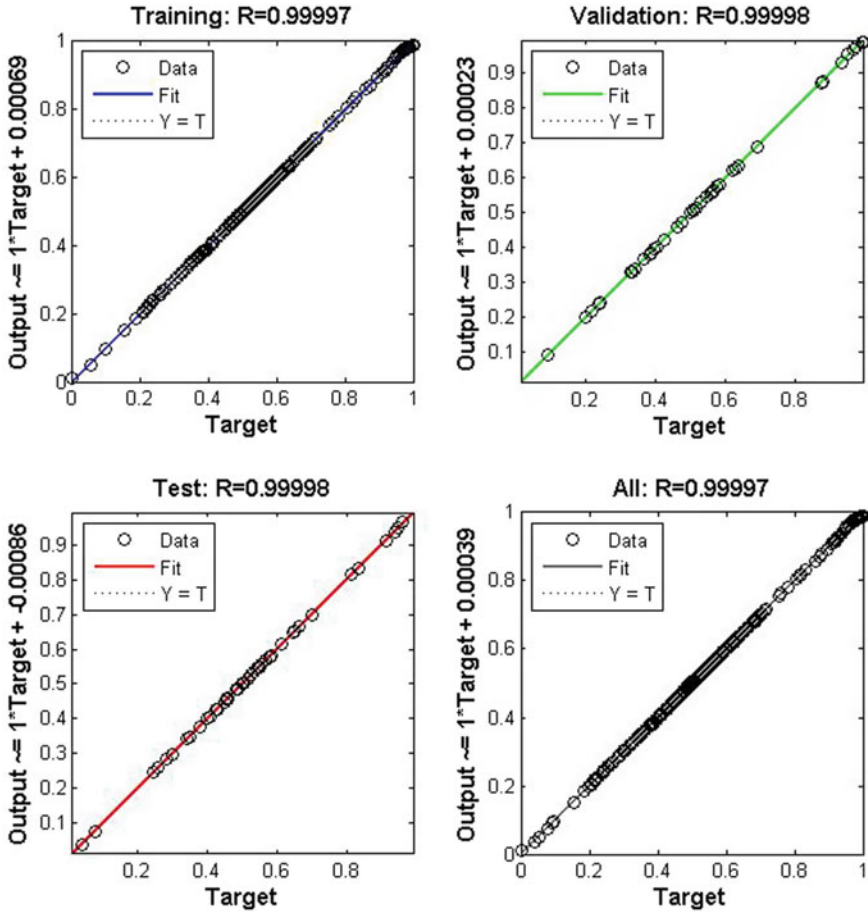


Fig. 7 Regression plot for stage 1

## References

1. Lange K, Hettig A, Knoerr M (1992) Increasing tool life in cold forging through advanced design and tool manufacturing techniques. *J Mater Process Technol* 35:495–513
2. Ahn SH, Kim TH, Kim BM, Choi JC (1997) A study on the prediction of fatigue life in an axi-symmetric extrusion die. *J Mater Process Technol* 71:343–349
3. Hambli R, Soulat D, Chamekh A (2009) Finite element prediction of blanking tool cost caused by wear. *Int J Adv Manuf Technol* 44:648–656
4. Kashid S, Kumar S (2014) Prediction of life of punches of compound die using artificial neural network. In: 5th international and 26th all India manufacturing technology, design and research conference. IIT Guwahati
5. Kashid S, Kumar S (2014) Prediction life of compound die using artificial neural network. *Key Eng Mater* 622–623, 664–671
6. Sachin Kashid, Kumar S, Hussein HMA (2015) Selection, modeling and prediction of life of stripper of compound die. *Key Eng Mater* 639:501–508

7. Salunkhe Sachin, Rajamani D, Balasubramanian E, Chandrasekhar U (2019) Prediction of life of piercing punches using artificial neural network (ANN) and adaptive neuro fuzzy inference systems (ANFIS). *Int J Mater Eng Innov* 10(1):20–33
8. Salunkhe Sachin, Rajamani D, Balasubramanian E (2018) Application of artificial neural network ANN and adaptive neuro fuzzy inference systems ANFIS for prediction of life of stripper. *Int J Mod Manuf Technol* 10(1):76–83
9. Salunkhe S, Rajamani D, Balasubramanian E (2019) Artificial neural network (ANN) and adaptive neuro fuzzy inference systems (ANFIS) for predicting the life of blanking Punch. *Adv Struct Mater*. [https://doi.org/10.1007/978-3-030-02257-0\\_1](https://doi.org/10.1007/978-3-030-02257-0_1)
10. Pan J, Sripichai K, Lin PC, Wang DA, Lin SH (2010) Mechanics modeling of spot welds under general loading conditions and applications to fatigue life predictions. In: Sun X (ed) *Failure mechanisms of advanced welding processes*. Woodhead Publishing, USA
11. Keller T (2010) *Failure mechanisms of advanced welding processes fatigue life prediction of bonded joints in composite structure*. In: Sun X (ed) *Failure mechanisms of advanced welding processes*. Woodhead Publishing, USA
12. Patel VK, Bhole SD, Chen DL (2014) Fatigue life estimation of ultrasonic spot welded Mg alloy joints. *Mater Des* 62:124–132
13. Naranje V, Salunke S, Kumar S, Ghodke A (2014) Prediction of life of deep drawing die using artificial neural network. *Advances in Material and Processing Technology*, Dubai



# Thermo-Mechanical Analysis of Unidirectional PALF Composites Using Micromechanical Approach



Anurag Jasti and Sandhyarani Biswas

**Abstract** In the past few years, natural fibers became one of the most widely used materials in place of synthetic fibers to develop composites as it attains some inherent characteristics like renewable resource and biodegradability. Pineapple leaf fiber (PALF) is one of the natural fibers which can be used as reinforcement to develop composites. The objective of the present work is to carry out the analytical study of mechanical and thermal properties of fiber-reinforced polymer composites. PALF in unidirectional form is used as reinforcement with varying fiber volume fraction ( $v_f$ ) ranging from 10 to 70% and epoxy as the matrix material to carry out the work. Representative elementary volume (REV)-based micromechanical analysis is used to determine elastic and thermal properties of composites. The results obtained from this analysis are compared with that of the existing analytical methods. The results show good agreement between the results of finite element analysis (FEA) and analytical methods.

**Keywords** REV · Micromechanical analysis · Pineapple leaf fiber · FEA

## 1 Introduction

The composite material can be characterized as a material consisting of two or more chemically distinct constituents, separated by an interface. Most composites have two constituents: one is reinforcement, and the other one is matrix. The individual parts are independently and autonomously inside the completed structure. The features like biodegradability, renewability, lightweight, and low-cost-made natural fibers gain popularity in the field of composites. A number of investigations have been carried out to assess the potential of natural fibers as reinforcement in polymers [1–4]. Among the various natural fibers such as jute, sisal, bamboo, coir, and banana, pineapple leaf fiber (PALF) is one of the most promising one due to its many advantages. But, a very few researches have been done on the use of PALF as reinforcement

---

A. Jasti (✉) · S. Biswas  
National Institute of Technology, Rourkela 769008, India  
e-mail: [anurag.jasti@gmail.com](mailto:anurag.jasti@gmail.com)

© Springer Nature Singapore Pte Ltd. 2020  
H. K. Voruganti et al. (eds.), *Advances in Applied Mechanical Engineering*,  
Lecture Notes in Mechanical Engineering,  
[https://doi.org/10.1007/978-981-15-1201-8\\_53](https://doi.org/10.1007/978-981-15-1201-8_53)

for polymer composites. George et al. [5] made an experimental study on the short PALF-reinforced LDPE composites. The influence of orientation, fiber loading, and length on the elastic properties of composites has been studied.

Most of the studies indicate that the mechanical and thermal properties of natural fiber composites are greatly influenced by many factors related to natural fibers. In order to determine the properties of composites, two types of approaches are generally used such as micromechanical approach and macromechanical approach. Micromechanical analysis helps to study the properties of composites at fiber and matrix level; whereas, macromechanical analysis considers the composite material as homogeneous orthotropic continuum [6]. In micromechanical analysis, the properties of composites are generally calculated using REV with either square or hexagonal geometry [7, 8]. Facca et al. [9] predicted the elastic modulus of different types of natural fiber-reinforced HDPE composites by varying the volume fraction of the fibers. Pal et al. [10] predicted the elastic properties of polypropylene fiber-based polymer composites by using REV model. Ramani et al. [11] studied the thermal conductivity of composites by finite element method with parallelepiped and spherical fillers. Cao et al. [12] estimated the thermal conductivity of fiber composites through REV with single and multiple fibers by using hybrid FEA based on homogenization technique. The present work is undertaken to study the mechanical and thermal behavior of unidirectional PALF-reinforced polymer composites.

## 2 Materials and Methods

In the present work, epoxy is taken as matrix phase and unidirectional pineapple leaf fiber (PALF) as reinforcement. The matrix and fibers are considered to be homogeneous and isotropic. For the ease of analysis, the fibers are considered to be arranged

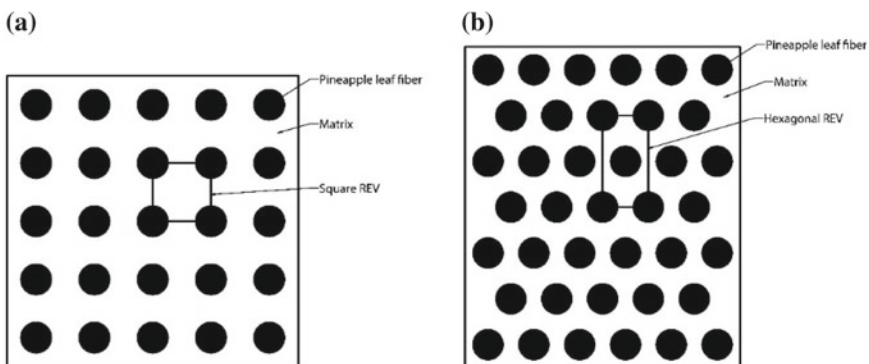


**Fig. 1** Fiber arrangement in **a** square REV with circular fiber and **b** hexagonal REV with circular fiber

**Table 1** Thermal and mechanical properties of epoxy and pineapple leaf fiber [2, 13]

Properties	PALF	Epoxy
Density ( $\text{g/cm}^3$ )	1.52	1.15
Young's modulus (Gpa)	62	3.76
Poisson's ratio	0.07	0.39
Shear modulus (Gpa)	28.97	1.28
Thermal conductivity (W/mK)	0.0273	0.363

and aligned perfectly (Fig. 1). The constituent materials properties are shown in Table 1.

## 2.1 Generation of REV

For the ease of analysis, the periodic arrangement of fibers is considered for micromechanical modeling of composites, where the unit cell or REV can be isolated. The  $\nu_f$  and elastic constants are the same for REV and composite. Hexagonal and square array are the commonly used periodic sequences for composite analysis.

Figure 2a, b represents square REV with circular and square fibers, respectively. Figure 2c, d represents hexagonal REV with circular and square fibers, respectively. Generally, more compact composite can be achieved with hexagonal packing geometry rather than square packing geometry.

## 2.2 Analytical Methods

To evaluate the properties of a composite, many analytical methods have been developed by many researchers over the years. From these models, some are selected for the analysis. This includes the rule of mixture, Halpin–Tsai model for analyzing elastic properties of composite. Chawla and Hashin models are most commonly used methods for predicting the thermal conductivity of unidirectional fiber-reinforced composite materials which are used here [14, 15].

## 2.3 FEA

There are many assumptions made for the ease of analysis. It is assumed that the arrangement and alignment of fibers in the matrix are regular, and the interface between the matrix and fiber is perfectly bonded. It is considered that the composite is free of voids. The axis 1 is aligned with the fiber direction, and axis 2 and 3 are perpendicular to the direction of fibers.  $\nu_f$  ranging from 0.1 to 0.7 is considered in

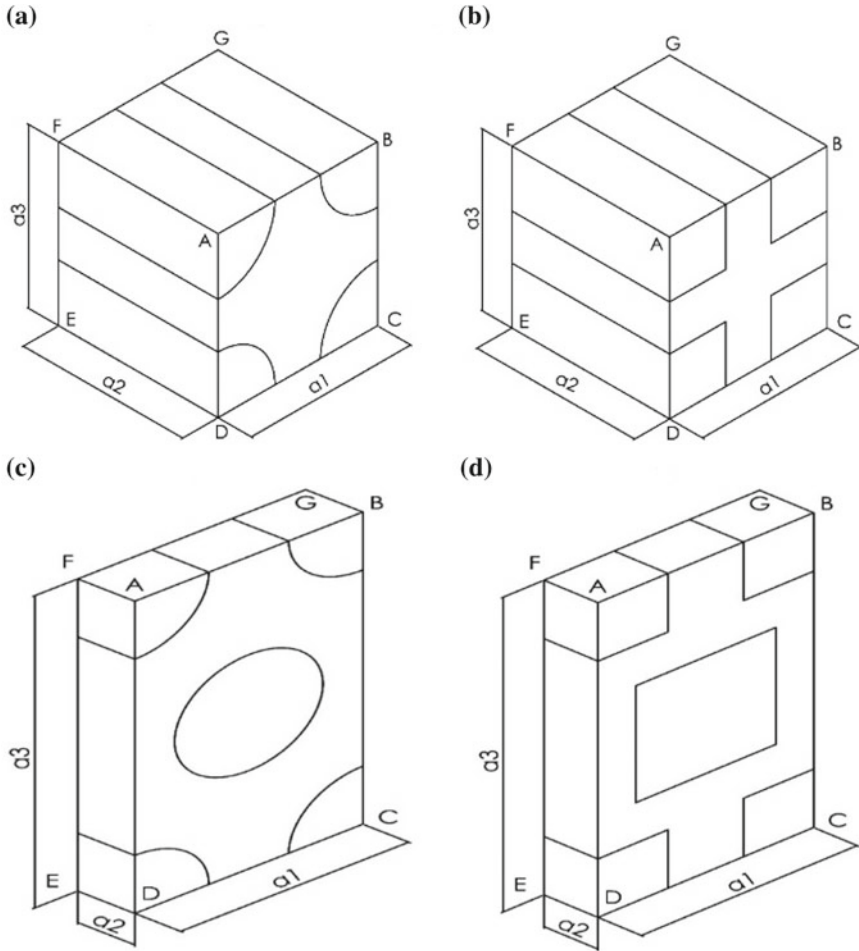


**Fig. 2** Unit cells of **a** square REV with circular fiber, **b** square REV with square fiber, **c** hexagonal REV with circular fiber, and **d** hexagonal REV with square fiber

the analysis. As REV models are considered for analysis, periodic boundary conditions are to be applied. After applying the corresponding boundary conditions for different load steps, various engineering constants were obtained using stress and strain equations of composites.

To predict the transverse and longitudinal thermal conductivity of the composite, steady state heat transfer simulations are done using FEA. For thermal analysis, a temperature difference of 100 K is applied between two opposite faces, and rest of the faces are subjected to insulation boundary condition. The heat flux was obtained

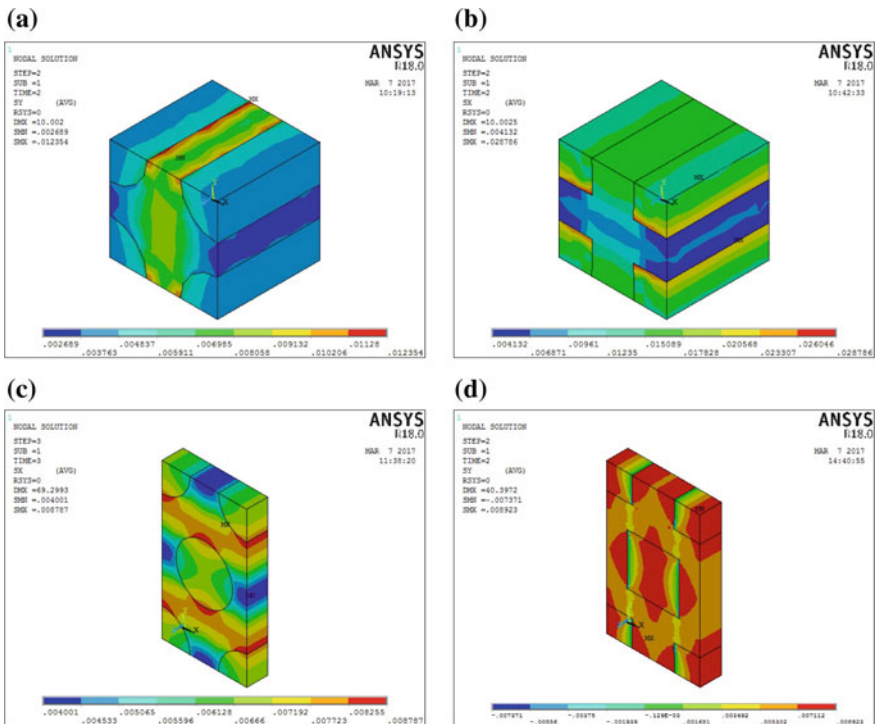
using the temperature gradient obtained from FEA. The heat conduction law is used to determine the effective thermal conductivity.

### 3 Results and Discussion

#### 3.1 Effect of Fiber Volume Fraction on Elastic Properties of Composites

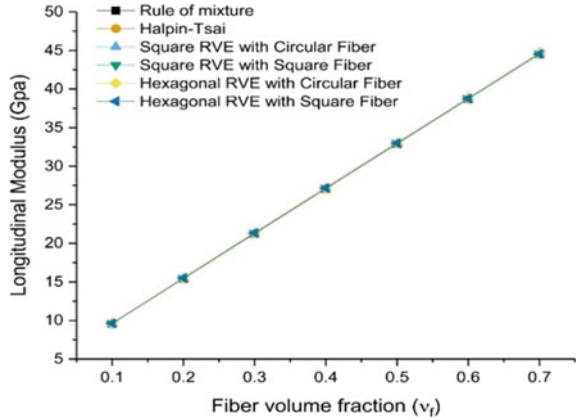
Figure 3 shows the stress distribution in hexagonal and square REV at 0.4  $v_f$ .

Figure 4 shows the effect of  $v_f$  on longitudinal modulus of composites analyzed by different methods. It is observed from the figure that longitudinal modulus of composites increases with increase in  $v_f$  irrespective of the analytical methods and FEA. Generally, with the increase in  $v_f$ , the stiffness of material increases which may lead to the increase in longitudinal modulus of composites. It is also observed that the results of FEA are in good agreement with the results obtained by the existing

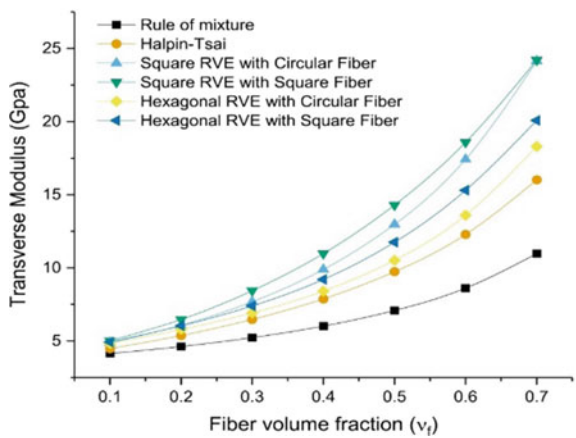


**Fig. 3** Stress gradient in **a** square REV with circular fiber, **b** square REV with square fiber, **c** hexagonal REV with circular fiber, and **d** hexagonal REV with square fiber

**Fig. 4** Effect of  $\nu_f$  on longitudinal modulus of composites



**Fig. 5** Effect of  $\nu_f$  on transverse modulus of composites



analytical methods. Figure 5 shows the variation of transverse modulus of composites with  $\nu_f$ . It can be seen that the transverse modulus increases with the increase in  $\nu_f$ . The results obtained by hexagonal REV are closer to Halpin–Tsai model. Figure 6 shows the variation of in-plane Poisson’s ratio with  $\nu_f$ . It is observed that the Poisson’s ratio of composites decreases with the increase in  $\nu_f$ . The results obtained by FEA are in good agreement with that of analytical methods. Similarly, Fig. 7 shows the effect of  $\nu_f$  on the in-plane shear modulus of composites. It is evident from the figure that the in-plane shear modulus of composites increases with the increase in  $\nu_f$ , and the results obtained by hexagonal REV are closer to the Halpin–Tsai model.

**Fig. 6** Effect of  $\nu_f$  on in-plane Poisson's ratio of composites

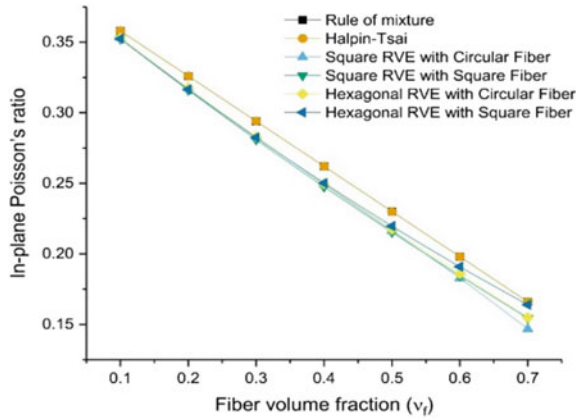
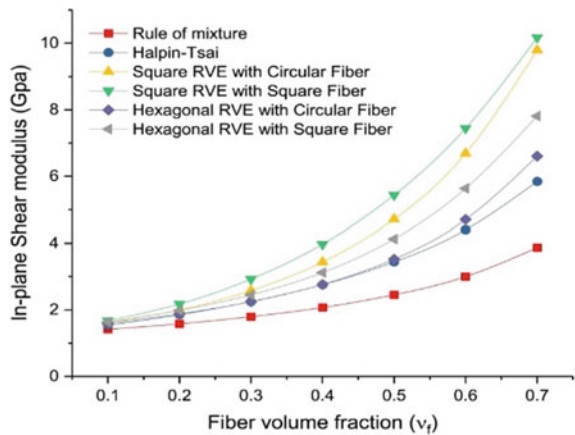


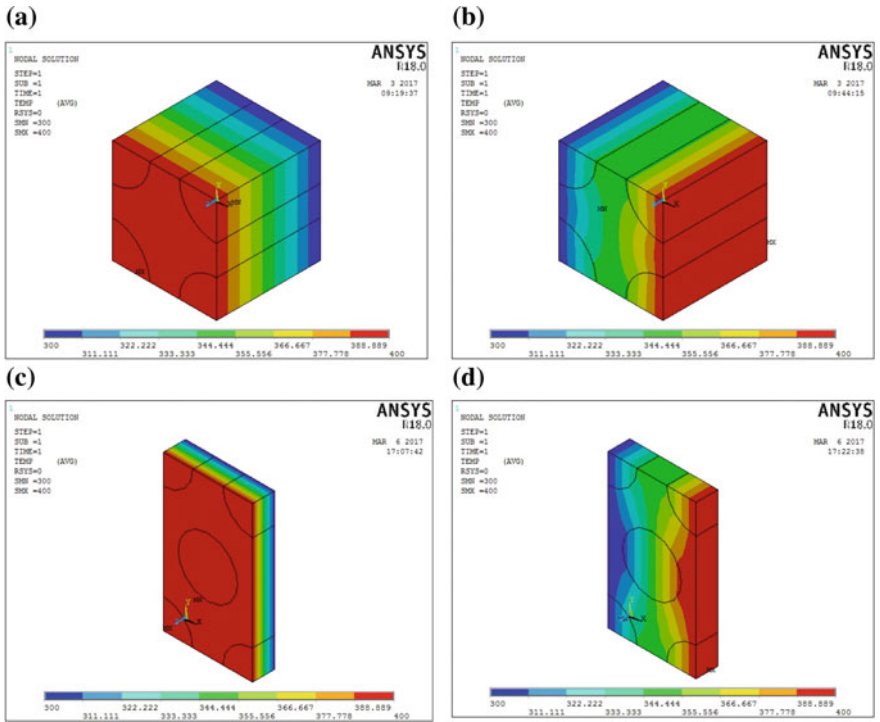
**Fig. 7** Effect of  $\nu_f$  on in-plane shear modulus of composites



### 3.2 Effect of Fiber Volume Fraction on Thermal Conductivity of Composites

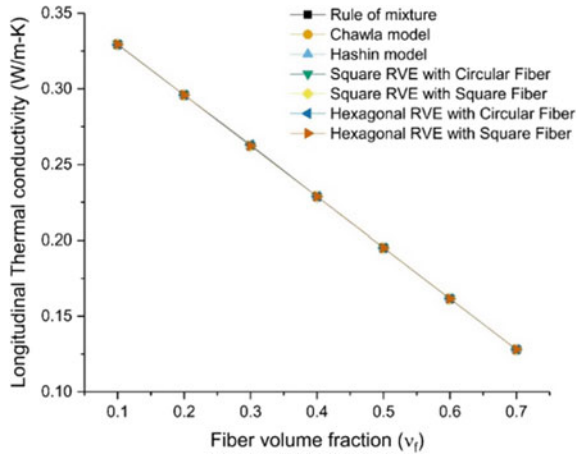
Figure 8 shows the longitudinal and transverse temperature gradient in hexagonal and square REV at 0.4  $\nu_f$ .

Figure 9 shows the variation of longitudinal thermal conductivity of composites with the  $\nu_f$  by different methods. It is observed from the figure that the longitudinal thermal conductivity of composites decreases with increase in  $\nu_f$ . It is also evident that the results of FEA are in good compliance with the results obtained by other analytical methods. Similarly, Fig. 10 shows the effect of  $\nu_f$  on transverse thermal conductivity of composites. From the graph, it is clear that the transverse thermal conductivity of composites decreases with the increase in  $\nu_f$ . The results obtained by FEA are in good agreement with Hashin model.



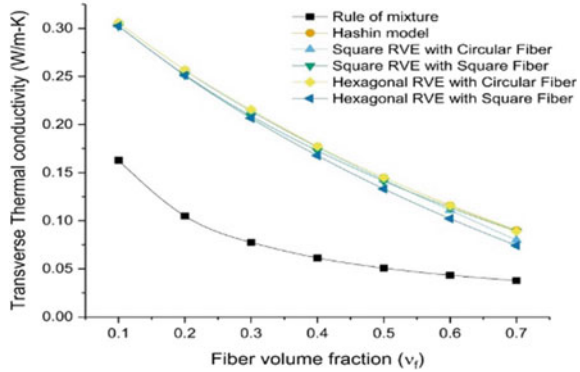
**Fig. 8** Longitudinal and transverse temperature gradient for square REV with circular fiber (a, b) and hexagonal REV with circular fiber (c, d), respectively

**Fig. 9** Effect of  $v_f$  on longitudinal thermal conductivity of composites





**Fig. 10** Validation of transverse thermal conductivity with varying  $v_f$



### 4 Conclusion

In the present study, the effective thermal and elastic properties of unidirectional PALF-reinforced epoxy composites with different  $v_f$  have been evaluated using micromechanical approach. The results obtained from FEA are compared with the different analytical methods. The present study leads to the following conclusions:

- The elastic properties of the composites such as in-plane Poisson’s ratio and longitudinal modulus predicted by FEA are in good agreement with the analytical methods. However, the in-plane shear modulus and transverse modulus values of composites predicted by FEA are closer to the results obtained by Halpin–Tsai model.
- The longitudinal thermal conductivity values obtained by FEA are in good compliance with the analytical methods. However, the transverse thermal conductivity values predicted by FEA are closer to Hashin model.
- From the study, it is clear that the effective thermal and elastic properties of unidirectional fiber-reinforced composites are significantly influenced by  $v_f$ .

### References

1. Biswas S (2013) Mechanical properties of bamboo-epoxy composites a structural application. *Adv Mater Res* 1:221–231
2. Devireddy SBR, Biswas S (2016) Physical and thermal properties of unidirectional banana-jute hybrid fiber-reinforced epoxy composites. *J Reinf Plast Compos* 35:1157–1172
3. Mishra V, Biswas S (2013) Physical and mechanical properties of bi-directional jute fiber epoxy composites. *Procedia Eng* 51:561–566
4. Monteiro SN, Terrones LAH, D’Almeida JRM (2008) Mechanical performance of coir fiber/polyester composites. *Polym Test* 27:591–595
5. George J, Bhagawan SS, Prabhakaran N, Thomas S (1995) Short pineapple-leaf-fiber-reinforced low-density polyethylene composites. *J Appl Polym Sci* 57:843–854

6. Aboudi J (1989) Micromechanical analysis of composites by the method of cells. *Appl Mech Rev* 42:193
7. Hashin Z, Rosen BW (1964) The elastic moduli of fiber-reinforced materials. *J Appl Mech* 31:223
8. Anurag J, Biswas S, Devireddy S (2017) Finite element analysis of mechanical and thermal properties of polymer matrix composites. In: *Primary and secondary manufacturing of polymer matrix composites*. CRC Press, Taylor & Francis Group, pp 121–141. 6000 Broken Sound Parkway NW, Suite 300, Boca Raton, FL 33487–2742 (2017)
9. Facca AG, Kortschot MT, Yan N (2006) Predicting the elastic modulus of natural fibre reinforced thermoplastics. *Compos Part A Appl Sci Manuf* 37:1660–1671
10. Pal B, Riyazuddin Haseebuddin M (2012) Analytical estimation of elastic properties of polypropylene fiber matrix composite by finite element analysis. *Adv Mater Phys Chem* 02:23–30
11. Ramani K, Vaidyanathan A (1995) Finite element analysis of effective thermal conductivity of filled polymeric composites. *J Compos Mater* 29:1725–1740
12. Cao C, Yu A, Qin Q-H (2012) Evaluation of effective thermal conductivity of fiber-reinforced composites. *Int J Archit Eng Constr* 1:14–29
13. Abdan K, Jawaid M, Dashtizadeh Z, Asim M, Nasir M, Ishak MR, Hoque ME (2015) A review on pineapple leaves fibre and its composites. *Int J Polym Sci* 2015:1–16
14. Wetherhold RC, Wang J (1994) Difficulties in the theories for predicting transverse thermal conductivity of continuous fiber composites. *J Compos Mater* 28:1491–1498
15. Chawla KK (1985) *Composite materials: science and engineering*. Springer-Verlag

# Analysis and Selection of Bio-stents Using Finite Element Method



Jannatul Bashar and K. Jayabal

**Abstract** Considerable research has been devoted to the design, optimization, and development of bio-stents in the last few decades. This paper reviews many existing stents and suggests an optimized structure of stent that satisfies all constraint functions including stress generation in the artery since the arteries also have some limitation in enduring stresses both in longitudinal and circumferential directions. The best stent structure among the seven optimized stents reported in the literature, based on the combined behavior of the artery and the stent-like foreshortening and elastic radial recoil, is suggested. A unit cell of the stent is considered along with a cylindrical artery to reduce the computational time. The finite element method is used to determine the mechanical integrity of the stents at various load conditions during and after its deployment. The stent is also analyzed for two different materials, stainless steel and Nitinol, that are used for stent manufacturing and the results are reported.

**Keywords** Bio-stent · Finite element method · Structural analysis

## 1 Introduction

The annual world data of the number of people who died as a result of specific diseases in 2016 shows that cardiovascular disease has taken the first place claiming 17.65 million lives that year alone. Stent research has always been at the forefront due to its high requirement all over the world. From the bibliometric analysis, 7790 journal papers and articles have published from 1986 to 2013. In the Web of Science databases, the USA ranks first for contributing 24% of the publications followed by Germany with 11% and others with 65% [1].

The PCI has been well-documented as a lifesaving therapy for patients who are suffering from heart problems and also as a pain-reducing treatment for individuals with multiple blocked arteries who are suffering from angina. In this process, inject a tiny flexible guide wire into the narrowed or blocked section of the coronary artery.

---

J. Bashar · K. Jayabal (✉)

Indian Institute of Information Technology, Design and Manufacturing, Kancheepuram, India  
e-mail: [jayabal@iiitdm.ac.in](mailto:jayabal@iiitdm.ac.in)

© Springer Nature Singapore Pte Ltd. 2020

H. K. Voruganti et al. (eds.), *Advances in Applied Mechanical Engineering*,

Lecture Notes in Mechanical Engineering,

[https://doi.org/10.1007/978-981-15-1201-8\\_54](https://doi.org/10.1007/978-981-15-1201-8_54)

After that, a thin tube called a balloon catheter is pushed over the guide wire whose function is to expand it radially and to assist in pushing plaque against the artery wall ensuring blood flow. The stent is nothing but a tiny wire mesh made up of superelastic material locates permanently into an artery to hold it open. After placing the stent, the catheter is withdrawn from the body.

The studies by Amirjani et al. [2] and Tammareddi et al. [3] through finite element analysis (FEA) and angioplasty tests have shown that the stent structure plays an essential role in Percutaneous Coronary Intervention (PCI). To analyze the best stent structure, we collected seven optimized stents structure reported in different pieces of literature and compared their mechanical behaviors and used various metrics such as recoiling and foreshortening to measure the adverse effects of stent deployment on damage to arterial and restenosis. This analysis is on a single blocked artery.

The stent dimensions depend on an individual's artery and plaque size; however, here, the analysis is considered for the same size artery. Selection of the best stent is based on defined necessitate functions. There are three major parts in this analysis, namely the stent, the balloon, and a cylindrically shaped artery. One-eighth part of the whole model has been taken for the analysis to gain the computational advantage. The best stent structure among the considered ones is suggested based on its performance accounting various factors.

## 2 Method

### 2.1 Stent Model

Seven models are considered from the previously published literature and named as Model A, Model B, Model C, Model D, Model E, Model F, and Model G in the present manuscript. The first two models, Model A and Model B, are based on the optimization of the stent parameters suggested by Amirjani et al. [2]. The Model C and Model D have a tapered strut profile to reduce strain fields along the strut axis as proposed by Alaimo et al. [4]. The Model E and Model F are developed whose diameter will vary depending upon the varying plaque size for a fixed artery diameter through altering the link angle, also known as apex angle,  $\alpha$ . To deal with such cases, the stents should have reduced diameter but without compromising its expansion or uncoiling ability. Thus, the parameters of Model E and Model F are the same as models A and B, respectively, however, differing only in the link angle. The structure of these two models E and F are slightly similar to the one suggested by Pauck et al. [5]. Model G is based on a multi-objective robust optimization [3]. All these seven models are taken for the present analysis.

The data available for coronary artery dimensions in an Indian population varies from 2.6 to 4.52 mm [6, 7]. Therefore, an established artery dimension has taken for appropriate comparison among seven stents. The inner and outer diameters of the artery are 2.8 mm and 3.5 mm, respectively, and the thickness of intima, media,

and adventitia are 0.3, 0.25, and 0.15 mm, respectively. All the models are shown in Fig. 1 and the meshing of parts is shown in Fig. 2. The parameters of the stent are given in Table 1.

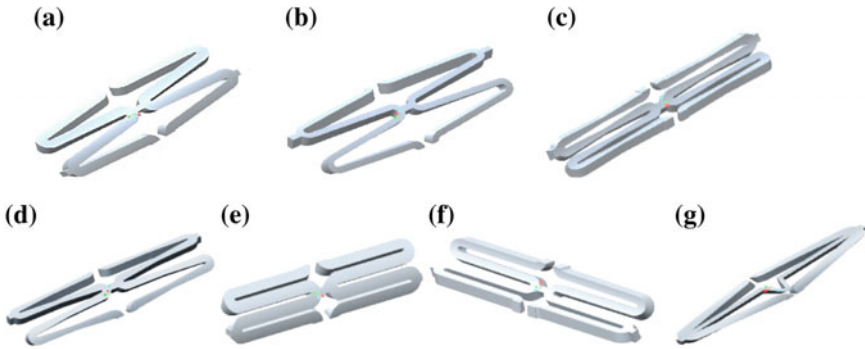


Fig. 1 Stent models a Model A b Model B c Model C d Model D e Model E f Model F g Model G

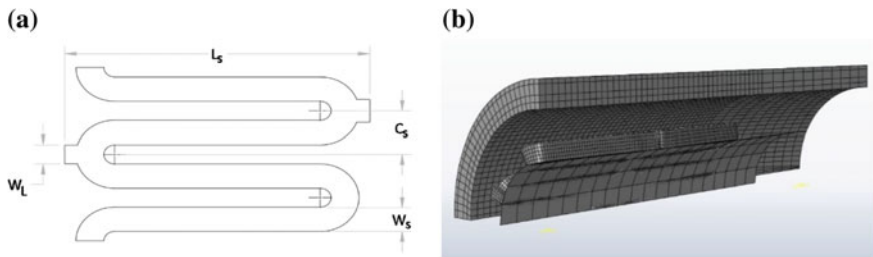


Fig. 2 a Dimensioning parameters. b Meshing of the artery, stent, and balloon

Table 1 Input parameters of the strut in mm

Stent	Outer Dia $D_o$	Thickness $t$	Length $l_s$	Strut width $W_s$	Centerline space $C_s$	Link width $W_1$	Link angle $\alpha^\circ$
Model A	2.03718	0.22	1.4	0.21	0.4	0.125	11.4
Model B	2.03718	0.22	1.4	0.13	0.4	0.125	11.4
Model C	2.03718	0.22	2.0	0.21	0.4	0.18	9.43
Model D	1.32417	0.18	2.0	0.21	0.26	0.21	0
Model E	2.03718	0.22	1.4	0.21	0.4	0.125	11.4
Model F	1.33769	0.18	1.4	0.163	0.26	0.125	0
Model G	1.32420	0.2	1.7	0.19	0.26	0.125	0

**Table 2** The coefficients of the constitutive model for each layer of the artery [5]

Artery layer	C10	C20	C30	C40	C50	C60
Intima	6.79E-03	0.54	-1.11	10.65	-7.27	1.63
Media	6.52E-03	4.89E-02	9.26E-03	0.76	-0.43	8.69E-02
Adventitia	8.27E-03	1.2E-02	0.52	-5.63	21.44	0.00

**Table 3** Material properties of stainless steel and Nitinol

Young's modulus (GPa)	Density (Kg/m <sup>3</sup> )	Poisson's ratio	Yield strength (MPa)	Plastic strain
Stainless steel 316 l				
196	8000	0.3	205	0
			515	0.6
Nitinol				
41	6450	0.33	140	0
			895	0.45

## 2.2 Material

Three coats of an artery, namely adventitia, media, and intima, are considered as incompressible isotropic hyperelastic material. For each layer, the coefficients of reduced polynomial strain energy potential are listed in Table 2. The six-ordered constitutive equation is described as,

$$U = \sum_{i+j=1}^N C_{ij} (\bar{I}_1 - 3)^i (\bar{I}_2 - 3)^j + \sum_{i=1}^N \frac{(J_{el} - 1)^{2i}}{D_i} \tag{1}$$

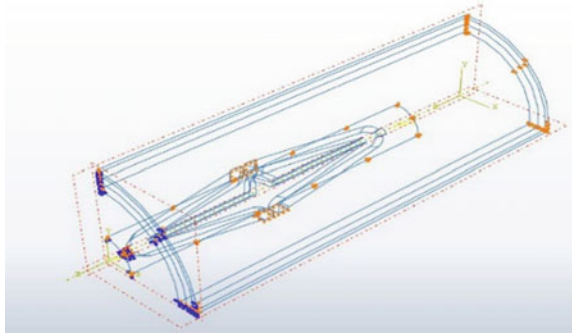
where  $I_1$  and  $I_2$  are the strain invariants and  $D_i$  indicate the compressibility. The material will become incompressible when the second term disappears in Eq. (1).

Elastic-plastic materials such as the stainless steel 316L (SST) [5] and the most biocompatible material Nitinol [8, 9] are used as the stent materials and their material properties are compiled in Table 3.

## 2.3 Finite Element Analysis

The following element types are used for the different parts in the assembly; an eight-node linear brick element C3D8R for the stent, a four-node quadrilateral surface element SFM3D4 for the balloon, and an eight-node linear brick hybrid element C3D8H for the artery.

**Fig. 3** Boundary condition applied for the models



The boundary conditions are enforced appropriately to the one-eighth part of the model as shown in Fig. 3. The radial displacements are specified to the balloon for its expansion instead of using pressure boundary conditions, as per reverse engineering by Jiao et al. [10].

## 2.4 Objective and Constraints

Our objective is to minimize the stress on the stent, stress on the artery, foreshortening Khosravi et al. [11], elastic radial recoil. The constraint functions subjected to, maximum circumferential arterial stress  $\leq 1.43$  MPa [4], maximum longitudinal arterial stress  $\leq 1.3$  MPa [4], recoil  $\leq 30\%$ , and the foreshortened length of stent  $\geq$  length of plaque.

## 3 Results

After completion of all simulations, the mechanical integrity such as the stress generation on the stent's curvature portion, arterial stress, PEEQ, foreshortening, recoil, and longitudinal stretch, also termed as foreshortening of the artery, are extracted from FEA output database. The maximum stress in the stent and the artery at each stage are obtained. As the stent acts as a scaffold, it uncoils its loop portion to hold artery permanently; therefore, the stent's curve portion experiences a plastic stage of the material that is measured by PEEQ, an equivalent plastic strain. The foreshortening is the reduction in length of the stent after the expansion and would affect the area of contact. The stent alone needs to hold the artery after the balloon deflation, and the arterial pressure acts on the stent's outer surface causing a decrease in its diameter, known as recoil. All these parameters related to mechanical integrity are compared for all the models chosen.

**Table 4** Maximum stress on the stent, arterial stress, PEEQ, foreshortening, recoil for each model of SST

Design name	Stent stress (MPa)	Artery stress (MPa)	PEEQ	Recoil (mm)	Foreshortening stent (mm)	Longitudinal stretch artery (mm)
Model A	307.04	6.49	0.198	0.060	0.101	0.767
Model B	247.27	7.62	0.082	0.100	0.084	0.661
Model C	250.27	8.06	0.088	0.090	0.065	0.901
Model D	241.91	0.33	0.071	0.690	0.028	0.211
Model E	299.85	0.09	0.183	0.300	0.060	0.111
Model F	228.75	0.25	0.046	0.289	0.050	0.164
Model G	275.17	0.435	0.165	0.255	0.000	0.167

### 3.1 Model Comparison

Initially, to compare all the models in view of choosing the optimized one, stainless steel is used as the stent material in all the stents. The model that is satisfying all the constraint functions is selected as the best stent structure among all of them. The results obtained are shown in Table 4, whereas the corresponding contour plots are displayed in Fig. 4. The plots are with respect to time that shows the mechanical integrity at each stage of PCI deployment.

From Table 4 and as per our objective, the maximum stent stress should be as low as possible. Accordingly, models B, C, D, F, and G are preferable over the other two models. Similarly, for arterial stress, the models D, E, F, and G are performing better than the other models. As far as PEEQ is concerned, the models A, E, and G can outperform the rest of the models. From the stent foreshortening point of view, the models D, E, F, and G outshine the other models. For recoil, the models A, B, C, E, F, and G are more effective than the Model D. Finally, for the longitudinal stretch of an artery, the models E, F, and G outperform the remaining models. From the above comparison, it is clear that the Model G performs better than the other models as it has satisfied all constraint and objectives functions.

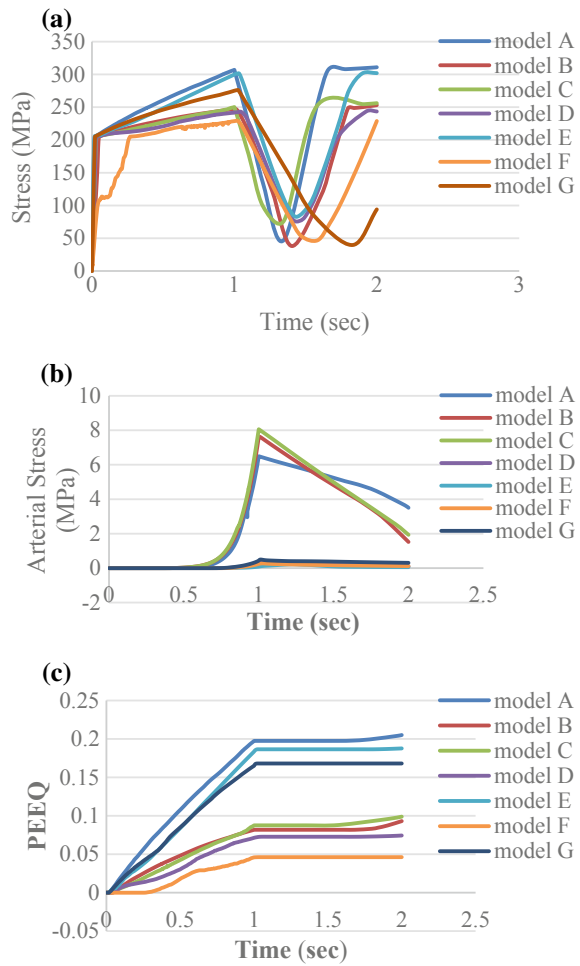
The stainless steel, the material used for all stents in previous comparisons, is now compared with Nitinol material for Model G restoring the same objective and constraint functions. The comparison result is shown in Fig. 5 and the mechanical integrities are listed in Table 5.

## 4 Conclusions

Seven bio-stent designs from the literature were chosen in this work in order to find out which one among them is better. Each model has its own advantageous and shortcomings attributing to various reasons. In the present work, we take several



**Fig. 4** a Stress on the stent. b Arterial stress and c PEEQ for all the models with respect to time



parameters to suggest the stent design that appears best among the seven chosen ones; stent stress, arterial stress, PEEQ, foreshortening, recoil, and foreshortening of the artery. It is suggested from the analysis that Model G with Nitinol material seems a better choice overall as compared with other stent models chosen for comparisons. This work may help to provide some additional input for further improvements in the bio-stent design.

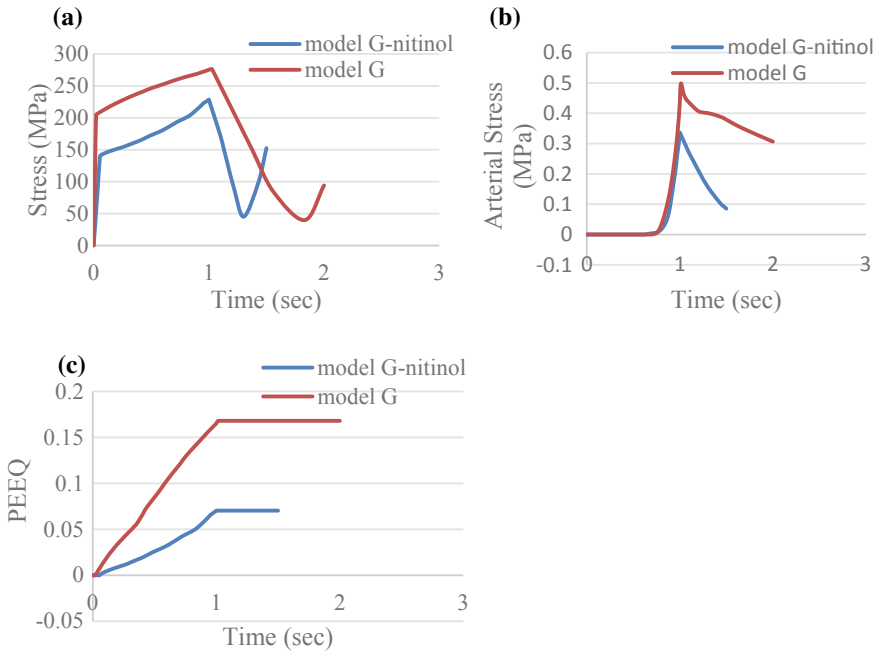


**Fig. 5** Comparison of Model G between stainless steel and Nitinol materials **a** stress on the stent **b** arterial stress and **c** PEEQ

**Table 5** Nitinol material results

Design name	Stent stress (MPa)	Artery stress (MPa)	PEEQ	Recoil (mm)	Foreshortening stent (mm)	Longitudinal stretch artery (mm)
Model G–Nitinol	228.5	0.336	0.07	0.105	-4.70E-03	0.143

## References

1. Ahn S, Sung JS, Choi B, Kim H, Sung YK (2014) Recent trends on the stent research for blood arteries by bibliometric analysis. *Biomater Res* 18(1):17
2. Amirjani A, Yousefi M, Cheshmaroo M (2014) Parametrical optimization of stent design; a numerical-based approach. *Comput Mater Sci* 90:210–220
3. Tammareddi S, Sun G, Li Q (2016) Multiobjective robust optimization of coronary stents. *Mater Des* 90:682–692
4. Alaimo G, Auricchio F, Conti M, Zingales M (2017) Multi-objective optimization of nitinol stent design. *Med Eng Phys* 47:13–24
5. Pauck RG, Reddy BD (2015) Computational analysis of the radial mechanical performance of PLLA coronary artery stents. *Med Eng Phys* 37(1):7–12
6. Raut BK, Patil VN, Cherian G (2017) Coronary artery dimensions in normal Indians. *Indian Heart J* 69(4):512–514

7. Holzapfel GA, Sommer G, Gasser CT, Regitnig P (2005) Determination of layer-specific mechanical properties of human coronary arteries with nonatherosclerotic intimal thickening and related constitutive modeling. *Am J Physiol* 289(5):H2048
8. McGrath DJ, O'Brien B, Bruzzi M, Kelly N, Clauser J, Steinseifer U, McHugh PE (2016) Evaluation of cover effects on bare stent mechanical response. *J Mech Behav Biomed Mater* 61:567–580
9. Puértolas S, Navallas D, Herrera A, López E, Millastre J, Ibarz E, Gabarre S, Puértolas JA, Gracia L (2017) A methodology for the customized design of colonic stents based on a parametric model. *J Mech Behav Biomed Mater* 71:250–261
10. Jiao GY, Li PP, Zhang RJ (2013) Application of periodic boundary conditions in studying stent expansion. *Appl Mech Mater* 419:286–291
11. Khosravi A, Bahreinizad H, Bani MS, Karimi A (2017) A numerical study on the application of the functionally graded materials in the stent design. *Mater Sci Eng, C* 73:182–188

# Electromechanical Responses of Dielectric Elastomers



Moumita Tewary and Tarapada Roy

**Abstract** Electroactive polymers (EAPs) have been widely employed as smart material for actuation and sensing in recent years. Dielectric elastomers (DEs) are a type of smart material which belongs to the class of EAPs. Their applications include soft sensing and actuation which require high sensitivity, flexibility and stretchability. They can be actuated under electric field responding to an electrostatic force. Compared with other electrical actuation technologies, the advantages of dielectric elastomer actuators include lightweight, good compliancy, high energy density, large actuation strain, quiet operation and low cost. The current research focuses on the electro-mechanical actuating behaviour of DEs embedded with composite using finite element approach. Analyses are carried out with three different support conditions of the composite, on which the elastomer is mounted, and with varying thickness and positions of elastomer on the composite at various voltage levels. Results indicate that strain in the composites increases with a decrease in the thickness of the elastomer.

**Keywords** Electroactive polymer · Dielectric elastomer · Electro-mechanical actuation

## 1 Introduction

Dielectric elastomers are a type of smart material which belongs to the class of electroactive polymers, which are made up of soft materials and are capable of changing their dimensions upon an electric stimulation. When in the generator mode, DEs convert mechanical energy to electrical energy, while they can also convert electrical energy to mechanical energy in actuator mode. DEs are a type of field-activated polymers that belong to the family of EAPs [1]. The typical assembly of a DE includes a dielectric material and two electrodes, wherein the dielectric material is sandwiched between the electrodes. These structures have high electromechanical efficiency and

---

M. Tewary (✉) · T. Roy  
National Institute of Technology, Rourkela 769008, India  
e-mail: [tewary.moumita@gmail.com](mailto:tewary.moumita@gmail.com)

© Springer Nature Singapore Pte Ltd. 2020  
H. K. Voruganti et al. (eds.), *Advances in Applied Mechanical Engineering*,  
Lecture Notes in Mechanical Engineering,  
[https://doi.org/10.1007/978-981-15-1201-8\\_55](https://doi.org/10.1007/978-981-15-1201-8_55)

can produce a large strain response, i.e. hyperelastic in nature. DEs can be used as generators, sensors and actuators based on the electromechanical effect. DEs have received significant interest in recent years for applications as electromechanical transducers, actuators, sensors and energy harvesters. The interest arises due to its attractive properties such as the ability to achieve large strains by inducing voltage, the fast deformation response, lightweight and cost-effectiveness.

DEs can be used in a wide range of applications which include structural health monitoring, robotic arms, energy harvesting, power generation, electronic skin and muscles, self-sensing actuators, sensors, etc. Some of these applications involve the use of composites. This allows an opportunity to test the elastomers when mounted on composites. The primary objective of this research is to study the electromechanical behaviour of dielectric elastomers.

## 2 Literature Review

### 2.1 On Electroactive Polymers

Electroactive polymers are those that respond to electrical signals, and significant change in dimensions is observed. The most important characteristic is the ability to induce large displacements and strains.

Much before EAPs existed, electroactive ceramics [EAC] and shape memory alloys [SMA] were the only source of actuation for smart structures and mechanisms. Application of these materials includes robotics, active damping, vibration isolation, manipulation, articulation and many others. On the other hand, little attention is given to EAPs due to the availability of lesser number of materials and their limited actuation capability [2, 3].

During the last ten years, many new and effective EAP materials have been identified and improved fabrication techniques have emerged that have demonstrated potential capabilities of these materials. Table 1 shows the comparison of some of the relevant properties of EAP, SMA and EAC [4, 5]. EAPs can induce strains that are as higher than EACs. The EAPs are broadly classified into two categories according

**Table 1** VHB tape and composite properties [21–23]

Property	Elastomer	Composite	Unit
Young's modulus	3.6e6	0.465e9	Pa
Poisson's ratio	0.4999	0.3	
Relative electrical permittivity	8.8		
Free-space permittivity	8.854e−12		F/m
Density	720	1158	kg/m <sup>3</sup>

to their mechanism; they are ionic and electric EAPs [6]. The dielectric elastomer comes under the category of electric EAPs.

## ***2.2 On Dielectric Elastomer Actuators***

Dielectric elastomer actuators (DEAs) gained popularity in the field of sensing and actuation since Pelrine et al. published their work on electrostriction of polymer dielectrics with compliant electrodes in 1999 [7]. DEAs are made of a rubbery soft dielectric elastomer sandwiched between two compliant electrodes. The two compliant electrodes act as a capacitor. The columbic force, generated due to the electric field, generates Maxwell stress between the two plates, compressing the dielectric elastomer layer due to the attraction of both the plates. This induces expansion in the DEA due to the incompressibility of the elastomer. In general, the operating voltage of DEAs is as high as  $\sim 1\text{--}10$  kV [8] which is around 100 MV/m of electric field and considerably high actuation strain over 100% [9] can be reached in the meantime.

## ***2.3 On Modelling of Elastomers***

Design and optimization are the important steps in the modelling and simulation of DE systems. This can be described by mainly two challenges. They are (i) the passive mechanical response of elastomer with history and time dependence and with large strains, and (ii) the mechanical response generated by the application of electric field (electromechanical coupling). Vast research has been done on the mechanical characterization of the elastomers [10–15] but no researchers focused on the electromechanical coupling behaviour of elastomers. No research exists on simulation of elastomers on composites, although only a few works exist on the modelling and simulation of dielectric elastomers [16–20].

# **3 Materials and Methods**

## ***3.1 Materials***

The elastic properties of 3 M VHB tapes allow to distribute loads over a larger area by accommodating differential expansion and absorbing dynamic loads. Composite made of MWCNT embedded in epoxy is used in this study. Table 1 shows the properties of 3 M VHB tapes and the composite material.

### 3.2 Methodology

A dielectric elastomer is placed between two compliant electrodes which is in turn attached to a composite beam represented in Fig. 1. An applied electric field causes the dielectric elastomer to elongate in length and compress in thickness which is represented in Fig. 2, due to Maxwell stress. This deformation in the elastomer causes the composite to bend or elongate based on the boundary conditions of the composite beam.

Due to the Maxwell stress, the elastomer film contracts in the thickness direction and expands in the film's planar directions. The direction of Maxwell stress acts in perpendicular to the DE film and the mechanical stress in radial direction ( $\sigma_r$ ) during planar actuation.

An electroelastic analysis is performed to determine the deformed shape and strain in the thickness direction ( $\epsilon_z$ ) for a static load. The position of the elastomer is varied, namely two end positions and middle position. The elastomer and the composite beam are meshed accordingly. Boundary conditions are applied based on the different supports, namely cantilever, both sides fixed and fixed roller beam. These supports are represented in Figs. 3, 4 and 5, respectively.

Fig. 1 Elastomer on composite beam

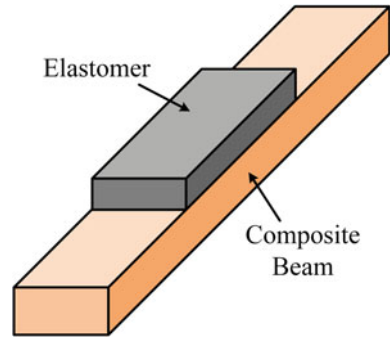
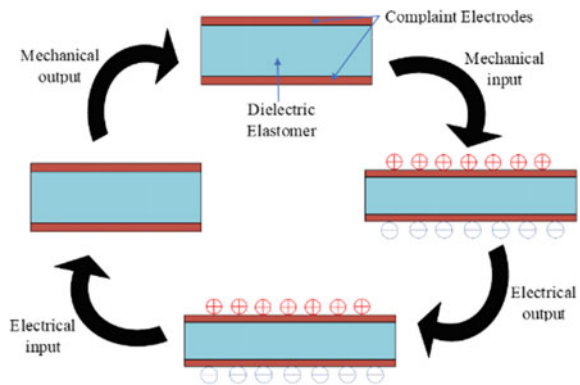
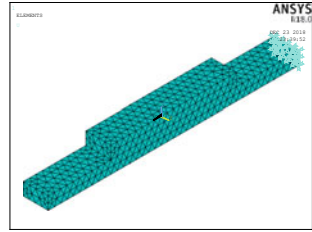


Fig. 2 Working of a dielectric elastomer



**Fig. 3** Cantilever support



**Fig. 4** Both ends fixed support

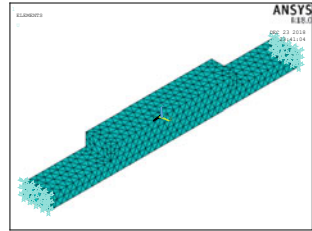
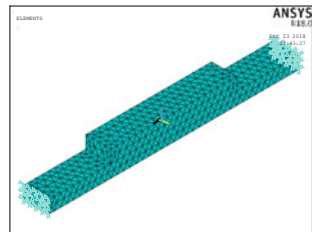


**Fig. 5** Fixed roller support



For the cantilever support, one side of the beam end is fixed in all the directions and the other end is kept free. For the both ends fixed support, both the ends are fixed in all the directions. One side of the beam is fixed in all directions, and the other end is fixed in y-direction and z-direction and allowed to move in x-direction in fixed roller support. The nodes are coupled in the top and bottom surfaces of the elastomer separately, in order to model the two compliant electrodes. For both the compliant electrodes to work, the least node on the respective faces is coupled with all the other nodes on the particular face on the elastomer. Voltage is applied on both the least nodes of both the coupled surfaces. As a voltage difference is created between the two faces, the elastomer tends to expand or compress based on the voltage difference created. The voltage is varied from 500 to 5500 V.



### 4 Results and Discussion

The deformation of the beam is measured on the free side of the cantilever beam, bottom side (i.e. side opposite to the side of the attached elastomer) of the beam with both sides fixed and on both the roller and bottom side for fixed roller beam support. Figure 6 depicts the deformation of the composite beam in cantilever support, both ends fixed support and fixed roller support when voltage is applied on the elastomer (middle position) with thickness ‘t’.

Figure 7 shows the strain in the cantilever beam for various voltages when the elastomer position is at fixed end, middle and free end. From Fig. 7, it is evident that as voltages increases, strain in the composite beam also increases. It is inferred that with reduction in the thickness of the elastomer, a higher strain can be obtained in the composite beam for a particular voltage level. This is due to the fact that the same amount of electromotive force acts on the elastomer even if the thickness varies. So, a greater deformation is obtained for a low thickness elastomer than a higher thickness elastomer for the same voltage level. It can also be seen that elastomers with higher thickness can withstand higher voltage levels.

Figures 8 and 9 show the strain for various positions of elastomer at different voltage levels for both ends fixed beam and fixed roller beam, respectively. The strains in both the cases follow the same trend as in the case of the cantilever beam.

Figure 10a shows the strain in the composite beam in cantilever support for elastomer thickness ‘t’ at different positions. From the graph, it can be inferred that

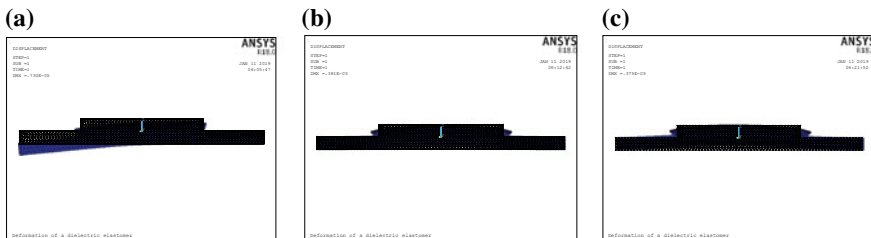


Fig. 6 a Cantilever support, b both ends fixed support and c fixed roller support

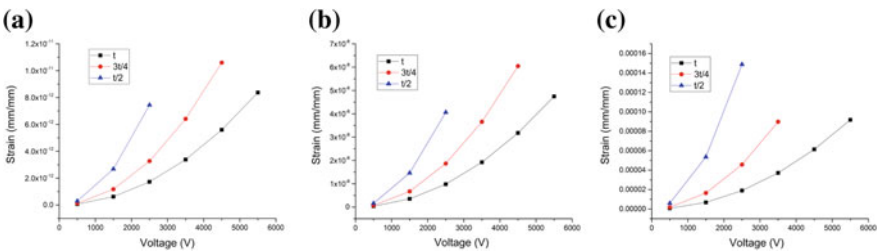


Fig. 7 Strain in cantilever beam when elastomer position is at a fixed end, b middle and c free end

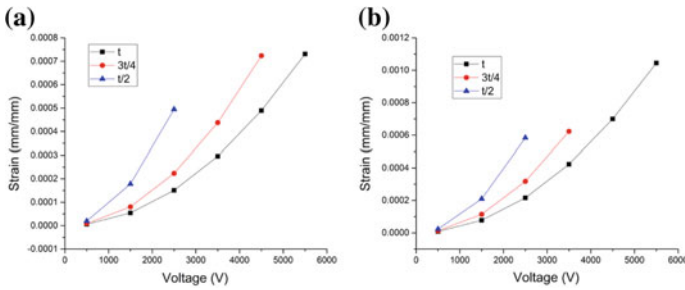


Fig. 8 Strain in both ends fixed beam when elastomer position is at **a** fixed end and **b** middle

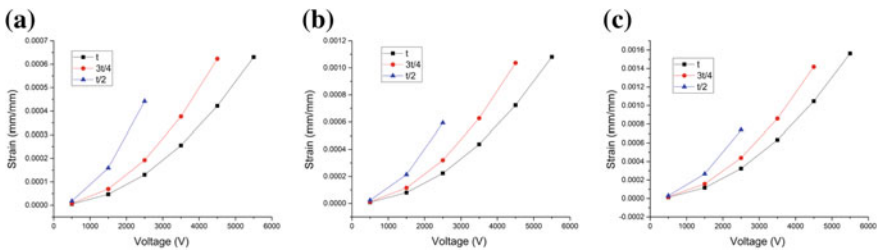


Fig. 9 Strain in fixed roller beam when elastomer position is at **a** fixed end, **b** middle and **c** roller end

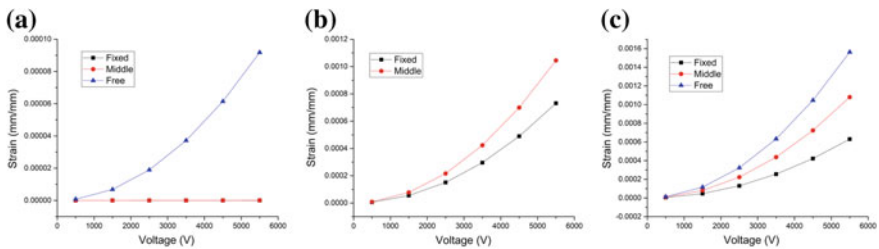


Fig. 10 Strain for various voltages in composite for different positions of elastomer and at thickness 't' for **a** cantilever, **b** both ends fixed and **c** fixed roller support

strains are very high when the elastomer is placed at free end as compared to that of the other two cases. We know that maximum displacement occurs at the free end in a cantilever beam and as the elastomer position moves from free end to fixed end, the point of application of forces moves from free end to fixed end, which in turn increases the displacement in the cantilever beam at the free end. Figure 10b shows the strain in the composite beam in both ends fixed support for elastomer thickness 't' at different positions. From the graph, it is evident that strain is more in the case of elastomer at the middle position. In general, when both the ends are fixed, maximum

deformation occurs at the middle. And if the elastomer is placed in the middle position, more force is acting at that position, which in turn produces more deformation. The variation in deformation for various positions is less as compared to that of the other supports. Figure 10c shows the strain in composite beam in the fixed roller support for elastomer thickness 't' at different positions. This case similar boundary conditions as that of the both ends fixed support, but only horizontal movement is allowed at the roller end. Similar trends in strains are observed as cantilever support. Similar trends are observed for other elastomer thickness ( $\frac{3t}{4}$ ,  $\frac{t}{2}$ ) for their respective beam supports.

## 5 Conclusion

The present research on the elastomers led to the following conclusions:

- Modelling and electroelastic analysis of dielectric elastomer on composite through finite element approach has been done for various composite beam supports and different elastomer positions and thickness.
- It is observed that, elastomers with low thickness tend to produce more deformation at lower voltages than elastomers with higher thickness, but they fail at higher voltages.
- It is observed for higher thickness elastomers; they have low deformations at lower voltages but the deformations increase exponentially with increasing voltage. They sustain higher voltages than low thickness elastomers and fail way above them.
- The position of the elastomer has a major impact on the strain in the composite. From the findings, it can be concluded that in the case of the cantilever and fixed roller support, as the elastomer positions are varied from fixed to free/roller side, the strain in the composite increases. In the case of fixed-fixed support, maximum strain occurs when the elastomer position is in the middle.

## References

1. Kim SY, Park S, Park HW, Park DH, Jeong Y, Kim DH (2015) Highly sensitive and multimodal all-carbon skin sensors capable of simultaneously detecting tactile and biological stimuli. *Adv Mater* 27:4178–4185
2. Bar-Cohen Y (2002) Electroactive polymers: current capabilities and challenges. In: *Smart structures and materials 2002: electroactive polymer actuators and devices (EAPAD)*. International Society for Optics and Photonics, pp 1–7
3. Liu C, Bar-Cohen Y, Leary SP (1999) Electrostatically stricted polymers (ESSP). In: *Smart structures and materials 1999: electroactive polymer actuators and devices (EAPAD)*. International Society for Optics and Photonics, pp 186–190
4. Yang Y, Zhu B, Yin D, Wei J, Wang Z, Xiong R, Shi J, Liu Z, Lei Q (2015) Flexible self-healing nanocomposites for recoverable motion sensor. *Nano Energy* 17:1–9

5. Kornbluh RD, Pelrine R, Joseph J, Heydt R, Pei Q, Chiba S (1999) High-field electrostriction of elastomeric polymer dielectrics for actuation. *Smart Struct. Mater. 1999 Electroact. Polym Actuators Devices* 3669:149–161 (1999)
6. Trung TQ, Lee N-E (2016) Flexible and stretchable physical sensor integrated platforms for wearable human-activity monitoring and personal healthcare. *Adv Mater* 28:4338–4372
7. Pelrine RE, Kornbluh RD, Joseph JP (1998) Electrostriction of polymer dielectrics with compliant electrodes as a means of actuation. *Sens Actuators Phys* 64:77–85
8. Kim KJ, Tadokoro S (2007) *Electroactive polymers for robotic applications*. Springer
9. Smela E, Inganäs O, Lundström I (1995) Controlled folding of micrometer-size structures. *Science* (80-.). 268:1735–1738 (1995)
10. Goulbourne N, Mockensturm E, Frecker M (2005) A nonlinear model for dielectric elastomer membranes. *J Appl Mech* 72:899
11. Kofod G, Sommer-Larsen P (2005) Silicone dielectric elastomer actuators: finite-elasticity model of actuation. *Sens Actuators A Phys* 122:273–283
12. Plante J-S, Dubowsky S (2006) Large-scale failure modes of dielectric elastomer actuators. *Int J Solids Struct* 43:7727–7751
13. Wissler M, Mazza E (2005) Modeling and simulation of dielectric elastomer actuators. *Smart Mater Struct* 14:1396–1402
14. Wissler M, Mazza E (2005) Modeling of a pre-strained circular actuator made of dielectric elastomers. *Sens Actuators A Phys* 120:184–192
15. Wissler M, Mazza E (2007) Mechanical behavior of an acrylic elastomer used in dielectric elastomer actuators. *Sens Actuators A Phys* 134:494–504
16. Bar-Cohen Y (2004) *Electroactive polymer (EAP) actuators as artificial muscles : reality, potential, and challenges*. SPIE Press
17. Kim H, Oh S, Hwang K, Choi H, Jeon J, Nam J (2001) Actuator model of electrostrictive polymers (EPs) for microactuators. In: *Smart Structures and Materials 2001: electroactive polymer actuators and devices*. International Society for Optics and Photonics
18. Carpi F, De Rossi D (2004) Dielectric elastomer cylindrical actuators: electromechanical modelling and experimental evaluation. *Mater Sci Eng, C* 24:555–562
19. Sommer-Larsen P, Kofod G, Shridhar MH, Benslimane M, Gravesen P (2002) Performance of dielectric elastomer actuators and materials. In: Bar-Cohen Y (ed) *Smart structures and materials 2002: electroactive polymer actuators and devices*. International society for optics and photonics, pp 158–166
20. Goulbourne N, Frecker MI, Mockensturm EM, Snyder AJ (2003) Modeling of a dielectric elastomer diaphragm for a prosthetic blood pump. In: Bar-Cohen Y (ed) *Smart structures and materials 2003: electroactive polymer actuators and devices*. International society for optics and photonics, p 319
21. ANSYS (2016) *ANSYS Mechanical APDL theory reference*. ANSYS Inc
22. Coleman JN, Khan U, Blau, WJ, Gun'ko YK (2006) Small but strong: a review of the mechanical properties of carbon nanotube–polymer composites. *Carbon N.Y.* 44:1624–1652 (2006)
23. Allaoui A (2002) Mechanical and electrical properties of a MWNT/epoxy composite. *Compos Sci Technol* 62:1993–1998

# Design, Manufacturing, and Testing of Feeding and Bending Mechanism



Vijay V. Mehta, Vedant K. Parmar, Nirav P. Maniar and Jasmin P. Bhimani

**Abstract** With the growing need of fast production to meet the requirement of the industry, mass production machines like hydraulic, tracer control machine tool, special purpose automatic and semi-automatic machines were introduced with the advancement of technology. The use of these machines has considerably reduced production costs by way of reduced machining time and labor cost. This has excited the research to develop another special purpose machine—CNC 2D rod bending machine. Presently, available CNC 2D bending machine is very costly. The present research work focusses on developing a low-cost CNC 2D bending machine using pneumatic and single-axis CNC system, capable of bending metal rod ranging from 3 to 6 mm diameter, in the length range from 1 foot to 8 feet, of rod material mainly stainless steel and mild steel with maintaining cladding material and appearance. The methodology is applied to design the feeding and bending mechanism to overcome the above-stated problems. The mechanisms are not only designed but also manufactured. Its cost reduced by 35–45% compared to available machines in the market. It sets the classical example of design for manufacturing.

**Keywords** Metal rod bending · Bending mechanism · Feeding mechanism

## 1 Introduction

Automation industry is currently the most booming industry for fast and easy production. Automation takes place in various product manufacturing. Automation has been covering many industrial applications like manufacturing, inspection, research and development, dispatch, material handling process, inventory control, food processing, medical, agriculture, power plants, automobile industries, etc.

---

V. V. Mehta (✉) · V. K. Parmar · N. P. Maniar · J. P. Bhimani  
Mechanical Engineering Department, V.V.P. Engineering College, Rajkot 360005,  
Gujarat, India  
e-mail: [vijay.mehta.me@vvpedulink.ac.in](mailto:vijay.mehta.me@vvpedulink.ac.in)

N. P. Maniar  
e-mail: [nirav.maniar.me@vvpedulink.ac.in](mailto:nirav.maniar.me@vvpedulink.ac.in)

© Springer Nature Singapore Pte Ltd. 2020  
H. K. Voruganti et al. (eds.), *Advances in Applied Mechanical Engineering*,  
Lecture Notes in Mechanical Engineering,  
[https://doi.org/10.1007/978-981-15-1201-8\\_56](https://doi.org/10.1007/978-981-15-1201-8_56)

Metal rod bending machine means, “A machine which bends the rod by applying a specific angle consisting of different axis to control the feeding mechanism and bending mechanism by giving angle control.” Metal rod bending machines are classified into two different categories, one is 2D metal rod bending machine and another is 3D metal rod bending machine. Both classifications are based on working of axis in bending machine. In 2D metal rod bending machine, two different axes are available; *X*-axis as feeding axis and *Y*-axis as bending axis, whereas in 3D metal rod bending machine, one feeding axis and two bending axes, *X*-axis as feeding axis, *Y*- and *Z*-axis are bending axis.

Authors of published technical papers highlight the mechanical design of the rod bending mechanism. It is related to the construction of rod, its structure, and effect of rod materials on different mechanical properties after bending. Feeding mechanism literature involves its components’ working behavior while feeding the rod.

The feeding mechanism of bending machine is equipped with either a hydraulic system or pneumatic system in addition to an original power source providing to feed the rod. It is necessary to get an increment of the rod with high accuracy to eliminate the errors in the final product. Servo pneumatic is utilized for various industrial applications to obtain position accuracy. Advantage of this device is cleanliness, high power absorption, easy maintenance, anti-explosive, and long working life [1]. Nonlinear characteristics of the electro-hydro actuator result in a time-varying load uncertainty. That can be controlled by the approximate control model system which is integrated with position feedback control system [2]. Both systems have clamping devices for rod. The force for clamping the rod has to be optimum to stick with clamp while bending it. Pneumatic system does not require a feedback system. Therefore, pneumatic system is cost-effective while the hydraulic system involves a high cost of the feeding mechanism.

Most of the literatures are dealing with analytical behavior of bending the rod in bending mechanism. For example, if fabrication of coil from the metal wire is done, then breath by height is affected. The small size of breath end increased and this portion should be machined after fabrication. Height is not affected compared with the breath [3]. The pretension force increases the parallel strength, but this strength effect is limited [4]. As an increase in the curvature, bending moment increases in the direction of the moment, that becomes unobvious and instability appears in product [5]. These parameters should be considered during the metal rod bending condition. The spur gear is the best cost-effective component in the bending mechanism. So, the research relates to the vibration of spur gear is also important. Vibration can be reduced by linear function and periodic function model [6].

The research gap is founded to design and manufacture a feeding and bending mechanism for the machine in such a way that it does not change the cladding material and its appearance.

## 2 Feeding and Bending Mechanism of 2D CNC Bending Machine

### 2.1 Statement of Problem

Different mechanisms are available for bending operation. Various analyses have been done to improve the parameters of different components of bending machine. Among them, some parameters like size of machine, cost, easy operating, easy assembly, and easy maintenance have been recognized for commercial use.

The objective is to design and manufacturing of compact size and lower-cost CNC 2D metal rod bending machine which can maintain metal rod cladding and appearance.

### 2.2 Machine Details

2D metal rod bending machine's specification has been dealing with different machine components. Some of the generalized components are base table, bending mechanism, feeding mechanism, operating system of bending mechanism, operating system of feeding mechanism, case cover of body, controller system, and feedback system.

Above all are generalized component of 2D metal rod bending machine which has required to design as per the application of machine. The major dimension of the machine is base table size, see Table 1. It is comparatively compact size compared to available machines in recent market.

The machine contains servo motor, pneumatic system, proximity sensors, and single-axis CNC controller to feed the metal bar.

Feeding mechanism is input mechanism for the machine. It feeds the rod to the bending mechanism. It has to be designed simply with low maintenance costs. Designed feeding mechanism is shown in Fig. 1.

Bending mechanism used to bend the metal rod by giving an angle. The development of this mechanism is very important for giving a low-cost solution. This mechanism satisfies the unique solution of machine as well as provides easy operating and low maintenance. The axes details are shown in Fig. 2.

**Table 1** Machine details

S. No.	Description	Dimension (Metric)	
1	Table size	Length	1700 mm
2		Width	900 mm
3	Metal rod range	Diameter	2–6 mm
4	Metal rod range	Length	1–8 mm

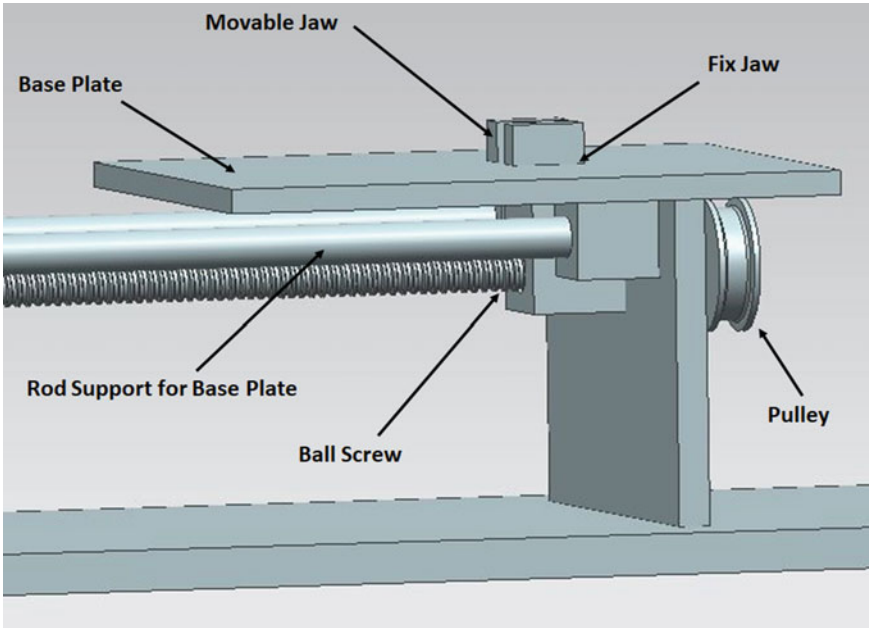


Fig. 1 Assembly of feeding mechanism

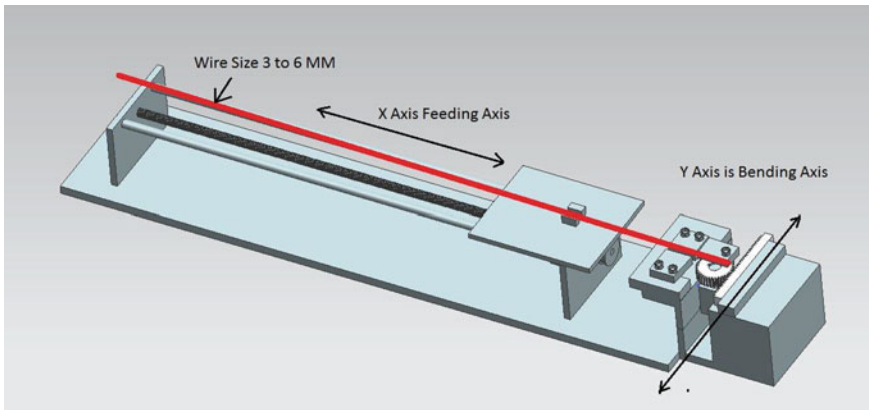


Fig. 2 Assembly of bending mechanism

The final assembly of machine is done with feeding and bending mechanisms together with required components. It is shown in Fig. 3. The final product of stainless steel metal rod of diameter 6 mm which has to bend perfectly at 90° is shown in Fig. 4.





**Fig. 3** Manufactured machine



**Fig. 4** Final bending metal rod

### 2.3 Analytical Calculations of Bending Mechanism

**Case 1:** 3 mm diameter 250 MPa yield strength of MS bar.

$$\partial b = \frac{MY}{I} \text{ Bending stress (Based on Yield stress limit)} \quad (1)$$

$$\partial b = \frac{Fl}{I/y} = \frac{F * 10}{(\pi/32)d^3} = \frac{F * 10}{(\pi/32)3^3}$$

$$F_1 = \frac{250(\pi/32)3^3}{10} = 66.267 \text{ N}$$

**Case 2:** 6 mm diameter 250 MPa yield strength of MS bar.

$$\partial b = \frac{MY}{I} \text{ Bending stress (Based on Yield stress limit)} \quad (2)$$

$$\partial b = \frac{Fl}{I/y} = \frac{F * 10}{(\pi/32)d^3} = \frac{F * 10}{(\pi/32)6^3}$$

$$F_2 = \frac{250(\pi/32)6^3}{10} = 530 \text{ N}$$

**Case 3:** 3 mm diameter 215 MPa yield strength of SS bar.

$$\partial b = \frac{MY}{I} \text{ Bending stress (Based on Yield stress limit)} \quad (3)$$

$$\partial b = \frac{Fl}{I/y} = \frac{F * 10}{(\pi/32)d^3} = \frac{F * 10}{(\pi/32)3^3}$$

$$F_3 = \frac{215(\pi/32)3^3}{10} = 56.990 \text{ N}$$

**Case 4:** 6 mm diameter 215 MPa yield strength of SS bar.

$$\partial b = \frac{MY}{I} \text{ Bending stress (Based on Yield stress limit)} \quad (4)$$

$$\partial b = \frac{Fl}{I/y} = \frac{F * 10}{(\pi/32)d^3} = \frac{F * 10}{(\pi/32)6^3}$$

$$F_4 = \frac{215(\pi/32)6^3}{10} = 455.923 \text{ N}$$

These four cases finalize the required force to bend the metal rod. It needs to identify the pneumatic cylinder which will generate forces to bend the metal rod. Above forces calculated in Eqs. 1, 2, 3, and 4 are generating from the Janatics A12 series pneumatic cylinder.

$$\text{Pressure} = \frac{\text{Force}}{\text{Area}} \quad (5)$$

The A12 pneumatic cylinder generates 5 bar of pressure and it has 50 mm bore diameter. Equation 6 is showing the calculation of force for desired application. It has to be verified whether it is satisfying our requirement or not.

$$F_c = P \left( \frac{\pi}{4} \right) d^2 = 0.5 \left( \frac{\pi}{4} \right) 50^2 = 981.747 \text{ N} \quad (6)$$

Here, obtained result shows that  $F_c > F_1, F_2, F_3, F_4$ . Therefore, required force  $F_c$  is satisfying the bending requirement. As per this force, MS and SS rod of 3–6 mm can bend properly.

### 3 Conclusion

The bending mechanism and feeding mechanism are safe design for the 3–6 mm metal rod bending at  $90^\circ$ . This machine is utilizing mechanical components collaborating with the electronics components to generate interdisciplinary machine.

Important thing is to notice that during the rod bending process, there is no descaling of the metal from the bent portion. It is big achievement. This machine has been applied in kitchenware production successfully. It is observed that simple design of mechanism makes easy maintenance. This machine cost is nearly 35–45% less than available bending machines in the recent market with same configuration. It is very clear to conclude that this special purpose machine satisfies the aim of bending the metal rod for the customer.

**Acknowledgements** Special thanks to Mr. Mahesh Vyas and Mr. Kashyap, Archana Automation Pvt Ltd, Rajkot for giving support and admire work to manufacture this machine.

### References

1. Saravanakumar D, Mohanb B, Muthuramalingam T (2017) A review on recent research trends in servo pneumatic positioning systems. *Precis Eng* 49:481–492
2. Dinga W, Denga H, Xiaa Y, Duana X (2017) Tracking control of electro-hydraulic servo multi-closed-chain mechanisms with the use of an approximate nonlinear internal model. *Control Eng Pract* 58:225–241
3. Kuboki T, Muraoka T, Tsubouchi T, Kajikawa S (2017) Upset of bent wire/tube for fabrication of in-plane bent sheet metals with extremely large breadth and small bending radius. *CIRP Ann* 66:277–280
4. Yujie Y, Wang X, Chen Z (2016) A simplified finite element model for structural cable bending mechanism. *Int J Mech Sci* 113:196–210
5. Xing E, Zhou C (2016) Analysis of the bending behavior of a cable structure under microgravity. *Int J Mech Sci* 114:132–140
6. Zajíček M, Dupal J (2017) Analytical solution of spur gear mesh using linear model. *Mech Mach Theory* 118:154–167

# Design and Kinematics of a Coal Bunker Scraper Guide-Mechanism



**Bijoy Ramakrishnan, Alex Sherjy Syriac, Chetan Chaudhari, Aditya Shah and S. S. Chiddarwar**

**Abstract** The paper discusses the evolution of a robotic mechanism which can closely follow the perimeter walls of a coal bunker. A mechanism, which slides on a track along the perimeter and guides the scraper, is constructed. The robot is designed keeping in mind its rigidity and achieves its functionality. The most desired parameter of this robot is the proximity to the walls when the scraper moves to all altitude levels of the bunker. The mechanism discussed permits the scraper to be guided along the walls of a rectangular frustum. Design and selection of parts were done by conventional methods. Workspace analysis of the resultant mechanism was done in MATLAB to ascertain the reach of the scraper. The kinematic development of the mechanism is discussed in brief. The design criticality of structural members was analyzed numerically.

**Keywords** Scraping · Mechanism · Workspace · Coal

## 1 Introduction

A coal bunker is a large storage facility for coal in a power plant. Coal bunker scraping is a routine process of cleaning a coal bunker. Coal from bunker flows to the pulverizing mill. The continuous flow of coal is necessary for optimal operation of the power plant. Coal is expected to flow by gravity. While this arrangement works in dry coal, scraping becomes a necessary process in wet conditions, when coal sticks to the walls. The problem of scraping cannot be carried out effectively by human interference but needs a robotic entrance.

Considerable research and design have been made for a similar application as explained by Dandan et al. [1]. A review of cleaning techniques including whip type cleaning has been described by Dandan et al. [2] in another paper. However, most papers and patents discuss the lines where the material being handled is in powder form and small quantities [3]. There are numerous other commercial solutions as well

---

B. Ramakrishnan (✉) · A. S. Syriac · C. Chaudhari · A. Shah · S. S. Chiddarwar  
Department of Mechanical Engineering, Visvesvaraya National Institute  
of Technology, Nagpur, Maharashtra 440010, India

© Springer Nature Singapore Pte Ltd. 2020

H. K. Voruganti et al. (eds.), *Advances in Applied Mechanical Engineering*,

Lecture Notes in Mechanical Engineering,

[https://doi.org/10.1007/978-981-15-1201-8\\_57](https://doi.org/10.1007/978-981-15-1201-8_57)

[4] with little or no demarcating effect on each other. While most solutions may work to a good extent in circular Hoppers [5], the mechanism for a bunker with rectangular frustum is not explored. This paper discusses the generation of a mechanism and its design to meet these requirements. The mechanism proposed in this paper is built on the functional requirement of heavy payload, rugged construction keeping in tab the requirement of positioning, reach, and safety as well. The mechanism consists of a closed-chain mechanism, which guides the scraper to the required position in the bunker. While the scraper has to reach the walls [6], the projection of the scraper can be traced to an imaginary point on a plane on top of the bunker. This is the required point that has to be traced by the mechanism in order to position the scraper to the proximity of walls.

The use of a mechanized scraper reduces the industrial risk [7]. While most mechanisms are based on serial manipulation, some are based on parallel manipulation, which can handle a higher payload [8]. In this paper, a 2-DOF manipulator is modeled to position the end effector along the walls of the bunker. This is achieved using a P-R, R-P configuration [9]. The scraper guide trolley adds to it a concatenated effect of the actuator, which gives it two degrees of freedom. The paper discusses the development of the mechanism, the physical and industrial constraints it meets. The workspace of the end effector is of prime importance as it has to follow a path close to the walls. The given mechanism is most beneficial in the case of a rectangular cross-sectional bunker.

## 2 Development of Mechanism

The mechanism is a forced closed-chain mechanism. Taking inputs from Feng Gao [9], the mechanism follows an R-P'P'R-P configuration Fig. 1. The prismatic joint is superimposed on another prismatic joint. The spatial process that mechanism possesses is a translational motion by using the rotational and prismatic joints.

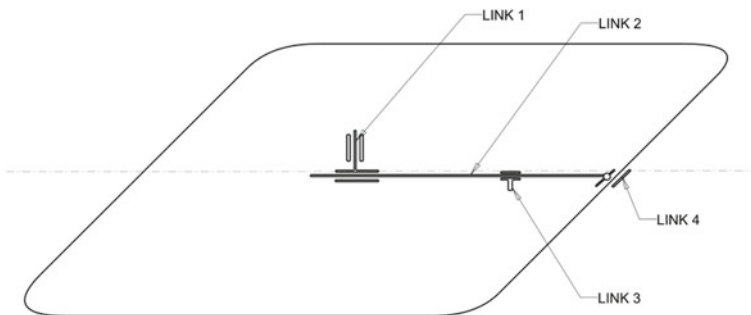


**Fig. 1** Kinematic arrangement of the mechanism

The first rotational joint is fixed to the top surface of the bunker. The type of constraint between links is pin type, allowing one degree of freedom. This is connected to the second link (beam) by a prismatic joint in a perpendicular plane. This joint allows the span of the link to change as per the contour of the guide track. The second link is not directly powered and is dependent on the guide track and hence does not contribute to the degree of freedom. The third link or the sliding link on the second link is the end effector. This part does not form a part of the chain, but is an actuated link on the second link. The second link is directly connected to the fourth link (trolley) by means of a pin joint. The fourth link is resting on a guide track. The trolley is the driven part and gives the tangential motion to the end effector link. This actuator achieves the first degree of freedom. The end effector link-2 itself being an actuated link adds a degree of freedom, hence giving the mechanism a two degree of freedom.

The complete mechanism consists of two actuators responsible for the beam rotation and the end effector motion, respectively, leading to 2-DOF translational capability of mechanism. The kinematic arrangement of such kind opens avenues for a higher degree of freedom to the mechanism which is uncalled for. This is the result of the higher pair at the sliding outer end of the mechanism. It can be constrained by keeping the tolerance of contacting parts in check.

### 3 Design Criticality

The mechanism must fulfill the following design requirements. First being the workplace requirement. The mechanism has to be transported to the bunker. In most cases, the bunkers are more than 20 m tall and have minimal approach paths to their loading area. Therefore, considering this aspect, it must have appropriate weight and size, or assembly should be possible at the place. Secondly, the entire equipment must be compact and robust for handling purposes so that it can enter a confined small opening for operation. The mechanism should facilitate reach to every location of the bunker at all the heights. In addition to it, the robot must be able to move inside the silo to scan the entire height from top to bottom, allowing the cleaning tools to reach every point of the interior surface. The mechanism should hold the end effector during the cleaning process. Maintenance of cleaning tools and supporting equipment at regular intervals should be possible (Table 1).

**Table 1** Link and constraints

Link number	Constraint	Degrees of freedom	Links connected
Link-1: Rotating axial support	Pin	1	Base and link-2
Link-2: Sliding beam	Sliding	Dependent	Link-1 and Link-4
Link-3: End effector	Sliding	1	Link-2
Link-4: Trolley	Sliding	1	Link-2 and base

The actual design of this mechanism includes many components. Hence, discussion on only critical parts is done here. The beam and the joint end at the trolley section are the critical components when subjected to loading conditions. Beam is the primary structural support as well as the main contributor of weight to the mechanism. In addition, the beam has to handle the loads at different spans and different locations of the beam. For facilitating the movement of the prismatic actuator, I-section beam is selected. For practicality of the mechanism, standard available beam sizes were chosen from data book and FEM analysis [10, 11] was done on the most optimal beam size. The MB150 beam has proved to be sufficient for given data. The initial guess on a range of beam size is based on the bending moment equation. The beam is expected to operate between a range of values for the given dimensions of bunker. This was calculated as 3-m and 5.61-m span, respectively. The data containing the extreme and minimum span length is given in Table 2 as well. The calculation for the beam taken is a similar approach as the one taken by Leszek Sowa [10]. The data is for a bunker with plan dimensions of 7-m breadth and 11-m length. The depth of the bunker is 20-m. The load is taken as 5 kN for all analysis purposes. The load taken is the consolidated weight of the mechanism and driving support. It is inclusive of service factors and safety factors. The dimensions have been taken from the actual bunker where this mechanism is being implemented.

The stress generated in the beam is well within the safety factor (Table 2) and will not cause any safety issue for forecasted dynamic loads to the end effector. The load considered on the beam is the consolidated weight of all the apparatus on the end effector to be used for scraping. Also, a factor of 1.5 in loading is taken, overseeing the reaction force experienced by the end effector. This service factor has been taken considering the design of scraper mechanism [11]. As seen in Fig. 2a, the beam is a propped beam. The end condition is fixed sliding at the central bearing and simply supported at the trolley end.

The trolley end of the mechanism (link-3) is also a critical part of the working. It was observed from stress analysis that a stress concentration zone forms at trolley pin joint. The stress was reduced by adding supports as required and increasing the dimension. Design details are limited to the identification of critical parts and concluded here to reduce trivial calculations.

**Table 2** Stress distribution at different loading

Position	Span (m)	Load position from track (m)	Maximum Stress (MPa)
1	3.00	0.5	17.956
2	5.61	0.5	24.550
3	3.00	1	23.219
4	5.61	1	33.880

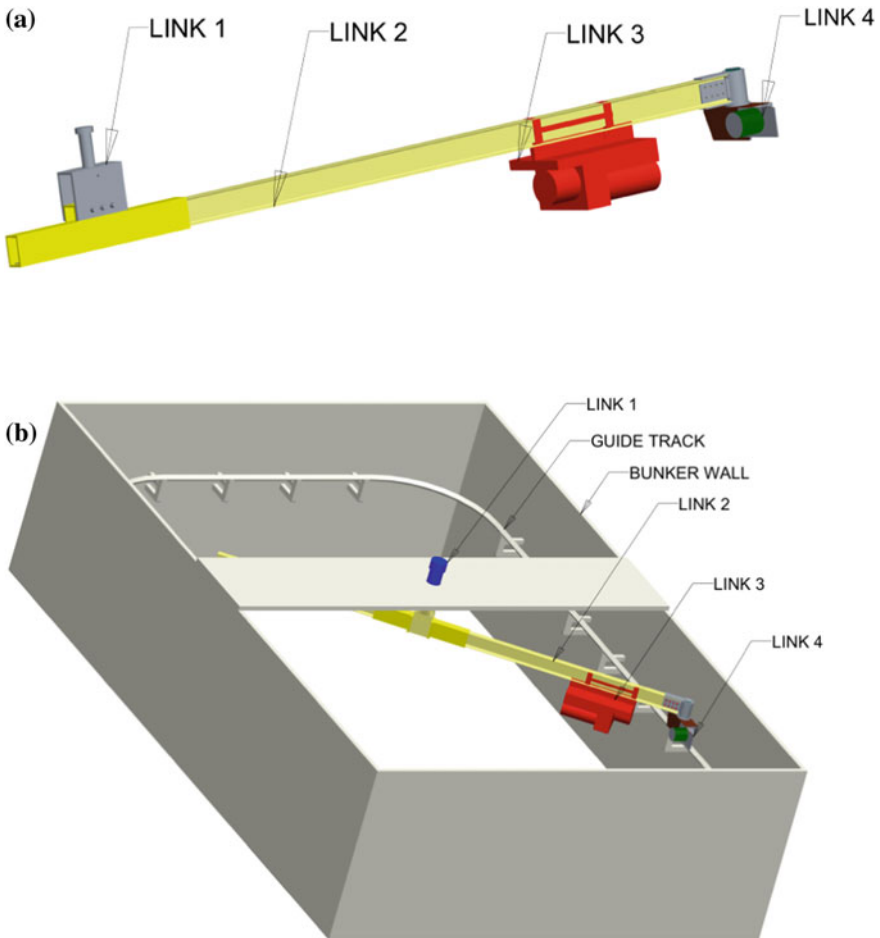


Fig. 2 a Design of mechanism structure. b Design of mechanism with end effector in the bunker

#### 4 Kinematic Workspace Analysis

The mechanism is conceptualized for a locus almost similar to the perimeter of the bunker. In actual case, the locus traced is not as perfect due to the different inclination of link-2 to the guide track at different positions. The kinematic workspace analysis is subject to boundary constraints of the bunker as well as the resolution of the servomotor driving the trolley of the mechanism.

The motor generates a dotted locus near the rectangular plot on the guide track. The distance between the dots is governed by the resolution of the motor coupled with the inertia of the system and braking accuracy. In this mechanism, endpoints of the effector generate coordinate data for almost all spatial points in the bunker. Such analysis would generate a lot of redundant data regarding workspace [12].



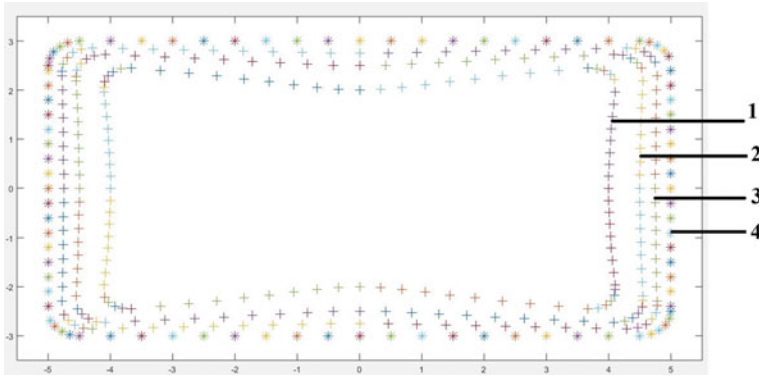


**Fig. 3** Locus of end effector for a fixed point on the beam position of track is (4) 0.5 m from wall position of end effector at (1) 1 m (2) 0.5 m (3) 0.25 m

In the current analysis method, three distant points of actual application are taken into consideration. In Fig. 3, the points are at a distance of 0.25 m, 0.5 m, and 1 m, respectively. The equation of line joining the track and central bearing was generated and a point at specified distance was taken on that line. For that fixed length, the points were plotted using MATLAB as in Fig. 3.

The locus of these points shows the coordinate of the end effector. Since the required position is parallel to the wall, the locus represents a modified position of the end effector. To achieve the actual position on the beam, the end effector has to move a bit to compensate for the distance. Symmetric points were taken along the trajectory of the end effector. The actuation of the end effector by the correction distances will lead to more precise positioning of it. The following function relates the angle theta generated at the center by the link to the initial and final pose of the sliding trolley on track. The initial coordinate of the pose being  $x_i, y_i$ , and  $x_{i+1}, y_{i+1}$  is the final coordinated of the slider on track.

$$\theta = \cos^{-1} \left( \frac{x_i x_{i+1} + y_i y_{i+1}}{\sqrt{(x_i^2 + y_i^2)(x_{i+1}^2 + y_{i+1}^2)}} \right) \tag{1}$$

where theta is the angle formed by the two positions (Fig. 4). The theta values found from Eq. 1 are used to find the motion required by the end effector to keep itself parallel to wall.

### 5 Conclusion

Scraping is a necessary part of a coal bunker. Coal bunker has existed for centuries and technology regarding them has evolved. The current mechanism has evolved based on the improvement in support systems which allow much precise motion

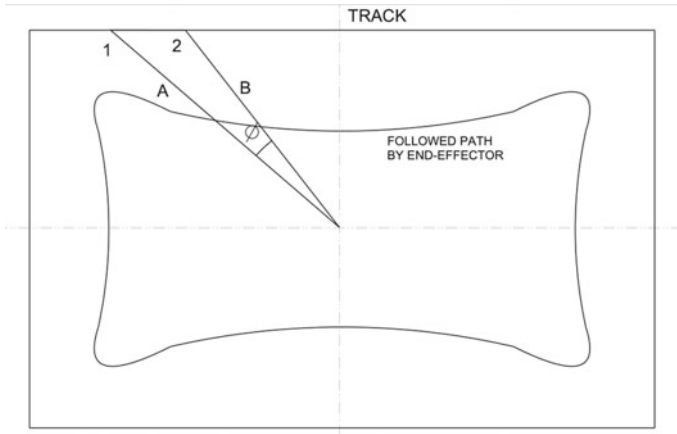


**Fig. 4** Track profile and the end effector profile generated. Here, A and B are the initial and final link length for position 1 and 2, respectively;  $\phi$  is the angle formed between them

of the arm. A robust mechanism with multiple constraints was generated by the constrained application of industrial functionality. A rigid mechanism of industrial grade and ease of handling was evolved. The mechanism greatly reduces the human interference in the process of scraping. In addition to that, the continuous operation of this mechanism increases the bunker operational capacity. An end effector base was created to facilitate the planar motion of a point. The mechanism proves to be practically feasible from an industrial, design, assembly, and safety point of view.

## References

1. Dandan K, Ananiev A, Kalaykov I (2013) SIRO: the silos surface cleaning robot concept. In: 2013 IEEE International Conference on Mechatronics and automation (ICMA). IEEE, pp. 657–661. Author F, Author S, Author T (eds) Book title. 2nd edn. Publisher, Location (1999)
2. Dandan K, Albitar H, Ananiev A, Kalaykov I (2016) Confined spaces: cleaning techniques and robot-based surface cleaning. *Am Sci Res J Eng, Technol, Sci (ASRJETS)*, 22:210–230LNCS Homepage. <http://www.springer.com/lncs>. Last accessed 21 Nov 2016
3. Yasui H, Mitani T, Komabashiri T (1989) Apparatus for cleaning a tank-like vessel. In: Google patents
4. Hartwigsen WD, Johnson AD, Beckham JC, White KL (1990) Silo cleaning apparatus. In: Google patents
5. Spencer MF, Clark FJ, Henningsen EA (1966) Silo unloader with wall cleaning means. In: Google patents
6. Farajun D (1986) Apparatus for silo clean out. In: Google patents
7. Botti L, Ferrari E, Mora C (2017) Automated entry technologies for confined space work activities: a survey. *J Occup Environ Hyg* 14:271–284
8. Tsai L-W (1999) *Robot analysis: the mechanics of serial and parallel manipulators*. Wiley
9. Gao F, Li W, Zhao X, Jin Z, Zhao H (2002) New kinematic structures for 2-, 3-, 4-, and 5-DOF parallel manipulator designs. *Mech Mach Theory* 37:1395–1411

10. Sowa L, Saternus Z, Kubiak M (2017) Numerical modelling of mechanical phenomena in the gantry crane beam. *Procedia Eng* 177:225–232
11. Gerdemeli I, Kurt S (2014) Design and finite element analysis of gantry crane. In: *Key engineering materials*. Trans Tech Publications, vol 572, pp 517–520
12. Bier ML (1959) Scraper attachment for silo unloader. In: *Google patents*

# Measurement of Elastic Modulus and Damping Properties of Friction Stir Processed Pure Metals Using Impulse Excitation Technique



K. Venkateswara Reddy, R. Bheekya Naik, Sandeep Yadav,  
G. Madhusudhan Reddy and R. Arockia Kumar

**Abstract** The impulse excitation technique (IET) is one of the most reliable and non-destructive techniques to measure dynamic elastic properties of materials. It is also possible to measure the damping factor and the resonant frequency of materials using this technique. In the current study, IET is used to measure Young's modulus, natural or resonant frequency ( $f_r$ ) and damping factor ( $Q^{-1}$ ) of friction stir processed pure metals with an intention to assess their vibration damping ability. Commercial pure aluminium (Al), copper (Cu) and magnesium (Mg) metals were subjected to single-pass friction stir processing employing 600 RPM of tool rotational speed and 60 mm/min of travel speed. The specimens for IET analysis and for microstructural observations were extracted from the stir zone of friction stir processed plates. The microstructure in the stir zone is severely refined by the friction stirring particularly the grain size of magnesium refined to 25.6  $\mu\text{m}$  from its initial size of 780  $\mu\text{m}$ . The measured Young's modulus and natural frequency for the processed Al and Cu samples were interestingly lower than their as-received counterparts. But the damping ability of these metals significantly improved after processing. However, for magnesium, the observed trends in the properties before and after processing were quite opposite to the other two metals. The crystal defects created during the friction stirring could be a reason for the observed trends.

**Keywords** Impulse excitation technique (IET) · Resonance frequency and damping factor · Friction stir processing

---

K. Venkateswara Reddy (✉) · R. Bheekya Naik · S. Yadav · R. Arockia Kumar (✉)  
National Institute of Technology, Warangal, TS 506004, India  
e-mail: [arockia@nitw.ac.in](mailto:arockia@nitw.ac.in)

G. Madhusudhan Reddy  
Defence Metallurgical Research Laboratory, Hyderabad, TS 500058, India

© Springer Nature Singapore Pte Ltd. 2020  
H. K. Voruganti et al. (eds.), *Advances in Applied Mechanical Engineering*,  
Lecture Notes in Mechanical Engineering,  
[https://doi.org/10.1007/978-981-15-1201-8\\_58](https://doi.org/10.1007/978-981-15-1201-8_58)

## 1 Introduction

Over a decade, the friction stir welding process has been established as a reliable technique to join non-ferrous alloys, particularly, aluminium alloys. Apart from establishing a joint, this process also significantly alters the microstructure of the materials. Friction stir processing (FSP) is a modification of the friction stir welding process that has extensively used to alter the surface microstructures of metallic materials [1]. Employing the same process, composite layers have also been prepared by incorporating hard ceramic particles into the surface [2]. The friction stir processed regime, in general, was observed to have a fine microstructure [3] and it is a well-established fact that fine microstructure improves the mechanical properties of metallic materials. These observations have been reported by several researchers [4, 5]. At the same time, it has to be remembered that the fine microstructure also influences the elastic modulus [6] and damping properties of the materials [7]. The ultrafine microstructures developed by equal channel angular extrusion [8, 9] and high-pressure torsion have been observed to exhibit reduced Young's modulus and improved damping properties. It is well known that Young's modulus is a key design parameter. Hence, it is essential to study the influence of processing on the modulus. The friction stir processing has widely been accepted by industries in processing non-ferrous alloys. Therefore, it is necessary to study the influence of this process in altering the modulus and damping properties. This knowledge would help the design engineers. The present study is an attempt to study Young's modulus and damping properties of friction stir processed commercial pure metals, i.e. aluminium, copper and magnesium. Indeed, there were some efforts in the recent past to determine the damping properties of surface composites fabricated by friction stir processing. Such studies employed dynamic mechanical analyser to study the elastic properties [10]. However, the present study employs the impulse excitation technique (IET) to measure the damping properties and Young's modulus. The impulse excitation technique (IET) is one of the simple and non-destructive techniques used to determine these properties.

## 2 Experimentation

Commercially pure metals (aluminium, copper and magnesium) are used in this study. They were cut into 200 mm × 70 mm × 6 mm samples. A tool made of high-speed steel having a threaded pin profile was used for the present study. The tool had a shoulder diameter of 15 mm, pin diameter of 6 mm and pin length of 4 mm. The FSP was carried out at tool rotational speed = 600 rpm; traverse speed = 60 mm/min and axial force = 10 kN. These are the optimum process parameters for these metals. Figure 1 shows the line diagram of experimental procedures. Specimens were obtained by cutting the friction stir processed plates at its centre perpendicular to the processing direction. Specimens were polished as per the standard metallographic

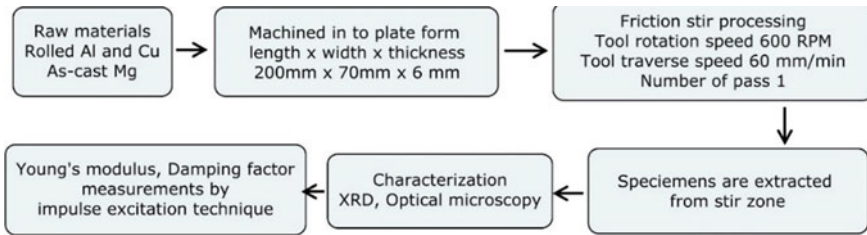


Fig. 1 Line diagram of the present study

procedure [11]. The microstructural characterisation of FSPed samples was carried out using an optical microscope and X-ray diffraction (XRD) analysis. The impulse of a light mechanical impact excites the suspended sample into the resonance frequency.

The sample’s vibration is collected by a microphone and the signal is processed by a software-based analysis program for the calculation of the resonance frequency, elastic modulus and damping. For rectangular samples, the elastic modulus can be calculated as the following formula [12].

$$E = 0.9465 \frac{mf_f^2}{b} \left( \frac{L^3}{t^3} \right) T_1$$

where  $E$  is the elastic modulus (Pa),  $f_f$  is the resonance frequency (Hz),  $m$  is the mass of the sample (g),  $T_1$  is the correction factor and  $L$ ,  $b$  and  $t$  are the length, width and thickness of the sample (mm).

The damping factor or internal friction ( $Q^{-1}$ ) can be calculated from

$$Q^{-1} = \frac{K}{\pi f_f}$$

where  $K$  is the exponential decay parameter.

### 3 Results and Discussions

Figure 2 shows decay of sound vibration as a function of time. The time required to decay the sound vibration represents the damping ability of the material. If the amplitude of vibration decays quickly, then it has better damping properties. It is evident from Fig. 2 that the time for decaying the vibration reduced in the case of friction stir processed aluminium and copper, whereas it takes more time to decay the vibration in the case of processed magnesium. The damping factor ( $Q^{-1}$ ) as calculated from these curves is shown in Fig. 3a. It is implied from the figure that damping factor increased for aluminium and copper after processing. Indeed for copper, the damping factor doubled after FSP, whereas for aluminium, the improvement in damping factor

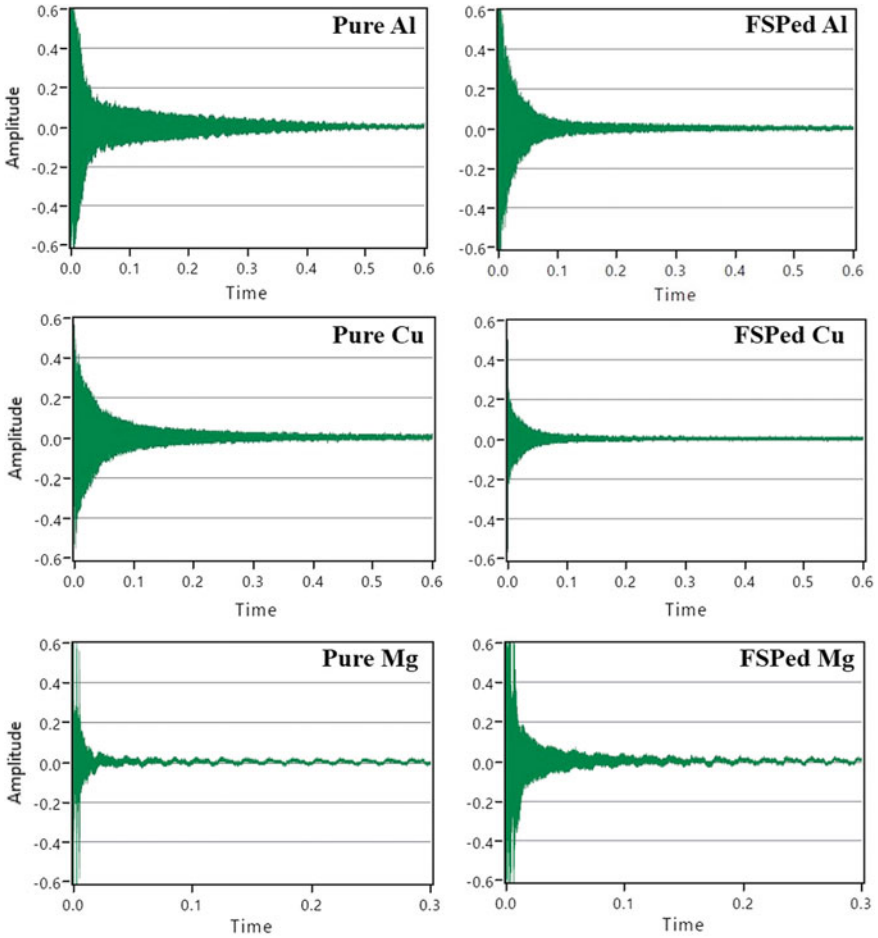


Fig. 2 Decay of sound vibration as a function of time for materials before and after FSP

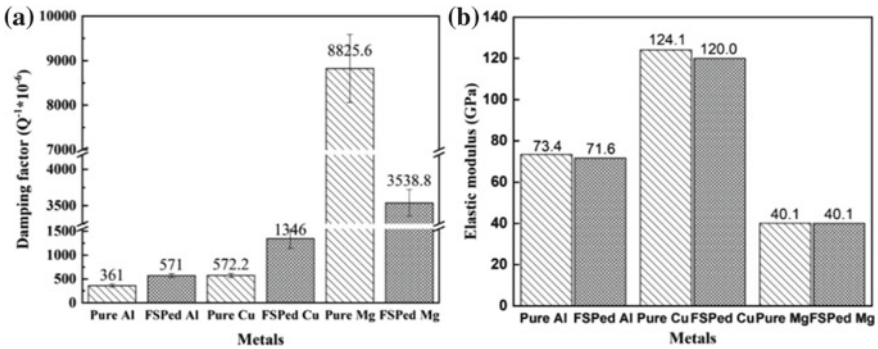
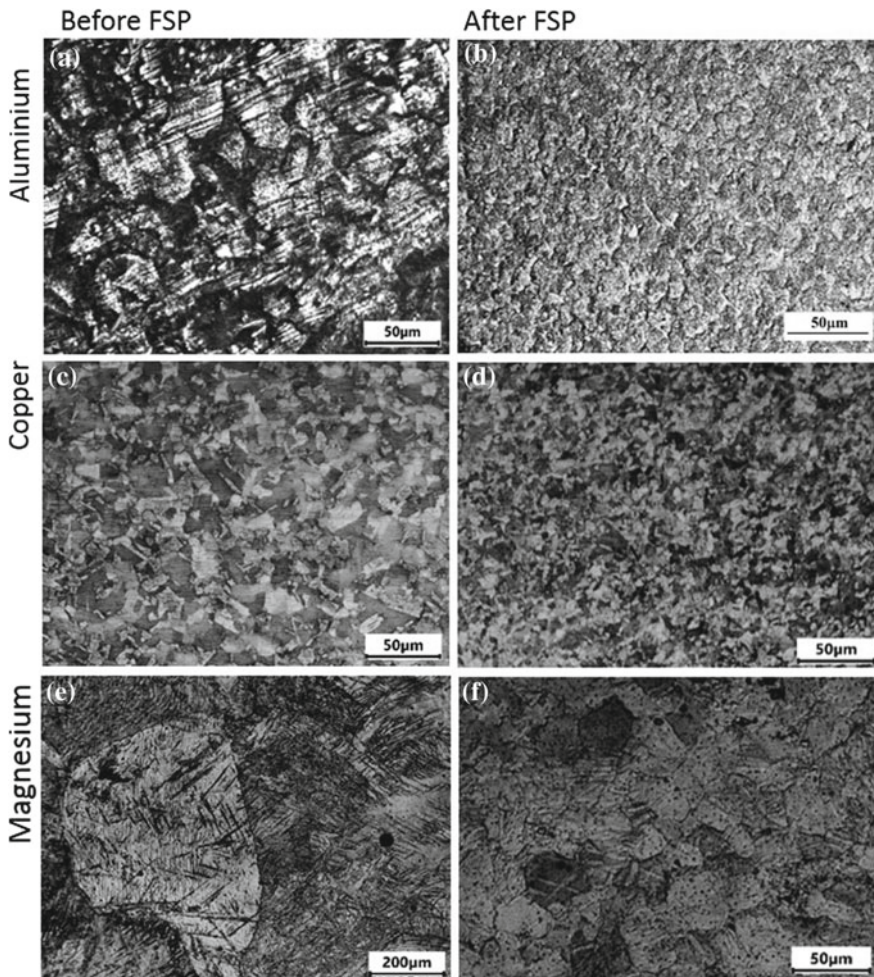


Fig. 3 a Damping factors and b elastic modulus of pure metals before and after FSP

is marginal. However, the damping factor for magnesium considerably decreased after FSP. The elastic modulus of copper and aluminium, in general, decreased after processing. However, for magnesium, it is unchanged. The observed changes in damping factor and elastic modulus might have been due to the microstructural changes that occurred during FSP. Hence, microstructural investigation was carried out to explain the observations. Figure 4 shows the optical micrographs of the base metals and the FSPed metals. In each sample, stir zone can be clearly distinguished from the base metals. From Fig. 4, it was observed that after FSP, the grains are qui-axed and grain size reduced to 10, 4 and 26  $\mu\text{m}$  for Al, Cu, and Mg, respectively.



**Fig. 4** Optical micrographs of pure metals before and after FSP



**Table 1** Calculated values of average grain size and dislocation density before and after FSP

S. No.	Material	Grain size ( $\mu\text{m}$ )		Dislocation density ( $\rho$ ) $\times 10^{12}/\text{m}^2$		
		Before FSP	After FSP	Before FSP	After FSP	%Change
1	Aluminium (Al)	44	10	4.24	2.57	-39.3
2	Copper (Cu)	20	4	1.49	0.84	-43.6
3	Magnesium (Mg)	780	26	1.67	2.99	+79.0

The stir zone X-ray diffraction patterns (Fig. 5) of base and processed metals was obtained to calculate the density of dislocations.

It was observed that dislocation density decreased after processing in copper and in aluminium, whereas in magnesium, it is increased after processing (Table 1). The aluminium and copper plates used in this study were received in rolled condition. Then it is expected to have high dislocation density in as-rolled condition. But after FSP, the dislocation density was low because the microstructures are fully recovered and recrystallized by thermo-mechanical cycles endured by metal during FSP, whereas magnesium was received in as-cast condition. As-cast ingots expected to have only equilibrium number of dislocations. Hence, the number of dislocations increases after processing in the case of magnesium.

The defects, i.e. dislocations, grain boundaries, present in the material help to improve the inherent damping factor [13]. The vibrational energy dissipates at defects. The decrease in grain size (Fig. 4) implies that increase in grain boundary area [14]. This was believed to be responsible for the improvement of damping properties in aluminium and in copper, whereas in the case of magnesium, increase in grain boundary and dislocations leads to the formation of dislocation tangles thus led to poor damping. The tangled dislocation cannot be moved by applied vibrational energy; hence, it would not participate in dissipating the energy. A decrease in damping was reported for ECAE processed pure magnesium supports the present observation [8].

The creation of defects particularly an increase in grain boundary area led to decrease in density. Otherwise, free volume increases as grain boundary fraction increases. This results in softening of material thus decreased in elastic modulus. It is evident from Fig. 4 that microstructure of aluminium and copper is significantly refined after FSP, i.e. increase in grain boundary area. Pal-Val et al. also observed that materials exhibit reduced elastic modulus after being subjected to severe plastic deformation for the same reason supports the present findings [9].

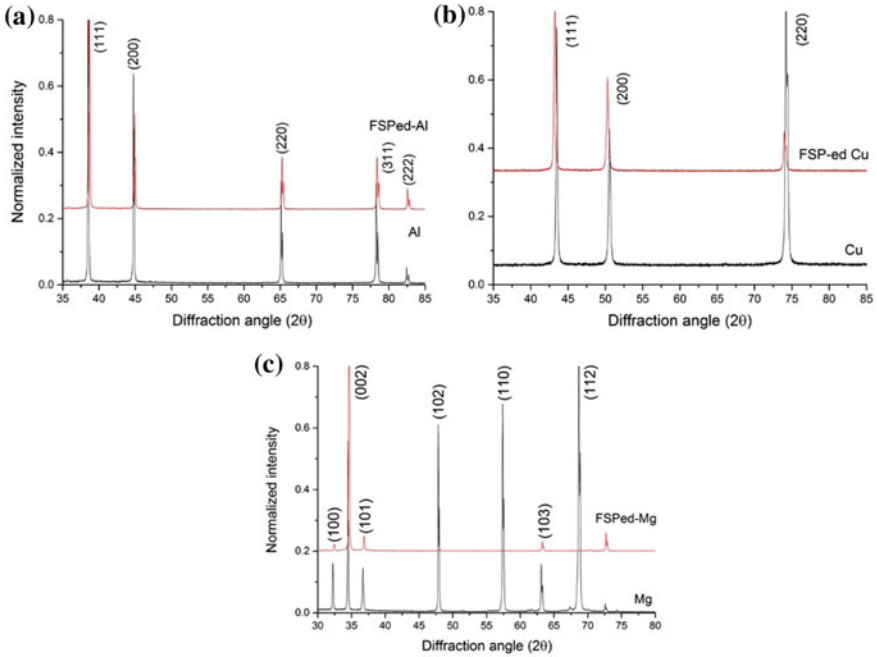


Fig. 5 X-ray patterns of pure metals before and after friction stir processing

### 4 Conclusion

1. The damping factor of aluminium (+58%) and copper (+135%) was increased after friction stir processing due to an increase in the grain boundary area.
2. The elastic modulus of aluminium and copper was marginally decreased after processing.
3. The damping factor of magnesium decreased (−60%) owing to an increase in dislocation density after processing.
4. The elastic modulus of magnesium was found to be unchanged after processing.

**Acknowledgements** The authors would like to thank DST-SERB for funding this research work through project No. ECR/2017/00122. Authors also grateful to DRDO-DMRL for extending their facility to conduct friction stir processing.

### References

1. Mishra RS, Ma ZY (2005) Friction stir welding and processing. Mater Sci Eng R 50
2. Gangil N, Siddiquee AN, Maheshwari S (2017) Aluminium based in-situ composite fabrication through friction stir processing: a review. J Alloy Compd 715

3. Morishige T, Hirata T, Tsujikawa M, Higashi K (2010) Comprehensive analysis of minimum grain size in pure aluminum using friction stir processing. *Mater Lett* 64
4. Yadav D, Bauri R (2012) Effect of friction stir processing on microstructure and mechanical properties of aluminium. *Mater Sci Eng A* 539
5. Yang Y, Zhao Y, Kai X, Tao R (2017) Superplasticity behavior and deformation mechanism of the in-situ  $Al_3Zr/6063Al$  composites processed by friction stir processing. *J Alloy Compd* 710
6. Abrosimova G, Afonikova N, Estrin Y, Kobelev N, Kolyvanov E (2010) Orientation dependence of elastic properties and internal stresses in sub-microcrystalline copper produced by equal channel angular pressing. *Acta Mater* 58
7. Jiang HJ, Liu CY, Zhang B, Xue P, Ma ZY, Luo K, Ma MZ, Liu RP (2017) Simultaneously improving mechanical properties and damping capacity of Al-Mg-Si alloy through friction stir processing. *Mater Charact* 131
8. Fan GD, Zheng MY, Hu XS, Xu C, Wu K, Golovin IS (2012) Improved mechanical property and internal friction of pure Mg processed by ECAP. *Mater Sci Eng A* 556
9. Pal-Val PP, Loginov YuN, Demakov SL, Illarionov AG, Natsik VD, Pal-Val LN, Davydenko AA, Rybalko AP (2014) Unusual Young's modulus behavior in ultrafine-grained and microcrystalline copper wires caused by texture changes during processing and annealing. *Mater Sci Eng A* 618
10. Singh S, Pal K (2017) Influence of surface morphology and UFG on damping and mechanical properties of composite reinforced with spinel  $MgAl_2O_4$ -SiC core-shell microcomposites. *Mater Charact* 123
11. ASM Hand Book (1992) *Metallogr Microstruct* 9
12. Swarnakar AK, Donzel L, Vleugels J, Van der Biest O (2009) High temperature properties of ZnO ceramics studied by the impulse excitation technique. *J Eur Ceram Soc* 29
13. Liu CY, Jiang HJ, Zhang B, Ma ZY (2018) High damping capacity of Al alloys produced by friction stir processing. *Mater Charact* 136
14. Chen Y, Liu CY, Zhang B, Ma ZY, Zhou WB, Jiang HJ, Huang HF, Wei LL (2018) Effects of friction stir processing and minor Sc addition on the microstructure, mechanical properties, and damping capacity of 7055 Al alloy. *Mater Charact* 135

# Dynamic Response of FGM Kirchhoff's Plate



Pratikshya Mohanty and Rabindra Kumar Behera

**Abstract** The study proposes a new rectangular finite element of 16° of freedom based on hermitic cubic polynomials, for investigating the strength of a thin rectangular FG plate compared to conventional materials like pure ceramic or pure metals on the aspects of static and dynamic performance. A power law variation in material properties is assumed across the plate thickness. Mori–Tanaka homogenization scheme is employed for micromodeling of the FGM. A thin plate of particulate silicon carbide and aluminum matrix functionally graded composite is designed which is analyzed based on classical laminate plate theory and tested to clamped and cantilevered boundary conditions. The results are generated using MATLAB programming and validated using ANSYS commercial FEA package.

**Keywords** Finite element method · Functionally graded materials · Modal analysis · Classical laminated plate theory

## 1 Introduction

Since the launch of functionally graded materials in Japan, researchers have been studying and utilizing graded composites in various engineering applications. FGMs are of two kinds: continuous and discretely layered. FG materials perform better in terms of optimum strength with high thermal stability. Particulate FGMs are far less susceptible to de-bonding and thermal fracture that are caused due to inter-laminar localized stresses as observed in laminated composites or short whisker FGMs. Therefore, efficiency in load transfer mechanism is retained in FGMs [1]. Usually, vapor deposition, powder-stacking methodology, electrostatic, and thermal plasma techniques are employed for fabrication of functionally graded materials [2]. The process of homogenization is understood as the determination of effective properties of the composite based on the properties of the parent materials. Usually,

---

P. Mohanty (✉) · R. K. Behera  
Department of Mechanical Engineering, National Institute of Technology,  
Rourkela, Odisha 769008, India  
e-mail: [pratikshya2010@gmail.com](mailto:pratikshya2010@gmail.com)

© Springer Nature Singapore Pte Ltd. 2020  
H. K. Voruganti et al. (eds.), *Advances in Applied Mechanical Engineering*,  
Lecture Notes in Mechanical Engineering,  
[https://doi.org/10.1007/978-981-15-1201-8\\_59](https://doi.org/10.1007/978-981-15-1201-8_59)

Voigt’s and Ruess rule of mixture is applied for the homogenization of advanced composites but when it comes to randomly oriented particulate FGM such as Al-SiC, Mori–Tanaka scheme provides an effective method for the accurate prediction of the characteristics of inhomogeneous isotropic FGM laminae [3]. A 3D iso-geometric and mesh-free coupling was proposed by Tan et al. [4] for the parametric analysis of FG plates and shell. Wang et al. [5] investigated the vibration response of (FG-GPLRC) beam traversed by double mass using Navier analytical solution. It was proposed that gradient index  $n = 5$  sufficiently yields accurate result for FGM modeling. The modal analysis of FGM plate was carried out by Ramu and Mohanty [6] using a rectangular non-conforming element. Esen [7] made use of four nodal rectangular plate elements with 24 d.o.f for the dynamic analysis of isotropic plate. Therefore, it is motivating to apply a conforming rectangular element with 16 d.o.f for the astute approximation of static and dynamic responses of FGM structures under multiple boundary and loading conditions without compromising on either accuracy or computational ease.

## 2 Material Modeling

The metal ceramic composite is composed of embedded silicon carbide particles in an aluminum matrix thus generating a FGM governed by power law variation in density, Young’s modulus, and Poisson’s ratio over the plate thickness as shown in Eq. (1).

$$V_p = \left(0.5 + \frac{z + d}{h}\right)^n \left(-\frac{h}{2} \leq z \leq \frac{h}{2}, 0 \leq n \leq \infty\right) \tag{1}$$

where  $V_p$  is the volume fraction of reinforcement,  $z$  is lamina thickness,  $h$  is overall thickness, power law gradient index is represented by  $n$ , and  $d$  is the offset of neutral axis from geometric axis [6] of the thin rectangular plate given by Eq. (2).

$$d = \frac{\int_{-h/2}^{h/2} E(z_m)(z_m)dz_m}{\int_{-h/2}^{h/2} E(Z_m)dz_m} \tag{2}$$

where  $E(z_m)$  is the effective Young’s modulus of the lamina.  $K, K_p, K_m$  and  $G, G_p, G_m$  are the bulk moduli and shear moduli of the FGM, reinforcement, and matrix material, respectively. The Mori–Tanaka homogenization scheme [8] in Eqs. (3) and (4) given below effectively predicts the material properties of FGM.

$$\frac{K - K_p}{K_m - K_p} = \frac{(1 - V_p)}{1 + \frac{(V_p)(K_m - K_p)}{K_p + 1.333G_p}} \tag{3}$$

$$\frac{G - G_p}{G_m - G_p} = \frac{(1 - V_p)}{1 + \frac{(V_p)(G_m - G_p)}{G_p + B}} \quad \text{where, } B = \frac{G_p(9K_p + 8G_p)}{6(K_p + 2G_p)} \quad (4)$$

Using the classical laminate plate theory in which it is assumed that no deformation occurs in the neutral axis of the composite, the material matrix in plane stress condition is given by Eq. (6). The stress and strain vectors are related by the material matrix as shown in Eq. (7).

$$[Q] = \frac{E}{1 - \nu^2} \begin{bmatrix} 1 & \nu & 0 \\ \nu & 1 & 0 \\ 0 & 0 & \frac{1-\nu}{2} \end{bmatrix} \quad (6)$$

$$\{\sigma_{xx} \ \sigma_{yy} \ \tau_{xy}\}^T = [Q]\{\epsilon_{xx} \ \epsilon_{yy} \ \gamma_{xy}\}^T \quad (7)$$

The differential equation of motion for the dynamic analysis of a plate without damping in the plate is given by Eq. (8). Considering variation in Poisson's ratio,  $D$  is the flexural rigidity as mentioned in Eq. (9), while the product of  $\rho$  (density) and  $h$  (plate thickness) represents value of mass per unit area. ( $A_{ij}$ ,  $B_{ij}$ ,  $D_{ij}$ ) represent the extensional, coupling, and bending stiffness, respectively.

$$D \left[ \frac{\partial^4 w}{\partial x^4} + 2 \frac{\partial^4 w}{\partial x^2 \partial y^2} + \frac{\partial^4 w}{\partial y^4} \right] + \rho h \frac{\partial^2 w}{\partial t^2} = 0 \quad (8)$$

$$D = D_{ij} - B_{ij}^2/A_{ij}, \quad (A_{ij}, B_{ij}, D_{ij}) = \int_{-h/2}^{h/2} Q_{ij}(1, z, z^2) dz, \quad (9)$$

The FGM plate is modeled based on the parent materials presented in Table 1.

**Table 1** Material properties of the matrix and particulate reinforcements

Material properties	Aluminum	Silicon carbide
Density (Kg/m <sup>3</sup> )	2700	3200
Young's modulus (N/m <sup>2</sup> )	72.1e9	431e9
Shear modulus (N/m <sup>2</sup> )	26.9e9	181.1e9
Poisson's ratio	0.34	0.19
Bulk modulus (N/m <sup>2</sup> )	7.43e10	3.31e11
Thermal conductivity (W/m <sup>-1</sup> K <sup>-1</sup> )	187	252.5

### 3 Finite Element Modeling

Due to the incapacity of obtaining the analytical solutions for governing equations of plate beyond the simple boundary conditions, a need for astute approximation methods such as finite element method originated. Commonly, a 12 degree of freedom element is in usage for plate analysis [4]. However, this element, although computationally simple, fails to capture the deformation in the plate element accurately as it makes the element too stiff. Therefore, in this study, a conforming element following  $C^{(1)}$  continuity with 16 d.o.f is utilized for the parametric study of Al-SiC particulate FGM. There exist four displacements per node instead of three as shown in Eq. (10). The twist at plate corners is also taken into account.

$$\{W\} = \left\{ w, \frac{\partial w}{\partial y}, -\frac{\partial w}{\partial x}, \frac{\partial^2 w}{\partial x \partial y} \right\}_i^T, \quad i = 1, 2, 3, 4 \quad (10)$$

Using hermitic polynomials of cubic nature [9], the following shape functions are obtained as mentioned in set of Eqs. (11)–(26).

$$N_1 = \frac{1}{a^3}(a^3 - 3ax^2 + 2x^3) \frac{1}{b^3}(b^3 - 3by^2 + 2y^3) \quad (11)$$

$$N_2 = \frac{1}{a^2}(a^2x - 2ax^2 + x^3) \frac{1}{b^3}(b^3 - 3by^2 + 2y^3) \quad (12)$$

$$N_3 = \frac{1}{a^3}(a^3 - 3ax^2 + 2x^3) \frac{1}{b^2}(b^2x - 2by^2 + y^3) \quad (13)$$

$$N_4 = \frac{1}{a^2}(a^2x - 2ax^2 + x^3) \frac{1}{b^2}(b^2x - 2by^2 + y^3) \quad (14)$$

$$N_5 = \frac{1}{a^3}(a^3 - 3ax^2 + 2x^3) \frac{1}{b^3}(3bx^2 - 2y^3) \quad (15)$$

$$N_6 = \frac{1}{a^2}(a^2x - 2ax^2 + x^3) \frac{1}{b^3}(3bx^2 - 2y^3) \quad (16)$$

$$N_7 = \frac{1}{a^3}(a^3 - 3ax^2 + 2x^3) \frac{1}{b^2}(y^3 - by^2) \quad (17)$$

$$N_8 = \frac{1}{a^2}(a^2x - 2ax^2 + x^3) \frac{1}{b^2}(y^3 - by^2) \quad (18)$$

$$N_9 = \frac{1}{a^3}(3ax^2 - 2x^3) \frac{1}{b^3}(3bx^2 - 2y^3) \quad (19)$$

$$N_{10} = \frac{1}{a^2}(x^3 - ax^2) \frac{1}{b^3}(3bx^2 - 2y^3) \quad (20)$$

$$N_{11} = \frac{1}{a^3}(3ax^2 - 2x^3)\frac{1}{b^2}(y^3 - by^2) \tag{21}$$

$$N_{12} = \frac{1}{a^2}(x^3 - ax^2)\frac{1}{b^2}(y^3 - by^2) \tag{22}$$

$$N_{13} = \frac{1}{a^3}(3ax^2 - 2x^3)\frac{1}{b^3}(b^3 - 3by^2 + 2y^3) \tag{23}$$

$$N_{14} = \frac{1}{a^2}(x^3 - ax^2)\frac{1}{b^3}(b^3 - 3by^2 + 2y^3) \tag{24}$$

$$N_{15} = \frac{1}{a^3}(3ax^2 - 2x^3)\frac{1}{b^2}(b^2x - 2by^2 + y^3) \tag{25}$$

$$N_{16} = \frac{1}{a^2}(x^3 - ax^2)\frac{1}{b^2}(b^2x - 2by^2 + y^3) \tag{26}$$

$K_e$  and  $M_e$  being the elemental stiffness and mass matrix, respectively, of size  $16 \times 16$  can be calculated from Eqs. (27) and (28).

$$k_{ij}^e = D^* \int_0^b \int_0^a \left[ \frac{\partial^2 N_i}{\partial x^2} \frac{\partial^2 N_j}{\partial x^2} + \nu \frac{\partial^2 N_i}{\partial x^2} \frac{\partial^2 N_j}{\partial y^2} + \nu \frac{\partial^2 N_i}{\partial y^2} \frac{\partial^2 N_j}{\partial x^2} + \frac{\partial^2 N_i}{\partial y^2} \frac{\partial^2 N_j}{\partial y^2} + 2(1 - \nu) \frac{\partial^2 N_i}{\partial x \partial y} \frac{\partial^2 N_j}{\partial x \partial y} \right] dx dy \tag{27}$$

$$m_{ij}^e = \rho h \int_0^b \int_0^a N_i(x, y) N_j(x, y) dx dy \tag{28}$$

The elemental mass and stiffness matrices are assembled to produce the global matrices ( $[K]$ ,  $[M]$ ). The equation of motion of the plate shall yield natural frequencies  $\omega$  by solving Eq. (29).

$$([K] - \omega^2[M])\{W\} = 0 \tag{29}$$

### 4 Results and Discussions

Mori–Tanaka homogenization scheme produces an average value of FGM properties between the upper bound and lower bound rule of mixture scheme. It neither underestimates nor overestimates the plate stiffness (see Fig. 1).

As mentioned in Fig. 2, FGM modeled using power law with gradient index  $n \geq 1$  shows smooth transition in material properties from pure aluminum in the first layer to pure silicon carbide layer on the top. While in modeling based on  $n < 1$ , the initial volume fraction of reinforcement ranges between near about 0.2–0.6.



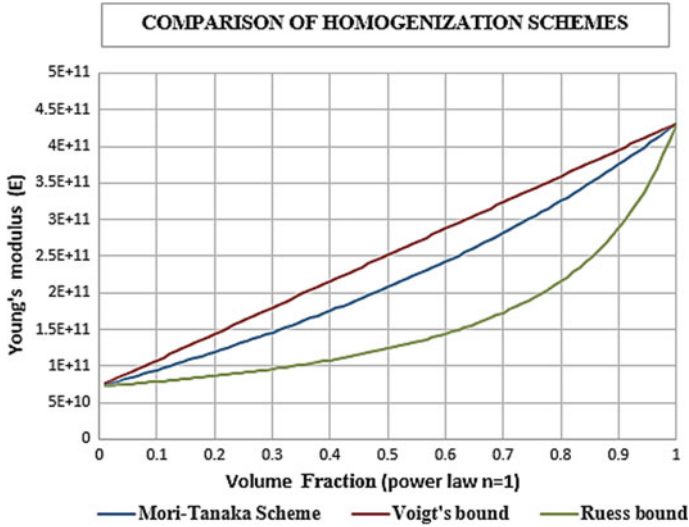


Fig. 1 Variation of Young's modulus over the volume fraction through the thickness of a FGM plate with gradient index  $n = 1$ , is micro-modeled based on three different homogenization schemes: Mori–Tanaka, Voigt's (upper bound), and Ruess's (lower bound)

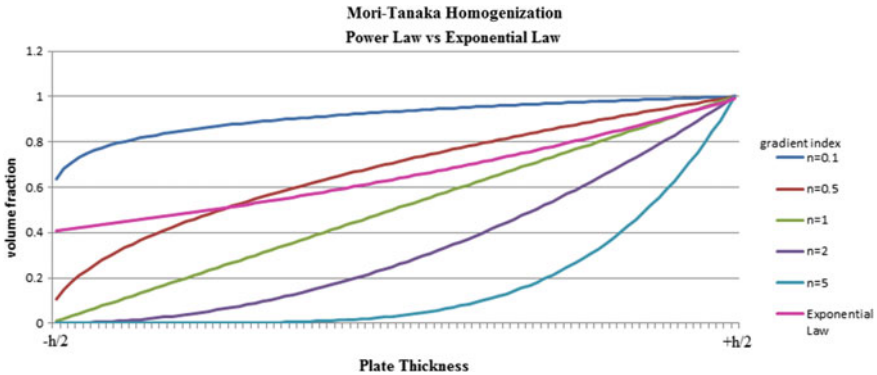


Fig. 2 Variation of volume fraction over the plate thickness with different gradients of power law vs exponential law using Mori–Tanaka homogenization scheme

The chosen system for FG plate is of Mori–Tanaka scheme with power law variation (with gradient index = 1). The plate thickness is  $6.3e-3$  m and area is  $(0.1 \times 0.1) \text{ m}^2$ . This FG plate is tested against pure aluminum and pure SiC plate under an external pressure on 2Gpa as plotted in Table 2.

The natural frequency of the FGM plate is obtained using 16-d.o.f element and 12-d.o.f element; for a mesh size of  $20 \times 20$  divisions is shown in Table 3, and mode shapes are portrayed in Fig. 3.

**Table 2** Total deformations (in mm) in plates made of different materials

Boundary conditions	Pure aluminum	Ceramic (Silicon carbide)	Functionally graded plate
All sides clamped	0.16113	0.0290	0.0635
Cantilevered	15.487	2.7341	6.08

**Table 3** Natural Frequency of FGM plate using different finite elements (in Hertz)

Boundary conditions	Mode number	Non-conforming element (12 d.o.f)	Conforming element (16 d.o.f)	ANSYS validation
All sides clamped	1st	9517	8327.3	8406.3
	2nd	19,393	16,514	16,650
Cantilevered	1st	921.18	833.12	839.43
	2nd	2265	2033.9	2013.2

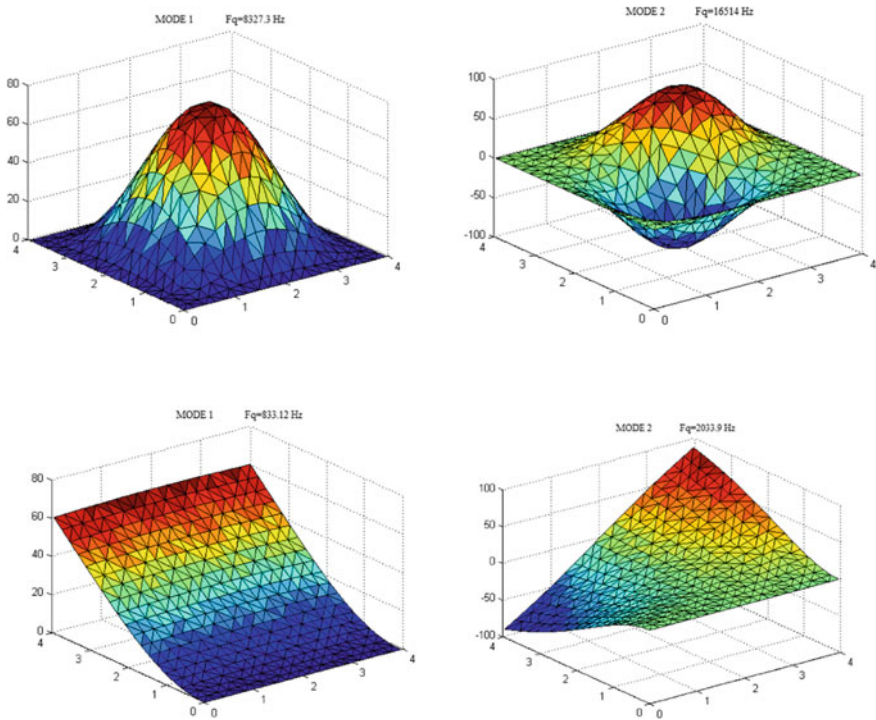


**Fig. 3** First and second mode shapes of clamped plate and cantilever plate, respectively

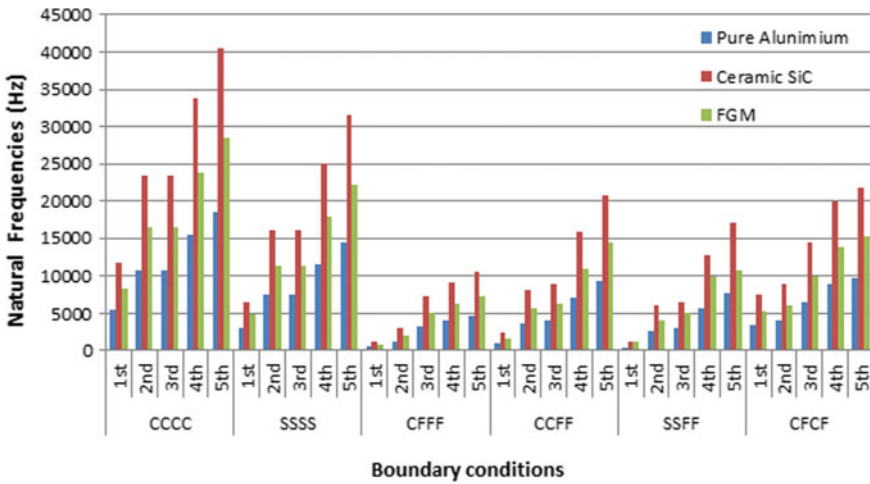


Fig. 4 Performance comparison of FGM ( $n = 1$ , Mori–Tanaka scheme) to metal and ceramic

The dynamic performance of FGM compared to its parent materials in various other boundary conditions up to five modes of vibration is portrayed in Fig. 4.

### 5 Conclusion

The stiffness of FG materials is larger than aluminum. It imbibes the optimum properties of ceramic plate as it can be utilized in high-temperature environment. FG materials should be modeled based on power law variation with gradient index greater than 1 as they show smooth transition in material properties in a FGM as expected to vary from pure aluminum to pure ceramic. Mori–Tanaka homogenization scheme renders an effective inhomogenous isotropic material, which can be then analyzed as isotropic conventional materials. The application of transformed bending matrix with consideration to variation in Poisson’s ratio is the accurate way to model FGM. This fact was long ignored in previous literatures. The conforming finite element is better able to capture the actual plate deformations that were under-evaluated by non-conforming finite element. Non-conforming elements are too stiff and therefore, overestimate the natural frequency of the structures that add to material cost. Thus, it is mathematically viable to utilize conforming element for computational modeling of engineering structure in favor of result accuracy and quick convergence than non-conforming finite element of 12 degrees of freedom.

## References

1. Jha D, Kant T, Singh R (2013) A critical review of recent research on functionally graded plates. *Compos Struct* 96:833–849. <https://doi.org/10.1016/j.compstruct.2012.09.001>
2. Bastwros M, Kim G (2015) Fabrication of aluminum–SiC laminate nanocomposite by ultrasonic spray deposited sheet bonding I. *J Micro Nano-Manuf* 3:031005. <https://doi.org/10.1115/1.4030705>
3. Mehar K, Panda S, Mahapatra T (2017) Theoretical and experimental investigation of vibration characteristic of carbon nanotube reinforced polymer composite structure. *Int J Mech Sci* 133:319–329. <https://doi.org/10.1016/j.ijmecsci.2017.08.057>
4. Tan P, Nguyen-Thanh N, Rabczuk T, Zhou K (2018) Static, dynamic and buckling analyses of 3D FGM plates and shells via an isogeometric-meshfree coupling approach. *Compos Struct* 198:35–50. <https://doi.org/10.1016/j.compstruct.2018.05.012>
5. Wang Y, Xie K, Fu T, Shi C (2019) Vibration response of a functionally graded graphene nanoplatelet reinforced composite beam under two successive moving masses. *Compos Struct* 209:928–939. <https://doi.org/10.1016/j.compstruct.2018.11.014>
6. Ramu I, Mohanty S (2014) Modal analysis of functionally graded material plates using finite element method. *Procedia Mater Sci* 6:460–467. <https://doi.org/10.1016/j.mspro.2014.07.059>
7. Esen İ (2015) A new FEM procedure for transverse and longitudinal vibration analysis of thin rectangular plates subjected to a variable velocity moving load along an arbitrary trajectory. *Lat Am J Solids Struct* 12:808–830. <https://doi.org/10.1590/1679-78251525>
8. Sharma K, Kumar D (2017) Elastoplastic stability and failure analysis of fgm plate with temperature dependent material properties under thermomechanical loading. *Lat Am J Solids Struct* 14:1361–1386. <https://doi.org/10.1590/1679-78253747>
9. Szilard R (2004) *theories and applications of plate analysis*, 1st ed. Wiley, USA, ISBN: 9780471429890

# Comparative Study of Various Defects in Monolayer Graphene Using Molecular Dynamics Simulation



Kritesh Kumar Gupta, Aditya Roy and Sudip Dey

**Abstract** The present study uses the molecular dynamics approach to study the various defects available in graphene sheet and also to record its effect on the strength and stiffness of graphene. The graphene sheet is uniaxially deformed in its armchair and zigzag direction. In order to examine the fracture behaviour of defective graphene, molecular dynamics (MD) simulations based on AIREBO interatomic potential field and Nose-Hoover thermostat and barostat techniques are implemented. The present study shows that with the introduction of the defects, the fracture/yield strength of graphene reduces up to some extent in both of its direction. However, the presence of crack reduces the strength of graphene significantly more. Further, the study also concludes that the graphene withholds much higher stress when loaded in its zigzag direction in comparison with loading it in armchair direction.

**Keywords** Molecular dynamics simulation · Monolayer graphene · Defects

## 1 Introduction

The exceptional properties of monolayer graphene have been used to explore the possibilities in developing nanoresonators [1], biosensors [2], nano-composites [3] and many more nanoelectromechanical systems (NEMS). The very first time, Professor Sir Andre Geim and Professor Sir Kostya Novoselov extracted the single-layer graphene sheet (SLGS) from graphite in 2004. Since then graphene has been researched by a lot of researchers in order to determine its exact mechanical properties and strength. After the invention of graphene, Lee et al. in 2008 experimentally found that the graphene is one of the lightest ( $0.77 \text{ mgm}^{-2}$ ) and still stiffest material known. Its fracture strength and Young's modulus were recorded as 130 GPa and 1 TPa, respectively [4]. Experimentally, one of the common methods to extract graphene from graphite is chemical vapour decomposition (CVD), which is performed at elevated temperatures. It is obvious that during extraction, some defects

---

K. K. Gupta (✉) · A. Roy · S. Dey  
Department of Mechanical Engineering, National Institute of Technology, Silchar, India  
e-mail: [kriteshamie@gmail.com](mailto:kriteshamie@gmail.com)

© Springer Nature Singapore Pte Ltd. 2020  
H. K. Voruganti et al. (eds.), *Advances in Applied Mechanical Engineering*,  
Lecture Notes in Mechanical Engineering,  
[https://doi.org/10.1007/978-981-15-1201-8\\_60](https://doi.org/10.1007/978-981-15-1201-8_60)

539

may be introduced to the graphene structure by vacancy, chemical reactions with foreign elements or by a change in the bond structure at elevated temperatures. This leads to getting incorrect desired results from the experimentation. The irregularities in the graphene structure remarkably impact the strength of graphene, which in return may affect the desired performance. In past, researchers have made a lot of efforts to gather the exact characteristics of graphene. Such as Lopez-Polin et al. [5] investigated the relationship between vacancies concentration induced in the graphene and its elastic modulus. In their study, they revealed that by the controlled density of vacancy in the monolayer graphene, the elastic modulus of graphene may be improved. By inducing merely 0.2% of vacancy concentration in graphene, its Young's modulus becomes twice of the earlier value. On the contrary, Mortazavi and Ahzi [6] concluded that with the introduction of 0.25% defect concentration, the thermal conductivity of graphene reduces by 50% and the reduction in the failure stress and strain is observed. This reveals the fact that the defect concentration in graphene has a profound effect on its mechanical properties. In this regard, Zandiataashbar et al. [7] carried out his study to report that how the mechanical properties of graphene are influenced by the  $sp^3$  defects and the vacancy defects, and they used diamond AFM nano-indentation and Raman spectroscopy to gather the results. The similar study was presented by the Dewapriya and Meguid [8] to successfully tailor the fracture strength of graphene by intentionally introducing strategic placement of vacancy in cracked graphene. Apart from vacancy and the crack, the presence of Stone–Thrower–Wales (STW) defect also plays the important role for manipulating the mechanical properties of pristine; to study the influence of Stone–Thrower–Wales defect over the fracture toughness of the graphene, Rajasekaran and Parashar [9] presented a molecular dynamics approach. They also proposed that the proper placement of STW defects near the crack faces may improve the fracture behaviour of monolayer graphene. In the same manner, Verma and Parashar [10] also presented the MD study to improve the fracture toughness of pristine and hydrogenated graphene by inducing STW defects.

The modelling of nano-materials helps in analysing the actual characteristics of the material in a better manner. It is because of the fact that user can regulate critical parameters such as temperature and pressure using the tools available. In physical experimentation, regulating these critical parameters becomes an expensive and tedious task to perform. Therefore using MD simulation as the analysis tool gives the edge over, understanding the complex nano-materials in a better way. The present study analyses the strength and stiffness of the perfect SLGS along with the graphene with various defects such as single vacancy, Stone–Wales defect, nanopore, and crack, using MD simulation. The modulus of elasticity, fracture stress, and failure strain are determined for both armchair and zigzag directions of graphene. The strength and mechanical properties of defective graphene are further compared with those of perfect graphene.

## 2 Molecular Dynamics Simulation

### 2.1 Numerical Methodology

The nano-mechanical modelling is one of the best methods to analyse the properties of nano-materials; it can be differentiated into three main categories—the first-principle approaches such as density functional theory (DFT), semi-empirical methods such as molecular dynamics simulation and the third one is the modified continuum model. The molecular dynamics is computationally affordable in comparison with the first-principle approaches. Apart from that, MD is extremely fast and can handle much larger systems when compared with the first-principle methods. Although MD relies on several assumptions associated with the interatomic potential function, the interatomic potential functions are created by the calibration of previous experimental results using the curve fitting methods. These interatomic potential functions describe the interactions between the constituent atoms. The MD simulation considers the material as the collection of individual atoms which interact by exerting forces on each other and follow Newton's law of motion. The simulation procedure in MD initiates by determining the force acting on an individual atom by the neighbouring atoms. Force acting on atom  $i$

$$f_i = -\frac{\partial E_i}{\partial r_i} \quad (1)$$

where  $E_i$  represents the potential energy of atoms. The potential energy between the atoms is approximated by interatomic potential field. After the determination of forces, the accelerations are determined using Newton's equation of motion

$$f_i = m_i \frac{d^2 r_i}{dt^2} = m_i a_i \quad (2)$$

Further, the atoms are allowed to accelerate for certain duration, known as time-step. At the end of each time-step, the new positions and velocities are determined using numerical integration algorithms such as velocity verlet. The use of statistical ensemble such as NPT, NVT and NVE allows, controlling the temperature and pressure of the system [11].

### 2.2 Modelling and Simulation

We used the open-source software Visual Molecular Dynamics (VMD) [12] for modelling the square shape perfect graphene sheet of 5-nanometre edge length with 1008 carbon atoms. Further, an open-source atom manipulator, Avogadro [13] is used to introduce the vacancy defect, Stone–Wales defect, nanopore and crack in

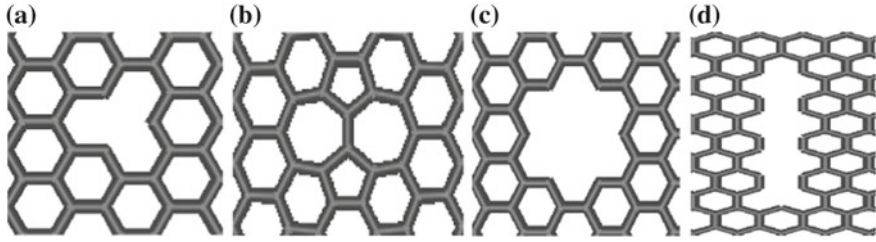


**Fig. 1** Defected graphene with **a** single vacancy, **b** Stone–Wales defect, **c** nanopore and **d** crack

the perfect graphene sheet. The *data files* containing the coordinates of atoms were generated by using the *topotool* plugin of VMD. Figure 1 depicts the various defects considered in the fracture analysis. The Stone–Wales defect shown in Fig. 1b is formed by a bond rotation of  $90^\circ$  between two adjacent carbon atoms, which results in the formation of pentagon-heptagon pairs. The nanopore shown in Fig. 1c has the dimension 5.63 angstroms in the armchair direction and 7.36 angstrom in the zigzag direction. And the crack shown in Fig. 1d has the length 12.28 angstrom and width 4.25 angstrom.

Both the sheets (perfect and defected) were uniaxially deformed in an armchair and zigzag direction using LAMMPS, which is an open-source code by Sandia National Laboratories, USA. In the simulation, AIREBO interatomic potential [14] is used to mimic the interactions between the carbon–carbon atoms. To avoid free edges, all three directions were applied with periodic boundary conditions. The sheets were firstly equilibrated to minimize the energy of the system, over 60 picoseconds before applying strain, using timestep of 1 femtosecond. In the relaxation period, the pressure component of the x-direction and y-direction was maintained zero using NPT ensemble. The NPT uses Nose-Hoover technique to maintain the desired temperature and pressure of the system. Furthermore, to uniaxially deform the sheets, a strain was imposed by elongation of the simulation box in both (armchair and zigzag) dimension and the applied strain rate was  $10^9 \text{ s}^{-1}$ . The stress components in y-direction and z-direction were kept at zero during simulating the tensile deformation of graphene by keeping in check the pressure component in the said directions using NPT ensemble. To determine the atomistic stress, the virial stress is computed, which is defined as [15]:

$$\sigma_{ij} = \frac{1}{V} \sum_{\alpha} \left[ \frac{1}{2} \sum_{\beta=1}^N \left( R_i^{\beta} - R_i^{\alpha} \right) F_j^{\alpha\beta} - m^{\alpha} v_i^{\alpha} v_j^{\alpha} \right] \quad (3)$$

where  $\alpha$  and  $\beta$  refer to the number assigned to an atom and the number assigned to the neighbouring atom, respectively, while  $i$  and  $j$  signify the directional indices,  $m^{\alpha}$  and  $v_i^{\alpha}$  are the mass and velocity of the atom  $\alpha$ , respectively.  $R_i^{\beta}$  is the location of atom  $\beta$  in  $i$  direction;  $F_j^{\alpha\beta}$  is the force due to an atom  $\beta$  on atom  $\alpha$  along the  $j$ -direction;  $V$  refers to the total volume of the material system. The virial stress represents a product



of stress and volume, i.e. the stress value computed by LAMMPS [16] would be in the units of pressure\*volume, in order to extract the stress from the computed value it is essential to divide the value calculated by the LAMMPS with the total volume. Furthermore, in order to calculate the virial stress, the instantaneous volume is used, i.e. when the imposed strain is ' $\epsilon$ ', the value of volume at the given instant would be  $V_0(1 + \epsilon)$ , where  $V_0$  represents the initial volume of the system.

### 3 Results and Discussion

The Young's modulus, elastic constants, Poisson's ratio and ultimate strength are determined and show a good agreement with the literature values. The aforesaid values are determined for the perfect graphene, which is expressed as follows (Table 1).

The stress-strain behaviour of perfect and defective graphene is recorded in the armchair and zigzag directions. The stress-strain plots are illustrated in Fig. 2.

It is evident from the stress-strain behaviour of the perfect and defective graphene in both the directions; the zigzag direction has higher fracture strength. It is also clear that the defective graphene shows a considerable yielding prior to failure when loaded in the armchair direction. However, the defects do not affect much Young's modulus of graphene, apart from the crack which shows a drastic reduction in Young's modulus of the graphene. The stress-strain behaviour shows that failure strain is high in case of loading in a zigzag direction. This shows that the zigzag direction graphene shows more resistance to failure, as Tables 2 and 3 show the values of elastic constants, modulus of elasticity, Poisson's ratio and fracture strength of the perfect and defective graphene sheet in an armchair and zigzag directions, respectively. From the comparison of mechanical properties in an armchair and the zigzag direction, it is clear that the graphene is stiffer in armchair direction and stronger in a zigzag direction.

**Table 1** Validation of mechanical properties of graphene

Properties	Present study	Literature values
C11 (in GPa)	1033.7	1094 (Thomas et al. 2014)
C12 (in GPa)	142.6	136 (Thomas et al. 2014)
Young's modulus (in TPa)	1.014	1.020 (Lee et al. 2008)
Poisson's ratio	0.1379	0.1248 (Thomas et al. 2014)
Fracture strength (in GPa)	165.7	130 (Lee et al. 2008)

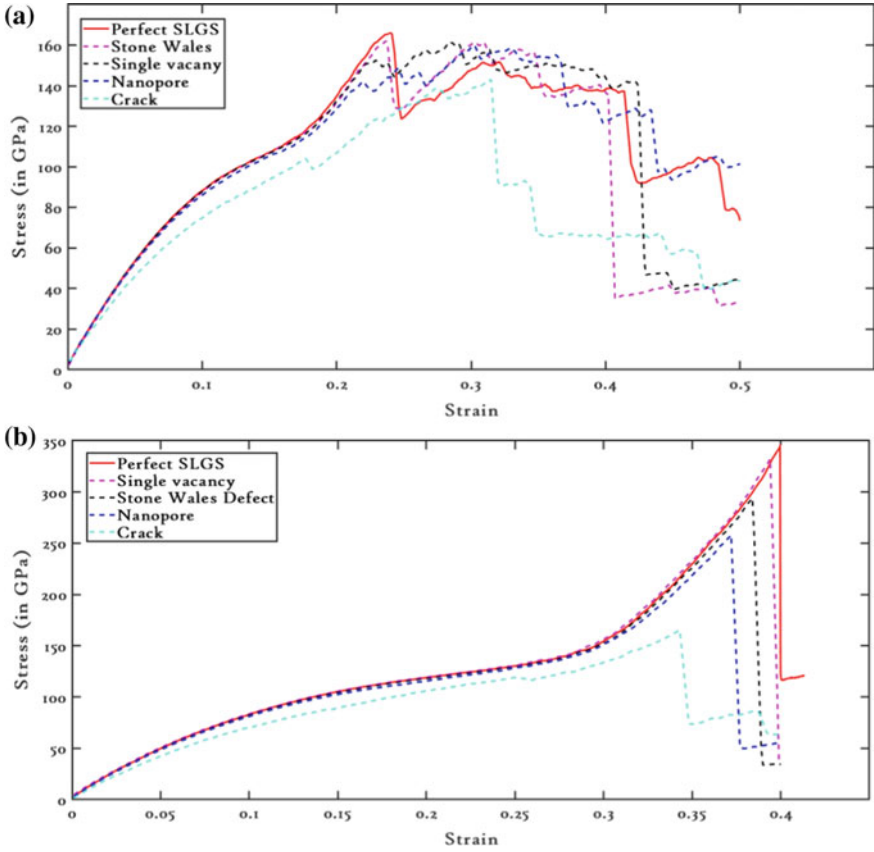


**Fig. 2** Stress–Strain behaviour of perfect and defective graphene in **a** armchair direction and **b** zigzag direction

**Table 2** Comparison of mechanical properties in armchair direction

	$C_{11}$ (in GPa)	$C_{12}$ (in GPa)	Young's modulus (in TPa)	Poisson's ratio	Fracture strength (in GPa)
Perfect SLGS	1074.08	169.04	1.047	0.1573	165.7
Stone-wales defect	1058.34	181.90	1.027	0.1718	161.9
Vacancy defect	1070.78	123.90	1.056	0.1157	151.1
Nanopore	1055.86	164.92	1.030	0.1562	141.4
Crack	935.32	180.16	0.9	0.192	143.1

**Table 3** Comparison of mechanical properties in zigzag direction

	$C_{11}$ (in GPa)	$C_{12}$ (in GPa)	Young's modulus (in TPa)	Poisson's ratio	Fracture strength (in GPa)
Perfect SLGS	1025	273.29	0.952	0.266	346.2
Stone-Wales defect	1009.12	253.46	0.945	0.251	332.2
Vacancy defect	992.99	257.94	0.925	0.259	294.2
Nanopore	970.43	235.86	0.913	0.243	257.9
Crack	848.67	233.83	0.784	0.275	165.2

## 4 Conclusion

The present study uses the MD simulations to uniaxially deform the perfect and defective (Stone–Wales defect, vacancy defect, nanopore and crack) SLGS in both of its loading directions. The AIREBO potential is used to incorporate the interatomic interactions between the constituent atoms. The Nose-Hoover barostat is used to control the atomistic pressure of the system by using the NPT ensemble. The mechanical properties of the perfect and defective graphene sheet are observed in both the directions and it is concluded that defects have the profound impact on the strength of graphene in both the directions, whereas it does not affect the stiffness much, apart from the case of crack present in graphene. It is also seen that the graphene has more resistance to failure in its zigzag direction than armchair direction. However, the graphene has a high value of stiffness in its armchair direction. It is also evident that by introducing defects in graphene and loading it in armchair direction, graphene shows the considerable yielding before failure which remains absent in zigzag direction.

**Acknowledgements** The author(s) would like to acknowledge the financial support provided by the TEQIP-III to attend the conference of ICAMER 2019 at NIT Warangal.

## References

1. Dai MD, Kim CW, Eom K (2012) Nonlinear vibration behaviour of graphene resonators and their applications in sensitive mass detection. *Nanoscale Res Lett* 7(1)
2. Kuila T, Bose S, Khanra P, Mishra AK, Kim NH, Lee JH (2011) Recent advances in graphene-based biosensors. *Biosens Bioelectron* 26:4637–4648
3. Wang G, Wang B, Wang X, Park J, Dou S, Ahn H, Kim K (2009) Sn/graphene nanocomposite with 3D architecture for enhanced reversible lithium storage in lithium ion batteries. *J Mater Chem* 19:8378–8384

4. Lee C, Wei X, Kysar JW, Hone J (2008) Measurement of the elastic properties and intrinsic strength of monolayer graphene. *Science* 321:385–388
5. Lopez-Polin G, Gomez-Navarro C, Parente V, Guinea F, Katsnelson MI, Perez-Murano F, Gomez-Herreto J (2014) Increasing the elastic modulus of graphene by controlled defect creation. *Nat Phys* 11:26–31
6. Mortazavi B, Ahzi S (2013) Thermal conductivity and tensile response of defective graphene: a molecular dynamics study. *Carbon* 63:460–470
7. Zandiatashbar A, Lee GH, An SJ, Lee S, Mathew N, Terrones M, Hayashi T, Picu CR, Hone J, Koratkar N (2014) Effect of defects on the intrinsic strength and stiffness of graphene. *Nat Commun* 1–9
8. Dewapriya MAN, Meguid SA (2018) Tailoring fracture strength of graphene. *Comput Mater Sci* 141:114–121
9. Rajasekaran G, Parashar A (2017) Enhancement of fracture toughness of graphene via crack bridging with stone-thrower-wales defects. *Diam Relat Mater* 74:90–99
10. Verma A, Parashar A (2017) The effect of STW defects on the mechanical properties and fracture toughness of pristine and hydrogenated graphene. *Phys Chem Chem Phys* 19:16023–16037
11. Lee JG (2017) *Computational Materials Science An Introduction*, 2nd edn. CRC Press, Florida
12. Humphrey W, Dalke A, Schulten K (1996) VMD- visual molecular dynamics. *J Molec Graphics* 14:33–38
13. Hanwell MD, Curtis DE, Lonie DC, Vandermeersch T, Zurek E, Hutchison GR (2012) Avogadro: an advanced semantic chemical editor, visualization, and analysis platform. *J Cheminformatics* 4(17)
14. Stuart SJ, Tutein AB, Harrison JA (2000) A reactive potential for hydrocarbons with intermolecular interactions. *J Chem Phys* 112(14)
15. Thompson AP, Plimpton SJ, Mattson W (2009) General formulation of pressure and stress tensor for arbitrary many-body interaction potentials under periodic boundary conditions. *J Chem Phys* 131
16. Plimpton S (1995) Fast parallel algorithms for short-range molecular dynamics. *J Comp Phys* 117:1–19

# Application of Single-Sided NMR and Acousto-Ultrasonic Methods for NDE of Composite Structures



S. K. Sahoo, R. N. Rao, Srinivas Kuchipudi and M. K. Buragohain

**Abstract** New advanced non-destructive evaluation (NDE) methods such as single-sided nuclear magnetic resonance (NMR) and Acousto-ultrasonic methods are being developed for their advantages and high resolution for defect detection in composite structures. Glass fiber-reinforced plastics (GFRP) composites are being used for many industrial applications. Rubber lining in layers is done to the composite inner surface to meet the industrial requirements. The interface of GFRP composite and rubber lining is very critical. Any de-bond (separation of adhesively bonded liner from composite surface) at the interface and delamination between rubber layers may lead to failure of composite structure due to corrosive gases and liquids. NDE of such structures is challenging due to their high attenuation of ultrasound and poor radiography defect signatures. The present study reports application of proton single-sided NMR method to evaluate the de-bonds of rubber liner with composite and delamination between rubber layers. Results are compared with Acousto-ultrasonic method, which uses low-frequency mechanical waves for inspection. Results indicate application of both these techniques for evaluation of bonded interfaces. Advantages of both the techniques over conventional techniques have been discussed.

**Keywords** Composite · NDE · NMR · Acousto-ultrasonic · Defect

## 1 Introduction

Fiber-reinforced composite cylindrical structures with polymer matrix are widely used for many industrial applications including aerospace, petrochemical, automotive, sports and marine industries. Composite structures are fabricated with multiple interfaces in multi-layered configuration for specific applications in industries.

---

S. K. Sahoo · R. N. Rao  
Department of Mechanical Engineering, National Institute of Technology,  
Warangal, Telangana 506004, India

S. K. Sahoo (✉) · S. Kuchipudi · M. K. Buragohain  
Advanced Systems Laboratory, DRDO, Kanchanbagh PO, Hyderabad 500058, India  
e-mail: [sahoosanjayk@rediffmail.com](mailto:sahoosanjayk@rediffmail.com)

© Springer Nature Singapore Pte Ltd. 2020

H. K. Voruganti et al. (eds.), *Advances in Applied Mechanical Engineering*,

Lecture Notes in Mechanical Engineering,

[https://doi.org/10.1007/978-981-15-1201-8\\_61](https://doi.org/10.1007/978-981-15-1201-8_61)

Often such structures are protected from corrosive and moist environments using rubber/elastomeric layers [1]. These layers are adhesively bonded to the composite structure for structural purposes. Integrity of these adhesively bonded layers is important to serve the intended purposes such as oil transportation or hot gases or other industrial uses. During usage, these adhesively bonded structures have to be non-destructively evaluated to avoid the possible failures due to defects such as de-bond, delamination and bulges. Composite structure can fail catastrophically due to weakening of strength when defects occur. NDE of such adhesively bonded structures using various physics-based techniques has been of interest to both industry and NDE community. Reliable NDE methods for bond-quality evaluation of bonded interfaces have been topic of research in industry. Any de-bond at the interface may weaken the structure due to uneven erosion of rubber liner leading to opening of lining, thus exposing composite materials. Many NDE methods are being used to access the bond quality. However, increased reliability of bond quality is both a requirement and necessity to take decision about replacement of the structure. Ultrasonic, X-ray radiography are widely used for bonded interfaces. These techniques have limitations in measuring the thickness of the bond. Both qualitative and quantitative techniques are required for taking decision for replacement of the structure.

Single-sided NMR technique uses chemical signature of the material present within rubber layers as well as the adhesive at the interface [2]. The present study is focused on developing NMR methods for defect detection in glass/epoxy composite cylinder lined with rubber. Proton single-sided NMR system is unique as compared to conventional NMR systems wherein samples are to be taken in vials and inserted into the bore of the magnet to achieve magnetization whereas in single-sided NMR system, magnetic field is outside the core of the magnets. By superimposing AC magnetic field over DC magnetic field, a sensitive volume is generated which can be moved inside the sample by shifting magnets using stepper motor assembly. The present study uses commercially available single-sided NMR system for NDE applications. Advantages of single-sided inspection are access to only one side of structure is required, non-contact inspection, no couplant is required during inspection, safe for operator, portable, qualitative and quantitative assessment of defect is possible [3, 4].

Results of single-sided NMR technique are compared with low-frequency Acousto-ultrasonic method. Low-frequency Acousto-ultrasonic scanning (AUS) is an emerging NDE technique for characterizing and inspecting composite structures with multi-layered configurations. The technique uses low-frequency ultrasonic waves to evaluate the composite structures. It needs only one side access and no couplant is required during the inspection [5, 6]. With the use of tone burst excitation and single frequency in cyclic sinusoidal excitation, it is possible to penetrate deeper into the composite structures through the multiple interfaces to achieve the NDE of the composite structures. The features of AUS that make it suitable and challenging NDE tool over the conventional NDE techniques are ability to penetrate thick multi-layered composite structures, inspection of elastomeric interfaces, no couplant is required during testing, testing can be done from one side, single sided (reflection method) or single sided (pitch-catch method) inspection, provides contact

**Fig. 1** GFRP composite cylinder with rubber lining



mode or non-contact mode of testing and cost-effective inspection setup. Areas of application of AUS include bond-quality evaluation, determining thickness variation and defect detection [7–9]. Inspection of glass/epoxy composite cylinder with known implanted defects by proton single-sided NMR technique and low-frequency ultrasonic methods are presented in this paper.

## 2 Fabrication of Composite Cylindrical Specimen

The glass/epoxy composite cylinder was fabricated using filament winding machine. First the mandrel was prepared by applying Plaster of Paris (PoP) over a metalling rod. Then, the PoP was machined to the desired diameter (i.e., inner diameter (ID) of the cylinder) using conventional lathe machine. The hoop winding process was adopted for winding glass filaments over the rotating mandrel. The mandrel rotates around the spindle while a delivery eye on a carriage traverses horizontally in line with the axis of the rotating mandrel, laying down fibers in the desired hoop winding pattern. The glass filaments are impregnated in a bath with epoxy resin as they are wound on to the mandrel. Once the mandrel is completely covered to the required thickness, the component is sent for curing in an oven. After the component is cured, the mandrel is removed leaving the hollow composite cylinder. Glass/epoxy cylinder of 220 mm ID and 5 mm thick is used for the present study. Nitrile-based rubber of 2 layers (2 mm thick each layer) is used as insulation. Rubber-based adhesive is used for bonding glass/epoxy cylinder with rubber layers. Defects such as de-bond/air-gap and delamination within rubber layers are introduced for study as shown in Fig. 1.

## 3 Experimental Work

Single-sided profile NMR-MOUSE system is based on the principle of inside-out NMR where the sample is outside the magnet. These systems are provided with

stepper motor for precise lifting of magnets to magnetize the region of interest inside the sample. For the present study, commercially available proton solid state NMR system with 12.88 MHz RF frequency as shown in Fig. 2 is used. The profile NMR-MOUSE (PM 25) system is a portable open NMR sensor equipped with a permanent magnet (Bo equivalent to 0.3T) geometry that generates a highly uniform gradient perpendicular to the scanning surface outside the magnets. A flat sensitive volume is excited and detected by a surface RF coil (frequency 12.88 MHz) placed on top of the magnet at a position that defines the maximum penetration depth into the sample. By repositioning the sensitive slice across the object, this scanner produces one-dimensional profiles of the sample with a spatial resolution of 30  $\mu\text{m}$ . The present study reports result from experiments performed with CPMG (Carr-Purcell-Meiboom-Gill) pulse sequence at pre-defined position programmed using PROSPA software. The sensor excites a sensitive volume at a fixed distance from the magnet surface as per the program. By mechanically moving the sensor, the sensitive volume is stepped through the sample and the CPMG sequence is then applied at each position with an echo-time of 60  $\mu\text{s}$ . Then signal from each position is plotted as amplitude versus depth plot to generate depth profile of the sample.

The experimental setup for low-frequency Acousto-ultrasonic inspection consists of tone burst excitation pulser and broadband receiver system (frequency range of 10 kHz to 20 MHz) along with pre-amplifier electronics and low-frequency ultrasonic probes. The entire electronics and back-up power supply are housed in a safety certified composite enclosure. The system is portable for testing at the shop floor. The test signals were captured in A-scan mode for further analysis. In A-scan mode, amplitude versus time of flight of tone burst excitation received using broadband receiver is captured. Two cycles of sinusoidal burst of 75 kHz frequency are used for

**Fig. 2** Profile NMR system with sample on the top



**Fig. 3** Acousto-ultrasonic system used for testing glass/epoxy structure with rubber lining





testing. One probe for excitation and other probes for receiving were used in pitch-catch mode. Figure 3 shows the Acousto-ultrasonic system used for the present study.

### 4 Results and Discussion

CPMG sequence is used for obtaining data at each of the depth during profile experiments. From the CPMG fast data, normalized peak integral value is plotted as a function of depth. Figure 4a, b shows normalized peak integral value of glass/epoxy cylinder bonded with rubber as a function of depth (in microns) and weighted function of normalized peaks, respectively. Depth profile data shows no signature of glass/epoxy cylinder whereas adhesive-rubber interface shows steep increase in amplitude at the depth corresponding of 5 mm. This is because of low proton signature from epoxy resin and it may also be noted that glass fiber does not have protons. Hence, no signal is obtained from composite sample, whereas the signal from rubber is observed until the entire thickness of the rubber is scanned. Beyond rubber thickness of 4 mm, the signal value falls to baseline indicating absence of protons beyond the rubber material. Weighted function of amplitude of peaks versus depth also clearly indicates the signature of rubber. From the weighted function, the thickness of rubber layers can be clearly ascertained. Figure 5 shows Acousto-ultrasonic data of the test specimen over the defect-free region. Number of bunch of ultrasonic signals received at the receiver in pitch-catch mode is observed. The signal is characteristic of the sample on a defect-free zone. Experiments were again performed on test specimen on other zones with suspected defects. Figure 6a, b shows normalized peak integral value of glass/epoxy sample bonded with rubber as a function of depth (in microns) and weighted function of normalized peaks, respectively at delamination zone (defect

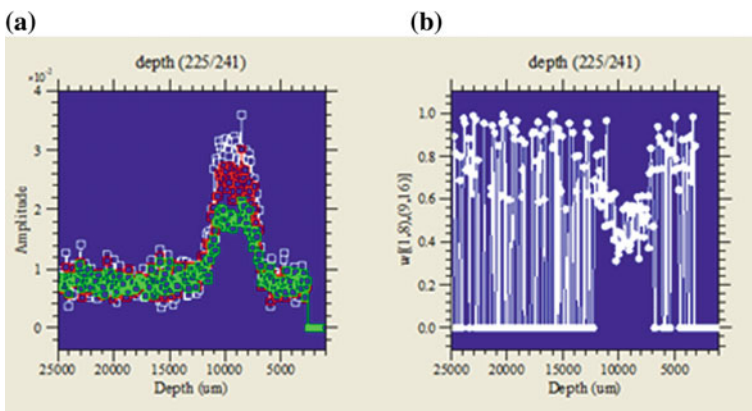
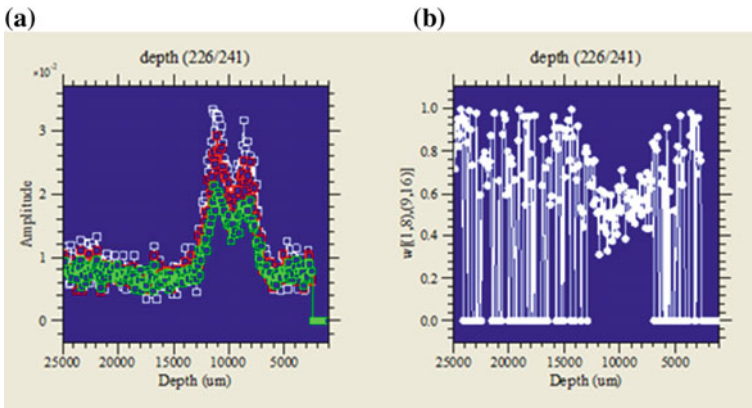
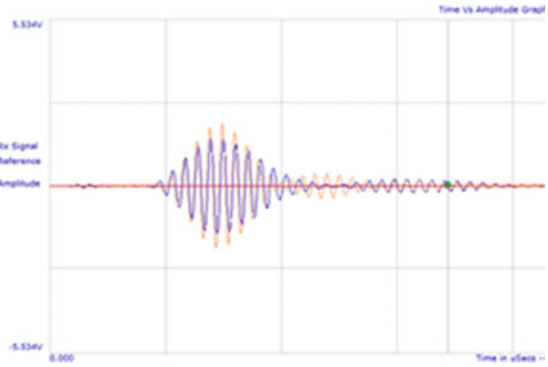


Fig. 4 a, b Profile NMR data at defect-free zone

**Fig. 5** AUS data at defect-free zone

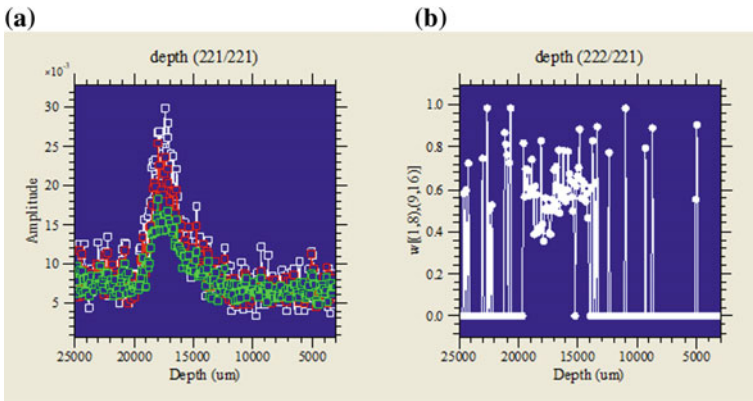
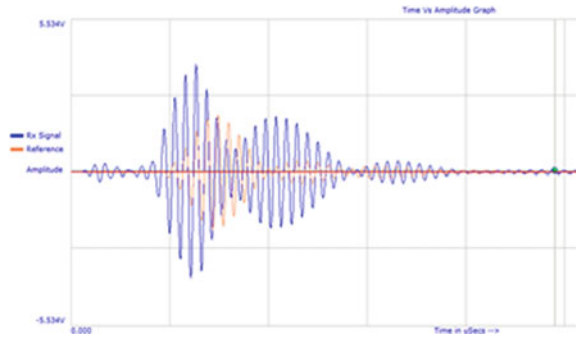


**Fig. 6** a, b Profile NMR data at delamination zone (within rubber layers)

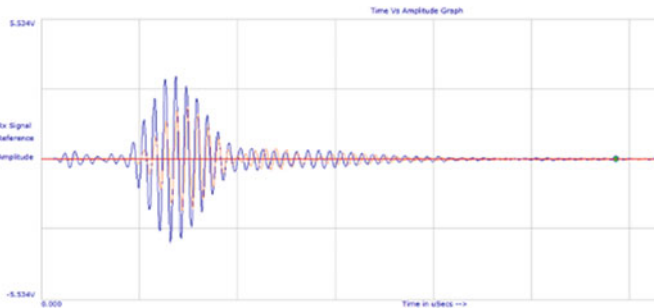
within rubber layers). Dip in the rubber signal data is clearly seen. It is also observed that increase in the width obtained using weighted function indicating extended proton signature due to separation of rubber layers. The separation of two rubber layers was further confirmed from X-ray radiography data taken using tangential method.

Figure 7 shows Acousto-ultrasonic data over defective region. Signal shows multiple peaks appearing over time domain indicating multiple reflections occurring from different regions. Composite specimen was further tested at de-bond zone. From Fig. 8a, b, there is no notable change in the signature of the rubber; however, the depth of the rubber is observed to be shifted to higher values indicating the presence of air-gap when compared with Fig. 4a, b. The air-gap thickness can be calculated from the shifted value taken from the X-axis. In this case, the air-gap thickness is  $7000 + 30 \mu\text{m}$ . Figure 9 shows the Acousto-ultrasonic data of the test sample over the defect region (de-bond). It is observed to show increase in amplitude as compared to Fig. 5 (non-defect region). This is due to the increased energy of the ultrasound due to reflection from de-bond. In case of the bonded zone, energy of the ultrasound

**Fig. 7** AUS data at delamination zone



**Fig. 8** a, b Profile NMR data at de-bond zone



**Fig. 9** AUS data at de-bond zone

gets attenuated whereas over the de-bond zone, the ultrasonic energy gets reflected back from the interface and more energy is received at the receiver end.

Table 1 gives the comparison of profile NMR data for all the three zones. From the comparison, it is observed that thickness of glass/epoxy composite and rubber can

**Table 1** Comparison of profile NMR data

Zone	Beginning of rubber signature ( $\mu\text{m}$ )	Ending of rubber signature ( $\mu\text{m}$ )	Difference ( $\mu\text{m}$ )
Defect free	7000	12,000	5000
Defect within rubber layers	7000	13,000	6000
De-bond	14,000	19,000	5000

be ascertained clearly. Initial delay in beginning of rubber signature indicates discontinuities like de-bond, air-gap, foreign material inclusion, etc., at the glass/epoxy and rubber interface. Presence of delamination or air-gap within rubber layers can also be seen clearly with dip or kink in rubber signal data and also increase in the width indicating increased proton density.

## 5 Conclusion

Single-sided profile NMR technique is observed to be qualitative as well as quantitative NDE tool for evaluating bond quality of glass/epoxy-rubber bonded interfaces. Defects such as de-bonds, air-gaps, delamination and wrinkles or folds within rubber layers including thickness of rubber layers were evaluated. Acousto-ultrasonic inspection method works as a complementary NDE tool with defect information obtained qualitatively. Both the techniques are safe to be used on the shop floor for qualitative and quantitative assessment of defects.

**Acknowledgements** The authors are thankful to the Director, ASL for providing an opportunity, support and encouragement to carry out this work.

## References

1. Buragohain MK (2017) Composite structures: design, mechanics, analysis, manufacturing and testing. CRC Press (2017)
2. Saalwachter K (2006) Chain dynamics in elastomers as investigated by proton NMR. *Macromolecules* 39:3291–3303
3. Dykstra R, Callaghan RT, Eccles D, Hunter M (2005) Portable NMR systems for non destructive testing. *Non-destr Testing Aust* 1:15–18
4. Srinivas K et al (2015) Single sided NMR for NDE of GFRP—rubber interface. *e-J Non-destr Testing* 20(6):ISSN 1435–4934
5. Raju PK (1997) Acousto-ultrasonic technique for non-destructive evaluation of composites and structures. *J Acoust Soc Am* 102:3082
6. Mareeswaran S, Sasikumar T (2017) The acousto—ultrasonic technique: a review. *Int J Mech Eng Technol* 8(6):418–434

7. Srivastava VK (1995) Acousto—ultrasonic evaluation of interface bond strength of coated glass fibre—reinforced epoxy resin composites. *Compos Struct* 30:281–285
8. Kwon O-Y, Lee S-H (1999) Acousto-ultrasonic evaluation of adhesively bonded CFRP-aluminum joints. *NDT&E Int* 32:153–160
9. Daniel IM, Luo JJ, Hsiao HM (1998) Acousto-ultrasonic techniques for evaluation of bond integrity of composite repair patches. *Rev Prog Quant Non-destr Eval* 17:1331–1338

# Effect of Material Damping on the Vibration Response of Cantilever Beams in Dynamic Environment



L. Viswanadham, R. N. Rao and Ch. Sri Chaitanya

**Abstract** In the present study, the dynamic response of the cantilever was studied by exciting it using a vibration exciter. The aluminium cantilever beam was excited with random and sine vibration conditions, and the response of the beam was obtained using accelerometers. The natural frequency and the free end oscillations were studied. The natural frequency varied with material due to their stiffness. The displacements at free end were higher for shock loads whereas they were lower for random vibrations. The trends of the vibration response with acceleration remain same for both types of vibration but the variation between them was visible only at higher accelerations.

**Keywords** Vibration · Response · Cantilever beams · Vibration excitation

## 1 Introduction

The vibration analysis of cantilever beams has been widely studied by researchers. Most of the structures used in engineering application experience excitation by external forces. When the excitations applied to these structures vary, the response will be uncertain. This uncertainty leads to an interest to study these responses. The sensitive components like electronics which are mounted in aerospace, aircraft and missile structures endure serious damages due to the vibrations caused by the engine movement and atmospheric loads. The structures on which these components were mounted can be assumed as cantilever beams and the study of the response of these beams to the vibrations can be used to design the mounting of electronic equipment on aerospace structures. These studies can also be used to check the structural integrity of the aerospace structures. The cost of failure in aerospace structures is very high and utmost care must be taken while designing. Hence, the study of response of the aerospace structures for the vibration environment during flight is necessary.

---

L. Viswanadham (✉) · R. N. Rao · Ch. Sri Chaitanya  
Department of Mechanical Engineering, National Institute of Technology,  
Warangal, Telangana 506004, India  
e-mail: [visu\\_rci@yahoo.co.in](mailto:visu_rci@yahoo.co.in)

© Springer Nature Singapore Pte Ltd. 2020  
H. K. Voruganti et al. (eds.), *Advances in Applied Mechanical Engineering*,  
Lecture Notes in Mechanical Engineering,  
[https://doi.org/10.1007/978-981-15-1201-8\\_62](https://doi.org/10.1007/978-981-15-1201-8_62)

The vibration controllers do not consider the nonlinear accelerations and when the high performance is required from the structure, the performance of the vibration controllers will be poor [1]. Hence, the structures made using the materials with good inherent responses will improve the performance. The aerospace structures are subjected to a wide range of frequency and the study of the response of these structures is difficult to analyse using theoretical models [2]. The damping in the structure due to the material characteristics has the major impact compared to that the damping due to the surrounding environment and the mounting methods [3]. Tang et al. [4] analysed the bolted joined cylindrical shells and the effect of the number of bolts used to join the shell, the stiffness of the joint and the length ratio on the natural frequencies are studied. The natural frequency of the system varied irregularly with number of bolts when the number of bolts used for the joint is small but when they are large in number the frequency of the structure increased with the increase in number of bolts but the variation tends to become stable very quickly. The sensitivity of the natural frequency with the stiffness of the joint is more apparent with the unsymmetrical assembly. The stable natural frequency changes if the stiffness is large enough. The length ratio also has significant effect on the natural frequency but the length can easily be controlled. The stiffness of the material is varied by inducing the damage to the structure and its effect is studied and observed that the bending failures do not vary the first mode natural frequency [5]. It is reported in the literature that the variation in acceleration of the structure effects its angle of attack and also varies the stress distribution in it [6]. The modal testing of the structures by using vibration excitation is an easy and accurate method to study the inherent material properties and also the failure modes for quality inspection. These tests can also be used to study the elastic constants, creep, fracture toughness, damage and degradation, etc. [7].

From the literature, it is evident that the major focus on the material properties and the shape effecting the vibration response of the structures. Current study focuses on the response of the same material and size with variation of the vibration imparted to the structure.

## 2 Materials and Methods

Aluminium alloy (AA2014), stainless steel and magnesium were chosen as a base material for the current study. The alloy was cast into a block and then machined to the shape of a cantilever beam of dimensions 74 mm wide, 80 mm length and thickness of 5 mm. The cantilever beam is mounted on the vibration exciter by drilling four holes of 5 mm diameter along one edge of the beam and using bolts as shown in Fig. 1.

The response of the cantilever because of the mounting was obtained using accelerometers. The control acceleration was given to the specimen. A 20–2000 Hz

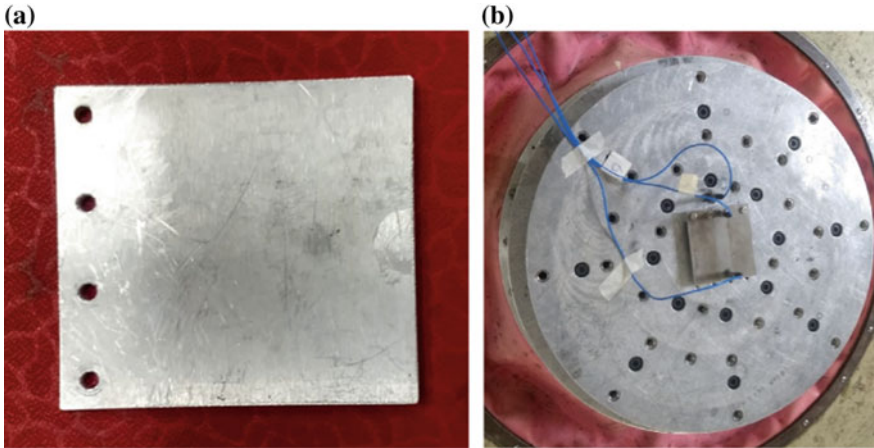


**Fig. 1** **a** The cantilever beam used in the current study with M5 holes at the mounting edge. **b** The sample that is mounted on the vibration exciter and accelerometers attached to acquire the response

sweep was given to the cantilever beam using both the sine and random type vibrations. The response was visualized and analysed using a computer and data acquisition software. The vibration excitation was achieved by using a current-carrying coil around the movable base of the vibration exciter. When the current was induced to the armature coil around the base, a force (Biot–Savart’s law) is exerted on the base. The response was acquired using accelerometers. The accelerometers were mounted at the base and the free end of the cantilever beam. The forces due to the vibration motion will stress the piezoelectric structures present in the accelerometers which generate a potential. This response from accelerometers will be converted into the displacement and the result was used in the study.

### 3 Results and Discussion

The vibrations are imparted to the cantilever beam made of aluminium, magnesium and steel at the sine and random modes. The response of the cantilever beams was obtained using accelerometers and the variations were compared.

#### 3.1 *Random Vibrations*

The cantilever beam system was forced to vibrate in random vibration environment. The vibrations were accelerated from 20 Hz to 2000 Hz at 1grms to 5grms. The responses of the cantilever beam at the free end of the cantilever beam were obtained



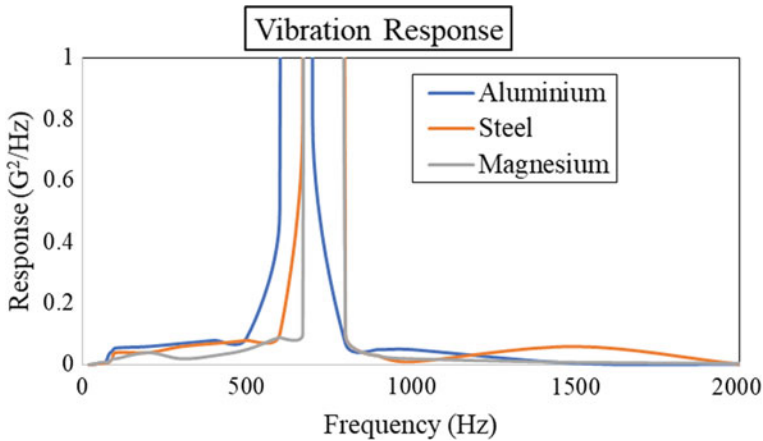


**Fig. 2** Vibration response of aluminium, steel and magnesium cantilever beams in vibration sweep cycle of 20–2000 Hz in random vibration mode

using the uniaxial accelerometers which were visualized using a computer. From Fig. 2, it is observed that the natural frequency of the system magnesium has higher natural frequency and the vibrations were lower. At higher frequencies, the steel beams show higher response.

### 3.2 Sinusoidal Vibrations

For sinusoidal vibrations, the similar pattern as that of the random vibrations was followed. The vibrations were accelerated from 20 Hz to 2000 Hz at 1G to 5G. The magnesium cantilever beam has higher range of natural frequency. The displacements are also lower for magnesium at higher frequencies. The response of the beams measured at the free end during the vibration sweep of sinusoidal vibrations at an acceleration of 5G was shown in Figs. 3 and 4.

The natural frequency of the aluminium, steel and magnesium cantilever beam system can be seen at around 650, 400 and 800 Hz, respectively. This variation in the natural frequency between the materials may be due to their differences in material damping caused by different stiffness. Figure 5 shows that the magnesium beams have higher damping properties and can be used in the structures to mount the electronic equipment in aerospace vehicles.

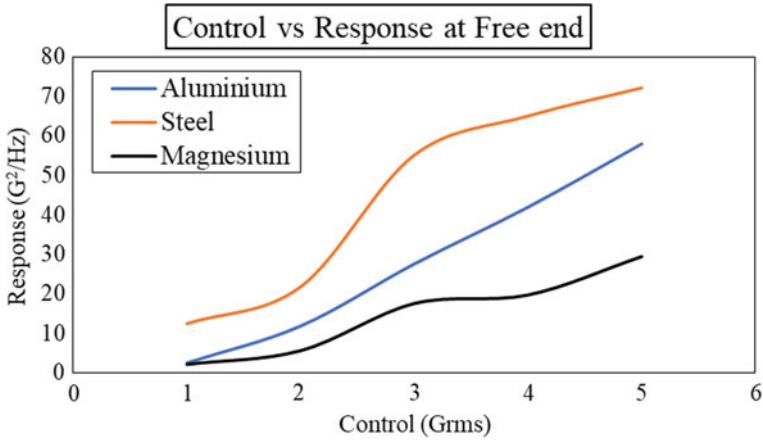


**Fig. 3** Control versus response of cantilever beams with variation of control acceleration during the 20–2000 Hz random vibration sweep

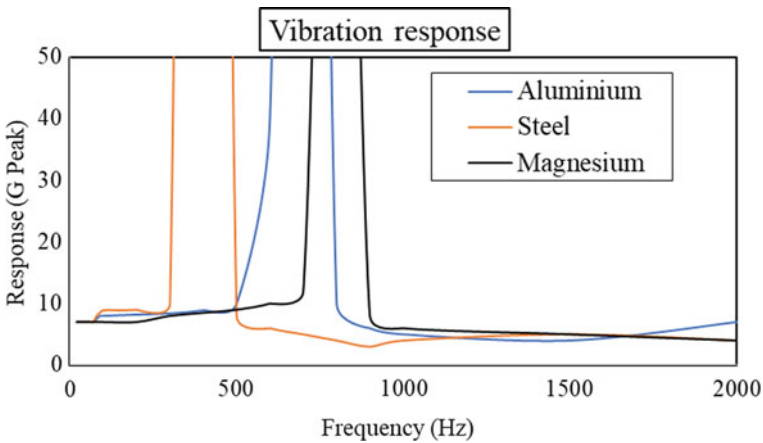


**Fig. 4** Vibration response of aluminium, steel and magnesium cantilever beams in vibration sweep cycle of 20–2000 Hz in sinusoidal vibration mode

### 4 Conclusion

- The natural frequency of the magnesium was higher than that of the other two materials used in both the random and sinusoidal vibration conditions.
- For random vibrations, the response of magnesium was lower and clearly distinguishable.
- Deflections of the magnesium beams were lower in all the conditions, this may be due to the high stiffness of magnesium material.

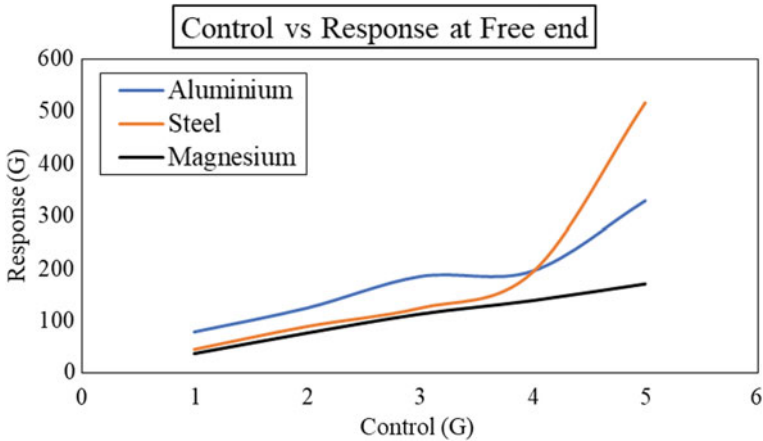


**Fig. 5** Control versus response of cantilever beams with variation of control acceleration during the 20–2000 Hz sinusoidal vibration sweep

- The trends of the response of beams are similar to each other which implies the variation in response does not depend on the material.

## References

1. Mori Y, Tagawa Y (2018) Vibration controller for overhead cranes considering limited horizontal acceleration. *Control Eng Pract* 81:256–263
2. Aykan M, Celik M (2009) Vibration fatigue analysis and multi-axial effect in testing of aerospace structures. *Mech Syst Sig Process* 23(3):897–907
3. Foong FM, Thein CK, Yurchenko D (2019) On mechanical damping of cantilever beam-based electromagnetic resonators. *Mech Syst Sig Process* 119:120–137
4. Tang Q, Li C, She H, Wen B (2018) Vibration analysis of bolted joined cylindrical-cylindrical shell structure under general connection condition. *Appl Acoust* 140:236–247
5. Viglietti A, Zappino E, Carrera E (2018) Free vibration analysis of locally damaged aerospace tapered composite structures using component-wise models. *Compos Struct* 192:38–51
6. Gledhill IMA, Forsberg K, Eliasson P, Baloyi J, Nordström J (2009) Investigation of acceleration effects on missile aerodynamics using computational fluid dynamics. *Aerospace Sci Technol* 13(4–5):197–203
7. Gibson RF (2000) Modal vibration response measurements for characterization of composite materials and structures. *Compos Sci Technol* 15(60):2769–2780

# Active Vibration Control in Turbocharger Rotor System with the Use of Electromagnetic Actuator



Rajasekhara Reddy Mutra and J. Srinivas

**Abstract** This work presents an active vibration control scheme in high-speed turbocharger rotor system. The working speed of these rotors is very high so a small vibration may damage the system, so there is a requirement to control such unwanted vibrations. Most of the cases these rotors are supported on the floating ring bearings. Initially, the rotor model is developed with finite element method to get the dynamic response of the system due to unbalance and gravity forces. The nonlinear hydrodynamic bearing forces are computed and the equations of motion of multi-degree of freedom turbocharger model are solved with time integration scheme. After obtaining the parametric effects of the bearing on overall system response an electromagnetic actuator system is adopted to control the vibration amplitudes in the system. The methodology is found to be reliable and reduces the vibration amplitudes considerably.

**Keywords** Bearing forces · Frequency response · Turbocharger · Active control

## 1 Introduction

Rotor-bearing systems are important elements in heavy machinery including turbo-compressors and turbo-pumps. The fluid film journal bearings are widely used in turbochargers. Under high-speed operations, this kind of bearing supports large radial loads. During the last two decades, several works focused on various approaches such as utilizing modal data, time and frequency responses as well as wavelet data for identification of the faults in rotors. The turbocharger rotates with very high speeds even small vibration can destroy the system so the vibration control in turbocharger rotor-bearing system is very essential task. There are various methods to control the

---

R. R. Mutra (✉)

Vignan's Institute of Information Technology, Visakhapatnam, Andhra Pradesh 530046, India  
e-mail: [rajmech03@gmail.com](mailto:rajmech03@gmail.com)

J. Srinivas

National Institute of Technology, Rourkela, Odisha 769008, India

© Springer Nature Singapore Pte Ltd. 2020

H. K. Voruganti et al. (eds.), *Advances in Applied Mechanical Engineering*,

Lecture Notes in Mechanical Engineering,

[https://doi.org/10.1007/978-981-15-1201-8\\_63](https://doi.org/10.1007/978-981-15-1201-8_63)

vibrations in rotor-bearing system such as active and semi-active vibration control techniques.

Dorier and Tichy [1] investigated the lubrication flow behavior in viscous fluids with Bingham method. In order to use the continuous constitutive law, the generalized Reynold's equation was used. A planar slider bearing in 2-D flow and two plates in parallel with an applied pressure in 3-D flow were studied. The stress and strain rate parameter effects on the fluid were explained. Williams et al. [2] explained the electroreological fluids (ERF) non-Newtonian behavior with a mathematical model. Aoyama and Inasaki [3] explained the usage of ER fluids in the machine tool elements, this was helped to increase the machine tool dynamic characteristics. Nikolakopoulos and Papadopoulos [4, 5] presented an experimental analysis of high-speed journal bearings with ER fluids as lubricants. As a function of an electric field, the shear stress, dynamic yield stress and relative viscosity were identified from experiments. Sharma and Khatri [6] explained the influence of the ERF on the reliability of the hybrid journal bearings. Forte et al. [7] explained the design procedure of a magnetorheological (MR) squeeze film damper for rotor applications. As a function of magnetic field strength, the dynamic behavior of the damped rotor was analyzed numerically. Bompos and Nikolakopoulos [8] presented the computational fluid dynamics and finite element methods to study the simulation of the MR fluid journal bearing. In this analysis, the magnetic field and  $L/D$  ratios are considered as functions to estimate the bearing parameters. Kazakov et al. [9] proposed an analytical method to measure the power characteristics of the magnetorheological dampers with magnetorheological fluid as a lubricant. Vance and Ying [10] investigated experimentally the stiffness and damping coefficients of the bearing with the use of two types ER fluid in the turbomachinery. Lim et al. [11] used semi-active vibration control scheme in high-speed spindle system with ER fluid damper.

Basumatary et al. [12] described the numerical study on the effect of magnetic actuator on the stability of rigid rotor supported on bump type gas foil bearings. Kim et al. [13] explained the design and modeling of the controllable semi-active squeeze film dampers (SFD) using magnetorheological (MR) fluids. The influence of critical design parameters on the performance of the MR-SFD was studied. Rotor system supported on active magnetic bearings (AMB) was used to characterize the dynamic behavior of the prototype model. Ferfecki and Zapomel [14] explained the steady state vibration of the rotor, which was placed with the stationary part controlling constraint elements. In this analysis, two design variants are considered the first one was rolling elements bearings with magnetorheological squeeze film damper and the second one was journal bearings with movable housing. Wang et al. [15, 16] presented a measuring method of rotor dynamic coefficients of a controllable floating ring bearing and semi-floating ring bearings. Calvo et al. [17] proposed a method to control the whistling noise in the turbocharger. In order to maintain the acoustic comfort of the automobile, the unbalanced force variation has been suggested. A test procedure to estimate the vibration performance in turbocharger in the vehicle was established. Feng et al. [18] explained the analysis of the active bump foil bearings with controllable mechanical preloads. In this analysis, the active and compliant foil structure model was developed theoretically. Das et al. [19, 20] proposed a method of

an active vibration control of an unbalanced rotor-shaft system on excited base was studied. Electromagnetic control force is given by an actuator, and it contains four electromagnetic exciters were used to place on the stator in a correct plane around the rotor shaft.

In the present work, an active vibration controls scheme in high-speed turbocharger rotor system. Initially, the rotor model is developed with finite element method to get the dynamic response of the system due to unbalance and gravity forces. The equations of motion of multi-degree of freedom turbocharger model are solved with time integration scheme. After obtaining the parametric effects of the bearing on overall system response an electromagnetic actuator system is adopted to control the vibration amplitudes in the system. Remainder of the paper is organized as follows: Sect. 2 describes the mathematical modeling of rotor system using finite analysis. Section 3 presents the methodology employed and the proposed scheme in brief. Section 4 gives the results and discussion.

## 2 Rotor-Bearing System Model

The rotor-bearing system is shown in Fig. 1. The rotor model is formulated using quasi-finite element analysis with lumped floating ring masses considered at the bearing locations. The shaft is considered as flexible member and disks are treated as rigid. Each node has four degrees of freedom (DOF) including two translations ( $u_x, u_y$ ) and two bending slopes ( $\theta_x, \theta_y$ ).

The equations of motion of the rotor are expressed as:

$$\mathbf{M}\ddot{\mathbf{q}} + [\mathbf{C} + \Omega\mathbf{G}]\dot{\mathbf{q}} + \mathbf{K}\mathbf{q} = \mathbf{F} \tag{1}$$

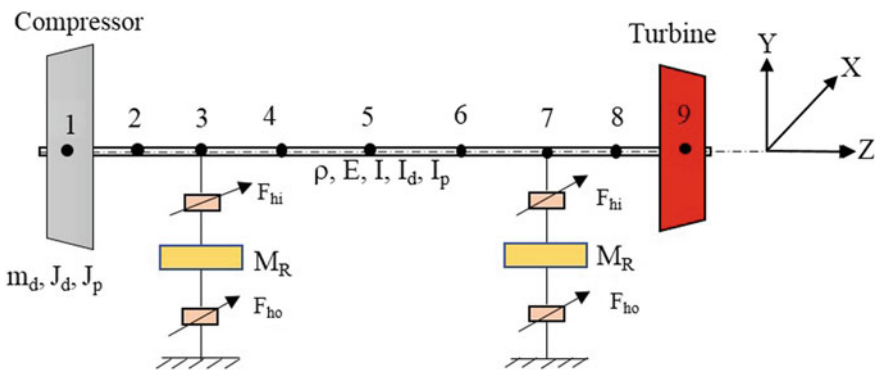


Fig. 1 FE model used

Here,  $\mathbf{M}$ ,  $\mathbf{C}$ ,  $\mathbf{G}$  and  $\mathbf{K}$  denote, respectively, the assembled mass, damping, gyroscopic and stiffness matrices of size  $N \times N$ . Also,  $q$  is the  $N \times 1$  displacement vector,  $F$  is unbalanced and gravity force vector at the disks.

## 2.1 Bearing Forces

The floating ring bearing (FRB) model developed in this article refers to the Capone model in Refs. [21–23]. The components of forces from the pressure distribution at the inner and outer films are as follows:

$$\begin{Bmatrix} F_{ix} \\ F_{iy} \end{Bmatrix} = \mu_i (\Omega_j + \Omega_r) R_j L_i \left( \frac{R_j}{C_1} \right)^2 \left( \frac{L_i}{2R_j} \right)^2 \begin{Bmatrix} f_{ix} \\ f_{iy} \end{Bmatrix} \quad (2)$$

$$\begin{Bmatrix} F_{ox} \\ F_{oy} \end{Bmatrix} = \mu_o \Omega_r R_{ro} L_o \left( \frac{R_o}{C_2} \right)^2 \left( \frac{L_o}{2R_{ro}} \right)^2 \begin{Bmatrix} f_{ox} \\ f_{oy} \end{Bmatrix} \quad (3)$$

where  $f_{ix}, f_{iy}$  and  $f_{ox}, f_{oy}$  indicate the component forces on the journal and bearing, respectively, as given in the reference.

## 3 Methodology Used in the Present Analysis

To reduce the vibration amplitude of the system appropriate magnetic force should have applied by the actuator force should act in the opposite direction of motion and should increase with displacement. The magnetic force, on the other hand, depends upon the pole winding current of an electromagnet, so by controlling pole winding currents, the system response can be controlled. Proportional–Derivative (PD) control is generally used for faster response. Proportional control increases the control input in proportion to the error  $e(t)$  within the acceptable range of error. Derivative control changes the control input in proportion rate of change of error. The control system logic is shown in Fig. 2.

Here, the proportional and derivative gains  $l_p$  and  $l_v$  are selected as 10 and 0.1, respectively. Other parameters include:  $A_a = 240 \text{ mm}^2$ ,  $N_c = 106$ ,  $\psi = 22.5^\circ$ ,  $B = 0.9 \text{ mm}$  and  $I_b = 3 \text{ A}$ . The instantaneous current components  $i_1$  and  $i_2$  depend on the displacements  $x$  and  $y$  at the eighth node.

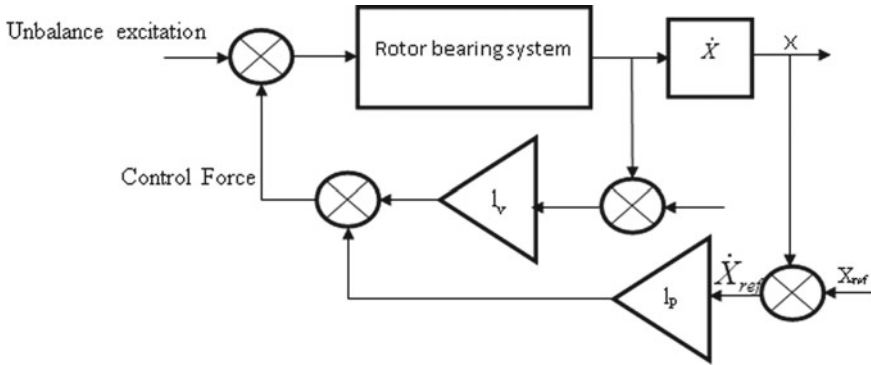


Fig. 2 PD control strategy for controlling vibrations

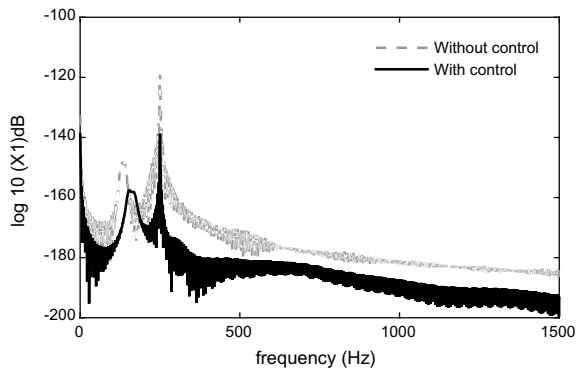
### 4 Results and Discussion

Dimensional data of the rotor-bearing system considered is depicted from Ref. [24]. The MATLAB program is changed such that the right-hand side force vector carries additional magnetic force components at the eighth node. With and without control frequency response of rotor is shown in Fig. 3. It is observed that the amplitudes with control are reduced at all the modes. The methodology can be extended for other nodes of interest also.

The phase plot and Poincare map at the eighth node, when shaft speed of 1000 rpm is shown in Fig. 4. It is observed that the motion is of non-synchronous vibratory nature.

As the shaft speed reaches higher, the motion becomes multi-periodic as observed in Fig. 5. The electromagnetic actuator is designed in order to reduce the amplitudes at the eighth node of the rotor over the entire operating speed range so the electromagnetic actuator target is to achieve the null value of displacement and velocity at the eighth node of the rotor. The influence of the axial deformation is not accounted

Fig. 3 Frequency response with and without control





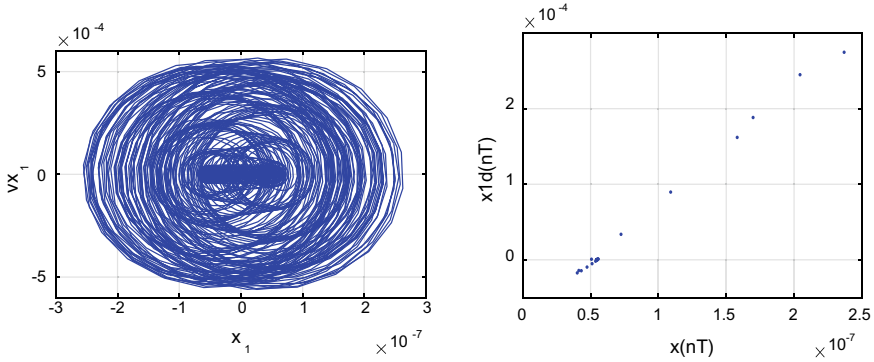


Fig. 4 Phase plot and Poincare diagram at eighth node of rotor system

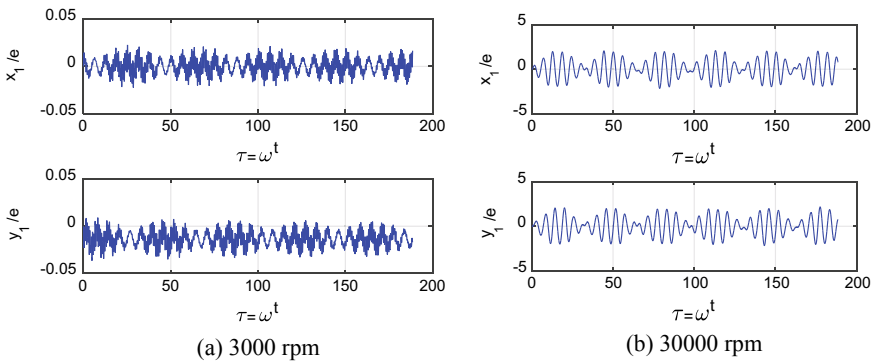
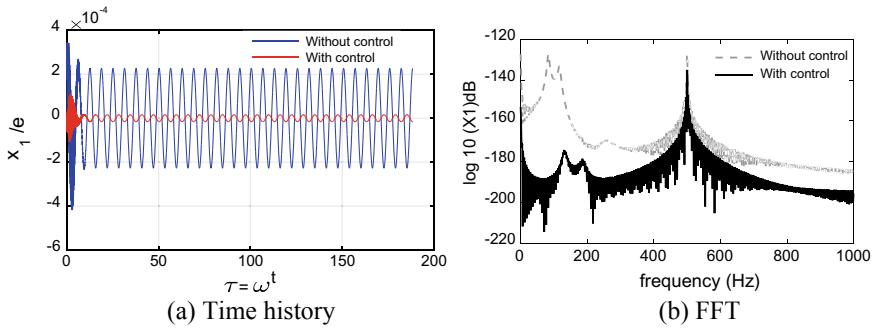


Fig. 5 Time histories at eighth node of rotor system

while modeling. To eliminate the rotational degrees of freedom static condensation is implemented and all the initial conditions are considered as zero.

The non-dimensional time history and FFT at the eighth node in the x-direction both with and without control are shown in Fig. 6. It is observed that the shaft resonates at 150 Hz and after applying, the control of the unstable motion persists due to the rotary force generated by internal damping of the rotor. It can be identified from above plots that with the use of proportional derivative the larger amplitudes are decreased to the reasonable levels. The focus of control is to attenuate large amplitudes in the operations and to prevent the rotor from dangerous damaging conditions.



**Fig. 6** Time response and FFT before and after control

## 5 Conclusion

This work presented an active vibration control scheme in high-speed turbocharger rotor system. The rotor model was developed with finite element method to get the dynamic response of the system due to unbalance and gravity forces. The equations of motion of multi-degree of freedom turbocharger model were solved with time integration scheme. The parametric effects of the bearing on overall system response were studied. An electromagnetic actuator system was adopted to control the vibration amplitudes in the system. The methodology was found to be reliable and reduces the vibration amplitudes considerably.

## References

1. Dorier C, Tichy J (1992) Behavior of a bingham-like viscous fluid in lubrication flows. *J Non-Newton Fluid Mech* 45:291–310
2. Williams EW, Rigby SG, Sproston JL, Stanway R (1993) Electrorheological fluids applied to an automotive engine mount. *J Non-Newton Fluid Mech* 47:221–238
3. Aoyama T, Inasaki I (1997) Application of electrorheological fluid dampers to machine tool elements. *CIRP Ann* 46:309–312
4. Nikolakopoulos PG, Papadopoulos CA (1996) High speed journal bearings lubricated with electro-rheological fluids: an experimental investigation. *Int J Mod Phys B* 10:3045–3055
5. Nikolakopoulos PG, Papadopoulos CA (1998) Controllable high speed journal bearings, lubricated with electro-rheological fluids. An analytical and experimental approach. *Tribol Int* 31:225–234
6. Sharma SC, Khatri CB (2017) Electro-rheological fluid lubricated textured multi-lobe hole-entry hybrid journal bearing system. *J Intell Mater Syst Struct* 29:1600–1619
7. Forte P, Paternò M, Rustighi E (2004) A magnetorheological fluid damper for rotor applications. *Int J Rotating Mach* 10:175–182
8. Bompos DA, Nikolakopoulos PG (2011) CFD simulation of magnetorheological fluid journal bearings. *Simul Model Pract Theory* 19:1035–1060
9. Kazakov YB, Morozov NA, Nesterov SA (2017) Development of models of the magnetorheological fluid damper. *J Magn Magn Mater* 431:269–272

10. Vance JM, Ying D (2000) Experimental measurements of actively controlled bearing damping with an electrorheological fluid. *J Eng Gas Turbines Power* 122:337–344
11. Lim S, Park SM, Kim KI (2005) AI vibration control of high-speed rotor systems using electrorheological fluid. *J Sound Vib* 284:685–703
12. Basumatary KK, Kumar G, Kalita K, Kakoty SK (2017) A Numerical study on effect of electromagnetic actuator on rigid rotor supported on gas foil bearing. In: ASME 2017 gas turbine India conference. ASME, Bangalore, India, pp 1–9
13. Kim KJ, Lee CW, Koo JH (2008) Design and modeling of semi-active squeeze film dampers using magneto-rheological fluids. *Smart Mater Struct* 17:035006–035010
14. Ferfecki P, Zapoměl J (2012) Investigation of vibration mitigation of flexibly support rigid rotors equipped with controlled elements. *Procedia Eng* 48:135–142
15. Wang X, Li H, Meng G (2017) Rotordynamic coefficients of a controllable magnetorheological fluid lubricated floating ring bearing. *Tribol Int* 114:1–14
16. Wang X, Li H, Lu W, Meng G (2017) Stiffness and damping properties of (semi) floating ring bearing using magnetorheological fluids as lubricant. *J Tribol* 139:051701–051711
17. Calvo JA, Diaz V, San Roman JL (2005) Controlling the turbocharger whistling noise in diesel engines. *Int J Veh Noise Vib* 2:17–28
18. Feng K, Guan HQ, Zhao ZL, Liu TY (2018) Active bump-type foil bearing with controllable mechanical preloads. *Tribol Int* 120:187–202
19. Das AS, Nighil MC, Dutt JK, Irretier H (2008) Vibration control and stability analysis of rotor-shaft system with electromagnetic exciters. *Mech Mach Theory* 43:1295–1316
20. Das AS, Dutt JK, Ray K (2010) Active vibration control of unbalanced flexible rotor–shaft systems parametrically excited due to base motion. *Appl Math Model* 34:2353–2369
21. Adiletta G, Guido AR, Rossi C (1996) Chaotic motions of a rigid rotor in short journal bearings. *Nonlinear Dyn* 10:251–269
22. Ying G, Meng G, Jing J (2009) Turbocharger rotor dynamics with foundation excitation. *Arch Appl Mech* 79:287–299
23. Wang JL, Cao DQ, Huang WH (2010) A new fluid film force model of elliptical bearing: Modelling and case studies. *Proc Inst Mech Eng Part J: J Eng Tribol* 224:595–608
24. Bonello P (2009) Transient modal analysis of the non-linear dynamics of a turbocharger on floating ring bearings. *Proc Inst Mech Eng Part J: J Eng Tribol* 223:79–93

# Coupled Analysis of Underwater System by Numerical Approach



V. Rama Krishna, B. Ajay Kumar, O. R. Nandagopan, N. Ravi kumar and U. Urban Kumar

**Abstract** Underwater weapons in defense application are used to hit against enemy ships and submarines. These are designed to operate under extreme depths which require minimization of structural weight for increasing the performance, speed and operating range. This paper deals with the design and analysis of assembled system made of aluminum alloy and CFRP material. It mainly consists of different subsystems. These subsystems are used to accommodate different varieties of electronics and other systems required for underwater applications. These subsystems generate the heat fluxes which are transferred to both ends of the system. In addition, this underwater system also subjected to external hydrostatic pressure during functioning. Hydrostatic and thermal loads can cause system failure due to shell expansion and O-ring failure and can cause water leakage into the vehicle compartments. This paper mainly concerns about the avoidance of system failures and increase the efficiency of underwater vehicle. Coupled analysis (thermal and hydrostatic) carried out for existing design using ANSYS finite element analysis software. With this analysis stresses, deformations and strains of vehicle are found out for existing design. Buckling analysis also carried out for subsystem shells for finding the buckling pressure. This analysis proves the stresses and buckling pressures are within the limits. This analysis is used to identify the weak zone and most affected area of the vehicle which helps for the modifications and remedies for underwater vehicle.

**Keywords** Homing · External hydro static pressure and coupled analysis

---

V. Rama Krishna (✉) · O. R. Nandagopan · U. Urban Kumar  
Naval Science and Technological Laboratory, Visakhapatnam, India  
e-mail: [ramki40@gmail.com](mailto:ramki40@gmail.com)

B. Ajay Kumar · N. Ravi kumar  
Department of Mechanical Engineering, VRSEC, Vijayawada, India

© Springer Nature Singapore Pte Ltd. 2020  
H. K. Voruganti et al. (eds.), *Advances in Applied Mechanical Engineering*,  
Lecture Notes in Mechanical Engineering,  
[https://doi.org/10.1007/978-981-15-1201-8\\_64](https://doi.org/10.1007/978-981-15-1201-8_64)

# 1 Introduction

The underwater vehicles used for different purposes are developing more rapidly now days. Torpedoes are the principal armament of submarines and ships. These vehicles are designed to attack underwater targets such as submarines and ships and are autonomous underwater vehicles. Research is carrying out for increasing life, durability, effectiveness, speed and range of underwater vehicle. This system must also have high-speed maneuverability and must be capable of delivering payloads sufficient for target destruction. The cost of a system rises dramatically with its weight and volume. This system consists of different sub systems used to start, move in defined path (navigation) and propulsion system for vehicle movement. Different systems having different components for various application of underwater systems. Homing, signal processing unit, EX-Head, inertial navigation system, Battery with SBH, power electronic drive system, motor, actuation system and propulsor are the various subsystems of this vehicle.

This system accommodates various electronic equipments and plays a vital role in underwater applications. This system is designed for strength, stiffness and weight etc. The materials like aluminum alloys, composite and titanium become significant used in this system because of lightweight and high strength, and these materials are capable of taking the hydrostatic and hydro dynamic loads.

These systems are to be designed for higher depth operations where there is a higher pressures which is a difficult task. So there is a need to design these systems for under water applications like torpedoes, submarine, mines, decoys, AUVs etc. for their improved performance. These systems are designed for moderate and extreme depths, which require minimization of structural weight for increasing the performance, speed and operating range. Hence, it is better to design the lightweight materials like aluminum and composite materials for the underwater applications.

The carbon fiber/epoxy material is used for the battery shell. CFRP material has special characteristics of lightweight and high strength. Because of which this material is having high demand for different applications where weight is a constraint. This material has excellent high mechanical properties with low weight. Hence, this material is used for battery shell cover and withstands both the hydrostatic and thermal loads.

## 1.1 Literature Survey

There are numerous papers available in literature about the analysis of the systems for safe design. Ramesh [1] explained the design and static analysis of homing head shell of a torpedo. Here, various configurations of the homing head shells have been prepared and comparison study was made before finalizing the present design. Pulletikurti et al. [2] deals with the design and analysis of ring stiffened cylindrical shell

which is made of aluminum alloy forging. The design and analysis of the shell structure is mainly focused to obtain stresses and buckling load factors. Windenburg and Trilling [3] studied the design and analysis of thin cylindrical shells under external pressure. They also studying the collapse of the shell by external pressures and results are compared for different materials of shells. Little et al. [4] studied the buckling of 12 thin-walled geometrically imperfect tubes, which were tested for destruction under uniform external hydrostatic pressure. These experimental results are compared with theoretical and analytical results. Ross et al. [5] carried out theoretical and experimental investigations of the buckling characteristics of a series of six ring-stiffened circular cylinders that experienced general instability when subjected to external hydrostatic pressure.

### 1.2 Problem Statement

This system consists of different shells made up of aluminum alloy and the battery shell is made of CFRP composite material. These sub system shells are used to accommodate the various electronics and other systems. Some of these systems emits the heat flux which flows from one end to the other end and causes the thermal strains in the body. The other design requirement of this system is hydrostatic pressure of 60 bar at a depth of 600 m (i.e., for every 10 meters depth there is a 1 bar pressure acts). This combined load causes deformation in the shells and may lead to failure. For understanding the actual conditions, both thermal and hydrostatic pressure loads are acting on the system simultaneously which is called as coupled analysis. The material properties of aluminum and CFRP are shown in Tables 1 and 2, respectively.

Aluminum 24345(IS: 734).

**Table 1** Aluminum properties

Density	2.8 g/cc
Young’s modulus	71,000 Mpa
Poisson’s ratio	0.32
Yield strength	385 Mpa

**Table 2** CFRP material properties

Density	1.6 g/cc
Yong’s modulus in fiber direction ( $E_x$ )	158,700 Mpa
Yong’s modulus in transverse direction ( $E_y = E_z$ )	8615.4 Mpa
$\nu_{xy}$	0.292
$\nu_{yz} = \nu_{xz}$	0.3
Shear modulus ( $G_{xy}$ )	3523.4 Mpa
$G_{yz} = G_{xz}$	3523.4 Mpa

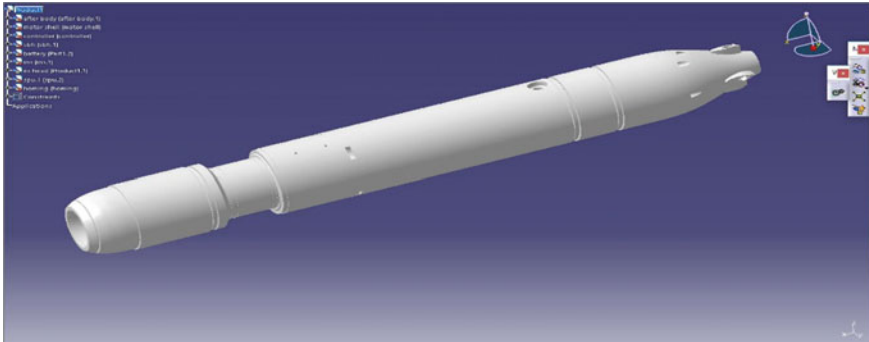


**Fig. 1** 3D model of assembled system

CFRP Material properties are taken from the TORAYCA T700G carbon fiber data sheet.

## 2 Methodology: Solid Modeling

This total system consists of individual shells which were modeled initially and all the shells are added to get assembled configuration. This systems contains complicated structures and are modeled using high-end software i.e., CATIA V5 R20. Initially, using part module and existing design documents, the 3D solid models of individual shells are designed. Using various commands like sketch, sketch-based features, dress up features, transformation feature and using 2D tools like circle, line, spline etc.... modeled the shells same procedure is followed for all the shells except battery shell. As the battery shell is made of composite material, it is designed using the composite module in the CATIA V5 R20. The layup sequences, layer direction, thickness and material are given using ply group in stacking option. Using these tools, composite shell is designed. Individual shells are assembled using assembly module by top down approach where individual components are imported using existing component tool. All D.O.F is arrested for the component using constrains like fix, coincide and contact. The 3D model of the assembled system is shown in Fig. 1.

## 3 Finite Element Analysis

Finite element analysis is a method which divides the solid model into elements and structural analysis is carried out using numerical procedure. The finite element procedure generates many simultaneous algebraic equations and solves on a digital

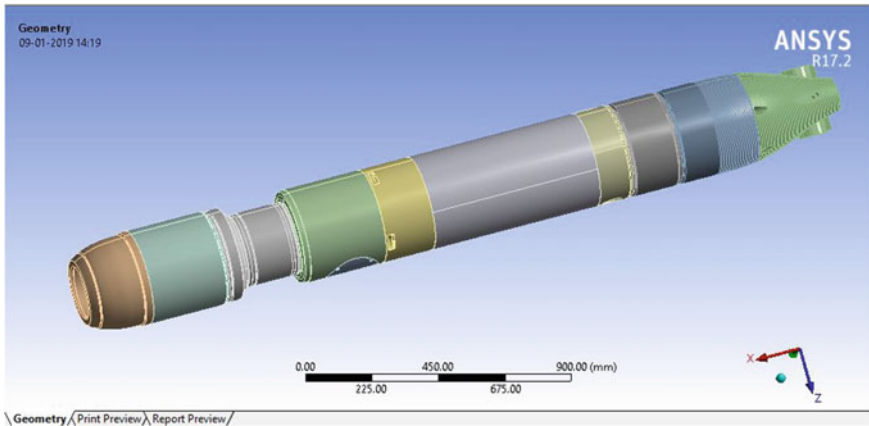


**Fig. 2** Finite element model before meshing

computer with in less time. Finite element method originated as a method of stress analysis. Finite element methods are also used to analyze problems of structural heat transfer, fluid flow, lubrication, electric and magnetic fields.

ANSYS Workbench is used for solving this problem. Engineering properties are assigned initially and then the 3D model is imported into the ANSYS Workbench. Finite element model of assembled system before meshing is shown in Fig. 2.

### 3.1 Finite Element Model

The properties of meshing are defined as below:

Element type: Tetrahedron elements (Hex mesh is difficult because of critical geometry of assembled system and computation limitation)

Element size: 15

Mesh type: Fine mesh.

Convergence check for various element sizes are shown in Table 3.

**Table 3** Convergence check for element size

Element size	Deformation (mm) maximum	Stress (Mpa) maximum
18	1.613	358.53
15	1.5925	352.74
12	1.59233	352.7367



### 3.2 Static Structural Analysis

**Boundary conditions:**

The boundary conditions for the above model are as follows

Front side = Fixed Support

Rear side = Axial Displacement.

**Loading conditions:** Except battery section and all other sections are applied circumferential pressure of 6 Mpa. At the rear end in axial direction 6 Mpa pressure is applied. At battery section 0.2, Mpa circumferential pressure is applied. Thermal loads of the system taken are 70 °C on the homing shell, 80 °C on battery shell and 110 °C on motor shell. The meshed model and boundary conditions are shown in Figs. 3 and 4, respectively.

### 3.3 Buckling Analysis

All the subsystem shells are modeled and static structural analysis was carried out before buckling analysis. The output of static analysis was given as input to buckling analysis. Solid model, meshed model and boundary conditions of homing system shell are shown in Fig. 5.

The same procedure is followed for remaining shells also. From the buckling analysis, it was found out the eigen buckling factor (load multiplier). From this factor, buckling pressure is calculated.

Buckling pressure = Applied Pressure \* Eigen buckling factor (load multiplier).

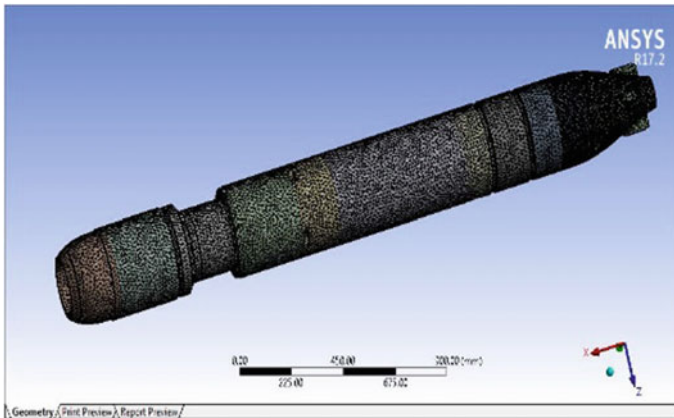


Fig. 3 Finite element model after meshing

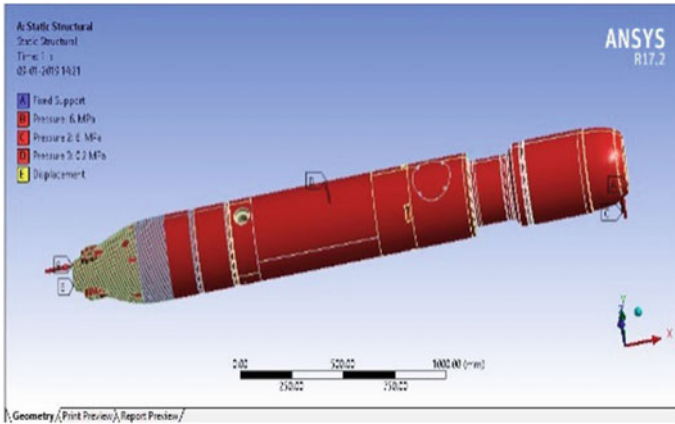


Fig. 4 Boundary conditions

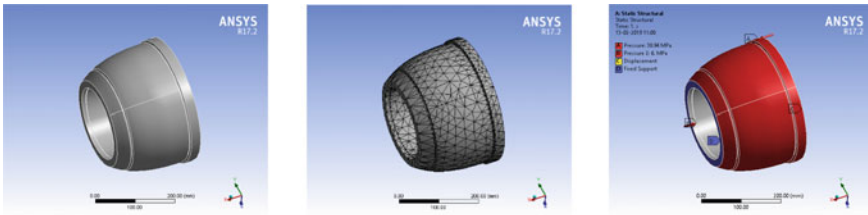


Fig. 5 Finite element model, mesh and boundary condition for homing shell

## 4 Results and Discussions

Hydro static and thermal loads are applied simultaneously, and coupled analysis was carried out using ANSYS Workbench 17.2. From this analysis, stresses, strains, deformations of assembled system and buckling modes of subsystem shells are found out using mechanical APDL Solver.

The results are as follows

1. Total deformation contour, equivalent (von-Mises) stress and equivalent strains contour is shown in Fig. 6
2. Buckling factors of subsystem shells are shown in Fig. 7
3. Buckling pressures of subsystem shells are shown in Table 4.

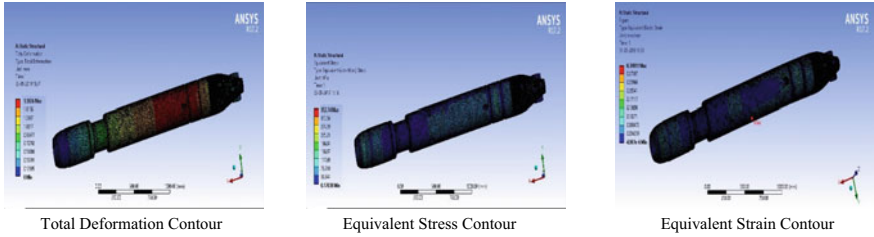


Fig. 6 Static structural analysis of assembled system

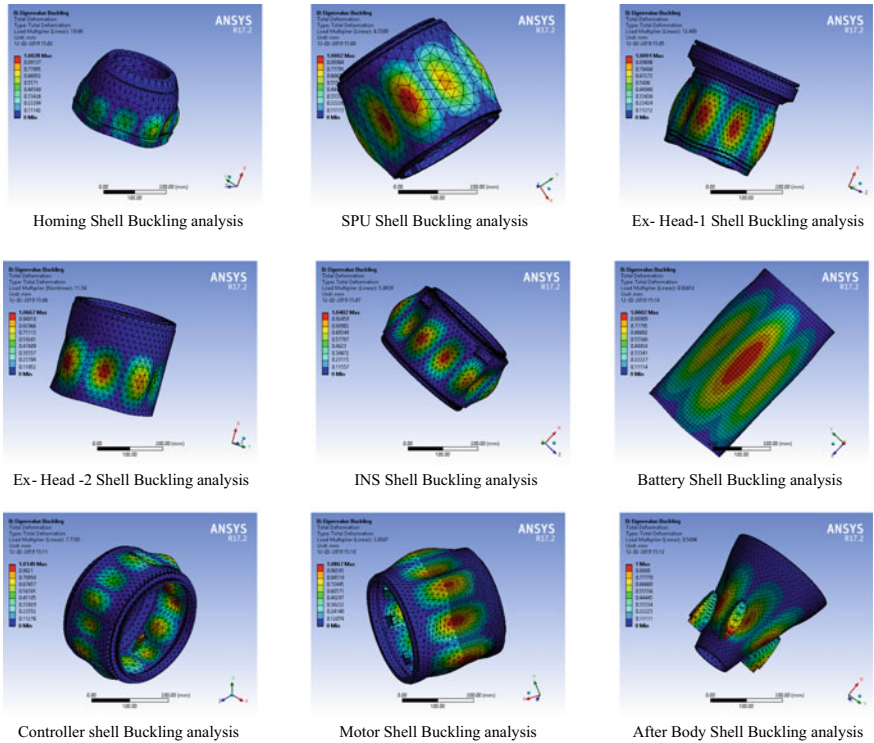


Fig. 7 Buckling factors of subsystem shells

### 5 Conclusion

1. Maximum stress observed on the aluminum shells is <math><188.05\text{ Mpa}</math>. Yield stress of aluminum is <math>414\text{ Mpa}</math>. Hence, Factor of safety is <math>2.02</math>.
2. Maximum deformation observed in the system is <math>1.5926\text{ mm}</math> i.e. on CFRP shell.
3. Maximum strain observed in the system is <math>0.33\text{ mm/mm}</math> i.e. at Battery Scoop bulk head.

**Table 4** Buckling Pressure of subsystem shells

Shell	Eigen buckling factor (load multiplier)	Applied pressure (Mpa)	Buckling pressure (Mpa)
Homing shell	19.88	6	119.28
SPU shell	6.5509	6	39.3054
EX—Head-1 shell	12.493	6	74.958
EX—Head-2 shell	11.56	6	69.36
INS shell	5.04	6	30.24
Battery shell	0.82612	6	4.95672
Controller shell	7.71	6	46.26
Motor shell	3.03	6	18.18
After body shell	9.54	6	57.24

4. Buckling pressures of subsystems are shown in Table 4 and all are within the limits.
5. In view of above, it was concluded that aluminum subsystems are safe. Further study was also carried out to reduce the deformation of battery shell by using stiffened ring at battery and INS joint.

**Acknowledgements** Authors wish to express their sincere gratitude to Dr. O. R. Nandagopan, Outstanding Scientist and Director, NSTL Visakhapatnam for permitting to publish this paper. The authors also wish to acknowledge Shri. P. Trimurtulu, Scientist ‘G’ and all Technology Directorates of NSTL, Visakhapatnam who helped to complete this work. Authors also wish to acknowledge R. V. College of engineering, Bangalore for their support.

## References

1. Ramesh JVR (2017) Design and static analysis of homing head shell of torpedo. *Int J Res Appl Sci Eng Technol (IJRASET)* 5(XI). ISSN 2321-9653
2. Manikanta PV, Ranga Raju P (2012) Computer aided design and analysis of ring stiffened cylindrical shell for underwater applications. *Int J (ESTIJ)* 2(4). ISSN 2250-3498
3. Windenburg DF, Trilling C (1934) Collapse by instability of thin cylindrical shells under external pressure. *Trans ASME APM-56-20*
4. Little APF (2008) Inelastic buckling of geometrically imperfect tubes under external hydrostatic pressure. *Ocean Sovereignty* 3(1)
5. Ross CTF (2008) Buckling by general instability of cylindrical components of deep sea submersibles. *Appl Mech Mater* 13–14:289–296
6. Cai M (2002) Buckling strength of thin cylindrical shells under localized axial compression. In: 15th ASCE engineering mechanics conference, 2–5 June 2002
7. Koiter IWT, Mikhailov GK (1980) *Theory of shells*. North-Holland Publishing Company, Amsterdam, New York

# Design and Analysis on Reinforced Carbon–Basalt Fibres Composite Laminate



S. Nagarjuna Reddy  and M. Trivikrama Sankar 

**Abstract** As the use of eco-friendly, natural products is currently increasing, reinforced composites from Basalt have recently been developed. These amorphous mineral fibres are a suitable alternative to low-cost carbon fibre and strong glass fibres. The basalt and carbon fibres of uni-directional and bi-directional with lay-up sequence of (0/90/±45/±45/0/90/±45/±45/90/0) that are used to strengthen composites by the vacuum bagging technique. A mechanical characterization is required in order to use reinforced composites for structural applications. Different tests such as tensile and flexural tests are carried out in both the experimental and analytical method to show mechanical characteristics. Finally, the obtained results propose to emphasize the behaviour of reinforced composite fibre. The enhanced properties put forward possible applications of such composite materials in various fields.

**Keywords** Carbon fibre · Basalt fibre · Uni-directional · Bi-directional

## 1 Introduction

Basalt is an inert volcanic rock that occurs naturally and can be found all over the world. Basalt materials are environmentally friendly and safe. Current basalt fibre production technology is similar to the one for the manufacture of e-glass. The principal difference is that e-glass is made of a complex batch of material, while basalt filament is made of melted basalt rock without additional additives and thus has a cost advantage. Due to the simplicity of the production process, less energy is required.

In addition, basalt fibres are highly chemical [1], non-toxic, non-fuel [2], and temperature resistant [3]. In addition, their mechanical characteristics are comparable or better than those of e-glass. Colombo et al. shown that in tensile and compressive mode, the basaltic-reinforced epoxy composites have shown higher mechanical

---

S. Nagarjuna Reddy (✉) · M. Trivikrama Sankar  
Department of Mechanical Engineering, BVRIT, Narsapur, Telangana 502313, India  
e-mail: [nagarjunareddysure@gmail.com](mailto:nagarjunareddysure@gmail.com)

properties with respect to vinyl ester, and failure mode is more compact, as fibres are not explosive

As the use of basalt fibre-reinforced polymer composites to watch over water immersion, water absorption, temperature, and cycling, further research [4] by the same authors reported tolerances for the use of environmental composites. For the glass-reinforced correlated composites, parallel tests have been conducted. A slight but significant decrease in the Young's modulus and tensile strength of the basalt combustibles has occurred which are 240 days old in salty water or normal water.

In most of the research carried out to date, glass and carbon have been used to enhance fibres in composite materials. The works of strengthened wooden elements, mainly of made with glass fibre, were investigated during the first publications [5–8]. P. D. L. R. Garcia et al. work showed that structures with greater rigidity and carrying capacity are created by reinforcement systems of basalt and carbon pine beams glued on the exterior [9]. The ultimate movement in the reinforced beams, however, is not increased and also that the rigidity of the beam increases with increasing grams of the fabrics.

The number of research projects using carbon fibre used to improve this type of element was increased [10] and carbon fibre was later introduced into the market. Some published conclusions show that beams strengthened with uni-directionally reinforced plastic carbon fibre (CFRP), in comparison to non-reinforced beams, can grow from 20 to 40% [11]. Tingley and Kent [12] study also showed a 21.5% increase in carriage capacity and a 5% increase in stiffness where reinforced beams were tested with CFRP.

The biggest problem with the use of carbon composites is the production costs which result in very low conditions of usage. The hybridization technique, which strengthens certain levels of carbon fibre with common ductile fibres with a common matrix, can resolve these difficulties, such as weakness and fragility. By doing so, weight could be reduced by 40–60%. This also can lead to cost advantages and improved mechanical and physical properties.

## 2 Methodology

With the vacuum bagging method, all structures were built with one lamination. This method involves the initial laying of the hand and then polymerization of the matrix in a flexible bag where a vacuum pump reaches negative pressure. Compared to the hand lay-up technology, vacuum bag technology brings certain advantages to its finishing characteristics. All laminates were cured for 24 h at room temperature and then post-cured for 8 h at 60 °C.

The carbon composite laminates consist of 14 carbon-matted layers of fibres, randomly oriented and 450 g/m<sup>2</sup> of areal weight in the epoxy resin matrix (i.e. SP 106) mixed with own hardener. Starting with the CFRP structure, the hybrid composites were produced to replace four carbon mats with four basaltic uniaxial layers, which are weighed 400 g/m<sup>2</sup>.

Epoxy resin (Araldite LY 556) with its hardener (Aradur HY 951) (10:1 ratio) is the chosen material for the production due to its various advantages, like a lower viscosity system without internal stress and excellent water resistance.

For the production of specimens, 40 and 60%, respectively, are fibre to matrix weight ratio (2:3) by vacuum bagging method. The dimension of the panel is  $25 \times 250 \text{ mm}^2$  to minimize the resin quantity and achieve success at room temperature within a short time. The thickness of the panels is nominally 2.5 mm; rectangular specimens are cut by a saw when ready.

### 3 Properties of Composite Laminates

#### 3.1 Mechanical Properties of UD Layer

In this work, the mechanical properties of the UD layer were calculated for each design case. Firstly, the density and moduli were obtained by using the rule of mixtures (ROM). The experimental evidence has been reported that the ROM provides an accurate prediction for the effective modulus of UD composite over a wide range of fibre volume fraction. By using ROM, the density and elastic properties were calculated as following equations:

$$\begin{aligned}
 \rho &= \rho_F V_F + \rho_M V_M \\
 \nu_{12} &= \nu_F V_F + \nu_M V_M \\
 E_{11} &= E_F V_F + E_M V_M \\
 \frac{1}{E_{22}} &= \frac{V_F}{E_{22F}} = \frac{V_M}{E_M} \\
 \frac{1}{G_{12}} &= \frac{V_F}{G_{12F}} = \frac{V_M}{G_M}
 \end{aligned} \tag{1}$$

where  $\rho$  is the density,  $\nu$  is the volume fraction of fibre,  $E_{11}$  and  $E_{22}$  are elastic moduli of the longitudinal direction and transverse direction, respectively,  $\nu$  is Poisson's ratio, and  $G_{12}$  are shear modulus. The subscripts F and M represent the fibre and matrix, respectively.

#### 3.2 Mechanical Properties of Entire Structure of Carbon and Basalt Mat Thermoplastic (CBMT)

The mechanical properties of entire structure of CBMT were calculated by using the classical laminated plate theory (CLPT) based on the obtained mechanical properties of each layer. It has been known that the CLPT is a common approach method used

to predict mechanical properties, especially for the thin plate composite structures. In the CLPT, individual laminate was assumed as homogeneous and orthotropic. The analytical stiffness of composite laminate is expressed as follows when there are no hydrothermal effects:

$$\begin{Bmatrix} F_x \\ F_y \\ F_{xy} \\ M_x \\ M_y \\ M_{xy} \end{Bmatrix} = \begin{bmatrix} A_{11} & A_{12} & A_{16} & B_{11} & B_{12} & B_{16} \\ A_{12} & A_{22} & A_{16} & B_{12} & B_{22} & B_{26} \\ A_{16} & A_{12} & A_{16} & B_{16} & B_{26} & B_{66} \\ B_{11} & B_{12} & B_{16} & D_{11} & D_{12} & D_{16} \\ B_{12} & B_{22} & B_{26} & D_{12} & D_{22} & D_{26} \\ B_{16} & B_{26} & B_{66} & D_{16} & D_{26} & D_{66} \end{bmatrix} \begin{Bmatrix} \varepsilon_x^0 \\ \varepsilon_y^0 \\ \varepsilon_{xy}^0 \\ k_x \\ k_y \\ k_{xy} \end{Bmatrix} \tag{2}$$

where  $F_x$ ,  $F_y$ , and  $F_{xy}$  are in-plane forces per unit length,  $M_x$ ,  $M_y$ , and  $M_{xy}$  are moments per unit length,  $\varepsilon$ 's are the strains of midplane and  $k_x$ ,  $k_y$ , and  $k_{xy}$  are the plate curvatures.  $[A]$  is the in-plane stiffness matrix,  $[B]$  is stretching–bending coupling matrix and  $[D]$  is the bending stiffness matrix. The bending–stretching coupling matrix  $[B]$  is identically zero when the stacking sequence of a laminate is symmetric about its midplane. In addition, this laminate is subjected to in-plane force  $\{F\}$  then the curvature  $\{k\}$  reduces to zero. Then, above Eq. (2) becomes

$$\begin{Bmatrix} F_x \\ F_y \\ F_{xy} \end{Bmatrix} = \begin{bmatrix} A_{11} & A_{12} & A_{13} \\ A_{12} & A_{22} & A_{26} \\ A_{13} & A_{26} & A_{66} \end{bmatrix} \tag{3}$$

and the in-plane stiffness matrix  $[A]$  can be calculated as follows:

$$A_{ij} = \sum_{k=1}^N [Q_{ij}]^{[k]} (z_k - z_{k-1}) \tag{4}$$

where are  $[Q_{ij}]^{[k]}$  the transformed reduced stiffness of the  $k$ th ply, and the  $z_k$  represents the displacement between midplane and  $k$ th ply. Then, the elastic properties of the entire CBMT laminate are calculated as follows:

$$\begin{aligned} E_x &= \frac{|A|}{h(A_{22}A_{66} - A_{26}^2)}, \\ E_y &= \frac{|A|}{h(A_{11}A_{66} - A_{16}^2)}, \\ G_{xy} &= \frac{|A|}{h(A_{11}A_{22} - A_{12}^2)} \\ \nu_{xy} &= -\frac{A_{16}A_{26} - A_{12}A_{66}}{A_{22}A_{66} - A_{26}^2}, \end{aligned}$$



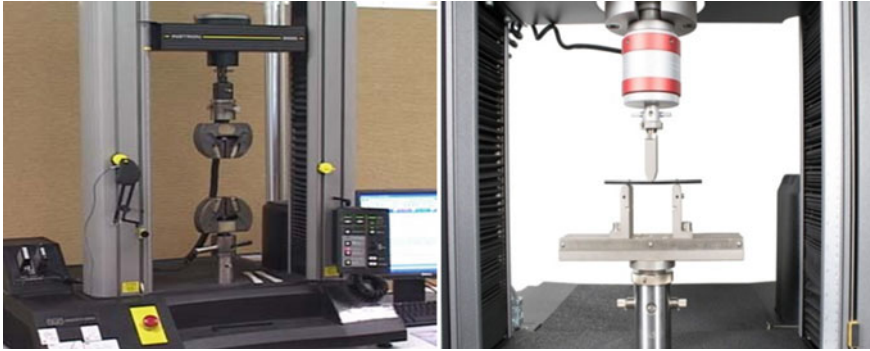


**Fig. 1** Experimental set-up for tensile and flexural test specimens

$$v_{yx} = -\frac{A_{16}A_{26} - A_{12}A_{66}}{A_{11}A_{66} - A_{16}^2} \quad (5)$$

where  $|A|$  is determinant of  $[A]$ ,  $E_x$ ,  $E_y$ , and  $G_{xy}$  are axial, transverse, and shear modulus of the laminate and  $v_{xy}$  and  $v_{yx}$  are Poisson's ratio.

## 4 Experimental Tests

### 4.1 Tensile Test

On standard ASTM D3039 machines with a load capacity of 100 KN, the static tensile test is carried out. Under normal humidity conditions, all static tensile tests are conducted at room temperature as shown in Fig. 1(left).

The experimental tests on reinforced composites are tensile testing and flexural testing. The following paragraphs describe the details of the experimental tests.

Testing shall be conducted at 2 mm/min crosshead speed in the displacement control. Dimensions of the specification are  $25 \times 250 \text{ mm}^2$ . The tabs of all specimens (length = 80 mm) are fitted to prevent the sample from failing at grips.

### 4.2 Flexural Test

The flexural test is carried out on the standard ASTM D790 machine. It measures the force to bend a beam in the loading conditions of three points. The flexural module is used as an indication of the rigidity of the material when bending. Due to the environmental temperature, the physical properties of thermoplastic materials vary. In order to assess the flexural strength, rectangular bars with the required dimensions

have been cut from fully cured samples and subjected to three-point bending tests. Figure 1(right) Shows the experimental configuration of bending test specimen.

In particular, bending tests were performed with five prismatic samples of 20 mm × 96 mm dimensions on each implemented structure with a load cell of 5KN. In each test, the range length is 80 mm and the speed of the crosshead is 4.26 mm/min.

### 4.3 Computational Test

The model is to be created by input constants and material characteristics for simulation by ANSYS according to required ASTM standards. The main menu on the left of the screen will display the window. It is selected as a type for the composite material in this Shell 3D Node 181 element. Then, material characteristics are given and the modelling is carried out using the necessary dimensions or 3D model can be imported from CATIA. Meshing is also possible with various mesh types, by selecting the required accuracy. In “pre-processor > sections” option in the main menu, fibre orientation can also be given for composite materials, as well as for each layer with the required thickness different material characteristics can be given.

The application of load and boundary conditions is an important step for an analysis. After meshing as shown in Fig. 2 a, cantilever condition is applied, as it is fixed at one end and free at the other for the tensile test in ANSYS APDL. Similarly, a simply supported condition is applied for the bending test and the loads applied are of similar to the experimental condition, i.e. 100 KN for tensile at the free end and 5 KN for flexural at the middle of specimen.

The stress and strain resulting from the ANSYS Nodal solution is calculated using certain finite element mathematical analysis solutions applied in the ANSYS. The analytical solution for maximum strain and maximum stress are given in Eqs. (6) and (7). Tensile modulus ( $E$ ) can be calculated by applying the maximum strain and

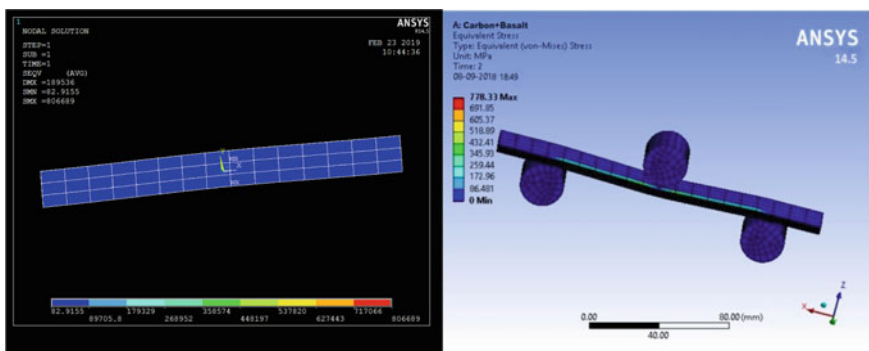


Fig. 2 Simulation image of composite laminate for tensile and flexural strength

**Table 1** Experimental results for tensile test specimens

Property	Composites			
	Basalt	Carbon	Basalt + carbon (uni-directional)	Basalt + carbon (bi-directional)
Flexural strength (MPa)	762	69	985	549

maximum stress obtained from finite element analysis (FEA).

$$\int \sigma_{ij} \delta \varepsilon_{ij} dV = \int_s f_i^B \delta u_i dV + \int_s f_i^S \delta u_i dS \tag{6}$$

$$\sigma_{ij} = \sigma'_{ij} - \delta_{ij} \bar{P} = \sigma_{ij} + \delta_{ij} P - \delta_{ij} \bar{P} \tag{7}$$

where

- $\sigma_{ij}$  Cauchy stress component
- $\varepsilon_{ij} = \frac{1}{2} \left( \frac{du_i}{dx_j} + \frac{du_j}{dx_i} \right)$  deformation tensor
- $u_i$  displacement
- $x_i$  current coordinate
- $f_i^B$  component of body force
- $f_i^S$  component of surface fraction
- $V$  volume of deformed body
- $S$  surface deformed body on which tractions are prescribed
- $\delta_{ij}$  Kronecker delta
- $\sigma'_{ij}$  Cauchy stress from constitutive law.

## 5 Results and Discussions

### 5.1 Tensile Strength

Table 1 shows the experimental results for tensile test specimens. This table shows that the use of epoxy as matrix increases mechanical static (tensile) properties.

### 5.2 Flexural Strength

Table 2 shows the results for flexural test due to variation of load. The use of epoxy as matrix and adding of different materials with better properties increases mechanical properties.

**Table 2** Experimental results for flexural test specimens

Property	Composites			
	Basalt	Carbon	Carbon + Basalt (uni-directional)	Carbon + Basalt (bi-directional)
Tensile strength (MPa)	468	584	742	105
Elongation (%)	18.91	23.01	21.29	14.42

**Table 3** Comparison of experimental and analytical results

Composites	Properties			
	Tensile strength (MPa)		Flexural strength (mpA)	
	Experimental results	Analytical results	Experimental results	Analytical results
Carbon	584	592	869	871.12
Basalt	468	482	762	778.33
Carbon + Basalt (uni-directional)	742	806	985	992
Carbon + Basalt (bi-directional)	105	189	549	594.36

Table 3 shows the comparison of experimental and analytical values between the tensile and flexural tests. By observing the table, it will confirm that both the experimental and analytical values are close enough suggesting the results obtained are correct.

## 6 Conclusion

A Carbon–basalt fibre composite with 14 layers of laminates is manufactured by vacuum bagging, and the material properties of the composite are determined by means of the tensile and flexural test. Three points of bending and tensile tests indicate that, compared to CFRP laminates, the presence of four layers of basalts in uni-directional results in the improvement of mechanical characteristics of the hybrid laminates. Finally, the finite element analysis, confirmed with the results of the experiment, shows the distribution of stress in the sample layers. When all test results have been observed, the refinement of carbon and basalt fibres with 0° angle, i.e. Uni-directional results have been better.

## References

1. Wei B, Cao H, Song S (2015) *Mat Sci Eng: A* 640:481
2. Cerny M, Glogar P, Chlup Z et al (2009) Partially pyrolyzed composites with basalt fibres—mechanical properties at laboratory and elevated temperatures. *Compos Part A* 40:1650–1659
3. Liu Q, Shaw MT, Parnas RS, McDonnell AM (2006) Investigation of basalt fibre composite aging behaviour for applications in transportation. *Polym Compos* 27:475–483
4. Gentile C, Svecova D, Saltzberg W, Rizkalla SH (2000) Flexural strengthening of timber beams using GFRP. In: *Proceedings of advanced composite materials in bridges and structures, Canada*, pp 637–44
5. Hallstrom S, Grenestedt JL (1997) Failure analysis of laminated timber beams reinforced with glass fibre composites. *Wood Sci Technol* 31:17–34
6. Johns KC, Lacroix S (2000) Composite reinforcement of timber in bending. *Can J Civil Eng* 27:899–906
7. Pavez A, Ansell MP, Smedley D (2009) Mechanical repair of timber beams fractured in flexure using bonded-in reinforcements. *J Compos: Part B* 40(2):95–106
8. García PDLR, Escamilla AC, García MNG (2013) Bending reinforcement of timber beams with composite carbon fibre and basalt fibre materials. *Compos Part B Eng* 55:528–536
9. Borri A, Corradi M, Grazini A (2003) FRP reinforcement of wood element under bending loads. In: *Proceedings of structural faults and repair, London*
10. Borri A, Carrodi M, Grazini A (2005) A method for flexural reinforced of old wood beams with CFRP materials. *J Compos: Part B* 36(2):143–153
11. Triantafillou T, Deskovic N (1992) Pre stressed FRP sheets as external reinforcement of wood members. *ASCE J Struct Eng* 118(5):1270–1284
12. Tingley D, Kent S (2001) Structural evaluation of fibre reinforced hollow wood beams. In: *Proceedings of international conference of advanced composite materials in bridges and structures, Malta*, pp 367–72

# Optimum Geometry of Steering Mechanism for an Automobile



R. Venkatachalam and A. Padma Rao

**Abstract** Steering mechanism is very essential for any road vehicle. The commonly used mechanism for steering is the Ackermann mechanism. The perfect steering demands that the extensions of the axes of the two front wheels intersect at a point on the extension of the common rear wheel axis. The Ackermann mechanism does not give perfect steering always. In this paper, an attempt is made to arrive at optimum dimensions of the links of the mechanism which make the error in steering minimum.

**Keywords** Steering · Ackermann mechanism · Optimization · A two-dimensional surface · Global optimum

## Notation

$E$	Total squared error
$H$	Wheel base
$L_i$	Lengths of links of Ackermann mechanism, $i = 1-4$ $L_1 = W$ ; $L_2$ and $L_4 =$ lengths of track arms; $L_3 =$ length of track rod
$W$	Track width, also $L_1$ the distance between the pivots
$W_i$	Weightage factor, $i = 1$ to $n$
$x_1$	Length of track arms ( $L_2, L_4$ )
$x_C, y_C$	Coordinates of point C
$x_D, y_D$	Coordinates of point D
$\alpha, \beta$	Angles made by track arms with the link $L_1$
$\gamma$	Angle between the track arm and corresponding stub axle
$\emptyset, \theta$	Angles turned by inner and outer stub axles, respectively

---

R. Venkatachalam  
Mechanical Engineering, National Institute of Technology, Warangal 506004, India  
e-mail: [chalamrv@yahoo.com](mailto:chalamrv@yahoo.com)

A. Padma Rao (✉)  
Mechanical Engineering, B.V. Raju Institute of Technology, Narsapur 502313, India  
e-mail: [padmarao.are@bvrit.ac.in](mailto:padmarao.are@bvrit.ac.in)

© Springer Nature Singapore Pte Ltd. 2020

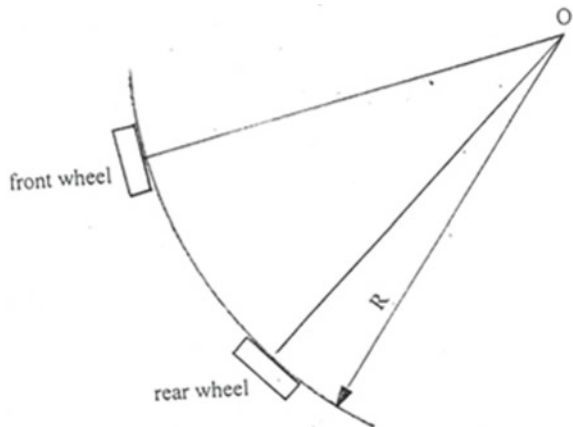
H. K. Voruganti et al. (eds.), *Advances in Applied Mechanical Engineering*,  
Lecture Notes in Mechanical Engineering,  
[https://doi.org/10.1007/978-981-15-1201-8\\_66](https://doi.org/10.1007/978-981-15-1201-8_66)

## 1 Introduction

One of the important systems of an automobile is the steering system. In a two-wheeler, the rider turns the front wheel–handlebar. The vehicle starts moving in a circular path whose centre is located at  $O$  the point of intersection of the axes of the rear and front wheels as shown in Fig. 1. It is to be observed that the planes of rotation of the wheels are tangential to the circular path. In a four-wheeler, right-side front and rear wheels may be imagined to form one two-wheeler and left-side front and rear wheel to form another two-wheeler. It is a common practice to provide steering only to the front wheels. If the front wheels are turned arbitrarily as shown in Fig. 2, then the right-side front and rear wheels try to follow a circular path whose centre is at  $O_2$ . Similarly, the left-side front and rear wheels follow a circular path whose centre is at  $O_1$ . Clearly, these two circular paths are not concentric and the motion of the wheels is not going to be smooth. That is, the front wheels start skidding on the road. It is therefore observed that if the vehicle has to take a turn smoothly, the two circular paths must be concentric which demands a condition that the  $O_1$  and  $O_2$  should be the same point as shown in Fig. 3. The whole vehicle follows a circular path whose centre is at  $O$ . The two front wheels will make rolling on the road without skidding. This is treated as perfect steering. The condition for perfect steering may now be stated as when the axes of the two front wheels are extended, they should intersect at a point on the extension of the common axis of the rear wheels. In Fig. 3, the vehicle is shown taking a right turn.

The mechanical element on which the wheel is free to rotate is called stub axle. From Fig. 3, the stub axles of the front wheel are shown to be rotated about points  $A$  and  $B$ . The distance between  $A$  and  $B$  is called track width,  $W$ . The distance between  $AB$  and common rear wheel axle  $EF$  is called wheel base,  $H$ . In Fig. 3, the inner wheel is shown to rotate by an angle  $\phi$  and the outer wheel is shown to rotate by an angle  $\theta$ . It is observed that  $\phi > \theta$ . From the geometric consideration of the perfect steering condition shown in Fig. 3, a relation connecting  $\phi$  and  $\theta$  may be derived as

**Fig. 1** A bicycle taking a right turn



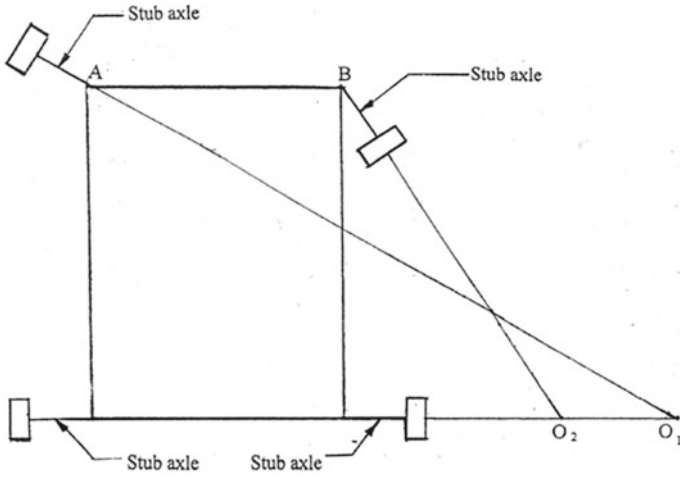


Fig. 2 Steering offered by the Ackermann mechanism

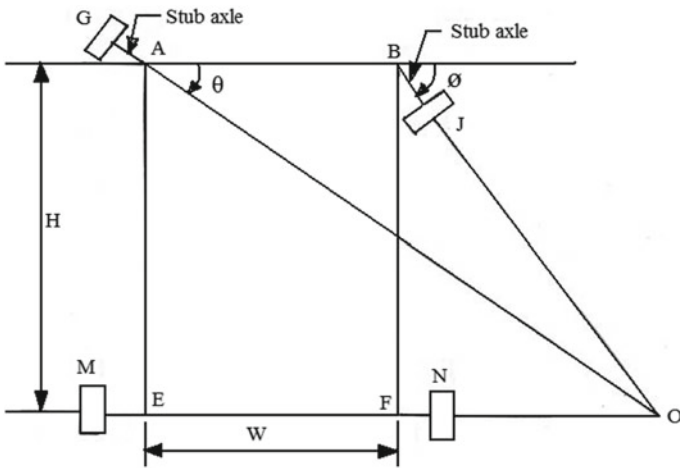


Fig. 3 A car taking right turn

$$\cot\theta - \cot\phi = W/H \tag{1}$$

The condition in Eq. (1) is known as a condition for perfect steering. It is to be observed that the angles  $\theta$  and  $\phi$  are related to the physical dimensions  $W$  and  $H$  of the vehicle. For a given value of  $W/H$ , one can numerically solve Eq. (1) for  $\phi$  for different values of  $\theta$ . Table 1 gives a typical set of pairs of values of  $\theta$  and  $\phi$ . In actual road vehicles, the inner wheel stub axle normally does not turn more than  $30^\circ$ . That is why the values are computed for  $0 \leq \theta \leq 30^\circ$ .



**Table 1** A typical set of pairs of values of  $\theta$  and  $\emptyset$  for  $W/H = 0.57$

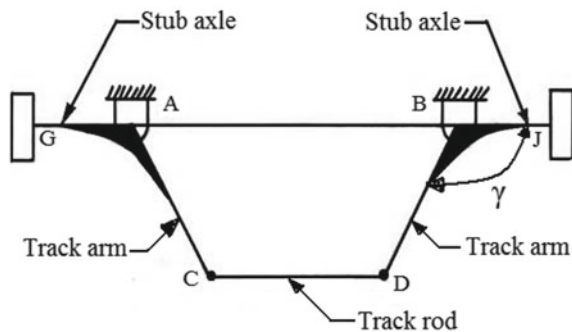
$\theta$ (°)	$\emptyset$ (°)	$\theta$ (°)	$\emptyset$ (°)	$\theta$ (°)	$\emptyset$ (°)
0	0.00	11	12.33	22	27.70
1	1.01	12	13.59	23	29.26
2	2.04	13	14.84	24	30.83
3	3.09	14	16.21	25	32.43
4	4.16	15	17.55	26	34.05
5	5.26	16	18.92	27	35.70
6	6.38	17	20.32	28	37.36
7	7.52	18	21.74	29	39.04
8	8.68	19	23.19	30	40.73
9	9.87	20	24.67		
10	11.09	21	26.17		

## 2 Steering Mechanism

A perfect steering mechanism must be such that it should provide angles turned by the front wheels  $\theta$  and  $\emptyset$  should execute the condition for correct steering expressed in Eq. (1). Attempts have been made to have the steering control through microprocessor. When one wheel is turned through an angle, that information is taken by a microprocessor and decides through how much angle, should other wheel be turned according to correct steering condition given in Eq. (1). The information is then fed to a stepper motor, and it turns the outer stub axle through the required angle. Arrangement involving microprocessor totally eliminates the mechanism. But it suffers from disadvantages such as reliability of operation of microprocessor, slow response of a stepper motor, and a non-positive drive offered. Mechanical arrangement is foolproof, and response is immediate and positive.

One mechanism which is popularly being used is the Ackermann mechanism which is shown in Fig. 4. The mechanism consists of two bell crank levers GAC

**Fig. 4** Ackermann steering mechanism



and JBD. A metallic link in the form shown in Fig. 5 is called bell crank lever. It is hinged at point A, and the whole piece is capable of rotating about A. In the actual four-wheeler, the bell crank link is hinged to the chassis of the vehicle. Similarly, JBD is another bell crank lever which is hinged to chassis at point B. The actual mechanism is ABDC which is in the form of a quadrilateral, and A, B, D, and C are the hinges. Such a mechanism is called a four-bar mechanism. In Fig. 4, AC and BD of the bell crank levers are called the track arms. GA and BJ of the bell crank levers form the stub axes on which the front wheels are free to rotate. When the mechanism is operated, it may occupy a position such as ABD'C' as shown in Fig. 6. As the bell crank levers GAC and JBD rotate about A and B, respectively, as single units, BJ' and AG' are the new positions of the stub axes. The front wheels are now steered. The

Fig. 5 Bell crank lever

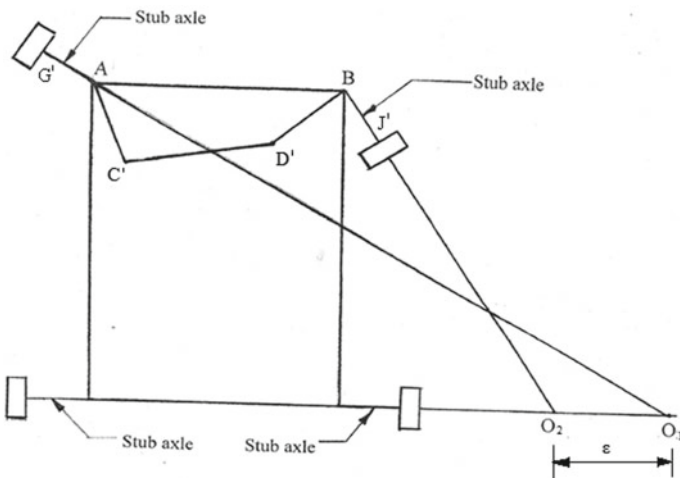
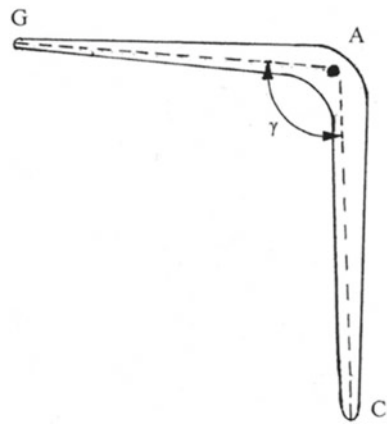


Fig. 6 Steering offered by the Ackermann mechanism

Ackermann mechanism ABDC shown in Fig. 4 represents the vehicle moving along a straight path. The Ackermann mechanism shown in Fig. 6 is a general position. One side front and rear wheels act as inner wheels in one side (say right side) turn and act as outer wheels in the other side (say left side) turn. Since the same mechanism produces similar turns for both right and left turns, the mechanism is expected to be symmetric about vehicle centreline. Figure 4 shows the Ackermann mechanism while the vehicle is moving on a straight path. It is to be observed that the mechanism ABDC is in the form of isosceles trapezium ( $AC = BD$ ). The link CD is called track rod. In Fig. 6, the steering offered by the Ackermann mechanism is shown. Clearly, it is not a perfect steering. The Ackermann mechanism may give perfect steering in three positions namely while moving along a straight path, one particular position in the left turn and one similar position in the right turn. Though this mechanism cannot give perfect steering always, it is widely accepted in the automobile industry because of its simple constructional features.

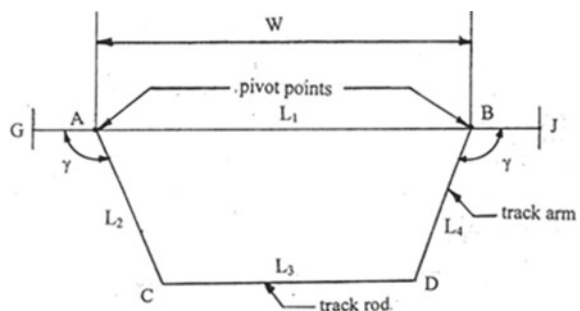
Deep studies on the Ackermann mechanism must have been performed by the automotive industries. But they are not available in the published literature, maybe because of confidentiality. References [1–7] are on some of the recent studies suggesting modifications on the Ackermann mechanism. The authors [8] presented a method of analysis of the Ackermann mechanism for studying its performance. The method proposed by the authors helps to estimate the skidding of the tires due to incorrect steering.

In this paper, an attempt is made to arrive at important dimensions for the mechanism with a view to make the mechanism closer to an ideal mechanism by minimizing the errors produced in steering. Simple optimization principles are applied, and interesting results are obtained.

### 3 Formulation of the Problem

For the sake of convenience, various links are named as shown in Fig. 7.  $L_1$  represents distance between pivot points A and B which is also the track width  $W$ .  $L_2$  and  $L_4$  are

**Fig. 7** Ackermann mechanism essentially a four-bar mechanism



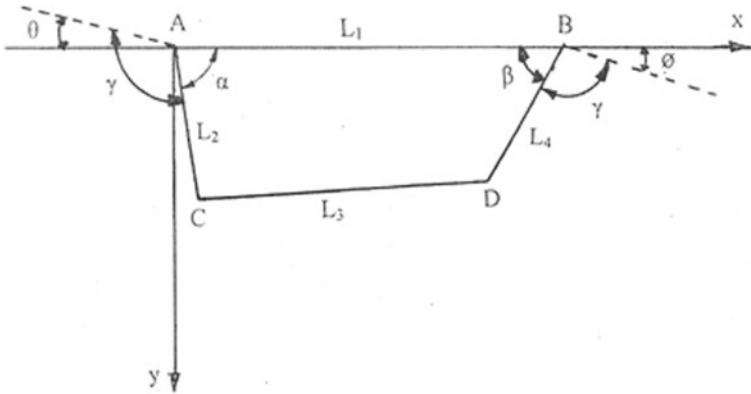


**Fig. 8** Position of the Ackermann mechanism when the vehicle is taking a right turn

the lengths of the track arms. For the reason mentioned above,  $L_2 = L_4$ . The length of the track rod is  $L_3$ . Angle  $\gamma$  represents the angle of the bell crank lever.

In a given situation,  $W$  is a fixed quantity.  $\gamma$  and  $L_2$  can fix the value of  $L_3$  as

$$L_3 = L_1 + 2 L_2 \cos \gamma \tag{2}$$

Therefore, the variables are only  $\gamma$  and  $L_2$ .

Figure 8 shows a general position of the Ackermann mechanism when the vehicle is taking a right turn. The inner stub axle BJ is shown to turn by an angle  $\theta$ , and the outer stub axle AG is shown to turn by an angle  $\theta$ . The angles  $\alpha$  and  $\beta$  are the angles made by  $L_2$  and  $L_4$  with AB. They may be expressed in terms of  $\theta$  and  $\theta$  as

$$\alpha = 180 - \gamma + \theta \tag{3}$$

$$\beta = 180 - \gamma - \theta \tag{4}$$

For the sake of convenience, an  $xy$  coordinate system with its origin at A and  $x$ -axis along AB may be considered as shown in the figure.

The length  $L_3$  may be expressed as

$$(L_3)^2 = (x_C - x_D)^2 + (y_C - y_D)^2 \tag{5}$$

where  $(x_C, y_C)$  and  $(x_D, y_D)$  are the coordinates of points C and D, respectively.

From the geometry, suitable expressions for these coordinates may be substituted, and the length  $L_3$  may be expressed as

$$(L_3)^2 = [L_2 \cos \alpha - L_1 + L_4 \cos \beta]^2 + [L_2 \sin \alpha - L_4 \sin \beta]^2 \tag{6}$$

which may be reduced to

$$(L_3)^2 = L_1^2 + L_4^2 + L_2^2 + 2 L_1 L_2 \cos(\alpha + \beta) - 2 L_1 L_2 (\cos \alpha + \cos \beta) \quad (7)$$

Substituting for  $L_3$  from Eq. (2) in Eq. (7), an expression in relating various variables of the mechanism may be obtained as

$$(2x_2^2 - 1)A - x_2\sqrt{1 - x_2^2}B - (L_1/x_1)x_2C - (L_1/x_1)\sqrt{1 - x_2^2}D - (2x_2^2 - 1) = 0 \quad (8)$$

where

$$A = \cos(\emptyset - \theta) \quad (9)$$

$$B = 2 \sin(\emptyset - \theta) \quad (10)$$

$$C = 2 - \cos \theta - \cos \emptyset \quad (11)$$

$$D = \sin \emptyset - \sin \theta \quad (12)$$

$$x_1 = L_2 \text{ or } L_4 \quad (13)$$

$$x_2 = \cos \gamma \quad (14)$$

The variables of interest are renamed as  $x_1$  and  $x_2$ .

If the mechanism is ideal and is offering perfect steering always, and if  $\theta$  and  $\emptyset$  according to Eq. (1) are substituted, then Eq. (8) should be satisfied always. However, the mechanism is unable to offer the perfect steering. If  $\theta$  and  $\emptyset$  desired by an ideal mechanism are substituted in Eq. (8), it will not yield a value zero but some residue. The idea behind the optimization process may be stated as what should be the values of  $x_1$  and  $x_2$  such that the residues are minimum. For this purpose, an objective function is constructed as

$$E = \sum_{i=1}^n W_i \left\{ (2x_2^2 - 1)A_i - x_2\sqrt{1 - x_2^2}B_i - (L_1/x_1)x_2C_i - (L_1/x_1)\sqrt{1 - x_2^2}D_i - (2x_2^2 - 1) \right\}^2 \quad (15)$$

where  $A_i$ ,  $B_i$ ,  $C_i$ , and  $D_i$  are the values of  $A$ ,  $B$ ,  $C$ , and  $D$  obtained by substituting  $i$ th pair of values of  $\emptyset_i$  and  $\theta_i$  (see Table 1).

The optimization problem may be stated as

$$\text{Find } \begin{Bmatrix} x_1 \\ x_2 \end{Bmatrix}$$

which minimizes

$$E = \sum_{k=1}^n w_i \left\{ (2x_2^2 - 1)A_i - x_2\sqrt{1 - x_2^2}B_i - (L_1/x_1)x_2C_i - (L_1/x_1)\sqrt{1 - x_2^2}D_i(2x_2^2 - 1) \right\}^2 \tag{16}$$

### 4 Results and Discussion

This is an unconstrained optimization problem with two variables. The necessary conditions may be written as

$$\frac{dE}{dx_1} = 0 \tag{17}$$

and

$$\frac{dE}{dx_2} = 0 \tag{18}$$

The objective function is nonlinear, and hence, it is very difficult to solve for the optimum values using the necessary conditions. Numerical techniques such as random search method, pattern search method, univariate method may be suitable for the present problem [9]. Gradient techniques such as steepest descent method may not be convenient for the present problem as these methods require evaluation of the derivatives of the objective function [9]. However, it is intended to evaluate the values of  $E$  for different sets of  $x_1$  and  $x_2$  and observe how  $E$  varies.

The  $x_1$  is varied from 200 to 2000 mm in steps of 200 mm. For each value of  $x_1$ , the value of  $x_2$  is varied from  $-1$  to  $+1$  in steps of 0.1. The objective function is evaluated for different values of  $x_1$  and  $x_2$ . Figure 9 shows the objective function plotted in  $x_1 - x_2$  space. It is very interesting to see the contours of  $E$  and also how the minimum is occurring. The optimum value of  $x_2$  is around  $-0.2$  giving the value of  $\gamma$  around  $101^\circ$  and the optimum value of  $x_1$  is around 1400 mm. The same values are plotted in three-dimensional isometric space as shown in Fig. 10 in order to give a more physical feel. Negative values of  $E$  are plotted in order to get a convex shaped surface. In most of the vehicles, the practical value of  $\gamma$  used is around  $100^\circ$ . The length of track arm is not taken so much as 1400 mm in view of space constraints to accommodate the mechanism. Usually, it is taken around 250–500 mm sacrificing some amount of steering error.

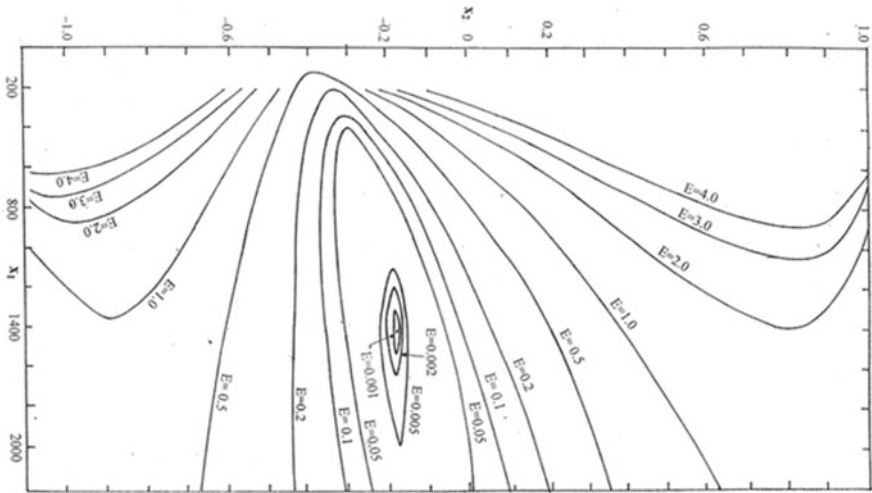
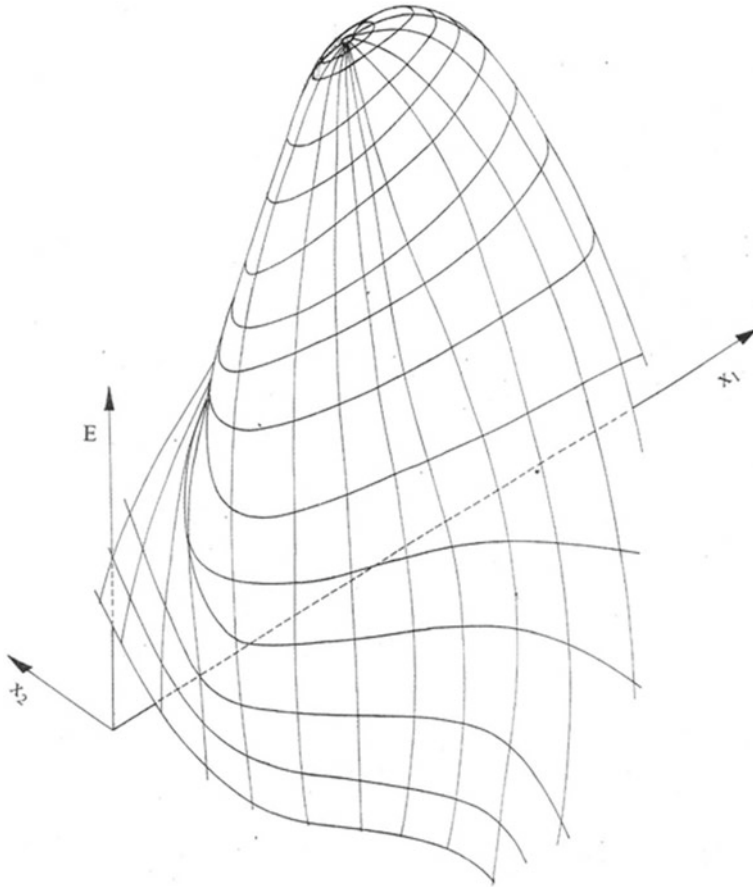


Fig. 9 Objective function plotted in  $x_1 - x_2$  space

## 5 Concluding Remarks

The significant conclusions that may be drawn based on the present work may be summarized as follows.

- i. The condition for perfect steering for a four-wheeler is described starting with simple principles.
- ii. The popularly used the Ackermann mechanism is described.
- iii. The necessity of the steering mechanism to be symmetric about vehicle centreline is explained.
- iv. Two variables are identified which may be varied in order to obtain an Ackermann mechanism which can reduce the steering error. The two variables are the length of the track arm and angle of the bell crank lever.
- v. An expression is derived connecting all the variables.
- vi. An optimization problem is formulated in which the objective function describes the sum of squares of residual errors.
- vii. The unconstrained optimization problem in two variables could not be solved in a classical way because the objective function is highly nonlinear.
- viii. Numerical methods could have been applied, but out of curiosity, the objective function is evaluated at different points and a three-dimensional surface is generated.
- ix. It is found interesting to watch the three-dimensional surface and locate the optimum value.
- x. The convexity of the surface clearly shows that the solution obtained represents a global optimum.



**Fig. 10** Three-dimensional surface representing the objective function

## References

1. Okamoto AA, Chikuma I (1977) The design concept of an integral power steering system for heavy duty trucks. SAE transactions. Report no. 770673, Steering Gear Division, Nippon Seiko
2. Nakahama M, Momiyama F, Ueda T (1985) Load and/or speed sensing power steering for medium and heavy trucks. SAE transactions. Report no. 770673, Hino Motors Ltd.
3. Kamner HJ (1967) Combined articulated and Ackermann steering system for vehicles. United States Patent No. 3 515 235
4. Hornagold JT, Beckley GH, Rathi RN (1978) Steering mechanism. United States Patent No. 4,109,747
5. Tapp GEE (1979) Steering mechanism. United States Patent No. 4,163,566
6. Kamble N, Saha SK (2005) Evaluation of torque characteristics of rack and pinion steering gear using ADAMS model 2005-01-1064. SAE 2005-Trans J Passengers Cars-Mech Syst 1217-1222
7. Kamble N, Saha SK (2006) Developing a virtual prototype of a rack and pinion steering system, Int J Veh Syst Model Testing



8. Venkatachalam R, Padma Rao A (2015) Estimation of skidding offered by Ackermann mechanism. *J Inst Eng (India)-Ser C* 97(2):149–156. Springer
9. Rao SS (2003) *Engineering optimization theory and practice*, 3rd edn. New Age International (P) Limited, New Delhi, pp 279–326

# Influence of Surface Textures by Ink-Jet Print Followed by Chemical Etching Process on the Performance of HSS Cutting Tool



K. Nagendra Prasad and Ismail Syed

**Abstract** In the present work, an attempt has been made to generate protruded and dimpled textures on the rake surface of high-speed steel (HSS) cutting tool by an ink-jet print followed by chemical etching (IPCE) process. The orthogonal turning of Aluminum 6063 alloy was conducted by using textured and non-textured tools. The results revealed that cutting forces and friction coefficient are reduced with textured cutting tools. Moreover, the protruded textured tool exhibits better performance than the dimple-textured tool.

**Keywords** Chemical etching · Protruded textured tool · Dimple-textured tool · Cutting forces · Friction coefficient

## 1 Introduction

Surface texturing is an emerging technique in metal cutting process to reduce tool wear and frictional forces by reduction of contact area and adhesiveness between the chip–tool interaction [1, 2]. Sasi et al. [3] fabricated dimpled texture on the HSS tool rake surface by laser surface texturing during the machining of aluminum alloy. Their results showed that chip–tool contact length is reduced with a textured tool, and it leads to a reduction in cutting forces. Sawant et al. [4] studied the influence of dimple and spot textures on HSS rake surface by micro-plasma transferred arc powder deposition ( $\mu$ -PTAPD) method. They concluded that spot-textured tool is more effective to reduce the cutting forces by increasing rake angle when chip flows over the spot texture. Obikawa et al. [5] fabricated different textures such as grooves, pits, and dots by photoresist spin coating followed by chemical etching. They observed that dot-textured tool was more effective in reducing chip–tool contact length. Jianxin et al. [6] made micro-holes on cemented carbide tool by micro-electrical discharge machining (micro-EDM). Their results showed that cutting forces have reduced up to 30% with a textured tool.

---

K. Nagendra Prasad · I. Syed (✉)

Department of Mechanical Engineering, NIT Warangal, Warangal, Telangana 506004, India  
e-mail: [syedismail7@nitw.ac.in](mailto:syedismail7@nitw.ac.in)

© Springer Nature Singapore Pte Ltd. 2020

H. K. Voruganti et al. (eds.), *Advances in Applied Mechanical Engineering*,

Lecture Notes in Mechanical Engineering,

[https://doi.org/10.1007/978-981-15-1201-8\\_67](https://doi.org/10.1007/978-981-15-1201-8_67)

From the above study, it has been observed that researchers have fabricated the textured cutting tool through different methods such as laser texturing,  $\mu$ -PTAPD, photoresist spin coating followed by chemical etching, and micro-EDM. These methods have inherent limitations, which require a unique experimental setup and involve high cost to make textures. The present work aims to develop a technique for fabrication of the textures with a simple and economical process. In this paper, the investigators have studied the experimental work on fabrication of protruded and dimple textures on HSS tool by an ink-jet print followed by chemical etching (IPCE) process. Moreover, performance of the textured tools has been compared with the non-textured tool in the dry turning of Aluminum 6063 alloy.

## 2 Experimental Work

T-42 grade high-speed steel was selected as a tool (supplied by Rohit tools under grade of 3X Square TB) for surface texturing and dry machining. Aluminum 6063 T6 (supplied by overseas aluminum) was selected as a workpiece material in the form of a hollow cylindrical pipe with an outer diameter of 73 mm. Table 1a, b represents the chemical composition of HSS cutting tool and aluminum 6063 alloy composition, respectively.

### 2.1 Fabrication of HSS Tool with Textured Surfaces

The fabrication of protruded textures on the rake surface of HSS tool is represented schematically in Fig. 1. The texturing can be done in three steps, i.e., transfer of the shape of textures on the tool surface, masking of surface, and chemical etching. In the first step, design of the texture is transferred on a rake surface of HSS tool by ink-jet print method using a Ronald LEF-20 UV printer. Afterward, masking is done with the insulation tape on the tool (except rake surface) to avoid unwanted etching. In the final step, the tool is immersed in a chemical etchant, which is a mixture of copper sulfate ( $\text{CuSO}_4$ ), sodium chloride ( $\text{NaCl}$ ), and hot water ( $70^\circ\text{C}$ ) in the ratio of 1:1:4 (15 mg: 15 mg: 60 ml) for 30 min. After the chemical etching process, ultrasonic cleaning process has been carried out to remove the burrs around the texture.

During the chemical etching process, the cutting edge of the tool suffers a damage due to the chemical reactions between tool and etchant (refer Fig. 1e). Therefore, polishing has been carried out to sharpen the cutting edge of the tool. Similar method has been applied to produce dimple textures on the rake surface of the tool. The developed textures on the rake surface have the following dimensions, i.e., diameter  $180\ \mu\text{m}$ , pitch  $500\ \mu\text{m}$ , and height/depth  $35\ \mu\text{m}$ . The characteristic features of textures on the rake surface of the tool are represented in Fig. 2. Height/depth of the textures was measured with the help of Quasmo 500 optical microscope by changing the depth of the focus.

**Table 1 a** Chemical composition of aluminum 6063 alloy [7] and **b** chemical composition of HSS T 42 [4]

Example	Al	Cr	Cu	Fe	Mg	Mn	Si	Ti	Zn	Other, total	
%	98.41	0.0067	0.0348	0.3495	0.5067	0.078	0.477	0.0236	0.1	0.0137	
Example	Co	W	Cr	Mo	V	Ni	Si	Mn	P	S	Fe
%	9.15	8.68	4.1	3.23	3.12	0.36	0.22	0.2	0.3	0.35	Bal

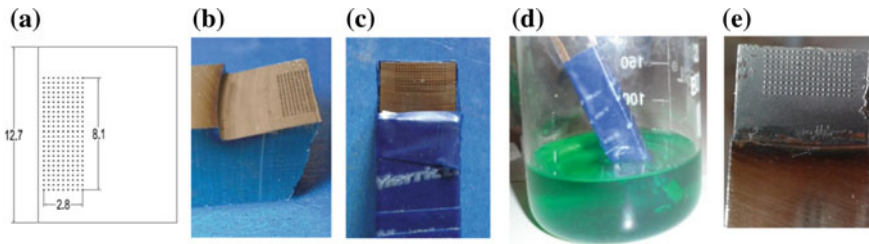


**Fig. 1** Schematic representation of ink-jet print chemical etching process. **a** protruded texture design, **b** image of designed textures after ink-jet print method, **c** masking, **d** chemical etchant, and **e** final protruded textured tool

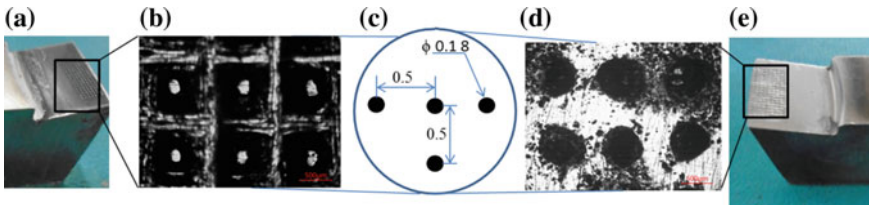


**Fig. 2** **a** protruded textured tool, **b** optical image (magnification 5X) for protruded texture design, **c** characteristics for texture design (all dimensions are in mm), **d** optical image (magnification 5X) for dimpled texture design, and **e** dimple-textured tool

## 2.2 Orthogonal Turning

Orthogonal dry turning experiments were carried out on a variable speed precision lathe with non-textured and textured cutting tools. The cutting tool has the following geometry: rake angle of  $10^\circ$  and the clearance angle of  $15^\circ$ . All turning experiments were conducted at a cutting speed of 110 m/min, feed of 0.103 mm/rev, and width of cut of 1.5 mm. Each orthogonal turning experiment was repeated three times with textured and non-textured tools. During the turning, cutting force ( $F_c$ ) and thrust force ( $F_t$ ) were measured with a three-axis Kistler dynamometer. In this test, the cutting edge of the tool was held perpendicular to the workpiece as shown in Fig. 3.

## 3 Results and Discussion

Frictional force ( $F_f$ ), cutting force ( $F_c$ ), and thrust force ( $F_t$ ) during the orthogonal turning can be expressed in the following equations [7].

$$F_f = A_w \tau_c \quad (1)$$

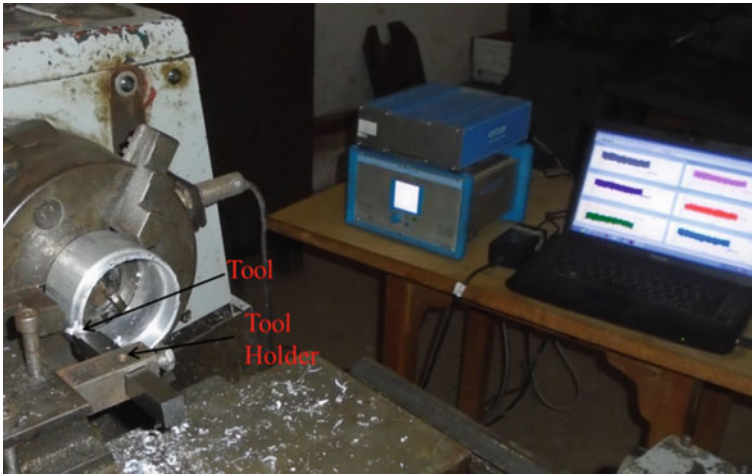


**Fig. 3** Schematic diagram of experimental setup for orthogonal turning

$$F_c = \frac{F_f \sin(\beta - \alpha)}{\sin(\beta)} \tag{2}$$

$$F_t = \frac{F_f \cos(\beta - \alpha)}{\sin(\beta)} \tag{3}$$

where  $A_w$  is the area of tool–chip contact,  $\tau_c$  is the shear strength at the tool–chip contact zone,  $\beta$  is the friction angle, and  $\alpha$  is rake angle.

It can be observed from the equations (1–3) that the cutting forces ( $F_c$  and  $F_t$ ) can be reduced by decreasing the chip–tool contact area ( $A_w$ ). Chip–tool contact area with textured tools can be understood by observing the morphology of the chip back surface using scanning electron microscope (SEM). Figure 4a–c shows the SEM

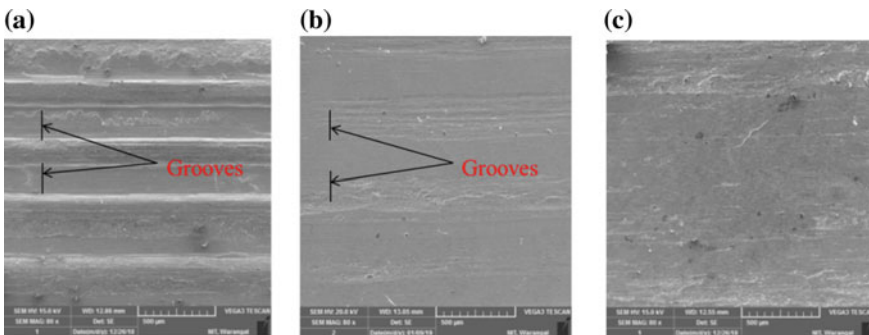


**Fig. 4** SEM images of the chip back surfaces when flow over. **a** protruded textured tool, **b** dimple-textured tool, and **c** non-textured tool

image of the chip back surface which flows over the protruded, dimpled and non-textured tools. It is observed that grooves were formed when the chips flowed over the textured tools; it led to an increase in the gap between chip and toolface, resulting in a reduction of the chip–tool contact area ( $A_w$ ). However, it can be observed that deep grooves are observed with protruded textured tool than the dimple-textured tool which results in higher reduction of the chip–tool contact area ( $A_w$ ).

Figure 5a represents the cutting forces during the machining of Al6063 T6 alloy with non-textured and textured tools. It can be observed that cutting force ( $F_c$ ) for the protruded textured tool has reduced by nearly 13% than the non-textured tool and nearly 4.8% than the dimple-textured tool. Similarly, thrust force ( $F_t$ ) for the protruded textured tool is reduced by almost 23 and 7.3% than the non-textured and dimple-textured tools, respectively.

The friction coefficient ( $\mu$ ) during orthogonal turning is calculated by using the mathematical expression [4].

$$\mu = \tan \beta = \frac{F_t + F_c \tan \alpha}{F_c - F_t \cos \alpha} \tag{4}$$

From Fig. 5b, it is observed that the calculated friction on protruded textured tool has reduced by nearly 11% than the non-textured tool and nearly 2.7% than the dimple-textured tool. The relation between shear angle ( $\phi$ ), friction angle ( $\beta$ ), rake angle ( $\alpha$ ), and chip thickness ( $h_c$ ) is expressed in the following equations [8].

$$\phi + \frac{\beta}{2} - \frac{\alpha}{2} = \frac{\pi}{4} \tag{5}$$

$$\phi = \tan^{-1} \left( \frac{h \cos \alpha}{h_c - h \sin \alpha} \right) \tag{6}$$

where  $h$  is the uncut chip thickness.

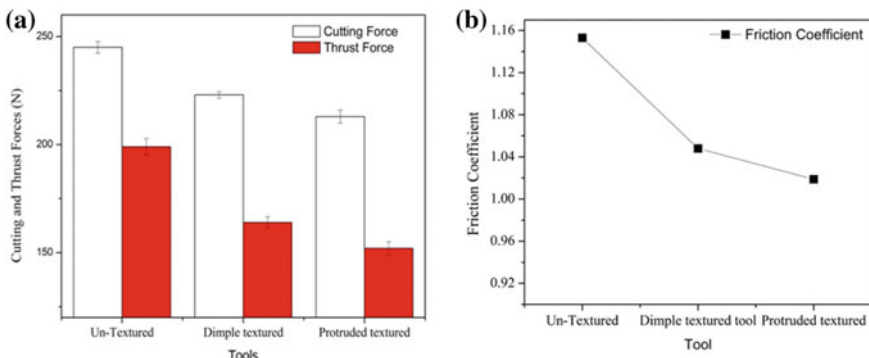


**Fig. 5** Comparison of **a** cutting force ( $F_c$ ) and thrust forces ( $F_t$ ), **b** friction coefficient with non-textured, dimpled, and protruded texture tools

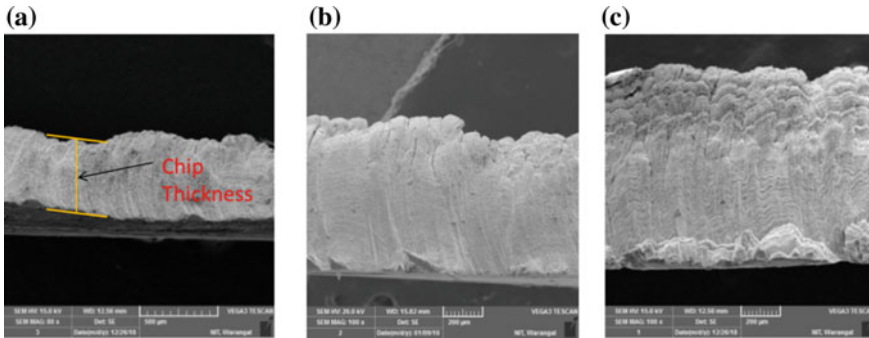


**Fig. 6** SEM images of the chip back surfaces when flow over. **a** Protruded textured tool, **b** dimple-textured tool, and **c** non-textured tool

Curl radius of chip is reduced when the chip flows over the protruded textured tool, and also it leads to an increase in the rake angle [4]. When chip flows over the dimple texture, chip gets sheared off and deposited inside the dimple which leads to the formation of built-up edge (BUE) on the rake surface. As time progressed, amount of BUE increases which leads to the formation of the bulges. The rake angle gets increased when the chip flows over these bulges [3].

The cutting force with the textured tool has reduced by an increase in shear angle because of the reduction in specific cutting energy [8]. Large shear angle in the textured tool can be proved by measuring chip thickness by using a digital micrometer. Chip samples were accumulated, measured at ten different locations, and taken its average. It has been observed that chip thickness with protruded textured tool, dimple-textured tool, and non-textured tool is 1.0188 mm, 1.048 mm, and 1.153 mm, respectively. Figure 6 shows the SEM images of the side surface of the chip when flows over the textured and non-textured tools. It can be observed that thinner chips have formed with textured tools.

## 4 Conclusion

This work proves that the IPCE method is an inexpensive, simple, and effective method to fabricate protruded and dimple textures on the rake surface of the HSS tool. It was also found that chip–tool contact length reduced with textured tools, which leads to reduction in cutting forces and friction coefficient. However, protruded texture has more effectively reduced the cutting forces by reducing the more contact area between chip and tool and causing an increase in rake angle.

**Acknowledgement** Authors would like to thank Hari Radium, Hanamkonda, Telangana 506001, to provide the UV printer to print the texture design on the rake surface of the HSS cutting tool.



## References

1. Enomoto T, Sugihara T (2010) Improving anti-adhesive properties of cutting tool surfaces by nano-/micro-textures. *Precis Eng* 59:229–237
2. Sugihara T, Enomoto T (2012) Improving anti-adhesion in aluminum alloy cutting by micro stripe texture. *Precis Eng* 36:229–237
3. Sasi R, Subbus K, Palani IA (2017) Performance of laser surface textured high speed steel cutting tool in machining of Al7075-T6 aerospace alloy. *Surf Coat Technol* 313:337–346
4. Sawant MS, Jain NK, Palani IA (2018) Influence of dimple and spot-texturing of HSS cutting tool on machining of Ti-6Al-4V. *J Mater Process Tech* 261:1–11
5. Obikawa T, Kamio A, Takaoka H, Osada A (2011) Micro-texture at the coated tool face for high performance cutting. *Int J Mach Tools Manuf* 51:966–972
6. Jianxin D, Wenlong S, Hui Z, Pei Y, Aihua L (2011) Friction and wear behaviors of the carbide tools embedded with solid lubricants in sliding wear tests and in dry cutting processes. *Wear* 270:666–674
7. Rathod P, Aravindan S, Rao V (2016) Performance evaluation of novel micro-textured tools in improving the machinability of aluminum alloy (Al6063). *Procedia Technol* 23:296–303
8. Sharma V, Pandey PM (2016) Recent advances in turning with textured cutting tools: a review. *J Clean Prod* 137:701–715

# Effect of Temperature on the Tribological Performance of MoS<sub>2</sub>–TiO<sub>2</sub> Coating Material



Avinash V. Borgaonkar and Ismail Syed

**Abstract** Recently, there is a growing interest in molybdenum disulphide (MoS<sub>2</sub>) to use as a solid lubricant to enhance the tribological properties. In the present work, composite MoS<sub>2</sub>/TiO<sub>2</sub> coatings were prepared and bonded on pre-treated steel substrate. The manganese phosphating process has been used as a pre-treatment which helps to improve the bond strength. The coating has been bonded onto the phosphated substrate using sodium silicate as a binder. A comparative study of these composite coatings was done at different temperature, load and speed conditions using pin-on-disc tribometer. The results depict that the tribological performance such as friction coefficient and specific wear rate has been improved by coating material as compared to uncoated material.

**Keywords** Molybdenum disulphide · Solid lubricant · Coating · Tribological properties

## 1 Introduction

Solid lubricants have been proven to be such materials that despite of its solid phase, they are able to provide improved tribological performance between the rolling/sliding interfaces. The solid lubricant can be either used as coatings or as filler element in self-lubricating composites [1]. From the past few decades, they have been used as a lubricant between the contact surfaces subjected to rolling and sliding movement. There are certain applications where only solid lubricants can be used, i.e. in severe conditions and in hostile environments such as high load and high temperature, ultra-low vacuum and cryogenic temperatures, strong radiation, dry and clean lubrication, resistance to contamination and protection against corrosion. The solid lubricants with their classification are as shown in Table 1 [2, 3].

From the past few decades, most of the researchers concentrated on MoS<sub>2</sub> as a solid lubricant due to its weak interatomic forces between the sulphide anions and strong

---

A. V. Borgaonkar · I. Syed (✉)  
Department of Mechanical Engineering, NIT Warangal, Warangal, Telangana 506004, India  
e-mail: [syedismail7@nitw.ac.in](mailto:syedismail7@nitw.ac.in)

© Springer Nature Singapore Pte Ltd. 2020  
H. K. Voruganti et al. (eds.), *Advances in Applied Mechanical Engineering*,  
Lecture Notes in Mechanical Engineering,  
[https://doi.org/10.1007/978-981-15-1201-8\\_68](https://doi.org/10.1007/978-981-15-1201-8_68)

**Table 1** Classification of solid lubricants

Classification	Key examples
Lamellar solids	Molybdenum disulphide
	Tungsten disulphide
	Hexagonal boron nitride
	Graphite
	Graphite fluoride
	Boric acid
	Monochalcogenides (GaSe, GaS, SnSe)
Soft metals	Silver
	Lead
	Gold
	Indium
	Tin
Mixed oxides	CuO–Re <sub>2</sub> O <sub>7</sub>
	CuO–MoO <sub>3</sub>
	PbO–B <sub>2</sub> O <sub>3</sub>
	CoO–MoO <sub>3</sub>
	Cs <sub>2</sub> O–MoO <sub>3</sub>
	NiO–MoO <sub>3</sub>
	Cs <sub>2</sub> O–SiO <sub>2</sub>
Single oxides	Re <sub>2</sub> O <sub>7</sub>
	MoO <sub>3</sub>
	TiO <sub>2</sub>
	ZnO
Halides and sulphates or alkaline earth metals	CaF <sub>2</sub> , BaF <sub>2</sub> , SrF <sub>2</sub>
	CaSO <sub>4</sub> , BaSO <sub>4</sub> , SrSO <sub>4</sub>
Carbon-based solids	Diamond
	DLC
	Glassy carbon
	Hollow carbon nanotubes
	Fullerenes
	Carbon–carbon and carbon–graphite-based composites
Polymers/organic materials	Zinc stearate
	Waxes
	Soaps
	Polytetrafluoroethylene

covalent bonds within molybdenum. Moreover, it is stable and unaffected by oxygen and diluted acids. As like graphite, it is also having asperity healing attributes, which helps to lower the friction values. On the other hand, it does not require any water vapour or moisture to provide the results which makes it suitable for vacuum applications. Shankara et al. [4] investigated the tribological performance of bonded pure MoS<sub>2</sub> as well as composite MoS<sub>2</sub>-zirconia and MoS<sub>2</sub>-graphite coating on steel substrate using sodium silicate as a binder. The test results reveal that in comparison with pure MoS<sub>2</sub>, composite MoS<sub>2</sub>-zirconia improves the tribological performance since zirconia is a ceramic material having high wear resistance. Beside MoS<sub>2</sub>-graphite also helps to enhance the tribological performance since by nature graphite is a very soft material [5]. Another study conducted by Ye et al. [6] used novolac epoxy resin as a binder to bond MoS<sub>2</sub> with the substrate. They observed significant improvement in tribological behaviour at relatively higher load range, since the sand blasting which has been used as a pre-treatment helps to improve the adhesion strength. Further with this same coating and binder material, Luo et al. [7] conducted the rotational fretting wear test. The findings were similar to the previous study. However, they observed that the wear mechanism was the combination of delamination, abrasive wear and tribo-oxidation. Tang et al. [8] examined the tribological performance of aramid fibre filled polyamide six different composites with and without addition of nano-MoS<sub>2</sub> under dry sliding contact conditions. They observed that the tribological properties enhanced significantly due to addition of nano-MoS<sub>2</sub>. Two main wear mechanisms such as micro-ploughing and plastic deformations were identified. The decrease in wear rate of a coating was observed with increase of aramid fibre content.

Hamilton et al. [9] conducted number of experiments on different five thin-film MoS<sub>2</sub> coatings such as MoS<sub>2</sub>-Ni, MoS<sub>2</sub>-Ti, MoS<sub>2</sub>-Sb<sub>2</sub>O<sub>3</sub>, MoS<sub>2</sub>-C-Sb<sub>2</sub>O<sub>3</sub> and MoS<sub>2</sub>-Au-Sb<sub>2</sub>O<sub>3</sub>. In order to study the macroscopic effect of temperature on the tribological properties, the temperature was varied from -80 to 180 °C. The decrease in COF values has been observed with increase in temperature since the thermally activated coatings exhibit stable interfacing layers due to which ultra-low wear occurs, whereas athermal behaviour leads to high rate of wear. Nowadays, the solid lubricants used at high-temperature conditions since most oils, greases and few organic polymers were oxidatively unstable for some appreciable time. Some of the materials can be used as self-lubricating composites and coatings such as dichalcogenides, graphite and graphite fluoride, polyimides, soft oxides, oxidatively stable fluorides and hard coatings to enhance the tribological performance of the contacting surfaces [10]. Zhang et al. [11] added Ag nano-particles to the MoS<sub>2</sub> in order to improve the tribological properties as well as the load bearing capacity since the addition of Ag nano-particles enhances strength of the tribofilm. Moreover at higher temperature, the composite coating demonstrates prolonged life as compared to conventional MoS<sub>2</sub> coating because of the formation of silver molybdate layers. Theiler et al. [12] examined the tribological performance of MoS<sub>2</sub>/ta-C bilayer coatings under different environments such as vacuum and air. In order to improve the bonding, a thin chromium interlayer has been introduced. The tribological performance of the coating found to be significantly improved in humid air environment since the coating deposited by laser-arc has relatively high roughness which enhances the endurance

of MoS<sub>2</sub>. Recently, Torres et al. [13] in 2018 from their extensive study summarized that from the transition metal dichalcogenides group MoS<sub>2</sub> being a cost-effective and the outstanding tribological performance in dry air and vacuum environment, since it possesses the weak van der Waals adhesion forces between sulphur-like atoms, leading to the formation of easy-to-shear lamellas. Further, Meng et al. [14] studied the tribological performance MoS<sub>2</sub> coating under dry sliding motion at high temperatures with different loads and speeds. It has been observed that MoO<sub>3</sub> results as an oxidation of MoS<sub>2</sub> (i.e. when working temperature is higher than the transition temperature) leads to lower the tribological performance. Renevier et al. [15] deposited MoS<sub>2</sub>/Ti (MoST) coating on machine tools to study the tribological behaviour. The results reveal that the tribological performance of the conventional MoS<sub>2</sub> coating has been significantly improved with the addition Ti since Ti possesses high resistance to wear.

From the literature, it has been observed that MoS<sub>2</sub> as a single as well as in combination with other different materials has been used as coating material at ambient and high-temperature applications. However in the previous literature, nobody addressed the use of composite MoS<sub>2</sub>/TiO<sub>2</sub> as a solid lubricant. Hence in this paper, the attempt has been made to analyse the performance composite MoS<sub>2</sub>/TiO<sub>2</sub> coating material at ambient and high-temperature conditions.

The objective of the present work involves the evaluation of the tribological performance of composite MoS<sub>2</sub>/TiO<sub>2</sub> coating on the steel substrate at ambient and high-temperature conditions. The study has been carried out at different temperatures including room temperature (RT), 100, 200, 300 and 400 °C. At the end, the tribological properties have been evaluated for summarizing the study.

## 2 Methodology

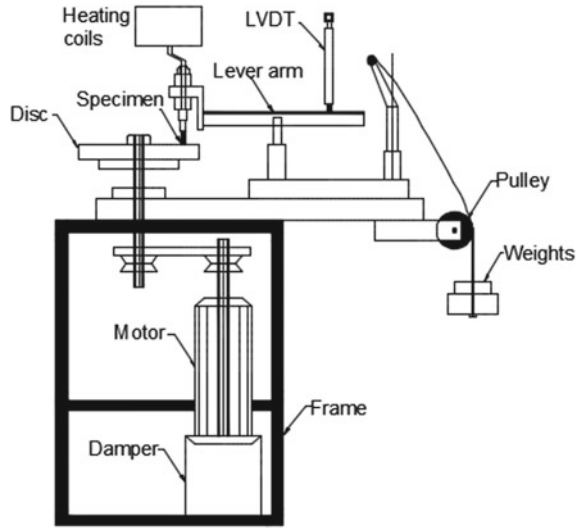
The pin samples were made of AISI 52100 steel (12 mm diameter and 25 mm length) used as the substrate. The AISI 52100 steel composed of 1% C, 1.5% Cr, 0.3% Mn, 0.25% Si, 1% C, with Fe as remaining. Before the experimental test, specimens were polished with SiC abrasive paper (from 220 to 1000-grit), cleaned ultrasonically using acetone and then dried. In order to improve bond strength, manganese phosphating employed as a pre-treatment for the steel substrates. The composite MoS<sub>2</sub>/TiO<sub>2</sub> coating applied on the phosphated substrates with the brushing and cured at 150 °C for two hours.

The friction tests were performed using pin-on-disc tribometer (Magnum, India) in accordance with ASTM standard G99-95 [16]. A schematic set-up of the pin-on-disc tribometer is shown in Fig. 1.

The counter disc is made up of EN31 steel. Before performing each test, the disc surface was cleaned using acetone and thoroughly dried. The sliding speed was kept constant by adjusting the rotational frequency and track radius using the formula:

$$V = 2\pi r * N \quad (1)$$

**Fig. 1** Experimental set-up for tribological study



where  $V$  is the sliding velocity,  $N$  is speed in rpm and  $r$  is the track radius. A data acquisition system was coupled to the tribometer to compute and record automatically, the tribological parameters between the coated specimen and the disc surface all the time of the experiments. The wear rate can be obtained using the formula:

$$W_R = W_V / P * D \tag{2}$$

where  $W_R$  is the specific wear rate in  $\text{mm}^3/\text{Nm}$ , is the wear volume in  $\text{mm}^3$ ,  $P$  is the applied load in  $N$  and  $D$  is the sliding distance in m. The wear volume was estimated by taking the weights of the samples before and at the end of wear test. Eventually to get the reliable data, each experiment was repeated three times.

The detailed test parameters and ranges are summarized in Table 2.

**Table 2** Test parameters and ranges

Sr. No.	Parameters	Operating conditions
1	Normal load	176, 442 and 707 kPa
2	Sliding speed	2, 4 and 6 m/s
3	Track radius	30 mm
4	Sliding distance	3000 m
5	Temperature	RT, 100, 200, 300 and 400 °C
6	Relative humidity	70 ± 5%

### 3 Results and Discussion

The pin-and-disc surfaces have been analysed before and after wear test to understand the tribological behaviour of the composite coating. The results show that at low load, the mechanism of wear is abrasion, and as the load increases, the coating material from the pin surface gets transferred to the disc surface. So with the increase in load and speed, the mechanism of wear changes from abrasion to adhesion as depicted in Fig. 2.

The experimental test performed at three different load and speed combinations varying the temperature from RT to 400 °C with a step of 100 °C. The values of coefficient of friction (COF) and specific wear rate ( $\text{mm}^3/\text{Nm}$ ) for different combinations have been obtained from the data acquisition system and plotted as shown in Figs. 3 and 4.

From the experimental results, it has been observed that friction coefficient (COF) decreases with increase in the temperature and load. At high load with increase in temperature, the coating layer worn out and transferred to the counter disc surface, due to which the reduced values of COF have been observed. The lowest COF value obtained is 0.065. Beside with increase in the temperature and load, the specific wear rate increases, and in the temperature range 300–400 °C, the values of specific wear rate found to be almost consistent. The lowest value of specific wear rate obtained is  $1.7 \text{ mm}^3/\text{Nm}$ .

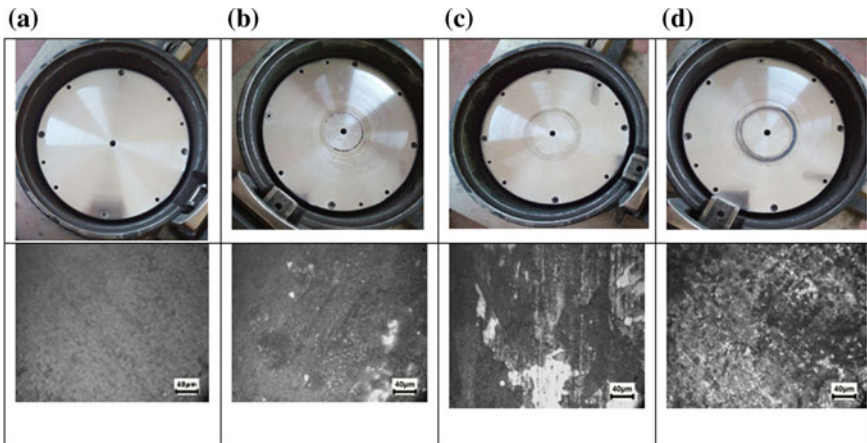


**Fig. 2** Disc and pin surface before test (a) and after test at constant load 176 kPa and different sliding speed 2 m/s (b), 4 m/s (c), 6 m/s (d)

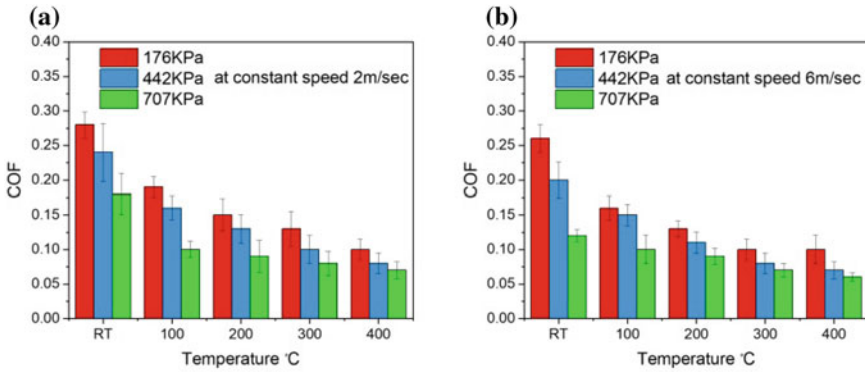


**Fig. 3** Coefficient of friction (COF). **a** At load 176, 442 and 707 kPa at constant low speed 2 m/s, **b** at constant high speed 6 m/s

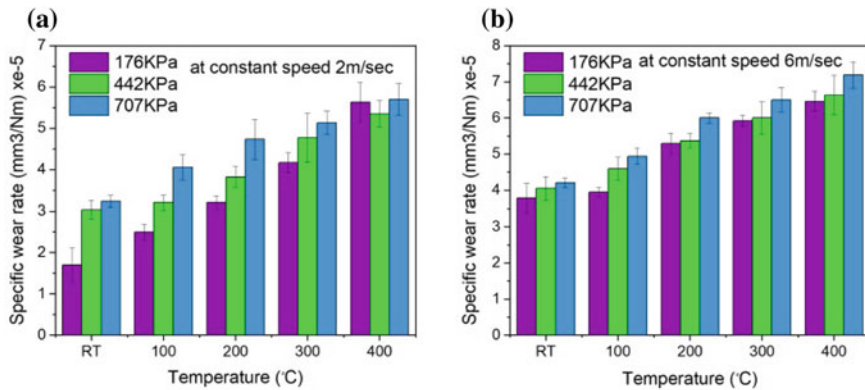


**Fig. 4** Specific wear rate (mm<sup>3</sup>/Nm). **a** At load 176, 442 and 707 kPa at constant low speed 2 m/s, **b** at constant high speed 6 m/s

### 4 Conclusion

Within the scope of this study, the tribological behaviour of composite of MoS<sub>2</sub>/TiO<sub>2</sub> coating at ambient as well as high temperature has been investigated. The results show that due to the synergistic effect of MoS<sub>2</sub> and TiO<sub>2</sub> at high temperature and high load, the friction coefficient was lower. However, due to the change in mechanism from abrasion to adhesion, the coating layers transformed from substrate surface to the counter disc surface with rise in temperature and load, which leads to increase in the specific wear rate. At higher temperatures (i.e. 300–400 °C), the specific wear rate found to be almost constant.



## References

1. Feng IM (1952) Lubricating properties of molybdenum disulfide. *Lubr Eng* 8:285–288
2. Sharma SM, Anand A (2016) Solid lubrication in iron based materials—a review. *Tribol Ind* 38(3)
3. Ingole SP, Menezes PL, Nosonovsky M, Lovell MR, Kailas SV (2013) *Tribology for scientists and engineers: from basics to advanced concepts*. Springer
4. Shankara A, Menezes PL, Simha KRY, Kailas SV (2008) Study of solid lubrication with MoS<sub>2</sub> coating in the presence of additives using reciprocating ball-on-flat scratch tester. *Sadhana* 33(3):207–220
5. Meng FM, Cui ZT, Cheng ZT, Han HL (2018) Experimental Study on Tribological Properties of Graphite-MoS<sub>2</sub> Coating on GCr<sub>15</sub>. *J Tribol* 140(5):051303
6. Ye Y, Chen J, Zhou H (2009) Microstructure, tribological behavior, and corrosion-resistant performance of bonded MoS<sub>2</sub> solid lubricating film filled with nano-LaF<sub>3</sub>. *J Dispersion Sci Technol* 30(4):488–494
7. Luo J, Zhu MH, Wang YD, Zheng JF, Mo JL (2011) Study on rotational fretting wear of bonded MoS<sub>2</sub> solid lubricant coating prepared on medium carbon steel. *Tribol Int* 44(11):1565–1570
8. Tang G, Huang W, Chang D, Nie W, Mi W, Yan W (2011) The friction and wear of aramid fiber-reinforced polyamide 6 composites filled with nano-MoS<sub>2</sub>. *Polym-Plast Technol Eng* 50(15):1537–1540
9. Hamilton MA, Alvarez LA, Mauntler NA, Argibay N, Colbert R, Burris DL, Muratore C, Voevodin AA, Perry SS, Sawyer WG (2008) A possible link between macroscopic wear and temperature dependent friction behaviors of MoS<sub>2</sub> coatings. *Tribol Lett* 32(2):91–98
10. Sliney HE (1982) Solid lubricant materials for high temperatures—a review. *Tribol Int* 15(5):303–315
11. Zhang W, Demydov D, Jahan MP, Mistry K, Erdemir A, Malshe AP (2012) Fundamental understanding of the tribological and thermal behavior of Ag–MoS<sub>2</sub> nanoparticle-based multi-component lubricating system. *Wear* 288:9–16
12. Theiler G, Gradt T, Österle W, Brückner A, Weihnacht V (2013) Friction and endurance of MoS<sub>2</sub>/ta–C coatings produced by laser arc deposition. *Wear* 297(1–2):791–801
13. Torres H, Rodríguez Ripoll M, Prakash B (2018) Tribological behaviour of self-lubricating materials at high temperatures. *Int Mat Rev* 63(5):309–340 (2018)
14. Meng F, Yang C, Han H (2018) Study on tribological performances of MoS<sub>2</sub> coating at high temperature. *Proc Inst Mech Eng Part J: J Eng Tribol* 232(8):964–973
15. Renevier NM, Hampshire J, Fox VC, Witts J, Allen T, Teer DG (2001) Advantages of using self-lubricating, hard, wear-resistant MoS<sub>2</sub>-based coatings. *Surf Coat Technol* 142:67–77
16. Standard A (2010) Standard test method for wear testing with a pin-on-disk apparatus, Annual book of ASTM standards, G99-053

# Topology Optimization Using Strain Energy Distribution for 2D Structures



Srinivasan Bairy, Rafaque Ahmad and Hari K. Voruganti

**Abstract** Optimization is carried out to achieve the best out of given resources while satisfying constraints on performance, state variables, and resources thus avoiding the excessive use of resources and decrease the cost associated. Structural systems need to be designed for a minimum of weight, compliance, displacement, frequency, etc., to save cost and get optimal performance. For this, structural optimization is carried out. Topology optimization is one type of structural optimization in which topology of the structure is changed. Generally, topology optimization is performed using methods like solid isotropic material with penalization (SIMP), level set-based methods, phase field method, evolutionary structural optimization (ESO), and bidirectional evolutionary structural optimization (BESO). In the present work, a modified evolutionary algorithm is proposed for structural optimization with consideration to strain energy distribution. Addition of material is performed on a partially void space instead of material removal. As the final optimum structure bears only a fraction of initial structure, the method of structure growth using addition approach is better for computational efficiency. This method initially takes a void input design domain but to make numerical computation easy, negligible density is assumed. The objective is to achieve critical strain energy per unit volume which is less than the modulus of resilience according to the maximum strain energy criterion. According to the maximum strain energy theory, a safe structure should have strain energy per unit volume less than the modulus of resilience. Hence, the objective is to find a structure satisfying the above criterion with minimum weight. The main focus of the work is to find optimum topology. Effect of multiple loads, rate of material addition, and effect of the magnitude of loads are also considered for structural optimization. The results are close to the results reported in the literature.

**Keywords** Topology optimization · Strain energy · Finite elemental analysis

---

S. Bairy · R. Ahmad · H. K. Voruganti (✉)  
Department of Mechanical Engineering, National Institute of Technology Warangal, Warangal,  
Telangana 506004, India  
e-mail: [harikumar@nitw.ac.in](mailto:harikumar@nitw.ac.in)

© Springer Nature Singapore Pte Ltd. 2020  
H. K. Voruganti et al. (eds.), *Advances in Applied Mechanical Engineering*,  
Lecture Notes in Mechanical Engineering,  
[https://doi.org/10.1007/978-981-15-1201-8\\_69](https://doi.org/10.1007/978-981-15-1201-8_69)

619

# 1 Introduction

The world is facing the scarcity of resources and there is a demand for only the best products in a very high-technological competitive market. To solve this problem and hence minimize the wastage of resources, there is a need to find the best solution among all the solutions of a design problem in such a way that that functionality of the design is not hampered. Structural optimization aims to utilize structural resources most efficiently. Today, optimization of structures has become mandatory for different applications. Structural optimization is much found in the aerospace and automotive industries where weight minimization is the key criteria for design. Structural optimization can be classified into size optimization, shape optimization, and topology optimization. Size optimization is carried out to determine the optimal size, dimensions of cross-sectional areas, thickness, moment of inertia, etc. Shape optimization helps in identifying the optimal geometry of boundaries for the structures carrying loads. Among these three, topology optimization is the most general and gives more design freedom to engineers by expanding the design space to look for the optimal solution, and hence, it is most rewarding economically.

Bendsoe and Sigmund [1] mentioned that topology optimization is carried out to get the best distribution of the material in a design domain. Topology optimization determines the best connectivity, shape, and location of voids in a design domain. Woon et al. [2] carried out shape optimization by moving the boundary and internal nodes of the structure. Optimal coordinates are found using genetic algorithm and also mirroring option helps in reducing the computational time of symmetrical problem to half. Ding [3] mentions that boundary of the physical problem can be represented by using the nodes, piecewise polynomials, and B-spline models. Smooth boundaries are required to avoid stress concentration and to make the manufacturing process easy. Bendsoe [4] described topology optimization as a process of removing the material from the places of negligible contribution to the load carrying capacity of the structural member. It is carried for minimizing the compliance of the structure by the method of solid isotropic material with penalization (SIMP). In topology optimization, material density is chosen as a continuous variable varying from zero to one within an element of finite element mesh. Optimal density is obtained through an optimization algorithm by choosing the densities of each element as variable as explained by Bendsoe [4, 5]. Solid isotropic material with penalization considers the density of element as a design variable and penalizes density based on this power law model such that less contributing elements have minimum effect on the final design, and penalization is applied as mentioned by Duysinx and Bendsoe [6].

An evolution algorithm is proposed by Xie and Steven [7] using a rejection ratio to remove the elements of lower stress. In optimization, constraints play a greater role in the outcome of the algorithm. Generally, in structural optimization, constraints are the volume, weight, and also sustaining the external loads. Xie and Grant [8] described a method for obtaining the optimal structure using an evolutionary structural optimization (ESO) method which works on the local stress of the individual

elements. In ESO algorithm, the material is removed from very low stressed locations in every iteration using a rejection ratio. Lagaros et al. [9] presented a hybrid method to reduce the computational cost combining genetical algorithm method with the SQP method. This hybrid method first uses the GA to get the nearest solution to optimum solution, and then in the second half, the SQP method is used to achieve convergence to optimal quickly. Chu et al. [10] developed an optimization algorithm with the objective as stiffness. Lower sensitivity elements of FEA are removed using stiffness sensitivity which is measured by the change in the strain energy.

Abolbashari and Shadi [11] examined the effect of mesh size, rejection ratio, and type of element on the optimal shape and found that the optimum shape is dependent on these parameters. Huang and Xie [12] developed a bidirectional algorithm to increase the rate of convergence of the optimal solution. This algorithm adds the material at critical locations and removes the material from low stressed areas. Tanskanen [13] studied the theoretical aspects of ESO method and found that this method is equivalent to the compliance minimization problem. Li et al. [14] worked on a reference factor for suppressing checkerboard pattern in the optimal solution. Li et al. [15] mentioned that Vonmises stress criteria and stiffness criteria are equivalent in the evolutionary structural optimization problems. Kwok et al. [16] proposed a topology optimization method based on the principal stress lines.

Genetic algorithms also have been used in structural topology optimization. Rajeev and Krishnamoorthy [17] used the genetic algorithm to optimize truss problems. Deb and Surendra [18] also used GA for optimizing the location of nodes for a truss member. Members having negligible area assumed to be absent in the final solutions. Balamurugan et al. [19] claimed that a two-stage adaptive genetic algorithm is converging quickly to obtain a global solution. Deepak et al. [20] studied and compared different formulations for the topology optimization of compliant mechanisms. Mutual strain energy formulation found to be better for compliant mechanisms. Jog [21] proposed topology optimization for reducing structural vibrations. Dynamic compliance is used to optimize the structures vibration levels. This ensures that natural frequency is away from the dynamic frequency of the structures. Nandy et al. [22] optimized the structures for reducing the radiated noise.

Querin et al. [23] applied the bidirectional evolutionary algorithm (BESO) for a fully stressed design using Vonmises stress criterion by removing elements where stress is low and adding elements to void regions near high-stress locations in the design domain. BESO is another method in evolutionary optimization techniques which has provisions of both adding and removing material simultaneously from design domain from less critical regions, i.e., places in design domain where sensitivity number is low and add material to void regions, where material required will be more based on high sensitivity number of void elements. The number of elements to be added and deleted is based on heuristic criteria, not on sensitivity of void elements which causes this method to fail without producing optimal topology and also causing numerical problems like mesh dependency problems and checkerboard. From the literature, the points are noted. (1) Many algorithms remove the material from the initial domain [1]. In this method, material addition method for topology optimization is proposed. (2) In the existing algorithms, strain energy distribution

as a criterion for structure topology design based on element addition approach is not presented. (3) Available algorithms did not consider the effect of change in the magnitude of loads, multiple loads on the structures. In our work, the addition of material is adopted instead of removal. The strain energy distribution is considered for optimization. We found the elements which are contributing more to the final solution so that they can be strengthened by adding material. Finite element analysis (FEA) is carried out to know these high contributing elements. As the entire process happens iterationwise, it is enough to check the given structure is safe or not according to the failure criteria chosen. This helps to stop the algorithm at safe design.

## 2 FEA Formulation

In our work, finite element analysis is used to know the critical locations in the structural component. FEA preprocessing divides the design domain into small finite elements and generates a mesh. Variation of field variables is approximated with shape functions. Rate of change of field variables variation gives the strain at required locations on the element. FEA analysis is carried out using the four-noded quadrilateral element. Isoparametric FEA method is used to approximate the field variables and geometric variables on the element at any location. Field variables are interpolated using nodal values (notation of nodal displacements at  $j$ th node are  $u_j$  and  $v_j$  in  $X$ -direction and  $Y$ -direction, respectively) and shape functions (notation of  $i$ th shape function is  $N_i$ ).

In an element, geometric variables are approximated using the following relations with four known geometric coordinates. The four shape functions for the quadratic element are shown below:

$$\begin{aligned} N_1 &= \frac{(1-r)(1-s)}{4}; N_2 = \frac{(1+r)(1-s)}{4}; \\ N_3 &= \frac{(1+r)(1+s)}{4}; N_4 = \frac{(1-r)(1+s)}{4} \end{aligned} \quad (1)$$

In an element, geometric variables are approximated by using the following relation with four known geometric coordinates.

$$\begin{Bmatrix} x \\ y \end{Bmatrix} = \sum_{i=1}^4 N_i \begin{Bmatrix} x_i \\ y_i \end{Bmatrix} \quad (2)$$

Displacement of field variables is approximated within the element with known displacements at the four nodes of the element.

$$\begin{Bmatrix} u \\ v \end{Bmatrix} = \sum_{i=1}^4 N_i \begin{Bmatrix} u_i \\ v_i \end{Bmatrix} \tag{3}$$

In FEA, the physical element in  $(x, y)$  coordinate is mapped to master element in  $(r, s)$  coordinate. Transformation matrix  $J$  is used to map the special derivatives available in  $(r, s)$  coordinate back into  $(x, y)$  coordinate. Strain vector  $\epsilon$  is determined using  $[\epsilon] = [B] \times [U]$ .  $[B]$  is the strain–displacement matrix and  $[U]$  is the displacement matrix. Stiffness for an element is calculated using the following relation. The thickness of the element is assumed as 1 unit.

$$[K] = \iint_{-1}^1 [B]^T [D] B |J| dr ds \tag{4}$$

where  $[D]$  is material constitutive matrix.

### 3 Proposed Method

A method is proposed with consideration to strain energy distribution. Initially, 2D design domain is divided into a certain number of finite elements having a partially dense material equivalent to a void space. The void space is ensured by multiplying regular density stiffness matrix with negligible density factor of 10–8 similar to SIMP methodology. Loading and boundary conditions are selected on nodes according to the physical problem. The field variable such as displacement and their derivatives such as strains and stresses are obtained with finite element analysis. Then critical elements (elements with high strain energy value) are identified among all elements in the design domain. The critical elements are strengthened at each iteration by adjusting the density factor to 1 for those elements. This procedure is continued until the maximum energy in any element is just below the critical level, i.e., the structure becomes safe so the density of all elements in optimum topology is one, and this gives distinctly sharp boundaries of the final design. The entire algorithm is implemented using MATLAB. The flowchart of the algorithm is shown in Fig. 1.

### 4 Results and Discussions

In this study, four case studies are considered. In each case study, the design domain is divided into 5000 finite elements and then assigned a density factor of 10–8. The properties of material considered are Young’s modulus ( $E$ ) = 200 GPa and Poisson’s ratio = 0.3. Plane stress conditions are considered. The final solution consists of elements whose density factor is 1.

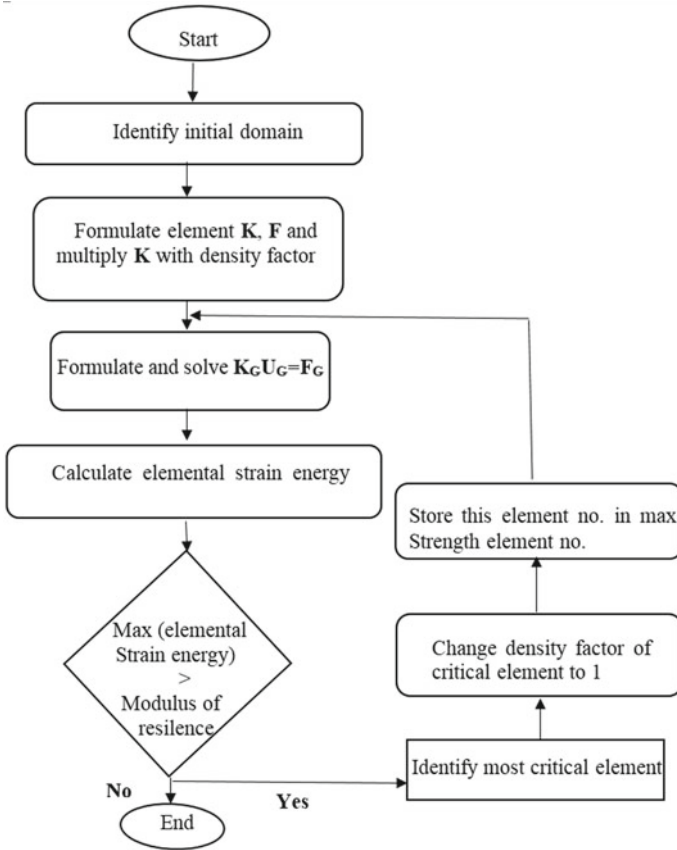


Fig. 1 Flowchart of the proposed algorithm

**4.1 Case Study 1: Effect of Dimensions of the Initial Domain on the Final Optimized Result**

Consider a simply supported beam of length 5 m and height 0.4 m with a load of 100 KN applied at the bottom of the mid-section and self-weight of the beam is not considered as shown in Fig. 2. The FEM formulation is based on 2D plane stress elements.

The structure is optimized using the proposed method and the final solution is consisting of 516 elements shown in Fig. 3. In each iteration, one element is added, and so, the total number of iterations is equal to the number of elements in the final solution. Initially, strain energy dropped significantly with the addition of the elements until connectivity between the load and the support is established. While establishing connectivity, the strain energy is almost constant. Again, it dropped while forming new connectivity. The strain energy plot with respect to the iteration

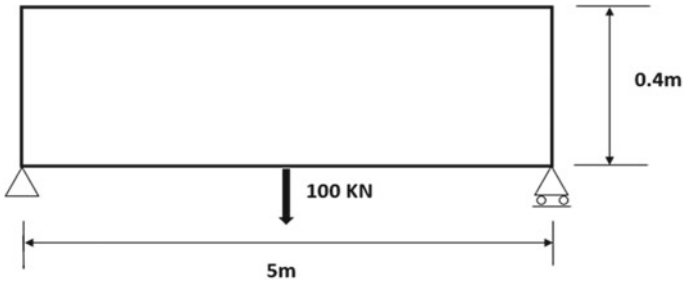


Fig. 2 Simply supported beam with applied load

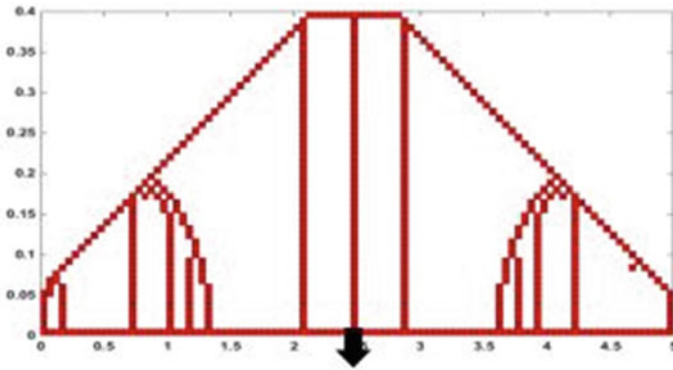


Fig. 3 Topology optimization of the simply supported beam

number is shown in Fig. 4. The percentage of final material with density factor 1 is 10.32 with respect to the initial domain.

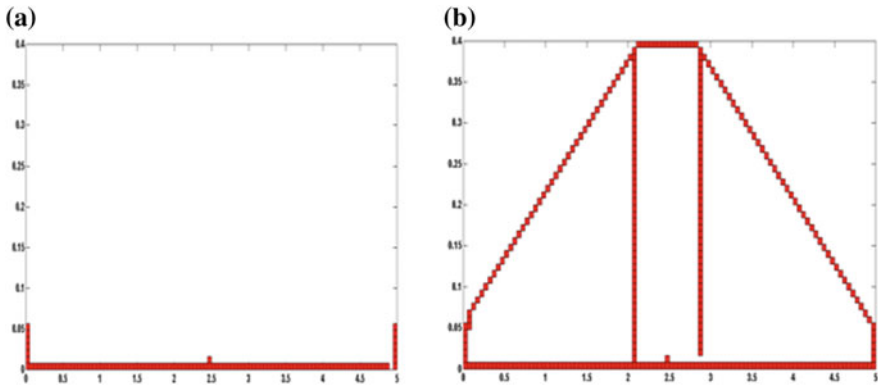
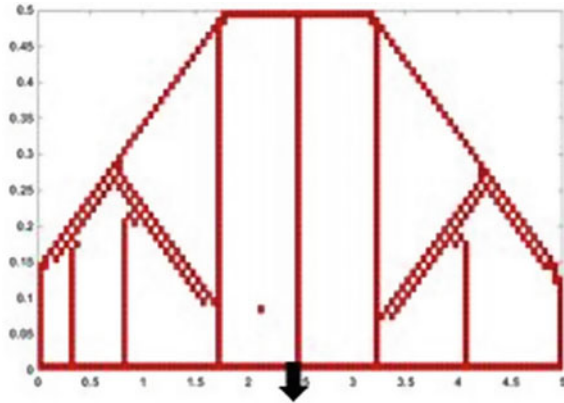


Fig. 4 a Iterative result at 109th iteration and b result at 300<sup>th</sup> iteration



**Fig. 5** Optimized result for different dimension (height = 0.5 m)



The representative intermediate results at iteration number 109 and at 300 where strain energy dropped considerably are shown in Fig. 4.

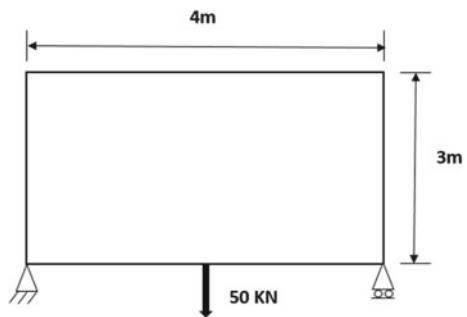
The dimensions of the beam are changed by increasing its height 0.5 m and the corresponding result is shown in Fig. 5. The percentage of final material is 10.4 with respect to the initial domain. This result shows that the optimal results will depend upon the dimensions of the initial domain.

### 4.2 Case Study 2: Effect of the Rate of Material Addition on the Optimization Result

In this case study, the effect of the rate of the amount of material addition on the final solution is studied. For this case, a simply supported beam with a length of 4 m and a height of 3 m is considered. A load of 50 kN is applied at the bottom of the middle section as shown in Fig. 6.

Rate of material addition has effect on final topology because if material added per iteration is more than it may cause inclusion of some elements which may be having

**Fig. 6** Initial domain of simply supported beam



less strain energy in other subsequent iterations, therefore, optimal topology may not be captured but it reduces computational time with less number of elements added per iteration topology development is more detailed with more computational effort. Optimal solution with the addition of 15 elements at a time is having 912 elements (18.24% of the initial domain) in the final solution as shown in Fig. 7, whereas with the addition of 5 elements per iteration, the solution is having 330 elements as shown in Fig. 8. The solution resulted in the addition of a single element per iteration (66% of the initial domain) is shown in Fig. 9. So, for more refined final topology, the low rate of material addition is better.

This effect is also studied with another example of a cantilever beam of 1.5 m length and 3 m height. It is loaded at the middle with 100 KN as shown in Fig. 10. Change in rate of addition gave the same shape structure but the number of elements in the final optimum solution is different as shown in Fig. 11. The optimal structure for the addition of single element per iteration is having 105 elements (2.5% of the

**Fig. 7** Optimized result for material addition rate of 15

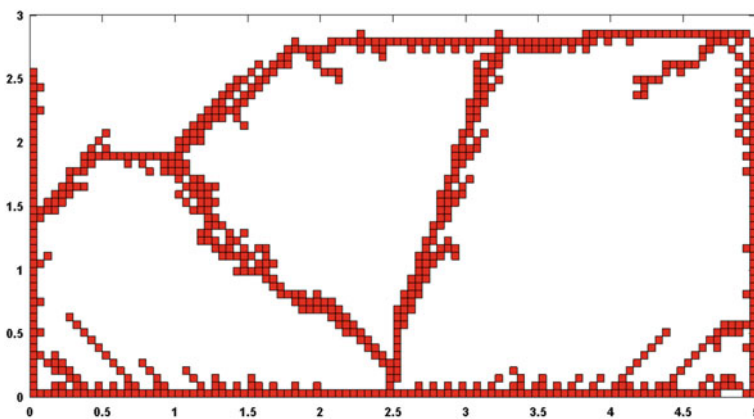
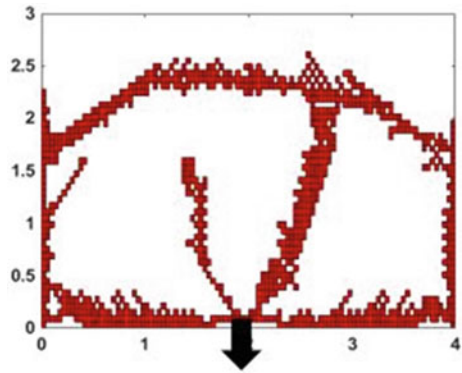


**Fig. 8** Optimized result for material addition rate of 5

**Fig. 9** Optimized result for material addition rate of 1

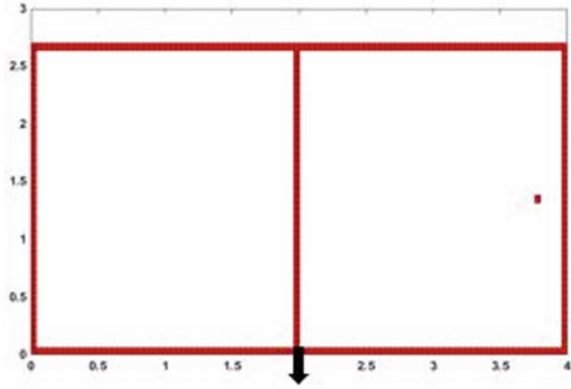
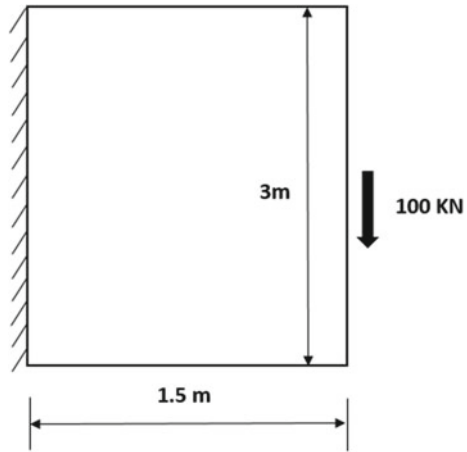


**Fig. 10** Initial domain for a cantilever beam



initial domain) and the optimal structure for the addition of 2 elements per iteration is having 156 elements (3.12% of the initial domain).

### ***4.3 Case Study 3: Effect of Magnitude of Applied Load on the Optimized Result***

Generally, if the magnitude of the load is changed, size optimization is carried out on the optimized topology so that structure can be strengthened at critical locations. Here, in our study, the effect of the magnitude of the load on optimized structure is shown without considering the size optimization. For this case, a cantilever beam of size is considered as shown in Fig. 12. The optimization process produces a solution with few members so the optimum result is truss-like structure when the beam is

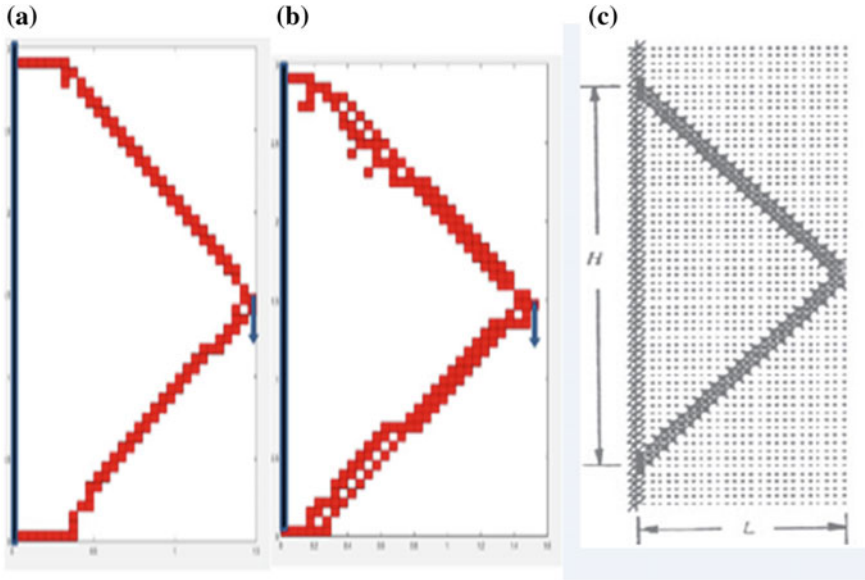
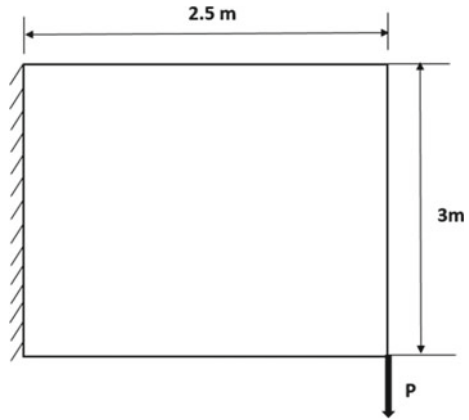


**Fig. 11** a Optimal shape for 1 element addition, b optimal shape for 2 element addition, and c Optimum shape from literature (Xie and Steven [7])

**Fig. 12** Initial domain for cantilever beam



subjected to smaller loads since for smaller loads, few members are sufficient. The optimized results for the cantilever beam with less load (150 KN) and a high load (1500 KN) are shown in Fig. 13.

Effect of increasing the load on the optimum solution causes the addition of more members in optimum topology. The percentage of material with 150 KN load is 3.8 and that with 1500 KN is 7.2.

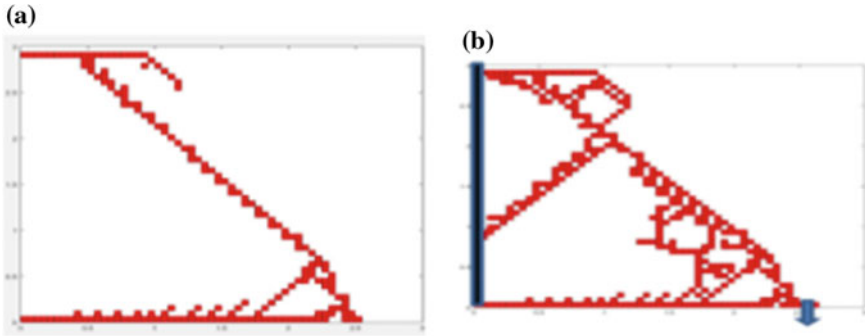


Fig. 13 a Solution for 150 kN and b solution for 1500 kN

### 4.4 Case Study 4: Effect of Multiple Loads

Consider a simply supported beam of length 5 m with a load of 150 kN as shown in Fig. 14. Two more loads of the same magnitude are added at 1.25 and 3.75 m as

Fig. 14 Simply supported beam with a single load

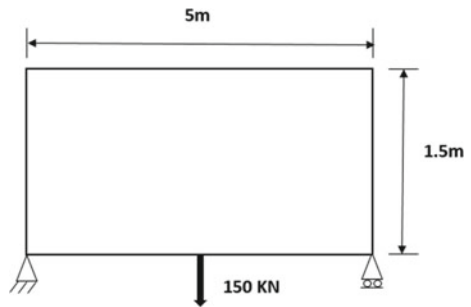
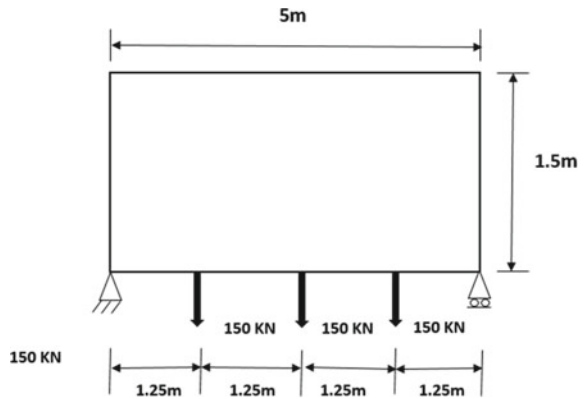
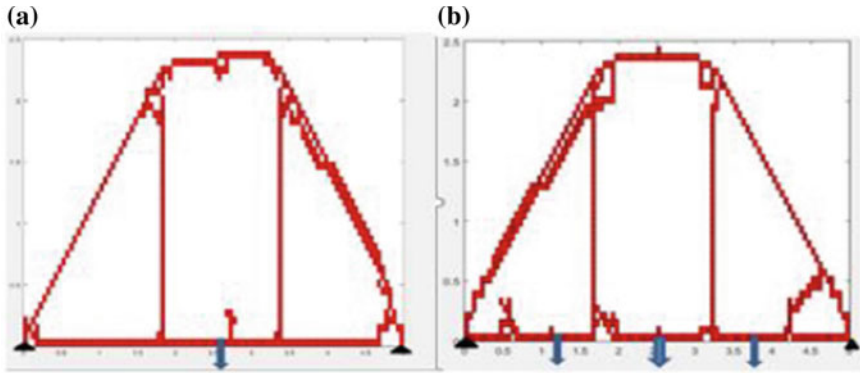


Fig. 15 Simply supported beam with multiple loads





**Fig. 16** **a** Simply supported beam with a single load and **b** simply supported beam with multiple loads

shown in Fig. 15. The optimum solution for single and multiple loads is shown in Fig. 16.

The multiple loads generate extra members between the point of application of load and support to give strength to structure. The percentage of final material with a single load is 7 and that of multiple loaded beams is 7.8.

## 5 Conclusion

In this paper, a modified evolutionary algorithm which is heuristic is proposed for topology optimization with strain energy distribution as a criterion. Optimum structures obtained using this method are close to the existing optimum solutions [8]. Proposed algorithm strengthens highly strained elements through increasing their density factor. This is a material addition process. Results depend on the chosen failure criteria. The algorithm ensures the optimum solution to be safe as per maximum strain energy criteria. From the case studies, it is observed that, if loads of a structure changes, the corresponding topology also changes. The multiple loaded beams have more intermediate members to bear extra loads than a single load case. The main focus of the work is to capture the topology well, and the results can be further improved so that the structures are manufacturable using the filter techniques [24]. The present work can be applied to other 2D structural domains and can be extended to 3D domains.

## References

1. Bendsøe MP, Sigmund O (2013) *Topology optimization: theory, methods, and applications*. Springer
  2. Woon SY, Querin OM, Steven GP (2001) Structural application of a shape optimization method based on a genetic algorithm. *Struct Multidiscip Optim* 22(1):57–64
  3. Ding Y (1986) Shape optimization of structures: a literature survey. *Comput Struct* 24(6):985–1004
  4. Bendsøe MP (1989) Optimal shape design as a material distribution problem. *Struct Multidiscip Optim* 1(4):193–202
  5. Bendsøe MP (1995) *Optimization of structural topology, shape, and material*. Springer, Berlin
  6. Duysinx P, Bendsøe MP (1998) Topology optimization of continuum structures with local stress constraints. *Int J Numer Methods Eng* 43(8):1453–1478
  7. Xie YM, Steven GP (1993) A simple evolutionary procedure for structural optimization. *Comput Struct* 49(5):885–896
  8. Xie YM, Grant PS (1997) Basic evolutionary structural optimization. *Evolutionary structural optimization*. Springer, London, pp 12–29
  9. Lagaros ND, Papadrakakis M, Kokossalakis G (2002) Structural optimization using evolutionary algorithms. *Comput Struct* 80(7):571–589
  10. Chu DN, Xie YM, Hira A, Steven GP (1996) Evolutionary structural optimization for problems with stiffness constraints. *Finite Elem Anal Des* 21(4):239–251
  11. Abolbashari Hossein M, Shadi K (2006) On various aspects of application of the evolutionary structural optimization method for 2D and 3D continuum structures. *Finite Elem Anal Des* 42(6):478–491
  12. Huang X, Xie YM (2007) Convergent and mesh-independent solutions for the bi-directional evolutionary structural optimization method. *Finite Elem Anal Des* 43(14):1039–1049
  13. Tanskanen P (2002) The evolutionary structural optimization method: theoretical aspects. *Comput Methods Appl Mech Eng* 191(47):5485–5498
  14. Li Q, Steven GP, Xie YM (2001) A simple checkerboard suppression algorithm for evolutionary structural optimization. *Struct Multidiscip Optim* 22(3):230–239
  15. Li Q, Steven GP, Xie YM (1999) On equivalence between stress criterion and stiffness criterion in evolutionary structural optimization. *Struct Multidiscip Optim* 18(1):67–73
  16. Kwok TH, Li Y, Chen Y (2016) A structural topology design method based on principal stress line. *Comput Aided Des* 80:19–31
  17. Rajeev S, Krishnamoorthy CS (1992) Discrete optimization of structures using genetic algorithms. *J Struct Eng* 118(5):1233–1250
  18. Deb K, Gulati S (2001) Design of truss-structures for minimum weight using genetic algorithms. *Finite Elem Anal Des* 37(5):447–465
  19. Balamurugan R, Ramakrishnan CV, Singh N (2008) Performance evaluation of a two-stage adaptive genetic algorithm (TSAGA) in structural topology optimization. *Appl Soft Comput* 8(4):1607–1624
  20. Deepak SR, Dinesh M, Sahu DK, Ananthasuresh GK (2009) A comparative study of the formulations and benchmark problems for the topology optimization of compliant mechanisms. *J Mech Robot* 1(1):011003
  21. Jog CS (2002) Topology design of structures subjected to periodic loading. *J Sound Vib* 253(3):687–709
  22. Nandy AK, Jog CS (2012) Optimization of vibrating structures to reduce radiated noise. *Struct Multidiscip Optim* 45(5):717–728
  23. Querin OM, Steven GP, Xie YM (2000) Evolutionary structural optimization using an additive algorithm. *Finite Elem Anal Des* 34(3):291–308
  24. Blaise B (2001) Filters in topology optimization. *Int J Numer Methods Eng* 50(9):2143–2158.
- Chu, Nha D (1996)

# Kinematic Analysis for Optimum Manipulability and Trajectory Planning of Human Leg



Abhijeet Dhoke, V. V. M. J. Satish Chembuly and Hari K. Voruganti

**Abstract** Inverse kinematics and trajectory planning are important for rehabilitation robotics and exoskeleton design. In this paper, a three-link three-dimensional kinematic model of a human leg is defined and its kinematic analysis is performed with the focus of optimizing its manipulability. The biomechanics data is used to obtain the range of motion limit and comfort zone of every joint. The forward kinematics of the leg is used to obtain the workspace of the human leg. Using inverse kinematics, the final joint angles for the desired three-dimensional position are obtained. The inverse kinematics of human leg model is formulated as a constrained optimization problem to get the optimum joint angles under different task constraints. The fifth-degree polynomial function is used to obtain trajectory from initial to final joint angles. Simulations have been performed on the kinematic model of a human leg for workspace evaluation, inverse kinematic solution, and trajectory planning.

**Keywords** Biomechanics · Manipulability · Forward kinematics · Workspace evaluation · Inverse kinematics · Optimization

## 1 Introduction

The inverse kinematics is the mapping that computes the joint angles for the desired pose of the end effector of the model. Most of the robots and living organisms have more degrees of freedom (DOF) than required for the tasks to be performed, which is called redundant DOF. This redundancy improves the flexibility in maneuvering the robots in narrow regions. Mapping of the redundant kinematic model is not one to one, i.e., there may exist many number of solutions for a given end-effector configuration [1] which makes the inverse kinematic problem challenging. There are different techniques to solve inverse kinematics and they can be classified as

---

A. Dhoke · V. V. M. J. Satish Chembuly · H. K. Voruganti (✉)  
Department of Mechanical Engineering, National Institute of Technology Warangal, Warangal,  
Telangana 506004, India  
e-mail: [harikumar@nitw.ac.in](mailto:harikumar@nitw.ac.in)



algebraic, geometric, and iterative [2]. Some of the alternative methods are neural networks [3] or genetic algorithms [1]. Aristidou et al. [4] presented a detailed review on different approaches used in inverse kinematics.

Inverse kinematics is important in the exoskeleton design [5], animation, game programming, robotics, rehabilitation [6], etc. Presently, the rehabilitation and exoskeleton robotics is becoming a research hotspot and some models have been invented as the research achievement [7]. For designing them, knowledge of the biomechanics of human, inverse kinematics, forward kinematics, and trajectory planning is necessary.

A real-time inverse kinematics approach for anthropomorphic limbs has proposed by Tolani et al. [8]. In this approach, they combined analytical and numerical methods to solve IK problems by considering position, orientation, and joint constraints as problem specifications. Głowiński and Krzyżyński [9] proposed an inverse kinematic algorithm for the human leg with an objective of maximizing the manipulability. The advantage of this approach is that the objective function used in it focuses on the comfort zone of the joints and for a living organism, it is very important criteria. This approach is limited for two-dimensional kinematic analysis of human leg model. The proposed work in this paper is focused on developing a three-dimensional kinematic model of a human leg.

In this paper, we proposed an optimization-based approach for evaluating the inverse kinematics solution and trajectory planning for a three-link kinematic model of the human leg in a three-dimensional workspace. In this approach, initially, the task of evaluating workspace of the kinematic model of a human leg has been performed using forward kinematics. Then inverse kinematics solution has determined by posing it as an optimization problem by using optimization functions of MATLAB package. Finally, trajectory planning has performed by interpolating the joint trajectories as a fifth-order polynomial equation. This work can be used for rehabilitation and exoskeleton robot design.

## ***1.1 Biomechanics of the Human Leg***

The human structure is constituted by a skeleton and several muscles, which are collectively called the human musculoskeletal system. Muscle contraction plays main role in producing and delivering the force/torque on the joints and between the body segments at a biomechanical standpoint [10]. A human skeleton can be represented as a kinematic chain model which allows the positioning of joints relative to other joints. The joint configurations can be determined using inverse kinematics.

The human leg consists of three segments, thigh, shank, and foot. The leg can be represented topologically using a kinematic chain structure in which links represent leg segments. Since our leg model has more degrees of freedom than those required to place the end effector in a specified goal, the model is kinematically redundant. To obtain the kinematic parameters, we make the following assumptions [9]:

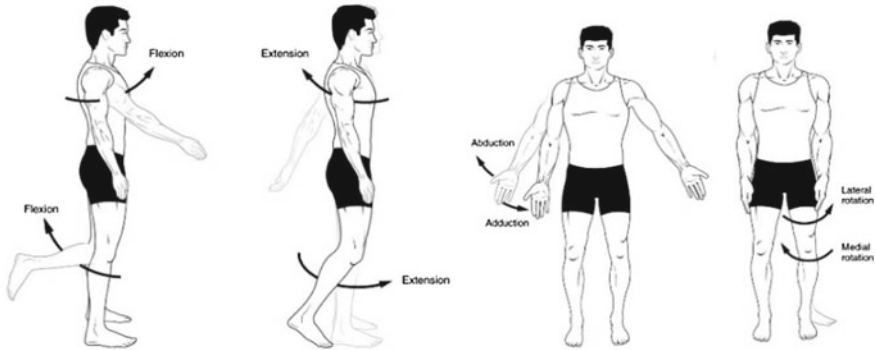


**Fig. 1** The average joint ROM's and joint comfort zones [15]

- The leg base or hip joint is located at the origin and is stationary.
- Lengths of the links are calculated as a function of human height  $H$  [m], thigh-bone  $l_t = 0.2450H$ , shank  $l_s = 0.2460H$ , length from ankle to metatarsal  $l_a = 0.0577H$ .
- Joints are revolute and their limits are known.
- The initial joint angles are known.
- The goal coordinates are given.
- All simulations are performed for the right leg.
- The world coordinate  $x$ -axis is taken downwards.

The range of motion (ROM) of every joint is not constant for every human being; it depends on certain factors, such as the use, body build, gender, health condition, age, and many other factors [11]. The comfort zone (CZ) of the joint is a subset of the corresponding joint ROM where we feel more comfortable.

In Fig. 1, technical terminologies of the human body movements are presented. Flexion, extension, abduction, adduction, etc. are the frequent term used for body movements. Table 1 shows the human joint mobility, range of motion, and comfort zones of the joints; it can be observed that the range of motion of any joint is also dependent on the configuration of other joints. Figure 2 shows the kinematic model of the human leg in two dimensions.

## 2 Forward Kinematics and Workspace Evaluation

Forward kinematics (FK) helps to determine the position and orientation of the end effector from specified values for the joint parameters. There are several methods to solve FK problem. Here, homogeneous transformation matrices are employed solving forward kinematics.

The workspace is the region reached by the end effector taking joints limit into consideration. The workspace analysis plays an important role in the rehabilitation

**Table 1** The average joint ROM's and joint comfort zones [8]

Joint mobility	ROM in degree	Comfort zone in degree	Conditions when
Hip flex/ext	113/−45	39.5/−15.75	Knee neutral 0°
	90/−30	31.5/−10.5	Knee flexes 90°
Hip abd/add	45/−40	15.75/−14	Knee 0° and hip neutral (vertical)
	53/−31	18.55/−10.8	Knee 0° and hip flexes 90° (horizontal)
Hip med/lat rotation	39/−34	13.65/−11.9	Knee 90° and hip neutral 0°
	31/−30	10.8/−10.5	Knee 90° and hip flexes 90°
Knee flexion	113 (Stand)	39.5	Hip neutral 0°
	125 (Prone)	43.75	
	159 (Kneel)	55.65	
	80 (Stand)	28	Hip flexes 90°
Knee med/lat rotation	43/−35	15/−12.25	Knee neutral 0°
	<43/−35	<15/−12.25	Knee flexes 90°
Ankle plan/dorsi	38/−35	19/−17.5	Knee neutral 0°
	36/−33	18/−16.5	Knee flexes 90°
Foot inversion/eversion	24/−23	12/−11.5	N/A
Toe flex/ext	35/−20	17.5/−10	N/A

of human leg, to understand maximum reachability in the workspace. The workspace coordinates of the human leg can be obtained by using forward kinematics for all the combinations of joint angles. For forward kinematics, we used *trchain* function of robotic toolbox [12].

The pose of the end effector [13] is given by

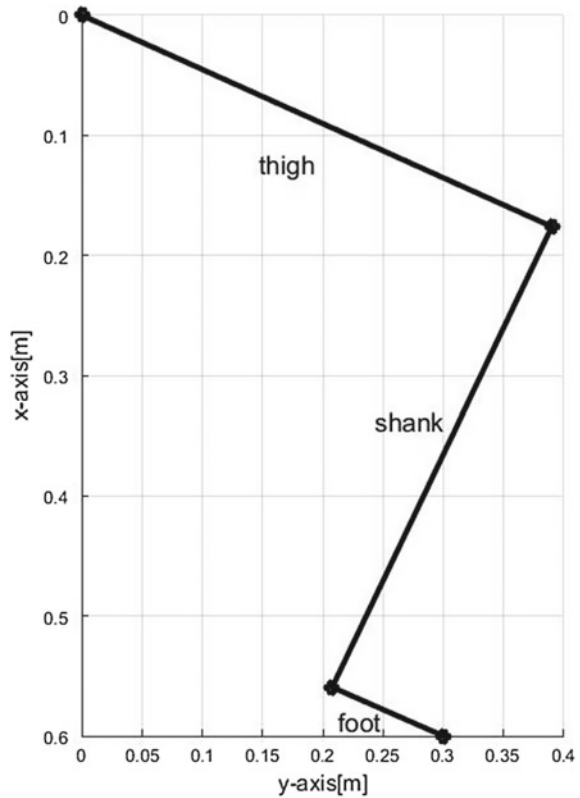
$$\begin{aligned}
 T = & R_z(q_1) * R_y(q_2) * R_x(q_3) * T_x(a_1) \\
 & * R_z(q_4) * R_y(q_5) * R_x(q_6) * T_x(a_2) \\
 & * R_z(q_7) * R_y(q_8) * R_x(q_9) * T_x(a_3)
 \end{aligned} \tag{1}$$

where

- $R_z$ ,  $R_y$ , and  $R_x$  are rotation matrices (4 \* 4) about z-, y-, and x-axis, respectively.
- $T_x$  is translation matrices (4 \* 4) about x-axis.
- $q_1, q_2, q_3, q_4, q_5, q_6, q_7, q_8$  and  $q_9$  are the quantitative values of rotation of the joints within their range of motions.
- $a_1, a_2$  and  $a_3$  are the thigh bone, shank, and ankle length, respectively.

Figure 3a–d shows different views of right leg workspace of a 1.75 m height person, with a joint range of motion constraints.

**Fig. 2** Kinematic model of human leg



### 3 Inverse Kinematics and Optimization

The inverse kinematics (IK) problem computes the joint angles for the desired pose of the end effector of the model. Nature has given us flexibility by providing more degree of freedom than required for general task. The proposed leg model is kinematically redundant; the IK problem is formulated as nonlinear constrained optimization problem. So, we can obtain a feasible solution which satisfies our criterion to the best extent. The criteria for optimization problems are range of motion, comfort zone, and the distance between the goal and end the effector. Optimization techniques are used to obtain optimal feasible solution [14]. A sequential quadratic programming (SQP)-based  $f_{\mincon}$  is used in the MATLAB simulation for finding optimal solution.

The IK procedure begins by providing end position coordinates of the leg and then optimization process is performed. The IK solution is a vector that consists of joint angles for the given final position. The objective function used for optimization should give the restriction on joint limits, which minimizes the distance from the comfort zone of joint and the range of joint motion. The objective function is expressed as

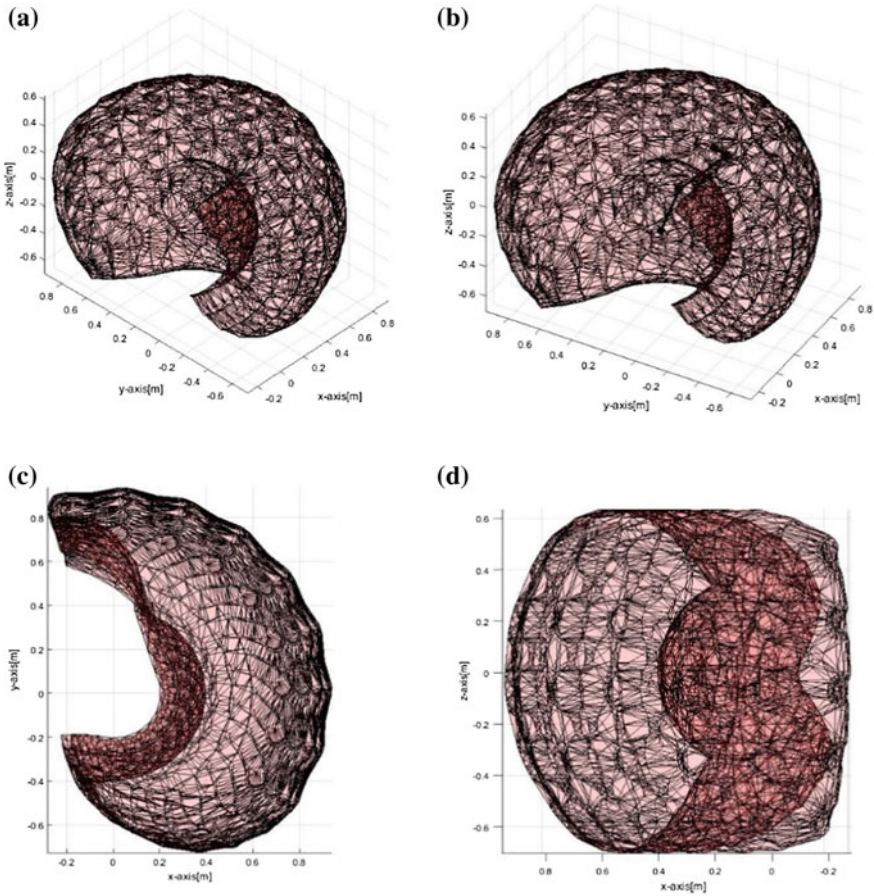


**Fig. 3** Workspace evaluation of kinematic model of human leg with different views. **a** 3D view of workspace, **b** workspace with human leg joint configurations, **c** XY plane view of workspace, **d** XZ plane view of workspace

$$\begin{aligned}
 f(\theta) = & \sum_{i=1}^3 \left( \frac{\theta_{h,i} - \theta_{h,i,opt}}{\theta_{h,i,max} - \theta_{h,i,min}} \right)^2 + \sum_{i=1}^3 \left( \frac{\theta_{k,i} - \theta_{k,i,opt}}{\theta_{k,i,max} - \theta_{k,i,min}} \right)^2 \\
 & + \sum_{i=1}^3 \left( \frac{\theta_{a,i} - \theta_{a,i,opt}}{\theta_{a,i,max} - \theta_{a,i,min}} \right)^2 \tag{2}
 \end{aligned}$$

Here,

- $\theta_{h,i,opt}$ ,  $\theta_{k,i,opt}$  and  $\theta_{a,i,opt}$  are the comfort zone centers of hip, knee, and ankle, respectively, which can be obtained by averaging the respective comfort zone limit.

- $\theta_{h,i,max}$  and  $\theta_{h,i,min}$  represent the upper and lower limit of range of motion of the respective joint.

In three dimensions, each joint has three-axis of rotation ( $i = 1, 2, 3$ )  
 The constraints used for the proposed optimization process is

$$\begin{aligned}
 |x_g - T(1, 4)| &< 0.0001 \\
 |y_g - T(2, 4)| &< 0.0001 \\
 |z_g - T(3, 4)| &< 0.0001
 \end{aligned}
 \tag{3}$$

Here,

- $x_g, y_g$  and  $z_g$  represent the goal position coordinates.
- $T$  is the transformation matrix mentioned in forward kinematics in Eq. 1.
- $T(1, 4), T(2, 4)$  and  $T(3, 4)$  are the  $x, y$  and  $z$  position's from the FK equation, respectively.

The minimization of the objective function expressed in Eq. 2 provides the final joint configuration which is close to its optimum value (i.e., the comfort zone of each joint). The constraints shown in Eq. 3 keep the end-effector position as close to the given goal position coordinates. Figure 4 shows the simulation result of the inverse kinematic algorithm of human leg for an input goal position (0.2, 0.6, 0.1) m. It is observed that the final leg position is very accurate with respect to goal position. Figure 4 shows two different views of joint configuration for a given goal position in the workspace.

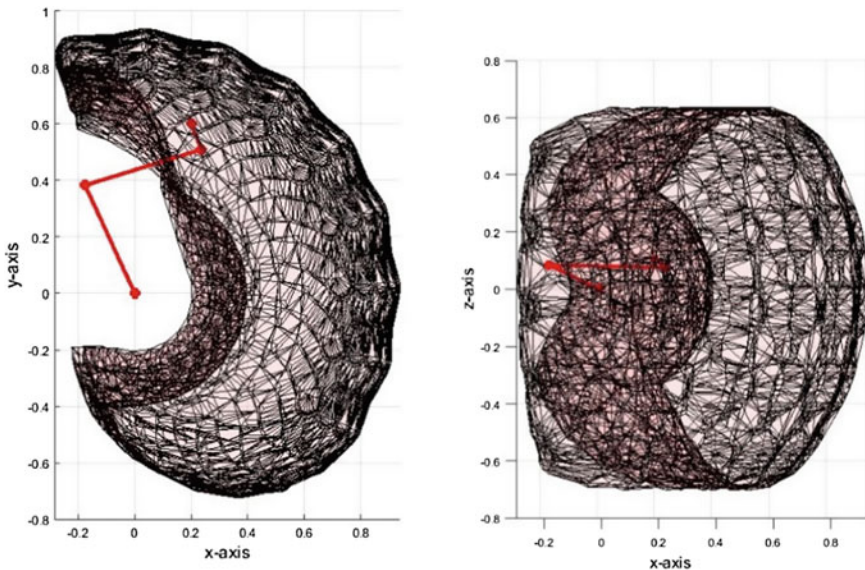


Fig. 4 Simulation of inverse kinematic algorithm of human leg

## 4 Trajectory Planning

Obtaining the joint trajectories for a human leg model is very essential in the rehabilitation process. This basically helps in determining the joint angle variation in a given time frame. For which, we have considered initial and final joint angles of human leg. Then a joint trajectory is required to guide the end effector of the human leg from initial to final position. To evaluate the joint trajectories, a fifth-degree polynomial equation is chosen as interpolating function of joint variable. This polynomial equation ensures a minimum jerk trajectory. The polynomial equation can be described as

$$\theta(t) = s_0 + s_1t + s_2t^2 + s_3t^3 + s_4t^4 + s_5t^5 \quad (4)$$

where  $s_0, s_1, s_2, s_3, s_4$  and  $s_5$  are the coefficients of the polynomial equation, which are unknown variables and  $\theta(t)$  is the joint angle at time  $t$ . Velocity and acceleration equations are

$$\dot{\theta}(t) = s_1 + 2s_2t + 3s_3t^2 + 4s_4t^3 + 5s_5t^4 \quad (5)$$

$$\ddot{\theta}(t) = 2s_2 + 6s_3t + 12s_4t^2 + 20s_5t^3 \quad (6)$$

with boundary conditions

$$\begin{aligned} \theta(0) &= \theta_0 & \dot{\theta}(0) &= 0 & \ddot{\theta}(0) &= 0 \\ \theta(t_f) &= \theta_f & \dot{\theta}(t_f) &= 0 & \ddot{\theta}(t_f) &= 0 \end{aligned} \quad (7)$$

For a minimum jerk condition, initial velocity, final velocity, initial acceleration, and final acceleration all are taken zero. By considering the boundary conditions given in Eq. 7, the equations of displacement, velocity, and acceleration have been solved to determine the coefficients of the interpolating polynomial function. As the coefficients are determined, the joint trajectories can be evaluated for a specific time interval.

Figure 5a shows different joint configurations of the human leg from initial to final position. It can be seen that the path is smooth and endpoint of leg is accurately positioned at target location. Figure 5b shows the variation of the joint angle, angular velocity, and acceleration with respect to time for initial joint angle  $0^\circ$  and final joint angle  $10^\circ$ . It can be observed that in the starting, velocity is increasing and is maximum at half of the trajectory time and then it starts decreasing. Acceleration and velocities are in the permissible range from the biomechanical point of view.

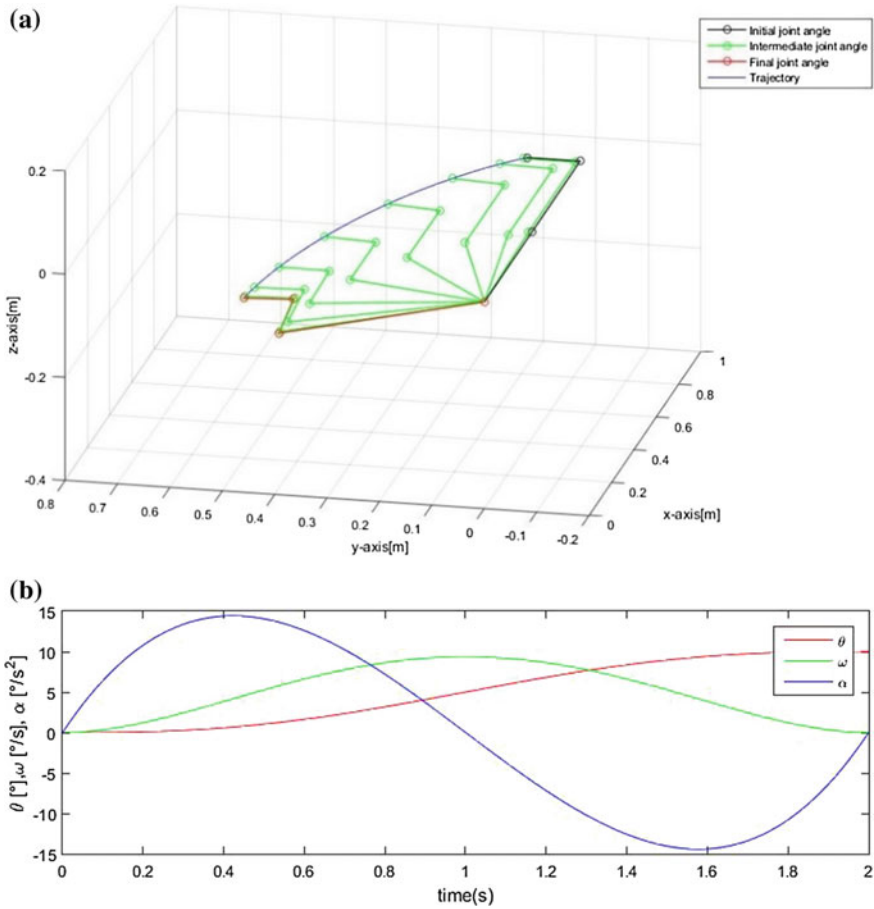


**Fig. 5** Simulation of three-dimensional trajectory of human leg, **a** Joint configurations from initial position to final position of leg, **b** trajectory of a joint angle (0–10°), angular velocity and angular acceleration

## 5 Conclusion

In this paper, an approach for modeling and simulation of the human leg kinematics is presented which can be used for designing rehabilitation and exoskeleton robot. In the simulation of human leg model, the tasks of evaluating workspace, inverse kinematics, and trajectory planning have been carried out and the simulation results are presented.

The proposed trajectory method is based on the fifth-degree polynomial which is minimum jerk trajectory. Results show that the trajectories obtained are smooth and are in the permissible range of biomechanical viewpoint. All the joint configurations obtained are very close to comfort zone of human leg, which makes the algorithm to



be used with virtual reality for ease and visualization in the rehabilitation process. Further improvements can be implemented by taking individual patient capabilities into consideration. Dynamic aspects can also be added to it to improve further in designing of rehabilitation robot.

## References

1. Parker JK, Khoogar AR, Goldberg DE (1989) Inverse kinematics of redundant robots using genetic algorithms. In: Proceedings, 1989 international conference on robotics and automation, vol 1, Scottsdale, AZ, pp 271–276
2. Craig John J (1989) Introduction to robotics: mechanics and control, 2nd edn. Addison-Wesley Longman Publishing Co., Inc., Boston, MA
3. Tejomurtula S, Kak S (1999) Inverse kinematics in robotics using neural networks. *Inf Sci* 116(2/4):147–164
4. Aristidou A et al (2018) Inverse kinematics techniques in computer graphics: a survey. *Comput Graph Forum* 37(6)
5. Głowiński S, Krzyżyński T, Pecolt S, Maciejewski I (2015) Kinematics and dynamics of an exoskeleton arm. *Arch Appl Mech* 85:75–87. <https://doi.org/10.1007/s00419-014-0900-8>
6. Wang H, Deng F, Ren L, Shi X, Zhang H, Xie L (2014) Design and analysis of a multi-joint lower limbs rehabilitation robot. In: Proceedings of the 2014 international conference on advanced mechatronic systems, Kumamoto, pp 49–54
7. Díaz I, Gil JJ, Sánchez E (2011) Lower-limb robotic rehabilitation: literature review and challenges. *J Robot* 2011:1–11
8. Tolani D, Goswami A, Badler NI (2000) Real-time inverse kinematics techniques for anthropomorphic limbs. *Graph Models* 62(5):353–388
9. Głowiński S, Krzyżyński T (2016) An inverse kinematic algorithm for the human leg. *J Theor Appl Mech* 54(1):53–61. ISSN 1429-2955
10. Gu EYL (2013) A journey from robot to digital human, mathematical principles and applications with MATLAB programming. Springer, Berlin
11. Chaffin D, Andersson G (1991) Occupational biomechanics, 2nd edn. Wiley, New York
12. Corke PI (1996) A robotics toolbox for MATLAB. *IEEE Robot Autom Mag* 3(1):24–32
13. Corke PI (2011) Robotics, vision & control. Springer, Berlin. ISBN 978-3-642-20143-1
14. Nocedal J, Wright SJ (1999) Numerical optimization. Springer, New York
15. <http://teachmeanatomy.info/the-basics/anatomical-terminology/terms-of-movement/>

# Structural Topology Optimization: Methods and Applications



Rafaque Ahmad and Hari K. Voruganti

**Abstract** This paper deals with basic concepts, methods and applications of continuum structural topology optimization. The three elements that are geometric modelling, analysis methods and optimization techniques which form the backbone of topology optimization are explained. Various approaches to perform topology optimization are also presented. The concepts are explained in an intuitive way such that new researchers can learn steeply and expand their knowledge by going through vast literature on this exciting research area.

**Keywords** Topology · Finite elements · Sensitivity · Filtering · Isogeometric analysis · Level set · Phase field

## 1 Introduction

Optimization is the task to get the best solution out of given available resources. Structural optimization deals with finding optimal structure with respect to weight, stiffness, strength, frequency, etc. satisfying resource and performance constraints such as volume, mass, deflection and stress. It is to be noted that topology optimization differs from size and shape optimization. Size optimization treats geometrical dimensions of structural members as design variables such as thickness and diameter of a predefined geometrical shape, and in shape optimization, design variables are the quantities which affect the shape of the structure of predefined topology, an example can be control points of a Bezier curve. Topology optimization (TO) task is to find the best distribution of material that is to find optimal location, shape, size and connectivity of holes in a design domain. It is most general in the hierarchy of structural optimization and there is no constraint on size and boundary of design domain, which gives engineers more design freedom and search space to look for optimal solution especially during the initial design phase.

---

R. Ahmad · H. K. Voruganti (✉)  
Department of Mechanical Engineering, National Institute of Technology, Warangal,  
Telangana 506004, India  
e-mail: [harikumar@nitw.ac.in](mailto:harikumar@nitw.ac.in)

© Springer Nature Singapore Pte Ltd. 2020  
H. K. Voruganti et al. (eds.), *Advances in Applied Mechanical Engineering*,  
Lecture Notes in Mechanical Engineering,  
[https://doi.org/10.1007/978-981-15-1201-8\\_71](https://doi.org/10.1007/978-981-15-1201-8_71)

The paper first explains different methods of topology optimization, advantages and drawbacks of each method and recent developments. It then describes various applications and issues during the process of optimization. The paper tries to classify topology optimization techniques into several classes so that the reader will have a clear view of the path ahead. Based on the continuity of structure dealt by topology optimization, it is classified into two types: discrete and continuous TO. In discrete TO, the aim is to find the optimum number, positions and connectivity of structural members. Topology optimization methods for continuous structures can be broadly classified as:

1. Homogenization-based method.
2. Density-based methods.
3. Evolutionary methods.
4. Boundary variation methods.

The topology optimization problem can be seen as a material distribution problem where the goal is whether to put material at a point in a domain or not, i.e. solid or to create a void such that objective function is optimized and constraints are satisfied. The topology optimization problem lacks the existence of solution in general [1] and therefore numerical methods face difficulties like no convergence or high mesh dependency. To formulate a well-posed problem, i.e. a problem whose optimum exists, ‘regularization’ is done to relax the design space. To have a well-posed problem, homogenization method is used to properly formulate the problem or appropriate constraints are added in the formulation of the problem.

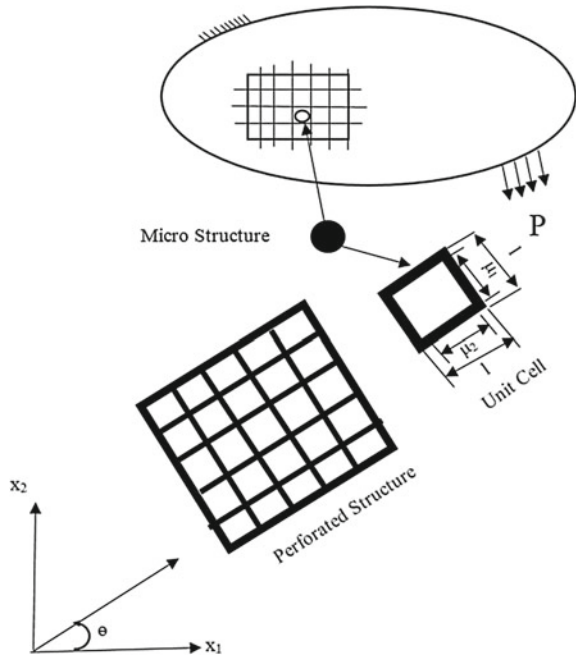
## 2 Homogenization Method

This method proposed by Bendsøe and Kikuchi [2] had a huge impact on TO of continuum structures. The basic idea was to relax the design space and design variable which can be interpreted as material density  $\rho$  can take all values from 0 (void) to 1 (solid). Using the homogenization technique which model porous material and their macroscopic material properties from a periodic microstructure (material model) defined on unit cell, effective material properties of microstructure can be determined.

Figure 1 shows a potential kind of material model named hole-in-cell. The hole-in-cell microstructure parameters are  $\mu_1$ ,  $\mu_2$ ,  $\theta$ , which are design variables. If  $\mu_1 = \mu_2 = 0$  means void, if  $\mu_1, \mu_2 = 1$  means solid and any other values of  $\mu_1, \mu_2$  means composite. The volume density of microstructure is given by  $\rho = 1 - \mu_1\mu_2$ . A single set of microstructure variables can be used for each finite element or a sub-mesh may be used for fine structures. The topology optimization problem is to determine the combination of microstructure variables corresponding to the optimal macro-scale distribution of properties that minimizes an objective function.

Minimization of compliance or strain energy, i.e. maximization of global stiffness for a given volume  $V^*$ , the optimization problem is written as:

**Fig. 1** Microstructure for 2D continuum topology optimization with the homogenization



**Minimize:**

$$\text{Strain energy} = \frac{1}{2} U^T K U \tag{1}$$

**Constraints:**

$$\begin{aligned} \sum_{e=1}^{e=N} (1 - \mu_1 \mu_2) v_e &\leq V^* \\ \mu_1 - 1 &\leq 0 \\ -\mu_1 &\leq 0 \\ \mu_2 - 1 &\leq 0 \\ -\mu_2 &\leq 0 \\ \mu_{1i}, \mu_{2i}, \theta_i & \quad i = 1 \text{ to } N \end{aligned} \tag{2}$$

where  $U$  is the global displacement vector,  $K$  is the global stiffness matrix and  $N$  is the number of finite elements.

The drawback of the homogenization method is the need for a large number of design variables and partial relaxation of design space. However, the method works well for compliance and eigenfrequency optimization. This method was very successful but new methods came which require few design variables having tuning

parameters and alternate formulations to alleviate numerical issues as explained below.

### 3 Density-Based Methods

This is most widely used TO technique and perhaps most used in commercial TO software. Finite element mesh is fixed and has one design variable per finite element. The variable is often understood as the element material density  $\rho$ . The material properties of each element, like Young's modulus, are expressed as a function of density design variables with the help of interpolation functions. To produce solid/void (1/0) design solution, intermediate densities are penalized [3]. For structural problems using solid isotropic material with penalization (SIMP) method, interpolation function with penalization is written as

$$E = \rho^p E^0 \quad (3)$$

where  $E^0$  elasticity modulus of isotropic solid material and  $p$  is penalization parameter, which is generally taken more than 3 in most applications.

#### 3.1 Finite Element Based TO

The density-based TO methods mostly uses finite element method for analysis. Here, the structure is discretized into finite elements and density design variables are assigned to each element. The mathematical formulation of density-based TO problem consists of an objective function, a set of constraints and bounds on density variables. General formulation of linear static structural finite element analysis can be given as:

**Minimize:**

$$F(\rho, U) \quad (4)$$

**Constraints:**

$$\begin{aligned} K(\rho)U &= F(\rho) \\ g_i(\rho, U) &\leq 0 \\ 0 < \rho_{\min} &\leq \rho \leq 1 \end{aligned} \quad (5)$$

where  $\rho$  is the vector of density design variables,  $U$  is the global displacement vector,  $K$  is the global stiffness matrix,  $F$  is the force vector and  $g_i$  are the constraints. Using this formulation, many problems can be solved considering compliance, stresses, displacement, fluid flow, nonlinear and multi-physics.

A very important factor to perform TO is the selection of appropriate interpolation function and penalization technique to relate to physical quantities of the problem. Several interpolation functions have been proposed like SIMP [3], rational approximation of material properties (RAMP) [4] and SINH [4] to force solution to solid/void form. There are some numerical issues related to interpolation functions such as checkerboarding and mesh dependency [4]. Checkerboarding is the formation of adjacent solid/void elements in the optimal design and mesh dependency is occurrence of different topologies with different FE mesh sizes (Figs. 2 and 3).

To alleviate these issues, ‘regularization’ techniques are used such as constraint methods and filters. Constraint methods use extra constraints that are added to the



Fig. 2 Numerical effect of checkerboarding

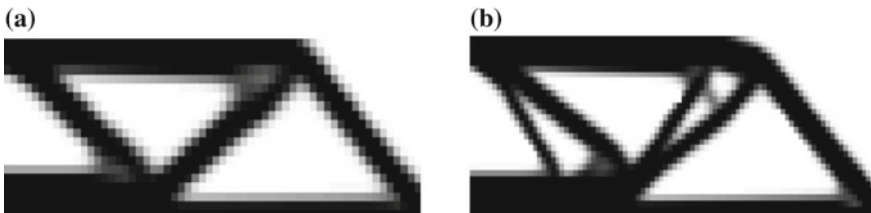


Fig. 3 Mesh dependency: a coarse mesh and b relatively fine mesh

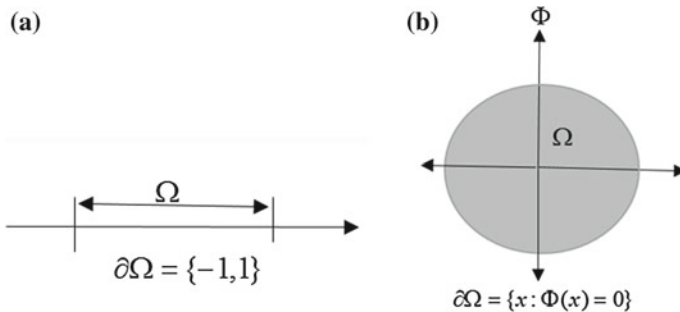


Fig. 4 a Explicit versus and b implicit representation of a design domain and boundaries

optimization problem such as the perimeter of structural boundaries [5] but its application depends on the problem. Filtering methods are easy to implement with little extra computational effort [6]. Projection methods and morphology filters [7] are used to remove grey transition material between solid and void regions to define a crisp boundary and to enforce length scale control.

FE-based TO is applied to solve problems in stress-based topology design [8], design-dependent loads [9], support design and multicomponent structures [10], non-linear response [11], fluid flow [12], multifunctional materials [13], heat transfer and thermoelastic problems [14] and aerospace design [15]. To further broaden the application area of FE-based TO, there is a need for efficient formulation of TO problem to model multi-physics and to take care of manufacturing limitations, feature control and adaption to additive manufacturing.

### ***3.2 Isogeometric Analysis-Based TO***

Isogeometric analysis (IGA) which is an analysis technique to solve partial differential equations [16] has been applied instead of finite element analysis (FEA) for structural TO. The IGA uses non-uniform rational B splines (NURBS) instead of the polynomial basis of FEA to represent both geometry and approximation functions and due to several interesting properties of NURBS basis, it seems to be ideal analysis technique for TO.

Material density is approximated using continuous NURBS basis functions; also, penalization technique similar to SIMP is used to prevent porous medium [17], and in this paper, control points of the material distribution function are taken as design variables. The results show no mesh dependency, smooth boundaries with higher-order NURBS and less intermediate material densities for more number of control points.

Trimmed spline surface which can represent complex topologies have been applied in TO [18]. Trimming data from CAD systems are used for analysis and sensitivity calculation for TO. Design variables in this approach are coordinates of control points of spline surface and trimming curves.

TO using moving morphable components (MMCs) and IGA are proposed in [19]. The domain is discretized using NURBS patches, and IGA was used for both response and sensitivity analysis. MMCs are used to represent the geometries of structural components. The central coordinates, half-length, half-width and inclined angles of MMCs are taken as design variables. The method uses both explicitness of MMCs, higher-order continuity and tighter link with computer-aided design (CAD).

TO using IGA also have been applied using level set method [20], phase field method [21], multi-scale TO of lattice materials [22] and multi-resolution multi-material TO using IGA [23].

## 4 Evolutionary Methods

These methods work by gradually removing/adding a finite amount of material from the design domain. The choice of element placement is heuristic and is not based on gradient information. The design space is not relaxed because either there is material or void but it very simple to use with finite element software packages and produce very clear defined structural boundaries with no intermediate density or greyscale material. The most well-known evolutionary method is evolutionary structural optimization (ESO) [24]. In ESO, criteria value is calculated for each element called sensitivity number and the inefficient element of low criteria value is removed. ESO-based algorithms also suffer from numerical instabilities like checkerboarding and mesh dependency.

A modification of ESO method is the provision of adding and removing elements called bidirectional evolutionary algorithm (BESO) [25] so that some of potential low criteria elements deleted from the domain can return back in future iterations and contribute to optimum design. The sensitivity of void elements can be calculated, and also mesh independency is achieved using nodal sensitivities by modified BESO.

Another version of BESO is to use the elements of very low density instead of completely removing elements from the computational domain [26], and admission criteria of elements can be calculated based on void elements and no extrapolation of densities of elements near solid boundaries is needed. Analytical sensitivities with respect to density are used in BESO to decide element admission or rejection.

Genetic algorithms (GA) have also been applied to for TO and its binary nature seems good to create solid/void designs. Connectivity of domain in GA-based TO is difficult because nature of GA is a stochastic also high computational cost associated with GA. The advantage of GA with respect other TO algorithms is a high probability to find global optima. Genetic evolutionary structural optimization (GESO) overcomes some challenges of GA [27].

These common and popular methods of evolutionary algorithms mentioned above have been applied to many fields like nonlinear problems for both material and geometrical nonlinearities [28]. Design-dependent loadings by modifying sensitivity number to capture load dependency [29], multi-criteria function optimization [30], heat transfer and thermoelasticity [31], biomedical design [32], civil engineering structures [33], vibration and buckling problems [34] and material microstructures optimization [35].

## 5 Boundary Variation Methods

Boundary variation methods are relatively new developments in TO compared to above-mentioned methods in this article. In these methods, implicit functions represent structural boundaries instead of explicit parameterization of the design domain. Figure 5 shows explicit parameterization of the domain  $\Omega$  between coordinates 0 and



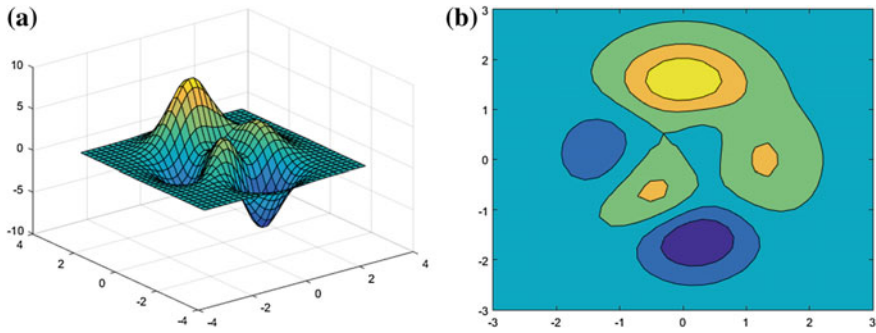


**Fig. 5** Level set representation of 2D topologies and their corresponding level set function

1 with boundaries explicitly defined as set  $\{-1, 1\}$ , whereas in Fig. 4b, boundary is defined implicitly by the contour of a scalar function  $\Phi(x)$ . These methods produce sharp smooth boundaries i.e. no greyscale and hence very little post-processing is required for structural features. The two boundary variation methods are level set and phase field methods.

### 5.1 Level Set Method

In level set method, boundaries are represented as zero level curve of a scalar function. The level set method was first used in TO by Sethian and Weigmann [36, 37] for linear elastic structural problems. Level set method allows movement of structural boundaries of level set function  $\Phi(x)$ , and the formation, disappearance, merger of void regions, which generates new topological design. Boundary shape is modified by controlling the motion of level set from physical problem and optimization condition. The level set method starts with specifying structural boundary as level set implicitly as a level surface of a 3D scalar function.

$$S = \{x : \Phi(x) = c\} \tag{6}$$

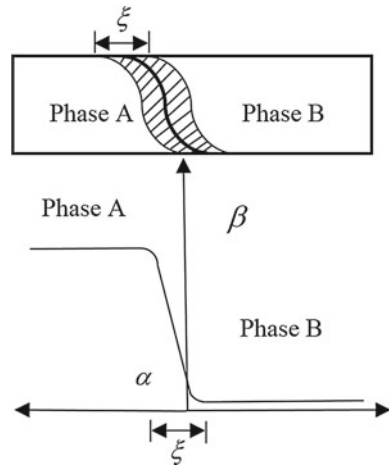
where  $c$  is arbitrary constant, and  $x$  is a point on the boundary. Structural optimization is performed by letting level set vary with time as

$$S(t) = \{x(t) : \Phi(x(t), t) = c\} \tag{7}$$

The time derivative of the above equation and application of chain rule yields the following the Hamilton–Jacobi equation.

$$\frac{\partial \Phi(x, t)}{\partial t} + \nabla \Phi(x, t) \frac{dx}{dt} = 0, \Phi(x, 0) = \Phi_0(x) \tag{8}$$

**Fig. 6** a 1D and 2D domain represented by the phase field function



$dx/dt$  be the movement of a point driven by the objective of optimization and it can be expressed as position  $x$  and geometry of surface at that point. The optimum boundary then can be found by solving the partial differential equation given above.

The level set method has an advantage over density-based methods as intermediate densities not used; however, one drawback of current level set formations is their dependency on the initial design, which is more severe than other methods. However, new developments have somewhat improved this deficiency.

### 5.2 Phase Field Method

The phase field method for TO is based on theories to simulate phase transition phenomenon. In this method, a phase field function  $\Phi$  is specified over a design domain  $\Omega$  that is composed of two phases, A and B, which are represented by values  $\alpha$  and  $\beta$  of  $\Phi$ . The boundary between phases is a continuously varying region of finite thickness  $\xi$ . In phase field topology optimization [38], this region defines the structural boundary and is modified by the dynamic evolution of phase field function. The governing equation of phase field is solved throughout domain, and like level set method, the boundary is not tracked during the optimization process and reinitialization is not needed (Fig. 6).

## 6 Learning Resources

For new researchers, the most useful resource to learn TO is monograph by Bendsøe and Sigmund [4]. There are several resources that are publicly available to learn

and implement various methods of TO. For density-based methods using SIMP, there are two MATLAB codes, a 99 line code by Sigmund [39] and a new version by Andreassen et al. [40]. Also, there is a web version of SIMP [41], a mobile application of SIMP for iPhone and Android [42].

For ESO/BESO manuscript by Huang and Xie [24] is a very good resource, in this MATLAB code for BESO is publicly available. MATLAB implementation of the discrete level set TO with implementation details can be found in [43].

## 7 Future Directions in TO

Future of TO seems to be exciting and several innovative application areas are still to be explored like in biomedical engineering and healthcare applications. TO based on stress criteria is another area where some work has been done but still, there are several issues unresolved. Additive manufacturing aids topology optimization and vice versa, by modelling residual stresses, constraining overhang angle and setting minimum deposition tolerances in TO formulations. TO should give more refined geometrical features which can be used for further shape, size design, and also, there is a need for algorithms to consider the features like fillets, extrusions, etc. TO methods should be robust to handle design-dependent loads; hence, new formulations are needed. It can be concluded that TO has vast usefulness for a design problem that can be formulated into a material distribution problem, which surely depends on imagination and ingenuity of the designer.

## References

1. Kohn RV, Strang Gilbert (1986) Optimal design and relaxation of variational problems, I. *Commun Pure Appl Math* 39(1):113–137
2. Bendsøe MP, Kikuchi N (198) Generating optimal topologies in structural design using a homogenization method. *Comput. Methods Appl. Mech. Eng.* 71(2):197–224
3. Bendsøe MP (1989) Optimal shape design as a material distribution problem. *Struct Optim* 1(4):193–202
4. Bendsøe MP, Sigmund O (2003) *Topology optimization: theory, methods and applications*, vol 2013, pp 16–18
5. Haber RB, Jog CS, Bendsøe MP (1996) A new approach to variable-topology shape design using a constraint on perimeter. *Struct Optim* 11(1-2):1–12
6. Bourdin B (2001) Filters in topology optimization. *Int J Numer Meth Eng* 50(9):2143–2158
7. Sigmund O (2007) Morphology-based black and white filters for topology optimization. *Struct Multidiscip Optim* 33(4-5):401–424
8. Le C et al (2010) Stress-based topology optimization for continua. *Struct Multidiscip Optim* 41(4):605–620
9. Chen B-C, Kikuchi N (2001) Topology optimization with design-dependent loads. *Finite Elem Anal Des* 37(1):57–70
10. Buhl T (2002) Simultaneous topology optimization of structure and supports. *Struct Multidiscip Optim* 23(5):336–346

11. Buhl T, Pedersen CBW, Sigmund O (2000) Stiffness design of geometrically nonlinear structures using topology optimization. *Struct Multidiscip Optim* 19(2):93–104
12. Borrvall T, Petersson J (2003) Topology optimization of fluids in Stokes flow. *Int J Numer Meth Fluids* 41(1):77–107
13. Zhou S, Li Q (2008) Computational design of microstructural composites with tailored thermal conductivity. *Numer Heat Transfer Part A: Appl* 54(7):686–708
14. B TE (2007) Topology optimization of convection-dominated, steady-state heat transfer problems. *Int J Heat Mass Transf* 50(15–16):2859–2873
15. Maute K, Allen M (2004) Conceptual design of aeroelastic structures by topology optimization. *Struct Multidiscip Optim* 27(1–2):27–42
16. Hughes TJR, Cottrell JA, Bazilevs Y (2005) Isogeometric analysis: CAD, finite elements, NURBS, exact geometry and mesh refinement. *Comput Methods Appl Mech Eng* 194(39–41):4135–4195
17. Hassani B, Khanzadi M, Tavakkoli SM (2012) An isogeometrical approach to structural topology optimization by optimality criteria. *Struct Multidiscip Optim* 45(2):223–233
18. Seo Y-D, Kim H-J, Youn S-K (2010) Isogeometric topology optimization using trimmed spline surfaces. *Comput Methods Appl Mech Eng* 199(49–52):3270–3296
19. Hou W et al (2017) Explicit isogeometric topology optimization using moving morphable components. *Comput Methods Appl Mech Eng* 326:694–712
20. Ghasemi H, Park HS, Rabczuk T (2017) A level-set based IGA formulation for topology optimization of flexoelectric materials. *Comput Methods Appl Mech Eng* 313:239–258
21. Dedè L, Borden MJ, Hughes TJR (2012) Isogeometric analysis for topology optimization with a phase field model. *Arch Comput Methods Eng* 19(3):427–465
22. Wang Y, Hang X, Pasini D (2017) Multiscale isogeometric topology optimization for lattice materials. *Comput Methods Appl Mech Eng* 316:568–585
23. L QX, Lee Jaehong (2017) A multi-resolution approach for multi-material topology optimization based on isogeometric analysis. *Comput Methods Appl Mech Eng* 323:272–302
24. Huang X, Xie M (2010) *Evolutionary topology optimization of continuum structures: methods and applications*. Wiley
25. Querin OM, Steven GP, Xie YM (1998) Evolutionary structural optimisation (ESO) using a bidirectional algorithm. *Eng Comput* 15(8):1031–1048
26. Rozvany G, Querin O (2002) Theoretical foundations of sequential element rejections and admissions (SERA) methods and their computational implementation in topology optimization. In: 9th AIAA/ISSMO symposium on multidisciplinary analysis and optimization
27. Zuo ZH, Xie YM, Huang X (2009) Combining genetic algorithms with BESO for topology optimization. *Struct Multidiscip Optim* 38(5):511–523
28. Huang XH, Xie Y (2007) Bidirectional evolutionary topology optimization for structures with geometrical and material nonlinearities. *AIAA J* 45(1):308–313
29. Ansola R, Canales J, Tárrago JA (2006) An efficient sensitivity computation strategy for the evolutionary structural optimization (ESO) of continuum structures subjected to self-weight loads. *Finite Elem Anal Des* 42(14–15):1220–1230
30. Proos KA et al (2001) Multicriterion evolutionary structural optimization using the weighting and the global criterion methods. *AIAA J* 39(10):2006–2012
31. Ansola R et al (2012) Evolutionary optimization of compliant mechanisms subjected to non-uniform thermal effects. *Finite Elem Anal Des* 57:1–14
32. Chen Y et al (2011) Design optimization of scaffold microstructures using wall shear stress criterion towards regulated flow-induced erosion. *J Biomech Eng* 133(8):081008
33. Liu Y et al (2008) A fixed-grid bidirectional evolutionary structural optimization method and its applications in tunnelling engineering. *Int J Numer Methods Eng* 73(12):1788–1810
34. Huang X, Zuo ZH, Xie YM (2010) Evolutionary topological optimization of vibrating continuum structures for natural frequencies. *Comput Struct* 88(5–6):357–364
35. Huang X et al (2013) Topology optimization of microstructures of cellular materials and composites for macrostructures. *Comput Mater Sci* 67:397–407

36. Sethian JA (1999) Level set methods and fast marching methods: evolving interfaces in computational geometry, fluid mechanics, computer vision, and materials science, vol 3. Cambridge University Press
37. Sethian JA, Wiegmann A (2000) Structural boundary design via level set and immersed interface methods. *J Comput Phys* 163(2):489–528
38. Takezawa A, Nishiwaki S, Kitamura M (2010) Shape and topology optimization based on the phase field method and sensitivity analysis. *J Comput Phys* 229(7):2697–2718
39. Sigmund O (2001) A 99 line topology optimization code written in Matlab. *Struct Multidiscip Optim* 21(2):120–127
40. Andreassen E et al (2011) Efficient topology optimization in MATLAB using 88 lines of code. *Struct Multidiscip Optim* 43(1):1–16
41. Tcherniak D, Sigmund O (2001) A web-based topology optimization program. *Structural and multidisciplinary optimization* 22(3):179–187
42. Aage N et al (2013) Interactive topology optimization on hand-held devices. *Struct Multidiscip Optim* 47(1):1–6
43. Challis VJ (2010) A discrete level-set topology optimization code written in Matlab. *Struct Multidiscip Optim* 41(3):453–464

# A Multi-objective Optimization Method Based on Nelder–Mead Simplex Search Method



Vivek Kumar Mehta and Bhaskar Dasgupta

**Abstract** In this paper, a method based on Nelder and Mead's simplex search method is developed for solving multi-objective optimization problems. Unlike other multi-objective optimization algorithms based on classical methods, this method does not require any *a priori* knowledge about the problem. Moreover, it does not need any pre-defined weights or additional constraints as it works without scalarizing the multi-objective problem. The algorithm works with a population of points and is capable of generating a multitude of Pareto optimal solutions. Equipped with the constraint handling strategy adopted in this work, the method is found to be competitive with respect to the existing algorithms.

**Keywords** Simplex search method · Multi-objective optimization · Pareto optimal solutions

## 1 Introduction

Nelder and Mead's simplex search method [14] is a well-known direct search classical algorithm for single-objective optimization. The method was introduced for solving the usual single-objective unconstrained optimization problems. In a problem having  $n$  design variables, it works with a simplex, which with its  $n + 1$  vertices forms a convex hull. Starting with an initial simplex in the design space, the method evaluates the objective function value at each vertex of the simplex and on the basis of these function values determines the worst  $\mathbf{x}_w$ , second worst  $\mathbf{x}_s$ , and the best  $\mathbf{x}_b$  among them. Next, the algorithm attempts to improve the current simplex by replacing the worst vertex with a potentially better point in the design space. It does so by exploring

---

V. K. Mehta (✉)  
Tezpur University, Tezpur, Assam, India  
e-mail: [vkmehta@tezu.ernet.in](mailto:vkmehta@tezu.ernet.in)

B. Dasgupta  
IIT Kanpur, Kanpur, India  
e-mail: [dasgupta@iitk.ac.in](mailto:dasgupta@iitk.ac.in)

© Springer Nature Singapore Pte Ltd. 2020  
H. K. Voruganti et al. (eds.), *Advances in Applied Mechanical Engineering*,  
Lecture Notes in Mechanical Engineering,  
[https://doi.org/10.1007/978-981-15-1201-8\\_72](https://doi.org/10.1007/978-981-15-1201-8_72)

the region around the points (other than the worst point) with the help of a reflection followed by a considered option of an expansion, contraction, or shrink.

In recent years, there have been attempts to exploit the potential of this algorithm for multi-objective optimization problems [7, 8, 11, 12]. Using simplex search method for local search along with the usual operations of reproduction, crossover, and mutation involved in genetic algorithm, Koduru et al. [7] proposed a hybrid algorithm, fuzzy simplex genetic algorithm (FSGA), which uses the concept of fuzzy dominance. Martnez and Coello [11] have proposed a method for hybridizing the NSGA-II algorithm with the simplex search method. They have also employed the simplex search method for local exploration and found their method performing better than NSGA-II. However, their method can only handle bound constraints. Kuriger and Grant [8] proposed a lexicographic Nelder–Mead-based simulation optimization (LNM-SO) method. They have used preemptive goal programming strategy for handling multiple objectives. In addition to setting the target value for each goal, the strategy demands the decision maker to rank the goals in order of decreasing importance.

Martinez et al. [12] proposed a nonlinear simplex search-based approach for solving unconstrained multi-objective optimization problems. They have adopted the penalty boundary intersection (PBI) approach [20], which uses weight vectors and a penalty value to convert the multi-objective problem to several single-objective problems. Then, they solve each of these subproblems using simplex search method to obtain several solutions on the Pareto front.

In this paper, a multi-objective optimization method based purely on Nelder–Mead’s simplex search method has been developed. The suggested method works without converting the multi-objective optimization problem into single-objective optimization problem and, yet, is capable of generating a multitude of Pareto optimal solutions. The proposed method uses only the basic operations of simplex search method and is capable of handling constraints efficiently. In Sect. 2, the proposed method has been described in detail. Section 3 describes the constraint handling strategy used with the proposed method. Sections 4 and 5 present the results obtained by the proposed method for unconstrained and constrained problems, respectively, followed by the conclusion in Sect. 6.

## 2 Proposed Algorithm

Evolutionary algorithms work with a population, because of which they are capable of generating several solutions for a multi-objective optimization problem in a single run. Like evolutionary algorithms, the simplex search method, in a way, also works with a population of points. One obvious question than one could ask is the following.

Could it be used to generate several solutions for a multi-objective optimization problem and that too in a single run?

This is precisely the question that has been addressed in this work, and the proposed method is an answer to this question. Though the proposed method is based on the simplex search method, it is different from the basic simplex method in two significant aspects.

1. The basic simplex method works with  $n + 1$  points and a single simplex, whereas the proposed method works with more than  $n + 1$  points and multiple simplices.
2. In the basic simplex method, two points in the design space are compared on the basis of objective function values, whereas in the case of the proposed method, two points are compared on the basis of dominance.

Moreover, in the proposed algorithm the number of vertices used to form a simplex,  $nps$ , is also taken as a parameter. In the usual simplex method, the number of vertices to form a simplex,  $nps$ , is taken as  $(n + 1)$ . To explore an  $n$ -dimensional space, it is imperative for a simplex to have  $(n + 1)$  vertices so that no region of the domain is outside the reach of such simplices. However, working with more than one simplex, in a multi-objective scenario, gives an opportunity to explore the effect of changing  $nps$  on the performance of the algorithm. Since the algorithm works with more than one simplices, a region of the domain left unexplored by one of the simplex could be covered by others.

**Algorithm** As discussed earlier, for solving an  $n$ -dimensional multi-objective optimization problem, the proposed algorithm which is based on simplex search method works with more than  $n + 1$  points and multiple simplices. Further, the number of vertices used to form a simplex,  $nps$ , is also considered as a parameter. Hence, it is must to decide the population size, the number of simplices, and the number of vertices for the simplex at the beginning of the algorithm. Let the population size be denoted as  $P_s$ , and the number of simplices is denoted as  $N$ . Now, the task in hand is to generate the new improved solutions using this initial population of solutions. For generating the new solutions, at each iteration,  $iter$ , usual operations of simplex search method, i.e., reflections, contraction, and expansion, are performed for each of the  $N$  simplices. The stopping criterion for the simplex loop is  $Smax_{iter}$ . New solutions are generated till the maximum iteration,  $Max_{iter}$ , is reached. Below are the steps involved in the proposed algorithm.

- Decide population size  $P_s$ , number of simplices  $N$ , number of vertices to form a simplex  $nps$ , maximum iteration of the outer loop  $Max_{iter}$ , and maximum iteration for the simplex loop or the inner loop  $Smax_{iter}$ .
- Generate  $P_s$  points to form the initial population and assign front value to each point of the population.
- Outer loop: For  $iter = 1$  to  $iter = Max_{iter}$ , generate random combination of points for  $N$  simplices.
  - Inner loop: For each simplex, follow the usual procedure of basic simplex method of reflection, expansion/contraction to generate new solutions and compare different solutions on the basis of domination.



It is interesting to note that if  $Smax_{iter} = 1$ , then by the end of every outer iteration, the algorithm must have generated and explored at most  $2N$  additional points (generated by reflection and expansion/contraction). It is quite possible that in one of the inner iterations, the algorithm accepts a point from the tenth front,<sup>1</sup> whereas in another it rejects a point which corresponds to the fifth front. Discarding or accepting points in every inner loop severely hampers the efficiency of the algorithm because in doing so it is quite likely that the algorithm discards a point having a better front value.

To overcome this difficulty, an additional population of points generated by reflection and expansion/contraction is maintained at the end of every outer loop iteration. This additional population is then combined with original  $P_s$  points. Out of these points,  $P_s$  points are chosen from the fronts having the highest front value. In the vocabulary of evolutionary algorithms, this can be seen as preserving *elites*.

While selecting  $P_s$  points from a combined population of points, a condition may arise when to complete the set of  $P_s$  points, and the algorithm needs to choose only a subset of points from the points available on a front. In that case, those points from the front can be chosen, which form a better spread of that front. This can be done by introducing another measure, *crowding distance* [3], that will help the algorithm identify such points from a front.

### 3 Constraint Handling with Simplex Search Method

A method for handling constraints with simplex search method for single-objective constrained optimization problems has been proposed by the authors [13]. It treats constraint violation and objective function separately and provides appropriate measures to handle all the cases of a simplex lying in any of the three regions, namely (i) feasible region: where all the points of the simplex are feasible, (ii) boundary region: where some of the  $n + 1$  points are feasible and other infeasible, and (iii) infeasible region: where all the points of the simplex are infeasible. In case all the points are either feasible or infeasible, the algorithm tries to minimize the objective function value or constraint violation, respectively. If the simplex lies in the boundary region, the infeasible points are assigned a consolidated function value which is equal to the sum of objective function value of the worst feasible point and the constraint violation of that infeasible point. In this way, the point having the largest value of constraint violation would become the worst point among  $n + 1$  points and the algorithm would try to move away from that point.

The same strategy of assigning function value is used here for handling constraints in multi-objective scenario. The function value assignment for each point of the population  $P_s$  is as follows:

---

<sup>1</sup>To compare two points on the basis of dominance, a front value is assigned to each point depending on the front on which the point lies. All the points on a particular front have the same front value which is equal to the number of points which are dominated by that front.

- For each point of the population, evaluate the constraint violations and identify the infeasible points.
- Evaluate the objective function values at all the feasible points, identify the worst feasible function value for all the objectives  $f_i, i = 1, 2, \dots, m$ , and store them in a vector  $\mathbf{f}^w = [f_1^{worst} \ f_2^{worst} \ \dots \ f_m^{worst}]^T$ .
- To each of the infeasible points, assign a consolidated value

$$\mathbf{F} = \mathbf{f}^w + cv[1 \ 1 \ \dots \ 1]_{R^{m \times 1}}^T,$$

where for a general multi-objective problem having inequality and equality constraints defined as  $g_i(\mathbf{x}) \leq 0$  for  $i = 1, \dots, p$ ,  $h_j(\mathbf{x}) = 0$  for  $j = 1, \dots, q$ ; the constraint violation ( $cv^2$ ) is defined as:

$$cv = \sum_{j=1}^p \max \{0, g_j(\mathbf{x})\} + \sum_{j=1}^q \max \{0, (|h_k(\mathbf{x})| - \delta)\} + R \sum_{j=1}^q |h_k(\mathbf{x})|^2.$$

Thus, all the points of the population will be assigned function values. The point having the highest constraint violation will be dominated by all the other points, and the proposed algorithm would try to move away from that point.

## 4 Unconstrained Problems

The proposed method has been tested on several unconstrained multi-objective test problems shown in Table 1. The results are compared with the NSS-MO [12] and NSGA-II [3] algorithms. The comparison with NSS-MO is on the basis of performance metrics spacing  $S$  [17] and hypervolume [22], whereas with NSGA-II, it is based on  $\mathcal{Y}$  and  $\Delta$  [3]. The metrics  $\mathcal{Y}$  and hypervolume measure the convergence of the solution points obtained to the global Pareto front, whereas the metrics  $\Delta$  and  $S$  give a measure of the diversity of the obtained solution set.

Martinez et al. [12] have compared their algorithm NSS-MO with that of Zhang and Li [20] for the problems LIS, FON, and DTLZ5 and concluded their algorithm to be superior than MOEA/D. For bi-objective problems LIS and FON, Martinez et al. have taken  $P_s = 100$  and maximum function evaluations to be 4000 and for three-objective problem, DTLZ5, they have taken  $P_s = 300$  and maximum function evaluations to be 12,000. For comparison, 30 independent runs of the proposed algorithm have been considered, with same  $P_s$  and maximum function evaluations, along with  $N = 100, nps = n + 1$  and  $Smax_{iter} = 1$ .

Figure 1 shows the typical convergence of the population points of the proposed algorithm for problems LIS, FON, and DTLZ5. Table 2 shows the comparison of the results obtained from the proposed algorithm with that of the NSS-MO (as reported in [12]). For each problem, boldface values correspond to the algorithm which performs

---

<sup>2</sup>For discussion on  $R$  and  $\delta$  in the expression, see Mehta and Dasgupta [13].

**Table 1** Unconstrained multi-objective optimization test problems

Problem	$n$	Variable bounds	Objective function	Nature of Pareto front
SCH Schaffer [16]	1	$[-10^3, 10^3]$	$f_1(x) = x^2$ $f_2(x) = (x - 5)^2$	Convex Connected
LIS Lis and Eiben [10]	2	$[-5, 10]$	$f_1(\mathbf{x}) = \sqrt[8]{x_1^2 + x_2^2}$ $f_2(\mathbf{x}) = \sqrt[4]{(x_1 - 0.5)^2 + (x_2 - 0.5)^2}$	Non-convex Connected
FON Fonseca et al. [6]	3	$[-4, 4]$	$f_1(\mathbf{x}) = 1 - \exp(-3 \sum_{i=1}^3 (x_i - \frac{1}{\sqrt{3}})^2)$ $f_2(\mathbf{x}) = 1 - \exp(-3 \sum_{i=1}^3 (x_i + \frac{1}{\sqrt{3}})^2)$	Non-convex Connected
POL Poloni et al. [15]	2	$[-\pi, \pi]$	$f_1(\mathbf{x}) = 1 + (A_1 - B_1)^2 + (A_2 - B_2)^2$ $f_2(\mathbf{x}) = (x_1 + 3)^2 + (x_2 + 1)^2$ $A_1 = 0.5 \sin 1 - 2 \cos 1 + \sin 2 - 1.5 \cos 2$ $A_2 = 1.5 \sin 1 - \cos 1 + 2 \sin 2 - 0.5 \cos 2$ $B_1 = 0.5 \sin x_1 - 2 \cos x_1 + \sin x_2 - 1.5 \cos x_2$ $B_2 = 1.5 \sin x_1 - \cos x_1 + 2 \sin x_2 - 0.5 \cos x_2$	Disconnected, Non-convex
KUR Kursawe [9]	3	$[-5, 5]$	$f_1(\mathbf{x}) = \sum_{i=1}^{n-1} (-10 \exp(-0.2 \sqrt{x_i^2 + x_{i+1}^2}))$ $f_2(\mathbf{x}) = \sum_{i=1}^n ( x_i ^{0.8} + 5 \sin x_i^3)$	Non-convex Disconnected
VNT Viennet et al. [19]	2	$[-3, 3]$	$f_1(\mathbf{x}) = 0.5(x_1^2 + x_2^2) + \sin(x_1^2 + x_2^2)$ $f_2(\mathbf{x}) = \frac{(3x_1 - 2x_2 + 4)^2}{8} + \frac{(x_1 - x_2 + 1)^2}{27} + 15$ $f_3(\mathbf{x}) = (x_1^2 + x_2^2 + 1)^{-1} - 1.1$ $\exp[-(x_1^2 + x_2^2)]$	Non-convex Disconnected
DTLZ5 Deb et al. [5]	12	$[0, 1]$	$f_1(\mathbf{x}) = \cos(\theta_1) \cos(\theta_2)(1 + g(\mathbf{x}_M))$ $f_2(\mathbf{x}) = \cos(\theta_1) \sin(\theta_2)(1 + g(\mathbf{x}_M))$ $f_3(\mathbf{x}) = \sin(\theta_1)(1 + g(\mathbf{x}_M))$ $g(\mathbf{x}_M) = \sum_{x_i \in \mathbf{x}_M} (x_i - 0.5)^2$ $\theta_1 = \frac{\pi}{2} x_1$ $\theta_2 = \frac{\pi}{4(1+g(\mathbf{x}_M))} (1 + 2g(\mathbf{x}_M x_2))$ $\mathbf{x}_M = [x_3, x_4, x_5, x_6, x_7, x_8, x_9, x_{10}, x_{11}, x_{12}]$	Non-convex Connected Degenerate

better. Clearly, as the convergence of the proposed algorithm is better in two out of three cases, whereas the spacing metric values are better for the NSS-MO algorithm in two cases, one cannot say which algorithm performs better on these problems. However, it is important to note that the proposed algorithm has performed similar to the NSS-MO without using any weight vector and penalty value and without converting the multi-objective problem to single-objective problem.

For comparison, the NSGA-II<sup>3</sup> algorithm has been run for 250 generations (or  $Max_{iter}$ ) with a population size of  $N = 100$ , crossover probability 0.9, and a mutation probability of  $1/n$  (where  $n$  is the number of design variables). The distribution indices for mutation and crossover operators were taken as  $\eta_m = 20$  and  $\eta_c = 20$ , respectively. To keep the function evaluations of the proposed algorithm same as that of NSGA-II, the runs for the proposed algorithm were taken with maximum number

<sup>3</sup>The authors gratefully acknowledge the availability of the source codes for NSGA-II algorithm on the Web site <http://www.iitk.ac.in/kangal/codes.shtml>, from where these were downloaded on September 8, 2011.

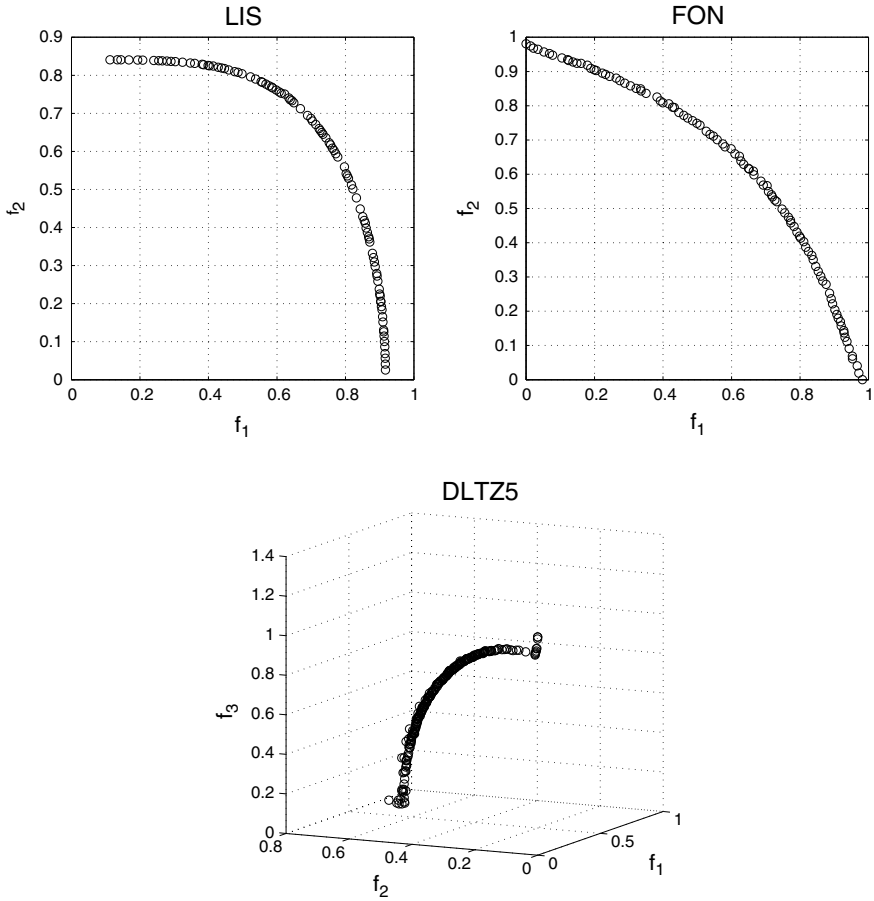


Fig. 1 Typical results of the proposed algorithm for problems LIS, FON, and DLTZ5

Table 2 Comparison of the proposed algorithm with NSS-MO. The hypervolume calculation is based on reference vector  $r = [1 \ 1]^T$  for LIS,  $r = [1.1 \ 1.1]^T$  for FON and  $r = [1.1 \ 1.1 \ 1.1]^T$  for DLTZ5

Problem	NSS-MO	Proposed algorithm	NSS-MO	Proposed algorithm
	Hypervolume		Spacing	
	Mean (variance)	Mean (variance)	Mean (variance)	Mean (variance)
LIS	<b>0.309713</b> (0.007686)	0.281162 (0.000029)	0.005861 (0.000812)	<b>0.005823</b> (0)
FON	0.542006 (0.001476)	<b>0.543569</b> (0)	<b>0.004454</b> (0.000218)	0.005823 (0.000001)
DLTZ5	0.429676 (0.000917)	<b>0.432870</b> (0.000006)	<b>0.007064</b> (0.001211)	0.019799 (0.000289)

**Table 3** Comparison of different algorithms of the basis of mean and variance of metrics  $\Upsilon$  and  $\Delta$

Problem	Algorithm	$\bar{\Upsilon}$	$\sigma_{\Upsilon}$	$\bar{\Delta}$	$\sigma_{\Delta}$	$\bar{N}_f$
SCH	NSGA-II	0.003173	0	0.430332	0.001196	25,000
	Proposed algorithm ( $n + 1$ )	<b>0.003162</b>	0	<b>0.393513</b>	0.000722	25,000
FON	NSGA-II	0.002589	0	0.373326	0.000566	25,000
	Proposed algorithm (2)	<b>0.002173</b>	0	<b>0.293504</b>	0.000539	25,000
	Proposed algorithm ( $n + 1$ )	0.002240	0	0.323102	0.000674	25,000
POL	NSGA-II	<b>0.014194</b>	0.000001	0.415517	0.001060	25,000
	Proposed algorithm (2)	0.015238	0.000001	0.339555	0.000244	25,000
	Proposed algorithm ( $n + 1$ )	0.016869	0.000001	<b>0.322245</b>	0.000290	25,000

of function evaluations as 25,000. Ten independent runs for each of the algorithms have been considered for those problems for which the true Pareto front is known. For the proposed algorithm, the run was carried out with two values of  $nps$ . The average performance of the algorithms, on the basis of  $\Upsilon$  and  $\Delta$ , is shown in Table 3. As is evident from the values shown in the table, except the value of  $\bar{\Upsilon}$  for the problem POL, all the results of the proposed algorithm are better than NSGA-II.

For the problems, KUR and VNT (for which the true Pareto front is not known), the results are compared using set converge metrics [21]  $C_{AB}$  and  $C_{BA}$ , where  $A$  corresponds to the solution set obtained by the proposed algorithm and  $B$  corresponds to the solution set obtained by the NSGA-II algorithm.

Table 4 shows the mean and standard deviation for these metrics. As discussed earlier, the metric  $C_{AB}$  gives the fraction of solutions in set  $B$ , which are dominated by solutions of set  $A$  and  $C_{BA}$  gives the fraction of solutions in set  $A$ , which are dominated by solutions of set  $B$ . As evident from the table, for the problem KUR, on an average more number of solutions of set  $A$ , *i.e.*, solutions obtained by the proposed algorithm are dominated by the solutions of set  $B$ . Hence, the algorithm NSGA-II performs better on the problem KUR. For the problem VNT, on an average more number of solutions of set  $B$ , *i.e.*, solutions obtained by the NSGA-II algorithm are dominated by the solutions of set  $A$ . So, the proposed algorithm performs better in case of the problem VNT.

**Table 4** Comparison of different algorithms on the basis of set converge metric

Problem	Algorithm	$\bar{C}_{AB}$	$\sigma_{C_{AB}}$	$\bar{C}_{BA}$	$\sigma_{C_{BA}}$	$\bar{N}_f$
KUR	A: Proposed algorithm ( $nps = n + 1$ ) B: NSGA-II	<b>0.0854</b>	0.0251	0.4227	0.0375	25,000
	A: Proposed algorithm ( $nps = 2$ ) B: NSGA-II	<b>0.1177</b>	0.0366	0.2219	0.0438	25,000
VNT	A: Proposed algorithm ( $nps = n + 1$ ) B: NSGA-II	0.1023	0.0303	<b>0.0774</b>	0.0290	25,000
	A: Proposed algorithm ( $nps = 2$ ) B: NSGA-II	0.1132	0.0344	<b>0.0667</b>	0.0248	25,000

## 5 Constrained Problems

The proposed multi-objective optimization algorithm equipped with the constraint handling procedure discussed in Sect. 3 is tried on some problems (Table 5) available in the literature. These problems include two problems of mechanical component design: two-bar truss design problem and welded-beam design problem. The results have been compared with NSGA-II. The results of NSGA-II were obtained with 250 generations (or  $Max_{iter}$ ), a population size of  $N = 100$ , crossover probability 0.9 and a mutation probability of  $1/n$  (where  $n$  is the number of design variables). The distribution indices for mutation and crossover operators were taken as  $\eta_m = 100$  and  $\eta_c = 20$ , respectively. To keep the function evaluations of the proposed algorithm same as that of NSGA-II, the results of the proposed algorithm have been obtained with the maximum number of function evaluations as 25,000.

Figure 2 shows the typical convergence of the proposed algorithm on these constrained test problems, along with that of NSGA-II. Except the welded-beam design problem, where both the algorithms have fallen short of locating the minimum of objective function  $f_1$ , the performance of both the algorithms is good, as all the points of the population have converged close to the actual Pareto front and a decent spread has been maintained by both the algorithms. To compare the average performance of the algorithms quantitatively, ten runs of both the algorithms were taken and mean and variance of the performance metrics  $\mathcal{Y}$  and  $\Delta$  are shown in Table 6. As shown in the table, except the SRN and truss design problem, the convergence metric  $\mathcal{Y}$

**Table 5** Constrained multi-objective optimization test problems

Problem	$n$	Variable bounds	Definition
DEB Deb et al. [3]	2	$x_1 \in [0.1, 1.0]$ $x_2 \in [0, 5]$	<b>Minimize</b> $f_1(\mathbf{x}) = x_1$ <b>Minimize</b> $f_2(\mathbf{x}) = \frac{1+x_2}{x_1}$ <b>Subject to</b> $g_1(\mathbf{x}) = 6 - x_2 - 9x_1 \leq 0$ $g_2(\mathbf{x}) = 1 + x_2 - 9x_1 \leq 0$
SRN Chankong and Haimes [1]	2	$x_1 \in [-20, 20]$ $x_3 \in [-20, 20]$	<b>Minimize</b> $f_1(\mathbf{x}) = (x_1 - 2)^2 + (x_2 - 1)^2 + 2$ <b>Minimize</b> $f_2(\mathbf{x}) = 9x_1 - (x_2 - 1)^2$ <b>Subject to</b> $g_1(\mathbf{x}) = x_1^2 + x_2^2 - 225 \leq 0$ $g_2(\mathbf{x}) = x_1 - 3x_2 + 10 \leq 0$
TNK Tanaka et al. [18]	2	$x_1 \in [-\pi, \pi]$ $x_2 \in [-\pi, \pi]$	<b>Minimize</b> $f_1(\mathbf{x}) = x_1$ <b>Minimize</b> $f_2(\mathbf{x}) = x_2$ <b>Subject to</b> $g_1(\mathbf{x}) = -x_1^2 - x_2^2 + 1 + 0.1 \cos(16 \arctan \frac{x_2}{x_1}) \leq 0$ $g_2(\mathbf{x}) = (x_1 - 0.5)^2 + (x_2 - 0.5)^2 - 0.5 \leq 0$
Welded beam Deb and Srinivasan [4]	4	$h \in [0.125, 5]$ $t \in [0.1, 10]$ $l \in [0.1, 10]$ $b \in [0.125, 5]$	<b>Minimize</b> $f_1 = (1.10471h^2l + 0.04811tb(14 + l))$ <b>Minimize</b> $f_2 = (2.1952/(t^3b))$ <b>Subject to</b> $g_1 = \tau - 13600$ $g_2 = \sigma - 30600$ $g_3 = h - b$ $g_4 = 6000 - P_c$ where $\tau_p = 6000/(\sqrt{2}hl)$ $\tau_{dp} = 6000(14 + 0.5l) \frac{\sqrt{0.25(l^2 + (h+t)^2)}}{(1.414h((l^2/12) + 0.25(h+t)^2)}$ $P_c = 64746.022(1 - 0.0282346t)tb^3$ $\sigma = 504000/(t^2b)$ $\tau = \sqrt{\tau_p^2 + \tau_{dp}^2 + \frac{t\tau_p\tau_{dp}}{\sqrt{0.25(l^2 + (h+t)^2)}}$
Two-bar Truss design Deb [2, pp. 450–451]	3	$x_1 \in [0, 0.01]$ $x_2 \in [0, 0.01]$ $y \in [1.0, 3.0]$	<b>Minimize</b> $f_1 = x_1\sqrt{16 + y^2} + x_2\sqrt{1 + y^2}$ <b>Minimize</b> $f_2 = \max(\sigma_{AC}, \sigma_{BC})$ <b>Subject to</b> $g_1 = \max(\sigma_{AC}, \sigma_{BC}) \leq 10^5$ where $\sigma_{AC} = \frac{20\sqrt{16+y^2}}{yx_1}$ $\sigma_{AC} = \frac{80\sqrt{1+y^2}}{yx_2}$

has a better value for the proposed algorithm. Also, the metric  $\Delta$ , which signifies the spread of the points of the population over the Pareto front, has better value in all the cases.

With the above discussions, it is clear that the proposed method which is based on a classical direct search algorithm is capable of generating a multitude of solutions for multi-objective optimization problems. The method is capable of handling constraints neatly and efficiently and can solve engineering problems. Apart from the problems discussed here, the proposed method has been tested on few other problems and the performance is found to be comparable with the existing algorithms.

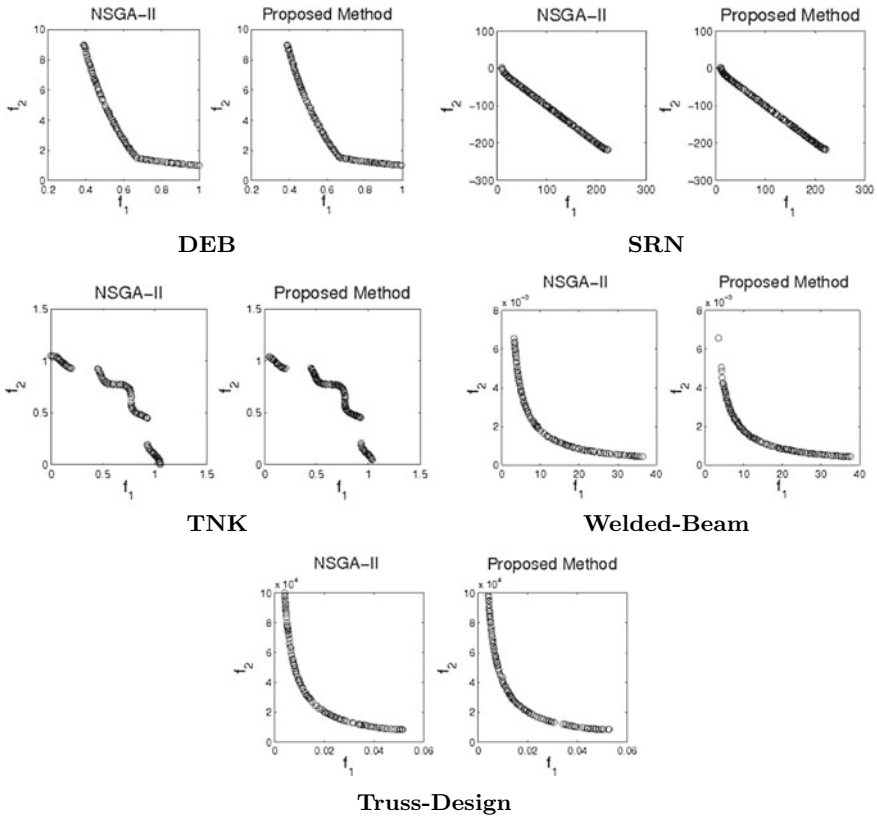


Fig. 2 Typical results of NSGA-II and the proposed algorithms for constrained problems

However, to exploit the true potential of the proposed algorithm and to further develop the idea of using the simplex search method as the multi-objective optimization tool, detailed studies on the area are needed.

## 6 Conclusion

In this paper, a multi-objective optimization method based on Nelder and Mead’s simplex search method has been developed. The method is easy to implement and unlike NSS-MO [12], which is another multi-objective algorithm based on Nelder and Mead’s simplex search method, is capable of handling constraints. The proposed method does not need any *a priori* and additional information about the problem, and it works without converting the multi-objective optimization problem to single-objective problem using weights or additional constraints.



**Table 6** Comparison of different algorithms of the basis of mean and variance of metrics  $\mathcal{V}$  and  $\Delta$

Problem	Algorithm	$\bar{\mathcal{V}}$	$\sigma_{\mathcal{V}}$	$\bar{\Delta}$	$\sigma_{\Delta}$	$\bar{N}_f$
DEB	NSGA-II	0.004666	0	0.691395	0.002342	25,000
	Proposed algorithm (2)	<b>0.004419</b>	0	0.604383	0.000834	25,000
	Proposed algorithm ( $n + 1$ )	0.005127	0	<b>0.568830</b>	0.000738	25,000
SRN	NSGA-II	<b>0.287146</b>	0.000615	0.380772	0.001154	25,000
	Proposed algorithm (2)	0.341309	0.000752	<b>0.365620</b>	0.000429	25,000
	Proposed algorithm ( $n + 1$ )	0.341737	0.000501	0.376241	0.000849	25,000
TNK	NSGA-II	0.005242	0	0.719209	0.000585	25,000
	Proposed algorithm (2)	<b>0.003374</b>	0	<b>0.626290</b>	0.001373	25,000
	Proposed algorithm ( $n + 1$ )	0.003420	0	0.630787	0.000284	25,000
Welded beam	NSGA-II	0.049928	0.000925	0.760862	0.004857	25,000
	Proposed algorithm (2)	0.100432	0.032677	0.730994	0.009236	25,000
	Proposed algorithm ( $n + 1$ )	<b>0.044968</b>	0.000030	<b>0.552562</b>	0.003877	25,000
Truss design	NSGA-II	<b>265.8680</b>	713.1869	0.740586	0.001752	25,000
	Proposed algorithm (2)	273.7213	976.5151	0.640583	0.001531	25,000
	Proposed algorithm ( $n + 1$ )	279.8505	782.431	<b>0.624337</b>	0.001124	25,000

It has been shown that the proposed algorithm is capable of generating multiple solutions closer to the true Pareto front of a problem with decent spread and that too in a single run, and its performance is comparable to well-established algorithm NSGA-II. It has been found that several parameters influence the performance of

the algorithm. A detailed study of these effects on the performance of the proposed method could be taken up further for understanding and enhancing the capabilities of the proposed method.

## References

1. Chankong V, Haimes Y (1983) Multiobjective decision making: theory and methodology, vol 8. North-Holland, New York
2. Deb K (2001) Multi-objective optimization using evolutionary algorithms, vol 16. Wiley, Hoboken
3. Deb K, Pratap A, Agarwal S, Meyarivan T (2002) A fast and elitist multiobjective genetic algorithm: NSGA-II. *IEEE Trans Evol Comput* 6(2):182–197
4. Deb K, Srinivasan A (2006) Innovization: innovating design principles through optimization. In: Proceedings of the 8th annual conference on genetic and evolutionary computation. ACM, pp 1629–1636
5. Deb K, Thiele L, Laumanns M, Zitzler E (2002) Scalable multi-objective optimization test problems. In: WCCI. IEEE, pp 825–830
6. Fonseca C, Fleming P (1995) An overview of evolutionary algorithms in multiobjective optimization. *Evol Comput* 3(1):1–16
7. Koduru P, Dong Z, Das S, Welch S, Roe J, Charbit E (2008) A multiobjective evolutionary-simplex hybrid approach for the optimization of differential equation models of gene networks. *IEEE Trans Evol Comput* 12(5):572–590. <https://doi.org/10.1109/TEVC.2008.917202>
8. Kuriger G, Grant F (2011) A lexicographic Nelder Mead simulation optimization method to solve multi-criteria problems. *Comput Ind Eng* 60:555–565
9. Kursawe F (1991) A variant of evolution strategies for vector optimization. In: Parallel problem solving from nature, pp 193–197
10. Lis J, Eiben Á (1996) A multi-sexual genetic algorithm for multiobjective optimization. In: 1997 IEEE international conference on evolutionary computation. IEEE, pp 59–64
11. Martínez, S., Coello, C.: A proposal to hybridize multi-objective evolutionary algorithms with non-gradient mathematical programming techniques. In: Parallel problem solving from nature—PPSN X, pp 837–846
12. Martinez S, Montanando A, Coello Coello C (2011) A nonlinear simplex search approach for multi-objective optimization. In: 2011 IEEE congress on evolutionary computation (CEC), pp 2367–2374. <https://doi.org/10.1109/CEC.2011.5949910>
13. Mehta VK, Dasgupta B (2012) A constrained optimization algorithm based on the simplex search method. *Eng Optim* 44(5):537–550
14. Nelder JA, Mead R (1965) A simplex method for function minimization. *Comput J* 7(4):308–313
15. Poloni C, Giurgevich A, Onesti L, Pediroda V (2000) Hybridization of a multi-objective genetic algorithm, a neural network and a classical optimizer for a complex design problem in fluid dynamics. *Comput Meth Appl Mech Eng* 186(2–4):403–420
16. Schaffer JD (1984) Some experiments in machine learning using vector evaluated genetic algorithms (artificial intelligence, optimization, adaptation, pattern recognition). Ph.D. thesis, Nashville, TN, USA. AAI8522492
17. Schott J (1995) Fault tolerant design using single and multicriteria genetic algorithm optimization. Technical report. DTIC Document
18. Tanaka M, Watanabe H, Furukawa Y, Tanino T (1995) GA-based decision support system for multicriteria optimization. In: IEEE international conference on systems, man and cybernetics. Intelligent systems for the 21st century, vol 2. IEEE, pp 1556–1561
19. Viennet R, Fonteix C, Marc I (1996) Multicriteria optimization using a genetic algorithm for determining a pareto set. *Int J Syst Sci* 27(2):255–260

20. Zhang Q, Li H (2007) MOEA/D: a multiobjective evolutionary algorithm based on decomposition. *IEEE Trans Evol Comput* 11(6):712–731. <https://doi.org/10.1109/TEVC.2007.892759>
21. Zitzler E (1999) *Evolutionary algorithms for multiobjective optimization: methods and applications*. Shaker Verlag, Aachen-Maastricht, *Berichte aus der Informatik*
22. Zitzler E, Thiele L (1998) Multiobjective optimization using evolutionary algorithms—a comparative case study. In: *Parallel problem solving from nature—PPSN V*. Springer, pp 292–301

# **Production and Industrial Engineering Section**

# Performance and Life Cycle Analysis of Soybean Oil-Based Minimum Quantity Lubrication in Machining of Ti6Al4V



Rukmini Srikant Revuru and Nageswara Rao Posinasetti

**Abstract** Titanium alloys are used in various applications due to their properties. However, these alloys are difficult to machine. Several techniques have been proposed in the literature to deal with the problem. This paper presents a study on the performance and life cycle analysis of the dry machining, flood lubrication and minimum quantity lubrication (MQL) of titanium alloy, Ti6Al4V. Machining was carried out at different speeds 30, 55 and 80 m/min. Soybean-based fluid was used in both flood lubrication and MQL. Cutting forces, tool wear and surface roughness were measured in all three cases. MQL was found to have better performance with longer tool life by almost two times, cutting forces by about 18% and surface roughness by about 10% compared to dry machining. Flood lubrication results were intermediate between the two. However, flood lubrication had the highest carbon footprint followed by dry machining and MQL.

**Keywords** Ti6Al4V · Machining · MQL · Carbon footprint

## 1 Introduction

Titanium alloys are popularly utilized to make parts for various applications in aerospace, energy and medical/dental sectors due to their superior properties such as high strength, biocompatibility and corrosion resistance compared to other metals or alloys [1]. Among the alloys, Ti6Al4V is most commonly used. These alloys have high yield strength, fatigue strength, heat resistance, specific strength, corrosion resistance, etc. [2, 3]. Due to high strength the alloys, cutting temperatures are usually high in their machining [4, 5]. Further, these alloys continue to have high strength even at elevated temperatures, and hence, cutting forces do not decrease with cutting speed. Also, as the titanium alloys have low thermal conductivity, heat due to machining is not dissipated; it remains in the tool/chip junction causing increased tool wear and early tool failure. Most of the heat (about 80%) is retained in the

---

R. S. Revuru (✉) · N. R. Posinasetti  
Department of Technology, University of Northern Iowa, Cedar Falls 50614, IA, USA  
e-mail: [rukmini.revuru@uni.edu](mailto:rukmini.revuru@uni.edu)

© Springer Nature Singapore Pte Ltd. 2020  
H. K. Voruganti et al. (eds.), *Advances in Applied Mechanical Engineering*,  
Lecture Notes in Mechanical Engineering,  
[https://doi.org/10.1007/978-981-15-1201-8\\_73](https://doi.org/10.1007/978-981-15-1201-8_73)

tool [6, 7]. This problem is more severe at high speeds. Also, great spring back is present in the materials, resulting in chatter and poor surface finish. This is extremely important due to the nature of the applications of the alloys. It was reported in the literature that the preferred machining speed for the titanium alloys is about 60 m/min with tungsten carbide/PVD-coated tools [8–10], which are usually the best tools for machining titanium alloys [11]. In addition, titanium alloys have high reactivity with cutting tool materials. This results in exacerbated tool wear and premature failure of the tool [12]. Thus, the machining of titanium alloys involves several problems. In recent years, several works are reported in the literature on the machining of titanium alloys. Various techniques such as flood lubrication, MQL and cryogenic cooling were tried by various researchers [13].

Dry machining results in high cutting temperatures and small tool life. Since cutting temperatures greatly depend on cutting speed, the allowable range of speeds in dry machining is usually limited. This reduces the productivity of the industry. Hence, investigations on techniques to effectively cool and lubricate the machining zone gained prominence. The usual technique to reduce cutting temperatures is applying the cutting fluids. Cutting fluids help in carrying away the heat and reduce the friction in the machining zone through lubrication. The fluids are generally applied with the nozzle in one or more of the three directions: underneath the chip, on the rake face of the tool or on the tool flank surface. To increase the carrying away of heat and lubrication, cutting fluids are applied in large quantities, called flood lubrication. This also helps to compensate the losses due to evaporation. For better convection of heat, cutting fluids are supplied under high-pressure delivery systems in the machining of titanium alloys. Further, high-pressure jet can help to break the chip and result in smaller tool/chip contact length leading to reduced friction. However, due to the complex nature of the ingredients, proper treatment is required by EPA before disposal. Some researchers have suggested cryogenic cooling in the machining of titanium. Nitrogen in its liquid form is applied in machining at  $-196\text{ }^{\circ}\text{C}$  [13]. This helps in reducing the temperatures and forms a layer at the tool/chip interface and reduces the friction. Due to its ability to reduce the temperature by over 59%, cryogenic cooling has become popular in the machining of titanium alloys. However, the cutting forces are very high, and the quality of product is poor. Extreme cooling causes various hardening of the workpiece and dimensional/form inaccuracies. As another solution, vegetable oils replaced the paraffin oil in the cutting fluids. However, even these oils require treatment and disposal. However, if used in MQL, there is no need for disposal. MQL reduces cutting forces, temperatures and tool wear and improves the quality of the product. Though MQL improves the machining performance, it needs fluids of very high quality to obtain significant cooling and lubrication.

Apart from the performance aspect of the cutting fluids, the environmental impact is important. Not many works are available in literature on the life cycle analysis. In one interesting work [14], total carbon footprint was calculated as:

$$CE = CE_{\text{elec}} + CE_{\text{tool}} + CE_{\text{coolant}} + CE_{\text{m}} + CE_{\text{chip}} \quad (1)$$

where  $CE_{elec}$ ,  $CE_{tool}$ ,  $CE_{coolant}$ ,  $CE_m$  and  $CE_{chip}$  are the carbon emissions due to production of electricity necessary for machining, producing cutting tools, production of cutting fluid, production of raw materials and chip removal. In the calculation of  $CE_{coolant}$ , only the carbon emissions of production and disposal are considered, without regard to the individual ingredients of the fluid. Hence, a vegetable-based oil or a petroleum-based oil would essentially give the same results.

In summary, though MQL is popularly used, its application in machining of titanium alloys is not popular, mostly due to inadequate cooling. Hence, the application of cutting fluids in MQL is a potential solution. Though few works dealing with MQL in titanium are found in literature, most of them deal with petroleum-based oils. Of the few works dealing with vegetable-based fluids, LCA analysis is not done. Many works, dealing with sustainability, consider only the reduced forces in machining and hence reduced power consumption, due to the use of cutting fluids. However, the energy consumption during the life cycle is often neglected. The present work attempts to test the performance of soybean-based cutting fluids in the machining of Ti6Al4V and studies the sustainability aspects through life cycle analysis.

## 2 Experimentation

In the present work, Ti6Al4V was machined on HAAS SL-20 turning center (20 HP) using TiN/TiAlN-coated carbide tools till the end of the tool life for different cutting conditions. Cutting speeds of 30, 55 and 80 m/min, feed rate of 0.3 mm/rev and depth of cut of 0.5 mm were selected.

Soybean-based cutting fluid was supplied at the rate of 40 mL/h using MQL system. The nozzle is so placed that the fluid is supplied behind the chip. Dry machining and flood cooling were also carried under the same cutting conditions for comparison. In flood lubrication, cutting fluid was diluted with 95% water and supplied at the rate of 100 L/h. In all cases, the limiting value of flank wear was taken to be 0.6 mm as per the ISO standards. Tool flank wear was measured using a toolmaker's microscope (Make: Mitutoyo) at different intervals of machining. Cutting forces and surface roughness were measured using lathe tool dynamometer (Make: Kistler) and surface roughness tester (Make: Mahr). The experimental setup is shown in Fig. 1.

## 3 Results and Discussions

Tool wear was significantly influenced by cutting speeds, and higher speeds resulted in higher tool wear. However, for each speed the trends for the three lubricating conditions were similar. Hence, tool wear data at cutting speed of 80 m/min only is presented in this paper for brevity (Fig. 2). It may be seen that tool wear is low for MQL compared to the other two conditions. Dry machining produces highest heat due to the absence of any coolant/lubricant and hence has highest tool wear. Flood

**Fig. 1** Experimental setup [14]

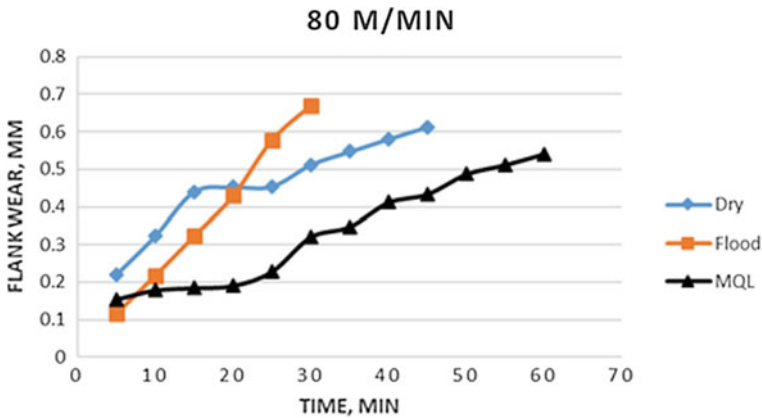


**Fig. 2** Tool wear at 80 m/min

lubrication effectively curtails heat and reduces the chance of plastic deformation of the tool, and however, the cutting fluid may not reach the actual machining zone (tool–chip interface, secondary shear zone) and hence may not reduce friction, especially at high cutting speeds. In MQL, the fluid is supplied underneath the chip in this study. When applied underneath the chip, the cutting fluid can reach the tool–chip junction via capillarity through the micro-cracks on the surface of the chip. Usually, lubrication is required in the secondary shear zone, where the chip is in contact with the rake face of the tool. The lubricant forms a thin lubricating film at the tool/chip interface and reduces the adhesion of the chip with the tool. This results in decrease in friction and thus tool wear. It may be seen that tool life (max. tool wear = 0.6 mm) was almost twice for MQL compared to dry machining and about 25% more compared to flood lubrication. The tool wear data was used to formulate tool life equation for TiN/TiAlN-coated tools in the machining of titanium (Eqs. 2–4).

$$VT^{0.69} = 533 \text{ (flood lubrication)} \tag{2}$$

$$VT^{0.588} = 495.26 \text{ (MQL)} \tag{3}$$



$$VT^{0.65} = 398 \text{ (Dry machining)} \tag{4}$$

where  $V$  = cutting speed, m/min and  $T$  = tool life, min. The cutting data for cutting speeds of 30 and 55 m/min was used to build the model, while the values at 80 m/min were used to test the model. The errors in prediction were found to be 9.2, 2.5 and 3.5% for dry machining, flood lubrication and MQL, respectively. The equations are helpful in predicting tool life under different cutting speeds. This will give the measure of tools spent and help to carry out the LCA of fluids.

Cutting forces and surface roughness were also recorded for the entire tool life. Surface roughness and cutting forces were observed to be less with MQL than other conditions (Figs. 3 and 4). Dry machining had the highest surface roughness followed by flood lubrication. Due to lesser tool wear, MQL resulted in least surface roughness about the considered conditions, about 6% less than flood lubrication and about 10% less than dry machining at the end of tool life. Cutting forces were found to be almost similar for different cutting speeds, despite the high tool wear at higher speeds. This may be due to the high amount of heat that is contained in the workpiece, which softens the workpiece, reducing the cutting forces. Since, titanium alloys have low thermal conductivity; most of the heat is not carried away by the chip, but is retained in the tool and workpiece. This causes the workpiece to get heated up very quickly. However, within the different conditions of lubrication, difference can be observed. Cutting forces are consistently low for MQL compared to dry machining and flood lubrication. Dry machining is devoid of any lubrication and hence obviously has higher forces. In flood lubrication, the cutting fluid helps mainly by cooling the machining zone, and however, the fluid may not reach the tool–chip interface. In case of MQL, the fluid reaches the secondary shear zone, thereby considerably reducing the cutting forces. Further, the lower tool wear helps in reducing the cutting forces in

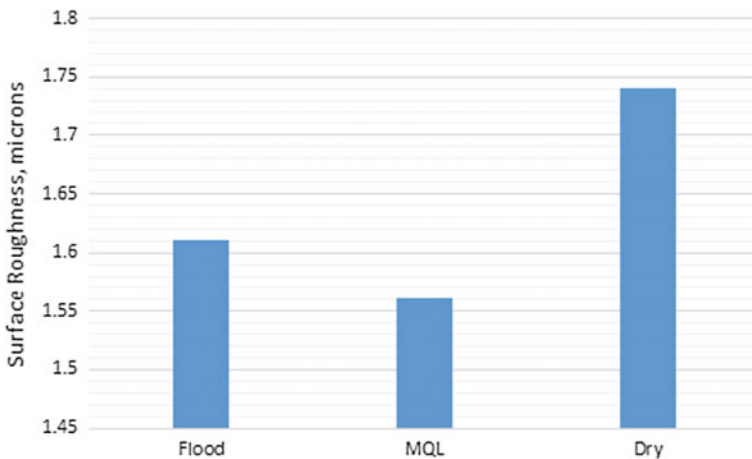


**Fig. 3** Surface roughness for different lubricating conditions at 80 m/min

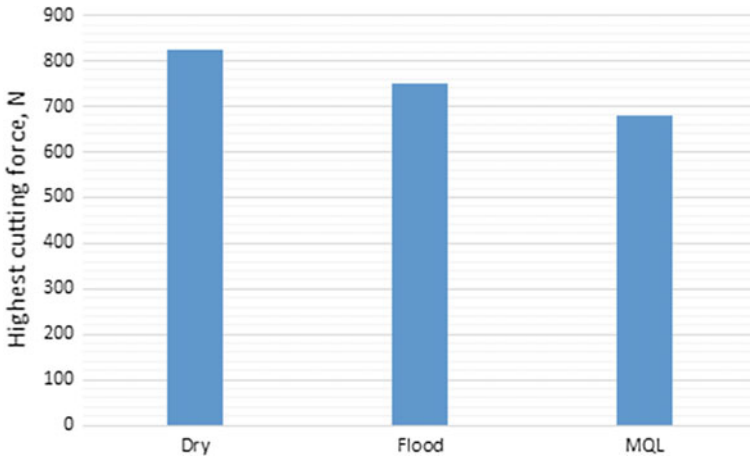


**Fig. 4** Highest cutting force recorded for different lubricating conditions at 80 m/min

**Table 1** Carbon footprint calculations

Cutting speed(m/min)	Carbon footprint (kg CO <sub>2</sub> )		
	Dry	Flood	MQL
30	10.267	10.256	10.230
55	10.419	10.427	10.372
80	10.559	10.644	10.546

case of MQL. It may be observed that MQL has about 18% lesser forces compared to dry machining and about 9% compared to flood lubrication.

LCA of titanium alloy machining was carried out based on the equations given in the literature [15]. The carbon footprint calculations are presented in Table 1. It may be seen that in many cases, flood lubrication leaves higher carbon footprint compared to the other two conditions. This is due to the fact that flood lubrication results in better performance than dry machining, and the impact of the production of the cutting fluid is high. In case of MQL, the carbon footprint is small due to the small quantity of fluid used and longer tool life/smaller cutting forces. Further, MQL does not need disposal, thus reducing the carbon footprint.

### 4 Conclusions

The following conclusions may be drawn based on the present work:

1. At the considered cutting conditions, MQL gave the best performance compared to dry and flood lubrication. Tool life was twice for MQL compared to dry machining and 25% more compared to flood lubrication. Similarly, MQL has

cutting forces reduced by 18 and 9% compared to dry machining and flood lubrication, respectively. Further, MQL resulted in improved surface roughness by 10% and 6%, respectively.

2. Better lubrication in MQL helped to reduce cutting forces, tool wear and surface roughness.
3. Flood lubrication was better than dry machining in terms of performance. However, LCA revealed that flood lubrication is not sustainable compared to the other two cases.
4. MQL is found to be the most sustainable under the considered conditions.

**Acknowledgements** The work has been carried out with the support of University of Northern Iowa in form of Professional Development Assignment to one author and Pre-tenure Grant (Office of Provost) and Faculty Research/Creative Activity Grant (CHAS) to the other author.

## References

1. Ulutan D, Ozel T (2011) Machining induced surface integrity in titanium and nickel alloys: a review. *Int J Mach Tools Manuf* 51(3):250–280
2. Shokrani A, Dhokia V, Newman ST (2016) Investigation of the effects of cryogenic machining on surface integrity in CNC end milling of Ti–6Al–4V titanium alloy. *J Manuf Process* 21:172–179
3. Singh P, Pungotra H, Kalsi NS (2016) On the complexities in machining titanium alloys. In: *CAD/CAM, robotics and factories of the future*, India, pp 499–507
4. Abdalla HS, Baines W, McIntyre G, Slade C (2007) Development of novel sustainable neat-oil metalworking fluids for stainless steel and titanium alloy machining. Part 1. Formulation development. *Int J Adv Manuf Technol* 34(1–2):21–33
5. Ezugwu EO, Bonney J, Yamane Y (2003) An overview of the machinability of aeroengine alloys. *J Mater Process Technol* 134(2):233–253
6. Welsch G, Boyer R, Collings EW (1993) *Materials properties handbook: titanium alloys*. ASM International
7. Pan W (2014) *The machining of titanium alloys with polycrystalline diamond tools*. Doctoral dissertation, RMIT University Melbourne, Australia
8. Sun FJ, Qu SG, Pan YX, Li XQ, Li FL (2015) Effects of cutting parameters on dry machining Ti–6Al–4V alloy with ultra-hard tools. *Int J Adv Manuf Technol* 79(1–4):351–360
9. Shokrani A, Dhokia V, Newman ST (2012) Environmentally conscious machining of difficult-to-machine materials with regard to cutting fluids. *Int J Mach Tools Manuf* 57:83–101
10. Pervaiz S, Deiab I, Darras B (2013) Power consumption and tool wear assessment. Power consumption and tool wear assessment when machining titanium alloys. *Int J Precis Eng Manuf* 14(6):925–36
11. Sun S, Brandt M, Dargusch MS (2015) Effect of tool wear on chip formation during dry machining of Ti–6Al–4V alloy, part 2: effect of tool failure modes. *Proc Inst Mech Eng Part B: J Eng Manuf* 231(9):1575–1586
12. da Silva RB, Machado AR, Ezugwu EO, Bonney J, Sales WF (2013) Tool life and wear mechanisms in high speed machining of Ti–6Al–4V alloy with PCD tools under various coolant pressures. *J Mater Process Technol* 213(8):1459–1464
13. Revuru RS, Posinasetti NR, VSN VR, Amrita M (2017) Application of cutting fluids in machining of titanium alloys—a review. *Int J Adv Manuf Technol* 91:2477–2498

14. Revuru RS, Zhang JZ, Posinasetti NR, Kidd T (2018) Optimization of titanium alloys turning operation in varied cutting fluid conditions with multiple machining performance characteristics. *Int J Adv Manuf Technol* 95(1–4):1451–1463
15. Li C, Tang Y, Cui L, Li P (2015) A quantitative approach to analyze carbon emissions of CNC-based machining systems. *J Intell Manuf* 26(5):911–922

# Investigations on Corrosion Behaviour in Micro-Milling of Biomedical Grade Ti-6Al-7Nb Alloy



S. P. Leo Kumar and D. Avinash

**Abstract** Titanium (Ti)-based alloy is extensively used in biomedical field due to its unique properties that promotes osseointegration. Present work deals with investigation on the effect of cutting conditions on corrosion resistance in micro-milling of Ti-6Al-7Nb alloy for enhanced biocompatibility. Experiments were carried out based on Taguchi  $L_9$  orthogonal array with selected process variables include cutting speed ( $v_c$ ), feed rate ( $f_n$ ) and depth of cut ( $a_p$ ). Micro-slot of size 700  $\mu\text{m}$  for a length of 10 mm was made using high-speed micromachining station under wet condition. Potentiostat setup with three electrodes and simulated body fluid (SBF) at 37 °C was used for corrosion resistance measurement and corresponding  $I_{\text{corr}}$  values were obtained from polarisation curve.  $I_{\text{corr}}$  values are found to be minimum at higher  $v_c$  and lower  $a_p$  conditions. Variation in process parameters influences the surface characteristics to a greater extent, which intern alters the corrosion resisting potential of surface. From the study, it is observed that Ti-6Al-7Nb alloy exhibits higher corrosion resistance under in vitro condition for enhanced biocompatibility for medical application.

**Keywords** Biocompatibility · Corrosion resistance · Micro-milling · Ti-6Al-7Nb alloy

## 1 Introduction

Titanium (Ti) is a non-cytotoxic element used for manufacturing biomedical implants. It is alloyed with many biocompatible elements like tantalum (Ta) and niobium (Nb) to reduce the Young's modulus value [1]. Eisenbarth et al. [2] described about the replacement of Ti-6Al-4V with Ti-6Al-7Nb, due to the toxic nature of

---

S. P. Leo Kumar (✉) · D. Avinash  
Department of Production Engineering, PSG College of Technology, Coimbatore 641004, India  
e-mail: [spleokumar@gamil.com](mailto:spleokumar@gamil.com)

vanadium (V); therefore, V is replaced with Nb. Even after replacement, metallurgical and mechanical properties of Ti–6Al–7Nb alloy are similar to Ti–6Al–4V alloy. Al-Mobarak et al. [3] investigated corrosion performance of Ti–6Al–7Nb alloy using Hank's solution and compared the results with Ti–6Al–4V alloy. Investigation results showed that Nb cations helped to increase resistance to corrosion by the formation of TiO<sub>2</sub> film with less number of anion vacancies. Luiz de Assis et al. [4] examined corrosion characteristics of Ti–6Al–4V, Ti–13Nb–13Zr and Ti–6Al–7Nb alloys by using Hank's solution and observed that these Ti alloys had two oxide layers. A porous oxide film formed above barrier layer enhanced the corrosion characteristics. The porous layer of Ti–6Al–7Nb alloy increases the ability of osseointegration.

Mohan et al. [5] studied the development of TiO<sub>2</sub> layer formation on surface of Ti–6Al–7Nb alloy in electrolytic solution containing hydrofluoric and sulphuric acid. Variation in porous diameter of oxide layer was observed when there is a change in applied voltage. This nanostructure helps in the improvement of osteoblast cells attachment. Kobayashi et al. [6] evaluated the existence and growth of protective layer in Ti–6Al–7Nb alloy using anodic polarisation and immersion test. It is inferred that there is no sign of pitting corrosion. Chrzanowski [7] presented the influence of various surface treatment on topographical and corrosion properties on Ti alloy. The experimental results proved that Ti–6Al–7Nb alloy possesses superior corrosion resistance in SBF condition. Henrique Lauro et al. [8] experimentally investigated Ti–6Al–7Nb alloy under micro-cutting conditions. The result shows that the cutting quality can be improved by increase of  $v_c$ . It was also indicated that spindle speed increment results minimisation of heat generation on the tool. Leo Kumar et al. [9] performed a review on tool-based micromachining process and mentioned the importance of surface characteristics for various micro-part fabrication.

From the literature, it is observed that Ti–6Al–7Nb alloy can be used as a biomaterial for medical implants. The human body is a highly corrosive environment; as a result, it is mandatory to investigate the corrosion resistance of machined implant surface.

## 2 Materials and Methods

In this work, Ti–6Al–7Nb is chosen due to its biocompatible properties and their availability. Taguchi experimental design has been incorporated, and process variables including  $f$ ,  $v_c$  and  $a_p$  are considered for the study of corrosion resistance. The workpiece of size 20 mm × 20 mm has been used for investigation. Micro-milling experiments are carried out in CNC micromachining station. The machine is precision enough to produce micro-feature with positional accuracy of  $\pm 1 \mu\text{m}$  with high spindle speed capable of running up to 60,000 rpm. Tungsten carbide tool of size 700  $\mu\text{m}$  diameter with two flute end mill cutter is used for experimentation. Micro-milling experiments were carried out under wet condition with mist cooling facility. Experimental setup is shown in Fig. 1.

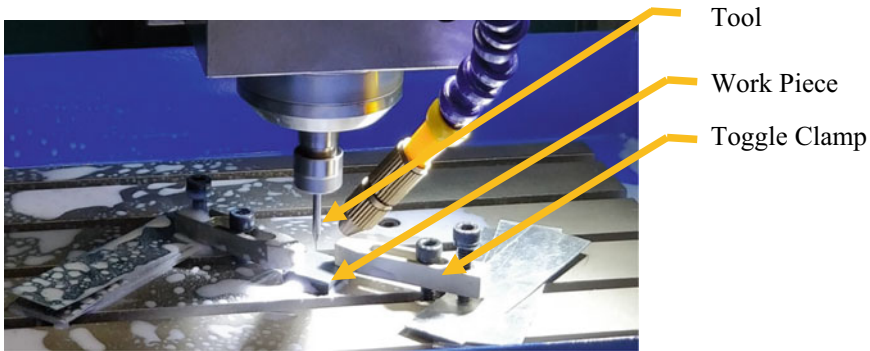


**Fig. 1** Micro-milling experimental setup

Corrosion test was carried out with the help of potentiostat setup. It consists of a flat cell and three electrodes, namely working electrode (work material), reference electrode (silver (Ag)), and counter electrode (graphite). In order to perform corrosion study, SBF is used for in vitro study. The solution possesses pH level of  $7.4 \pm 0.1$  with acid-base. The test was carried out for an hour at temperature of  $37 \pm 1.0$  °C. Fresh solution is prepared for each trial, and the potentiostat setup has been used for measuring corrosion resistance.

### 3 Results and Discussion

From potention-dynamic study, Nyquist plot and Tafel plot were generated from experimentation. Tafel plot is used to identify rate of pitting and corrosion susceptibility by plotting relation between electric potential and current density. Further, cathodic polarisation curve and anodic polarisation curve were extrapolated and their intersection point provides  $E_{\text{corr}}$  and  $I_{\text{corr}}$  values.  $E_{\text{corr}}$  value is open circuit potential of metal in a liquid environment, and  $I_{\text{corr}}$  values influence corrosion rate. Electrochemical impedance spectroscopy (EIS) or Nyquist plot is used to find electrochemical impedance of Ti alloy. Electrochemical impedance is the response of an electrochemical system to an applied potential which is complex in nature. Hence, in Nyquist plot  $Z_{\text{real}}$  is plotted against  $Z_{\text{imaginary}}$ , in which impedance is measured as a function of frequency.

From Tafel plot,  $I_{\text{corr}}$  and  $E_{\text{corr}}$  values are obtained as shown in Table 1. These values were further investigated to study effects of  $v_c$ ,  $a_p$  and  $f$  on corrosion behaviour. The Tafel and Nyquist plots for machining conditions of  $v_c = 47$  m/min,  $f = 1.5$  mm/min  $a_p = 150$   $\mu\text{m}$  are shown in Fig. 2a, b. The  $I_{\text{corr}}$  value is obtained from the polarisation curve by cathodic branch of polarisation curves to corrosion potential were found to be 576 nA and  $-522$  mV, respectively. The resistance offered by material increases with respect to time and initial increment is due to the formation

**Table 1** Experimental results on corrosion resistance

Ex. No.	Cutting speed (m/min)	Feed rate (mm/min)	Depth of cut ( $\mu\text{m}$ )	$E_{\text{corr}}$ (mV)	$I_{\text{corr}}$ ( $\text{nAm}^2$ )
1	31.4	0.5	100	-174	688
2	31.4	1	150	-290	3250
3	31.4	1.5	200	-250	2130
4	39	0.5	150	-491	711
5	39	1	200	-477	2290
6	39	1.5	100	-288	1120
7	47	0.5	200	-299	961
8	47	1	100	-318	1860
9	47	1.5	150	-522	576

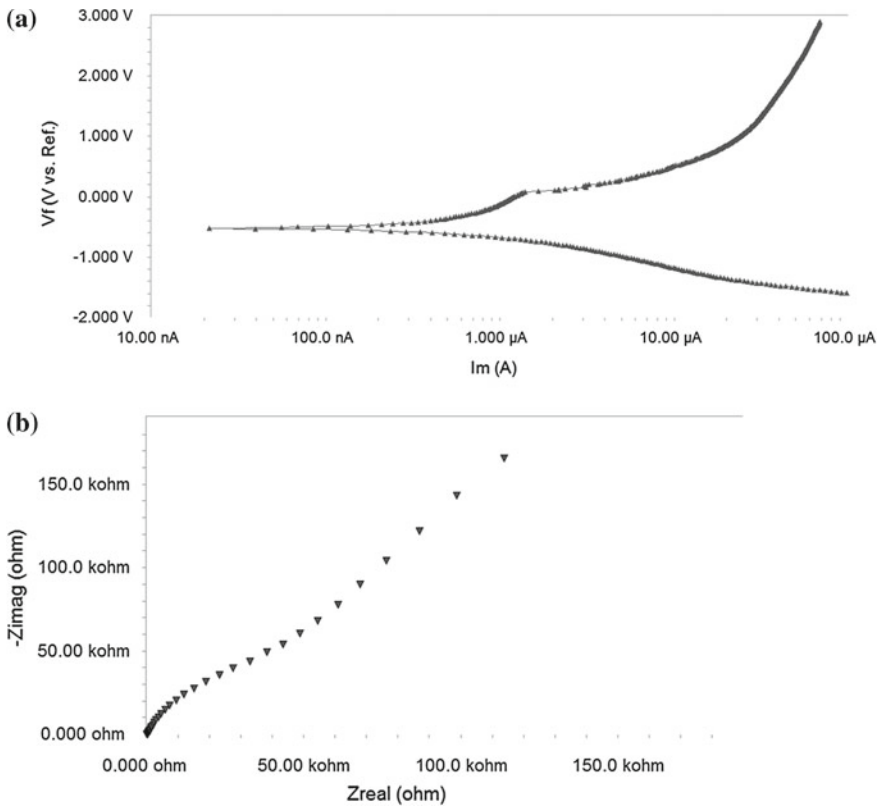


**Fig. 2** Tafel and Nyquist plots for cutting conditions of  $v_c = 47$  m/min,  $f = 1.5$  mm/min  $a_p = 150 \mu\text{m}$ . **a**Tafel plot, **b** Nyquist plot



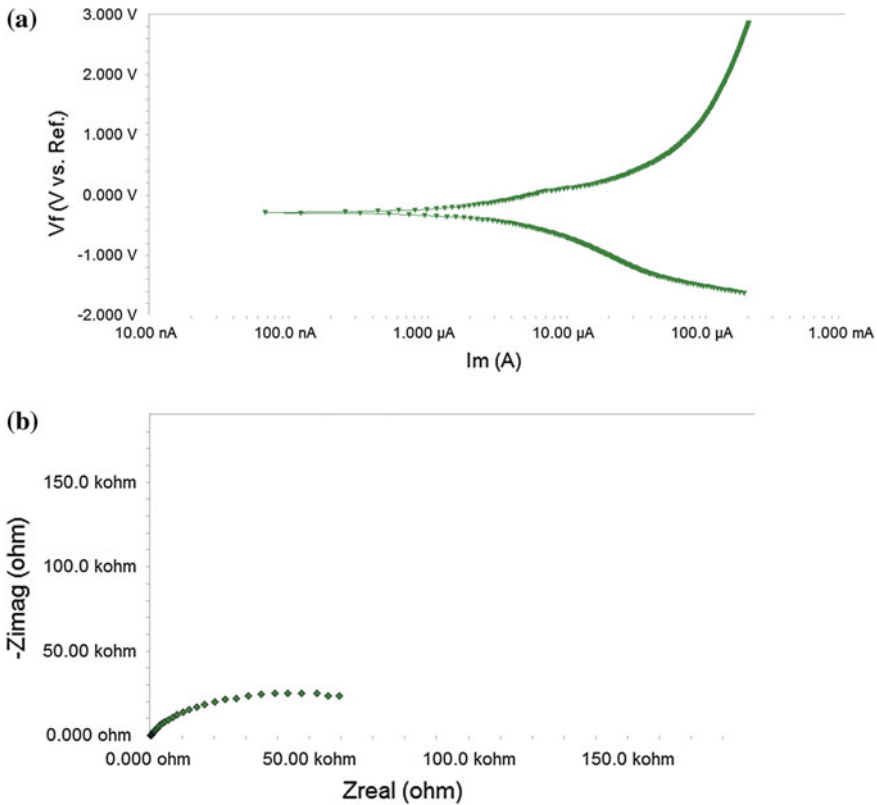


**Fig. 3** Tafel and Nyquist plots for cutting conditions of  $v_c = 31.4$  m/min,  $f = 1$  mm/min  $a_p = 150$   $\mu$ m. **a** Tafel plot, **b** Nyquist plot

of very thick oxide film on surface that leads to improvement of corrosion protection ability. The Tafel and Nyquist plots for cutting conditions of  $v_c = 31.4$  m/min,  $f = 1$  mm/min  $a_p = 150$   $\mu$ m are shown in Fig. 3a, b. A sharp increase in current density at level of potentials above 0.0 V (SCE) was identified. This suggests that oxide film is getting replaced gradually by a less protective passive film. The resulted passive film becomes stable approximately above 500 mV (SCE). The formation of protective passive film is distinguished by  $I_{corr}$  value of  $3.25 \mu\text{A}\cdot\text{m}^2$ .

### 3.1 Influence of Cutting Parameters on Response

The interaction of  $f$ ,  $v_c$  and  $a_p$  on corrosion resistance was investigated. From corrosion study, it is observed that implants should have very less  $I_{corr}$  value in order to have better corrosion resistance. It is identified that increment in  $v_c$  and decrease

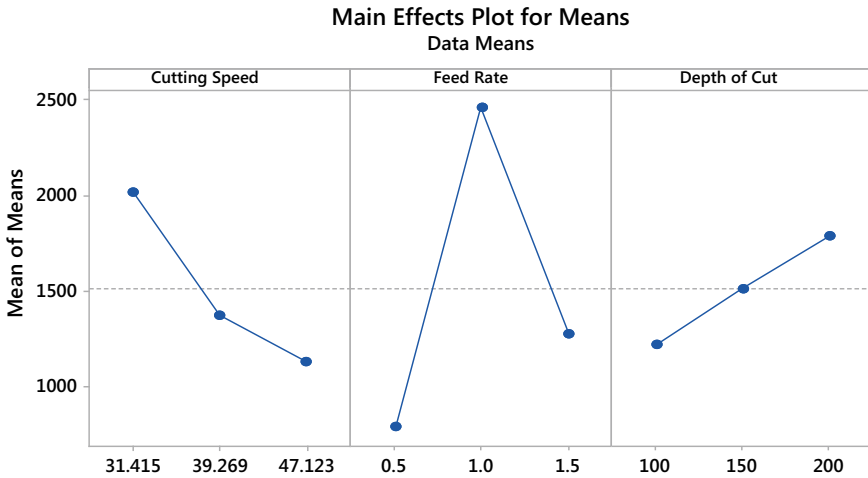


**Fig. 4** Effects of  $v_c$ ,  $f$  and  $a_p$  on current density ( $I_{\text{corr}}$ )

in  $a_p$  condition have major influence on corrosion resistance as shown in Fig. 4. It clearly shows that  $a_p$  and  $v_c$  have significant effects on  $I_{\text{corr}}$  value. It is attributed by improvement in surface quality creates residual compressive stress within the sub-surface, i.e., chemical species adsorption resistance along with low roughness which prevents initiations of surface pores and twinning which were potential in influencing corrosion. It is inferred that increase of  $v_c$  reduces micro-particle deposition that promotes better surface finish attributing to improved corrosion resistance.

## 4 Conclusion

In this work, an effort has been made to analyse the effect of micro-milling cutting conditions on corrosion behaviour in Ti-6Al-7Nb alloy.  $I_{\text{corr}}$  and  $E_{\text{corr}}$  values for the cutting conditions were obtained from Tafel and Nyquist plots, and the following conclusions are drawn:

- The potentiodynamic polarisation test shows that the influence of  $v_c$  and  $a_p$  on  $I_{\text{corr}}$  value is higher.
- The minimum value of  $I_{\text{corr}}$  obtained is 576 nA at  $v_c = 47$  m/min,  $f_n = 1.5$  mm/min.
- It is observed that at higher level of  $v_c$ , higher feed and lower  $a_p$  condition, the corrosion resistance of Ti-6Al-7Nb is found to be high under in vitro condition.
- Variation in process parameters influences the surface characteristics to a greater extent, which in turn alters the corrosion resisting potential of surface.
- Ti-6Al-7Nb alloy obtained very low current density in SBF solution. This is because of the formation of a firm passive film on the surface.

- The EIS result proves oxide film formed on Ti–6Al–7Nb is submissive at initial time, after which the curve indicates formation of a strong bi-layered oxide film.

From the investigation, it is inferred that the machined surface characteristics have a great influence on the corrosion behaviour of Ti–6Al–7Nb alloy.

**Acknowledgements** We would like to deliver our profound thanks to DST-SERB, Government of India for providing financial support throughout the Research Project No: ECR/2016/001330 to carry out this work.

## References

1. Abdel-Hady Gepreel M, Niinomi M (2013) Biocompatibility of Ti-alloys for long-term implantation. *J Mech Behav Biomed Mater* 20:407–415
2. Eisenbarth E, Velten D, Muller M, Thull R, Breme J (2004) Biocompatibility of  $\beta$ -stabilizing elements of titanium alloys. *Biomaterials* 25(26):5705–5713
3. Al-Mobarak NA, Al-Swayih AA, Al-Rashoud FA (2011) Corrosion behavior of Ti–6Al–7Nb alloy in biological solution for dentistry applications. *Int J Electrochem Sci* 6:2031–2042
4. Luiz de Assis S, Wolyneć S, Costa I (2006) Corrosion characterization of titanium alloys by electrochemical techniques. *Electrochim Acta* 51(8–9):1815–1819
5. Mohan L, Anandan C, Rajendran N (2015) Electrochemical behavior and effect of heat treatment on morphology, crystalline structure of self-organized TiO<sub>2</sub> nanotube arrays on Ti–6Al–7Nb for biomedical applications. *Mater Sci Eng C* 50:394–401
6. Kobayashi E, Wang TJ, Doi H, Yoneyama T, Hamanaka H (1998) Mechanical properties and corrosion resistance of Ti–6Al–7Nb alloy. *J Dent Cast* 8:567–574
7. Chrzanowski W (2008) Corrosion study of Ti<sub>6</sub>Al<sub>7</sub>Nb alloy after thermal, anodic and alkali surface treatments. *J Achiev Mater Manuf Eng* 31(2):10
8. Henrique Lauro C, Sergio LM, Filh, R, Cardoso Brandao L, Paulo Davim J (2016) Analysis of behaviour biocompatible titanium alloy (Ti–6Al–7Nb) in micro-cutting. *Measurement* 93:529–540
9. Leo Kumar SP, Jerald J, Kumanan S, Prabakaran R (2014) A review on current research aspects in tool based micro machining process. *Mater Manuf Process* 29(11–12):1291–1337

# Optimization of Machining Parameters for Multi-performance Characteristics in Milling of Composite Solid Propellants Using RSM



Kishore Kumar Katikani, A. Venu Gopal and Venkateseara Rao Vemana

**Abstract** The solid rocket motors (SRMs) produced with case-bonded composite solid propellant (CSP) grains are formulated with metallic aluminium (Al) powder as the fuel, ammonium perchlorate ( $\text{NH}_4\text{ClO}_4$ ) as the oxidizer and hydroxyl-terminated polybutadiene (HTPB) as a polymer binder. These CSPs are sensitive to fire hazard by mechanical stimuli such as friction, heat, impact load and static charge which are inevitably present in conventional machining operations. In order to machine this 'hazardous to machine' CSP material safely, using custom build cutting tool called 'turbine cutter' with minimum cutting power and for maximum material removal rate (MRR), experimental studies are carried out. The main objective of this study is to identify the optimum process input parameters for low cutting power (CP) and high MRR and further to enhance the safety in machining of 'hazard to machine' materials. To achieve this objective, the effect of machining parameters on CP and MRR was investigated. Full factorial experiments were carried out on live propellant grain using the turbine cutter on CNC vertical turn mill (VTM). In order to investigate the influence of process parameters in machining CSP material, two-factor interaction (2FI) models are developed, and subsequently, ANOVA is performed to evaluate the significant process parameters. Response surface methodology (RSM) is used to develop the mathematical models and also for multi-response optimization, using commercial software, Design-Expert. The optimum values of machining parameters attained with a desirability value of 0.88 are as follows: cutting velocity (CV) is 125 rpm (196 m/min), table feed rate (TFR) is 24 deg/min (0.418 m/min), and depth of cut is 4 mm for minimum CP and maximum MRR, and their values are  $15.75 \times 10^{-2}$  kW and  $1092.11 \times 10^{-6}$  m<sup>3</sup>/min, respectively.

---

K. K. Katikani (✉)

NSTL, DRDO, Visakhapatnam, Andhra Pradesh 530027, India

e-mail: [b4ukishorekk@rediffmail.com](mailto:b4ukishorekk@rediffmail.com)

A. Venu Gopal

National Institute of Technology Warangal, Warangal, Andhra Pradesh 506004, India

V. R. Vemana

DRDO, Hyderabad, Telangana 500058, India

© Springer Nature Singapore Pte Ltd. 2020

H. K. Voruganti et al. (eds.), *Advances in Applied Mechanical Engineering*,

Lecture Notes in Mechanical Engineering,

[https://doi.org/10.1007/978-981-15-1201-8\\_75](https://doi.org/10.1007/978-981-15-1201-8_75)

**Keywords** Composite solid propellant (CSP) · Desirability function · Multi-response optimization · Response surface methodology (RSM)

## 1 Introduction

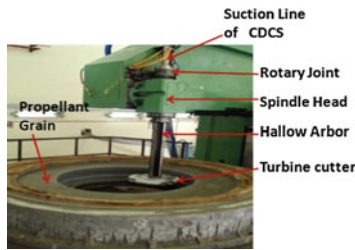
HTPB/AP/AL-based CSP material of SRM is produced by chemical casting under vacuum condition and machining of these materials which come under 1.3 hazard division classifications. Sutton and Biblarz [1] reported that ballistic requirement of SRM will not meet by simple casting. It requires machining on the propellant grain to generate the desired profile as initial ignition surface called grain configuration. In addition to this, uneven and porous surface of propellant grain, non-uniform deposition of propellant, extra propellant cast for machining allowance during casting of SRM segments require machining as secondary operation to bring the size of grain to exact dimensions for assembly of segments into motor as reported by Nagappa [2] and Devenas [3].

Safe machining practices have been highly emphasized to deal with heterogeneous CSP materials, especially highly filled CSP, which pose complex technological problems due to their sensitivity to fire hazard by mechanical stimuli. The viable method to exercise the safe machining operations on CSP grain, to control and maintain the cutting force at a prescribed safe level, is standardizing the cutting tool geometry as well as adjusting the machining parameters for minimum cutting energy simultaneously. To cater these functional and safety requirements of machining of hazard to machine CSP material, a custom build cutter called ‘turbine cutter’ is developed with suitable tool signature and by incorporating various safety features to mitigate the risk of hazard.

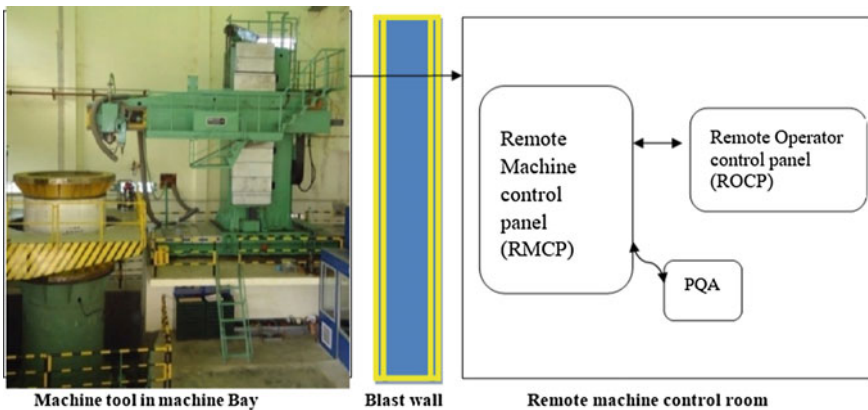
Data on process parameters on machining of CSP material is seldom found in the literature due to their strategic application and safety stringent and expensive infrastructure required to generate such data. Attempts are made in the present study to generate such valuable experimental data based on full factorial (27) experiments, using developed turbine cutter on special-purpose CNC VTM. The main goal of this study is to optimize the input machining parameters for desired performance characteristics, i.e., low cutting power (CP) and maximum material removal rate (MRR). Hence in the present study, response surface methodology (RSM) is used to develop desirability function for multi-response optimization of machining parameters for the two performance characteristics CP and MRR in milling of hazard to machine CSP materials. Mathematical models also developed for each response within the operating capacity of CNC VTM.

## 2 Experimental Method and Procedure

A special-purpose CNC VTM machine which can be operated and controlled remotely was used for experimentation whose illustration is shown in Fig. 1. Turbine cutter is connected to vacuum line of safety equipment called chip and dust collection system (CDCS) through a hollow arbour and rotary joint as shown in Fig. 1a for safe and instant chip disposal. Wu et al. [4] reported that the indirect measurement of cutting forces through cutting power is quite reasonable, economical, and it has an important application value with high compatibility in machining studies. Altintas [5] predicted cutting force and tool breakage in milling from feed drive current measurement while machining the metals. Kim et al. [6] investigated a simple and economical method to measure the cutting force indirectly, i.e., by measuring the power drawn by the servo motor drive of spindle in NC milling process and claimed to be the most economical solution compared to other alternatives. In line with the above references, for the present study cutting power is measured from the AC drive of spindle motor of SP CNC VTM machine using power quality analyser (PQA)—fluke makes. The schematic of general layout of experimental set-up is



(a) Cutter/arbour/CDCS setup



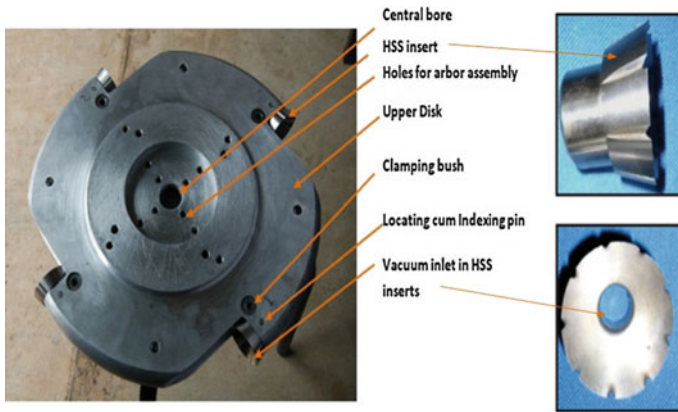
(b) Machine bay with control panels

Fig. 1 Schematic of machining experimental set-up for ‘hazard to machine’ materials

shown in Fig. 1. Monitoring and control of machining were done from this remote control room through remote operator panel as shown in Fig. 1b. CCTV cameras for visibility and safety interlocks of the machine are also employed in the experiments.

Experiments were conducted using a specially designed turbine cutter as shown in Fig. 2 on HTPB/AP/Al-based live CSP material of SRM. Customised conical HSS inserts in four numbers were integrated to the turbine shaped cutter as shown in Fig. 2. Due to explosive nature of the material, experiments were remotely monitored and controlled. Safe machining parameters were investigated by monitoring cutting temperature less than 50 °C using an infrared thermometer. The range of machining parameters and environmental conditions at which the experiments were conducted is summarized in Table 1.

Spindle power is measured from servo drives of the machine spindle using advanced power analyser having real-time electrical data acquisition system. These servo drives are located in the remote control room of the machine, isolating the machining ambience from source of electrical energies so as to eliminate the source of hazard. An additional machine inbuilt default display on operator panel as shown



**Fig. 2** Developed turbine cutter for CSP machining

**Table 1** Machining parameters and environmental factors

<i>Machining parameters</i>	
Cutting speed range	117–196 m/min
Rotary table feed	0.42–0.84 m/min
Depth of cut	2–4 mm
<i>Machining environment factors</i>	
Machine bay ambience temperature	28–32 °C
Relative humidity	75–85%
Coolant	Dry machining
Vacuum at the cutting edge	240 mm Hg below atm

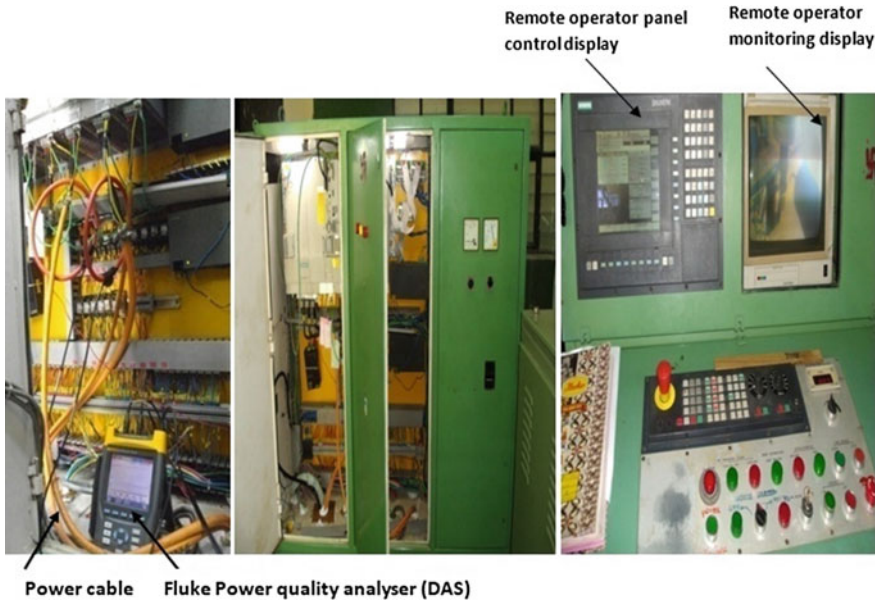


Fig. 3 Measurement of cutting power using PQA

in Fig. 3 was used as redundant provision for verification of measured cutting power values. MRR is measured from the volume of the chips collected in CDCS and CP in kW from PQA. The scheme of taping power from the machine power drives and measurement of CP using PQA is illustrated in Fig. 3. MRR is measured from the quantity of chips collected in CDCS.

### 3 Experimental Results and Analysis

Nayak and Shetty [7] used RSM for investigation of cutting force in elastomer machining under ambient and cryogenic conditions, and a similar approach is adopted in this study using commercial statistical software Design-Expert 7.1.0. With the limited and expensive resources, the possible approach would be to limit the number of levels to three (the minimum to study the nonlinear effects) and conducted full factorial experiments. However, the broad range was chosen in feed, speed range as limited by safety aspects and capabilities of resources as shown in Table 2.



**Table 2** Experimental factors and their levels

Parameters	Units	Levels		
		1	2	3
Cutting velocity (CV)	rpm (m/min)	75(117)	100(157)	125(196)
Table feed rate (TFR)	deg/min (m/min)	24(0.418)	36(0.628)	48(0.378)
Depth of cut (DoC)	mm	2	3	4

### 3.1 *Experimental Results*

The experiments conducted with the developed turbine cutter on live propellant and the results are as shown in Table 3.

### 3.2 *Analysis*

#### 3.2.1 **Analysis for Cutting Power**

The main effects of each parameter on CP are plotted on graphs shown in Fig. 4a–c. These figures clearly indicate the CP decreased with the increase in CV due to chip thinning and visco-elastic behaviour of CSP. CP increased with the increase in TFR and DoC due to resistance to large chip cross section.

#### 3.2.2 **Analysis for MRR**

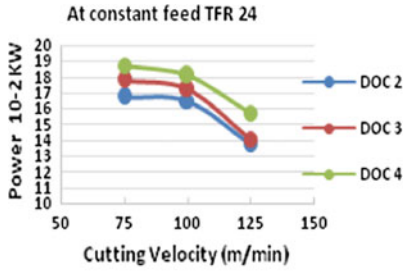
The main effects of each parameter on MRR are plotted on graphs shown in Fig. 5a–c. These figures clearly indicate the MRR increased with the increase in cutting velocity, table feed rate, depth of cut. However, depth of cut has large influence on MRR.

#### 3.2.3 **Analysis of Variance for Cutting Power and MRR and Its Regression Models**

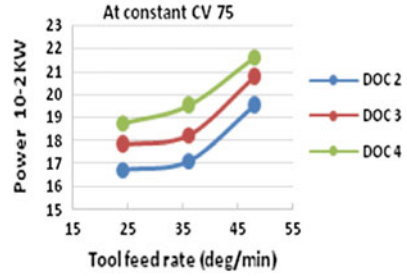
Since response cannot be assigned criteria, it has a model. ANOVA statistics and diagnostics graphs were used to check the design evaluation and to find the most influencing process parameters on cutting power. These tools are used to make sure the models provide a good estimate of the true response surface. From the results, it can be concluded that CV shows the most influencing process parameters on CP and is followed by TFR and DoC. ANOVA for MRR is shown that DoC is strongly influencing the MRR followed by CV and TFR. To obtain applicable and practical predictive quantitative relationships, it is necessary to model the machining responses

**Table 3** Experimental result

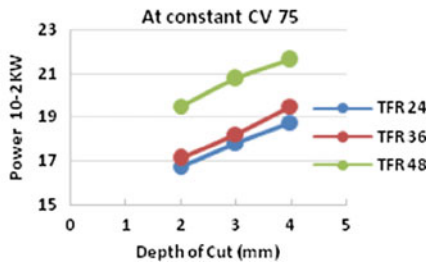
S. no.	CV (rpm)	TFR (deg/min)	DoC (mm)	CP (kW)	MRR (m <sup>3</sup> /min)	S. no.	CV (rpm)	TFR (deg/min)	DoC (mm)	CP (kW)	MRR (m <sup>3</sup> /min)
1	75	24	2	16.75	325.96	15	100	36	4	18.25	985.96
2	75	24	3	17.8	452.12	16	100	48	2	17.2	525.63
3	75	24	4	18.75	651.92	17	100	48	3	18.1	788.45
4	75	36	2	17.12	367.38	18	100	48	4	18.5	1051.27
5	75	36	3	18.23	551.07	19	125	24	2	13.75	546.05
6	75	36	4	19.5	734.76	20	125	24	3	14.12	819.08
7	75	48	2	19.5	391.71	21	125	24	4	15.75	1092.11
8	75	48	3	20.75	587.57	22	125	36	2	16	615.44
9	75	48	4	21.62	783.43	23	125	36	3	16.7	923.16
10	100	24	2	16.5	477.4	24	125	36	4	17.26	1230.88
11	100	24	3	17.25	656.1	25	125	48	2	16.5	656.2
12	100	24	4	18.1	904.12	26	125	48	3	17	984.31
13	100	36	2	16.81	492.98	27	125	48	4	17.5	1312.41
14	100	36	3	17.5	739.47	Cutting power: ( $\times 10^{-2}$ kW) MRR: (m <sup>3</sup> /min $\times 10^{-6}$ )					



(a) Main effects of cutting velocity on cutting power



(b) Main effects of feed rate on Cutting Power



(c) Main effect of Depth of Cut on Cutting Power

Fig. 4 Measurement of process parameters on cutting power

and the process variables. These models would be of great use during the optimization stage of milling of CSP materials

**Regression model for cutting power and MRR:**

$$\begin{aligned} \text{Cutting Power} = & 018 + (0.014 \times CV) - (0.0098 \times TFR) \\ & - (0.0083 \times DoC) + (0.0069 \times CV \times TFR) \end{aligned}$$

$$\begin{aligned} \text{MRR} = & 0.000728 - (0.00019 \times CV) + (0.00001 \times TFR) - (0.00024 \times DoC) \\ & + (0.0000128 \times CV \times TDR) + (0.000062 \times CV \times DoC) \\ & - (0.000011 \times TFR \times DoC) \end{aligned}$$

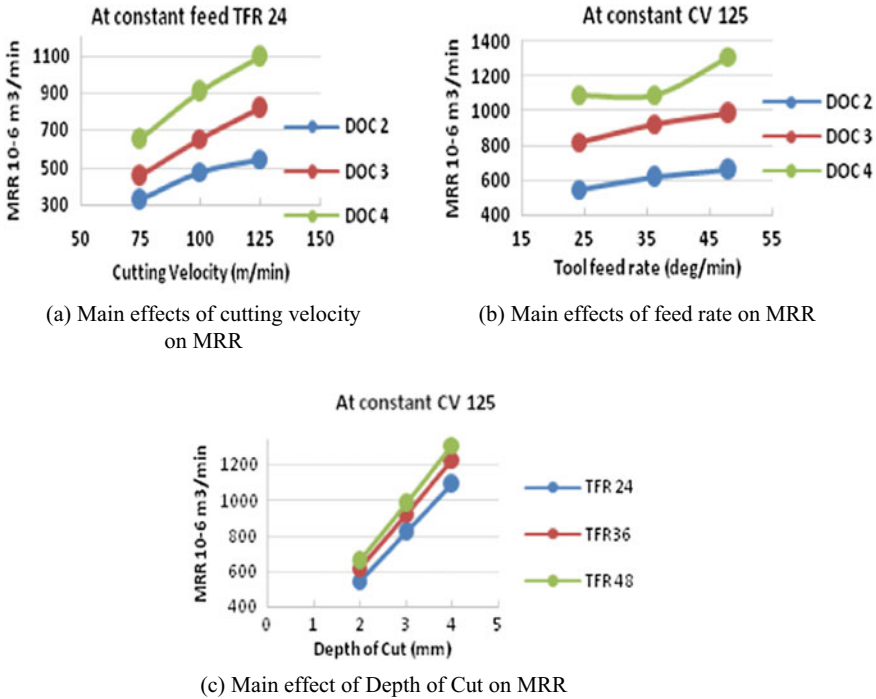


Fig. 5 Measurement of process parameters on MRR

### 3.3 Multi-response Optimization

The experimental results were used to model the various responses using multiple regression method and nonlinear fit among the responses and the corresponding significant parameters. In the present work, a commercially available statistical software Design-Expert 7.1.0 package was used for the computation of regression constants, parameters and mathematical modelling. In the present study, full factorial design, the most commonly used RSM design, is chosen for modelling and optimization to achieve the maximum MRR and minimum power. In RSM, a suitable approximation has been made to establish the relationship between the dependent and independent variables.

#### 3.3.1 Method Followed for Multi-response Optimization

The present approach uses desirability functions, after identification of performance characteristics, where independent desirability function for individual response will be made and combining them will form a two-sided desirability function. Solution to the two-sided desirability function will be the optimum combinations of parameters

for multi-response optimization. The present problem in the study is solved using the later one using Design-Expert software package, and the response yield is illustrated as follows.

### 3.3.2 Selection of Optimum Levels and Its Validation

Here, numerical optimization of process parameters for milling of CSP material with turbine cutter using Design-Expert (response surface methodology) is presented. The considered process parameters speed, feed, and depth of cut are optimized with considerations of multiple process characteristics including minimum cutting power and Maximum MRR. From Fig. 6, it can be concluded that for getting optimum condition, one can perform experiments at cutting velocity at level 3, table feed rate at level 1 and depth of cut at level 3 with desirability 0.88 from Fig. 6. Illustrated the graphical view of each optimal solution as ramps, optimal factor settings are shown with red points. Optimal response prediction values are displayed in blue.

### 3.3.3 Validation

The optimal parameter combination for achieving minimum cutting power and max MRR is obtained using the Design-Expert software is validated with the optimum conditions correlated with 21 run of the full factorial experiment shown in Table 3.

## 4 Conclusions

- Cutting power increases with the increase in DoC and TFR; this is because at larger feeds or DoC results, larger volume of the deformed material and consequently the resistance of the material to chip formation are greater. CP decreases with the increase in CV; this is because as CV increases, the following chips are thinner and shear angle increases and the increase in rake angle leads to decrease in tool-chip contact area; visco-elasticity, dewetting and dilation of CSP materials contribute for this result.
- MRR increases with the increase in CV, TFR and DoC; this is because at lower speeds, due to high coefficient of friction between tool and rubbery binder of work, material cutting forces are significantly high. In comparison with feed, the depth of cut influences largely on MRR.
- The finest combination of machining parameters values for maximizing the multiple performance characteristics is 125 m/min, 24 deg/min and 4 mm for CV, TFR and DoC, respectively. The result of optimum condition was correlated with the experiment results of full factorial experiments. The experimental results confirm the predicted results from mathematical modelling. The adopted approach for optimizing the cutting parameters was validated. The cutting power and MRR



Fig. 6 Constraints for the process parameters and performance characteristics and optimum levels

are  $15.75 \times 10^{-2}$  kW and  $1092.11 \times 10^{-6}$  m<sup>3</sup>/min, respectively, at the optimum machining parameters. The experimental results confirm the predicted results from mathematical modelling.

- The results of ANOVA have proved that the 2FI models can complete prediction of power and MRR with 95% confidence interval. Safe and effective cutting parameters for machining of CSP material using the developed cutter were established which has great value in production.

**Acknowledgements** The authors express their sincere thanks to GM, DRDO, Jagdalpur, and Director, NSTL, for the support of equipment and facility extended.

## References

1. Sutton GP, Biblarz O (1989) Rocket propulsion elements, 7th edn. Willey, New York
2. Nagappa R (2014) Evolution of solid propellant rockets in India. DRDO, Ministry of Defence, India (2014)
3. Devenas A (1992) Solid rocket propulsion technology. Pergmon Press, Oxford
4. Wu H, Turyagyenda G, Yang JG (2006) Modeling and real-time compensation of cutting force-induced errors in NC turning center, vol 315–316. Trans Tech Publications, Switzerland, pp 274–278
5. Altintas Y (1992) Prediction of cutting force and tool breakage in Milling from feed drive current measurement. ASME J Eng Ind 114:386–392
6. Kim T-Y, Woo J, Shin D, Kim J (1999) Indirect cutting force measurement in multi-axis simultaneous NC milling processes. Int J Mach Tools Manufact 39-11:1717–1731
7. Nayak R, Shetty S (2014) Investigation of cutting force in elastomer machining under ambient and cryogenic conditions using response surface methodology. In: III World conference on applied science, engineering and technology

# The Effect of ZrO<sub>2</sub> and TiO<sub>2</sub> Reinforcing Agent on the Microstructure and Mechanical Properties of Hydroxyapatite Nanocomposites



Vemulapalli Ajay Kumar, Penmetsa Rama Murty Raju, Nallu Ramanaiah and Siriyala Rajesh

**Abstract** The effect of additives like zirconia and titania on the mechanical properties of hydroxyapatite nanocomposites was investigated. Nanocomposites were manufactured through high-energy ball milling (HEBM) at 300 rpm for 1 h was adopted to produce the composite powders. The specimens were fabricated through compacting at 100 bar with a stay time of 150 s and sintered at 1200 °C. X-ray beam diffraction demonstrated that the crystallite and grain size estimate steadily diminished with the expansion in ZrO<sub>2</sub> and ZrO<sub>2</sub> + TiO<sub>2</sub> content till 20wt%, after which there was a sudden rise in crystallite and grain sizes of both the composites. An overwhelming ZrO<sub>2</sub> stage was seen in the X-ray beam diffraction (XRD) and smaller scale basic examination (Field Emission Scanning Electron Microscopy—FE-SEM) of the sintered samples. Mechanical properties were observed to be enhanced including 20wt% of ZrO<sub>2</sub> and ZrO<sub>2</sub> + TiO<sub>2</sub> at 1200 °C. There was a drop in the mechanical properties of HAp due to the expansion of 25 wt% of ZrO<sub>2</sub> and ZrO<sub>2</sub> + TiO<sub>2</sub> composites. The drop could be because of the expansion in grain size and prevailing particles of ZrO<sub>2</sub>.

**Keywords** High-energy ball milling · ZrO<sub>2</sub> · TiO<sub>2</sub> · Grain size · Mechanical properties

## 1 Introduction

Hydroxyapatite has been observed to be biocompatible and bioactive in the recent past. Its structure or compound arrangement is observed to be like human hard tissues, for example, bone and teeth [1]. HAp can give framework to the arrangement of the new bone tissues after implantation into the human body as a counterfeit

---

V. Ajay Kumar · P. Rama Murty Raju · S. Rajesh (✉)  
Department of Mechanical Engineering, S.R.K.R. Engineering College, China Amiram,  
Bhimavaram, AP 534204, India

N. Ramanaiah  
Department of Mechanical Engineering, A.U. College of Engineering, Andhra University,  
Visakhapatnam, AP 530003, India



material [2]. Calcium and phosphorous can be free from the material surface and absorbed by the body as new tissues. It is one of the vital viewpoints for human well-being in the field of drug and medical procedure. Among various classes of biomaterials, bioactive pottery, for example, HAp is appealing possibility for body's hard tissue substitution [3]. So as to enhance the mechanical properties of the HAp, expansion of nanoparticles has made an incredible intrigue. Among the available reinforcements,  $\text{TiO}_2$  and  $\text{ZrO}_2$  has been widely used for enhancing the mechanical properties of HAp composites [4]. Titanium oxide has been broadly utilized as biomaterial because of its incredible biocompatibility and superior corrosion resistance. Titanium oxide has been utilized to enhance the holding quality of the HAp layer and the Ti substrate, just as the high solidness, disintegration obstruction and erosion opposition [5]. Zirconia can be balanced out with different added substances, among which yttria and cerium are the most valuable stabilizers. Specifically, yttria-settled zirconia is known to be both hard and intense at room temperature [6, 7]. For better utilization of bioimplant,  $\text{Al}_2\text{O}_3$ ,  $\text{ZrO}_2$  and their composite ceramic have been considered as a lattice in the support stages because of their brilliant oxidation obstruction, great biocompatibility and wear opposition [8–10]. Que et al. [11] revealed the significant impact on the HAp structure and upgraded HAp properties on expansion of titania to HAp. The stage changes in the composites at higher sintering temperatures are seen because of the presentation of optional stages. Xihua et al. [12] described the manufacturing superior exhibitions of hydroxyapatite lattice ceramic composites with minimal effort, and alumina is presented in hydroxyapatite. Xihua et al. [13] observed the toughening effect of alumina on the mechanical properties of HAp bone bond. Guoa et al. [14] explored first of its thought, the creation of covered and practically evaluated HAp/Y-TZP composites by methods for the spark plasma sintering (SPS). The covered and practically evaluated HAp/Y-TZP (yttria balanced out tetragonal zirconia) composites are planned as a solid Y-TZP centre bioactive HAp layer structure, a non-symmetric Y-TZP layer to HAp later structure or a bioactive HAp centre solid Y-TZP layer structure. Aminzare et al. [15] considered the nanocomposite by high-vitality ball processing so as to acquire exceedingly thick articles with wanted mechanical properties. The impacts of alumina and titania nanoparticles on microstructure, stage deterioration and mechanical properties have been examined. Ahmed et al. [16] studied the HAp/ $\text{TiO}_2$  nanocomposites fabricated through HEBM. The impacts of titania expansion and sintering temperature and time on the shaped stages and their effect on the compressive quality of HAp were examined. Viswanath and Ravishankar [17] considered the interfacial responses in hydroxyapatite/alumina nanocomposite in which alumina responded totally with hydroxyapatite. Khalil et al. [18] contemplated HAp and HAp composites sintered at various temperatures by HFHS. The goal of their investigation was to blend and sinter HAp–3YSZ (yttria balanced out zirconia) powders with high hardness, high strength, fine grain estimate and homogeneous constituent conveyance. Oktar [19] considered the impact of sintering of composite materials, made of HAp, got from cow-like bone, with 5 and 10 wt% of  $\text{TiO}_2$ , on their mechanical properties. The exploratory outcomes uncovered that the created microstructure and the stages shaped amid sintering influence the densification and the mechanical properties of the delivered composite materials.

Mobasherpour et al. [20] confirmed a precipitation strategy to orchestrate nanocrystalline HAp and researched the impacts of ZrO<sub>2</sub>-Al<sub>2</sub>O<sub>3</sub> on the mechanical properties of nanocrystalline HAp powder. Byong et al. [21] considered Hap-(t-ZrO<sub>2</sub>)/Al<sub>2</sub>O<sub>3</sub>-(m-ZrO<sub>2</sub>) composite to enhance the mechanical properties utilizing the multi-pass expulsion process. Enhanced bowing and the rigidity of HAp by utilizing La<sub>2</sub>O<sub>3</sub>, ZrO<sub>2</sub> and TiO<sub>2</sub> as covers have been seen by Shin-Ike et al. [22]. Their investigation has demonstrated that doping can expand the bowing quality of HAp.

In the present investigation, the utilization of HEBM strategy to deliver HAp/ZrO<sub>2</sub> and HAp/ZrO<sub>2</sub> + TiO<sub>2</sub> nanocomposites and the impact of the expansion of ZrO<sub>2</sub> and ZrO<sub>2</sub> + TiO<sub>2</sub> to HAp on the miniaturized scale structure and mechanical quality of the composites were explored. The connection between the mechanical and small scale basic properties was methodically settled.

## 2 Materials and Methods

### 2.1 Sample Preparation

HAp and its composite powders of molecule size 20–40 nm are collected initially. Various weight %, i.e. 5, 10, 15, 20 and 25 wt. of ZrO<sub>2</sub> and ZrO<sub>2</sub> + TiO<sub>2</sub> were blended with HAp by HEBM at 300 rpm for 1 h. The processed powder was virus compacted at a weight of 100 bar with an abide time of 150 s. The powders were compacted to cylindrical shape of sizes 20 mm dia and 5 mm height for hardness and compression testing and square shape of sizes 40 × 10 × 3 mm (length × width × thickness) for flexural strength and fracture toughness testing. To solidify the samples, sintering was done at 1200 °C for 1 h in an electrical box furnace followed by furnace cooling.

### 2.2 Experimental Procedure

HAp and its composites are portrayed by X-ray beam diffractometer outfitted with Cu-K $\alpha$  radiation ( $\lambda = 1.5406 \text{ \AA}$ ). It was worked in the scope of 6–90° utilizing a stage size of 0.01°. Utilizing the deliberate width ( $\beta$ ) of their diffraction design, the normal crystallite measure ( $D$ ) was evaluated utilizing Scherer's recipe [16]. FE-SEM has been utilized to explore the miniaturized scale basic data. The synthesis of the components Ca, P, O and Zr is resolved utilizing energy dispersive analysis of X-ray beams (EDAX) joined with FE-SEM. The densities of the given composites were estimated utilizing Archimedes' standard. The compression test was completed under a semi-static stacking range, in which the underlying strain rate ( $\epsilon^*$ ) is set to  $0.001 \text{ s}^{-1}$ , i.e. the machine cross head speed ( $\dot{\nu} = \epsilon^* \cdot h_0$ ) is 0.005 mm/s, where  $h_0$  is the initial height of the specimen [16]. Knoop's hardness estimations of the cleaned

cross-areas of the HAp composites were performed utilizing the Shimadzu HMV-2000 miniaturized scale hardness analyser. A test heap of 4.905 N and a holding time of 15 s are utilized in the estimations as per ASTM E384. The indenter has a width to length proportion of 1:7.11. Its particular face plot for the long edge is 172°, and for the short edge is 130°. The space profundity is around (1/30)<sup>th</sup> of the more drawn out measurement.

The Knoop hardness ‘ $H$ ’ is communicated utilizing (Eq. 1) [14]

$$H = 14229 \frac{L}{d^2} \quad (1)$$

where ‘ $L$ ’ alludes to the load (in Newton), and ‘ $d$ ’ alludes to the longer diagonal of the indentation (in mm).

The elastic modulus ( $E$ ) (Eq. 2) over the reviewed composites was determined utilizing the accompanying condition [14]:

$$\frac{B'}{A'} = \frac{B}{A} - \alpha \frac{E}{H} \quad (2)$$

where  $B'/A'$  is the indent diagonal ratio after elastic recovery or after the indentation,  $B/A$  is the ratio of Knoop’s indenter dimensions (=1/7.11) and ‘ $\alpha$ ’ is a constant with a value of 0.045. The flexural strength of the nanocomposite was assessed through three-point bending test. The sintered examples (40 × 10 × 3 mm) were first arranged and cleaned to evacuate surface defects and after that put on a three-point bending testing set up. The heap (outline cross head speed of 0.05 mm/min) was connected from the best at centre purpose of the specimen.

Through the indentation technique, the fracture toughness ( $K_c$ ) (Eq. 3) was evaluated, and the qualities were controlled by utilizing the underneath condition [18]:

$$K_c = \xi * \left[ \frac{E}{H} \right]^{\frac{2}{5}} * \left[ \frac{P}{[d * l^{0.5}]} \right] \quad (3)$$

where ‘ $K_c$ ’ alludes to the fracture toughness, ‘ $E$ ’ is Young’s modulus and ‘ $H$ ’ is hardness (GPa). ‘ $P$ ’ alludes to the connected burden ( $N$ ), ‘ $\xi$ ’ alludes to the consistent that relies upon the geometry of the indenter ( $\xi = 0.0089$ ), ‘ $l$ ’ is the split length in mm and ‘ $d$ ’ is the half length of the indents.

### 3 Results and Discussion

#### 3.1 Microscopic Analysis

The morphologies of HAp and its composites are analysed by a FE-SEM. HAp is cross-connection with one another amid the development procedure, which gives a favourable condition to the grip and development of natural tissues. Figure 1 demonstrates XRD of HAp and standard HAp (PdF card no 74-0566). The watched diffraction example of HAp is in great concurrence with the standard HAp design, and no reflections from contaminations can be watched. At the point when unadulterated HAp is squeezed and sintered at 1200 °C, just pinnacles relating to HAp are distinguished, as appeared in Fig. 2. ZrO<sub>2</sub> powder is included and sintered under similar condition; more grounded pinnacles are identified alongside zirconium and HAp.

Fig. 1 XRD pattern of HAp sample and standard HAp

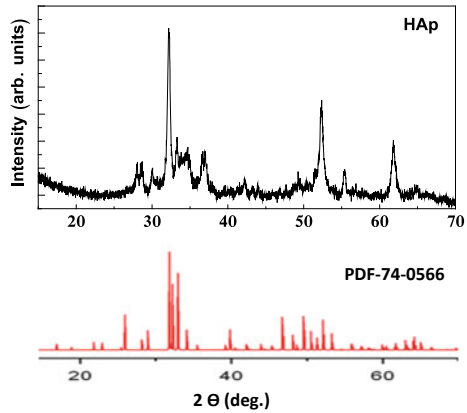
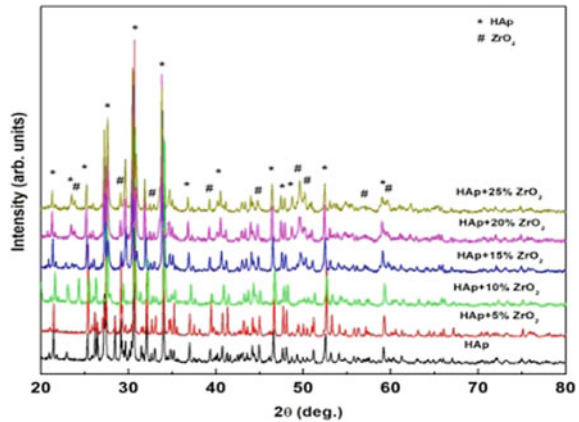
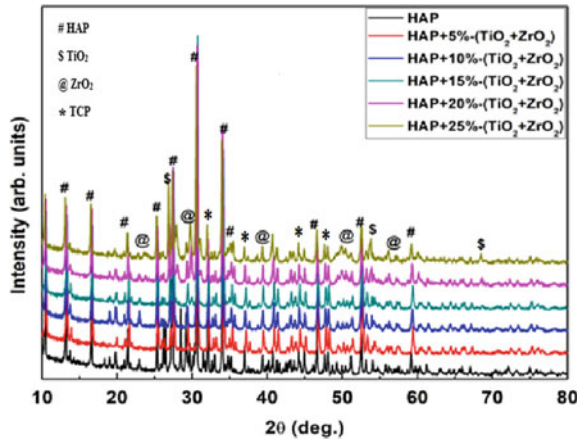


Fig. 2 XRD patterns of HAp/ZrO<sub>2</sub> composites after sintering



**Fig. 3** XRD patterns of HAP/ZrO<sub>2</sub> + TiO<sub>2</sub> composites after sintering



The ZrO<sub>2</sub> content of 5, 10, 15, 20 and 25 wt% is chosen to investigate the contribution of ZrO<sub>2</sub> in enhancing the properties of sintered composites. After compacting and sintering, the composition of the specimens sintered at 1200 °C is analysed by means of their XRD patterns which are shown in Fig. 2. The X-ray diffractograms of HAP and composites (ZrO<sub>2</sub> + TiO<sub>2</sub>) recorded are appeared in Fig. 3. The watched reflections were compared (HAP-set apart with '#') with its composites (TiO<sub>2</sub> (set apart with '\$') + ZrO<sub>2</sub> (set apart with '@')).

The observed increase in intensities of diffraction designs with expanding ZrO<sub>2</sub> + TiO<sub>2</sub> content is ascribed to ZrO<sub>2</sub> + TiO<sub>2</sub> structural stability. On expansion of ZrO<sub>2</sub> + TiO<sub>2</sub>, it is seen that ZrO<sub>2</sub> has appeared prevailing stage over TiO<sub>2</sub> which can be seen from the distinguished stages in Fig. 3. The crystallite sizes of all the diffraction designs are determined by utilizing Scherer's equation. HAp, in the majority of its applications is generally dictated by its morphology, piece and gem measure dissemination. Consequently, to control the mechanical properties of HAp, the impacts of combination conditions on such attributes as particles morphology and size conveyance just as morphology are much prescribed.

To know the effect of sintering on HAp and its composites, an investigation has been carried out by FE-SEM in Fig. 4. The analysis is performed both on sintered HAp and on the composites with ZrO<sub>2</sub>. The composites with ZrO<sub>2</sub> substance (various wt%) displays a remarkable development of adjusted molecule. Particles of ZrO<sub>2</sub> which are smaller in size are found to circulate in the framework, Fig. 4a-f. With increment in ZrO<sub>2</sub> content, the measure of ZrO<sub>2</sub> particles small in size expands which thoroughly adjusts the smaller scale auxiliary properties of the composites, Fig. 4. The adjustments in the smaller scale basic properties additionally influenced the mechanical properties of the composites.

In Fig. 5, HAp can be observed in the basic matrix with traces of melting. As stated earlier, the composites with ZrO<sub>2</sub> + TiO<sub>2</sub> contents also (5, 10, 15, 20 and 25 wt%) exhibit a unique growth of rounded particle which is small in size and the ZrO<sub>2</sub> + TiO<sub>2</sub> smaller particles are found to be distributed in the matrix, Fig. 5a-f. With

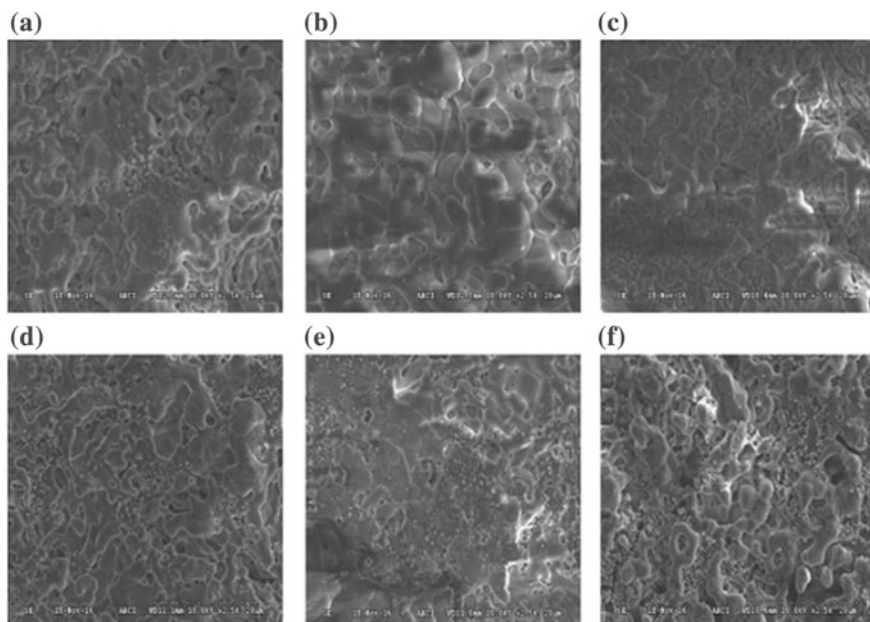


**Fig. 4** SEM images of **a** HAp and HAp/ZrO<sub>2</sub> composites, **b** 5 wt%, **c** 10 wt%, **d** 15 wt%, **e** 20 wt% and **f** 25 wt%

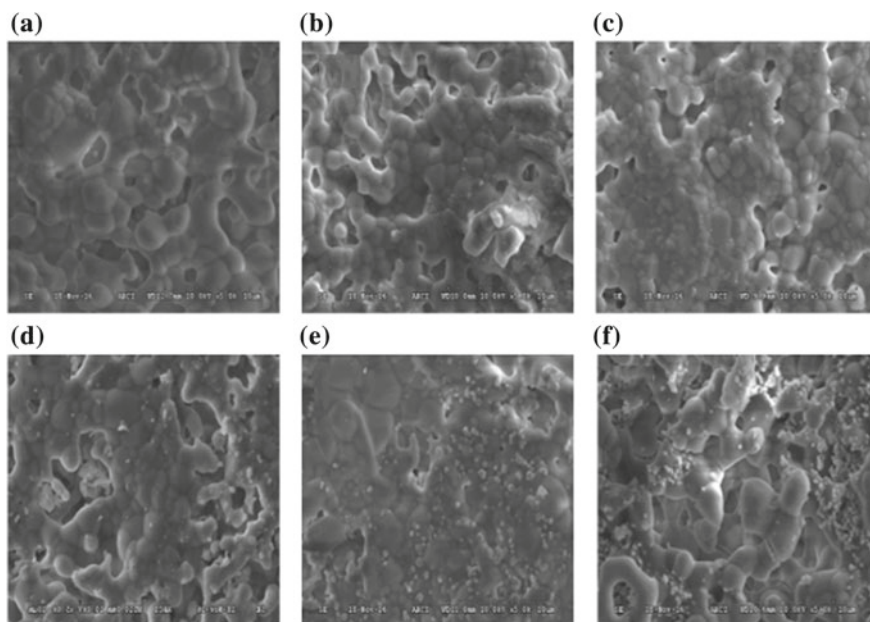


**Fig. 5** SEM images of **a** HAp and HAp/(TiO<sub>2</sub> + ZrO<sub>2</sub>) composites, **b** 5 wt%, **c** 10 wt%, **d** 15 wt%, **e** 20 wt%, **f** 25 wt%

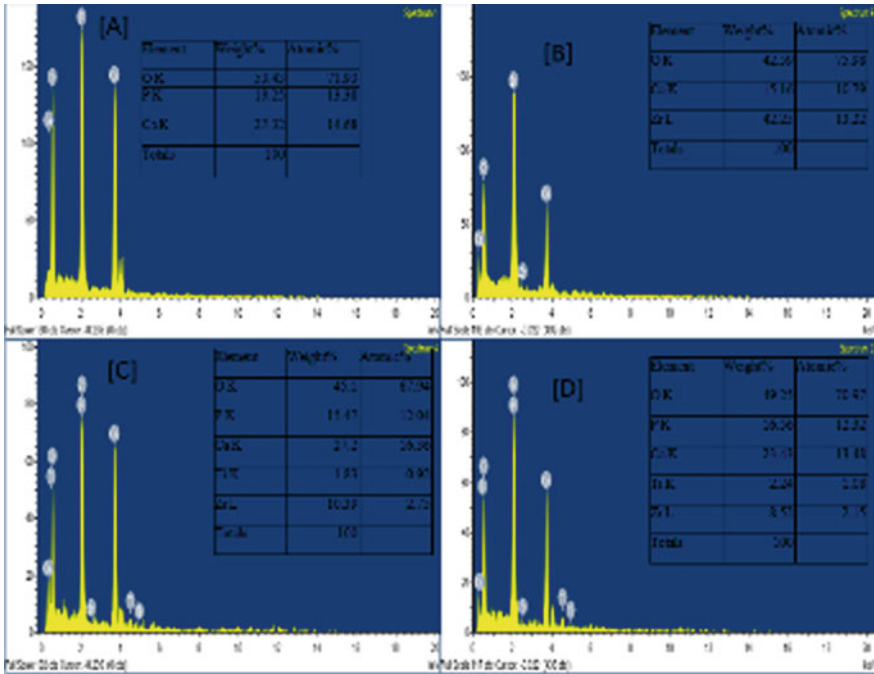


**Fig. 6** EDAX composition of **a** pure HAp and **b** HAp/20 wt% ZrO<sub>2</sub> and **c** HAp/10 wt% ZrO<sub>2</sub> + TiO<sub>2</sub> **d** HAp/15 wt% ZrO<sub>2</sub> + TiO<sub>2</sub>

the increase in ZrO<sub>2</sub> + TiO<sub>2</sub> content, the amount of rounded particles smaller in size also increased which in turn altered the micro-structural properties of the composites. Miao et al. [4] detailed the distending precious stones were recognized to be ZrTiO<sub>4</sub> compound, which was affirmed by the X-ray beam and EDX investigation. Figure 6a–b indicates EDAX investigation of HAp/ZrO<sub>2</sub> composite. The nearness Ca, P and Zr can be seen from the figure.

Figure 6c–d shows the EDX analysis of HAp/ZrO<sub>2</sub> + TiO<sub>2</sub> composite. The protruding crystals reveals Zr and Ti intensities in which background grains exhibited strong Zr intensity but weak Ti intensity, Fig. 6c–d. The XRD result shows the formation of the TCP phase matched well with the FE-SEM micrographs that showed the appearance of the protruding crystals. The above observations are in tune with the results obtained by Miao et al. [4] Fig. 7 shows the grain size of the composites evaluated from the ASTM line method [23]. It can be seen that there is a decline till 20 wt% past which a sudden increment has been seen with 25 wt%.

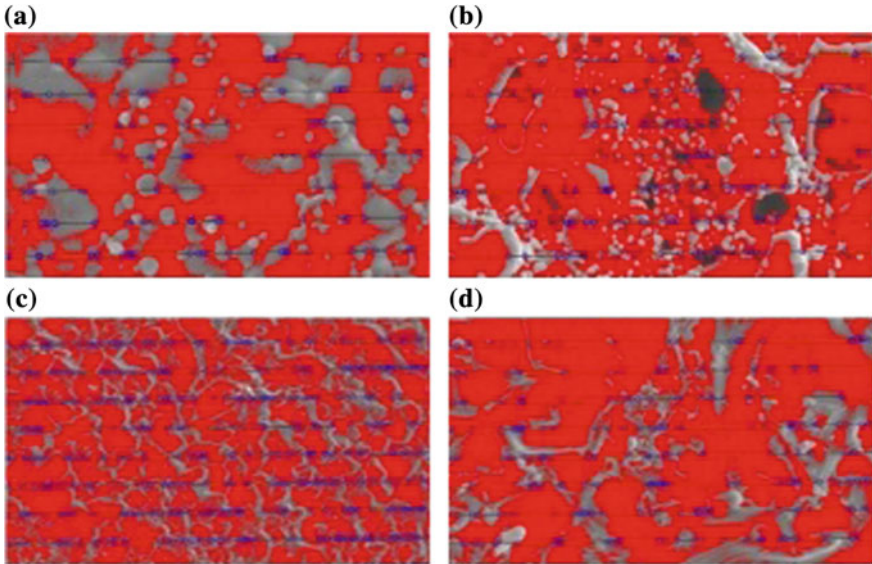
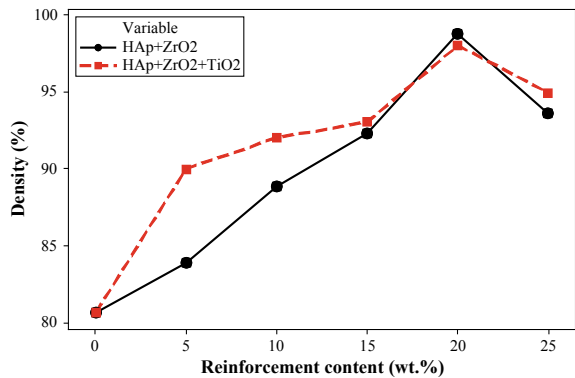


**Fig. 7** Grain size of the composites (ASTM line method) **a** HAp + 20wt%ZrO<sub>2</sub>, **b** HAp + 25 wt%ZrO<sub>2</sub> and **c** HAp/10 wt% ZrO<sub>2</sub> + TiO<sub>2</sub>, **d** HAp/15 wt% ZrO<sub>2</sub> + TiO<sub>2</sub>

### 3.2 Mechanical Properties

Based on the structural and morphological analysis, an attempt has been made to understand the formation mechanism of the composites ZrO<sub>2</sub> and ZrO<sub>2</sub> + TiO<sub>2</sub>. The measured density of HAp/ZrO<sub>2</sub> and HAp/ZrO<sub>2</sub> + TiO<sub>2</sub> composites is shown in Fig. 8. Determined densities of HAp/ZrO<sub>2</sub> and HAp/ZrO<sub>2</sub> + TiO<sub>2</sub>(various wt%) tests sintered at 1200 °C for 1 h are in close concurrence with hypothetical thickness. This can be credited to the expansion in the smaller particles of ZrO<sub>2</sub> stage with increment in ZrO<sub>2</sub> content as appeared in Fig. 4. The same pattern can be seen with

**Fig. 8** Variation of density in HAp/ZrO<sub>2</sub> and HAp/ZrO<sub>2</sub> + TiO<sub>2</sub> composites



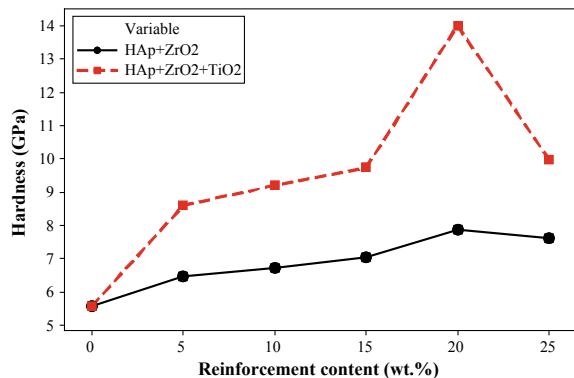


the HAp/ZrO<sub>2</sub> + TiO<sub>2</sub> nanocomposite. The thickness has appeared with straight increment with ZrO<sub>2</sub> just as with ZrO<sub>2</sub> + TiO<sub>2</sub> content till 20 wt%, after which it demonstrated a diminishing pattern. This affirms the most extreme thickness can be accomplished for both the composites, for example 20 wt%. This can be credited to the foundation grains with solid Zr intensity yet dominating Ti intensity [4] of HAp nanoorganizations, Fig. 5.

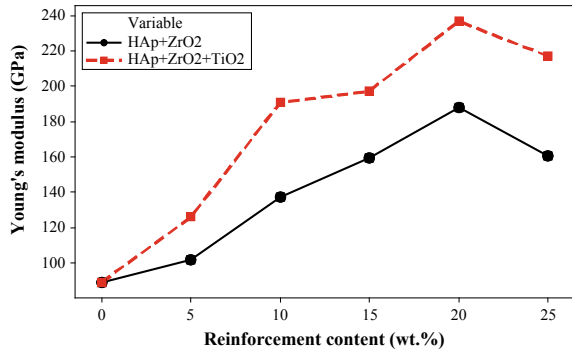
Khalil et al. [18] have mentioned comparative objective fact for HAp and HAp-20 vol.% 3YSZ composites, where sintering has been completed at various temperatures by HFIHS. The thickness of the examples is the capacity of sintering temperature, subsequently achieving most extreme at 1000 °C for HAp and 1100 °C for 20 vol.% 3YSZ-ZrO<sub>2</sub> and ZrO<sub>2</sub> + TiO<sub>2</sub> nanoparticles impacted on the mechanical properties of HAp. The impact of support on hardness of HAp has been concentrated as a component of thickness and grain measure. The hardness esteems are plotted against wt% of HAp composites as appeared in Fig. 9. The incremental hardness from 5.56 to 7.86 GPa has been found for the HAp and ZrO<sub>2</sub> composites. Among the composites of HAp and ZrO<sub>2</sub> (5, 10, 15, 20 and 25 wt%), most noteworthy hardness of 7.86 GPa is observed for the 20 wt% ZrO<sub>2</sub> content. It may be also seen that at 25 wt% of ZrO<sub>2</sub> content, a sudden increment in grain size, which brought the reduction in hardness. This is ascribed to the measure of HAp grain development that may be precluded as the measure of ZrO<sub>2</sub> content goes past 20 wt%. A comparable pattern has been observed for HAp/ZrO<sub>2</sub> + TiO<sub>2</sub> nanocomposite, the hardness of the composites HAp/ZrO<sub>2</sub> + TiO<sub>2</sub> expanded from 5.56 to 14.01 GPa, separately, with ZrO<sub>2</sub> + TiO<sub>2</sub> content. Among the composites, the most noteworthy hardness of 14.01 GPa was observed for the 20 wt% composite ZrO<sub>2</sub> + TiO<sub>2</sub> content. Knoop hardness was observed in great concurrence with the work directed by Guo et al. [14] and Salman et al. [24].

Figure 10 demonstrates elastic modulus of HAp/ZrO<sub>2</sub> and HAp/ZrO<sub>2</sub> + TiO<sub>2</sub> composites in sintered condition. Elastic modulus of the composites HAp and ZrO<sub>2</sub> are observed to be in the scope of 89.09–188.14 GPa. Whereas, for HAp/ZrO<sub>2</sub> + TiO<sub>2</sub> composites, elastic modulus(*E*) of the HAp composites was observed to be in the range of 89.09–328.08 GPa. Values of elastic modulus of HAp composites were

**Fig. 9** Variation of hardness in HAp/ZrO<sub>2</sub> and HAp/ZrO<sub>2</sub> + TiO<sub>2</sub> composites



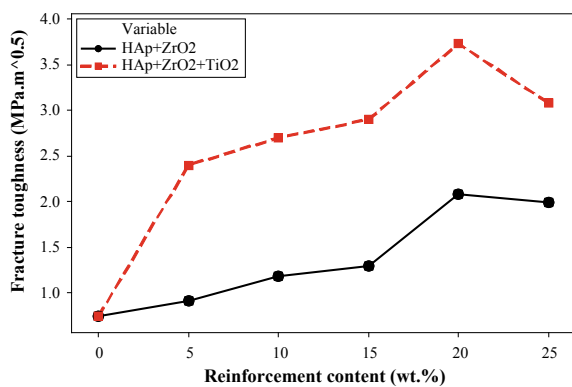
**Fig. 10** Variation of Young's modulus HAp/ZrO<sub>2</sub> and HAp/ZrO<sub>2</sub> + TiO<sub>2</sub> composites



increased with increased content of ZrO<sub>2</sub> and ZrO<sub>2</sub> + TiO<sub>2</sub>. For both the composites, the elastic modulus achieves a most extreme at 20 wt%, fortification substance pursued by a slight diminishing at 25 wt% composite. As clarified earlier, with increment in support content, grain measure diminishes and thickness increments thus hardness progressed. Que et al. [25] reported that the hardness and elastic modulus of the Pure HAp and the HAp/TiO<sub>2</sub> (10% mol) composites as an element of the sintering temperature. The most outstanding hardness and elastic modulus, which are 2.81 and 45.33 GPa separately, are obtained at the sintering temperature of 1100 °C.

Figure 11 demonstrates the relation between fracture strength of HAp/ZrO<sub>2</sub> and HAp/ZrO<sub>2</sub> + TiO<sub>2</sub> composites in sintered examples. Break sturdiness of HAp/ZrO<sub>2</sub> composite material are observed to be in the scope of 0.742 MPa m<sup>1/2</sup> to 2.08 MPa m<sup>1/2</sup>. Whereas for HAp/ZrO<sub>2</sub> + TiO<sub>2</sub> segments were observed to be in the range 0.742–3.73 MPa m<sup>1/2</sup>, for most extreme crack strength occurs at 20 wt% of composite material. These two HAp composites subsequently achieve a greatest at 20 wt%, trailed by a marginally decline at 25 wt% composite. Evidently, these outcomes are in great concurrence with consequences of hardness, elastic modulus and fracture durability which can be comprehended the advancement of the grain measure. Flexural strength information estimated utilizing three-point bend test uncovered that HAp

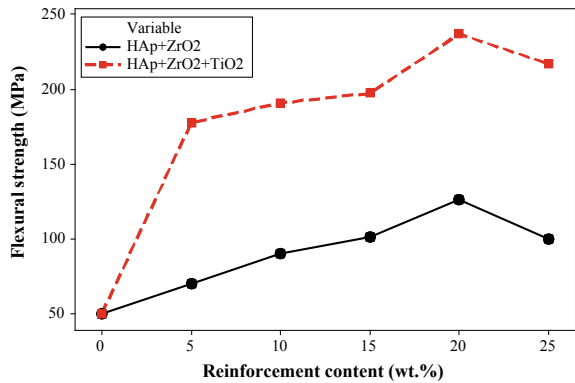
**Fig. 11** Variation of fracture toughness HAp/ZrO<sub>2</sub> and HAp/ZrO<sub>2</sub> + TiO<sub>2</sub> composites



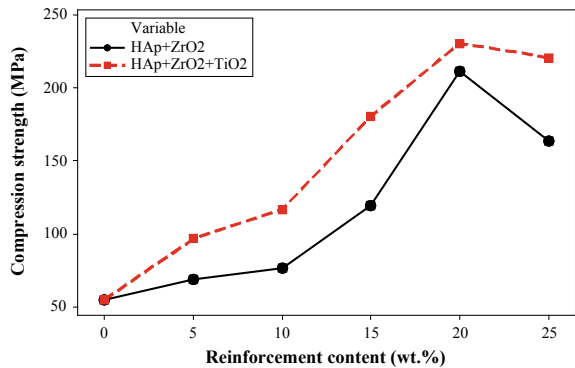
and HAp/ZrO<sub>2</sub> composite had flexural quality scope of 50 to 126.1 MPa. Additionally, flexural quality information uncovered that HAp/ZrO<sub>2</sub> + TiO<sub>2</sub> composites had flexural quality scope of 50–236.8 MPa, and separately, the most extreme flexural quality is seen at 20 wt% of composite after which it demonstrates a diminishing pattern as appeared in Fig. 12.

Figure 13 demonstrates that compressive qualities of HAp/ZrO<sub>2</sub> and HAp/ZrO<sub>2</sub> + TiO<sub>2</sub> with different wt%. HAp due to sintering, showed the base compressive quality of 54.72 MPa, and most extreme compressive quality of 211.4 MPa is accomplished for 20 wt% of ZrO<sub>2</sub>. A similar pattern has been seen with the HAp/ZrO<sub>2</sub> + TiO<sub>2</sub> having a greatest compressive quality of 230.67 MPa was accomplished for 20 wt%, after which it demonstrates a diminishing pattern as appeared in Fig. 13. It tends to be ascribed to the expansion in the scattering of fortification particles in the framework stage as seen from the small-scale basic highlights, Figs. 4 and 5. The results obtained in the current study are in good agreement with Salman et al. [24].

**Fig. 12** Variation of flexural strength HAp/ZrO<sub>2</sub> and HAp/ZrO<sub>2</sub>/TiO<sub>2</sub> composites



**Fig. 13** Variation of compression strength HAp/ZrO<sub>2</sub> and HAp/ZrO<sub>2</sub>/TiO<sub>2</sub> composites



## 4 Conclusions

The accompanying significant perceptions can be drawn from the present examination:

- Hardness estimations for HAp and ZrO<sub>2</sub> composites are 5.56–7.86 GPa, whereas the hardness estimations for HAp/ZrO<sub>2</sub> + TiO<sub>2</sub> composites are 5.56–14.01 GPa.
- The elastic modulus of the sintered HAp/ZrO<sub>2</sub> composites is from 89.09 to 188.14 GPa, whereas for the sintered HAp/ZrO<sub>2</sub> + TiO<sub>2</sub> composites are from 89.09 to 328.08 GPa.
- The fracture toughness HAp and ZrO<sub>2</sub> composites is observed to be in the range of 0.742–2.08 MPa m<sup>1/2</sup>, and for HAp/ZrO<sub>2</sub> + TiO<sub>2</sub> composites, fracture toughness was observed to be in the range of 0.742–3.73 MPa m<sup>1/2</sup>.
- The flexural quality of HAp/ZrO<sub>2</sub> composites enhanced from 50 to 126.1 MPa while the flexural quality of HAp/ZrO<sub>2</sub> + TiO<sub>2</sub> composites was found to increasing from 50 to 236.8 MPa.
- The compression strength of HAp/ZrO<sub>2</sub> composites for 20 wt% expansion is 211.4 MPa essentially higher than unadulterated HAp, while the compression strength of the 20 wt% HAp/ZrO<sub>2</sub> + TiO<sub>2</sub> composites is 230.67 MPa which higher than unadulterated HAp and HAp/ZrO<sub>2</sub>.
- Enhanced mechanical properties have been obtained with the expansion of (ZrO<sub>2</sub> + TiO<sub>2</sub>) to HAp composites. The acquired properties are turned out to be superior to HAp/ZrO<sub>2</sub> composites. The examined biocomposite materials can be utilized for implant applications.

## References

1. Pushpakanth S, Sriinivasan B, Sreehar B, Sastry TP (2008) An in situ approach to prepare nanorods of Titania-Hydroxyapatite nano composite by micro wave hydrothermal technique. *Mater Chem Phys* 107:492–498
2. Xihua Z, Changxia L, Musen L, Yunqiaiang B, Junlong S (2008) *Ceram Int* 35:1969
3. Mian X, Hu Y, Liu J, Huang X (2007) Hydroxyapatite coating on porous zirconia. *Mater Sci Eng C* 27:257–261
4. Miao Xigeng, Sun Dan, Hoo PuiWoon, Liu Jiani, Chea Yanming (2004) Effect of titania addition on Yttria-stabilised tetragonal zirconia ceramics sintered at high temperatures. *Ceram Int* 30:1041–1047
5. Faratash B, Liao H, Li J, Fouda N, Hermansson L (1995) Long-term evaluation of titania-based ceramics compared with commercially pure titanium in vivo. *J Mater Sci Mater Med* 6(8):451–454
6. Fu L, Khor KA, Lim JP (2002) Effects of yttria-stabilized zirconia on plasma-sprayed hydroxyapatite/yttria-stabilized zirconia composite coatings. *J Am Ceram Soc* 85(4):800–806
7. Wen C, Xu W, Hu W, Hodgson P (2007) Hydroxyapatite/titania sol-gel coatings on titanium zirconium alloy for biomedical applications. *Acta Biomater* 3:403–410
8. Lee BT, Sarkar SK, Gain AK, Yim SJ, Song HY (2006) Core/Shell volume effect on the micro structure and mechanical properties of fibrous Al<sub>2</sub>O<sub>3</sub>-(m-ZrO<sub>2</sub>)/t-ZrO<sub>2</sub> composites. *Mater Sci Eng A* 432:317–323

9. Gain AK, Lee BT (2006) Micro structure control of continuously porous t-ZrO<sub>2</sub> bodied fabricated by multi pass extrusion process. *Mater Sci Eng A* 419:269–275
10. Lee BT, Jang DH, Kang IC, Lee CW (2005) Relation between micro structures and mechanical properties of novel fibrous Al<sub>2</sub>O<sub>3</sub>-(m-ZrO<sub>2</sub>)/t-ZrO<sub>2</sub> composites. *J Am Ceram Soc* 88:2874–2878
11. Que W, Khor KA, Xu JL, Yu LG (2008) Hydroxyapatite/titaniana-nocomposites derived by combining high-energy ball milling with spark plasma sintering processes. *J Eur Ceram Soc* 28:3083–3090
12. Xihua Z, Changxia L, Musen L, Yunqiang B, Junlong S (2009) Fabrication of Hydroxyapatite/diopside/alumina composites by hot-press sintering process. *Ceram Int* 35:1969–1973
13. Yu W, Wang X, Zhao J, Tang Q, Wang M, Ning X (2015) *Ceram Int* 41:10600
14. Guoa H, Khorb K, Boeya YC, Miaoa X (2003) Laminated and functionally graded hydroxyapatite/yttria stabilized tetragonal zirconia composites fabricated by spark plasma sintering, *Bio Mater* 24:667–675
15. Aminzare M, Eskandari A, Baroonian MH, Berenov A, Razavi Z (2013) Hydroxyapatite nanocomposites: synthesis, sintering and mechanical properties. *Ceram Int* 39:2197–2206
16. Hannora AE, Ataya S (2016) Structure and compression strength of Hydroxyapatite/titanianano composites formed by high energy ball milling. *J Alloys Compd* 658:222–233
17. Viswanath B, Ravishankar N (2006) Interfacial reactions in hydroxyapatite/alumina nanocomposites. *ScriptaMaterialia* 55:863–866
18. Khalil KA, Kim SW, Kim HY (2007) Consolidation and mechanical properties of nanostructured hydroxyapatite (ZrO<sub>2</sub> + 3 mol%Y<sub>2</sub>O<sub>3</sub>) bioceramics by high frequency induction heat sintering. *J Mater Sci Eng A* 456:368–372
19. Oktar FN (2006) Hydroxyapatite–TiO<sub>2</sub> composites. *Mater Lett* 60:2207–2210
20. Mobasherpour I, SolatiHashjin M, RazaviToosi SS, Darvishikamachali R (2009) Effect of the addition ZrO<sub>2</sub>-Al<sub>2</sub>O<sub>3</sub> on nano crystalline Hydroxyapatite bending strength and fracture toughness. *Ceram Int* 25:1569–1574
21. Lee B-T, Lee C-W, Yeon M-H, Song HY (2007) Relationship between microstructure and mechanical properties of fibrous Hap-(t-ZrO<sub>2</sub>/Al<sub>2</sub>O<sub>3</sub>-(m-ZrO<sub>2</sub>) composites. *Mater Sci Eng A* 458:11–16
22. Shin-Lke M, Tsutsui J, Tanaka A, Murayama S, Fujita A (1989) Attempts to improve the strength of sintered lanthanum-containing hydroxyapatites. *J Osaka Odontol Soc* 52:854
23. Standard Test Methods for Determining Average Grain size Designation: E 112-96 (ASTM International)
24. Salman S, Gunduz O, Yilmaz S, Ovecoglu ML, Snyder RL, Oktar FN, Agathapoulos S (2009) *Ceram Int* 35:2965
25. Wenxiuque Q, Khor KA, Xu JL, Yu LG (2008) Hydroxyapatite/titania nanocomposites derived by combining High-energy ball milling with spark plasma sintering processes. *J Eur Ceram Soc* 28:3083–3090

# Optimization of Machining Parameters for Vibration-Assisted Turning of Ti6Al4V Alloy Using Analysis of Variance



D. Venkata Sivareddy, P. Vamsi Krishna and A. Venu Gopal

**Abstract** In this study, Taguchi-based analysis of variance (ANOVA) is adopted for optimization of lower-frequency vibration-assisted turning (LVAT) process parameters such as cutting speed, frequency, amplitude, and feed rate. Machining parameters are analyzed by evaluating maximum cutting force and tensile maximum circumferential residual stress (MCRS) in VAT of Ti6Al4V alloy. Finite element simulations are performed in ABAQUS according to  $L_{27}$  orthogonal array to find the optimum condition for maximum cutting force and MCRS (tensile). Results show that the vibrating parameters, frequency, and amplitude are most significant for maximum cutting force and MCRS (tensile), respectively. The optimum condition is obtained at 30 m/min of cutting speed, 150  $\mu\text{m}$  of amplitude, 600 Hz of frequency, and 0.05 mm/rev of feed rate for cutting force while the optimum condition for MCRS (tensile) is 45 m/min of cutting speed, 50  $\mu\text{m}$  of amplitude, 200 Hz of frequency, and 0.15 mm/rev of feed rate.

**Keywords** Vibration-assisted turning · Ti6Al4V alloy · Finite element modeling · ANOVA · Optimization

## 1 Introduction

Ti6Al4V is the most commonly used material in aerospace, automotive and medical industry due to its inherent properties like high strength-to-weight ratio and its corrosion resistance. Machinability of Ti6Al4V alloy in conventional turning (CT) is poor due to its high chemical affinity with cutting tool materials and low thermal conductivity which results in accumulation of heat generated during machining. Consequently, cutting tool causes rapid tool wear which results in poor surface finish and enhanced cutting forces. Vibration-assisted turning (VAT) is a promising machining process for high strength materials in which vibrations are superimposed

---

D. Venkata Sivareddy (✉) · P. Vamsi Krishna · A. Venu Gopal  
Department of Mechanical Engineering, National Institute of Technology Warangal, Warangal  
506004, India  
e-mail: [dvsivareddy2006@gmail.com](mailto:dvsivareddy2006@gmail.com)

© Springer Nature Singapore Pte Ltd. 2020  
H. K. Voruganti et al. (eds.), *Advances in Applied Mechanical Engineering*,  
Lecture Notes in Mechanical Engineering,  
[https://doi.org/10.1007/978-981-15-1201-8\\_77](https://doi.org/10.1007/978-981-15-1201-8_77)

on movement of the cutting tool [1, 2]. The fundamental feature of VAT is intermittent contact between tool and the workpiece at periodic intervals. This improves tool life and surface finish of machined component.

The stresses induced during machining remain even after the retrieval of the cutting tool from workpiece and are termed as residual stress. The generation of residual stress is due to thermoplastic deformation of material that occurs during thermo-mechanical loading. Plastic deformation of workpiece and friction between chip-tool interface acts as the main source of mechanical and thermal loads [3]. However, the stresses generated during machining can be either tensile or compressive. The residual stresses developed on machined surface will extend from surface of cut to certain depth will depend upon cutting conditions [4]. The tensile residual stresses generated on machined surface will have detrimental effect by initiating crack propagation. Hence, the fundamental mechanism and nature of residual stresses that develop due to VAT should be analyzed to enhance the performance. Few researchers worked to optimize the machining parameters for generation of residual stresses. Fu et al. [5] studied the effect of depth of cut and tool geometry on residual stresses. They found that compressive residual stresses were developed with an increase in nose radius and rake angle. Capello et al. [6] investigated the effect of tool geometry and machining conditions on residual stresses in turning by developing the empirical methodology. Naresh et al. [7] studied the effect of workpiece hardness on residual stresses and also discussed the variation of residual stresses in machined component from tensile to compressive with an increase in depth direction.

From the literature, it is found that there is no unique agreement between researchers with respect to the effect of machining parameters on the generation of residual stresses. It is also observed that very few works have been discussed the optimization of machining parameters for minimum residual stress generation in VAT process. In this study, a 3D FE model is developed in ABAQUS for both CT and VAT. An attempt is made to optimize the machining and vibration parameters for reducing maximum cutting force and tensile maximum circumferential residual stresses (MCRS). Taguchi experimental design is used to select simulations for VAT of Ti6Al4V alloy. Results obtained from simulations are analyzed with analysis of variance (ANOVA) to achieve the optimum machining conditions. ANOVA is applied to know the most influencing input parameter on output responses. Finally, confirmation tests are performed at optimum conditions.

## **2 FE Simulation of Ultrasonic Vibration-Assisted Turning**

### **2.1 FE Model**

A 3D FE orthogonal machining model is developed using ABAQUS. The workpiece and cutting tool materials considered for this model are Ti6Al4V alloy and tungsten carbide (WC), respectively. The workpiece is considered as isotropic plastic

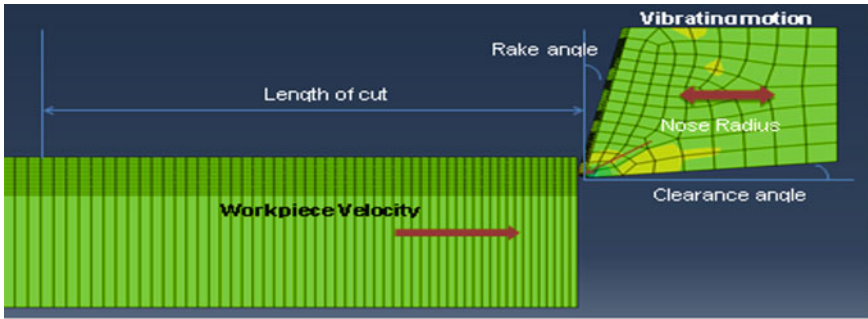


**Fig. 1** FE modeling of orthogonal vibration-assisted turning

material, whereas cutting tool is taken as rigid with rake angle of 10° and clearance angle of 5°.

In FE simulation, the type of element selected is an eight-node coupled temperature–displacement trilinear brick element; C3D8RT in ABAQUS is used to facilitate both mechanical and thermal analysis with reduced integration and hourglass control. The workpiece is meshed with approximately 6800 elements with element deletion. In vibration-assisted turning, 20 kHz frequency and 15 μm amplitude are imposed on cutting tool. Figure 1 shows the relative movement between tool and workpiece in FE modeling of VAT process.

In this FE model, workpiece moves with cutting speed,  $V_c$  is equal to 50 m/min. Kinematic boundary conditions are applied to bottom, left side, and right side of workpiece, whereas the top surface is free. The kinematic condition for workpiece at top surface is  $V_x = V_c$  and  $V_y = 0$ . The cutting tool is immovable for conventional turning, whereas it vibrates harmonically in cutting velocity direction during ultrasonic vibration-assisted turning simulation process as given by

$$v_x = -a \cos \omega t \text{ and}$$

$$v_y = 0$$

where angular velocity  $\omega = 2\pi f$ .

The cutting tool vibration velocity =  $a \omega \sin \omega t$  and  $a \omega = 1885 > V_c$  (800 mm/s). This satisfies the condition for separation of cutting tool from workpiece during harmonic vibrations.

## 2.2 Johnson Cook Material Model

The simulated results obtained from Johnson Cook (JC) material model are in close agreement with experimental results. This JC model considers the effect of material



hardening at constant strain rate condition and strain rate effect due to thermal softening in an adiabatic heating condition. This JC model represented in Eq. (1) gives relation between the equivalent stress as a function of strain hardening, strain rate, and thermal softening [5].

$$\sigma_{eq} = [A + B(\epsilon)^n] \left[ 1 + C \times \ln\left(\frac{\dot{\epsilon}^o}{\dot{\epsilon}_0^o}\right) \right] \left[ 1 - \left(\frac{T - T_{room}}{T_{Melt} - T_{room}}\right)^m \right] \quad (1)$$

### 2.3 Separation Criteria and Damage Equation

According to JC model, the chip separation and crack initiation in FE model are based on plastic strain at element integration point is given by Eq. (2)

$$D = \sum \left( \frac{\Delta \epsilon_p}{\epsilon_f} \right) \quad (2)$$

where  $D$  is damage parameters;  $\Delta \epsilon_p$  the incremental plastic strain which is updated at every analysis increment;  $\epsilon_f$  is an equivalent plastic strain in damaged element and strain rate  $\dot{\epsilon}_p$  and temperature  $T$  as given by Eq. (3).

$$\epsilon_f = \left[ D_1 + D_2 \exp\left(D_3 \frac{p}{q}\right) \right] \left[ 1 + D_4 \ln\left(\frac{\dot{\epsilon}_p}{\dot{\epsilon}}\right) \right] [1 + D_5 T^*] \quad (3)$$

where  $D_i$  ( $i = 1, 2, 3, 4, 5$ ) are JC material damage coefficients and its corresponding values for Ti6Al4V alloy are given in Table 1.

**Table 1** Material modeling and JC model parameters used in the simulation model

Density		4420 kg/m <sup>3</sup>				
Conductivity		7.264 W/m-°C				
Young's modulus		114 GPa				
Specific heat		526 kJ/kg-°C				
<i>JC-Parameters</i>						
A	B	C	n	m	Melting temperature	Strain rate
724.7	683.1	0.035	0.47	1	1650 °C	2000 s <sup>-1</sup>
<i>Damage parameters</i>						
D1		D2	D3		D4	D5
-0.09		0.28	0.48		0.014	3.18

### 2.4 Model Validation

A 3D FE model developed for VAT process is validated with experimental results available in literature [7]. Variation in cutting force and cutting temperature are observed to be 3.2% and 8.04%, respectively, in case of CT compared to experimental results, whereas the same are found to be 7.2% for force and 3.1% for temperature, respectively, in case of VAT. Variation in equivalent stress is observed to be 3.9% for CT and 5.9% for VAT, which is less than 10% in all cases as shown in Table 2 and Fig. 2.

**Table 2** Comparison of results from simulation and experimentation for CT and VAT

Process	Comparison	Stress (MPa)	Force (N)	Temp (°C)
CT	Literature Experiment	–	153	410
	Literature simulation (2D)	1340	160	420
	Present simulation (3D)	1392	158	443
VAT	Literature Experiment	–	110	330
	Literature simulation (2D)	1360	140	265
	Present simulation (3D)	1279	102	340

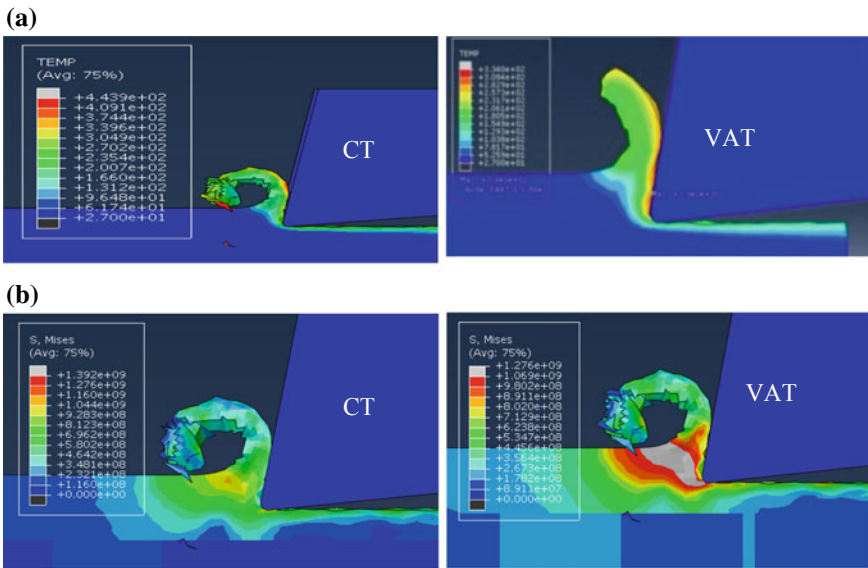


**Fig. 2** Comparison between CT and VAT **a** cutting temperature and **b** equivalent stress

**Table 3** Machining parameters and their levels for simulation with Ti6Al4V alloy

Parameters	Level 1	Level 2	Level 3
Cutting speed (A), m/min	30	45	60
Amplitude (B), $\mu\text{m}$	50	100	150
Frequency (C), Hz	200	400	600
Feed rate (D), mm/rev	0.05	0.1	0.15

## 2.5 Taguchi Experimental Design

Taguchi experimental design is used for optimization of machining parameters for low-frequency vibration-assisted turning (LVAT). The levels of machining parameters, such as cutting speed, frequency, amplitude, and feed rate, considered for LVAT process are selected to cover wide range of machining conditions as given in Table 3. The selected parameters have no interaction among them. The response parameters considered for this work are maximum cutting force and tensile maximum circumferential residual stress (MCRS-Tensile). According to Fraley et al. [8], Taguchi  $L_{27}$  ( $3^4$ ) array with four control parameters with three levels is used for this study.

## 3 Results and Discussion

The 3D FE model is developed in ABAQUS and simulations are conducted to study the machining parameters effect such as cutting speed, frequency, amplitude, and feed rate on maximum cutting force and MCRS (tensile) in LVAT of Ti6Al4V alloy. Table 4 shows the simulation results of 27 trails from  $L_{27}$  array.

### 3.1 Analysis of Process Parameters

In this technique, the output responses are transformed to average signal-to-noise ratio, delta, rank, and optimum level. The average  $S/N$  is used to measure the deviation of the response from the mean value. The response that is to be maximized is called larger-the-better and response that is to be minimized is called smaller-the-better. Rank is assigned to each factor according to its delta value. SNR characteristics, larger-the-better and smaller-the-better are calculated using Eqs. (4) and (5).

$$\eta = -10 \log_{10} \left( \frac{1}{n} \right) \sum_{i=1}^n \frac{1}{\sigma_i^2} \quad (4)$$

$$\eta = -10 \log_{10} \left( \frac{1}{n} \right) \sum_{i=1}^n \sigma_i^2 \quad (5)$$

**Table 4** Simulation results for max. cutting force and MCRS (tensile) at various machining conditions

Trial no	Speed (m/min)	Amplitude (μm)	Frequency (Hz)	Feed (mm/rev)	Max. cutting force (N)	MCRS (tensile) (MPa)
1	30	50	200	0.05	190	410
2	30	50	400	0.1	180	435
3	30	50	600	0.15	172	445
4	30	100	200	0.1	175	431
5	30	100	400	0.15	180	436
6	30	100	600	0.05	150	449
7	30	150	200	0.15	165	435
8	30	150	400	0.05	151	460
9	30	150	600	0.1	145	462
10	45	50	200	0.1	210	374
11	45	50	400	0.15	182	388
12	45	50	600	0.05	162	402
13	45	100	200	0.15	187	405
14	45	100	400	0.05	177	429
15	45	100	600	0.1	168	440
16	45	150	200	0.05	175	401
17	45	150	400	0.1	168	407
18	45	150	600	0.15	158	416
19	60	50	200	0.15	224	358
20	60	50	400	0.05	174	378
21	60	50	600	0.1	165	381
22	60	100	200	0.05	228	477
23	60	100	400	0.1	215	475
24	60	100	600	0.15	200	452
25	60	150	200	0.1	193	385
26	60	150	400	0.15	178	397
27	60	150	600	0.05	150	422

where  $n$  represents the average SNR of simulated values that indicates the simulated value of the  $i$ th simulation and  $n$  is the total no. of simulations. In order to observe the practical significance of machining parameters on responses, max. cutting force and MCRS (tensile), ANOVA is performed at 95% confidence level. The larger value of percentage contribution indicates the most significant on output parameters.

### 3.1.1 Effect of Parameters on Maximum Cutting Force

The response data for SNR and ANOVA of maximum cutting force are presented in Tables 5 and 6. From ANOVA results, it is observed that the influence of frequency (38.12% of contribution) on cutting force is more, whereas the influence of amplitude (28.63% of contribution) and cutting speed (20.69% of contribution) is less on cutting force. Figure 3 shows the variation of cutting force with cutting speed, feed rate, amplitude, and frequency.

As the frequency increases, it causes reduction in force due to less time of contact which allows the reduction in friction due to pulsating characteristics of VAT. Hence, in VAT process, frequency is more influencing parameter compared to other parameters. As the cutting speed increases, the rate at which workpiece is interacting with the cutting tool also increases which in turn increases the friction and so the cutting force. Therefore, lower value of cutting speed is preferred for low cutting force. As the amplitude value increases, the time of lapse also increases which allows the workpiece to relieve its stresses causing less cutting force. Therefore, higher value of amplitude is preferred. As the feed increases, the cutting force increases due to the higher interaction time at certain positions. So, lower value of feed is preferred.

**Table 5** Response table for SNR of max. cutting force

Level	Factors			
	Cutting speed (m/min)	Amplitude ( $\mu\text{m}$ )	Frequency (Hz)	Feed rate (mm/rev)
1	-44.45	-45.27	-45.71	-44.69
2	-44.90	-45.36	-44.99	-45.04
3	-45.58	-44.30	-44.22	-45.20
Delta	1.13	1.05	1.49	0.51
Rank	2	3	1	4
Optimum	1	3	3	1

**Table 6** ANOVA table for max. cutting force using SN data

Factors	DOF	SSTR	MSTR	F-Test	% Contribution (P)
Cutting speed	2	5.862	2.9310	10.25	20.69
Amplitude	2	6.128	3.0642	10.72	28.63
Frequency	2	9.950	4.9752	17.40	38.12
Feed rate	2	1.248	0.6239	2.18	4.40
Error	18	5.146	0.2859		8.16
Total	26	28.334			100.00

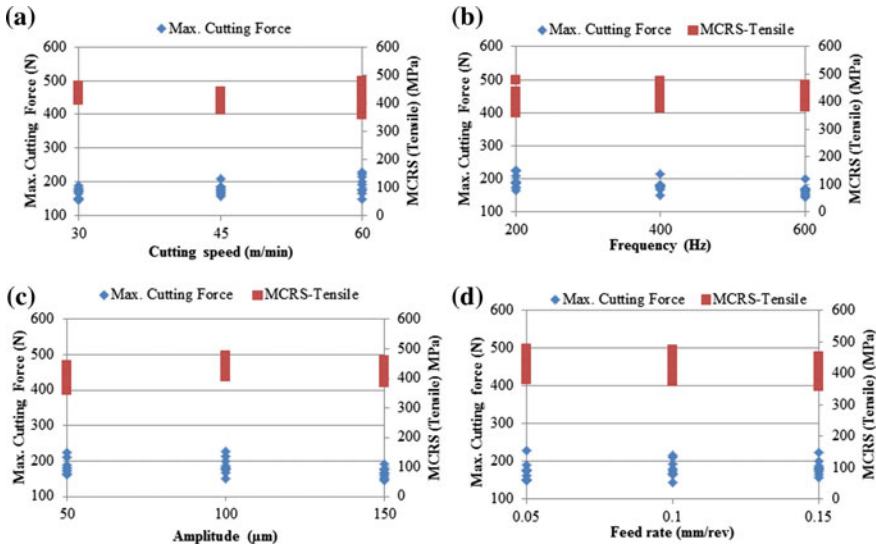


**Fig. 3** Variation of maximum cutting force and MCRS (tensile) with **a** feed rate, **b** cutting speed, **c** amplitude, and **d** Frequency

### 3.1.2 Effect of Machining Parameters on MCRS (Tensile)

Tables 7 and 8 depict the influence of each process parameter on MCRS (tensile). From ANOVA results, it is observed that the influence of amplitude (37.74% of contribution) is more on MCRS (tensile) than other parameters in LVAT process. Figure 3 shows the variation of MCRS on cutting speed, feed rate, amplitude, and frequency. The lower values of MCRS (tensile) are obtained at lower values of cutting speed and amplitude.

MCRS (tensile) mostly occurs in the forward movement of cutting tool onto the workpiece. If the amplitude is low, the speed with which it comes would be lower and causing less impact on the workpiece thereby lowering the MCRS (tensile). For

**Table 7** Response table for SNR of MCRS (tensile)

Level	Factors			
	Cutting speed (m/min)	Amplitude (μm)	Frequency (Hz)	Feed rate (mm/rev)
1	-52.87	-51.95	-52.19	-52.55
2	-52.18	-52.93	-52.50	-52.46
3	-52.29	-52.46	-52.65	-52.33
Delta	0.69	0.98	0.46	0.22
Rank	2	1	3	4
Optimum	2	1	1	3

**Table 8** ANOVA table for MCRS (tensile) using SN data

Factors	DOF	SSTR	MSTR	F-Test	% Contribution (P)
Cutting speed	2	2.4657	1.2329	6.34	21.42
Amplitude	2	4.3448	2.1724	11.17	37.74
Frequency	2	0.9809	0.4904	2.52	29.52
Feed rate	2	0.2212	0.1106	0.57	1.92
Error	18	3.4996	0.1944		9.40
Total	26	11.5121			100

minimizing MCRS, lower speeds are preferred as the heat generated in the workpiece is less which is the main source for generating tensile MCRS.

### 3.2 Optimum Design

The SSTR is used to quantify the variation between the treatment groups and error sum of squares (SSE) which is calculated from Eq. (4) [8].

$$SSE = (y_1 - 1)x_1^2 + (y_2 - 1)x_2^2 + \dots + (y_n - 1)x_n^2 \tag{4}$$

where “*n*” indicates each individual factor, “*x*<sup>2</sup>” indicates variance, and “*y*” indicates number of observations in the *n*th factor. The optimum levels of machining parameters are calculated with the help of response data from *S/N* ratio. The predicted output responses at optimum levels of control parameters are obtained by using the Eq. (5).

$$X = \bar{X} + (\bar{A}_o - \bar{X}) + (\bar{B}_o - \bar{X}) + (\bar{C}_o - \bar{X}) + (\bar{D}_o - \bar{X}) \tag{5}$$

$$\text{Maximum Cutting force Max } F_c = 10^{\frac{-x}{20}} \tag{6}$$

$$\text{MCRS (Tensile) } \sigma_{TR} = 10^{\frac{-x}{20}} \tag{7}$$

### 3.3 Confirmatory Test

The confirmatory test is conducted through FE simulation model which is already validated through experimental values. These simulations are done at optimum machining parameters, i.e., *V* = 30 m/min, *a* = 50 μm, *F* = 200 Hz, and *f* = 0.15 mm/rev

**Table 9** Predicted and simulated results

	Predicted value	Simulated value	% error
Max cutting force	151.2	137.2	9.1
MCRS (Tensile)	424.1	395.3	8.7

for output responses. Then, the predicted values from Eqs. (5) and (7) are compared with simulated values as shown in Table 9.

## 4 Conclusions

The influence of cutting speed, frequency, amplitude, and feed rate on maximum cutting force and MCRS (tensile) are analyzed using Taguchi-based ANOVA and following conclusions are drawn from this study.

- Cutting force, cutting temperature, and equivalent stress developed in VAT process are less when compared to CT due to relaxation between tool and workpiece in VAT.
- ANOVA at 95% confidence level gives frequency as the most significant parameter for maximum cutting force while amplitude as most significant parameter for MCRS (tensile).
- The optimum condition is obtained at 30 m/min of cutting speed, 150 μm of amplitude, 600 Hz of frequency, and 0.05 mm/rev of feed rate for maximum cutting force while the optimum condition for MCRS (tensile) is 45 m/min of cutting speed, 50 μm of amplitude, 200 Hz of frequency, and 0.15 mm/rev of feed rate.

## References

1. Brehl DE, Dow TA (2008) Review of vibration-assisted machining. *Precis Eng* 32:153–172
2. Skelton RC (1969) Effect of ultrasonic vibration on the turning process. *Int J Mach Tool Des Res* 9:363–374
3. Guo YB, Liu CR (2002) 3D FEA modeling of hard turning. *J Manuf Sci Eng* 124:189–198
4. Batalha GF, Delijaicov S, Aguiar JB, Bordinassi EC, Stipkovic Filho M (2007) Residual stresses modeling in hard turning and its correlation with the cutting forces. *J Achievements Mater Manuf Eng* 24(1)
5. Fu WE, Cohen PH, Ruud CO (2009) Experimental investigation of the machining induced residual stress tensor under mechanical loading. *J Manuf Processes* 11:88–96
6. Capello E (2005) Residual stresses in turning Part I: influence of process parameters. *Mater Process Technol* 160:221–228



7. Naresh Kumar M, Vamsi Krishna P, Jin X (2017) Assessment of high and low frequency vibration assisted turning with material hardness. *Int J Mach Mach Mater* 19:110–135
8. Fraley S, Oom M, Terrien B, Zalewski J (2007) Design of experiments via Taguchi methods: orthogonal arrays. <https://controls.engin.umich.edu/wiki/index.php/>

# Characterisation and Performance Measure Evaluation of Nanofluid Blended Thin-Film Temperature Gauges



P. Jayesh , Sheikh Afridhi  and Abhay Mohan 

**Abstract** The surface temperature history and convective heating rate are the vital design perspectives of the short duration facilities such as IC engines and gas turbines. With this motivation, ‘Thin film gauges’ (TFGs) have been developed by depositing transition metals blended with CNT nanofluid on the surface of highly polished ceramic substrates. For a precise temperature sensor of resistance based, the quality measures on temperature coefficient of resistance (TCR) are recommended. An experimental investigation is performed for finding the performance measures of the sensor. The experimental correlation of TCR is compared with the theoretical interpretation using XRD material characterisation method. An enhancement of performance is identified for CNT-blended TFG, and the performances were validated using analytical model.

**Keywords** Thin-film gauge · X-ray diffraction · TCR · Characterisation

## 1 Introduction

For applications such as shock tubes, I.C engines, gas turbines and high-speed aerodynamics, the heat flux and temperature measurement must have a good response time. The most recent advancement in the field of temperature measurement has been produced by thin-film technology. Since the 1970s, thin-film technique had been developed on heat flux measurement and used in a variety of applications. Kinnear and Lu [1] introduced a method for the design, construction, calibration and testing of thin-film platinum resistance–temperature detectors. Lei et al. [2] discussed the advancement of thin-film sensor techniques for temperature measurements, being developed at the NASA Lewis Research Center. Similar experimental studies on platinum (Pt) thin films and TCR measurements were conducted by Tsutsumi et al. [3]. Rakesh and Sahoo [4] identified that a thin-film gauge can also provide transient surface temperature measurement. The sensors were designed and fabricated by the

---

P. Jayesh · S. Afridhi (✉) · A. Mohan  
MVJ College of Engineering, Bangalore, India  
e-mail: [afridhi113@gmail.com](mailto:afridhi113@gmail.com)

© Springer Nature Singapore Pte Ltd. 2020  
H. K. Voruganti et al. (eds.), *Advances in Applied Mechanical Engineering*,  
Lecture Notes in Mechanical Engineering,  
[https://doi.org/10.1007/978-981-15-1201-8\\_78](https://doi.org/10.1007/978-981-15-1201-8_78)

725

platinum film is deposited on the insulating substrate for thin-film heat transfer gauge. Keblinski et al. [5] made an interesting review on the properties of nanofluids and future challenges in the field. Xu et al. [6] proposed the combination of aluminium-carbon nanotube composites and investigated their microstructural characteristics and disturbances of CNTs in the Al matrix. Lacy [7] evaluated the resistivity–temperature relationship for the RTDs and other conductors like platinum and nickel. A physical model was incorporated using the microscopic parameters associated with FCC lattice structure. Temperature coefficient of resistance symbolises the resistance change factor per degree of temperature change. For pure metals, this coefficient is a positive number, whereas for the elements like carbon, silicon, and germanium, this is a negative number, and even some metal alloys, the TCR is very close to zero. Thin-film gauges (TFGs) were the most competent dynamic temperature sensors because of their microseconds responsive time. It is identified from the literatures that a positive and high value of TCR is recommended as a measure of performance of thin-film gauges. Multilayered thin-film sensor and applications for dynamic temperature measurements discussed by Fen et al. [8]. Being the next-generation heat transfer fluids, the nanofluid's reliability to the transient metal-based TFG's on the performance measures is considered in this work.

## 2 Experimental Performance Measures Evaluation

The resistance-based transient temperature measurement gauge is designed and fabricated in-house. The standard preparation procedures for fabricating the thin-film gauges were maintained, as discussed by Kinnear and Lu [1]. To select the substrate and prepare it, assumptions of one-dimensional semi-infinite concepts were followed. Due to desirable properties like low thermal conductivity, Pyrex rods about 10 mm long with a diameter of 1.6 mm were used as substrate materials. This ensured the validity of the semi-infinite assumptions. The silver conductive adhesive paste was blended with multiwall carbon nanotubes (MWCNT) of 40–60 nm of diameter and 5–15  $\mu\text{m}$  length with a different composition for the gage materials. A suspension was obtained by mixing the functionalised CNTs with the silver solutions. The preparation and functionalization of CNT procedure are followed by Dobranski et al. [9]. A tip sonicator model VCX was used to disperse the carbon nanoparticles in the liquid. An ultrasonic pulse of 750 W at 20 kHz was generated by the ultrasonic tip in the nanofluid. During sonication, the container of the nanofluid was cooled with a water jacket and the temperature of the nanofluid was maintained at less than 35 °C for the sonication time of 60 min. Three gauges were prepared with different wt percentage of CNT (1wt%, 0.5wt%, 0.25wt%) in silver solutions, and the effect of CNT blend on the solution and their performance measures discussed in the next sections. The final step in the gauge construction was making the electrical connections to the metallic thin film. Aluminium wire ensured the structural stability of the leads for the electrical connection of the gauge. The primary excitation constant current of 10 mA was supplied to the sensor through the voltmeter. When subjected to a change in the

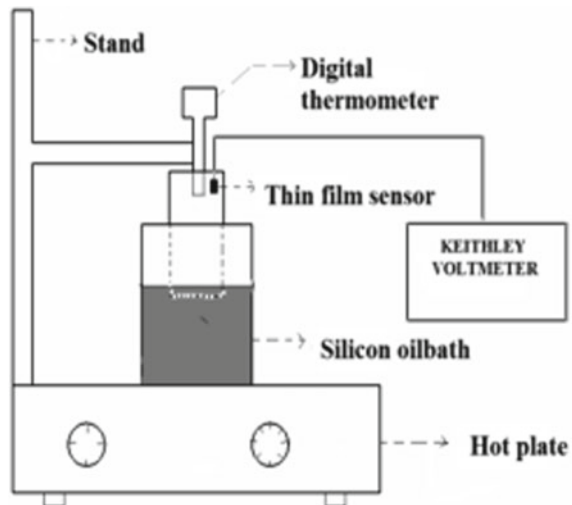
temperature field, the film acted as a thermometer and under some assumptions, it showed the temperature changes in the form of resistance changes, as Eq. (1).

$$R = R_0 + R_0\alpha_0(T - T_0) \tag{1}$$

The consistency and accuracy of the fabricated sensor were identified by the static oil bath bench calibration process, shown in Fig. 1. Due to thermal excitation, the electrical resistance of the conductor varies in accordance with its temperature and this forms the resistance based thin-film gauge. The effect is most commonly exhibited as an increase in resistance when the temperature increases, i.e. a positive temperature coefficient of resistance (TCR),  $\alpha$ . The calibration results in Figs. 2 and 3 identify the linearity of the gauges as well as the high value of positive TCR for the CNT-blended solution, ensuring the sensors best performance measures.

Silver chemical is mixed with CNT in three different wt% (0.25wt%, 0.5wt%, 1wt%) in scientific methods, and the TCR value is calculated for different wt% is shown in Fig. 3. There is found to be an increment in TCR values for the corresponding % wt of CNT increment. With respect to the basic TCR value of the silver thin film, the blended combinations exhibit a performance improvement in TCR values for different wt% (0.25wt%, 0.5wt%, 1wt%) respectively as 17.15%, 20.192%, 24.14%, shown in Table 1.

**Fig. 1** Schematic representation of the calibration



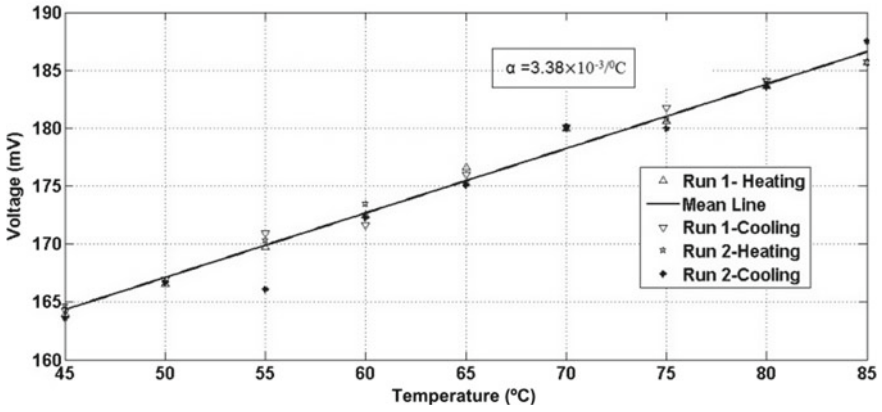


Fig. 2 Calibration curve of silver gauge

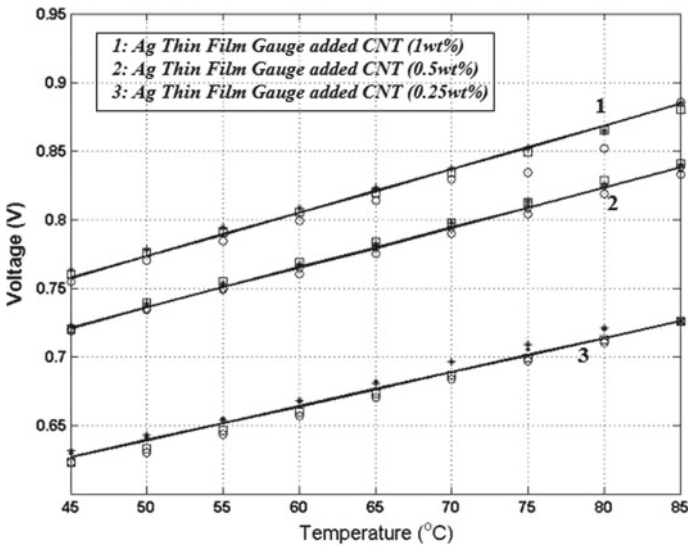


Fig. 3 Calibration results of CNT added Ag thin film

Table 1 TCR percentage performance improvement

Material	TCR [%c]	Enhancement of TCR (%)
Ag + 0 wt% CNT	$3.38 \times 10^{-3}$	—
Ag + 0.25 wt% CNT	$3.95 \times 10^{-3}$	17.15
Ag + 0.5 wt% CNT	$4.06 \times 10^{-3}$	20.19
Ag + 1.00 wt% CNT	$4.19 \times 10^{-3}$	24.14

### 3 Theoretical Investigations

Most of the metal-based thin film shows linearity in resistance–temperature characteristics, according to Eq. (1). The relation between the resistivity and temperature using for different gauge materials was evaluated using Lacy [7] 2D model for FCC crystal structure.

#### 3.1 XRD Characterisation and Analysis

The nondestructive XRD diffraction technique is used to monitor the phases, structure lattice parameter, strain and texture present in the film. The input parameters for the theoretical evaluations were taken from XRD characterisation studies. Lattice parameter constant ‘a’ of the face-centred cubic system (FCC) can be calculated from the equation standard miller indices values obtained correspondingly. The electrical resistivity for the materials is calculated from the model according to Eq. (2).

$$\rho = \rho_0 \left[ \frac{1}{\frac{[2\sqrt{\gamma/kT}-b]\left(\frac{\epsilon_1}{\epsilon_2}-1\right)}{2a+b} + 1} \right] \tag{2}$$

The composition of the blended solution is reflected by the peak shift in XRD Figs. 4 and 5. The difference in peak shift compared the silver solution with the CNT-blended silver solution. The molecular structure, atomic radius and lattice parameter

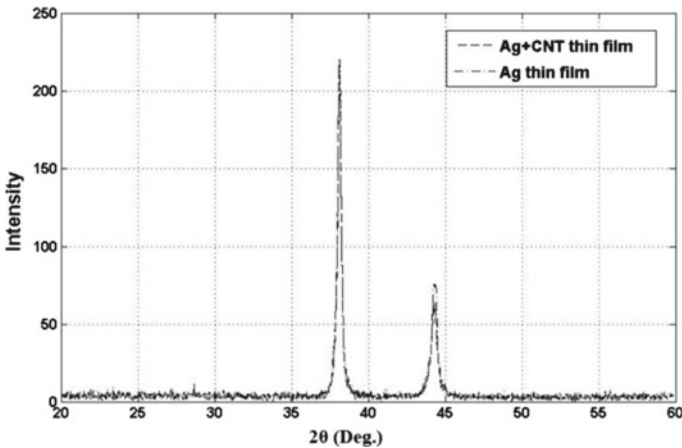
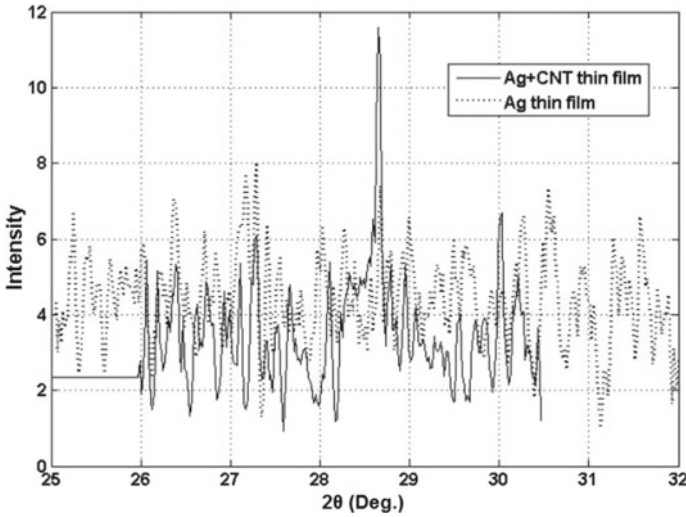


Fig. 4 XRD spectrum comparison



**Fig. 5** XRD spectrum for CNT peak on Ag-CNT thin film

**Table 2** Comparison of lattice parameter values and crystal size

Material	Lattice parameter ( $\times 10^{-10}$ ) [m] (from XRD data)	Crystal size(m)
Ag + 0 wt% CNT	$3.38 \times 10^{-3}$	–
Ag + 0.25 wt% CNT	$3.95 \times 10^{-3}$	17.15

can be evaluated from the XRD results and followed by basic miller indices equations along with Eq. (3). The lattice parameters constants and the crystal size were evaluated for 1% wt added of CNT-blended silver solution, noted in Table 2.

$$B(2\theta) = \frac{k\lambda}{L \cos \theta} \tag{3}$$

### 3.2 Modification of Lacy’s Resistivity–Temperature Relationship Model

Lacy [7] developed FCC structure 2D model for temperature resistive relationship for transition metals. The model is based on the theoretical molecular solid-state assumptions. A comparative modified modelled equation is predetermined, shown

in Fig. 8. For the constant lattice parameter values,  $\gamma$  and time constant ratios are adjusted to produce the best-fit equation, labelled in Fig. 8. The expected linear response is found very good match with the general linear Eq. (1). The temperature coefficient of resistance (TCR) of sensors and their comparison was plotted in Figs. 6 and 7.

Silver TFGs and silver–CNT nanofluid TFGs were successfully developed and calibrated in the laboratory for the use of short duration facilities. The initial resistance of Ag–CNT thin-film gauge was found to increase with the concentration of CNTs (Fig. 8).

The temperature coefficient of resistance of CNT-blended silver TFG over silver TFG is increased by 17.2%, 20.2% and 24% respectively with weight percentage of CNT in silver solutions of 0.25%, 0.5% and 1%, respectively. The linearity in performance is identified for all the cases. The composition of nanofluid in silver solution

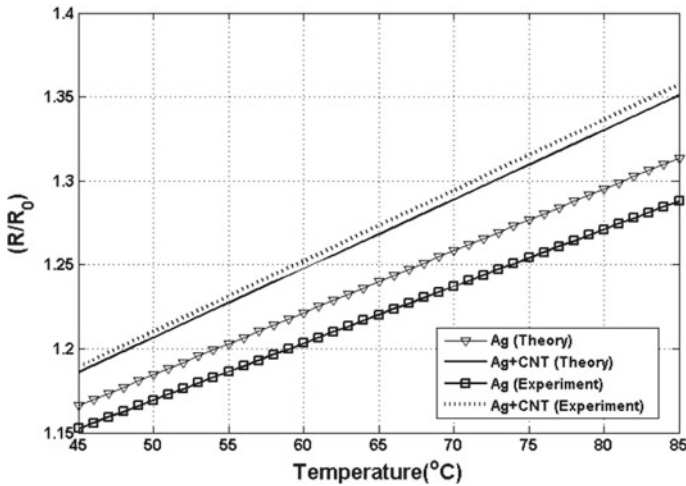
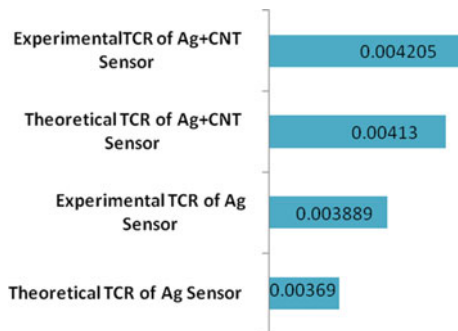


Fig. 6 Plot showing the TCRs of different sensors

Fig. 7 Comparison of TCRs obtained from different sensors





Thin Film	Parameter	Characterized Relationship	Experimental Relationship
Silver film	$\delta=1; a=1 \times 10^{-12} \text{ m};$ $b=3.23 \times 10^{-10} \text{ m};$ $(\tau_1/\tau_2)=2.0584$	$R = R_0 [1 + 3.69 \times 10^{-3} T]$	$R = R_0 [1 + 3.3889 \times 10^{-3} T]$
Ag-CNT film	$\delta=1; a=1 \times 10^{-12} \text{ m};$ $b=3.059 \times 10^{-33} \text{ m};$ $(\tau_1/\tau_2)=2.0084$	$R = R_0 [1 + 4.13 \times 10^{-1} T]$	$R = R_0 [1 + 4.205 \times 10^{-1} T]$

Fig. 8 Correlation comparison

and the dispersion in base solution is identified from the XRD characterisation analysis. Theoretical investigation of resistance–temperature relationship is found to be a very good agreement with the experiment results. The correlation comparison is the enhancement of TCR of Ag and Ag + CNT nanofluid based thin film was found to be 21% and 12% by experimental and theoretical investigation, respectively.

### 4 Conclusion

The reliability of the next-generation heat transfer fluids, i.e. effect of CNTs to base fluid and temperature measurement performances has been investigated. The sensitivity performance measure of thin-film gauge for transient temperature measurement for short duration facility is compared experimentally and analytically. The TCR value is found increasing with the percentage of weight added CNT in silver solution. The blended CNT weight is restricted to maximum of 1% due to the cost restriction and effectiveness of the sensor. However, the performance measure evaluation is conducted; this research paper addresses the limitations in real-time case studies of the quality conformance of the sensor.

### References

1. Kinnear KM, Lu FK (1998) Design, calibration and testing and transient thin film heat transfer gauges. Am Inst Aeronaut Astronaut, 1998–2504
2. Lei J-F (1997) Advances in thin film sensor technologies for engine applications. In: International conference on Gas Turbine Institute and the American Society of Mechanical Engineers, NASA TM 107418

3. Sutsumi KT, Yamashita A, Ohji H (2002) Experimental study of high TCR Pt thin films for thermal sensors. In: Proceedings of IEE, vol 2, pp 1002–1005
4. Rakesh K, Sahoo N, Kulkarni V, Anugrah S (2011) Laser based calibration technique for short duration transient measurements. *J Therm Sci Eng Appl* 3(4):0444041–0445046
5. Keblinski P, Eastman JA, Cahill DG (2005) Nanofluids for thermal transport. *J Mater Today* 8(6):36–44
6. Chunfeng D, Li X (2007) Fabrication of aluminum matrix composite reinforced with carbon nanotubes. *J Rare Mater* 26(5):450–455
7. Lacy F (2011) Evaluating the resistivity-temperature relationship for RTDs and other conductors. *J IEEE Sens* 11:1208–1213
8. Fen JL, Will HA (1998) Thin film thermocouples and strain gauge technologies for engine applications. *Sens Actuators A*:187–193
9. Dobrzanski LA, Pawlyta M, Krzton A, Liszka B, Tai CW, Kwasny W (2009) Synthesis and characterization of carbon nanotubes decorated with gold nanoparticles. In: The 8th Torunian carbon symposium, vol 118

# Base Transesterification of Ineffectual Soybean Oil Using Lab Scale Synthesized CaO Catalyst



Rakesh Singh Ningthoujam, Ronaldo Singh Naorem,  
Denin Singh Langpokpam, Thokchom Subhaschandra Singh  
and Tikendra Nath Verma

**Abstract** The present study involves the transesterification of ineffectual soybean oil using synthesized calcinated (duck eggshell) calcium oxide (CaO) as heterogeneous base catalyst. The catalyst was first prepared by exposing at a muffle furnace for about 180 min 800 °C and then characterized using X-ray diffraction (XRD), Fourier transform infrared spectrometry (FT-IR), scanning electron microscopy (SEM) and energy-dispersive x-ray spectroscopy (EDX). There is characterization of uncooked, ineffectual and transesterified ineffectual soybean oil using FT-IR spectrometry. The yield was obtained to be 94.55% when transesterified at 3% (wt%) catalyst loading, 10:1 alcohol to oil ratio, a reaction temperature of 70 °C and a reaction time of 60 min. The methyl ester underwent gas chromatography–mass spectrometer (GC-MS) test to check the contents of the yield oil. It was found that the cheap and ready to be discarded ineffectual soybean oil can be effectively used for producing biodiesel.

**Keywords** Base transesterification · Soybean oil · Duck eggshells · Calcination · Calcium oxide

## 1 Introduction

With advancements in production of biofuel from various sources, such as edible, non-edible oils, animal fats, microalgae, tire pyrolysis oil, waste plastic oil, and waste cooking oil [1–7], the researchers have been working round the clock in search of optimal parameters in utilizing less resources and obtaining optimum results. This is primarily due to ever-increasing pollution from commercial diesel engines [8]. It has been reported by many researchers that biodiesel/biofuels can provide lesser emissions without much compromise in performance and combustion characteristics. At present, there has been much literature which reports the use of various feed materials for production of biodiesel. Although NaOH and KOH were opted

---

R. S. Ningthoujam · R. S. Naorem · D. S. Langpokpam · T. S. Singh (✉) · T. N. Verma  
Department of Mechanical Engineering, National Institute of Technology Manipur, Langol,  
Imphal 795004, India  
e-mail: [th.s.singh@nitmanipur.ac.in](mailto:th.s.singh@nitmanipur.ac.in)

© Springer Nature Singapore Pte Ltd. 2020  
H. K. Voruganti et al. (eds.), *Advances in Applied Mechanical Engineering*,  
Lecture Notes in Mechanical Engineering,  
[https://doi.org/10.1007/978-981-15-1201-8\\_79](https://doi.org/10.1007/978-981-15-1201-8_79)

735

by many for performing acid-based transesterification, it was evident from many studies that the cost involved is very high. Hence, researchers are now opting for organic-based catalyst for performing the transesterification process. Kamila et al. (2017) developed a bench-scale transesterification reactor having capacity to give output of 3L Biodiesel. To optimize the set operating parameters, viz. methanol to oil molar ratio, catalyst concentration and reaction time, they used a full 23 factorial. Then, the reactor is used for the transesterification process as well as the recovery of methanol present in excess. Characterization of the product was done using gas chromatography. To determine the ester and calcium concentrations, liquid analysis has been used. A maximum yield of almost 100% was obtained at 3 wt% of the catalyst; reaction time is 75 min and methanol: oil molar ratio is 6:1 [9].

Shan et al. (2018) have stated that the catalyst made from renewable resources such as shells, ashes from plants and trees, natural sources, and large scale wastes generated in industries are more advantageous as they do not harm the environment and are the most cost-effective. [10]. Szulczyk et al. (2018) found that the reason of the cost of biodiesel being higher than normal diesel was the high cost of feed materials [11]. Samad et al. (2018) have converted 92.8% of free fatty acids (FFA) into fatty acid methyl esters (FAME) using sulfuric acid as catalyst with 10% w/w of the said FFA in the esterification process [12]. Mahmudul et al. (2017) have performed a research on the negative impact that is caused by fossil fuels to the environment and the development of renewable sources of energy. They found that biofuels are a very good alternative to normal diesel owing to it being biodegradable and renewable as well as having similar fuel properties [13].

Hasan et al. (2017) have mentioned that there are many advantages of using blend mixture of biodiesel and diesel like shorter ignition delay and lesser emission of HC, CO and PM [14]. Goli et al. (2018) produced biodiesel at which the catalyst was derived from waste chicken eggshell. The characterization of the catalyst was done by XRD, FT-IR, X-ray fluorescence (XRF), thermogravimetric analysis (TGA/DTA) and SEM. They could produce 93% of biodiesel with an expectation of 92.32% at a reaction time of 3 h, temperature of reaction 57.5 °C molar ratio of methanol to oil 10:1 and concentration of catalyst of 7 wt% [15]. Tan et al. (2015) have used ostrich eggshells as catalyst in the production of biodiesel from waste cooking oil and found that 12:1 methanol to oil ratio, 65 °C reaction temperature, 1.5 wt% catalysts, 2 h reaction time with a speed of 250 rpm gave the most desired results [16]. Sirisomboonchai et al. (2015) have performed a research work on the transesterification process of WCO with methanol by utilizing calcined scallop shell (CSS). According to their research, CSS showed higher catalytic activity as compared to commercial CaO [17]. Farooq et al. (2015) have discussed the depleting condition of fossil fuels and performed transesterification of used cooking oil for producing biodiesel using waste chicken bones as a source of catalyst [18].

Yin et al. (2016) have used duck eggshell as source of catalyst which was calcined at about 800 to 900 °C. At reaction time of 120 min, concentration of sulfuric acid as 1.5%, molar ratio 12:1 and reaction temperature of 60 °C with 10 wt% catalyst, the yield of biodiesel was 94.6%. Reusability of the catalyst was tested, and it was found that catalyst could be used at least five times [19]. Viriya-empikul et al. (2010) have

used eggshell and *meretrix* (L.) for biodiesel production using palm oil. They calcined the shells at 800 °C at 2–4 h and found that all catalysts exhibit high yield activity (90%) of fatty acid methyl ester (FAME) in reaction time of 2 h [20]. Marinkovi et al. (2016) have reported that the CaO-based catalysts are the best for biodiesel production [21].

Therefore, in light of the above findings of the researchers in the past, the authors believed that one such commonly available feed material is the used/ineffectual soybean oil. Duck eggshells were also obtained and calcined at 800 °C for 80 min. The catalyst and feed materials were characterized using XRD, FT-IR, SEM, EDX and GC-MS.

## 2 Materials and Method

### 2.1 Material Collection and Preparation

The materials used for feed was collected from the Canteen and Hostel Mess of National Institute of Technology Manipur, Langol, Imphal-795001, India (24.83°N latitude, 93.91°E longitude, 756 m elevation above sea level). Figure 1 shows the raw materials which have been used for the present study. Another sample of unused soybean oil is also taken for the present study to compare the characteristics between used and unused feed materials. In the study, 5 liters of the ineffectual soybean oil and 300 g of duck eggshells were used. The ineffectual soybean oil was preheated to an elevated temperature of about 110–120 °C for removing any moisture from the

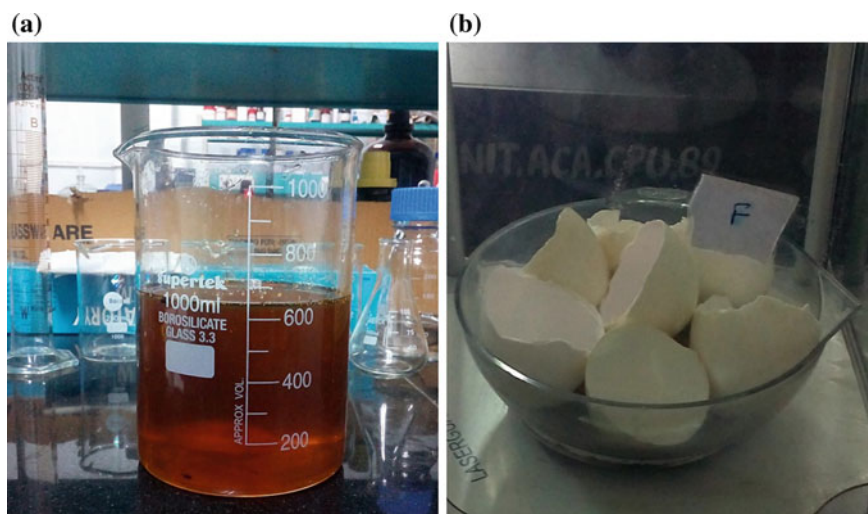


**Fig. 1** Feed materials for the present study **a** ineffectual soybean oil **b** duck eggshells

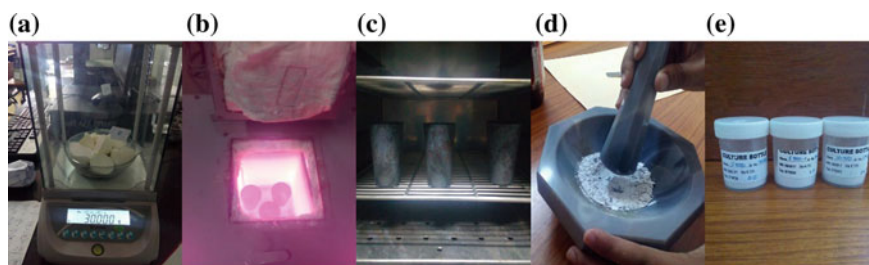


**Fig. 2** Calcination of the duck eggshells **a** weighing of the samples **b** calcination at muffle furnace **c** cooling down at oven **d** grinding of sample **e** bottling of samples

sample [1]. The duck eggshells were also pre-treated using a hot air oven (Make: Kelsons Testing Equipment). An electric muffle furnace is used for calcinations of the duck eggshell sample. Figure 2 shows the process of calcination of the duck eggshells at 800 °C for 180 min.

## 2.2 Transesterification

Figure 3 shows the process of transesterification of the samples. The transesterification started with filtration of the feed oil. About 100 ml of feed oil is taken for each process and the experiment was performed for three times to ensure correctness of the result. The alcohol to oil ratio is taken to be 10:1 and the catalyst loading rate is 3% (wt%). The beaker is kept above the hot plate magnetic stirrer at a temperature of about 70 °C. A thermometer is dipped into the beaker to check the temperature of the reaction. The reaction took place for about 60 min and finally kept in a separating funnel. The transesterification reaction is shown in Eq. (1). After the glycerol is separated, the alcohol and catalyst were recovered. Then the methyl esters underwent a washing process with warm water by vigorous shaking the mixture. After settling the mixture for about 3 days, the methyl esters were collected and measured to determine the yield, using the Eq. (2).

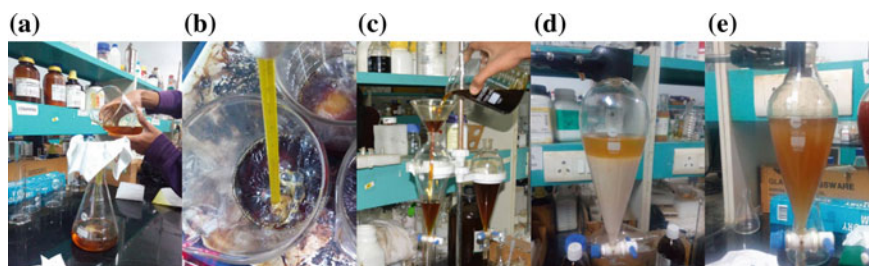
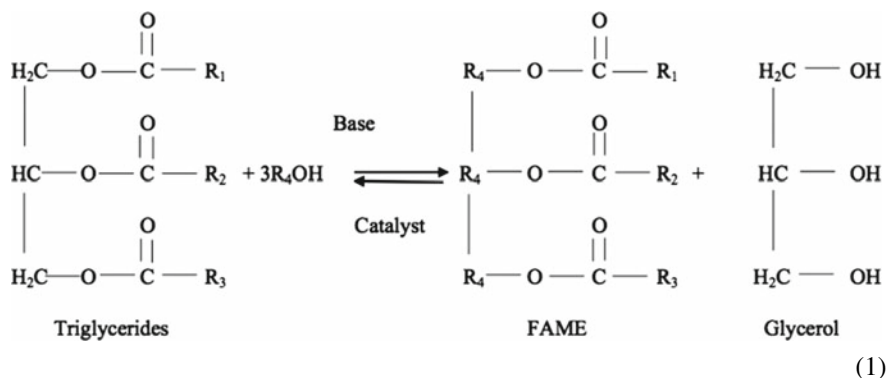


**Fig. 3** Transesterification process of the sample



$$\text{Yield} = \frac{\text{weight of methyl ester produced}}{\text{weight of oil procured}} \times 100 \quad (2)$$

Figure 3(a) shows preliminary filtration using a fine cloth [7], (b) glycerol formation during reaction (c) separation using funnel (d) washing of methyl esters and (e) filtered, washed and dried methyl esters.

### 3 Results and Discussion

During the process of transesterification, it was found that the yield of the present study was obtained to be 94.55%. The GC-MS result yield 9.6% of  $\alpha$ -linolenic acid (C-18:3), 51% of linolenic acid (C-18:2), 22.8% of oleic acid (C-18:1) and 16.6% of stearic (C-18:0) and palmitic acids (C-16:0).

#### 3.1 Characterization of Catalyst

The calcinated CaO from duck eggshells has been characterized using XRD, FT-IR, SEM and EDX. The corresponding results are shown in Fig. 4a–d, respectively. The diffraction peaks of  $29.68^\circ$ ,  $33.42^\circ$  and  $47.72^\circ$  from Fig. 4a correspond to (111), (200) and (220) of the face-centered cubic phase. From Fig. 4b, it is evident that the displayed bands of  $1411$  and  $875\text{ cm}^{-1}$  correspond to the asymmetric stretching of C=O. The extra stretch at  $412\text{ cm}^{-1}$  displayed the formation of CaO from the duck eggshell samples. Figure 4c, d shows the morphology of synthesized CaO. The EDX result shows the elemental composition of the sample, which was found to be 66.75 wt% & 42.01 atomic % (for Ca) and 22.58 wt% and 35.60 atomic % (for O). The findings are coherent to the findings of other researchers [1, 9, 10, 15–19].

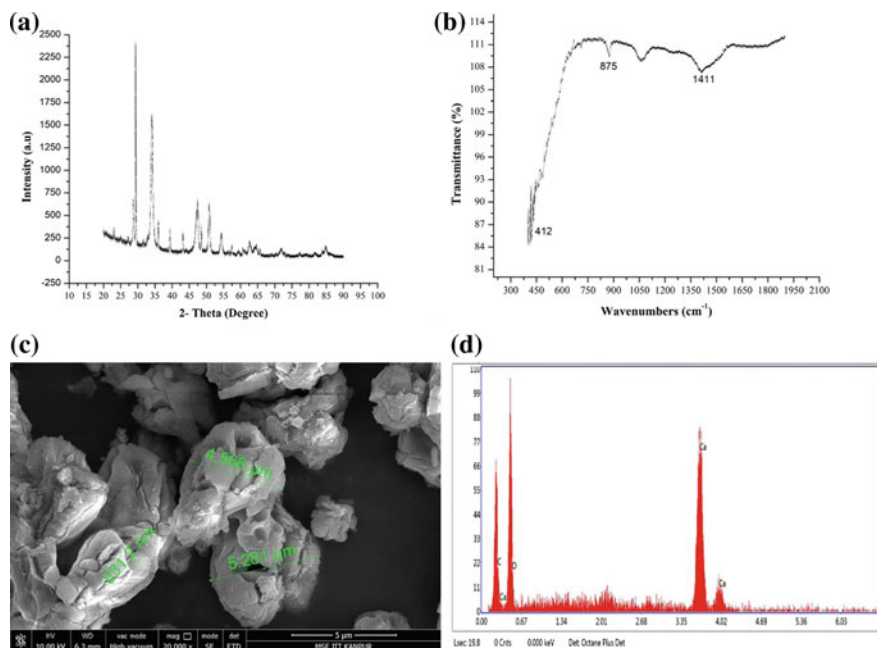


Fig. 4 Characterization of duck eggshells CaO catalyst

### 3.2 Characterization of Ineffectual Soybean Oil and Methyl Ester

The ineffectual soybean oil along with the uncooked soybean oil was also characterized using FT-IR alongside the transesterified ineffectual soybean. The corresponding graphs which have been plotted are shown in Fig. 5. The stretching of bonds for the various types of oil is tabulated in Table 1. The present findings were in good relation to those of the results obtained by other researchers [1, 9, 10, 16, 19, 21].

## 4 Conclusion

Transesterification reaction was performed using ineffectual soybean oil through the application of duck eggshell derived CaO as heterogeneous base catalyst.

Calcination of CaO at 800 °C for 180 min, showed that the synthesized CaO had favorable morphology and was in good relation with those of other researchers.

At 3% (wt%) catalyst loading rate, 10:1 alcohol to oil ratio, 70 °C reaction temperature and 60 min reaction time, the final methyl ester yield was found to be 94.55%.



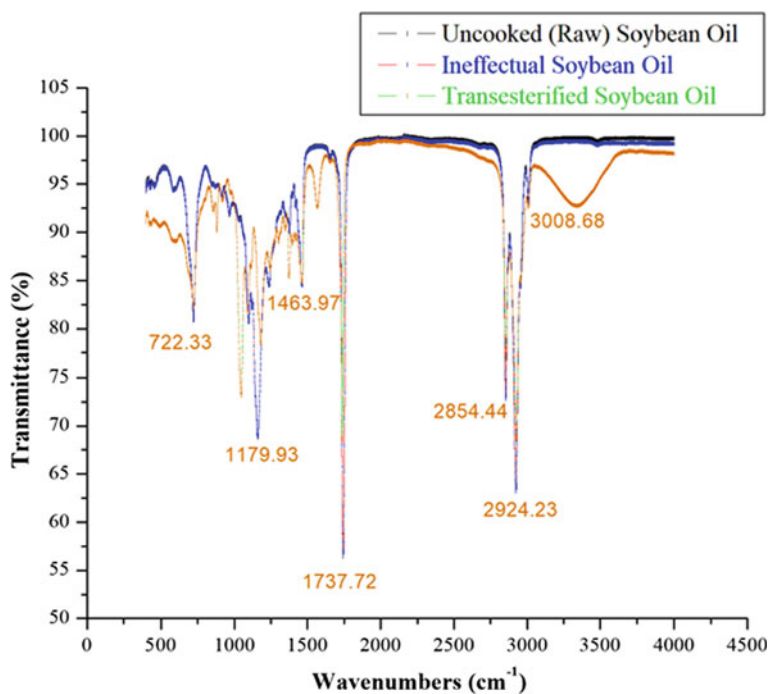


Fig. 5 FT-IR spectroscopy of uncooked, ineffectual and transesterified soybean oil

Table 1 Stretching of bonds for various types of oil sample

Wavenumber ( $\text{cm}^{-1}$ )			Remark [1, 9, 10, 15–22]
Raw soybean oil	Ineffectual soybean oil	Transesterified Ineffectual soybean oil	
3009.12	3009.10	3008.68	C–H stretch
2923.16	2923.16	2924.23	$\text{CH}_2$ presence
2853.64	2853.64	2854.54	$\text{CH}_2$ presence
1743.55	1743.52	1737.72	C=O
1464.61	1464.58	1463.97	$\text{CH}_2$ bending vibrations
1160.24	1160.36	1179.93	C–O ester
722.24	722.24	722.33	$\text{CH}_2$ rocking

Hence, the authors conclude that waste and ready to be thrown soybean cooking oil from various sources, can be effectively used for biodiesel production. Also acid-base catalyst can be substituted by readily available and easy to produce CaO from waste sources like duck eggshells.

**Acknowledgements** The authors acknowledge the support provided by Department of Chemistry NIT Manipur throughout the course of the project. The authors also thank IIT Kanpur and IIT Guwahati for extensive support in providing results of various tests.

## References

1. Singh TS, Verma TN (2019) Taguchi design approach for extraction of methyl ester from waste cooking oil using synthesized CaO as heterogeneous catalyst: response surface methodology optimization. *Energy Convers Manag* 182:383–397
2. Rajak U, Nashine P, Singh TS, Verma TN (2018) Numerical investigation of performance, combustion and emission characteristics of various biofuels. *Energy Convers Manag* 156
3. Rajak U, Verma TN (2018) Effect of emission from ethylic biodiesel of edible and non-edible vegetable oil, animal fats, waste oil and alcohol in CI engine. *Energy Convers Manag* 166(X):704–718
4. Rajak U, Verma TN (2018) Spirulina microalgae biodiesel—a novel renewable alternative energy source for compression ignition engine. *J Clean Prod* 201:343–357
5. Rajak U, Nashine P, Verma TN (2018) Assessment of diesel engine performance using spirulina microalgae biodiesel. *Energy* 166:1025–1036
6. Salam S, Verma TN (2019) Appending empirical modeling to numerical solution for behavior characterization of microalgae biodiesel. *Energy Convers Manag* 180:496–510
7. Subhaschandra Singh T, Verma TN (2019) Impact of tri-fuel on compression ignition engine emissions: blends of waste frying oil–alcohol–diesel. In: Agarwal A, Gautam A, Sharma N, Singh A (eds) *Methanol and the alternate fuel economy. Energy, environment, and sustainability*. Springer, Singapore
8. Singh TS, Verma TN, Nashine P, Shijagurumayum C (2018) BS-III diesel vehicles in Imphal, India: an emission perspective. In: Sharma N, Agarwal A, Eastwood P, Gupta T, Singh A (eds) *Air pollution and control. Energy, environment, and sustainability*. Springer, Singapore
9. Colombo K, Ender L, Barros AAC (2017) The study of biodiesel production using CaO as a heterogeneous catalytic reaction. *Egypt J Petrol* 26(2):341–349
10. Shan R, Lu L, Shi Y, Yuan H, Shi J (2018) Catalysts from renewable resources for biodiesel production. *Energy Convers Manag* 178:277–289
11. Szulczyk KR, Khan MAR (2018) The potential and environmental ramifications of palm biodiesel: evidence from Malaysia. *J Clean Prod* 203:260–272
12. Samad ATP, Putri DN, Perdani MS, Utami TS, Arbianti R, Hermansyah H (2018) Design of portable biodiesel plant from waste cooking oil. *Energy Proc* 153:263–268
13. Mahmudul H, Hagos F, Mamat R, Adam AA, Ishak W, Alenezi R (2017) Production, characterization and performance of biodiesel as an alternative fuel in diesel engines—a review. *Renew Sustain Energy Rev* 72:497–509
14. Hasan M, Rahman M (2017) Performance and emission characteristics of biodiesel-diesel blend and environmental and economic impacts of biodiesel production: a review. *Renew Sustain Energy Rev* 74:938–948
15. Goli J, Sahu O (2018) Development of heterogeneous alkali catalyst from waste chicken eggshell for biodiesel production. *Renew Energy* 128:142–154
16. Tan YH, Abdullah MO, Nolasco-Hipolito C, Taufiq-Yap YH (2015) Waste ostrich-and chicken-eggshells as heterogeneous base catalyst for biodiesel production from used cooking oil: catalyst characterization and biodiesel yield performance. *Appl Energy* 160:58–70
17. Sirisomboonchai S, Abudwayiti M, Guan G, Samart C, Abliz S, Hao X, Kusakabe K, Abudula A (2015) Biodiesel production from waste cooking oil using calcined scallop shell as catalyst. *Energy Convers Manag* 95:242–247

18. Farooq M, Ramli A, Naeem A (2015) Biodiesel production from low FFA waste cooking oil using heterogeneous catalyst derived from chicken bones. *Renew Energy* 76:362–368
19. Yin X, Duan X, You Q, Dai C, Tan Z, Zhu X (2016) Biodiesel production from soybean oil deodorizer distillate using calcined duck eggshell as catalyst. *Energy Convers Manag* 112:199–207
20. Viriya-Empikul N, Krasae P, Puttasawat B, Yoosuk B, Chollacoop N, Faungnawakij K (2010) Waste shells of mollusk and egg as biodiesel production catalysts. *Biores Technol* 101(10):3765–3767
21. Marinković DM, Stanković MC, Veličković AV, Avramović JM, Miladinović MR, Stamenković OO, Veljković VB, Jovanović DM (2016) Calcium oxide as a promising heterogeneous catalyst for biodiesel production: current state and perspectives. *Renew Sustain Energy Rev* 56:1387–1408
22. Buasri A, Worawanitchaphong P, Trongyong S (2014) Utilization of scallop waste shell for biodiesel production from palm oil—optimization using Taguchi method. *Proc Soc Behav Sci* 8:216–221. <https://doi.org/10.1016/j.apcbee.2014.03.030>

# Solid Lubricant Effect on the Microstructure and Hardness of the Functionally Graded Cemented Tungsten Carbide



Rityuj Singh Parihar, Srinivasu Gangi Setti and Raj Kumar Sahu

**Abstract** Cemented tungsten carbide (WC-Co) is preferred cutting tool material, having tungsten carbide (WC) reinforcement embedded in cobalt (Co) matrix. Higher hardness, fracture toughness and wear resistance are the essential characteristics for cutting tool materials and are inherited by cemented tungsten carbide. The controlled distribution of Co composition in the form of gradient makes functionally graded cemented tungsten carbide (FGCC) and results in customized material properties but the only difficulty is Co migration. Additionally, wear resistance of FGCC is further improved by including a solid lubricant in the form of a gradient. The desired gradient is developed by powder metallurgy route using spark plasma sintering (SPS), which eliminates the migration of Co. The present work deals with the development of FGCC with and without solid lubricant and comparisons of their microstructure and hardness. The obtained results confirm the variations of microstructure and hardness in both FGCC samples (with and without solid lubricant). The presence of solid lubricant decreases the hardness, so FGCC without solid lubricant is having a higher hardness.

**Keywords** Functionally graded cemented tungsten carbide · Spark plasma sintering · Solid lubricant

## 1 Introduction

Tungsten carbide (WC) is the most suitable cutting tool material due to its high hardness, but due to its brittle nature, it requires some binder phase. Usually, cobalt (Co) is preferred as a binder, addition of WC in Co matrix provides toughness to the cemented carbide [1]. In cutting tool application, the Co percentage varies from 5 to 15%. The increasing Co content improves toughness and reduces hardness. Hence, it is very difficult to get a balance of toughness and hardness. Functionally graded

---

R. S. Parihar (✉) · S. G. Setti · R. K. Sahu  
Department of Mechanical Engineering, National Institute of Technology Raipur, Raipur,  
Chhattisgarh 492010, India  
e-mail: [singhrityuj24@gmail.com](mailto:singhrityuj24@gmail.com)

© Springer Nature Singapore Pte Ltd. 2020  
H. K. Voruganti et al. (eds.), *Advances in Applied Mechanical Engineering*,  
Lecture Notes in Mechanical Engineering,  
[https://doi.org/10.1007/978-981-15-1201-8\\_80](https://doi.org/10.1007/978-981-15-1201-8_80)

material (FGM) is a new concept where composition can be varied according to the requirement; consequently, a balance between toughness and hardness can be achieved [2]. Hence, cemented carbide is prepared in such a manner that surface and core of material have high WC and Co content, respectively. In this way, a promising combination of hardness and fracture toughness can be achieved. Cemented carbide prepared with this kind of composition gradient is known as FGCC [3]. Although this concept of gradient is having enormous advantages, still it is a challenge to prepare effective gradient. Most commonly adopted method for preparation of cemented carbide is powder metallurgy (PM) route through liquid phase sintering. The gradient development using liquid phase sintering is difficult due to migrating nature of Co. As the processing temperature increased, it resulted in melting of Co and followed by migration and homogenization. This problem was effectively encountered by spark plasma sintering (SPS) method [1]. In this method, it is possible to perform compaction and sintering together at solid-state temperature with the high heating rate. This solid-state sintering at short span of time suppressed Co migration and initially deposited gradient is consolidated. FGCC is having a hard surface but its wear resistance decreased at high temperature due to low hot hardness while high-speed machining. This problem is encountered by proper cooling technique at the time of machining but due to the strict environmental policies, it would be better to adopt a dry machining process [4]. There are several methods are available for dry machining but the new area of research is the application of solid lubricant [4]. This solid lubricant will be included in the Co matrix as reinforcement.

The earlier studies revealed that the presence of a solid lubricant in composite matrix makes it self-lubricating but at the same time mechanical properties degraded [4–6]. Researchers have done extensive work to improve the mechanical properties and found that the preparation of solid lubricant gradient is the only solution to optimize the composition for performance enhancement. The solid lubricant is required only at surface so it would be better to provide composition gradient according to the application [1]. In addition to this, volume fraction and composition gradient can be optimized in such a way that there is development of compressive and tensile residual stresses at the surface and core respectively due to the material processing. The compressive residual stress will hinder the crack propagation and improve the life and properties of developed functionally graded material [7]. Xing et al. [8] proposed design model for symmetrical functionally gradient ceramic tool materials and developed  $\text{Al}_2\text{O}_3\text{--TiC}$  FGM in such a way that compressive residual stresses formed on the surface layers so that the stresses created from external loadings can be neutralized. Zhao et al. [9] developed  $\text{Al}_2\text{O}_3\text{--(W, Ti)C}$  and  $\text{Al}_2\text{O}_3\text{--TiC}$  symmetrical functionally graded ceramic tool materials and achieved improved thermal shock resistance by composition variation. Xu et al. [10] designed and developed self-lubricating functionally graded  $\text{Al}_2\text{O}_3\text{--(W,Ti)C}$  cutting tool material by incorporating solid lubricant  $\text{CaF}_2$ . Xu et al. [7, 9] showed that the wear resistance and antifriction property of cutting tools can be improved simultaneously by gradient self-lubricating ceramic material, with surface and middle layers having compressive and tensile stresses, respectively. Muthuraja et al. [4] have prepared monolithic cemented carbide (WC–Co) with solid lubricant ( $\text{CaF}_2$ ). The developed WC–Co– $\text{CaF}_2$  tested for abrasive as

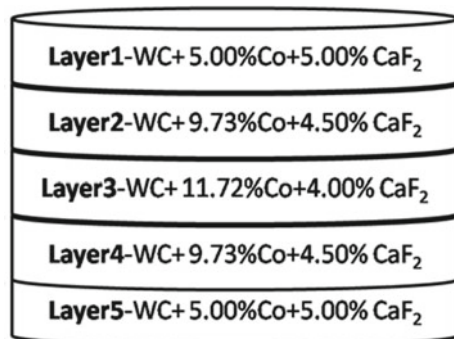
well as adhesive wear resistance and found the improvement in wear resistance [5, 6]. Parihar et al. [1] have also developed WC–Co–CaF<sub>2</sub> composite With Co and CaF<sub>2</sub> gradient using spark plasma sintering process. Although the material performance of conventional and self-lubricating cemented tungsten carbide tool has been compared, still research regarding the effect of solid lubricant on the material properties of FGCC is not yet reported.

The present work deals with the development of functionally graded cemented tungsten carbide with and without the addition of solid lubricant. The possibility of high heating rate in the spark plasma sintering process makes the choice for preparation of FGCC, results in smaller grain size and suppression of Co migration. The prepared samples are characterized by microstructure and hardness to show the effect of solid lubricant on the FGCC.

## 2 Experimental Procedure

WC-Co is a basic cutting tool material, and CaF<sub>2</sub> is adopted as a solid lubricant because of its capability to provide lubrication at high temperature. WC–Co–CaF<sub>2</sub> is adopted as a cutting tool material. WC is work as reinforcement in a Co binder (for cutting tool application 5–15 wt% Co), additionally CaF<sub>2</sub> (4–5 wt%) is also included. These materials are mixed in a planetary ball mill at a rotational speed of 250 rev/min with the powder to ball weight ratio as 1:5 for 40 h milling time using WC balls and vial. The ball-milled material is consolidated by SPS using graphite die and punch. The ball-milled materials are deposited in the form of the layer inside the die. In present development, five layers are selected due to die-size constraint. The layer composition is decided by “Power law” and optimized in such a way that compressive and tensile residual stresses are generated at the outer and middle layer, respectively. Figure 1 shows the arrangement of layers composition in the designed FGCC. The selected parameters are 1100 °C sintering temperature, 100 °C/min heating rate, 100 MPa consolidation pressure and 10 min holding time. In SPS, Joule heating is done by simultaneous application of pulsed electric current and pressure.

**Fig. 1** Composition distribution in FGCC



The consolidation process was monitored by the displacement of the punch while processing. The punch also worked as an electrode for generation of pulse current in deposited powder. This consolidation is performed by two mechanisms solid-state sintering and liquid phase sintering. The consolidated sample had a cylindrical shape (20 mm diameter and 5 mm thickness) and characterized for microstructure and hardness.

### 3 Result and Discussion

#### 3.1 Microstructural Characterization of Spark Plasma Sintered Sample

The microstructural examination of consolidated samples is done with the help of scanning electron microscope (SEM). This investigation is performed on cold-mounted polished samples. The polishing is performed using the different grades of paper and velvet cloth with diamond paste. These polished samples are etched by Murakami's reagent ( $K_3FeCN_6 + KOH + Water$ ) to reveal the grains and grain boundaries. The SEM micrographs were taken at particular layers along the thickness direction so the variation of microstructure with the composition can be observed. Figure 2 shows the SEM micrograph of FGCC without solid lubricant, each micrograph presents different layers. These layers are deposited symmetrically along the thickness, so outer layers (1 and 5) as well as layers 2 and 4 exhibit similar microstructure features. The sintering is performed at 1100 °C by solid-state sintering and results in Co neck formation between WC particles followed by Co melting, which leads to densification. The outer layers (1 and 5) are having more porosity than the middle

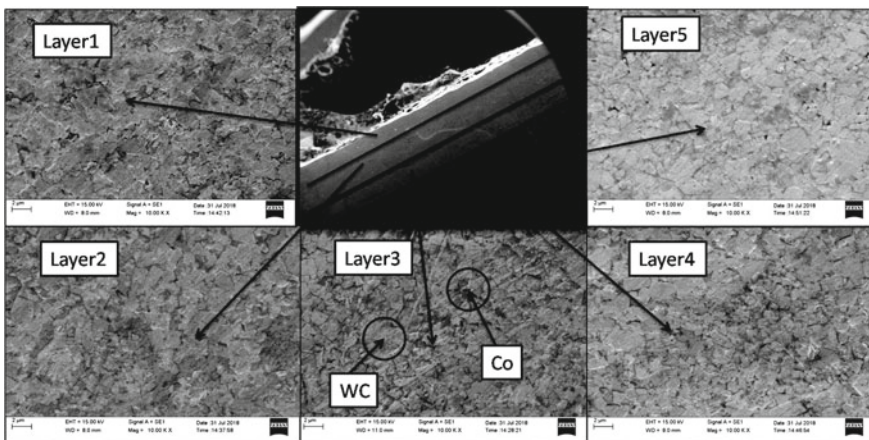
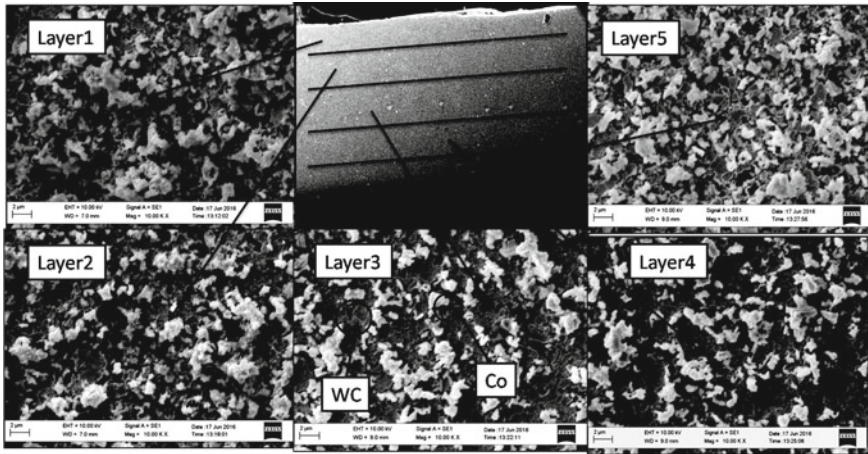


Fig. 2 Micrograph of FGCC without Solid lubricant (CaF<sub>2</sub>)



**Fig. 3** Micrograph of FGCC with Solid lubricant ( $\text{CaF}_2$ )

layer. Two kinds of phases are visible in the micrograph, dark and light grey phases (light grey phase represent WC and light grey phase Co). In the middle layer, the amount of dark grey phase is comparatively high.

FGCC with solid lubricant is also prepared at  $1100\text{ }^\circ\text{C}$  sintering temperature. Figure 3 shows SEM micrograph FGCC with solid lubricant. It is also having similar features as in Fig. 2, the light grey phase represents WC and dark grey phase Co. Layers 1, 5 and layers 2, 4 are similar to each other due to the same composition. The outer layers are having higher porosity than the middle layer. The outer layer is having less Co content as compared to middle and having less porosity due to more densification. The current microstructure observations are in line with the available literature [1, 11, 12].

### 3.2 Hardness of Spark Plasma Sintered Samples

The change in Co volume fraction is responsible for the microstructure variations. Similarly, this Co percentage causes variation in the hardness along its thickness direction. Higher Co percentage results in lower hardness and vice versa. The hardness measurement is performed using Vickers hardness tester along the thickness direction of the polished samples. The indenter is a diamond shape, dwell time is 10 s and load is 9.8 N. The hardness of FGCC without solid lubricant varied from 1341 to 1741 HV at 9.8 N load. The hardness value of FGCC with solid lubricant is varied from 1171–1357 HV. Higher hardness is obtained at the outer layer and lowest at the middle in both samples due to Co composition gradient. The obtained hardness values are in accordance with the available literature [1, 11]. The variation



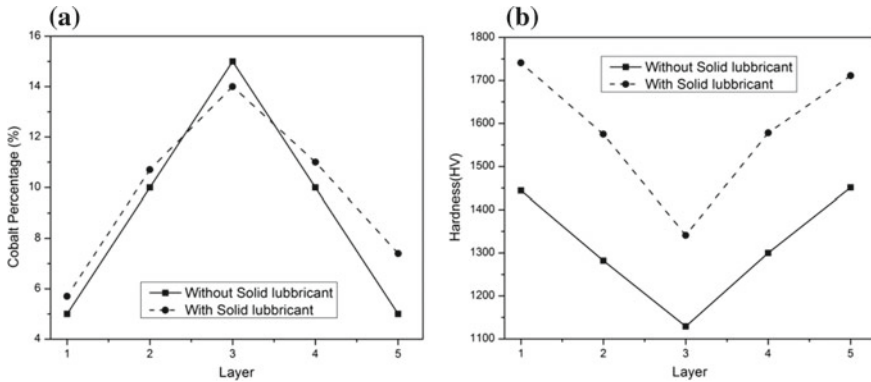


**Fig. 4** a Variation of Cobalt percentage along the thickness at different layers b Variation of hardness along the thickness at different layers

in Co volume fraction in the prepared samples is confirmed by the EDS analysis and the variation is given in Fig. 4a.

## 4 Conclusions

The FGCC with and without solid lubricant is successfully developed by the SPS process. The variation in SEM micrograph, hardness value, and EDS mapping confirm the presence of a gradient. The FGCC with solid lubricant has more porosity and is less hard than another sample due to the presence of  $\text{CaF}_2$  phase. The presence of  $\text{CaF}_2$  phase is responsible for the reduction in hardness of FGCC. The Co volume fraction gradient is also responsible for hardness variation; at the outer layer, higher hardness is observed as compared to the middle layer due to a lower Co volume fraction. Additionally, the outer layer exhibits higher porosity than the middle layer due to a lower Co volume fraction.

## References

1. Parihar RS, Setti SG, Sahu RK (2017) Preliminary investigation on development of functionally graded cemented tungsten carbide with solid lubricant via ball milling and spark plasma sintering. *J Compos Mater* 52(10):1363–1377
2. Parihar RS, Setti SG, Sahu RK (2016) Recent advances in the manufacturing processes of functionally graded materials: a review. *Sci Eng Compos Mater* 25(2):309–336
3. Wang X, Hwang KS, Koopman M (2013) Mechanical properties and wear resistance of functionally graded WC-Co. *Int J Refract Met Hard Mater* 36:46–51
4. Muthuraja A, Senthilvelan S (2015) Development of tungsten carbide based self-lubricant cutting tool material: preliminary investigation. *Int J Refract Metals Hard Mater* 48:89–96

5. Muthuraja A, Senthilvelan S (2015) Adhesive wear performance of tungsten carbide based solid lubricant material. *Int J Refract Metals Hard Mater* 52:235–244
6. Muthuraja A, Senthilvelan S (2015) Abrasive wear performance of tungsten carbide based self-lubricant cutting tool material. *Int J Refract Metals Hard Mater* 51:91–101
7. Xu C, Xiao G, Zhang Y, Fang B (2014) Finite element design and fabrication of  $\text{Al}_2\text{O}_3/\text{TiC}/\text{CaF}_2$  gradient self-lubricating ceramic tool material. *Ceram Int* 40:10971–10983
8. Xing A, Jun Z, Chuanzhen H, Jianhua Z (1998) Development of an advanced ceramic tool material—functionally gradient cutting ceramics. *Mater Sci Eng A* 248:125–131
9. Zhao J, Ai X, Deng J, Wang J (2004) Thermal shock behaviors of functionally graded ceramic tool materials. *J Eur Ceram Soc* 24:847–854
10. Xu CH, Wu GY, Xiao GC, Fang B (2014)  $\text{Al}_2\text{O}_3/(\text{W}, \text{Ti})\text{C}/\text{CaF}_2$  multi-component graded selflubricating ceramic cutting tool material. *Int J Refract Metals Hard Mater* 45:125–129
11. Cha SI, Hong SH, Kim BK (2003) Spark plasma sintering behavior of nanocrystalline WC-10Co cemented carbide powders. *Mater Sci Eng A* 351:31–38
12. Eriksson M, Radwan M, Shen Z (2013) Spark plasma sintering of WC, cemented carbide and functional graded materials. *Int J Refract Metal Hard Mater* 36:31–37

# Experimental and Microstructural Analysis of TIG and MIG Welding on Dissimilar Steels



A. Aravind Reddy and Abu Sufyan Malik

**Abstract** Mild steel and stainless steels are the two utmost steels used in the automotive industries as well as in various constructional and industrial applications. Welding of these steels with lesser defects and higher strengths is the most important need of the current industries. In this paper, TIG and MIG welding is performed between two dissimilar steels. Transitional changes happen frequently in physical and microstructural properties; therefore, this study carries out an experimental and microstructural analysis to determine the properties like hardness, impact strength, tensile strength and microstructure of the weld zone.

**Keywords** Steels · Welding · Microstructure

## 1 Introduction

In the modern era, most of the industries have a high demand of lightweight, high-strength structures with desired product properties which depend on the joining of dissimilar materials for manufacturing. According to Md. Gaffar et.al in their paper published in International Journal of Current Engineering and Technology, they have found that TIG and MIG welding have high hardness and brittleness using filler rod ER304L and ER70S6 [1].

In **TIG welding**, tungsten electrode is placed centrally in the torch. During the inert gas supplied through the annular space between torch and electrode, the filler material is supplied using a separate rod and shielding undertaken by covering the weld zone with a blanket of gases (argon, helium) which prevent the exposure of weld metal to oxygen and hydrogen of the air.

---

A. Aravind Reddy  
Vasavi College of Engineering, Hyderabad 500031, India  
e-mail: [amaramaravindreddy8@gmail.com](mailto:amaramaravindreddy8@gmail.com)

A. S. Malik (✉)  
Mahaveer Institute of Science & Technology, Hyderabad 500005, India  
e-mail: [malikabusufyan@gmail.com](mailto:malikabusufyan@gmail.com)

© Springer Nature Singapore Pte Ltd. 2020  
H. K. Voruganti et al. (eds.), *Advances in Applied Mechanical Engineering*,  
Lecture Notes in Mechanical Engineering,  
[https://doi.org/10.1007/978-981-15-1201-8\\_81](https://doi.org/10.1007/978-981-15-1201-8_81)

In **MIG welding**, the arc is struck between the workpiece and the wire, which act as electrode and filler material; the arc and weld pool were shielded by inert gas. Depending upon the work material, the shielding gas may be argon, helium and carbon dioxide. In this case, the bare metal electrode (consumable electrode) in the form of continuous wire is fed through welding torch with the help of electrical motor and feed rolls [2].

## 1.1 Steels

Mild steels are the carbon steels which generally contain less than about 0.60–1.4 wt% of carbon. The alloy of mild steel with chromium, magnesium, vanadium, tungsten and molybdenum is used as knives, razors, cutting tool, dies, hacksaw blades and crankshaft.

The stainless steels are highly resistant to corrosion in a variety of environments, especially ambient atmosphere. Their predominant alloying element is chromium; a concentration of at least 11 wt% Cr is required. Equipments employed for these steels include gas turbines, high-temperature steam boilers, heat-treating furnaces, aircraft, missiles and nuclear power-generating units.

## 2 Experimental Process

### 2.1 Material and Filler Rod Selection

#### Mild Steel (MS1040) and Stainless Steel (304L)

**AISI 1040** carbon steel has high carbon content and can be hardened by heat treatment followed by quenching and tempering to achieve 150–250 ksi tensile strength.

The chemical composition of **MS1040** plate is: **iron (Fe)**: 98.6–99%; **manganese (Mn)**: 0.6–0.90%; **carbon(C)**: 0.370–0.440%; **sulphur(S)**:  $\leq 0.050\%$ ; **phosphorus (P)**:  $\leq 0.040\%$ .

The mechanical properties of **MS1040** plate are: **tensile strength**: 620 MPa; **yield strength**: 415 MPa; **elastic modulus**: 190–210 GPa; **elongation at break**: 25%; **hardness (Brinell)**: 93; **impact**: 45 J.

**304L** stainless steel is a sought-after material for use in severely corrosive conditions. This steel grade is found in a variety of commercial sectors, particularly in the chemical industry.

The chemical composition of **SS304L** plate is: **iron (Fe)**: 60–65%; **chromium (Cr)**: 18–20%; **nickel (Ni)**: 8–12%; **manganese(Mn)**:  $\leq 2\%$ ; **aluminium(Al)**: 0.100%; **silicon (Si)**: 0.750%; **phosphorus(P)**: 0.045%; **carbon (C)**: 0.03%; **sulphur (S)**: 0.03%.

The mechanical properties of **SS304L** plate are: **tensile strength**: 564 MPa; **yield strength**: 210 MPa; **elastic modulus**: 193–200 GPa; **elongation at break**: 58%; **hardness (Brinell)**: 82; **impact**: 78 J [3].

### Filler Rod for TIG Welding (SS304L) and MIG Welding (ER70S-6)

This **SS304L** welding electrode is a heat-resistant, titanium-stabilized, austenitic alloy that is commonly used for service in the 1000–1600 °F temperature range. It is the grade of choice for applications combining high strength, resistance to scaling and phase stability with resistance to subsequent aqueous corrosion.

The chemical composition of filler rod for TIG welding **SS304L** is: **iron (Fe)**: 60–65%; **chromium (Cr)**: 18–20%; **nickel (Ni)**: 8–12%; **manganese (Mn)**: ≤2%; **silicon (Si)**: 0.750; **phosphorus (P)**: 0.045%; **carbon(C)**: 0.03%; **sulphur(S)**: 0.03%.

Type **ER70S-6** is a copper-coated MS electrode with higher levels of deoxidizers; this wire is suitable for welding of steels with moderate amounts of scale or rust which is used for MIG welding.

The chemical composition of filler rod used in MIG welding **ER70S-6** is: **iron (Fe)**: 95%; **manganese (Mn)**: 1.4–1.85%; **silicon (Si)**: 0.80–1.15%; **copper (Cu)**: 0.50%; **molybdenum (Mo)**: 0.15%; **nickel (Ni)**: 0.15%; **chromium (Cr)**: 0.15%; **carbon (C)**: 0.06–0.15%; **sulphur (S)**: 0.035%; **vanadium (V)**: 0.03%; **phosphorus (P)**: 0.025%.

## 2.2 Welding Procedure

### Metal Cutting

The specimen is built up as per the dimension provided in Table 1 by the grinder cutting machine.

### Edge Preparation

Edge preparation demands for a workpiece which has more than 5 mm thickness. The plates we used for welding are of 10 mm thick. So edge preparation is done. Bench grinding machine is used for edge preparation of a “**V Groove**” at an angle of 60° which means each workpiece possesses 30° angle.

**Table 1** Specimen dimensions

Material	Length (mm)	Width (mm)	Thickness (mm)
Mild steel (MS1040)	150	100	10
Stainless steel (304L)	150	100	10

**Fig. 1** TIG-welded plates**Fig. 2** MIG-welded plates

### Parameter Considered for TIG and MIG Welding

*TIG welding* can be done with either AC or DC current; here, TIG welding is done by DC current, the selected range of DC current and voltage to perform welding require 160 A and 24 V with the negative polarity of electrode. The shielding gas used is argon. The non-consumable electrode exhausted is made of 98% tungsten and 2% thoriated. The diameter of non-consumable electrode is 3 mm. The flow rate of shielding gas is 10 L/min.

*MIG welding* is carried out by employing of DC current of 150 A and 20 V along with the positive polarity of electrode. The shielding gas used is CO<sub>2</sub>. Electrode is made of copper-coated MS wire which has a diameter of 1.2 mm, and the flow rate for gas is 10 L/min (Figs. 1 and 2).

## 3 Visual Inspection of Welded Joint

External features of a welded joint can be inspected through visual inspection like weld bead profile which indicates weld width, bead angle and external defects. The weld bead parameters are measured on profilometer (Table 2).

**Table 2** TIG and MIG visual inspection

Filler used	SS304L (TIG)	Filler used	MSER70S6 (MIG)
Weld bead width	8 mm	Weld bead width	9.5 mm
Weld bead height	6.2 mm	Weld bead height	6.2 mm
Penetration	4 mm	Penetration	11 mm
Reinforcement	2 mm	Reinforcement	3 mm
Weld quality	High	Weld quality	High
Surface defects	Moderate	Surface defects	Moderate

## 4 Destructive Test Results and Analysis

The welding procedure, specification and assessing the suitability of a welded joint are usually performed by destructive testing such as tensile test, impact test and Rockwell hardness test.

### 4.1 Tensile Test

A tensile test measures the response of a material to the stress by applying a pulling force. The specimen is prepared geometrically according to ASME SEC-IX: 2015 standard. The universal testing machine of model TUE-C-600 is undertaken to conduct this test. The method carried out in this experiment entitled as ASTM A370-2015 (Fig. 3; Table 3).

The above details indicate that a satisfactory weld joint performed on welding mild steel with stainless steel can be achieved with both TIG and MIG welding process. The overall tensile test results unfold that the best tensile strength can be acquired with TIG welding process using ER304L filler when we compare it with MIG welding.

Load at yield and the yield stress describes the plastic nature of a material. In TIG welding, the load at yield is 28.8 kN and the yield stress is 230.61 N/mm<sup>2</sup>, so the plasticity starts in TIG welding on 28.8 kN or 230.61 N/mm<sup>2</sup>, whereas in MIG welding it starts at 21.57 kN or 173.183 N/mm<sup>2</sup>, and the plasticity starts at lower

**Fig. 3** Tensile test specimen (ASME SEC-IX: 2015)

**Table 3** Tensile test results

Input data		Output data		
		Properties	MIG Welding	TIG Welding
Specimen shape	Flat	Load at yield	21.57 kN	28.8 kN
Material type	Steel	Yield stress	173.183 N/mm <sup>2</sup>	230.631 N/mm <sup>2</sup>
Specimen description	MIG Welding (MS + SS)	Load at peak	21.720 N/mm <sup>2</sup>	32.250 N/mm <sup>2</sup>
Specimen width	12.48 mm	Tensile strength	174.387 N/mm <sup>2</sup>	258.258 N/mm <sup>2</sup>
Specimen thickness	9.98 mm	% Elongation	9	8
Initial gauge length	50 mm			
Pre load value	0 kN			
Max. load	600 kN			

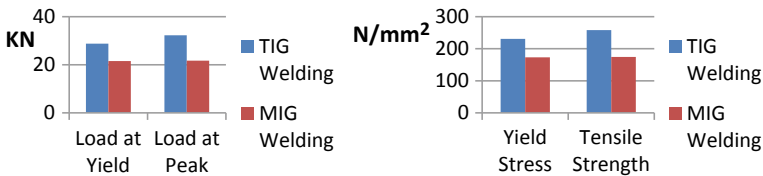


**Fig. 4** Tensile test results

values in MIG welding which shows MIG welding has high plastic nature than TIG welding.

% Elongation describes the ductility of a material, so the % elongation of TIG welding is 8, whereas in MIG welding, it is 9 which indicates that the joint with MIG welding will have higher ductility than TIG welding (Fig. 4).

### 4.2 Impact Test

The research paper undertakes the impact test method for evaluating the toughness and sensitivity of a material. The specimen was made as per ASTM A 370-2015 as shown in Fig. 5. The notch created has depth of 2 mm, and test is conducted on machine model FIT 300(EN) (Table 4).

The above data indicates that MIG-welded joint can bear high toughness, while TIG-welded joint has lesser impact toughness compared to MIG welding. If any sudden load will be applied on the welding part, the TIG welding joint will tend to failure before MIG welding.



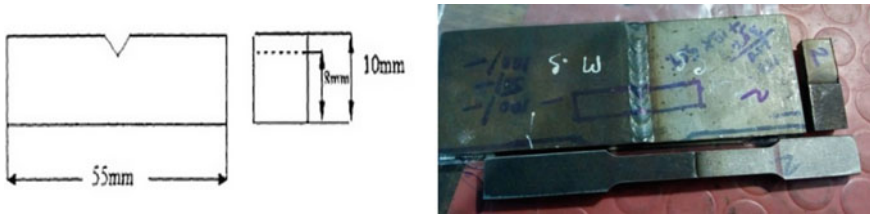


Fig. 5 Specimen for impact test

Table 4 Impact test result

Type of welding and filler rod	Impact strength (Joules)
TIG welding (SS 304 L filler rod)	22
MIG welding (ER70S6 filler wire)	26

### 4.3 Hardness Test

In this experiment, the Rockwell hardness test using C scale was carried out at the weld zone of mild steel and stainless steel. The specimen for the hardness was prepared according to standards. A diamond indenter was used for the test, and the test was deployed with minor load 10 kg and major 140 kg load.

The below results indicate that the hardness of TIG weld bead is harder than MIG; hence, TIG welding can be preferred if hardness is a criterion. Due to unequal heating and cooling of base metals, different hardnesses are found at different parts (Table 5).

## 5 Microstructural Analysis

The microstructural analysis is carried out by optical microscope (MET SCOPE-1) and the method ASTM E 407-07 and ASTM E 3-11. The microstructure is undertaken on magnification of 200x. The etching agent used is aqua regia and nital.

Table 5 Hardness test result

Type of welding and filler rod	Hardness on weld bead
TIG welding (SS 304 L filler rod)	80
MIG welding (ER70S6 filler wire)	62

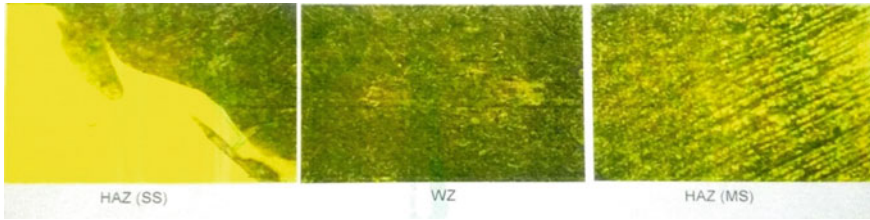


**Fig. 6** Microstructure of TIG welding

### **5.1 TIG Welding Microstructure**

Microstructure includes grain structure of austenite, pearlite and ferrite matrix. Microstructures comprise with fine austenite, pearlite and ferrites grains are uniformly distributed on weld zone to base material. No cracks observed at HAZ. As the microstructure indicates distribution of phases like fine austenite and pearlite with uniform distribution of ferrite grains, it implies that the weld bead has both strength and ductility. Hence, optimum mechanical properties are obtained and can be further improved by heat treatment. It can be observed that the distribution of pearlite in welding zone is more; it indicates that it has maximum ductility and tensile strength but has low toughness (Fig. 6).

### **5.2 MIG Welding Microstructure**

Microstructure consists of fine grain structure of austenite, pearlite and ferrite matrix. Microstructures consist of fine austenite and pearlite ferrites grains are uniformly distributed on weld zone to base material. No cracks observed at HAZs.

The microstructure indicates distribution of phases like fine austenite and pearlite with uniform distribution of ferrite grains. It implies that the weld bead has both strength and ductility. Hence, optimum mechanical properties are obtained and can be further improved by heat treatment (Fig. 7).



**Fig. 7** Microstructure of MIG welding

## 6 Conclusion

This paper elaborates about the effects of TIG and MIG welding between two dissimilar steels and results in these following points.

- (1) TIG welding with filler rod SS304L has more tensile strength and yield stress as compared to MIG welding with filler rod ER70S6.
- (2) MIG welding has higher percentage of elongation as compared to TIG welding.
- (3) MIG welding has higher toughness.
- (4) The hardness of TIG welding at weld bead is higher as compared to MIG welding, so TIG welding can be employed when strength is the criterion for manufacturing.
- (5) By visual inspection, we found that TIG welding has superior quality than MIG welding.
- (6) The microstructure of both TIG welding and MIG welding indicates that they have uniform strength and ductility.

## References

1. Gaffar M, Shankar M, Kumar PS, Satyanarayana VV (2017) Experimental investigation on welded joints of dissimilar steels. *Int J Curr Eng Technol* 7(3). E-ISSN:2277-4106, P-ISSN:2347-5161
2. Kaynak I (2016) The welding of dissimilar materials with copper based consumables. *Usak Univ J Mater Sci*
3. Callister Jr WD, Rethwisch DG (2010) *Material science and engineering an introduction*, 8th edn. Wiley, Hoboken (2010)

# Thermal Management of Avionic Packages Using Micro-blower



K. Velmurugan, V. P. Chandramohan, S. Karunanidhi  
and D. Sai Phaneendra

**Abstract** Thermal management of avionic packages mostly involves bringing down conduction and radiation resistance between the components and the sink. Fans and blowers are not recommended because of the acoustic noise generated and the EMI/EMC disturbance created by them. In this paper, an attempt has been made to find the utility of micro-blower for local cooling of high-power components. The micro-blower is operated by piezoelectric vibrators whose frequency is beyond 20 kHz. These blowers are compact and draw very less power. Moreover, no acoustic noise and EMI/EMC disturbances are encountered. Experimental study has been carried out to find the velocity of air flow with respect to distance from the exit for different input power. To assess the cooling effect of micro-blower on components, components are simulated with patch heater and the case temperature is found for packages with and without blowers, respectively. To find the effect of orientation of components in an electronic package (generally not known), measurements have been carried out for different component orientation. Based on the experiment, the maximum temperature drop and minimum temperature drop were found to be 10 °C and 8.6 °C, respectively. This work facilitates the use of micro-blower for the local cooling of electronic components for avionic applications.

**Keywords** Piezoelectric · IR camera · Micro-blower · Anemometer

---

K. Velmurugan (✉) · S. Karunanidhi · D. Sai Phaneendra  
RCI, DRDO, Hyderabad, India  
e-mail: [velmurugan.k@rcilab.in](mailto:velmurugan.k@rcilab.in)

S. Karunanidhi  
e-mail: [Karunanidhi.s@rcilab.in](mailto:Karunanidhi.s@rcilab.in)

D. Sai Phaneendra  
e-mail: [phani.dintyala@gmail.com](mailto:phani.dintyala@gmail.com)

V. P. Chandramohan  
National Institute of Technology Warangal, Warangal 506004, Telangana, India  
e-mail: [vpcm80@nitw.ac.in](mailto:vpcm80@nitw.ac.in)

# 1 Introduction

The working principle of the micro-blower can be explained in four simple steps: (a) no-load state, (b) suction (piezo bending down), (c) discharge (piezo return to normal state) and (d) discharge (piezo bending up) as shown in Fig. 1 [2–4].

The micro-blower consists of a piezoelectric element, diaphragm, separator and nozzle. The nozzle dimension is 1.6 mm, and it is circular in cross section [2]. The diaphragm is bonded to a piezoelectric element. Indirect piezoelectric effect causes the piezoelectric element to vibrate when subjected to an AC voltage. The diaphragm is bonded to piezoelectric element as shown in Fig. 2, which causes it to vibrate with AC input signal. During the process, the diaphragm is bent down creating partial vacuum inside the blower which forces air from outside to enter into the blower (phase 2). When the piezoelectric element bends up, air inside the blower is pushed through the nozzle provided on the top (phase 4).

To derive the optimal operating frequency of piezoelectric blower for use in drug delivery, Qifeng et al. [1] conducted numerical simulation and concluded that first natural frequency generates higher flow rate compared to others and that silicon offers a lower natural frequency compared to SiO<sub>2</sub> and steel. Hitara et al. [2] invented a device related to piezoelectric micro-blower which is suitable for compressive fluid such as air. Application of voltage to the piezoelectric element causes the diaphragm

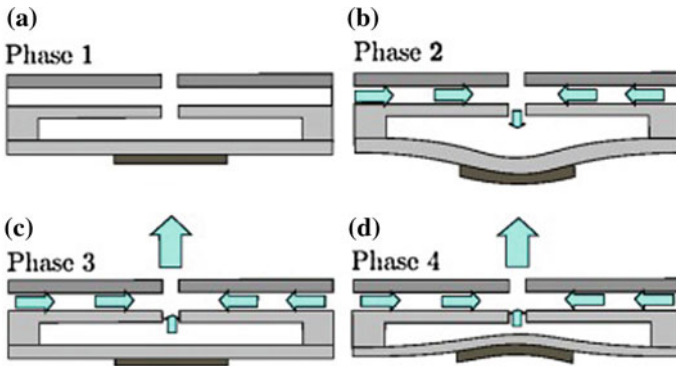
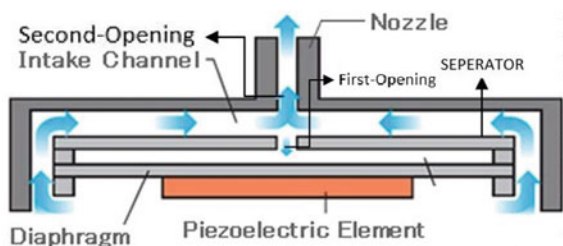


Fig. 1 Stages in working of piezoelectric micro-blower

Fig. 2 Cross-sectional view of micro-blower



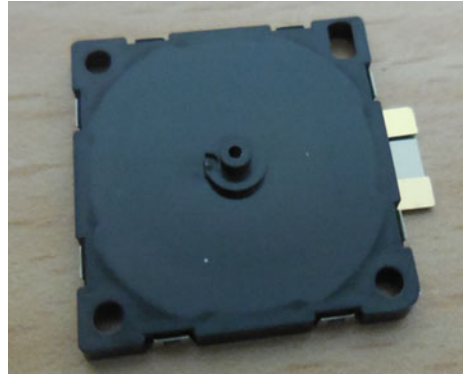
to vibrate so that gas can be drawn from inlet and discharged through the nozzle. Fukue et al. [3] obtained the cooling performance of heat sink of a novel miniature piezoelectric micro-blower using numerical simulation. Different patterns of heat sink (plate with fins) were modelled and analysed using FlowTherm-10.1 simulation software, and inline finned heat sink was found to be the most preferable. Fukue et al. [4] conducted an experiment using micro-blower manufactured by MORATA to know the effect of obstruction on P–Q curves at inlet and outlet. The micro-blower achieved a high cooling performance regardless of packing density without causing any significant changes in both the cases.

Settling time ( $t_s$ ) is the parameter used to define whether the amplitude of actuator becomes steady or not. Covet et al. [5] did experimental research and numerical study on control of flow separation and concluded that in the span of reaching the settling time, the membrane deflects more and the deflection reduces once the membrane becomes steady. It was observed that with increase in the value of actuation frequency, the settling time also increases and that with increase in frequency, settling time, duty cycle and voltage, the velocity of the air increases. Phase-locked particle image velocimetry (PIV) measurements were done to detect the velocity behaviour, i.e., the penetration length. It was observed that the reattachment point came down and the separation of flow reduced to some extent by the use of micro-blowers. The parameter named forcing frequency ( $s_f$ ) is defined as the value at which maximum velocity is obtained. Fan et al. [6] have done numerical study on piezoelectric, valveless, micro-pump and have observed the changes in membrane deflection shape at various frequencies. For frequencies less than 7.5 kHz, both pumping rate and membrane deflection amplitude increase with the increase in actuation frequency, and for frequencies greater than 7.5 kHz, pumping rate decreases and the membrane deflects in undesirable way with increase in actuating frequency. Similarly for frequencies greater than 50 kHz, both pumping rate and membrane deflection amplitude decrease with increase in actuating frequencies. Gaffari et al. [7] conducted an experimental investigation using particle image velocimetry (PIV) method to observe the flow and to know the optimal jet-to-surface spacing ratio. Based on the Nusselt number, it was concluded that H/D ratio of 10–15 is preferable and that the preferred operating frequency of the piezoelectric actuator is 25 kHz which falls in the ultrasonic region meaning that the device can function with low noise. Gopinadh et al. [8] performed numerical analysis using the fluid–structure interaction interface of COMSOL Multiphysics software to analyse jet formation of piezoelectric actuated micro-blower and found that there is no change in the volume flow rate and jet formation for the micro-blower.

## 2 Experimental Set-up

In the present study, experimental investigation is carried out to find the variation of velocity with distance along the direction of flow, the variation of velocity with change in input voltage and the thermal performance of micro-blower. A commercially

**Fig. 3** Micro-blower  
(muRata,  $20 \times 20 \times$   
1.85 mm)



available product muRata MZB1001E00 ( $20 \text{ mm} \times 20 \text{ mm} \times 1.85 \text{ mm}$ ) micro-blower was used for study and is shown in Fig. 3.

Thermal performance test was carried out for different configurations of micro-blower. All the experiments were performed at RCI (Research Centre Imarat), DRDO, Hyderabad, India.

**i. Velocity Measurement test:**

Velocity is one of the key parameters as it decides the amount of heat that can be removed by forced convection from the heat-generating components of the avionics package. The experimental test set-up consists of a PC with software (AccuTrac™), DC power supply (TDK-Lambda,36-6/U, U.S.A), hot-wire anemometer (DegeeControls-UAS1500, U.S.A,  $\pm 0.025 \text{ m/sec}$ ) and micro-blower with driver circuit (muRata-MZB1001E00, Japan). The measurements were carried out in longitudinal direction for different operating input voltages and for different distances between an aluminium plate and the micro-blower. The experimental set-up for velocity measurement is shown in Fig. 4. DC power source is used to send controlled DC voltage ( $0\text{--}36 \text{ V}$ ) to the driver circuit of micro-blower. Soldering of positive and negative wires to micro-blower and driver circuit was carried out using lead-free solder maintained at  $350 \text{ }^\circ\text{C}$  with a contact time of 3 s.

Square input signal was given to micro-blower and operated at 25 kHz frequency [5]. The driver circuit takes DC voltage as input and supplies AC voltage at 25 kHz to micro-blower. The velocity readings from anemometer were saved data with the help of logging PC and AccuTrac™ software. The experiment was carried out to know longitudinal variation of velocities (along the flow) from the blower exit for three different operating voltages ( $10 V_{P-P}$ ,  $15 V_{P-P}$  and  $20 V_{P-P}$ ).

**ii. Thermal Performance of Micro-blower:**

The present work mainly concentrates on the heat removal from heat source which is generated by the electronic components of avionic packages. Experiments were carried out to know the heat reduction capacity of the blower. In avionic applications, the space and orientation of the components are decided by many factors. The

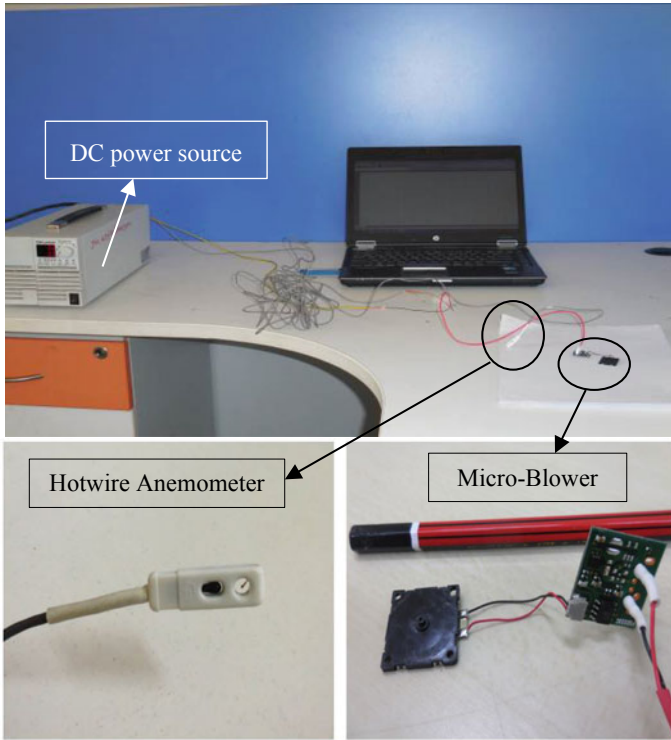


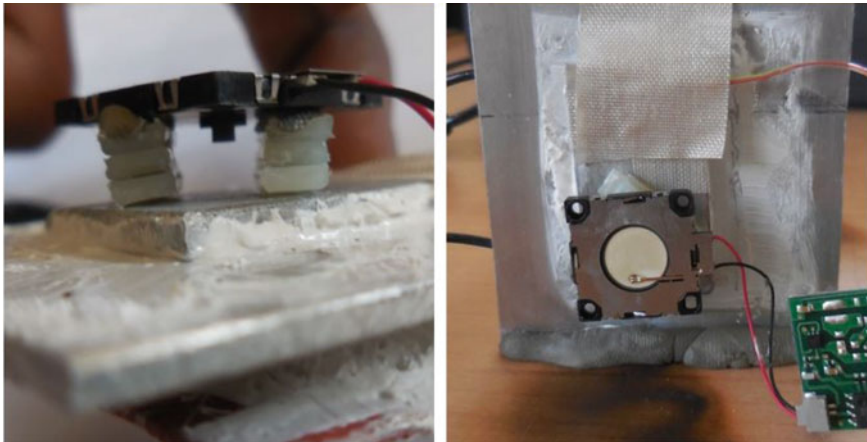
**Fig. 4** Experimental test set-up for velocity measurement test

performance of the blower may not be same in all directions. To know the effect of orientation on the performance of micro-blower, the measurements were carried out for two types of alignment, viz. heater facing up blower facing down (vertical alignment) and heater and blower side by side (horizontal alignment) as shown in Fig. 5.

As per existing literature, “Every 10 °C Increase in Component Temperature Reduces Component Life by Half”. The distance between blower and heat-generating component was maintained at 5 mm due to high velocity. Thermal performance test set-up consists of nichrome test heater of square domain (OmegaLux-SRMU100202P0, 120 V, 0.34 A, 50.8 mm × 50.8 mm), aluminium plate (60 mm × 60 mm × 2 mm), data acquisition system (Hoiki-8421-51, Japan), DC power supply (TDK-Lambda, 36-6/U, U.S.A), K-type thermocouples (OMEGA-M0503, U.S.A) and micro-blower (muRata-MZB1001E00, Japan).

The nichrome heater was attached to aluminium plate and thermal paste was added in between heater and plate to reduce contact thermal resistance. Nichrome heater generates heat by taking 120 V, 0.34 A current as input and transfers heat to aluminium plate attached to the heater. The aluminium plate was used as a constant heat source to measure the temperature variations.





(a) Vertical alignment

(b) Horizontal alignment

**Fig. 5** Different alignments of the heat source and micro-blower

To provide 120 V constant AC voltage to the nichrome heater, a step-down transformer was used. The output voltage of step-down transformer and DC power supply were continuously monitored using a multi-meter. K-type thermocouple was used to measure the temperature on plate. Sensor end of the thermocouple was attached to surface of aluminium plate, and the other end was connected through a data acquisition system to the PC. DC power supply was used to power the driver circuit of the micro-blower.

The experimental set-up for thermal performance test is shown in Fig. 6. Entire test was conducted at an ambient temperature of 32 °C. The heat source was placed near the exit of the micro-blower. The air coming from the blower exit with specific flow rate and velocity impinges on to the heat source.

The experiment was carried out with the aluminium plate heated to 100 °C. It was ensured that the temperature of the aluminium plate reached the steady state before switching on the micro-blower to ensure exact measurement of the temperature drop.

### 3 Results

The results of velocity measurement experiment and thermal performance test are discussed below.

#### i. Velocity Measurement:

Variation of velocity with distance along the direction of flow (longitudinal) for different input voltages was observed and plotted in Fig. 7.

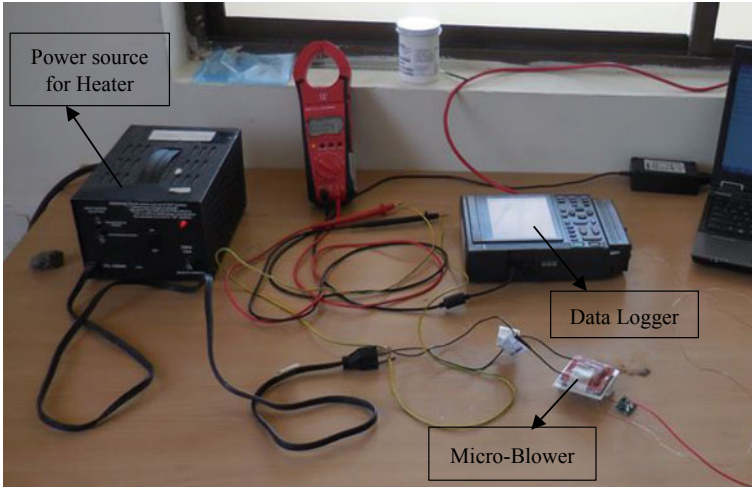


Fig. 6 Experimental test set-up for thermal performance test

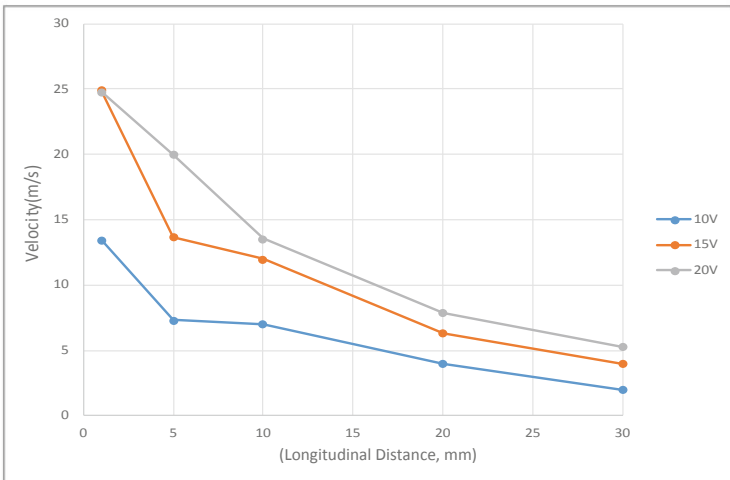
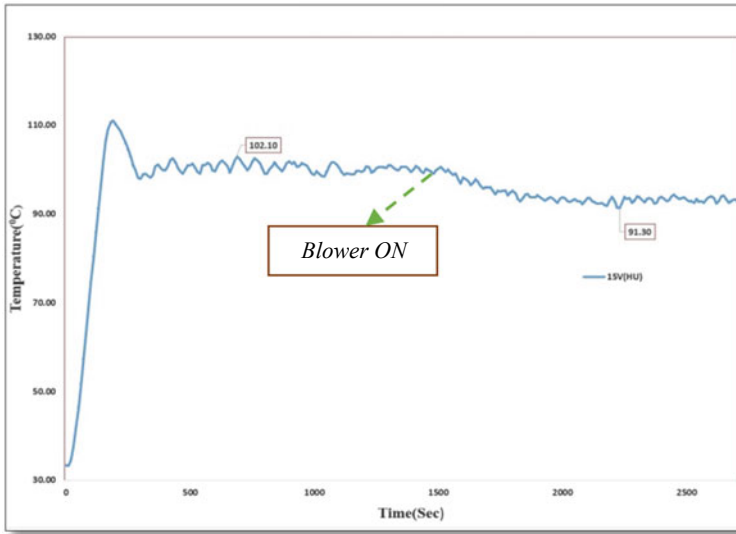


Fig. 7 Variation of velocity with longitudinal distance from micro-blower

Figure 7 shows the plot between longitudinal distance and velocity. From results, it can be observed from the plot that magnitude of velocity reduces as the longitudinal distance between the blower exit and heat source increases. Also magnitude of velocity increases as the input voltage to blower increases. Speed of blower output air reduces due to entertainment of resistance offered by still ambient air which also reduces the heat transfer coefficient. With increase in impinging distance, the amount and strength of recirculation also decrease.



**Fig. 8** Temperature drop of heated plate for vertical alignment of blower

**ii. Thermal performance:**

The micro-blower was operated with 25 kHz frequency at 20 V input power, and the temperature drop of aluminium heater plate was observed for different orientations of the micro-blower. K-type thermocouples were placed at fixed position for all the cases.

Figure 8 shows temperature versus time plot for vertical alignment of the blower after it is switched ON. From the result of vertical alignment of the blower, when the heater is facing up and blower facing down, there is a maximum of 10 °C variation in temperature which was observed.

Figure 9 shows temperature versus time plot for horizontal alignment of the blower after it is switched on. For horizontal alignment of the blower, a maximum of 8.6 °C variation in temperature was observed.

From thermal performance test results, it was observed that there is no considerable variation between horizontal alignment and vertical alignment. It is due to the fact that there is no variation in the resistance offered to flow with change in alignment. The reduction in heat-carrying capacity in case of horizontal arrangement is due to flow coming from aluminium surface which is hot when compared to impinging air. The air is sucked again by blower as the hot air flows upward due to density difference.

The workplace was kept clean as micro-blower affected by dirty environment, and it was ensured that constant velocity and temperature are maintained and no external parameter influences the test results.

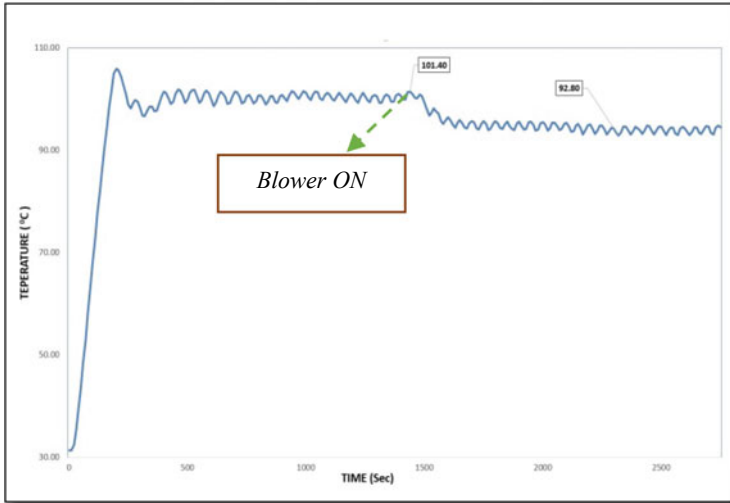


Fig. 9 Temperature drop of heated plate for horizontal alignment of blower

iii. **IR images of Thermal Performance Test:**

IR images are also called as thermal images and are captured using IR camera (thermal camera). All objects in nature emit infrared energy (heat) as a function of temperature. Hotter the body, higher will be radiation that it emits.

A thermal camera is a kind of heat sensor that can detect tiny differences in temperature by collecting the infrared radiation from the objects and creates an electronic image based on the information available about temperature differences.

Thermal imaging is a method of differentiating the objects with distinct colour codes (thermal contours according to temperature emitted by them). In the present study, thermal images were captured by using IR camera during thermal performance test. Images captured before and after the test are shown in Figs. 10 and 11, respectively. During the experiment, it was observed that the temperature of the micro-blower remained at 32 °C even though the temperature of the aluminium plate reached 100 °C.

**4 Conclusion**

Velocity response and thermal performance of the micro-blower were investigated at different operating conditions.

The distance between heat-generating component and micro-blower should be less than 5 mm for optimal velocity along longitudinal direction of flow at all operating

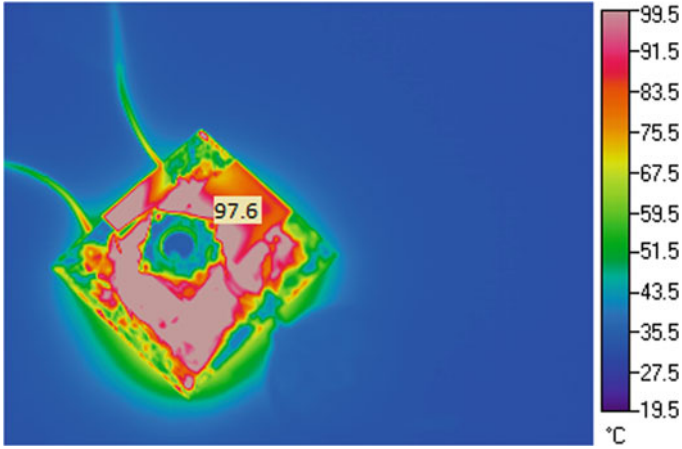


**Fig. 10** IR image of the heat source with the blower switched off

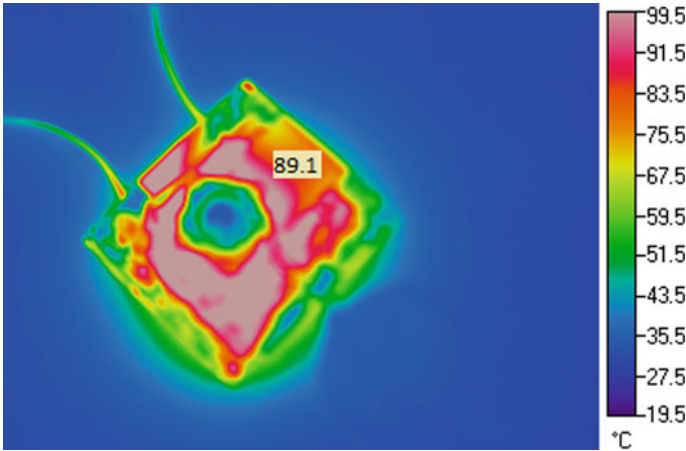


**Fig. 11** IR image of the heat source with blower switched on

input voltages of micro-blower. Beyond 5 mm, there is a significant drop in velocity was perceived which effects the heat-removing capacity of the blower.

Thermal performance test shows that there is a remarkable heat reduction and a temperature drop of about 10 °C with the use of micro-blower which can double the life of electronic component. For an optimal distance of 5 mm between aluminium plate and micro-blower, it is observed that there is a 10 °C of temperature reduction (as shown in Fig. 8) for vertical alignment. There is no significant difference in temperature which was noted with difference in alignment. Higher the temperature difference between heat-generating component and ambient air, higher the heat-removing capacity of micro-blower. Also, it is noticed that at higher voltages, the

blower can reduce more amount of heat as the velocity is increasing with respect to input voltage for the blower. From the results, it can be concluded that the micro-blower is effective in cooling of electronic components in avionic packages and will help in increasing their reliability, performance and life span.

## 5 Scope for Future Work

- Further study by performing the thermal performance test at high altitude.
- Improve heat removal using heat sink with fins and rough surface.

**Acknowledgement** The authors gratefully acknowledge the support of NIT (National Institute of Technology) Warangal and RCI (Research Centre Imarat), Hyderabad, DRDO, India.

## References

1. Cui Q, Liu C, Zha XFW (2006) Design and simulation of a piezoelectrically actuated micropump for the drug delivery system. In: Proceedings of IEEE-2006, International conference, Shanghai, China
2. Hitara A, Kamitani G, Wada H, Sunaga M, Kanal S (2014) Piezoelectric micro-blower, US patent No: 8,978,787, 25<sup>TH</sup> March, 2014
3. Fukue T, Matsura Y, Hirose K, Terao H (2014) Evaluation of cooling performance of a piezoelectric micro-blower in narrow flow passage. In: ICEP 2014 proceedings
4. Fukue T, Matsura Y, Hirose K, Terao H (2014) Effect of obstruction in front of a piezoelectric micro-blower on performance characteristics. In: IEEE, 06 Mar 2014. <https://doi.org/10.1109/icsj.2013.6756109>
5. ChovetC, Lippert M, Keirsbuck L, Foucaut JM (2016) Dynamic characterization of piezoelectric micro-blower, Science Direct, vol 249, 1st October 2016
6. Fan B, Song G, Hussain F (2005) Simulation of piezoelectrically actuated valve less micro pump, vol 14. Institute of Physics Publications, 4 Mar 2005
7. Ghaffari O, Solovitz SA, Ikhlaiq M, Arik M (2016) An investigation into flow and heat transfer of an ultrasonic micro-blower for electronic cooling applications, Science Direct, 16 June 2016
8. Gopinadh KV, Kumar PM, Velmurugan K (2016) Design and simulation of bimorph piezoactuated micro blower. Int J Sci Res Sci Eng Technol 2(6):317–330. Print ISSN: 2395-1990

# Evaluation of Mechanical Properties of Banana and S-glass Fiber-Reinforced Hybrid Nanosilica Composite



P. Srinivas Manikanta, M. Somaiah Chowdary  
and M. S. R. Niranjan Kumar

**Abstract** The aim of the present work is to evaluate the mechanical properties of banana and S-glass fiber-reinforced hybrid nanosilica composite. The glass and other synthetic fiber-reinforced polyester composites give high strength when compared with the natural fiber-reinforced composite, but their applications are limited because of the high cost of fabrication. So to overcome the cost of fabrication and to meet the high strength as of synthetic composite, a new hybrid composite is fabricated by using 50% of natural fiber and 50% of synthetic fiber. The new composite is fabricated by reinforcing the stacking layers of woven banana and s-glass fibers with the polyester resin as a matrix and nanosilica as filler material. Different samples were prepared by changing the stacking sequence of fiber placed in the composite and weight percentage of nanosilica powder that is mixed into the resin. The fabrication is done by the hand layup method. The mechanical properties like tensile strength, flexural strength, tensile modulus, and flexural modulus were studied. The morphological study is done through a scanning electron microscope to observe the fibers pullout, stacking of fibers, and the behavior of matrix in the hybrid composite. The change of weight percentage of nanosilica and the stacking sequence of fibers in the composite show the improvement in mechanical properties.

**Keywords** Stacking sequence of fibers · Polyester resin · Nanosilica

---

P. Srinivas Manikanta

Department of Mechanical Engineering, Prasad V Potluri Siddhartha Institute of Technology,  
Vijayawada 520007, Andhra Pradesh, India  
e-mail: [srinu4633@gmail.com](mailto:srinu4633@gmail.com)

M. Somaiah Chowdary (✉) · M. S. R. Niranjan Kumar

Department of Mechanical Engineering, Prasad V Potluri Siddhartha Institute of Technology,  
Vijayawada 520007, Andhra Pradesh, India  
e-mail: [somaiahchowdary@pvpsiddhartha.ac.in](mailto:somaiahchowdary@pvpsiddhartha.ac.in)

M. S. R. Niranjan Kumar

e-mail: [coe@pvpsiddhartha.ac.in](mailto:coe@pvpsiddhartha.ac.in)

© Springer Nature Singapore Pte Ltd. 2020

H. K. Voruganti et al. (eds.), *Advances in Applied Mechanical Engineering*,

Lecture Notes in Mechanical Engineering,

[https://doi.org/10.1007/978-981-15-1201-8\\_83](https://doi.org/10.1007/978-981-15-1201-8_83)

## 1 Introduction

A composite material generally consists of two or more macro constituents with different chemical composition and having a distinct interface which separates each other. The constituents are also insoluble in each other. The constituent which is harder and stronger than the other constituent is called as a reinforcement which is a discontinuous phase, and the other constituent is called as a matrix which is a continuous phase. The discontinuous phase may consist of one or more phases. Nano- or micropowders can be taken as filler material in the matrix. There are three types of matrix materials; they are metal matrix, ceramic matrix, and polymer matrix out of which polymer matrix has wide applications. The reinforcement may be fibrous or non-fibrous. The fibers which are extracted from plants and other living species are called natural fibers, and man-made fibers are called as synthetic fiber. The fiber mainly acts as the load-carrying members in the composite.

By the combination of two or more different types of fibers as reinforcement in a matrix, we obtain a hybrid composite material. The hybridization of natural fiber and synthetic fibers shows a significant strength value and low cost of fabrication. Natural fiber shows moderate mechanical properties, but they available abundantly and at very low cost, whereas synthetic fiber possesses high mechanical properties, but they are high in cost. The fabrication of new hybrid composite of high strength and low cost of fabrication is made by combining both synthetic and natural fibers as reinforcement in this composite. With this, we can reduce 50% cost of production and we can obtain a significant strength value.

Banana fiber is the waste product of banana cultivation, which is extracted from the stems of banana trees. So, it is abundantly available at low cost. Banana shows an energy saving replacement of synthetic fibers. It is a natural bast fiber which has a wide range of applications and it can be developed into mats, ropes, and twines, but it uses only 10% of its pseudostem.

A number of extremely fine fibers of glass will constitute a glass fiber. It is available at moderate cost when compared to other synthetic fibers. They are significantly less brittle, very strong, and relatively lightweight when used in the composite. They are mainly used in building thermal insulation.

Silicon dioxide nanoparticles are also known as silica nanoparticles or nanosilica. They have a great deal of research due to their stability, and they have a very low level of toxicity. Nanosilica powder appears to be in the form of white powder. Nanosilica is a good additive to the plastics and rubbers. It is also used as strengthening filler for composites concrete and other construction composites.

Polymer matrix are two types; they are thermosets and thermoplastics. Polyester resin is a thermosetting polymer. It is adequately resistant to water, a variety of chemicals, temperature, and aging. It has good wetting properties of glass fibers, and they are mainly used in sheet molding compounds and bulk molding compounds. It is very popular for its simple fabrication methods and low cost.

From the references, [1] has studied the mechanical properties and tribological behavior of nanofiller reinforced polymer nanocomposites with a different stacking



sequence of the fiber. The mechanical properties increase as a weight percentage of nanopowder increases up to three weight percent of nanopowder. The study says that the stacking sequence and weight percentage of nanofiller are important factors for tensile and flexural strengths. Many studies show that hybrid composite mainly contains either natural fiber or synthetic fibers as a reinforcement which gives moderate mechanical properties [2–18]. A less number of studies have been carried on both natural and synthetic fiber-reinforced hybrid composites with the nanofiller material. Therefore, the aim of the present study is to fabricate a new type of composite with woven banana and s-glass reinforced hybrid polyester composite with nanosilica as filler material.

## 2 Methodology

### 2.1 Material

To fabricate the laminated hybrid composite used in this study uses the following material and the composites with stacking sequence and percentage of mass are represented in Table 2 . The physical properties of banana and s-glass fiber are shown in Table 1.

- Polyester resin: The general polyester resin is used and is mixed with a catalyst (MEKP) and hardener (cobalt) for curing.
- Banana fiber: The banana fiber is used in the woven mat form.
- S-glass fiber: The S-fiber is used in the woven mat form.

**Table 1** Physical properties of banana and S-glass fiber

Physical properties	Banana fiber	S-glass fiber
Density ( $g/cm^3$ )	1.3	2.4
Tensile strength (MPa)	54	4700–4800
Flexural modulus (GPa)	2–5	4.5–4.9
Young's modulus (GPa)	3.48	86–93

**Table 2** Stacking sequence and weight fractions (%) of fiber and resin in the composite

Stacking sequence	wt% of fibers		Fiber weight fraction (%) in composite	Polyester resin weight fraction (%) in composite
	Banana	S-glass		
BGGB	50	50	26	74
GBBG	50	50	26	74
GBGB	50	50	26	74

G = Woven S-glass fiber and B = Woven Banana fiber

## 2.2 Fabrication

Firstly, the surface of the mold is cleaned with a thinner solution and was allowed to dry for 10 min. Now applying the grease as releasing agent to all sides of the mold and the base plate and few minutes. A few minutes is given to mold to get it set for mold layup. The polyester resin, catalyst, and hardener are mixed in 100:1.5:1.5 proportion, and nanosilica is used as filler material; the curing time of the resin is observed carefully from the chart of the laboratory that is usually notified. The care must take so that the resin does not cure in the curing vessel itself. A constant watch-over is maintained while mixing of resin, hardener, catalyst, and nanosilica using a stopwatch. The woven banana fiber mat is cleaned gently and is kept in the sunlight for 1–2 h. The size of the laminate which is to be fabricated is restricted to 200 mm × 170 mm × 3 mm. Every laminate consists of four layers of fibers out of which two layers are woven banana fiber and two layers are s-glass fiber. The laminate is prepared by placing the fiber mats one over the other in the polyester resin which is mixed up with nanosilica. The fabrication is done by the hand layup method. Similarly, different laminates were prepared by changing the stacking sequence of fibers and the weight percentage of nanosilica. Now, all the hybrid composite laminates were cured under the general loading conditions for 12 h. The woven banana fiber and s-glass fiber used in the fabrication are shown in Figs. 1 and 2.

**Fig. 1** Woven banana fiber



**Fig. 2** Woven S-glass fiber



### 3 Mechanical Properties of Hybrid Composite

#### 3.1 Tensile Test

The flat tension test specimens were prepared according to the ASTM D638M-89, and the length of the specimen is 160 mm. The test is carried out on the tensometer, by means of applying load with a crosshead speed of 10 mm/min on the specimen until the results are observed before the specimen gets a failure. Five samples of each laminate were tested to get the mean values. The same method is followed for all the tensile test specimens of different compositions to get the mean tensile strength and tensile modulus values from the mean load and elongation values. The tensile test specimens before and after the tests are shown in Figs. 3 and 4.

**Fig. 3** Tensile test specimens before fracture

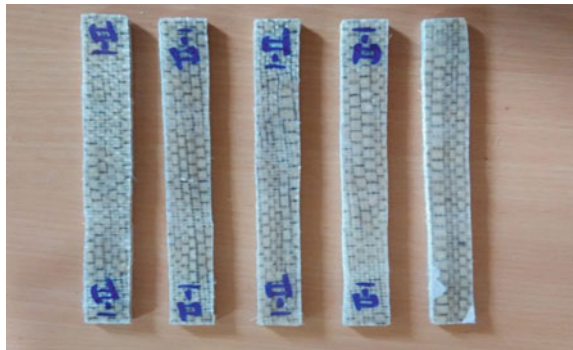


**Fig. 4** Tensile test specimens after fracture



### 3.2 Flexural Test

The flat flexural test specimens were prepared according to the ASTM D638M-89, and the length of the specimen is 100 mm. The test is carried out on the tensometer, by means of 3-point flexural loading method. The load is applied with a crosshead speed of 10 mm/min on the specimen until the results are observed before the specimen gets a failure. Five samples of each laminate were tested to get the mean loading and slope of bending curve values. The same method is repeated for all the nine laminates, and the results are compared. The flexural test specimens before and after the tests are shown in Figs. 5 and 6.

## 4 Results and Discussions

In the above methodology total, 9 laminates were prepared by changing the stacking sequence of fibers and the weight percentage of nanosilica. Five samples for tensile

**Fig. 5** Impact test specimens before fracture



**Fig. 6** Impact test specimens after fracture

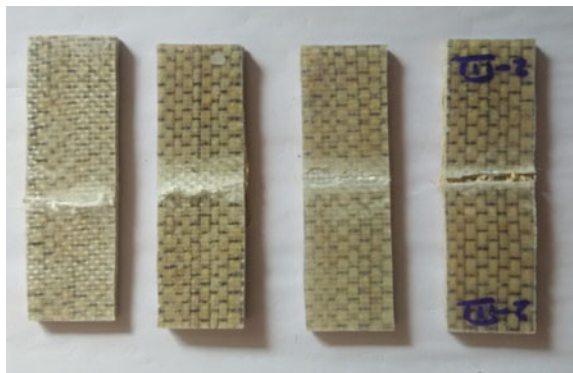


**Table 3** Mechanical properties of the hybrid composite with the addition of nanosilica

Composite sample	Tensile strength (MPa)	Flexural strength (MPa)	Tensile modulus (GPa)	Flexural modulus (GPa)
Polyester	19.76	35.5	0.23	0.88
BGGB + 1wt% nanosilica	91.2	281.33	4.43	5.14
BGGB + 2wt% nanosilica	101.44	345.34	4.16	4.74
BGGB + 3wt% nanosilica	112.64	176	3.36	4.5
GBBG + 1wt% nanosilica	93.97	238.67	3.31	3.01
GBBG + 2wt% nanosilica	96.64	268	3.5	4.15
GBBG + 3wt% nanosilica	100.1	321.33	4.6	3.5
GBGB + 1wt% nanosilica	98.93	304	3.21	3.14
GBGB + 2wt% nanosilica	102.99	380	3.31	5.3
GBGB + 3wt% nanosilica	101.49	302.67	4.8	3.03

G = Woven S-glass fiber and B = Woven Banana fiber

test and 5 samples for the flexural test from each laminate are tested as per standard ASTM methods. The results are observed, and strength and modulus values are calculated. The values are given in Table 3.

### 4.1 Tensile Strength and Tensile Modulus

The tensile strength and tensile modulus values are observed, and the corresponding graphs are plotted. The graph for tensile strength and tensile modulus of BGGB hybrid composite laminate is shown in Figs. 7 and 8, respectively. From the graph, it is observed that the tensile strength is maximum at 3wt% nanosilica and is minimum at 1wt% nanosilica. The tensile modulus value is maximum at 1wt% nanosilica and minimum at 3wt% nanosilica. As the percentage of nanosilica increases, the bonding of resin with the fiber increases, but the further increase may increase the viscosity of the resin which leads to lower adhesion process. The presence of both glass layers at the center also causes the increased strength.

Now, the graph for tensile strength and tensile modulus of GBBG hybrid composite laminate is shown in Figs. 9 and 10, respectively. From the graph, it is observed that the tensile strength is maximum at 3wt% nanosilica and is minimum at 1wt%

**Fig. 7** Tensile strength variation for different wt% of nanosilica

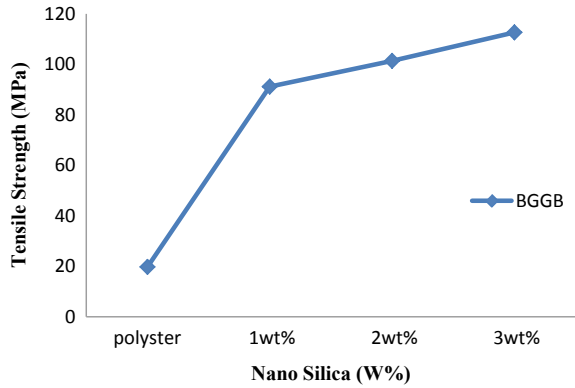


**Fig. 8** Tensile modulus variation for different wt% of nanosilica

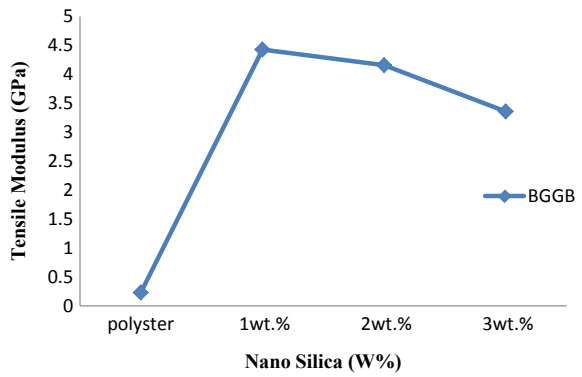
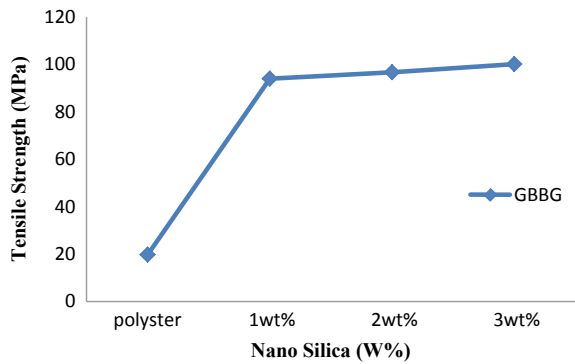
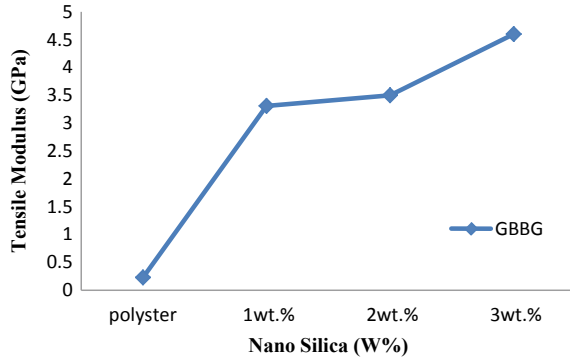


**Fig. 9** Tensile strength variation for different wt% of nanosilica



nanosilica. The tensile modulus value is maximum at 3wt% nanosilica and minimum at 1wt% nanosilica. As the percentage of nanosilica increases, the bonding of resin with the fiber increases, but the further increase may increase the viscosity of the resin which leads to lower adhesion process.

**Fig. 10** Tensile modulus variation for different wt% of nanosilica



Now, the graph for tensile strength and tensile modulus of GBGB hybrid composite laminate is shown in Figs. 11 and 12, respectively. From the graph, it is observed that the tensile strength is maximum at 2wt% nanosilica and is minimum at 3wt%

**Fig. 11** Tensile strength variation for different wt% of nanosilica

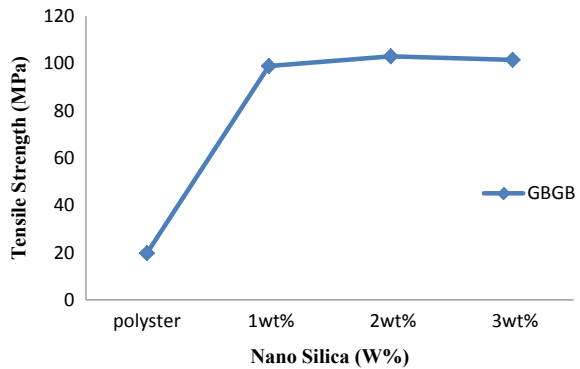
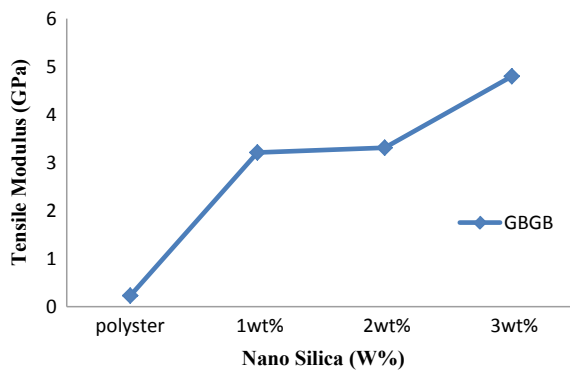


**Fig. 12** Tensile modulus variation for different wt% of nanosilica



nanosilica. The tensile modulus value is maximum at 3wt% nanosilica and minimum at 1wt% nanosilica. Here, the stacking sequence shows the influence on tensile strength over the polyester resin and nanosilica. The presence of banana layer in between the two glass layers decreases the strength of the composite.

### 4.2 Flexural Strength and Flexural Modulus

The flexural strength and flexural modulus values are observed, and the corresponding graphs are plotted. The graph for flexural strength and a flexural modulus of BGGB hybrid composite laminate is shown in Figs. 13 and 14, respectively. From the graph, it is observed that the flexural strength is maximum at 2wt% nanosilica and is minimum at 3wt% nanosilica. The flexural modulus value is maximum at 1wt% nanosilica and minimum at 3wt% nanosilica. Here, the stacking sequence shows the influence on tensile strength over the polyester resin and nanosilica. Since the presence of banana layers on the outer surfaces of the composite, the fiber gets fractured before the strongest glass fiber gets fractured.

**Fig. 13** Flexural strength variation for different wt% of nanosilica

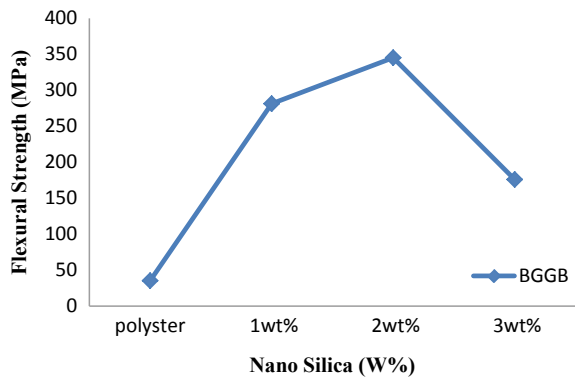


**Fig. 14** Flexural modulus variation for different wt% of nanosilica

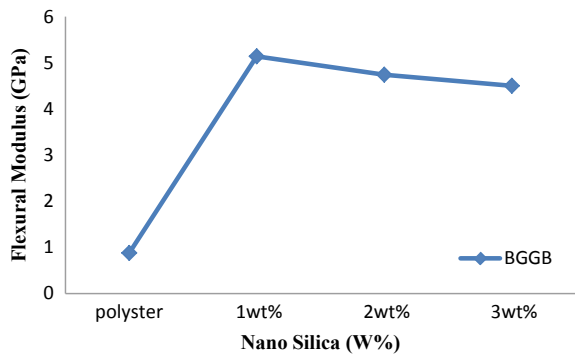




**Fig. 15** Flexural strength variation for different wt% of nanosilica

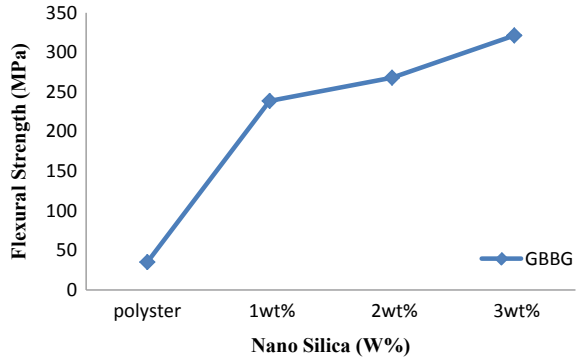
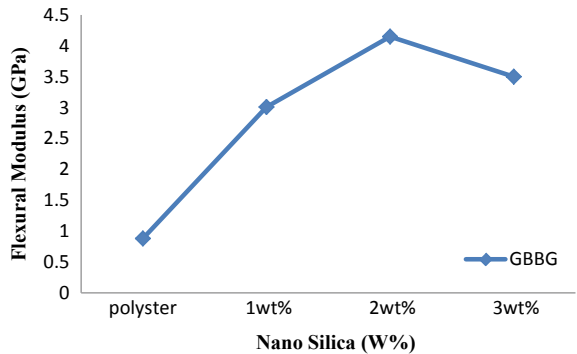


**Fig. 16** Flexural modulus variation for different wt% of nanosilica



Now, the graph for flexural strength and a flexural modulus of GBBG hybrid composite laminate is shown in Figs. 15 and 16, respectively. From the graph, it is observed that the flexural strength is maximum at 3wt% nanosilica and is minimum at 1wt% nanosilica. The flexural modulus value is maximum at 2wt% nanosilica and minimum at 1wt% nanosilica. Here the presence of glass layers on the outer surfaces of the composite, the composite withstand up to 3wt% nanosilica.

Now, the graph for flexural strength and a flexural modulus of GBGB hybrid composite laminate is shown in Figs. 17 and 18, respectively. From the graph, it is observed that the flexural strength is maximum at 2wt% nanosilica and is minimum at 3wt% nanosilica. The flexural modulus value is maximum at 2wt% nanosilica and minimum at 3wt% nanosilica. Here, the presence of banana layer in between the two glass layers decreases the strength of the composite 3wt% nanosilica.

**Fig. 17** Flexural strength variation for different wt% of nanosilica

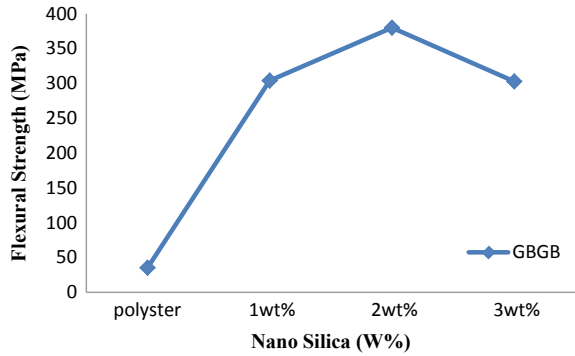
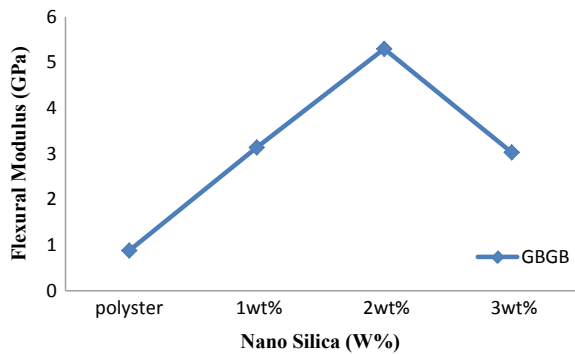


**Fig. 18** Flexural modulus variation for different wt% of nanosilica



### 4.3 Scanning Electron Microscope

The following figures show the morphological study of the hybrid composites through a scanning electron microscope. The fiber pullout from the matrix, fractured fibers, cracking of resin, internal structure, and voids are observed through the images of the scanning electron microscope. Figure 19 shows the woven banana fiber pullout from the resin under loading. Figure 20 shows the cracking of the matrix besides fiber under loading conditions. Figure 21 shows the arrangement of glass fiber in the matrix. Figure 22 shows the glass fiber pullout from the matrix under loading. With this morphological study, we observe the behavior of the banana fiber, glass fiber, and matrix in the hybrid composite.

**Fig. 19** Fiber pullout under loading



**Fig. 20** Cracking of the matrix under loading

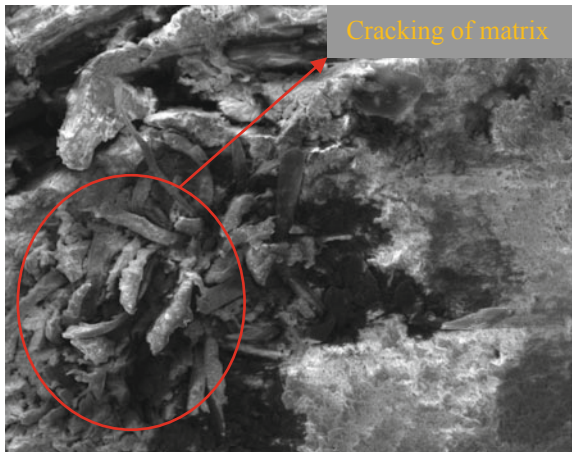


**Fig. 21** Stacking of glass layers in the matrix

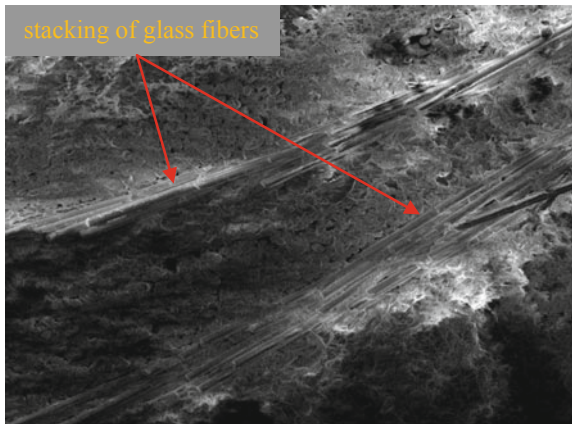
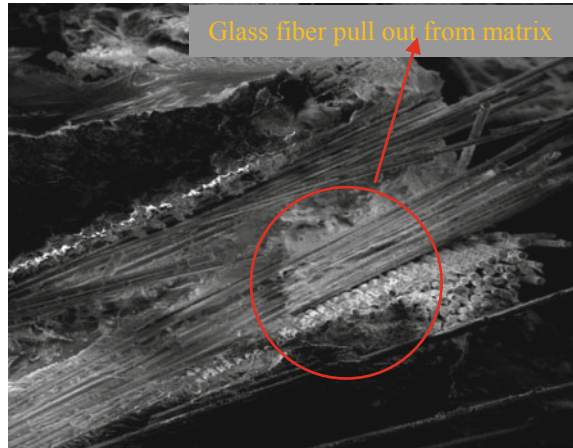


**Fig. 22** Glass fiber pullout under loading



## 5 Conclusions

In the present study, the hybrid composite laminates were fabricated with low cost having an overall lightweight. The tensile and flexural properties of hybrid composite laminates were evaluated, and the following observations were made from this study.

- The tensile strength comparisons of different hybrid composite laminates reveal the stacking sequence of BGGB hybrid composite laminate with 3wt% of nano silica has 112.64 MPa exhibits higher tensile strength than other hybrid composite laminates. This is because two layers of S-Glass is placed in between the two layers of banana fiber forms a stronger layer in that laminate. This also shows that as the percentage of nanopowder increases, the tensile strength is also increased, but the further increase may cause failure because of its brittle nature.
- Similarly, the comparison of flexural strength reveals that the stacking sequence of GBGB hybrid composite laminates with 2wt% of nanosilica as filler material exhibits higher flexural strength as 380 MPa. In the stacking sequence GBGB, more load is taken by the lower glass fiber and next to banana fiber, and so on. Since the glass fiber can withstand the more load so, the high strength is obtained in this laminate.
- The morphological study is done through a scanning electron microscope. The fibers pullout from the composite, stacking of fibers, and the behavior of matrix in the hybrid composite are observed.
- This paper shows that the stacking sequence or placing of fiber in the composite plays an important role in obtaining good mechanical properties. Thus, it can be concluded that replacing 50% of synthetic fiber with natural fiber gives high mechanical strength as that of complete synthetic fiber-reinforced composites. It also shows that the fabrication of composite is of low cost and applications also increase, when compared to synthetic fiber. These results gave good opportunities

to fabricate a new type of composite with low cost of fabrication and a wide range of application.

## References

1. Somaiah Chowdary M, Niranjan Kumar MSR (2015) Effect of Nano clay on the mechanical properties of polyester and S-glass fiber (Al). *Int J Adv Sci Technol* 74:35–42
2. Gujjala R, Ojha S, Acharya SK, Pal SK (2013) Mechanical properties of woven jute–glass hybrid-reinforced epoxy composite. *J Compos Mater* 48(28):3445–3455 (First Published September 11, 2013)
3. Bhoopathi R, Ramesh M, Deepa C (2014) Fabrication and property evaluation of Banana-Hemp-Glass fiber reinforced composites. *Proc Eng* 97:2032–2041
4. Amir N, Abidin KAZ, Shiri FBM (2017) Effects of fibre configuration on mechanical properties of Banana fibre/PP/MAPP natural fibre reinforced polymer composite. *Proc Eng* 184:573–580
5. Ramesh M, Palanikumar K, Hemachandra Reddy K (2013) Comparative evaluation on properties of hybrid glass fiber-Sisal/Jute reinforced epoxy composites. *Proc Eng* 51:745–750
6. Alavudeen A, Rajini N, Karthikeyan S, Thiruchitrambalam M, Venkateshwara N (2014) Mechanical properties of banana/kenaf fiber-reinforced hybrid polyester composites: effect of woven fabric and random orientation, Elsevier
7. Ramesh M, Sri Ananda Atreya T, Aswin US, Eashwar H, Deepa C (2014) Processing and mechanical property evaluation of Banana fiber reinforced polymer composites. *Proc Eng* 97:563–572
8. Yahaya R, Sapuan SM, Jawaid M, Leman Z, Zainuddin ES (2014) Effect of layering sequence and chemical treatment on the mechanical properties of woven kenaf–aramid hybrid laminated composites, Elsevier
9. Ramesh M, Palanikumar K, Hemachandra Reddy K (2012) Mechanical property evaluation of sisal–jute–glass fiber reinforced polyester composites, Elsevier
10. Alsaadi M, Bulut M, Erklig A, Jabbar A (2018) Nano-silica inclusion effects on the mechanical and dynamic behavior of fiber reinforced carbon/Kevlar with epoxy resin hybrid composites. *Compos B* 152:169–179
11. Zhang L, Zhang G, Chang L, Wetzel B, Jim B, Wang Q (2016) Distinct tribological mechanisms of silica nanoparticles in epoxy composites reinforced with carbon nanotubes, carbon fibers, and glass fibers. *Tribol Int* 104:225–236
12. Sapuan SM, Maleque MA (2005) Design and fabrication of natural woven fabric reinforced epoxy composite for household telephone stand. *Mater Des* 26:65–71
13. Sapuan SM, Leenie A, Harimi M, Beng YK (2006) Mechanical properties of woven banana fiber reinforced epoxy composites. *Mater Des* 27:689–693
14. Cai D, Zhou G, Wang X, Li C, Deng J (2017) Experimental investigation on mechanical properties of unidirectional and woven fabric glass/epoxy composites under off-axis tensile loading. *Proc Eng* 184:573–580
15. Boopalan M, Niranjana M, Umapathy MJ (2013) Study on the mechanical properties and thermal properties of jute and banana fiber reinforced epoxy hybrid composites, Elsevier
16. Braga RA, Magalhaes PAA Jr (2015) Analysis of the mechanical and thermal properties of jute and glass fiber as reinforcement epoxy hybrid composites. *Mater Sci Eng C* 56(1):269–273
17. Sanjay MR, Arpitha GR, Yogesha B (2015) Study on mechanical properties of natural - glass fibre reinforced polymer hybrid composites: a review. *Mater Today: Proceedings* 2:2959–2967
18. Idicula M, Malhotra SK, Joseph K, Thomas S (2005) Dynamic mechanical analysis of randomly oriented intimately mixed short banana/sisal hybrid fiber reinforced polyester composites. *Compos Sci Technol* 65:1077–1087

# Tribological Behaviour of Carbon Fibre Polymer Composites Reinforced with Nano-fillers



Shylesh K. Siddalingappa, Bhaskar Pal, M. R. Haseebuddin  
and K. Gopalakrishna

**Abstract** Nano-fillers reinforced with polymer-based composites have found to enhance the tribological properties in polymer composites. Alumina ( $\text{Al}_2\text{O}_3$ ) and molybdenum-di-sulphide ( $\text{MoS}_2$ ) were selected as nano-fillers in the present research work.  $\text{Al}_2\text{O}_3$  and  $\text{MoS}_2$  fillers were mixed with the epoxy resin in the concentration of 0.1, 0.2, 0.4 and 0.7% by volume of the epoxy resin. The reinforced epoxy resin was used as a matrix material along with the aircraft grade carbon fabric as the primary reinforcement. Test panels were fabricated using vacuum-assisted resin transfer moulding technique (VARTM), and samples were extracted using water jet cut as per the dimensions given in the ASTM standards of three-body wear (ASTM G-65) and two-body wear (ASTM G-99). Scanning electron microscopic (SEM) studies revealed the even distribution of the  $\text{MoS}_2$  when disbursed with ultrasonicator than by manual mixing. The three-body and two-body wear tests were carried out at a load of 24 and 48 N. The composite reinforced with 0.4% of  $\text{MoS}_2$  particulate has shown the decrease in wear rate by 20.45% as compared to that of the  $\text{Al}_2\text{O}_3$  particulate-based composites in three-body wear test when the applied load was 48 N, whereas in two-body wear test, the composite reinforced with 0.4% of  $\text{MoS}_2$  particulate has shown the decrease in wear rate by 16.13% as compared to that of the  $\text{Al}_2\text{O}_3$  particulate-based composites. SEM studies of worn-out surfaces revealed that the mode of failure in worn-out samples was due to delaminate at the fibre matrix interface. SEM images also revealed that better bonding between fibre and matrix can be well achieved for the 0.4% concentration of nano-reinforcements as compared to that of the composites with 0.2% concentration of nano-reinforcements.

---

S. K. Siddalingappa (✉) · B. Pal  
Department of Mechanical Engineering, School of Engineering, Presidency University,  
Bengaluru, Karnataka 560064, India  
e-mail: [is.shyleshks@gmail.com](mailto:is.shyleshks@gmail.com)

M. R. Haseebuddin  
Department of Mechanical Engineering, Dayananda Sagar College of Engineering, Bengaluru,  
Karnataka 560078, India

K. Gopalakrishna  
Jyothy Institute of Technology, Bengaluru, Karnataka 560082, India

**Keywords** Carbon fibres · Molybdenum-di-sulphide · Vacuum-assisted resin transfer moulding (VARTM) · Nano-composites

## 1 Introduction

Carbon fibre-reinforced polymer composites command the major share in the structural polymer composite industry. It is widely used for various applications such as aerospace, aeronautical, automobile, locomotive, and recreational applications. Amongst the various advantages, the polymer composites offer one noticeable advantage which is its flexibility in allowing the user to tailor the properties as per the end application needs. The few amongst them are higher strength-to-weight ratio, higher stiffness and higher fatigue resistance. Profound tests were carried out to determine the array of properties related to structural as well as tribological properties of the carbon fibre-reinforced polymer composites [1]. However, the research work to evaluate the significance of nano-sized reinforcements on the tribological properties of the carbon fibre-reinforced polymer composites has not been dealt in an intense manner [2]. Hence, this research work aimed at studying the significance of reinforcing the carbon fibre-reinforced composites with alumina ( $\text{Al}_2\text{O}_3$ ) and molybdenum-di-sulphide ( $\text{MoS}_2$ ) separately and compared their effect on the tribological properties based on test results that obtained by three-body wear tests and two-body wear tests.

## 2 Literature Review

GuangShi et al. had assessed the impact of nano-sized alumina fillers on the sliding wear behaviour on the epoxy-based polymer composites. The researchers were successful in reducing the specific wear rate by 97% when the volume of the nano-alumina used was 0.24 vol.% than compared to the bare epoxy resin [3]. B Suresha et al. evaluated the tribological properties of carbon-epoxy and glass-epoxy-reinforced polymer composites using pin-on-disc apparatus. It was found that carbon-epoxy samples showed lower friction and lower slide wear loss [3, 4]. A Shafiei-Zarghani et al. had developed the  $\text{Al}_2\text{O}_3$  nano-composite surface layer on an Al alloy using friction stir welding (FSP). FSP made significant enhancement in the mean microhardness of the nano-composite layered composite by three times as compared to the bare aluminium substrate [5].

V.P. Gordienko et al. studied the significance of adding additives less than one micrometer ( $<1 \mu\text{m}$ ) with polyolefin such as polyethylene and polypropylene by hot pressing under a pressure of 35 MPa for 20 min by adding inorganic additive molybdenum-di-sulphide in the range of 0.1 to 10% by volume. It was found that there was increase in the hardness due to the addition of molybdenum in a tracer quantity of 0.3 to 0.5% which enhanced the wear resistance of the composite by 8 to 10% [6]. Zhu Peng et al. conducted the study of the tribology performance

of molybdenum-di-sulphide reinforced thermoplastic polyamide under dry and wet lubrication conditions. It was found that mechanical performances were superior the thermoplastic filled with molybdenum-di-sulphide [7]. P. H. Sivaraman et al. studied the influence of molybdenum-di-sulphide composition on the wear characteristics of the composites fabricated. SEM images were used to study the worn surfaces. It was found that there was a significant improvement in the composite properties which were doped with molybdenum-di-sulphide than compared with that of the bare composite [8].

From the above discussion, it was concluded that there is enough documented research work carried out in fabrication polymer-based nano-composites using nano-sized alumina and nano-sized molybdenum-di-sulphide. Most of the work involved fabricating the samples from hand layup and compression moulding. But no evident was found about fabrication of composite using VARTM method and testing the composites with three-/two-body abrasive wear test and traditional pin-on-disc apparatus. Hence, the present research work concentrated on developing the VARTM fabricated nano-composites reinforced with nano-sized filler in different proportions and conducting three-body abrasive wear and two-body abrasive wear for performance study.

### 3 Materials and Method of Fabrication

Structural grade carbon fabric used as a primary fibre and epoxy resin HTR 212 were mixed with hardener HTR-386-99 for preparing the composites. These materials were procured from Aircraft Spruce, USA. It is noted from the supplier that the size of alumina ( $Al_2O_3$ ) particles is about 18 nm and the size molybdenum-di-sulphide ( $MoS_2$ ) particle is in range of 80 nm–100 nm with 99.9% purity. These particles were used as nano-fillers in the volume of 0.1, 0.2, 0.4 and 0.7% to develop nano-filler-reinforced polymer composites. Vacuum-assisted resin transfer moulding (VARTM) method was used for fabricating the composite panels. The ultrasound powered ultrasonicator is used for uniform distribution of the nano-fillers in the pure epoxy resin. The whole set-up is shown in Fig. 1. Panels were fabricated resembling the size of the VARTM mould, and samples were extracted by water jet cutting as per the

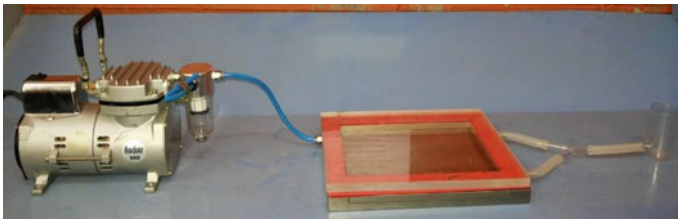


**Fig. 1** Vacuum-assisted resin transfer moulding



**Fig. 2** Composite panels extracted from water jet cutting



ASTM standards. The photographs of the extracted samples are as shown in Fig. 2. The scanning electron microscope (SEM) studies were conducted to understand the significance of using the ultrasonicator to mix the nano-reinforcements into the epoxy resin as compared to that of the manual mixing. The SEM micrographs reveal that MoS<sub>2</sub> nano-filler in the epoxy resin is evenly distributed when it is mixed with ultrasonicator. The SEM micrographs also disclose that the porosity level is almost nil due to ultrasonication.

## 4 Experimental Testing

### 4.1 Three-Body Abrasive Wear Test

Three-body abrasive wear tests were conducted in accordance with ASTM G-65. The equipment used for conducting the three-body wear test is shown in Fig. 3. The initial weight of the specimen was recorded. The velocity and test time were set. Abrasive particles from the hopper were introduced between the test specimen and rotating chlorobutyl rubber tyre abrasive wheel (hardness; Durometer-A 58-62). At the end of the set duration, specimen was removed and cleaned thoroughly. The final weight of the tested specimen was recorded for measuring the wear loss. The above procedure was repeated for varying abrading radius for different concentrations of the nano-fillers. These experiments were carried out at two different loads, i.e., 24 N and 48 N [8].

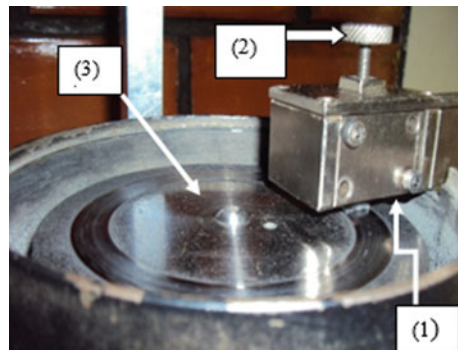
**Fig. 3** Three-body abrasive wear test set-up



## 4.2 Two-Body Wear Test

Two-body abrasive wear tests were conducted in accordance with ASTM G-99. The rotating disc of the apparatus was cleaned using the acetone to remove any dirt, grease or any material debris attached from the previous test. Initial weight of the sample was measured and recorded, and the specimen was fixed to the sleeve based upon the preselected abrading radius. The specimen was loaded by the predefined magnitude of weight and brought in contact with the rotating disc. As the machine was switched on, the specimen in contact with the rotating disc abraded gradually. The test was performed for a fixed duration of time as per standard, and finally, the weight of the specimen measured after the test was conducted, thus measuring the wear loss. The above procedure was repeated for varying abrading radius for different concentrations of the nano-fillers used at two different weights of 24 N and 48 N [9] (Fig. 4).

**Fig. 4** Two-body abrasive wear test set-up: 1. Pin holder with screw, 2. specimen with holder, and 3. rotating disc



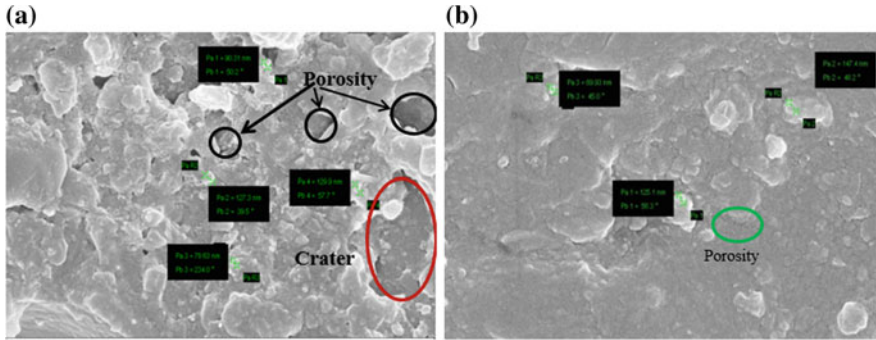


**Fig. 5** Scanning electron microscope images showing the distribution of the reinforcement in the composite structure when the reinforcements were mixed manually (a) and by ultrasonicator (b)

## 5 Results and Discussions

### 5.1 Scanning Electron Microscope (SEM) Studies

Figure 5 shows the SEM images of MoS<sup>2</sup> dispersion into the epoxy resin matrix done manually as well as by using the ultrasonicator. The figure reveals composites developed by the dispersing the reinforcements by manually mixing (Fig. 5a) is more porous that the dispersion done using the ultrasonicator (Fig. 5b).

### 5.2 Three-Body Wear Test

The plots shown in Figs. 6 and 7 show the variation of wear rate against the abrading distance for the various reinforcements (Al<sub>2</sub>O<sub>3</sub> and MoS<sub>2</sub>) used at an operating load of 24 N and 48 N, respectively. The three-body wear test was conducted at above-mentioned loads at various (0.0, 0.1, 0.2, 0.4 and 0.7%) concentrations of Al<sub>2</sub>O<sub>3</sub> and MoS<sub>2</sub>. In the plots shown in Figs. 6 and 7, it can be observed that the wear rate was

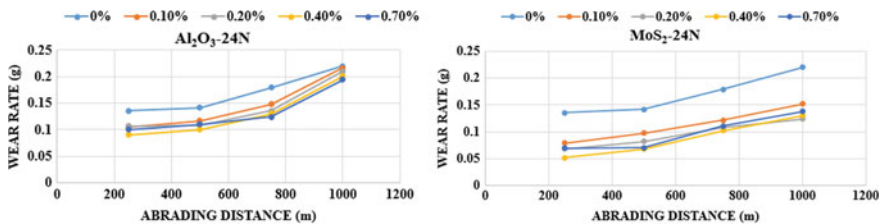


**Fig. 6** Three-body abrasive wear test results showing the variation of wear rate against the abrading distance for different concentrations of Al<sub>2</sub>O<sub>3</sub> and MoS<sub>2</sub> at 24 N

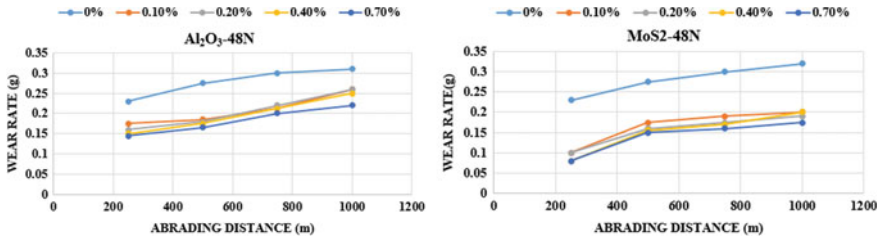


**Fig. 7** Three-body abrasive wear test results showing the variation of wear rate against the abrading distance for different concentrations of Al<sub>2</sub>O<sub>3</sub> and MoS<sub>2</sub> at 48 N

directly proportional to the abrading distance; hence, the gradual increase in the wear rate can be observed for all the concentrations of reinforcement studied irrespective of whether it was Al<sub>2</sub>O<sub>3</sub> reinforced composites or MoS<sub>2</sub> reinforced composite. But however the detailed observation of the plots demonstrated that the wear rate in MoS<sub>2</sub> reinforced composites is substantially lower as compared to that with composites reinforced with Al<sub>2</sub>O<sub>3</sub>. For instance, at 0.4% concentration Al<sub>2</sub>O<sub>3</sub> sample wear rate was 0.135 units whereas that of the MoS<sub>2</sub> was 0.1 units; i.e., the wear resistance of the MoS<sub>2</sub> was approximately 25% more than that of the Al<sub>2</sub>O<sub>3</sub> reinforced composites. This behaviour of the material could be attributed for the fact that Al<sub>2</sub>O<sub>3</sub> being a hard reinforcement gets wore out and material gets removed from the specimens in the form of flakes; hence, the volume of material removed is higher, whereas in the case of MoS<sub>2</sub>, the very nature of the MoS<sub>2</sub> is to act as a lubricating agent which in turn reduces the friction during the abrasion and also MoS<sub>2</sub> is a soft reinforcement; hence, the material gets removed in the form of small powders, thereby reducing the rate of the material removal and hence the lesser wear rate. The behaviour of the samples tested at a load of 48 N has shown the similar trend.

### 5.3 Two-Body Wear Test

With reference to the above discussion in Sect. 5.2, the results obtained in the two-body wear test are shown in the plots given in Figs. 8 and 9. The results showed

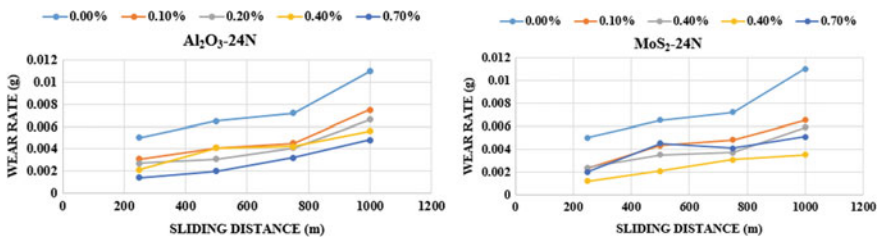


**Fig. 8** Two-body abrasive wear test results showing the variation of wear rate against the sliding distance for different concentrations of Al<sub>2</sub>O<sub>3</sub> and MoS<sub>2</sub> at 24 N

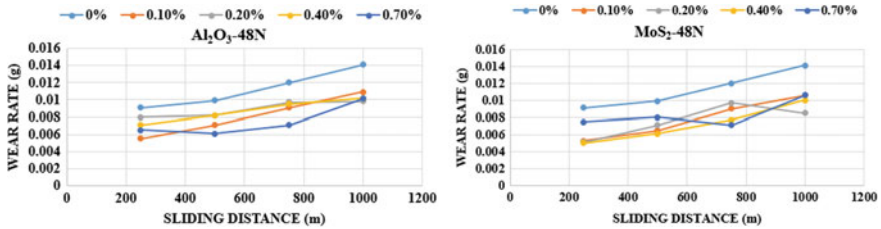


**Fig. 9** Two-body abrasive wear test results showing the variation of wear rate against the sliding distance for different concentrations of  $\text{Al}_2\text{O}_3$  and  $\text{MoS}_2$  at 48 N

the similar trends as that in case of three-body wear test. However, the wear rate obtained was far more less as compared to that of the three-body wear results. The abnormalities in the last plot shown in Figs. 8 and 9 can be attributed for the reason of loose gripping of sample in the pin-on-disc machine.

#### 5.4 Surface Morphology

Figures 10 and 11 show the SEM images of the worn-out surfaces of the composites with  $\text{Al}_2\text{O}_3$  and  $\text{MoS}_2$  as nano-reinforcements with 0.2% and 0.4% of the concentrations. The severity of the wear in composites with 0.2% alumina is more than compared to that of composites reinforced with 0.2%  $\text{MoS}_2$ . In the SEM micrographs shown in Fig. 10a, b it is evident that the failure is due to delamination at the fibre matrix interface. However, in the composites reinforced with 0.4% of  $\text{Al}_2\text{O}_3$  and

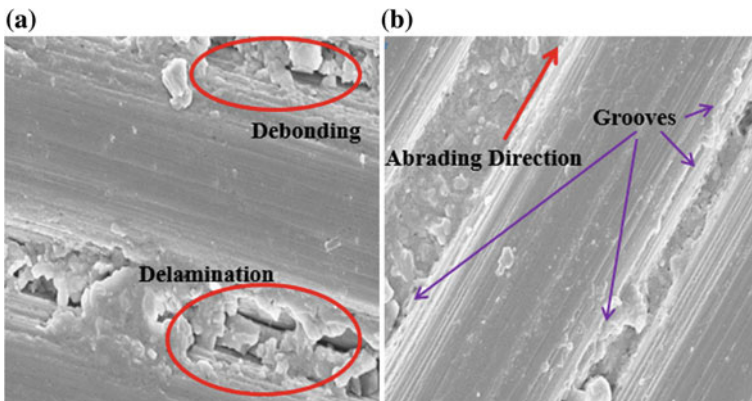


**Fig. 10** Scanning electron microscope images showing the abraded surfaces of composites reinforced with 0.2%  $\text{Al}_2\text{O}_3$  concentration (a) and composites reinforced with 0.2%  $\text{MoS}_2$  concentration (b) during three-body wear test with an applied load of 48 N

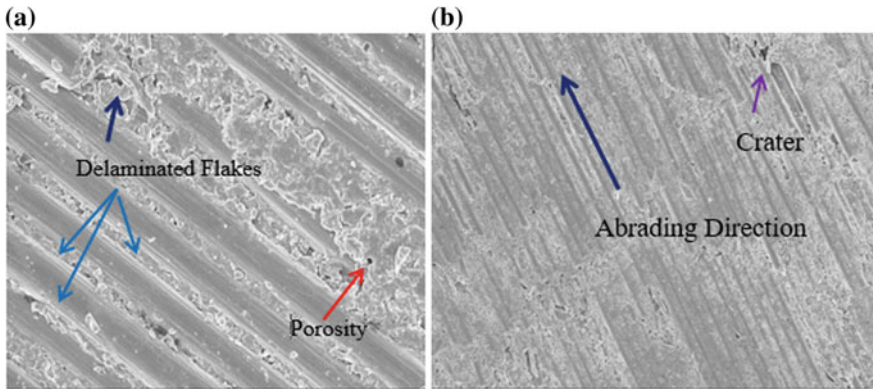


**Fig. 11** Scanning electron microscope images showing the abraded surfaces of composites reinforced with 0.4%  $\text{Al}_2\text{O}_3$  concentration (a) and composites reinforced with 0.4%  $\text{MoS}_2$  concentration during three-body wear test with an applied load of 48 N

$\text{MoS}_2$  as nano-reinforcements, the bonding is better as compared to the composites with 0.2% of the nano-reinforcements of  $\text{Al}_2\text{O}_3$  and  $\text{MoS}_2$  as shown in Fig. 11a, b.

## 6 Conclusions

- i. Composite panels with  $\text{Al}_2\text{O}_3$  and  $\text{MoS}_2$  nano-fillers were fabricated using vacuum-assisted resin transfer moulding (VARTM) in the varying concentrations discussed above, and performance study has been carried out in three-body and two-body abrasive wear test.
- ii. The nano-reinforcement of  $\text{MoS}_2$  was well distributed by the use of ultrasonicator as shown in the figure.
- iii. The results obtained clearly depicted that composites reinforced with  $\text{MoS}_2$  showed better wear resistance at all the concentrations studied as compared to that of the composites reinforced with  $\text{Al}_2\text{O}_3$  nano-filler.
- iv. The  $\text{Al}_2\text{O}_3$  being a hard reinforcement gets wore out in the form of flakes; hence, the wear rate is more as compared to  $\text{MoS}_2$ , which by very nature acts as a lubricating agent which in turn reduces the friction during the abrasion as shown in Figs. 6.4 and 6.5.
- v.  $\text{MoS}_2$  is a soft reinforcement; hence, the material gets removed in the form of small powders, thereby reducing the rate of the material removal and hence the lesser wear rate.
- vi. The SEM images shown in Fig. 6.4 depict the severity of the worn-out surfaces of the composites 0.2% of nano-reinforcement of  $\text{Al}_2\text{O}_3$  and  $\text{MoS}_2$  signifies that the mode of failure is due to fibre and matrix debonding.

- vii. The SEM micrographs shown in Fig. 6.5 reveal that the composites fabricated with 0.4% of nano-reinforcement of  $\text{Al}_2\text{O}_3$  and  $\text{MoS}_2$  showed better bonding than that of the composites with 0.2% of nano-reinforcements.

## References

1. Mallick PK (2007) Fiber reinforced polymer composites, materials, manufacturing and design. CRC Press, New York
2. Gopala Krishnaa K, Divakar C, Venkatesha K, Mohana CB, Mahesh Lohith KS (2010) Bulk temperature estimation during wear of a polymer composite pin. *Wear* 268:346–351
3. Soutis C (2005) Fiber reinforced composites in aircraft construction. *Program Aero Sci* 41(2):143–151
4. Shi G, Zhang MQ, Rong MZ, Wetzel B, Friedrich K (2004) Sliding wear behavior of epoxy containing nano- $\text{Al}_2\text{O}_3$  particles with different pretreatments. *Wear* 256:1072–1081
5. Suresha B, Chandramohan G, Samapthkumaran P, Seetharamu S, Vynatheya S (2006) Friction and wear characteristics of carbon-epoxy and glass-epoxy woven roving fiber composites. *J Reinf Plast Compos* 25(7):771–782
6. Gordienko VP, Sal'nikov VG, Podlesnyi RV, Kasperskii AV (2009) Hardness and wear resistance of certain polyolefins with additions of molybdenum-di-sulphide. *Plasticheskie Massy (Plastic Weight)* 10:13–15
7. Peng Z, Xiao W, Xiao-dong W, Pei H, Jun S (2013) Tribology performances of molybdenum disulfide reinforced thermoplastic polyimide under dry and water lubrication conditions. *Ind Lubr Tribol* 58(4):195–201
8. Sivaraman PH, Vimal R, Badrinarayanan S, Vignesh Kumar R (2017) Study of wear properties of jute/banana fibers reinforced molybdenum-di-sulphide modified epoxy composites. *Mater Today Proc, Part A* 4(2):2910–2919
9. ASTM G65-04 (2004) Standard test method for measuring abrasion using the dry sand/rubber wheel apparatus, *Annual Book of ASTM Standards*, vol 03.02
10. ASTM G99-17 (2017) Standard test method for wear testing with a pin-on-disk apparatus, ASTM International, West Conshohocken, PA

# Environment Effect on Impact Strength of Pistachio Shell Filler-Based Epoxy Composites



Sandeep Gairola, Somit Gairola and Hitesh Sharma

**Abstract** This paper studies the effect of pistachio shell microfillers on the impact strength of epoxy composites. In the present research endeavor, the potential of pistachio shell as natural filler is examined with the epoxy matrix. Pistachio shell filler-based composites were developed by varying the content of fillers 0, 5, 10, and 15% (by weight). Charpy impact test and moisture absorption test were performed on developed composite specimen. An increase in moisture absorption was observed with the incorporation of filler. The effect of different environmental conditions, i.e. water, petrol, and kerosene, on impact strength was also studied, and test results of specimen were compared with the neat epoxy composite. With incorporation of 10% filler, an increase of 36.56% in impact strength was observed under ambient conditions. Further decrease in impact strength was observed for sample subjected to different environmental conditions. Morphological study of all developed specimen was also done which revealed the brittle nature of fractured surface. The study revealed that the pistachio shell filler has got potential to be successful filler in developing epoxy composites.

**Keywords** Composite · Pistachio shell · Impact strength

## 1 Introduction

Over the last two decades, natural fibers/fillers are being extensively used in polymer-based composites as a reinforcement. This natural reinforcement has various environmental and economic benefits [1]. In addition of this, natural fibers/fillers as reinforcement in composites are environment-friendly, renewable, cost-effective, and abundant in nature. Due to these advantages, natural fillers became a potential reinforcement in polymer matrix composite. Incorporation of these fillers results in lower processing cost and increases the physical and mechanical properties of polymer matrix composite. Pistachio shell, ground nut shell, rice husk, peanut shell,

---

S. Gairola (✉) · S. Gairola · H. Sharma  
Mechanical Department, National Institute of Technology Uttarakhand, Uttarakhand, India  
e-mail: [sandeepgairola.12345@gmail.com](mailto:sandeepgairola.12345@gmail.com)

© Springer Nature Singapore Pte Ltd. 2020  
H. K. Voruganti et al. (eds.), *Advances in Applied Mechanical Engineering*,  
Lecture Notes in Mechanical Engineering,  
[https://doi.org/10.1007/978-981-15-1201-8\\_85](https://doi.org/10.1007/978-981-15-1201-8_85)



cashew nut shell, and wall nut shell have been extensively used as a potential filler. It has been reported that incorporation of these natural filler in polymer matrix composite gives a remarkable change in the mechanical and physical properties of the composites [2–9].

Pistachio shell is generally a biowaste which is not used extensively as a natural filler with the epoxy-based composite; also its chemical constituents (cellulose, lignin, hemicellulose, etc.) can be comparable with the other natural filler, i.e., ground nut shell, cashew shell, wood flour, etc. Chemical configuration of ligno-cellulose pistachio shell fillers consists of three main components: cellulose (42%) hemicellulose (3.11%), and lignin (13.5%), which are known to present very complex structure. The cellulose content of pistachio shell filler is much more than that of, coconut coir, and bamboo, hemp, kenaf and sisal fibers which is responsible for its greater hydrophilic nature [10]. The study of environment effect on properties of composite also plays an important role in order to elaborate the complete behavior of composite material under different circumstances. It has been reported that under different exposure of environment i.e. humid, aqueous solution, petrol, vegetable oil significantly affect the mechanical properties of natural reinforcement polymer composites [11–13]. Various studies have been reported using pistachio shell filler and polyester as a matrix, but with epoxy as a matrix the potential is still unknown. In this study, pistachio shell filler is used as reinforcement with the epoxy matrix and their impact behavior and moisture absorption are studied.

## 2 Experimental Details

### 2.1 Material and Methods

Epoxy LY 556 which is a bisphenol A was used as resin along with hardener HY 951 in 10:1 ratio. Pistachio shell fillers were obtained by grinding the pistachio shells in a kitchen grinder (Make: Maharaja White line 500 W). Before grinding, the pistachio shell fillers were kept in a hot air oven (Make: Apollo Lab India) for 24 h at 80 °C. After grinding, the fillers in particle form were sieved through a 500 micron sieve in order to get uniform size filler material. Pistachio shell filler-based epoxy composites were fabricated using casting method. Pistachio filler is mixed with the epoxy with 5, 10, and 15 wt%. The mixture is stirred for 20 min in order to get a homogeneous mixture. This mixture was then poured into a glass mold of size  $200 \times 200 \times 5 \text{ mm}^3$ . The mixture was left to cure for 24 h at room temp of about  $23 \pm 2 \text{ }^\circ\text{C}$  (Figure 1 and Table 1).

Optical micrograph was taken from a camera of resolution  $4\times$  to show the dispersion of filler in the epoxy matrix composites. It is evident from Fig. 2 that there is uniform dispersion of fillers in epoxy matrix. However, there is slight difference in color of the developed micrograph which can be attributed to increment filler percentage.



**Fig. 1** Mixing and pouring of mixture

**Table 1** Samples with different specification

Sample No.	Specification	Designation
1.	Neat epoxy	S <sub>1</sub>
2.	Epoxy + 5% filler	S <sub>2</sub>
3.	Epoxy + 10% filler	S <sub>3</sub>
4.	Epoxy + 15% filler	S <sub>4</sub>

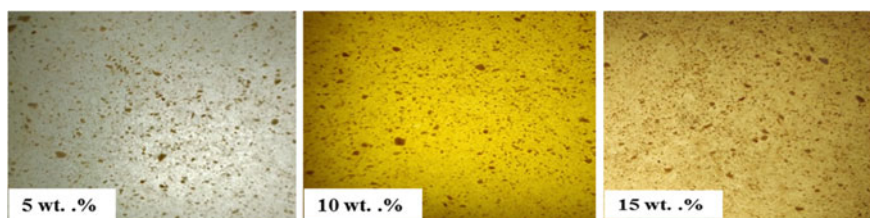


**Fig. 2** Optical micrograph of samples

### 3 Testing and Analysis

#### 3.1 Moisture Absorption Test

Moisture absorption test was performed according to ASTM D 570-98 standard for moisture absorption of plastics. The samples were immersed into plain water for different time periods 24, 48, and 72 h. The samples were taken out after every two hours and wiped with clean cotton cloth every time the weight was measured. The amount of water uptake by each sample was calculated by weighing initial ( $W_i$ ) and final weight ( $W_f$ ) immediately, using a precise balance machine. The change in weight percentage is measured by the given equation (Table 2).

$$W\% = (W_f - W_i)W_f \tag{1}$$

**Table 2** Moisture absorbed by the samples

Sample			Weight(gm)				
	0	24 (hrs)	% change	48 (hrs)	% change	72 (hrs)	% change
S <sub>1</sub>	8.72	8.725	0.057	8.728	0.092	8.729	0.10
S <sub>2</sub>	9.73	9.736	0.06	9.741	0.13	9.743	0.30
S <sub>3</sub>	7.24	7.36	1.657	7.42	2.486	7.46	3.038
S <sub>4</sub>	9.141	9.143	0.0218	9.146	0.0546	9.146	0.0546

**Table 3** Impact strength of samples

Specimen	Average Impact Strength(kJ/m <sup>2</sup> )			
	Ambient	Water	Petrol	Kerosene
S <sub>1</sub>	16.60	16.62	16.61	16.60
S <sub>2</sub>	19.21	20.28	16.70	18.84
S <sub>3</sub>	22.67	16.62	22.72	22.64
S <sub>4</sub>	20.17	19.90	17.77	20.12

### 3.2 Impact Test

The samples were cut as per ASTM-D256 and were subjected to Charpy impact test. The test is performed on 3 samples using a digital pendulum impact tester. Three un-notched sample of dimension  $55 \times 10 \times 5 \text{ mm}^3$  was taken from each specification. The samples are also subjected to different environmental conditions (i.e., plain water, kerosene, petrol) for 10 days. For each observation, experiment was triplicated and the average values are given in Table 3.

### 3.3 SEM Analysis

In order to understand the morphology of pistachio shell filler-based epoxy composites, the developed samples were subjected to SEM analysis using scanning electron microscope(Make: LEO England). The samples were cut to  $10 \text{ mm} \times 10 \text{ mm}$  and given a gold coating to enhance the conductivity.

## 4 Results and Discussion

From moisture absorption test as shown in Fig. 3, it is revealed that rate of water absorption solely depends on the filler content. As the filler content increases, moisture absorption increases and further decreases after 10% filler. The reason of this

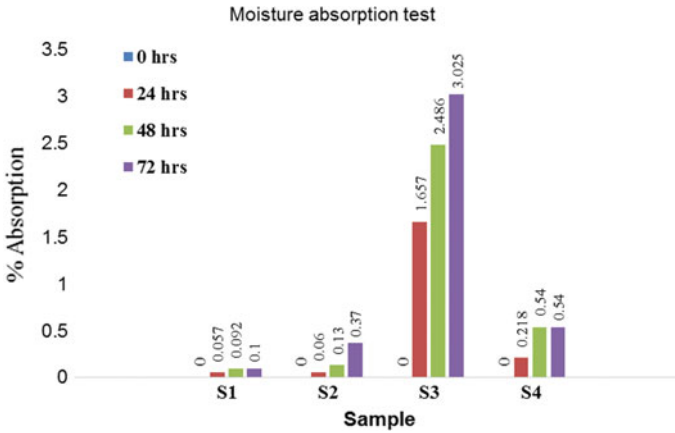


Fig. 3 Moisture absorption with varying filler content

may be due to the fact that as content of natural filler increases, the number of free OH groups present in cellulose also increases in the composite. These free OH groups result in weight gain in the composites due to come in contact with moisture and form hydrogen bond [13]. In spite of this, the moisture absorption also depends upon the voids present in the material. It is observed that maximum moisture is absorbed by sample of 10 wt% filler. This is caused due to the presence of large amount of filler and void present in it which absorbed more water. In the case of S<sub>4</sub> sample, the filler content increases but with this void present in the sample gets reduced that's why showing reduction in moisture absorption in spite of high filler content [12].

As shown in Fig. 4, the impact strength in ambient condition firstly increases about 15.72% in 5% pistachio shell filler content, going maximum for optimum filler content of 10 wt% and then starts decreasing at higher content. The highest impact strength of 22.67 kJ/m<sup>2</sup> was observed for 10% wt., while that of unfilled

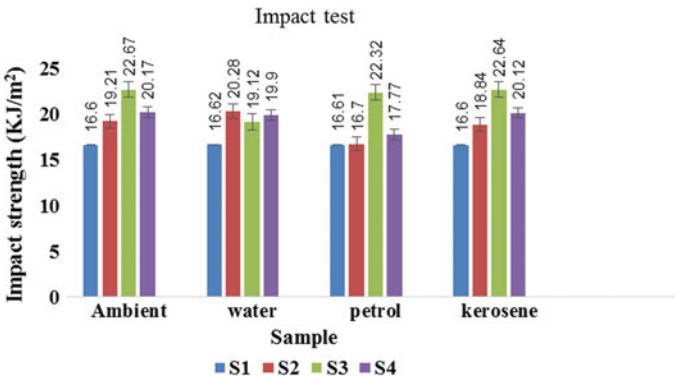


Fig. 4 Impact strength with varying filler content

epoxy was  $16.6 \text{ kJ/m}^2$  corresponding to an increment of 36.56%. This may be due to the better compatibility of the pistachio filler with the epoxy. As filler content increases, the load carrying proportion between the filler and matrix gets changed. For optimum filler content, it gives the maximum strength. As filler content increases from 10 to 15 wt%, the compatibility between filler and epoxy gets decreased due to excess amount of filler, and also it could be due to the decrease in stress transfer efficiency [16].

When samples were subjected to different environmental conditions, a decrease in impact strength was observed. It was found that sample immersed in water shows a decrease in strength due to the fact that as sample absorbs the moisture, the interfacial bonding gets weakened in nature and leads to decrease in strength. The  $S_3$  sample absorbs more moisture and hence shows the maximum decrement in strength. A similar type of results was observed by Prakash et al. [13] and Raghavendra et al. [14] in the arhar and jute fiber epoxy composites, respectively.

Sample subjected to the petrol environment shows the small decrement in impact strength as petrol moisture intake is less and presence of hydrocarbon in petrol may reduce the interfacial bonding strength. Similar observation is observed in sample subjected to kerosene environment. Hence, in sample  $S_3$  water absorption affects the impact strength more as compared to other environment; the reason may be due to hydroxyl group present in water and hydrophilic nature of filler, which is not present in other environments, and therefore, the compatibility between filler and matrix gets reduced [16, 17]. This indicates that pistachio shell filler potentially can improve the impact strength significantly.

The morphological study revealed the void content in developed epoxy composites which keeps on increasing with increase in filler content. Figure 5 shows the filler pullout and the voids which can be the reason for decreased strength as mentioned in Sect. 4 which can be the reason for low absorption of moisture.

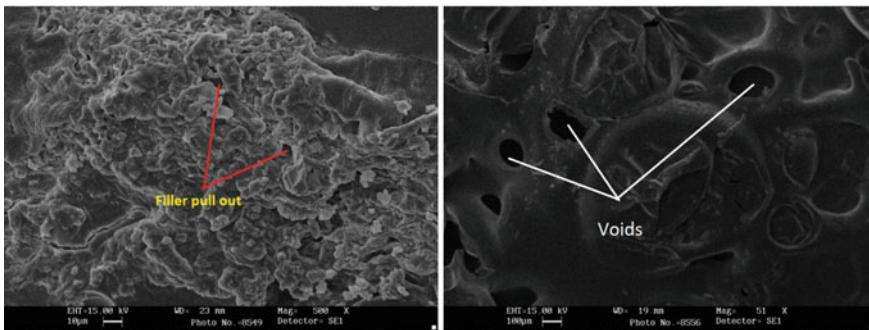


**Fig. 5** SEM images of the developed sample  $S_4$  depicting voids and filler pullout

## 5 Conclusion

The following conclusions can be drawn from the above study:

- (1) Water absorption study showed that water absorption solely depends upon the filler content and voids present in the developed composite.
- (2) The addition of pistachio shell filler significantly affects the impact strength of developed sample. The energy absorbed by samples reached a maximum value with 10% of pistachio shell filler and then decreased with increasing content.
- (3) The samples subjected to different environments when tested for impact strength, S<sub>3</sub> subjected to water environment lost more strength in comparison with other environments.
- (4) Sample subjected to water environment validates the effect with other researchers also, and rest of samples show inconsistent behavior, but it can be concluded that use of pistachio shell as a filler results in improved impact properties as compared to neat epoxy.
- (5) As waste filler pistachio shell can be utilized for developing bio-friendly composites, reducing the percentage of epoxy will result in reducing plastic consumption which will lead toward green manufacturing.

## References

1. Silva RV, Spinelli D, Bose Filho WW, Neto SC, Chierice GO, Tarpani JR (2006) Fracture toughness of natural fibers/castor oil polyurethane composites. *Compos Sci Technol* 66(10):1328–1335
2. Alsaadi M, Erklığ A, Albu-khaleefah K (2018) Effect of Pistachio shell particle content on the mechanical properties of polymer composite. *Arab J Sci Eng* 1–8
3. Marhoon II (2016) Effects of the addition of Pistachio shell particles on the properties of polyurethane matrix composite
4. Nitin S, Singh VK (2013) Mechanical behavior of walnut reinforced composite. *J Mater Environ Sci* 4(2):233–238
5. Raju GU, Kumarappa S (2011) Experimental study on mechanical properties of groundnut shell particle-reinforced epoxy composites. *J Reinf Plast Compos* 30(12):1029–1037
6. Prabhakar MN, Shah AUR, Rao KC, Song JI (2015) Mechanical and thermal properties of epoxy composites reinforced with waste peanut shell powder as a bio-filler. *Fibers Polym* 16(5):1119–1124
7. Mwaikambo LY, Ansell MP (2003) Hemp fibre reinforced cashew nut shell liquid composites. *Compos Sci Technol* 63(9):1297–1305
8. Sharma H, Komal UK, Singh I, Misra JP, Rakesh PK (2019) Introduction to green composites. <https://doi.org/10.1007/978-981-13-6019-0>
9. Komal UK, Sharma H, Singh I (2019) Lignocellulosic polymer composites: processing, challenges, and opportunities
10. Akovali G (ed) (2001) Handbook of composite fabrication. iSmithers Rapra Publishing
11. Costa FHMM, d'Almeida JRM (1999) Effect of water absorption on the mechanical properties of sisal and jute fiber composites. *Polym-Plast Technol Eng* 38(5):1081–1094

12. Rashdi AAA, Sapuan SM, Ahmad MMHM, Khalina A (2010) Combined effects of water absorption due to water immersion, soil buried and natural weather on mechanical properties of Kenaf Fibre Unsaturated Polyester Composites (KFUPC). *Int J Mech Mater Eng* 5(1):11–17
13. Prakash MO, Raghavendra G, Panchal M, Ojha S, Bose PSC (2018) Influence of distinct environment on the mechanical characteristics of Arhar fiber polymer composites. *Silicon* 10(3):825–830
14. Raghavendra G et al (2015) Moisture absorption behavior and its effect on the mechanical properties of jute-reinforced epoxy composite. *Polym Compos.* 1–7. <https://doi.org/10.1002/pc.23610>
15. Lila MK, Singh B, Pabla BS, Singh I (2018) Effect of environmental conditioning on natural fiber reinforced epoxy composites. *Mater Today: Proceedings* 5(9):17006–17011
16. Swain PTR, Biswas S (2017) Effect of moisture absorption on the mechanical properties of ceramic filled Jute/Epoxy hybrid composites. In: *IOP conference series: materials science and engineering*, vol 178, no 1. IOP Publishing, p 012010
17. Yallem TB, Aregawi S, Kumar P, Singh I (2018) Response of natural fiber reinforced polymer composites when subjected to various environments. *Int J Plast Technol* 22(1):56–72

# Performance Improvement of Nanofluid Minimum Quantity Lubrication (Nanofluid MQL) Technique in Surface Grinding by Optimization Using Jaya Algorithm



Sharad Chaudhari, Rahul Chakule and Poonam Talmale

**Abstract** The recent industries are more concise about clean, green, and sustainable machining process for better quality and productivity. The conventional cutting fluid is gradually replaced by nanofluid due to heat transfer and the lubricating properties of nanoparticles. The effect of material hardness on grinding performance in terms of surface roughness is determined under different cooling environments such as conventional flooded, MQL, and Nanofluid MQL. The result shows that surface finish of hard material is obtained better at 0.30 vol.% concentration of nanofluid compared to conventional flooded, MQL and 0.15 vol.% concentrations of Nanofluid MQL process. In present work, the modeling and optimization of process parameters for EN 31 soft material are carried out using Jaya algorithm to improve the process performance. The process parameters such as table speed, depth of cut, dressing depth, coolant flow rate, and nanofluid concentration are considered the input parameters and surface roughness as the response parameter for model development. The optimal values obtained by Jaya algorithm for soft steel material in Nanofluid MQL process are table speed (7000 mm/min), depth of cut (20  $\mu\text{m}$ ), dressing depth (10  $\mu\text{m}$ ), coolant flow rate (750 ml/hr), and nanofluid concentration (0.22 vol.%). The result shows that Nanofluid MQL process significantly reduced the surface roughness by 14% over the conventional technique. The confirmation experiments are conducted to validate the regression model by comparing the experimental results with predicted values obtained from Jaya algorithm at optimal setting.

**Keywords** Cooling environments · Jaya algorithm · Modeling · Surface roughness

---

S. Chaudhari · R. Chakule (✉)

Department of Mechanical Engineering, Yeshwantrao Chavan College of Engineering, Nagpur, Maharashtra 441110, India

e-mail: [r\\_chakule@rediffmail.com](mailto:r_chakule@rediffmail.com)

P. Talmale

Department of Mechanical Engineering, Late G.N. Sapkal College of Engineering, Nasik, Maharashtra 422213, India

© Springer Nature Singapore Pte Ltd. 2020

H. K. Voruganti et al. (eds.), *Advances in Applied Mechanical Engineering*,

Lecture Notes in Mechanical Engineering,

[https://doi.org/10.1007/978-981-15-1201-8\\_86](https://doi.org/10.1007/978-981-15-1201-8_86)



## 1 Introduction

The large amount of heat generates at contact zone due to complex material removal mechanism of grinding process and abrasive workpiece contact for microseconds. The large heat affects on workpiece quality, tool life, specific grinding energy, and finally on machine efficiency. The more amount of coolant is used to improve the process performance. It helps to dissipate the heat generated during machining, but the process is not economical and eco-friendly. The problem associated with the conventional grinding process of excess coolant usage is discussed [1]. In minimum quantity lubrication (MQL), the small amount of cutting fluid (ml/hr) is used in mist form by compressed air and then penetrates effectively at contact interface. The result of MQL grinding is better compared to conventional flooded, but lubricating effects are poor as cutting fluid is soluble oil. Recently, the Nanofluid MQL technique is more cost-effective, eco-friendly and human-friendly [2–4]. The features of nanoparticles are better thermal conductivity, large relative surface area, high mobility, and better suspension stability [5, 6]. The application of nanofluid using MQL (Nanofluid MQL) can reduce the friction, cutting forces, and temperature in cutting region due to better heat transfer, tribological characteristics of nanoparticles, and better penetration of nanofluid [7–10]. The hardness effect of workpiece on MQL process performance is studied in paper [11].

From the literature study, it is observed that the traditional method of optimization can use to find the optimal values of process parameters but the accurate guess of the initial solution is not possible and may trap into local optima. The problem is more critical for Nanofluid MQL grinding, where more parameters are involved. To overcome the limitations of traditional methods, Jaya algorithm is used to optimize the process parameters. It has only one phase and does not require any algorithm-specific parameter for optimization. The execution of Jaya algorithm is easy and simple [12].

In the present study, the performance of EN31 hard and soft steel materials in terms of surface roughness is analyzed experimentally using response surface methodology (RSM). The main purpose of this work is to study the Nanofluid MQL process for hard and soft EN31 steels and further to improve the performance of soft steel using optimized values obtained from Jaya algorithm. The mathematical model is developed using RSM based on significant parameters. The mathematical model is treated as the fitness function for evaluation in Jaya algorithm.

## 2 Experimental Procedure

Experiments are conducted on EN31 rectangular plate of hard and soft types having size 100 \* 50 \* 25 mm using hydraulic surface grinding machine. The grinding wheel size of 350 \* 50 \* 75.2 mm and type AA46-54-K5-V8 is used for experimentation. The soluble oil ratio of 1:20 is used for conventional/wet and MQL

experiments. The water-based  $Al_2O_3$  nanofluid of 0.15 and 0.30 vol.% concentrations is used for experimentation of Nanofluid MQL process. The average particle size of  $Al_2O_3$  is 30–50 nm and is used for experimentation. The concentration (0) indicates that the experiments are conducted using MQL technique. The average value of response is considered for analysis. The EN31 steel is extensively used to manufacture the drawing dies and molds in various forming operations. The good tolerance and better surface finish in dies and molds is the basic requirement that depends on material selection and process performance. The levels of parameters shown in Table 1 are determined considering the industry practices, literature survey, and conducting the pilot experiments. The experiments are conducted as per design matrix obtained by response surface methodology (RSM) using Minitab 17 software. The minimum experimental runs are determined using statistical technique called design of experiments [13]. The experimental setup of NanoMQL process is shown in Fig. 1.

The surface finish which determines the performance and service life of machine components is measured in terms of Ra value at three points along the grinding direction. The SRT-6200-type surface roughness tester is used to measure surface roughness. The speed and sampling length of 0.5 mm/s and 2 mm are used. The cutting forces are recorded using strain gauge dynamometer positioned properly under the workpiece clamping device. The normal ( $F_n$ ) and tangential ( $F_t$ ) cutting forces are measured at three locations on workpiece after 14, 32, and 46 passes of grinding wheel on workpiece surface. The resultant average of cutting force is

**Table 1** Levels of process parameters

Level	Table speed (mm/min)	Depth of cut ( $\mu\text{m}$ )	Dressing depth ( $\mu\text{m}$ )	Coolant flow rate (ml/hr)	Nanofluid concentration (vol.%)
Low	7000	20	10	250	0
Medium	10,000	30	20	500	0.15
High	13,000	40	30	750	0.30

**Fig. 1** Experimental setup



considered for result analysis. The coefficient of friction ( $\mu$ ) is determined using the ratio tangential force and normal force value ( $F_t/F_n$ ).

### 3 Results and Discussion

The tangential force increases with friction that is generated along with the reciprocating movement of worktable. The other cutting force component called normal force obtained is mostly affected by workpiece hardness. The coefficient of friction obtained is lowest for harden material in Nanofluid MQL technique. The reason of better results may be due to efficient lubrication and cooling effects of nanofluid at contact zone compared to wet and MQL techniques. The lubricating properties of nanofluid and effective penetration using compressed air at contact zone help to form tribofilm of nanofluid on ground surface and wheel abrasive. The slurry effect of lubrication helps to restore the sharpness of grits better than soluble cutting fluid. The material removal is more shearing in hard material, whereas due to ductility nature, the material removal is shearing and plastic deformation of soft steel. Thus, the better surface finish is obtained by reducing the surface roughness value in hard steel using Nanofluid MQL. For better improvement of results in soft steel, it is important to optimize the machine process parameters. Figures 2 and 3 show the tribological characteristics such as tangential force, coefficient of friction and response value, namely surface roughness of hard and soft EN31 steels under different grinding environments.

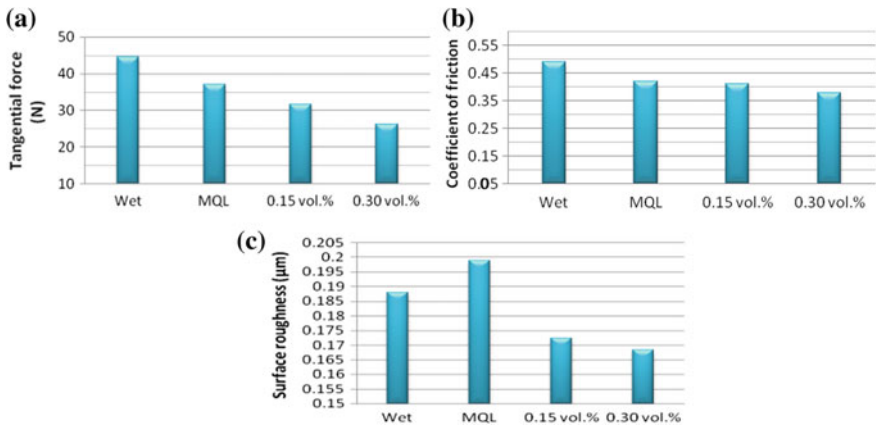


**Fig. 2** Grinding parameters under different cutting environments (hard steel): **a** Tangential force, **b** coefficient of friction, **c** surface roughness

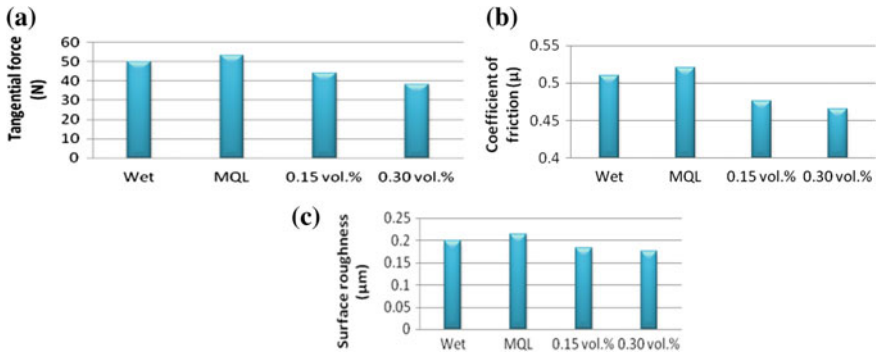


**Fig. 3** Grinding parameters under different cutting environments (soft steel): **a** Tangential force, **b** coefficient of friction, **c** surface roughness

### 3.1 Development of Mathematical Model

The quadratic model of surface roughness is developed using RSM. The equation of surface roughness (Ra) in coded form is given in Eq. (1). The input factors are coded as table speed ( $x_1$ ), depth of cut ( $x_2$ ), dressing depth ( $x_3$ ), coolant flow rate ( $x_4$ ), and nanofluid concentration ( $x_5$ ).

$$\begin{aligned}
 \text{Surface roughness (Ra)} = & 0.13301 + 0.000009x_1 + 0.000628x_2 \\
 & - 0.000424x_3 - 0.000049x_4 \\
 & - 0.2187x_5 + 0.5461x_5^*x_5 - 0.000011x_1^*x_5 \\
 & + 0.000001x_3^3x_4 + 0.000078x_4^*x_5 \quad (1)
 \end{aligned}$$

The analysis of variance (ANOVA) of the response surface quadratic model of surface roughness shows the multiple regression coefficients ( $R^2$ ) value of 0.9797. The predicted R-squared value 0.9605 is also in reasonable agreement with adjusted  $R^2$  value 0.9715. The value indicates that the model well fitted the data. The  $P$ -value of model in ANOVA is less than 0.05, indicates the model terms are significant. The lack of fit is not significant. This indicates that the model is adequate to study the relationship between response parameter in concerned with machining process parameters. The papers [14–18] are reviewed on modeling and optimization to find optimal machining process parameters.

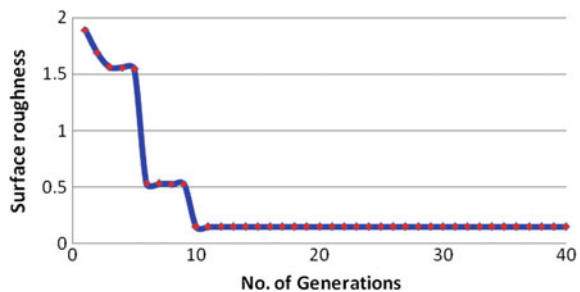
### 3.2 Optimization Using Jaya Algorithm

The literature studies on optimization stated that evolutionary algorithms are probabilistic. They require common controlling parameters like population size and number of iterations and algorithm-specific control parameters besides the common controlling parameters. The improper tuning of algorithm-specific parameters and common controlling parameters increases the computational effort or obtained the local optimal solution. To overcome these limitations, recently developed Jaya algorithm is used in this case study. The special features of Jaya algorithm are simplicity and do not have any algorithm-specific parameters. In addition to this, it gives optimal solutions in less number of function evaluations. The different papers [19–22] are reviewed to understand the Jaya algorithm and its execution. The optimized values of process parameters are determined using Jaya algorithm for soft steel material.

$$X'_{m,n,i} = X_{m,n,i} + r_{1,m,i}(X_{m,best,i} - |X_{m,n,i}|) - r_{2,m,i}(X_{m,worst,i} - |X_{m,n,i}|) \quad (2)$$

where  $r_{1,m,i}$  and  $r_{2,m,i}$  are the two random numbers for “ $m$ ” variable during  $i$ th iteration in the range of [0, 1]. The term “ $r_{1,m,i}(X_{m,best,i} - |X_{m,n,i}|)$ ” indicates the tendency of solution to move closer to the best solution, and the term “ $r_{2,m,i}(X_{m,worst,i} - |X_{m,n,i}|)$ ” shows the ability of solution to avoid the worst solution.  $X'_{m,n,i}$  solution is accepted if it gives a superior function value. All the accepted function values at the end of iteration are considered as input to the next iteration. The algorithm tries to get the best optimal solution and rejects the worst solution. The absolute value of  $X_{m,n,i}$  is considered in Eq. (2). The objective function is subjected to significant parameter and range constraints such as  $7000 \leq x_1 \leq 13,000$ ;  $20 \leq x_2 \leq 40$ ,  $10 \leq x_3 \leq 30$ ,  $250 \leq x_4 \leq 750$ , and  $0 \leq x_5 \leq 0.30$ . The convergence curve for optimizing surface roughness value is shown in Fig. 4. The confirmation experiments are conducted at feasible optimized values obtained from Jaya algorithm such as table speed (7000 mm/min), depth of cut (20  $\mu$ m), dressing depth (10  $\mu$ m), coolant flow rate (750 ml/hr), and nanofluid concentration (0.22 vol.%). It is also observed that the percentage error of surface roughness is 5.49% at optimized values. The good agreement of surface roughness result is obtained as predicted values from Jaya algorithm and experimental values are closer.

**Fig. 4** Convergence curve of surface roughness



## 4 Conclusions

The present work analyzed the modeling and optimization of Nanofluid MQL process for soft EN31 steel to improve the process performance in terms of surface roughness. The surface roughness value is determined at optimized parameters obtained from Jaya algorithm. Based on current investigations, the following findings are summarized as follows:

- (1) The significant reduction of surface roughness in hardened steel is observed by 14% using Nanofluid MQL grinding at 0.30 vol.% concentrations over conventional flooded technique. The stable nanofluid and better cooling-lubrication effect at contact interface may be the reason to obtain better surface quality. In soft steel, the surface roughness value found poor compared to hard steel in all cutting environments. The more material deformation due to the ductility nature of material may be the reason for poor surface finish in soft steel.
- (2) The second-order quadratic model of surface roughness is developed for significant parameters, and its adequacy is checked by analysis of variance to predict the response at 95% confidence interval. The optimal values obtained for soft EN31 steel using Jaya algorithm in Nanofluid MQL process are table speed (7000 mm/min), depth of cut (20  $\mu\text{m}$ ), dressing depth (10  $\mu\text{m}$ ), coolant flow rate (750 ml/hr), and nanofluid concentration (0.22 vol.%). The convergence speed of Jaya algorithm found very high, and optimum response is obtained in less function evaluations.
- (3) The confirmation experiments are conducted at optimized feasible values of parameters obtained from Jaya algorithm to validate the results. The predicted value of surface roughness obtained from Jaya algorithm is 0.14933  $\mu\text{m}$  and experimental value of 0.158  $\mu\text{m}$ . Thus, the percentage error of 5.49% is observed for surface roughness.

## References

1. Kim H-J, Seo K-J, Kang KH, Kim D-E (2016) Nano-lubrication: a review. *Int J Precis Eng Manuf* 17(6):829–841
2. Setti D, Sinha MK, Ghosh S, Rao PV (2015) Performance evaluation of Ti-6Al-4V grinding using chip formation and coefficient of friction under the influence of nanofluids. *Int J Mach Tools Manuf* 88:237–248
3. Brinksmeier E, Meyer D, Huesmann-Cordes AG, Herrmann C (2015) Metalworking fluids—mechanisms and performance. *CIRP Ann Manuf Technol* 64(2):605–628
4. Hadad M (2015) An experimental investigation of the effects of machining parameters on environmentally friendly grinding process. *J Cleaner Prod* 108:217–231
5. Lee J, Yoon YJ, Eaton JK, Goodson KE, Bai SJ (2014) Analysis of oxide ( $\text{Al}_2\text{O}_3$ , CuO, and ZnO) and CNT nanoparticles disaggregation effect on the thermal conductivity and the viscosity of nanofluids. *Int J Precis Eng Manuf* 15(4):703–710

6. Chiam HW, Azmi WK, Mamat R, Adam NM (2017) Thermal conductivity and viscosity of  $\text{Al}_2\text{O}_3$  nanofluids for different based ratio of water and ethylene glycol mixture. *Exp Thermal Fluid Sci* 81:420–429
7. Sinha MK, Madarkar R, Ghosh S, Rao PV (2017) Application of eco-friendly nanofluids during grinding of inconel 718 through small quantity lubrication. *J Cleaner Prod* 141:1359–1375
8. Wang Y, Li C, Zhang Y, Yang M, Zhang X, Zhang N, Dai J (2017) Experimental evaluation on tribological performance of the wheel/workpiece interface in minimum quantity lubrication grinding with different concentrations of  $\text{Al}_2\text{O}_3$  nanofluids. *J Cleaner Prod* 142(4):3571–3583
9. Paul S, Singh AK, Ghosh A (2017) Grinding of Ti-6Al-4V under small quantity cooling lubrication environment using alumina and MWCNT nanofluids. *Mater Manuf Processes* 32(6):608–615
10. Wang Y, Li C, Zhang Y, Li B, Yang M, Zhang X, Guo S, Liu G (2016) Experimental evaluation of the lubrication properties of the wheel/workpiece interface in MQL grinding with different nanofluids. *Tribol Int* 99:198–210
11. Rabiei F, Rahimi AR, Hadad MJ, Ashrafi M (2015) Performance improvement of minimum quantity lubrication (MQL) technique in surface grinding by modeling and optimization. *J Cleaner Prod* 86:447–460
12. Rao RV, Rai DP, Balic J (2017) A new optimization algorithm for parameter optimization of nano-finishing processes. *Sci Iranica* 24(2):868–875
13. Montgomery DC (2013) *Design and analysis of experiments*, 8th edn. Wiley, New York
14. Mia M, Bashir MA, Khan MA, Dhar NR (2017) Optimization of MQL flow rate for minimum cutting force and surface roughness in end milling of hardened steel (HRC 40). *Int J Adv Manuf Technol* 89(1–4):675–690
15. Lin YC, Tsao CC, Hsu CY, Hung SK, Wen DC (2012) Evaluation of the characteristics of the microelectrical discharge machining process using response surface methodology based on the central composite design. *Int J Adv Manuf Technol* 62:1013–1023
16. Nam JS, Kim DH, Chung H, Lee SW (2015) Optimization of environmentally benign micro-drilling process with nanofluid minimum quantity lubrication using response surface methodology and genetic algorithm. *J Clean Prod* 102:428–436
17. Liu G, Li C, Zhang Y, Yang M, Jia D, Zhang X (2018) Process parameter optimization and experimental evaluation for nanofluid MQL in grinding Ti-6Al-4V based on grey relational analysis. *Mater Manuf Processes* 33(9):1–14
18. Gupta MK, Sood PK, Sharma VS (2016) Optimization of machining parameters and cutting fluids during nanofluid based minimum quantity lubrication turning of titanium alloy by using evolutionary techniques. *J Clean Prod* 135:1276–1288
19. Rao RV, Rai DP, Ramkumar J, Balic J (2016) A new multi-objective Jaya algorithm for optimization of modern machining processes. *Adv Prod Eng Manage* 11(4):271–286
20. Rao RV (2017) A multi-objective algorithm for optimization of modern machining processes. *Eng Appl Artif Intell* 61:103–125
21. Rao RV, Rai DP (2017) Optimization of submerged arc welding process parameters using quasi-oppositional based Jaya algorithm. *J Mech Sci Technol* 31(5):2513–2522
22. Abhishek K, Rakesh Kumar V, Datta S, Mahapatra SS (2017) Application of JAYA algorithm for the optimization of machining performance characteristics during the turning of CFRP (epoxy) composites: comparison with TLBO, GA and ICA. *Eng Comput* 33(3):457–475

# Wear Resistance of Structural Steels Having Ultra-Low Carbon to High Carbon Concentration



Soumya Sourav Sarangi, Lavakumar Avala and D. Narsimhachary

**Abstract** The tribological behavior of the different structural steels with carbon concentration ranging from 0.002 to 0.7% was evaluated through ball on disk wear testing method. Testing was carried out at three different loads, i.e., 30, 40, and 50 N to understand the wear behavior at different loading conditions. The wear resistance of the spheroidized high carbon steel (0.7%) is found to be lesser than that of steels containing pearlite in their microstructures, i.e., low carbon (0.19%) steel and medium carbon (0.32%) steel. Enhanced strain hardening of the pearlite structure was held responsible for the increased wear resistance. As expected if steel showed least wear resistance due to its softer ferrite content. The SEM images of the worn structures are correlated with the macroscopic wear resistance data.

**Keywords** Wear testing · If steel · SEM micrographs · Worn structures

## 1 Introduction

Wear occurs when two surfaces come in contact with each other. Generally, wear process involves the relative movements of the surfaces. Wear is basically a surface phenomenon, where the surface of the material gets removed continuously due to delamination of the surface layer because of various processes undergoing at the subsurface level [1]. The environmental condition along with the crack generation at the subsurface level has an important role to play during wear property evaluation [2]. Wear resistance of steels or any metals is correlated with various

---

S. S. Sarangi (✉) · L. Avala  
Department of Metallurgical & Materials Engineering, Veer Surendra Sai University of Technology, Odisha 768018, India  
e-mail: [soumyasouravsarangi33@gmail.com](mailto:soumyasouravsarangi33@gmail.com)

L. Avala  
Department of Materials Science and Engineering, Kyoto University, Kyoto, Japan

D. Narsimhachary  
Department of Metallurgical and Materials Engineering, National Institute of Technology, Rourkela, Rourkela, Odisha 769008, India

© Springer Nature Singapore Pte Ltd. 2020  
H. K. Voruganti et al. (eds.), *Advances in Applied Mechanical Engineering*,  
Lecture Notes in Mechanical Engineering,  
[https://doi.org/10.1007/978-981-15-1201-8\\_87](https://doi.org/10.1007/978-981-15-1201-8_87)



factors like microstructure, mechanical work history, and composition. Extensive studies have been carried out to understand the generalized mechanism of wear occurring under various conditions. Mang et al. have attempted to describe wear behavior of metals through predictive mathematical equations [3]. But the aim of predicting wear with respect to few specific properties has been largely unsuccessful. This is concluded by Hurricks et al. that only the knowledge of composition and bulk mechanical properties of materials is not sufficient to understand wear behavior. Rather, the knowledge of microstructure and the influence of microstructure over the wear properties carry equal importance [1]. While a steel surface undergoes wear, various complex mechanisms like crack or void formation, pulling off colonies of pearlite, dissolution of carbides etc. come into play [4, 5]. These properties affect the wear behavior of steels to a vast extent.

Therefore, steels with varying microstructures are selected for this study, so that an understanding can be built on the effect of microstructure on wear properties.

## 2 Experimental Procedure

Five different steels with varying carbon concentration were selected for the present study. The samples selected are spheroidized high carbon steel (0.7% C), medium carbon steel (0.32% C), low carbon steel (0.19% C), microalloyed steel (0.07% C), and if steel (0.002% C). The wear testing for the samples was carried out in DUCOM ball on disk wear testing machine in dry condition to study the wear behavior at different loading conditions; wear test was carried out at three normal loads, i.e., at 30 N, 40 N, and 50 N load, respectively. Three samples with dimensions 1 cm × 1 cm × 1 cm were cut and metallographically prepared for the wear testing. For the testing, a diamond indenter was held against the specimen surface with a wear track diameter of 4 mm. The samples were rotated at a speed of 25 rpm for a time period of 15 min. Finally, HITACHI SU3500 Scanning Electron Microscope (SEM) was used to observe the worn-out surface of the steels.

## 3 Results and Discussion

The plots showing the wear rate in microns as a function of sliding distance for the steels selected in the study are given in Fig. 1 (Fig. 1a–e). For all the specimens, the amount of wear increases with wear load. It can be observed from Fig. 1a–e that initially, the wear rate is quite high which gets stabilized after a certain sliding distance. This is seen in all the specimens. Another conclusion that can directly be followed from Fig. 1 is that the increase in wear rate with load for the specimens can not be said to be directly related to the carbon concentration. For medium carbon steel,

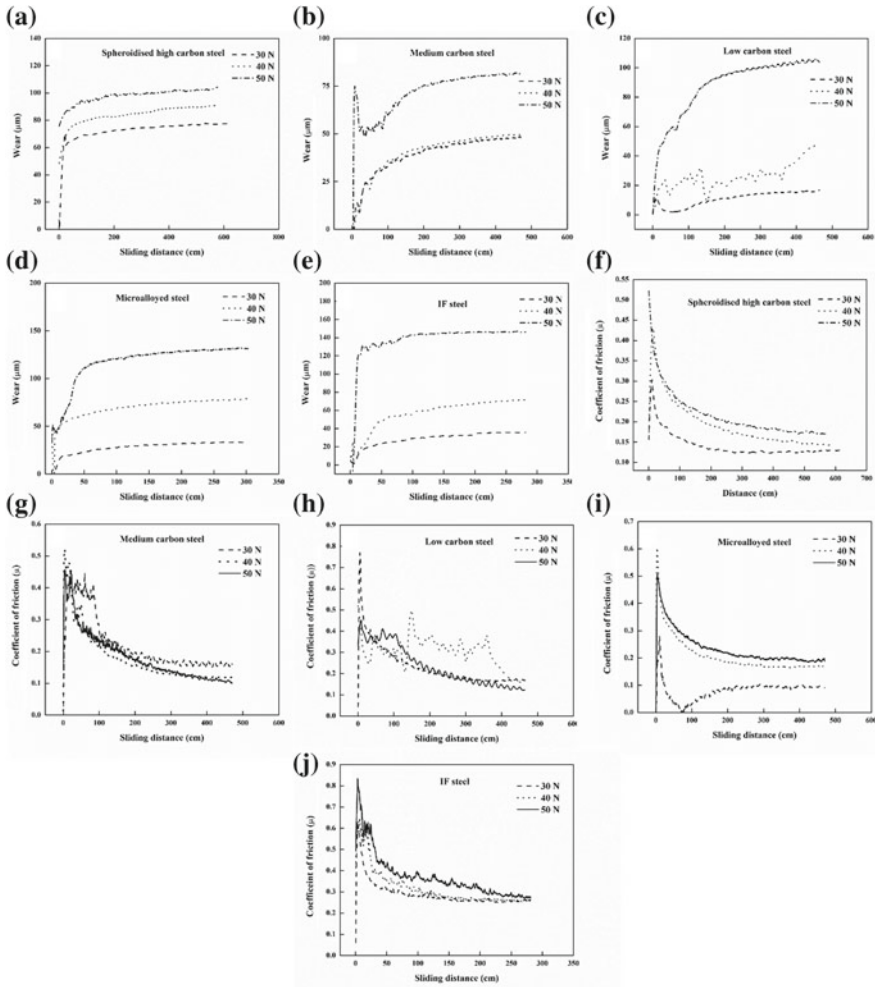


**Fig. 1** Wear rate versus sliding distance for **a** spheroidized high carbon steel, **b** medium carbon steel, **c** low carbon steel, **d** microalloyed steel and **e** if steel variation of coefficient of friction value with sliding distance for **f** spheroidized high carbon steel, **g** medium carbon steel, **h** low carbon steel, **i** microalloyed steel, and **j** if steel

the wear rate observed for 30 and 40 N loads is quite similar, whereas a considerable amount of increase in wear rate can be detected at 50 N load.

The amount of wear in the specimens is a strong function of the constituent phases inside the material. For if steel and microalloyed steel, the wear rate shows a little difference at 30 and 40 N loads. But at 50 N if steels, wear rate is considerably higher than that of microalloyed steel due to softer ferritic matrix in the former. Similar is the case with low carbon and medium carbon steels, where the wear amount and wear rate in medium carbon steel are lower than that of low carbon steel due to the

presence of a higher fraction of pearlite in its microstructure. The wear rate versus distance plot in low carbon steel at 40 N load (Fig. 1c) seems to be distorted. This might be the result of uneven sample surface encountered during testing.

In spite of having the highest surface hardness, spheroidized high carbon steel shows lower resistance to wear deformation than that of low carbon and medium carbon steels. This can be observed from the comparison of variation of wear rate with sliding distance for all samples given in Fig. 1. The presence of softer ferritic matrix in spheroidized high carbon steel explains the poor wear resistance of the above-mentioned steel. This result agrees with previous studies carried out by Y. Wang et al., where steels having pearlite in their microstructure showed higher wear resistance than that of the steel with spheroidized microstructure [6].

The influence of surface hardness over the wear properties of the steels during sliding conditions is quite complex and it is difficult to relate the surface hardness of the materials directly with their wear properties [7]. Instead, the thermal stability of the phases in the microstructure of the steels plays an important role in this phenomenon. With ongoing sliding contact wear process the temperature of the test piece increase, their surface hardness decrease. This might explain the observation of higher wear rate in steels with a higher surface hardness [6].

The high wear resistance of the medium carbon steel and low carbon steel is attributed to the presence of lamellar pearlite in their microstructure. With successive wear of the surface, the surface layers work hardens appreciably. As it is known that pearlite has excellent work hardening capability due to the orientation of carbides in lamellar form, the wear in pearlite becomes considerably smaller than structures with similar hardness or in some cases than structures with higher surface hardness [8]. The phase fraction of pearlite in the considered medium carbon steel is nearly 50%. This explains the highest wear resistance observed in the medium carbon steel.

The similar concept of work hardening can be employed to explain the wear behavior observed in if steel and microalloyed steel. Both the if steel and microalloyed steel contain ferrite phase in their microstructures due to very less carbon content. The grain size in the case of microalloyed steel is quite smaller than that of the if steel, which imparts greater strain hardening capability to the microalloyed steel. It can be observed the wear resistance at smaller loads (30 and 40 N) in both the steels is similar, i.e., the degree of work hardening in both the steels is similar at lower loading conditions. But at 50 N load, fine grain microstructure of microalloyed steel work hardens more and shows higher resistance to wear deformation.

Figure 1f–j shows the variation of coefficient of friction with sliding distance for each steel at different loads. A sharp decrease in the value of coefficient of friction with little initial fluctuation is the common feature in all the steels. The rapid decrease in the value of coefficient of friction implies the very fast increase in the wear resistance of steels by virtue of their own deformation, i.e., work hardening.

The coefficient of friction value at lower loads of low carbon steel shows a lot of fluctuation which may be the effect of carrying out tests with an uneven specimen. The transition in coefficient of friction values with progressing wear test indicates toward the change of wear mechanism with time. It can be observed that the coefficient of

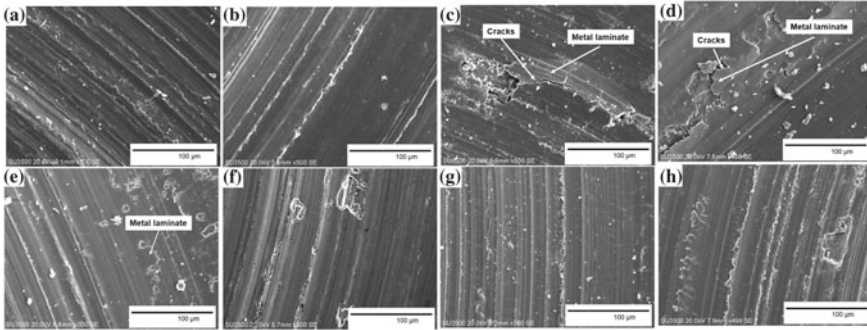


**Fig. 2** SEM images of worn surface of **a** if steel at 50 N load, **b** microalloyed steel at 30 N load, **c** microalloyed steel at 50 N load, and **d** low carbon steel at 50 N load. SEM images of worn-out surface of **e** medium carbon steel at 50 N, **f** spheroidized high carbon steel at 30 N, **g** spheroidized high carbon steel at 40 N, and **h** spheroidized high carbon steel at 50 N

friction values for all specimens increases slightly with increase in load from 30 to 40 N, whereas an appreciable inflation in coefficient of friction values is seen when transition of load occurred from 40 to 50 N.

The wear resistance of the above steels can directly be related to the appearance and features on the worn-out surfaces. Figure 2 (Fig. 2a–h) shows selective SEM images of the wear track at different loads for the samples. Figure 2a shows the wear track of if steel sample at a load of 50 N. The evidence of microcutting of the steel specimen can be found from this picture, which indicates abrasive wear has taken place in if steel [9]. When a metal surface work hardens with time, then cracks form in the subsurface region. These cracks join together and eventually sheets of metal are separated from the surface exposed to wear. This is known as delamination [10]. Delamination and subsurface cracking can be observed in microalloyed and low carbon steels (Fig. 2c, d). This indicates considerable strain hardening occurring during wear of these steels, which in turn enhances their wear resistance.

Spheroidized high carbon steel, in spite of its highest surface hardness, shows inferior wear resistance than that of the plane carbon steels having lesser carbon concentration. This is evident from Fig. 2 (Fig. 2f–h). Spheroidized high carbon steel specimen even at lower load, i.e., at 30 N load shows the removal of patches of metal from localized sites (Fig. 2f). In spheroidized high carbon steel, hard cementite particles are uniformly distributed in the softer ferritic matrix. During sliding wear, the huge plastic deformation can cause the nucleation of cracks at the hard cementite particles [11, 12]. This is responsible for more material loss from the spheroidized structure and hence more wear rate. The removal of the material from surface of spheroidized high carbon steel seems more prominent at the higher load (50 N) as can be seen in Fig. 2h.

## 4 Conclusions

1. The wear of the steel samples with sliding distance was measured. At 50 N load, medium carbon steel showed highest wear resistance, whereas if steel showed the least.
2. The carbon concentration cannot directly be related to the wear resistance of the steels. The importance of microstructure of the surface exposed to wear is more toward determining the wear resistance than the composition.
3. The coefficient of friction values showed a rapid increase in value followed by a relatively stable regime. This indicates a change in wear mechanism or changes in surface condition of the steels while testing.
4. The features observed in the SEM micrograph of the worn surface of the samples at particular loads are related to the wear rate shown by the specimen at those particular loads.

## References

1. Suh NP (1973) The delamination theory of wear. *Wear* 25(1):111
2. Aglan H, Fateh M (2007) Fracture and fatigue crack growth analysis of rail steels. *J Mech Mater Struct* 2(2):335–346
3. Meng HC, Ludema KC (1995) Wear models and predictive equations: their form and content. *Wear* 181:443–457
4. Rigney DA, Glaeser WA (1978) The significance of near surface microstructure in the wear process. *Wear* 46(1):241–250
5. de Oliveira APM, Houmard M, Labiapari WDS, Godoy C (2019) Erosive Wear Study of the AISI 201LN Stainless Steel: a comparison with the AISI 304 and AISI 410 Stainless Steels. *Metall Mater Trans A* 50(4):1663–1671
6. Wang Y, Lei T, Liu J (1999) Tribo-metallographic behavior of high carbon steels in dry sliding: II. Microstructure and wear. *Wear* 231(1):12–19
7. Rigney DA (1997) Comments on the sliding wear of metals. *Tribol Int* 30(5):361–367
8. Langford G (1977) Deformation of pearlite. *Metall Trans A* 8(6):861–875
9. Sahoo KL, Krishnan CSS, Chakrabarti AK (2000) Studies on wear characteristics of Al–Fe–V–Si alloys. *Wear* 239(2):211–218
10. Yin CH, Liang YL, Liang Y, Li W, Yang M (2019) Formation of a self-lubricating layer by oxidation and solid-state amorphization of nano-lamellar microstructures during dry sliding wear tests. *Acta Mater* 166:208–220
11. Fleming JR, Suh NP (1977) Mechanics of crack propagation in delamination wear. *Wear* 44(1):39–56
12. Hasan SM, Chakrabarti D, Singh SB (2018) Dry rolling/sliding wear behaviour of pearlitic rail and newly developed carbide-free bainitic rail steels. *Wear* 408:151–159

# Experimental Investigation on Laser Beam Welded Joints of Dissimilar Metals and Optimization of Process Parameters Using Firefly Algorithm



B. Narayana Reddy, P. Hema, Y. Prasanth Reddy and G. Padmanabhan

**Abstract** Laser beam welding (LBW) is extensively being used in modern industry for joining of metals and alloys due to its advantages of controlled heating, narrow weld bead, low heat-affected zone (HAZ). Further, its ability is to weld a wide range of metals and dissimilar metals. With a new generation of high power lasers, LBW makes the process possible for welding of dissimilar metals used in shipbuilding, offshore structures, pipelines, power plants and other industries. In addition, LBW is suitable for joining at high process speed, low heat input to achieve high productivity, leading to reduced process costs. Therefore, an attempt is made in the present paper with an objective to investigate the mechanical properties of dissimilar metal joints of AISI 4130 and AISI 316 steels. Experiments are conducted with LBW considering 2-mm-thick dissimilar metals by varying laser beam power, welding speed, beam incident angle, focal point position and focal length. The experimental output results of ultimate tensile strength and impact strength are measured. ANOVA is carried out to obtain the influence of process parameters and validation of results by statistical analysis. Firefly optimization algorithm is used to determine the best combination of the process parameters of LBW.

**Keywords** Laser beam welding (LBW) · Mechanical properties · Analysis of variance · Firefly algorithm

## 1 Introduction

AISI 316 stainless steel (SS) is the second most commonly used metal after 304 austenitic stainless steel. The marine grade SS 316L usually contains Cr, Ni and Mo. AISI 316 SS is used in various industries such as oil, gas, petrochemical, pharmaceutical, food industries, for manufacturing of pipes and sheets, but it is more costlier in comparison with 304 SS. AISI 4130 steel is a medium carbon steel consisting of Cr, Mo and Mn. It is used in oil industry and power plants, due to its very good strength

---

B. Narayana Reddy · P. Hema (✉) · Y. Prasanth Reddy · G. Padmanabhan  
Department of Mechanical Engineering, Sri Venkateswara University, Tirupati 517502, India  
e-mail: [hemasvumech@gmail.com](mailto:hemasvumech@gmail.com)

© Springer Nature Singapore Pte Ltd. 2020  
H. K. Voruganti et al. (eds.), *Advances in Applied Mechanical Engineering*,  
Lecture Notes in Mechanical Engineering,  
[https://doi.org/10.1007/978-981-15-1201-8\\_88](https://doi.org/10.1007/978-981-15-1201-8_88)

at high temperatures developed in heat exchangers and generators. It is also used in normalized, quenched and tempered states.

Welded joints of dissimilar SS and low alloy steels with high strength have plenty of applications in a variety of industries, oil, gas, petrochemical, thermal power plants and food industry. In many of the above-said industries, the fluid transfer tube lines and nozzles are made of SS, whereas the tanks made of low alloy steels subjected to pressure parts of the systems are welded by the conventional welding methods. In view of the extensive applications of dissimilar steel metal joints, optimizing the process parameters of such joints has always been the critical case. In past, some research has been published concerning with the joints conventional processes of 4130 and 316 steel plates, but with some drawbacks. To overcome such of the drawbacks, LBW offers significant advantages due to its ability to weld complex geometries with close tolerances, high strength and narrow HAZ, with high-quality joining [1, 2].

## 2 Literature Review

In any welding process of dissimilar metals, it is important to use optimal process parameters. Optimal parameters can be obtained by scientific optimization techniques. In the present work, Taguchi-based orthogonal array is chosen to conduct experiments. Published literature shows the usability of optimization techniques for both non-fusion and fusion welding including LBW of different materials. A brief literature is presented in the following:

Mechanical behaviour joints of AISI 4130 steel obtained by TIG and LBW are studied by comparing with each other process. It is shown that the LBW is more suitable for mechanical characterization, Souza Neto et al. [3]. GTAW method is used for investigating the properties of dissimilar joints of AISI 4130 and AISI 316 steels by Mostaan et al. [4] and analysed the interface structure by SEM and EDS. Experimental study on the hardness and corrosion resistance of joining similar metals (304) and dissimilar metals (304/A36) has shown that the welding speed and corrosion resistance influence the quality of the welding, Mahmoud et al. [5]. The dissimilar metals (304/4130) joints obtained by EBW are found to be having better tensile strength over the joints obtained by GTAW and FSW, Arivazhagan et al. [6]. The recent publication on evolutionary algorithm firefly algorithm (FA) based on nature is found to be a good optimization tool leading to multi-objective optimization problem, Yang [7]. Further, it is also shown that the FA can perform better than PS optimization algorithm particularly in the case noisy nonlinear optimization problems at higher level of noises, Pal et al. [8]. Later on, the recent advantages and applications of FA are shown in Yang et al. [9]. Though the literature shows that the joint properties of the LBW of dissimilar steel joints are affected by power (W), speed (m/min) beam angle, focal point position (mm) and focal length (mm), but they are limited to one or two input parameters. Therefore, experiments are carried out with various levels of process parameters in the present work.

## 2.1 An Objective of Research Paper

The objective of the present research paper is to investigate the mechanical properties of dissimilar metals joints of AISI 4130 and 316 steels by LBW. Experimental results are analysed using ANOVA followed by the application of FA for optimization of process parameters.

## 3 Experimental Procedure

To achieve the objective, experiments are conducted after the preparation of samples by joining of two plates of dissimilar metals. Samples of two plates of base metals (AISI 4130 and AISI 316) with dimensions of  $2 \times 80 \times 280$  mm are cut to size and used for welding. Figure 1a shows the arrangements of sample pieces as per AWS standards. The pieces are cleaned with acetone to prevent the formation of any defects.

### 3.1 Welding Process

Experiments are conducted with a CO<sub>2</sub> LBW system of 4 kW (Trump Model), by keeping the average power of the CO<sub>2</sub> LBW constant at 4 KW. However, the pulse repetition (frequency) and focal length of 16 mm are used. Welding parameters consist of power-A (1400, 1600, 1800, 2000, 2200 W), welding speed-B (1.2, 1.4, 1.6, 1.8, 2.0 m/min), beam angle-C (88°, 89°, 90°, 91°, 92°), focal point position-D (-0.2, -0.1, 0.0, 0.1, 0.2 mm), and focal length-E (16, 17, 18, 19, 20 mm). Taguchi approach consisting of L<sub>25</sub> (25) orthogonal array for five levels of these parameters is selected for experimentation. Different combinations of parameters to weld specimens for the five levels and five factors are shown in Table 1. Experiments are conducted to obtain 25 joints, but the results of 5 sample joints are shown in Fig. 1b.

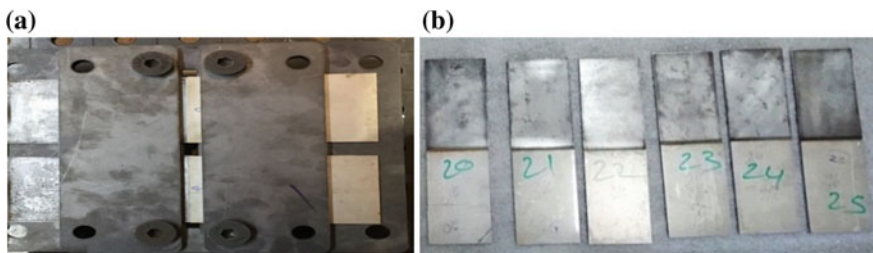


Fig. 1 LBW workpieces: a position of workpieces and b welded joints



**Table 1** LBW process parameters combination and mechanical properties of joints

S. no.	Input process parameters					UTS (MPa)	IS (J)
	A	B	C	D	E		
1	1400	1.2	88	-0.2	16	513.85	26
2	1400	1.4	89	-0.1	17	519.23	22
3	1400	1.6	90	0.0	18	177.69	4
4	1400	1.8	91	0.1	19	341.54	25
5	1400	2.0	92	0.2	20	610.00	24
6	1600	1.2	89	0.0	19	664.61	23
7	1600	1.4	90	0.1	20	684.61	12
8	1600	1.6	91	0.2	16	681.54	18
9	1600	1.8	92	-0.2	17	593.85	27
10	1600	2.0	88	-0.1	18	569.23	26
11	1800	1.2	90	0.2	17	585.38	28
12	1800	1.4	91	-0.2	18	688.46	21
13	1800	1.6	92	-0.1	19	616.15	24
14	1800	1.8	88	0.0	20	730.77	26
15	1800	2	89	0.1	16	685.00	28
16	2000	1.2	91	-0.1	20	167.69	26
17	2000	1.4	92	0.0	16	688.46	27
18	2000	1.6	88	0.1	17	731.54	28
19	2000	1.8	89	0.2	18	246.15	15
20	2000	2.0	90	-0.2	19	603.07	26
21	2200	1.2	92	0.1	18	533.07	28
22	2200	1.4	88	0.2	19	572.31	26
23	2200	1.6	89	-0.2	20	510.00	28
24	2200	1.8	90	-0.1	16	369.23	26
25	2200	2.0	91	0.0	17	513.84	24

### 3.2 Mechanical Properties Measurements

Test specimens are prepared by using CNC wire cut EDM machine as per standards of ASTM E 8M-01 for UTS and ASTM E23 for IS. The tested specimens for tensile test (FIE UTM) are shown in Fig. 2a, followed by the specimens for Charpy impact in Fig. 2b. The test results of each joint sample are presented in Table 1 (Columns UTS and IS).

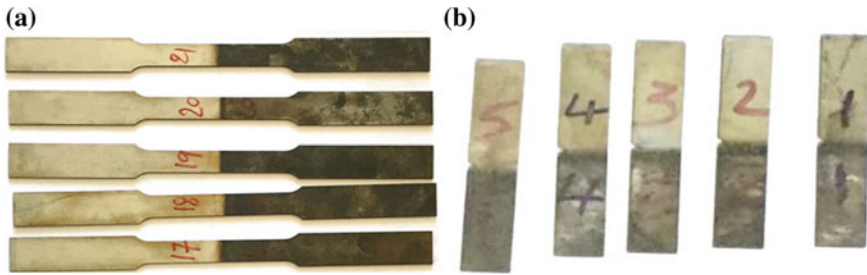


Fig. 2 Tested specimens as per ASTM: **a** tensile test and **b** impact test

### 4 Analysis of Variance

Statistical analysis is conducted on the experimental results by ANOVA for UTS and is shown in Table 2 and IS results in Table 3. The tables show the degrees of freedom,  $SS^2$ , adj SS, adj MS,  $F$ -value,  $P$ -value and percentage of contribution each parameters (%C). Similarly, the columns in Table 3 show the results ANOVA for IS with the same parameters and symbols.

Table 2 ANOVA for means of UTS

S	DF	$SS^2$	Adj SS	Adj MS	$F$ -value	$P$ -value	% C
A	4	201,576	201,576	50,394	1.88	0.277	31.33
B	4	102,646	102,646	25,661	0.96	0.516	15.96
C	4	93,493	93,493	23,373	0.87	0.550	14.53
D	4	66,765	66,765	16,691	0.67	0.645	10.38
E	4	71,882	71,882	17,971	0.62	0.670	11.17
F	4	106,980	106,980	26,745			16.63
T	24	643,343	–	–			100.0

$$S = 163.5 \quad R^2 = 83.4\%$$

Table 3 ANOVA for means of IS

S	DF	$SS^2$	Adj SS	Adj MS	$F$ -value	$P$ -value	%C
A	4	145.04	145.04	36.26	1.18	0.437	18.22
B	4	125.04	125.04	31.26	1.02	0.493	15.70
C	4	168.64	168.64	42.16	1.38	0.383	21.18
D	4	77.84	77.84	19.46	1.28	0.408	9.78
E	4	157.04	157.04	39.26	0.63	0.665	19.72
E	4	122.64	122.64	30.66			15.40
T	24	796.24	–	–			100.0

$$S = 5.537 \quad R^2 = 84.6\%$$

F-Test for laser power - null hypotheses (Ho): No significant difference between the experimental and theoretical values  $F_{\text{calculated}} = 1.88$ ,  $F_{(0.05, 4, 4)}$  table value = 6.39. Since the calculated value is less than the table value, null hypothesis is accepted at 5% of risk or at 95% of confidence level. There is no significant difference between the experimental and theoretical results; hence, the experiments conducted are correct. Similarly, the F-test is conducted for other results and all the results found to be within the acceptance of 95% confidence levels. Hence, the experiments conducted are correct and proved by statistical validation.

Percentage of the contribution of each parameter for UTS is shown in Table 2. It is clear from the experimental, that the percentage of contribution by laser power is 31.33%, welding speed is 15.96%, beam angle 14.53%, focal length 11.17% and focal point position 10.38%, respectively. It can be seen that the laser power has greater influence on UTS.  $R^2 = 83.4\%$  confirms the reliability of model, since the ANOVA is a way to find out the parametric influence of experimental results; thus from the results, it is clear that the laser power is the major factor with 31.33%, which is to be selected to obtain better UTS. Similarly, the percentage of contribution of each parameter for IS is shown in Table 3. It is clear from the results, that the percentage of contribution by beam angle is 21.18%, focal length 19.72%, laser power 18.22%, welding speed 15.70% and focal point position 9.78%, respectively. It is observed that the beam angle has the major influence on UTS.  $R^2 = 84.6\%$  confirms the reliability of model. It is also clear from the results that the beam angle is the major influencing factor (21.18%), which is to be selected to obtain better IS.

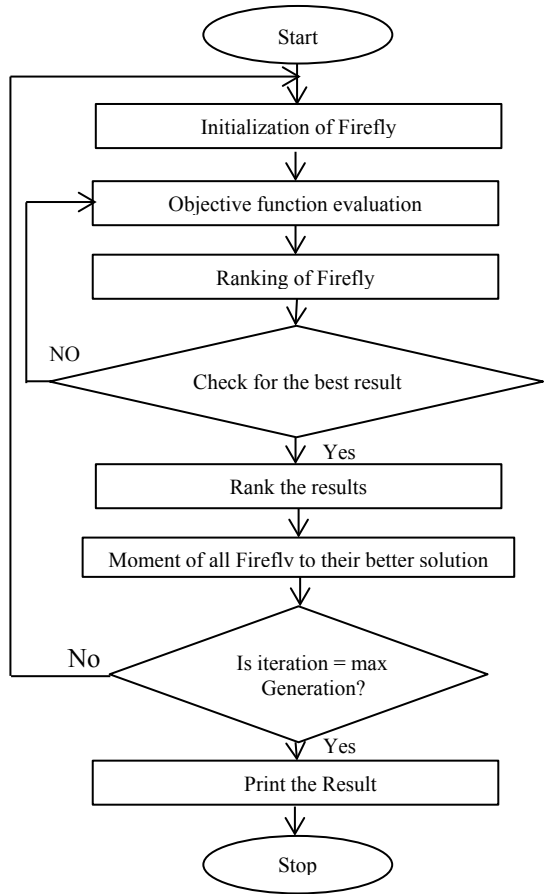
## 5 Optimization Using Firefly Algorithm (FA)

FA is a nature-inspired metaheuristic algorithm introduced in 2008 by Yang to solve optimization problems. The algorithm is based on the social flashing behaviour of fireflies in nature. Fireflies or lightning bugs belong to a family of insects that are capable to produce natural light to attract a mate or prey, whereas firefly algorithm regression analysis is being used to generate equations of UTS and IS which are shown in Eqs. (1) and (2). The flowchart of FA is shown in Fig. 3. The objective functions are converted into multi-objective function by weighted sum approaches. Such approach helps to solve multi-objective optimization by assigning a weightage  $W_j$  to each objective function. The single objective problem with a scalar objective function is shown in Eq. (3). The weightage is considered for  $w_j = 0.5$ . The multi-objective function is shown in Eq. (4), which converts the minimization function to maximization by using Eq. (5).

$$z_1 = 1447 - 0.008A + 16B - 7.7C + 61D - 12.3E \quad (1)$$

$$Z_2 = 27.8 + 0.0078A + 0.5B - 0.12C - 7.4D - 0.46E \quad (2)$$

**Fig. 3** Flowchart of firefly algorithm



$$Z = w_1 z_1 + w_2 z_2 \tag{3}$$

$$\text{Min } Z = 737.4 - 0.0001A + 8.25B - 3.91C + 26.8D - 6.38E \tag{4}$$

$$Z_{\text{max}} = -Z_{\text{min}} \tag{5}$$

$$\text{Max } Z = 737.4 - 0.0001 + 8.25B - 3.91C + 26.8D + 6.38E \tag{6}$$

The maximization of multi-objective regression Eq. (6) is used and then for optimization by the application of FA. The optimal combination of process parameter are  $A$  1568.1 W,  $B$  1.9 m/min,  $C$  88.6°,  $D$  0.1 mm,  $E$  16.3 mm and the optimal values are UTS = 588.2452 Mpa, IS = 22.1112 J.

## 6 Conclusions

Conclusions based on the experimental results are shown in the following:

- Sound welds are obtained on joining of dissimilar AISI 316 and AISI 4130 steels by LBW.
- LBW is suitable for welding AISI 4130 with AISI 316 steels for industrial applications owing to high welding speed and highest UTS 731.54 MPa and IS 28 J as obtained for the experimental joints. The specific applications are milk carrying tanks, turbines, polyester manufacturing pipelines, body structures of ships, airplanes, rockets, underground water pipelines, boilers shells in thermal power plants.
- ANOVA results show that the power 31.33% is the major influencing process parameter on UTS, whereas beam angle 21.18% on IS.

The multi-optimal combination of processes parameters obtained by the application of FA are: power 1568.1 W, speed 1.9 m/min, angle 88.6°, focal point position 0.1 mm, focal length 16.3 mm for the UTS 588.24 MPa and impact strength 22.11 J.

**Acknowledgements** The authors are grateful acknowledge welding of Magod Laser Machining Pvt. Ltd., Bengaluru-560105, India, for permitting to conduct the experiments.

## References

1. Narayana Reddy B, Hema P, Eswara Reddy C, Padmanabhan G (2017) Role of Laser Beam in welding and assembly: a status review. In: Proceeding of 10th international conference on precision, meso, micro and nano engineering manufacturing engineering section, Department of Mechanical Engineering, IIT Madras, 20–23 Dec, 1056–1060
2. Narayana Reddy B, Hema P, Padmanabhan G (2018) Influence of CO<sub>2</sub> Laser Beam Welding process parameters on mechanical properties of lowalloy AISI 4130 Steel welded joints. In: Proceedings of the 1st international congress on latest innovations in materials engineering & technology, Lendi Institute of Engineering & Technology, 24–27 June
3. Souza Neto F, Neves D, Silva OMM, Limac MSF, Abdallac AJ (2015) An analysis of the mechanical behavior of AISI 4130 Steel after TIG and Laser Welding process. *Proc Eng* 114:181–188
4. Mostaan H, Poorkabirian M, Rafiei M (2018) The interface structure in dissimilar welding of AISI 4130 to AISI 316L Steels using ERNiCr-3 filler metal. *Int J ISSI* 15(1):1–8
5. Mahmoud MT (2015) Effect of laser welding speed on the hardness and corrosion resistance of (304/304 Stainless Steels) and (304 Stainless Steel/A36 Carbon Steel). *Int J Adv Tech Eng Sci* 3:47–56
6. Arivazhagan N, Surendra S, Satya P, Reddy GM (2011) *Mater Des* 32:3036–3050
7. Yang XS (ed) (2010) Nature inspired metaheuristic algorithm. In: *Firefly algorithm*, 2nd edn. Luniver Press, University of Cambridge, UK, pp 81–89
8. Pal S, Rai CS, Singh A (2012) Comparative study of firefly algorithm and particle swarm optimization for noisy non-linear optimization problems. *Int J Intell Syst Appl* 1(10):50–57
9. Yang XS, He X (2013) Firefly algorithm recent advances and applications. *Int J Swarm Intell* 1(1):36–50

# Parametric Optimization of Electrical Discharge Grinding on Ti–6Al–4V Alloy Using Response Surface Methodology



Murahari Kolli and Adepu Kumar

**Abstract** In this paper, an experimental study of electrical -discharge grinding (EDG) process of Ti–6Al–4V alloy on material removal rate (MRR) and surface roughness (SR) through response surface methodology (RSM). Wheel speed (WS), discharge current ( $I_p$ ), pulse on time ( $T_{on}$ ), and pulse off time ( $T_{off}$ ) are considered the important parameter. RSM-central composite design (CCD) of four parameters with three levels has been employed. ANOVA results were performed to identify the significant parameters and the establishment of the mathematical model of MRR and SR. Furthermore, mathematical models and experimental values were correlated; the results were verified and found to be within the range of 7.57% and 4.68% of MRR and SR, respectively.

**Keywords** Electrical discharge grinding · Ti–6Al–4V alloy · Response surface methodology · Analysis of variance

## 1 Introduction

EDM is thermo-electric machining processes in which the electrode and workpiece do not come into direct contact and eliminate the mechanical stress, chatter, and vibration problems during machining [1]. Nowadays, EDM process is used in various advanced materials such as composites, ceramics, HSTR steels, nickel, and titanium. Selection of control factors plays a significant role in EDM, which effects the performance characteristics resulting in lower MRR and high rate of tool wear rate (TWR) and surface and subsurface damage creation of thin and brittle heat-affected zone(HAZ). In order to overcome these EDM limitations, a hybrid EDM process is used. One of the unconventional hybrid techniques is electrical discharge

---

M. Kolli (✉)

Department of Mechanical Engineering, Lakireddy Bali Reddy College of Engineering, Mylavaram, AP 521230, India

A. Kumar

Department of Mechanical Engineering, National Institute of Technology, Warangal, Warangal, Telangana 506004, India

© Springer Nature Singapore Pte Ltd. 2020

H. K. Voruganti et al. (eds.), *Advances in Applied Mechanical Engineering*,

Lecture Notes in Mechanical Engineering,

[https://doi.org/10.1007/978-981-15-1201-8\\_89](https://doi.org/10.1007/978-981-15-1201-8_89)

grinding (EDG). EDG was developed by replacing the stationary electrode used in EDM with rotating electrode. In EDG process, an electrically conductive disk shape is used as a tool electrode at horizontal axis instead of stationary tool electrode. The rotation of disk wheel, the flushing efficiency, enhanced between discharge gaps. Due to the dielectric, flushing affects result enrichment in MRR, lower the surface finish and HAZ [2, 3].

Many attempts have been made by different researchers regarding applications of EDG for different workpiece materials and performance in terms of MRR, SR, and TWR. Chandrasekhar et al. fabricated a self-made an experimental setup of EDG in face grinding type. The process parameters such as  $I_p$ ,  $T_{on}$ ,  $T_{off}$ , and wheel rotations per minute (RPM) were selected on the performance characteristics MRR and SR with machining of high carbon steel (HCS) and high-speed steel (HSS) workpieces [4]. The result is observed that MRR enhances with enhance in WS for both HCS and HSS. The MRR is high while machining the HCS workpiece compared to the HSS workpiece for the same parameter settings. Yadav et al. conducted experiments on self-developed electrical discharge diamond cut-off grinding (EDDCG) of Ti–Al–Mo–V alloy. They found that the MRR increases with an increase in wheel RPM,  $I_p$ , and  $T_{on}$  [5]. Modi et al. examined the experimental study on Ti–6Al–4V alloy with in-house developed powder-mixed electrical discharge diamond surface grinding (PMEDDSG). It concluded that better surface finished and higher MRR obtained at PMEDDSG [6]. Shih et al. investigated the EDG using a rotary disk to mimic the machining process of a surface grinder with horizontal spindles of cold-worked tool steel AISI D2. The results concluded that lower EWR and higher MRR were obtained at rotary disk electrode when positive polarity was selected [7].

Singh et al. optimized the EDM parameters to improve the surface finish of titanium alloy adopted the Taguchi's technique.  $T_{on}$ ,  $T_{off}$ , and  $I_p$  were as process parameters, copper tools used as an electrode material. It concluded that  $I_p$  and  $T_{on}$  have a significant effect on SR [8]. Shu et al. investigated the performance characteristics of EDG on metal matrix composites (MMCs) electrode (Cu/SiCp). It was concluded that MRR enhanced three to seven times compared to the without attachment of EDM. Electrode rotating speed, SiCp particles size, and  $I_p$  were significant parameters of MRR [9]. Mohan et al. studied the EDM process parameters of Al–SiC MMC with rotary tube electrode. The factors were polarity,  $I_p$ , electrode material, pulse duration, and rotation of electrode on performance characteristics like MRR, TWR, and SR. The increase in the electrode speed resulted in positive effect with MRR, TWR, SR than the stationary electrode material [10].

The literature survey reveals that most of the researchers have concentrated on EDM process with conventional dielectric fluids; it is observed that a scarce amount of research focuses on EDG with parameters optimization of Ti–6Al–4V alloy with RSM approach. WS,  $I_p$ ,  $T_{on}$ , and  $T_{off}$  are the EDG variable factors. So, the main objective of the present work is to maximize the MRR and minimize the SR using the EDG factors adopted the design of experiments (DoE). The experiments were planned and conducted by using RSM-CCD approach. ANOVA analysis was conducted to finalize the significant parameters, interaction and to develop empirical relation.

## 2 Experimental Setup

The EDG attachment has been used on EDM Formatics 50 Machine (Make: India). The EDG setup has been placed on the ram of the EDM machine. The experimental setup is shown in Fig. 1. The EDG setup consists of electrically conductive rotating non-abrasive grinding wheel (brass), motor, shaft, belt, pulley, and bearing. The brass with dimensions of 100 mm diameter and 10 mm thickness is used as the grinding wheel. The fabricated attachment has been replaced by the original tool holder of die-sinking EDM. The EDG assembly is partially dipped in a dielectric within the dielectric tank [2].

The  $WS$ ,  $I_p$ ,  $T_{on}$ , and  $T_{off}$  are the process parameters of the EDG process. The variable factors and their ranges are observed in Table 1. Ti-6Al-4V alloy is selected as a workpiece material for the experimentation. Ti-6Al-4V alloy of dimensions  $100 \times 50 \times 5$  mm is taken. Drinking water was used as a dielectric fluid. The experiments were conducted for a fixed time period, i.e., 15 min. To calculate the MRR, weight differences are measured by electronic digital weighing machine (Make: citizen, India) having least count 0.0001 g. Machining time was measured by the EDM machine time counter. Surface finish was measured by using handy surf (Make: Zeiss, India).

**Fig. 1** Grinding wheel setup attached the EDM machine

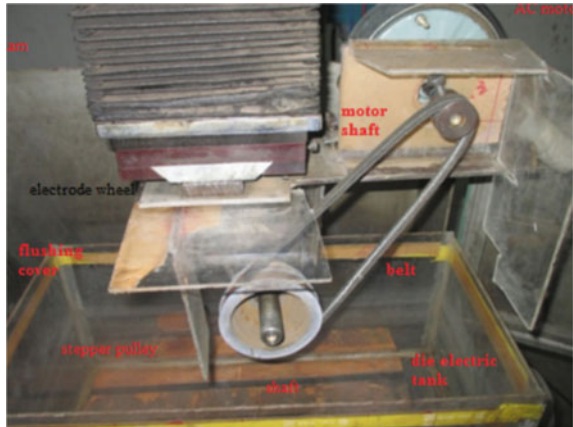


**Table 1** Process parameters factor and their levels

Process parameters	Units	Level 1	Level 2	Level 3
		-1	0	1
Wheel speed (rpm)	$WS$ : (A)	400	550	700
Current (A)	$I_p$ : (B)	10	15	20
Pulse on time( $\mu$ s)	$T_{on}$ : (C)	25	45	65
Pulse off time ( $\mu$ s)	$T_{off}$ : (D)	24	36	48



### 3 Design of Experiments

Response surface methodology (RSM) is a statistical technique for representing optimum variable factors and developing response performance measures, i.e., MRR and SR. In this paper, RSM-central composite design (CCD) was used. Due to its flexibility, ability to run sequentially and efficiency, CCD approach is the most popular among the different categories of RSM design in providing the overall experimental error in a minimum number of experimental runs. In CCD technique, for the construction of a second-order polynomial model as given in Eq. (1), each factor is varied at three levels (+, 0, -). The specific advantage of this technique was not necessary to run experiments all combinations of factors when the number of factors four. The factors part of the design can be executed using a fraction of the total number of variable combinations. The possible design options can be either regular fractional factorials or minimum run experimental resolution.

$$Z = b_0 + \sum_{n=1}^n (b_i Y_i) + \sum_{i=1}^n (b_{ii} Y_i^2) + \sum_{i=1}^{n-1} \sum_{j=1}^n (b_{ij} Y_i Y_j) \quad (1)$$

where  $b_0$  is constant,  $b b_{ii} b_{ij}$  are linear coefficient, quadratic, and interaction coefficients. The RSM models were developed for the sustainable measures of optimum response values using design expert<sup>®</sup> 11.0 statistical software. The aim is to identify the best response values and these are influenced by variable dependent factors from the DoE. The considered factors are WS,  $I_p$ ,  $T_{on}$ , and  $T_{off}$ . It has a smooth function that enhances the best performance characteristics of a particular study due it eliminates the unwanted parameters/factors. To reduce the effect of noise and they allow for the use of derivative-based algorithms. And also gives us maximum yield and minimum cost, the following output factors which are modeled by using polynomial second-order equation.

### 4 Results and Discussion

Experiments are planned and conducted according to RSM-CCD layout. The experimental layout and their result for MRR and SR are observed in Table 2. The results were analyzed using design of expert<sup>®</sup> 11.0 statistical software.

#### 4.1 ANOVA and Mathematical Model for MRR ( $mm^3/min$ )

The ANOVA analysis for the MRR shows that there are many insignificant terms in the model. Therefore, model reduction using the backward elimination process has been performed to improve the model. To adjust the fitted quadratic model while

**Table 2** Experimental plan and their results values

Std. ord	Run ord	WS: (A)	$I_p$ : (B)	$T_{on}$ : (C)	$T_{off}$ : (D)	MRR (mm <sup>3</sup> /min)	SR (μm)
1	5	400	10	25	24	4.7911	5.70
2	16	700	10	25	24	6.1670	5.40
3	25	400	20	25	24	10.0312	6.20
4	21	700	20	25	24	13.7162	6.00
5	30	400	10	65	24	10.3703	7.56
6	11	700	10	65	24	15.0429	6.10
7	9	400	20	65	24	32.2573	7.95
8	2	700	20	65	24	40.7720	6.80
9	3	400	10	25	48	6.7923	5.75
10	10	700	10	25	48	7.3725	5.10
11	17	400	20	25	48	9.4131	6.30
12	6	700	20	25	48	13.1624	5.80
13	1	400	10	65	48	11.6365	8.00
14	12	700	10	65	48	16.0687	7.00
15	29	400	20	65	48	32.7146	8.30
16	23	700	20	65	48	39.3417	7.20
17	20	400	15	45	36	14.1923	7.10
18	15	700	15	45	36	19.5938	6.20
19	24	550	10	45	36	6.8660	7.60
20	13	550	20	45	36	19.5175	8.40
21	28	550	15	25	36	8.9880	6.30
22	19	550	15	65	36	22.7389	7.70
23	27	550	15	45	24	14.2646	5.90
24	7	550	15	45	48	14.4175	6.35
25	14	550	15	45	36	14.3194	6.90
26	26	550	15	45	36	14.1125	6.90
27	18	550	15	45	36	14.8088	7.05
28	22	550	15	45	36	14.6985	7.10
29	8	550	15	45	36	14.8915	7.10
30	4	550	15	45	36	14.6914	7.00

maintaining the model hierarchy, it eliminates the negligible terms. The model F-value of 551.75 with its Prob > value less than 0.0001 indicates that the model is significant for MRR.

The values of prob > F less than 0.05 indicate the significant of the model terms. Values which are greater than 0.1000 indicate that the model terms are not significant. In this MRR model, WS,  $I_p$ ,  $T_{on}$ , WS \*  $I_p$ , WS \*  $T_{on}$ ,  $I_p$  \*  $T_{on}$ ,  $I_p$  \*  $T_{off}$ , and WS<sup>2</sup>,  $I_p$ <sup>2</sup>,

**Table 3** Model summary statistics for the MRR

Source	Std. Dev.	R-Squ	Adjusted R-Squ	Predicted R-Squ	Press	Recommended
Linear	3.9514	0.8408	0.8153	0.7222	681.1041	
2FI	1.6397	0.9791	0.9682	0.9384	150.8365	
Quadratic	0.5628	0.9980	0.9962	0.9911	21.79117	Suggested
Cubic	0.3555	0.9996	0.9985	0.9586	101.3182	Aliased

and  $T_{on}^2$ , are significant model terms. It indicates that the most significant parameters for MRR are WS,  $I_p$ ,  $T_{on}$ , and  $WS * T_{on}$ .

The lack of fit F-values of 4.6281 implies the model to fit with the experimental data. When it approaches to unity, the response model fits better to the experimental (actual) data and shows less variation between the predicted and actual values. The values of  $R^2$  and  $R^2$  (pred.) for MRR models are 0.9980 and 0.9962, respectively (Table 4). According to the results of model summary statistics for the MRR was indicated in Table 3. From Table 4 shows the ANOVA results for MRR suggested that significant model and important parameters on the EDG process. Response surface plots on the MRR were observed in Fig. 2.

**Regression equation for MRR:** In terms of actual factors, second-order regression equation for the performance characteristic of MRR in terms of input process parameters can be expressed by the following equation.

$$\begin{aligned}
 \text{MRR} = & +32.35407 - 0.12748 * \text{WS} + 0.73158 * I_p - 0.74433 * T_{on} + 0.27612 * T_{off} \\
 & + 9.59485E - 004 * \text{WS} * I_p + 3.09484E - 004 * \text{WS} * T_{on} - 9.93132E 005 * \text{WS} * T_{off} \\
 & + 0.044229 * I_p * T_{on} - 7.96310E - 003 * I_p * T_{off} - 1.86766E - 004 * T_{on} * T_{off} \\
 & + 1.06543E - 004 * \text{WS} \wedge 2 - 0.052164 * I_p \wedge 2 \\
 & + 3.41898E - 003 * T_{on} \wedge 2 - 1.07507E - 003 * T_{off} \wedge 2
 \end{aligned}$$

### 4.2 ANOVA and Mathematical Model for the SR ( $\mu\text{s}$ )

The ANOVA analysis for the SR shows that there are many insignificant terms in the model. The backward elimination process is used for improving the model into significant. The model F-value of 86.74 with its Prob > value less than 0.0001 indicates that the model is significant for SR. The values of prob > F less than 0.0500 indicate the significance of the model terms. The values which are greater than 0.1000 indicate that the model terms are not significant. In this SR model, WS,  $I_p$ ,  $T_{on}$ ,  $T_{off}$ ,  $WS * I_p$ ,  $WS * T_{on}$ ,  $WS * T_{off}$ ,  $I_p * T_{on}$ ,  $I_p * T_{off}$ ,  $T_{on} * T_{off}$  and  $WS^2$ ,  $I_p^2$ ,  $T_{on}^2$ , and  $T_{off}^2$  are significant model terms. The model indicated that the most significant terms for SR are WS,  $I_p$ ,  $T_{on}$ ,  $T_{off}$ ,  $WS * T_{on}$ ,  $T_{on} * T_{off}$  and  $WS^2$ ,  $I_p^2$  and  $T_{off}^2$ . The lack of fit F-value of 2.65 implies the model to fit with the experimental data. When it approaches to unity, the response model fits better to the experimental (actual) data

**Table 4** ANOVA results for the MRR

Source	Sum of SS	DoF	Mean SS	F-value	P-value Pro > F	Recommended
Model	2447.271	14	174.8051	551.7537	1.02E-17	Significant
A-WS	84.67147	1	84.6715	267.2566	5.73E-11	
B-I	879.4751	1	879.4751	2775.9700	1.93E-18	
C-T <sub>on</sub>	1096.842	1	1096.8420	3462.0650	3.71E-19	
D-T <sub>off</sub>	0.683701	1	0.6837	2.1580	0.162485	
AB	8.285503	1	8.2855	26.1523	0.000127	
AC	13.79235	1	13.7924	43.5340	8.47E-06	
AD	0.511304	1	0.5113	1.61388	0.2233	
BC	312.9925	1	312.9925	987.9280	4.18E-15	
BD	3.652475	1	3.6525	11.5286	0.003995	
CD	0.032147	1	0.0321	0.1014	0.754468	
A <sup>2</sup>	14.88915	1	14.8892	46.9960	5.46E-06	
B <sup>2</sup>	4.406365	1	4.4064	13.9082	0.002014	
C <sup>2</sup>	4.845785	1	4.8458	15.2952	0.00139	
D <sup>2</sup>	0.062094	1	0.0621	0.1959	0.664292	
Residual	4.752257	15	0.3168			
Lack of fit	4.290228	10	0.4290	4.6428	0.052004	Not significant
Pure error	0.462029	5	0.0924			
Cor total	2452.023	29				

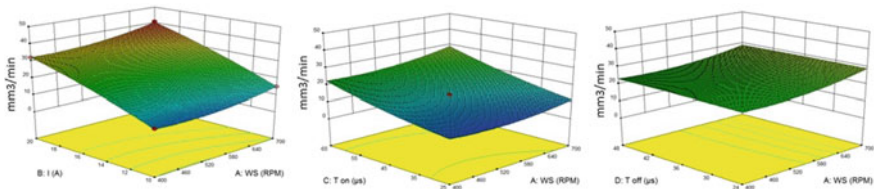


**Fig. 2** Response surface plots show the two variable on MRR (WS: I<sub>p</sub>, WS: T<sub>on</sub> and WS: T<sub>off</sub>)

and shows less variation between the predicted and actual values. The values of  $R^2$  and  $R^2$  (pred) for SR models are 0.9878 and 0.9764, respectively. Similar to MRR, ANOVA result was performed for SR. Model summary and important parameters on their suggested values were observed in Tables 5 and 6, respectively. Response interaction plots show the two input parameters on the SR observed in Fig. 3.

**Table 5** ANOVA results for the SR

Source	Sum of SS	DoF	Mean SS	F-value	P-value Pro > F	Recommended
Model	21.4447	14	1.5318	86.7392	9.53E-12	Significant
A-WS	2.9282	1	2.9282	165.8148	1.64E-09	
B-I	1.2482	1	1.2482	70.6817	4.65E-07	
C-T <sub>on</sub>	10.9824	1	10.9824	621.9001	1.26E-13	
D-T <sub>off</sub>	0.2544	1	0.2544	14.4071	0.001759	
AB	0.0132	1	0.0132	0.7489	0.400457	
AC	0.5852	1	0.5852	33.1395	3.79E-05	
AD	0.0012	1	0.0012	0.0694	0.795843	
BC	0.0361	1	0.0361	2.0442	1.73E-01	
BD	0.0121	1	0.0121	0.6852	0.420782	
CD	0.3721	1	0.3721	21.0709	0.000354	
A <sup>2</sup>	0.4169	1	0.4169	23.6084	2.08E-04	
B <sup>2</sup>	2.3327	1	2.3327	132.0926	7.78E-09	
C <sup>2</sup>	0.0068	1	0.0068	0.3837	0.54492	
D <sup>2</sup>	2.3439	1	2.3439	132.7284	7.53E-09	
Residual	0.2649	15	0.0177			
Lack of fit	0.2228	10	0.0223	2.6472	0.147081	Not significant
Pure error	0.0421	5	0.0084			
Cor total	21.7096	29				

**Table 6** Model summary statistics for the SR

Source	Std. Dev.	R-Squ	Adjusted R-Squ	Predicted R-Squ	Press	Recommended
Linear	0.5018	0.7099	0.6635	0.6059	8.5555	
2FI	0.5269	0.7569	0.6290	0.5144	10.5414	
Quadratic	0.1328	0.9877	0.9764	0.9263	1.5987	Suggested
Cubic	0.0939	0.9971	0.9882	0.8112	4.0972	Aliased

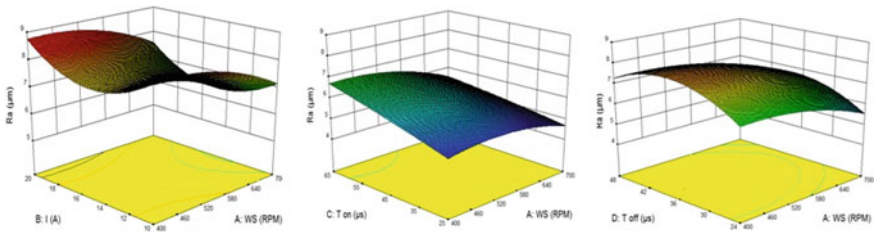


**Fig. 3** Response surface plots show the two variables on SR (WS:  $I_p$ , WS:  $T_{on}$  and WS:  $T_{off}$ )

### 4.3 Validation Model

Once the optimal levels of the machining parameters were identified, the final step was to predict and verify the improvement of performance characteristic using optimal levels of the input parameters. The estimated RSM layout using levels of the machining parameters can be calculated as,

$$\hat{\eta} = \eta_m + \sum_{i=1}^o (\hat{\eta}_i - \eta_m) \quad (2)$$

where  $\eta_m$  is the total mean value,  $\hat{\eta}_i$  is the mean value at the optimal level, and  $o$  is the number of main design parameters that affect the quality characteristic. Based on Eq. (2), the estimated RSM values optimal input parameters were obtained. Table 7 shows results of validation condition using optimal experimental conditions. It clearly shows that the optimum performance characteristic in the EDG process is significantly improved than the above results obtained.

## 5 Conclusion

The present work has successfully established the development of EDG attachment and studied the effect of input parameter on response characteristic. A model was prepared by RSM. The conclusions drawn from the present work are as follows:

- Higher MRR was found at  $I_p$ ,  $T_{on}$ , and WS are at maximum of their level. MRR was observed through ANOVA results;  $T_{on}$  and  $I_p$  are the most influential parameters than the reaming parameters.
- Lower SR was found at minimum levels of  $I_p$ , WS, and  $T_{off}$ . SR was found from the ANOVA results;  $T_{on}$  is the most dominated parameter among the four parameters.
- The fit summary recommended that the quadratic models are statistically significant for analysis of MRR and SR.
- The empirical equations for the MRR and SR were formed through the RSM-CCD approach and then found the error between experimental and predicted values are lied within 7.57% and 4.68%, respectively.

**Table 7** EDG validation results for MRR and SR model

WS (A)	$I_p$ (B)	$T_{on}$ (C)	$T_{off}$ (D)	Exp MRR	Pre MRR	Error (%)	Exp SR	Pre SR	Error (%)
700	10	25	48	7.39	7.74	4.74	6.2	5.91	4.67
400	10	25	48	6.29	6.90	7.94	5.54	5.96	7.58
550	10	25	48	10.14	9.09	9.91	6.98	6.78	1.63
Average of error						7.53			4.68

## References

1. Ho KH, Newman ST (2003) State of the art electrical discharge machining (EDM). *Int J Mach Tools Manuf* 43:1287–1300
2. Sahu AS, Kolli M, Rao GV, Kumar A (2014) International colloquium on materials, manufacturing and metrology, ICMMM, 8–9 Aug, IIT Madras, IIT, Chennai, India
3. Kolli M, Kumar A (2016) Optimization of the parameters for the surfactant-added edm of a Ti-6Al-4V alloy using the Gra-Taguchi method. *Materiali in Tehnologije* 50:229–238
4. Chandrasekhar AB, Yadava V, Singh GK (2010) Development and experimental study of electro discharge face grinding. *J Mater Manuf Processes* 25:482–487
5. Yadav S, Yadava V (2013) Investigation of electrical discharge diamond cut-off grinding of Ti Alloy. *J Mater Manuf Processes* 28:557–561
6. Modi M, Agarwal G (2013) Powder mixed electro discharge diamond surface grinding process: modelling, comparative analysis and multi-output optimisation using weighted principal components analysis. *Adv Mater Res J Mech Eng* 59(12):725–747
7. Shih HR, Shu KM (2008) A study of electrical discharge grinding using a rotary disk electrode. *Int J Adv Manuf Technol* 38:59–67
8. Singh SK, Kumar N (2013) Optimizing the EDM parameters to improve the surface roughness of Titanium Alloy (Ti-6AL-4V). *Int J Emerg Sci Eng* 10:2016–2023
9. Shu KM, Tu GC (2003) Study of electrical discharge grinding using metal matrix composite electrodes. *Int J Mach Tools Manuf* 43:845–854
10. Mohan B, Rajadurai A, Satyanarayana GK (2002) Effect of SiC and rotation of electrode on electric discharge machining of Al-SiC composite. *J Mater Process Technol* 124:297–304



# Mathematical Modeling of Material Removal Rate Using Buckingham Pi Theorem in Electrical Discharge Machining of Hastelloy C276



P. Ravindranatha Reddy, G. Jayachandra Reddy and G. Prasanthi

**Abstract** In today's world, to meet the requirements of the extreme applications, the need for precisely manufactured components becomes necessary. The new materials developed for the extreme applications are difficult to machine by conventional machining processes due to their high hardness. Most of the materials irrespective of their hardness can be easily machined by EDM. In this present work, a prediction model for MRR in machining of Hastelloy C276 on EDM using Buckingham Pi theorem is developed to study the influence of process parameters. Further, the linear programming using MS-solver was applied to perform the optimization and the sensitivity analysis for the model developed. The theoretical and experimental results are compared and found that the predicted model results are satisfactory.

**Keywords** EDM · Hastelloy C276 · Buckingham Pi theorem · MS-solver

## 1 Introduction

In an electrical discharge machining (EDM), a material removal takes place by the action of series of electrical sparks repeated between the electrodes with the introduced gap of 5–100  $\mu\text{m}$  (depends on electrical parameters) in the medium of dielectric fluid [1]. EDM has become extensively used since its inception in the mid-1940s for producing the components such as molds/dies, aircraft engine parts, medical instruments, etc. The more precise and accurate components involving complex shapes and sizes can be obtained by this process [2].

---

P. Ravindranatha Reddy (✉)

Research Scholar, Faculty of Mechanical Engineering, JNTUA, Ananthapuramu, AP 515002, India

G. Jayachandra Reddy

Professor, Department of Mechanical Engineering, YSR Engineering College of YVU, Proddatur, AP 516360, India

G. Prasanthi

Professor, Department of Mechanical Engineering, JNTUA College of Engineering, Ananthapuramu, AP 515002, India

© Springer Nature Singapore Pte Ltd. 2020

H. K. Voruganti et al. (eds.), *Advances in Applied Mechanical Engineering*,

Lecture Notes in Mechanical Engineering,

[https://doi.org/10.1007/978-981-15-1201-8\\_90](https://doi.org/10.1007/978-981-15-1201-8_90)

A nickel alloy Hastelloy C276 having about 57% of nickel is widely used in chemical industries, nuclear plants, aerospace industries, petrochemical units as it exhibits high strength and corrosion resistance even at very high temperatures. Because of distinctive characteristics such as low thermal diffusivity, affinity to react with tool material and work hardening makes it difficult to machine [3]. Hence, a non-traditional method EDM is most advantageous to use for machining of these materials. The most common influencing parameters on performance in EDM are peak current ( $I$ ),  $T_{on}$ , and  $T_{off}$ . Ghewade [4] reported the influencing machining parameters on output responses of material removal rate, electrode wear rate, half taper angle, and radial overcut in machining of Inconel 718. Aliakbari [5] evaluated the effect of rotary tool in EDM on surface finish. An integrated approach of Taguchi method and artificial intelligence was applied to optimize response process parameter design and proved the improvement in setting the optimal parameters set [6].

A semi-empirical model is introduced based on the concept of DA between the parameters of process and performance measures [7]. Mangesh [8] has been successfully utilized Buckingham Pi theorem approach in deriving the mathematical expression for the material removal rate and power consumption in turning of ferrous materials. The tool wear in boring operation can be easily predicted by having the equation and that will be derived conveniently by the DA concept [9]. In machining of metal matrix composites, a semi-empirical model for material removal rate has been developed by employing dimensional analysis by Bains et al. [10]. Ravindranath et al. [11] developed a model for MRR and Ra employing dimensional analysis and considering thermo-mechanical properties. Kishan et al. [12] established a mathematical model for predicting MRR on EDM and also determined the contribution of each factor on MRR. A simulation model of MRR using a composite tool has been developed and tested for its adequacy [13].

Few researchers focused on developing mathematical models considering thermo-mechanical properties of workpiece for MRR in EDM. In the current work, an attempt is made to establish the relation between process parameters, thermo-mechanical properties, and performance measures using Buckingham Pi theorem. The linear programming using MS-solver was used to perform optimization and sensitivity analysis for the developed model. The selected machining variables are peak current, pulse-on time, pulse-off time, density, electrical resistivity, thermal conductivity, and specific heat after conducting several experiments.

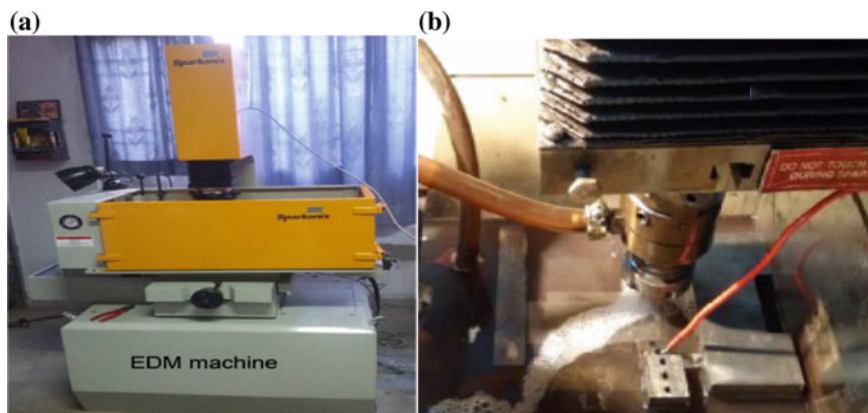
### ***1.1 Electrode Materials and Experimental Conditions***

A nickel alloy of 57% nickel, Hastelloy C276, and tool electrode of pure copper are selected for this work. The properties of Hastelloy C276 superalloy [14] are given in Table 1.

Figure 1 shows the machining setup of EDM process and the specifications of EDM machine used for experimentation are as follows.

**Table 1** Properties of Hastelloy C276 superalloy

Melting range (°C)	1325–1370
Density (g/cm <sup>3</sup> )	8.89
Modulus of elasticity (GPa)	205
Specific heat (J/kg °K)	427
Electrical resistivity (μΩ-m)	1.3
Thermal conductivity (W/m °K)	10.2

**Fig. 1** Photographs of EDM machine and machining process

Make:	Sparkonix
Model:	SZNC 50 A
Work tank size (in mm):	900 × 550 × 375
X, Y, Z movement:	350 mm, 250 mm, 250 mm
Maximum electrode weight:	50 kg
Maximum workpiece weight:	500 kg
Maximum workpiece height:	325 mm
Filtration:	10microns
Dielectric tank:	240 lts

The experimental conditions in detail are given in Table 2 and process parameters and their levels are given in Table 3, which are taken within the permissible range for better performance [15].

## 1.2 Experimental Design

Using Taguchi technique [7], L9 orthogonal array is selected and performed nine experiments randomly. At each set of process parameters, the experiments were

**Table 2** Experimental conditions in EDM

Workpiece	20 mm × 20 mm × 10 mm plate
Electrode	Copper tool (diameter = 10 mm)
Dielectric	Commercial EDM oil (grade 30)
Dielectric flushing	Side flushing with pressure
Polarity	Positive (workpiece '+ve' and tool '-ve')
Work time	20 min
Gap voltage	30 V (constant)

**Table 3** Process parameters and their levels

Process parameter	Symbol	Selected levels		
		1	2	3
Peak current (A)	A	12	15	18
Pulse-on time (μs)	B	5	20	50
Pulse-off time (μs)	C	20	50	100

repeated three times to avoid an experimental error. The average value of MRR for three trials is calculated for the final analysis. The MRR (m<sup>3</sup>/s) is calculated using formula,

$$MRR = (m_1 - m_2) / \rho \cdot T \tag{1}$$

where

$m_1$  = Initial mass of the workpiece in kg

$m_2$  = Final mass of the workpiece in kg

$\rho$  = density of the workpiece in kg/m<sup>3</sup>

$T$  = machining time in seconds

## 2 Dimensional Analysis

The following are the two methods for dimensional analysis:

- (a) Buckingham Pi theorem
- (b) Rayleigh’s method

### Buckingham Pi theorem:

In this work, Buckingham Pi theorem is used for dimensional analysis to elicit the functional relationship between the process parameters and MRR in exponential form. The independent variables and their dimensional formulae used for predicting the response MRR are shown in Table 4.

**Table 4** Process parameters of EDM and their dimensional formulae

Process parameters	Units	Dimensional formula
Current ( $I$ )	A	$A$ (or) $I$
Pulse-on Time ( $T_{on}$ )	$\mu S$	$T$
Pulse-off Time ( $T_{off}$ )	$\mu S$	$T$
Density ( $\rho$ )	$kg/m^3$	$ML^{-3}$
Electrical resistivity ( $R$ )	$\mu\Omega\text{-m}$	$ML^3T^{-3}I^{-2}$
Thermal conductivity ( $k$ )	$W/m\ ^\circ K$	$MLT^{-3}\theta^{-1}$
Specific heat ( $C_v$ )	$J/kg\ ^\circ K$	$L^2T^{-2}\theta^{-1}$
Metal removal rate (MRR)	$m^3/S$	$L^3T^{-1}$
SR (Ra)	$\mu m$	$L$

Number of  $\pi$  terms = Number of variables – Number of primary dimensions  
 $I, T_{on}, k, \rho, C_v$  are the selected repeating variables.

Calculation of  $\pi$  terms:

$$\begin{aligned} \pi_1 &= I^{A1} T_{on}^{B1} \rho^{C1} k^{D1} C_v^{E1} (\text{MRR}) \\ [M^0 L^0 T^0 I^0 \theta^0] &= [I]^{A1} [T]^{B1} [ML^{-3}]^{C1} [MLT^{-3}\theta^{-1}]^{D1} [L^2 T^{-2} \theta^{-1}]^{E1} [L^3 T^{-1}] \\ \pi_2 &= I^{A2} T_{on}^{B2} \rho^{C2} k^{D2} R^{E2} (R) \\ [M^0 L^0 T^0 I^0 \theta^0] &= [I]^{A2} [T]^{B2} [ML^{-3}]^{C2} [MLT^{-3}\theta^{-1}]^{D2} [L^2 T^{-2} \theta^{-1}]^{E2} [ML^3 T^{-3} T^{-2}] \\ \pi_3 &= I^{A3} T_{on}^{B3} \rho^{C3} k^{D3} R^{E3} (T_{off}) \\ [M^0 L^0 T^0 I^0 \theta^0] &= [I]^{A3} [T]^{B3} [ML^{-3}]^{C3} [MLT^{-3}\theta^{-1}]^{D3} [L^2 T^{-2} \theta^{-1}]^{E3} [T] \end{aligned}$$

On equating the powers of the fundamentals units in the above sets on both sides, the following equations are obtained.

$$\pi_1 = I^0 T_{on}^{-0.5} \rho^{1.5} k^{-1.5} C_v^{1.5} (\text{MRR}) \tag{2}$$

$$\pi_2 = I^2 T_{on}^0 \rho^2 k^{-3} C_v^3 (R) \tag{3}$$

$$\pi_3 = I^0 T_{on}^{-1} \rho^0 k^0 C_v^0 (T_{off}) \tag{4}$$

$$\pi_1 = f(\pi_2, \pi_3)$$

Assuming exponential form as a probable exact mathematical form,

$$\pi_1 = M(\pi_2)^a (\pi_3)^b$$

$$\left[ \frac{(\text{MRR})\rho^{1.5} C_v^{1.5}}{T_{on}^{0.5} k^{1.5}} \right] = M \left( \frac{I^2 \rho^2 C_v^3 R}{k^3} \right)^a \left( \frac{T_{off}}{T_{on}} \right)^b$$

Taking logarithm on both sides

$$\log \left[ \frac{(\text{MRR})\rho^{1.5}C_v^{1.5}}{T_{\text{on}}^{0.5}k^{1.5}} \right] = \log M + a \log \left( \frac{I^2\rho^2C_v^3R}{k^3} \right) + b \log \left( \frac{T_{\text{off}}}{T_{\text{on}}} \right) \tag{5}$$

Let,  $Z = \log \left[ \frac{(\text{MRR})\rho^{1.5}C_v^{1.5}}{T_{\text{on}}^{0.5}k^{1.5}} \right]$   $Y = \log \left( \frac{T_{\text{off}}}{T_{\text{on}}} \right)$   $X = \log \left( \frac{I^2\rho^2R}{T_{\text{on}}^3\rho^{-3}} \right)$   $c = \log M$   
 Then Eq. (5) is written as,

$$Z = aX + bY + c \tag{6}$$

The above equation is a regression equation. The equation consists of three unknowns and it requires minimum of three experimental data to determine the unknown quantities. To accomplish all the experimental data in the determination of unknown parameter values, it has been applied least square method.

Writing normal equations

$$\Sigma Z = a\Sigma X + b\Sigma Y + Nc \tag{7}$$

$$\Sigma XZ = a\Sigma X^2 + b\Sigma XY + c\Sigma X \tag{8}$$

$$\Sigma YZ = a\Sigma XY + b\Sigma Y^2 + c\Sigma Y \tag{9}$$

On solving normal Eqs. (7), (8), and (9), the constants are as follows:

$a = -0.0773713$ ,  $b = 0.3033778$ ,  $c = 1.548602$ ,  $M = 35.36731$

Finally, the mathematical equation for MRR is written as

$$\text{MRR} = 35.36731 \left( \frac{I^2\rho^2C_v^3R}{k^3} \right)^{-0.0773713} \left( \frac{T_{\text{off}}}{T_{\text{on}}} \right)^{0.3033778} \left( \frac{T_{\text{on}}^{0.5}k^{1.5}}{\rho^{1.5}C_v^{1.5}} \right) \tag{10}$$

### 3 Results and Discussion

#### 3.1 Model Formulation

The mathematical model for material removal rate is shown below:

$$\text{MRR} = 35.36731 \left( \frac{I^2\rho^2C_v^3R}{k^3} \right)^{-0.0773713} \left( \frac{T_{\text{off}}}{T_{\text{on}}} \right)^{0.3033778} \left( \frac{T_{\text{on}}^{0.5}k^{1.5}}{\rho^{1.5}C_v^{1.5}} \right)$$

In order to validate it, the average error is calculated as in Table 5:

$$\text{Error (\%)} = \left| \frac{\text{Experimental results} - \text{Predicted value}}{\text{Experimental results}} \right| \times 100 \tag{11}$$

**Table 5** Observed and predicted values of MRR

Exp. No.	Peak current $I$ (A)	Pulse-on time $T_{on}$ ( $\mu$ S)	Pulse-off time $T_{off}$ ( $\mu$ S)	MRR (Experimental) ( $mm^3/min$ )	MRR (Predicted) ( $mm^3/min$ )
1	12	5	20	12.2100	6.364
2	12	20	50	9.3474	11.348
3	12	50	100	12.2886	16.307
4	15	5	50	8.5428	8.118
5	15	20	100	9.6174	13.156
6	15	50	20	8.0028	9.668
7	18	5	100	8.6892	9.739
8	18	20	20	8.5092	7.849
9	18	50	50	16.452	12.411
Mean MRR:				10.407	10.551
%error:				1.38	

The average prediction error based on a model is 1.38%. It is obvious that the predicted values and experimental results are approaching very near to each other. Therefore, the model is well fitted between machining parameters and response.

### 3.2 Model Optimization

To achieve the maximum output, it is required to find an optimum set of input variables. As the model has nonlinear form, it is to be converting into a linear form for simple analysis. This has been done as follows:

Taking logarithm to Eq. (10), we get

$$\log(\text{MRR}) = \log(35.36731) - 0.0773713 \log\left(\frac{I^2 \rho^2 C_v^3 R}{k^3}\right) + 0.3033778 \log\left(\frac{T_{off}}{T_{on}}\right) + \log\left(\frac{T_{on}^{0.5} k^{1.5}}{\rho^{1.5} C_v^{1.5}}\right)$$

$$Z = 1.548602 - 0.0773713 \log \pi_4 + 0.3033778 \log \pi_5 + \log \pi_6$$

$$Z = 1.548602 - 0.0773713X_1 + 0.3033778X_2 + X_3 \tag{12}$$

where  $Z = \log(\text{MRR})$ ,  $X_1 = \log \pi_4$ ,  $X_2 = \log \pi_5$ ,  $X_3 = \log \pi_6$

The objective function is written as

$$\text{Max } Z = 1.548602 - 0.0773713X_1 + 0.3033778X_2 + X_3$$

Subject to the following constraints

**Table 6** Optimized values of response variables

	Log values of $\pi$ terms	Antilog values of $\pi$ terms
Z	-9.2624	$5.465 \times 10^{-10} \text{m}^3/\text{s}$ (or) $32.79 \text{mm}^3/\text{min}$
$X_1$	9.03559	$1.0854 \times 10^9$
$X_2$	1.30103	20
$X_3$	-10.5066	$3.11458 \times 10^{-11}$

$$1 \times X_1 + 0 \times X_2 + 0 \times X_3 \leq 9.38777 \tag{12}$$

$$1 \times X_1 + 0 \times X_2 + 0 \times X_3 \geq 9.03559 \tag{13}$$

$$0 \times X_1 + 1 \times X_2 + 0 \times X_3 \leq 1.30103 \tag{14}$$

$$0 \times X_1 + 1 \times X_2 + 0 \times X_3 \geq -0.39794 \tag{15}$$

$$0 \times X_1 + 0 \times X_2 + 1 \times X_3 \leq -10.50661 \tag{16}$$

$$0 \times X_1 + 0 \times X_2 + 1 \times X_3 \geq -11.00661 \tag{17}$$

MS-solver is used to solve the above-formulated problem and  $X_1, X_2, X_3$  values are listed in Table 6. The optimum value of MRR is  $32.79 \text{mm}^3/\text{min}$ .

### 3.3 Sensitivity Analysis

Further, sensitivity analysis has been done to know the influence of various independent  $\pi$  terms. The change in dependent  $\pi$  term on introducing  $\pm 10\%$  change in the independent  $\pi$  terms is evaluated (one at a time). This is called sensitivity. These results are listed in Table 7.

## 4 Conclusion

Dimensional analysis modeling has been found to be the easiest technique to perform the analysis of MRR with respect to various independent parameters including thermo-mechanical properties of workpiece. A designer can subsequently select the best combination of design variables with the mathematical model obtained for achieving optimum MRR. This will eventually reduce the machining time. The error



**Table 7** Sensitivity analysis of MRR

$\pi_4$	$\pi_5$	$\pi_6$	MRR (mm <sup>3</sup> /min)
$1.0854 \times 10^9$	2	$3.11452 \times 10^{-11}$	16.30704
$1.19394 \times 10^9$	2	$3.11452 \times 10^{-11}$	16.18722
$0.97686 \times 10^9$	2	$3.11452 \times 10^{-11}$	16.44051
Change (%)			1.55
$1.0854 \times 10^9$	2.2	$3.11452 \times 10^{-11}$	16.78543
$1.0854 \times 10^9$	1.8	$3.11452 \times 10^{-11}$	15.79403
Change (%)			6.08
$1.0854 \times 10^9$	2	$3.425972 \times 10^{-11}$	17.93773
$1.0854 \times 10^9$	2	$2.491616 \times 10^{-11}$	13.04562
Change (%)			30

calculated is 1.38% only which means the model is very closely approached the experimental results. Hence, the dimensional analysis (DA) technique can be employed to obtain a mathematical model for performance measures involving many process parameters in electrical discharge machining process.

## References

1. Pandey PC, Shah HS (1980) Modern machining processes. Tata Mcgraw-Hill, New Delhi
2. McGeough JA (1988) Advanced methods of machining, Chapman and Hall
3. Raghavan M, Berkowitz BJ, Scanlon JC (1982) Electron microscopic analysis of heterogeneous precipitates in Hastelloy C-276. *J Metall Trans A* 13(6):979–984
4. Ghewade DV, Nipanikar SR (2011) Experimental study of electro discharge machining for Inconel material. *J Eng Res Stud II(II)*:107–112
5. Aliakbari E, Baseri H (2012) Optimization of machining parameters in rotary EDM process by using the Taguchi method. *Int J Adv Manuf Technol* 62:1041–1053
6. Sibalija TV, Majstorovic VD (2012) An integrated approach to optimise parameter design of multi-response processes based on Taguchi method and artificial intelligence. *J Intell Manuf* 23:1511–1528
7. Tsai K, Wang P (2001) Semi-empirical model of surface finish on electrical discharge machining. *Int J Mach Tools Manuf* 41:1455–1477
8. Phade MR, Tatwawadi VH (2015) Mathematical models of material removal rate & power consumption for dry turning of ferrous material using dimensional analysis in Indian prospective. *Jordan J Mech Ind Eng* 9(1):27–38
9. Kadu RS, Awari GK, Sakhale CN, Modak JP (2014) Formulation of mathematical model for the investigation of tool wears in boring machining operation on cast iron using carbide and CBN tools. *Proc Mater Sci* 6:1710–1724
10. Bains PS, Sidhu SS, Payal HS (2016) Semi empirical modeling of magnetic field assisted ED machining of metal matrix composites. In: *Proceedings of the American Society for Composites*
11. Ravindranath B, Madhu V, Gogia AK (2015) Modeling and analysis of material removal rate and surface roughness in wire-cut EDM of armour materials. *Int J Eng Sci Technol* 1–5

12. Kishan B, Premkumar BS, Gajananab S, Buchaiah K, Gaffara MA (2018) Development of mathematical model for metal removal rate on EDM using Copper & Brass electrodes. *Mater Today: Proceedings* 5:4345–4352
13. Zhang S, Zhang W, Wang P, Liu Y, Ma F, Yang D, Sha Z (2019) Simulation of material removal process in EDM with composite tools. *Adv Mater Sci Eng* 1–11
14. Khidhir BA, Mohamed B (2010) Study of cutting speed on surface roughness and chip formation when machining nickel-based alloy. *J Mech Sci Technol* 24:1053–1059
15. Rajender O, Koduri M, Bhargav M (2017) Modeling and analysis of electrical discharge machining process parameters using fuzzy logic. *Int J Res* 4(10):860–870

# Effect of Exfoliated Vermiculite as Thickening and Foaming Agent on the Physical Properties of Aluminium Foam



V. V. K. Lakshmi, V. Arun Vikram, K. V. Subbaiah, K. Suresh and B. Surendra Babu

**Abstract** In this paper, exfoliated vermiculite (EV), a siliceous non-metallic particle is used as both thickening and foaming agent to fabricate low-density metal foam via the oxidation reduction method. Aluminium Alloy 5083 is used as base metal. EV particles 0.1 mm size that were dehydrated by preheating were added as thickening agents and EV particles 1 mm size containing 5% moisture are used as foaming agent to produce bubbles. The density of the foam produced is reduced by about 50% when compared to pure Al5083. The macrostructure reveals that 1.5% EV particle addition resulted in uniform foam. Average pore size varied from 0.1 to 2 mm with varying EV %. With an increase in amount of thickening agent percentage, the pore size decreased, but when the thickening agent increased beyond 1.5%, the pores size increased. The density of foam increased with increase in percentage of thickening agent. From the compressive stress–strain curves, at strain rate of 1 mm/min, the plateau stress increased with the density. The energy absorption for the foam is found to be 4 MJ/m<sup>3</sup> for 1.5% EV particles. The energy absorption efficiency is 65%.

**Keywords** Metal foam · Composite · Vermiculite · Aluminium

## 1 Introduction

Aluminium closed-cell foams due to lightweight find applications in automobile, shipping, aviation, packaging and military equipment where load bearing and heat insulation are of prime concern. Metal foams possess low strength-to-weight ratio stiffness, low densities and good impact energy absorption in comparison to solid

---

V. V. K. Lakshmi (✉) · V. Arun Vikram · K. Suresh · B. Surendra Babu  
Department of Mechanical Engineering, GITAM Institute of Technology, Vizag,  
Andhra Pradesh, India  
e-mail: [Lakshmi.vennela@gmail.com](mailto:Lakshmi.vennela@gmail.com)

K. V. Subbaiah  
Department of Mechanical Engineering, AU College of Engineering (A), Vizag,  
Andhra Pradesh, India

© Springer Nature Singapore Pte Ltd. 2020  
H. K. Voruganti et al. (eds.), *Advances in Applied Mechanical Engineering*,  
Lecture Notes in Mechanical Engineering,  
[https://doi.org/10.1007/978-981-15-1201-8\\_91](https://doi.org/10.1007/978-981-15-1201-8_91)

metals. By proper engineering of size, shape of the pores desired mechanical properties can be achieved [1, 2]. Closed-cell metal foams are formed by gas foaming techniques, whereas open-cell foams are formed by infiltration technique. The methods generally adopted for fabrication of metal foams are powder metallurgy technique, stir cast method and infiltration technique. It is important to maintain the viscosity of the melt molten metal to prevent escaping of the gas bubbles. Therefore, thickening agents like calcium, copper, silicon carbide siliceous materials like perlite, etc. which increase viscosity are added to melt as gas formed cannot escape from thick for aluminium and its alloys [3, 4]. Siliceous materials obtained from miner processing such as wollastonite and barite are also used as thickening agents [5]. The gas bubble formation in the melt is done by adding foaming agents such as hydrides, polymeric agents, carbonates, sulphates or organic compounds as they release gases at the temperature by either vaporization or decomposition. The commonly used foaming agents are  $\text{TiH}_2$ ,  $\text{CaH}_2$  and  $\text{CaCO}_3$  [6–10]. The mechanical properties of foam metals greatly depend on the uniformity of the pores, pore size which in turn depend on foaming agent size, quantity, time of exposure, temperature of the melt [11–13]. SiC effect as thickening agent on porosity and density of foams was studied and reported the foam density 0.4–0.86  $\text{g/cm}^3$ . Addition of 5% by weight of  $\text{CaCO}_3$  in melt is reported as best % addition at 1400 rpm speed which gives optimum cell wall thickens and porosity [14]. Silicon carbide ( $\text{SiC}_p$ ) as foaming agent and AA2014 base metal composite foam was fabricated [15, 16]. Till date, to the best of knowledge of the author(s), exfoliated vermiculite (EV) is not used as a thickening or foaming agent. And in addition, literature reports only one kind of material usage as either thickening agent or foaming agent. Hence, this work shows a novelty of usage of EV as both thickening and foaming agents simultaneously with base material as aluminium alloy (Al-5083). The magnesium in Al-5083 readily reacts with steam and aids in the bubble formation for foaming. Water carrying agent, vermiculite is used as foaming agent and foaming was done via the oxidation reduction method. The exfoliated vermiculite EV, particles have layered like structure and belongs to mica group. Vermiculite belongs to silicate group of minerals with oxides of alumina, magnesium and silicon. It costs less, light in weight, offers better resistance to fire at elevated temperatures, non-toxic and has wide applications in packaging, insulation application [17]. EV also acts as a mild lubricant due to plate like structure.

## 2 Materials and Methods

Exfoliated vermiculite which has accordion like structure with an average size of 0.1–1 mm and density: 0.36  $\text{g/cc}$  is considered for the study. The composition by weight of EV particles is  $\text{SiO}_2$ : 40.52%,  $\text{Al}_2\text{O}_3$ : 16.74%,  $\text{Fe}_2\text{O}_3$ : 4.32%,  $\text{TiO}_2$ : 0.63%,  $\text{CaO}$ : 0.47%,  $\text{MgO}$ : 3.68%, Loss 11.05% and moisture: 7.89%. EV particles used for foaming are approximately an average size 0.1 mm and contain moisture. The composition by weight of the base material Al-5083 is 0.4% Si, 4% Mg, 0.4% Fe, 0.15% Ti, 0.4% Mn, Cu 0.1% and remainder Al. Al5083 alloy having density of

2.66 g/cc has good cast ability and high reactivity of magnesium content which readily reacts with oxygen to form bubbles [18, 19] and apart from it, presence of Mg improves the wet ability.

Stir casting technique is used for fabrication of foam formation. The Al5083 is melted above solidus temperature to 680 °C where liquid and solid phases coexist. Dehydrated EV particles with 0.1 mm are added with weight% of 1.5% as thickening agent to the Al5083 melt. The slurry which is in plastic range is made to have uniform dispersion of the particles by means of stirring at speed of 1200 rpm for 2 min. Later, the temperature is raised to 1000 °C above liquidus phase and EV particles of average size 1 mm with weight% of 0.5, 1.0, 1.5 and 2% containing moisture are added and stirred at 1200 rpm to aid steam generation and bubble formation. The mixture is held at the temperature for one minute in the graphite mould of the furnace for movement of bubbles. Then, the mixture with mould is immersed in water and cooled. Thus, the obtained mixture is cut into piece for testing and analysis like thermalgravimetric analysis, microstructures, density, volume fraction, viscosity and bubble velocity evaluation of metal foams and quasi-static compression tests.

### 3 Results and Discussion

#### 3.1 Thermogravimetric Analysis

The thermalgravimetric analysis (TGA) of EV of average size 1–2 mm is shown in Fig. 1. TGA plot shows the loss weight of particles with increase in temperature from 50 to 300 °C and also found around 10% mass loss during heating from 0 to 1000 °C. Initial mass loss occurred at 50 °C due to hydration of water molecules present on the surface, while mass loss of 2.5% observed between 50 and 300 °C which is due to hydration of free molecules hydroxyl molecules present in the inter lamella spaces. Loss of mass between 300 and 800 °C is due to loss of water molecules and chemical reactions between cations [20].

#### 3.2 Microstructure

The microstructure structure of EV particles consists of pores in between the plate like lamellar structures as shown in Fig. 2. The clay mineral has silica tetrahedral layer represented by  $(\text{Si}_2\text{O}_5)_2$ . The energy-dispersive X-ray spectrometer (EDS) provides a semi-quantitative analysis of minerals present in the vermiculite particles.

EV particles with 0.5% as thickener exhibited a large pore size due to less viscosity. The bubbles rose rapidly, collapsed and formed irregular distribution of voids, while with 1.5% weight of EV particles showed average pore size of 0.5 mm uniformly distributed.

**Fig. 1** a TGA of vermiculite particles. b TGA of vermiculite particles

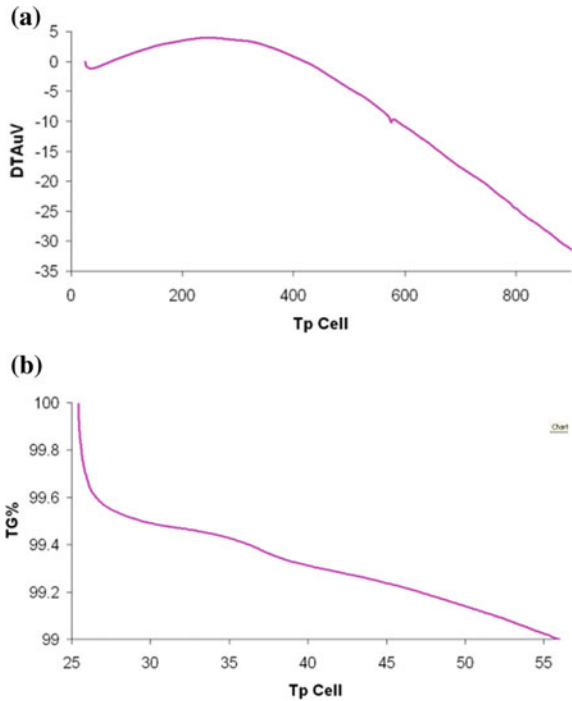
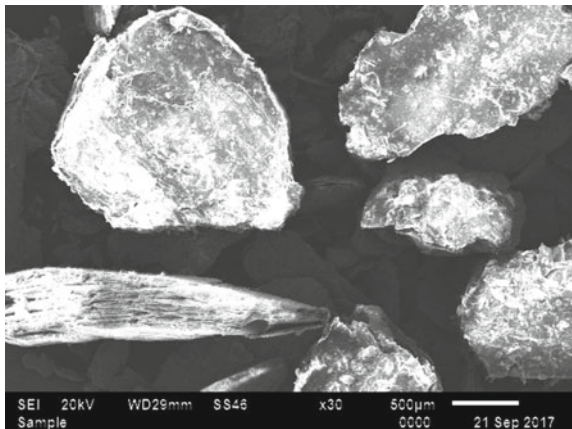
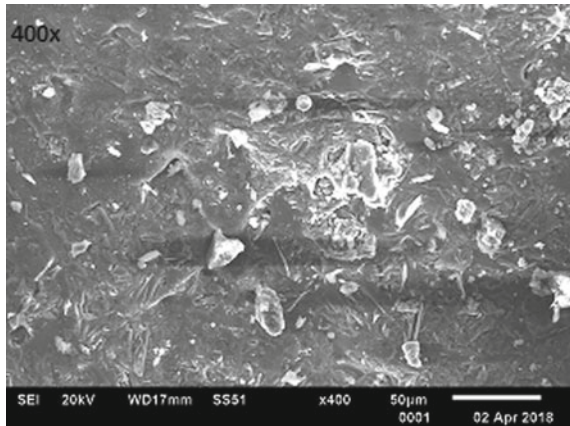


**Fig. 2** SEM of EV particles



The SEM shown in Fig. 3 shows a larger amount of oxygen (steam) at interface of EV particle and metal, which is due to addition of moisture containing EV particles. The alloy contains 4% magnesium which readily reacts with steam at high temperatures and so it reacts with the steam to form MgO, thereby releasing H<sub>2</sub> gas. The release of H<sub>2</sub> is oxidation–reduction process which forms bubbles. These oxides and films formed damp the surface waves in liquid metal preventing the rapture of

Fig. 3 SEM showing oxides



the film [1, 2]. The foam is stabilized due to melt viscosity maintained by addition of thickener. The liquid layer is thick for 1.5% EV addition, and hence, particles are drawn towards the oxide film and also the oxide layer restrains the EV particles to progress further down.

**Density, volume fraction, viscosity and bubble velocity evaluation of metal foams.** The density of the foam was measured based on weight and volume of pieces. Density of the EV flakes is 0.64–1.12 g/cc. The density and porosity variation with respect to EV% are shown in Fig. 4a, b. The average porosity ranges from 60 to 80% [21]. The pore size is mainly dependent on the bubble formation and moving velocity in melt. The bubble velocity can be determined by the Stokes equation (i.e. Eq. 1) for gas–liquid two-phase flow [11]. Assume pore size equal to the bubble size of the formed gas.

$$V = 1/18gd^2(\rho_1 - \rho_g)1/\mu \tag{1}$$

where ‘g’—acceleration due to gravity, ‘d’—diameter of pore, ‘ $\rho_1$ ’—density of Al,  $\rho_2$ —density of gas and ‘ $\mu$ ’—dynamic viscosity of melt.

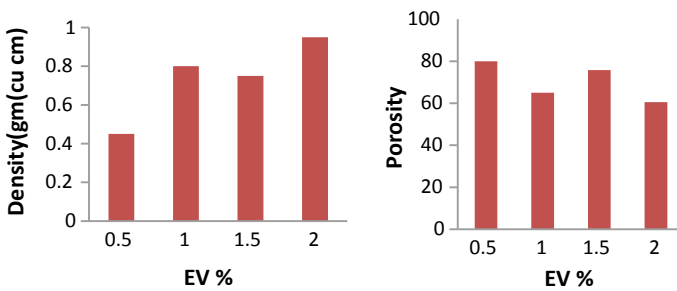


Fig. 4 a Density versus % EV. b Porosity versus % EV

Greater the pore (bubble) size, greater the velocity with which it rises in the melt. The literature mentions 1.5% EV particles rather than 0.5% exhibit less velocities with all bubble diameters [11]. Hence, in this paper, EV particles with 1.5% and velocities of bubble as 0.393 m/s for of  $\Phi 1.5$  mm and 0.043 m/s for  $\Phi 0.5$  mm bubble size are considered. It is evident from Fig. 4a, b that as the density increased, the porosity decreased which happened due to increase in thickening agent.

*Quasi-Static Compression tests.* The compression properties of the foam are evaluated experimentally at low strain rate using a uniaxial computer-controlled INSTRON testing machine. The test samples for compression test are as per ASTM E9 specifications with dimensions of 30 mm \* 20 mm \* 20 mm. The crosshead speed is taken as 0.01 mm/s and the quasi-static compressive stress test specimens before and after failure of the foam at rate of 1 mm/min are shown in Fig. 5. The quasi-static compressive stress test results of foam are graphed and presented in Fig. 6. It is observed that as density increases, the compressive stress increased.

Plateau stress is a prime parameter that influences the cushion effect and is observed in the range of 5–40% of the strain. An earlier drop in stress for sample 1.5% EV particles can be attributed to two causes. It can be either due to strain hardening or collapse of pores. If the drop is due to first cause, then the stress curve should exhibit a steady rise due to dislocations. But in the graph, the stress is almost constant after the initial drop, and hence, the drop is due to early collapse of few pores [13]. The plateau stress increased with density. As the EV particles increases from 0.5 to 2%, the compressive yield strength increased. For metal foams with significant plateau region, the area under the plateau portion of graph gives the energy absorption capability of the foam [12, 16].

The foam energy absorbing capacity is 1.3–12 MJ/m<sup>3</sup> and is shown in Fig. 7. As the %EV particles increased, the viscosity of melt increased which prevented the

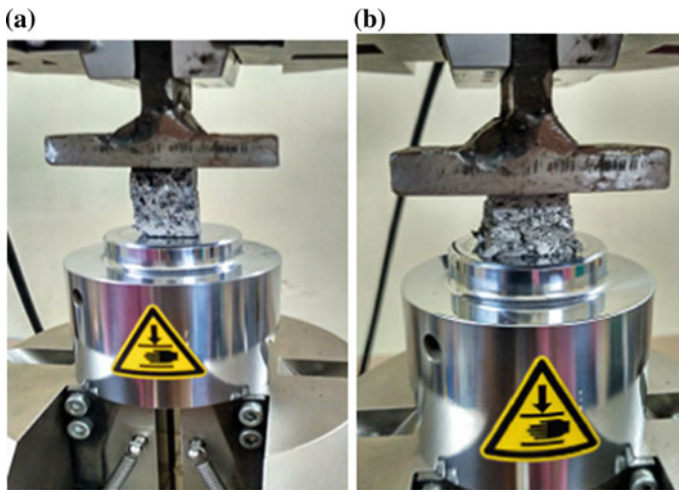


**Fig. 5** Quasi-static compressive test (INSTRON) **a** Before load. **b** After failure



**Fig. 6** Compressive stress versus strain

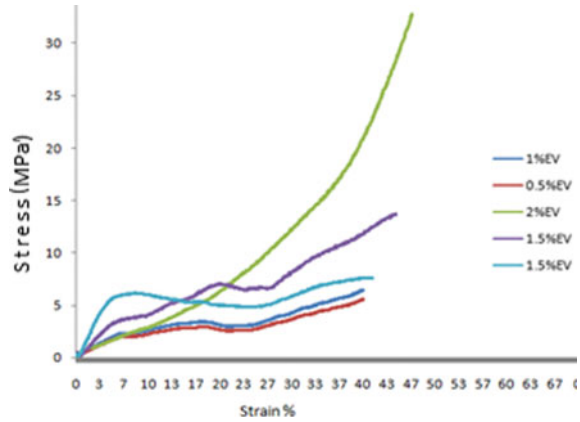
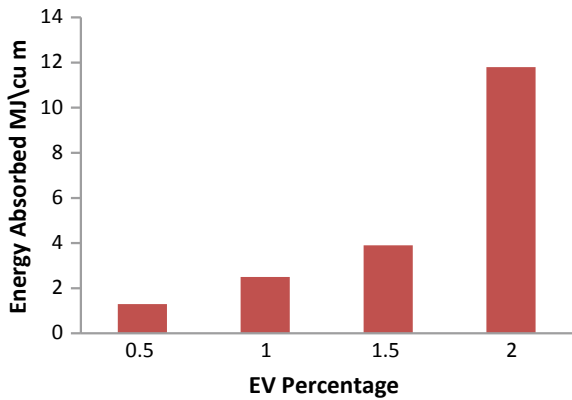


**Fig. 7** Energy absorbed by foam versus EV %



foaming process and the bubble movement into the melt. Addition of 0.5% thickening agent could not increase the melt viscosity substantially, and hence, the pores moved rapidly and pore coalesced to form an elliptical large pores there by reducing the cell wall thickness.

### 4 Conclusions

In this research, exfoliated vermiculite is successfully used as foaming and thickening agent to fabricate foam via oxidation–reduction technique.

- EV particles with 1.5% are suggested as superior foam properties such as pore size, and shape uniformity was observed. 0.5% EV particle as thickeners resulted a very low density 0.58 mm/cc and 70% porous foam. But the pore size was 2 mm

and energy absorbing capacity was low. Hence, 1.5% EV particle addition resulted in good foam properties.

- It is observed that in the process, the time of holding the mixture in the furnace post addition of foaming agent if too long the bubbles settle and if less the pores are not dispersed uniformly.
- It is observed that the addition of EV particles as thickening agents, the pore size increased from 0.01 to 2 mm.
- The constant stress region from strain 5–30% is observed in all samples except the sample with 2% EV particle foam with density of 1.2 g/cc and porosity 50% which behaved like a metal rather than foam.

## References

1. Banhart J (2001) *Prog Mater Sci* 46:559–632
2. Banhart J, Baumeister J (1998) *J Mater Sci* 33:1431–1440
3. Mondal DP, Das S, *Werkstofftech M-WU* (2010) 41(5)
4. Heidarzadeh A, Emamy M, Rahimzadeh A, Soufi R, Heidary DSB, Nasibi S et al (2014) *J Mater Eng Perform* 23:469–476
5. Nava MG, Cruz-Ramírez A, Rosales MÁ, Gutiérrez-Pérez VH, Sánchez-Martínez A (2017) *J Alloy Compd* 698:1009–1017
6. Aboraia M, Sharkawi R, Doheim MA (2011) *J Eng Sci Assiut Univ* 39:441–451
7. Mater J, Cambronero LEG, Ruiz-Roman JM, Corpas FA, Prieto JMR (2009) *Process Technol* 209:1803–1809
8. Nava MG, Cruz-Ramírez A, Rosales MÁ, Gutiérrez-Pérez VH, Sánchez-Martínez A (2017) *J Alloys Compd* 698:1009–1017
9. Madhu HC, Kailas SV (2018) *Mater Charact*
10. Birla S, Mondal DP, Das S et al (2017) *Trans Indian Inst Met* 70:1827
11. Lakshmi VVK, Subbaiah KV, Babu BS (2018) *Mater Today Proceedings* 5:19424–19430
12. Avinash G, Harika V, Sandeepika Ch, Gupta N (2018) *IOP Conf Ser: Mater Sci Eng* 338:012010
13. Rohatgi PK, Weiss D, Gupta N (2006) *JOM* 58:71–76
14. Rajak DK, Kumaraswamidhas LA, Das S (2016) *Mater Sci Technol* 32:1338–1345
15. Rajak DK, Mahajan NN, Das S (2019) *Materials and Manufacturing Processes* 34(4):379–384
16. Sahu S, Mondal DP, Cho JU, Goel MD, Ansari MZ (2019) *Compos Part B: Eng* 160:394–401
17. Haesche M, Lehmkus D (2010) *J Mater Sci Technol* 26:845–850
18. Suvorov SA, Skurikhin VV (2013) *Refract Ind Ceram* 44:186–193
19. Taherishargh M, Belova IV, Murch GE, Fiedler T (2014) *Mater Sci Eng A* 604:127–134
20. Mondal DP, Das S, Ramakrishnan N, Uday Bhasker K (2016) *Compos Part A: Appl Sci Manuf* 40:279–288
21. Marcos C, Arango YC, Rodriguez I (2009) *Appl Clay Sci* 42:368–378

# Multi-response Optimization of Process Parameters in Turn-Milling Processes—An Experimental Approach



K. Arun Vikram, C. Ratnam, V. V. K. Lakshmi and R. D. V. Prasad

**Abstract** The present study focuses on multi-response optimality of machining parameter using grey relational analysis combined with principal component analysis coupled with Taguchi SN ratios. The responses like roughness and hardness of the machined surface are considered for study while machining in tangential and orthogonal turn-milling processes. Subsequently, study of individual optimality and empirical regression modelling of machining parameters like end mill cutter (tool) speed, rate of feed and depth of cut on responses are also carried on. A-axis CNC Vertical Milling centre is considered for the process of single cut plain turning operations using high-speed steel end mill cutters. Brass rods material is taken as work material under dry condition. Experimentation results show that tangential turn-milling is more efficient than orthogonal turn-milling in generating the responses for same machining parameter combinations.

**Keywords** Grey relational analysis · Principal component analysis · Optimization · Turn-milling

---

K. Arun Vikram (✉) · V. V. K. Lakshmi  
Department of Mechanical Engineering, GITAM Institute of Technology, Vizag,  
Andhra Pradesh, India

C. Ratnam  
Department of Mechanical Engineering, AU College of Engineering (A), Vizag,  
Andhra Pradesh, India

R. D. V. Prasad  
Department of Mechanical Engineering, ANITS Engineering College, Vizag,  
Andhra Pradesh, India

## 1 Introduction

Turn-mill machining is based on the concept of actively driven rotary tool mechanism with rotating workpiece. The rotary tool and workpiece are rotated with an external agency. It has wider advantages over conventional lathe and milling mechanisms in generating desired objectives. Turn-milling processes emerged from the foreseen advantages of James Napier in 1868 but kinematics between rotary tool and rotation of workpiece is complex and so the work is suppressed and came into light after the work of M. C. Shaw and his co-workers in 1950s [1]. Turn-milling processes are one such technologies which can bridge the gap of high quality, high quantity, less cutting forces and temperatures when compared to ordinary turning and milling processes due to relativity between rotational tool and workpiece [2, 3].

The microscopic level interaction between the rotary tool with multiple edges and rotary workpiece in turn-milling processes describes the burnishing activity between them, which results in surface hardness variations. Researchers reported that burnishing processes generate improved finish and hardness of machined surfaces, dimensional and tensile strength consistency, etc. by introducing residual compressive stress in the workpiece [4]. In turn-milling processes, the tool gives pressure contact on the workpiece surface due to depth of cut, while advancement of the rotary tool generates crest and trough irregularities, which are filled and pressed by the preceding tooth of the rotary tool. Hence, the end mill cutter acts as a burnishing tool making burnishing process on the workpiece surface and thereby varies hardness over the surface. In orthogonal turn-milling process, the edge tips of the end mill cutter behave like a ball burnishing tool make cold flow of work material from the peaks of the roughness of machined surface to valleys of the workpiece. The cold working on the surface of the workpiece increases the surface finish and surface hardness, whereas in case of process of tangential turn-mill, the sides/helix of the cutter act like a burnishing roller tool to increase surface finish and surface hardness.

In this work, process variables with four levels each are considered for optimal study on generating the responses like roughness of machined surface ( $R_a$ ) and surface hardness ( $H$ ) in turn-milling processes. The Taguchi design of experiments (TDOE) based on Taguchi philosophy which has wide publicity for efficiently optimizing the experiments in manufacturing process has been adopted and  $L_{16}$  combination of experimental runs-based orthogonal arrays are derived for experimentation. The signal-to-noise (SN ratio) ratios of the responses are considered for study of optimality. Optimization is very much essential in every sector like layout design, health care, logistics, scheduling, manufacturing, etc. due to competitive increase in demand of products and services. The optimization techniques are developed based on mining of the data [5, 6]. In case of manufacturing process/product optimization, Taguchi's philosophy stands as the starting point; however, this philosophy is being worldwide criticized due to its inability to solve multi-response optimization problems [7]. To overcome this draw back of Taguchi philosophy, application of grey relational analysis (GRA), utility theory, TOPSIS, fuzzy inference system, principal component analysis (PCA), entropy method, etc. are individually integrated with Taguchi method

by converting multiple responses into an equivalent single response function, which can finally be optimized by the Taguchi method. However, these approaches rely on some assumptions. Hence, in this paper, multi-response optimization technique, like GRA developed by Deng [8] and PCA developed by Hoteling [9, 10], is adopted.

To the best of knowledge of the author, experimentations on roughness of machined surface are investigated in process of turn-mill. But none of the research focused on multi-response optimization of roughness ( $R_a$ ) and hardness of surface ( $H$ ) of the workpiece material using GRA–PCA and findings related to them. In addition, relative comparisons between the two types of process of turn-milling like tangential and orthogonal are also not attempted so far. Hence, this paper focuses on considerations of the above said based on Taguchi fractional factorial study in turn-milling processes.

## 2 Experimental Design and Conditions

This paper focus on plain turning with operation in processes of turn-milling (i.e. tangential and orthogonal) carried on CNC Vertical Milling centre (VMC-1050) using A-axis with high-speed steel (HSS) end mill cutters under dry condition. The machining parameters like cutter speed (r/min), rate of feed (mm/min) and depth of cut (mm) with 20 r/min workpiece constant rotation based on Taguchi ( $L_{16}$ ) fractional factorial study in turn-mill processes are taken for study on roughness of machined surface and hardness of surfaces of machined materials. SN ratio is useful in finding the optimal parametric setting values that directly influence the response and are mentioned in Eqs. 1–2 [11, 12].

$$(SN)_{\text{Lower-is-better}} = -10 \log \left( \frac{1}{n} \sum_{i=1}^n y_i^2 \right) \tag{1}$$

$$(SN)_{\text{Higher-is-better}} = -10 \log \left( \frac{1}{n} \sum_{i=1}^n \frac{1}{y_i^2} \right) \tag{2}$$

where ‘ $n$ ’—number of observations and ‘ $y_i$ ’—observation values.

Leaded brass (IS:319-2007-Grade:1-Half Hard) having wide range of customer and industrial applications [12] is taken for lathe plain turning study as workpiece material in processes of turn-mill. Commercially available long parallel shank HSS end mill cutters of 10 mm diameter with 30° helix with standards of BS: 122 (part-1)-1953 are used. The rotation of workpiece do not influence the cutter speed but only relates to the axial movement of the cutter, and hence, workpiece with 20 r/min constant rotation is adopted, while the variables and their levels are shown in Table 1a.

**Table 1 a** Machining factors and their levels. **b** Experimental values measured and their SN ratios

		Level 1		Level 2		Level 3		Level 4	
S: Cutter speed (r/min)		2400		2650		2900		3150	
F: Rate of feed (mm/min)		3.27		5.05		8.76		10.0	
C: Depth of cut (mm)		0.25		0.50		0.75		1.0	

Exp. No.	Machining parameters				Process of tangential turn-mill				Process of orthogonal turn-mill			
	S	F	C	R <sub>a</sub>	H	SN ratio R <sub>a</sub>	SN ratio H	R <sub>a</sub>	H	SN ratio R <sub>a</sub>	SN ratio H	
1	1	1	1	0.78	142.3	2.16	43.0	4.82	120.0	-13.7	41.5	
2	1	2	2	1.11	145.9	-0.91	43.2	5.65	134.0	-15.0	42.5	
3	1	3	3	1.83	151.3	-5.25	43.6	6.50	143.7	-16.3	43.1	
4	1	4	4	2.30	151.5	-7.23	43.6	7.30	148.0	-17.3	43.4	
5	2	1	2	0.56	156.7	5.04	43.9	4.41	134.7	-12.9	42.5	
6	2	2	1	0.73	153.3	2.73	43.7	5.35	127.3	-14.6	42.1	
7	2	3	4	1.80	163.0	-5.11	44.2	5.93	154.0	-15.5	43.7	
8	2	4	3	1.88	158.4	-5.48	44.0	7.12	145.0	-17.1	43.2	
9	3	1	3	0.50	170.0	6.02	44.6	2.95	148.7	-9.40	43.4	
10	3	2	4	0.77	172.3	2.27	44.7	4.10	156.7	-12.3	43.9	
11	3	3	1	1.08	161.0	-0.67	44.1	5.50	125.0	-14.8	41.9	
12	3	4	2	1.50	162.3	-3.52	44.2	6.18	136.0	-15.8	42.6	
13	4	1	4	0.34	177.3	9.37	44.9	1.89	163.0	-5.53	44.2	

(continued)

**Table 1** (continued)

Exp. No.	Machining parameters			Process of tangential turn-mill				Process of orthogonal turn-mill			
	S	F	C	$R_a$	H	SN ratio $R_a$	SN ratio H	$R_a$	H	SN ratio $R_a$	SN ratio H
14	4	2	3	0.42	175.4	7.54	44.8	2.74	151.3	-8.76	43.6
15	4	3	2	0.84	167.7	1.51	44.4	4.65	141.7	-13.4	43.0
16	4	4	1	1.01	162.3	-0.09	44.2	5.70	128.3	-15.1	42.1
				$\eta_{avg} =$		0.52	44.1	$\eta_{avg} =$		-135	42.9
				$\eta_{ideal S} =$		4.58	44.6	$\eta_{ideal S} =$		-10.6	43.2
				$\eta_{ideal F} =$		5.64	44.1	$\eta_{ideal F} =$		-10.3	43.0
				$\eta_{ideal C} =$		1.03	44.3	$\eta_{ideal C} =$		-12.6	43.8
				<b>Response<sub>opt</sub> =</b>		<b>0.31</b>	<b>177.0</b>	<b>Response<sub>opt</sub> =</b>		<b>2.1</b>	<b>162.1</b>

The determined SN ratios of the responses are used for determining the individual optimality and multi-response optimality. Using Eqs. 3–4 [13] are used for calculating individual optimum response values.

$$\eta_{\text{opt}} = \eta_{\text{avg}} + \sum_{i=1}^n (\eta_{\text{ideal}} - \eta_{\text{avg}}) \quad (3)$$

$$\text{Response}_{\text{optimum}} = \sqrt{10^{\pm(\eta_{\text{opt}}/10)}} \quad (4)$$

where ‘ $n$ ’ number of observations, ‘ $\eta_{\text{opt}}$ ’ SN ratio optimum value, ‘ $\eta_{\text{avg}}$ ’ average SN ratio value and ‘ $\eta_{\text{ideal}}$ ’ ideal level of SN ratio of each parameter.

## 2.1 Experimental Procedure

Work material rods of diameter 40 mm and length 225 mm are taken and are divided into parts of 5 (i.e.  $4 \times 40 \text{ mm} + 65 \text{ mm}$  extra length so that tool holder does not hit the chuck of VMC). Average roughness ( $R_a$ ) and hardness ( $H$ ) of surface are measured on the three diametrical points as the responses. Surface roughness tester (Surface Test SJ-301) is used to measure  $R_a$  and for hardness measurement, universal hardness testing machine is used as per ASTM E92. A new HSS cutter is used for each new speed. Cutter speed (r/min), rate of feed (mm/min) and depth of cut (mm) in conjunction with 20 r/min of workpiece constant rotational speed are taken along with TDOE, as shown in Table 1a, b. The SN ratio for  $R_a$  to be minimum, so lower-the-better formula used; while for “ $H$ ” SN ratio to be maximum and so higher-the-better formula used. The SN ratio values are shown in Table 1b.

## 3 Analysis of Individual Optimality and Regression Modelling

Based on Eqs. 1–2, the SN ratios are computed for  $R_a$  and  $H$ , considering lower-is-better for roughness of machined surface and higher-is-better for hardness and are tabulated as shown in Table 1b. The average ideal SN ratio of cutter speed, rate of feed and depth of cut are taken from the determined SN ratios for calculating individual optimal value of responses using Eqs. 3 and 4.

### Calculation of optimal roughness of machined surface for S4-F1-C1 in tangential turn-milling:

Based on the response table over SN ratios as given in Table 1b, the ideal SN ratio of cutter speed, rate of feed and depth of cut are 4.58, 5.6 and 1.03, respectively, so



$$\begin{aligned}\eta_{\text{opt}} &= \{0.52 + [(4.58 - 0.52) + (5.6 - 0.52) + (1.0 - 0.52)] \\ &= 10.19 \& (R_a)_{\text{opt}} = \sqrt{(10^{\pm 1.019})} = 0.31 \mu\text{m}.\end{aligned}$$

### 3.1 Discussions on Individual Optimality

The individual optimal levels of cutting parameters depends on individual ideal mean effect of SN ratios and are found as S4-F1-C1 and S4-F1-C4 for tangential and orthogonal turn-mill processes for generating  $R_a$  and evaluated as 0.31  $\mu\text{m}$  and 2.1  $\mu\text{m}$ , respectively. Similarly, the optimal levels of cutting parameters are found as S4-F2-C4 and S4-F2-C4 in process of tangential and orthogonal turn-mill while generating  $H$  and evaluated as 177.01 HV and 162.18 HV respectively.

### 3.2 Regression Modelling

Empirical regression models are mostly used in exercise of predicting the behaviour of parameters of machining. They aid the selection of working parameters as per required response. Empirical regression models with second-order linear equations are developed for predicting and analysing ' $R_a$ ' and ' $H$ '. The regression models revealed a significance of confidence level more than 95%, shown in Table 2a. The regression analysis based on statistical analysis using analysis of variance (ANOVA) is carried to indicate the significance of process parameters on the models. The regression models indicates all the parameters are significant excluding depth of cut to be less significant in generating  $R_a$  in both the processes, while all parameters are significant in generating  $H$  with less significance of rate of feed and shown in Table 2b–c.

## 4 Multi-response Optimization

The methodology of hybridizing grey relational analysis (GRA) with principal component analysis (PCA) for finding the optimal combination of experiment for the correlated response for multi-objective optimization [10] is shown in Fig. 1. The multi-response optimal values determined using GRA–PCA coupled with Taguchi gives S4-F1-C4 combination for  $R_a$  of 0.34–1.89  $\mu\text{m}$ , while  $H$  of 177.3 HV and 163.0 HV in turn-mill process of tangential and orthogonal, respectively.

**Sample calculations of algorithm of roughness of machined surface in tangential turn-milling:**

**Table 2 a** Regression models generated in both turn-mill processes. **b** Regression response analysis in tangential turn-milling. **c** Regression response analysis in orthogonal turn-milling

<b>(a)</b>							
Process	Second-order linear empirical regression model						R <sup>2</sup> (%)
<i>For roughness of machined surface</i>							
Tangential	$1.75 - 8 \times 10^{-5}S + 0.031F + 0.335C - 19 \times 10^{-8}S^2 + 0.01F^2 + 0.17C^2$						98
Orthogonal	$-5.5 + 95 \times 10^{-4}S + 0.33F - 1.29C - 229 \times 10^{-8}S^2 + 0.0073F^2 + 0.39C^2$						96
<i>For surface hardness</i>							
Tangential	$-117 + 0.16S + 1.6F + 21.6C - 233 \times 10^{-7}S^2 - 0.14F^2 - 4.6C^2$						96
Orthogonal	$93.9 - 0.0023S + 1.89F + 56.56C - 2.6 \times 10^{-6}S^2 - 0.166F^2 - 12.8C^2$						97
<b>(b)</b>							
Source	Df	SS	MS	F	P	F-critical	Significance
<i>For roughness of machined surface</i>							
Regression	3	15.9	5.3	1387	0.00	2.81	High significant (HS)
S	1	4.8	4.8	1270	0.00	4.06	HS
F	1	9.9	9.9	2598	0.00	4.06	HS
C	1	1.1	1.1	294	0.00	4.06	Significant (S)
<i>For surface hardness</i>							
Regression	3	4575	1525	382	0.00	2.81	HS
S	1	3591	3591	900	0.00	4.06	HS
F	1	52.4	52.4	13	0.00	4.06	S
C	1	931	931	233	0.00	4.06	HS
<b>(c)</b>							
Source	Df	SS	MS	F	P	F-critical	Significance
<i>For roughness of machined surface</i>							
Regression	3	104	34.7	430	0.00	2.81	HS
S	1	38.3	38	475	0.00	4.06	HS
F	1	63.4	63.4	785	0.00	4.06	HS
C	1	2.4	2.4	30	0.00	4.06	S
<i>For surface hardness</i>							
Regression	3	6783	2261	686	0.00	2.81	HS
S	1	555	555	168	0.00	4.06	HS
F	1	37	37	11.3	0.00	4.06	S
C	1	6191	9191	1880	0.00	4.06	HS

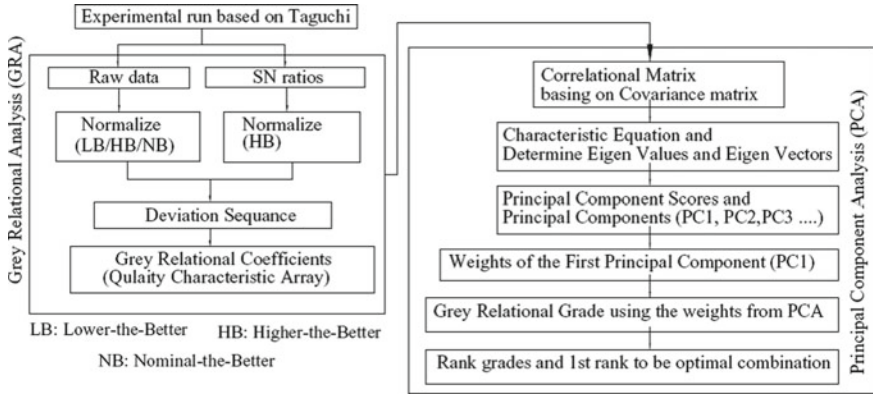


**Fig. 1** Procedural methodology of GRA-PCA

For normalization, higher-is-better (HB):

$$x_i^*(j) = \frac{[x_i(j) - \min(x_i(j))]}{\max(x_i(j)) - \min(x_i(j))} \rightarrow x_i^*(j) = \frac{2.16 - (-7.23)}{9.37 - (-7.23)} = 0.5657$$

For deviation sequence,  $\Delta_{oi}(k) = \|X_o(k) - X_i(k)\| \rightarrow \Delta_{o1}(1) = \|0.5657 - 1.000\| = 0.4343$

$$\text{Grey relational coefficient } \gamma_i = \frac{\Delta_{\min} + \zeta \Delta_{\max}}{\Delta_{oi}(k) + \zeta \Delta_{\max}} = \frac{0.0 + 0.5 * 1.0}{0.4343 + 0.5 * 1.0} = 0.5351$$

Generate a characteristic equation with help of covariance and correlation matrix which is of quadratic polynomial, as shown:  $\lambda^2 - 2\lambda + 0.51 = 0$ . It gives two eigenvalues (eigenvectors) as shown  $\{0.3 (-1.0; 1.0)$  and  $1.7 (1.0; 1.0)\}$ . The proportions, cumulative and principal component contribution are given in Table 3.

So, grey relational grade and ranks is evaluated as  $Y_i(k) = \sum_{j=1}^n x_i^*(j)\beta_{kj}$  and giving the  $L_{13}$  experiment as optimal in both the turn-mill processes.

**Table 3** Contribution for principal components in tangential turn-mill process

	$R_a$	$H$	Quality characteristic	First principal component (PC1)	Contribution of PC1 (weights)
Eigen values	1.74	0.25	<i>Tangential turn-milling</i>		
Proportion	0.87	0.12	$R_a$	0.707	0.50
Cumulative	0.87	1.00	$H$	0.707	0.50

## 5 Results and Discussions

Results between first two machining factors that are predominant on the responses interprets that  $R_a$  to be increasing with the rate of feed but is decreasing with cutter speed, whereas  $H$  to be increasing with the depth of cut and cutter speed, in both the processes of turn-milling. The results of optimal design reveal that the proposed approach of combining GRA and PCA can acquire cutting parameters optimal combination effectively and can be an improving tool of cutting performance of turn-milling processes. From ANOVA, it is clear that the cutter speed is highly effective in generating the combined and individual responses in process of tangential. Similarly, in process of orthogonal, depth of cut is undoubtedly effective in generation of individual and combined responses but rate of feed is less effective.

The depth of cut seems to be increasing the surface hardness, due to the fact that the cutter acts as a burnishing tool pressing towards the workpiece surface throughout the machining, which increases surface finish and thereby inducing surface hardness in both the turn-mill processes. While increase in rate reduces the duration of filling the roughness valleys over the surface by the cutter which is acting as a burnishing tool, thereby at high feeds, the roughness of surface increased.

## 6 Conclusions

The investigation of this study is on individual and multi-response optimal process parameters on ' $R_a$ ' and ' $H$ ' in processes of turn-milling.

- The improved surface finish increases surface hardness in both the processes of turn-mill. But the process of tangential turn-mill when compared with process of orthogonal turn-mill, the process of tangential turn-mill looks to generate better surface finish and surface hardness. More research is required for predicting the stresses, micro-structural changes and surface integrity generation in the surface layers, which are responsible for development of cracks, corrosion and cavitations.
- Individual optimization of a single response depends on its own ideal mean effect of SN ratios of the parameters, but if we require optimizing multi-responses, then combined effect of all the responses with highest SN ratio can be treated as optimal combination. In this context, one has to choose multi-response optimization, if he has a weightage or priority of responses to be generated and on the other hand for single optimization, weightage can be given 100%.

## References

1. Shaw MC, Smith PA, Cook NH (1952) The rotary cutting tool. *Trans ASME* 74:1065–1076
2. Choudhury SK, Mangrulkar KS (2000) Investigation of orthogonal turn-milling for the machining of rotationally symmetrical work pieces. *J Mater Process Technol* 99:120–128
3. Savas V, Ozay C (2008) The optimization of the surface roughness in the process of Tangential Turn-milling using genetic algorithm. *Int J Adv Manuf Technol* 37:335–340
4. Juha H, Sampsa VA, Laakso (2012) Integrity of surfaces finished with ultrasonic burnishing. *IMEchE Part B J Eng Manuf* 227(1):45–53
5. Ali A, Moradi B (2014) Simulation optimization of facility layout design Problem with safety and ergonomics factors. *Int J Ind Eng Theor Appl Pract* 21(4):209
6. Liu J, Kachitvichyanukul V (2015) A pareto-based particle swarm optimization algorithm for multi-objective location routing problem. *Int J Ind Eng Theor Appl Pract* 22(3):1314–329
7. Ahilan C, Kumanan S, Sivakumaran N (2010) Application of Grey Based Taguchi Method in Multi-response Optimization of Turning Process. *Adv Prod Eng Manage* 5(3):171–180
8. Krishna MA, Rajendra BS, Palani KK, Davim JP (2012) Application of grey fuzzy logic for the optimization of drilling parameters for CFRP composites with multiple performance characteristics. *Measurement* 45:1286–1296
9. Kumar A, Saurav D, Mahapatra S (2015) Optimization of thrust, torque, entry, and exist delamination factor during drilling of CFRP composites. *Int J Adv Manuf Tech* 76:401–416
10. Lu HS, Chang CK, Hwang NC, Chung CT (2019) Grey relational analysis coupled with principal component analysis for optimization design of the cutting parameters in high-speed end milling. *J Mat Pro Tech* 209:3808–3817
11. Cetin O, Vedat S (2012) The optimization of Cutting Parameters on Surface Roughness in Tangential Turn-milling using Taguchi Method. *Adv Nat Appl Sci* 6(6):866–874
12. Arun Vikram K, Ratnam CH, Sankaranarayana K, Satish BB (2015) Assessment of surface roughness and MRR while machining brass with HSS tool and carbide inserts. *Indian J Eng Mat Sci* 22(3):321–330
13. Madhav Phadke S (1989) *Quality engineering using robust design*. PTR Prentice-Hall Inc.

# On the Role of Amylum Additive-Based Cutting Fluids in Machining—An Experimental Investigation



R. Padmini, P. Vamsi Krishna and P. Jeevan Kumar

**Abstract** This work deals with the application of amyllum additive-based cutting fluids while turning AISI 304 steel using carbide inserts. Amyllum additive is dispersed in vegetable oil at varying percentages. Absorbance of the additive in pure bio-oil is examined using spectrophotometer, and thermal conductivity of these formulations is also obtained. Machining performance is assessed by comparing dry, synthetic cutting fluid, and pure oil for fixed cutting conditions. After basic machining, percentage of amyllum additive is changed, and machining is done to examine the best concentration (0.3–0.9%) of additive in pure oil through minimal quantity lubrication technique. Machining performance is obtained by measuring cutting tool temperatures, surface roughness, and tool flank wear. It is inferred that, when compared to dry machining, synthetic fluid, and pure oil-assisted machining, amyllum-assisted cutting fluids have resulted in improved machining performance owing to the reduction in cutting temperatures and better lubricity. Hence, it can be comprehended that amyllum additive has the potential to be used as an additive in biodegradable oils in view of eco-friendly and user compatible machining operations.

**Keywords** Amyllum additive · MQL · Cutting fluids · User compatible machining

---

R. Padmini (✉) · P. Jeevan Kumar  
Department of Industrial Engineering, GITAM Institute of Technology, Visakhapatnam, Andhra Pradesh 530045, India  
e-mail: [padhmini.r@gmail.com](mailto:padhmini.r@gmail.com)

P. Vamsi Krishna  
Department of Mechanical Engineering, National Institute of Technology, Warangal, Warangal, Telangana 506004, India

© Springer Nature Singapore Pte Ltd. 2020  
H. K. Voruganti et al. (eds.), *Advances in Applied Mechanical Engineering*,  
Lecture Notes in Mechanical Engineering,  
[https://doi.org/10.1007/978-981-15-1201-8\\_93](https://doi.org/10.1007/978-981-15-1201-8_93)

## 1 Introduction

Synthetic cutting fluids applied during machining lead to various technical and environmental issues. It was observed that wide use of synthetic cutting fluids leads to derma-related problems to machinists [1, 2]. They hinder the ecological balance, being toxic and non-biodegradable [3, 4]. High amounts of cutting fluids in million metric tons are utilized by manufacturing industries [5]. Researchers experimented with solid lubricant-assisted machining and pinpointed the friction reducing ability of MoS<sub>2</sub>. They noted that this behavior is affirmative for machining, and it is due to the physical and chemical properties of MoS<sub>2</sub> surface layers [6]. Suresh and Rao [7] worked with solid lubricants like graphite and molybdenum disulfide (MoS<sub>2</sub>). They inferred that milling using MoS<sub>2</sub> minimized friction, main cutting force, and specific energy required by 28%. It was inferred through experimentation that application of solid lubricants in hard turning operation was beneficial compared to dry machining [8]. Moving ahead to vegetable oil-based cutting fluids, Susan [9] worked with the lubricative nature of biodegradable fluids and found that they can be used in machining due to film formation capacity of these fluids on the job. Enhancement in tool life and minimization of cutting tool wear and forces by using vegetable oils were reported [10]. Machining results were found to be encouraging as reported by other researchers by applying different vegetable oils like canola and castor oils [11, 12]. Nanofluids as additives comprise good thermal and physical properties due to higher surface area to volume ratio. Investigators developed various relations to find the thermal properties of nanofluids [13, 14]. It was noted that due to enhancement in thermal properties, nanofluids can reduce the cutting temperatures during machining operations [15, 16]. Next to mention, MQL involves very low quantity of cutting fluid (10 ml/min). Shen [17] estimated the effect of Al<sub>2</sub>O<sub>3</sub>, nanodiamond, and zinc oxide (nano) in grinding operation through MQL and found affirmative results. Researchers observed an enhancement in surface integrity of workpiece during turning with high cutting tool pressure by implementing MQL [18]. Abiodun [19] conducted experiments to examine the performance of amyllum starch dispersed cutting fluids in turning and found improvement in machining performance. Flood mode of supply was implemented in this work. Research works on the applicability of natural additives like amyllum or maize starch to biodegradable oils through MQL mode have not been explored, and the present work attempts to address this aspect.

## 2 Materials and Methods

The methodology implemented to examine the impact of additive-based cutting fluids is discussed in the following sections.

## ***2.1 Formulation of Additive-Based Cutting Fluids***

The cutting fluids are formulated through ultra-sonication process using a bath-type sonicator. Pre-weighed quantity of amyllum is dispersed in coconut oil (CCO) and sonicated thoroughly for a period of 60 min for thorough mixing of additive in base oil. These fluids are prepared at different weight percentages varying in the range from 0.3 to 0.9% of amyllum (Amy) additive.

## ***2.2 Absorbance and Thermal Conductivity***

Before being applied as cutting fluids, it is important to understand the level of dispersion of additive in the base fluid. Spectral analysis is one method to assess the absorbance of formulated cutting fluids. Absorbance is analyzed by using a UV–Visible spectrometer. The cutting fluids being applied at the machining zone must possess good thermal properties. Thermal conductivity is an important property of cutting fluids due to which heat generated during machining is dissipated.

## ***2.3 Machining***

After evaluation of thermal conductivity of the formulated cutting fluids, experiments are conducted to assess the influence of these fluids while turning AISI 304 grade steel at fixed machining conditions (speed: 60 m/min, feed: 0.17 mm/rev, depth of cut: 0.5 mm), using coated carbide insert. Cutting temperatures are measured online using k-type shielded/embedded thermocouple. Tool flank wear is obtained by using optical microscope. Surf test SJ-301 equipments are used to measure surface roughness. All the experiments and tests are conducted thrice, and average values are taken to obtain precise results.

## **3 Results and Discussion**

This work aims at investigating the role of additive-based biodegradable cutting fluids in machining using amyllum as additive 0.3, 0.6, and 0.9%. Absorbance and thermal conductivity are tested to check the viability of these cutting fluids to be applied in machining. Machining performance is assessed by measuring cutting temperatures, tool wear, and surface roughness at constant cutting conditions. In this section, graphical results are presented, and comparative analysis is done and discussed.



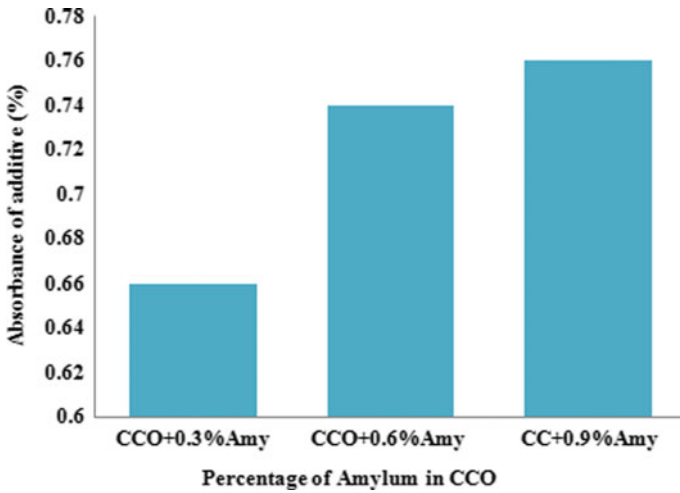


**Fig. 1** Absorbance of additive at varying percentages in base fluid (CCO)

### 3.1 Absorbance

Extent of dispersion of additive particles in coconut oil is presented in Fig. 1. It is observed that absorbance has significantly increased from 0.3% AMY in CCO to 0.6% AMY in CCO approximately by 12%. The increase in absorbance at 0.9% AMY from 0.6% is very less that is 2%. This can be attributed to the agglomeration of additive in base fluid as percentage additive is increased. Hence, increase in % additive does not proportionally increase the absorbance.

### 3.2 Thermal Conductivity

Results of thermal conductivity of additive-based cutting fluids are shown in Table 1. With increase in % additive thermal conductivity is also found to increase. Thus, this aspect makes the cutting fluid formulated from amyllum additive in coconut oil to be viable in machining applications. Increase in thermal conductivity makes the cutting fluid reduce the cutting temperatures.

**Table 1** Thermal conductivity (kW/m K) of additive-based cutting fluids

Base fluid	Percentage of amyllum additive			
CCO	0	0.3	0.6	0.9
	0.1815	0.1826	0.1830	0.1848

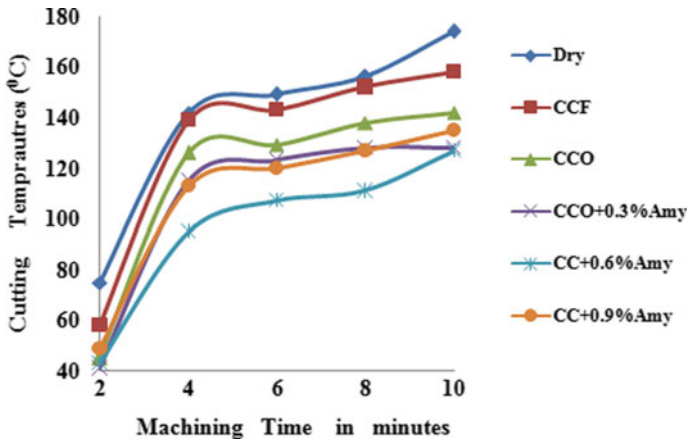


Fig. 2 Variation in cutting temperature with machining time under various lubricant environments

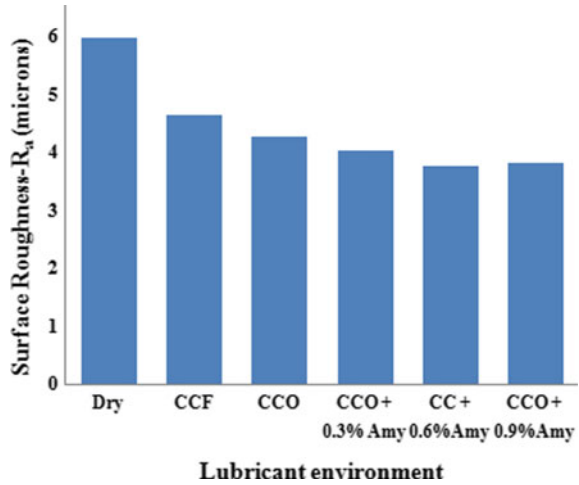
### 3.3 Cutting Temperatures

Variation of cutting temperatures with machining time is reflected in Fig. 2. It is noticed that cutting temperatures increase with an increase in machining time. Maximum temperatures are recorded during dry machining. Cutting temperatures are found to be minimum by applying CCO + 0.6% Amy compared to CCO + 0.3% Amy and pure CCO. Increase in % of amyllum additive does not show a proportionate reduction in cutting temperatures. This is due to the extent of absorbance of additive in base fluid, though there is increase in thermal conductivity with enhancement in % additive. Due to agglomeration, at higher percentages of additive in CCO ability to reduce friction at the contact surfaces and thereby cutting temperatures reduction is affected. It can be inferred that inclusion of additive in base fluid has reduced the temperatures to an extent of 28% and 19% when compared to dry and pure oil-assisted machining, respectively.

### 3.4 Surface Roughness

It is noticed that amyllum additive-based cutting fluids have reduced surface roughness of workpiece. The results are presented in Fig. 3. It is seen that under dry machining environment, maximum the workpiece is subjected to maximum surface roughness; while at 0.6% Amy in CCO, it is found to be less compared to other lubricant environments. Reduction in surface roughness can be attributed to the combined effects of reduction in cutting temperatures and tool wear as well. Film formation ability of the additive-based cutting fluids leads to reduction in surface roughness. The

**Fig. 3** Variation in surface roughness— $R_a$  under various lubricant environments



extent of reduction in surface roughness by using 0.3% Amy in CCO is observed to be 37 and 12% when compared to dry and pure oil-assisted machining environments.

### 3.5 Tool Wear

Results of tool wear obtained under different lubricant environments are presented in Fig. 4. It is evident that for all the conditions tool wear has increased with machining time. Under dry cutting condition, tool wear is maximum, under pure oil-assisted

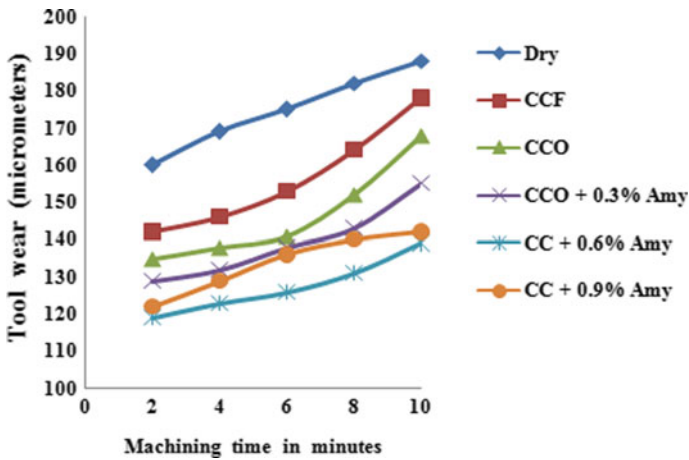


**Fig. 4** Variation in tool wear with machining time

machining (CCO), tool wear is found to be less compared to dry machining, and by applying CCO + 0.6% Amy tool wear is found to be least. This is due to reduced cutting temperatures and ability of the additive to form a thin film of lubricant between the surfaces in contact. Percentage reduction in tool wear is 29 and 13% in comparison with dry and CCO-assisted machining.

## 4 Conclusions

- Experimental investigations to examine the performance of amyllum or maize starch-based additive in coconut oil are carried out. Absorbance is found to increase with increase in percentage of additive in base fluid up to 0.3% and not beyond. Thermal conductivity increased with increase in % additive. Consistent increase in the basic properties with varying amount of additive does not mean that the same behavior should be exhibited by additive-based cutting fluids during machining.
- It is observed that 0.6% Amy in CCO resulted in reduced cutting temperatures, tool wear, and surface roughness. Extent of reduction in machining performance parameters is approximately 31 and 12% compared to dry machining while working with CCO + 0.6% Amy.
- Hence, the application of natural additives like amyllum to vegetable oils is an amicable alternative to explore eco-friendly and sustainable alternatives to conventional cutting fluids.

## References

1. Passman FJ, Roossmore HW (2002) Re assessing the health risks associated with employee exposure of metal working fluid microbes. *Lubr Eng* 58(7):30–38
2. Bennett EO (1983) Water based cutting fluids and human health. *Tribol Int* 16(3):133–136
3. Korde VM, Phelps TJ, Bienkowski PR, White DC (1993) Biodegradation of chlorinated aliphatics and aromatic compounds in total-recycle expanded-bed reactors. *Appl Biochem Biotechnol* 45(46):731–740
4. Zeman A, Sprengel A, Niedermeier D, Spath M (1995) Biodegradable lubricants-studies on thermo oxidation of metal-working fluids by differential scanning calorimetry (DSC). *Thermochim Acta* 268:9–15
5. Kline & Company, Inc. (2006) Competitive intelligence for the global lubricants industry, 2004–2014. Kline & Company
6. Dilbag S, Rao PV (2007) Performance improvement of hard turning with solid lubricants. *Int J Adv Manuf Technol* 32:170–177
7. Suresh Kumar Reddy N, Rao PV (2005) Performance improvement of end milling using graphite as a solid lubricant. *Mater Manuf Process* 20:673–686
8. Krishna PV, Rao DN (2008) The influence of solid lubricant particle size on machining parameters in Turning. *Int J Mach Tools Manuf* 48(1):107–111
9. Susan W (2005) Vegetable oil-based metalworking fluids can provide better performance and environmental results than mineral oil-based fluids. *Cutting Tool Mag* 57(2):1–3

10. Belluco W, De Chiffre L (2002) Surface integrity and part accuracy in reaming and tapping stainless steel with new vegetable based cutting oils. *Tribol Int* 35:865–870
11. Alves SM, Oliveira JFG (2005) Vegetable based cutting fluids: An environmental alternative to grinding process. In: Proceedings of the 15th CIRP international conference on life cycle engineering. Elsevier, pp 664–668
12. Ion IS, Camelia C, George C (2002) On the future of biodegradable vegetable lubricants used for industrial tribo systems. *Ann Univ "Dunarea De Jos" Galati Fascicle* 8:94–98
13. Wong KV, De Leon O (2010) Applications of nanofluids: current and future. In: *Advances in Mechanical Engineering* (Available online)
14. Das SK, Choi SU, Yu W, Pradeep T (2008) *Nanofluids: science and technology*. Wiley-Interscience, USA
15. Putra Nandy, Roetzel Wilfried, Das Sarit K (2003) Natural convection of nano-fluids. *Heat Mass Transf* 39:775–784
16. Xuan Y, Li Q (2000) Heat transfer enhancement of nanofluids. *Int J Heat Fluid Flow* 21:58–64
17. Shen B, Shih A, Tung SC (2008) Application of nanofluids in mql grinding. *Tribol Lubr Technol* 51:730–737
18. Diniz AE, Ferreira JR, Filho FT (2003) Influence of refrigeration/lubrication condition on SAE 52100 hardened steel turning at several cutting speeds. *Int J Mach Tools Manuf* 43:317–326
19. Abiodun MO, Adetan DA, Oladejo KA (2011) A Study of the performance of maize starch based cutting fluids in the turning of AISI 304 Stainless Steel. *Int J Eng Res Afr* 6:13–24

# Tensile Property of Ultra-High Molecular Weight Polyethylene Fibre and Its Composite Laminate



Arun Kumar Singh, Dharmendra Kumar Shukla and N. Eswara Prasad

**Abstract** The present paper reports the uniaxial tensile property of fibre and laminated composite of Dyneema<sup>®</sup> HB80 prepreg under quasi-static conditions. A detailed experimental work on tensile testing of fibre/filament and its laminated composite has been presented. It has also been discussed about the easy slipping out problem of Dyneema<sup>®</sup> grade test specimen during experimental work. The tensile strength of the filament of Dyneema<sup>®</sup> HB80 has been evaluated and found to be 2.96 GPa with an average elongation of 4.15%, closely agreed with the test data of manufacturer, although tensile strength of laminated composite has been found quite low as compared to fibre tensile strength. The effect of curing temperature on the tensile strength has also been studied and found higher strength for the laminate cured at a comparatively lower temperature. The SEM analysis of the fractured samples showed weak macro fibrils resulted in higher degree of damage to the fibre laminate, and hence, lower tensile strength.

**Keywords** Dyneema<sup>®</sup>HB80 · Composite material · Filament

## 1 Introduction

Ultra-high molecular weight polyethylene (UHMWPE) is a crystalline polymer with a wide range of structural applications from aerospace to defence industry. The UHMWPE-based composites exhibit excellent mechanical properties, adequate elongation and fatigue response, apart from high rigidity, high strength and good energy absorption capabilities [1–3]. Due to these attractive properties, the UHMWPE material finds application in many important protective gears development such as bulletproof armour, ballistic helmets and bulletproof vest [4, 5].

---

A. K. Singh · N. Eswara Prasad  
Defence Materials & Stores R&D Establishment, DRDO, Kanpur 208013, India

A. K. Singh · D. K. Shukla (✉)  
Department of Mechanical Engineering, Motilal Nehru National Institute of Technology,  
Allahabad 211004, India  
e-mail: [dkshukla@mnit.ac.in](mailto:dkshukla@mnit.ac.in)

© Springer Nature Singapore Pte Ltd. 2020  
H. K. Voruganti et al. (eds.), *Advances in Applied Mechanical Engineering*,  
Lecture Notes in Mechanical Engineering,  
[https://doi.org/10.1007/978-981-15-1201-8\\_94](https://doi.org/10.1007/978-981-15-1201-8_94)

The UHMWPE fibres have been commercialized in the late 1970s by the Dutch chemical company, DSM under trade name Dyneema<sup>®</sup> having chemical formula –  $[\text{CH}_2-\text{CH}_2]_n$ . Nowadays, there are many grade of Dyneema<sup>®</sup> fabrics/prepregs available in the market under the trade name of Dyneema<sup>®</sup>HB80, Dyneema<sup>®</sup>HB50, Dyneema<sup>®</sup>HB210, Dyneema<sup>®</sup>HB212, etc., for the moulding of hard ballistic armour panel.

Many investigations were carried out earlier on UHMWPE material. These investigations were oriented towards impact response, quasi-static response, creep response, etc., of UHMWPE fibres [6, 7]. Peijs et al. [8] extended these studies to UHMWPE fibre-reinforced laminate and reported mechanical properties of the laminate with the aim of its potential uses in high-end structural applications. An initial numerical study on the ballistic performance of UHMWPE fibre laminate has been reported by Grujicic et al. [9]. The properties of a fibre used in fibrous composite have their own bearing on the overall properties of composites. It has been observed that none of the literatures available in the public domain are describing overall tensile properties UHMWPE-based Dyneema<sup>®</sup> fibre and its laminate.

Under the present study, comprehensive experimental work has been carried out to evaluate tensile properties of Dyneema<sup>®</sup>HB80 grade fibre and its laminated composite under quasi-static loading condition. The findings of the experimental work and post experiment analysis using scanning electron microscopy (SEM) and optical microscope have been reported in this paper with an emphasis on failure behaviour of fibre and its laminate.

## 2 Experimental Details

In this section, the description of material system and experimental details for tensile testing of fibre and its composite has been discussed.

### 2.1 Material and Its Processing Descriptions

The manufacturer of UHMWPE Dyneema<sup>®</sup> produces fibre that consists of smaller units, which are called filaments as shown in Fig. 1a. In a sheet/prepreg, the fibres are equally distributed and flattened in unidirectional layers as shown in Fig. 1b. The fibres cannot be visually distinguishable, and only the filaments can be seen. The layers are rotated by 90° with respect to the adjacent layers; each sheet is a non-woven cross ply. The Dyneema<sup>®</sup> filament/fibre is bonded together by small amount of polyurethane rubber (PUR) matrix material.

Dyneema<sup>®</sup> composites are fabricated by pressing number of Dyneema<sup>®</sup> prepregs sheets together at elevated temperature and on application of adequate level of pressure using a suitable capacity hot press. Applied pressure and heat during the moulding process depend on the thermal and rheological properties of the resin. Therefore,

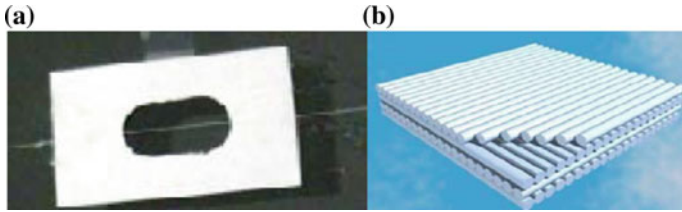
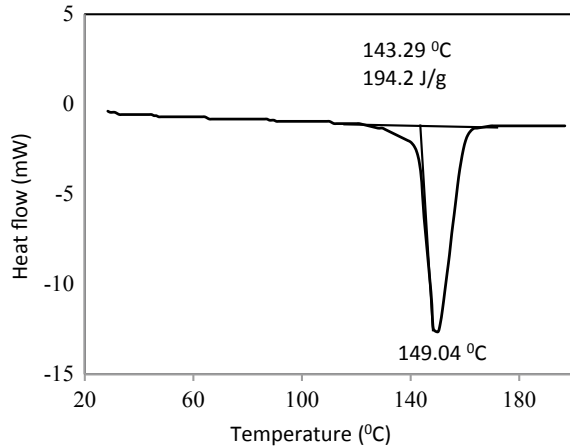


Fig. 1 Dyneema®HB80 a filament, b prepreg

Fig. 2 DSC curve of polyurethane rubber (PUR) resin



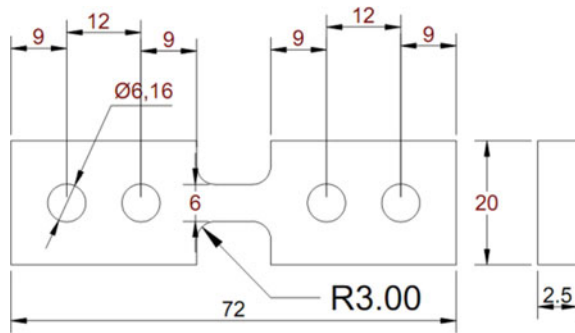
differential scanning calorimetry (DSC) has been chosen as an experimental tool for analysis of resin used in Dyneema®HB80 prepreg before fabrication of composite. The progress of the curing reaction and its softening behaviour has been investigated by Q200 differential calorimeter (TA Instrument). A sample of 5 mg. of PUR resin has been put into calorimeter and heated at constant rate of 10 K/min from ambient to 200 °C. The graph of DSC as shown in Fig. 2 indicates that the melting temperature of PUR resin is around ~150 °C with 194.2 J/g associated enthalpy. It indicates also that the extent of crystallinity is quite high in PUR resin.

## 2.2 Experimental Work

One of the most important tests that provides basis for all the mechanical properties is the uniaxial, quasi-static tensile test. This experimental investigation of Dyneema® HB80 fibre/filament and laminated composite allows the determination of ultimate tensile strength (UTS), Young’s modulus and elongation. Additionally, tensile toughness too can be determined.



**Fig. 3** Test specimen and dimensional details of specimen



In this work, the single fibre/filament testing of Dyneema®HB80 has been carried out using the Favimat instrument (Textechno, Germany). The Favimat measures the fineness of fibres utilizing the vibroscopic technique. Fibre strength and elongation have been measured at constant loading rate of extension of the measuring head, gauge length 20 mm and a constant head speed of 2 mm/min using samples of 20 filaments of Dyneema®HB80. The breaking force and elongation as well as the tenacity to elongation have also been measured for a fibre as per ASTM C1557. The load cell used for the tensile testing was 1200 cN, and a pretension of 0.5 cN/tex was applied to the fibre.

Similarly, the tensile testing of Dyneema® composite has been carried out by computerized universal testing machine (Model Instran 5967) of 3 kN load cell capacity. The geometry of the test specimens of Dyneema®HB80 composite employed for testing is shown in Fig. 3 [10]. Special tabs with riveted arrangement in the test specimens have been applied to have adequate and proper gripping.

### 3 Results and Discussion

#### 3.1 Fibre Testing

Figure 4 shows the load elongation plot of the 20 numbers of test samples tested at similar conditions. Microscopic examination of post test specimens using a Zeiss optical microscope at a magnification of 20× has been shown in Fig. 5. The figure shows that there are multiple and gradual breakages of the fibre during the tensile test corresponding to different displacement values. From the test result, the tensile strength of the fibre/filament has been found 2.96 GPa at 4.15% maximum elongation.

Based on manufacturer test values, Dyneema® fibre should fail at approximately 3.3–3.9 GPa at an elongation of 3–4% [11]. The experimental result has been found close to the manufacturer datasheet. Since the filaments were gripped directly to the gripper of the machine, the difference of the failure strength may be due to small slippage of the test samples. Another possibility of difference in failure strength of

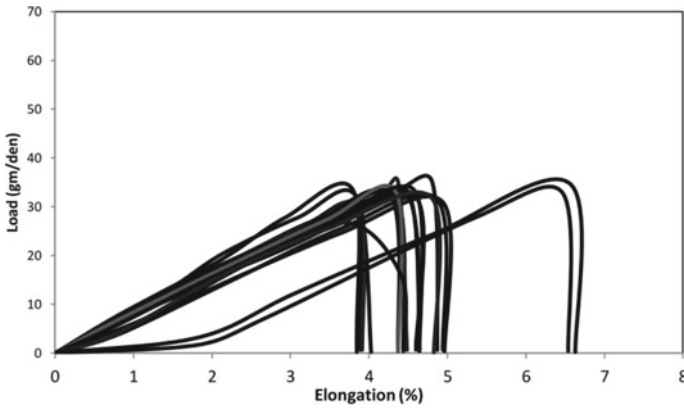
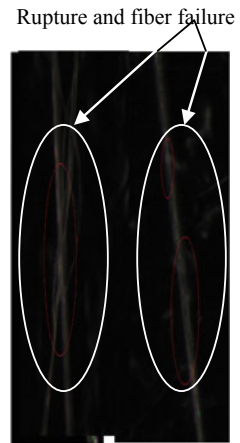


Fig. 4 Load elongation curves of filament

Fig. 5 Microscopic examination of the tested specimen



experimental result and manufacture test value may be due to the use of fibre of different spool. The closeness of experimental results with Dyneema<sup>®</sup> datasheet also gives greater confidence of the application of the direct gripping method for the testing of Dyneema<sup>®</sup> fibres.

### 3.2 Composite Testing

Tensile testing of Dyneema<sup>®</sup>HB80 composite has been carried out for 15 sets of specimen processed at different pressure, curing temperature and curing time as shown in Tables 1 and 2 and shows an average value of ultimate tensile strength (UTS) of each set of experiment comprising of testing of 03 numbers of specimens.

**Table 1** Range of various process variables

S. No.	Process parameters	Range
1.	Pressure ( $P$ ) (MPa)	9.8–17.65
2.	Temperature ( $T$ ) ( $^{\circ}$ C)	125–135
3.	Time ( $t$ ) (min)	10–20

**Table 2** Variables and experimental results

Test set no.	Level of process variables			UTS (MPa)
	$P$ (MPa)	$T$ ( $^{\circ}$ C)	$T$ (min)	
1	9.80	125	15	67.07
2	17.65	125	15	65.67
3	9.80	135	15	65.68
4	17.65	135	15	59.49
5	9.80	130	10	60.95
6	17.65	130	10	60.24
7	9.80	130	20	59.61
8	17.65	130	20	54.80
9.	13.73	125	10	60.67
10	13.73	135	10	40.74
11	13.73	125	20	53.12
12	13.73	135	20	65.72
13	13.73	130	15	49.42
14	13.73	130	15	49.31
15	13.73	130	15	49.52

The experimental results show that when the applied pressure is 9.8 MPa, curing temperature 125  $^{\circ}$ C and curing time is 15 min, the maximum ultimate tensile strength was achieved (Test set no. 1). In the case of Test set no. 10, where, the applied pressure, curing temperature and curing time were 13.73 MPa, 135  $^{\circ}$ C and 10 min, respectively, the minimum ultimate tensile strength has been achieved. From the above results, it is clear that the temperature effect is more significant than the pressure. The fibre softening and matrix/resin melting behaviour has been observed at higher temperature beyond a critical value. Therefore, comparatively poor ultimate tensile strength has been found in the test specimens cured at temperature 135  $^{\circ}$ C.

Scanning electron microscopy (SEM) of tensile fractured surface is carried out to study the nature of fractured surface morphology and associated failure mechanism. Figures 6 and 7 show SEM morphologies of the tested specimens corresponding to the lowest (see Test set no. 10, Table 2) and highest (see Test set no. 1, Table 2) UTS. These results can be explained in terms of the extent of delamination of filament and the fibres. In order to achieve higher UTS of such composite laminate, the selection of processing temperature is very critical. It has been observed that even if the processing

**Fig. 6** Morphology of the tensile fractured sample of Test set no. 10

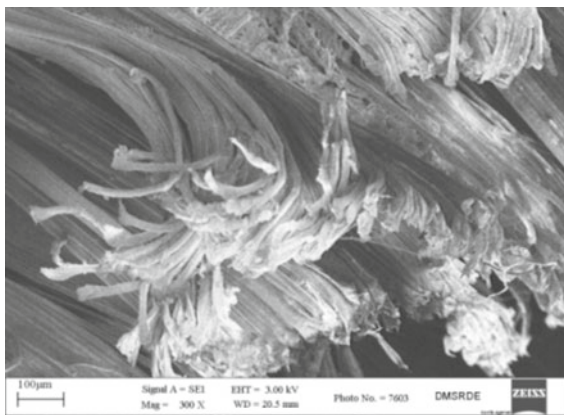
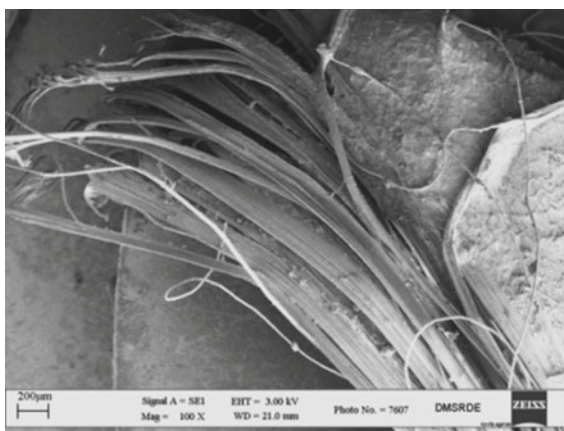


**Fig. 7** Morphology of the tensile fractured sample of Test set no. 1



pressure is kept minimum, curing temperature should be sufficient enough to melt the resin between inter layers of specimen. It has been observed that strong micro fibril in the SEM image of test specimens is processed at suitable temperature range.

The failure of the fibre always occurs at the macro fibril scale via internal friction within the amorphous regions due to chain slippage, leading to a highly localized adiabatic heating and softening, followed by localized failure of the material. Thus, the morphology of the tensile test of the Test set no. 1 also supports the claim of higher strength as compared to the tensile strength of the Test set no. 10 where comparatively weak macro fibrils can be seen (see Fig. 7).

## 4 Conclusions

This research work concludes the following:

- The ultimate tensile strength of filament of Dyneema®HB80fibre (2.90 GPa) has been found comparatively very high (>40 times) as compared to the composite laminates (40–70 MPa).
- The ultimate tensile strength of Dyneema®HB80 composite has been seen to be dependent on the applied pressure and curing temperature.
- The microstructure analysis of composite reveals that if the applied pressure and curing temperature are maintained for an appropriate time, the voids between two filaments are vanished, and the ultimate tensile stress is further increased.

## References

1. Luyu Z, Xianbo L (2013) A comparative study of UHMWPE multifilament and aramid multifilament. *Adv Mater Res* 709:84–88
2. Liu G, Thouless D, Deshpande VS (2014) Collapse of a composite beam made from ultra-high molecular weight polyethylene fibers. *J Mech Phys Solids* 63:320–335
3. Wei Z, Zihan H, Yan Z (2013) Gel-spun fibers from magnesium hydroxide nanoparticles and UHMWPE nanocomposite: rhe physical and flammability properties. *Compos Part B* 51:276–281
4. Long N, Shannon R, Stephen C (2015) The effect of target thickness on the ballistic performance of ultra-high molecular weight polyethylene composite. *Int J Impact Eng* 75:174–183
5. Miranda G, Celeste P, Alexandra F (2013) The effect of carbon nanotubes on viscoelastic behaviour of biomedical grade ultra-high molecular weight polyethylene. *Compos Struct* 105:263–268
6. Jacobs M, Heijnen N, Bastiaansen C, Lemstra J (2000) A novel, efficient route for the crosslinking and creep improvement of high modulus and high strength polyethylene fibres. *Macro Mol Mater Eng* 283:120–125
7. Govaert E, Lemstra J (1992) Deformation behavior of oriented UHMW-PE fibers. *Colloid Polym Sci* 270:455–464
8. Peijs A, Catsman P, Govaert E, Lemstra J (1990) Hybrid composites based on polyethylene and carbon fibres part 2: influence of composition and adhesion level of polyethylene fibres on mechanical properties. *Composites* 21:513–521
9. Grujicic M, Glomski S, Arakere G, Bell C, Cheeseman A (2009) Material modeling and ballistic resistance analysis of armor-grade composites reinforced with high performance fibers. *J Mater Eng* 18:1162–1182
10. Lifshitz JM, Leber H (1998) Response of fiber-reinforced polymers to high strain-rate loading in interlaminar tension and combined tension/shear. *Compos Sci Technol* 58:987–996
11. <https://issuu.com/Dyneema>. Comprehensive fact sheet. Last Accessed on 25 Mar 2019

# Experimental and Numerical Modeling of ECMM on Al 7075 T6 Alloy



K. Samson Praveen Kumar and G. Jaya Chandra Reddy

**Abstract** Electrochemical micromachining (ECMM) is a nontraditional machining technique in the area of mechanical engineering. It is more essential to meet the increasing demand of the industries from aero to medical. ECMM is the promising technique, since it has been growing popularity in various areas of applications. In the present study, the optimal combination and influence of process parameters on ECMM while machining Al 7075 T6 alloy are presented using Taguchi analysis and ANOVA. A bare electrode (cathode) has been used for this purpose. Later on, using an optimum combination of process parameters, the hole is drilled with insulated electrode. The ECMM process model has been developed and simulated with a bare tool and insulated tool using COMSOL Multiphysics V5.3a software. The effect of tip reaction on anode profile and stray current machined zone is identified with the electric field, temperature field, and fluid field. The results are validated with experimental results. The simulated predicted model is in close conformity with an experimental model.

**Keywords** Electrochemical micromachining (ECMM) · Stray current machining · Multiphysics · Modeling and simulation

## 1 Introduction

In the current development, the demand for microproducts has been rapidly increasing in the field of automotive, bio-medical, aerospace, etc. [1]. The materials which are difficult-to-machine like superalloys have considerably increased because of their improved properties [2]. While machining such materials using conventional machining process, a lot of issues like heat-affected zone, tool wear, etc. are being occurred

---

K. Samson Praveen Kumar (✉) · G. Jaya Chandra Reddy  
Department of Mechanical Engineering, YSR Engineering College of YVU, Proddatur, Kadapa  
516360, Andhra Pradesh, India  
e-mail: [ksamsonpraveen@yahoo.com](mailto:ksamsonpraveen@yahoo.com)

G. Jaya Chandra Reddy  
e-mail: [jcr.yvuce@gmail.com](mailto:jcr.yvuce@gmail.com)

© Springer Nature Singapore Pte Ltd. 2020  
H. K. Voruganti et al. (eds.), *Advances in Applied Mechanical Engineering*,  
Lecture Notes in Mechanical Engineering,  
[https://doi.org/10.1007/978-981-15-1201-8\\_95](https://doi.org/10.1007/978-981-15-1201-8_95)

[3]. To overcome this issue, various methods have been developed [4]. ECMM is a nonconventional machining technique emerging to be assuring method because of its additional advantages [5]. The use of different tapered tooltips for machining micro-holes and the effect of the spherical tip of a tool [6–8]. The researcher approaches multiphysics model for prediction of process performance characteristics [9, 10]. In the past simulations, the side-insulated layers are simplified to one-dimensional electrically insulated limit [11, 12]. On the other hand, the researcher focused only on the bare tool, electrical field and shows the importance of insulated layers, ensuing in a clear inconsistency among simulation and experiment. For this reason, multiphysics analysis is necessary for ECMM process to precisely know the cause of the tool on the machining accuracy. The electric field supply in the inter-electrode gap (IEG) using bare tool and insulated tool is shown in Fig. 1a, b.

The present investigation focuses on the optimum combination and influence of the process parameters (voltage, electrolyte concentration, and frequency) on dimensional overcut with the bare tool using ECMM process. Then the influence of the insulated tool on diametrical overcut with the optimum process parameters has been determined. After that, a multiphysics model for ECMM process was developed to find the parametric and structural effects on the electrical field distribution, fluid, and temperature fields. Finally, validate the obtained results from simulations with the experimental results.

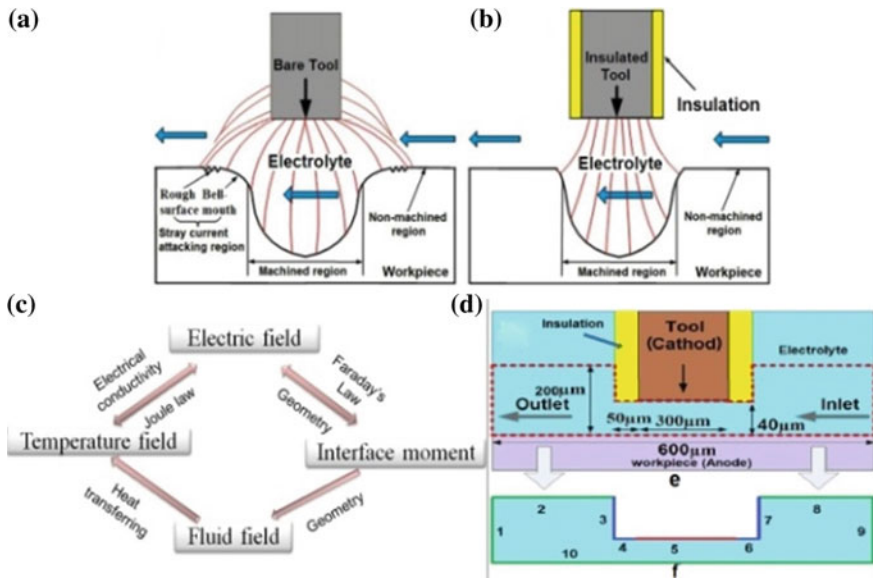


**Fig. 1** The schematic of the ECMM process. **a**Using bare tool with flat cathode tip. **b** Using side-insulated tool with flat cathode tip. **c** Schematically illustration of the coupling correlation multiphysical fields. **d** Geometry model. **e** The schematic of the electrolytic cell used in ECMM process. **f** The developed geometry model

## 2 Experimental Procedure

The process parameters used for machining are voltage, electrolyte concentration, and frequency which are considered as variables. The other parameters like current 0.8 A, feed rate 28.2  $\mu\text{m/s}$ , and duty cycle 60% are considered as constants. The tool diameter as 300  $\mu\text{m}$ , electrolyte as  $\text{NaNO}_3$ , and tool material as copper have been used to conduct the experiments. The corresponding values and levels of process parameters are chosen based on the past literature and preliminary experiments conducted are (6, 8, 10) V, (25, 30, 35) g/l, and (40, 50, 60) Hz, respectively. The experimental work was designed based on  $L_{27}$  orthogonal array method to perform microholes on Al 7075 T6 of thickness 0.3 mm and size 20 mm  $\times$  20 mm using ECMM process. The output of dimensional overcut has to be calculated for each trail. In this study, the target is to have lower overcut. To achieve this, optimization technique has to perform with the help of Taguchi analysis and ANOVA. Then with the optimum combination of process parameters, machining has been done with an insulated tool where the insulating material is PVC. After completion of the experiments, the microhole entrance was examined with SEM.

## 3 Numeric Model

A two-dimensional model was developed with the same machining conditions of experiments and simulated using COMSOL Multiphysics. The ECMM model has several physical domains like electrical field, deformed geometry interface, fluid field, and temperature field has been set up to analyze the interactions between the tool and workpiece. The modeled multiphysical field coupling correlation is shown in Fig. 1c. The coupled model of the above fields can be interfaced with the physical fields in ECMM with the following assumptions. The ECMM process is assumed to be ideal, i.e., the changes in composition of the electrolyte are negligible, the reaction products of heat, bubbles, and ions are neglected, the model is isothermal, the thermal conductivity of an electrolyte is assumed to be constant, and the fluid properties of the electrolyte are considered constant. In the electrolyte, the variations of composition are negligible as the electrode initiation over potential is negligibly small.

### 3.1 Geometry Model

The two-dimensional geometry model contains four domains namely cathode, anode, electrolyte, and insulation. The IEG initially maintained as 40 microns and the electrolyte flows from inlet right to outlet left. The geometry model was developed for ECMM process according to the experimentation as shown in Fig. 1d.



### 3.2 Physics

**Material Dissolution.** The material dissolution was carried out together with the interface of electric current and deformed geometry models. The domain of the electrolyte was assigned to water and defined with an electric conductivity of 0.165 S/m according to the performed experimental investigations. The boundary conditions of the mode electric current according to Fig. 1d are listed in Table 1. The ECMM follows Faraday’s law as functional principle for anodic dissolution of material due to electric potential  $Q$ . The material removed in volume  $V$  is calculated as.

$$V = \eta \times \frac{M}{\rho \cdot z \cdot F} \times Q \tag{1}$$

where  $\eta$  is the current efficiency,  $M$  is the molar mass,  $F$  the Faraday constant,  $z$  the electrochemical valence of the material, and  $\rho$  the density. The material removal velocity  $\vec{v}_n$  in normal direction depends on the current density  $\vec{j}_n$  in a normal direction.

$$\vec{v}_n = \eta(J) \times \frac{M}{\rho \cdot z_A \cdot F} \times \vec{j}_n \quad \eta(J) = \begin{cases} 1 & \text{for } J > J_{\min} \\ 0 & \text{for } J \leq J_{\min} \end{cases} \tag{2}$$

The current density  $J_{\min}$  was taken as 10 A/cm<sup>2</sup> according to past literature. Other parameters require calculating erosion according to Eq. (2) are current efficiency as 100%, molar mass as 190894.3856 g/mol, valency as 3, mass density as 2.81 g/cm<sup>3</sup>, and Faraday’s constant as  $9.65 \times 10^4$  C/mol.

**Deformed Geometry.** The deformed geometry interface can be used to study how physics changes in case the geometry shrinks by the removal of material. The interface requires a domain selection and has to select the geometry shape order as

**Table 1** Boundary conditions of multiphysics model

Boundary settings of the electric model			
Boundary condition	Electric potential	Electrical insulation	Ground
Boundary No.	5	1, 2, 3, 4, 6, 7, 8, 9	10
Setting	$U_0 = 6 \text{ V}$	$n \cdot j = 0$	$U_0 = 0$
Boundary settings for fluid model			
Boundary condition	Inlet	Outlet	No-slip wall
Boundary No.	9	1	2, 3, 4, 5, 6, 7, 8, 10
Setting	$u = -u_{\text{in}} \cdot n$	$P = 1 \text{ atm}$	$u = 0$
Boundary settings for heat transfer model			Temperature reference
Boundary condition	Heat flux	Thermal insulation	
Boundary No.	5	1, 2, 8	3, 4, 6, 7, 9, 10
Setting	$-n \cdot q = d_z q_0 \quad (q = -d_z \cdot k \nabla T)$	$-n \cdot q = 0$	$T = T_0$

1 and mesh smoothing type as Laplace. The free displacement has to be activated where Lagrange–Eulerian (ALE) method shape function uses same order for mesh position in domains.

**Non-isothermal Electrolyte Flow.** The non-isothermal laminar flow interface is used to simulate the couple between fluid flow and heat transfer and it combines the laminar flow and heat transfer in fluids.

*Laminar Flow.* The laminar flow interface has been solved with the incompressible laminar Navier–Stoke equation where the flowing velocity  $u$  can be expressed.

$$\rho \nabla(u) = 0 \quad \rho \frac{\partial u}{\partial t} + \rho(u \nabla)u = \nabla[-Pl + \mu(\nabla u + (\nabla u)^T)] + F \quad (3)$$

where  $\rho$  is electrolyte density,  $p$  is the fluid pressure, and  $\mu$  is the dynamic viscosity. The boundary conditions of the laminar flow according to Fig. 1d are listed in Table 1. The normal in-flow velocity is taken as 0.1 m/s, density of the electrolyte is taken as 1908 kg/m<sup>3</sup>, pressure as 1 atm and dynamic viscosity is taken as 00.00125 pa s.

*Heat Transfer in Fluids.* When the current is passed through two electrodes, resisting heating is generated known as Joule’s heating which increases temperature in the electrolyte and thus increases the conductivity of the electrolyte. The boundary conditions for heat transfer in fluids model according to Fig. 1d are listed in Table 1. The boundary 5 is defined as heat flux and is approximately taken 106 w/m<sup>2</sup>.

Here, for the simulation of heat transfer in fluids, the results of laminar flow were used coupled with primary current model. The heat transfer in fluids model uses the following Eq. (4)

$$\rho C_p \left( \frac{\partial T}{\partial t} + u \nabla T \right) = \nabla(k \nabla T) + Q \quad (4)$$

where  $C_p$  is the specific heat at constant pressure and is taken as 1655 J/(kg-K),  $u$  is velocity of the electrolyte 0.1 m/s,  $T$  is the temperature 273.15 K, and  $Q$  is the heat source which comes from electric current.

**Mesh.** An unstructured mesh has been used to the geometry. To attain this mesh, user-defined mesh has been chosen and in the settings, minimum and maximum element sizes are 50 μm and 500 μm, respectively. Then a free triangular mesh was chosen in that for size1, the minimum and maximum element sizes are 1 μm and 50 μm has been assigned to boundary 5 and for size 2, the minimum and maximum element sizes are 1 μm and 50 μm has been assigned boundary 10.

## 4 Results and Discussion

### 4.1 Experimental Results

The experimental results are analyzed through Taguchi analysis and ANOVA using statistical software, MINITAB 18 are listed in Tables 2 and 3. From Table 2, the factor voltage has the desired level is 1, because of the overcut value is minimum. Similarly, the desired levels for the electrolyte and frequency are 2 and 1, respectively. Therefore, the optimal process parameters are voltage as 6 V, the electrolyte as 30 g/l, and frequency as 40 Hz.

The parameters which significantly influence the output characteristics are with  $p$ -value  $\leq 0.05$  under 95% confidence levels. It is clear from Table 3 that the voltage is the most influencing factor and the electrolyte is also a significantly influenced factor.

The effect of various process parameters during machining is shown in Fig. 2a that the overcut increases with the increase of voltage. The ions increase in the electrochemical cell which increases the material removal and also increases the current flow through IEG. For the higher values of current, there will be the more current density which leads to higher removal of material at the edges of a hole as a result of higher overcut. Therefore, lower values of voltage are preferable for minimum overcut. The influence of the electrolyte concentration on overcut is when concentration increases, overcut reduces at moderate values and increases further at higher values because of the increase of ions association in the machining zone. A higher ion concentration improves the current density in the IEG resulting in increasing to overcut. Thus, the moderate value of the electrolyte concentration is

**Table 2** Mean effective response (smaller the better)

Level	Voltage (V)	Electrolyte (g/l)	Frequency (Hz)
1	69.11	91.67	101.78
2	95.78	86.78	113.22
3	172.11	158.56	122.00
Delta	103.00	71.78	20.22
Rank	1	2	3

**Table 3** Analysis of variance results

Source	DF	Adj SS	Adj MS	F-value	P-value	% of contribution
Voltage (V)	2	4.0570	2.0285	10.48	0.001	67.79
Electrolyte (g/l)	2	1.7149	0.8574	4.43	0.026	28.65
Frequency (Hz)	2	0.2129	0.1065	0.55	0.585	3.56
Error	20	3.8699	0.1935			
Total	26	9.8547				

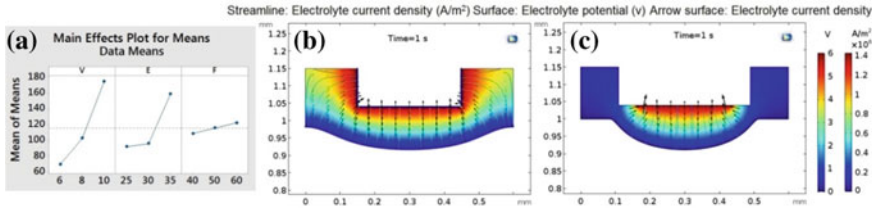


**Fig. 2** a Effect of various process parameters, b current density and the electrolyte potential distribution of the bare tool, and c insulated tool

preferable. The influence of frequency is not much higher when compared to voltage and the electrolyte concentration. Here, as the frequency increases, overcut also increases.

### 4.2 Simulation Results

**Material Dissolution.** The simulation results for material dissolution of the bare tool and insulated tool for current density distribution and the electrolyte potential distribution are shown in Fig. 2b, c. Obviously, it is clear that the insulated tip is helpful to restrict the effect of stray current in the IEG. The arrows in Fig. 2b bare tool and Fig. 2c insulated tool show the moment of ions which clearly indicating that the ions are moving more in the case of bare tool simulation than insulated tool simulation. The insulated layer confined the current attack on more localized area, which conforms the reducing of stray corrosion and overcut in ECMM process.

The effect of the bare tool and insulated tool on anode profile and current density distribution was investigated here, as shown in Fig. 3a, b. The light gray shaded rectangle shows position of the tool. Figure 3a shows that when bare tool is chosen, the distribution of current density is evidently dispersed an extensive range of the nearby surface go through stray current of the machined region. The removal of material from this region is known as stray current attacking [13], which generally caused bell-mouth profile [14]. On the other hand, Fig. 3b shows, when insulated tool is used, the current density distribution focuses on the machined zone. The current spreading from the cathode can be limited by the insulated layer and restricted to a lesser region.

**Non-Isothermal Laminar Flow.** The non-isothermal laminar flow simulation starts with independent simulation of the laminar fluid flow. The outcome of this simulation depends on the flow field characterization through velocity field. Figure 3 shows the electrolyte velocity magnitude (c) with bare tool and (d) with insulated tool. It is clear from Fig. 3c that the velocity is more in the machined zone because of the formation of bell-mouth and in the case of an insulated tool, the velocity is comparatively less. The velocity profile has an influence on temperature distribution, where the temperature occurs because of Joule’s heating, conduction, and convection.

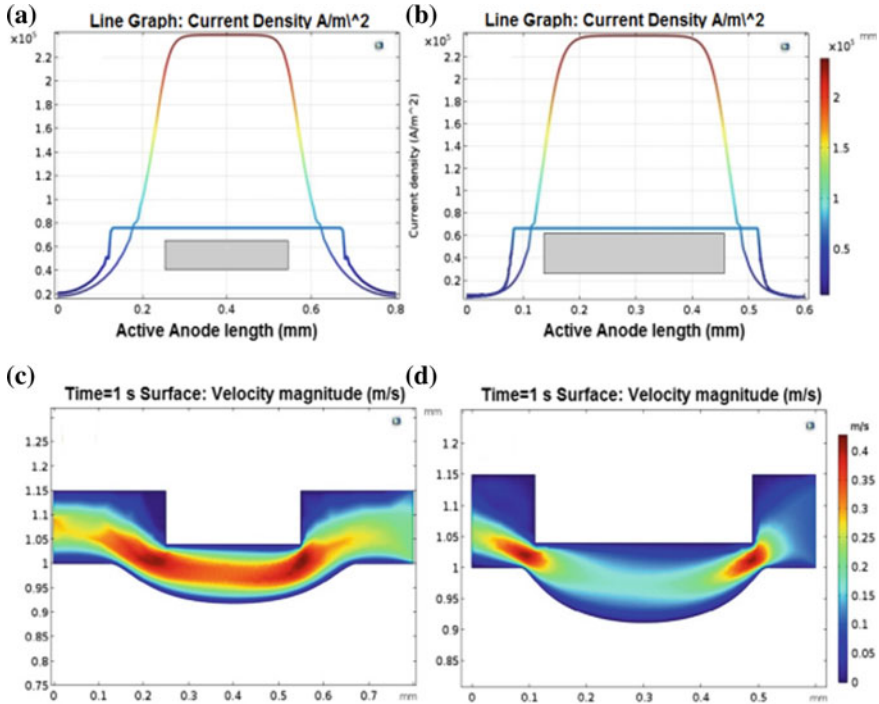


**Fig. 3** Current density distribution and anode profile of, **a** bare tool, **b** insulated tool, velocity magnitude, **c** with bare tool, and **d** with insulated tool

The temperature distribution simulation of the electrolyte follows the velocity profile computation. Comparing Fig. 4a, b with c, d, it can be observed that the distribution of temperature with bare tooltip is extremely asymmetric.

With insulated tooltip, the distribution of temperature turns out to be more symmetric because of the insulated layer restricting effect on the electrolyte convection. Comparing Fig. 4a, b, it can be observed that with the increasing of time in bare

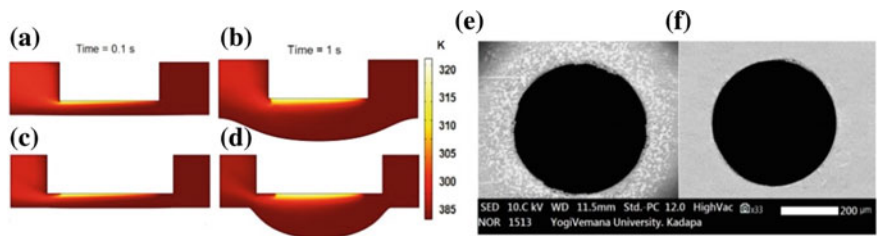


**Fig. 4** Temperature distribution of bare tool, **a** at time = 0.1 s, **b** at time = 1 s and insulated tool, **c** at time = 0.1 s, **d** at time = 1 s, SEM images of the machined hole with, **e** bare tool, **f** insulated hole

tooltip, the distribution of temperature becomes more symmetric. The temperature increases to some extent and presents even trends only in the case of insulated tooltip. Therefore, to obtain high machining accuracy, a stable environment temperature is predicated.

## 5 Experimental Verification

The experiments for both the bare tool and insulated tool of the optimum combination process parameters were conducted for compression. The simulation results are qualitatively compared with experimental results. The surface quality and entrance shape are used to estimate the machine accuracy. Figure 4e, f shows the SEM images of the machined holes at entrance. The Fig. 4e which is machined with the bare tool clearly shows evidence of a stray current attack region, entrance shape is fairly asymmetric and has bell-mouth shape. Insulated tool machined hole is shown in Fig. 4f which is clearly evident for no stray current attack. The experimental results thus well agree with the simulation results of a more intense current density distribution and better non-isothermal fluid flow using insulated tip tool.

## 6 Conclusion

In this paper, an experimental investigation has been carried out to know optimal combination levels of process parameters using Taguchi analysis method and also to find the influence of process parameters using ANNOVA method during machining microhole on Al 7075 T6 alloy on diametrical overcut using ECMM process. It has been made an attempt to model and simulate the ECMM process for an optimum combination of process parameters with the bare tool and insulated the tool using COMSOL Multiphysics V5.3a software. Based on the experimental and simulated results and analysis, the following conclusions can be made.

1. The optimal combination levels of process parameters were voltage of 6 V, the electrolyte concentration of 30 g/l, and frequency of 40 Hz.
2. From ANNOVA analysis, the most significant process parameter that influences lower OC is voltage and the electrolyte is also considerably influenced factor.
3. The multiphysics simulation results very closely agree with the experimental results. Therefore, it can be selected as substitute for the costly trial and error method.
4. The simulated and experimental results propose the use of the insulated tool which is able to produce the high-quality hole without any stray current attacking zone, good from minimum overcut, and accuracy.

**Acknowledgements** The authors thank the management of Sona College of Technology (Autonomous Institution), Salem, Tamil Nadu for the encouragement and support. The authors also thank Dr. P. Suresh in-charge for CNM/CMM lab, Department of Mechanical Engineering, Sona College of Technology, Salem, Tamil Nadu for his supervision and allowing me to utilize the microECM setup with pulse rectifier and optical microscope.

## References

1. Rajurkar KP, Levy G, Malshe A, Sundaram MM, McGeough J, Hu X, Resnick R, DeSilva A (2006) Micro and nano machining by electro-physical and chemical processes. *CIRP Ann Manuf Technol* 55(2):643–646
2. Ott EA, Groh JR, Banik A, Dempster I, Gabb TP, Liu X, Mitchell A, Sjoberg GP, Wusatowska-Sarnek A (2010) Superalloys, the most successful alloy system of modern times-past, present and future. TMS (The Minerals, Metals & Materials Society) (2010)
3. Muthuramalingam T, Mohan B (2015) A review on influence of electrical process parameters in EDM process. *J Arch Civ Mech Eng* 15(1):87–94
4. Ryu SH (2009) Micro fabrication by electrochemical process in citric acid electrolyte. *J Mater Process Technol* 209(6):2831–2837
5. Spieser A, Ivanov A (2013) Recent developments and research challenges in electrochemical micromachining ( $\mu$ ECM). *Int J Adv Manuf Technol* 69:563–581
6. Ghoshal B, Bhattacharyya B (2015) Investigation on profile of microchannel generated by electrochemical micromachining. *J Mater Process Technol* 222:410–421
7. Ghoshal B, Bhattacharyya B (2014) Shape control in micro borehole generation by EMM with the assistance of vibration tool. *Precision Eng* 38(1):127–137
8. Deconinck D, Van Damme S, Deconinck J (2012) The temperature dependent multi-ion model for time accurate numerical simulation of the electrochemical machining process. Part I: Theoretical basis. *Electrochim Acta* 60:321–328. <https://doi.org/10.1016/j.electacta.2011.11.070>
9. Fang X, Qu N, Zhang Y (2014) Effect of pulsating electrolyte flow in electrochemical machining. *J Mater Process Technol* 214(1):36–43
10. Wu J, Wang H, Chen X, Cheng P, Ding G, Zhao X, Huang Y (2012) Study of a novel cathode tool structure for improving heat removal in electrochemical micro-machining. *Electrochim Acta* 75:94–100
11. Kawanaka T, Kato S, Kunieda M (2014) Selective surface texturing using electrolyte jet machining. *Procedia CIRP* 13:345–349. <https://doi.org/10.1016/j.procir.2014.04.058>
12. Jain VK, Lal GK, Kanetkar Y (2005) Stray current attack and stagnation zones in electrochemical drilling. *Int J Adv Manuf Technol* 26(5–6):527–536
13. Chen X, Qu N, Li H, Guo Z (2015) Removal of islands from micro-dimple arrays prepared by through-mask electrochemical micromachining. *Precis Eng* 39:204–211
14. Liu Y, Zhu D, Zeng Y, Yu H (2011) Development of microelectrodes for electrochemical micromachining. *Int J Adv Manuf Technol* 55(1–4):195–203

# FEM Modeling of Coated Tools to Study the Influence of Coating Thickness



M. Khirod Kumar, Manne Hareesh, P. Vamsi Krishna  
and S. Sambhu Prasad

**Abstract** The aim of this paper is to study the performance of coated tools in machining with multilayer coatings. The coatings are made usually by using PVD or CVD techniques, and the coating material should be in such a way that it should make a very strong bond with the base material. In this paper, FEM model is developed by considering workpiece as AISI 1045 and tool as three-layered (TiC/Al<sub>2</sub>O<sub>3</sub>/TiN) coated tungsten carbide. Deform 2D software is used to simulate the model. Initially, the model is simulated at a different feed rate to observe the temperature distributions, and then, outcomes are compared with the experimental values to validate the model. After ensuring the accuracy of the developed model, the performance of tungsten carbide coated tool is studied by using this model. The influence of coating thickness is observed at the same machining conditions. Cutting forces, cutting temperature and effective strains are measured for all the combination of coatings selected in this study.

**Keywords** Coated tools · Multilayer coating · FEM analysis

## 1 Introduction

In conventional machining processes, getting good dimensional accuracies and surface finish is difficult. Available alternatives to get the quality of the product in the machining technologies are cutting fluids, nanofluids, minimum quantity lubrication (MQL), solid lubricates, coating technologies, etc. Coating technology has become more significant in machining technologies, and most of the coated tools are produced by Chemical Vapor Deposition (CVD) or Physical Vapor Deposition (PVD).

---

M. Khirod Kumar (✉) · Manne Hareesh · P. Vamsi Krishna  
Department of Mechanical Engineering, National Institute of Technology,  
Warangal, Warangal, India  
e-mail: [khirodmech@gmail.com](mailto:khirodmech@gmail.com)

S. Sambhu Prasad  
Department of Mechanical Engineering, Pragathi Engineering College, Surampalem, India

© Springer Nature Singapore Pte Ltd. 2020  
H. K. Voruganti et al. (eds.), *Advances in Applied Mechanical Engineering*,  
Lecture Notes in Mechanical Engineering,  
[https://doi.org/10.1007/978-981-15-1201-8\\_96](https://doi.org/10.1007/978-981-15-1201-8_96)



The primary coating was a layer of TiC of 10–12  $\mu\text{m}$  of thickness produced by CVD; during the deposition, some part of carbon was taken from the hard substrate thereby having imbalance of carbon at the interface coating and substrate, and it causes brittle nature and leads to the chipping of cutting edge; next development was TiN which prevents decarburizing of hard metal surface, but the coating is in gold color, and it does not adhere much well to hard substrate; TiN is a good diffusion barrier than TiC, but TiC has good abrasion resistance. And to get the thermal insulation, ceramic coatings came into the picture which includes  $\text{Al}_2\text{O}_3$ ,  $\text{Cr}_2\text{O}_3$ , etc.

Bhatt et al. [1] observed that the three-layered (TiCN/ $\text{Al}_2\text{O}_3$ /TiN) CVD coating shows the maximum wear resistance at high speeds and low feeds. Jindal et al. [2] investigated performance of TiN, TiCN and TiAlN PVD coatings at high and low-speed machining Grzesik [3]. It was observed that the difference in the measured values of the interface temperatures when comparing single and three-layered coatings reached 290 °C. Grzesik et al. [4] observed that in three-layered coated tools, the maximum differences of chip-tool interface temperature were about 10%. PalDey and Deevi [5] studied that hard coatings can enhance the performance of cutting tools in high-speed machining. Loladze [6] and Nouari and Molinari [7] were the first to transfer the described methodology to three-dimensional tool wear analysis simulating the tool wear for the machining of AISI 1045 with uncoated WC tools. Binder et al. [8] reported tool wear simulation by using the Usui model for coated (TiAlN) and uncoated tools.

In the present work, the model is simulated by using Deform 2D by considering workpiece as AISI 1045 and tool as three-layered (TiC/ $\text{Al}_2\text{O}_3$ /TiN) coated (WC) tungsten carbide. Initially, the model is simulated at a different feed rate to observe the temperature distributions and then comparing with the literature for the validation of the model. Once the validation is done, by changing the coating thickness, few combinations are made, and the model is simulated at all the combination by keeping all input parameters constant. From each combination, cutting forces in both the directions, cutting temperature and effective strains are measured, and among all the combination, one is selected such that all the output parameters are optimized.

## 2 Modeling and Simulation

In this work, the model is simulated by turning of AISI 1045 steel using three-layered CVD coated (TiC/ $\text{Al}_2\text{O}_3$ /TiN) WC tool. DEFORM 2D is used for FEA. DEFORM 2D working is based on an implicit Lagrangian method. At the starting stage of simulation, the process parameters for workpiece and tool insert must be defined. During simulation, an initial temperature of 20 °C, shear friction factor of 0.5, heat transfer coefficient of 45 N/s/mm/°C and no coolant are used. The thickness of the coating layers has been defined as 6  $\mu\text{m}$  for TiC, 3  $\mu\text{m}$  for  $\text{Al}_2\text{O}_3$  and 1  $\mu\text{m}$  for TiN, and a three-layered CVD coated (TiC,  $\text{Al}_2\text{O}_3$  and TiN) and tungsten carbide tool are used. In the simulation, the workpiece and tool insert are assumed as plastic and rigid

**Fig. 1** Coated tool with mesh before the simulation

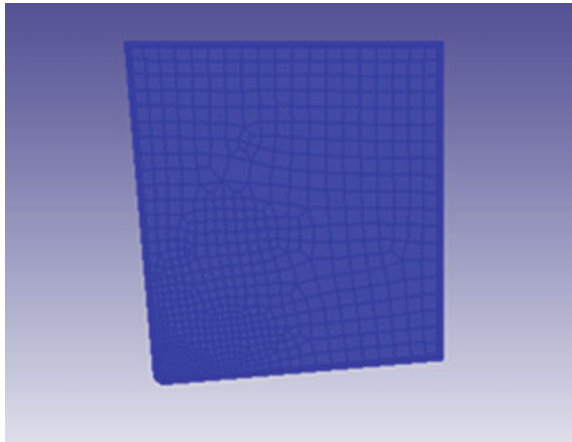
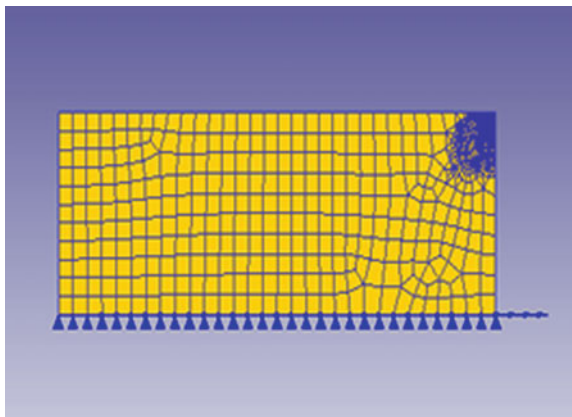


**Fig. 2** Workpiece with mesh generation before the simulation



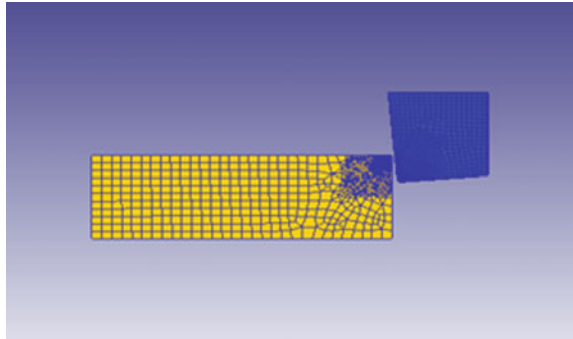
material. The total length for workpiece has been taken as 3 mm, and length of cut has been taken as 2 mm.

The physical and mechanical properties of AISI 1045 steel are density 7800 kg/m<sup>3</sup> modulus of elasticity 205 GPa, specific heat capacity[c] 420 J/kg °C, thermal conductivity[k] 38 W/m/K, melting. Figures 1, 2 and 3 show mesh generation of the tool, workpiece and positioning before simulation starts.

## 2.1 Material Modeling

Johnson–Cook model is suitable for modeling material because high strain, strain rate, strain hardening and nonlinear material properties are involved in the turning process. The material model is given in Eq. (1)

**Fig. 3** Positioning of the workpiece and tool before the simulation



$$\sigma = (A + B\epsilon^n) \left( 1 + C \ln \left( \frac{\dot{\epsilon}}{\dot{\epsilon}_0} \right) \right) \left[ 1 - \left( \frac{T - T_r}{T_m - T_r} \right)^m \right] \tag{1}$$

The first is the elastic–plastic term, and it represents strain hardening. The second one is the viscosity term, and it shows that flow stress of material increases when the material is exposed to high strain rates. The last one is temperature softening term. *A*, *B*, *C*, *n* and *m* are material constants that are found by material tests. *T* is instantaneous temperature, *T<sub>r</sub>* is room temperature, and *T<sub>m</sub>* is the melting temperature of a given material. Johnson–Cook material model assumes that flow stress is affected by strain, strain rate and temperature independently. The model constants for tool and workpiece are shown in Tables 1, 2 and 3.

**Table 1** Johnson–Cook model constants for AISI 1045 [8]

<i>A</i> (MPa)	<i>B</i> (MPa)	<i>C</i> (–)	<i>n</i> (–)	<i>m</i> (–)	<i>T<sub>m</sub></i> (K)	Strain rate (S <sup>-1</sup> )
546	487	0.25	0.027	0.631	1733	0.631

**Table 2** Johnson–Cook model constants for WC coated tool

<i>A</i> (MPa)	<i>B</i> (MPa)	<i>C</i> (–)	<i>n</i> (–)	<i>m</i> (–)	<i>T<sub>m</sub></i> (K)	Strain rate
1200	1100	0.35	0.475	1	2800	1

**Table 3** Cutting conditions and tool geometry used in the simulation

Tool rake angle (°)	5
Tool clearance angle (°)	–5
Cutting edge radius (µm)	0.33
Length of cut (mm)	2
Cutting speed (m/min)	103.2

## 2.2 *MultiLayer Coatings*

The single-layer coating is useful for many engineering applications, although there is some situation where single-layer coating does not give optimum results which lead to the development of multilayer coatings.

## 2.3 *Results and Discussions*

In this, the workpiece AISI1045 steel and three-layered WC coated tool have been selected to perform the simulation. The aim is to evaluate the influence of various output parameters, i.e., cutting forces in *X*- and *Y*-directions, effective strain and temperature by varying coating thicknesses (TiC/Al<sub>2</sub>O<sub>3</sub>/TiN).

## 2.4 *Effects of Coatings*

The main aim of the coatings is to provide high hardness, resistance to wear and chemical stability. Besides, coatings are helpful to increase the tool life by 2–3 times by decreasing the wear rate in high-speed machining of steel and cast. Tool life is increased in a large amount by coating with one layer of TiN produced by CVD process because a single layer of TiN acts as a diffusion barrier TiC provides good surface roughness and reduction of built up edge (BUE) when compared with the uncoated ones. The inert nature of Al<sub>2</sub>O<sub>3</sub> and TiC will reduce the cratering and has high resistance to abrasion and hence low flank wear. Al<sub>2</sub>O<sub>3</sub> also acts as a thermal barrier because of very low thermal conductivity.

## 2.5 *Validation of the Model*

The model is simulated by considering different feed rates at constant cutting speed (220 m/min) and depth of cut (1 mm). The multilayered (TiC/Al<sub>2</sub>O<sub>3</sub>/TiN) coated tool has coated thicknesses of 5 μm each. The interface temperature is observed at all feed rates and compared with the experimental values [3] shown in Table 4. The values which are observed to be compared by the experimental values and error are tabulated.

Figure 4 shows that the temperature obtained from the simulation is compared with experimental values for the validation. As the feed rate increases, temperature increases.

**Table 4** Comparison between simulation and experimental values (cutting speed = 220 m/min, depth of cut = 1 mm)

S. No.	Feed rates (mm/rev)	Temperature observed in simulation (°C)	Temperature in literature (°C)	Error (%) (°C)
1	0.05	551	560	1.6
2	0.1	602	630	4
3	0.15	625	640	2.38
4	0.2	639	670	4.68
5	0.25	731	720	1.25

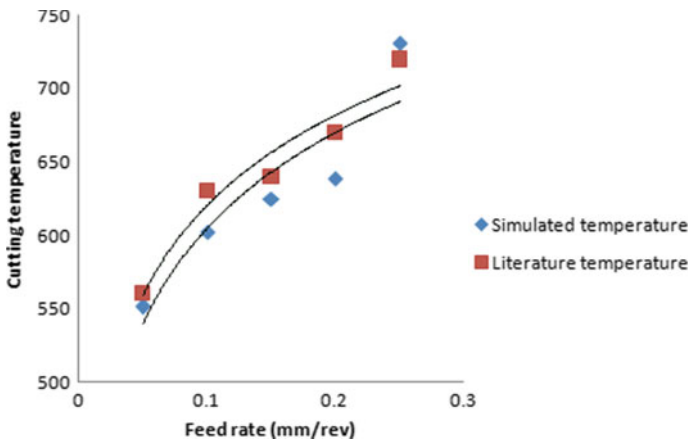


**Fig. 4** Temperature at different feed rates

### 2.6 Study on Multilayer Coatings Performance in Orthogonal Cutting

The model is simulated by considering process parameters, i.e., cutting speed of 103.2 m/min, depth of cut of 0.3 mm and feed rate is 0.16 mm/rev by varying coating layer thicknesses of TiC, Al<sub>2</sub>O<sub>3</sub> and TiN. Here, present work is focused to find the best combination of thicknesses of coated materials where the output parameters, i.e., cutting force, temperature, effective strains are observed. All the input parameters and the combination of coating layer thicknesses are shown in Table 5.

**Table 5** Combination of layer thicknesses used in the simulation ( $v = 103 \text{ m/min}$ ,  $f = 0.12 \text{ mm/rev}$  and depth of cut =  $0.3 \text{ mm}$ )

S.No.	TiC ( $\mu\text{m}$ )	$\text{Al}_2\text{O}_3$ ( $\mu\text{m}$ )	TiN ( $\mu\text{m}$ )
1	6	3	1
2	5	3	1
3	7	3	1
4	6	4	1
5	6	2	1
6	6	3	2
7	6	3	3

### 2.7 Cutting Force

Figure 5 shows a variation of cutting forces in both direction  $X$  and  $Y$  when the coating thicknesses of TiC is  $6 \mu\text{m}$ ,  $\text{Al}_2\text{O}_3$  is  $3 \mu\text{m}$ , and TiN is  $1 \mu\text{m}$  at constant cutting conditions. The average cutting forces at the tool-chip interaction in  $X$ - and  $Y$ -directions from the simulation are observed to be  $642$  and  $222 \text{ N}$ .

Cutting forces always reduce by using coatings on the cutting tool when compared with the uncoated cutting tool. For TiC, as the coating thickness varies from  $5$  to  $7 \mu\text{m}$ , the forces in  $x$  and  $y$ -direction changed as shown in Fig. 6, as the coating thickness varies cutting force increased from  $618$  to  $642 \text{ N}$  and then again increased to  $649 \text{ N}$ , consequently the force in  $y$  the direction force is constant at thicknesses  $5$  and  $6 \mu\text{m}$  and then increased to  $224 \text{ N}$ , it is observed that the force in  $Y$ -direction did not affect much because the main cutting action is carried out in the  $X$ -direction. As the thickness of coating increases, the sharpness of cutting edge gets reduced, so it requires more force to cut the material.

For  $\text{Al}_2\text{O}_3$ , as the coating thickness varies from  $2$  to  $4 \mu\text{m}$ , the forces in  $x$ - and  $y$ -direction changed as shown in the figure below, as the coating thickness varies, cutting force increased from  $612$  to  $630 \text{ N}$  and again increased from  $630$  to  $641 \text{ N}$ ,

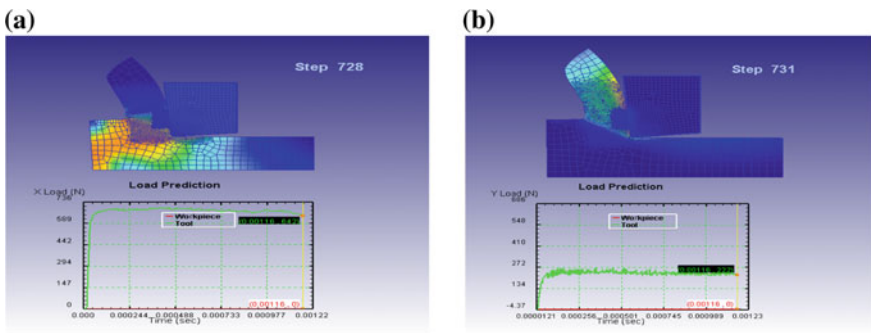


**Fig. 5** a, b Cutting forces in  $X$ - and  $Y$ -directions at TiC =  $6 \mu\text{m}$ ,  $\text{Al}_2\text{O}_3 = 3 \mu\text{m}$  and TiN =  $1 \mu\text{m}$

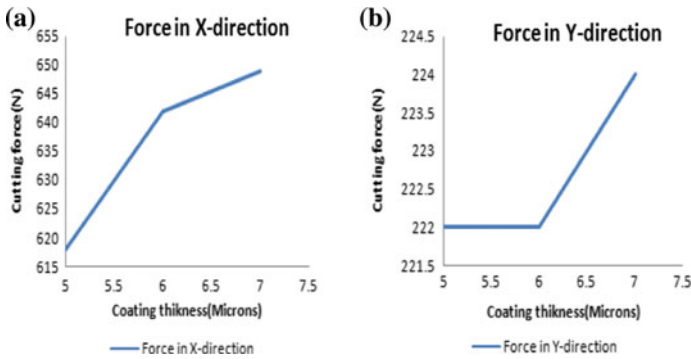


Fig. 6 a, b Cutting forces in X- and Y-directions when TiC varied from 5 to 7  $\mu\text{m}$

consequently the force in y the direction force is increased from 219 to 222 N and then decreased to 222–213 N.  $\text{Al}_2\text{O}_3$  does not have much effect on cutting forces when many alternating layers of two materials are deposited can lead to improvement in performance over a mixed coating even if two materials do not have specific functional requirements in the intended application (Fig. 7).

As TiN provides low friction, the values of cutting forces reduce if TiN coating is used. For TiN, as the coating thickness varies from 1 to 3  $\mu\text{m}$ , the forces in x- and y-direction changed as shown in Fig. 8, as the coating thickness varies, cutting force increased from 618 to 630 N and then again increased from 603 to 643 N, consequently the force in y the direction force increased from 222 to 223 N and then reduced from 223 to 220 N.

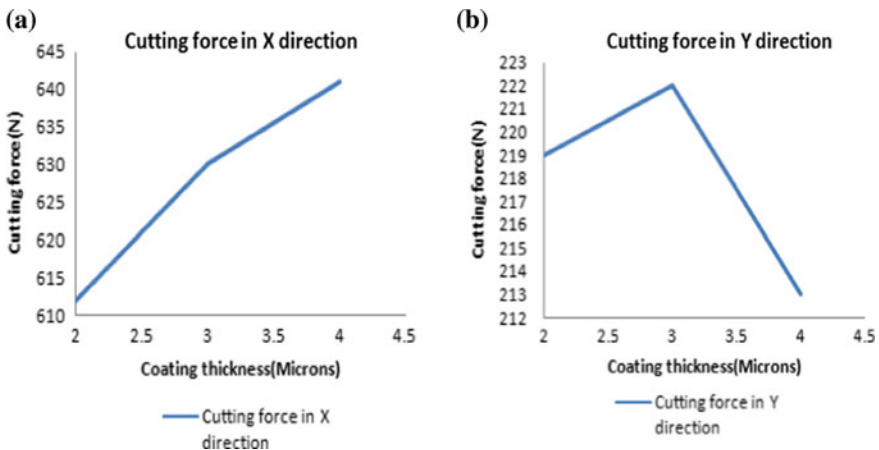
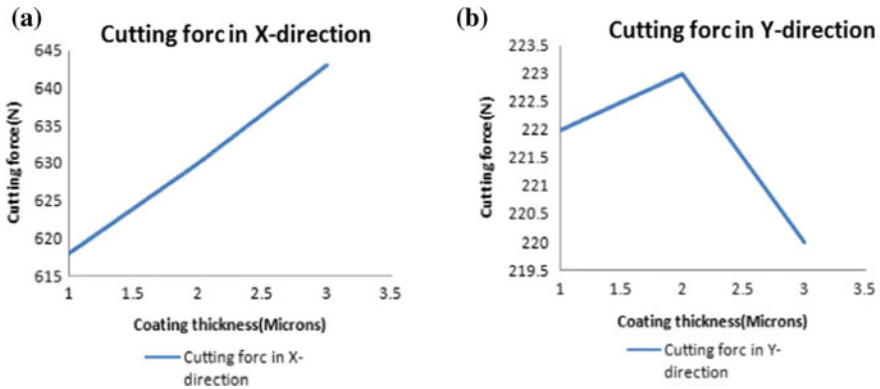


Fig. 7 a, b Cutting forces in X- and Y-directions when  $\text{Al}_2\text{O}_3$  varied from 2 to 4  $\mu\text{m}$



**Fig. 8 a, b** Cutting forces in X- and Y-direction when TiN varied from 1 to 3  $\mu\text{m}$

### 2.8 Cutting Temperature

The model is simulated at constant cutting conditions; the temperature is observed at the tool-chip interface is around 641  $^{\circ}\text{C}$ .

In Fig. 9, as the coating thickness varied from 5 to 6  $\mu\text{m}$ , cutting temperature reduced from 648 to 641  $^{\circ}\text{C}$ , and then, if thickness varied from 6 to 7  $\mu\text{m}$ , then the temperature reduced from 641 to 640  $^{\circ}\text{C}$ . Because of being inert nature of TiC, as the coating thickness increases, temperature reduces gradually.

Figure 10 indicates the variation of temperature when the thickness of  $\text{Al}_2\text{O}_3$  varies from 2 to 4  $\mu\text{m}$ , and as the coating thickness varied from 2 to 4  $\mu\text{m}$ , cutting temperature reduced from 642 to 641  $^{\circ}\text{C}$  and then again decreased from 641 to 635  $^{\circ}\text{C}$ . As the thickness of  $\text{Al}_2\text{O}_3$  increases, temperature reduces because  $\text{Al}_2\text{O}_3$  has low  $k$  value, and it does not allow heat produced in machining through it. Figure 11 shows that as the coating thickness varied from 1 to 3  $\mu\text{m}$ , cutting temperature reduced

**Fig. 9** Variation of temperature when the thickness of TiC varied from 5 to 7  $\mu\text{m}$

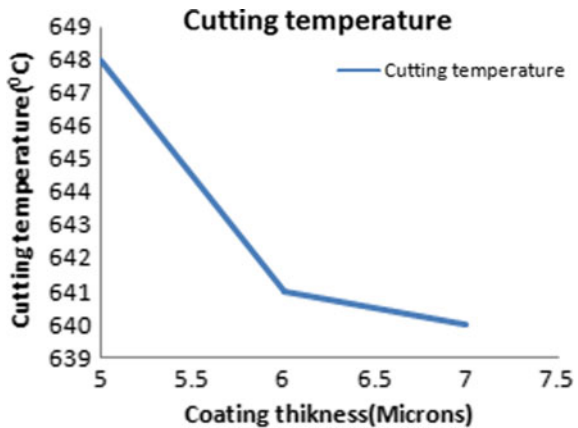




**Fig. 10** Variation of temperature when the thickness of  $Al_2O_3$  varied from 2 to 4  $\mu m$

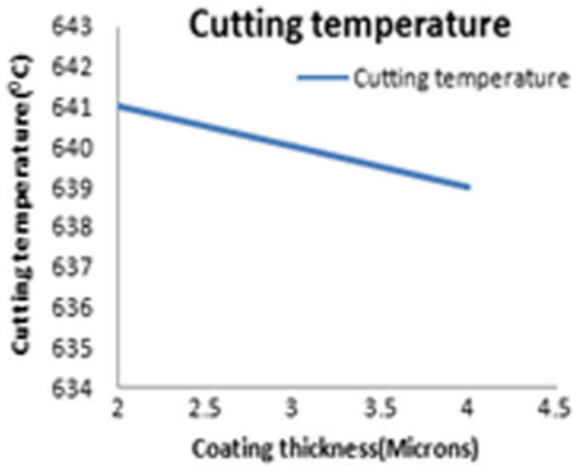
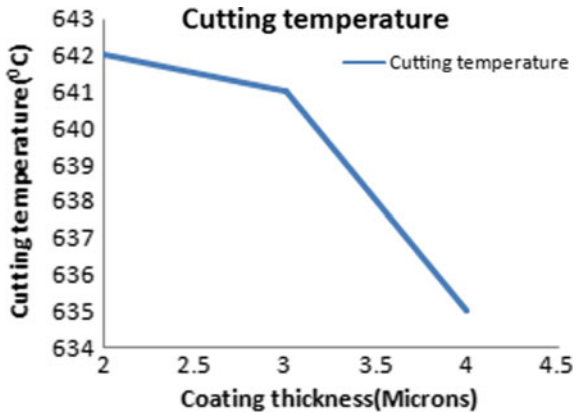


**Fig. 11** Variation of temperature when the thickness of TiN varied from 1 to 3  $\mu m$



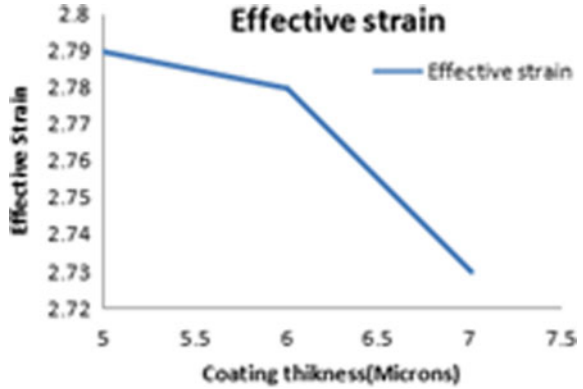
from 641 to 640 °C and then again reduced 640–639 °C, and as coating thickness of TiN increases, temperature reduced.

### 3 Effective Strain

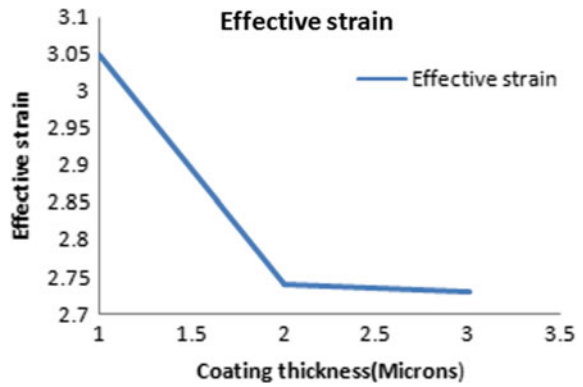
Figure 12 shows effective strain when coated layer thicknesses of Ti C is 6  $\mu m$ ,  $Al_2O_3$  is 3  $\mu m$ , and TiN is 1  $\mu m$ . Model is simulated at constant condition; effective strain is observed to be 2.73

Figure 13 indicates the variation of effective strain when the thickness of  $Al_2O_3$  varies from 1 to 3, and as the coating thickness varied from 1 to 2  $\mu m$ , then the effective strain is decreased from 3.05 to 2.74 and the constant from 2 to 3  $\mu m$ . Cutting

**Fig. 12** Variation of effective strain when the thickness of TiC changes from 5 to 7  $\mu\text{m}$



**Fig. 13** Variation of effective strain when the thickness of  $\text{Al}_2\text{O}_3$  changes from 2 to 4  $\mu\text{m}$



temperature is related to the effective strain. As the plastic deformation increases, temperature increases which in turn leads to the increase in effective strain. Figure 14 indicates the variation of effective strain when the thickness of TiN varies from 1

**Fig. 14** Variation of effective strain when the thickness of TiN changes from 1 to 3  $\mu\text{m}$

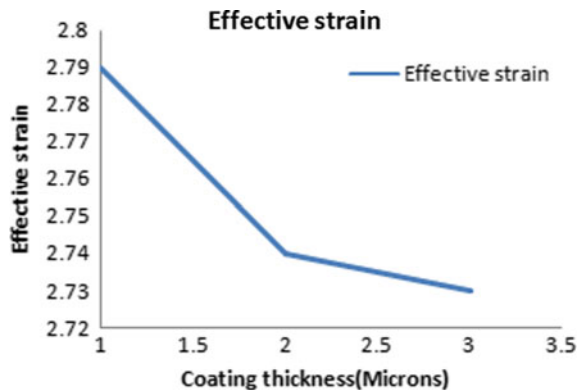


**Table 6** Results for all the combinations of coating thicknesses

S.No	TiC ( $\mu\text{m}$ )	Al <sub>2</sub> O <sub>3</sub> ( $\mu\text{m}$ )	TiN ( $\mu\text{m}$ )	$F_x$ (N)	$F_y$ (N)	Temp ( $^{\circ}\text{C}$ )	Effective strain
1	6	3	1	642	222	641	2.78
2	5	3	1	618	222	648	2.79
3	7	3	1	649	224	640	2.73
4	6	4	1	641	213	635	2.73
5	6	2	1	612	219	642	3.05
6	6	3	2	630	223	640	2.77
7	6	3	3	643	220	639	2.74

to 3, and as the coating thickness varied from 1 to 3  $\mu\text{m}$ , then the effective strain is increased from 2.74 to 2.7.

Table 6 shows the results for all the combination of coating thicknesses. After ensuring the accuracy of the developed model, the performance of tungsten carbide coated tool is studied by using this model. The influence of coating thickness is observed at the same machining conditions. Cutting forces, cutting temperature and effective strains are measured for all the combination of coatings selected in this study. Based on the results, it observed that forces are optimized when TiC = 6  $\mu\text{m}$ , Al<sub>2</sub>O<sub>3</sub> = 2  $\mu\text{m}$  and TiN = 1  $\mu\text{m}$ . Favorable results for temperature and effective strain are at TiC = 6  $\mu\text{m}$ , Al<sub>2</sub>O<sub>3</sub> = 4  $\mu\text{m}$  and TiN = 1  $\mu\text{m}$ .

## 4 Conclusion

The aim of the present work is to find the best combination of thicknesses of coated materials where the output parameters like cutting force, temperature and effective strains are observed. After ensuring the accuracy of the developed model, the performance of tungsten carbide coated tool is studied by using this model. The influence of coating thickness is observed at the same machining conditions. Cutting forces, cutting temperature and effective strains are measured for all the combination of coatings selected in this study. Based on the results, it observed that cutting forces are optimized when TiC = 6  $\mu\text{m}$ , Al<sub>2</sub>O<sub>3</sub> = 2  $\mu\text{m}$  and TiN = 1  $\mu\text{m}$ . Favorable results for temperature and effective strain are at TiC = 6  $\mu\text{m}$ , Al<sub>2</sub>O<sub>3</sub> = 4  $\mu\text{m}$  and TiN = 1  $\mu\text{m}$ .

## References

1. Bhatt A, Attia H, Vargas R, Thomson V (2010) Wear mechanisms of WC coated and uncoated tools in finish turning of Inconel 718. Tribol Int 43:1113–1121

2. Jindal PC, Santhanam AT, Schleinkofer U, Shuster AF (1999) Performance of PVD TiN, TiCN, and TiAlN coated cemented carbide tools in turning. *Int J Refract Metal Hard Mater* 17:163–170
3. Grzesik W (1999) Experimental investigation of the cutting temperature when turning with coated indexable inserts. *Int J Mach Tools Manuf* 39:355–369
4. Grzesik W, Bartoszek M, Nieslony P (2005) Finite element modelling of temperature distribution in the cutting zone in turning processes with differently coated tools. *J Mater Proc Technol* 164–165:1204–1211
5. PalDey S, Deevi SC (2003) Single layer and multilayer wear resistant coatings of (Ti, Al) N. *Mater Sci Eng A* 342:58–79
6. Loladze TN (1981) Of the theory of diffusion wear. *CIRP Ann Manuf Technol* 30:71–76
7. Nouari M, Molinari A (2005) Experimental verification of a diffusion tool wear model using a 42CrMO<sub>4</sub> steel with an uncoated cemented tungsten carbide at various cutting speeds. *Wear* 259:1151–1159
8. Binder M, Klocke F, Lung D (2015) Tool wear simulation of complex shaped coated cutting tools. *Wear* 330–331:600–607

# Effect of Graphene Nanofluid on Machining Inconel 718



Siva Bevara, M. Amrita, Sanjay Kumar and B. Kamesh

**Abstract** Cutting fluids have superior convective and conductive heat transfer coefficient, good lubrication and better chip removal rate from the cutting zone. But when applied in large quantities, as flood machining, its treatment, and disposal increase the economic burden on industries. Application of just sufficient quantity of cutting fluid exactly at the cutting zone as Minimum Quantity Lubrication (MQL) is found to be an alternative approach to flood machining. But it requires the use of cutting fluids with enhanced properties. Researchers suggested that nanofluid is the latest concept to achieve high performance of cooling and lubrication effect in machining. This project mainly focuses on performance evaluation of Minimum Quantity Lubrication (MQL) application of graphene nano cutting fluid while turning Inconel 718 alloy at constant cutting conditions. Different weight proportions (0.1wt%, 0.3wt%, 0.5wt%) of graphene are mixed with soluble oil using TX 100 as a surfactant. Machining performance is evaluated by measuring cutting forces, cutting temperature, surface roughness and tool wear. Performance is compared with dry machining and MQL application of cutting fluid without graphene.

**Keywords** Minimum quantity lubrication · Tool wear · Graphene · Inconel 718

## 1 Introduction

Nickel-based superalloys (Inconel 718) are widely used in the aerospace industry due to its unique properties like oxidation resistance, corrosion resistance and ability to retain mechanical strength even at very high temperatures. But their lower thermal conductivity, work hardenability, hardness, and affinity for tool material, causes the cutting tools to wear very rapidly. Cutting fluid is widely used for cooling and lubrication, disposal of chip, improvement of machining accuracy and surface finish

---

S. Bevara · M. Amrita (✉) · S. Kumar · B. Kamesh  
Gayatri Vidya Parishad College of Engineering (A), Visakhapatnam 530048,  
Andhra Pradesh, India  
e-mail: [amrita@gvpce.ac.in](mailto:amrita@gvpce.ac.in)

© Springer Nature Singapore Pte Ltd. 2020  
H. K. Voruganti et al. (eds.), *Advances in Applied Mechanical Engineering*,  
Lecture Notes in Mechanical Engineering,  
[https://doi.org/10.1007/978-981-15-1201-8\\_97](https://doi.org/10.1007/978-981-15-1201-8_97)

and extension of tool life. But their treatment and disposal are of economic concern to industries. Also, cutting fluids impose serious respiratory-related problems in employees. In order to have a sustainable environment, application of cutting fluid as Minimum quantity lubrication is an alternative approach, where a small amount of cutting fluid is sprayed to the tooltip with compressed air. Many researchers worked on machining of Inconel 718 using different conditions: Dry machining, flood machining, MQL application, cryogenic machining, use of coated and self-lubricating tools. Kaynak [1] performed machining on Inconel 718 workpiece using dry, MQL, and cryogenic cooling conditions. Cutting forces, flank, notch and crater wear, temperatures, surface roughness, and chip morphology were studied. MQL application showed least cutting forces at low speed while cryogenic machining at high speeds. Numbers of nozzles were found to be significant in cryogenic machining. Paturi et al. [2] studied the effect of solid lubricant assisted minimum quantity lubrication (MQL) turning on finish quality of a machined surface. Tungsten Disulfide ( $WS_2$ ) solid lubricant powder was dispersed (0.5% wt.) in emulsifier oil-based cutting fluid. Compared to the MQL machining,  $WS_2$  solid lubricant assisted MQL machining gave a good improvement on finish quality of work material by 35%. Shokrani et al. [3] investigated the performance of cryogenic cooling, Minimum Quantity Lubricant (MQL) machining, and CryoMQL, to improve machinability and surface integrity of difficult to machine materials. Rapeseed oil was used at 60 ml/h. Cryogenic cooling resulted in increased hardness of material and hence rapid tool wear while CryoMQL doubled tool life by reducing tool wear and improved surface roughness by 18%. Sidik et al. [4] reviewed applications of nanofluids in MQL machining. Several aspects like preparation methods of nanofluids and enhancement in their thermal conductivity were discussed. Application of  $Al_2O_3$ , CNT,  $MoS_2$  and diamond nanoparticles in MQL machining was discussed in detail and they were found to reduce the coefficient of friction and wear effect. The stability and cost of production were identified as challenges in the application of nanofluid to machining. Najiha et al. [5] used water-based  $TiO_2$  nanofluids in MQL machining (milling) on aluminum alloy, AA6061-T6 at three different speeds: 5200, 5400 and 5600 rpm. 0.65 ml/min and 1.0 ml/min are used as flow rates for MQL machining.  $TiO_2$  nanoparticles were used in 0.5, 2.5 and 4.5%. Lesser adhesion and edge integrity were found to take place at higher MQL flow rate. 2.5% was found to be the best with respect to tool damage. Behera et al. [6] prepared nanofluids by mixing different concentrations of alumina ( $Al_2O_3$ ) and colloidal solution of silver (Ag) nanoparticles with water. Performed MQL machining and dry machining on the nickel-based alloy. Cutting forces, tool wear, chip thickness, surface tension and contact angle were measured.  $Al_2O_3$  nanofluid at 125 ml/h showed least cutting force due to the formation of tribofilm which reduced the sliding friction. Chip thickness, coefficient of friction is found to be less in MQL machining. Revuru et al. [7] presented a detailed review on different lubricating conditions such as dry machining, cryogenic machining, flood machining and MQL machining with nanofluids in machining titanium alloys. MQL was found to perform better than dry and flood machining, as it has the capability to enter the tool-chip interface via capillary action providing lubrication. Cryogenic cooling could provide lesser tool wear, forces, and better finish initially but extreme

cooling led to the increased hardness of machined surface leading to further increase in cutting forces and surface roughness.

Graphene has high thermal conductivity, lubricating property, high specific surface area and reduced particle clogging [8] compared to other nanoparticles. Ahammed et al. [9] reported higher enhancement in thermal conductivity with small concentration of graphene compared to metal oxides ( $\text{Fe}_3\text{O}_4$ ,  $\text{Al}_2\text{O}_3$ ,  $\text{TiO}_2$ ,  $\text{MgO}$ ) taken in relatively higher concentrations in water. In the present work, graphene-based cutting fluids of different concentrations are applied as MQL in machining Inconel 718 and their performance is compared with dry machining and MQL application of the conventional cutting fluid.

## 2 Experimentation

Graphene-based nanofluids are prepared in different concentrations: 0.1wt%, 0.3wt% and 0.5wt% by dispersing graphene in conventional soluble oil (1:20). Graphene of grade 'C' with an average diameter of 2 microns, thickness 6–8 nm and surface area  $500 \text{ m}^2/\text{g}$  procured from XG Sciences, USA is used. A Surfactant used is Triton X 100 in the same concentration as graphene to maintain stable dispersion. Graphene along with Triton X100 is first added to water and ultra-sonicated for an hour to get stable dispersion. Concentrated cutting oil is added to it in ratio 1:20 to form graphene dispersed cutting fluid. Cutting experiments are conducted using CDL6236 lathe machine with coated carbide tool CNMG120408MS KC5010 on Inconel 718 rod of 150 mm length and 30 mm diameter at constant cutting conditions: cutting velocity 74 m/min, depth of cut 0.5 mm and feed of 0.14 mm/rev. Machining is performed at different machining conditions such as dry machining, MQL machining using soluble oil without graphene (0wt%), MQL machining using 0.1wt%, 0.3wt% and 0.5wt% graphene dispersed cutting fluid. Cutting forces are measured by using Kistler dynamometer, cutting temperatures are measured by using Infra-Red (IR) thermometer Extech42570 and IR Camera Optris PI160. Tool wear is measured by using Metzer Toolmaker's Microscope with image acquisition. Surface roughness is measured by using Surftest 301 J. The emissivity value of Inconel 718 is taken as 0.33. An experimental setup is shown in Fig. 1.

## 3 Results and Discussion

### 3.1 Cutting Forces

Mean values of the feed force ( $F_y$ ), radial force ( $F_x$ ) and tangential force ( $F_z$ ) obtained from Kistler dynamometer are presented in Fig. 2 and are used for further analysis.

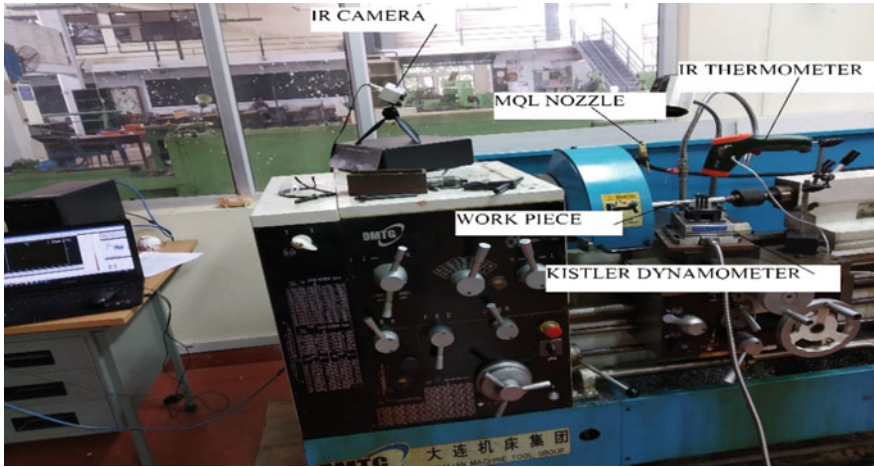
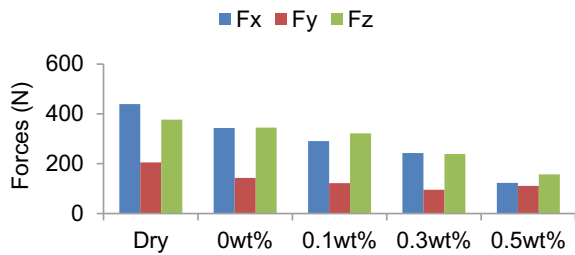


Fig. 1 Experimental setup

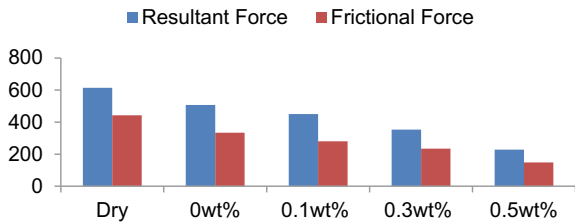
Fig. 2 Variation in radial force ( $F_x$ ), feed force ( $F_y$ ) and tangential cutting force ( $F_z$ )



Resultant forces and frictional forces in machining are calculated and are presented in Fig. 3.

Among all the components of forces, the feed force is found to be minimum. MQL machining showed less force when compared to dry machining. Almost all components of forces are found to decrease with an increase in the concentration of graphene. Resultant and frictional forces are also found to decrease with increase in the concentration of graphene. Cutting fluid with 0.5wt% showed the least cutting forces. The protective layer formed using suspended graphene helped in reducing

Fig. 3 Variation of resultant force and frictional force





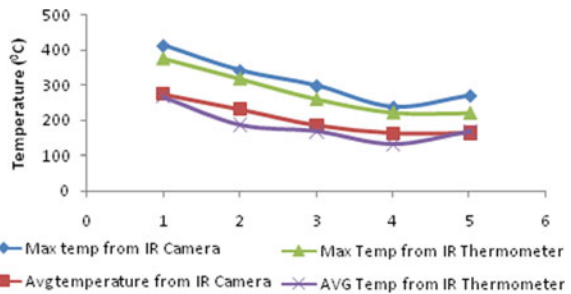
the cutting forces. Due to an increase in the volume of graphene in nano cutting fluid of 0.5wt% graphene nanofluid, the lubrication property became more, which led the cutting forces to decrease.

### 3.2 Cutting Temperature

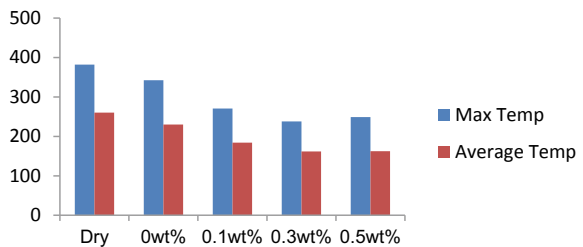
Figure 4 shows the variation of maximum and average cutting temperatures measured using both IR Thermometer and IR Camera. Variation in temperature was found in range 10°–50° with both devices. As IR Camera could measure temperature over an area, compared to IR thermometer which measures at a single point, IR camera showed higher temperatures.

Figure 5 shows the variation of maximum as well as average cutting temperature measured using IR Camera for all cases. Dry machining showed maximum temperature. MQL machining could reduce the temperature by providing cooling. The temperature was found to further decrease with the addition of graphene in cutting fluid. There may be enhanced thermal conductivity of the cutting fluid due to the addition of graphene. 0.5wt% graphene showed slightly higher average cutting temperature and maximum temperature than 0.3wt%. This may be due to an increase in viscosity of cutting fluid with increase in concentration of graphene as well as surfactant or there may be negative effect of more surfactant on thermal conductivity.

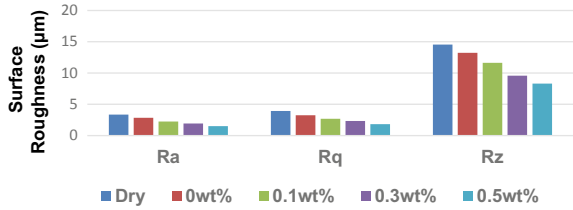
**Fig. 4** Variation in temperature for different machining operations



**Fig. 5** Variation in cutting temperature for different cases



**Fig. 6** Variation in surface roughness



### 3.3 Surface Roughness

Variation in all the measured values of surface roughness ( $R_a$ ,  $R_q$ ,  $R_z$ ) for all machining operations is shown in Fig. 6. Surface roughness values are less for MQL machining process when compared with dry machining. Among the different weight proportions of graphene nanofluids, 0.5wt% gave less surface roughness values. An increase in volume of graphene in nanofluid may have enhanced the lubrication property resulting in smooth machined surface.

### 3.4 Tool Wear

One of the most important parameters which have direct effect on the final quality of the product is tool wear. The performance of the tool and tool life is influenced by tool wear. Variation in the tool flank wear is shown in Fig. 7. Tool wear was found

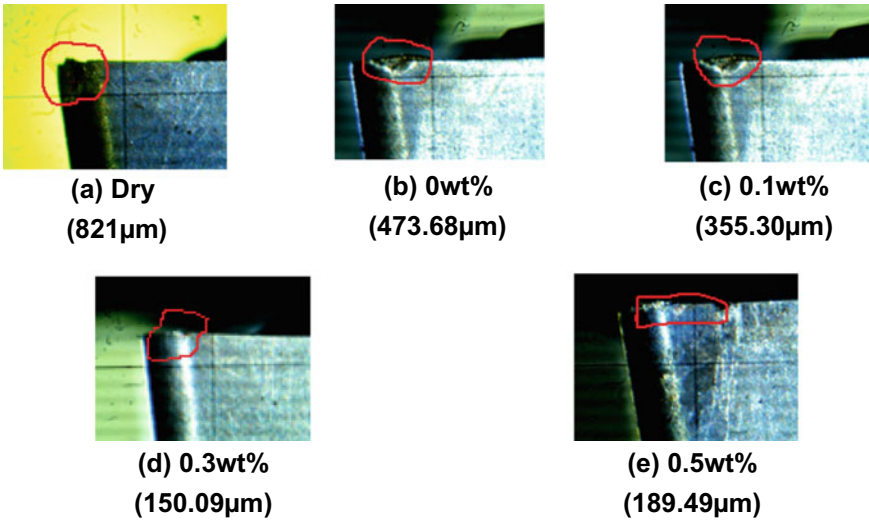


**Fig. 7** Variation of tool wear

to be maximum for dry machining, i.e. 821  $\mu\text{m}$ . MQL machining led to reduction in tool wear. Addition of 0.1wt% and 0.3wt% graphene insoluble oil led to a further reduction in tool wear. Addition of graphene and increase in its concentration may have increased the lubricating properties and thermal conductivity leading to reduced tool wear. Tool wear was found to increase with 0.5wt% compared to 0.3wt%. This is in line with the results obtained from cutting temperature. There may be reduction in the thermal properties or increase in viscosity of 0.5wt% compared to 0.3wt% which might have led to increase in tool wear. Increase in viscosity may have increased the size of MQL droplets preventing them to enter the cutting zone effectively.

## 4 Conclusions

1. The cutting forces decreased when the concentration of graphene increased. MQL machining with 0.5wt% of graphene showed least force with 74% reduction when compared to dry machining.
2. Cutting fluid with 0.5wt% showed slightly higher average cutting temperature and higher maximum temperature compared to 0.3wt%.
3. 0.5wt% graphene nanofluid gave least surface roughness.
4. Tool wear was found to be minimum with 0.3wt% graphene nanofluid.

**Acknowledgements** This work was supported by Science & Engineering Research Board F NO. ECR/2017/001172 as a research project. The authors are grateful to the Science & Engineering Research Board for providing financial support.

## References

1. Kaynak Y (2014) Evaluation of machining performance in cryogenic machining of Inconel 718 and comparison with dry and MQL machining. *Int J Adv Manuf Technol* 72(5–8):919–933
2. Paturi UMR, Maddu YR, Maruri RR, Narala SKR (2016) Measurement and analysis of surface roughness in WS2 solid lubricant assisted minimum quantity lubrication (MQL) turning of Inconel 718. *Procedia CIRP* 40:138–143
3. Shokrani A, Dhokia V, Newman ST (2017) Hybrid cooling and lubricating technology for CNC milling of Inconel 718 nickel alloy. *Procedia Manufacturing* 11:625–632
4. Sidik, NAC, Samion S, Ghaderian J, Yazid MNAWM (2017) Recent progress on the application of nanofluids in minimum quantity lubrication machining: a review. *Int J Heat Mass Transf* 108:79–89
5. Najiha MS, Rahman MM, Kadirgama K (2016) Performance of water-based TiO<sub>2</sub> nanofluid during the minimum quantity lubrication machining of aluminium alloy, AA6061-T6. *J Cleaner Prod* 135:1623–1636
6. Behera BC, Ghosh S, Rao PV (2016) Application of nanofluids during minimum quantity lubrication: a case study in turning process. *Tribol Int* 101:234–246
7. Revuru RS, Posinasetti NR, VSN VR, Amrita M (2017) Application of cutting fluids in machining of titanium alloys—a review. *Int J Adv Manuf Technol* 91(5–8):2477–2498

8. Sadeghinezhad E, Mehrali M, Saidur R, Mehrali M, Latibari ST, Akhiani AR, Metselaar HSC (2016) A comprehensive review on graphene nanofluids: recent research, development and applications. *Energy Convers Manag* 111:466–487
9. Ahammed N, Asirvatham LG, Titus J, Bose JR, Wongwises S (2016) Measurement of thermal conductivity of graphene–water nanofluid at below and above ambient temperatures. *Int Commun Heat Mass Transf* 70:66–74

# Mechanical Properties of AA 7075-Nano ZrO<sub>2</sub> Reinforced Matrix Composites



B. Prasanna Nagasai, S. Srikanth and J. A. Ranga Babu

**Abstract** Zircon reinforced composites are referred as a unique composite that exhibits relatively improved mechanical properties like high tensile strength and micro hardness compared to pure AA 7075 base metal. The present work aims to investigate that influence of reinforcement of ZrO<sub>2</sub> nanoparticles are mechanical properties of AA 7075 alloy and composites prepared through stir casting method. Samples are fabricated through varying the weight percentage of ZrO<sub>2</sub> 2 and 4 wt%. Mechanical properties of AA 7075 and composites were observed in particulars of density, porosity, micro hardness, XRD of ZrO<sub>2</sub> and tensile properties. Increased reinforcement contents enhance 15.92% of micro hardness, and 28.46% of tensile strength was noticed. However, the increase of particle concentration of reinforcement leads to diminishing of the percentage elongation.

**Keywords** AA 7075 · Nano ZrO<sub>2</sub> · Stir casting · Mechanical characterization

## 1 Introduction

Composite materials are the most promising material in exhibiting enhanced mechanical and technological properties compared to conventional materials for many real-time engineering applications. AMMCs have been subject of passion for scientists as they overcome the drawbacks of ferrous materials. MMCs join the metallic properties of base materials with ceramic properties of reinforcements and lead to rise tensile and compressive strengths and higher operating temperature capabilities. Zirconia is strong, adaptable and extensible material, it is highly resistant to corrosion and heat, chemical composition of zirconia is near of titanium, lighter than steel, and hardness is equal to copper. Ceramic-based metal matrix nano (1–100 nm) zirconia composites were suitable for automobile and aerospace applications, and it shows the good strength and hardness, developing the strength of casting, structure with useful weight savings due to their size [1]. Rao et al. [2] observed that the wear and

---

B. Prasanna Nagasai (✉) · S. Srikanth · J. A. Ranga Babu  
Department of Mechanical Engineering, Gudlavalleru Engineering College, Gudlavalleru, India  
e-mail: [nagasaibellamkonda143@gmail.com](mailto:nagasaibellamkonda143@gmail.com)

© Springer Nature Singapore Pte Ltd. 2020  
H. K. Voruganti et al. (eds.), *Advances in Applied Mechanical Engineering*,  
Lecture Notes in Mechanical Engineering,  
[https://doi.org/10.1007/978-981-15-1201-8\\_98](https://doi.org/10.1007/978-981-15-1201-8_98)

921

tensile properties are improved with increasing wt% of TiC particles to AA 7075. Baradeswaran et al. [3] reported that at 5 wt% of graphite and 2–8 wt% of  $Al_2O_3$  to AA 7075 decreasing the frictional coefficient.

Dipin Krishna et al. [4] noticed that the density, hardness, tensile strength, corrosion resistance increased with addition  $ZrO_2$  into the Al-7050 and impact strength is initially increased than decreased at 10 wt%  $ZrO_2$ .

Balaji Krishna et al. [5] reported that the addition of 2 wt% of fly ash and 3–7 wt% graphite to AA 7075 increasing the tensile strength compared to zirconia and graphite composites. Zirconia and graphite composites increased density and hardness compared to fly ash and graphite composites.

Pandiyarajan et al. [6] observed that the mechanical properties of 2–6 wt% of  $ZrO_2$  and graphite reinforced Al-6061 composites. Tensile properties and hardness were directly proportional to wt% of  $ZrO_2$  in Al-6061.

## 2 Materials and Methodology

### 2.1 Materials

AA 7075 is the base metal, in which Zinc major alloying element, which exhibits good casting properties and reasonable strength. It is strong, with excellent fatigue strength and medium machinability, weldability and has low resistance to corrosion compared to other alloys. Tables 1 and 2 show chemical constituents of AA 7075 and  $ZrO_2$ .

$ZrO_2$  particles of 20 nm size are used as reinforced at 2 and 4% weight and it is shown in Fig. 1b. It is observed as monoclinic and cubic structure.

**Table 1** Chemical constituents of AA 7075

Cr	Ti	Mn	Si	Fe	Cu	Mg	Zinc	Al
0.18	0.2	0.3	0.4	0.45	1.2	2.3	5.8	Bal.

**Table 2** Chemical constituents of  $ZrO_2$

$ZrO_2$	$Fe_2O_3$	$TiO_2$	$SiO_2$	Others
99.6	0.001	0.008	0.10	0.38



**Fig. 1** a Al-7075 round bar pieces. b ZrO<sub>2</sub> in powder form. c Magnesium turnings

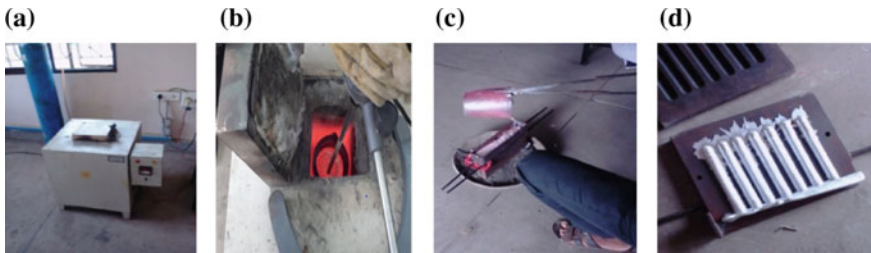


**Fig. 2** a Electric furnace for casting. b Stir casting. c Pouring molten metal into mould. d Casted fingers

## 2.2 Experimental Procedure

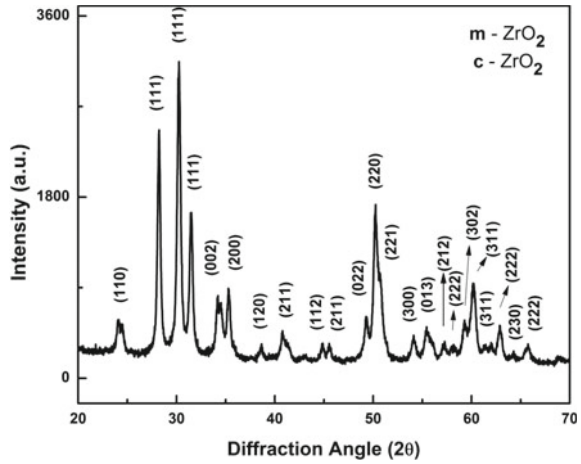
The synthesis of the AA 7075 and composite was prepared through stir casting. By using an electric furnace, AA 7075 was taken into a graphite crucible and melted. At the temperature of 800 °C, a vortex was built using mechanical stirrer. To improve wettability, magnesium turnings as shown in Fig. 1c were added to the alloy. While stirring in progress, the preheated ZrO<sub>2</sub> particulates were introduced into the molten metal. Molten metal was stirred at 800 rpm for 4 min under inert gas environment to ensure uniform distribution of particulate in base metal and then poured into metallic die (Fig. 2).

## 3 Results

### 3.1 XRD Analysis

The XRD pattern of ZrO<sub>2</sub> nanoparticles is shown in Fig. 3. All the diffraction peaks are indexed to the monoclinic zirconia. However, the characteristics reflections for cubic phases are located, and hence the diffraction pattern of ZrO<sub>2</sub> could be attributed to the monoclinic and cubic phases [7, 8]. The peaks indicated with “diamond”

**Fig. 3** XRD pattern of ZrO<sub>2</sub> nanoparticles



symbol for monoclinic ZrO<sub>2</sub> (m-ZrO<sub>2</sub>) with while the “dot” symbol for cubic ZrO<sub>2</sub> (c-ZrO<sub>2</sub>). The average grain size was measured by using Debye Scherer’s formula and was calculated as 21.01 nm.

### 3.2 Density

The AA 7075 and composite densities are determined by using Archimedean’s principle. By using the rule of mixture, the theoretical values of densities are determined.

$$\rho_{MMC} = (m) / ((m - m1) \times \rho_{H_2O}) \tag{1}$$

The density of composite can be estimated from the Eq. 2.

$$\rho_{composite} = V_r \rho_r + (1 - V_r) \rho_m \tag{2}$$

The porosity of the composites was determined from the following equation.

$$\text{Porosity}(\%) = (1 - (\text{experimental density} / \text{theoretical density})) \times 100 \tag{3}$$

Michael et al. [9] reported that the increase in reinforcement leads to the decreasing of density and fracture toughness. Antony Vasantha Kumar and Selwin Rajadurai [10] studied that the increasing in titanium dioxide leads to the increase of density. Ravi Kumar et al. [11] reported that the increase in ZrO<sub>2</sub> and CSA composites at the beginning decreased and then raised. It was observed that the addition of ZrO<sub>2</sub> into the AA 7075 positively increased the density and porosity as shown in Fig. 4.



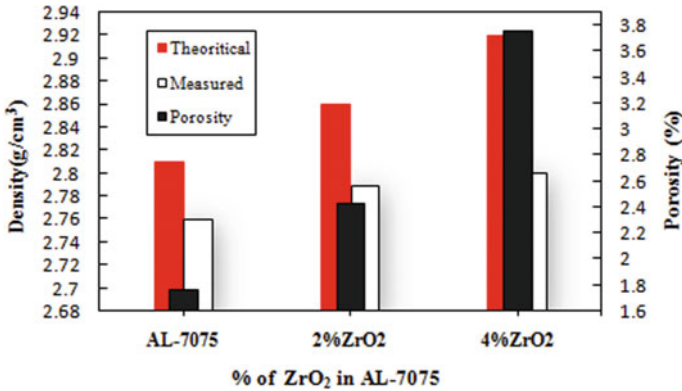


Fig. 4 Density variation of composite

This is due to the fact that the high density of ZrO<sub>2</sub> 5.68 g/cc. Praveen Kumer et al. [12] reported that the maximum porosity 2.52% is observed at 6% bamboo leaf ash. In AMMCs, from various researchers it was obtained that the maximum allowable porosity level is 4%. In the present study, the maximum acquired porosity 3.76% at 4% ZrO<sub>2</sub>, which is lower than the admissible porosity percentage.

### 3.3 Micro Hardness

Hardness is the resistance of a material to plastic deformation, usually through indentation. Vickers micro hardness number (VHN) was estimated for the polished specimens of AA 7075 and its composites using Vickers micro hardness tester. Figure 5a shows the form of indentation. In this work we measured three average readings for

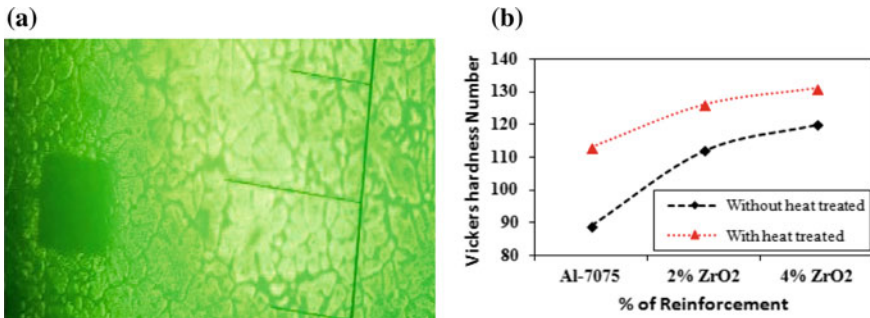


Fig. 5 a Micrograph report the form of indentation. b Graph of ZrO<sub>2</sub> composition versus Vickers hardness number

each sample at various points to prevent the possible effects of particle discrimination, the VHN is increased for composites reinforced with  $ZrO_2$  compared to base metal. The enhancement in the hardness may be developed to the existence of fixed and hard zirconium in  $ZrO_2$ .

The grain size of the reinforcement is also one of the senses for the development of hardness. Related conclusions were observed by [1, 2] authors. A comparison is also made between with and without heat-treated specimens. Hardness increased from 89 to 111 and 119 VHN for AA 7075, 2 wt% and 4 wt% of  $ZrO_2$  for without heat-treated specimens and 113 for AA 7075 alloy to 126 and 131 VHN for 2 wt% and 4 wt% of  $ZrO_2$  with heat-treated specimens as shown in Fig. 5b. It is noticed that 15.92% hardness is increased for with heat-treated specimens.

### 3.4 Tensile Strength

Universal testing machine (UTM) (Model: 9036TD) is used for tensile testing at room temperature. The specimens of the test were machined as per ASTM E8 standards and values are used to determine the tensile properties in particulars of elongation. ASTM E8 standard tensile specimens with dimensions are given in Fig. 6 and tensile specimens after testing are given in Fig. 7.

Figure 8a is evident for the enhanced tensile and yield strength with increased  $ZrO_2$  in wt%. Tensile strength of AA 7075 is 130 Mpa and it increases to a highest of

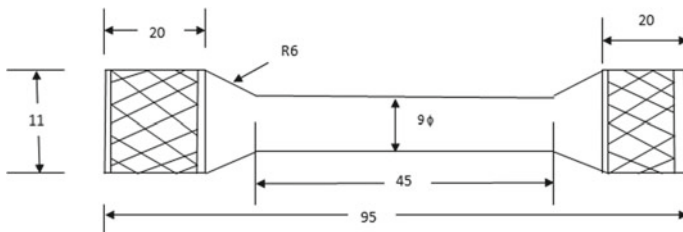


Fig. 6 As per ASTM E8 Tensile specimen



Fig. 7 Tested tensile specimen

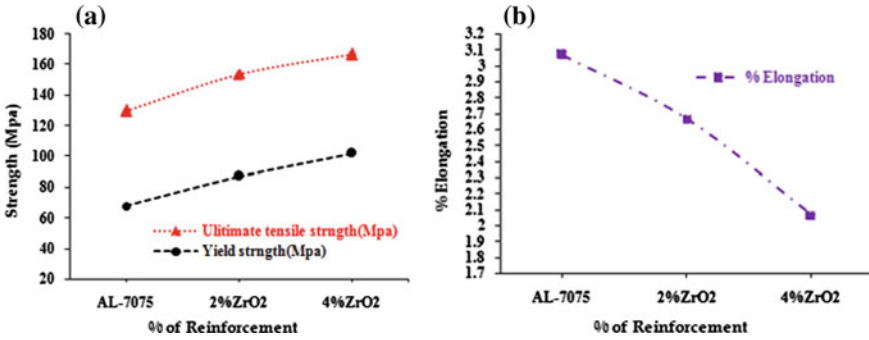


Fig. 8 a Tensile properties with reinforcement content. b Elongation (%) versus wt% ZrO<sub>2</sub>

167 Mpa for 4 wt% reinforced composite. Composites also recorded an enhanced tensile strength of 28.46%, for 4% wt. ZrO<sub>2</sub> reinforced composites compared with AA 7075 alloy. Ravi kumar et al. [11] studied that the addition of ZrO<sub>2</sub> particles increases with tensile strength. Madhusudhan et al. [1] observed the increased reinforcement in weight percentage increases with the tensile strength. Increasing the weight percentage of ZrO<sub>2</sub> in base metal leads to progressive decreasing of the elongation of MMC's.

Figure 8b shows the experimental elongation of ZrO<sub>2</sub> reinforced AA 7075 alloy. 3.07% is elongation of specimen AA 7075 this expense is reduced to 2.07% for specimen AA7075 4 wt% reinforcement. The load bearing capacity and delays crack ignition are enhanced by clean interfaces of composites.

### 4 Conclusion

AA 7075 and nano-ZrO<sub>2</sub> composites were well prepared through stir casting method. Stir casted composites have shown increase in density by 3.9%. At 2 and 4 wt%, ZrO<sub>2</sub> composite shows the greater results of micro hardness and tensile strength compared to AA 7075 alloy. Composites also recorded an enhanced tensile strength of 28.46%, hardness of 15.92%, for 4 wt% ZrO<sub>2</sub> reinforced composites and due to size of Zirconium oxide in aluminium matrix its usage as reinforcement is highly appraisable. Yield strength is increased and percentage of elongation is decreased at 4 wt% ZrO<sub>2</sub> compared to pure AA 7075 alloy. Crack initiation might have taken place because of the presence of ZrO<sub>2</sub> phase in the developed composites.

## References

1. Madhusudhan M, Naveen GJ, Mahesha K (2017) Mechanical behaviour of AA7068-ZrO<sub>2</sub> matrix composites. *Mater Today Proc* 4:3122–3130
2. Rao VRK, Sarcar MMM (2016) Wear properties of aluminium metal matrix composites AA7075 reinforced with TIC particles. *Int J Adv Sci Technol* 88:13–26
3. Baradeswaran A, Elaya Perumal A (2014) Study on mechanical and wear properties of Al 7075/Al<sub>2</sub>O<sub>3</sub>/graphite hybrid composites. *Composites: Part B* 56:464–471
4. Dipin Krishna J, Ajai Anil Kumar S, Mohan Kumar S, Ravi Kumar V (2017) Electrochemical corrosion studies and mechanical characterization of Al7050 metal matrix composite reinforced with ZrO<sub>2</sub> particulate by stir casting method. *Int J Mech Eng Technol* 8(11):949–957
5. Krishna NB, Unnikrishnan P, Ilangovan S (2018) Synthesis and characterization of zircon/graphite and flyash/graphite reinforced Aluminium7075 Alloy: a comparative study. *J Mater Environ Sci* 9(1):26–31
6. Pandiyarajan R, Maran P, Marimuthu S, Ganesh KC (2017) Mechanical and tribological properties of the matrix composite AA6061/ZrO<sub>2</sub>/C. *J Mech Sci Technol* 31(10):4711–4717
7. Otroshchenko TP, Kondratenko VA, Rodemerck U, Linke D, Kondratenko EV (2017) Non-oxidative dehydrogenation of propane, n-butane, and isobutane over bulk ZrO<sub>2</sub>-based catalysts: effect of dopant on the active site and pathways of product formation. *Catal Sci Technol* 7:4499–4510
8. Kantserova MR, Orlik SN, Shvets AV (2014) Effect of the composition of an oxide coating and the preparation method of block catalysts on their activity in the deep oxidation of methane. *Catal Ind* 6(2):88–93. ISSN 20700504
9. Bodunrina MO, Alaneme KK, Chown LH (2015) Aluminium matrix hybrid composites: a review of reinforcement philosophies; mechanical, corrosion and tribological characteristics. *J Mater Res Technol* 4(4):434–445
10. Antony Vasantha Kumar C, Selwin Rajadurai J (2016) Influence of rutile (TiO<sub>2</sub>) content on wear and microhardness characteristics of aluminium-based hybrid composites synthesized by powder metallurgy. *Trans Nonferrous Met Soc China* 26:63–73
11. Ravi Kumar K, Pridhar T, Sree Balaji VS (2018) Mechanical properties and characterization of zirconium oxide (ZrO<sub>2</sub>) and coconut shell ash(CSA) reinforced aluminium (Al 6082) matrix hybrid composite. *J Alloy Compd*
12. Kumar BP, Birru AK (2017) Microstructure and mechanical properties of aluminium metal matrix composites with addition of bamboo leaf ash by stir casting method. *Trans Nonferrous Met Soc China* 27:2555–2572

# Experimental Investigation on Friction Stir Welding of HDPE Reinforced with SiC and Al and Taguchi-Based Optimization



S. Ramesh Babu, S. R. K. Hudgikar and Y. Poornachandra Sekhar

**Abstract** Lightweight thermoplastics are the most prominent concerns of manufacturers due to their high performance characteristics in the current trend. Weld strength and weld quality are the performance measures of the thermoplastic materials, and determining the optimum weld parameters is the major research problem. This paper presents the optimization of weld parameters required for friction stir welding (FSW) of silicon carbide and aluminum reinforced in high-density polyethylene. The improved mechanical properties of these composites are the resultant effects of the optimum process parameters like welding speed, rotational speed, tilt angle, and percentage of reinforcement; hence it is very essential to determine them and to study their influence on composites weld joint. The experimental analysis was carried out for three levels in each and different combinations of weld parameters in order to measure the tensile strength and hardness. The optimum set of nine experiments was designed based on L9 Taguchi's design. The elicited test results convey that rotation speed of the tool is the most influential weld parameter for tensile strength and weld speed is the most responsible for hardness response of FSW butt joint. Maximum weld strength is 74.66% of the base material and hardness of 41.90 BHN at the weld portion is obtained. The analysis reveals that the added silicon carbide and aluminum particles enhance the ductility and brittle characteristics to base HDPE sheet causing improved weld strength and in turn ensures the weld quality.

**Keywords** Friction stir welding · High-density polyethylene sheet · Taguchi · Weld strength · Weld quality

---

S. Ramesh Babu (✉)  
VTU, Belagavi, Karnataka 590018, India  
e-mail: [s.ramesh737@gmail.com](mailto:s.ramesh737@gmail.com)

S. R. K. Hudgikar  
Lingaraj Appa Engineering College, Bidar, Karnataka 585403, India

S. Ramesh Babu · Y. Poornachandra Sekhar  
AITS, Rajampeta 516126, India

© Springer Nature Singapore Pte Ltd. 2020  
H. K. Voruganti et al. (eds.), *Advances in Applied Mechanical Engineering*,  
Lecture Notes in Mechanical Engineering,  
[https://doi.org/10.1007/978-981-15-1201-8\\_99](https://doi.org/10.1007/978-981-15-1201-8_99)

## 1 Introduction

Polymer matrix composite (PMC) widens its potential to become part in various industries such as aerospace and automotive due to its low-cost and high thermo-mechanical characteristics as well as high strength to weight ratio [1]. These composites generally need joining process for the larger and complex parts such as walls of cold storage plants, shipbuilding industry, and submersions [2, 3]. Welding is the most significant method to join the similar or dissimilar parts without losing the characteristics of the parent material. Friction stir welding (FSW) is a solid-state welding method invented in 1991 (British TWI), which consists of a cylindrical shoulder and a pin on its crest serves the purpose of heat development and then joining is performed with the pressure exerted by the shoulder [4–6]. In contrast with the traditional welding methods, FSW can effectively overcome some drawbacks like porosity formation, gas cavities, and inclusions, etc. which are observed in the normal welding process.

Friction stir welding-based investigations have been initiated on aluminum alloys [7–11], and later on magnesium alloys [12–14], but in recent years, plastic materials like low-density polyethylene (LDPE) and high-density polyethylene (HDPE), polypropylene (PP), nylon, polycarbonate, and acrylonitrile butadiene styrene (ABS) have been studied in the process of joining [1–4, 15–20]. Hence from the various investigations, it is evidenced that friction stir welding can be used for welding of unfilled thermoplastic and can study significant effects weld parameters on the performance of the welded joint. Yousefpour et al. [21] indicate that friction stir welding is the suitable method for welding thermoplastic composites.

Bilici et al. [20] used polypropylene (PP) sheet to study its bond strength and identified the dwell time as the most dominant weld parameter than tool rotation speed and plunge depth. Kiss et al. [22] investigation on polypropylene reveals that the tool geometry has a stronger effect compared to rotational and linear speeds. Payeganeh et al. [23] showed that the pin geometry has significant effect on mechanical properties of polypropylene composite welds such as weld surface appearance and tensile strength. Dashatan et al. [24] study on polymethyl methacrylate and acrylonitrile butadiene styrene (ABS) sheets of friction stir spot welding (FSSW) shows that the most effective parameter was found to be tool plunge rate on the weld strength.

The hardness of welded polymers in the FSW reduces due to the partially completed orientation of its molecular chains, which is the resultant effect by the stirring, fusion, and rapid cooling in very less span. Raza et al. [25] attempted to improve the hardness of HDPE by the graphite, silica, SiC, and alumina reinforcements and observed that the hardness of alumina and SiC-reinforced weld joints improved due to ductile behavior of composites. Emamian et al. [26] stated that square pin profile threaded cylindrical and conical pin profile joints will produce the sound joints. Hence in this study, the effect of conical pin with threaded profile has been considered for the significant improvement of stirring process.

The literature reveals that there are few publications related to friction stir welding applications of high-density polyethylene (HDPE) especially with nonferrous

and ceramic composites. Hence, this study attempts to investigate the effect of weld parameters on mechanical properties of friction stir welded HDPE sheets. The key objectives are set to be: (1) To examine the weld joint characteristics by the reinforcement of SiC and Al nanoparticles in HDPE weld joint. (2) To identify best combination of composites on HDPE at the weld portion. (3) To determine the optimum set of welding parameters to improve the weld strength and hardness of the weld joint.

## 2 Materials and Methods

In this work, the commercial HDPE sheets of 6 mm thick are welded to form butt joint by using friction stir welding process, and the schematic diagram of FSW process is shown in Fig. 1. The physical properties of selected HDPE sheets are given in Table 1.

For the effective stirring of composites, a conical profile FSW tool is employed for the investigation which has been machined from H13 tool steel having a shoulder diameter of 22 mm, pin diameter 3–6 mm and pin length 4.5 mm as shown in Fig. 2 with its cross-sectional view aside.

The HDPE sheets were butt welded using HMT FN2 vertical milling machine maintaining zero gap as shown in Fig. 3. Different combinations of Al and SiC particles are reinforced in-between the joining line (grooved portion) and pin face at

**Fig. 1** Typical Butt-joint welding procedure by a rotating shoulder [27]

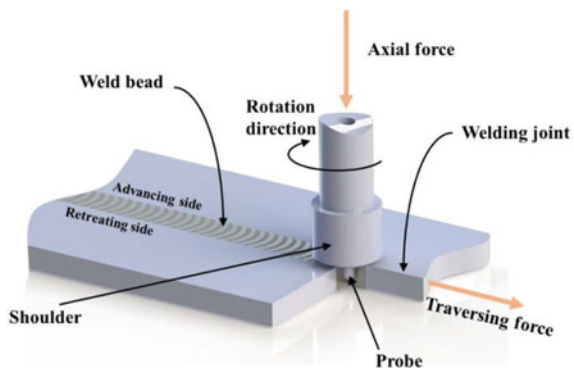


**Table 1** Physical properties of HDPE

Molecular weight (g)	Density (g/cc)	Young's modulus (N/mm <sup>2</sup> )	Melting temperature (°C)	Thermal conductivity (W/m K)	Softening temperature (°C)	Ultimate tensile strength (MPa)	Brinell hardness (BHN)
28.0	0.930–0.965	1035	135	0.40–0.47	112–130	26–33	17.46

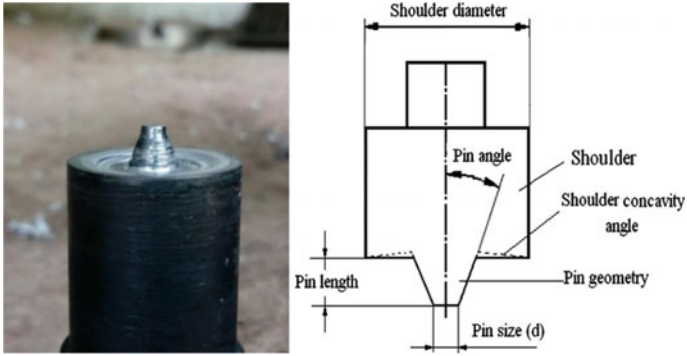


**Fig. 2** Conical pin tool along with its cross-sectional view

**Fig. 3** Experimental setup



the weld joint. The tool was traversed along that line of joining so as to reinforce the Al and SiC particles into HDPE sheets.



**Table 2** Levels in weld parameters

Weld parameters	Units	Range	Level 1	Level 2	Level 3
Rotational speed	Rpm	560–900	900	710	560
Welding speed	mm/min	16–30	30	20	16
Tool tilt angle	degrees	1°–3°	1°	2°	3°
Composition	%	50–100	HDPE (Al)	HDPE (Al + SiC)	HDPE (SiC)

### 3 Experimental Work

#### 3.1 Input Parameters

The key input variables of the experimental procedure consist of three levels taken randomly within the permissible range, identified to be suitable for effective performance [26]. The each selected welding parameters such as tool rotational speed (N), welding speed (S), tool tilt angle (TA), and percentage of composition are shown in Table 2.

#### 3.2 Taguchi’s Design of Experiments

Taguchi L9 orthogonal array is selected to perform optimum set of experiments based on the process parameters [3, 15]. Design of the experimental sets according to L9 orthogonal array for the four welding input process parameters is shown in Table 3.

The term ‘S—signal’ represents the desired output mean value and the term ‘N—noise’ represents the undesirable value of it, the S/N ratio ( $\eta$ ) can be calculated as product of  $-10$  and natural log of mean square deviation (MSD). For butt

**Table 3** Design of experiments using Taguchi L9 orthogonal array

S. No.	Rotational speed (rpm)	Weld speed (mm/min)	Tilt angle (°)	Compositions (%)
1	900	30	1	HDPE (AL)
2	900	20	2	HDPE (AL + SiC)
3	900	16	3	HDPE (SiC)
4	710	30	2	HDPE (SiC)
5	710	20	3	HDPE (AL)
6	710	16	1	HDPE (AL + SiC)
7	560	30	3	HDPE (AL + SiC)
8	560	20	1	HDPE (SiC)
9	560	16	2	HDPE (AL)

**Table 4** Tensile test results and S/N ratio values

Exp. No.	Rotational speed (rpm)	Weld speed (mm/min)	Tilt angle (°)	Compositions (%)	Ultimate tensile strength (MPa)
1	900	30	1	HDPE (AL)	24.464
2	900	20	2	HDPE (AL + SiC)	17.732
3	900	16	3	HDPE (SiC)	18.829
4	710	30	2	HDPE (SiC)	17.490
5	710	20	3	HDPE (AL)	18.003
6	710	16	1	HDPE (AL + SiC)	18.829
7	560	30	3	HDPE (AL + SiC)	11.985
8	560	20	1	HDPE (SiC)	15.512
9	560	16	2	HDPE (AL)	4.789

joint, both tensile strength and hardness are suitable to provide the larger-the-better characteristic [28]. MSD for larger-the-better optimal characteristic is expressed as:

$$MSD = \frac{1}{n} \sum_{i=1}^n \frac{1}{T_i^2} \tag{1}$$

where,  $n$  is the number of tests and  $T_i$  is the value of tensile or hardness test. The S/N ratios of experimental results for the weld strength and hardness are represented in Tables 4 and 6.

## 4 Results and Discussion

### 4.1 Tensile Test

Figure 4 shows the sample weld specimen prepared for tensile test. The test results for finding the tensile strength are shown in the Table 4, and it can be observed that a maximum tensile strength of 24.464 MPa was obtained at rotational speed 900 rpm, traverse speed 30 mm/min, tilt angle 10 and HDPE (with Al). The observed ultimate strength weld sample exhibits about 74.67% of strength of base material. Similar observation was made by Sayeedi and Givi on welded polyethylene sheet and obtained joint 75% of base material [17]. Bagheri et al. [19] observed 88% joint efficiency on welding of ABS sheet using a hot shoe.

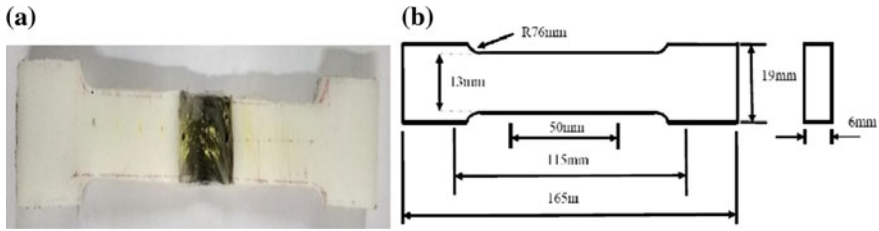


Fig. 4 a Sample specimen prepared for tensile test and b dimensional view [15]

### 4.2 Effect of Weld Parameters on Tensile Strength

The main effects plots along with contour plots are shown in Fig. 5 considering the influences of weld parameters on weld strength of the joint. The results in Table 5 shows that the highest ranked tool rotational speed as the most effecting weld parameter on weld strength and tilt angle as next important parameter. As the heat generation is majorly governed by the rotational speed, raise in the rotational speed from 560 to 900 rpm causes to generate more heat for deformation of the thermoplastic and to mix properly with Al and SiC particles and also increases the rates of material softening and liquidity, which will ensure the high weld strength at the joint portion. On the other hand at low tool rotational speed, the amount of weld strength is less due to low melting and deformation of thermoplastic.

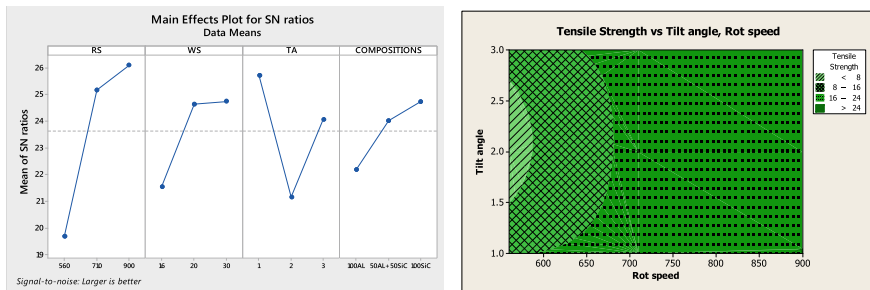


Fig. 5 Mean S/N ratio and contour plots for tensile strength

Table 5 S/N response table for weld strength

S. No.	Weld parameter	Mean S/N ratio				
		Level-1	Level-2	Level-3	Max.–min.	Rank
1	Rotational speed	19.66	25.15	26.08	6.42	1
2	Weld speed	21.53	24.63	24.73	3.20	3
3	Tilt angle	25.69	21.15	24.06	4.55	2
4	Compositions	22.16	24.01	24.72	2.56	4

**Table 6** Hardness test results and S/N ratio values

Exp. No	Rotational speed (rpm)	Weld speed (mm/min)	Tilt angle (°)	Compositions (%)	Hardness (BHN)
1	900	30	1	HDPE (AL)	30.56
2	900	20	2	HDPE (AL + SiC)	30.56
3	900	16	3	HDPE (SiC)	30.56
4	710	30	2	HDPE (SiC)	41.90
5	710	20	3	HDPE (AL)	30.56
6	710	16	1	HDPE (AL + SiC)	35.63
7	560	30	3	HDPE (AL + SiC)	41.90
8	560	20	1	HDPE (SiC)	35.63
9	560	16	2	HDPE (AL)	30.56

### 4.3 Brinell Hardness Test (BHN)

Hardness test is conducted along the joint portion with 60 kg f applied load, 2.5 mm diameter of indenter and the results are presented in the Table 6. It was observed that the maximum hardness of 41.90 BHN obtained at 710 rpm rotational speed, 30 mm/min weld speed, 20 tilt angle, and HDPE (with SiC), which is more than that of the un-welded base material (17.46 BHN).

### 4.4 Effect of Parameters on Hardness

Table 7 shows the response S/N ratios and the main effects as well as contour plots are shown in Fig. 6. From these it was observed that the weld speed is the major factor responsible for hardness of the weld joint. The maximum hardness of 41.90 BHN observed at weld speed 30 mm/min, rotational speed 710 rpm and tilt angle 20 for SiC + HDPE composite. The hardness across the SiC-reinforced weld joints is increasing

**Table 7** S/N response table for hardness

S. No.	Weld parameter	Mean S/N ratio				
		Level-1	Level-2	Level-3	Max.–min.	Rank
1	Rotational speed	31.06	31.06	29.07	1.36	2.5
2	Weld speed	30.15	30.15	31.53	1.38	1
3	Tilt angle	30.59	30.62	30.62	0.02	4
4	Compositions	29.70	31.06	31.06	1.36	2.5

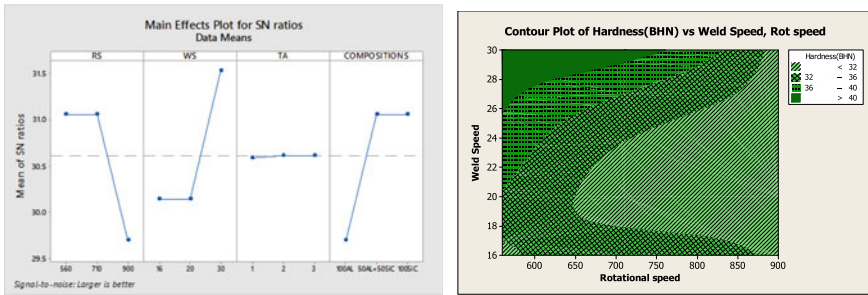


Fig. 6 Mean S/N ratio and contour plots for hardness

with the increase in weld speed, while that Al composite remains constant at minimum value for the variations of weld parameters. This observation is in accordance with reduction in ductile nature depicted by the SiC + HDPE weld joint and the moderate ductile behavior exhibit by the Al + HDPE weld joint.

## 5 Conclusions

Study the effects of SiC and Al particles reinforcement on HDPE in addition with other weld parameters over the weld strength, and hardness of weld joints was the objective of this work in the friction stir welding process. From the experimental analysis, the following conclusions are drawn:

- The rotational speed and weld speed are the main influencing factors on weld strength and hardness, respectively; it means the weld quality is proportional to the speeds of the FSW tool at weld zone.
- The optimum weld parameters for retaining 74.66% base material weld strength are 900 rpm rotational speed, 30 mm/min traverse (weld) speed, 1° tilt angle and HDPE combined with Al particles. The maximum hardness of 41.90 BHN at welded portion, obtained at 710 rpm, 30 mm/min, 20 and HDPE combined with SiC parameters set.
- It is observed that the weld quality of joint is also dependent of reinforced particles of SiC and Al. The effect of improved tensile strength is in accordance of better Al particle entrapment in base HDPE sheets during stirring process causes ductility, whereas hardness is due to the SiC particles enhancing the contrast nature to base materials.

## References

- Zohoor M, Besharati Givi MK, Salami P (2012) Effect of processing parameters on fabrication of Al-Mg/Cu composites via friction stir processing. *Mater Des* 39:358–365
- Aydin M (2010) Effects of welding parameters and pre-heating on the friction stir welding of UHMW-polyethylene. *Polym Plast Technol Eng* 49(6):595–601
- Bilici MK, Yüklér AI, Kurtuluş M (2011) The optimization of welding parameters for friction stir spot welding of high density polyethylene sheets. *Mater Des* 32(7):4074–4079
- Arici A, Sinmazcelik T (2005) Effects of double passes of the tool on friction stir welding of polyethylene. *J Mater Sci* 40:3313–3316
- Nandan R, DebRoy T, Bhadeshia HKDH (2008) Recent advances in friction-stir welding—process, weldment structure and properties. *Prog Mater Sci* 53(6):980–1023
- Casalino G, Campanelli S, Mortello M (2014) Influence of shoulder geometry and coating of the tool on the friction stir welding of aluminium alloy plates. *Procedia Eng* 69:1541–1548
- Hwang YM, Kang ZW, Chiou YC, Hsu HH (2008) Experimental study on temperature distributions within the workpiece during friction stir welding of aluminum alloys. *Int J Mach Tools Manuf* 48(7–8):778–787
- Amancio-Filho ST, Sheikhi S, dos Santos JF, Bolfarini C (2008) Preliminary study on the microstructure and mechanical properties of dissimilar friction stir welds in aircraft aluminium alloys 2024-T351 and 6056-T4. *J Mater Process Technol* 206(1–3):132–142
- Balasubramanian V (2008) Relationship between base metal properties and friction stir welding process parameters. *Mater Sci Eng A* 480(1–2):397–403
- Liu P, Shi Q, Wang W, Wang X, Zhang Z (2008) Microstructure and XRD analysis of FSW joints for copper T2/aluminium 5A06 dissimilar materials. *Mater Lett* 62(25):4106–4108
- Kwon YJ, Shigematsu I, Saito N (2008) Dissimilar, Friction stir welding between magnesium and aluminum alloys. *Mater Lett* 62(23):3827–3829
- Serindag H, Serindag HT, Kiral BG (2016) Friction stir welding of Az31 magnesium alloys—a numerical and experimental study. *Latin Am J Solids Struct* 14(1):113–130
- Bretz GT, Lazarz KA, Hill DJ, Blanchard PJ (2014) Adhesive bonding and corrosion protection of a die cast magnesium automotive door. *Essent Readings Magnes Technol* 9781118858:609–615
- Park SHC, Sato YS, Kokawa H (2003) Effect of micro-texture on fracture location in friction stir weld of Mg alloy AZ61 during tensile test. *Scr Mater* 49(2):161–166
- Sahu SK, Mishra D, Mahto RP, Pal SK, Pal K (2016) Friction stir welding of HDPE sheets: a study on the effect of rotational speed, ISBN: 978-93-86256-27-0, pp 1065–1068
- Kurabe Y, Miyashita Y, Hori H (2017) Joining process and strength in PVC friction stir spot welding with fabricating composite material at welding area. *Weld Int* 31(5):354–362
- Saeedy S, Givi MKB (2011) Investigation of the effects of critical process parameters of friction stir welding of polyethylene. *Proc Inst Mech Eng Part B: J Eng Manuf* 225(8):1305–1310
- Panneerselvam K, Lenin K (2014) Joining of Nylon 6 plate by friction stir welding process using threaded pin profile. *Mater Des* 53:302–307
- Bagheri A, Azdast T, Doniavi A (2013) An experimental study on mechanical properties of friction stir welded ABS sheets. *Mater Des* 43:402–409
- Bilici MK (2012) Application of Taguchi approach to optimize friction stir spot welding parameters of polypropylene. *Mater Des* 35:113–119
- Yousefpour A, Hojjati M, Immarigeon JP (2004) Fusion bonding/welding of thermoplastic composites. *J Thermoplast Compos Mater* 17:303–341
- Kiss Z, Czigány T (2012) Microscopic analysis of the morphology of seams in friction stir welded polypropylene. *Expr Polym Lett* 6(1):54–62
- Payganeh GH, Arab NBM, Asl YD, Ghasemi FA, Boroujeni MS (2011) Effects of friction stir welding process parameters on appearance and strength of polypropylene composite welds. *Int J Phys Sci* 6(19):4595–4601
- Dashatan SH, Azdast T, Ahmadi SR, Bagheri A (2013) Friction stir spot welding of dissimilar polymethyl methacrylate and acrylonitrile butadiene styrene sheets. *Mater Des* 45:135–141

25. Raza K, Shamir M, Qureshi MKA, Shaikh AS, Zain-ul-abdein M (2018) On the friction stir welding, tool design optimization, and strain rate-dependent mechanical properties of HDPE–ceramic composite joints. *J Thermoplast Compos Mater* 31(3):291–310
26. Emamian S, Awang M, Yusof F (2017). A review of friction stir welding pin profile 1–18. <https://doi.org/10.1007/978-981-10-4232-4>
27. Rezaee Hajideh M, Farahani M, Alavi SAD, Molla Ramezani N (2017) Investigation on the effects of tool geometry on the microstructure and the mechanical properties of dissimilar friction stir welded polyethylene and polypropylene sheets. *J Manuf Processes* 26:269–279
28. Singh R, Kumar V, Feo L, Fraternali F (2016) Experimental investigations for mechanical and metallurgical properties of friction stir welded recycled dissimilar polymer materials with metal powder reinforcement. *Compos B Eng* 103:90–97

# Design and Simulation of Porous Ti–6Al–4V Alloy Structures for Additive Manufacturing of Bioimplants



A. Rudra Kumar, S. Rambabu and K. Sri Harsha

**Abstract** This paper presents the efforts made in the design and finite element simulation of porous Ti–6Al–4V alloy structures to determine the elastic modulus of porous parts produced with the additive manufacturing technology for biomedical applications. The major problem concerning with the typically used metallic bioimplants is the mismatch of elastic modulus between the implant and the human bone, which resulted in the degradation of surrounding bone structure and disassociation of the implant. The present work is focused on designing the porous Ti–6Al–4V alloy structures and also on studying the influence of porosity on the elastic modulus of implants made of Ti–6Al–4V alloy material. The three-dimensional strut-based cellular structure is employed to build the porous structures ranging from 10 to 50% porosity volume. This work established the appropriate porosity to minimize the mismatch of elastic modulus between the implant and the bone by adding the porosity to the implant structure. It is found that the Ti–6Al–4V structure with the porosity of 40 vol.% possesses the elastic modulus about 74 GPa. These results demonstrate the proof of tailoring the elastic modulus of bioimplants.

**Keywords** Additive manufacturing · Elastic modulus · Porosity · Ti–6Al–4V alloy

## 1 Introduction

Additive manufacturing (AM) is a process that produces the parts by adding the material together, typically layer-by-layer method, based on the three-dimensional (3D) computer-aided design (CAD) data. The AM technology allows complex designs and also impacts on the manufacturing procedures in various fields including automobile, aerospace and biomedical engineering. Due to the improvement in additive manufacturing technology and the availability of various materials, the AM technology is used to produce orthopaedic implant structures and scaffolds. In general,

---

A. Rudra Kumar · S. Rambabu (✉) · K. Sri Harsha  
Department of Mechanical Engineering, Vignan's Institute of Information Technology,  
Visakhapatnam, Andhra Pradesh 500049, India  
e-mail: [ramu.sarimalla@gmail.com](mailto:ramu.sarimalla@gmail.com)

© Springer Nature Singapore Pte Ltd. 2020  
H. K. Voruganti et al. (eds.), *Advances in Applied Mechanical Engineering*,  
Lecture Notes in Mechanical Engineering,  
[https://doi.org/10.1007/978-981-15-1201-8\\_100](https://doi.org/10.1007/978-981-15-1201-8_100)

941



the implants are used as structural reinforcements inside the human body for load-bearing applications. The temporary implants include screws and plates, whereas the permanent implants include hip and knee joints and require more toughness, sufficient strength and resistance to wear between the joints. The various AM technologies are available for metals including selective laser melting, direct metal laser sintering and electron beam melting, which are capable of manufacturing functional metallic parts for orthopaedic applications in a single step. However, the major issue with bio-metallic implants is the mismatch of modulus between the bone and the implant which results in disassociation of the implant [1]. Moreover, the bone formation and in-growth are less for the dense implant. These problems can be minimized by using the porous implant structures. This paper presents the proof of tailoring the elastic modulus of Ti-6Al-4V material.

Additive manufacturing technology has the potential to build the intricate geometries, functionally graded materials, porous lattice structures, conformal cooling channels, based on the requirement of structures used in the aerospace, automotive, tooling, medical applications, etc. A lattice structure is a periodic arrangement of unit cells with two- or three-dimensional structures and is linked to cellular solids. The structures of cellular solids can be categorized into two types such as stochastic and non-stochastic structures based on the spatial arrangement of their unit cells [2, 3]. The materials having stochastic structures are characterized by a random distribution of their unit cells, whereas the materials with non-stochastic structures are characterized by an ordered distribution of their unit cells. Figure 1 presents the broad classification of cellular solid structures. Figure 2a–f presents the cellular structures of open-cell foam, closed-cell foam, 2D honeycomb structure, 3D strut-based cellular structure, 3D triply periodic minimal surface (TPMS)-based gyroid and diamond cellular structure. The lattice structures possess superior properties, which result in promising solution for various applications such as lightweight structures, heat exchangers, energy absorbers, acoustic insulators to reduce the noise and vibrations

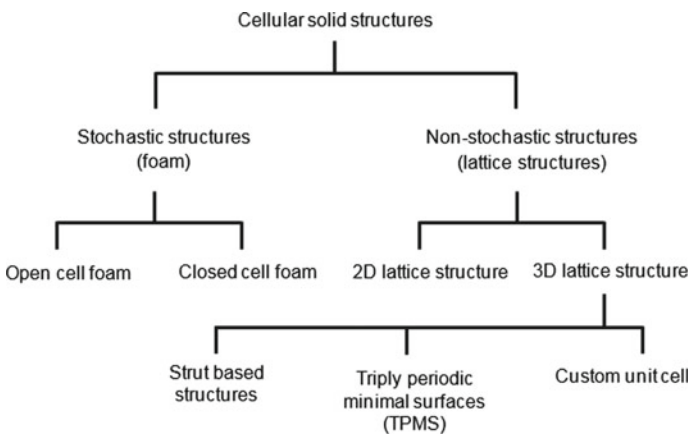
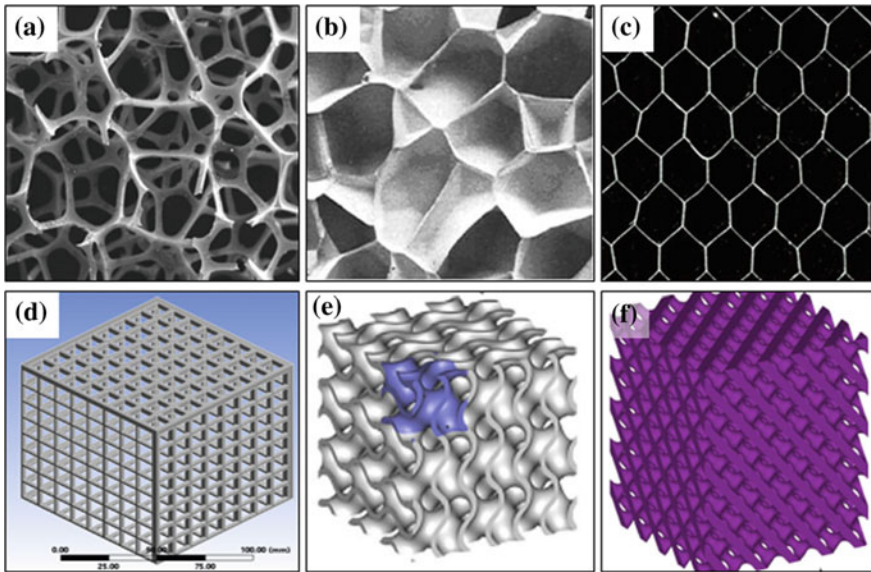


Fig. 1 Classification of cellular solid structures



**Fig. 2** **a** Stochastic open-cell foam, **b** stochastic closed-cell foam, **c** 2D honeycomb structure, **d** 3D strut-based cellular structure, **e** 3D triply periodic minimal surface (TPMS)-based gyroid cellular structure and **f** 3D TPMS-based diamond cellular structure

and orthopaedic implants. Due to the unique capabilities of additive manufacturing technology, it makes possible to manufacture the parts with desired porosity. This work covers the design and FEA simulation of porous structures to predict the elastic modulus of implant structures produced by additive manufacturing technologies.

## 2 Methodology

### 2.1 Design of Porous Ti–6Al–4V Alloy Structures

The important factor for the structural design of various porous structures is the relationship between the porosity volume and the elastic modulus. The simple cube is developed with different porosities ranging from 10 to 50% using square holes. Figure 3a–c presents the porous cube structures with 10% porosity, 30% porosity and 50% porosity. The FEA simulation was carried out by applying the boundary conditions as shown in Fig. 4a.

The finite element analysis using commercial software ANSYS was performed to estimate the elastic modulus of porous structures using von Mises stress and the strain. The key steps involved in design and simulation for predicting the elastic modulus of porous structures are presented in Fig. 4b. The elastic modulus was estimated by

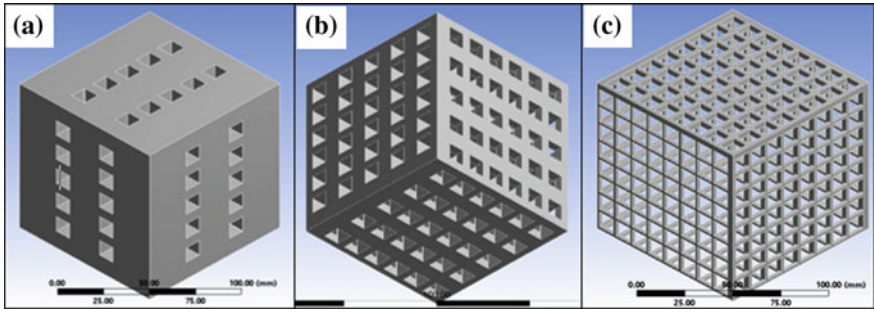


Fig. 3 Design of simple cube structures with a 10% porosity, b 30% porosity and c 50% porosity

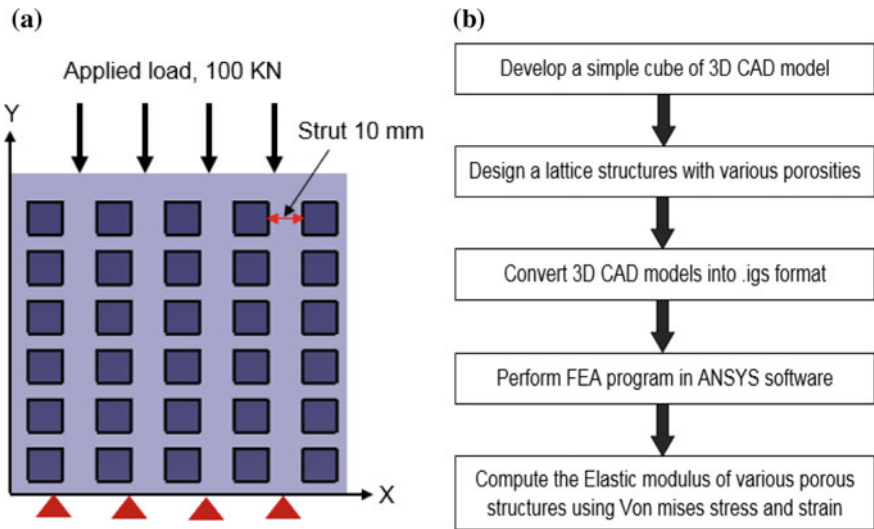
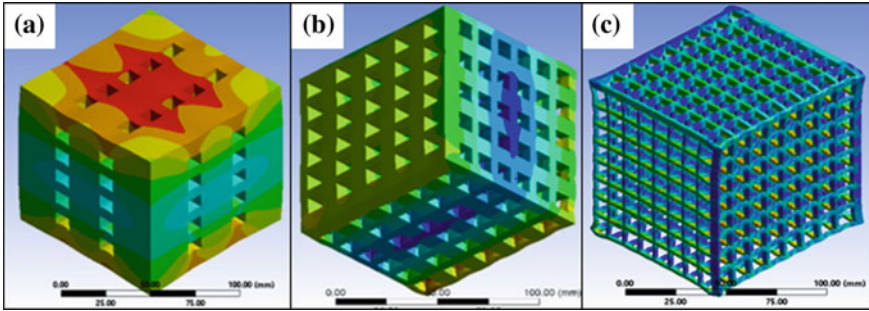


Fig. 4 a Porous cube structure with boundary conditions and b sequence of steps in design and FEA simulation for estimating the elastic modulus of porous structures

using the relationship between the von Mises stress and the strain obtained from the FEA simulation. The influence of strut size, number of pores and pore size on the elastic modulus of porous structures was studied.

### 3 Results and Discussion

The simple cube structures with porosities ranging from 10% to 50% were designed using the 3D CAD model. From the FEA simulation, it was found that the von Mises stress decreased with increasing the porosity volume up to 40%, and beyond that,

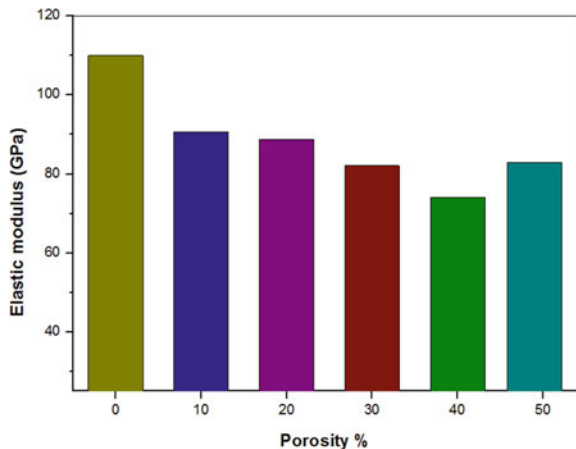


**Fig. 5** FEA contour plots for stress distribution in porous structures with **a** 10% porosity, **b** 30% porosity and **c** 50% porosity

the stress was increased. The FEA contour plots for stress distribution in porous structures are presented in Fig. 5a–c.

The effect of porosity volume on the elastic modulus was presented in Fig. 6. From the results presented in Fig. 6, it is clear that the elastic modulus of Ti-6Al-4V alloy without porosity possesses 110 GPa and gradually decreased from 90 to 74 GPa while increasing the porosity volume from 10% to 40%, respectively. However, the elastic modulus of porous structure increased from 74 to 83 GPa with increasing the porosity from 40 to 50%. This can be attributed to the densification phenomena of the porous structure, and it behaves like a solid structure due to increasing the self-contacting surfaces [4]. Also, it is found that the strut size influenced the elastic modulus than the pore size and number of pores [5].

**Fig. 6** Effect of porosity on elastic modulus



## 4 Conclusions

This work demonstrates the proof of tailoring the elastic modulus of the porous Ti–6Al–4V alloy structures. From the results, it is found that the Ti–6Al–4V alloy structure with the porosity of 40 vol.% possesses the elastic modulus about 74 GPa. From the results, it is clear that the elastic modulus of the bioimplants can be tailored by developing the implant structures with the designed porosity using additive manufacturing technology. Future work includes the experimental validation of elastic modulus of the porous Ti–6Al–4V alloy structures developed using additive manufacturing technology with the present results.

## References

1. Krishna BV, Bose S, Bandyopadhyay A (2007) Low stiffness porous Ti structures for load-bearing implants. *Acta Biomater* 3(6):997–1006
2. Tamburrino F, Graziosi S, Bordegoni M (2018) The design process of additively manufactured mesoscale lattice structures: a review. *J Comput Inf Sci Eng* 18(4):040801
3. Al-Ketan O, Rowshan R, Abu Al-Rub RK (2018) Topology-mechanical property relationship of 3D printed strut, skeletal, and sheet based periodic metallic cellular materials. *Add Manuf* 19:167–183
4. Maskery I, Aremu AO, Parry L, Wildman RD, Tuck CJ, Ashcroft IA (2018) Effective design and simulation of surface-based lattice structures featuring volume fraction and cell type grading. *Mater Des* 155:220–232
5. Jayanthi P, Starly B, Shiv kumar R (2011) A design for the additive manufacture of functionally graded porous structures with tailored mechanical properties for biomedical applications. *J Manuf Processes* 13:160–170

# Effect of Tool Geometry and Heat Treatment on Friction Stir Processing of AA6061



Karan Chauhan, M. V. N. V. Satyanarayana and Adepu Kumar

**Abstract** In this study, AA6061 plates of 6 mm thickness were subjected to friction stir processing with 50% pin overlapping to produce bulk area fine grain structure using three different tool geometries. Post-processing heat treatment was carried for all samples to investigate the effect of different tool geometries on microstructure and micro-hardness of AA6061. 3D optical microscope and Vickers micro-hardness tester were employed to examine the microstructure and micro-hardness, and results have been reported. From an analysis, it was observed that post-processing heat treatment improved the properties and among three different tool geometries, the samples processed with the hexagonal pin profile yield the best results.

**Keywords** Friction stir processing · Fine-grained structure · AA6061

## 1 Introduction

Huang et al. addressed new developments in the processing of fine-grained (FG) structured materials. FG structured materials possess a wide range of properties such as super-plasticity, high toughness, high strength, etc. [1]. A wide variety of processes are available for producing fine-grained structured materials such as equal channel angular processing (ECAP) [2], high-pressure torsion (HPT) [3], accumulative roll bonding (ARB) [4] and friction stir processing (FSP) [5, 6]. Grain refinement occurs in the above processes due to recovery and recrystallization. But in the first three processes, bulk area FG cannot be produced and in addition to that, they induce large strains and require large temperatures. To avoid these difficulties, FSP was studied

---

K. Chauhan (✉) · M. V. N. V. Satyanarayana · A. Kumar  
Department of Mechanical Engineering, National Institute of Technology,  
Warangal, Warangal 506004, Telangana, India  
e-mail: [karanchauhan884@gmail.com](mailto:karanchauhan884@gmail.com)

M. V. N. V. Satyanarayana  
e-mail: [veeru.satti@gmail.com](mailto:veeru.satti@gmail.com)

A. Kumar  
e-mail: [adepu\\_kumar7@yahoo.co.in](mailto:adepu_kumar7@yahoo.co.in)

© Springer Nature Singapore Pte Ltd. 2020  
H. K. Voruganti et al. (eds.), *Advances in Applied Mechanical Engineering*,  
Lecture Notes in Mechanical Engineering,  
[https://doi.org/10.1007/978-981-15-1201-8\\_101](https://doi.org/10.1007/978-981-15-1201-8_101)

and the results were very good compared to other processes. FSP is derived from friction stir welding (FSW) [6] but instead of joining the materials, it focuses on the enhancement of properties of the desired material. This process is widely used when enhancement of properties is required without other disadvantages and so FSP is an effective method for producing fine grain structure [7, 8]. AA6061 alloy is extensively used in the aircraft industry for wing tension members, shear webs and ribs. It requires FG structure for improving mechanical properties and formability.

Kwon et al. [9] produced UFG of AA 1050 alloy with the variation of process parameters and found that temperature is an important parameter and less heat input is required to obtain UFG. Su et al. [7] produced bulk UFG with overlapping passes, concluded that fine grains were obtained with rapid cooling and found low dislocations in the bottom region. Liu et al. [10] fabricated UFG of 6061 Al alloys with different rotation rates and by employing water cooling to reduce the grain size. Xue et al. [11] used pure Cu with five passes of FSP and obtained bulk area UFG structure by varying process parameters and cooling medium. Gandra et al. [12] studied the effect of overlapping direction in multi-pass FSP and concluded that surface characteristics are improved as a result of material flow which is asymmetric in nature, uniform layer thickness is formed in the processed layer when overlapping is on advancing side and hardness is more or less same in processed layer. Johannes and Mishra [13] created a staggered pass sample of aluminium 7075 from one to four passes and concluded that four-pass material is superplastic and single-pass material contains more elongation. Ramesh et al. [14] used rolled aluminium 5086 with twelve passes and two methods of intermittent multi-pass FSP (IMP) and continuous multi-pass FSP (CMP) were used and concluded that material processed with IMP showed better mechanical properties compared to material processed with CMP except for high traverse speeds.

## 2 Experimental Procedure

Plates of AA6061 aluminium alloy with 6 mm thickness were used as a base metal for this study. Table 1 shows the chemical composition of AA6061. All experiments were performed on a 3-Ton capacity CNC-based friction stir welding machine. AISI H13 tool steel was selected as the tool material as it has an excellent combination of abrasion and shock resistance along with better hardenability. The composition of tool material is shown in Table 2. Three different tools with different geometries were taken for experimentation and their description is shown in Table 3. The plates were

**Table 1** Composition of AA6061

Element	Al	Cu	Mg	Si	Fe	Mn	Cr
Composition (wt%)	Remainder	0.15–0.4	0.8–1.2	0.4–0.8	Max 0.7	Max 0.15	0.04–0.35

**Table 2** Composition of AISI H13

Element	Cr	Mn	C	Mo	P	S	Si	V
Composition (wt%)	4.75–5.5	0.2–0.5	0.32–0.45	1.1–1.75	Max 0.03	Max 0.03	0.8–1.2	0.8–1.2

**Table 3** Tool geometry

Tool No.	Tool geometry	Notation
Tool-1	Square pin with ridges	T-1
Tool-2	Hexagonal pin with concentric circles	T-2
Tool-3	Triangle pin with scrolls	T-3

processed with a tool rotational speed of 800 rpm and a traverse speed of 40 mm/min. FSP with 50% pin overlapping was conducted to produce the bulk area FG structure in AA6061. A total of five overlapping passes were done. After FSP, samples were solutionized at 530 °C for 1 h followed by water quenching to hold the constituents. The same samples were aged in a furnace at 160 °C for 16 h followed by air-cooling to improve the properties. For analysis, samples were cut transverse to the processing zone by using a power hacksaw. The samples were polished with different grades of emery papers followed by disc polishing and polished surface was cleaned with acetone to remove the dirt and contaminants on the polished surface. Keller's reagent was used to etch the polished surface and the etching time was 150 s. Microstructures were examined with a 3D optical microscope. Vickers micro-hardness tester was used for measurement of hardness with a load of 100 g for 10 s dwell time using diamond indenter. The hardness was measured along the processed zone with an interval of 0.5 mm.

### 3 Results and Discussion

#### 3.1 Microstructure

The microstructures of heat-treated (HT) samples with single-pass FSP without overlapping in stir zone (SZ) are shown in Fig. 1a–c. From the microstructures of the HT samples, it was observed that fine equiaxed grains along with uniform precipitates were obtained in SZ. This is due to dynamic recrystallization and plastic deformation that occurred because of high temperature and stirring action. Microstructure results witnessed the grain refinement is more in the sample processed with T-2. These results indicate that shearing is more in stir zone in sample processed with T-2 due to the six sharp edges of the hexagonal pin profile. Coarse grains were observed in stir zone of T-3 due to the less shearing action caused by the less number of edges. The grain refinement in stir zone of T-1 is in between the grain refinement of T-2 and



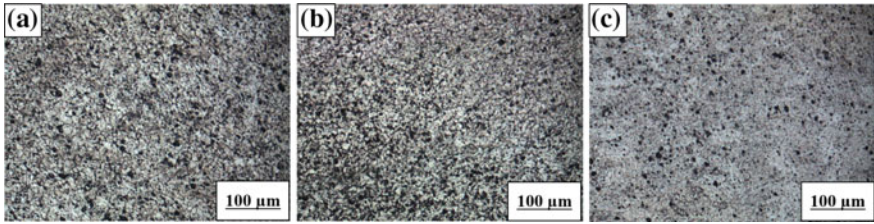


**Fig. 1** Microstructures of stir zone in first pass for **a** Tool-1 (T-1) **b** Tool-2 (T-2) **c** Tool-3 (T-3)

T-3. Figure 2a–c shows the microstructures of HT samples in overlapped SZ. From the microstructures, it was seen that the grains were further refined as they were subjected to two-pass FSP. As discussed in a previous analysis, dynamic recrystallization caused by severe plastic deformation is the reason for grain refinement; two-pass FSP enhances grain refinement compared to single-pass FSP. Figure 3a–c represents the microstructures of the thermo-mechanically affected zone (TMAZ) and shows grain coarsening as compared to SZ. The microstructures of all samples consisted of large elongated grains of Al-matrix with some amount of precipitates. This is due to the fact that TMAZ experiences temperature changes with a small effect of stirring action. During HT, the precipitates grow in size and size of the precipitates is high enough to stop the grain boundary sliding, which leads to improve the hardness in HT samples. The solution HT resulted in formation of precipitates at elevated temperatures. Figure 4a–c displays the microstructures of heat-affected

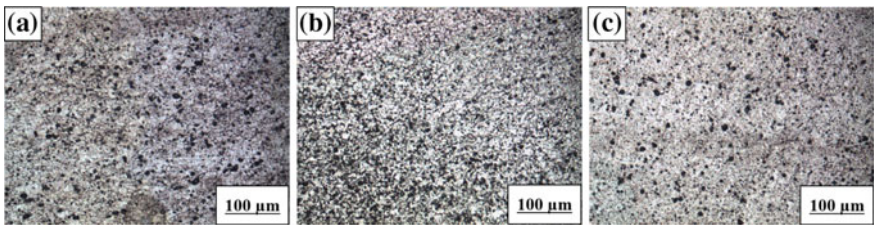


**Fig. 2** Microstructures of stir zone in overlapping pass for **a** Tool-1 (T-1) **b** Tool-2 (T-2) **c** Tool-3 (T-3)

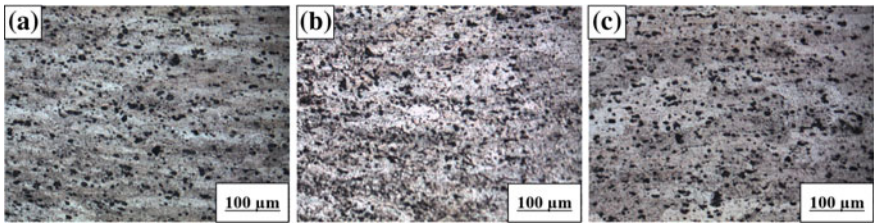


**Fig. 3** Microstructures of TMAZ for **a** Tool-1 (T-1) **b** Tool-2 (T-2) **c** Tool-3 (T-3)

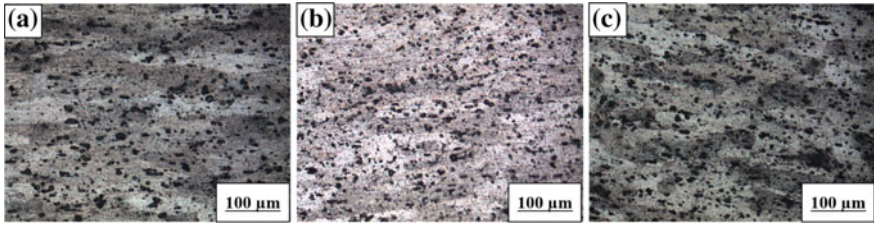


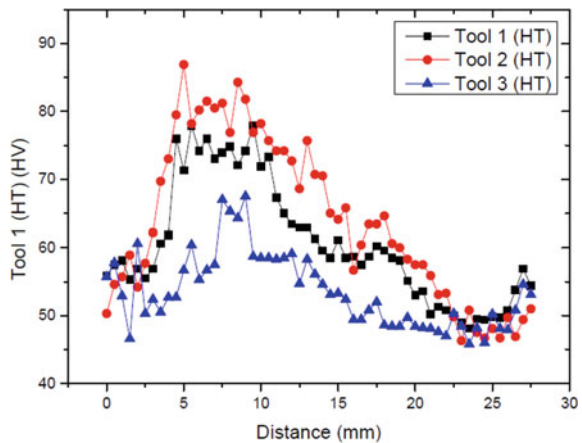
Fig. 4 Microstructures of HAZ for a Tool-1 (T-1) b Tool-2 (T-2) c Tool-3 (T-3)

zone (HAZ). Compared to all other zones, grain coarsening is more in HAZ due to the absence of pinning action and temperature changes.

### 3.2 Hardness

Figure 5 displays the micro-hardness profiles of HT samples. Uniform hardness was achieved in the stir zone of all samples. Sample processed with T-2 possessed the highest hardness in SZ. The more grain refinement in T-2 sample is the reason for more hardness according to the Hall–Petch equation. The lowest hardness in the SZ was obtained in the sample processed with T-3. These results are attributed to grain coarsening during FSP. All these hardness values were compared with hardness values of NON-HT samples and results have been represented in the graph form shown in Fig. 6a–c. The average hardness in the stir zone for HT sample processed with T-1 in the stir zone was 64.61 HV, which is 19.95% higher than NON-HT as shown in Fig. 6a. From Fig. 6b, it was observed that the average hardness in the stir zone for HT sample for T-2 in stir zone, which is 7.56% higher when compared to NON-HT sample. For T-3, there was an improvement of 12.76% in HT sample

Fig. 5 Hardness profile of HT samples



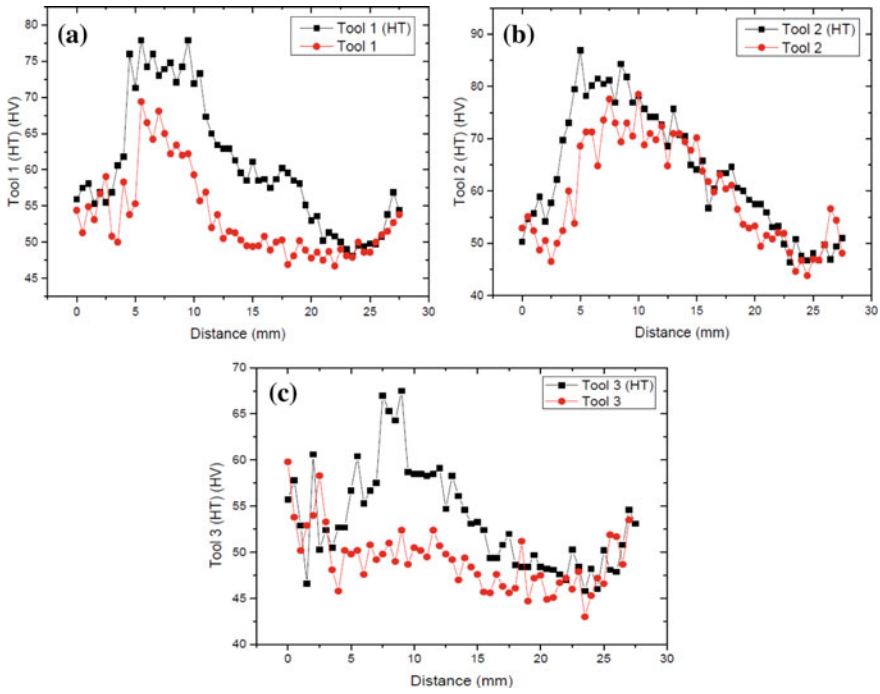


**Fig. 6** Comparison of hardness profiles of HT and NON-HT samples of **a** T-1 **b** T-2 **c** T-3

**Table 4** Average hardness values of HT and NON-HT samples in stir zone

Tool	HT (HV)	NON-HT (HV)
T-1	64.61	53.86
T-2	69.39	64.51
T-3	54.88	48.47

compared to NON-HT sample shown in Fig. 6c. These results witnessed precipitation behaviour in SZ. The average hardness values of HT and NON-HT samples in SZ are shown in Table 4.

### 4 Conclusions

In this investigation, a large bulk area FG structure was prepared with 50% pin overlapping using different tool geometries, post-processing heat treatment was carried and the following results were extracted.

- For all tool geometries, single-pass FSP grains were refined due to the severe plastic deformation and dynamic recrystallization and the grains size was further refined in overlapped passes.
- Sample processed with T-2 has more grain refinement than other profiles due to more number of edges of hexagonal pin profile and resulted in more plastic deformation.
- The highest average hardness was recorded in T-2 sample; the lowest average hardness was recorded for T-3 sample due to the grain refining and grain coarsening.
- Better hardness was obtained in HT samples compared to NON-HT samples as a result of precipitation hardening behaviour.

**Acknowledgements** The authors are very much thankful to the Aeronautical Research Board and Development (ARDB), New Delhi, India, for providing the financial assistance through the grant CCTM/TM/ARDB/GIA/16-17/0332, dated 17/01/2017 and National Institute of Technology, Warangal, India, for providing the laboratory facilities to carry out the project smoothly.

## References

1. Huang Yi, Langdon TG (2013) Advances in ultrafine-grained materials. *Mater Today* 16:85–93
2. Iwahashi Y, Wang J, Horita Z, Nemoto M, Langdon TG (1996) Principle of equal-channel angular pressing for the processing of ultra-fine grained materials. *Scripta Mater* 35:143–146
3. Naderi M, Peterlechner M, Divinski SV, Wilde G (2017) The effect of pre-annealing on defects, microstructure and recrystallization of ultra-fine grained Al produced by high-pressure torsion. *Mater Sci Eng A* 708:171–180
4. Tsuji N, Saito Y, Utsunomiya H, Tanigawa S (1999) Ultra-fine grained bulk steel produced by accumulative roll-bonding (ARB) process. *Scripta Mater* 40:795–800
5. Ma ZY (2008) Friction stir processing technology: a review. *Metall Mater Trans A* 39A:642–658
6. Mishra RS, MA ZY (2005) Friction stir welding and processing. *Mater Sci Eng R* 50:1–78
7. Su JQ, Nelson TW, Sterling CJ (2005) Friction stir processing of large-area bulk UFG aluminium alloys. *Scripta Mater* 52:135–140
8. Kumar N, Mishra RS, Huskamp CS, Sankaran KK (2011) Microstructure and mechanical behavior of friction stir processed ultrafine grained Al-Mg-Sc alloy. *Mater Sci Eng A* 528:5883–5887
9. Kwon YJ, Shigematsu I, Saito N (2003) Production of ultrafine-grained Al alloy using friction stir process. *Mater Trans* 44:1343–1350
10. Liu CY, Qu B, Xue P, Ma ZY, Luo K, Ma MZ, Liu RP (2018) Fabrication of large-bulk ultrafine grained 6061 aluminum alloy by rolling and low-heat-input friction stir welding. *J Mater Sci Technol* 34:112–118
11. Xue P, Xiao BL, Ma ZY (2013) Achieving large-area bulk ultrafine grained cu via submerged multiple-pass friction stir processing. *J Mater Sci Technol* 29:1111–1115
12. Gandra J, Miranda RM, Vilaca P (2011) Effect of overlapping direction in multipass friction stir processing. *Mater Sci Eng A* 528:5592–5599
13. Johannes LB, Mishra RS (2007) Multiple passes of friction stir processing for the creation of superplastic 7075 aluminum. *Mater Sci Eng A* 464:255–260
14. Ramesh KN, Pradeep S, Pancholi V (2012) Multipass friction-stir processing and its effect on mechanical properties of aluminum alloy 5086, *The Minerals. Metall Mater Soc Trans A* 43A:4311–4319

# Analysis of Micro-cracks and Micro-hardness in White Layer Formation on Machined Surfaces in EDM Process



K. Leela Kumar, Ch. Srinivasa Rao, B. Sateesh and M. S. R. Viswanath

**Abstract** In spite of huge advancement in machining process and much promising surface integrity, die-sinking EDM process is unavoidable. Micro-crack formation in the white layer zone in EDM leads to damage the quality of machined surface. This paper furnishes a quantitative investigation of micro-crack formation, in terms of crack width and orientation of micro-cracks formed in the white layer zone. The impact of processing conditions like peak current ( $I_p$ ) and pulse on duration ( $T_{on}$ ) on crack formation is examined by utilizing the perceptions of scanning electron microscope (SEM). In this work, micro-hardness is measured at different zones that are deposited layer, heat-affected zone (HAZ) and base metal. It is observed that significant improvement in the hardness value of the recast layer (9.175 Gpa) as compared to base metal (3.115 Gpa) of M<sub>2</sub> die steel.

**Keywords** Peak current ( $I_p$ ) · Pulse on duration ( $T_{on}$ ) · Micro-cracks and hardness · White layer formation

## 1 Introduction

Die-sinking electrical discharge machining is a thermal method that uses spark discharges to electrode, electrically conductive materials. A formed electrode decides where spark erosion can occur; it leads to cavity or hole within the workpiece. Due to experimental advantage and accuracy, die-sinking EDM is utilized in die manufacturing. Much of the cases, as in tools, die and aviation parts manufacturing, extreme pressure and thermal loads are experienced. To keep away from conceivable disappointments emerging from the surface imperfections of die-sinking EDMed parts,

---

K. L. Kumar (✉) · B. Sateesh · M. S. R. Viswanath  
Department of Mechanical Engineering, Vignan's IIT(A), Visakhapatnam 530049, India  
e-mail: [leelamech36@gmail.com](mailto:leelamech36@gmail.com)

Ch. S. Rao  
Department of Mechanical Engineering, AUCE, Andhra University, Visakhapatnam 530003, India

it is imperative that there ought to be a sufficient comprehension of the nature and degree of surface damage granted under different machining conditions [1].

In most engineering material, the formation of the recast layer and the surface cracks while machining through die-sinking EDM observed. The extreme heat created and connected with each discharge amid machining results serious temperature gradients in the machined surface [2]. Due to discontinuance of the discharge, the surface layers cool rapidly and build up tensile stress which causes crack formation in the machined surface [3]. Like many cases, the cracks terminate inside the recast layer. Be that as it may if they enter similar to the parent material, a noteworthy decrease in the fatigue strength, abrasive resistance, and corrosion resistance is observed [4]. Thus, the die-sinking EDM process is for the most part pursued by some type of post-preparing treatment to expel the recast layer with the end goal that the mechanical respectability of the machined segment can be checked. Anyway, this treatment procedure reaches out to manufacturing procedure as well as expands its expense. Therefore, it will be attractive to distinguish the processing conditions which eliminate the formation of recast layer with the end goal that the requirement for post-treatment can be wiped out and improve the mechanical properties of the machined part.

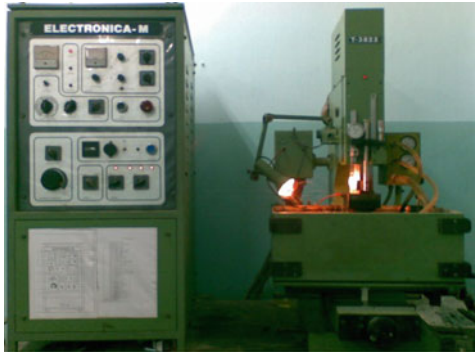
The present investigation underlines to connect the higher-order influences of major die-sinking EDM parameters like peak current ( $I_p$ ) and pulse on duration ( $T_{on}$ ) with various viewpoints of surface integrity like white layer thickness (WLT) and surface crack width while machining  $M_2$  die steel. In this work, micro-hardness is estimated at various zones that are deposited layer, heat-affected zone and base metal.

## 2 Experimental Procedure

A die-sinking EDM (Model T-3822, make Electronica machine tools Ltd., India) shown in Fig. 1 is used for the study. This machine has different current settings with a peak capacity of 12 A maximum. It can be run in both polarities. It has up to 520  $\mu$ s.

The targets of present experimental analysis have been performed for different combinations to find effective aggregate parameters. At ambient temperature, die steel with  $M_2$  hardened annealed sample (12 mm  $\times$  12 mm  $\times$  12 mm) as a work material with a composition of 0.85% C, 6.25% W, 4% Cr, 5% Mo, 2% V and remaining Fe. Experimentation was carried out to examine the effect of various EDM process parameters on white layer average thickness and surface crack width. Subsequently measurements of micro-hardness at different heat-affected zones (HAZ) are estimated.

A blind hole of 6 mm diameter and 2 mm depth was prepared on die steel work samples with a copper electrode. Castrol oil (ILO CUT-400) was chosen as a dielectric with its specific properties like dielectric quality, high flash point and low viscosity. Using DC power source, the impacts of peak current (1–12 A) and pulse on duration



### Specifications

Maximum work piece height: 125 mm  
 Maximum work piece weight: 80 kg  
 Longitudinal travel (X – axis): 200 mm  
 Transverse travel (Y – axis): 125 mm  
 Least count of hand wheel graduations with vernier scale: 0.02 mm  
 Maximum table quill distance: 340 mm  
 Minimum table quill distance: 190 mm  
 Work tank dimensions: 600 X 350 X 240 mm  
 Travel of the quill: 150 mm  
 Marching current maximum (A): 12  
 Open gap output voltage (V):  $135 \pm 5 \%$   
 Pulse duration: 2  $\mu$ s to 520  $\mu$ s

**Fig. 1** EDM experimentation setup

(2–520  $\mu$ s) were verified during experimentation with all other machining parameters constant.

The work sample is cleaned with acetone and the average white layer thickness is measured by using optical micrographs for each sample at  $500 \times$  magnification. Finally, the surface crack widths of work samples are observed by using SEM micrographs for different peak currents at pulse on duration (462  $\mu$ s) [5, 6]. Prepared copper electrode, work holding device and a sectional view of the machined work sample are shown in Figs. 2, 3 and 4, respectively.

**Fig. 2** Copper electrode



Fig. 3 Work holding setup

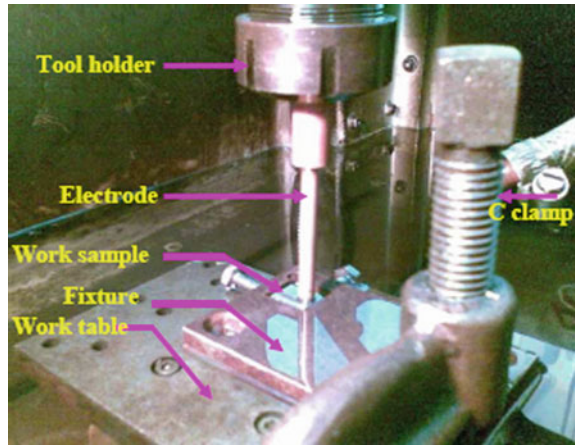
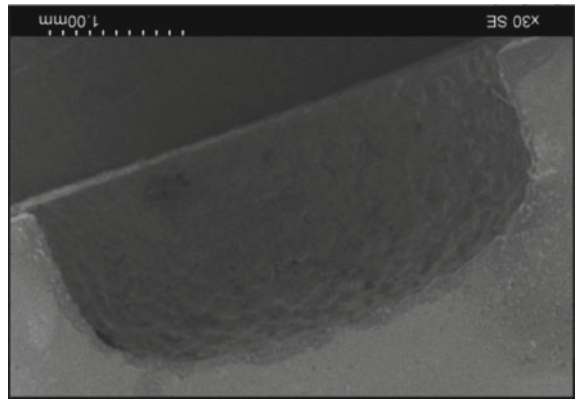


Fig. 4 Sectional view of workpiece



### 3 Design of Experiments

The principal goal in the use of experimental design is to provide the most and accurate information in the results, alongside the maximum efficient use of existing information. The experimental design method is implemented to optimize the dependability of results and set of experimentation without loss of accuracy. Experimental analysis has been performed and the effect of pulse on duration ( $T_{on}$ ) and peak current ( $I_p$ ) on the white layer thickness (WLT) and surface crack width is studied.

A  $2^k$  factorial with central composite second-order rotatable design (CCRD) is used (where the number of variables,  $k = 2$ ) and aggregate levels of the parameter, which cause a positive efficient response, can also be located. Experimental analysis is performed at four corner points at +1 level, four axial points at  $\gamma = +1.414$  and centre point at zero level with five iterations, and pure error was estimated. To allow



**Table 1** Actual and respective coded values for each parameter

Parameter	Coded value at different levels				
	1	2	3	4	5
	- 1.414	-1	0	+1	+1.414
Pulse on duration ( $T_{on}$ ) in $\mu$ S	42	104	252	400	462
Peak current ( $I_p$ ) in A	3.0	3.5	5.0	6.5	7.0

rotability, the axial points are picked, so that at all points, the variance of the model prediction is constant equidistant from the design centre [7]. Table 1 shows the actual and respective coded values for each parameter.

It is mandatory to repeat the test at the centre to the impartial estimate of the experimental errors. The precision of the predicted surface does no longer rely on the orientation of design with respect to the true response surface or the course of the search for optimum conditions results is shown in Table 2. The coded number for variables is obtained from the following transformation equation:

$$X_i = (\text{Chosen parametric values} - \text{Central rank value}) / (\text{Incremental parametric value})$$

**Table 2** Experimental results for training of the models based on CCD

Expt No.	Coded variables		Machining parameters		WLT ( $\mu$ m)
	$X_1$	$X_2$	Pulse on time ( $T_{on}$ ) $\mu$ s	Peak current ( $I_p$ ) A	
1	-1	-1	104	3.5	7.41
2	1	-1	400	3.5	16.6
3	-1	1	104	6.5	9.13
4	1	1	400	6.5	20.6
5	-1.414	0	42	5	5.95
6	1.414	0	462	5	20.39
7	0	-1.414	252	3	10.1
8	0	1.414	252	7	17.91
9	0	0	252	5	13.98
10	0	0	252	5	9.51
11	0	0	252	5	12.47
12	0	0	252	5	11.21
13	0	0	252	5	10.6

### 4 Experimental Results and Discussions

#### (i) Effect of pulse on duration ( $T_{on}$ ) and peak current ( $I_p$ ) on white layer thickness

The variation of white layer thickness different peak current is shown in Fig. 5. It is seen that the WLT increases as the pulse on duration ( $T_{on}$ ) increases. The higher pulse on duration permits the electro-discharge energy to enter further into the material, as a result, the thickness of the molten metal builds, which do not escape by the deficient detonating pressure of the dielectric at last outcomes in greater white layer thickness.

Figure 5 shows the effect of peak current on white layer thickness. It is observed that the average white layer thickness directly proportional to peak current and heat energy transferred into the specimen. This molten material solidified up to the recast layer under cooling effect and depth also formed as per the volume of liquid metal.

Figure 6 shows the various ( $I_p/T_{on}$ ) parametric combinations of 3A/462, 3.5A/462, 5A/462, 6.5A/462 and 7A/462  $\mu s$  and reveals the proportionality of average white layer thickness with peak current.

#### (ii) Effect of machining parameters on surface crack width

In specific, under tensile loading conditions, cracking is one of the most critical surface imperfections that decrease material resistance, fatigue as well as corrosion. Figure 7 shows quantify the variation of crack width with peak current at a constant

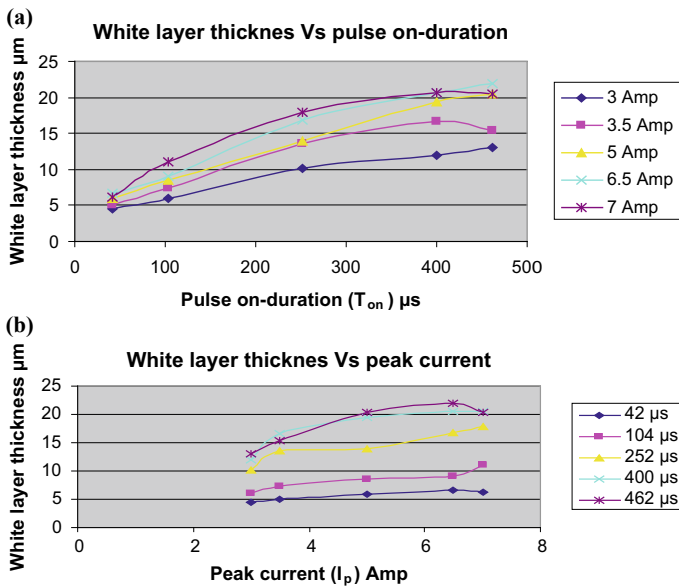
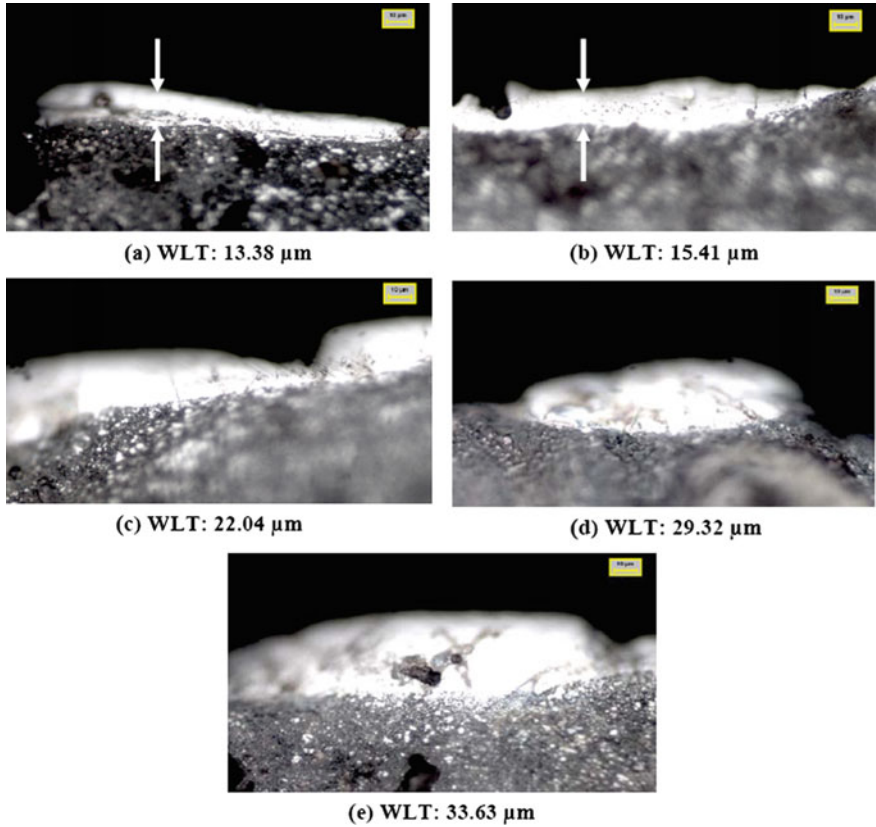


Fig. 5 a Pulse on duration vs white layer thickness and b Peak current vs white layer thickness



**Fig. 6** Optical micrographs of white layer at (a) 3A/462  $\mu$ s (b) 3.5A/462  $\mu$ s (c) 5A/462  $\mu$ s (d) 6.5A/462  $\mu$ s (e) 7A/462  $\mu$ s ( $I_p/T_{on}$ )10  $\mu$ m

pulse on duration. It illustrated that for a constant pulse on duration, there is a significant increase in surface crack width with increasing peak current. At peak current of 3 A, the crack width is very low and high at 7 A.

(iii) **Variation of hardness at different recast layers zones**

Figure 8 shows the measurement of micro-hardness of different zones, i.e. white layer zone, heat-affected zone and base metal. It is observed that hardness value of the white layer is 9.175 GPa, at the junction 7.57 GPa and at the base metal 3.115 GPa. It illustrates that the hardness value of the recast layer is larger as compared to base metal.

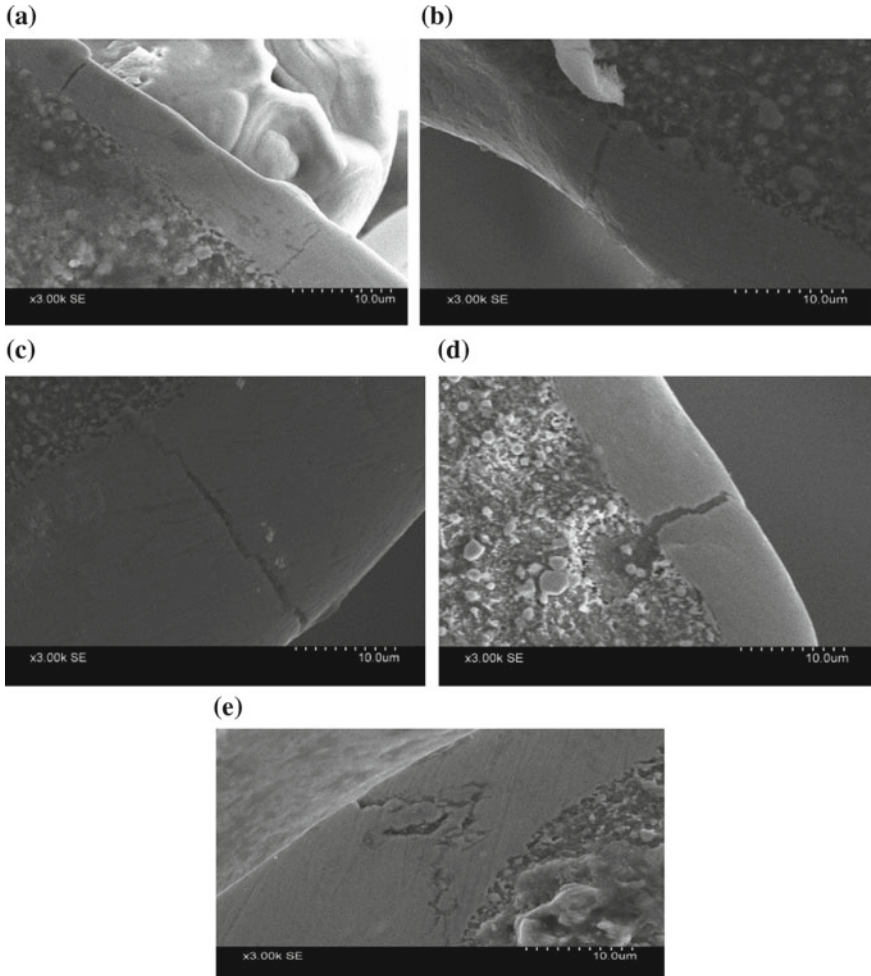
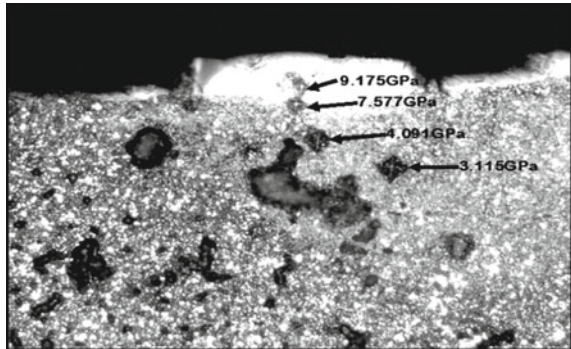


**Fig. 7** SEM micrographs of surface cracks at (a) 3A/462 μs (b) 3.5A/462 μs (c) 5A/462 μs (d) 6.5A/462 μs (e) 7A/462 μs ( $I_p/T_{on}$ )

## 5 Conclusions

- (i) From parametric investigation, it is observed that average white layer thickness, as well as surface crack width, is directly proportional to peak current and pulse on duration.
- (ii) Minimum white layer thickness is observed at the pulse on duration in the range of 42–252 μs and peak current in the range of 3–5 A.
- (iii) Minimum crack width is observed below 3.5 A at constant pulse on duration of 462 μs.

**Fig. 8** Micro-hardness at different zones of the transverse section



- (iv) From the experimental study, it is observed that hardness 9.175 Gpa of the recast layer is larger as compared to base metal hardness 3.115 Gpa.

## References

1. Bhattacharyya B, Gangopadhyay S, Sarkar BR (2007) Modeling and analysis of EDM<sub>ED</sub> job surface integrity. *J Mater Process Technol* 189(1–3):169–177. <https://doi.org/10.1016/j.jmatprotect.2007.01.018>
2. Abu Zeid OA (1997) On the effect of electro discharge machining parameters on the fatigue life of AISI D6 tool steel. *J Mater Process Technol* 68:27–32
3. Tai TY, Lu SJ, Chen YH (2011) Surface crack susceptibility of electrodischarge machined steel surfaces. *Int J Adv Manuf Technol* 57(9):983–989
4. Rebelco JC, Dias AM, Kremer D, Lebrun JL (1998) Influence of EDM pulse energy on the surface integrity of martensite steels. *J Mater Process Technol* 84:90–96
5. Lee SH, Li X (2003) Study of the surface integrity of the machined work piece in the EDM of the tungsten carbide. *J Mater Process Technol* 139:315–321
6. Lee LC, Lim LC, Wong YS, Lu HH (1990) Towards a better understanding of the surface features of electro-discharge machined tool steels. *J Mater Process Technol* 24:513–523
7. Hewidy MS, El-Taweel TA, El-Safty MF (2005) Modelling the machining parameters of wire electrical discharge machining of Inconel 601 using RSM. *J Mater Process Technol* 169:328–336

# Multi-objective Optimization of Submerged Friction Stir Welding Process Parameters for Improved Mechanical Strength of AA6061 Weld Bead by Using Taguchi-L18-Based Gray Relational Analysis



Laxmana Raju Salavaravu and Lingaraju Dumpala

**Abstract** Submerged friction stir welding (SFSW) is a moderation tool in the manufacturing industry. SFSW is used to join the AA6061-T6 plates in the seawater environment to different processes of parameters that are tool rotation speed, feed rate, and tilt angle. The experiments are done by using optimization method. To obtain a single optimum combination of parameters for these two types of responses, gray relational analysis has been utilized. Gray relational grade and a single optimum setting have been acquired for the SFSW of AA6061-T6. One of the most affecting and influencing processes of parameter is to find by applying ANOVA and the maximum orderly tool rotational speed is 61.63%, tool feed rate is 17.95% and finally, tool tilt angle is 12.47% of contribution in the entire process.

**Keywords** Submerged friction stir welding (SFSW) · Taguchi's method · Gray relational analysis (GRA) · Ultimate tensile strength (UTS) · Micro hardness (HV)

## 1 Introduction

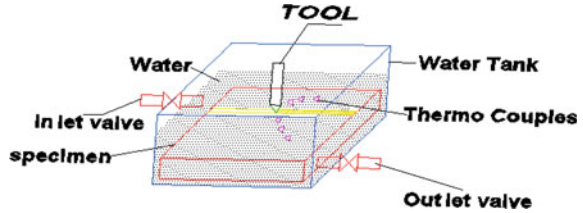
FSW is a moderate technique developed by TWI Cambridge for joining of aluminum alloys. This process is widely used in so many industries such as aircraft, aerospace, automobile, naval. FSW joints with high strength, low weld defects, low distortion, and low cost are the main advantages of this method. FSW is comprised of a non-consumable specially designed rotating tool is inserted into the edges of the two plates heating the workpiece by the friction between tool and workpiece the tool transverse along the line of joint the material flows from advancing side to retreating

---

L. R. Salavaravu  
Mechanical Engineering Department, Sri Sivani College of Engineering,  
Chilakapalem, Andhra Pradesh 532402, India

L. Dumpala (✉)  
Mechanical Engineering Department, JNTUK UCEK, Kakinada,  
Andhra Pradesh 533003, India

**Fig. 1** Schematic view of the submerged FSW process



side the producing joint in a solid state (Fig. 1). The FSW joints have three affected microstructural zones: heat-affected zone (HAZ), nugget zone (NZ), and thermo-mechanical affected zone (TMAZ) [1].

AA6061 is a heat treatable alloy having high corrosion resistance, high toughness, and good strength. The FSW joint mechanical properties mainly affected on the process of parameters are the tool rotation speed, the tool transverse feed, the tool pin geometry, and tilt angle. Sakurada et al. [2] initially used submerged friction stir welding for AA6061. Its is observed that the required amount of heat generated is sufficient enough for submerged friction stir welding. Fratini et al. [3] founded FSW of aluminum alloy plates with a cooling of water by the rotating tool during the process. The strength of the weld joint was observed to be more than that of NFSW. Zhang et al. [4] investigated that the underwater FSW increases the tensile strength of NFSW AA2219 joints at low welding speed and observed no conspicuous impact in the higher welding speeds. It depends on the water cooling rate. Liu et al. [5] found that the TMAZ was the failure zone in the friction stir welded joint, and the tensile fracture was exactly occurred, and the hardness improvement in the joint is essential to improve the tensile strength of the joint. Sabari et al. [6] found that the UFSW joint having higher tool traverse feed exhibited higher tensile properties. In these conditions, we find various aspects, i.e., the lower heat generation, high grain boundary strengthening, more volume fraction of particles, and the low hardness distribution region. In the normal FSW process, temperature is affected on the stir zone, and the base material is not affected in the process. The stir zone properties are drastically changed into the base material. Instead of this process, water cooling is used to yield better weld joint properties. This process is termed as SFSW process.

Kasan et al. [7] and Kumar et al. [8] studied TM with GRA approach for the optimization of FSW process parameters for different combinations and dissimilar aluminum alloys and found that the tool feed is the most effective parameter for gray relational grade. Rajakumar et al. [9] conducted to study the effects of tool geometry and FSW process parameters on tensile strength and microhardness of AA6061 FSW joints. They showed that the tool rotational speed and tool shoulder diameter are the most influential factors on mechanical properties. The effect of the FSW process parameters on the tensile strength of the joint was established by using tools such as Taguchi, analysis of variance (ANOVA), and RSM which were used to optimize the FSW parameters. Singarapu et al. [10] studied ANOVA test that was conducted to find out the significant values of FSW process parameters on mechanical properties such as UTS, YS, %EL, impact toughness, and microhardness and found that the rotational

speed has the highest % of contribution on UTS and microhardness, whereas tool transverse feed has the lowest mechanical properties such as UTS, YS, % EL, impact toughness, and microhardness values. Ilangovan et al. [11] observed that dissimilar joints of AA6061-AA5086 aluminium alloy joints were having good tensile strength, hardness and fine microstructure in all weld zones.

Nevertheless, the joining of AA6061-T6 plates using SFSW with the optimization of control variables using gray-Taguchi analysis is very limited. In this paper, multi-response optimization method, i.e., gray-Taguchi technique was applied to analyze the experimental results of mechanical properties of weld joints. Analysis was done for SFSW AA6061-T6 weld joints. Control variables used in the examination were tool rotational speed (rpm), tool transverse feed (mm/min), and tool tilt angle. For decreasing the experimental runs and getting the optimum conditions of control variables and their interactions based on the design of experiment by using an  $L_{18}$  orthogonal array in the Taguchi technique. The effect of these control variables on the response characteristics such as UTS and microhardness was examined to attain the optimal condition of the process factors. Analysis of variance (ANOVA) was used to evaluate the contribution of each control factor and its interactions on mechanical properties of weld joints.

## 2 Experimentation

The base material (BM) used for the experiments is a 6-mm-thick 6061 aluminum alloy; the chemical compositions values and mechanical properties of BM and tool material are listed in Table 1. The plates were prepared into rectangular shaped plates with the dimension of 230 mm long by 60 mm width, and the edges are prepared in a straight manner. After cleaned by acetone, the samples were clamped in a straight manner tool travel line to the backing plate in a tank, and then, the water at room temperature was poured into the tank to submerge the top surface of the work plates.

Butt weld joints were manufactured under seawater by utilizing an FSW machine which are at various welding speeds and various rotation speeds along the tool travel direction. The  $H_{13}$  welding tool of an 18 mm shoulder diameter and a cylindrical conical shaped pin with the length of 5.7 mm and the maximum diameter of 6 mm minimum diameter of pin is 3 mm. During the FSW, a  $1^\circ$  and  $2^\circ$  tilt angles and an axial load of 4.6 KN were applied to the welding tool. By using Taguchi orthogonal array,  $L_{18}$  OA ( $2^1$  &  $3^2$ ) is used, and the process parameters are placed in Table 2.

After the welding the samples are prepared by using water jet cutting machine for tensile test, Metallographic analyses and Vickers hardness tests.

Microhardness values were measured from the centerline of the thickness and polished cross sections with spacing from the weld centerline of 1 mm between the adjacent indentations. The testing load was 3 N for 10 s.

The tensile test specimens are prepared as per the ASTM-E8 standard. The tensile test is conducted at a crosshead speed of 1 mm/min at room temperature by utilizing a computer-controlled testing machine (Instron-8801). The tensile properties are



**Table 1** Chemical composition of AA6061

Element present	Si	Fe	Cu	Mn	Mg	Zn	Tn	Cr	Al	Others
6061 % present	0.4-0.8	0-0.7	0.15-0.4	0.0-0.15	0.8-1.2	0.0-0.25	0-0.15	0.04-0.35	Balance	0.05-0.15

**Table 2** Process parameters

Factor	Type	Levels	Values		
Tilt angle T (degrees)	Fixed	2	1	2	null
Rotational speed N (rpm)	Fixed	3	1100	1200	1400
Tool feed F (mm/min)	Fixed	3	22	45	60

evaluated using two specimens cut from the same joint. The prepared tensile specimens were subjected to tensile test, and its ultimate tensile strength is evaluated. The experiments were conducted according to the designed L18 OA. Table 3 will give the values of designed experimental layout.

### 3 Optimization Steps Using Taguchi-Based Gray Relation Analysis

In the gray relational analysis (GRA), experimental results (UTS, Microhardness) are first standardized in the range somewhere in the range of zero and one, which is additionally called the normalization. Next, the gray relational coefficient is determined from the standardized experimental data to express the connection between the ideal and experimental test information. At that point, the Gray Relational Grade (GRG) is evaluated by averaging the gray relational coefficients relating to each process response. The general assessment of the various procedure responses depends on the GRG. Accordingly, the optimization of the confounded different process responses can be changed over into the enhancement of a single GRG. At the end of the day, the GRG can be treated as the general assessment of experimental data for the multi-response process. Optimization of SFSW process parameters is the level with the highest GRG. By using the below equations, GRA is as follows:

Normalization of the data of UTS and microhardness by considering larger is better performance characteristics is evaluated by using Eq. (1).

$$x_i^*(k) = \frac{x_i^o(k) - \min x_i^o(k)}{\max x_i^o(k) - \min x_i^o(k)} \tag{1}$$

where  $k = 1 \dots n$ ,  $i = 1 \dots 9$ ,  $n$  is the performance characteristic, and  $i$  is the trial number. The gray relation coefficient can be calculated as follows:

$$x_i^*(k) = \frac{\max x_i^o(k) - x_i^o(k)}{\max x_i^o(k) - \min x_i^o(k)} \tag{2}$$

$\min_{\nabla j \in k} \|x_0^*(k) - x_i^0(k)\|$  is the smallest value of  $\Delta_{0i}$ ,  $\Delta_{\max} = \max_{\nabla j \in k}$ ,  $\max_{\nabla j \in k} \|x_0^*(k) - x_i^0(k)\|$  is the largest value of  $\Delta_{0i}$ .

After calculating gray relational coefficients, the GRG is obtained as follows:

**Table 3** GRA analysis

S no.	Tilt angleT	Rotation speed N	Tool feed F	UTS	HV	Normalizing Step-I			Gray relational coefficient			Rank
						UTS	HV	UTS	UTS	HV	GRG	
1	1	1100	22	163	96	0.368	0.376	0.442	0.445	0.443	15	
2	1	1100	45	160	91	0.211	0.108	0.388	0.359	0.373	17	
3	1	1100	60	156	89	0.000	0.000	0.333	0.333	0.333	18	
4	1	1200	22	165	100	0.474	0.565	0.487	0.534	0.511	11	
5	1	1200	45	162	98	0.316	0.457	0.422	0.479	0.451	14	
6	1	1200	60	161	95	0.263	0.296	0.404	0.415	0.410	16	
7	1	1400	22	174	105	0.947	0.860	0.905	0.782	0.843	2	
8	1	1400	45	172	103	0.842	0.753	0.760	0.669	0.715	4	
9	1	1400	60	169	99	0.684	0.538	0.613	0.520	0.566	8	
10	2	1100	22	167	100	0.579	0.591	0.543	0.550	0.547	9	
11	2	1100	45	166	98	0.526	0.465	0.514	0.483	0.498	12	
12	2	1100	60	164	99	0.441	0.511	0.472	0.505	0.489	13	
13	2	1200	22	170	103	0.711	0.753	0.633	0.669	0.651	5	
14	2	1200	45	168	101	0.632	0.645	0.576	0.585	0.580	7	
15	2	1200	60	166	101	0.500	0.618	0.500	0.567	0.534	10	
<b>16</b>	<b>2</b>	<b>1400</b>	<b>22</b>	<b>175</b>	<b>108</b>	<b>1.000</b>	<b>1.000</b>	<b>1.000</b>	<b>1.000</b>	<b>1.000</b>	<b>1</b>	
17	2	1400	45	173	104	0.895	0.823	0.826	0.738	0.782	3	
18	2	1400	60	171	100	0.789	0.591	0.704	0.550	0.627	6	

The bold values represent optimum values

$$\frac{1}{n} \sum_{i=1}^n \xi_i(k) = \gamma_i \tag{3}$$

Normalized Gray relational coefficients and GRG of experimental results of UTS and HV are placed in the tabular form 3.

### 4 Taguchi Method/Gray Relational Analysis

By using GRG values, apply Taguchi analysis. In this analysis, larger is better for both UTS and HV combined GRG. In the Taguchi method by using mean value of GRG optimum is identified at the Level of factors are affected to the responses by determined using ranking. In this response of mean in the SFSW process, the main affecting parameter is the tool rotation speed which is having first rank, and the feed rate having the second affecting parameter, and finally, the tool tilt angle is the least affecting parameters. Those values are placed in the tabular form Table 4.

Optimum levels of the factor are analyzed by using analysis of variance (ANOVA) in Minitab17 software. The average GRG for each level of the factor is computed in Table 4. The higher the GRG implies better quality characteristics. Based on the higher GRG the optimal of the each controllable factor is determined. The average GRG and the optimal levels of the affective factors are listed in Table 8. The optimum levels of the process parameters based on the GRG, the tilt angle is the third affected parameter at the level 2 of 2° and Tool rotation speed is the main affected parameter at the level 3 of 1400 rpm and feed rate is the second priority parameter at 1st level of 22 mm/min. The order is writing as T2N3F1. Finally, the UTS and microhardness are affected by the order of tool rotational speed, feed rate, and tilt angle.

The prediction value is calculated by using GRG values = T2 + N3 + F1 - 2  
 \*average mean = 0.905

The ANOVA summary results of the GRG, as appeared in Table 5, indicates the tool tilt angle, tool rotation speed, and feed rate significant SFSW process parameters, respectively, for influencing the different performance characteristics. This result

**Table 4** Response table for means

Level	Tilt angle T	Tool rotational speed N	Feed F
1	0.5162	0.4473	<b>0.6659</b>
2	<b>0.6342</b>	0.5227	0.5666
3		<b>0.7555</b>	0.4931
Delta	0.1180	0.3082	0.1728
Rank	3	1	2

The bold values represent optimum values  
 GRG mean value = 0.575188

**Table 5** Analysis of variance (ANOVA)

Source	DF	Adj SS	Adj MS	F-Value	P-Value	Contribution %
Tilt angle T (degree)	1	0.06269	0.062695	18.84	0.001	12.47
Rotational speed N (rpm)	2	0.30973	0.154863	46.53	0.000	61.63
Tool feed F (mm/min)	2	0.09020	0.045102	13.55	0.001	17.95
Error	12	0.03994	0.003328			7.95
Total	17	0.50257				

concur with the consequences of the response table for the GRG, as appeared in Table 5. Based on the past discussions, the optimal SFSW process for the best multiple performance characteristics is predicted to be the case of tool rotation speed at level 3 of 1400 rpm, tool tilt angle at level 2 of 2 degree, and transverse speed at level 1 of 22 mm/min. The last step is to predict and check the optimal SFSW process parameter combinations for the best multiple performance characteristics. Yet, standard SFSW processing parameters are not available in the literature because SFSW is a novel material joining technique. The process parameters are contributed in this order: The tool rotation speed is maximum affecting process parameter of 61.63%, tool feed rate is 17.95%, tilt angle is 12.47%, and the error percentage in this experimental is 7.95. The predicted value of GRG is 0.905 at optimal process parameters, and from the experimental results, GRG is 1.00 and the deviation is 0.095

## 5 Conclusion

By using the Taguchi based-gray relational analysis to optimize the SFSW process with the multiple objectives has been reported in this research paper. A gray relational analysis of the UTS and microhardness objectives from the single objective is called the GRG. The optimal conditions of SFSW have been obtained for the weld joints of AA6061. The optimal SFSW process parameter combinations are tool rotation speed at 1400 rpm, feed rate at 22 mm/min, and tilt angle at 2° for the best multiple objectives. The most affective SFSW process parameter in the line of order is the higher tool rotation speed 61.63, lower tool feed rate 17.95, and higher tool tilt angle 12.47% of contribution.

## References

1. Prado RA, Murr LE, Shindo DJ, Soto KF (2001) Tool wear in the friction-stir welding of aluminum alloy 6061+20% Al2O3: a preliminary study. Scripta Mater 45:75–80

2. Sakurada D, Katoh K, Tokisue H (2005) Underwater friction welding of 6061 aluminum alloy. *J Japan Institute Light Met* 52:2–6
3. Fratini L, Buffa G, Shivpuri R (2010) Mechanical and metallurgical effects of in process cooling during friction stir welding of AA7075-T6 butt joints. *Acta Mater* 58(6):2056–2067
4. Zhang Z, Xiao BL, Ma ZY (2014) Influence of water cooling on microstructure and mechanical properties of friction stir welded 2014Al-T6 joints. *Mater Sci Eng A* 614:6–15
5. Liu HJ, Jie HJ, Lei Yu (2011) Homogeneity of mechanical properties of underwater friction stir welded 2219-T6 aluminum alloy. *J Mater Eng Perform* 20(8):1419–1422
6. Sabari SS, Malarvizhi S, Balasubramanian V (2016) Influences of tool traverse speed on tensile properties of air cooled and water cooled friction stir welded AA2519-T87 aluminium alloy joints. *J Mater Process Technol* 237:286–300
7. Kasan S, Yenier Z (2014) Analyzing dissimilar friction stir welding of AA5754/AA7075. *Int J Adv Manuf Technol* 70:145–156
8. Kumar S, Kumar S (2015) Multi-response optimization of process parameters for friction stir welding of joining dissimilar Al alloys by gray relation analysis and Taguchi method. *J Braz Soc Mech Sci Eng* 37:665–674
9. Rajakumar S, Muralidharan C, Nadu T, Balasubramanian V, Nadu T (2011) Response surfaces and sensitivity analysis for friction stir welded AA6061-T6 aluminium alloy joints. *Int J Manuf Res* 6(3):215–235
10. Singarapu U, Adepu K, Arumalle SR (2015) Influence of tool material and rotational speed on mechanical properties of friction stir welded AZ31B magnesium alloy. *J Magnesium Alloys* 3(4):335–344. <https://doi.org/10.1016/j.jma.2015.10.001>
11. Ilangovan M, Boopathy SR, Balasubramanian V (2015) Microstructure and tensile properties of friction stir welded dissimilar AA6061–AA5086 aluminium alloy joints. *Trans Nonferrous Met Soc China* 25:1080–1090

# Investigation on Wear Behaviour of AA5052/SiC/Al<sub>2</sub>O<sub>3</sub> Hybrid Composite Fabricated Using Stir Casting Process



V. G. Shanmuga Priyan, R. Malayalamurthi and S. Kanmani Subbu

**Abstract** This project aims to increase the wear resistance of aluminium alloy 5052 (AA5052), which has very good corrosion resistance, ductility, excellent thermal and electrical conductivity. Composites were fabricated using AA5052 reinforced with silicon carbide 3% and alumina 3 & 4% by weight of the matrix, melting temperature 700 & 750 °C and stirring time 3 & 5 min. Maximum micro-hardness and tensile Strength were achieved for the combination of silicon carbide—3%, alumina—4%, melting temperature—750 °C and stirring time—3 min. Composite fabricated for the above said condition is used for wear analysis. The design of experiments was planned in full factorial method with load, speed, time and track diameter as input factors and wear as the response or output factor. The test was performed in pin-on-disc tribometer as per design of experiments. The process parameter combination of 2 kg load, 500 rpm speed, 5 min time and 70 cm track diameter was found to be the optimum condition for minimum wear of the fabricated hybrid composite. Wear resistance was increased by 51%. Speed has the maximum influence with 45.52% contribution, whereas time has the least influence with 7.02% contribution.

**Keywords** Stir casting · Hybrid composite · Pin-on-disc apparatus · Full factorial method

## 1 Introduction

Aluminium-based metal matrix composites are being extensively used in various fields owing to their superior mechanical properties like low weight, high strength-to-weight and stiffness-to-weight ratio and good corrosion resistance. It is commonly

---

V. G. Shanmuga Priyan (✉) · S. Kanmani Subbu  
Mechanical Engineering, Indian Institute of Technology  
Palakkad, Palakkad, Kerala 678557, India  
e-mail: [shanmu0122@gmail.com](mailto:shanmu0122@gmail.com)

R. Malayalamurthi  
Department of Mechanical Engineering, A.C College of Engineering  
and Technology, Karaikudi, Tamilnadu 630004, India

© Springer Nature Singapore Pte Ltd. 2020  
H. K. Voruganti et al. (eds.), *Advances in Applied Mechanical Engineering*,  
Lecture Notes in Mechanical Engineering,  
[https://doi.org/10.1007/978-981-15-1201-8\\_104](https://doi.org/10.1007/978-981-15-1201-8_104)

used in marine and aerospace applications. Among the various methods available to process metal matrix composites (MMC) like powder metallurgy, diffusion bonding, deformation bonding and squeeze casting, stir casting is the most commonly used and economic method. Composite materials have become a significant part of engineering materials that find applications starting from day-to-day applications to advanced technologies.

Saravanan et al. [1] made a detailed review of the effect of particulate reinforcements on aluminium metal matrix composites and their different fabrication techniques. They have also provided guidelines and criteria for selection of process parameters like stirring speed, time, melt temperature, reinforcements and die pre-heat temperature, etc. in stir casting process. Sozhamannan et al. [2] studied the effect of stir casting parameters like melting temperature and holding time on tensile strength, hardness and impact strength for Al/SiC composite. They concluded that 700–800 °C melting temperature is optimum for better and uniform distribution of reinforcement in the matrix. Prabu et al. [3] concluded that particle clustering occurred when stirring speed and stirring time were less. Homogenous distribution of SiC in the matrix was reported when the stirring speed and time were increased to 600 rpm and 10 min, respectively. Uvaraja et al. [4] suggested that for a sliding speed of 4.5 m/s, applied load of 10 N, sliding time of 5 min and reinforcement content of 15%, both coefficient of friction and the wear rate were optimum. Percentage reinforcement, applied load and speed had the contributions of 30.99, 29.96 and 29.86%, respectively. Baradeswaran et al. [5] made AA6061/B<sub>4</sub>C/graphite and AA7075/B<sub>4</sub>C/graphite hybrid composites and studied their properties. They concluded that 10 N applied load, 0.8 m/s sliding speed and 2000 m sliding distance were the optimum conditions for minimum wear of the fabricated composites. Kumar et al. [6] studied the mechanical and tribological properties of AA6061/SiC and AA7075/Al<sub>2</sub>O<sub>3</sub> composites and concluded that the reinforcement particles increased the overall properties in comparison to the respective base alloys. Venkataraman et al. [7] attempted to analyse the influence of mechanically mixed layer (MML), that forms during the sliding wear tests, by studying the dry sliding wear behaviour of aluminium, AA7075 and AA7075/SiC composites. They concluded that non-formation or fracture of the MML causes severe wear.

## 2 Experimental Work

### 2.1 Composite Fabrication

The composites were fabricated in bottom pouring type stir casting machine supplied by SwamEquip, Chennai. The experimental set-up consists of an electric resistance type furnace and a mechanical stirrer. The furnace has a crucible capacity of 2 kg. The maximum temperature that can be achieved during operation is 1000 °C. The current rating of the furnace is single phase 230 V AC, 50 Hz. AA5052 rods of



the required weight were heated in the crucible until they were completely molten and maintained at 700 & 750 °C. Reinforcement powders silicon carbide (3%) and alumina (3 & 4%) were preheated externally to a temperature of 250 °C to remove surface impurities that ensure proper mixing and were introduced into the melt pool and stirred at 600 rpm for 3 & 5 min. Argon gas was passed into the molten metal to remove the soluble gases present in the liquid state metal. The completely molten hybrid composite was poured into the die of required length and diameter.

## 2.2 Design of Experiments

Design of experiment is a suitable tool to model and analyse the effect of process variables or factors on a specific variable or response, which is an unknown function of the process variables. Design of experiments was planned in full factorial design method. It is a multi-factor design that not only tests the individual effect of factors, but also the combined effect or interaction of the factors on response. The number of experiments required in a factorial design is higher than that in a Taguchi design or fractional design, but it delivers accurate results. The parameters chosen for analysis were load, speed, time and track diameter and the response parameter is wear. Table 1 shows the parameters, their levels and the number of experimental runs conducted.

**Table 1** Wear test results

S.No.	Load (kg)	Speed (rpm)	Time (min)	Track diameter (cm)	Wear ( $\mu\text{m}$ )
1	2	500	5	70	89
2	3	500	5	70	113
3	2	600	5	70	122
4	3	600	5	70	142
5	2	500	7	70	103
6	3	500	7	70	122
7	2	600	7	70	125
8	3	600	7	70	153
9	2	500	5	80	103
10	3	500	5	80	129
11	2	600	5	80	129
12	3	600	5	80	158
13	2	500	7	80	109
14	3	500	7	80	146
15	2	600	7	80	154
16	3	600	7	80	165

### 2.3 Wear Test

All the fabricated hybrid composites were tested for micro-hardness and tensile strength. The average micro-hardness and tensile strength was 88 HV and 237 N/mm<sup>2</sup>, respectively. Maximum tensile strength and micro-hardness were achieved for the combination silicon carbide—3%, alumina—4%, melting temperature—750 °C and stirring time—3 min. This composite was selected for wear analysis. A pin-on-disc test tribometer supplied by Ducom Instruments was used to study the dry sliding wear behaviour of the composites in accordance with ASTM G99-95 standards. Pins of 20 mm height and 10 mm diameter were cut from the samples and polished. All these tests were conducted at room temperature. The wear test was carried out for 2 & 3 kg load, 500 & 600 rpm speed, 5 & 7 min time and 70 & 80 cm track diameter as per the design of experiments. The pin is held and loaded vertically into the rotating steel disc of material EN32 and hardness 65 HRC by an arm. Once the specimen has run for the specified time, it is removed, cleaned and the process is repeated.

### 2.4 Microstructural Study of Worn Surface

Morphological feature of worn surface is an important quantitative aspect of wear surface analysis. Wear measurement depends on tribological features at interspaces. The worn specimen was removed from the tribometer and studied in an inverted microscope supplied by Mitutoyo. The workpiece mounted on the stage can be moved in *X*-direction and *Y*-direction with the help of concentric knobs which facilitate coarse and fine adjustments. The objective lens extends and retracts along the vertical direction to provide the necessary focusing.

## 3 Results and Discussion

The wear value for each run was noted from the data acquisition system. The results of the test are given in Table 1 where the wear values for each specimen are entered against its parameter combination. The wear graphs of the Samples 1 & 16 are shown in Fig. 1. Samples 1 and 16 showed a wear of 89 μm and 165 μm, respectively, which are the minimum and maximum values in the entire set. While Sample 1 was tested for the condition load—2 kg, speed—500 rpm, time—5 min and track diameter—70 cm, Sample 16 was tested for the condition load—3 kg, speed—600 rpm, time—7 min and track diameter—70 cm. The differences in the load, speed and time caused a substantial difference in wear. Sample 1 showed gradual wear in the initial stage, but towards the end the wear shot up. Sample 16 showed steady increase in wear right from the start. This may be due to the removal of reinforcement particles from the matrix.

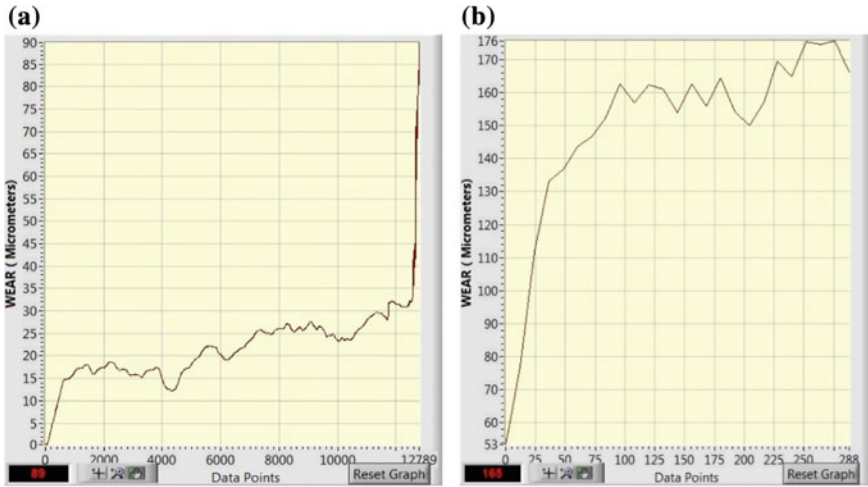


**Fig. 1** Wear graphs of samples **a** Sample 1, load—2 kg, speed—500 rpm, time—5 min and track diameter—70 cm **b** Sample 16, load—3 kg, speed—600 rpm, time—7 min and track diameter—70 cm

### 3.1 Optimization

The results obtained from wear test were optimized for minimum wear. Figure 2 depicts the main effects plot for wear, which shows the individual influence of load, speed, time and track diameter on the response wear. The mean of wear has a linear relation with the factors. The rotational speed of the disc decides the relative motion between the tribo-pairs. The higher the speed, the higher will be the relative motion between the tribo-pairs in the given time and hence higher wear. Load decides the force applied on the specimen, higher the load the higher is the coefficient of friction and wear. Track diameter controls the sliding distance and time duration for which the specimen is in contact with the rotating disc. Increase in both the factors has similar effect as the other factors, and the final result is the increase in wear. The slope of the curves obtained shows the influence of the corresponding parameter. From Figs. 2a and 2b, it can be seen that when the load changes from 2 to 3 kg or when the speed increases from 500 to 600 rpm, the mean of wear shows a significant difference. However, in Fig. 2c and 2d, when the time or track diameter is increased, the difference in mean of wear is not so pronounced. From this, it can be understood that speed has maximum influence and time the minimum. The minimum value of wear occurred for the condition load—2 kg, speed—500 rpm, time—5 min and track diameter—70 cm.

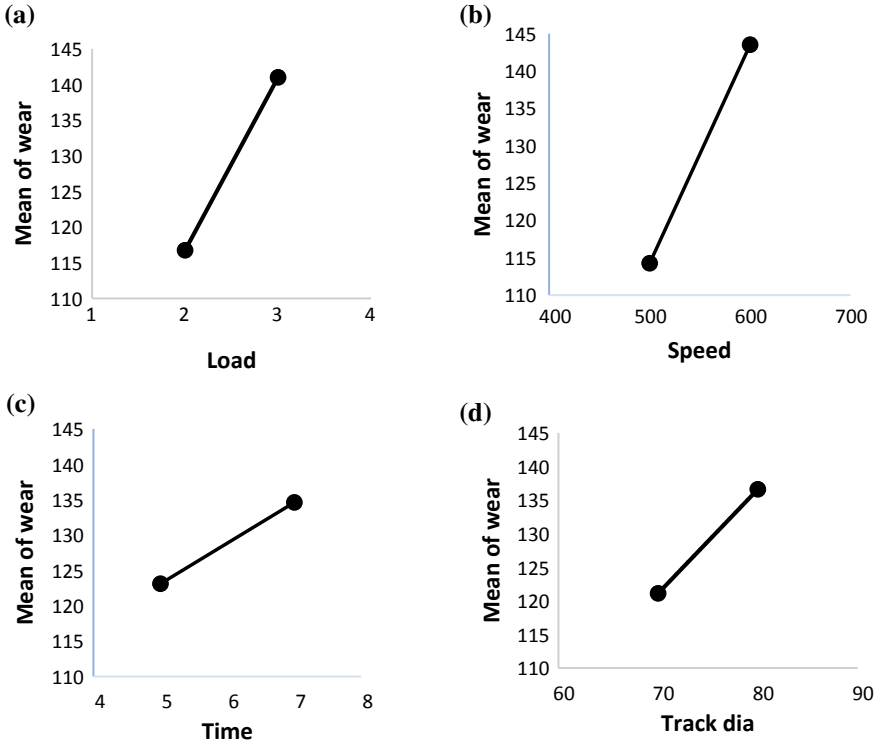


**Fig. 2** Plot for main effects of parameters **a** load **b** speed **c** time and **d** track diameter on mean of wear

### 3.2 ANOVA (Analysis of Variance)

ANOVA test gives the statistical significance of the model. The confidence limit is taken as 95% for all the factors. Factors with *P*-value less than 0.05 are considered to be significant. Table 2 shows the values obtained for ANOVA test and it can be

**Table 2** ANOVA test for wear analysis

Source	DF	Seq SS	Contribution (%)	Adj SS	Adj MS	<i>F</i> -value	<i>P</i> -value
Load	1	2352.3	31.29	2352.3	2352.25	102.17	0.000
Speed	1	3422.3	45.52	3422.3	3422.25	148.65	0.000
Time	1	529.0	7.04	529.0	529.00	22.98	0.001
Track dia	1	961.0	12.78	961.0	961.00	41.74	0.000
Error	1	253.3	3.37	253.3	23.02		
Total	5	7517.8	100.00				

seen that all the factors are significant. Speed has the maximum influence on wear at 45.52% followed by load at 31.29%, track diameter at 12.78% and time at 7.04%.

### 3.3 Multiple Linear Regression Model

The data adequacy and analysis of the model designed in full factorial model can be evaluated using multiple linear regression model. Regression test also gives the regression Eq. (1), which is a generalized equation corresponding to the effects of all the factors on the responses. Substituting the optimum conditions namely load—2 kg, speed—500 rpm, time—5 min and track diameter—70 cm in the regression equation the optimum value of wear obtained is 88.6  $\mu\text{m}$

$$\text{Wear} = -243.4 + 24.25 \text{ Load} + 0.2925 \text{ Speed} + 5.75 \text{ Time} + 1.550 \text{ Track dia} \quad (1)$$

### 3.4 Worn Surface Microstructural Study

Figure 3 shows the micrographs of the worn surface of the samples studied. The mechanism of the wear that occurred on the specimens can be understood from the micrographs. Sample 1 shows ploughing—removal or displacement of material in chunks, and Sample 7 shows grooves—linear cuts on the surface of the specimen. Both are characteristics of abrasive wear that occurs between a soft and comparatively hard surface. In this case, the hardened steel disc removed material from the samples. In Sample 1, due to low speed and load, the material displaces sideways from the hard

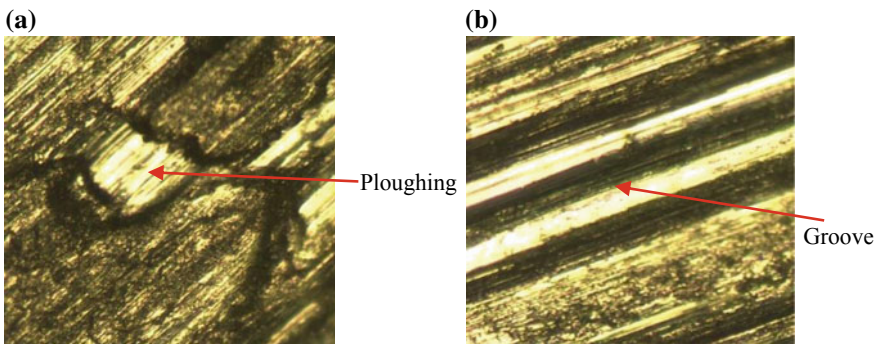


**Fig. 3** Worn surface micrograph of samples **a** Sample 1, load—3 kg, speed—600 rpm, time—7 min and track diameter—70 cm **b** Sample 7, load—2 kg, speed—600 rpm, time—7 min and track diameter—70 cm

surface and causes cavities. In Sample 7, due to high speed and load, the material gets removed in the form of chips or debris. The presence of reinforcement particles over the worn surface acts as a resistance to the material's wear.

## 4 Conclusion

The hybrid composite samples of AA5052 as matrix, and SiC and alumina as reinforcements were successfully fabricated using stir casting process. The wear behaviour and worn surface micro-structure were investigated for the fabricated samples. From the results, it is observed that the dual particulate reinforcements have shown an impact in the wear properties of the composite.

- The minimum wear obtained is 89  $\mu\text{m}$ , and in other words, the wear resistance has increased by 51%.
- The process parameter combination of 2 kg load, 500 rpm speed, 5 min time and 70 cm track diameter was found to be the optimum condition for minimum wear of the fabricated hybrid composite.
- Speed is the most significant factor for wear with 45.52% contribution followed by load at 31.29%, track diameter at 12.78% and time at 7.04%.

This hybrid composite can be explored for use in marine applications like ship hulls, underwater natural gas tanks and pipelines.

## References

1. Saravanan C, Subramanian K, Krishnan VA, Narayanan RS (2015) Effect of particulate reinforced aluminium metal matrix composite—a review. *Mech Mech Eng* 19:23
2. Sozhamannan GG, Prabu SB, Venkatagalapathy VS (2012) Effect of Processing parameters on metal matrix composites: stir casting process. *J Surf Eng Mater Adv Technol* 2:11
3. Prabu SB, Karunamoorthy L, Kathiresan S, Mohan B (2006) Influence of stirring speed and stirring time on distribution of particles in cast metal matrix composite. *J Mater Process Technol* 171:268
4. Uvaraja VC, Natarajan N (2012) Optimization of friction and wear behaviour in hybrid metal matrix composites using Taguchi technique *J Miner Mater Charact Eng* 11:352
5. Baradeswaran A, Vettivel SC, Perumal AE, Selvakumar N, Issac RF (2014) Experimental investigation on mechanical behaviour, modelling and optimization of wear parameters of B4C and graphite reinforced aluminium hybrid composites. *Mater Des* 63:620
6. Kumar GBV, Rao CSP, Selvaraj N, Bhagyashekar MS (2010) Studies on Al6061-SiC and Al7075-Al<sub>2</sub>O<sub>3</sub> metal matrix composites. *J Miner Mater Charact Eng* 9:43
7. Venkataraman B, Sundararajan G (2000) Correlation between the characteristics of the mechanically mixed layer and wear behaviour of aluminium, Al-7075 alloy and Al-MMCs. *Wear* 245:22

# Numerical Modelling of High Energy Density Beam-Assisted Machining of Hardened Armour Steel



A. Sahu, A. N. Jinoop, C. P. Paul, Adepu Kumar and K. S. Bindra

**Abstract** High energy density beam-assisted machining (HEDBAM) finds huge applications in machining of difficult-to-machine materials such as hardened steels and super alloys. Among these materials, armour steel is widely deployed in military and civil applications where resistance to ballistic protection is essential. In the present work, a numerical model is developed to investigate HEDBAM of high hardness armour steel. A fully coupled thermo-mechanical analysis model is developed for predicting the cutting forces and thrust forces using commercial software Abaqus/Explicit. The developed model for orthogonal cutting is validated with previously published literature on thermally assisted machining of titanium alloy with a maximum error of 9%. Further, the model is extended to of armour steel at four different temperature levels (20, 220, 420 and 620 °C), and a maximum reduction in 19 and 24% in the cutting and thrust force, respectively, is obtained at 620 °C. The work paves way for HEDBAM of different hardened high strength materials.

**Keywords** High energy density beam-assisted machining · Armour steel · FEM · 2D orthogonal cutting

## 1 Introduction

High hardness armour steel (HHAS) is used for the resistance to ballistic protection in military and civil applications due to its high hardness (~500 HB) and high ultimate tensile strength (~1640 MPa) [1]. Due to its high strength and hardness, machining of HHAS is difficult resulting in low material removal rates (MRR), large cutting forces

---

A. Sahu · A. Kumar  
National Institute of Technology, Warangal, Warangal, Telangana 506004, India

A. N. Jinoop · C. P. Paul (✉) · K. S. Bindra  
Laser Development & Industrial Applications Division, Raja Ramanna Centre for Advanced Technology, Indore, Madhya Pradesh 452013, India  
e-mail: [paulcp@rrcat.gov.in](mailto:paulcp@rrcat.gov.in)

Homi Bhabha National Institute, Anushaktinagar, Mumbai, Maharashtra 400094, India

© Springer Nature Singapore Pte Ltd. 2020  
H. K. Voruganti et al. (eds.), *Advances in Applied Mechanical Engineering*,  
Lecture Notes in Mechanical Engineering,  
[https://doi.org/10.1007/978-981-15-1201-8\\_105](https://doi.org/10.1007/978-981-15-1201-8_105)

and reduced tool life. High energy density beam-assisted machining (HEDBAM) finds key application in the machining of such difficult-to-machine materials.

HEDBAM is a hybrid machining process in which high energy density source, such as laser and plasma, is used for localized heating of the material to predetermined temperature before the material removal. In HEDBAM, the machining performance is predominantly governed by material removal. The material heating results in the reduction in material strength and hardness, thereby yielding higher material removal rate (MRR) with improved tool life. A comprehensive literature survey shows that HEDBAM can considerably improve the machinability of titanium alloys [2–5], nickel alloys [6, 7] and ceramics [8, 11].

Also, a number of models have been presented to estimate various output parameters during laser-assisted machining. Xi et al. [4] developed a 2D model for thermally assisted machining of Ti–6Al–4V at four different machining temperatures (20 °C, 150 °C, 250 °C, 350 °C) and predicted the chip formation behaviour and cutting force reduction. A very good correlation between the calculated and experimental cutting forces was predicted. Singh et al. [9] developed a 3D orthogonal laser-assisted machining (LAM) model to predict the temperature profile, cutting forces and stress generated during machining of D2 tool steel. It was observed that the flow stress and cutting forces reduced by 28% and 32%, respectively, after LAM. Tian et al. [10] developed a 3D thermal model for LAM of silicon nitride and found good agreement between experimental results and surface temperature from thermal modelling. German [12] developed a thermo-mechanical model for machining of 42CrMo steel in which temperature results from laser heating used for the initial temperature of the workpiece. Changyi Liu [13] presented analytical and finite element method-based (FEM) model for laser-assisted milling. Temperature distribution for moving laser source and effect of temperature on the cutting forces are evaluated in analytical model. In FEM model, Johnson–Cook constitutive law was used to consider the strain hardening, strain rates and thermal softening of the materials. Johnson–Cook failure criteria have been used for the chip formation during the cutting process. FEM results and analytical results show good agreement with the experimental data.

Thus, there is limited literature available in the public domain on HEDBAM of HHAS. In the present work, a 2D orthogonal machining model is developed, and the effect of different workpiece temperature on the cutting forces and thrust forces is estimated.

## 2 Finite Element Modelling

In the metal cutting process, the heat is generated in the materials due to two main phenomena—friction between cutting tool workpiece and plastic deformation. Hence, in the proposed model, thermo-mechanical coupling is considered for orthogonal machining process. First, initial boundary temperature is applied in structural mesh, and heat generated is calculated. Subsequently, the generated heat is transferred to the thermal mesh to compute the temperature distribution. The computed temperature is



transferred to the structural mesh for the thermal softening of the materials. A plain strain 2D thermo-mechanical model is used in the commercially available finite element Abaqus/Explicit software. A plastic deformable workpiece of size  $6 \times 3 \text{ mm}^2$  is used for the analysis. Cutting tool is modelled with rake angle  $\alpha = 0$  and clearance angle  $\gamma = 7^\circ$ . Further, the workpiece temperature considered for the study is assumed to be equal to the temperature generated by the high energy beam source on the workpiece surface at different energy levels. Machining parameters such as cutting speed, feed and depth of cut are kept constant during the simulation. The cutting speed, feed and depth of cut selected for the simulation are 100 m/min, 0.20 mm/rev and 1 mm, respectively, for all values of workpiece temperature. Workpiece temperature values of 20, 220, 420 and 620 °C are used for analysis.

### 2.1 Material Properties and Constitutive Models

HHAS is used as the workpiece material, and tungsten carbide (WC) is used as the tool material. Mechanical and thermal properties of the workpiece and tool are presented in Table 1.

During the cutting process, the material undergoes high strain rate deformation, and hence, Johnson–Cook constitutive model is used [1].

Flow stress of material during the process is presented in Eq. 1

$$\sigma = (A + B\varepsilon^n)(1 + C \ln\left(\frac{\dot{\varepsilon}}{\dot{\varepsilon}_o}\right)\left(1 - \left\{\frac{T - T_r}{T_m - T_r}\right\}^m\right) \tag{1}$$

where  $A$  is the yield strength,  $B$  is the hardening modulus,  $C$  is the coefficient of strain rate,  $n$  is the hardening coefficient,  $m$  is the thermal softening coefficient,  $T_m$  is the melting temperature,  $T_r$  room temperature,  $T$  is the material temperature at an instant, and  $\dot{\varepsilon}_o$  is the reference plastic strain rate. The material constants deployed for the present work are shown in Table 2.

**Table 1** Material property of HHAS and WC [1, 4]

Material Properties	HHAS	WC
Density (Kg/m <sup>3</sup> )	7860	14,500
Young’s modulus (GPA)	205	640
Poisson’s ratio	0.293	0.22
Specific heat (J/kg-°K)	452	220
Thermal expansion coefficient	$9 \times 10^{-6}/\text{K}$	–
Thermal conductivity(W/m-°K)	20	75.4

**Table 2** Johnson–Cook material model [1]

A (MPa)	B (MPa)	C	<i>m</i>	<i>n</i>	$\dot{\epsilon}_o$	<i>T<sub>m</sub></i> (K)	<i>T<sub>m</sub></i> (K)
1200	300	0.003	1.17	0.8	1	1783	293

### 2.2 Chip Separation Criteria and Contact Law

A plastic strain criterion is used for the chip separation from the workpiece. Johnson and Cooks damage model considering the sensitivity of the material to temperature, strain rates and hydrostatic pressure is used for the analysis (refer Eqs. 2 and 3).

$$D = \sum (\Delta \epsilon / \epsilon^f) \tag{2}$$

$$\epsilon^f = (D_1 + D_2 e^{(D_3 \sigma^*)}) \left( 1 + D_4 \ln \left( \frac{\dot{\epsilon}}{\dot{\epsilon}_o} \right) \right) \left( 1 + D_5 \left\{ \frac{T - T_r}{T_m - T_r} \right\} \right) \tag{3}$$

where  $\Delta \epsilon$ ,  $\epsilon^f$  and  $\sigma^*$  denote the increment in equivalent plastic strain at each incremental step, equivalent plastic strain at fracture points and ratio of average of normal stress to the von Mises stress, respectively. The fracture initiates when the variable  $D = 1$  for each element. The material parameters  $D_i$  are determined by tensile and torsion tests. The values of constants  $D_1, D_2, D_3, D_4$  and  $D_5$  for Johnson Cook damage model for HHAS are 0.1, 0.93,  $-1.08$ , 0.000014 and 0.65, respectively. Surface-to-surface contact method is employed to define the interaction between tool and workpiece. It is assumed that the friction coefficient  $\mu = 0.4$  is constant throughout the cutting process. To avoid penetration between elements, kinematic contact method is used. Coulomb friction law is assumed to model the friction between tool and workpiece as presented in Eq. 4.

$$\zeta < \mu \sigma \tag{4}$$

### 2.3 Element Types and Boundary Condition

Four-node plain strain thermo-coupled quad elements (CPE4RT) integration is used for the chip parts. Hourglass control and reduced integration is used for the large element deformation. For tool and bottom surface of workpiece, a three-node plain strain thermally coupled triangular element (CPE3T) is used. For the chip region, the element size is 10  $\mu\text{m}$ , and for the rest of the workpiece a courser mesh is used. The workpiece consists of 7574 elements, and tool consists of 79 elements. External boundaries of workpiece and tool are assumed to be adiabatic to avoid heat loss by convection and radiation.

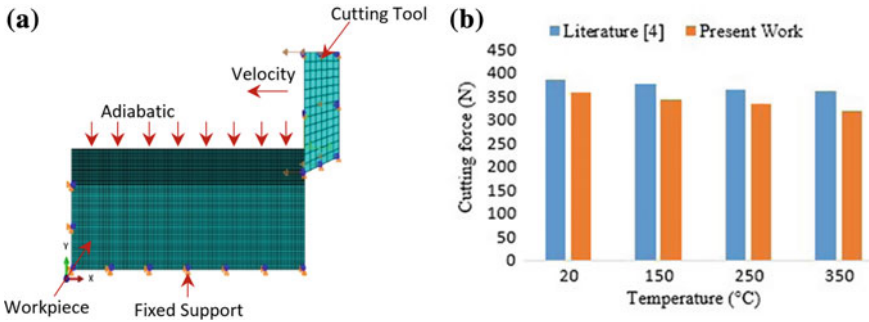


**Fig. 1** HEDBAM modelling **a** mesh model and boundary condition **b** model validation

For tool, velocity boundary condition is applied in *X*-direction and constrained in *Y*-direction. All the nodes of the left side and bottom side of workpiece are constrained in *X*- and *Y*-directions. It is assumed that all the frictional energy is converted into heat, and 50% of its total heat is distributed into chip region. Heat generated by plastic deformation in the materials is 90%. Figure 1a shows the mesh and boundary condition applied on the workpiece and tool.

### 3 Results and Discussion

The developed model is validated with previously published work on titanium alloy [4], and the cutting force is estimated. Figure 1b presents the cutting force obtained at different temperatures (20–350 °C), and maximum error of 9% is observed from previously published literature.

Figures 2a and 2b shows the chip formation during the orthogonal cutting process and maximum temperature generated in the secondary shear zone, respectively. Cutting forces and thrust forces generated during the contact between cutting tool and workpiece are presented in Fig. 2c. It is observed that continuous chips are formed due to the ductile mode failure of HHAS for all workpiece temperature. Shear stress is the failure criteria in ductile mode failure, and as the temperature increases, shear stress inside the materials decreases resulting in reduced cutting forces.

A reduction in 7%, 15% and 19% is obtained in the cutting forces at 220 °C, 420 °C and 620 °C, respectively, as compared to the room temperature cutting forces (20 °C). Further, a reduction in 9%, 17.3% and 24% in the thrust forces is obtained at 220 °C, 420 °C and 620 °C, respectively, as compared to the room temperature thrust force.

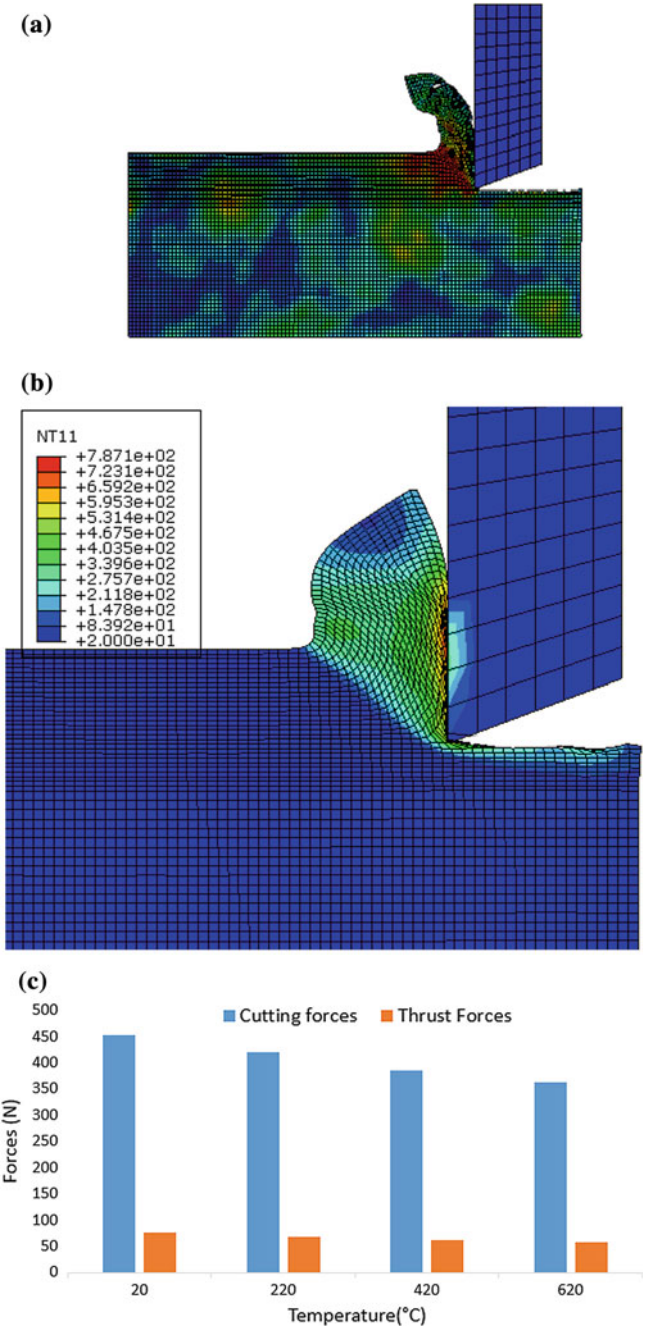


**Fig. 2** a Chip formation during orthogonal cutting b temperature profile during room temperature machining c forces at different workpiece temperature

## 4 Conclusion

HEDBAM process finds a large number of applications in machining of difficult-to-machine materials. Finite element method-based model to estimate the cutting forces during HEDBAM of HHAS is developed. The developed model for orthogonal cutting is validated with previously published literature on HEDBAM of titanium alloy with maximum error of 9%. Further, numerical modelling of HEDBAM of HHAS shows a maximum reduction in 19% and 24% in the cutting and thrust force, respectively, at 620 °C. Continuous chips are formed during the machining of HHAS showing ductile failure. The work will be further extended to the experimental studies on the machining of HHAS and ceramic materials.

## References

1. Polyzois I (2010) M.S. thesis. University of Manitoba, Canada
2. Ayed Y, Germain G, Salem WB, Hamdi H (2014) Experimental and numerical study of laser-assisted machining of Ti<sub>6</sub>Al<sub>4</sub>V titanium alloy. *Finite Elem Anal Des* 92:72
3. Rashid RAR, Sun S, Wanga G, Dargusch v (2012) An investigation of cutting forces and cutting temperatures during laser-assisted machining of the Ti–6Cr–5Mo–5V–4Al beta titanium alloy. *Int J Mach Tools Manuf* 63:58–69
4. Xi Y, Bermingham M, Wang G, Dargusch M (2013) Finite element modeling of cutting force and chip formation during thermally assisted machining of Ti6Al4 V alloy. *J Manuf Sci Eng* 135(6):061014
5. Dandekar CR, Shin YC, Barnes J (2010) Machinability improvement of titanium alloy (Ti–6Al–4V) via LAM and hybrid machining. *Int J Mach Tools Manuf* 50(2):174–182
6. Venkatesan K, Kanubhai J, Raval GV, Vipulkumar SH (2017) A study on prediction of forces and cutting temperature in laser-assisted machining of inconel 718 alloy using numerical approach. In: Anthony MX, Prasad KD VY, Jeyapandiarajan P, Joel J (eds) Conference 2017, vol 5. ICM MM, Elsevier, pp. 12339–12348
7. Xuefeng W, Jianfeng C (2018) The temperature process analysis and control on laser-assisted milling of nickel-based super alloy. *Int J Adv Manuf Technol* 2(5):223–235
8. Hossein R, Mohammad RM (2016) Analysis of heat transfer in laser assisted machining of slip cast fused silica. In: Wertheim R, Ihlfeldt S, Carsten H, Putz (eds) Conference 2016, HPC, vol 46. Elsevier, pp. 571–574
9. Gurpreet S, Mahesh T, Samanta A, Ramesh S (2011) Finite element modeling of laser-assisted machining of AISI D2 tool steel. *Mater Manuf Process* 28(4):443–448
10. Tian Y, Shin YC (2005) Multiscale finite element modeling of silicon nitride ceramics undergoing laser-assisted machining. *J Manuf Sci Eng* 129:287–295
11. Saurabh RV, John AP (2009) Numerical simulations and analysis of the thermal effects on silicon carbide during ductile mode micro-laser assisted machining. In: Editor F, Editor S (eds) Asme conference 2009, MSEC, vol 1. Springer, Heidelberg, pp. 409–416
12. Germain G, Dal Santo P, Lebrun JL (2011) Comprehension of chip formation in laser assisted machining. *Int J Mach Tools Manuf* 51(3):230–238
13. Changyi L, Yuhao S (2014) Modelling and simulation of laser assisted milling process of Ti-tanium alloy. In: Berend D, Pedro JA, Dragos A, Yusuf A, Tojiro A (eds) 5th machining innovations conference 2014, MIC, vol. 24. Springer, Heidelberg, pp. 134–139

# Experimental Investigation of Electro-Discharge Machining on NIMONIC 80A Through Response Surface Methodology



G. Vishnu Pramod Teja, K. Saraswathamma, P. Murali Krishna and G. Tejeswara Rao

**Abstract** Electro-discharge machining (EDM) is one of the most popular advanced machining processes for machining conductive material irrespective of material physical properties. In the present study, effect of electro-discharge machining parameters such as current ( $A$ ), pulse on time ( $T_{on}$ ) and pulse off time ( $T_{off}$ ) on machining characteristics such as material removal rate (MRR), tool wear rate (TWR) and surface roughness (SR) of NIMONIC 80A is focused. The Box–Behnken design (BBD) of response surface methodology (RSM) was used to design the experiments, and also, analysis of variance (ANOVA) was conducted in order to know the most significant parameters. ANOVA results show that current and pulse on time were the most significant factors for material removal rate, and only current was significant parameter for tool wear rate and surface roughness. Multi-objective optimization process was conducted to maximize the MRR and to minimize the TWR and SR, and optimized parameters are “3 A” current, “900  $\mu s$ ” pulse on time and “30  $\mu s$ ” pulse off time with the desirability value of 0.988.

**Keywords** Electro-discharge machining (EDM) · Box–Behnken design (BBD) · Analysis of variance (ANOVA)

---

G. Vishnu Pramod Teja (✉) · K. Saraswathamma  
Department of Mechanical Engineering, University College of Engineering (A),  
Osmania University, Hyderabad, Telangana 500007, India

P. Murali Krishna  
Department of Mechanical Engineering, Government Polytechnic,  
Srikakulam, Srikakulam, Andhra Pradesh 532001, India

G. Tejeswara Rao  
Department of General Section, Government Polytechnic,  
Amadalavalasa, Amadalavalasa, Andhra Pradesh 532185, India

## 1 Introduction

NIMONIC 80A is mostly used in gas turbine components (viz., blades, rings and disks), automobile exhaust valves, die-casting inserts and core, nuclear boiler tube supports and bolts. This superalloy contains high resistance to corrosion, strength as well as other mechanical properties in extreme temperatures, and it is very difficult to machine using conventional methods [1, 2]. To overcome these inferences, unconventional machining method is a best choice. Among unconventional machining methods, electro-discharge machining (EDM) is one of the most excellent choices for machining high-strength superalloys. EDM is an electro-thermal process where material is removed from the parent material with an electrode by the repetitive sparks.

Gowthaman et al. [3] examined “the effect of parameters namely pulse on time, pulse off time, discharge current and gap voltage on electrical discharge machining of MONEL superalloy with copper electrode. They reported that discharge current is the most significant parameter for MRR and Ra. As the discharge current increases, MRR and Ra were increased.” Chandramouli et al. [4] studied “electrical discharge machining of 17–4 PH steel using Taguchi method of input parameters such as current, pulse on time, pulse off time and tool lifetime. MRR and Ra were increased with increasing the current and pulse on time.” Vikram et al. [5] investigated “effect of machining parameters such as current, pulse on time and pulse off time on electrical discharge machining of aluminum alloy 6082 and the machining characteristics such as MRR, TWR and SR were studied. This research shows that increase in the current and pulse on time leads to increasing the machining characteristics, i.e. MRR, TWR and SR.” Neelesh Singh et al. [6] investigated “the effect of input parameters such as peak current, gap voltage and pulse on time on machining characteristics, i.e. MRR and SR of Inconel 601. In this paper, experiments were designed using Box–Behnken design of RSM. They reported that MRR and Ra increase with increasing the current.” Mohanty et al. [7] investigated “the various machining parameters such as open-circuit voltage, discharge current, pulse on time, duty factor, flushing pressure and different tool materials, i.e. copper, brass and graphite on electrical discharge machining of Inconel 718. In this paper, experiments were designed using Box–Behnken design of RSM and optimization was done by using multi-objective particle swarm algorithm. They reported that increase in discharge current and pulse on time leads to increase in the MRR, EWR, SR and ROC and copper tool gives a higher MRR and lower EWR than other tools.”

From the literature review, it is understood that a few research work was focused on multi-objective optimization study of input parameters which will lead to maximize the MRR and minimize the TWR and SR on NIMONIC 80A in EDM. Hence, this research study was mainly focused on multi-objective optimization of input parameters such as current, pulse on time and pulse off time of EDM on better machining characteristics such as high material removal rate and low tool wear rate and surface roughness on NIMONIC 80A. Box–Behnken design of response surface methodology is a useful tool for planning, analyzing and optimizing the experiment by

combining different input factors and characteristics. In this paper, experiments were designed and analyzed using Box–Behnken design of response surface methodology.

## 2 Materials and Methods

### 2.1 Materials

In this work, NIMONIC 80A and copper were chosen as a work material and electrode material, respectively, and chemical composition of NIMONIC 80A is shown in Table 1. NIMONIC 80A pieces were cut into sizes of 15 mm × 15 mm × 6 mm, whereas the electrode was made into Ø10 mm × 50 mm length. Machining time for each experiment was maintained as 10 min. Experiments were conducted on ARD ARTM30D Die-sink EDM using commercial grade “EDM oil.” The experimental arrangement and EDM machined samples are shown in Fig. 1.

### 2.2 Design of Experiments

Box–Behnken design (BBD) from response surface methodology was used for designing the experiments. Machining parameters and their levels are listed in Table 2, and experiment layouts and the recorded results are listed in Table 3.

The material removal rate and tool wear rate are calculated using Eqs. (1) and (2). In both cases, the weight before and after machining was measured using the Contech analytical balance having resolution of 0.0001 gm. The Taylor Hobson Surtronic 3 + surface roughness tester was used to measure the surface roughness.

MRR and TWR were calculated as

**Table 1** Chemical composition of NIMONIC 80A

Elements	C	Si	Mn	Cu	Cr	Fe	Ti	Al	Co	Ni
%	0.031	0.363	0.053	0.0403	20.03	2.268	2.63	1.387	0.4013	Bal

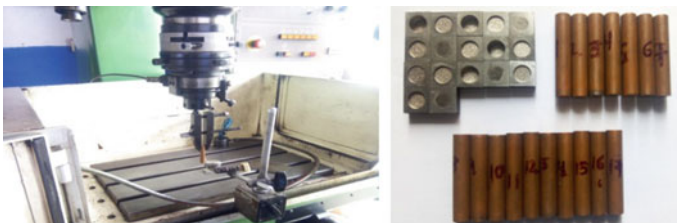


**Fig. 1** Experimental arrangement and EDM machined samples



**Table 2** Machining parameters and their levels

Factors	Units	Levels		
		Low (-1)	Medium (0)	High (1)
Current	A	3	9	15
Pulse on time ( $T_{on}$ )	$\mu s$	300	600	900
Pulse off time ( $T_{off}$ )	$\mu s$	30	60	90

**Table 3** Experimental layout and recorded results

Exp. run	Input parameters			Output parameters		
	Current (A)	$T_{on}$ ( $\mu s$ )	$T_{off}$ ( $\mu s$ )	MRR (gm/min)	TWR (gm/min)	SR ( $\mu m$ )
1	3	300	60	0.00251	0.00066	1
2	15	300	60	0.29843	0.00274	7.5
3	3	900	60	0.00205	0.00062	1.4
4	15	900	60	0.34988	0.00279	7.4
5	3	600	30	0.00221	0.00074	1.2
6	15	600	30	0.30673	0.00225	6.8
7	3	600	90	0.00211	0.00147	1.2
8	15	600	90	0.2253	0.00238	8.1
9	9	300	30	0.09691	0.00082	5.6
10	9	900	30	0.04035	0.00086	5
11	9	300	90	0.06554	0.00215	5.8
12	9	900	90	0.04906	0.00194	4
13	9	600	60	0.06608	0.00157	4.8
14	9	600	60	0.07427	0.00152	5.5
15	9	600	60	0.06998	0.00172	5.2
16	9	600	60	0.06705	0.00192	5.6
17	9	600	60	0.05517	0.00068	3.8

$$MRR = \frac{W_{wb} - W_{wa}}{t} \tag{1}$$

$$TWR = \frac{W_{tb} - W_{ta}}{t} \tag{2}$$

whereas  $W_{wb}$  and  $W_{wa}$  are the weight of the Nimonic 80A before and after machining correspondingly.

$W_{tb}$  and  $W_{ta}$  are the weight of the copper electrode before and after machining correspondingly,  $t$  = time of machining (min).

### 3 Results and Analysis

The Stat-Ease Design Expert 11 software is used to analyze the experimental machining characteristics and it is shown in Table 3. ANOVA is performed, to check the goodness and suitability of fitness of the model, and the model adequacy examination comprises: the test for significance of the regression model, test for significance on model coefficients and test for lack of fitness.

#### 3.1 Material Removal Rate

Fitness test summary from statistical analysis is a recommended quadratic model for material removal rate. Non-significant terms, i.e., *p*-value greater than 0.1, are eliminated by the backward elimination in order to improve model accuracy. The reduced ANOVA model for MRR is shown in Table 4. Obtained regression equation for MRR is shown in Eq. 3.

$$\frac{1}{\text{SQUARE ROOT(MRR)}} = 32.40230 - 5.19928 \times \text{CURRENT} + 0.006579 \times T_{\text{on}} - 0.016653 \times T_{\text{off}} - 0.000315 \times \text{CURRENT} \times T_{\text{on}} - 0.000032 \times T_{\text{on}} \times T_{\text{off}} + 0.209462 \times \text{CURRENT}^2$$

**Table 4** Reduced ANOVA for MRR

Source	Sum of squares	DOF	Mean	F-value	p-value	
Model	1000.19	7	142.88	4032.58	<0.0001	Significant
A—Current	753.78	1	753.78	21273.80	<0.0001	
B— <i>T</i> <sub>on</sub>	2.38	1	2.38	67.09	<0.0001	
C— <i>T</i> <sub>off</sub>	0.1326	1	0.1326	3.74	0.0851	
AB	1.28	1	1.28	36.23	0.0002	
BC	0.3349	1	0.3349	9.45	0.0133	
A <sup>2</sup>	240.08	1	240.08	6775.72	<0.0001	
C <sup>2</sup>	0.3841	1	0.3841	10.84	0.0093	
Residual	0.3189	9	0.0354			
Lack of fitness	0.1224	5	0.0245	0.4982	0.7682	Non-significant
Pure error	0.1965	4	0.0491			
Cor total	1000.51	16				
<i>R</i> <sup>2</sup> = 0.9997			Adeq precision = 159.119			
Adjusted <i>R</i> <sup>2</sup> = 0.9994			Predicted <i>R</i> <sup>2</sup> = 0.9989			

$$+ 0.000335 \times T_{\text{off}}^2 \tag{3}$$

**Influence of machining parameters such as current (A),  $T_{\text{on}}$  and  $T_{\text{off}}$  on MRR**

The influence of current on MRR at constant  $T_{\text{on}}$  (600  $\mu\text{s}$ ) and  $T_{\text{off}}$  (60  $\mu\text{s}$ ) is shown in Fig. 2. It shows that MRR increases with increasing the current. Spark discharge is increased with increase in the input energy, i.e., current. Hence, melting and vaporization of the metal take place. Hence, increase in MRR is observed. The effect of  $T_{\text{on}}$  on MRR at constant current (15 A) and  $T_{\text{off}}$  (90  $\mu\text{s}$ ) is shown in Fig. 3. It shows that MRR increases with increase in pulse on time. This is to be happened due to the fact that rise in  $T_{\text{on}}$ , spark per input energy increases; it results in high-level erosion on the workpiece. Hence, results in the increase of MRR. The effect of  $T_{\text{off}}$  on MRR at constant current (9 A) and  $T_{\text{on}}$  (600  $\mu\text{s}$ ) is plotted in Fig. 4. It shows that MRR decreases with increase in pulse off time. This happens due to fact that increase in  $T_{\text{off}}$  causes the reduced plasma channel, which reduces the positive ions on the work surface, resulting in decreased MRR.

**Fig. 2** Influence of current on MRR

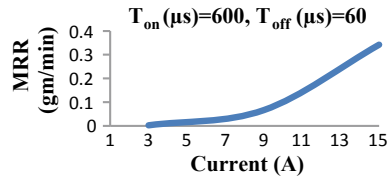


**Fig. 3** Influence of  $T_{\text{on}}$  on MRR

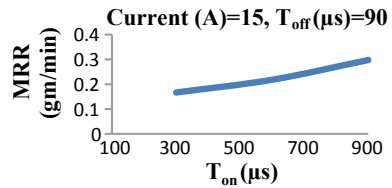
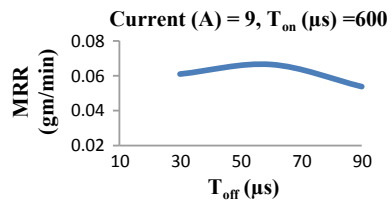


**Fig. 4** Influence of  $T_{\text{off}}$  on MRR



### 3.2 Tool Wear Rate

Fitness test summary from statistical analysis is a recommended linear model for tool wear rate. Separate ANOVA was conducted for tool wear rate also, and the model *F*-value is 12.08 and lack of fit *F*-value is 0.5917. From this, one can conclude that the model is significant. Regression equation for TWR is

$$TWR = -0.000450 + 0.000136 \times \text{CURRENT} - 3.67908E - 09 \times T_{on} + 0.000014 \times T_{off} \tag{4}$$

#### Influence of machining parameters such as current (A), *T<sub>on</sub>* and *T<sub>off</sub>* on TWR

The effect of current on TWR at constant *T<sub>on</sub>* (600 μs) and *T<sub>off</sub>* (60 μs) is shown in Fig. 5 and increase in the TWR was observed with increase in the current. With increase in the current, sparks (discharges) will be more, which results in more melting and vaporization of tool material. The effect of *T<sub>on</sub>* on TWR at constant current (9 A) and *T<sub>off</sub>* (60 μs) is shown in Fig. 6. It shows no variation in TWR with increase in *T<sub>on</sub>*. This may be due to the deposition of carbon on the tool, which results in no variation on the TWR. The effect of *T<sub>off</sub>* on MRR at constant current (9 A) and *T<sub>on</sub>* (600 μs) is shown in Fig. 7, and it was observed that TWR slightly increases with the increase in the pulse off time. Pulse off time directly connects to the flushing time. If the pulse off time is more means flushing time is also more. During flushing, debris as well as loosely connected material to the electrode cleared between the inter-electrode gap may result in increase in the TWR.

Fig. 5 Influence of current on TWR

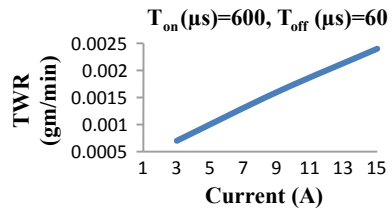
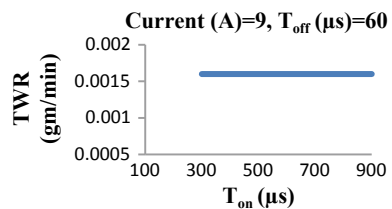
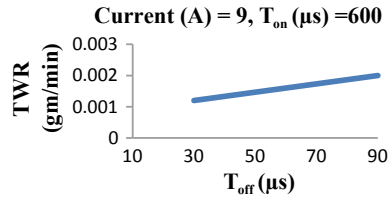


Fig. 6 Influence of *T<sub>on</sub>* on TWR



**Fig. 7** Influence of  $T_{off}$  on TWR



### 3.3 Surface Roughness

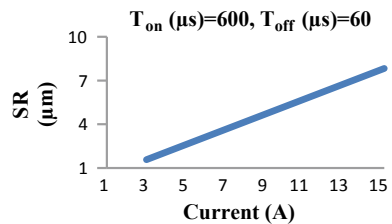
Fitness test summary from statistical analysis is a recommended linear model for surface roughness. Separate ANOVA was conducted for surface roughness also, and the model  $F$ -value is 51.74 and lack of fit  $F$ -value is 0.9324. From this, one can conclude that the model is significant. Obtained regression equation for the SR is shown below.

$$SR = +0.412500 + 0.520833 \times CURRENT - 0.000875 \times T_{on} + 0.002083 \times T_{off} \tag{5}$$

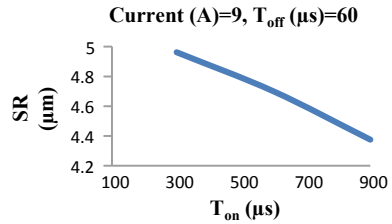
#### Influence of machining parameters such as current (A), $T_{on}$ and $T_{off}$ on SR

Figure 8 relates the effect of current on surface roughness for a constant  $T_{on}$  (600  $\mu s$ ) and  $T_{off}$  (60  $\mu s$ ). From the ANOVA, it was observed that current is the most contributing parameter with  $F$ -value 154.06. With increase in the current, surface roughness increases and increase is almost linear. Due to increase in the current, the discharge energy increases and generates violent sparks and impulse force. So, deeper and larger craters are formed on the surface of workpiece, and after sparking, debris was not properly washed out on the surface of the workpiece. Hence, the residues stay behind at the crater edge to form rough surface. Figure 9 shows the effect of  $T_{on}$  on surface roughness for a constant current (9 A) and  $T_{off}$  (60  $\mu s$ ). It shows that surface roughness linearly decreases with increase in pulse on time. This may be happened due to more material gets melted on surface of the work. As  $T_{off}$  was 60  $\mu s$ , proper flushing was done, resulting in the cleaner surface with less or no debris. Hence, results in lesser surface roughness. Figure 10 shows the effect of  $T_{off}$  on surface roughness for a constant current (9 A) and  $T_{on}$  (600  $\mu s$ ). It shows that with pulse off time surface roughness increases. As the pulse off time increases, re-solidification

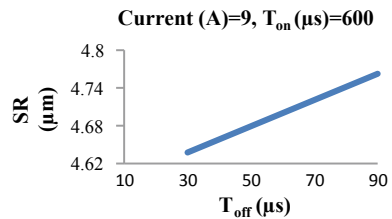
**Fig. 8** Influence of current on SR



**Fig. 9** Influence of  $T_{on}$  on SR



**Fig. 10** Influence of  $T_{off}$  on SR



time increases on the machined surface. Hence, results in increase in the surface roughness.

### 3.4 Optimization

Optimization was performed using desirability function in Stat-Ease Design Expert 11 software. The optimized parameters are as follows: maximum value of MRR (0.002 gm/min) and minimum value of TWR (0.0001 gm/min) and SR (0.004  $\mu m$ ), respectively, at “3 A” current, “900  $\mu s$ ” pulse on time and “30  $\mu s$ ” pulse off time with the desirability value 0.988. In order to confirm this optimization level, two confirmation experiments were conducted and the confidence levels were checked. Hence, this model can be used for predication of MRR, TWR and SR at 95% level of confidence.

## 4 Conclusions

The following conclusions were noted as per the experimental study.

1. The ANOVA results show the current and pulse on time are the most significant parameters of MRR and only current is contributing parameter for TWR and SR.
2. MRR increases with the current and pulse on time and decreases with pulse off time.
3. TWR increases with the current and pulse off time and not much variation in pulse on time.

4. SR increases with increase in the current and pulse off time and decreases with increase in pulse on time.
5. The optimum parameters are as follows: maximum value of MRR and minimum value of TWR and SR are current **3 A**, pulse on time **900  $\mu$ s** and pulse off time **30  $\mu$ s** with the desirability value **0.988**.

## References

1. Ezugwu EO, Wang ZM, Machado AR (1999) The machinability of nickel-based alloys: a review. *J Mater Process Technol* 86:1–16
2. Goswami A, Jatinder K (2014) Optimization in wire-cut EDM of Nimonic 80A using Taguchi's approach and utility concept. *Eng Sci Technol Int J* 17:173–184
3. Gowthaman S, Balamurugam K, Manoj Kumar P, Ahamed Ali SK, Mohan kumar KL, Vijaya Ram Gopal N (2018) Electrical discharge machining studies on monel-super alloy. *Procedia Manuf* 20:386–391
4. Chandramouli S, Eswaraiah K (2018) Experimental investigation of EDM process parameters in machining of 17–4 PH steel using Taguchi method. *Mater Today Proc* 5:5058–5067
5. Vikram Reddy V, Shiva Krishna B, Vamshi Krishna P, Shashidhar M (2016) Influence of process parameters on performance characteristics during EDM of aluminium alloy 6082. *Int J Eng Res Technol* 5
6. Sourabh S, Raj B, Amaresh K (2017) Investigation of material removal rate and tool wear rate on electrical discharge machining of Incoloy 800HT by using response surface methodology. *Mater Today Proc* 4:10603–10606
7. Mohanty CP, Mahapatra SS, Singh MR (2014) A particle swarm approach for multi-objective optimization of electrical discharge machining process. *J Intell Manuf* 6:1171–1190

# Optimization of Minimum Quantity Lubrication Parameters



M. Amrita , R. R. Srikant  and V. S. N. Venkata Ramana 

**Abstract** Cutting fluids are inevitable in manufacturing industries due to their cooling and lubricating properties. But their applications in large quantities pose serious threat to biological bodies in the oceans and rivers when disposed untreated. Strict rules and fines imposed by most of the countries on such industries created an economic and environmental concern. This led to research in finding alternative methods to either eliminate or reduce the usage of cutting fluids. Minimum quantity lubrication (MQL) is one of such methods being widely tested to replace flood machining. Application of cutting fluid as MQL requires decision of choosing the optimum MQL parameters, i.e., air pressure, cross-sectional area of nozzle and coolant flow rate. The present paper deals with optimizing these MQL system parameters in order to minimize cutting forces and surface roughness using conventional soluble oil as coolant. Coolant flow rate and quantity of air supplied were found to contribute the most to cutting forces and surface roughness, respectively.

**Keywords** Minimum quantity lubrication · Air metering screw · Cutting forces · Surface roughness

---

M. Amrita (✉)

Gayatri Vidya Parishad College of Engineering (A), Visakhapatnam, Andhra Pradesh 530048, India

e-mail: [amrita@gvpce.ac.in](mailto:amrita@gvpce.ac.in)

R. R. Srikant

Department of Technology, University of Northern Iowa, Cedar Falls, IA 50614, USA

e-mail: [r.r.srikant@gmail.com](mailto:r.r.srikant@gmail.com)

V. S. N. Venkata Ramana

GITAM (Deemed to be University), Visakhapatnam 530045, India

e-mail: [vsnvr74@gmail.com](mailto:vsnvr74@gmail.com)

© Springer Nature Singapore Pte Ltd. 2020

H. K. Voruganti et al. (eds.), *Advances in Applied Mechanical Engineering*,

Lecture Notes in Mechanical Engineering,

[https://doi.org/10.1007/978-981-15-1201-8\\_107](https://doi.org/10.1007/978-981-15-1201-8_107)



## 1 Introduction

Almost all manufacturing industries involve a section containing machine tools used for metal cutting operations. In order to increase the tool life and to reduce the cost of machining, cutting fluids are applied in large quantities as flood machining. Disposal of untreated used cutting fluids to water bodies like rivers and oceans poses serious threat to biological bodies. Strict rules and fines are imposed by most of the countries on such industries. This created economic and environmental concern, which led to research in finding alternative methods to either eliminate or reduce the usage of cutting fluids [1]. Minimum quantity lubrication (MQL) is one of such methods being widely tested to replace flood machining. Most of the researchers applied MQL to machining and found it to be effective over dry and flood machining [2–5]. Awale et al. [2] investigated the influence of different machining conditions on surface integrity while grinding hardened H13 die steel. Machining conditions used were dry machining, flood machining and MQL application using three types of fluids: distill water, paraffin oil and vegetable oil. MQL application of all three fluids resulted in improved surface finish compared to dry and flood machining. MQL application of vegetable oil showed best surface integrity compared to other MQL applications due to its high viscosity which provided better lubrication. Lohar and Nanavaty [3] evaluated effectiveness of MQL application over dry and flood machining while performing hard turning of AISI 4340 using CBN cutting tool. Machining was performed at varying speed, feed and depth of cut. Taguchi designs of experiments are used. MQL was found to reduce the cutting forces compared to dry and flood machining. Machining temperatures were found to reduce by approximately 36%, and surface finish was found to improve by 30% with the application of cutting fluid as minimum quantity lubrication. NareshBabu et al. [4] performed end milling of AISI 304 steel using flood lubrication and MQL application of olive oil. MQL application of olive oil was found to reduce surface roughness and tool wear. Compared to flood machining, MQL application reduced tool wear by 70% and surface roughness by 66%. Ball bearing effect of minute droplets of MQL led to better lubrication than flood machining. Maruda et al. [5] investigated the influence of minimum quantity lubrication (MQL), minimum quantity cooling and lubrication (MQCL) and extreme pressure and anti-wear additives in minimum quantity lubrication (MQL + EP/AW) in turning hard to machine material—*austenitic steel 316L*. Machining was performed in the range for speed: 70–400 m/min, feed: 0.05–0.35 mm/rev and depth of cut 0.5 mm. In the considered range, extreme pressure and anti-wear additives in minimum quantity lubrication showed best surface finish. Surface valley depths were found to be more with MQL + EP/AW which acted as reservoirs for cutting oil providing better lubrication, while surface peak heights were found to be more with dry machining, which reduced contact area and hence high contact pressure. In order to further increase the effectiveness of MQL, application of nanofluids is being investigated. Few of the researchers performed machining using nanofluids, which are applied as MQL during machining [6–10]. Babu et al. [6] evaluated performance of copper-dispersed coconut oil as flood machining and minimum quantity

lubrication while machining EN24 steel at varying speeds and feeds. Application of cutting fluid as MQL was found to be effective over flood machining in improving surface finish and reducing tool wear. Use of copper nanoparticles has reduced the surface roughness and tool wear in flood application as well as MQL application. This improvement in performance was due to enhanced thermal conductivity of copper-dispersed oil. Sharma et al. [7] investigated the influence of MQL application of cutting fluid containing hybrid nanoparticles, molybdenum disulfide ( $\text{MoS}_2$ ) and alumina ( $\text{Al}_2\text{O}_3$ ) at varying speeds, feed, depth of cut and volume concentrations. Tribological tests were also performed which showed least coefficient of friction with hybrid mixture of  $\text{MoS}_2$ - $\text{Al}_2\text{O}_3$  compared to individual nanoparticles in base fluid. Same combination showed best performance in machining also. Yildirim et al. [8] investigated the performance of MQL application of hexagonal boron nitride in ester-based cutting oil, while machining Inconel 625 0.5 vol.% hBN MQL showed highest tool life and best surface finish. Hegab et al. [9] simulated nanofluid application in machining and found good agreement in cutting forces from experimental as well as simulated conditions. Li et al. [10] investigated effect of different nanofluids and its concentration on surface tension and contact angle. Surface tension was found to increase, and contact angle was found to decrease with use of nanoparticles and also with increase in the concentration of nanoparticles. Though a lot of work is being done on application of cutting fluids as MQL, tests should be performed at optimum MQL parameters to get best output.

MQL systems may be classified as MQL with external supply and MQL with internal supply. In the former case, cutting fluid is supplied externally, while in latter case, cutting fluid is supplied through the tool. MQL can be externally supplied in two ways as shown in Fig. 1: MQL-1, where cutting fluid along with compressed air is supplied to a nozzle and aerosol is formed just after the nozzle; and MQL-2, where aerosol is prepared separately in a closed chamber and is supplied to the cutting zone using conventional nozzle. Before the application of cutting fluid as MQL to any machining, a proper study of all the process parameters has to be carried out, to understand its influence in machining responses. The present work deals with the study of effect of process parameters of MQL Unist coolubricator on cutting forces and surface roughness while machining AISI 1040 steel.

## 2 Experimentation

Machining is performed on widely used medium carbon steel AISI 1040 at constant cutting parameters: cutting speed of 560 rpm, feed: 0.15 mm/rev and depth of cut: 0.5 mm. Unist coolubricator shown in Fig. 2 is used to apply conventional cutting fluid (Servo Cut—water soluble oil mixed with water in ratio 1:19) as minimum quantity lubrication. It consists of different parts like air filter, solenoid valve, positive displacement metering pump which precisely supplies cutting fluid at 0.03 ml/stroke, pneumatic pulse generator which controls the pump cycle rate (pulses/min), air metering screw which controls the supply of air, pump stroke adjustment to control the

**Fig. 1** External MQL supply [1]

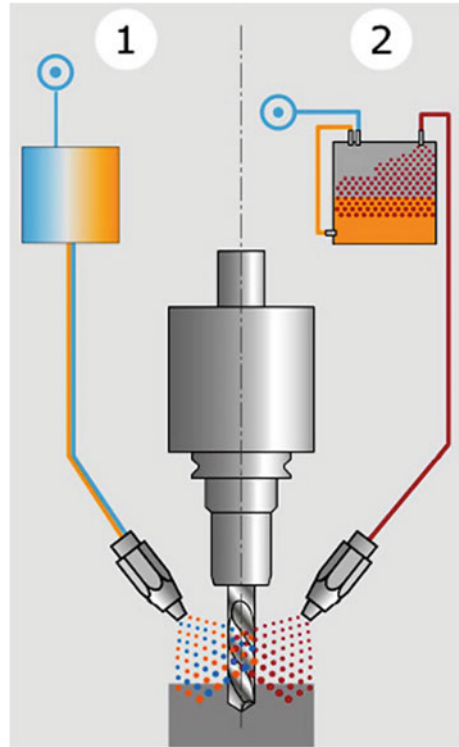


**Fig. 2** Unist coolubricator

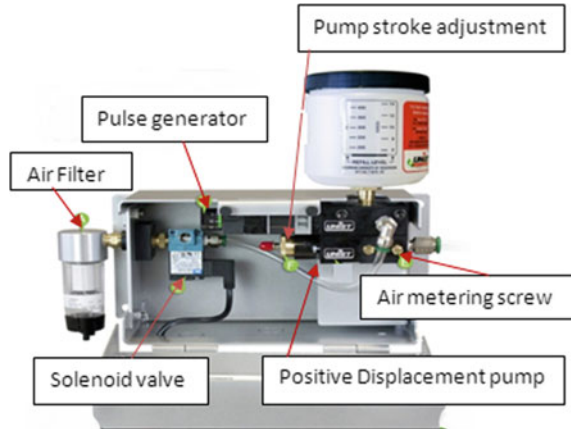


**Table 1** Levels and parameters considered

	Level 1	Level 2	Level 3
Air pressure (psi) (A)	70	75	80
Cross-sectional area of nozzle (mm <sup>2</sup> ) (B)	2	4	6
Coolant flow rate (ml/min) (C)	0.3	0.6	1.2

quantity of coolant/lubricant and fluid reservoir to store cutting fluid. Of all the parts, three main MQL system parameters are air pressure; air quantity, which is controlled by air metering screw; and lubricant/coolant quantity, which is controlled by pulse generator. Air quantity is varied by adjusting the air metering screw to half turn, three fourth turn and full turn, which changes the outlet cross-sectional area of air nozzle from 2 mm<sup>2</sup> to 4 mm<sup>2</sup> to 6 mm<sup>2</sup>. Quantity of lubricant is varied by adjusting the pulse generator to 10, 20 and 40 which supplies lubricant at rate 0.3 ml/min, 0.6 ml/min and 1.2 ml/min, respectively. Levels and parameters considered are shown in Table 1. Taguchi L9 experiments are conducted. Each experiment is conducted thrice. Nozzle is placed such that cutting fluid is applied at the back of the chip. Cutting forces are measured using Kistler dynamometer (model: 9272) and their resultant is used for further analysis. Surface roughness is measured using Mitutoyo Surftest 301 J.

### 3 Results and Discussions

Table 2 shows the input parameters and responses, i.e., resultant cutting forces and surface roughness with all experiments. Figure 3 shows the main effect plots for resultant cutting force and surface roughness. Table 3a shows the response table for cutting forces, and Table 3b shows the response table for surface roughness.

The main effect plot for resultant cutting forces (Fig. 3a) shows that with increase in air pressure, cutting forces decreased and then increased. Increase in air pressure from 70 to 75 psi may have caused effective entry of cutting fluid to the cutting zone, leading to better lubrication and hence decrease in cutting forces. Further increase in air pressure reduces the quantity of lubricant and hence led to increase in cutting forces. Increase in air pressure may have increased the spray angle, leading to reduced entry of coolant in the cutting zone. Adjusting the pulse generator led to change in number of strokes per minute, leading to increase in supply of coolant at rates 0.3 ml/min, 0.6 ml/min and 1.2 ml/min. Main effect plot shows that with increase in coolant flow rate, cutting forces have decreased. More quantity of coolant may have caused better lubrication leading to decrease in cutting force. The response table for cutting forces is shown in Table 3a, and it shows that coolant flow rate influences cutting forces the most followed by cross-sectional area of nozzle.

Main effect plots for surface roughness (Fig. 3b) show that with increase in air pressure, surface roughness has reduced. Increase in air pressure led to easier evacuation of chips from the cutting zone, preventing them from rubbing against the

**Table 2** Input parameters and responses for all experiments

Expt No.	Air pressure (psi) (A)	Cross-sectional area of nozzle (mm <sup>2</sup> ) (B)	Coolant flow rate (ml/min) (C)	Resultant cutting force (N)		Surface roughness ( $\mu\text{m}$ )	
1	70	2	0.3	409.13	400.23	4.93	5.01
2	70	4	0.6	384.56	375.58	3.75	3.87
3	70	6	1.2	308.34	306.43	3.90	3.91
4	75	2	0.6	364.34	366.04	3.88	4.31
5	75	4	1.2	256.84	260.23	3.48	3.70
6	75	6	0.3	265.34	271.28	3.32	3.51
7	80	2	1.2	219.47	221.24	3.89	4.46
8	80	4	0.3	605.32	606.51	3.27	3.37
9	80	6	0.6	336.20	324.57	3.34	3.27

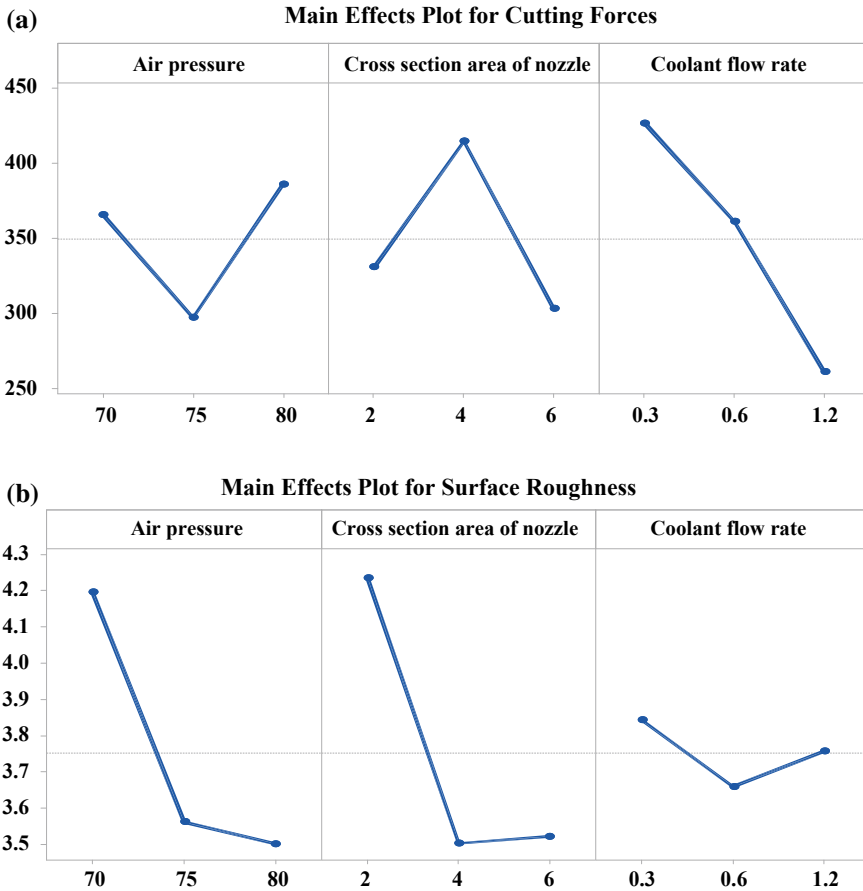


Fig. 3 a Main effect plot for resultant cutting forces, b main effect plot for surface roughness

workpiece, leading to better surface finish. With increase in area of cross section of nozzle from 2 to 4 mm<sup>2</sup>, surface roughness has decreased and then slightly increased. With increase in the area of cross section of nozzle from 2 to 4 mm<sup>2</sup>, quantity of air supplied increased, leading to better mist formation. This might have lead to better lubrication in cutting zone leading to improved surface finish. With further increase in opening of cross section of nozzle from 4 to 6 mm<sup>2</sup>, surface finish remained stable showing no further increase in lubrication. Variation in coolant flow rate does not have much influence on surface roughness, as the inclination of the line is less. This can also be seen from response Table 3b, which shows that area of cross section of nozzle highly influenced surface roughness followed by air pressure.

Tables 4 and 5 show the ANOVA table for cutting forces and surface roughness respectively. ANOVA table for cutting forces shows that factor C, i.e., coolant flow rate, contributes to cutting forces the most, followed by factor B, i.e., cross-sectional area of nozzle. This is in line with the conclusion drawn from response

**Table 3** (a) Response table for resultant cutting forces, (b) response table for surface roughness

Level	Air pressure (psi) (A)	Cross-sectional area of nozzle (mm <sup>2</sup> ) (B)	Coolant flow rate (ml/min) (C)
<i>(a)</i>			
1	365.2	330.6	426.3
2	297.1	414.4	360.9
3	385.7	303.0	260.9
Delta	88.6	111.4	165.4
	3	2	1
<i>(b)</i>			
1	4.198	4.237	3.843
2	3.562	3.503	3.660
3	3.502	3.522	3.758
Delta	0.697	0.733	0.183
	2	1	3

**Table 4** ANOVA for cutting forces

Source	DF	Seq SS	Adj SS	Adj MS	F	p	% Contribution
A	2	38,718	38,718	19,359	4.44	0.025	12.43
B	2	60,565	60,565	30,282	6.95	0.005	19.45
C	2	124,937	124,937	62,468	14.33	0.000	40.12
Error	20	87,164	87,164	4358			
Total	26	311,383					

**Table 5** ANOVA for surface roughness

Source	DF	Seq SS	Adj SS	Adj MS	F	p	% Contribution
A	2	2.68287	2.68287	1.34143	16.60	0.000	35.3
B	2	3.14802	3.14802	1.57401	19.48	0.000	41.4
C	2	0.15152	0.15152	0.07576	0.94	0.408	1.99
Error	20	1.61572	1.61572	0.08079			
Total	26	7.59812					

Table 3a. ANOVA table for surface roughness shows that factor B, i.e. cross-sectional area of nozzle, contributes to surface roughness the most, followed by factor A, i.e., air pressure. This is in line with the conclusion drawn from response Table 3b. Figure 3a shows that optimal MQL parameters which minimize cutting forces are A<sub>2</sub>B<sub>3</sub>C<sub>3</sub> and that minimize surface roughness are A<sub>3</sub>B<sub>2</sub>C<sub>2</sub>.

## 4 Conclusions

1. Coolant flow rate contributes the most followed by cross-sectional area of nozzle to cutting forces generated during machining AISI 1040.
2. Air metering screw, which controls the cross-sectional area of nozzle and hence the quantity of air supplied, contributes the most followed by air pressure to surface roughness generated during machining AISI 1040.
3. Optimum MQL parameters which minimize cutting forces are  $A_2B_3C_3$ , i.e., air pressure of 75 psi, nozzle cross-sectional area of 6 mm<sup>2</sup> and coolant flow rate of 1.2 ml/min with conventional soluble oil as coolant.
4. Optimum MQL parameters which minimize surface roughness are  $A_3B_2C_2$ , i.e., air pressure of 80 psi, nozzle cross-sectional area of 4 mm<sup>2</sup> and coolant flow rate of 0.6 ml/min with conventional soluble oil as coolant.

## References

1. Astakhov VP (2008) Machining—Fundamentals and Recent Advances. In: Ecological machining: near-dry machining. Springer, Berlin
2. Awale AS, Srivastava A, Vashista M, Yusufzai MK (2019) Influence of minimum quantity lubrication on surface integrity of ground hardened H13 hot die steel. *Int J Adv Manuf Technol* 100(1–4):983–997
3. Lohar DV, Nanavaty CR (2013) Performance evaluation of minimum quantity lubrication (MQL) using CBN tool during hard turning of AISI 4340 and its comparison with dry and wet turning. *Bonfring Int J Ind Eng Manage Sci* 3(3):102–106
4. NareshBabu M, Anandan V, Muthukrishnan N, Santhanakumar M (2019) End milling of AISI 304 steel using minimum quantity lubrication. *Measurement* 138:681–689
5. Maruda RW, Wojciechowski S, Krolczyk GM, Pimenov DY, Legutko S (2019) The influence of EP/AW addition in the MQL method on the parameters of surface geometrical structure in the process of turning 316L steel. In: *Advances in manufacturing engineering and materials*. Springer, Cham, pp 341–350
6. Babu MN, Anandan V, Muthukrishnan N (2019) Analysis of EN24 steel in turning process with copper nanofluids under minimum quantity lubrication. *J Brazilian Soc Mech Sci Eng* 41(2):101
7. Sharma AK, Singh RK, Dixit AR, Tiwari AK, Singh M (2019) An investigation on tool flank wear using Alumina/MoS<sub>2</sub> hybrid nanofluid in turning operation. In: *Advances in manufacturing engineering and materials*. Springer, Cham, pp 213–219
8. Yıldırım ÇV, Sarıkaya M, Kıvak T, Şirin Ş (2019) The effect of addition of hBN nanoparticles to nanofluid-MQL on tool wear patterns, tool life, roughness and temperature in turning of Ni-based Inconel 625. *Tribol Int* 134:443–456
9. Hegab H, Kishawy HA, Umer U, Mohany AA (2019) Model for machining with nano-additives based minimum quantity lubrication. *Int J Adv Manuf Technol* 1–16
10. Li Y, Zhao W, Gong Y (2019) Experimental investigation on the surface tension and contact angle of Al<sub>2</sub>O<sub>3</sub>-oil and SiO<sub>2</sub>-oil nanofluids. *Int J Nanomanuf* 15(1–2):80–91



# Experimental Investigation and Mathematical Modeling for Material Removal and Tool Wear in Making of Rectangular Channels by Electric Discharge Machining (EDM) on Aluminum–Boron Carbide Composite Sintered Preform



Suresh Gudipudi, Selvaraj Nagamuthu, Kanmani Subbu Subbian and Surya Prakasa Rao Chilakalapalli

**Abstract** Boron carbide ( $B_4C$ ) particulate Aluminum (Al) metal matrix composites (MMCs) are highly demanded due to their specific strength in aerospace, defense, and nuclear sectors. The controllable porosity which causes the good toughness and the forming limit values can be obtained for these MMCs synthesized by powder metallurgy route. But the porosity level had great influence on the machinability of these MMCs by electric discharge machining (EDM). In the present work, cold compaction followed by sintering of Al and  $B_4C$  powders was used to fabricate the MMC specimen. The density and hardness were estimated by Archimedes principle and Vickers microhardness test, respectively. The feasibility of EDM of the fabricated MMC at high porosity level (12%) was evaluated through pilot experimental runs. The full factorial experimental design with three parameters of three levels each (total runs  $3^3 = 27$ ) is used for experimentation. The influence of electrical process conditions such as discharge current (I), pulse-on duration (T-On), and pulse-off duration (T-Off) on material removal rate (MRR) and tool wear rate (TWR) was studied. A mathematical model was formulated to represent the process. Analysis of variance (ANOVA) was performed to identify the significant parameters affecting the material removal rate (MRR) and tool wear rate (TWR). Results revealed that the developed model was adequate to represent the process with R-square values of

---

S. Gudipudi (✉) · S. Nagamuthu  
Department of Mechanical Engineering, National Institute of Technology Warangal, Warangal,  
Telangana 506004, India  
e-mail: [gudipudi.suresh@gmail.com](mailto:gudipudi.suresh@gmail.com)

K. S. Subbian  
Discipline of Mechanical Engineering, Indian Institute of Technology Palakkad, Palakkad,  
Kerala 678557, India

S. P. R. Chilakalapalli  
National Institute of Technology Andhra Pradesh, Tadepalligudem, Andhra Pradesh 534102,  
India

94.9%, and 83.82% for MRR and TWR, respectively. Results also showed that the discharge current had a significant effect on the MRR and TWR.

**Keywords** B<sub>4</sub>C · Porosity · Electric discharge machining (EDM) · Material removal rate (MRR)

## 1 Introduction

The specific mechanical properties of Al–B<sub>4</sub>C particulate MMCs are highly appreciable in the high technology industries such as nuclear, friction, and computer hard disks [1]. These MMCs had great flexibility during processing by solid-state powder synthesis route to achieve significant improvement of required property in the specified application. The flexibility in terms of varying processing conditions which affect the desired property was explored by researchers [2]. The effect of compaction pressure, sintering temperature and milling time on density, and bending strength of these MMCs (Al–10 wt%B<sub>4</sub>C) were extensively studied by Abinojar et al. [3]. Mohanty et al. [4] explored the effect of weight proportion of the B<sub>4</sub>C particles in the range of 0–25% for density, electrical conductivity, hardness, and flexural strength. Karako [5] studied the effect of B<sub>4</sub>C wt% on mechanical properties and suggested the 10 wt% and 5 wt% for improved fracture toughness and tensile strength, respectively. Chang et al. [6] developed models to predict the electrical resistivity of the MMCs and compared experimentally. The high-temperature mechanical properties are also witnessed by Onoro et al. [7] of Al alloy–B<sub>4</sub>C MMCs. The tremendous improvement in mechanical properties of Al–15 wt% B<sub>4</sub>C–1.5 wt% Co MMC was also reported by Ghasali et al. [8].

The machinability studies of these MMCs by conventional machining methods are also found rarely. Moreover, those methods phasing challenges are because of the presence of hard B<sub>4</sub>C particles such as premature failure of the cutting tool, high temperature at work–cutting tool–chip interfaces, fluctuation in cutting forces, worn out cutting tool profile geometry, dimensional inaccuracy and lack of surface integrity of the finished product [9]. Therefore, a non-conventional method, electric discharge machining (EDM), is being reported as a potential process to overcome these limitations while machining of MMCs. In EDM, the material removal takes place by precisely controlled sparks that occur between a tool (electrode) and a workpiece separated with a specific small gap (spark gap) in the presence of a dielectric fluid such as hydrocarbon oil or deionized water. Vaporization of work material occurs due to intensive heat of generated spark (high frequency) between tool and work electrodes for a very short span of time (microseconds). Non-contacting type, low MRR during EDM/Micro EDM process is attributed to attaining high surface finish and dimensional accuracy [10–12].

From the reported literature, it was observed that the level of porosity and the volume/weight fraction of B<sub>4</sub>C particles had a great impact on the electrical, thermal, and mechanical properties of the MMCs. The high-level porosity and unavoidable

changes in the electrical conductivity in the fabricated MMCs by this powder metallurgy route will affect the machining (EDM) performance [13]. Therefore, the present study is conducted to check the feasibility of EDM of the high porous (12%) Al-6 wt% B<sub>4</sub>C MMC and to optimize the process conditions to improve MRR.

## 2 Materials and Methods

### 2.1 Fabrication of MMC Work Specimen and Tool Electrode

Pure aluminum in the powder form of 325 mesh (99.9% pure, SRL laboratory) and the B<sub>4</sub>C particles of average size 35 μm (99.9% pure, Supertek dies, Delhi.) were used as matrix and reinforcement (RF) phases, respectively. The scanning electron microscope image and X-ray diffraction pattern of B<sub>4</sub>C particulates were shown in Fig. 1a, b. The B<sub>4</sub>C particulates of 6 weight percentage (wt%) were added to the Al powder particles and mixed thoroughly in a ceramic bowl manually for 30 min. The matrix and RF particle mix were compacted (cross section of 30 mm × 30 mm) at room temperature in the metallic die under 500 kN capacity hydraulic press. The loading rate and dwell during compaction were set as 1 mm/sec and 90 min, respectively, till the pressure of 280 MPa is achieved. The compacted green specimen was sintered in a tubular furnace under argon atmosphere. The theoretical and experimental densities of the sintered MMC specimen were measured by a rule of mix and Archimedes principle. The hardness (HV) was measured by Vicker’s microhardness test (model: Economet VH 1MD) at a load of 100 g with dwell about 10 s. The microstructure was studied under the optical microscope (Model HUVITZ LUSIS HC-30MU). The XRD pattern of the MMC specimen was compared to the pure Al as shown in Fig. 1c. The photographs of a die, hydraulic press setup, and compacted MMC specimen were shown in Fig. 2. The sintering of MMC was carried out under argon atmosphere in tubular furnace. The sintering cycle consists of heating the MMC at rate of 2 °C/min up to 100 °C (hold for 20 min), 1.5 °C/min up to 250 °C

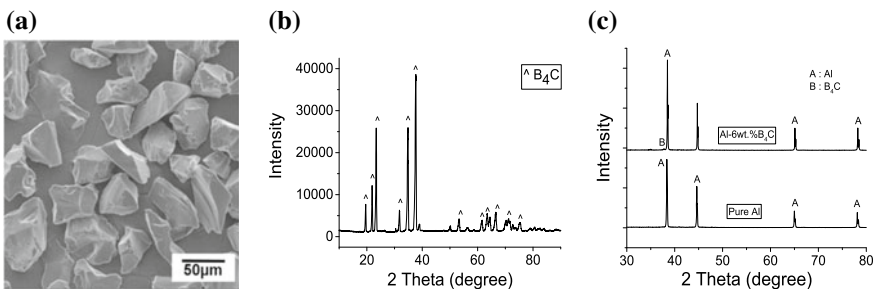


**Fig. 1** a SEM micrograph of B<sub>4</sub>C particulates, b XRD pattern of B<sub>4</sub>C, c Comparison of XRD pattern of pure Al and Al-6 wt% B<sub>4</sub>C

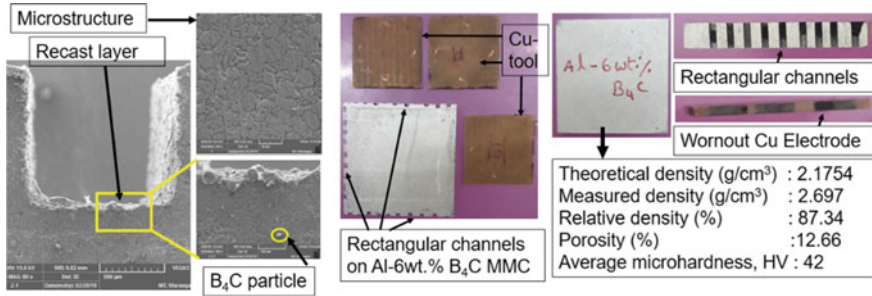


**Fig. 2** Photographs and SEM micrographs of Al-6 wt% B<sub>4</sub>C MMC and Cu-tool

(hold for 10 min), and 7 °C/min up to 600 °C (hold for 90 min) followed by furnace cooling (approximately 270 min).

## 2.2 Sinker EDM of a Rectangular Channel—Experimental

The diesinker EDM machine (Model PSR-20, Ratnaparkhi, India.) was used to make the rectangular channels in the fabricated Al-6 wt% B<sub>4</sub>C MMC specimen. The tool material made of copper (Cu) of 1 mm thickness was precisely machined through wire EDM. The average surface roughness of the tool electrode and MMC work specimens were measured with a surface profilometer (Model: Taylor Hobson Surtronic S128) as 1.02 μm and 1.03 μm, respectively. The tool-work arrangement of positive polarity was continuously flushed with commercial EDM oil as a dielectric. Tool electrode was vertically fed toward the work until it reaches the spark discharge gap of 0.25 mm. At this stage, a high electric potential (105 ± 10 V) was applied to initiate the plasma in the spark gap by the breakdown of the dielectric. The discharge voltage was maintained to the value 55 ± 10 V. As a result, melting and vaporization of the work material were occurred due to the intensive heat of generated plasma (high frequency) in a very short span of time (microseconds). Hence, the crater was created on the working specimen which replicates the shape of the tool electrode. Pilot experimental runs were conducted based on the available specifications of the EDM setup to fix the range for input experimental conditions. The varied input parameters with their levels and the full factorial experimental design were represented in Tables 1 and 2, respectively. The present study considered the material removal rate (MRR) and tool wear rate (TWR) for fixed machining time of 2 min as response variables. MRR and TWR were estimated by the weight difference before and after machining of unit time upon the measured density. The photographs of the tool (Cu) and work specimens of EDM machined slots were shown in Fig. 2.

**Table 1** Representation of EDM experimental conditions

Fixed parameters	Type/value		
Polarity	Straight (Positive)		
Spark open voltage	105 ± 10 V		
Discharge gap voltage	65 V		
Tool electrode	Cu		
Machining time	2 min		
Work	Al-6 wt%B <sub>4</sub> C MMC		
Thickness of the tool	1.00 ± 0.04 mm		
<i>Varied parameters and their levels</i>			
Factor code, Parameter	Level 1	Level 2	Level 3
A. Discharge current, I (A)	4	6	8
B. Pulse duration on time, T-on (μs)	25	45	65
C. Pulse duration off time, T-off (μs)	24	36	48
<i>Performance output (response variable)</i>			
Response variable 1	Material removal rate, MRR (mm <sup>3</sup> /min)		
Response variable 2	Tool wear rate, TWR (mm <sup>3</sup> /min)		

### 3 Results and Discussion

The full factorial experimental representation for response values is shown in Table 2. The regressions equation was developed to represent the process for the responses and ANOVA was performed. The multiple regression coefficients of the developed models indicate that the model can explain variation in MRR and TWR to the extent of 94.90% and 83.82%, respectively. Thus, the developed mathematical models are adequate to represent the EDM process. ANOVA revealed that the discharge current having *p*-values as 0.000 and 0.007 for both the MRR and the TWR, respectively. Hence, the discharge current is the most significant parameter affecting both responses. The main effect and interaction plots for MRR and TWR were shown in Figs. 3 and 4, respectively. From these plots, it was observed that the high discharge current values improve the MRR and TWR. The reason is the amount of heat energy transferred to both the tool and work increases as current increases (Tables 3 and 4).

#### 3.1 Regression Equation for MRR

$$MRR = 1.41 + 0.127 A + 0.0163 B - 0.0895 C - 0.0024 A^2 - 0.000669 B^2 + 0.00101 C^2 + 0.00538 A * B + 0.00240 A * C + 0.000183 B * C$$

**Table 2** Representation of full factorial experimental design

Standard Order	Run order	Factor, A Current (A)	Factor B, T-On (μs)	Factor C, T-Off (μs)	Response 1 MRR (mm <sup>3</sup> /min)	Response 2 TWR (mm <sup>3</sup> /min)
10	1	6	25	24	2.119	0.065
22	2	8	45	24	3.188	0.091
13	3	6	45	24	2.328	0.049
3	4	4	25	48	0.995	0.006
21	5	8	25	48	2.572	0.117
23	6	8	45	36	2.508	0.013
14	7	6	45	36	1.655	0.085
1	8	4	25	24	1.203	0.04
4	9	4	45	24	0.618	0.06
27	10	8	65	48	2.954	0.103
6	11	4	45	48	1.331	0.036
19	12	8	25	24	2.137	0.099
12	13	6	25	48	2.248	0.089
26	14	8	65	36	2.995	0.038
9	15	4	65	48	0.379	0.015
16	16	6	65	24	1.462	0.038
18	17	6	65	48	1.308	0.036
5	18	4	45	36	0.731	0.001
2	19	4	25	36	1.117	0.017
24	20	8	45	48	2.867	0.109
15	21	6	45	48	1.898	0.061
25	22	8	65	24	1.894	0.075
20	23	8	25	36	2.071	0.075
17	24	6	65	36	1.386	0.031
7	25	4	65	24	0.402	0.026
8	26	4	65	36	1.016	0.069
11	27	6	25	36	1.17	0.045

### 3.2 Regression Equation for TWR

$$TWR = 0.185 + 0.0087 A + 0.00143 B - 0.01294 C - 0.00011 A^2 - 0.000004 B^2 + 0.000142 C^2 - 0.000255 A * B + 0.000463 A * C + 0.000003 B * C$$

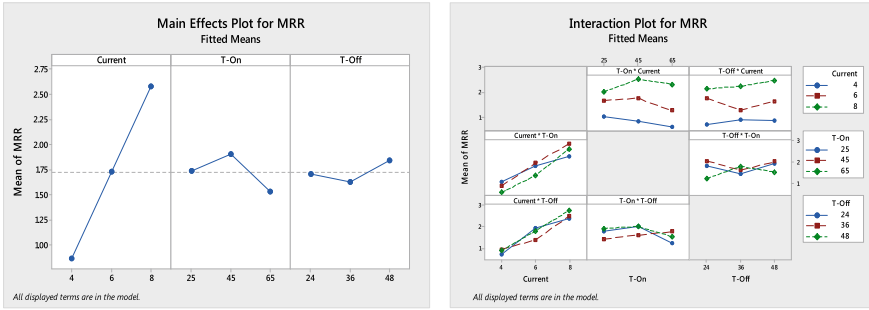


Fig. 3 Main effect and interaction plots for MRR

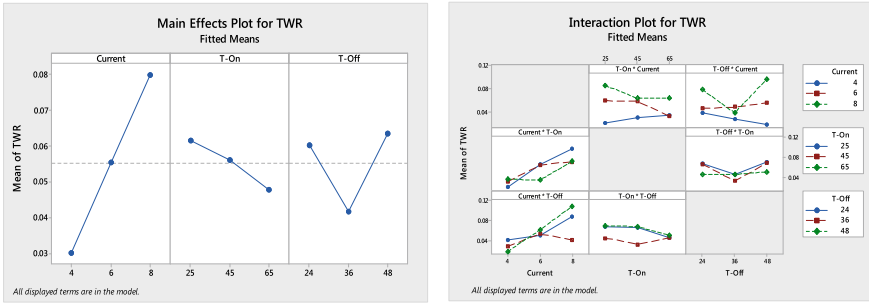


Fig. 4 Main effect and interaction plots for TWR

Table 3 ANOVA for MRR

Source of variation	Degree of freedom	Sum of square	Mean square	F-value	P-value
Model	18	16.4353	0.9131	8.27	0.002
Linear	6	13.9891	2.3315	21.13	0.000
A	2	13.1658	6.5829	59.66	0.000
B	2	0.6175	0.3088	2.80	0.120
C	2	0.2058	0.1029	0.93	0.432
2-Way interactions	12	2.4462	0.2039	1.85	0.195
AB	4	0.8620	0.2155	1.95	0.195
AC	4	0.6252	0.1563	1.42	0.312
BC	1	0.9590	0.2397	2.17	0.163
Error	8	0.8827	0.1103		
Total	26	17.3181			

**Table 4** ANOVA for TWR

Source of variation	Degree of freedom	Sum of square	Mean square	F-value	P-value
Model	18	0.024061	0.001337	2.30	0.115
Linear	6	0.014622	0.002437	4.20	0.033
A	2	0.011241	0.005621	9.68	0.007
B	2	0.000842	0.000421	0.73	0.513
C	2	0.002539	0.001269	2.19	0.175
2-Way interactions	12	0.009438	0.000787	1.36	0.341
AB	4	0.002739	0.000685	1.18	0.389
AC	4	0.005643	0.001411	2.43	0.133
BC	1	0.001056	0.000264	0.45	0.767
Error	8	0.004643	0.000580		
Total	26	0.028704			

## 4 Conclusions

The Al-6 wt% B<sub>4</sub>C composite was successfully fabricated by powder synthesis route. The porosity (due to fabrication method and conditions) and the electrical conductivity (due to less conductive B<sub>4</sub>C particle inclusion) of the composite affect the EDM. The reason is the discharge phenomenon directly affected by the electrical conductivity of the tool and the work material. The porosity level and the size distribution of pore in the composite will affect the crater volume and debris evacuation from the machining zone. Hence, the present study proved that the machining of these MMCs by EDM is possible, and the developed model was adequate to represent the process.

**Acknowledgements** The authors would like to thank the Department of Science and Technology-Science and Engineering Research Board (DST-SERB), New Delhi, India for supporting this work under the Early Career Research scheme (File No. ECR/2017/001320). The authors would like to thank Dr. M. J. Davidson, MED, NIT, Warangal, for valuable suggestions and support in fabricating the MMC.

## References

1. Miracle DB (2005) Science and metal matrix composites—from science to technological significance. *Compos Sci Technol* 65:2526–2540
2. Venkateswarlu K, Ray AK, Chaudhury SK, Pathak LC, Venkateswarlu K, Ray AK (2002) Development of aluminium based metal. National Metallurgical Laboratory, Jamshedpur India, pp 171–180
3. Abenojar J, Valasco F, Martinez MA (2007) Optimization of process parameters for the Al-10% B<sub>4</sub>C system obtained by mechanical alloying. *J Mater Process Technol* 184:441–446



4. Mohanty RM, Balasubramanian K, Seshadri SK (2008) Boron carbide-reinforced aluminium 1100 matrix composites: Fabrication and properties. *Mater Sci Eng A* 498(1–2):42–52
5. Karako H (2016) Influence of B<sub>4</sub>C particle reinforcement on mechanical and machining properties of Al6061/ B<sub>4</sub>C composites. *Compos B Eng* 101:87–98
6. Chang S, Chen C, Lin S, Kattamis TZ (2003) Electrical resistivity of metal matrix composites. *Acta Mater* 51:6191–6302
7. Onoro J, Salvador MD, Cambroner LEG (2009) High temperature mechanical properties of aluminium alloys reinforced with boron carbide particles. *Mater Sci Eng A* 499:421–426
8. Ghasali E, Alizadeh M, Ebadzadeh T (2016) Mechanical and microstructure comparison between microwave and spark plasma sintering of Al–B<sub>4</sub>C composite. *J Alloy Compd* 655:93–98
9. Bains PS, Sidhu SS, Payal HS (2016) Fabrication and machining of metal matrix composites: a review. *Mater Manuf Process* 31(5):553–573
10. Rajurkar KP, Levy G, Malshe A, Sundaram MM, McGeough J, Hu X (2006) Micro and nano machining by electro-physical and chemical processes. *CIRP Ann Manuf Technol* 55(2):643–666
11. Pandey PC, Shan HS (2005) *Modern machining processes*. Tata McGraw-Hill Publishing Company Limited, Delhi, p 84
12. Rajurkar KP, Sundaram MM, Malshe AP (2013) Review of electrochemical and electrodischarge machining. *Procedia CIRP* 6:13–26
13. Zou R, Yu Z, Li W, Guo M, Li J (2016) Influence of porous structure on the machining performance of micro EDM. *J Mater Process Technol* 232:43–51

# Investigation on the Microstructure and Mechanical Properties of AZ91D Magnesium Alloy Plates Joined by Friction Stir Welding



Nagabhushan Kumar Kadigithala and C. Vanitha

**Abstract** Friction stir welding (FSW) is an effective technique to join magnesium-based alloys which are difficult to fusion weld. In this work, similar AZ91D Mg alloy sheet of 3 mm thick butt joint was produced via friction stir welding at welding parameters such as rotational speed, welding speed, and tilt angle. The rotational speed was kept constant of 720 rpm, the welding speed varied from 25 to 75 mm/min, and tilt angle from 1.5° to 2.5°. Defect-free weld was obtained under 75 mm/min welding speed and tilt angle of 1.5°. The microstructure of the parent alloy consists of phases, namely primary  $\alpha$  and eutectic  $\beta$  ( $Mg_{17}Al_{12}$ ) in the as-received condition (gravity die-cast) which was confirmed by X-ray diffraction (XRD) analysis. Microscopic studies, tensile tests, hardness test, and fractographic studies were conducted. Metallographic studies revealed different features in each zone depending on their thermomechanical condition. A significant increase in hardness was observed in the stir zone of weldment compared to parent alloy due to the recrystallized grain structure. The dendrite grain structure present in weldment was completely disappeared and was transformed to fine grains in stir zone (SZ). The transverse tensile test result of the weld specimen indicated that weldment was about 44.9% higher than the parent alloy. Fractographic analysis of the friction stir welded specimen indicated that the weld specimen failed through the brittle failure.

**Keywords** AZ91 D mg alloy · Friction stir welding · Microstructure · Dynamic recrystallization

---

N. K. Kadigithala (✉) · C. Vanitha  
Department of Metallurgical and Materials Engineering, National Institute of Technology,  
Warangal, Warangal 506004, Telangana State, India  
e-mail: [knbkumar.ind@gmail.com](mailto:knbkumar.ind@gmail.com)

© Springer Nature Singapore Pte Ltd. 2020  
H. K. Voruganti et al. (eds.), *Advances in Applied Mechanical Engineering*,  
Lecture Notes in Mechanical Engineering,  
[https://doi.org/10.1007/978-981-15-1201-8\\_109](https://doi.org/10.1007/978-981-15-1201-8_109)

1021

## 1 Introduction

Mg-based alloys are transpiring as eminent material in the field of engineering, peculiarly in the automotive and aeronautics field cause of their superior damping strength and reusability, predominant strength-weight ratio, lower bulk density [1]. This material possesses a density of almost about 70% of Al materials, which are auspicious engineering materials to enhance propellant efficiency peculiarly in industries like automobile [2, 3]. Currently, these materials are predominantly utilized to originate cast-based components. Their usability in wrought nature is lesser, and predictions for the future are to advance in forthcoming years. However, the major disadvantage of these materials for structural applications is enormous chemical activity primarily on numerous occasions due to low joining and corrosion resistance [4]. Traditional fusion welding of these alloys involve variety of challenges in obtaining defect free welds [5].

The fusion welding of magnesium-based alloys is unreliable due to the above reasons. Friction stir welding (FSW) is an appropriate bulk form technique to combine Mg alloys that abolish joining imperfections collaborated with traditional fusion joining methods. Weldments originated through FSW route manifest superior mechanical characteristics like elasticity, tensile strength, and hardness with respect to traditional joining techniques. FSW is a bulk form welding process that was innovated at TWI (UK) in 1991 and was preliminarily implemented to combine Al alloys [6]. Because of this dominance, FSW suits as a magnificent strategy for combining divergent metals like Ni-based alloys, Ti and Steel alloys [7]. Contrasting these superior strength alloys, Mg materials have a lesser melting point and low strength that are suitable for FSW like Al materials [1]. Numerous industrial grade Mg materials like AZ31, ZM21 [8–10], and Mg–Zn–Y–Zr [11] are combined utilizing FSW route, producing great outcomes above traditional fusion joining methods.

Nakata [12] had demonstrated numerous FS-joined Mg materials. Scholar delineated that physical characteristics were enhanced above traditional fusion joining route. Lee et al. [13] scrutinized specimen features of FSWed AZ91D Mg alloy weldments and delineated that  $\beta$  intermetallic form was dissolved in stir region, because of frictional heat involved. Cao et al. [14] have scrutinized impacts of probe dimensional length and revolving speed on Friction stir lap weld of AZ31B-H24 Mg material having 2 mm dimensional thickness and demonstrated that by ascending speed of rotation of tool, tensile shear load escalates preliminarily but de-escalates by furthermore extending of rotational speed. Xunhong et al. [15] had scrutinized FS butt joint AZ31 Mg material plates of 4 mm dimensional thickness and delineated that tensile characteristics of the specimen obtained 93% of the metal in bulk form and breakage position was in HAZ region. Afrin et al. [10] explored FSWed AZ31B Mg materials and delineated that grain in stir region and thermo-mechanically impacted region encountered recrystallization and enlargement and the dimensional shape of uniform grains, having tiny values of dual aspect proportion and fractal dimension. Cavaliere et al. [16] has explored the impact of FSP on superplastic behavior of Mg material, i.e., AZ91 and outlined that it manifested superior strength and ductile

characteristics because of the tiny composition by processing technique at ambient temperature with respect to bulk metal. Darras et al. [17] scrutinized the impact of FSW on techno-commercial AZ31 Mg material and delineated that uniformity of microstructure and purification of grain are attained in a solo FSP pass over the facet of metal in bulk form. Zeng et al. [18] scrutinized the impact of FSW on AM50 Mg materials and delineated that microstructural homogenization introduce finer size of uniform grains accommodating  $\alpha$ -Mg matrix and  $\beta$  phase. Rose et al. [19] scrutinized the impact of length-wise force throughout FSW of AZ61A Mg material and delineated that it has a noteworthy impact on the generation of imperfections, grain size, hardness if tensile strength, and stir region. Cavaliere et al. [20] checked the FS-joined AZ91 fatigue-life cycle and found an improved fatigue-life compared to that of as-cast bulk material. Chai et al. [21] explored immersed FS-processed AZ91 and outlined that after processing larger  $\beta$  Mg<sub>17</sub>Al<sub>12</sub> form, grid altered into particles affixed on grain frontiers. Park et al. [22] established texture and movement design in FSWed AZ61 Mg materials and delineated that onion ring form in stir region and nugget form are connected with the availability of (0002) basal plane possess elliptical trace facet. Park et al. [23] explored FSW of thixomolded Mg material AZ91D and delineated that microscopic structure comprising elementary solid fragments is altered to tiny homogenized grains of  $\alpha$ -Mg form throughout processing. The toughness of stir region was improved with de-escalating grain dimensional size in correlation with the Hall–Petch equation. Nowadays, welding of dissimilar metals such as magnesium alloys [24, 25] and magnesium to aluminium alloys [26–28] has been getting attention among research groups. Literature survey confirmed that only a limited amount of work has been carried out on the FSW of magnesium-based alloys when compared to Al alloys. The present manuscript reports our primary results on FS-welded AZ91 Mg alloy (gravity die-cast), which is widely used in automobile and aerospace industries.

## 2 Experimental Procedures

### 2.1 Base Metal

The AZ91D Mg alloy used in the present work was supplied in the form of as-cast blocks; 3 mm thick plates were prepared from the blocks of dimension 130 × 45 mm using wire cut electrical discharge machine (EDM); and the chemical composition is presented in Table 1.

**Table 1** Chemical Composition of AZ91D Mg alloy

Element	Al	Zn	Si	Cu	Ni	Mn	Mg
wt%	8.84	0.59	0.22	0.05	008	0.21	Balance

**Table 2** Process parameters used for the present study

Nomenclature	Corresponding processing parameters
Tool details	H13 tool steel tapered cylindrical pin (left-hand metric threads, 0.5 mm pitch) Pin diameter: 7 mm (shoulder end) and 2 mm (tip end) Pin length: 2.6 mm Shoulder diameter: 18 mm
Other details	Rotation speed: 720 rpm, Welding speed: 25, 50, 75 mm/min Tilt angle: 1.5°, 2°, 2.5°
Dwelling time	10 s

## 2.2 Friction Stir Welding of AZ91D Mg Alloy Plates

Prior to welding, surface oxides of plates are removed by stainless steel brush, and then, the 3 mm thick plates were cleaned with acetone in order to remove any surface pollutant. At a constant rotational speed of 720 rpm, welding speeds varied from 25 to 75 mm/min, and tilt angle varied from 1.5° to 2.5°, the welding operations were performed. Butt joint welds, 3 mm thick, were produced using a commercially available vertical milling machine at IIT, Roorkee. The process parameters used in this study are listed in Table 2.

## 2.3 Metallography

The specimens were prepared by the standard metallographic polishing procedure. The weld specimens were etched with acetic glycol for 10–15 s prior to examination using optical microscopy and scanning electron microscopy.

Microstructural and elemental analysis of the weldments and fractured surfaces was analyzed using a VEGA 3 TESCAN scanning electron microscope.

## 2.4 X-Ray Diffraction (XRD) Analysis

Phase investigation of the bulk material and joints was explored utilizing an XRD, (X'pert Powder Diffractometer: PANalytical, Netherland) through Cu K $\alpha$  radiation.

## 2.5 Tensile Testing

Transverse tensile experiments were executed to diagnose the specimen strength of the weldments. Test samples were assembled following the standard ASTM E8

through a wire cut EDM. The tensile investigations were executed at ambient temperature utilizing Instron Model no. S500 testing machine, at crosshead velocity of 2 mm/min.

### 2.6 Microhardness Testing

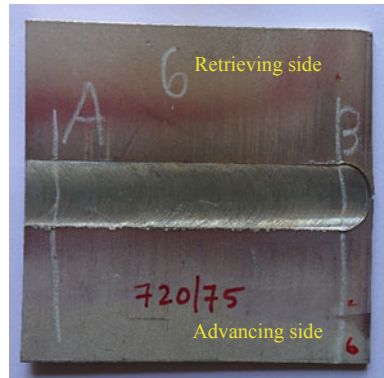
Microhardness was conducted using Shimadzu microhardness tester using a load of 200 g applied for 15 s.

## 3 Results and Discussion

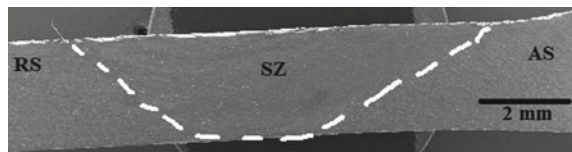
Defect-free weldment was produced at a rotational speed of 720 rpm, travel speed of 75 mm/min, and tilt angle of 1.5° as shown in Fig. 1. The same has been confirmed through X-ray radiography, and visual inspections are accomplished on the FSW joints to inspect defects generated during the welding process. Microstructure analysis, tensile, and hardness tests were conducted at this weld parameter. A moderate and constant rotational velocity of 720 rpm was maintained throughout the welding process [29, 30] as too low or too high speed results in inadequate and excess heat generation, respectively.

Figure 2 shows the macrostructure of the cross section of the joint which was welded at 720 rpm of rotational speed and 75 mm/min of travel speed. The top

**Fig. 1** Surface appearance at welding condition of 500 rpm, 75 mm/min, and 1.5°



**Fig. 2** Macrograph of cross-sectional joint



surface of weld nugget was wider than the bottom surface due to contacting tool shoulder with the top surface has experienced functional heat. The profile of nugget is influenced by tool pin profile, type of material and thermal conductivity. As shown in figure 2 no defects in the weld zone was observed.

### 3.1 Microstructure of the Weld Zones

The parent alloy consists of a mixture of primary  $\alpha$  phase and  $\beta$  intermetallic compound (eutectic  $\beta$  ( $Al_{12}Mg_{17}$ )) as shown in Fig. 3.

Figure 4 shows the microstructure of the weldment in different zones. The zones named as (a) heat affected zone (HAZ), (b) thermo-mechanically affected zone (TMAZ), and (c) stir zone (SZ), respectively. Each zone exhibits unique features, depending upon thermal and mechanical conditions. In HAZ, due to the thermal effect produced by the tool, the volume fraction of  $\beta$  intermetallic compound undergoes resolution and was reduced to a smaller fraction. In TMAZ, due to combined effects of thermal and plastic deformation, it is composed of partially observed recrystallization grains and eutectic  $\beta$ . The eutectic  $\beta$  is located around the tool rotation direction in TMAZ. In the SZ, the grain structure was transformed into a fine equiaxed grain structure. The stir zone undergoes dynamic recrystallization (DRX).

Figure 5 illustrates the XRD patterns of parent alloy and weldment, and the presence of  $\alpha$  and Eutectic  $\beta$  ( $Mg_{17}Al_{12}$ ) phase is confirmed.

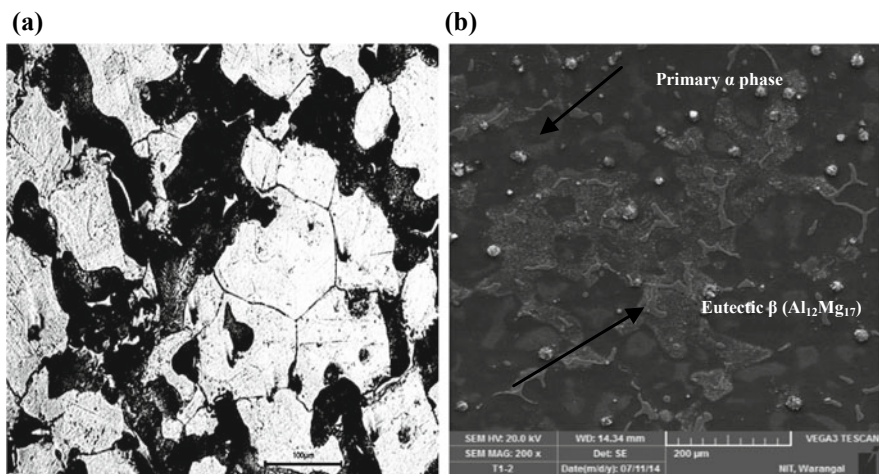


Fig. 3 Showing micrograph of AZ91D Mg alloy a optical microscopy image at 100 X b SEM image at 200 X

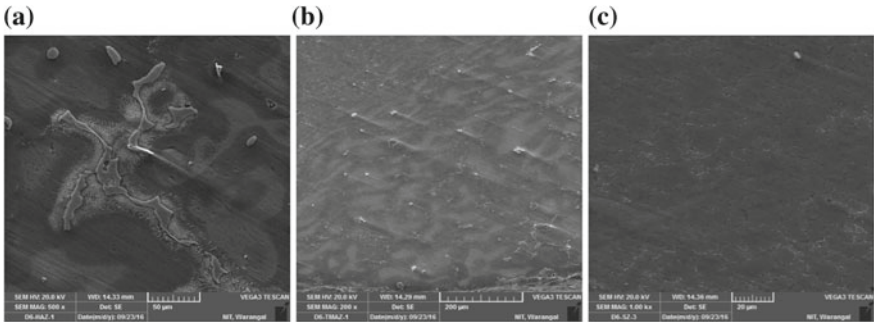


Fig. 4 SEM micrographs of AZ91D Mg alloy weldment of condition 720 rpm, 75 mm/min at a HAZ, b TMAZ, c SZ

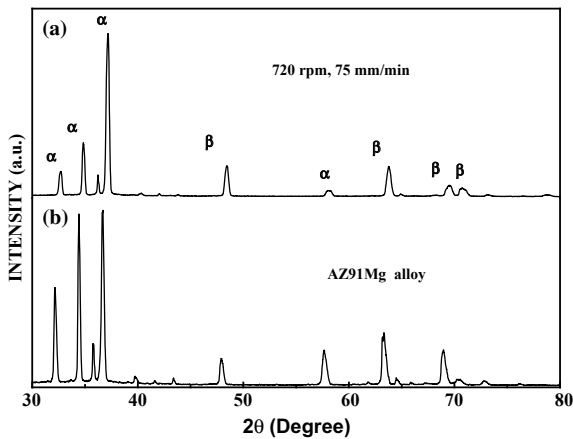


Fig. 5 XRD patterns of a parent alloy b weldment

### 3.2 Microhardness Testing Results

Figure 6 shows the microhardness result of the weldment. The hardness of parent alloy was about 68 HV. The hardness of SZ is improved significantly due to the recrystallized grain structure. The stir zone undergoes dynamic recrystallization (DRX) compare to the SZ, and the TMAZ and HAZ showed lower hardness.

### 3.3 Tensile Testing

The parent alloy exhibited lower tensile strength (109 MPa) and elongation value (3%) when compared to the weldment. The weldment showed the maximum ultimate



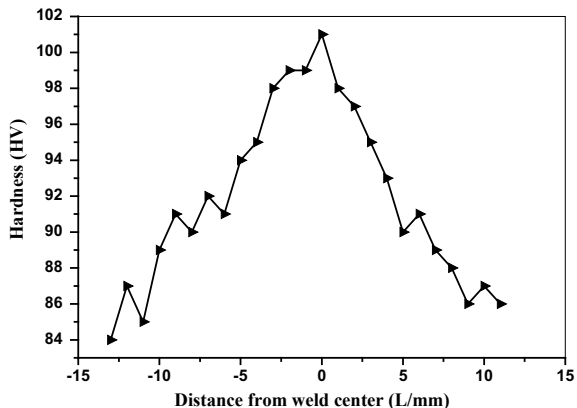


Fig. 6 Hardness profile of the weldment of condition 720 rpm, 75 mm/min

tensile strength of 158 MPa, which is about 44.9% greater and elongation of 4.7% which is about 56.6% higher than the elongation of parent alloy.

### 3.4 Fractographic Analysis

Figure 7 shows the fractured surface of the parent alloy and weldment. It was observed that fracture occurred at the interface of the weld specimen and image clearly indicates that fracture occurred in the brittle mode. The unevenly distributed eutectic  $\beta$ -Al<sub>12</sub>Mg<sub>17</sub> was responsible for preferential crack initiation. Due to this specimen

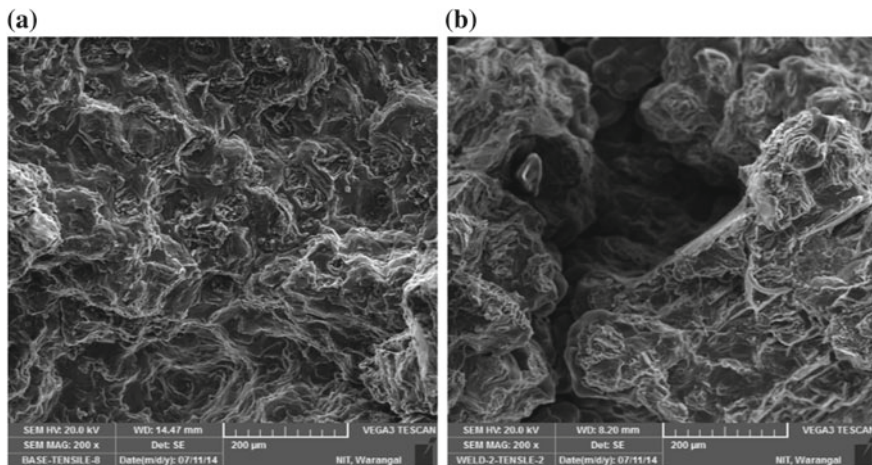


Fig. 7 SEM images of the fractured surface a AZ91D Mg alloy and b weldment

fractured at weld-base material interface, the existence of quasi-cleavage surfaces in Fig. 7a, b confirms that parent alloy and welded specimen failed through the brittle mode of failure.

## 4 Conclusion

Similar AZ91D magnesium alloy plates of 3 mm thick were successfully welded at a welding speed of 75 mm/min and tilt angle of 1.5°. The conclusions drawn from the present study are as follows:

1. The original dendritic grain structure present in weldment was completely eliminated in the stir zone. Due to the frictional heat input produced by the tool shoulder in contact with the workpiece, it was replaced with fine grains and  $\beta$  intermetallic phase was dissolved in stir zone.
2. In the stir zone, the grains undergo grain refinement due to dynamic recrystallization.
3. The mechanical properties such as tensile strength of the weldment were about 44.9% higher than the parent alloy.
4. Hardness was improved significantly when compared to other zones due to grain refinement.
5. The mode of fracture in the weldment was observed to be brittle in nature

**Acknowledgements** Authors would like to acknowledge the National Institute of Technology Warangal for financial support to carry out the experimentation of Mr. K. N. B. Kumar, Research Scholar, Enrollment Number (701251), under the guidance of Dr. C. Vanitha, Associate Professor in Department of Metallurgical and Materials Engineering—NIT Warangal, India.

## References

1. Harikrishna KL, Dilip JJS, Ramaswamy Choudary K, Subba Rao VV, Koteswara Rao SR, Janaki Ram GD, Sridhar N, Madhusudhan Reddy G (2010) Friction stir welding of magnesium alloy ZM21. *Trans Indian Inst Met* 63:807–811
2. Su SF, Lin HK, Huang JC, Ho NJ (2002) Electron-beam welding behavior in Mg-Al-based alloys. *Metall Mater Trans A* 33:1461–1473
3. Benartzy A, Munitz A, Kohn G, Brining B, Shtechman A (2010) In: *Proceedings Magnesium Technology*. TMS, Seattle, WA, USA, pp 295–302
4. Liu L (2010) *Welding and joining of magnesium alloys*, 1st edn. Woodhead Publishing, Cambridge
5. Cao X, Jahazi M, Immarigeon JP, Wallace W (2006) A review of laser welding techniques for magnesium alloys. *J Mater Process Technol* 171:188–204
6. Marzbanrad J, Akbari M, Asadi P, Safaee S (2014) Characterization of the influence of tool pin profile on microstructural and mechanical properties of friction stir welding. *Metall Mater Trans B* 45:1887–1894

7. Bhadeshia HKDH, DebRoy T (2009) Critical assessment: friction stir welding of steels. *Sci Technol Weld Joining* 14:193–196
8. Padmanaban G, Balasubramanian V (2009) Selection of FSW tool pin profile, shoulder diameter and material for joining AZ31B magnesium alloy—an experimental approach. *Mater Des* 30:2647–2656
9. Suhuddin UFHR, Mironov S, Sato YS, Kokawa H, Lee C-W (2009) Grain structure evolution during friction-stir welding of AZ31 magnesium alloy. *Acta Mater* 57:5406–5418
10. Afrin N, Chen DL, Cao X, Jahazi M (2008) Microstructure and tensile properties of friction stir welded AZ31B magnesium alloy. *Mater Sci Eng A* 472:179–186
11. Xie GM, Ma ZY, Geng L, Chen RS (2007) Microstructural evolution and mechanical properties of friction stir welded Mg–Zn–Y–Zr alloy. *Mater Sci Eng A* 471:63–68
12. Nakata K (2009) Friction stir welding of magnesium alloys. *Weld Int* 23:328–332
13. Lee WB, Kim JW, Yeon YM, Jung SB (2003) The joint characteristics of friction stir welded AZ91D magnesium alloy. *Mater Trans* 44:917–923
14. Cao X, Jahazi M (2011) Effect of tool rotational speed and probe length on lap joint quality of a friction stir welded magnesium alloy. *Mater Des* 32(1):1–11
15. Xunhong W, Kuaishe W (2006) Microstructure and properties of friction stir butt-welded AZ31 magnesium alloy. *Mater Sci Eng A* 431:114–117
16. Cavaliere P, De Marco PP (2007) Superplastic behaviour of friction stir processed AZ91 magnesium alloy produced by high pressure die cast. *J Mater Process Technol* 184:77–83
17. Darras BM, Khraisheh MK, Abu-Farha FK, Omar MA (2007) Friction stir processing of commercial AZ31 magnesium alloy. *J Mater Process Technol* 191:77–81
18. Zeng RCh, Dietzel W, Zettler R, Jun CHEN, Kainer KU (2008) Microstructure evolution and tensile properties of friction-stir-welded AM50 magnesium alloy. *Trans Nonferrous Met Soc China* 18:s76–s80
19. Rose AR, Manisekar K, Balasubramanian V (2011) Effect of axial force on microstructure and tensile properties of friction stir welded AZ61A magnesium alloy. *Trans Nonferrous Met Soc China* 21:974–984
20. Cavaliere P, De Marco PP (2007) Fatigue behaviour of friction stir processed AZ91 magnesium alloy produced by high pressure die casting. *Mater Charact* 58:226–232
21. Chai F, Zhang D, Li Y (2015) Microstructures and tensile properties of submerged friction stir processed AZ91 magnesium alloy. *J Magnesium Alloys* 3:203–209
22. Park SHC, Sato YS, Kokawa H (2003) Basal plane texture and flow pattern in friction stir weld of a magnesium alloy. *Metall Mater Trans A* 34:987–994
23. Park SHC, Sato YS, Kokawa H (2003) Microstructural evolution and its effect on Hall-Petch relationship in friction stir welding of thixomolded Mg alloy AZ91D. *J Mater Sci* 38:4379–4383
24. Won S, Seo B, Park JM, Kim HK, Song KH, Min SH, Ha TK, Park K (2018) Corrosion behaviors of friction welded dissimilar aluminum alloys. *Mater Charact* 144:652–660
25. Ratna Sunil B, Pradeep Kumar Reddy G, Mounika ASN, Navya Sree P, Rama Pinneswari P, Ambica I, Ajay Babu R, Amarnadh P (2015) Joining of AZ31 and AZ91 Mg alloys by friction stir welding. *J Magnesium Alloys* 3(4):330–334
26. Peiqi L, Guoqiang Y, Hengyu W, Wei G, Xin T, Sha L (2019) Friction stir welding between the high-pressure die casting of AZ91 magnesium alloy and A383 aluminum alloy. *J Mater Process Technol* 264:55–63
27. Prasad BL, Neelaiah G, Krishna MG, Ramana SVV, Prakash KS, Sarika G, Kumar Reddy P, Dumpala R, Sunil BR (2018) Joining of AZ91 Mg alloy and Al6063 alloy sheets by friction stir welding. *J Magnesium Alloys* 6(1):71–76
28. Benfer S, Straß B, Wagner G, Fürbeth W (2016) Manufacturing and corrosion properties of ultrasound supported friction stir welded Al/Mg-hybrid joints. *Surf Interface Anal* 48(8):843–852
29. Lee WB, Kim JW, Yeon YM, Jung SB (2003) The joint characteristics of friction stir welded AZ91D magnesium alloy. *Mater Trans* 44(5):917–923
30. Dai N, Kazuyoshi K, Hiroshi T (2008) Some characteristics of AZ31/AZ91 dissimilar magnesium alloy deposit by friction surfacing. *Mater Trans* 49(5):1137–1141

# Mechanical Characterization of Unidirectional Banana–Glass Fiber-Reinforced Hybrid Composites



Ch. Naveen Reddy, M. Bhargav and Ajay Kumar Kaviti 

**Abstract** Natural fibers are playing very important role in supporting the environmental balance and partially substitute to the structural applications. In this paper, hybrid composites are fabricated using unidirectional banana and unidirectional glass fibers into epoxy resin mixture. Percentage weight of unidirectional banana fibers considered in this study is varied from zero to 100% weight of fibers in the intervals of 20% weight of the total fibers. The objective of the present work is to evaluate and compare the mechanical properties of laminates such as tensile strength, flexural strength, and impact strength of different stacking sequences of unidirectional banana and glass fabrics. It is found that as the glass layer in the laminates increases, its mechanical properties enhance. When the natural fiber is hybridized with glass fiber, a moderate strength is observed in the composites. These hybrid composites can be used for medium load-bearing applications.

**Keywords** Hybrid composites · Tensile strength · Flexural strength · Impact strength

## 1 Introduction

In recent years, there has been an increasing environmental consciousness and awareness of the need for sustainable development, which has raised the interest to engineers, scientists, professionals, and research scholars to focus on natural fibers. Natural fibers act as an alternative reinforcement for composites because of its advantages like low density, high specific weight and low cost, eco-friendly, and biodegradable in nature to replace the synthetic fibers [1]. However, the main disadvantage of these natural fiber polymer composites seems to be the compatibility between the hydrophilic natural fibers and the hydrophobic matrix that makes necessary to

---

Ch. Naveen Reddy (✉) · A. K. Kaviti  
VNR VJMET, Hyderabad 500090, India  
e-mail: [chnaveenreddy316@gmail.com](mailto:chnaveenreddy316@gmail.com)

M. Bhargav  
NIT Warangal, Warangal 506004, India

© Springer Nature Singapore Pte Ltd. 2020  
H. K. Voruganti et al. (eds.), *Advances in Applied Mechanical Engineering*,  
Lecture Notes in Mechanical Engineering,  
[https://doi.org/10.1007/978-981-15-1201-8\\_110](https://doi.org/10.1007/978-981-15-1201-8_110)

1031

use coupling agents in order to improve the adhesion between fiber and matrix [2]. This good ecological friendly feature makes the materials exceptionally mainstream in building markets, like automobile and construction development industry [3]. The fusion of natural fibers with glass fiber increases its mechanical properties, and these composites can be utilized for medium-strength applications [4]. Shadrach Jeyasekaran et al. [5] studied the tensile properties of unidirectional banana and glass fiber-reinforced epoxy composites and compared the results with single-reinforced composite in both experimental and numerical analysis tests. From the test results, it is found that unidirectional glass fiber-reinforced composite possesses higher tensile strength 567 MPa than the unidirectional banana-glass-reinforced composites. Sanjay et al. [6] presented the mechanical and physical properties of banana and E-glass fabrics-reinforced polyester hybrid composites. In this, different compositions of banana and E-glass fabric laminates are fabricated by using hand layup and vacuum bagging methods. The testing of composite specimens is performed according to the ASTM standards. From the test results, it is observed that the higher tensile strength, flexural strength, impact strength, and hardness values are found in glass fabric laminate, while it is low for banana fabric laminate. Devireddy et al. [7] presented the physical and mechanical properties of unidirectional banana/jute fiber-reinforced epoxy-based hybrid composites and compared it with the single natural fiber-reinforced composites. Ramesh et al. [8] investigated the processing and mechanical evaluation of banana fiber reinforced with epoxy-based composites. In the present work, unidirectional banana/glass fiber hybrid composites are fabricated and evaluated the mechanical properties of laminates such as tensile strength, flexural strength, and impact strength of different stacking sequences of unidirectional banana and glass fabrics.

## 2 Experimental Details

### 2.1 Materials

The materials which are used in the fabrication process is unidirectional banana fabric, unidirectional E-glass fabric, epoxy resin LY556, hardener HY951, acetone, wax, and the transparent sheet. The unidirectional banana fabric is purchased in the form of Mats from Go Green Products Private Ltd. from Chennai, India. The unidirectional E-glass fabric, epoxy resin, hardener, and acetone are bought from a local retailer in Hyderabad.

**Table 1** Stacking sequence of laminates

Laminates	Composition of fiber (%)		Stacking sequence
	Banana (B)	Glass (G)	
L-1	0	100	G + G+G + G+G
L-2	20	80	G + G+B + G+G
L-3	40	60	G + B+G + B+G
L-4	60	40	B + G+B + G+B
L-5	80	20	B + B+G + B+B
L-6	100	0	B + B+B + B+B

## 2.2 Preparation of Composite Laminates

In this preparation process, the hand layup method is adopted for the fabrication of composite laminates [7]. Before to start the process, the mold of dimensions 365 mm × 365 mm has to be cleaned with acetone in order to remove impurities present on the mold surface. Then the transparent sheet is placed over the mold surface, and wax is applied to it for easy removal of laminates from the mold. The unidirectional banana and unidirectional E-glass fibers are cut according to the mold dimensions. The epoxy resin LY556 and hardener HY951 are mixed in the proportion of 10:1 and mix thoroughly with the help of mechanical stirrer. For every laminate, the different combinations of banana and E-glass fabric laminates are fabricated to obtain the required thickness of the laminates and subjected to post-curing at room temperature for 24 h. The laminates named as L-1, L-2, L-3, L-4, L-5, and L-6. The detailed composition and designations are given in Table 1.

## 3 Mechanical Testing

### 3.1 Tensile Strength

In the present study, the tensile test is performed on flat specimens using ASTM D 3039 [9]. The dimensions of the composite specimen as per ASTM standard are 250 mm × 25 mm × 3 mm for longitudinal direction. The tensile test is performed in computerized UTM of model Instron 1195 at a crosshead speed of 10 mm/min, and the results were used to calculate the tensile strength of the composite samples. For each composite type, three identical specimens were tested and the mean value is reported as the property of that composite.

### ***3.2 Flexural Strength***

The flexural test was carried out on rectangular specimens of composite samples using UTM of model Instron 1195 according to the procedure described in ASTM D 790 [10]. The dimensions of the composite specimen as per ASTM standard are 125 mm × 13 mm × 3 mm for longitudinal direction. The test was conducted using the load cell of 25 kN at 10 mm/min rate of loading. For each composite type, three identical specimens were tested and the mean value is reported as the property of that composite.

### ***3.3 Impact Strength***

The impact test was carried out on rectangular flat specimens. The standard for impact properties of fiber-reinforced composites has the designation ASTM D 256 [11]. The dimensions of the specimen are 100 mm × 10 mm × 3 mm for longitudinal direction. In the present work, the impact test conducted was Charpy impact test the specimen with a pendulum hammer, measuring the spent energy and relating it to the cross section of the specimen. For each composite type, three identical specimens were tested and the mean value is reported as the property of that composite.

## **4 Results and Discussion**

In this preliminary study, natural fibers like banana fiber are reinforced with synthetic fiber like E-glass fiber with epoxy resin, i.e., two different fibers act as the reinforcement material in the preparation of the hybrid composites. Their mechanical properties like ultimate tensile strength, flexural strength, and impact strength were evaluated. Experimental results are summarized in the charts.

### ***4.1 Tensile Strength Analysis***

The ultimate tensile strength and ultimate tensile load of unidirectional banana–glass fiber reinforced with varying wt% combination of the hybrid composite were studied here, and its failure mode is shown in Fig. 1. The comparative bar graph charts for ultimate tensile strength of different laminates are presented in Fig. 3. Among all six laminates, the average ultimate tensile strength of the laminate L-1 is noted as 510 MPa with average ultimate tensile load 61 kN and average ultimate tensile strength laminate L-6 is noted as 55 MPa with average ultimate tensile load 6 kN.



**Fig. 1** Tensile test specimen failure mode



**Fig. 2** Flexural test specimen failure mode

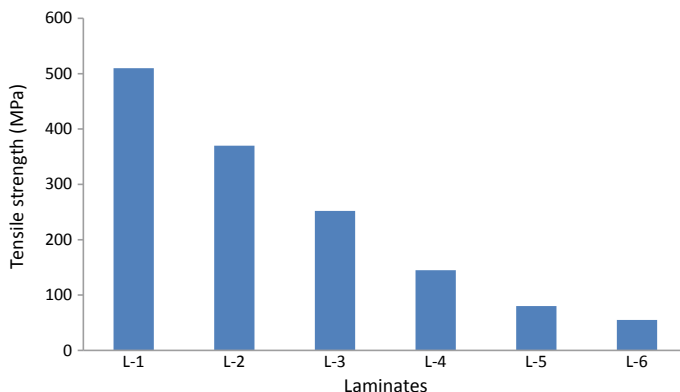


**Fig. 3** Ultimate tensile strength comparison chart

From this set of results, tensile strength values are obtained when the natural banana fiber is hybridized with glass fiber and a moderate strength is observed.

### 4.2 Flexural Strength Analysis

The flexural strength of unidirectional banana–glass fiber-reinforced epoxy hybrid composites was studied here, and its failure mode is shown in Fig. 2. The comparative charts for flexural strength of different laminates are presented in Fig. 4. Among all six laminates, the average flexural strength of the laminate L-1 is noted as 168 MPa and average flexural strength laminate L-6 is noted as 31 MPa. From this set of



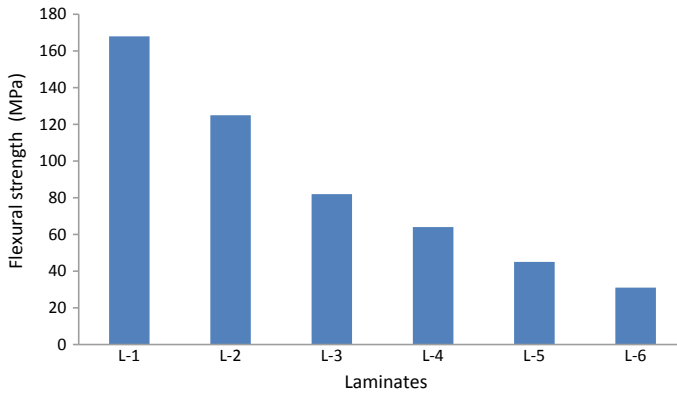


**Fig. 4** Flexural strength comparison chart

flexural values obtained when the natural banana fiber is hybridized with glass fiber a moderate strength is observed (Fig. 3).

### 4.3 Impact Strength Analysis

The impact strength and energy absorbed of banana–glass fiber-reinforced hybrid composite were studied here. Hybridization of banana with glass plays a major role in the impact strength. The comparative charts for impact strength of laminates are presented in Fig. 5. Among all six laminates, the average impact strength of the laminate L-1 is noted as  $0.222 \text{ J/mm}^2$  and average impact strength of the laminate L-6 is noted as  $0.04 \text{ J/mm}^2$ . The impact strength of the samples decreases linearly with the increase in banana fiber content. The impact strength of a composite is influenced by

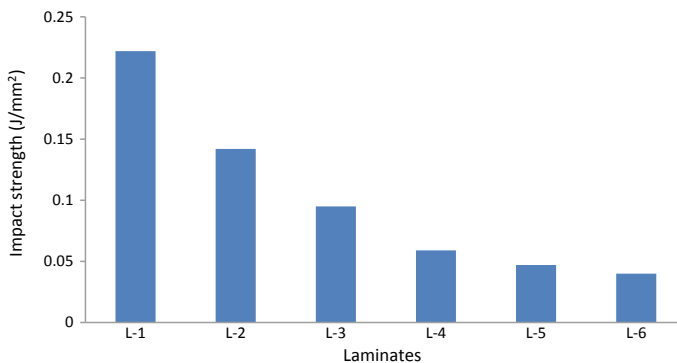


**Fig. 5** Impact strength comparison chart

many factors including the matrix-fracture, fiber/matrix debonding, and fiber pullout. Frictional losses due to fiber pullout are the major cause for enhancement of impact strength in increased glass fiber content in the hybrid composite. With increasing glass fiber reinforcement in the banana/glass hybrid composite, frictional losses as the fiber is pulled out of the matrix might be a major contributor to the observed increase in impact strength of the hybrid samples.

## 5 Conclusions

The unidirectional banana–glass fiber-reinforced epoxy-based hybrid composites were fabricated by simple hand layup technique. It is found that as the glass layer in the laminates increases, its mechanical properties enhance. When the natural fiber is hybridized with glass fiber, a moderate strength is observed in the composites. These hybrid composites can be used for medium load-bearing applications.

The unidirectional glass fiber composite possesses higher ultimate tensile strength among all the laminates and can withstand at the ultimate tensile strength of 510 MPa at load 61 kN. The unidirectional banana composite possesses a lower ultimate tensile strength of 55 MPa at a load of 6 kN. From the flexural test results, it is shown that laminate L-1 has a higher flexural strength 168 MPa and laminate L-6 has the lowest flexural strength 31 MPa. From the Charpy impact test results, it is noticed that the impact strength is high for the laminate L-1 of  $0.222 \text{ J/mm}^2$ , while it is low for the laminate L-6 of  $0.04 \text{ J/mm}^2$ .

**Acknowledgements** This research is funded by VNR Vignana Jyothi Institute of Engineering and Technology.

## References

1. Sathishkumar TP, Naveen J, Satheeshkumar S (2014) Hybrid fiber reinforced polymer composites—a review. *J Reinf Plast Compos* 5:454–471
2. Aquino EMF, Sarmiento LPS, Oliveira W, Silva RV (2007) Moisture effect on degradation of jute/glass hybrid composites. *J Reinf Plast Compos* 26(2):219–233
3. Mohammed L, Ansari MNM, Pua G, Jawaid M, Islam MS (2015) A review on natural fiber reinforced polymer composite and its applications. *Int J Polym Sci*
4. Dixit S, Goel R, Dubey A, Shivare PR, Bhalavi T (2017) Natural fiber reinforced polymer composite materials—a review. *Polym Renew Res* 2:71–78
5. Shadrach Jeyasekaran A, Palanikumar K, Rajarajan S (2016) Numerical and experimental analysis on tensile properties of banana and glass fibers reinforced epoxy composites. *Indian Acad Sci* 41(11):1357–1367
6. Sanjay MR, Arpitha GR, Laxmana L (2016) Studies on mechanical properties of banana/e-glass fabric reinforced polyester composites. *J Mater Environ Sci* 7:3179–3192
7. Devireddy SB, Biswas S (2016) Physical and mechanical behaviour of unidirectional banana/jute fiber reinforced epoxy based hybrid composites. *J Reinf Plast Compos* 35:1157–1172

8. Ramesh M, Sri AnandaAtreya T, Aswin US, Eashwar H, Deepa C (2014) Processing and mechanical property evaluation of banana fiber reinforced polymer composites. *Procedia Eng* 97:563–572
9. ASTM D3039 (2014) Standard test method for tensile properties of polymer matrix composite materials. ASTM International, West Conshohocken, PA
10. ASTM D790 (2007) Standard test methods for flexural properties of unreinforced and reinforced plastics and electrical insulating materials. ASTM International, West Conshohocken, PA
11. ASTM D256 (2006) Standard test methods for determining the impact resistance of plastics. ASTM International, West Conshohocken, PA

# Experimental Investigation of Ultrasonic Flaw Defects in Weld Clad Materials Using NDT Technique



P. Ravindra Kumar, G. Vijay Kumar, K. Naga Murali  
and R. B. S. S. Kishore

**Abstract** Automated ultrasonic testing method will be used in the many industries to locate discontinuities and to detect internal defects under test inside the workpiece material. The lowest defect size in weld material may start from 0.5 mm onwards. Ultrasonic testing is a fast and automated method, because the signals are available in electronic form to be tested in plates and pipes. This is mainly used for whether the material will be accepted or rejected easily based on internal cracks. “Modsonic Einstein II TFT (MODSONIC)” software package has been extensively using in many industries to find flaws and cracks. The objective of the work is to find the flaws in various materials like mild steel (M.S) plate clad with mild steel (M.S) electrode, mild steel plate clad with brass electrode, mild steel plate clad with stainless steel electrode, mild steel pipe clad with mild steel electrode. To detect the flaws at various angles, the probes are placed at 45°, 60° and 70°. When the size of the weld plate is less than 25 mm, then it will be preferable to use and find flaws in materials with 70° probe angle. With MODSONIC software package, it is found that mild steel pipe welded with mild steel electrode highlighted more internal flaws at 70° probe angle from experimental analysis.

**Keywords** Ultrasonic testing (UT) · Flaw detector machine · Probes · Weld clad materials · Distance amplitude curves (DAC) and MODSONIC software

---

P. Ravindra Kumar (✉) · G. Vijay Kumar · K. Naga Murali · R. B. S. S. Kishore  
Department of Mechanical Engineering, Lakireddy Bali Reddy College of Engineering,  
Mylavaram, Andhra Pradesh 521456, India  
e-mail: [pasupuletirk@gmail.com](mailto:pasupuletirk@gmail.com)

G. Vijay Kumar  
e-mail: [vijay@futurendt.com](mailto:vijay@futurendt.com)

K. Naga Murali  
e-mail: [nagamurali19957@gmail.com](mailto:nagamurali19957@gmail.com)

R. B. S. S. Kishore  
e-mail: [rbskishore@gmail.com](mailto:rbskishore@gmail.com)

© Springer Nature Singapore Pte Ltd. 2020  
H. K. Voruganti et al. (eds.), *Advances in Applied Mechanical Engineering*,  
Lecture Notes in Mechanical Engineering,  
[https://doi.org/10.1007/978-981-15-1201-8\\_111](https://doi.org/10.1007/978-981-15-1201-8_111)

## 1 Introduction

Nondestructive testing (NDT) is an extensive and huge range collection of investigation methods utilized in fabrication and manufacturing industries to discover the defects of a weld material like minute cracks and flaws within the device components. NDT does not change the shape of article after inspection. But it is extremely valuable technique that can be applied on weld clad materials to find weld defect flaws that can save time and money in product assessment. NDT is a kind of a process to investigate various trials on estimating substances, components or assemblies for discontinuities or break-ups and variations in traits without altering the serviceability of the element or gadget. The part can be reused once again after the inspection or test is completed depending on test results. Apart from NDT, there are other destructive tests which can be applied on a limited quantity of samples in place of materials, parts or assemblies that may honestly place into the provider. The detrimental checks are regularly carried out to discover the mechanical properties of materials like impact resistance, yield electricity, ductility, ultimate tensile strength, fracture sturdiness and fatigue strength. Today NDT techniques are using in small scale to large scale industries applying in fabrication, manufacturing, job related inspections and in repaired working parts to ensure the quality of product reliability and integrity to control the flaws in weld-clad materials. This technique also reduces the production costs and maintains a uniform level in quality. NDT is used to ensure the quality of metal-clad flaws both in fabrication and production phases.

Vural et al. [1] investigated the ultrasonic testing (UT) on spot-welded different steel sheets. In this study, they have fabricated two steel sheets clad each other using resistance spot weld. The specimens and nugget diameters were tested in a special ultrasonic test apparatus designed for spot-welded sheets of AISI 304—galvanized steel sheet combination subjected to the fatigue test up to 25% stiffness drop. Any rupture or fatigue in spot-welded joints after fatigue test is found. Ammirato et al. [2] carried out the ultrasonic testing of different metal welds in boiling water reactors and pressurized water reactor vessels and highlighted the complications of ultrasonic testing of dissimilar metal welds. They have developed a conventional shear wave transducer for testing the dissimilar metal welds in the nozzle. For welds, thickness less than 38 mm and transducer frequency of 2.1 MHz have used and were successful in constantly detecting the weld fissures with pits around 22% of the metal plate thickness and more. For large thickness welds, 1 MHz transducer element is required. With larger angles of refraction, the quality flaw detection performance was received.

Bindal et al. [3] have done the work on water-centred couplant for general-purpose use for ultrasonic NDT applications. Studies show that the newly developed couplant provides 3 decibels better coupling as compared to the other conventional couplant. Engel and Geiger [4] have done work on radiographic testing and ultrasonic testing in stainless steel bead in TIG welding. Jolly et al. [5] highlighted the review of nondestructive testing strategies and its applicability to thick-walled composites of a flywheel made of carbon fibre-reinforced plastic (CFRP) thickness which is 30mm. They carried out a NDT method of computer tomography which has given better

results. Kleinert [6] explained the importance of distance amplitude curves (DAC) and distance gain size (DGS) methods in the textbook of Defect Sizing Using Non-destructive Ultrasonic Testing. Kemnitz et al. [7] reported the radiographic testing on Lockheed Missiles. Yusof and Jamaluddin [8] have highlighted the various welding defects and its associated flaws for various applications in welding industries. Wevers et al. [9] discussed new developments in NDT technology.

After thoroughly understanding the literature study on NDT techniques, authors feel a little bit gaps on lack of work carried out on ultrasonic testing on different weld clad materials using A-Scan report presentations. Hence, authors carried out work on different weld clad materials to identify the weld defect flaws present in prepared experimental samples.

## 2 Experimental Set-up of Ultrasonic Test Equipment

A distinctive ultrasonic testing equipment is shown in Fig. 1 comprise pulsar receiver (i.e generate short and large amplitude ultrasonic pulses and propagated into materials), display devices, probes and transducers. Detection of cracks in samples using oscilloscope or flaw detector screen is shown in Fig. 2. A pulse-echo testing equipment which is a part of ultrasonic equipment shown in Fig. 3 is a digital tool that may produce excessive voltage electric pulse pushed with the aid of the pulsar. The transducer generates excessive frequency ultrasonic energy.

The sound energy is introduced and propagates via the substances in the form of waves. Whilst there may be a discontinuity (collectively with a crack) in the ultrasonic

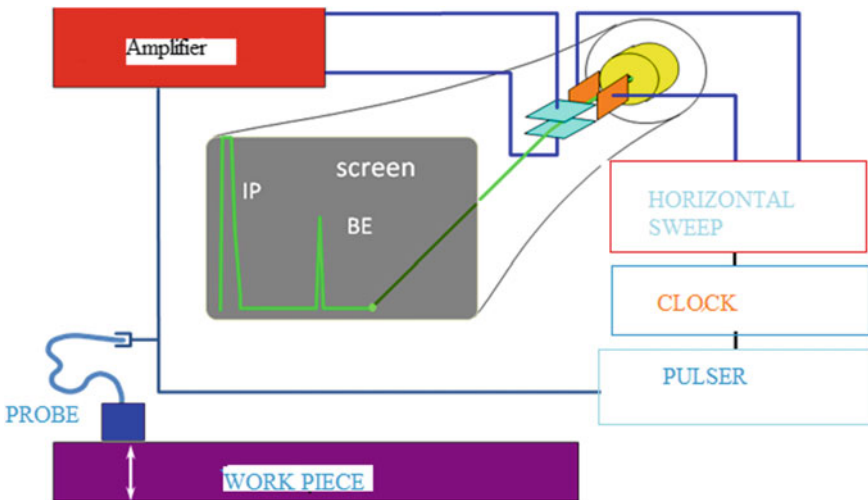


Fig. 1 Ultrasonic testing equipment

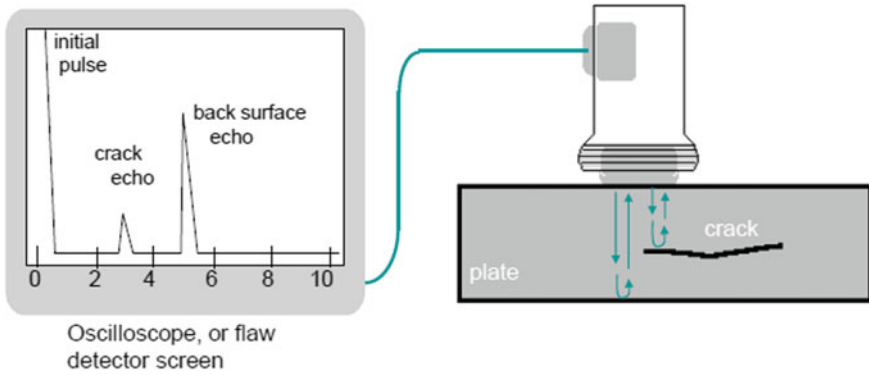


Fig. 2 Detection of cracks in samples using oscilloscope or flaw detector screen

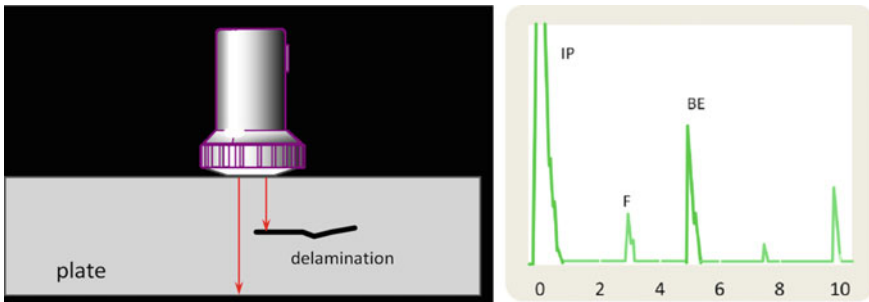


Fig. 3 Pulse-echo testing

sound course, a part of the strength may be contemplated back from the flaw surface, part of energy will be transmitted through the object and part of energy will be absorbed within the material. The reflected ultrasonic sound signal is transformed to electrical signal via transducer and showed on a display monitor called cathode ray tube (CRT). The reflected signal is displayed with respect to the time and strength (amplitude). Signal travel time can be right away related to the distance that the signal is travelled. From the signal, records approximately the discontinuity region, period, orientation and one of a kind capabilities can once in a while be received.

The main advantage of pulse-echo testing shows the depth of defect and can observe the sound beam path on range scale ( $X$ -axis). The time dimension starts with the electrical transmission pulse and the initial pulse (IP); this is an exceedingly brief electric discharge which triggers a legitimate pulse at the probe crystal. This pulse travels through the weld material and is reflected by using way of a discontinuity or the opposing wall and returns back to the probe. The received oscillations are transformed into an electrical pulse which stops the time limit.

To examine the echoes at the display monitor, there is a grid at the inside of the cathode ray tube. The scale attached which is exchangeable has a horizontal scale

with 10 graduations, shown in Fig. 3 called the display scale. High-frequency sound waves are introduced into a material, and they may be reflected back once again from surface defect flaws. The reflected sound energy is displayed on timescale, and the inspector can visualize a specimen showing the intensity of functions that reflects the sound.

### 2.1 Experimental Procedure

Butt welds may be of entire penetration or incomplete penetration depending upon whether the penetration is complete or incomplete through the metal thickness. Commonly, a description of welded joints requires a demonstration of the type of each the joint and the weld. ASME B16.5, B16.9, B16.25 and B16.34 cover the instruction of butt welding of plate and pipe components to be joined through welding [10]. It includes necessities for welding bevels, for external and internal shaping of heavy wall thickness of metals. In butt welding, the specimens to be connected ought to match perfectly and may be protected up for welding. In addition, butt welding requires the shaping of the surfaces to be joined. Full penetration butt welds are customary, whilst the components are connected collectively within the thickness of the parent metal.

Welds are also categorized in keeping their function into flat, horizontal, vertical and overhead. Flat welds are least expensive to make, whilst overhead welds are the most hard and highly priced (Fig. 4).

Based on the experimentation, the following parameters are considered in the specimen preparation which is shown in Table 1.

For this test, the struts used to support the work at frequency of five MHz. Echo techniques could be employed to discover the cracks. Tool can be tuned to a frequency of five MHz. The best couplant used ought to have corrosion, or a different damage may appear. Within the route of the inspection, a test specimen could be employed and the calibration may be executed at the standard reference, if one wishes to take the readings. The amount of couplant must be adequate in the transducer section areas of fitting. The show is probably monitored for crack indicators.

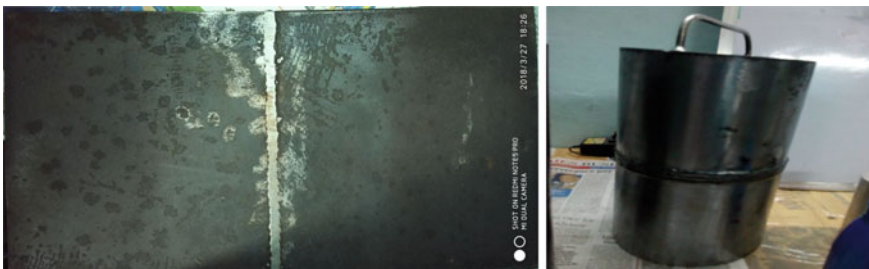


Fig. 4 Samples of prepared test plate and pipe specimen



**Table 1** Fixed and variable parameters of welding

Fixed parameters	Variable parameters
Electrode size = 4 mm, length = 450 mm	Welding current = 120–160 A for M.S. plate = 80–110 A for S. S. plate = 50–240 A for Brass = 120–220 A for M.S. pipes
Polarity = DC reverse polarity (DCEP)	Welding voltage = 20 V for Mild Steel plate = 21 V for Stainless Steel = 18 V for Brass = 23 V for Mild Steel pipes
Electrode work angle 45° between two pieces of metal	Welding speed = 105–110 mm/min for M.S. Plate = 115–125 mm/min for S.S. Plate = 85–90 mm/min for Brass = 65–75 mm/min for M.S. pipes
Metal thickness = 25 mm	

The following steps must be applied during the experiment to identify crack signals.

**Step 1:** Adequate quantity of couplant is to be applied at the location where inspection is being carried out.

**Step 2:** For the round specimens, the struts can be positioned within the corresponding place inside the device. Sufficient couplant is to be applied at the tool and on probe.

**Step 3:** For the flat specimens, no device is needed; however, couplant has to be quality carried out between the inspected floor and the probe.

**Step 4:** A distinctive attention should be paid on the vicinity, wherein feasible cracks exist.

**Step 5:** A break-up like a crack produces a height on the display monitor.

**Step 6:** Care should be given to take delivery of motion of the viable top caused by the cracks at the specimen.

## 2.2 *Mathematical Formulations*

Acoustic impedance ( $Z$ ) of a material is the product of density ( $\rho$ ) and acoustic velocity ( $V$ ) and can be found for the given workpiece material.

$$Z = \rho * V \quad (1)$$

The acoustic impedance is vital within the determination of acoustic transmission and reflection at the boundary of workpiece substances having unique acoustic

impedance, inside the layout of ultrasonic transducers, in assessing the absorption of sound in a medium.

The reflector space can now be calculated as from the below given correlation:

$$S = \frac{CT}{2} \tag{2}$$

- $S$  = sound path [mm]
- $C$  = sound velocity [km/s]
- $T$  = time of flight [ms].

Reflection is how much sound energy coming back whilst hitting an interface.

Transmission is how much energy transmitted from one medium to another medium.

The impedance mismatch ( $Z$ ) can be stated as ultrasonic wave's reflection at the boundaries, where there may be a distinction in acoustic impedance of the material on each side of the boundary.

$$R = ((Z_2 - Z_1)/(Z_2 + Z_1)) \tag{3}$$

Percentage of transmission coefficient is determined by

$$Tr = (1 - R) \tag{4}$$

where

- $Z_1, Z_2$  are impedances of different materials,  $R$  = parentage of reflection coefficient
- $T$  = percentage of transmission coefficient,  $p$  = density of material
- $V$  = sound velocity in that material.

**Relation Between Time Period ( $t$ ) and frequency ( $f$ )**

For cyclical techniques, along with rotation, oscillations, or waves, frequency is defined as some of the cycles in line with unit time. The duration, usually denoted by  $T$ , is the time frame taken via one cycle and is the reciprocal of the frequency  $f$ .

$$T = \frac{1}{f} \tag{5}$$

**Relation Between Wave Velocity, Frequency and Wavelength**

The relation between wave velocity ( $V$ ), wavelength ( $\lambda$ ) and frequency ( $f$ ) can be stated as

$$V = f * \lambda \tag{6}$$

Wave velocity is defined as the distance travelled by the wave in one second.

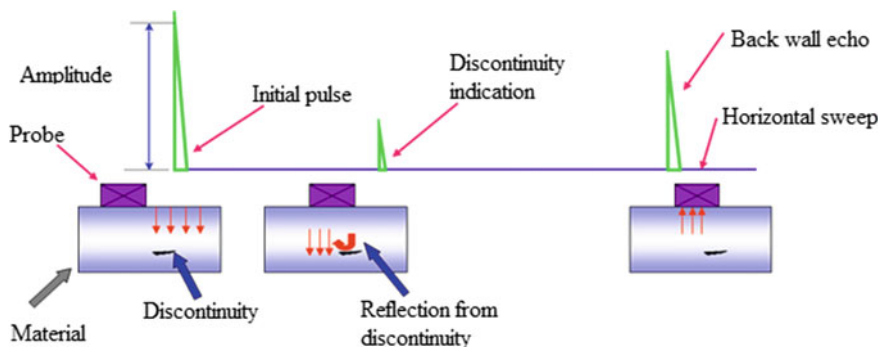


Fig. 5 A-scan presentation

$$\text{Wave velocity} = \frac{\text{Distance travelled by one wave}}{\text{Time taken by one wave}} \tag{7}$$

or

$$\text{Wave velocity} = \text{Wavelength} \times \text{frequency}$$

Exhaustive instructions for operation of individual samples can be obtained from the operation and maintenance guide for the specific instrument being tested. The amount of energy received from ultrasonic machine is a function of time with A-scan presentation shown in Fig. 5.

The amount of energy received is plotted on Y-axis, and the elapsed time is displayed on X-axis. The display monitor with A-scan will permit the sign to be showed in its natural frequency shape and completely rectified into a radio frequency signal or as half of both the positive and negative radio frequency signal. Ultrasonic flaw detector system is shown in Fig. 6 and angle beam transducer is shown in Fig. 7.

### 3 Results and Discussions

A-Scan display indicates the distance amplitude correction (DAC) shows a method of establishing a graphic “Reference-Level Sensitivity” as a function of sweep distance. DAC allows the signals to be reflected from break-up areas, wherein the signal attenuation as a characteristic of intensity has been associated. A-Scan display monitor moreover indicates the DAC to permit for loss in amplitude over a specimen depth (time), electronically by using positive devices graphically. The near area period and beam unfold may range in step with the transducer size, speed, frequency and substances’ attenuation. For every state of affairs, DAC curve has to be mounted. It could be employed in shear and longitudinal modes of operation.



Fig. 6 Ultrasonic flaw detector machine

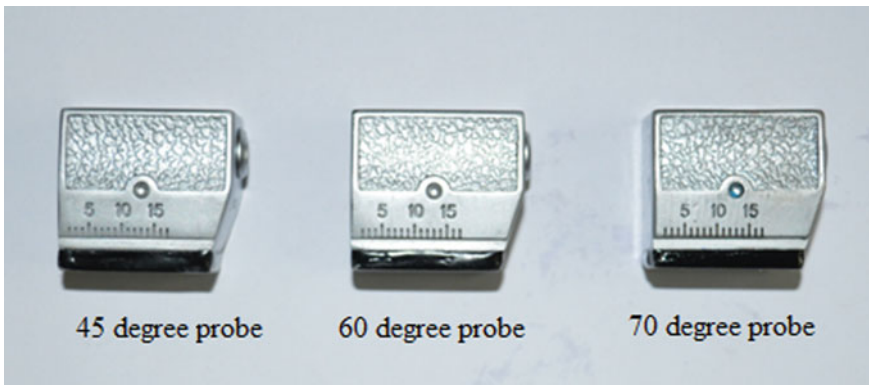
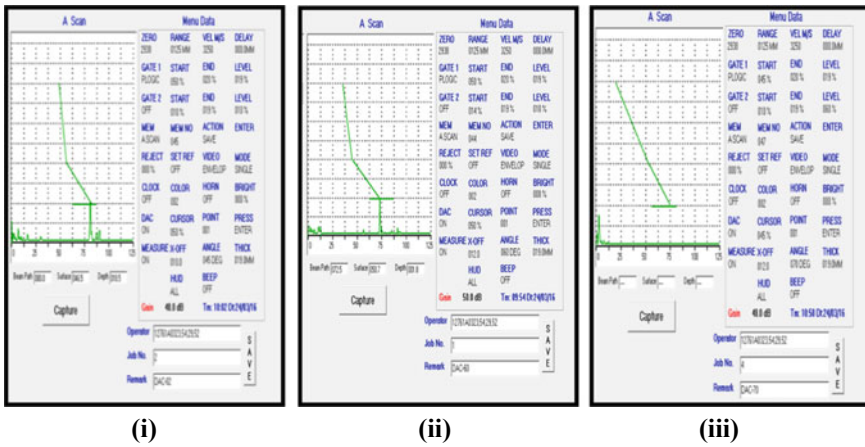


Fig. 7 Angle beam transducer

Distance amplitude correction curves of probes of 45°, 60° and 70° are shown in Fig. 8. But DAC curve probes are available at various angles. The main aim of the above figures is to find flaws in the curve region and to draw the curve by using the side-drilled block hole. The above figures are mainly used to find the welding defects and flaws above and below 25-mm plate or pipe.

Weld defect is present in the prepared specimen at a distance of 14.7 mm depth and at a sub-surface distance of 27.4 mm as shown in Fig. 9. This type of defect is identified as lack of penetration, and the reason is due to the too large weld puddle and the travel speed is too low. The other side of Fig. 9 presents welding defect at a depth of 15.1 mm and at a sub-surface distance of 39.1 mm. The type of defect is due to lack of penetration and porosity due to poor welding technique.



**Fig. 8** Distance amplitude correction curves of A-scan presentation with different probes. **a** 45° probe, **b** 60° probe, **c** 70° probe

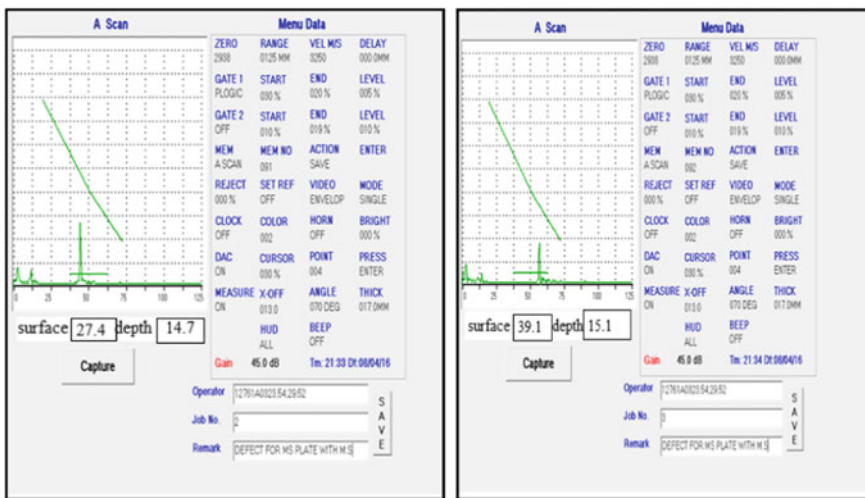


**Fig. 9** Defects in mild steel plate clad with mild steel electrode at different surface distances and depths

Welding defect is present in M.S plate clad with S.S. electrode as shown in Fig. 10. This indicates that the flaw at 8.8 mm depth and at sub-surface distance of 28.8 mm. The type of defect is identified as porosity, the reason for this defect is the absorption of some gases in the molten weld pool, and these gases are released on solidification. The other side of Fig. 10 shows welding defect at a distance of 1 mm depth and at sub-surface distance of 35.4 mm. The type of defect is classified as crack, the reason is base metal contamination, and preheating is not done before welding is started.

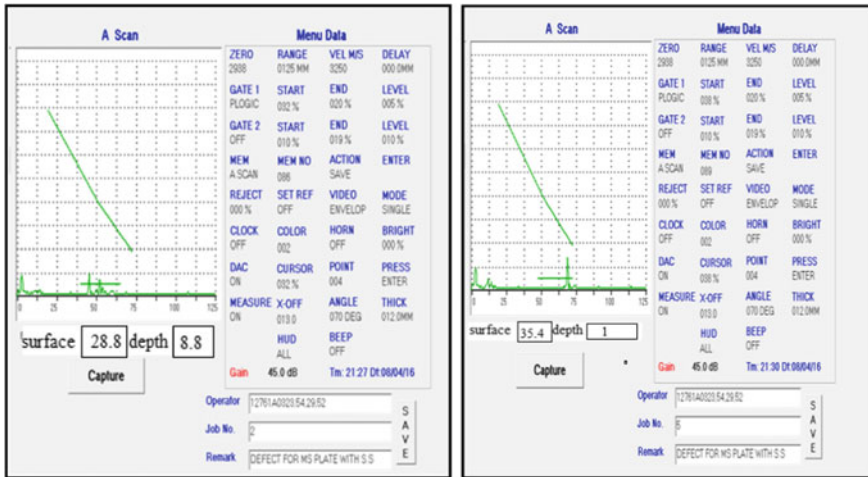


Fig. 10 Defects in mild steel plate clad with stainless steel electrode

Figure 11 represents a welding defect of M.S. plate clad with brass electrode which shows crack defect present at 18.6 mm depth and at a surface distance of 38.6 mm. The type of defect is detected as crack, and this is occurred due to residual stress caused by the solidification shrinkage. The side figure also presents the welding defect in 20.5 mm depth and at a surface distance of 43.3 mm. The type of defect is identified as lack of penetration and this occurred due to both sides' root regions of the joint infused.

Flaws present in M.S. pipe clad with M.S electrode is shown in Fig. 12 identified a welding defect at a 12.6 mm depth at sub surface distance of 34.9 mm for the

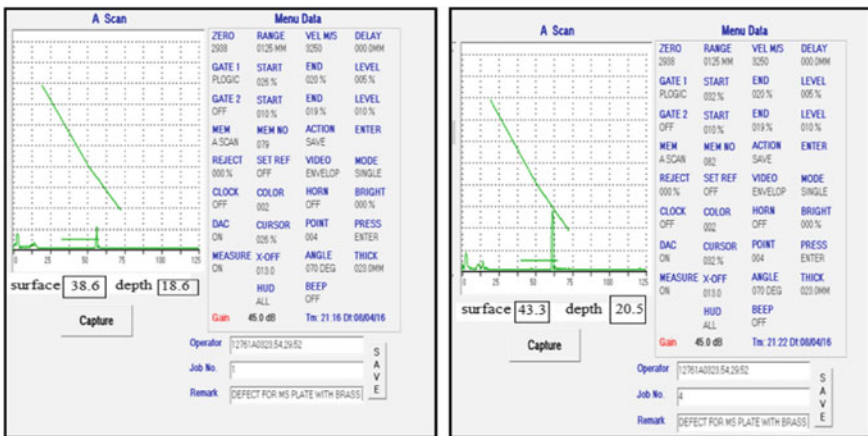


Fig. 11 Defects in mild steel plate clad with brass electrode

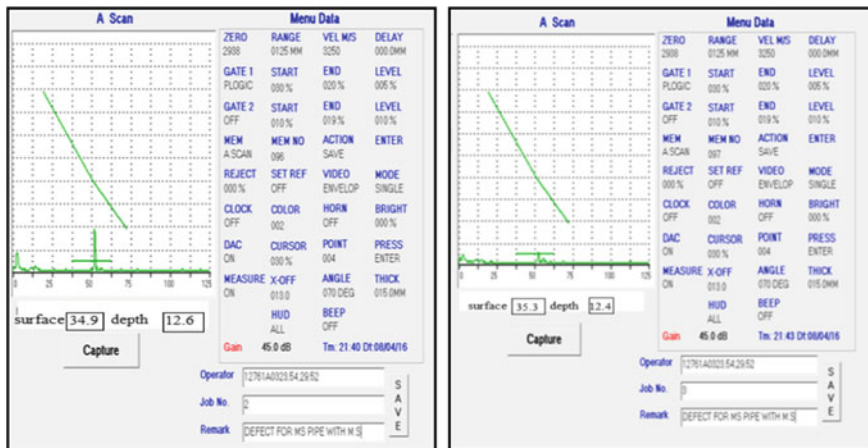


Fig. 12 Defect flaw present in mild steel pipe clad with mild steel electrode

prepared sample specimen. The type of defect flaw identified as lack of penetration due to wide melting range. The side figure shows welding defect in 12.4 mm depth and at a surface distance of 35.3 mm. The type of defect identified is porosity due to the presence of contaminants on the job surface and trapped moisture between joining surfaces.

### 4 Conclusions

In both the government and private sectors, especially in irrigation sector, welding is extensively used in the fabrication, maintenance and repair of structural parts. To ensure its quality, the welding should be flawless. Ultrasonic testing is conducted to locate discontinuities within the material under test and often used to detect internal defects by using the “MODSONIC software”. Ultrasonic testing can easily be computerized, because it is a fast method, and the signals are available in electronic form.

1. After studying the various inspections and testing techniques used in welding, it is found that NDT is very important tool used in the modern industries especially in the design of pressure vessels, welding of pipelines in the irrigation sector. Out of all NDT methods, to detect the welding defect flaws in metals, it is found that ultrasonic testing is more economical and less time-consuming.
2. Using different types of transducer degree probes like 45°, 60° and 70° are mainly used to draw the distance amplitude curves to find the welding defect flaws within the metals.
3. Ultrasonic testing is conducted on four different specimens. Those are M.S plate welded with M.S. electrode, M.S. plate welded with stainless steel electrode,

M.S. plate welded with brass electrode, M.S. pipe welded with M.S. electrode. It can be concluded that M.S pipe welded with M.S. electrode highlighted more internal flaws at 70° probe angle from the experimental results.

4. It was also found that M.S plate clad with stainless steel electrode got good welding joint with minor errors.
5. The specific characteristic of ultrasonic testing is used to find the position, size, type of defect and sub-surface cracks which can be detected instantly.
6. Ultrasonic testing is more suitable to detect sub-surface cracks and flaws, internal flaws and discontinuities, non-metallic inclusions like slag and porosity and for laminated composite materials for ferrous welds, steel and iron castings.

**Acknowledgements** Authors would like to acknowledge Mr. G. Vijay Kumar, Managing Director, The Future NDT Pvt. Ltd. helped to carry out the importance of work in manufacturing and fabrication Industries.

## References

1. Vural M, Akkus A (2004) On the resistance spot weldability of galvanized interstitial free steel sheets with austenitic stainless steel sheets. *J Mater Process Technol* 153–154C:1–6
2. Ammirato F, Shankar R, Edelmann X (1988) Ultrasonic examination of dissimilar-metal welds in BWR and PWR plants. *Int J Press Vessels Pip* 35(1–4):37–56
3. Bindal VN (1999) Transducer for ultrasonic flaw detector. Narosa publishing House, New Delhi, pp 180–196
4. Stancu-Niederhorn S, Engel U, Geiger M (1996) Ultrasonic investigation of friction mechanism in metal forming. *J Mater Process Technol* 45(1–4)
5. Jolly MR, Prabhakar B, Sturzu K, Hollstein R, Singh S, Thomas Foote P, Shaw A (2015) Review of non destructive testing techniques and their applicability to thick walled composites. *CIRP Procedia* 38:129–136
6. Kleinert W (2016) Defect sizing using nondestructive ultrasonic testing. Lecture notes in mechanical engineering. Springer International Publishing, Switzerland, pp 7–19. <https://www.springer.com/gp/book/9783319328348>. [https://doi.org/10.1007/978-3-319-32836-2\\_2](https://doi.org/10.1007/978-3-319-32836-2_2)
7. Kemnitz P, Richter U, Klüber H (1997) Measurements of the acoustic field on austenitic welds: a way to higher reliability in ultrasonic tests. *Nucl Eng Design* 174(3):259–272
8. Yusof F, Jamaluddin MF (2014) Welding defects and implications on welded assemblies. *Compr Mater Process* 6:125–134. <https://doi.org/10.1016/B978-0-08-096532-1.00605-1>
9. Wevers M, Meester De P, Devolder S, Stoffels A (2010) New developments in NDT techniques. In: 10th ECNDT, Moscow, 7–11 June 2010
10. Lampan SR, Theodore ZB (2015) Nondestructive evaluation and quality control. In: *Metals handbook*, 9th edn, vol 17. ASM International Handbook Committee, New York



# An Effective and Economical Method to Improve Structural Homogeneity and Mechanical Properties of Al–Mg Alloy Processed by ECAE



Ananda Babu Varadala, Swami Naidu Gurugubelli and Sateesh Bandaru

**Abstract** The formation of the dead metal zone (DMZ) in equal channel angular extrusion (ECAE) process significantly affects the deformation uniformity and mechanical properties of work material. The aim of the present study is to investigate the effect of the dead metal zone on structural homogeneity and hardness of Al 5083 alloy processed by ECAE and suggest the way to minimize that adverse effect. In this work, the rectangular billets with 1-mm-thick copper casing on two longitudinal faces and square billets with no casing are processed by ECAE up to four passes in route A. It was observed that the soft and ductile nature of the copper casing allows smooth flow of the work material at low pressing loads as compared to the alloy ECAE'd without a casing. Field emission scanning electron microscope (FESEM) images of the processed material with casing show the noteworthy improvement in structural homogeneity and grain refinement than another set of billets. The obtained structural homogeneity indicates the uniform strain distribution in the processed material is achieved by minimizing the formation of the dead metal zone at the intersection of ECAE die channels. The higher hardness and tensile strength measurements of the processed materials indicate the significance of grain refinement and uniform strain distribution. The variations in the test results confirm the non-homogeneous strain distribution caused by the dead metal zone is high for the billets processed with no copper casing.

**Keywords** ECAE · DMZ · Casing · Structural homogeneity · Hardness · Strength

---

A. B. Varadala (✉)

Mechanical Engineering, Vignan's Institute of Engineering for Women, Visakhapatnam, Andhra Pradesh 530049, India  
e-mail: [varadalaanand@gmail.com](mailto:varadalaanand@gmail.com)

S. N. Gurugubelli

Metallurgical Engineering, JNTUK-UCEV, Vizianagaram, Andhra Pradesh 535003, India

S. Bandaru

Mechanical Engineering, Vignan's Institute of Information Technology, Visakhapatnam, Andhra Pradesh 530049, India

© Springer Nature Singapore Pte Ltd. 2020

H. K. Voruganti et al. (eds.), *Advances in Applied Mechanical Engineering*,

Lecture Notes in Mechanical Engineering,

[https://doi.org/10.1007/978-981-15-1201-8\\_112](https://doi.org/10.1007/978-981-15-1201-8_112)

## 1 Introduction

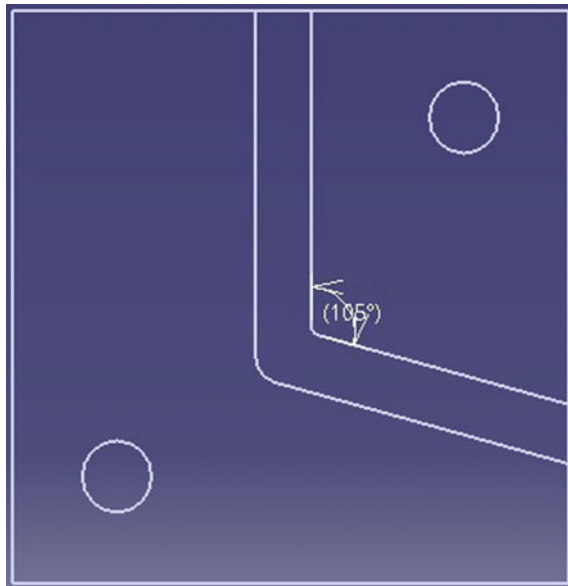
ECAE is the widely used severe plastic deformation (SPD) method in which a high amount of strain is induced in the work material with no cross-sectional changes [1]. The work material experiences the severe strain while passing through the intersection of the channels of ECAE die and forms the ultrafine grain (UFG) structure which improves the strength and hardness as per the Hall–Petch equation [2]. The amount of effective strain and the deformation patterns of the processed material mostly depend on the selection of die geometry and operational parameters [3]. The ECAE die geometry consists of the channel angle ( $\Phi$ ), outer corner angle ( $\Psi$ ), corner radii and the type of cross section of the channels [4]. The processing route, temperature, coefficient of friction and number of passes are the important operational parameters of the ECAE process [4]. Out of all, the channel angle, outer corner angle, corner radius and a frictional coefficient between work material and the channel walls are the significant parameters which influence the formation of the dead metal zone at the intersection of channels [5]. Eivani and Karimi Taheri have studied the effect of DMZ on strain and required forming force in ECAE and they found that the chances of dead zone formation increase with increasing the friction between the die walls and the billets and by decreasing channel angles. They also found that the amount of required extrusion force increases with increasing the friction coefficient [5]. Balasundar et al. performed numerical and physical modelling of ECAE using die channel angle  $90^\circ$ , outer corner angles  $30^\circ$  and outer corner radius ranging from 1 to 5 mm. They noticed that no corner angle and a high coefficient of friction causes the sticking of metal to the lower surfaces of the channels and forms the dead metal zone. They reported that by providing low corner angles and less friction coefficient, there may be a chance of reducing the formation of the dead zone and increases the uniform strain distribution [6]. Ferrasse et al. reported that even with the smooth flow and pointed corners, the DMZ exists. In their opinion, this effect can be reduced by using a movable bottom wall [7]. Hasani et al. studied the deformation field variations in ECAE'd AA 6061 with backpressure and they expressed that the backpressure increases the swelling of the sample and required pressing force which leads to the formation of the dead metal zone [8]. Djavanroodi et al. conducted the finite element analysis to identify the effect of the ultrasonic-assisted ECAP on the required forming force at different vibration amplitudes, billet lengths, friction factors and channel angles. They reported that the decrease of a load was observed by using ultrasonic vibrations, larger billet lengths, more friction factor and die channel angles in the range of  $65^\circ$ – $135^\circ$  [9].

In the present study, the authors are attempted to introduce the concept of casing/shielding to minimize the DMZ in ECAE process in an inexpensive way. The copper sheets with 1 mm thickness were considered as a casing to the work material in view of less frictional coefficient between sliding components of copper and die steel.

## 2 Experimental Methods

Al–Mg alloy with 4.5%Mg is selected as a feedstock in the present study. The square billets of 16 mm × 16 mm and rectangular billets of 16 mm × 14 mm were prepared from the rolled slab. The longitudinal faces of the billets were well polished before ECAE to accelerate the smooth flow when they are pressed through die channels. Due to the more formability nature and having a low frictional coefficient between the sliding parts of the copper and steel [10], 1-mm-thick copper sheets were considered as a casing to the rectangular billets. The feedstock and copper casings were heat treated for 1 h at 530 °C and 400 °C, respectively. The die geometry used in this work as shown in Fig. 1 is used in this study. MoS<sub>2</sub> lubricant is applied to the sliding elements before every pass to reduce the rubbing forces. The rectangular billets with 1-mm-thick copper casing and square billets with no casing were extruded as shown in Fig. 2, in route A (without any rotation about its axis) up to four times at a speed of 2 mm/s. The cumulative strain of 3.452 induced in the extruded material for the considered angles. After the ECAE, the billets were sectioned across the longitudinal direction and polished as per the standard specimen preparation procedures. The structural analysis of the billets before and after ECAE is performed by the field emission scanning electron microscope (FESEM). To observe the improvement in the properties of the processed material with ultrafine grain structure, the Vickers microhardness tester was used. The hardness tests were conducted at 200 g load and for a dwell period of 15 s. The tensile tests are also performed on the specimens prepared from processed material along the longitudinal direction as per ASTM E8M at room temperature.

**Fig. 1** Schematic of ECAE die



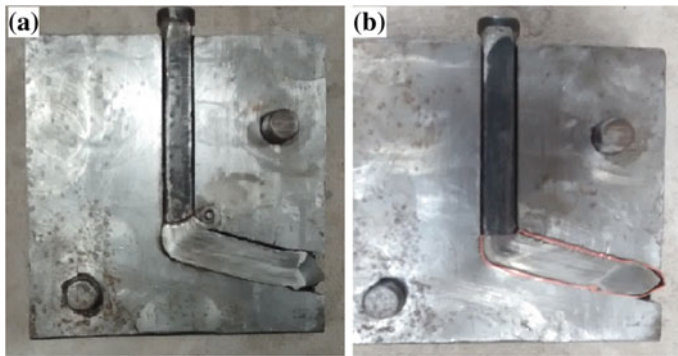


**Fig. 2** ECAE of Al-Mg alloy **a** with no casing, **b** with casing

### 3 Results and Discussions

#### 3.1 Forming Force

The requirement of forming forces in ECAE of Al-Mg alloy with and without casing is shown in Fig. 3. It is noticed that the alloy ECAE'd without casing required more force than the alloy covered with copper casing in view of high rubbing forces between the sliding elements even with the sufficient lubrication provided.

A noteworthy reduction in required forming force is observed for the billets extruded with copper casing due to less coefficient of friction between sliding parts, i.e. copper sheet and steel die [5]. The copper sheet takes its advantage of high ductility and allows the smooth flow of the billets and this reduction in forming force continues up to four passes. The observation of forming forces required in this study is in good agreement with the other studies [11].

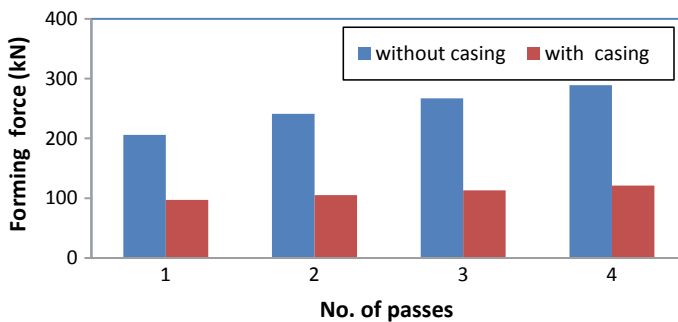


**Fig. 3** Forming forces in ECAE of Al-Mg alloy

### 3.2 Structural Analysis

Figure 4 shows the FESEM images of Al–Mg alloy after ECAE process. The average grain size of the material is measured using the line intercept method. The coarse grains of an alloy with a grain size of 60  $\mu\text{m}$  were refined to a few hundreds of nanometres after the very first pass of ECAE due to the severe strain induced in the work material. From Fig. 4a, b, it is clear that the grain sizes are significantly reduced to  $\sim 750$  and  $\sim 500$  nm after the first and fourth passes, respectively, in the ECAE'd alloy. Even the submicron size grains produced after the first pass, some structural defects were observed in the processed material without copper casing and the severity of defects was reduced after the successive passes. Figure 4c, d shows the homogeneous ultrafine grain structure of the severely deformed alloy with copper shielding after the first and the fourth passes with an average grain size of  $\sim 710$  and  $\sim 420$  nm, respectively. The ductile copper casing causes the uniform strain distribution and reduces the formation of DMZ by occupying the area at the intersection of channels during the pressing. The use of copper covering avoids the cracking on the top longitudinal surfaces of the billets and the formation of DMZ. The average grain sizes of an alloy after the first and fourth passes are presented in Fig. 5.

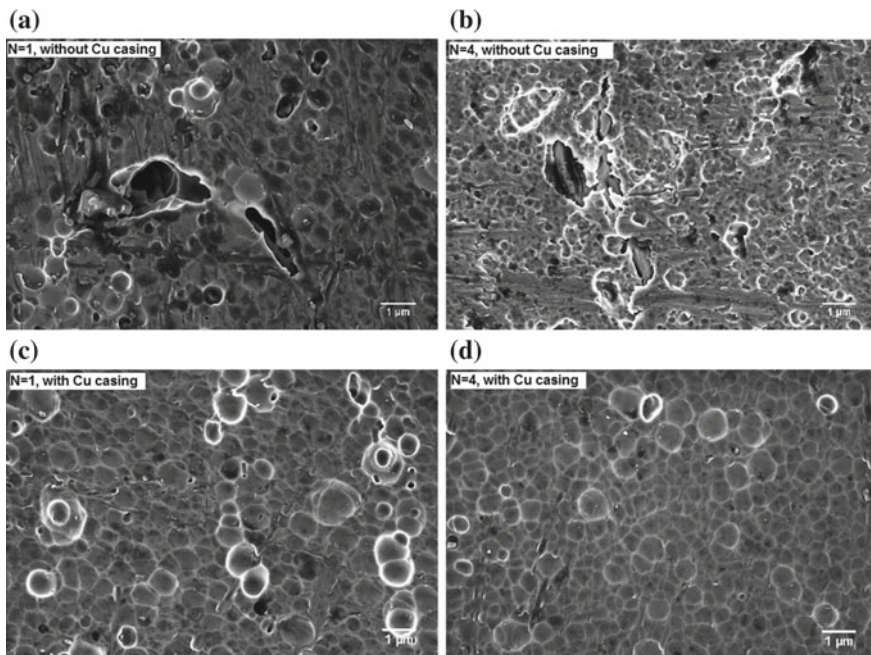


**Fig. 4** SEM photographs of Al–Mg alloy **a** without Cu casing after first pass, **b** without Cu casing after fourth pass, **c** with Cu casing after first pass, **d** with Cu casing after fourth pass

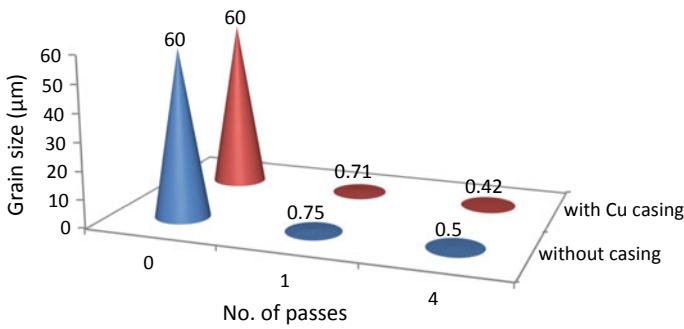
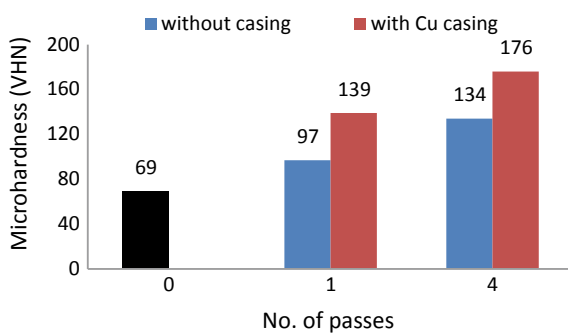


**Fig. 5** Grain sizes of Al-Mg alloy before and after ECAE

**Fig. 6** Microhardness of Al-Mg alloy before and after ECAE



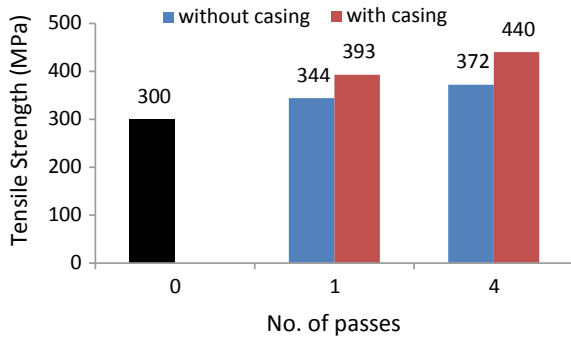
### 3.3 Vickers Microhardness

The hardness of the alloy ECAE'd without copper casing increases from 69 VHN to 97 VHN and 134 VHN after the first and fourth passes, respectively as shown in Fig. 6. Due to the development of non-homogeneous structure with few defects, the hardness values vary in different regions along the cross section of the billets. Whereas the uniform strain distribution produces homogeneous ultrafine grain in the alloy ECAE'd with the copper casing. A fully dense ultrafine grain structure with no structural defects improves the average hardness value to 139 VHN and 176 VHN after the first and fourth passes, respectively. The pattern of test results presented in this study is similar to the results reported by Reza Naseri et al. [12].

### 3.4 Tensile Strength

As shown in Fig. 7, the tensile strength of the alloy significantly increased after ECAE process due to the formation of ultrafine grains. The tensile strength of the billets ECAE'd without and with copper casing increased from 300 MPa to 344 MPa and

**Fig. 7** Tensile strength of Al–Mg alloy before and after ECAE



393 MPa, respectively, after the first pass. The rate of increase is 14.6 and 31% for the alloy ECAE'd without and with casing shielding, respectively, after the first pass. The repetition of ECAE process improves the strength further and the tensile test results obtained after the fourth pass are 372 and 440 MPa for the alloy ECAE'd without and with copper casing, respectively. From the test results, it is clearly observed that the uniform strain distribution develops the homogeneous ultrafine grain structure which directly satisfies the Hall–Petch relation [13] and improves the mechanical behaviour of the processed material.

## 4 Conclusions

The summary of the observations of this work are:

- The effect of DMZ and the non-uniform strain distribution on the structural homogeneity and hardness is high for the alloy pressed with no copper shielding.
- The requirements of forming force are significantly reduced by minimizing the rubbing forces when copper sheets are employed as a casing to the work material.
- The smooth flow of the billet avoids the formation of DMZ, improves the strain distribution and develops the homogeneous ultrafine grains.
- The hardness and tensile strength of severely deformed Al–Mg alloy with copper shielding increased more as compared to another case due to the formation of a fully dense ultrafine grain structure.

## References

1. Segal VM (1995) Materials processing by simple shear. *Mater Sci Eng, A* 197(2):157–164
2. Kawasaki M, Langdon TG (2014) Producing ultrafine-grained materials through severe plastic deformation. *Emerg Mater Res* 3(6):252–260

3. Djavanroodi F, Omranpour B, Ebrahimi M, Sedighi M (2012) Designing of ECAP parameters based on strain distribution uniformity. *Progr Nat Sci Mater Int* 22(5):452–460
4. Djavanroodi F, Ebrahimi M (2010) Effect of die parameters and material properties in ECAP with parallel channels. *Mater Sci Eng, A* 527(29):7593–7599
5. Eivani AR, Karimi Taheri A (2008) The effect of dead metal zone formation on strain and extrusion force during equal channel angular extrusion. *Comput Mater Sci* 42(1):14–20
6. Balasundar I, Sudhakara Rao M, Raghu T (2009) Equal channel angular pressing die to extrude a variety of materials. *Mater Design* 30(4):1050–1059
7. Ferrasse S, Segal VM, Alford F, Kardokus J, Strothers S (2008) Scale up and application of equal-channel angular extrusion for the electronics and aerospace industries. *Mater Sci Eng A* 493(1):130–140
8. Hasani A, Lapovok R, Tóth LS, Molinari A (2008) Deformation field variations in equal channel angular extrusion due to back pressure. *Scripta Mater* 58(9):771–774
9. Djavanroodi F, Ahmadian H, Koohkan K, Naseri R (2013) Ultrasonic assisted-ECAP. *Ultrasonics* 53(6):1089–1096
10. Shaeri M, Djavanroodi F, Sedighi M, Ahmadi S, Salehi MT, Sayyedien SH (2013) Effect of copper tube casing on strain distribution and mechanical properties of Al-7075 alloy processed by equal channel angular pressing. *J Strain Anal Eng Design* 48(8):512–521
11. Varadala AB, Gurugubelli N, Bandaru S (2018) Equal channel angular extrusion of semicircular AA 5083 covered with copper casing. *Emerg Mater Res* 7(3):160–163
12. Naseri R, Kadkhodayan M, Shariati M (2017) An experimental investigation of casing effect on mechanical properties of billet in ECAP process. *Int J Adv Manuf Technol* 90(9–12):3203–3216
13. Hansen N (2004) Hall-petch relation and boundary strengthening. *Scripta Mater* 51(8):801–806



# Characterization of Kenaf/Aloevera Fiber Reinforced PLA-Hybrid Biocomposite



P. Ramesh, B. Durga Prasad and K. L. Narayana

**Abstract** This paper examines the influence of hybridization on mechanical and thermal properties of biocomposites. Kenaf and Aloevera fibers were treated by NaOH treatment to improve the bonding with Poly(lactic acid). Kenaf (30 wt%) reinforced Poly(lactic acid) (70 wt%) and Aloevera (30 wt%) reinforced Poly(lactic acid) (70 wt%) biocomposites, and Kenaf/Aloevera (15/15 wt%) reinforced Poly(lactic acid) (70 wt%) hybrid biocomposite are prepared by extruder and compression molding process. The fabricated bio and hybrid biocomposites were used to illustrate the impact and thermal properties of biocomposites. Treated Kenaf/Aloevera fiber (15/15 wt%) reinforced Poly(lactic acid) (70 wt%) hybrid biocomposite exhibits higher mechanical and thermal properties than other biocomposites.

**Keywords** Kenaf/Aloevera fiber · PLA · Thermal-mechanical properties · Hybrid biocomposite

## 1 Introduction

Eco-friendly composites are non-toxic and purely bio-degradation via composting process (in soil) [1]. In various green (biodegradable) thermo plastics (bio-polymers), PLA offers an exclusive opportunity and numerous of works have been studied [2, 3]. The corn (renewable)-based Poly(lactic acid) offered prospective alternative medium for synthetic (conventional) polymers in market [4]. The PLA offers greater strength

---

P. Ramesh (✉)

Research Scholar, JNTUA Ananthapuramu, Anantapur, Andhra Pradesh 515002, India  
e-mail: [rameshvt@gmail.com](mailto:rameshvt@gmail.com)

B. Durga Prasad

Department of Mechanical Engineering, JNTUA Ananthapuramu, Anantapur, Andhra Pradesh 515002, India

K. L. Narayana

Department of Mechanical Engineering, SVCET, Chittoor 517127, Andhra Pradesh, India

© Springer Nature Singapore Pte Ltd. 2020

H. K. Voruganti et al. (eds.), *Advances in Applied Mechanical Engineering*,

Lecture Notes in Mechanical Engineering,

[https://doi.org/10.1007/978-981-15-1201-8\\_113](https://doi.org/10.1007/978-981-15-1201-8_113)

and easy processability but costly material; for diverse useful appliances the modification is necessary [5]. Hence, natural fibers inclusion in PLA is a right (alteration) system to develop cost-effective material, which has most recently attained thought to substitute (glass and carbon) synthetic fibers [6, 7]. The synthetic (conventional) fibers are substituted by environmentally friendly natural fibers; because they are abundant, recyclable, non-toxicity, cheaper, biodegradable, and capable of non absorbing moisture, permeable and competitive mechanical properties [8]. The incompatibility between (polymer) matrix and (natural) fiber is a main negative aspect; it is overcome by fiber chemical treatment method [9, 10]. In the various kinds of natural assets, Kenaf fiber has a prospective alternating medium to replace the synthetic (conventional) fibers as reinforcement in composites; it diminishes the waste, creates the jobs and contributes healthier atmosphere [11]. On the other hand, Aloe vera plant (*Aloe barbadensis* Miller) was used for drugs since thousands of years. Aloe vera plants were widely cultivated in Florida, India, South Texas, United States (South California), Africa, South and Central America, Australia, Iran and Caribbean [12]. Its look like a sisal plant, but in reality different in nature; the former's point of view Aloe vera fiber provides economic benefit [13]. Islam et al. [14] have reported that hybridization (Kenaf/Coir/PP) enhanced mechanical, water absorption and biodegradable properties than of the Coir/PP composite. Asaithambi et al. [15] developed and studied the cause of hybridization on flexural, impact and tensile properties of the PLA/Banana/Sisal biocomposites; the hybridization enhanced the tensile, impact and flexural properties than other biocomposites. Ramesh et al. [16] concluded that purely biocomposites with kenaf reinforced composite works are needed. A few researchers have tried to find out suitable hybrid biocomposites with required properties [15, 16].

The main key factor of this investigation is to produce a completely eco-friendly green composite through renewable resources using Polylactic acid (matrix) and a grouping of treated Kenaf and Aloe vera Fiber (reinforcement). As for instigators knowledge no work is carried out based on PLA-Treated Kenaf/Aloe vera Fiber hybrid biocomposites by compression molding Technique. Furthermore, the effect of hybridization of PLA-Treated Kenaf/Aloe vera Fiber on impact and thermal properties were examined and evaluated.

## 2 Experimental

### 2.1 Materials

Pellet formed 3052D PLA with  $1.24 \text{ g/cm}^3$  (specific gravity), (melting temp) 145–160 and 55–60 °C (glass transition) material acquired from Nature Tech. The fibers like Kenaf and Aloe vera supplied through Go-Green Products, India. The NaOH was supplied by SR-Scientific Chemicals, Tirupati (AP, India). The 1–3 mm long chopped fibers are used.

**Table 1** Formations of composites

Sample	Code	PLA, wt%	Kenaf fiber, wt%	Aloevera, wt%	NaOH, wt%
PLA-30TKF	PLA/K	70	30	0	6
PLA-30TAF	PLA/A	70	0	30	6
PLA-30TKAF	PLA/K/A	70	15	15	6

## 2.2 Methods

### Fabrication of Bio and Hybrid Biocomposites

The produced composites formations were tabulated in Table 1. Prior to fabrication of sample MMT clay, PLA, Aloevera and Kenaf fibers were held in oven at 110 °C for 1 h. The compositions (Kenaf and Aloevera chopped fibers, PLA and MMT) were physically pre-mixed and then compounded through twin-screw extruder (ZV 20 model, Baroda), and then pelletized composites (PLA, fibers and MMT) went for two roll mill and compression molding machine (for compounding of bio and hybrid bio composites, screw speed and temperature profile were set to 78 rpm and 155–190 °C, respectively). Then, compounded pellets were kept in (hot air) oven for dry at 80 °C for 4 h. After drying, immediately the compound pellets were pre-melted at 185 °C in a counter rotating (two roll mill) internal mixer through a revolve speed of 50 rpm). During the compression process keep the temperature 185 °C and 30 ton force applied (up stroke); then compacted at 165 °C bar pressure for 30 min followed by cool under pressure and then composite sheet is separated from platens and cut into desired form for impact and thermo gravi metric evaluations. The manufacture of bio and hybrid biocomposites line diagram is as shown in Fig. 1.

## 3 Results and Discussion

### 3.1 Mechanical Properties

The PLA-biocomposite and PLA-hybrid biocomposites obtained impact strength (ASTM D256) is shown in Fig. 2. It is obvious that PLA/Kenaf and Aloevera fiber hybrid biocomposite improved the impact strength (Fig. 1). The PLA/Treated Kenaf and PLA/Treated Aloevera biocomposites impact strengths are 49.34 and 50.39 kJ/m<sup>2</sup>, respectively. The PLA/Treated Kenaf and Aloevera fiber hybrid biocomposite impact strength is improved to 69.29 kJ/m<sup>2</sup>. The fiber hybridization influences the impact strength of biocomposite. Previously the same trend was observed by Zainudin et al. [17], they concluded that hybridized coir/oil palm EFB/PP composite enhanced higher mechanical properties than alone coir or oil palm EFB-based

**Fig. 1** Experimental line diagram

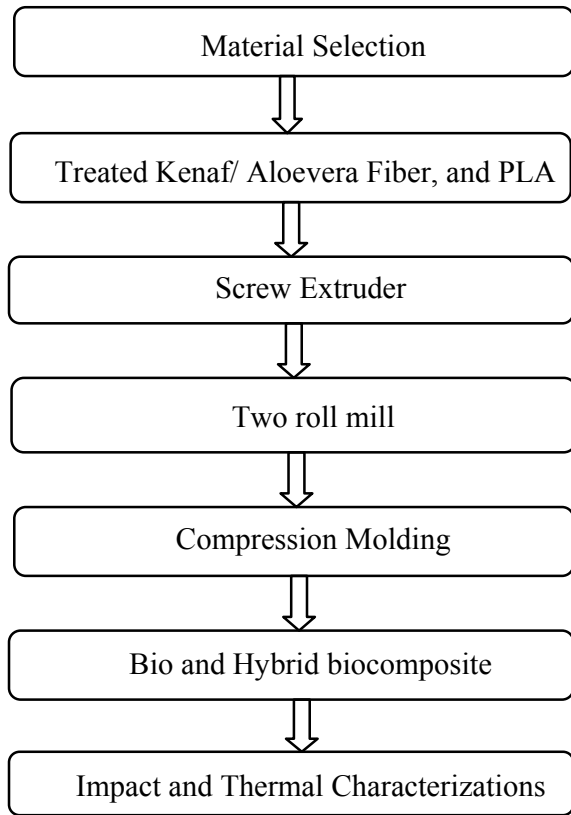
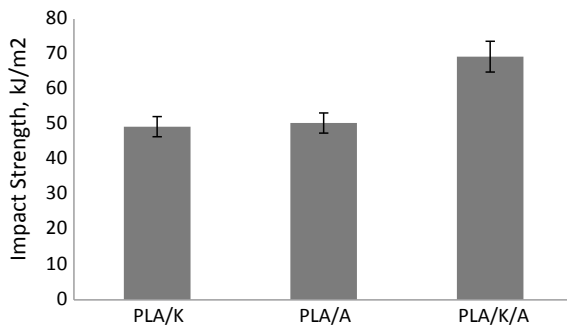


**Fig. 2** Impact strength of bio and hybrid bio composites



composites. Jacob et al. [18] also finding that, sisal/oil palm reinforced rubber composite shows improved mechanical properties than alone sisal or oil palm-based composites.

### 3.2 Thermal Properties

Thermal stability of PLA-biocomposite and PLA-hybrid biocomposites were investigated by thermo gravimetric analysis (TGA). Figure 3 shows PLA-biocomposites and PLA-hybrid biocomposites of the TGA curve. The fiber hybridization improved thermal stability of biocomposite as evidenced from Thermo gravimetric curve. The  $T_{75\%}$  of hybrid biocomposite improved 337–343 °C (Table 2). The decomposition takes place in three-stages. In the primary stage, moisture evaporation occurred up to 150 °C and in second phase due to lignin, cellulose and hemi celluloses. Finally, depolymerisation of PLA takes place. For 10% mass loss PLA-30TKF, PLA-30TAF and PLA-30TAKF were degraded at 280, 295 and 291 °C, respectively. For 75% loss PLA-30TKF, PLA-30TAF and PLA-30TAKF are decomposed at 337, 338 and 343 °C, respectively. The PLA-30TAKF shows maximum decomposition temperature 343 °C (75%) due to chemical treatment and hybrid of biocomposite.

Previously the same trend was observed by Boopalan et al. [19], they concluded that the hybridization enhanced superior thermal stability. The chemical treatment and hybrid posse better thermal stability of hybrid biocomposite.

**Fig. 3** TGA curve of PLA/K, PLA/A and PLA/K/A

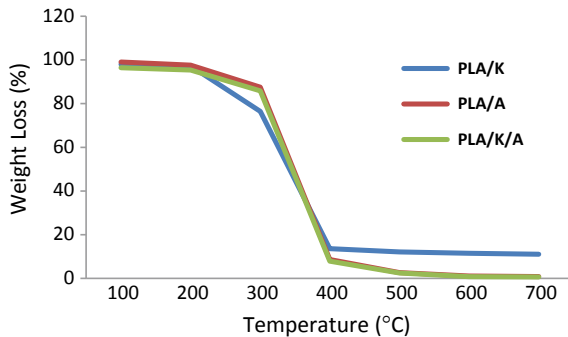


**Table 2** TGA Characterization of bio and hybrid biocomposites

Sample	Denotation	Decomposition temperature (°C)	
		10% (weight loss)	75% (weight loss)
PLA-30TKF	PLA/K	280	337
PLA-30TAF	PLA/A	295	338
PLA-30TAKF	PLA/K/A	291	343

## 4 Conclusion

The characterization (impact and thermal stability) of bio and hybrid biocomposites has been presented. The higher impact strength  $69.29 \text{ kJ/m}^2$  obtained for PLA/K/A hybrid biocomposite. The hybrid biocomposites impact strength improved 40.46 and 37.57% than PLA-30TKF, PLA-30TAF. TGA curve demonstrates the PLA/K/A hybrid biocomposite exhibits highest decomposition temperature  $343 \text{ }^\circ\text{C}$  (75% weight loss) than other. Finally, concluded that, the chemical treatment and hybrid biocomposite exhibits higher mechanical and thermal properties than other biocomposites.

## References

1. Lee SH, Wang S (2006) Biodegradable polymers/bamboo fiber biocomposite with bio-based coupling agent. *Compos A* 37(1):80–91
2. Oksman K, Skrifvars M, Selin JF (2003) Natural fibers as reinforcement in polylactic acid (PLA) composites. *Compos Sci Technol* 63(9):1317–1324
3. Huda MS, Drzal LT, Mohanty AK, Misra M (2007) The effect of silane treated- and untreated talc on the mechanical and physicmechanical properties of poly(lactic acid)/newspaper fibers/talc hybrid composites. *Compos B* 38(3):367–379
4. Lim LT, Auras R, Rubino M (2008) Processing technologies for poly (lactic acid). *Prog Polym Sci* 33(8):820–852
5. Huda MS, Drzal LT, Mohanty AK, Misra M (2006) Chopped glass and recycled news paper as reinforcement fibers in injection molded poly (lactic acid) composites: a comparative study. *Compos Sci Technol* 66(11–12):1813–1824
6. Ochi S (2008) Mechanical properties of kenaf fibers and kenaf/PLA composites. *Mech Mater* 40(4–5):446–452
7. Shanks RA, Hodzic A, Riddehof D (2006) Composites of poly (lactic acid) with flax fibers modified by interstitial polymerization. *J Appl Polym Sci* 101(6):3620–3629
8. Shekeil YAE, Sapuan SM, Jawaid M, Shuja OMA (2014) Influence of fiber content on mechanical, morphological and thermal properties of kenaf fibres reinforced poly (vinyl chloride)/thermoplastic polyurethane poly-blend composites. *Mater Des* 58:130–135
9. Jing Z, Honghong L, Jialiang Y, Tianwei T (2011) Effect of natural fiber surface modification on mechanical properties of poly (lactic acid)/sweet sorghum fiber composites. *Polym-Plast Technol Eng* 50:1583–1589
10. Vilay V, Mariatti M, Taib RM, Togo M (2008) Effect of fiber surface treatment and fiber loading on the properties of bagasse fiber-reinforced unsaturated polyester composites. *Compos Sci Technol* 68:631–638
11. Akil HM, Omar MF (2011) Kenaf fiber reinforced composites: a review. *Mater Des* 32:4107–4121
12. Moghaddasi SM, Verma SK (2011) *Int J Biol Med Res* 2:466
13. Chaitanya S, Singh I (2016) Novel Aloe Vera fiber reinforced biodegradable composites—development and characterization. *J Reinf Plast Compos* 1–13
14. Islam Md S, Hasbullah NAB, Hassan M, Talib ZA, Jawaid M, Haafiz MKM (2015) Physical and mechanical and biodegradable properties of kenaf/coir hybrid fiber reinforced polymer Nanocomposites. *Mater Today Commun* 4:69–76
15. Asaithambi B, Ganesan G, Anand Kumar S (2014) Biocomposites: development and mechanical characterization of banana/sisal fiber reinforced polylactic acid (PLA) hybrid composites. *Fibers Polym* 15(4):847–854

16. Ramesh P, Durga Prasad B, Narayana KL (2018) Characterization of kenaf fiber and its composites: a review. *J Reinf Plast Compos* 37(11):731–737
17. Zainudin ES, Lim HY, Haniffah WH, Jawaid M, Alothman OY (2014) Effect of coir fiber loading on mechanical and morphological properties of oil palm fibers reinforced polypropylene composites. *Polym Compos* 35:1418–1425
18. Jacob M, Thomas S, Varughese KT (2004) Mechanical properties of sisal/oil palm hybrid fiber reinforced natural rubber composites. *Compos Sci Technol* 64:955–965
19. Boopalan M, Niranjana M (2013) MJ Umaphathi, Study on mechanical properties and thermal properties of jute and banana fiber reinforced epoxy hybrid composites. *Compos B* 51:54–57

# Performance Analysis of Different Tool Shape in Electric Discharge Machining Process with Vegetable Oil as Dielectric Fluid



B. Singaravel, K. Chandra Shekar, G. Gowtham Reddy and S. Deva Prasad

**Abstract** Electric discharge machining (EDM) is used to produce complex geometries from difficult-to-cut materials in the area of making dies, mold, and tools. Complex geometries involve different shapes, and electrode plays a major role in reproducing the shape on component. In EDM, hydrocarbon oil-based dielectric fluid is used which is causing environmental issues. Recently, researchers attempted by using vegetable oil as dielectric fluid in EDM process which is a natural product and lead to sustainability in machining. In this analysis, machining performance of different cross sections of electrode is analyzed with vegetable oil (sunflower oil) as dielectric fluid, and the results are compared with conventional dielectric fluid (kerosene). The different cross sections of electrode used in the work include circle, square, rectangle, and hexagon. Material removal rate (MRR), tool wear rate (TWR), and surface roughness (SR) are observed with two sets of energy levels during the process. The result observed that vegetable oil has similar dielectric properties and erosion mechanism compared with conventional dielectric, and it could be used as dielectric fluid in EDM process.

**Keywords** EDM · Dielectric fluid · Vegetable oil · Electrode shape

## 1 Introduction

In EDM process, hydrocarbon-based dielectric fluids are used which generate harmful elements, and it affects environmental as well as operator health [1]. To overcome these issues, some of the steps are taken by researchers to adapt EDM process into green process. One of the approaches is dry EDM, which uses gaseous medium as dielectric, but it has limitation of low MRR and has debris particle suspended in the gaseous medium. Some other approaches are near-dry EDM, water as dielectric,

---

B. Singaravel (✉) · K. Chandra Shekar · G. Gowtham Reddy · S. Deva Prasad  
Department of Mechanical Engineering, Vignan Institute of Technology and Science, Deshmukhi,  
Hyderabad, Telangana, India



additives added in dielectrics, and cryogenic approaches. There are few issues to solve those methods to convert green EDM process [2–4]. Recently, vegetable oil-based dielectric is attempted to attain sustainable idea in EDM process. As earlier stated, EDM process is used to produce complex geometries which involve circle, square, triangle, rectangle, and hexagon. Generally, the cross section of electrode will be reproduced during EDM process, and electrode must be same cross sections and dimensions. The cross sections of electrode are important for producing cavity with sharp corners in bottom as well as in side of the wall [5–7].

## 2 Literature Review

Khan et al. [5] used various cross sections of electrode influence on performance of EDM process. The influence of cross sections of electrode (circle, square, diamond, and triangle) on MRR, TWR, wear ratio, and SR was investigated. The result revealed that diamond shape of electrode was given high value of MRR, and circular cross section electrode was given minimum SR. Yu et al. [6] discussed the performance of square cross section of electrode. In order to obtain accurate machined surface, tool wear compensation, tool path, and cutting steps were used. The result concluded that accurate square cavities are with sharp corners. Sohani et al. [7] investigated the shape of electrodes using response surface methodology. The electrode shape considered was circle, square, triangle, and rectangle. The result highlighted that the circle cross section shape of electrode provided good MRR and TWR than other electrodes used.

Valaki and Rathood [8] attempted sustainability enhancement in EDM process by applying vegetable oil as dielectric fluid. Two categories of dielectric fluids were used, such as hydrocarbon oil-based and vegetable oil-based dielectric fluids. The result concluded that process performances were enhanced vegetable oil as dielectric fluid. Sadagopan and Mouliprasanth [9] used different dielectric fluids (biodiesel, transformer oil, and kerosene), and their machining performances were studied. The result shows that biodiesel as dielectric fluid was given good machining performance than other dielectric fluids. Ng et al. [10] investigated the vegetable oil as dielectric fluids on EDM process of bulk metallic glass and titanium alloy. The result revealed that the proposed dielectric fluids were having dielectric properties and given good machining performance. Valaki et al. [11] used Jatropa oil as dielectric fluid, and the results were compared with conventional dielectric fluid for enhancement of sustainability in EDM process. The effect of current, pulse on time, pulse off time, and voltage on MRR, TWR, SR, and surface hardness were studied. The result pointed out that Jatropa oil-based dielectric could be used as alternative dielectric to conventional dielectric fluid.

From the literature review, the limited studies are reported in the area of different shapes of electrodes (circle, square, rectangle, and hexagon) and vegetable oil as dielectric (sunflower oil) in EDM process. A detailed investigation is to be carried out for understanding the performance of cross sections of electrode using vegetable oil as a dielectric. Hence, in this chapter, an attempt has been made to study the effect of dielectric fluid (kerosene and sunflower oil) when different cross sections of electrode used while machining AISI D2 steel in EDM process.

### 3 Experimental Setup

Die-sinking EDM is used to conduct experiments (Fig. 1). In this work, AISI D2 steel is used as workpiece material, and copper is used as electrode material. AISI D2 steel is used to make die which is categorized into difficult-to-machine material. Copper is widely used as electrode materials with various cross sections such as circle, square, hexagon, and rectangle being used. Figure 2 shows various cross sections of copper electrodes. Table 1 shows the different electrode cross sections and their dimensions. Two categories of dielectric fluids are used, namely hydrocarbon oil-based (kerosene) and vegetable oil-based (sunflower oil). Input process parameters include current, pulse on time, pulse off time, and voltage. Table 2 shows the input parameters and their values. Figure 3a, b shows the machined samples.

The following procedures are used to obtain the output values of MRR, TWR, and SR. Equations (1) and (2) are used to calculate the MRR [11] and TWR [12], respectively. A precision weighing machine is used to find out weight difference

Fig. 1 EDM



**Fig. 2** Electrodes and its various cross sections

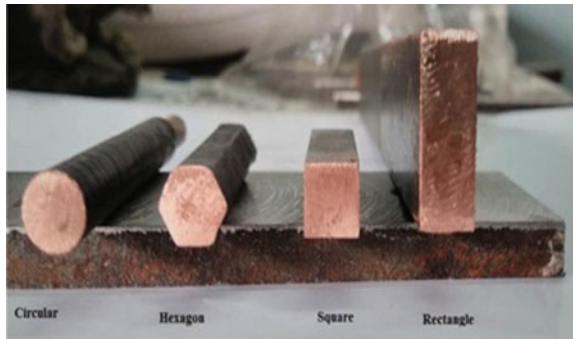


**Table 1** Electrodes' shape and their dimensions

Sl. No.	Electrode cross section	Electrode dimension
1	Circle	Diameter = 8 mm
2	Square	Side = 8 mm
3	Hexagon	Side to side = 8 mm
4	Rectangle	Length = 20 mm width = 8 mm

**Table 2** Process parameters and their values

Sl. No.	Process parameters and their values
Energy Level 1	Pulse on time = 500 $\mu$ s, pulse off time = 300 $\mu$ s and current = 7 Amps
Energy Level 2	Pulse on time = 300 $\mu$ s, pulse off time = 100 $\mu$ s and current = 9 Amps

**Fig. 3 a, b** Machined samples **a** kerosene as dielectric fluid and **b** sunflower oil as dielectric fluid



**Table 3** Experimental results

Sl. No.	Electrode cross sections	Energy level	Kerosene as dielectric fluid			Sunflower oil as dielectric fluid		
			MRR in mm <sup>3</sup> /min	TWR in mm <sup>3</sup> /min	SR in μm	MRR in mm <sup>3</sup> /min	TWR in mm <sup>3</sup> /min	SR in μm
1	Circle	Energy Level 1	2.883	0.448	1.82	5.060	1.362	2.39
		Energy Level 2	4.0729	0.996	2.45	6.683	1.528	2.96
2	Square	Energy Level 1	5.093	0.771	1.490	5.194	1.081	2.47
		Energy Level 2	7.992	1.129	1.886	8.513	1.345	2.54
3	Hexagon	Energy Level 1	2.72	0.476	2.348	5.493	0.918	2.68
		Energy Level 2	6.079	0.712	3.346	11.057	1.126	3.69
4	Rectangle	Energy Level 1	6.431	1.332	2.592	8.831	1.557	2.722
		Energy Level 2	10.743	1.820	2.630	13.986	2.841	2.993

between before and after machining of workpiece and electrode materials. Table 3 shows the experimental results.

$$MRR = \frac{W_{wbm} - W_{wam}}{t \times \rho_w} \times 1000 \text{ mm}^3/\text{min} \tag{1}$$

$$TWR = \frac{W_{ebm} - W_{eam}}{t \times \rho_e} \times 1000 \text{ mm}^3/\text{min} \tag{2}$$

where  $W_{wbm}$  = weight of the workpiece before machining (g),  $W_{wam}$  = weight of the workpiece after machining (g),  $W_{ebm}$  = weight of electrode before machining,  $W_{eam}$  = weight of electrode after machining  $t$  is the machining time (min), and  $\rho_w$  and  $\rho_e$  are the density of workpiece and electrode material (g/cm<sup>3</sup>), respectively. Surface roughness of the machined sample is measured by Talysurf SJ 210 surface roughness tester.

## 4 Results and Discussions

In this analysis, different cross sections of electrodes are processed with kerosene and sunflower oil as dielectric fluid. Two sets of process parameters are chosen, and the output parameters MRR, TWR, and SR are analyzed. Figures 4a-c and 5a-c shows the performance of different cross sections of electrodes with kerosene and sunflower oil as dielectric fluids.

Increased MRR is observed using vegetable oil as dielectric fluid than conventional dielectric fluid. This is due to low breakdown voltage, and high viscosity of dielectric

leads to high-spark energy density, hence improved melting and vaporization. Higher thermal conductivity and low specific heat retain ionization state for long time. Higher TWR is observed using vegetable oil as dielectric because of high oxygen content creates strong conductive discharge channel. Also, high viscosity accumulates more heat and thus increased erosion in electrode [13, 14]. The effect of process parameters such as pulse on time and current is increased in MRR, TWR, and SR. Increased pulse on time provides longer duration of discharge energy due to its widen discharge. Also, pulse on time creates more positive ions that strike on the electrode surface. At higher pulse on time, vaporization and melting cause deeper crater surfaces. Hence, it is increased MRR, TWR, and SR [15, 16]. At high values of current, similar types of result as pulse on time is observed. Increased more number of electron strike on the work piece surface and workpiece materials at high values of current. Also, it produces more energy penetration and more SR values [17].

Generally, complex shapes involve different cross sections. Producing complex cavities through EDM process completely depends on the cross section of electrode. This study highlights instead of moving directly regular electrode into and along the cavity, one can use various shape of electrodes such as circle, square, hexagon and rectangle to produce complex geometries on the workpiece. Electrodes with other than circular sections such as square, rectangle, and hexagon have sharp edges and tips. These types of various cross section of electrodes could be used to machining cavities involving sharp corners in bottom as well as in side [7].

## 5 Conclusion

The comparative analysis is carried out using different categories of dielectric fluid effect with different cross sections of electrodes during EDM process of AISI D2 steel.

- Vegetable oil is attempted as dielectric fluid, and it is observed that higher value of MRR than conventional dielectric. Hence, it is understood that it has similar dielectric properties of erosion principle compared with conventional dielectric.

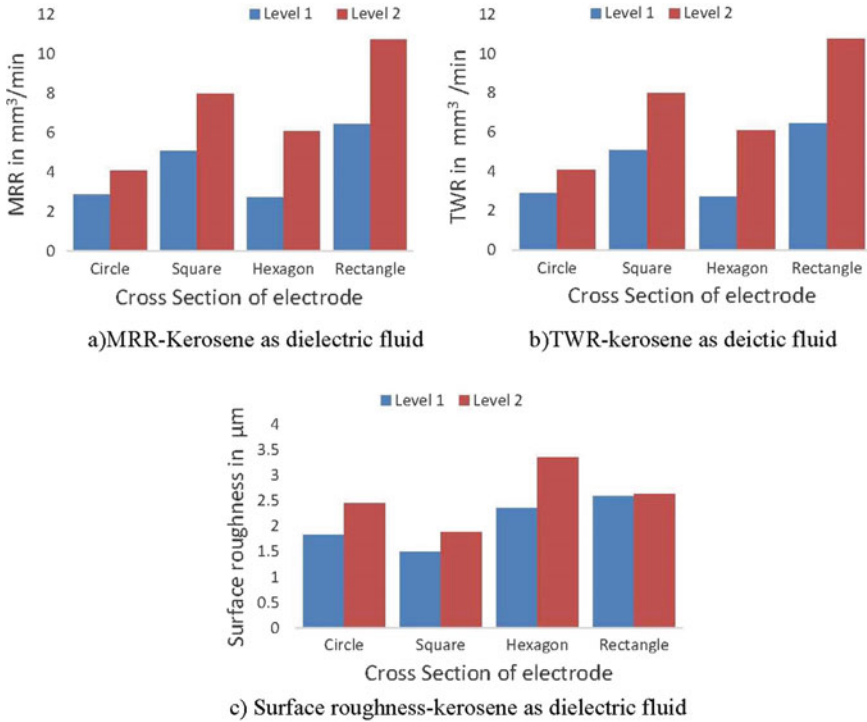


**Fig. 4** Performance (MRR, TWR and SR) of kerosene as dielectric fluid **a** MRR-kerosene as dielectric fluid **b** TWR-kerosene as dielectric fluid **c** Surface roughness-kerosene as dielectric fluid

- Different cross sections of electrode is used to produce complex geometries such as square, rectangle, and hexagon with sharp corners of bottom side as well as side wall.
- Sunflower oil as dielectric fluid is given good performance than kerosene for all cross sections of electrodes.
- The result of TWR and SR is observed as high with vegetable oil as dielectric fluid, and further studies are required to reduce the same.
- Vegetable oils are less toxicity and biodegradable; hence, it is useful for the implementation of sustainability in EDM.

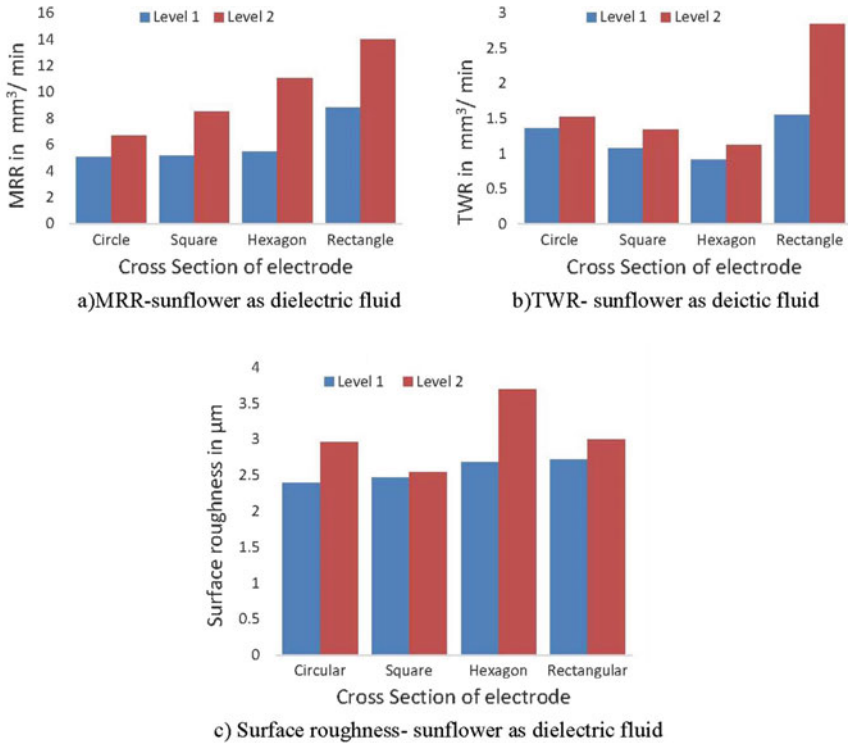


**Fig. 5** Performance (MRR, TWR and SR) of sunflower as dielectric fluid **a** MRR-sunflower as dielectric fluid **b** TWR-sunflower as dielectric fluid **c** Surface roughness-sunflower as dielectric fluid

**Acknowledgements** The authors would like to thank IEI R&D cell for supporting and funding this research work. Ref.: RDPG2017006.

## References

1. Pragadish N, Kumar MP (2015) Surface characteristics analysis of dry EDMed AISI D2 steel using modified tool design. *J Mech Sci Tech* 29:1737–1743
2. Puthumana G, Joshi SS (2011) Investigations into performance of dry EDM using slotted electrodes. *Int J Precis Eng Manuf* 12:957–963
3. Gholipour A, Baseri H, Shabgard MR (2015) Investigation of near dry EDM compared with wet and dry EDM processes. *J Mech Sci Tech* 29:2213–2218
4. Tang L, Du YT (2014) Multi-objective optimization of green electrical discharge machining Ti–6Al–4V in tap water via Grey-Taguchi method. *Mater Manuf Process* 29:507–513
5. Khan A, Ali A, Haque MM (2009) A study of electrode shape configuration on the performance of die sinking EDM. *IJMME* 4:19–23
6. Yu Z, Masuzawa T, Fujino M (1998) 3D micro-EDM with simple shape electrode. *Int J Elect Mach* 3:7–12

7. Sohani MS, Gaitonde VN, Siddeswarappa B, Deshpande AS (2009) Investigations into the effect of tool shapes with size factor consideration in sink electrical discharge machining (EDM) process. *Int J Adv Manuf Technol* 45:1131
8. Valaki JB, Rathod PP (2016) Investigating feasibility through performance analysis of green dielectrics for sustainable electric discharge machining. *Mater Manuf Process* 31:541–549
9. Sadagopan P, Mouliprasanth B (2017) Investigation on the influence of different types of dielectrics in electrical discharge machining. *Int J Adv Manuf Technol* 92:277–291
10. Ng PS, Kong S, Yeo SH (2017) Investigation of biodiesel dielectric in sustainable electrical discharge machining. *Int J Adv Manuf Technol* 90:2549–2556
11. Valaki JB, Rathod PP, Sankhavara CD (2016) Investigations on technical feasibility of *Jatropha curcas* oil based bio dielectric fluid for sustainable electric discharge machining (EDM). *J Manuf Process* 22:151–160
12. Kumar S, Singh R, Batish A, Singh TP (2017) Modeling the tool wear rate in powder mixed electro-discharge machining of titanium alloys using dimensional analysis of cryogenically treated electrodes and workpiece. *Proc Inst Mech Eng Part E J Process Mech Eng* 231:271–282
13. Giakoumis EG (2013) A statistical investigation of biodiesel physical and chemical properties, and their correlation with the degree of un saturation. *Ren Energy* 50:858–878
14. Wang X, Liu Z, Xue R, Tian Z, Huang Y (2014) Research on the influence of dielectric characteristics on the EDM of titanium alloy. *Int J Adv Manuf Technol* 72:979–987
15. Daneshmand S, Kahrizi EF, Abedi E, Abdolhosseini MM (2013) Influence of machining parameters on electro discharge machining of NiTi shape memory alloys. *Int J Electrochem Sci* 8:3095–3104
16. Shabgard MR, Seyedzavvar M, Oliaei SNB (2011) Influence of input parameters on characteristics of EDM process. *Stroj Vestn J Mech Eng* 57:689–696
17. Wu KL, Yan BH, Huang FY, Chen SC (2005) Improvement of surface finish on SKD steel using electro-discharge machining with aluminum and surfactant added dielectric. *Int J Mach Tool Manuf* 45:1195–1201



# Experimental and Finite Element Analysis of Fracture Toughness of Chilled LM13 MMC



H. S. Harshith and Joel Hemanth

**Abstract** There was a remarkable increase in the mechanical properties and fracture toughness by using chills during the development of composites. In the present work, metallic and non-metallic chills were used to develop the LM13 alloy-fused SiO<sub>2</sub> metal matrix composite reinforcement which varied from 3 to 12%, in steps of 3%. The fracture toughness experiment revealed a toughness of 9.7 Mpa√m for the composite with 9 wt%. Beyond 9 wt%, the fracture toughness declined. The increase in the fracture toughness can be attributed to uniform distribution of the hard reinforcement particles. SEM fractography of fracture toughness specimen reveals that the matrix alloy exhibits fine and shallow dimples with high plastic deformation, thus clearly indicating that the type of fracture is ductile. For validity purpose, the experimental results of the fracture toughness were assessed through FE analysis and found that the results are converging within the limits, i.e. 5%.

**Keywords** Fracture toughness · LM13 · Fused SiO<sub>2</sub> · Chills · SEM

## 1 Introduction

Aluminium-based composites are known for their blend of properties, texture and processing choices due to which they are widely used in the aviation and automobile sectors [1]. The industries are looking to have aluminium composites free from defects. Aluminium-based composite casting is subjected to micro-shrinkage during casting because of its freezing range. Also, composite with desired properties can be obtained by suitably reinforcing the matrix alloy [2, 3].

Spray deposition, stir casting technique and powder metallurgy are used to develop particulate-reinforced MMCs. The matrix or base alloy is combined with excellent strength material known as reinforcement to obtain a composite. Certain materials

---

H. S. Harshith (✉)

Channabasaveshwara Institute of Technology, Tumkur, Karnataka 572216, India  
e-mail: hshmech.29@gmail.com

J. Hemanth

Presidency University, Bengaluru, Karnataka 560064, India

© Springer Nature Singapore Pte Ltd. 2020

H. K. Voruganti et al. (eds.), *Advances in Applied Mechanical Engineering*,

Lecture Notes in Mechanical Engineering,

[https://doi.org/10.1007/978-981-15-1201-8\\_115](https://doi.org/10.1007/978-981-15-1201-8_115)

can be workable even at 1700 °C, which include silicon nitride, silicon carbide, silicon dioxide, etc. Carbon–carbon composite retains much of its strength even at 2500 °C [4–8].

Chilling lessens grain of the composites down to an interface-controlled structure, to get a material with new utilitarian properties. Hardness, wear and fracture strength properties of aluminium composites fundamentally reliant on processing methods, dispersoid content, chill conditions, microstructure, and interfacial bonding attributes. Wise positioning of chills will subjugate micro-shrinkage or dispersed porosity in composites [9].

Most of the times where the experimental works are complicated and costly, we use finite element analysis to obtain an approximate result of the desired work [10, 11].

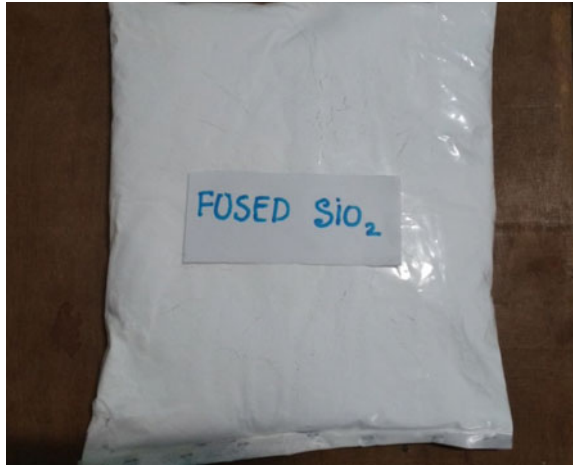
## 2 Experimental Procedure

LM13 ingot shown in Fig. 1 shows good casting properties with density of 2.7 gm/cc, melting temperature of 615 °C and fair strength, and hence it was chosen as the base matrix alloy.

Fused SiO<sub>2</sub> as shown in Fig. 2 is a smooth white mineral powder that has almost zero thermal expansion, thermal shock resistance and chemically inert and stable at high temperatures but dissolves in hydrofluoric acid. The fused SiO<sub>2</sub> is odourless/colourless but might have blue or green colour depending on the impurities. Fused SiO<sub>2</sub> is the most popular ceramic material with a density of 2.7 gm/cc, melting temperature is 1660 °C and coefficient of thermal expansion is  $0.54 \times 10^{-6}$  μm/m. Fused SiO<sub>2</sub>, a ceramic reinforcement, is chemically very stable and possess high hardness and Young's modulus with excellent thermal stability.

Fig. 1 Al alloy (LM13)



**Fig. 2** Fused SiO<sub>2</sub>

## 2.1 Composite Preparation

Stir casting technique is used to produce Al alloy (LM13) and fused SiO<sub>2</sub>-reinforced MMCs. This technique involves various processing parameters such as speed of stirrer, processing temperature, pouring temperature, mould temperature and reinforcement feeding rate, which can be controlled, and sound castings can be obtained. The aluminium ingots were placed in a graphite crucible. The molten metal was heated to red hot condition. The pre-heated fused SiO<sub>2</sub> particles were introduced into melt. Vortex was created in the molten metal, and the wetting of the particles and the matrix was ensured by constant stirring using mechanical impeller.

The constant stirring was carried out for more than 20 min to avoid agglomeration. The scum powder was used as slag removing agent and degassing tablet hexachloroethene was added to completely remove any gases in the molten metal and continued reheating to a super-heated temperature (710 °C), then it was poured into the prepared mould fitted with chills to reduce the micro-porosity and enhance the mechanical properties, and finally, the castings were obtained. The composites were cast using various metallic copper and mild steel, non-metallic chills silicon carbide and graphite to ensure directional solidification.

## 2.2 Fracture Toughness Test

A closed-loop Instron servo-hydraulic material testing system was used to perform fracture toughness test on the test samples of MMCs and matrix alloy in accordance with ASTM E399-1990 standards. The test samples were subjected to three-point bending of machined specimen which was pre-cracked by fatigue. A sketch of single edge notch bend (SENB) specimen with a chevron notch was prepared as per the

**Fig. 3** Fracture specimens  
(before test)



dimensions. A notch of initial length  $a_o = 1.27$  mm was produced by using CNC wire cutting machine. Figure 3 shows fracture specimens with various % weight reinforcement addition, cast using chill.

During the fatigue loading, a minimum load of 0.296 KN and maximum load of 0.457 KN were maintained. The process of introducing a crack with a plastic zone at the vicinity of the notch with the influence of fatigue load is called fatigue pre-cracking. In pre-cracking, a crack of length  $ap = 2.27$  mm is introduced. For the ratio  $a/W = 0.3881$ ,  $f(a/W)$  is noted down as 3.812 for further validations. The fractured test samples are shown in Fig. 4.

### 3 Results and Discussions

The fracture toughness  $K_{IC}$  of the single edge notch bend specimen is indicated in Table 1. The load was varied from 0.1 to 0.5 KN.

It is observed from Table 1 that increasing the reinforcement content and chilling has an effect on the fracture toughness of the material. The fracture toughness of the MMC increases up to 9 wt% reinforcement addition cast with different chills, and beyond 12 wt%, a decrease in fracture toughness was observed.

The possible three micro-mechanisms controlling the fracture behaviour during cyclic loading are indicated below:

- Effective transfer of load between the soft Al alloy (LM13) and the hard  $\text{SiO}_2$  ceramic particle.
- Hardening arising from constrained plastic flow and triaxiability in the Al alloy (LM13) matrix due to the presence of the brittle reinforcements.

**Fig. 4** Fracture specimens (after test)

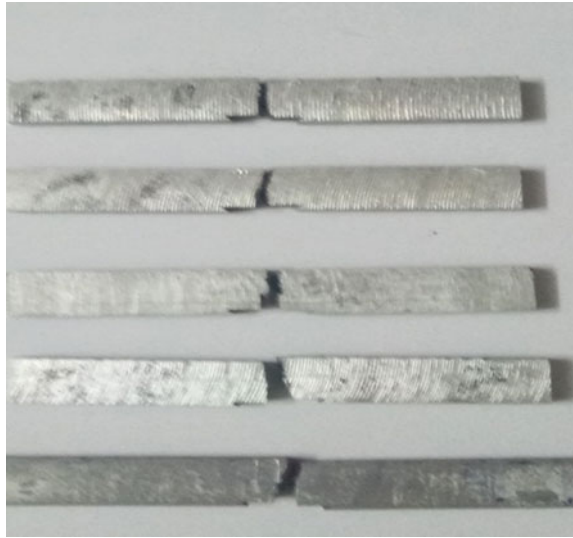


**Table 1** Fracture toughness ( $K_{IC}$ ) of MMC with different wt% reinforcement addition cast using different chills

Type of chill	Fracture toughness $K_{IC}$ ( $\text{MPa}\sqrt{\text{m}}$ )			
	wt% reinforcement			
	3	6	9	12
Copper	7.840	7.546	9.706	7.227
Mild steel	5.970	6.592	9.632	6.148
Silicon carbide	5.250	7.170	9.070	4.830
Graphite	5.187	6.352	8.059	3.959

- The soft Al alloy (LM13) matrix and the hard  $\text{SiO}_2$  ceramic particle reinforcement leads to residual stresses due to the mismatch in thermal coefficient between the components of the composite.

Figure 5 shows an increase in the fracture toughness of the MMCs developed which could be primarily attributed to the presence and uniform dispersion of hard  $\text{SiO}_2$  particulates in Al alloy (LM13). Also, good bonding and compaction of reinforcement with the matrix alloy and effective load distribution between the soft matrix alloy and harder ceramic particles leads to higher fracture toughness (Figs. 6, 7 and 8).

**FEA Results of Fracture Specimen**

The fracture toughness values as obtained by experimental and FEA as shown in Table 2 are in close agreement with each other and marginal variation of 3–4% has

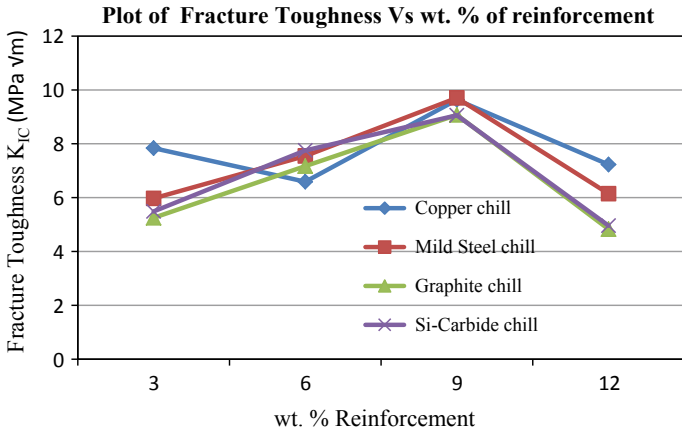


Fig. 5 Plot of  $K_{IC}$  as a function of wt% of reinforcement

Fig. 6 3D model of fracture specimen

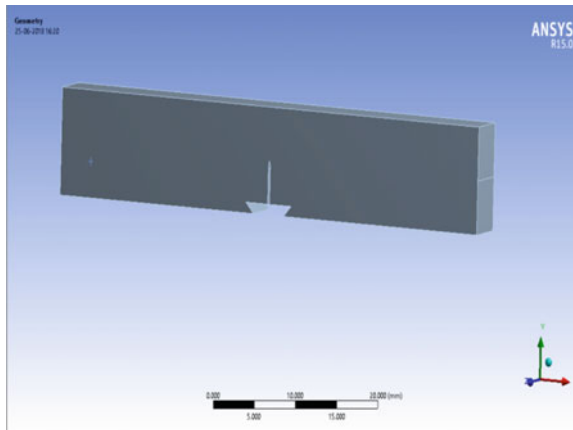
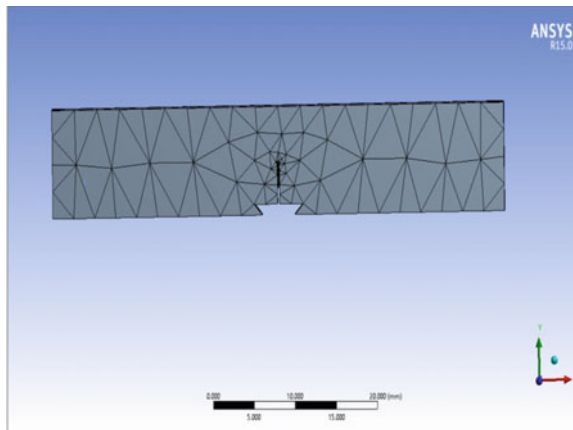
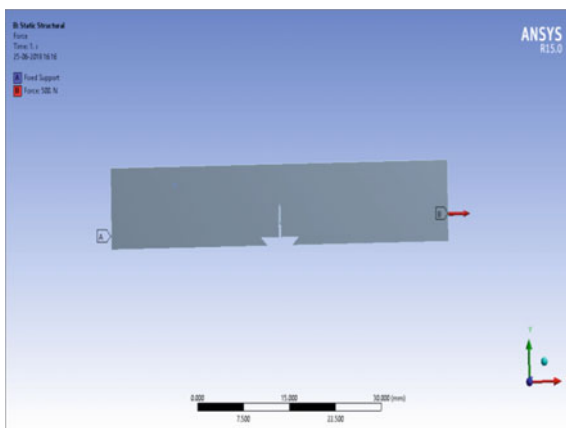


Fig. 7 Meshed model



**Fig. 8** 3D meshed model after applying boundary conditions



**Table 2** FEA results of fracture toughness test for various wt% reinforcement and different chills

	Fracture toughness ( $\text{MPa}\sqrt{\text{m}}$ )			
	wt%	$K_{IC}$ (Expt)	$K_{IC}$ (FEA)	Error %
Copper chill	3	7.840	7.760	1.02
	6	6.592	6.532	0.91
	9	9.432	9.265	1.77
	12	5.927	5.628	5.04
Mild steel chill	3	5.970	5.860	1.84
	6	7.346	7.210	1.85
	9	9.706	9.562	1.48
	12	6.245	6.159	1.37
Silicon carbide chill	3	5.950	5.850	1.68
	6	6.700	6.625	1.11
	9	9.170	9.150	0.21
	12	4.430	4.321	2.46
Graphite	3	5.587	5.534	0.94
	6	7.952	7.824	1.60
	9	9.120	9.085	0.38
	12	4.559	4.321	5.22

been seen. This is a clear indication of uniform distribution of reinforcement particles in the matrix Al alloy (LM13).

## 4 Conclusion

Fracture toughness was highest for composite with 9 wt% reinforcement and is 17% higher in comparison with unreinforced matrix alloy.

The fracture toughness showed an increasing trend till 9 wt% reinforcement, and beyond which there is decreasing trend which might be due to cluster formation.

FEA and experimental results are in close agreement with each other.

## References

### 1. Journal Article

1. Kutumbarao GV, Panchanathan V (1972) An evaluation of parameter controlling the soundness of long freezing range alloy castings. *J Br Foundry Man* 66:135–145
2. Yuen HC, Ralph B, Lee WB (1993) Novel preparation for an aluminum-alumina MMC by a hot roll bonding process. *Scr Metall Mater* 29:695–670
3. Ralph B, Yuen HC, Lee WB (1997) The processing of MMCs: an overview. *Mater Process Technol* 63:1–8
4. Wei ZG, Tang CY, Lee WB (1997) Design and fabrication of intelligent composites based on shape. *Mater Process Technol* 63:68–75
5. Hemanth J (2011) Finite element wear behavior modeling of Al/Al<sub>2</sub>SiO<sub>5</sub>/C chilled hybrid metal matrix composites (CHMMCs). *Mater Sci Appl* 2:878–812
6. Agarwal BD, Lifshitz JM (1974) Elastic-plastic finite element analysis of short fiber composites. *Fiber Sci Technol* 7:45–53

### 2. Book

7. Kainer KU (ed) (2003) *Metal matrix composites*. Wiley
8. Davidson DL (1989) *Eng Fract Mech* 33:965

### 3. Conference Proceedings

9. Reinforced aluminum based MMCs fabricated by squeeze casting method. *Trans Nonferrous Met Soc China* 21(7):1441–1448
10. Morse T, Sasuda T, Okabe M (1995) Proceedings of 28th Japan congress on material research. Tokyo, Japan, pp 231



#### **4. Conference Paper**

11. Jacob S, Drouzy M (1970) Solidification behavior of aluminum alloy castings. Foundrie 15:395-403

# Design and Fabrication of Die Back Door for Manufacturing of Cylinder Liners



T. Vadivelu, C. Vijaya Bhaskar Reddy and G. Prasanthi

**Abstract** The centrifugal die casting process was observed at VACPL, at Vijayawada in India. In the present observation, for the production of cylinder liners, resin sand was used at the front door of the centrifugal die casting machine, and also, resin sand was dressed at the inner surface of the die. However, no resin sand is used at the back door, which results in the direct melt to metal contact at the back door and which increases the hardness of the casting excess than required, due to rapid cooling rate between the casting and die back door zone. Due to this hot spot, defects appear on the back door, and it decreases life of the back door and increases the scrap rate. The chilling length is removed by the parting operation, which increases the cost of production. In this research work, to eliminate that hot spot defect, the die back door was design and fabricated to introduce resin sand, and also, the temperature distributions of the die back doors were simulated by using ANSYS 18 software. Both old and new rear-end casting samples can be examined using the FE-SEM and EDX technique for microanalysis. Result in, no direct metal to metal contact, increasing the life of back door and the hardness of the cylinder casting is limited to as per requirement, parting operation and hot spot defects are eliminated. Instead of parting operation, facing operation is adopted. The time required for facing operation is 1/6th of the parting operation.

**Keywords** Die casting · Chilling · Back door · Resin sand

---

T. Vadivelu (✉)  
JNTUA, Ananthapuramu, Andhra Pradesh 515002, India  
e-mail: [Vadimay28@gmail.com](mailto:Vadimay28@gmail.com)

C. Vijaya Bhaskar Reddy  
Department of Mechanical Engineering, SVCET, RVS Nagar, Chittoor, Andhra Pradesh 517127, India

G. Prasanthi  
Department of Mechanical Engineering, JNTUA College of Engineering, Ananthapur, Andhra Pradesh 515002, India

## 1 Introduction

Centrifugal casting is one of the superior-quality cylindrical or tubular casting techniques widely used in casting industries, in which melt is poured into a rotating die or mould. Due to centrifugal force, the die is rotated [1] about its axis at high speed (500–1500 rpm), so that the melt to be casted spreads over the die surface and becomes a hollow cylindrical casting. These types of castings are fine grained on the outer diameter, while the inside surface has more inclusions and impurities; these are gathered by centrifugal force towards the centre of the case that can be machined away. In this type of castings are free from defects when compared to statically [2] casting process and have higher production rate and superior mechanical properties. Centrifugal casting machines are generally three types based on the direction of the mould spinning axis: they are vertical, horizontal and inclined centrifugal casting machines. The present research work carries out on the horizontal centrifugal casting machine. The horizontal centrifugal casting machines are generally used to cast pieces with a uniform internal diameter or with a high length-to-diameter ratio component. Products include cylinder sleeves, tubes, pipes, and cylindrical or tubular castings [3] that are simple in shape. Thoroddsen et al. [4] have been explored the experimental study of coating flows in partially-filled horizontally rotating cylinder. Lu et al. [5] have been examined the filling and temperature field of cantilever-type horizontal centrifugal casting of a wet-type cylinder liner which was simulated based on the pro-CAST software, and solidification processes and temperature field were also simulated in the time of cooling process.

However, hot spot defects have not been examined in the horizontal centrifugal die casting process. Hot spot defects are shown in Fig. 3, which occur when casting area cools more rapidly than the reaming area and also dies back door, in the time of hot molten metal contact to the die back door and resulting, excess hardness occurs at a rear end side of the casting up to 6–10 mm length (chilling ring and its pieces) as shown in Fig. 4.

In this study, die's back door is designed and fabricated to introduce resin sand instead of bentonite coating, and also, the temperature of die back door is simulated through ANSYS 18 software, and also, hot spot defects were analysed. It is expected that the result would help to minimize the scraps and improve the quality of the cylinder liner, manufactured by horizontal centrifugal die casting.

## 2 Material for Cylinder Liner

Generally, ferrous and non-ferrous materials are used in the preparation of the cylinder liners. Based on the present work, grey cast iron was selected due to its low cost and wide range of properties. Grey iron contains graphite in the form of flakes, and it has great lubricating nature due to graphite flakes, excellent machinability,

and moderate hardenability, toughness, optimum strength and considerable corrosion resistance excellent damping capacity and wear resistance. Grey cast irons have a chemical composition of 2.5–4.0% carbon, 1–2.5% silicon, 0.6–1% manganese, 0.2–0.4 chromium, 0.3% phosphorus, 0.05 sulphur and the remainder iron.

### 3 Experimental Set-up

To control the excess hardness at the rear-end side of the casting and eliminating the hot spot defect on the die back door, the new die back door is designed [5] based on old die back door and fabricated as per the drawing shown in Fig. 1a, b, with an outer diameter 130 mm and intermediate step diameter 119.5 mm. In the fresh die back door, additional step is created (i.e. 96 mm diameter) based on the inner diameter of the casting. At the top of the die, an 8 mm hole is drilled due to send the sand into the die, and its drawing is shown in Fig. 1c.

A suitable supporting door instrument is designed and fabricated as shown in Fig. 2, to support the resin sand until the resin sand solidifies. 8 mm bottom diameter, 12 mm top diameter and 50 mm length, tap per rod is used for closing the 8 mm hole on the die; otherwise, the liquid metal may come outside and affects the workers.

The resin sand was sent into the die through a pipe with 2 kg/m<sup>2</sup> pressures (to close the 8 mm hole with tap per rod); its drawings and fabricated instrument are shown in Figs. 1b. The resultant diagram is shown in Fig. 6a. Due to pressure force, resin sand cannot withstand at the circular portion that gap also filled with resin with help of a funnel (at this particular instant that 8 mm hole can be opened). The elliptical portion which is completely filled by the resin sand is shown in Fig. 6b. At the time of melt pouring into the die carefully closed that the 8 mm hole with the tapered rod.

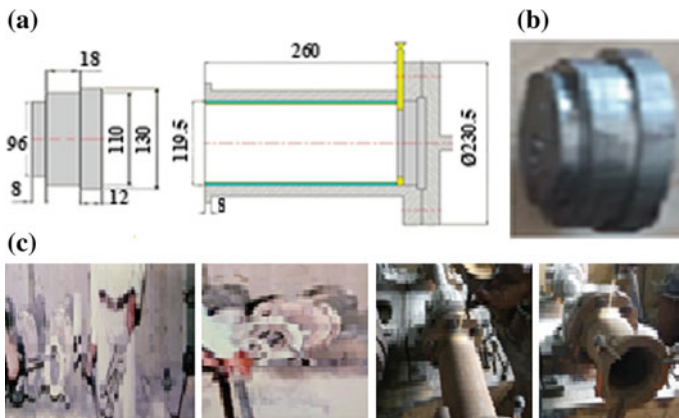


**Fig. 1** a New die back door design. b New die back door fabrication. c Sand sends through pipe and funnel



**Fig. 2** Supporting door instrument design and fabrication



**Fig. 3** Old die back door and its hot spot defect



**Fig. 4** Old and new castings' parting rings



**Fig. 5** Both old and new method cast castings rear side parting rings (chilled portion) can be made small pieces and its polished hardness tested specimens

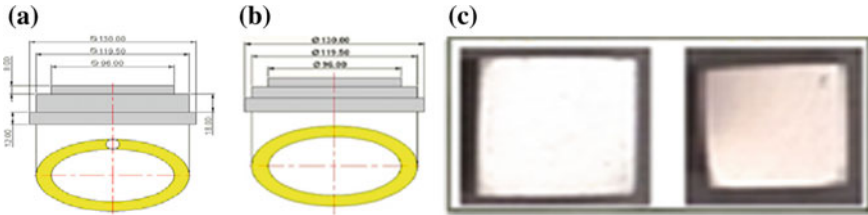


**Fig. 6** a, b Die in side resin sand formation (circular/elliptical shape) on die back door. c Smooth polished microstructure tested specimens

Every day before production starting the die back door and die are preheated (i.e., 200 °C) directly without sand, which helps the resin sand to form adhesive nature on the die back door and also which maintains the pouring temperature constantly. After dressing the die with quartz and resin sands, the molten metal is poured into the die with the help of the spout. After few minutes, the molten metal will solidify, and the casting will be separated from the die for cooling. The new method produces effective castings without chill and hot spot defects. Parting operation is completely eliminated to introduce a new method, and the corresponding visuals are shown in Fig. 4, which clears that the white cast iron is completely terminated on the rear-end side of the casting and its different sample variations (these rings are not presented white colours) which are shown in Fig. 4. The machined casting becomes a liner (Fig. 3).

The hardness of the cast sample was evaluated using Rockwell’s hardness testing machine in C Scale (i.e. HRC Series). The excess hardness portion can be taken by a small piece (both old and new cast cylinder castings at rear-side ring portion can be made small pieces, and then hardness can be examined), and then it can be grinded and polished by grinding machine and CC-22 P800 silicon carbide electro cathode abrasive paper.

The microstructure investigation was performed using field emission scanning electron microscopy (FE-SEM): it is the high-resolution electron imaging, and over 1000,000X (>10 nm at 1 kV) can be performed with very low accelerating voltages (50–150 kV are scanned across the specimen). Specimens for microstructural examination were cut from the rear-end side of the castings (old casting 10 mm chilling ring portion was taken and makes it into small pieces and also newly cast 10 mm rear-side casting portion), and these samples were grinded and polished by using grinding machine and abrasive paper. The etching of the samples was carried out using 98 ml ethanol +2 ml nitric acid (HNO<sub>3</sub>) before the microstructural examination was performed, using field emission scanning electron microscope. The microstructure examined specimens are shown in Fig. 6c (Fig. 5).

## 4 Heat Transfer Transient Analysis

The calculation of the temperature distribution for the die back door, based on unsteady-state heat conduction, was found by solving the governing equation for fluid flow and heat transfer conduction for a solid sphere, considering the following equations are employed.

$\frac{d}{dr} \left( x^2 \frac{dT}{dr} \right) + \frac{x^2 q}{k} = 0$  In  $0 \leq x \leq x_0$ ,  $\frac{dT}{dr} = 0$  at  $x = 0$  &  $T = T_0$  at  $x = x_0$ , where  $q$  = Uniform heat flow,  $x$  = radius of sphere,  $k$  = thermal conductivity of sphere material,  $T$  = temperature variation and  $d_r$  = spherical shell thickness. Heat transfer behaviour during mould filling and solidification is given as follows: conservation of mass,  $\frac{\partial \rho}{\partial t} = \nabla \cdot (\rho \mathbf{u} = 0)$ , and the energy equation during mould filling is governed by the equation:  $\rho C_p \left( \frac{\partial T}{\partial t} + \mathbf{u} \cdot \nabla T \right) = \nabla \cdot (k \nabla T) + Q$  where  $C_p$  and  $K$  are the specific heat and thermal conductivity of the molten metal,  $\mathbf{u}$ : velocity component,  $\rho$  = density,  $T$  is the temperature, and  $Q$  is an internal power source. In the inner free surface and outside of mould/die, the radiation effect must be considered in both flow melt and solidified metal. Heat loss due to convection and radiation is determined from the equation:  $-\lambda \cdot \frac{\partial T}{\partial x} = h \cdot (T_{w1} - T_{w2}) + \sigma \cdot \epsilon \cdot (T_{w1} - T_{sur1})$ , where  $\lambda$ : thermal conductivity,  $T$ : temperature,  $h$ : convection heat transfer coefficient,  $\sigma$ : Stefan–Boltzmann’s constant,  $\epsilon$ : the emissivity.

Initial conditions: The initial preheated temperature of 200 °C was applied to the mould and resin sand coating. The pouring temperature of the liquid is  $1350 \pm 50$  °C which was applied to the casting. The moving fluid flow speed of 1 kg/s was applied over the mould surface, and fluid filling time is approximately 30 s.

Rotational speed of the die: use the following formula to calculate the rotational speed of the mould

$$N = 29.9 (G/R_i)^{0.5} \quad (i)$$

where  $N$  is the rotational speed of the die in RPM,  $R_i$  is the inner surface radius of the casting in metres, and  $G$  is the coefficient of gravity. For metal moulds (cast iron, steel),  $G$  value generally adopts a range of 50–120. The speed of 1400 RPM was selected after  $G$  value was calculated.

Boundary conditions: the mould and casting were cooled in atmospheric air, and the ambient temperature of outer mould surface is considered as 20 °C. The surface heat transfer coefficient of 25 W/m<sup>2</sup> K was applied to the die back door, resin sand and outer surface on the mould.

## 5 Result and Discussions

The result section covers three different subsections as hardness measurement, microstructure analysis and also the temperature distribution of the die back door which were simulated by using ANSYS 18 software.

The values of hardness for each cast sample (based on old method) are measured in Rockwell hardness testing machine in C Scale series (HRC series). The chill portion parting ring was taken and makes it into small pieces. The casting samples were polished to obtain a flat and smooth surface finish. Multiple tests were performed on each sample, average hardness values are taken as a consideration, and these hardness values are as shown in Table 1.

From Fig. 7, it can be noted that at chill portion, from 1 to 6 mm distance (from rear side of casting to front side) the hardness is found very high and excess than required; at 7–8 mm distance, the hardness values are gradually decreased and moderate and 9–10 mm; it found constant and required amount of hardness values. The above similar procedure can be followed for new method castings, and its hardness values are shown in Table 2, and from Fig. 8, it can be seen that all sides of casting sample values are found constant hardness values (i.e. required amount of hardness values).

The micrographs show that the microstructure of chilled portion of the (old method producing casting piece at a rear-end side) casting is characterized with a high percentage of cementite and little amount or no graphite flakes as shown in Fig. 9. Chilling nature is formed due to fast cooling rate at the die and dies' back door zone (due to molten metal hits directly to the die back door, result in lower the Si and carbon percentage), resulting in much of the carbon in a molten cast iron forms iron carbide( $Fe_3C$ -in a pearlite matrix) instead of graphite upon solidification. This type

**Table 1** Hardness values obtained by used in old die back door

Samples	Chilling length in mm				
	2	4	6	8	10
Series 1	47	41	36	30	24
Series 2	47	40	35	29	24
Series 3	46	40	34	28	23
Series 4	45	39	33	27	22

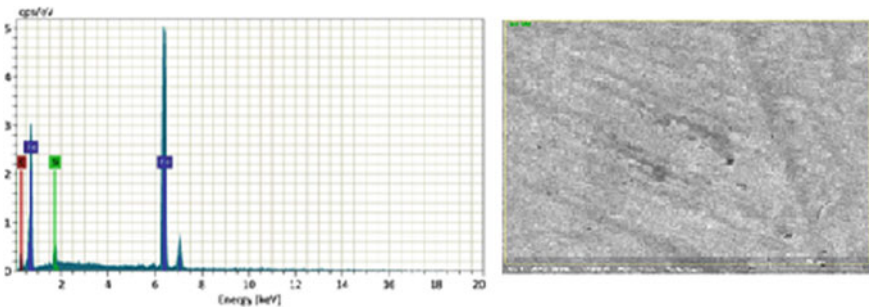


**Fig. 7** High magnification view (2500x) of the white cast iron specimen (microstructure and ED's analysis)



**Table 2** Hardness values obtained by using old die back door

Samples	Chilling length in mm				
	2	4	6	8	10
Series 1	24	23	22	22	22
Series 2	24	23	22	22	22
Series 3	24	23	22	22	22
Series 4	24	23	22	22	22

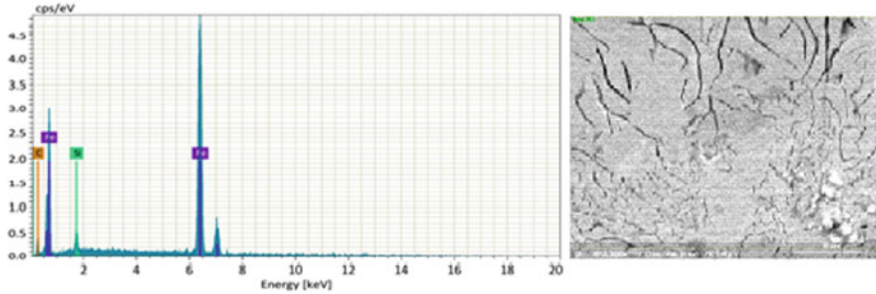


**Fig. 8** Grey cast iron specimen etched with 2% nital (Microstructure and ED’s analysis)

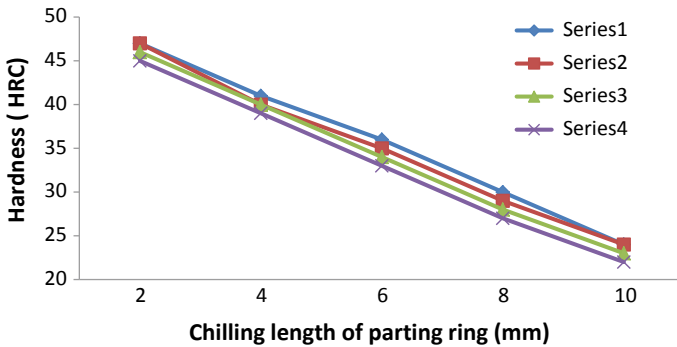
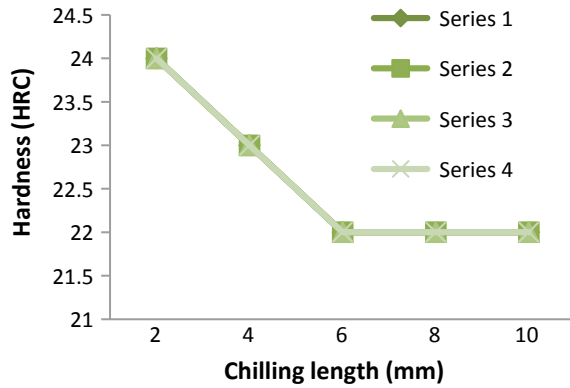


**Fig. 9** Casting hardness values (by using old die back door) graph

of cast iron is also called white cast iron because of the white crystalline appearance on the fracture surface, which is hard and brittle, and almost impossible to machine.

The micrographs show that the microstructure of a rear-side portion of the (new method casting piece at a rear-end side) casting is characterized (hardness is constant thought out the cylinder casting with a required amount) distinct graphite flakes with fine sizes uniformly distributed and randomly oriented. This type of graphite is typical of type-graphite as shown in Fig. 10, which is usually preferred for most casting applications.

**Fig. 10** Casting hardness values (by using new die back door) graph



The EDS/EDX analysis of the chilled surface by FE-SEM/EDS result (Fe, Si and C element mass%) is shown in Fig. 9 and also given in Table 3. FE-SEM/EDS analysis of the newly casted casting pieces at a rear-end side of the casting was observed (Fe, Si and C element mass%) and as shown in Fig. 10 and also given in Table 4. Alloy concentration is expressed in atomic per cent (atom %). It can be seen that chill region contains lower Si and C percentage compared to new casting pieces.

**Table 3** EDS analysis for sample 2 (big size—WCI)

Element	At. No.	Mass [%]	Mass norm [%]	Atom[%]	Abs. error [%] (1 sigma)	Rel. error [%](1 sigma)
Fe	26	72.55	81.31	50.12	2.06	2.84
C	6	14.67	16.44	47.12	3.76	25.66
Si	14	2.25	2.25	2.76	0.15	7.46
		89.23	100.00	100.00		

**Table 4** EDS analysis for sample 1 (small size—G.CI)

Element	At. No.	Mass[%]	Mass norm [%]	Atom [%]	Abs. error [%] (1 sigma)	Rel. error [%] (1 sigma)
Fe	26	84.98	87.74	62.67	2.33	2.74
C	6	10.15	10.48	34.80	2.40	23.63
Si	14	1.72	1.78	2.53	2.53	6.95
		96.85	100.00	100.00		

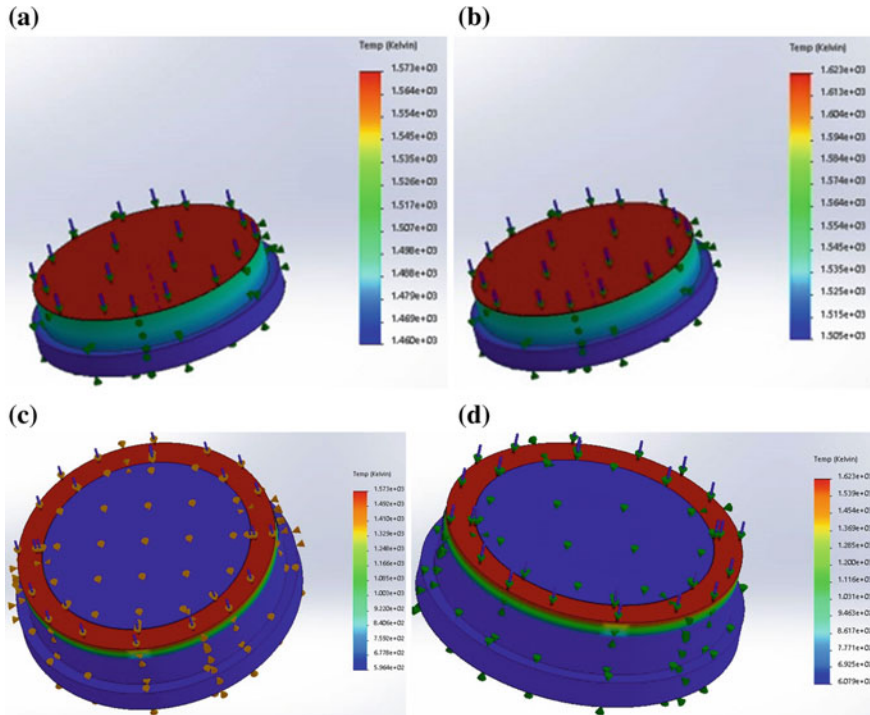


**Fig. 11** Temperature distribution of die back door with bentonite coating {**a** max: 1573 K, min: 1460 K and **b** max: 1623 K, min: 1505 K}. **c, d** Temperature distribution of the die back door with resin sand {**a** max: 1573 K, min: 596.4 K and **b** max: 1623 K, min: 607.9 K}

## 6 Simulation Results

Based on the above simulation, condition's simulation of die back door is carried out. The aim is to simulate the temperature and heat flux field (both temperature and heat flux analysis are shown in Figs. 11 and 12) of the die back door to increase the life of back door and remove the hot spot defect.

## 7 Conclusion

The new method was observed to be free of cementite as compared to an old method, and it gives to the required amount of hardness due to slower cooling rate and additionally promotes hypo-eutectic as-cast grey iron with a uniform distribution of randomly oriented graphite flakes (A-type).

The microstructure of white cast iron is observed after etching, noting that the inter-dendritic cementite (white) appearance. Austenite is formed as the pro-eutectic

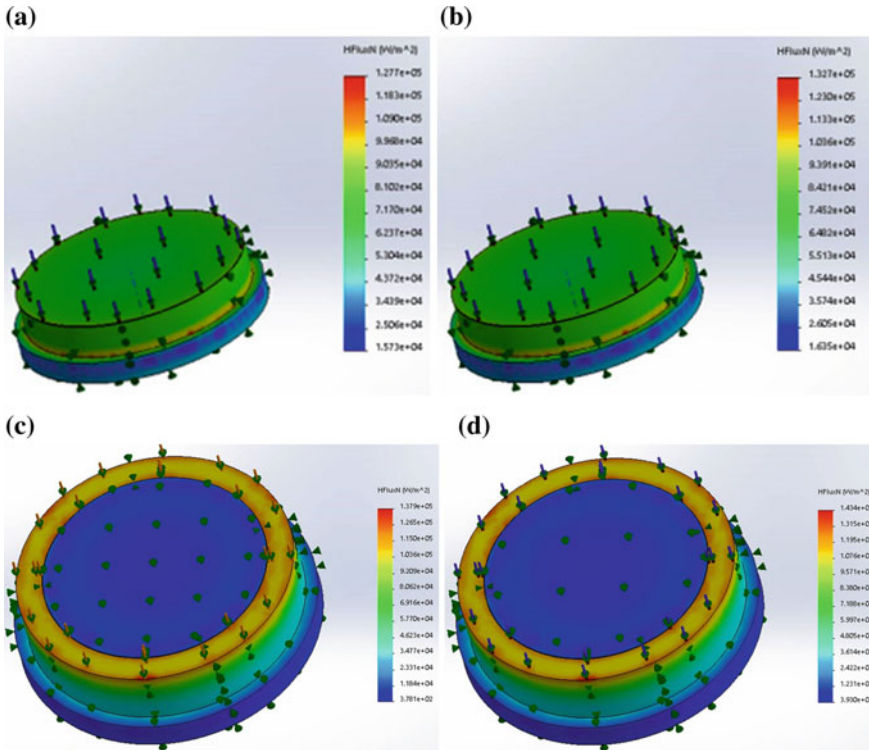


**Fig. 12** Heat flux distribution of die back door with bentonite coating (at 1573 K max heat flux value:  $1.277 \times 10^5$  W/m<sup>2</sup>, min heat flux value:  $1.573 \times 10^4$  W/m<sup>2</sup> and at 1623 K max heat flux value:  $1.327 \times 10^5$  W/m<sup>2</sup>, min heat flux value:  $1.635 \times 10^4$  W/m<sup>2</sup>). **c, d** Heat flux distribution of die back door with resin sand (at 1573 K max heat flux value:  $1.379 \times 10^5$  W/m<sup>2</sup>, min heat flux value:  $3.781 \times 10^2$  W/m<sup>2</sup> and at 1623 K, max heat flux value:  $1.434 \times 10^5$  W/m<sup>2</sup>, min heat flux value:  $3.93 \times 10^2$  W/m<sup>2</sup>)

constituent before the eutectic reaction (liquid transforms to austenite and cementite) and later transforms to pearlite and cementite upon cooling below the eutectoid temperature.

The simulation results show that there is no difference between input temperatures (for old die) and output temperatures, the old die back door faced directly almost pouring temperature, and this temperature affects the die back door and develops the hot spot defect at a particular back door zone, due to cause its life expired within three days. However, new designed to die back doors facing preheat output temperature (this temperature can't affects the die back door), due to cause its life increased up to a minimum one year and eliminate the hot spot defect. Temperature analysis values are shown in Fig. 11. New die back door heat flux values also are favourable, and then, old die back door and its heat flux analysis are shown in Fig. 12.

Die back door with resin sand technique is more effective in minimizing under cooling of metal during a solidification process. Using this technique, the machining

allowance of the casting can be reduced by 14 mm length at the rear end of the casting. The machining allowance of the casting can be reduced by 14 mm length (i.e. 10 mm chilling length +2 mm front and back side machining allowance +2 mm parting ring cutting tool width).

Each one mm length of the casting requires 17.3 grams of metal. Thus, an amount of 242.2 grams of metal, i.e. 6%, can be reduced each casting. It causes the reduction in scrap rate by 6.45%, electrical power consumption by 8.56% and machining cost by 16.65%. Analyses of scrap rate, power consumption and machining cost values are shown in Table 5 (i.e. in the appendix).

**Acknowledgements** The authors would like to gratefully acknowledge to SVCET for providing financial support during the work and also gratefully acknowledge to M/s VACPL, Vijayawada, for allowing carrying out this research work.

## Appendix

See Table 5.

**Table 5** Analysis of scrap rate, power consumption and machining cost

Item	Quantity	Item	Quantity
<i>(i) Scrap rate analysis</i>			
Total number of dies used for producing	20.00 Nos	Average time taken for facing operation/casting	9.7 s
Cylinder castings (i.e. liners) Raw material used per round	75.00 kg	Average time taken for parting operation/casting	61.5 s
Raw material used per/casting (75/20)	03.75 kg	Average time saving to eliminate parting operation (61.5–9.7)/casting	51.8 s
Averagely total castings produced/day	1260 kg		
Total raw material used/day(1260 × 3.75)	4725 kg		
Average parting ring weight	242 g	<b>Average time saving to eliminate parting operation/day (1260 × 51.8)</b>	<b>65,268 s or 18.13 h</b>

(continued)

**Table 5** (continued)

Item	Quantity	Item	Quantity
Total average parting ring weight produced/day (1260 × 242) or day-wise scrap collected through parting rings/day	304.92 kg	Time taken for to make facing operation of 1260 castings (1260 × 9.7)/day	12,222 s or 3.4 h
<b>Scrap rate saved to eliminate parting rings/day {(304.92 × 100)/4725}</b>	<b>6.45%</b>		
<i>(ii) Power calculation</i>		<i>(iii) Machining cost calculation</i>	
		Time taken for to make parting operation of 1260 castings (1260 × 61.4)/day	77,364 s or 21.49 h
Average power used to melt 1 kg of raw material or scrap	0.94 units	Average time taken for ID and OD surface finishing (2 + 2)	4 min
Average power used to melt 4725 kgs of raw material (4725 × 0.94)	4441.5 units	Time taken for to make ID and OD surface finishing of 1260 castings (1260 × 4)	5040 min or 84 h
Power used to melt 304.92 kg of raw material produced through parting ring (304.5 × 0.94)	286.63 units	Total time machining taken for machining (21.49 + 3.4 + 84) 14 workers required for machining operation; each one gets Rs. 10,000 per month (26 working days/month). So one hour machining cost: Averagely Rs. 224.36	108.89 h
Average rejecting castings due to parting operation/day	2.1%		
Total rejected castings/day {(2.1 × 1260)/100}	26.5 castings		
Weight of 26.5 castings (26.5 × 3.75)	99.4 kg		
Power used to melt 99.4 kg of raw material (99.4 × 0.94)	93.44 units	108.89 h machining cost	Rs. 24,430.6

(continued)

**Table 5** (continued)

Item	Quantity	Item	Quantity
Total power used to effect on producing parting ring (286.63 + 93.44)	380.07 units	18.13 h machining cost	Rs. 4067.65
<b>% of power saved to eliminate the parting ring <math>\{(380.07 \times 100)/4441.5\}</math></b>	<b>8.56%</b>	<b>Total machining cost saving to eliminate parting operation/day <math>\{(4067.7 \times 100)/24,430.6\}</math></b>	<b>16.65%</b>

Note Abbreviations, VACPL: Vijayawada alloy casting private limited, SVCET: Sri Venkateswara College of Engineering and Technology)

## References

1. Kim KT (2007) Fabrication and characterization of BSCCO-2212 tube prepared by Centrifugal Casting. *Physica C* 460–463
2. Jones MC (1970) Investigation of centrifugal casting techniques. *Foundry Trade J* 1003–1017
3. Cumberland (1963) Centrifugal casting techniques. *The British Foundry Man* 26–46
4. Thoroddsen ST, Mahadevan L (1997) Experimental study of coating flows in a partially-filled horizontally rotating cylinder. *Exp Fluids* 23(1):1–13
5. Lu S-L, Xiao F-R, Zhang S-J, Mao Yong-Wei, Liao Bo (2014) Simulation study on the centrifugal casting wet-type cylinder liner based on Pro-CAST. *Appl Therm Eng* 73:51019

# Fabrication and Characterization of Functionally Graded Composites Using Friction Stir Processing



B. Venkatesh, T. Sadasiva Rao and Adepu Kumar

**Abstract** Functionally graded materials (FGM) are the composite materials that are heterogeneous wherein the compositions or microstructures vary locally resulting in certain variation in the local material properties. Moreover, certain challenges exist in their manufacturing techniques. In this study, functionally graded composites were manufactured by integrating SiC particles of particle size: 20–30  $\mu\text{m}$  in a groove on aluminium alloy 6082-T6 plate using friction stir processing (FSP) route. Three sets of samples with variation in a volume percentage of SiC along the thickness were processed by one to three passes. The effect of multipass on microstructure, microhardness and wear behaviour of graded materials has been analyzed. The functionally graded composite layer produced with three FSP passes has shown the superior wear resistance of 0.25  $\text{mm}^3/\text{m}$ ; that is, because of its greater microhardness value of 110 HV which is 1.8 times greater than the base metal. The modifications were mainly because of microstructural alterations through FSP, better particle dispersion, decreased particle clustering and fine grain size (6.39  $\mu\text{m}$ ).

**Keywords** FGM · FSP · Silicon carbide · Mechanical properties

## 1 Introduction

FGM is a new concept for implementing the innovative characteristics and/or functions which conventionally homogeneous materials cannot accomplish. A property in an FGM grading reduces thermal stress, residual stress and stress in traditional composites. The designer can customize the material responses to satisfy design criteria by an FGM gradient of material properties [1]. Hence, an FGM has great potential in different areas like structural, aerospace and nuclear energy applications where these materials come to great use as these areas require materials with different grades of hardness and toughness to get the Myriad compositions of functions

---

B. Venkatesh (✉) · T. Sadasiva Rao · A. Kumar  
Department of Mechanical Engineering, Warangal, National Institute of Technology, Warangal,  
Telangana 506004, India  
e-mail: [venkatesh.bnitw@gmail.com](mailto:venkatesh.bnitw@gmail.com)

© Springer Nature Singapore Pte Ltd. 2020  
H. K. Voruganti et al. (eds.), *Advances in Applied Mechanical Engineering*,  
Lecture Notes in Mechanical Engineering,  
[https://doi.org/10.1007/978-981-15-1201-8\\_117](https://doi.org/10.1007/978-981-15-1201-8_117)

1103



such as refractoriness or chemical inertness. Further, FGMs enhance reliability and efficiency. There are different processing methods available today to manufacture FGMs such as physical and chemical vapour deposition, plasma sintering, powder metallurgy, friction stir processing, solid freeform fabrication, etc. [2–4].

Friction stir processing (FSP) is a variation of the friction stir welding (FSW). If so, it is based on the same principles but cannot modify the microstructure of certain areas in order to improve local properties. Recently, FSP was considered as a less costly and versatile process for producing FGM, in which reinforcement particles are packed into a longitudinal groove along which friction stirring takes place which is mainly controlled by rotation and transverse speed of the tool [5–8]. A precise control, homogenization, microstructural refining, densification and variable depth of the processed zone are the advantages that differentiate FSP from other processes. In addition, FSP is environmentally friendly and utilizes less energy without changing its size or shape. FSP may also be utilized for the manufacture of polymer composites. In the energy materials field such as materials in fusion reactors that includes vanadium alloy processing and joining, they play a very vital role. Yoshihiko Hangai et al. fabricated FG aluminium foams by varying the size of the pores and density distribution by employing friction stir processing [9]. J. Gandra et al. attempted to fabricate aluminium-based functionally graded composite by SiC particles using a friction surfacing multilayering approach [10]. Mishra et al. developed surface MMC by friction stir processing and obtained good bonding with Al/SiC composite gradient of 50–200  $\mu\text{m}$ . It was noticed that microhardness of composite doubled with silicon particles up to 27 vol. % [11]. More recently, Miranda et al. reported that compositionally graded surface can be produced in several ways by making U-shaped grooves filled with reinforcement particles or by pre-deposition of particles on the top surface of the substrate before performing FSP and a third way of producing is by preparing consumable tool [12]. The authors in the present article focus on fabrication of functionally graded Al–SiC composite from lower to higher volume fraction of SiC particles (cumulative percentage of 6, 8, and 10%) at different passes.

## 2 Experimental Procedure

AA6082-T6 rolled plates with dimensions 220 mm  $\times$  150 mm  $\times$  6 mm and SiC powder with an average diameter of 20–30  $\mu\text{m}$  was chosen as the matrix and the reinforcement. The chemical constituents of AA6082-T6 are given in Table 1. Three

**Table 1** Elemental composition of the AA6082-T6 (wt%)

Mg	Mn	Fe	Si	Cu	Cr	Al
0.82	0.61	0.29	0.82	0.1	0.23	Bal

types of H13 tool steel with taper cylindrical-threaded pin having 24 mm of shoulder diameter, 8 mm of pin diameter and 6 mm with a length of 5.2 mm (Tool-A), 3.2 mm (Tool-B) and 1.7 mm (Tool-C) were utilized for making functionally graded composites which are shown in Fig. 1. The FSP process was conducted on a friction stir welding machine (NCFWS-3T) at a constant rotational speed of 900 rpm and transverse rate of 20 mm/min. The axis of the tool was inclined by 1° along vertical axis of the surface plate.

Figure 2 shows the schematic representation of fabrication of FG sample using FSP. Initially, a groove is machined on the aluminium plate with measurements of 180 mm × 1.5 mm × 5.4 mm and it is packed with 6% volume ratio of SiC particles. To avoid the escape of SiC particles during the processing, initially, the groove was sealed using tool which has only shoulder without pin through Tool-A, the samples were subjected to single pass and in order to create a functionally graded composite a groove with width of 2.1 mm and depth of 3.2 mm was machined in the middle of

Fig. 1 Tools for making FG composite

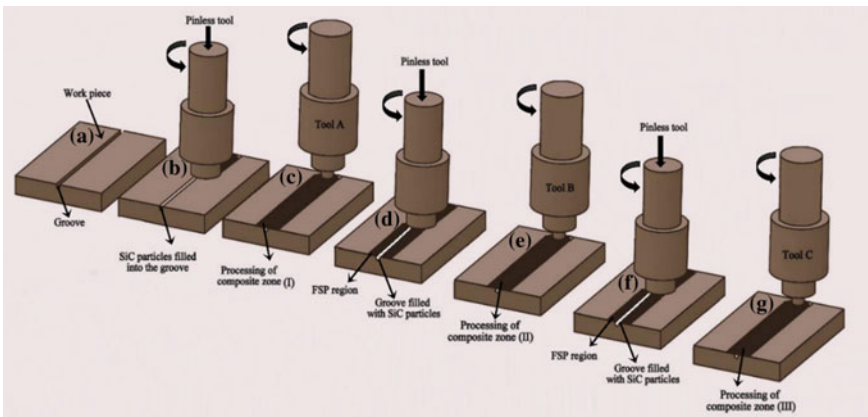
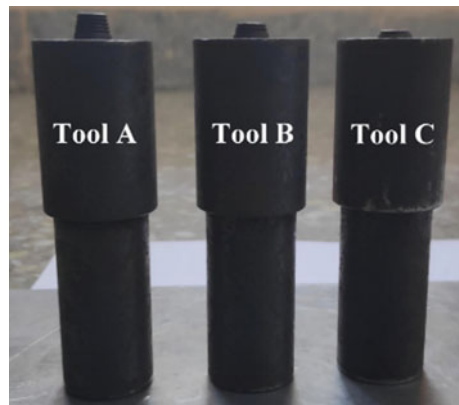


Fig. 2 Schematic diagram of FGM fabrication through FSP

the processed zone and is filled with 8% volume (cumulative) of SiC particles and the same procedures which was followed for Tool-A are repeated with Tool-B and Tool-C by differing number of passes. At last, properties of the fabricated graded composite were evaluated by microhardness, optical microscopy and pin-on-disc equipment.

### 3 Results and Discussion

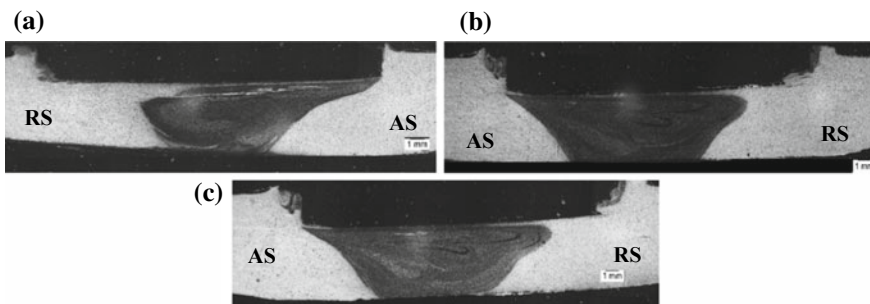
#### 3.1 Microstructure

Microstructural observations were carried out at the nugget zone (NZ) of FG composites which was normal to the FSP direction by using an optical microscope, (Huvtiz, South Korea). The specimens were prepared by polishing and etching was performed using Keller's reagent (2 ml HF, 20 ml HNO<sub>3</sub>, 3 ml HCl, and make it up to 200 ml with H<sub>2</sub>O).

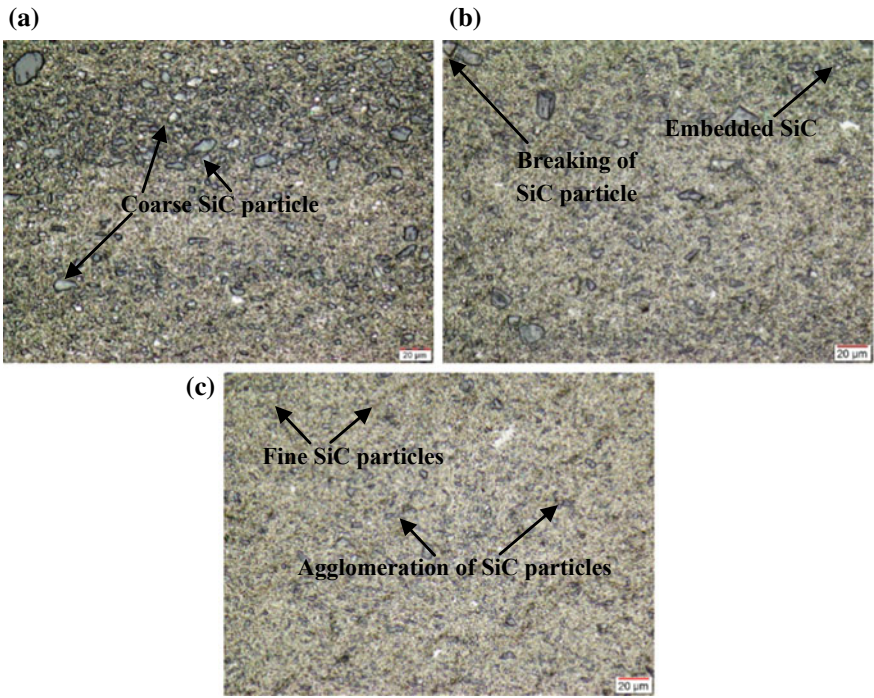
Figure 3a shows the macrograph of a single pass FG sample that has tapered cylindrical-threaded tool where SiC particles are embedded into the aluminium. Figure 3a–c are the macrostructures of the FG sample at different passes. Similarly, Fig. 4a–c show the microstructures of the FG samples at different passes. It is observed that most of the material is moved to the advancing side present in the stir zone. Therefore, plastic flow here is inadequate for the generation of particle recirculation flow [13]. However, the particle distribution in the second pass was increasingly uniform which can be seen in Figs. 3b and 4b.

Figure 4b shows non-uniform particle distribution in the upper as well as lower regions of the stir zone. In order to avoid this, the third pass is applied where the reinforcing particles distribution is uniform in the stir zone, see Fig. 4c.

Figure 5 shows SEM micrographs showing particle distribution of FG samples at different passes where the quality of the stir zone was good; no defects like porosity,



**Fig. 3** Macrographs of FG sample using SiC particles when **a** 1st pass approach is used **b** 2nd pass approach is used **c** 3rd pass approach is used



**Fig. 4** Micrographs of showing particle distribution in FG sample when **a** first pass is used **b** the second pass is used **c** the third pass is used

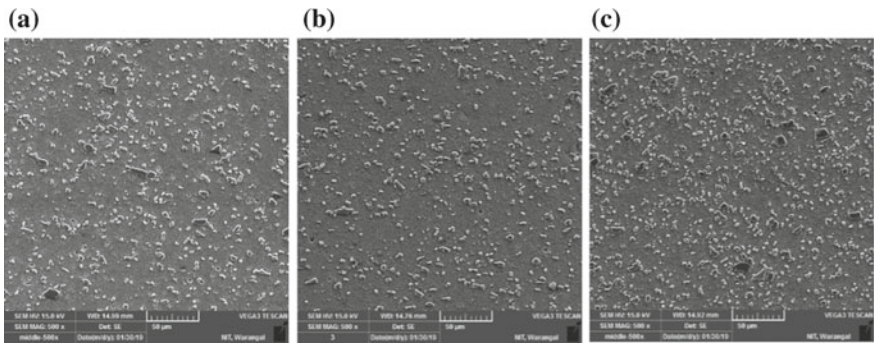


**Fig. 5** SEM micrographs showing particle distribution of FG sample in **a** first pass **b** second pass **c** third pass

blow holes were found. The distribution of particle is generally an important feature of FG sample. Figure. 5c shows the average grain size of  $6.39 \mu\text{m}$  for the third pass which is smaller than  $8.60 \mu\text{m}$  (second pass) and  $12.68 \mu\text{m}$  (third pass). The reason could be due plastic deformation, suitable mixing of particles in the stir zone and breakdown of cluster particles due to an increase in passes.

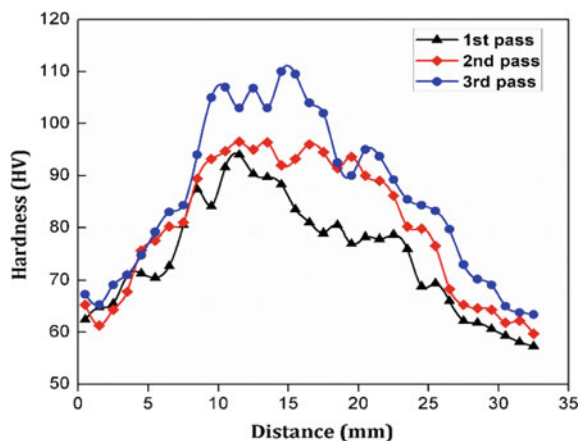
### 3.2 Microhardness

Microhardness profiles were measured across the stir zone using a digital Vickers indenter (ECONOMET, Chennai) with 100 gf load and a dwell time of 10 s. Figure 6 shows the plot of microhardness versus distance for FG samples were the measured hardness values reduces gradually in all the three passes. It tends to be noticed that the increase in silicon carbide volume percentage rises the microhardness of the FG sample. The composite surface layer of 8 wt% of SiC with the third pass showed the highest hardness value of about  $110 \pm 2 \text{ HV}$ . It is observed that at a distance in between 10 and 15 mm, hardness values are shown to be high due to severe plastic deformation and frictional heat during FSP results in the formation of fine recrystallized grains in the stir zone.

After the first pass, there is significant variation in the hardness due to the void occurrence and non-uniform material distribution in the stir zone. But the distribution of hardness is even more homogeneous with an increased number of passes, where the average hardness in stir zone rises from  $82 \pm 3 \text{ HV}$  to  $93 \pm 3 \text{ HV}$ . This is due to grain refinement and uniform particle distribution achieved by FSP.

In the third pass, the particle distribution is more uniform when compared with the second pass, where the hardness is  $110 \pm 2 \text{ HV}$  which is probably due to an agglomeration of particles. The increasing values of microhardness in FG composites are

**Fig. 6** Profile of microhardness along the stir zone using different passes



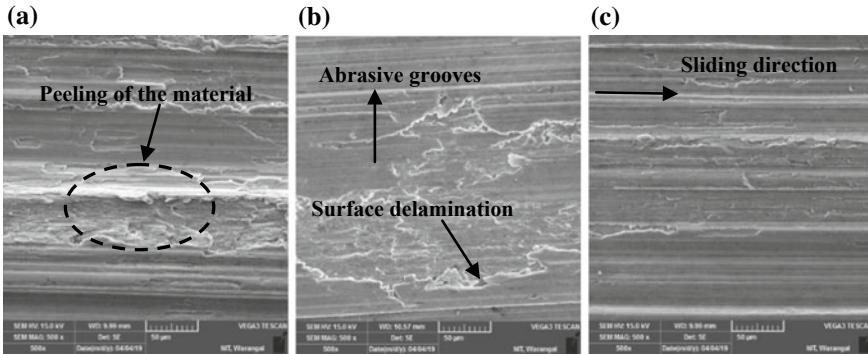


**Fig. 7** Worn-out surface at 5N load at **a** first pass **b** second pass **c** third pass

mainly by the reason of grain refinement which is caused by dynamic recrystallization along with Orowan strengthening effect [14]. The hardness values increased from 82 HV to 110 HV because of induced development of strain and the pinning effect of SiC particles.

### 3.3 Wear Analysis of FG Composite

The wear performance of FG composite at different passes was conducted by a pin-on-disc machine at a sliding distance of 75 m and applied a load of 5 N. In FG composite after wear, non-uniform wear consisting of grooves, microcutting and scratches, which are formed by reinforcing materials are noticed in Fig. 7. After the wear test, the surface observed is non-uniform wear consisting of grooves, microcutting and scratches that are formed due to reinforcing particles which indicate that wear is caused due to abrasion. The wear surface also shows delamination resulting in the subsurface crack which grow gradually and ultimately shear onto a surface forming a thin layer.

The wear rates of FG composite for the 1st pass, 2nd pass and 3rd pass were  $0.3386 \pm 2 \text{ mm}^3/\text{m}$ ,  $0.30425 \pm 1 \text{ mm}^3/\text{m}$  and  $0.25477 \pm 1 \text{ mm}^3/\text{m}$ . Improvement in wear resistance in third pass composite is due to its higher hardness value and uniform dispersion of SiC particles in the matrix. Hence, the surface examination shows that wear is more for the sample which has less number of pass.

## 4 Conclusions

A new process of fabricating functionally graded composites using friction stir processing is conferred with variation in volume percentage along with the thickness. From the present study, following conclusions are drawn.

- Microstructural observations showed that the dispersion of SiC particles in AA6082-T6 matrix was homogeneous.
- It is found that the optimal distribution of reinforcing particles has been achieved by means of three FSP passes, which increase hardness and wear resistance.
- In the FG sample, the highest microhardness of 110 HV was obtained which is 1.8 times greater than the base metal.
- The superior wear performance of fabricated FG sample can be attributed due to increased microhardness, hard ceramic particles and grain refinement of the matrix.

**Acknowledgements** The authors acknowledge the Department of Mechanical Engineering, National Institute of Technology-Warangal, India, for providing the research facilities to carry out the work.

## References

1. Kawasaki A, Watanabe R (1997) Concept and P/M fabrication of functionally gradient materials. *Ceram Int* 8842:73–83
2. Miyamoto I, Yoshinari (1999) *Functionally graded materials: design, processing, and applications*. Springer Science & Business Media
3. Naebe M, Shirvanimoghaddam K (2016) Functionally graded materials: a review of fabrication and properties. *Appl Mater Today* 5:223–245
4. Parihar RS, Setti SG, Sahu RK (2018) Recent advances in the manufacturing processes of functionally graded materials: a review. *IEEE J Sel Top Quantum Electron* 25:309–336
5. Suresh S, Mortensen A (1998) *Fundamentals of functionally graded materials*. The Institute of Materials
6. Mishra R, Ma Z (2005) Friction stir welding and processing. *Mater Sci Eng* 50:1–78
7. Thomas WM, Nicholas ED, Needham JC, Murch MG, Temple-Smith P, Dawes CJ (1991) International patent application no. PCT/GB92/02203 and GB patent application no. 9125978.8 and US patent application no. 5,460,317
8. Nandan R, DebRoy T, Bhadeshia HKDH (2008) Recent advances in friction-stir welding - process, weldment structure and properties. *Prog Mater Sci* 53:980–1023
9. Hangai Y, Oba Y (2011) Fabrication of A1050-A6061 functionally graded aluminum foam by friction stir processing route. *Metall Mater Trans A* 42:3585–3589
10. Gandra J, Mirandaa R, Vilaca P, Velhinho A, Teixeira JP (2011) Functionally graded materials produced by friction stir processing. *J Mater Process Technol* 211:1659–1668
11. Mishra RS, Ma ZY, Charit I (2003) Friction stir processing: a novel technique for fabrication of surface composite. *Mater Sci Eng A* 341:1–4
12. Miranda RM, Santos TG, Gandra J, Lopes N, Silva RJC (2013) Reinforcement strategies for producing functionally graded materials by friction stir processing in aluminium alloys. *J Mater Process Technol* 213:1609–1615

13. Yang M, Xu C, Wu C, Lin KC, Chao YJ, An L (2010) Fabrication of AA6061/Al<sub>2</sub>O<sub>3</sub> nano ceramic particle reinforced composite coating by using friction stir processing. *J Mater Sci* 45:4431–4438
14. Cavaliere P (2005) Mechanical properties of friction stir processed 2618/Al<sub>2</sub>O<sub>3</sub>/20p metal matrix composite. *Compos Part A* 36:1657–1665



# Multi-Parametric Optimization of Electrical Discharge Machining of Inconel-690 Using RSM-GRA Technique



Bhavani Marturi, Murahari Kolli, Adepu Kumar, Seelam Pichi Reddy and Sai Naresh Dasari

**Abstract** In many industries, alloys of nickel have extensive range of applications for their noteworthy properties like corrosion resistance, high temperature tolerance and resistance to creep rupture. Nickel-chromium (Ni 690) alloys being precipitation hardenable are broadly employed in aircraft structures, gas turbines, rocket engine thrust chambers, pressure vessels and nuclear reactors. Machining of Inconel 690 is very hard by traditional routes because of their strong strain hardening nature, poor thermal conductivity and high strengths at very high temperatures. EDM has a thermal process which can be used irrespective of workpiece strength and hardness, to machine Inconel 690 alloy by electrical erosion. In this paper, the investigation of chosen input parameters current ( $I_p$ ), pulse on time ( $T_{on}$ ), gap voltage ( $V$ ) and pulse off time ( $T_{off}$ ) of EDM on Ni-690 alloy on resulting process parameters like surface roughness (SR) and material removal rate (MRR) is considered. Primarily, the experiments were planned and designed with RSM-CCD approach. Grey relational analysis (GRA) was adapted to multi optimize the performance parameters on MRR and SR. In further stages, analysis of variance (ANOVA) approach was selected to reveal the impact of the variables on the performance characteristics of SR and MRR. GRA results show that the EDM performance in the Ni-690 machining process can be improved at confirmation test conditions.

**Keywords** EDM · Inconel-690 alloy · RSM-GRA · Multi optimization

---

B. Marturi · M. Kolli (✉) · S. Pichi Reddy · S. Naresh Dasari  
Department of Mechanical Engineering, Lakireddy Bali Reddy College of Engineering,  
Mylavaram, Andhra Pradesh 521230, India  
e-mail: [kmhari.nitw@gmail.com](mailto:kmhari.nitw@gmail.com)

A. Kumar  
Department of Mechanical Engineering, National Institute of Technology Warangal, Warangal,  
Telangana State 506004, India

## 1 Introduction

Nickel-based alloys can perform satisfactorily at high temperatures with outstanding corrosion resistance and mechanical properties. These materials have extensive applications in manufacturing of jet engine components, combustion chambers, turbine bodies, turbine blades, tanks, exhaust valves, etc. [1, 2]. Inconel 690 alloy has high strength, superior hardness and poor thermal conductivity because of these reasons it is not favourable to cut these materials through conventional routes. Hence, in order to obtain a complex geometry while machining in the end product of Inconel 690 alloy with appreciable dimensional accuracies, non-traditional machining process such as electrical discharge machining (EDM) is being employed [3]. Rahul et al. attempted EDM studies on various materials like Inconel 601, 625, 718 and 825 alloys and successfully considered five-factor four-level  $L_{16}$  orthogonal array (OA) for variables such as  $T_{on}$ ,  $I_p$ ,  $V$ , duty factor (%) and flushing pressure for yielding suitable parameters of machining for good electrode wear rate (EWR), surface crack density (SCD), SR and MRR [4].

Neelesh Singh et al. discussed cryogenically cooling the electrode, machined Inconel 601 alloy through EDM process with various electrodes and also reported significant improvements in MRR and SR of the workpiece and reduced tool wear rate (TWR) by up to 33% when compared to conventional copper electrode [5]. Upadhyay et al. attempted to optimize machining parameters during EDM on Inconel 601 alloy by applying utility-based Taguchi method evaluating SCD and white layer thickness (WLT) by the machinability [6]. Torres et al. investigated the effect on EDM variables for different polarities of graphite electrode's EWR, MRR and SR of Inconel 600 alloy. It concluded that negative polarity results were higher MRR, lower TWR, and superior SR was obtain [7]. Rao and Venkaiah studied influencing parameters of WEDM of Inconel 690 alloy on micro-hardness and SR in addition to recast layer thickness (RLT) and compared the parent metal's hardness with EDM'ed surface hardness and reported an inverse proportionate relation of recast layer microhardness and RLT with WEDM variables [8]. Using modified flower pollination algorithm, Rao et al. were successful in estimating precise values of global responses in optimization of Inconel 690 alloy on WEDM variables. They also introduced a new two-stage initialization theory comparing RSM and FPA methods. It is concluded that  $T_{on}$  and  $I_p$  and their interaction had influenced SR and MRR. This data has given a field of future research to industry [9]. To predict machining performance on Inconel 690 alloy, an advancement was attempted by Binayak et al. on an intellectual ANFIS-based system [10].

The reviewed literature on Inconel 690 alloy revealed that it is a challenging task to machine Inconel 690 alloy because of supreme temperature resistance, excessive stressing of cutting edges and pressure at petite area throughout the machining process in conventional processing. Also, a very scarce amount of research is available in WEDM process and almost no research was reported on EDM of Inconel 690 alloy. Hence, in the current study, multi optimization by RSM-GRA approach is employed

to maximize MRR and minimize SR. Furthermore, ANOVA analysis was employed to reveal the significance of the parameters and their contributions.

## 2 Experimental Setup

The tests are conducted using die-sinking EDM of Electronica CNC export 1 model as shown in Fig. 1. The workpiece is made of Inconel 690 alloy with dimensions  $100 \times 75 \times 7$  mm. The electrode is a copper rod of length 70 mm and diameter  $\text{Ø}10$  mm. The machining surface of the workpiece and the contact surface of the electrode are polished prior to the commencement of the experimentation using emery papers of various grades. Both the workpiece and the tool are flooded by the EDM oil at a flushing pressure of  $0.90 \text{ kg/cm}^2$ . EDM spark erosion 450-grade oil is used as the dielectric fluid. Mass loss of tool and workpiece are calculated to find TWR and MRR, respectively. The input process parameters and their corresponding layouts used for experimentation are shown in Table 1. MRR and SR are the chosen performance characteristics in this study. The responses of these performance characteristics are in turn used to evaluate the performance of EDM process by varying the levels of input parameters.

**Fig. 1** Experimental setup of die-sink EDM

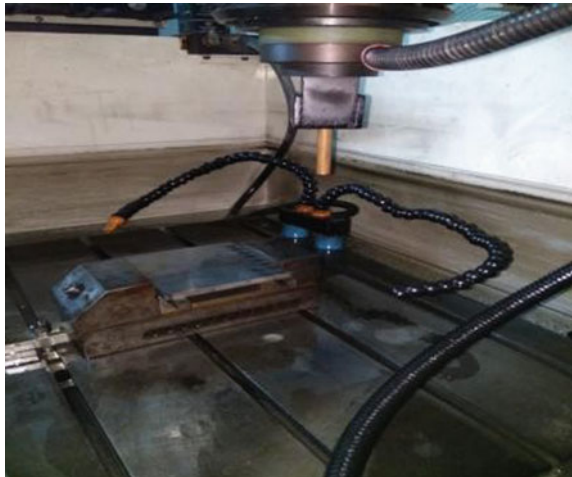


**Table 1** Experimental layout and their values

Ex. No.	Current (A)	Ton (B)	Voltage (C)	Toff (D)	MRR (mm <sup>3</sup> /min)	SR (μm)
1	6	45	50	33	22.1793	5.98
2	12	45	50	54	24.5873	6.46
3	9	15	50	33	25.8123	5.49
4	9	45	50	12	16.6765	6.97
5	9	75	50	33	28.9742	6.34
6	9	45	70	33	24.0209	5.23
7	9	45	50	33	26.2347	5.87
8	9	45	30	33	31.2913	6.39
9	9	45	50	33	26.2536	5.98
10	9	45	50	33	26.2537	5.85
11	12	15	30	54	24.7703	8.11
12	12	15	70	12	25.7843	6.52
13	9	45	50	33	25.7865	5.78
14	6	75	70	12	11.4705	6.89
15	6	75	30	54	30.6689	7.17
16	12	75	30	12	28.0143	6.84
17	6	15	30	12	24.3517	7.27
18	9	45	50	33	26.2314	5.79
19	12	75	70	54	34.7376	5.81
20	6	15	70	54	16.0762	5.11
21	12	75	30	54	39.6263	6.45
22	6	75	70	54	19.3907	6.39
23	9	45	50	33	26.1253	5.73
24	12	15	70	54	23.6875	5.96
25	12	15	30	12	25.6334	8.37
26	6	15	30	54	23.8083	6.78
27	12	75	70	12	22.5245	6.45
28	6	15	70	12	18.4127	5.76
29	6	75	30	12	24.1567	7.89
30	9	45	50	33	26.5245	5.82

### 3 Design of Experiments

#### 3.1 Response Surface Methodology (RSM)

RSM is a statistical method to represent optimum variable factors and developing responses for performance measures, i.e. MRR and SR. In the present study, RSM central composite design (CCD) is used. CCD has been the most noteworthy technique among the various classes of RSM designs available for its consecutiveness, flexibility and efficiency in providing the net experimental error in minimum runs.

#### 3.2 Grey Relational Analysis (GRA)

GRA is an incidence analysis method in grey system theory initially established by Dr. Deng which effectively identifies the uncertainty in knowledge in a given system. RSM method along with GRA is being employed for optimizing the EDM process parameters with multi-performance characteristics. In grey relation generation, MRR and a corresponding higher the better (HB) criterion can be expressed as:

$$x_i(k) = \frac{y_i(k) - \min y_i(k)}{\max y(k) - \min y(k)} \tag{1}$$

Similarly, SR and lower the better (LB) criterion can be expressed as:

$$x_i(k) = \frac{\max y_i(k) - y_i(k)}{\max y_i(k) - \min y_i(k)} \tag{2}$$

The original sequence is to be normalized if a definite target value is to be attained. This can be done in the form:

$$x_i(k) = 1 - \frac{|y_i(k) - OB|}{\max\{\max y_i(k) - OB, OB - \min y_i(k)\}} \tag{3}$$

where OB is the target value. Instead, the native order can be normalized by dividing the original sequence by first value of sequence.

$$x_i(k) = \frac{y_i(k)}{y_i(1)}$$

where

- $x_i(k)$  value after grey relation generation (data processing),
- $y_i(k)$  original sequence,
- $\max y_i(k)$  largest value of  $y_i(k)$  for the  $k$ th response,

$\min y_i(k)$  smallest value of  $y_i(k)$  is the desired value.

$y_i(k)$  ( $k = 1, 2, 3, \dots, m$ ) is ideal sequence for the responses. Furthermore, a grey relation coefficient (GRC) is calculated in order to establish a relation for actual and ideal normalized experimental results while pre-processing the data using the expression:

$$\xi_i(k) = \frac{\Delta_{\min} + \zeta \Delta_{\max}}{\Delta_{0i}(k) + \zeta \Delta_{\max}} \quad (4)$$

where  $\Delta_{0i}(k)$  are the deviation sequence of the reference sequence  $x_i(k)$  and the comparability sequence  $y_i(k)$ ;  $\Delta_{0i} = \|x_0(k) - x_i(k)\|$  = difference of the absolute value between  $x_0(k)$  and  $x_i(k)$ ;  $\zeta$  = Distinguishing coefficient (0 ~ 1)

$$\begin{aligned} \Delta_{\min} &= \forall j^{\min} \in i \forall k^{\min} \|x_0(k) - x_i(k)\| \\ \Delta_{\max} &= \forall j^{\max} \in i \forall k^{\max} \|x_0(k) - x_i(k)\| \end{aligned}$$

The average of grey relational coefficient gives the grey relational grade ( $\gamma$ ) (GRG)

$$\gamma_i = \frac{1}{n} \sum_{k=1}^n \xi_i(k) \quad (5)$$

Also, the capability of comparability sequences to influence reference sequence is reported by GRA. Hence, the GRG's for the reference sequence and comparability sequences would be greater than other GRG's when a comparability sequence is comparatively more significant than the other comparability sequence and reference sequences. In this technique, the comparability sequence and reference sequence both are given equal preference [11].

## 4 Results and Discussion

The sequential procedure of RSM with GRA for EDM of Inconel 690 alloy is as follows:

1. Record the test results for MRR and SR.
2. Normalize the test results of MRR and SR.
3. Find out the equivalent GRC.
4. Find out the GRG by assigning suitable weights to the components.
5. Estimate the ANOVA analysis results.
6. Identify the best possible levels and conditions of EDM variables.
7. Conduct the confirmation tests.

At the initial stage, the tests are run and results are tabulated in Table 1 of Sect. 2. Normally, MRR is considered as larger the better and SR is considered as smaller

the better. In general, all MRR and SR experimental values are transformed to normalized values and substituted in Eqs. 1 and 2 respectively and also the results are tabulated in Table 2. As mentioned earlier by Deng, improved performance is indicated by larger normalized values and the higher normalized values are unity. Further, using Eq. 3, GRC of initially recorded MRR and SR parameters are calculated. The calculated deviation sequence ( $\Delta_i$ ) values are mentioned in Table 3. For obtaining

**Table 2** Normalized values

S. No.	MRR (larger the better)	SR (smaller the better)
Ideal sequence	1	1
1	0.3803	0.7331
2	0.4659	0.5859
3	0.5094	0.8834
4	0.1849	0.4294
5	0.6217	0.6227
6	0.4457	0.9632
7	0.5244	0.7669
8	0.7040	0.6074
9	0.5250	0.7331
10	0.5250	0.7730
11	0.4724	0.0798
12	0.5084	0.5675
13	0.5085	0.7945
14	0.0000	0.4540
15	0.6819	0.3681
16	0.5876	0.4693
17	0.4575	0.3374
18	0.5243	0.7914
19	0.8264	0.7853
20	0.1636	1.0000
21	1.0000	0.5890
22	0.2813	0.6074
23	0.5205	0.8098
24	0.4339	0.7393
25	0.5030	0.0000
26	0.4382	0.4877
27	0.3926	0.5890
28	0.2466	0.8006
29	0.4506	0.1472
30	0.5347	0.7822

**Table 3** Deviation sequences

S. No.	MRR (larger the better)	SR (smaller the better)
Ideal sequence	1	1
1	0.6197	0.2669
2	0.5341	0.4141
3	0.4906	0.1166
4	0.8151	0.5706
5	0.3783	0.3773
6	0.5543	0.0368
7	0.4756	0.2331
8	0.2960	0.3926
9	0.4750	0.2669
10	0.4750	0.2270
11	0.5276	0.9202
12	0.4916	0.4325
13	0.4915	0.2055
14	1.0000	0.5460
15	0.3181	0.6319
16	0.4124	0.5307
17	0.5425	0.6626
18	0.4757	0.2086
19	0.1736	0.2147
20	0.8364	0.0000
21	0.0000	0.4110
22	0.7187	0.3926
23	0.4795	0.1902
24	0.5661	0.2607
25	0.4970	1.0000
26	0.5618	0.5123
27	0.6074	0.4110
28	0.7534	0.1994
29	0.5494	0.8528
30	0.4653	0.2178

GRC, distinguishing coefficients  $\zeta$  are plugged into Eq. 4.  $\zeta$  is in the range of 0–1, in the present study  $\zeta$  is taken as 0.5. The GRGs are calculated by substituting Eq. 5 and the values are represented in Table 4.



**Table 4** Grey relational coefficient and grade for each performance

Number	Grey relational coefficient		Grey relational grades	
	MRR	SR	Average value	Rank
1	0.3495	0.5551	0.452	17
2	0.3840	0.4457	0.415	21
3	0.4043	0.7407	0.573	5
4	0.2900	0.3685	0.329	26
5	0.4681	0.4688	0.468	14
6	0.3753	0.9005	0.638	3
7	0.4118	0.5882	0.500	11
8	0.5294	0.4589	0.494	12
9	0.4122	0.5551	0.484	13
10	0.4122	0.5946	0.503	10
11	0.3869	0.2657	0.326	28
12	0.4038	0.4350	0.419	19
13	0.4039	0.6184	0.511	8
14	0.2498	0.3788	0.314	30
15	0.5114	0.3451	0.428	18
16	0.4467	0.3856	0.416	20
17	0.3804	0.3345	0.357	25
18	0.4118	0.6149	0.513	7
19	0.6573	0.6080	0.633	4
20	0.2848	1.0000	0.642	2
21	1.0000	0.4476	0.724	1
22	0.3166	0.4589	0.388	23
23	0.4098	0.6365	0.523	6
24	0.3704	0.5609	0.466	16
25	0.4012	0.2498	0.326	29
26	0.3721	0.3940	0.383	24
27	0.3541	0.4476	0.401	22
28	0.3065	0.6255	0.466	15
29	0.3774	0.2808	0.329	27
30	0.4171	0.6046	0.511	9

#### 4.1 Statistical Analysis of GRG

From the obtained GRG data, statistical analysis was carried out, through RSM-CCD approach by using statistical software Design of expert<sup>®</sup> 11.0. The trial conditions

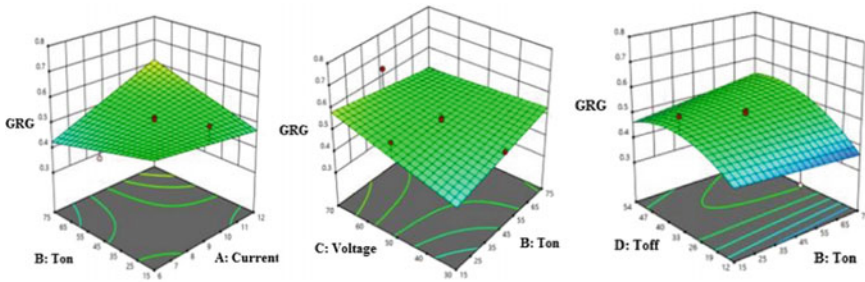


**Fig. 2** Response surface plots show the two variable on GRG (A: B, B: C and B: D)

and obtained results are tabulated in Table 1. GRG regression analysis was employed to reveal the relation between input variables and GRGs in Table 4.

### 4.2 ANOVA and Mathematical Model for GRG

The quadratic model of GRG results analyzed by ANOVA reported many irrelevant terms in the model. Hence, in order to improve the model, the reduction of the model is carried out by backward elimination process which eliminated the non-influencing parameters and adjusted the fixed quadratic model simultaneously holding the hierarchy of the model. The *F*-value at 11.47 with its probability less than 0.01% indicates that the model is significant for GRG.

The values of  $\text{prob} > F < 0.01\%$  indicates the importance of the model conditions. Values which are  $> 0.1000$  point out that the model terms are not important. In this GRG model, A, C, D,  $A * B$ ,  $B * C$ ,  $B * D$ , and  $D^2$  are significant model terms. The lack of fit *F*-values of 25.43 implies the model to fit with the experimental data. The response model fits better to the experimental (actual) data and shows less variation between the predicted and actual values, when it approaches unity. The values of  $R^2$  and  $R^2$  (pred.) for GRG models are 0.8137 and 0.7427, respectively (Table 4). Table 4 observed the ANOVA results for GRG. Response surface plots on the GRG observed in Fig. 2.

### 4.3 The Equation of Regression for GRG

Second-order regression equation for the performance attributes of GRG in terms of input variables can be expressed by the following equation,

$$\text{GRG} = 0.5121 + 0.0314939 \times A + 0.03245 \times C + 0.0577 \times D + 0.06412 \times AB - 0.0476 \times BC + 0.029 \times BD - 0.069 \times D^2.$$

**Table 5** ANOVA results for the GRG

Source	Sum of SS	DoF	Mean SS	F-value	p-value	
Model	0.2583	8	0.0323	11.47	<0.0001	Significant
A-Current	0.0174	1	0.0174	6.19	0.0213	
B-Ton	0.0011	1	0.0011	0.4035	0.5322	
C-Voltage	0.0189	1	0.0189	6.73	0.0169	
D-TOFF	0.0603	1	0.0603	21.42	0.0001	
AB	0.0658	1	0.0658	23.37	<0.0001	
BC	0.0363	1	0.0363	12.89	0.0017	
BD	0.0135	1	0.0135	4.78	0.0403	
D <sup>2</sup>	0.0385	1	0.0385	13.69	0.0013	
Residual	0.0591	21	0.0028			
Lack of fit	0.0582	15	0.0039	25.43	0.0003	Significant
Pure error	0.0009	6	0.0002			
Total	0.3174	29				

GRG versus A and B are plotted in Fig. 2. If GRG increases B decreases if GRG decreases then A increases. Based on the response curve of GRG, higher current the spark intensity is higher resulting in increased the heat flux within the gap. From this graph, it is found that maximum GRG is achieved between 0.40 and 0.65 when current is 12 A (Table 5).

#### 4.4 Confirmation Tests

The confirmation tests are processed to verify the performance characteristics improvement, after the best possible EDM variables set was obtained. Confirmation runs are compared with the grey theory prediction of the designed operating parameters and outcome of the orthogonal array [12]. GRA prediction and experimental results are normal errors that are obtained, so multiple optimization techniques are useful for reduced the SR and enhanced the MRR (Table 6).

**Table 6** Conformation results for MRR and SR model

Optimum combination				MRR	SR	Error
Current	Pulse on time	Voltage	Pulse off time	(mm <sup>3</sup> /min)	(μm)	%
A(I <sub>p</sub> )	B(T <sub>on</sub> )	C(V)	D(T <sub>off</sub> )			
6	15	30	12	24.3417	7.17	5.67
9	15	30	12	28.6754	4.49	4.39
12	75	30	40	39.8767	4.55	6.85

## 5 Conclusion

The above work has successfully proposed a hybrid approach of RSM-GRA for EDM process and studied the effect of input parameters on response characteristics like MRR and SR. Optimization of the multiple responses was converted into optimization of a single response performance parameter by using GRA. The conclusions drawn from the present work are as follows.

- The highest MRR value 39.6263 mm<sup>3</sup>/min was obtained at  $I_p$ -12,  $T_{on}$ -75, V-30 and  $T_{off}$ -40.
- Lower SR was found as 4.55 μm at  $I_p$ -12,  $T_{on}$ -75, V-30 and  $T_{off}$ -40.
- Variations in the values of current, voltage and pulse off time and their interaction responses have shown significant influence over MRR and SR.
- The found MRR and SR quadratic models are statistically significant for analysis as reported by fit summary.
- The empirical equations of GRG were formed through the RSM-CCD approach, and the error between experimental and predicted values is lying within the range.

## References

1. Bunsch A, Kowalska J, Witkowska M (2012) Influence of die forging parameters on the microstructure and phase composition of Inconel 718 alloy. *Arch Mech Mat* 57(4):929–935
2. Guan H, Cai Z, Ren Y, Jing J, Wang W, Zhu M (2017) Impact-fretting wear behavior of Inconel 690 alloy tubes effected by pre compressive stress. *J Al Com* 724, 910–920
3. Rahul DS, Biswal BB, Mahapatra SS (2019) Machinability analysis of inconel 601, 625, 718 and 825 during electro-discharge machining: on evaluation of optimal parameters setting measurement. <https://doi.org/10.1016/j.measurement.019.01.065>
4. Blaizot J, Chaise T, Nelias DM (2015) Constitutive model for nickel alloy 690 (Inconel 690) at various strain rates and temperatures. *Int J Pla* 80:139–153
5. Neelesh S, Routara BC, Nayak RK (2018) Study of machining characteristics of Inconel 601 with cryogenic cooled electrode in EDM using RSM. *Proc* 5:24277–24286
6. Upadhyay C, Datta S, Masanta M, Mahapatra SS, Manoj M (2017) An experimental investigation emphasizing surface characteristics of electro discharge machined Inconel 601. *J Braz Soc Mech Sci Eng* 39(8):3051–3066
7. Torres A, Puertas I, Luis CJ (2016) EDM machinability and surface roughness analysis of INCONEL 600 using graphite electrodes. *Int J Adv Manu* 84(9–12):2671–2688
8. Rao MS, Venkaiah N (2018) Experimental investigations on surface integrity issues of Inconel-690 during wire cut electrical discharge machining process. *J Eng Manu* 232(4):731–741
9. Sreenivasa RM, Venkata Naresh Babu A, Venkaiah N (2018) Modified flower pollination algorithm to optimize WEDM parameters while machining Inconel-690 alloy. *Mat Today Proc* 5(2):7864–7872

10. Sen U, Mandal K, Mondal SP (2017) Advancement of an intelligent system based on ANFIS for predicting machining performance parameters of Inconel 690—A perspective of metaheuristic approach. *Measurement* 109:9–17
11. Kolli M, Kumar A (2016) Optimization of the parameters for the surfactant added edm of a Ti-6Al-4V alloy using the Gra-Taguchi method. *Mat Tech* 50(2):229–238
12. Kolli M, Kumar A (2017) Surfactant and graphite powder assisted electrical discharge machining of titanium alloy. *J Manu* 231(4):641–657

# Effect of Nanoparticles Addition on Microstructural and Mechanical Properties of Friction Stir Welded 2014 Aluminium Alloy



Kethavath Kranthi Kumar, Adepu Kumar and Divya Sachan

**Abstract** Effect of aluminium oxide nanoparticles ( $\text{Al}_2\text{O}_3$  NPs) was studied on the microstructural and mechanical properties of friction stir welded 2014 aluminium alloy to overcome softening in nugget zone. A joint with and without  $\text{Al}_2\text{O}_3$  NPs was welded to compare the microstructure, tensile and hardness results. Optical and scanning electron microscope (SEM) was used for investigation of distribution, grain size and grain structure in the stir zone. Transverse tensile test and hardness across the weld surface were carried out to compare the mechanical properties of the joints. The FSW parameters fixed throughout the experiments were 1100 rpm, 30 mm/min of rotation speed and traverse speed, respectively. Microstructure observation indicated that the  $\text{Al}_2\text{O}_3$  NPs were distributed uniformly after the third pass and the  $\text{Al}_2\text{O}_3$  NPs settled at the grain boundaries in the stir zone which leads to an increase in the weld strength. The grain refinement was successfully achieved after reinforcing nanoparticles in the stir zone of FSW joint. The tensile strength of reinforced FSW joint got enhanced about 22% to that of normal FSW joint. Due to a decrease in grain size and the presence of nanoparticles in the stir zone, the average hardness across the stir zone of the reinforced joint was improved.

**Keywords** Aluminium oxide nanoparticles · Grain refinement · Softening

## 1 Introduction

Due to the high strength to weight ratio and good corrosion properties, aluminium alloys are widely used in automobile, defence and marine industries [1]. The most important issue with the fusion welding of aluminium alloys is softening at the weld nugget due to the dissolution of strengthening precipitates and decrease in dislocation density [2]. FSW is a solid-state joining method where a tool with a pin at its end is plunged into the abutting edges of the joint and traversed with specified

---

K. Kranthi Kumar · A. Kumar (✉) · D. Sachan  
Department of Mechanical Engineering, National Institute of Technology, Warangal, Telangana  
506004, India  
e-mail: [kranthikethavath@student.nitw.ac.in](mailto:kranthikethavath@student.nitw.ac.in)

© Springer Nature Singapore Pte Ltd. 2020  
H. K. Voruganti et al. (eds.), *Advances in Applied Mechanical Engineering*,  
Lecture Notes in Mechanical Engineering,  
[https://doi.org/10.1007/978-981-15-1201-8\\_119](https://doi.org/10.1007/978-981-15-1201-8_119)

1127

rotation and travel speed. Heat is generated due to friction between tool shoulder and workpiece material as well as severe plastic deformation occurs where material gets soften around the rotating pin and the material is pushed back to form a joint. The temperature reached during this process is below the solidus temperature of the metal. FSW was invented by W. Thomas (TWI) in the UK in 1991 [3]. Friction stir processing (FSP), a new surface modification method similar to that of FSW, has been developed for grain refinement along the processed line, to produce a surface composite by adding different sized reinforcements [4]. AA2014 is precipitation hardened high-strength aluminium alloy and is very challenging to get higher joint efficiency due to formation of a soft region in the nugget zone. Researchers have focused on improving the joint properties by adding different reinforcing particles such as SiC, TiC and Ti particles into the stir zone to improve joint properties.

Microstructural evolution, grain refinement and mechanical properties of the aluminium alloys have been studied till now by various researchers in the literature. Al<sub>2</sub>O<sub>3</sub> NPs have extensively used in preparing surface nanocomposite to improve the mechanical properties of the aluminium alloy surfaces. Sun et al. [5] developed a novel method by adding ceramic particles in the stir zone to completely change the stir zone to metal matrix composite. Zhao et al. [6] studied the influence of tool geometry on mechanical properties, and produced enhance tensile strength. Ghetiya et al. [7] conducted submerged friction stir welding and mechanical properties were improved. Bahrami et al. [8] added SiC particles for welding AA 7075 and reported tensile strength increment by 31%. Barmouz et al. [9] have studied the effect of multi-passes on the distribution of particles and concluded that particle distribution is highly influenced by no. of passes. His research also resulted that grain refinement takes place by varying the process parameters and also simultaneously prepared Cu-based SiC reinforced composite. No studies till now were carried on reinforcing the Al<sub>2</sub>O<sub>3</sub> NPs to eliminate the effect of softening behaviour. The present study is to investigate the effect of the addition of Al<sub>2</sub>O<sub>3</sub> NPs on the microstructural and mechanical behaviour of the SZ in the FSW joint. Microhardness, tensile and wear test were conducted to evaluate the mechanical properties of the welds.

## 2 Experimental Procedure

Rolled aluminium alloy 2014-T651 with 6.35 mm thickness sheets was utilized in this study and elemental composition of AA2014 and mechanical properties at that tempered condition of the alloy are shown in Table 1. The aluminium plate with a size of 140 × 280 mm was prepared for longitudinal butt joint configuration on a three-ton capacity friction stir welding machine. The welding is done along the rolling direction of the plate. Process parameters of 1100 rpm rotational speed, 30 mm/min traverse speed and 1° tool tilt angle were optimized to get defect-free joint. FSW tool as shown in Fig. 1 of H13 tool steel material with hardness 56HRC after heat treatment and with a tapered conical pin profile was used for welding. The shoulder diameter, average pin diameter and pin length are 24 mm, 7 mm and 5.8 mm, respectively.

**Table 1** Elemental composition (in wt%) and mechanical properties of AA2014-T651

Si	Fe	Cu	Mn	Mg	Zn	Ni	Ti	Al	Tensile strength (MPa)	Yield strength (MPa)	Elongation (%)
0.65	0.4	4.2	0.8	0.5	0.25	0.1	0.15	Balance	476	412	9.35



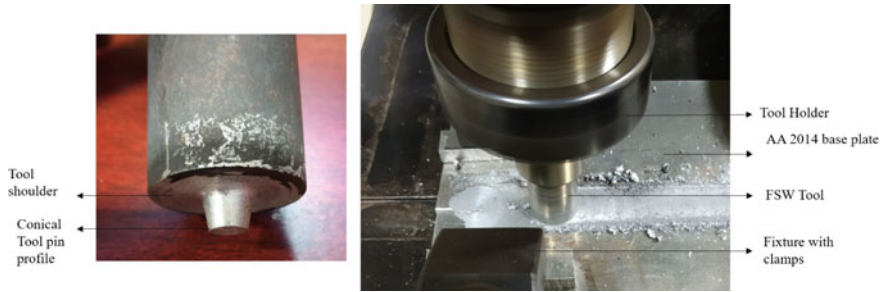


**Fig. 1** FSW tool and experimental set-up

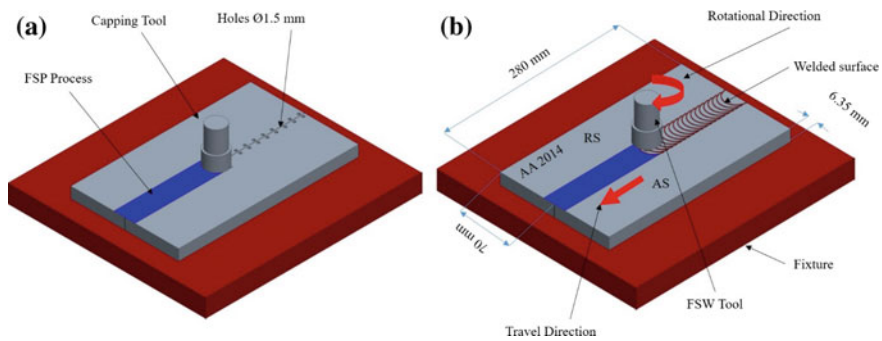


**Fig. 2** Schematic representation of FSW/FSP process

The shoulder plunge depth during the process was maintained 0.2 mm. The holes are drilled (1.5 mm diameter and 5.5 mm depth) on the left and right side of the centre line as shown in Fig. 2. The  $Al_2O_3$  NPs (nearly 20–30 nm) were filled manually in each hole tightly and the powder was preheated initially to 200 deg Celsius for 1 h before filling into the holes. To get a joint, there are two processes which are done. Firstly, friction stir processing is done initially to close the holes filled with powder particles by using a capping tool. Figure 2a. Secondly, friction stir welding was done on the friction stir processed zone by using a cylindrical tapered pin FSW tool Fig. 2b.

After FSW, the samples were cut along the traverse direction of the welds for macro and microstructural examinations. The standard polishing method was followed to get a mirror-like surface finish for microstructural analysis. Keller’s reagent was applied for 15 s to the polished surfaces before capturing the microstructure. An optical microscope was used for capturing macrostructure and microstructure at different magnifications. Grain size measurement by using the line intercept method was done for the captured images at 100× magnification. Multi-pass friction stir welding was done for up to three passes to reduce the clusters and distribute the powder uniformly in the stir zone. The non-reinforced joint was also processed for three times for comparison. SEM analysis was done on polished samples of friction stir welded reinforcement and non-reinforced joint by using a scanning electron microscope.

Elemental analysis at the selected locations of the microstructure was done using EDX (energy-dispersive X-ray spectroscopy). Vickers hardness testing (Economet VT-1) instrument was used for microhardness test along the weld surface. A constant load of 100 g, dwell time of 10 s and the 0.5 mm distance between each indentations were maintained on all the samples. Dimensions used to prepare the tensile samples are followed as per ASTM E8 standard.

### 3 Results and Discussion

#### 3.1 Microstructural Observation

Optical microscopy (OM) of the normal FSW joint and  $\text{Al}_2\text{O}_3$  NPs reinforced joint is shown in Figs. 3 and 4, respectively, with typical areas such as heat-affected zone (HAZ), Thermo-mechanically affected zone (TMAZ), stirred zone or nugget zone (SZ) interface between stir zone and TMAZ. Figure 3a shows TMAZ, while Fig. 3f, h show the interface of the joints at AS and RS of the welded sample with stir zone and elongated grains with sudden reduction of grain size. Figure 4a shows the top area of the stir zone with recrystallized grain size. In stir zone of the non-reinforced joint, the plasticized metal experiences severe plastic deformations result in grain refinement at elevated temperatures due to continuous dynamic recrystallization (CDRX). In case of the reinforced joint, the particles distributed were found as the preferred

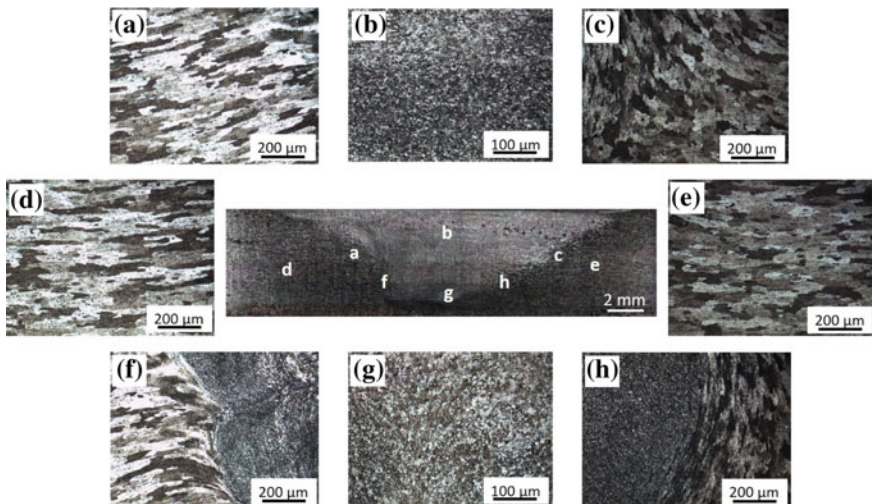


**Fig. 3** Microscopy image at different magnifications across the cross section of the non-reinforced sample. **a** AS TMAZ, **b** the top stir zone, **c** RS TMAZ, **d** AS HAZ, **e** RS HAZ, **f** interface on the AS, **g** the bottom stir zone and **h** interface on the RS

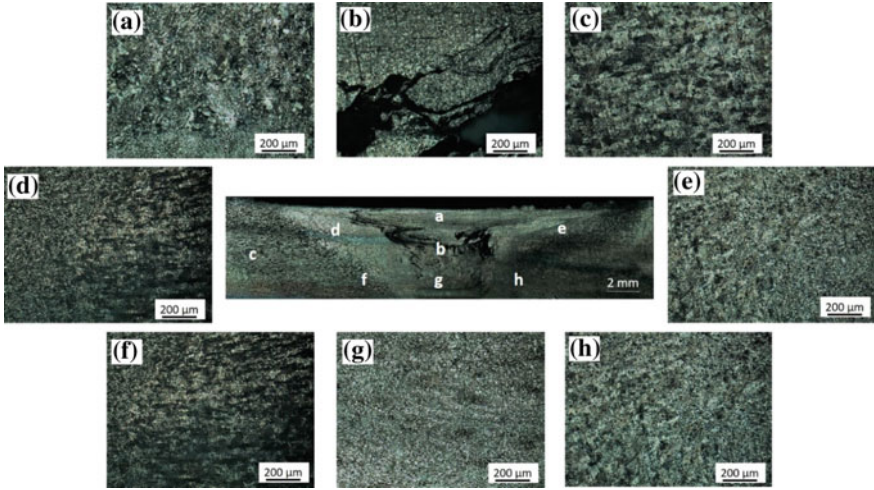


**Fig. 4** Microscopy images different magnifications at the cross section of the reinforced sample. **a** The top stir zone, **b** the middle stir zone, **c** the base material, **d** the RS interface, **e** AS interface on the, **f** RS TMAZ, **g** the bottom stir zone and **h** base material

location for the formation of new grains and CDRX can be promoted, based on the particles stimulate nucleation mechanism, as in the literature reported by Bahramani et al. [8] and Barmouz et al. [9]. Some of the authors such as Azizieh et al. [10] and El-Rayes and El-Danaf [11] addressed that the later grain growth after CDRX can be prevented with the particles, which impinges the grain boundary from grain growth, thus finer grains are formed. The average grain size of AA2014 in weld nugget of reinforced and non-reinforced FSW joints was 6 and 11  $\mu\text{m}$ , respectively.

SEM images of the reinforced joint are shown in Fig. 5a–c. The refined grain structure of the AA2014 base is seen in image Fig. 5a. However, grain refinement is due to a mechanism called dynamic recrystallization [12]. The particles of the  $\text{Al}_2\text{O}_3$  at the grain boundary are seen in the reinforced joint as shown in Fig. 5b. Due to the

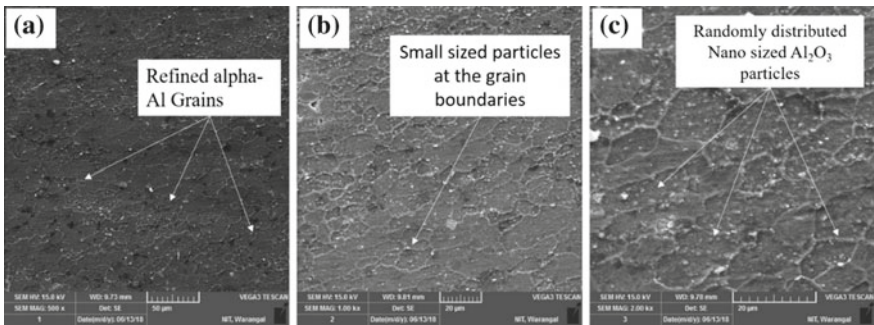


**Fig. 5** SEM images of the  $\text{Al}_2\text{O}_3$  NPs reinforced sample

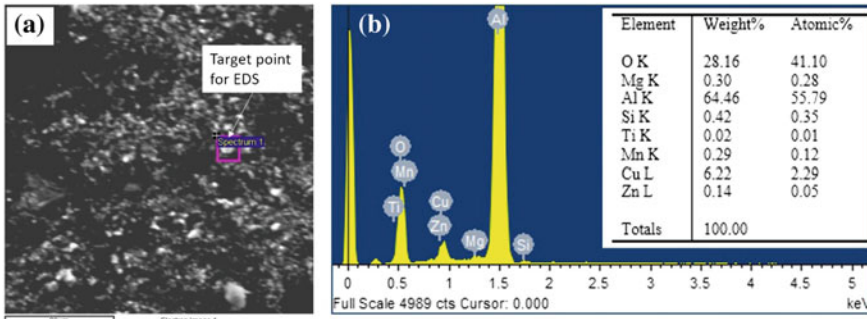


**Fig. 6** SEM-EDAX Analysis of the Al<sub>2</sub>O<sub>3</sub> NPs reinforced sample

stirring action, the particles are been distributed evenly as shown in Fig. 5c. Figure 6 shows the EDS analysis which was done along with the SEM imaging analysis. EDS analysis was done to study particles for identifying the element phase of the particles present in the stir zone. From the mapping, it is seen that the higher peaks are of Al<sub>2</sub>O<sub>3</sub> particles that are distributed uniformly in the stir zone.

### 3.2 Microhardness

Figure 7 shows the comparison of the microhardness of normal FSW joint and reinforced FSW joint samples. The hardness in the stir zone is quite difficult to predict whether it increases or decreases after the FSW joint. Whereas in AA2014 at T6 condition, depending on the processing parameters, the hardness varies. This is due to the high heat generation, where dissolution of strengthening precipitates is more

**Fig. 7** Microhardness behaviour across the centreline of samples of normal FSW and reinforced FSW joints

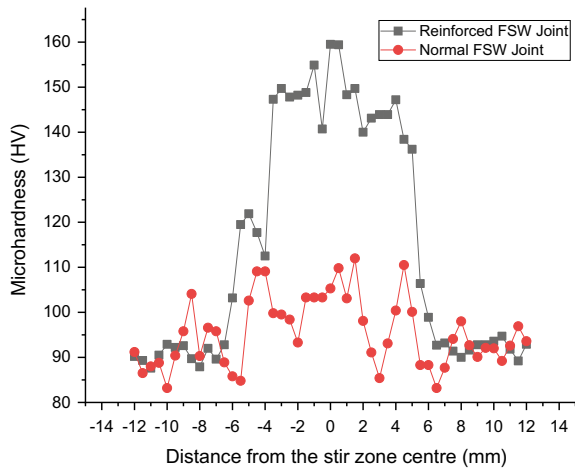


**Table 2** Tensile test values of AA2014 base metal and FSW joints

Material conditions	Ultimate tensile strength (MPa)	Yield strength (MPa)	Joint efficiency (%)
Base material	476	412	–
Normal FSW	289	201	60.7
Reinforced FSW	337	234	70.8

than compared to a decrease in grain size. Hence, the reinforced joint eliminates the effect of softening during the welding and the hardness is drastically increased compared to that of normal FSW joint. The higher hardness of the NZ in both reinforced joint and normal FSW joint was attributed to the grain refinement of the SZ. As mentioned earlier, grain refinement and increase in hardness at the stir zone are because of grain boundary pinning which creates a barrier for dislocation movement.

### 3.3 Tensile Properties

The results of the yield strength and ultimate tensile strength of base metal, normal FSW joint and reinforced FSW joint are shown in Table 2. The yield strength (YS) and ultimate tensile strength (UTS) were less than the base material because of dissolution of precipitates and decrease in dislocation density present in the AA2014 alloy with high generation. Tensile properties of different joints are illustrated in Fig. 8. The findings stated by Abdollahzadeh and Azizieh are that strengthening

**Fig. 8** UTS and YS values of the welds

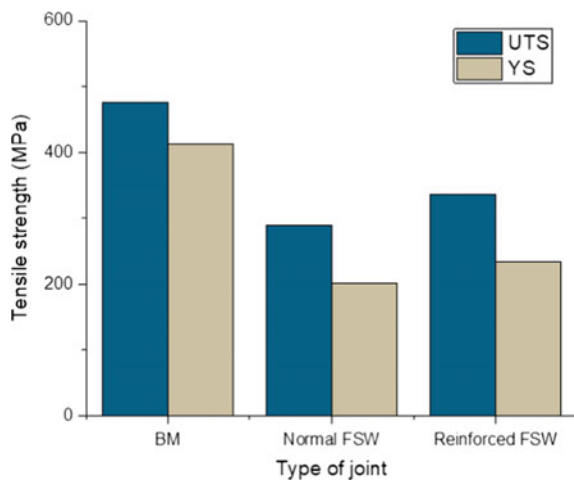




**Fig. 9** Fractured lines after tensile test of **a** BM, **b** normal FSW joint **c** reinforced joint

of the joint is high when grain size and interparticle spacing reduce. This relates to the improved strength of the reinforced sample was because of grain refinement and restricting the deformation by bearing the load by the reinforced particles. The fractured samples are shown in Fig. 9, both the reinforced joint and normal FSW joint failed near to the advancing side of the stir zone, where high temperature is generated and softening occurs [12]. Though the total softening effect could not be eliminated, the joints formed by the reinforced  $\text{Al}_2\text{O}_3$  NPs were with higher joint efficiency compared to that of normal FSW joint.

## 4 Conclusions

Major findings resulted from the present studies are as follows:

- (1) The nano-sized  $\text{Al}_2\text{O}_3$  particles were successfully introduced into the NZ by FSW process and the  $\text{Al}_2\text{O}_3$  particles were distributed uniformly after three pass friction stir welding.
- (2) A refined grain structure was formed by introducing nanoparticles in the stir zone with a decrease in grain size from 11 to 6  $\mu\text{m}$  of normal FSW joint to Reinforced FSW joint, respectively.
- (3) Average microhardness values increased significantly at the stir zone of the reinforced joint from 114.5 HV to 95.5 HV that of the normal FSW welded joint.
- (4) UTS increased to 337 MPa for the reinforced joint to that of normal FSW joint of 289 MPa attributed to the nanoparticles distribution at the grain boundaries restricting the dislocation movement.

**Acknowledgements** The authors thank the Aeronautical Research and Development Board (ARDB), New Delhi, and National Institute of Technology, Warangal, India, for financially supporting under the scheme of ARDB sponsored research project sanction no. CCTM/TM/ARDB/GIA/16-17/0332 dated 17/01/2017.

## References

1. Rajamanickam N, Balusamy V, Madhuhanna Reddy G, Natarajan K (2009) Effect of process parameters on thermal history and mechanical properties of friction stir welds. *Mater Des* 30:2726–2731
2. Threadgill PL, Leonard AJ, Shercliff HR, Withers PJ (2009) Friction stir welding of aluminium alloys. *Int Mater Rev* 54:49–93
3. Mishra RS, Ma ZY (2005) Friction stir welding and processing. *Mater Sci Eng R: Rep* 50:1–78
4. Barmouz M, Asadi P, Besharati Givi MK, Taherishargh M (2011) Investigation of mechanical properties of Cu/SiC composite fabricated by FSP: effect of SiC particles' size and volume fraction. *Mater Sci Eng A* 528:1740–1749
5. Sun YF, Fujii H (2011) The effect of SiC particles on the microstructure and mechanical properties of friction stir welded pure copper joints. *Mater Sci Eng A* 528:5470–5475
6. Zhao YH, Lin SB, Wu L, Qu FX (2005) The influence of pin geometry on bonding and mechanical properties in a friction stir weld 2014 Al alloy. *Mater Lett* 59:2948–2952
7. Ghetiya ND, Patel KM (2015) Prediction of tensile strength and microstructure characterization of immersed friction stir welding of aluminium alloy AA2014-T4. *Indian J Eng Mater Sci* 22:133–140
8. Bahrami M, Dehghani K, Besharati Givi MK (2014) A novel approach to develop aluminium matrix nano-composite employing friction stir welding technique. *Mater Des* 53:217–225
9. Barmouz M, Besharati Givi MK (2011) Fabrication of in situ Cu/SiC composites using multipass friction stir processing: evaluation of microstructural, porosity, mechanical and electrical behaviour. *Compos Part A* 42:1445–53
10. Azizieh M, Kokabi AH, Abachi P (2009) Effect of rotational speed and probe profile on microstructure and hardness of AZ31/Al<sub>2</sub>O<sub>3</sub> nanocomposites fabricated by friction stir processing. *Mater Des* 32:2034–2041
11. ERayes MM, El-Danaf EA (2012) The influence of multipass friction stir processing on the microstructure and mechanical properties of aluminium alloy 6082. *J Mater Process Technol* 212:1157–1168
12. Mokabberi SR, Movahedi M, Kokabi AH (2018) Effect of interlayers on softening of aluminium friction stir welds. *Mater Sci Eng A* 727:1–10

# Investigation on Influence of Hybrid Nanofluid/MQL on Surface Roughness in Turning Inconel-718



Mechiri Sandeep Kumar, V. Vasu and A. Venu Gopal

**Abstract** Inconel 718 alloy is, in exacting superalloy, used extensively in the most sophisticated application such as aerospace, chemical, marine and high-speed racing cars. However, the characteristics of this material make it difficult to machine due to poor thermal conductivity (11 W/mK) and work hardening. The turning process is classified as a process that produces continuous chips and experiences elevated temperatures. With emerging new and efficient MQL delivery systems, the industry has shown drift from flood and dry lubrications towards MQL. Having this in mind, to further improve the cutting fluids, a novel hybrid nanocomposite of Cu–Zn was developed in situ with mechanical alloying. Cu–Zn/vegetable oil (groundnut oil) hybrid nanofluids were prepared by dispersing the synthesized nanocomposite powder in vegetable oil. A unist MQL system combined with a compressor is used to supply nanofluid mist to the cutting zone. The inserts used were TiAlN coated beyond blast insert from Kennametal with ISO designation CNGG 120408. The insert holder used was from Kennametal beyond blast with ISO designation MCLNL 2525 M12BB. The intent of this work is to haul out the effect of cutting parameters like speed, feed, depth of cut, volume of fluid and air pressure, when machined under dry, MQL/vegetable oil and MQL/nanofluid conditions. The results were compared while machining with dry and Veg/MQL lubricating conditions. A 39% reduction in surface roughness was obtained when compared to dry machining.

**Keywords** Hybrid nanofluid · Minimum quantity lubrication · Vegetable oil · Turning · Surface roughness

---

M. Sandeep Kumar (✉)

Department of Mechanical Engineering, B V Raju Institute of Technology, Narsapur, Medak, Telangana 502313, India

e-mail: [sand.mechiri@gmail.com](mailto:sand.mechiri@gmail.com)

V. Vasu · A. Venu Gopal

Department of Mechanical Engineering, National Institute of Technology Warangal, Warangal, Telangana 506004, India

© Springer Nature Singapore Pte Ltd. 2020

H. K. Voruganti et al. (eds.), *Advances in Applied Mechanical Engineering*,

Lecture Notes in Mechanical Engineering,

[https://doi.org/10.1007/978-981-15-1201-8\\_120](https://doi.org/10.1007/978-981-15-1201-8_120)

1137



## Nomenclature

MQL	Minimum quantity lubrication
C	Cooling condition
$V_c$	Cutting speed (m/min)
$f$	Feed rate (mm/rev)
$a$	Depth of cut
Ra	Arithmetic average roughness (mm)
$F$	Variance ratio
$P$	Probability of significance
$R^2$	Determination coefficient
DOE	Design of experiments
ANOVA	Analysis of variance
PCR	Percentage of contribution

## 1 Introduction

Nickel-based alloys have found use in various industries like aerospace, marine, nuclear due to extensive properties that it possess [1]. Inconel 718, a nickel-based alloy, is one such material which has found more frequent application as it possesses good thermal and mechanical properties. This superalloy does not possess good machinability, which leads to an increase in heat generation affecting the tool life, surface quality, etc. Usually, the industry uses conventional cutting fluids, which create health problems, and has an adverse effect on environment also [2, 3]. With the increase in awareness towards the environmental and health impacts of industry, manufactures are forced to reduce the use of conventional lubricants. Minimum quantity lubrication (MQL) also known as near-dry lubrication with biodegradable oils has shown promising results and counters the problems arising from conventional lubricants [4, 5]. This resulted in reducing the consumption of cutting fluids and has shown positive results, as the lubricating oil penetrates deep into the tool–chip–workpiece interfaces [6].

Vegetable oil used with minimum quantity lubrication (MQL) mode to turning of AISI 9310 alloy steel resulted in remarkable improvement in metal removal rate (MRR) and surface finish [7]. With the emerging trend of nanotechnology, fluids possessing high thermal conductivity called nanofluids have evolved. Addition to ultrafine particles in the base fluid, the thermophysical properties of the fluid can be enhanced [8]. The applicability of the fluids as coolants is mainly due to their enhanced thermophysical properties resulting from nanoparticle inclusion [9]. In the past decade, many researchers have reported enhancement in thermophysical properties of cutting fluid with the inclusion of ceramic and metallic nanoparticles [10–16]. Nanofluids with ceramic nanoparticles possess good stability and low thermal conductivity when compared to fluid with metallic nanoparticles. Metallic nanoparticles

possess high thermal conductivity with less stability and reactivity. Therefore to prevail over this problem, hybrid nanoparticles are prepared [17]. Hybrid nanofluids are a rank of fluids containing a blend of two or more dissimilar solid nanoparticles, which are effectively dispersed in the fluid medium.

The heat transfer and rheological characteristics of various hybrid nanofluids mixed with hybrid nanoparticles were studied and compared with nanofluids incorporated with single-particle nanofluids [18–22]. Study reported an increase in heat transfer coefficient with the increase in volume concentration. In our previous work, a comparative study was carried out between nanofluids containing individual particles of Zn, Cu and hybrid Cu–Zn (50:50 wt%). The results reported an increase in thermal conductivity and viscosity in case of hybrid Cu–Zn (50:50 wt%) compared to nanofluids with individual particles [23].

In the present work, an attempt is made to study the influence of hybrid cutting fluid on surface roughness as a function of cutting parameters, considering the information of the recent developments in cutting fluids. In situ developed hybrid nanoparticle is used as inclusions in vegetable oil to prepare hybrid nanofluids [23]. A unist MQL system combined with a compressor is used to supply nanofluid mist to the cutting zone. The intent of this work is to haul out the effect of cutting parameters like speed, feed, depth of cut, volume of fluid and air pressure, when machined under dry, MQL/vegetable oil and MQL/nanofluid conditions.

## 2 Materials and Methods

The work material used in the study is Inconel 718, as received material was prepared under ASTM B637 standard with  $\varnothing$  40 mm and length 300 mm. The inserts used were TiAlN coated beyond blast insert from Kennametal with ISO designation CNGG 120408. The insert holder used was from Kennametal beyond blast with ISO designation MCLNL 2525 M12BB. Beyond blast system delivers coolant directly and precisely to the cutting edge, significantly reducing temperatures at the point of the cut.

Unist coolubricator JR was used to create air/oil mist which continuously produces precisely metered lubricant and has provision to adjust outputs from 4 to 200 injection cycles per minute with 0.1–3.0 drops of lubricant per cycle. A durable, vented 474-ml lubricant is combined with air in the patented co-axial nozzle tip. It maintains the atomization and distribution of the liquid consistent regardless of the hose length. In situ developed nanofluids [23] are used for cooling and lubricating. A new class of nanofluids are used, which consists of hybrid nanoparticle inclusions and vegetable oil as base fluid.

In situ nanofluids were prepared by dispersing hybrid nanoparticles composite of Cu and Zn. Hybrid nanocomposite was prepared in mechanical alloying process, using Retsch planetary ball mill PM 100. The prepared nanocomposite was characterized using TEM and XRD [24], and the results are shown in Fig. 1. Hybrid nanofluids were prepared by collecting the essential amount of nanoparticles and

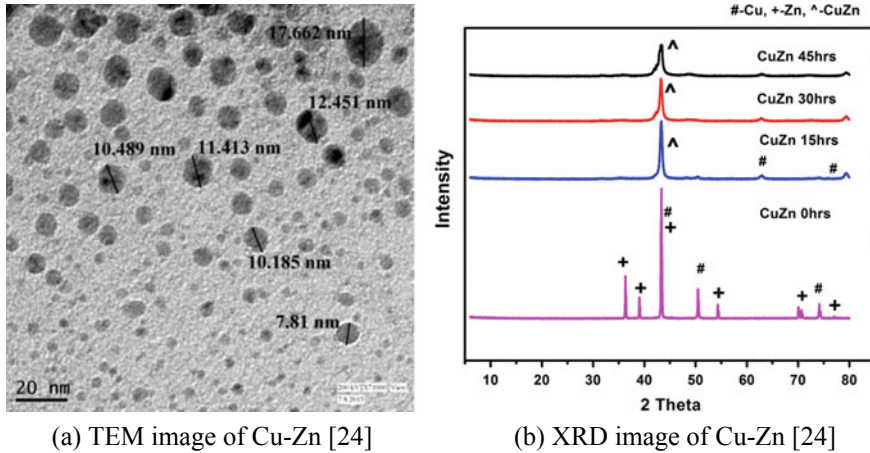


**Fig. 1** Characterization of in situ prepared Cu–Zn hybrid nanocomposite

calculated using the law of mixture and dispersant with one-tenth of the weight of the powder. The collected powder and the dispersant were added to vegetable oil and mixed using ultrasonicator. Ultrasonication for the sample of hybrid nanofluids was carried out for 2 h each.

Machining test was carried out on magnum precision lathe (Fig. 2). The aim of this present study is to haul out the influence of the cutting fluids medium on surface roughness. The percentage contribution of the process parameters on the responses with relation to the cutting fluid medium is also studied. Design of the experiment layout is used to carry out experiments with process parameters, and their levels are shown in Table 1. L9 orthogonal array was considered for conducting experiments in dry condition, with process parameters—speed, feed and DOC. L18 orthogonal array was used for MQL/vegetable oil and MQL/nanofluid-based experiments, with process parameters—speed, feed, DOC, volume of fluid and air pressure. The surface roughness was measured using a Taylor Hobson Talysurf Surtronic S-100.

### 3 Experimental Results and Discussions

#### 3.1 Surface Roughness

SR is critical for the components machined from Inconel-718, because these alloys are termed as difficult to cut materials. The current work presents the effects of in situ developed hybrid nanofluid on SR, compared with dry cutting and MQL/vegetable oil. Experiments were carried out according to L9 and L18 array, and the ANOVA is used to analyse the effect of cutting medium on SR. ANOVA values of the surface roughness experiments are shown in Table 2. PCR values were taken into consid-

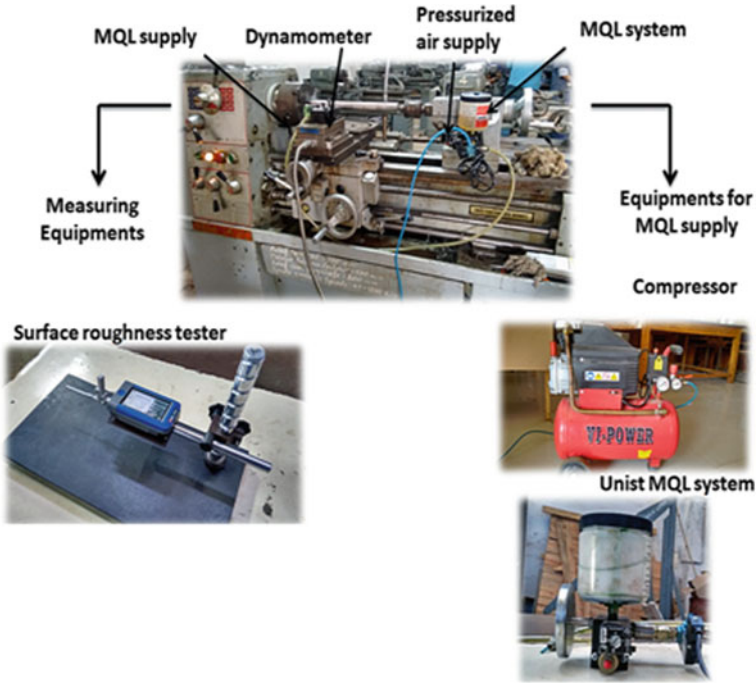


Fig. 2 Experimental set-up for turning Inconel 718

Table 1 Process parameters

Factors	Level 1	Level 2	Level 3
DOC (mm)	0.5	0.75	1
Feed (mm/rev)	0.082	0.137	0.178
Speed (m/min)	80	120	160
Volume of fluid (ml/h)	40	80	120
Air pressure (bar)	3	5	7
Cutting fluid	Dry	MQL/Veg	MQL/NF

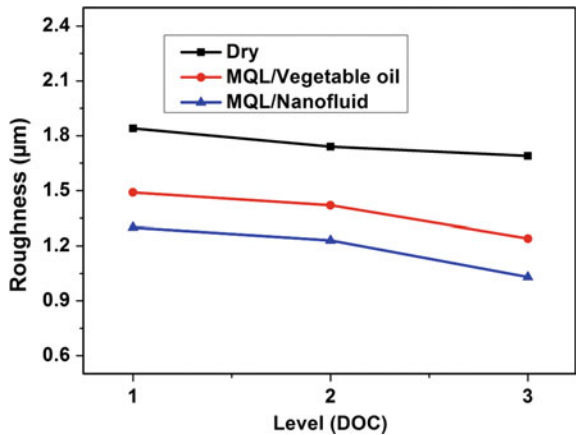
eration to identify the significance of the variable on the response. From Table 2, it is seen that, when machining with the MQL/vegetable oil and MQL/nanofluids as cutting fluids, it is seen that the PCR of speed, feed and depth of cut reduces, and feed is the major influencing factor for SR, with a contribution of 69.9% in dry machining.

As MQL reduced average auxiliary flank wear and notch wear on auxiliary cutting edge, surface roughness also grew very slowly under MQL conditions [25]. With the addition of hybrid nanoparticles, the wettability of the cutting fluids increases, resulting in better heat transfer from the cutting zone. Figure 3 shows the effect of cutting fluid on SR, at different levels of DOC, when machined under different

**Table 2** ANOVA for surface roughness results

	Source	Sum of squares	df	Mean square	F value	p-value	Percentage contribution
L9	DOC	0.082733	2	0.012544	2.063985	0.3264	7.176176
	Feed	0.806769	2	0.420678	69.21572	0.0142	69.97802
	Speed	0.251231	2	0.137144	22.5649	0.0424	21.79144
	Error	0.012156	2	0.006078			1.054356
		1.152889	8				100
<i>R</i> -Squared 0.9895, Adj. <i>R</i> -Squared 0.9578							
L18	Cutting fluid	0.1152	1	0.1152	6.982602	0.0384	6.629666
	DOC	0.113776	2	0.117706	7.134471	0.0259	6.54772
	Feed	0.993631	2	0.479439	29.06016	0.0008	57.18264
	Speed	0.171193	2	0.042156	2.555169	0.1575	9.852036
	Vol of fluid	0.150178	2	0.047339	2.869346	0.1335	8.642609
	Air pr	0.094678	2	0.075089	4.551353	0.0627	5.448642
	Error	0.098989	6	0.016498			5.69673
		1.737644	17				100
	<i>R</i> -Squared 0.9430, Adj. <i>R</i> -Squared 0.8386						

**Fig. 3** Effect of cutting fluid with DOC on SR at various depths of cuts compared to dry machining



kinds of lubricating conditions. The percentage reduction in SR values is 19–24% in case of MQL/vegetable oil and 30–39% in case of MQL/nanofluids compare to dry machining. Figure 4 shows the effect of cutting fluid on SR, at different levels of feed. A reduction of 20–23% and 35–37%, respectively, for MQL/vegetable oil and MQL/nanofluids is obtained and compared to dry machining. Speed is the second most influencing factor on roughness and with the CS, reduction of 19–27% for MQL/vegetable and 35–38% (Fig. 5) reduction in SR for MQL/nanofluids is

**Fig. 4** Effect of cutting fluid with feeds on SR at various feeds compared to dry machining

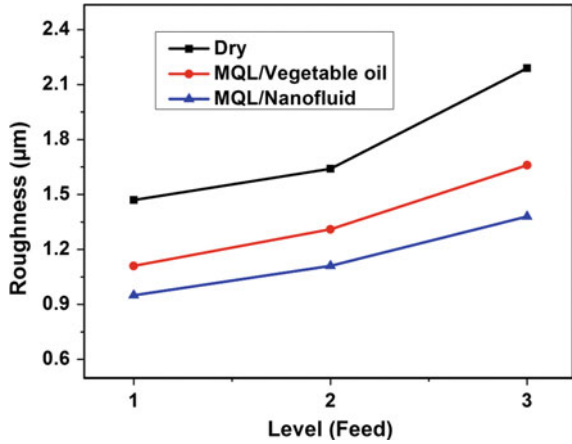
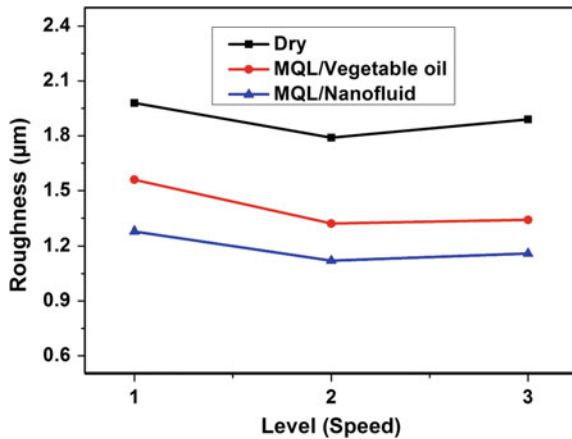


**Fig. 5** Effect of cutting fluid with speed on SR at various cutting speeds compared to dry machining



obtained. Improved performance can be attributed to the combination of lubrication and cooling at the same time.

### 4 Conclusions

This work demonstrated machining of Inconel-718 with hybrid nanofluid (MQL/nanofluid) as cutting fluid and compared its performance with dry and MQL/vegetable oil conditions. MQL/nanofluid and MQL/vegetable oil in general demonstrated contribution in improving performance if used with suitable cutting parameters. MQL provides the benefits mainly by reducing the cutting temperature, which improves the chip–tool interaction and maintains sharpness of the cutting

edges. Surface finishes improved mainly due to the reduction of wear and damage at the tooltip by the application of MQL [25]. Hybrid nanofluids increase the wettability and heat transfer rate of the cutting fluids. Feed rate is the major contributor for surface roughness followed by speed and DOC. With the use of MQL, the contribution of these parameters is reduced.

## References

1. Ezugwu EO (2005) Key improvements in the machining of difficult to-cut aerospace superalloys. *Int J Mach Tool Manuf* 45(12–13):1353–1367
2. Ezugwu EO, Bonney J, Yamane Y (2003) An overview of the machinability of aeroengine alloys. *J Mater Proc Technol* 134(2):233–253
3. Hong SY, Zhao Z (1999) Thermal aspects, material considerations and cooling strategies in cryogenic machining. *Clean Prod Proc* 1:107–116
4. Klocke F, Eisenblätter G (1997) Dry cutting. *CIRP Ann Manuf Technol* 46:519–526
5. Attanasio A, Gelfi M, Giardini C, Remino C (2006) Minimal quantity lubrication in turning: effect on tool wear. *Wear* 260:333–338
6. Ezugwu EO, Bonney J, Yamane Y (2003) An overview of the machinability of aeroengine alloys. *J Mater Proc Technol* 134:233–253
7. Lawal SA, Choudhury IA (2011) Application of vegetable oil-based metalworking fluids in machining ferrous metals—a review. *Int J Mach Tools Manuf*. <https://doi.org/10.1016/j.ijmachtools.2011.09.003>
8. Eastman JA, Phillpot SR, Choi SUS, Keblinski P (2004) Thermal transport in nanofluids. *Annu Rev Mater Res* 34:219–230
9. Vasu V, Rama Krishna K, Kumar ACS (2007) Exploitation of thermal properties of fluids embedded with nanostructured materials. *Int Energy J* 8:178–186
10. Masuda H, Ebata A, Teramae K, Hishinuma N (1993) Alteration of thermal conductivity and viscosity of liquid by dispersing ultra-fine particles (dispersion of  $\gamma$ - $\text{Al}_2\text{O}_3$ ,  $\text{SiO}_2$ , and  $\text{TiO}_2$  ultra-fine particles). *Netsu Bussei* 4:227–233
11. Murshed SMS, Leong KC, Yang C (2005) Enhanced thermal conductivity of  $\text{TiO}_2$ —water based nanofluids. *Int J Therm Sci* 44:367–373
12. Murshed SMS, Leong KC, Yang C (2008) Investigations of thermal conductivity and viscosity of nanofluids. *Int J Therm Sci* 47:560–568
13. Patel HE, Das SK, Sundararajan T (2003) Thermal conductivities of naked and monolayer protected metal nanoparticle based nanofluids: manifestation of anomalous enhancement and chemical effects. *Appl Phys Lett* 83:2931–2933
14. Lee JH, Hwang KS, Jang SP, Lee BH, Kim JH, Choi SUS, Choi CJ (2008) Effective viscosities and thermal conductivities of aqueous nanofluids containing low volume concentrations of  $\text{Al}_2\text{O}_3$  nanoparticles. *Int J Heat Mass Transf* 51:2651–2656
15. Das SK, Putra N, Thiesen P, Roetzel W (2003) Temperature dependence of thermal conductivity enhancement for nanofluids. *ASME J Heat Transf* 125:567–574
16. Yu W, Xie H (2012) A review on nanofluids: preparation, stability mechanisms, and applications. *J Nanomaterials* 17
17. Suresh S, Venkataraj KP, Selvakumar P, Chandrasekar M (2011) Synthesis of  $\text{Al}_2\text{O}_3$ —Cu/water hybrid nanofluids using two step method and its thermo physical properties. *Colloids Surf A Physicochemical Eng Aspects* 388:41–48
18. Baghbanzadeh M, Rashidi A, Rashtchian D, Lotfi R, Amrollahi A (2012) Synthesis of spherical silica/multiwall carbon nanotubes hybrid nanostructures and investigation of thermal conductivity of related nanofluids. *Thermochim Acta* 549:87–94

19. Madhesh D, Parameshwaran R, Kalaiselvam S (2014) Experimental investigation on convective heat transfer and rheological characteristics of Cu–TiO<sub>2</sub> hybrid nanofluid. *Exp Therm Fluid Sci* 52:104–115
20. Sundar LS, Singh MK, Sousa ACM (2014) Enhanced heat transfer and friction factor of MWCNT–Fe<sub>3</sub>O<sub>4</sub>/water hybrid nanofluids. *Int Commun Heat Mass Transf* 52:73–83
21. Baghbanzadeha M, Rashidib A, Soleimanisalimc AH (2014) Investigating the rheological properties of nanofluids of water/hybrid nanostructure of spherical silica/MWCNT. *Thermochimi Acta* 578:53–58
22. Tadjarodi A, Zabihi F (2013) Thermal conductivity studies of novel nanofluids based on metallic silver decorated mesoporous silica nanoparticles. *Mater Res Bull* 48:4150–4156
23. Kumar MS, Vasu V, Venu Gopal A (2015) Thermal conductivity and viscosity of vegetable oil–based Cu, Zn, and Cu–Zn hybrid nanofluids. *J Test Eval* 44:1–7. <https://doi.org/10.1520/jte20140286>. ISSN 0090–3973
24. Mechiri SK, Vasu V, Venu Gopal A (2016) Investigation of thermal conductivity and rheological properties of vegetable oil based hybrid nanofluids containing Cu–Zn hybrid nanoparticles. *Exp Heat Transfer* 30:205–217. <https://doi.org/10.1080/08916152.2016.1233147>, ISSN 1521-0480
25. Dhar NR, Kamruzzaman M, Ahmed M (2006) Effect of minimum quantity lubrication (MQL) on tool wear and surface roughness in turning AISI-4340 steel. *J Mater Process Technol* 172:299–304



# Fuzzy Logic and Regression Modelling of Machining Parameters in Turning AISI 1040 Steel Using Vegetable-Based Cutting Fluids with Extreme Pressure Additive



B. Satheesh Kumar, Neelam Parimala and P. Vamsi Krishna

**Abstract** This study focuses on the prediction of cutting force, tool flank wear and surface roughness with extreme pressure (EP) additive included vegetable-based cutting fluids (VBCFs) using fuzzy logic and regression. Cutting force, tool flank wear and surface roughness are measured during turning of AISI 1040 steel according to L9 orthogonal array. A model depends on fuzzy logic is established, and the results obtained from fuzzy logic are compared with the results from regression and experimentation. Fuzzy logic model gives closer values to experimental results than the regression model. It has been concluded that fuzzy rule-based modelling helps in predicting cutting force, surface roughness and tool flank wear. Confirmation experiment results revealed that fuzzy logic model is better than regression model for predicting cutting force, tool wear and surface roughness in turning.

**Keywords** Vegetable-based cutting fluids · EP additive · Turning · Fuzzy logic · Regression

## 1 Introduction

Machining process generates great amount of heat due to friction at tool–workpiece interface leading to high temperatures. Cutting fluids are utilised to overcome the demerits of high temperatures. Usage of conventional cutting fluids leads to environmental pollution and damage operators' health [1]. Vegetable oils are evolved as an alternative to conventional cutting fluids due to their biodegradability and environmental friendliness [2, 3]. The requirements of the machining operation drive us towards the addition of sulphur or sulphurised fats as extreme pressure (EP) additives

---

B. Satheesh Kumar (✉)

Department of Mechanical Engineering, N.B.K.R.I.S.T., Vidyanagar 524413, India  
e-mail: [satheeshkumar76svu@gmail.com](mailto:satheeshkumar76svu@gmail.com)

N. Parimala · P. Vamsi Krishna

Department of Mechanical Engineering, National Institute of Technology,  
Warangal, Warangal 506004, India

© Springer Nature Singapore Pte Ltd. 2020

H. K. Voruganti et al. (eds.), *Advances in Applied Mechanical Engineering*,

Lecture Notes in Mechanical Engineering,

[https://doi.org/10.1007/978-981-15-1201-8\\_121](https://doi.org/10.1007/978-981-15-1201-8_121)

in cutting fluids because of their anti-wear, antioxidation properties and strong EP characteristics [4].

Less tool wear was reported with soybean-based cutting fluid when compared to petroleum-based cutting fluid in CNC turning operation [5]. In another study [6], better results were achieved with coconut oil with 0.5% boric acid suspension in turning AISI 3014 steel. The effects of EP additive added VBCFs were investigated during machining of AISI 304 stainless steel (SS) with end milling by comparing cutting force, tool life and surface roughness [7]. Experiments were conducted using different VBCFs having 8% extreme pressure additive (EPA) that includes sunflower oil, canola oil and semisynthetic cutting fluid, and the results indicated that canola oil with EPA showed better performance than others. Friction and wear behaviour are also studied under different lubricating conditions such as without lubrication and with lubrication (base oil, base oil with single and composite EPA) with tribo-tester. Composite EPA in base oil significantly reduced the friction coefficient compared to base oil [8]. Fuzzy rule models were used to predict thrust force and surface roughness in drilling of glass fibre-reinforced plastic composites and achieved good results in prediction with minimum errors [9, 10]. A comparative study of dry machining and wet machining showed rice bran oil and coolant oil improved surface roughness and tool life as the cutting fluids in a CNC turning of plain carbon steels EN8 and EN9 [11]. The results indicated that the best cutting conditions were obtained for coolant oil followed by rice bran oil. In the current study, a model that depends on fuzzy logic approach is established on the prediction of turning parameters with EP additive added VBCFs, and the results from fuzzy logic modelling are compared with the results from regression and experimentation.

## 2 Experimental Details

The current work deals with the effectiveness of the EPA during machining of AISI 1040 heat-treated steel on lathe machine where the machining performance is evaluated considering the terms cutting force, surface roughness and tool flank wear. The EPA used to prepare VBCFs (with 5%, 10% and 15% EPA to canola, sesame and coconut oils) is sulphur-based in order to achieve lower viscosity, better water solubility and lubrication properties [12].

For preparing cutting fluid, initially the mixture is made in the ratio of emulsifier to vegetable oil as 15:85 by weight, respectively, and then EPA is added to it. The VBCF mixture has oil to water ratio of 9:100. The details of lubricant supply to the machining zone are shown in Fig. 1. Chemical composition of AISI 1040 steel workpiece is shown in Table 1. The experimental details are depicted in Table 2. The levels of the turning parameters are presented in Table 3.

From the literature, it is observed that 8% EP additive performed well. To identify the better percentage in the present work, for different combination of tool-workpiece and cutting fluid composition 5, 10 and 15% EP additive in cutting fluid is considered. Similarly, the process parameter levels for cutting speed and feed values



**Fig. 1** Detailed experimental set-up

**Table 1** Chemical composition of AISI 1040 steel (wt%)

C	Si	Mn	S	P	Fe
0.40	0.025	0.80	0.025	0.015	Balance

**Table 2** Experimental details

Work material type	AISI 1040
Hardness	30 ± 2 HRC
Tool holder	PSRNR12125F09
Cutting tool (insert)	CNMG120408NC6110 coated carbide (TiCN/Al <sub>2</sub> O <sub>3</sub> coating)
Cutting speed (m/min)	60, 80 and 100
Feed (mm/rev)	0.14, 0.17 and 0.20
Depth of cut (mm)	0.5 (constant)
Cutting fluids	Sesame, canola and coconut-based cutting fluids
EP additive inclusion (%)	5, 10 and 15

**Table 3** Levels of turning factors

Symbol	Parameter	Unit	Level 1	Level 2	Level 3
EP	EP additive	%	5	10	15
<i>V</i>	Cutting speed	m/min	60	80	100
<i>f</i>	Feed	mm/rev	0.14	0.17	0.20

are considered at which the responses are more influential. Cutting fluids utilised in the present work are abbreviated as follows: cutting fluids with base fluid sesame (SCF), canola (CNCF) and coconut (CCF).

Cutting forces ( $F_c$ ) are measured using a KISTLER dynamometer. Flank wear ( $V_b$ ) is measured using an optical projector having a magnification of  $5\times$ . The measurement of surface roughness is done by surface roughness tester (Ra).

### 3 Results and Discussion

Cutting force, surface roughness and tool flank wear are measured for sesame, canola and coconut-based cutting fluids with varying proportions of EP additive as per L9 orthogonal array are presented in Table 4. In general, coconut-based cutting fluid with 10% of EP additive gave lower values of cutting force, tool flank wear and surface roughness due to better viscosity property of coconut oil-based cutting fluid that reduces friction at tool–chip and tool–workpiece interfaces. The reason for decrease in the responses with 10% of EP additive is due to the formation of lead sulphide as EP additive which reacts with the surface and eases up plastic deformation.

A fuzzy system model is in the form of If-Then rules instead of a mathematical equation. The components of the fuzzy system are fuzzifier, fuzzy inference engine and a defuzzifier as shown in Fig. 2. In the current study, the input parameters taken into consideration are cutting speed, feed and proportion of EP additive; whereas, cutting force, surface roughness and tool flank wear are considered to be the performance characteristics as shown in Fig. 3. Initially, in fuzzy logic, the range of machining parameters and performance characteristics values is identified. For fuzzification, trapezoidal membership is used to obtain fuzzy sets. Here, the input and output numerical values are converted to linguistic forms such as low, medium and high. The range of membership function value is between 0 and 1. Membership functions with their range values of input parameters for the proportion of EP additive (Fig. 4), cutting speed (Fig. 5) and feed (Fig. 6) are shown in figures. Finally, to obtain output, trapezoidal membership is used for defuzzification. The conversion of fuzzy quantity into precise quantity is defined as defuzzification. In the present study, the centroid of the area is evaluated using the method of centroid defuzzification of the membership function.

The equation for the trapezoidal membership function is given in Eq. (1)

$$f(x, a, b, c, d) = \left\{ \begin{array}{ll} 0 & x \leq a \\ \frac{x-a}{b-a} & a \leq x \leq b \\ \frac{d-x}{d-c} & c \leq x \leq d \\ 0 & d \leq x \end{array} \right\} \tag{1}$$

where  $f$ : membership functions of the fuzzy set;  $a, b, c, d$ : parameters;  $x$ : variable.

**Table 4** Machining parameters and experimental results

Trial run	Machining parameters			Experimental results											
	EP (%)	V (m/min)	f (mm/rev)	Average $F_c$ values (N)			Average $V_b$ values ( $\mu\text{m}$ )			Average $R_a$ values ( $\mu\text{m}$ )					
				SCF	CNCF	CCF	SCF	CNCF	CCF	SCF	CNCF	CCF			
1	5	60	0.14	101.0961	87.8690	74.6419	91.80	76.00	60.21	4.14	3.54	2.95			
2	5	80	0.17	157.9813	111.6723	85.4395	130.50	107.16	83.83	5.16	4.49	3.83			
3	5	100	0.20	123.2514	85.3574	67.5290	239.18	166.61	94.05	4.53	4.03	3.52			
4	10	60	0.17	91.8209	80.2927	68.7046	87.20	78.62	70.04	3.91	3.38	2.85			
5	10	80	0.20	156.1680	139.4391	122.7103	209.53	144.1	78.66	6.13	5.22	4.22			
6	10	100	0.14	58.4193	53.7297	48.1403	105.05	81.9	58.76	3.80	3.11	2.42			
7	15	60	0.20	127.3058	113.1471	98.9884	155.68	124.84	94.00	5.22	4.58	3.95			
8	15	80	0.14	162.6940	112.4050	98.1120	125.60	97.05	68.5	5.35	4.56	3.77			
9	15	100	0.17	125.8062	85.7831	62.7600	154.73	127.81	101.62	4.54	3.89	3.26			

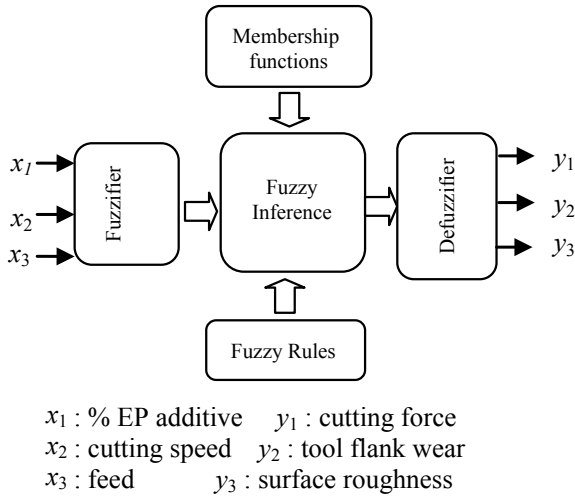


Fig. 2 Structure of fuzzy logic system

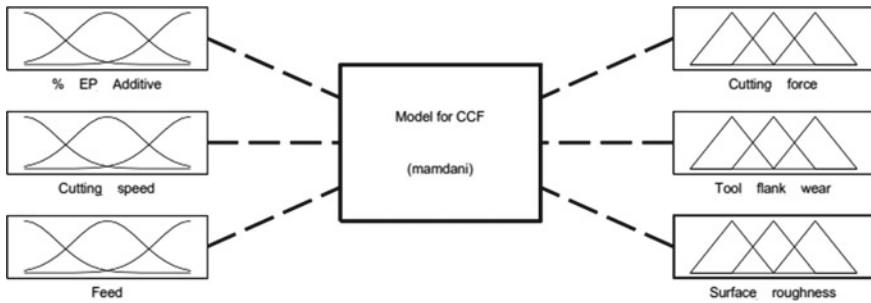


Fig. 3 Fuzzy inference system

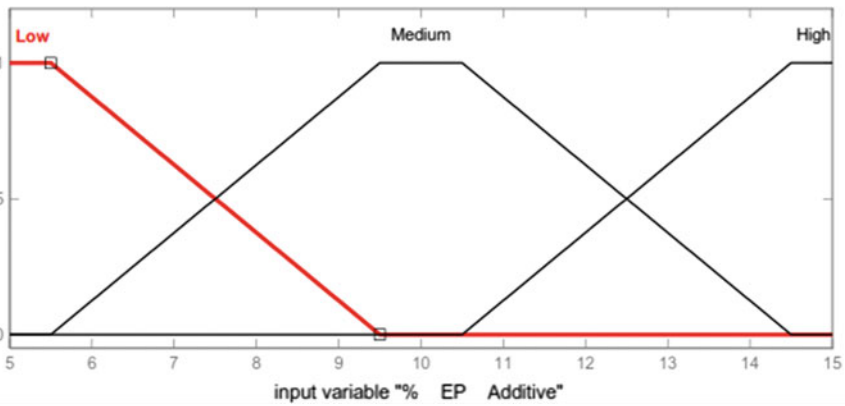


Fig. 4 Membership function for % EP additive

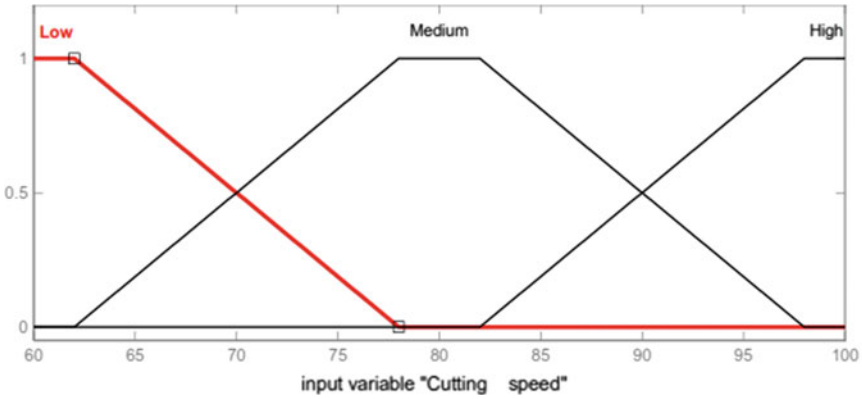


Fig. 5 Membership function for cutting speed

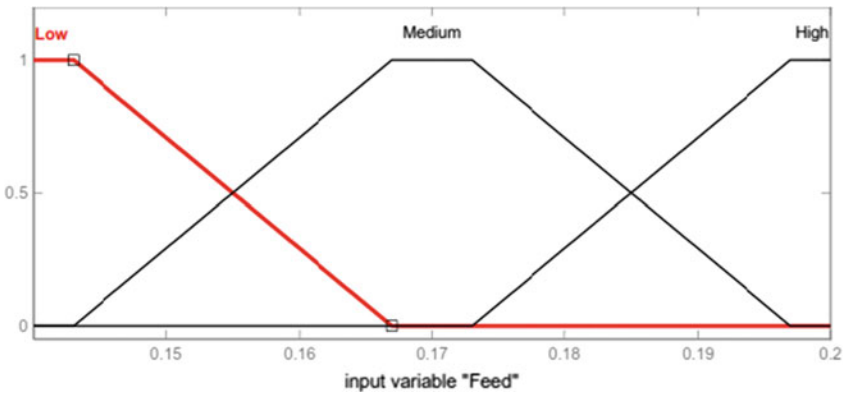


Fig. 6 Membership function for feed

Regression analysis is carried out for modelling and analysis of various parameters which describes the relationship between the dependent and independent variables. Mathematical models are developed from regression analysis to predict cutting force, tool flank wear and surface roughness in terms of % EP additive, cutting speed and feed rate. The mathematical models developed for cutting force are as follows:

For SCF:

$$F_c = 40 + 1.12EP - 0.106V + 470f R^2 = 0.968$$

For CNCF:

$$F_c = 46.2 + 0.88EP - 0.470V + 466f R^2 = 0.946$$

For CCF :

$$F_c = 48.1 + 1.07EP - 0.533V + 380f R^2 = 0.962$$

where cutting force ' $F_c$ ' in N, EP is % EP additive,  $V$  is cutting speed in m/min, and  $f$  is feed in mm/rev.

The mathematical models developed for tool flank wear are as follows:

For SCF:

$$V_b = -223 - 0.85EP + 1.37V + 1566fR^2 = 0.959$$

For CNCF:

$$V_b = -124 - 0.00EP + 0.807V + 1003fR^2 = 0.972$$

For CCF :

$$V_b = -24.8 + 0.868EP + 0.251V + 440fR^2 = 0.995$$

where  $V_b$  is tool flank wear in  $\mu\text{m}$ .

For surface roughness, the mathematical models developed are as follows:

For SCF:

$$R_a = 2.15 + 0.0427EP - 0.0033V + 14.4fR^2 = 0.963$$

For CNCF:

$$R_a = 1.60 + 0.0323EP - 0.0039V + 14.6fR^2 = 0.978$$

For CCF :

$$R_a = 1.15 + 0.0227EP - 0.0046V + 14.2fR^2 = 0.994$$

where  $R_a$  is the surface roughness in  $\mu\text{m}$ .

$R^2$  is the value of correlation coefficient in regression analysis, and it should be between 0.8 and 1. In the present study,  $R^2$  value of cutting force, tool flank wear and surface roughness for all cutting fluids is very close to 1, which indicates an excellent relationship between dependent and independent variables.

The validity of the fuzzy model is measured by comparing the predicted values with experimental and regression results. The relationship between predicted values and experimental results is plotted and illustrated in Figs. 7, 8 and 9. From the plots, it is seen that the values obtained from fuzzy model are very close to experimental results. From the results, it is concluded that fuzzy logic modelling can be successfully utilised for predicting cutting force, tool flank wear and surface roughness in turning of AISI 1040 steel.

Confirmation test is conducted in order to verify the developed model, and the results are shown in Figs. 10, 11 and 12. Confirmation experiments are conducted at 15% of EP additive, 100 m/min of cutting speed and 0.2 mm/rev of feed at higher cutting conditions investigated in the present work.

The results (Figs. 10, 11 and 12) revealed that fuzzy logic model is better than the regression model for predicting cutting force, tool flank wear and surface roughness.



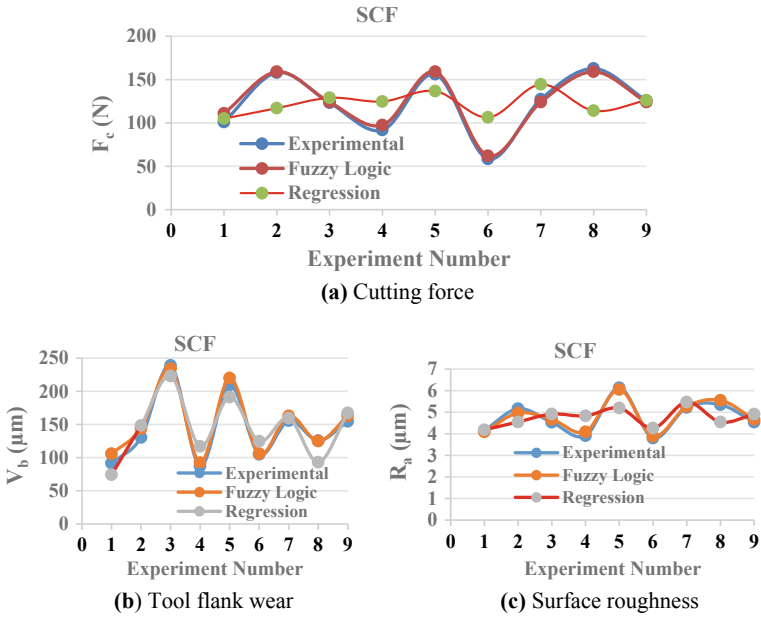


Fig. 7 Comparison of experimental and predicted results using SCF for a  $F_c$  b  $V_b$  c  $R_a$

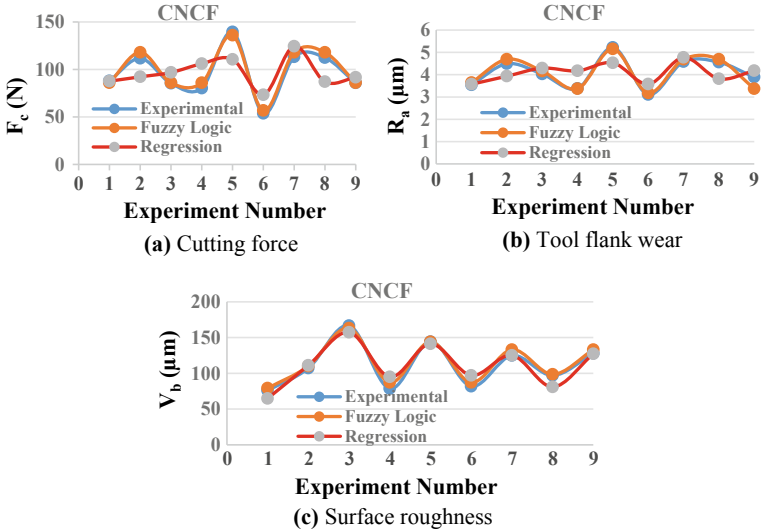
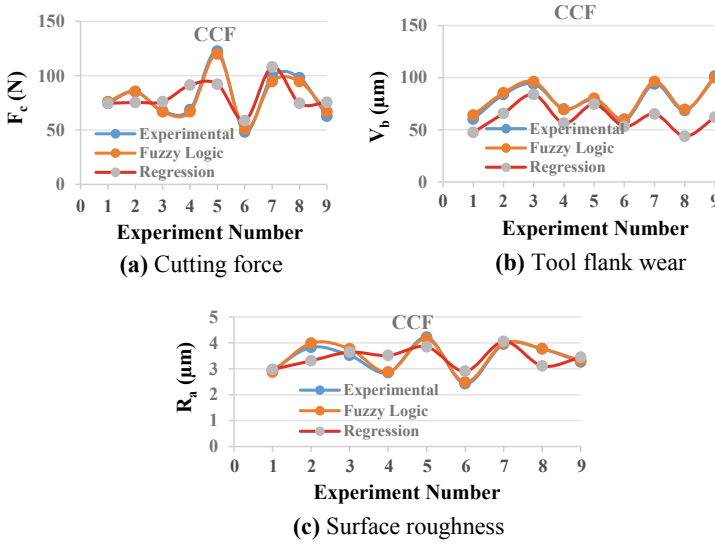
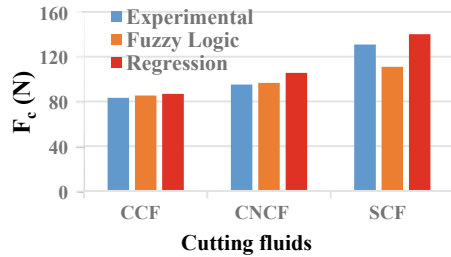


Fig. 8 Comparison of experimental and predicted results using CNCF for a  $F_c$  b  $V_b$  c  $R_a$



**Fig. 9** Comparison of experimental and predicted results using CCF for **a**  $F_c$  **b**  $V_b$  **c**  $R_a$

**Fig. 10** Confirmation experiment results for  $F_c$  using SCF, CNCF and CCF



**Fig. 11** Confirmation experiment results for  $V_b$  using SCF, CNCF and CCF

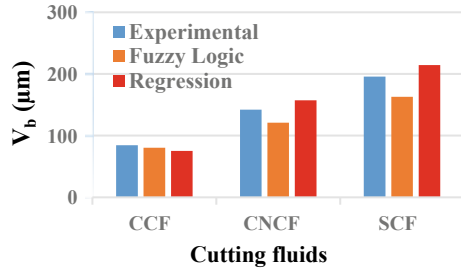
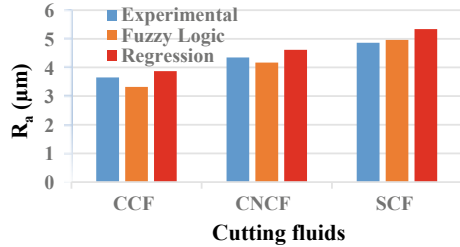


**Fig. 12** Confirmation experiment results for  $R_a$  using SCF, CNCF and CCF



## 4 Conclusions

In the current study, a model that depends on fuzzy logic approach to predict machining performance with EP additive included VBCFs is compared with experimentation and regression.

The lower cutting force, tool wear and surface roughness are achieved with coconut-based cutting fluid with 10% EP additive as compared with other cutting fluids used in the present work.

The values predicted using fuzzy logic model are very close to experimental results, and hence, the fuzzy logic model can be successfully used for predicting cutting force, tool flank wear and surface roughness.

Confirmation experiment results revealed that the fuzzy logic model is better than the regression model for predicting cutting force, tool flank wear and surface roughness in turning of AISI 1040 steel.

## References

- Howes TD, Toenshoff HK, Heuer W (1991) Environmental aspects of grinding fluids. *Ann CIRP* 40(2):623–629
- Adhvaryu A (2004) Tribological studies of thermally and chemically modified vegetable oils for use as environmentally friendly lubricants. *Wear* 257:359–367
- Fox NJ, Stachowiak GW (2007) Vegetable oil based lubricants—a review of oxidation. *Tribol Int* 40:1035–1046
- Rastogi RB, Yadav M (2004) Suspension of molybdenum-sulfur complexes in paraffin oil as extreme pressure lubricants. *Tribol Int* 37:87–92
- Rao PN, Zhang J, Eckman M () Experimental study and regression modeling of tool wear in CNC turning operation using soybean based cutting fluid. *J Mech Eng* 10(1):1–6
- Sodavadia KP, Makwana AH (2014) Experimental investigation on the performance of coconut oil based nano-fluid as lubricants during turning of AISI 304 Austenitic Stainless Steel. *Int J Adv Mech Eng* 4(1):55–60
- Kuram E, Babur O, Bilgin TS, Erhan D (2013) The effect of extreme pressure added vegetable based cutting fluids on cutting performance in milling. *Ind Lubr Tribol* 65(3):181–193
- Yan XD, Sun JL, Xiong S, Hou YQ (2017) Insights into the sliding wear behavior of a copper-steel pair with oils containing extreme-pressure additives. *Wear* 386:211–217
- Latha B, Senthil Kumar VS (2009) Analysis of thrust force in drilling glass fiber reinforced plastic composited using fuzzy logic. *Mater Manuf Processes* 24:509–516

10. Latha B, Senthil Kumar VS (2010) Modeling and analysis of surface roughness parameters in drilling GFRP composites using fuzzy logic. *Mater Manuf Processes* 25:817–827
11. Gokul G, Smitha GN (2016) Case study on effect of cutting fluids in turning operation. *Int J Mech Ind Technol* 3(2):79–84
12. Santos FDD, Guillemet F (2002) New water soluble EP additive for environment friendly fluids. *Ind Lubr Tribol* 54:285–290

# A New Approach in Establishing Stable Machining Parameters Using Frame Statistics and Kurtosis



V. Srinivasa Rohit, A. Venu Gopal and L. Rama Krishna

**Abstract** Sensors have become an integral part of the current manufacturing systems. However, gaining insight into the data collected from sensors is a complex task. The current paper presents an approach to identify stable machining parameters by applying frame statistics and kurtosis to cutting force signal. The approach is presented in finish turning of aluminum metal matrix composites (Al-MMC) using coated carbide inserts. It was found that the process parameters suitable for finish turning Al-MMC are 80 m/min cutting speed, 0.103 mm/rev feed and 0.1 mm depth of cut. The approach presented can be applied to other machining processes, and as it is computationally efficient, it can be used in online monitoring systems.

**Keywords** Frame statistics · Kurtosis · Turning · Signal analysis

## 1 Introduction

Computer-based data acquisition systems have provided a low-cost approach to monitor manufacturing processes. This has led to the development of online monitoring and predictive maintenance in manufacturing processes. The field of machining has always been forefront in adapting sensor-based technologies to improve productivity. Tlustý et al. [1], Tonshoff et al. [2], Byrne et al. [3] and Teti [4] give a detailed review of the developments in sensor-based applications in machining processes. However, algorithm-based monitoring systems require large amounts of historical data regarding the processes. Before collecting such data, the process needs to be analyzed and established. A process is generally established either through trial and error methods or through use of experimental design methodology [5, 6]. The experimental data is generally optimized for a required objective like material removal rate surface

---

V. Srinivasa Rohit · A. Venu Gopal (✉)

Department of Mechanical Engineering, National Institute of Technology, Warangal, Warangal, Telangana 506004, India  
e-mail: [venu@nitw.ac.in](mailto:venu@nitw.ac.in)

L. Rama Krishna

Center for Engineered Coatings, ARCI, Hyderabad, Telangana 500005, India

© Springer Nature Singapore Pte Ltd. 2020

H. K. Voruganti et al. (eds.), *Advances in Applied Mechanical Engineering*,

Lecture Notes in Mechanical Engineering,

[https://doi.org/10.1007/978-981-15-1201-8\\_122](https://doi.org/10.1007/978-981-15-1201-8_122)

quality. [7–10]. The design of experiments approach has also been used in industrial applications as a tool in six sigma methodology. However, only the average value of the force signal is measured in most cases, the process is assumed steady, ignoring the dynamics of the process. By the use of frame statistics, time-based variation in the process can also be evaluated. The purpose of this study is to present an approach in establishing stable machining parameters using frame statistics and kurtosis along with the design of experiments. To illustrate, the effectiveness of the approach is applied to the force signals acquired from finish turning of aluminum metal matrix composites. As the analysis and methodology are simple and are similar to an already established industrial practice, it can be used in practical applications.

The metal matrix composites (MMC) are being widely used in the automotive sector because of their properties like high strength to weight ratio, lower costs and greater wear resistance. Li et al. [11] and Manna et al. [12] have presented accelerated tool wear issues in machining MMC. The presence of hard particles was found to be one of the main reasons for tool chip off. The present study presents a method to analyze the effect of these hard particles and establish process parameters where their effect is minimal.

## 2 Methods

In the current study, the application of frame statistics for sensor signal analysis is presented through analyzing cutting force signal in dry turning of aluminum metal matrix composites. The following sections present the details of the experiments.

### 2.1 *Materials and Experimental Setup*

The turning experiments were conducted on a lathe (Magnum SSM 1430) attached with a piezoelectric dynamometer (Kistler 9257B) as shown in Fig. 1. A cylindrical workpiece of length 200 mm and diameter 35 mm, made of aluminum matrix with 6% SiC and 3% C, was used as the workpiece. A coated carbide insert (Widia CNMG 120408TN-4000) was used to machine it.

### 2.2 *Design of Experiments*

The process parameters considered for the analysis are speed, feed and depth of cut. The range of the parameters was selected based on the recommendations of the tool manufacturer [13] and initial trial experiments. The levels of the parameters are shown in Table 1.



**Fig. 1** Precision lathe with dynamometer

**Table 1** Process parameter levels

Symbol	Parameters	Unit	Level -1	Level 0	Level 1
A	Speed	m/min	40	60	80
B	Feed	mm/rev	0.103	0.175	0.264
C	Depth of cut	mm	0.1	0.2	0.3

A half-fractional factorial design with two levels [14] was used to conduct the experiments efficiently. Further, two experiments were conducted at the center of the parameter range for better understanding of the process. The order of experiments was randomized to minimize errors due to uncontrollable conditions during machining. The experimental designs along with the levels at which the experiments were conducted are shown in Table 2.

The experiments were conducted as mentioned above, and the force signal for each experiment was logged at a sampling rate of 1000 Hz. Sampling frequency was

**Table 2** Half-factorial experimental design

S. No	Cutting speed (A)	Feed (B)	Depth of cut (C)
1	1	1	1
2	-1	1	-1
3	0	0	0
4	0	0	0
5	1	-1	-1
6	-1	-1	1

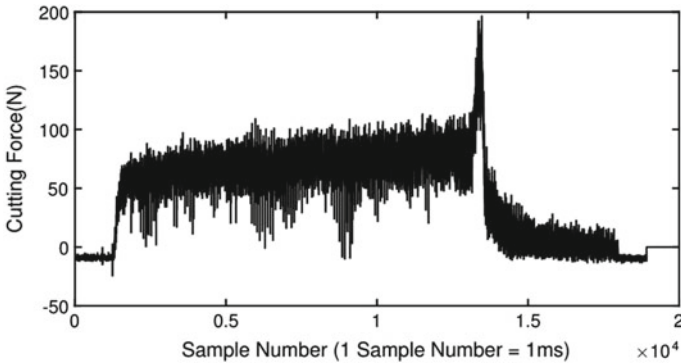


**Fig. 2** Cutting force signal for experiment 1

decided based on the Nyquist criteria, to avoid aliasing, and the sampling frequency needs to be at least twice the maximum frequency being measured [15]. It was stored in a computer using the data acquisition system. The signal data was then exported to MATLAB using comma specified value (CSV) format for further analysis.

### 2.3 Signal Analysis

The cutting force signal from dynamometer is shown in Fig. 2. The signal was processed as follows:

1. The entry and exit part of the signal were removed, and steady cutting zone was considered (Fig. 3).
2. The linear trend present in the signal was removed (Fig. 4).
3. The signal was divided into frames of 500 samples without overlap.
4. The low, high and mean values of each frame were plotted in an error-bar chart (Fig. 5).
5. The kurtosis value for each frame was evaluated and plotted as shown in Fig. 6.

The detailed steps in signal processing are as follows:

#### Signal Preprocessing

Signal preprocessing involves preparing the signal for the analysis. In the current study, the transient parts, entry and exit of the process were not considered for analysis. The steady part of the signal can be obtained using matrix slicing options in MATLAB. As can be seen from Fig. 3, the signal has an upward trend. This trend from the signal generally removed before conducting further analysis, and the de-trended signal is shown in Fig. 4. In this case, the trend was linear; hence, a straight line fit for the equation was determined and subtracted from the signal. This can be accomplished in MATLAB using de-trend function. During trial experiments, the



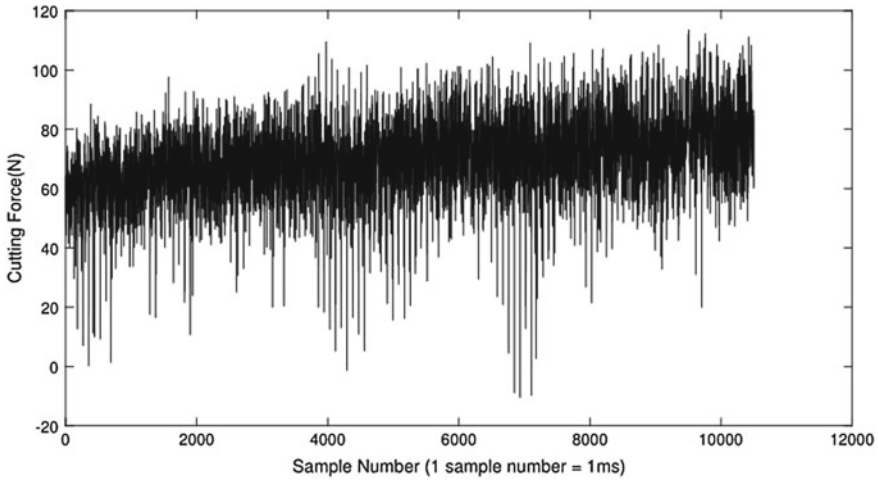


**Fig. 3** Steady part of the cutting force signal

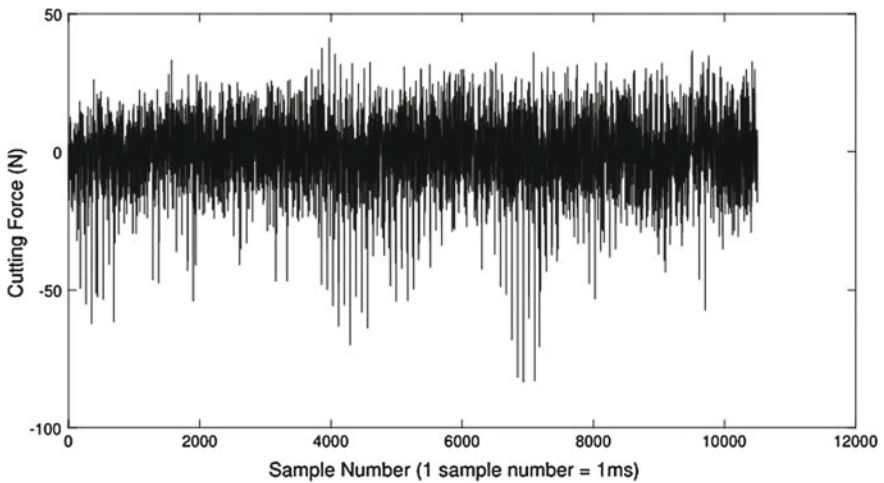


**Fig. 4** Cutting force signal after removing trend

frequency content of the force signal was analyzed; the high-frequency content was negligible, and hence, the signal was not filtered using a low-pass filter.

**Frame Statistics**

Analyzing a signal as shown in Fig. 4 can be difficult as there are many data points. Frame statistics involves dividing the signal into frames of equal size and determining statistical parameters like low, high, mean, range and standard deviation. Each statistical parameter can then be plotted with respect to time to analyze the system. This reduces the complexity and helps in visualizing the process conditions. In the

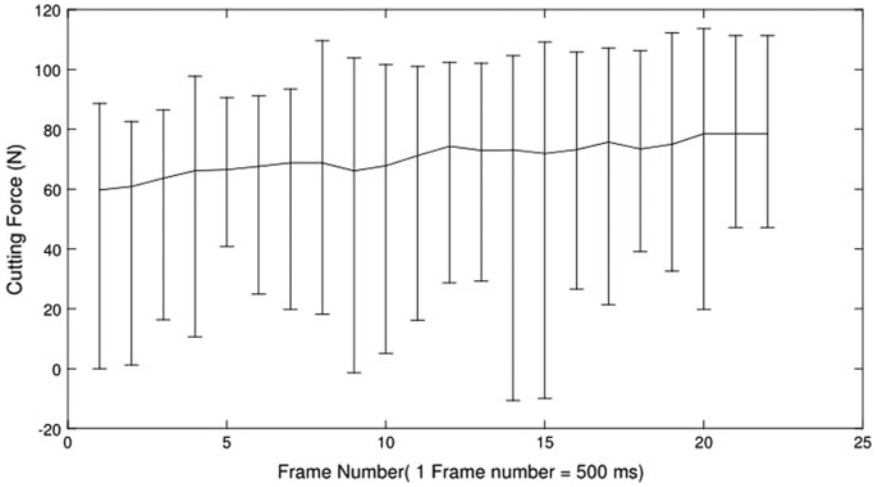


Fig. 5 Error-bar plot for cutting force signal

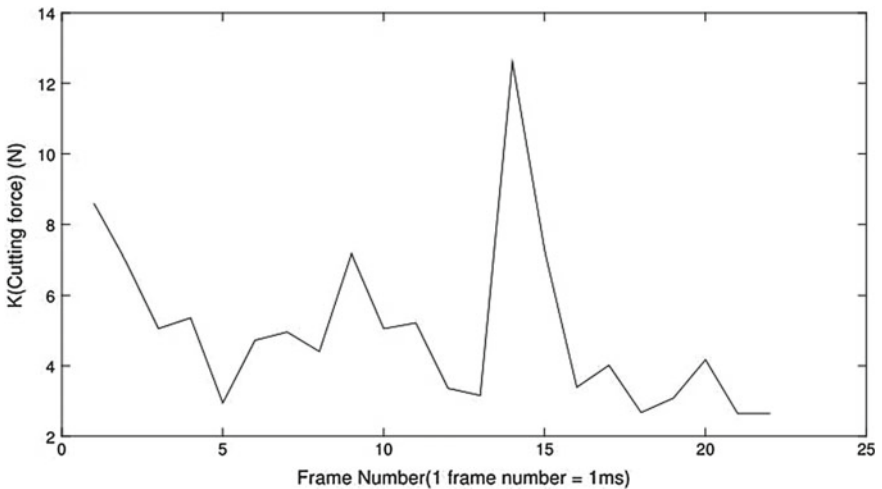


Fig. 6 Kurtosis plot for the steady zone of the signal

current study, the signal was divided into frames of equal size of 500 samples (i.e., 0.5 s) without any overlap, i.e., each frame does not share any samples from the adjacent frame. After the signal was divided, low, high and mean values were calculated for each frame and plotted as shown in Fig. 5. This plot is useful to visualize mean and dynamic variation in the cutting force value. Error-bar plots are generally useful for preliminary analysis about the process. Moreover, by plotting the kurtosis value with respect to time, it can be used to understand the process stability for the given cutting parameters.

**Kurtosis**

For data  $x_1, x_2, \dots, x_n$ , kurtosis is given by

$$K = \frac{\sum_{i=1}^N (x_i - \bar{x})^3 / N}{s^3} \tag{1}$$

where  $s$  is the standard deviation [16]. Kurtosis compares how the data is distributed when compared with the standard normal distribution. The kurtosis value for the standard normal distribution is 3. Larger kurtosis value is an indication of the presence of extreme data. Hence, kurtosis is a measure of extremes. It helps in finding if there are any sudden changes. In the present study, the aluminum metal matrix composite consists of hard SiC particles. When they come in contact with the tool, they cause a sudden impact, resulting in sudden increase in cutting force. Thus, kurtosis can be used to measure the effect of such impact loads.

The experiments were conducted based on Table 2, and the signal analysis was done to evaluate kurtosis for every frame. The results for the six experiments have been summarized in Fig. 7 and Table 3. As mentioned in the previous section, kurtosis is a measure of any sudden impact loads on the tool. It has to be noted that it is a dimensionless parameter, and hence, physical interpretation is only possible through comparison.

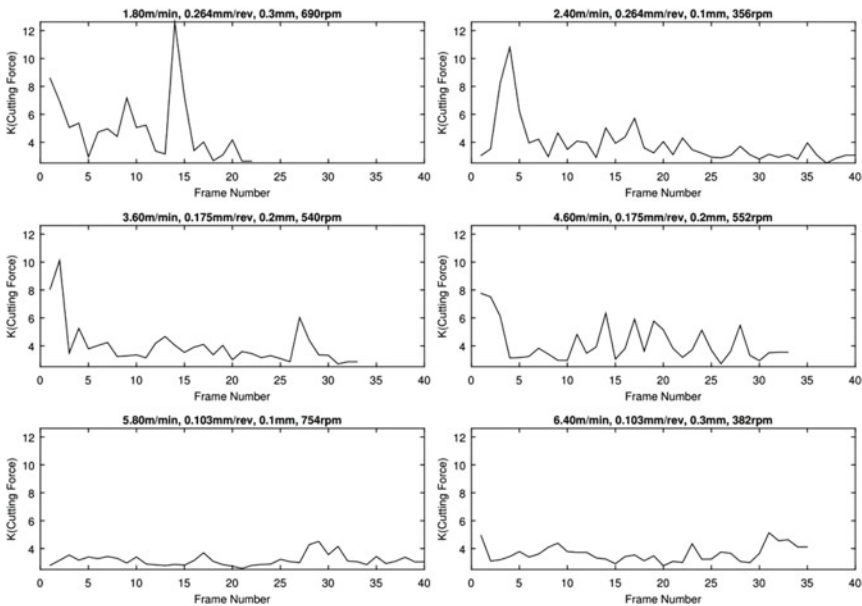


**Fig. 7** Plot of kurtosis values for each frame in all experiments

**Table 3** Peak kurtosis value for the experiments

S. No	Cutting speed (m/min)	Feed (mm/rev)	Depth of cut (mm)	Peak kurtosis value
1	80	0.264	0.3	12.61
2	40	0.264	0.1	10.8
3	60	0.175	0.2	10.12
4	60	0.175	0.2	7.764
5	80	0.103	0.1	4.512
6	40	0.103	0.3	5.14

### 3 Results and Discussion

As shown in Fig. 7, plot of kurtosis values for each frame in all experiments, the peak is largest in the first experiment, where all the process parameters are at the maximum value. Moreover, there are a couple of smaller peaks in experiment 1. Large peaks can also be seen in experiments 3 and 4. Though experiments 3 and 4 were conducted at same process parameters, slight variation can be observed in experiment 4 with multiple smaller peaks. This could be possibly due to the presence of hard SiC particles that were not completely removed in previous passes. Experiments 5 and 6 have kurtosis values close to 3, and hence, are not affected much by the presence of hard particles. In both these cases, feed is low. Low feed results in low uncut chip thickness, thus smaller area of the tool is interacting with the cutting tool, leading to lower number of SiC particles coming in contact with the tool. Experiments 5 and 6 have lower kurtosis values, and hence, they are affected the least by the hard particles. The parameters in experiment 5 are beneficial as it results in lower cutting times, better surface finish and lower wastage of material due to smaller depths of cut. Through this analysis, the effect of hard SiC particles was found to be minimum in experiment 5. The peak values have been summarized in Table 3. As the hard particles causing catastrophic tool failure is the main reason for tool wear, minimizing it results in longer tool life.

### 4 Conclusions

The paper presented an application of using frame statistics and kurtosis in dry finish turning of aluminum metal matrix composites. The following conclusions can be made from the study:

1. Frame statistics reduces the load data into a manageable graph that can be analyzed based on the mechanics of the manufacturing process.
2. Kurtosis was presented as a measure of impact loads on the cutting tool.

3. As kurtosis is computationally inexpensive, it can be used for online monitoring of the machining process.
4. In finish turning aluminum metal matrix composites, better process conditions were found when feed was low. The best process parameters in the machining range were found at 80 m/min cutting speed, 0.103 mm/rev feed and 0.1 mm depth of cut.
5. The methodology can be applied to other machining processes.

## References

1. Tlustý J, Andrews GC (1983) A critical review of sensors for unmanned machining. *CIRP Ann Technol* 32(2):563–572
2. Tönshoff HK, Wulfberg JP, Kals HJJ, König W, Van Luttervelt CA (1988) Developments and trends in monitoring and control of machining processes. *CIRP Ann Technol* 37(2):611–622
3. Byrne G, Dornfeld D, Inasaki I, Ketteler G, König W, Teti R (1995) Tool condition monitoring (TCM)—the status of research and industrial application. *CIRP Ann Technol* 44(2):541–567
4. Teti R, Jemielniak K, O'Donnell G, Dornfeld D (2010) Advanced monitoring of machining operations. *CIRP Ann Technol* 59(2):717–739
5. Chang C-W, Kuo C-P (2007) Evaluation of surface roughness in laser-assisted machining of aluminum oxide ceramics with Taguchi method. *Int J Mach Tools Manuf* 47(1):141–147
6. Tsao CC, Hocheng H (2004) Taguchi analysis of delamination associated with various drill bits in drilling of composite material. *Int J Mach Tools Manuf* 44(10):1085–1090
7. Ramanujam R, Muthukrishnan N, Raju R (2011) Optimization of cutting parameters for turning Al-SiC (10p) MMC using ANOVA and grey relational analysis. *Int J Precis Eng Manuf* 12(4):651–656
8. Seeman M, Ganesan G, Karthikeyan R, Velayudham A (2010) Study on tool wear and surface roughness in machining of particulate aluminum metal matrix composite—response surface methodology approach. *Int J Adv Manuf Technol* 48(5–8):613–624
9. Sahoo AK, Pradhan S, Rout AK (2013) Development and machinability assessment in turning Al/SiCp-metal matrix composite with multilayer coated carbide insert using Taguchi and statistical techniques. *Arch Civ Mech Eng* 13(1):27–35
10. Bhushan RK, Kumar S, Das S (2010) Effect of machining parameters on surface roughness and tool wear for 7075 Al alloy SiC composite. *Int J Adv Manuf Technol* 50(5–8):459–469
11. Li X, Seah WKH (2001) Tool wear acceleration in relation to workpiece reinforcement percentage in cutting of metal matrix composites. *Wear* 247(2):161–171
12. Manna A, Bhattacharayya B (2003) A study on machinability of Al/SiC-MMC. *J Mater Process Technol* 140(1):711–716
13. Widia (2010) *Widia 2010 Turning Catalog*
14. Montgomery DC (2001) *Design and analysis of experiments*. Wiley, Hoboken
15. Brandt A (2011) *Noise and vibration analysis: signal analysis and experimental procedures*. Wiley, Hoboken
16. Natrella M (2010) *NIST/SEMATECH e-handbook of statistical methods*. NIST/SEMATECH

# Design and Ergonomic Work Posture Evaluation of Garbage Disposal Pushcart



P. Jayesh, A. Gopala Krishna, M. Vishal, Abhay Mohan and Sheikh Afridhi

**Abstract** Garbage management is a continually growing problem both at global and regional frontiers. Solid waste arises from human, animal, and industrial activities. User-friendly products are essential for garbage collectors and residents to improve the utility. In this study, the main concerns are addressed to design an economically frugal garbage transportation cart which would be viable for commercialization. The new design is engineered keeping in mind present-day conditions and is built to cater to the needs of the pourakarmikas. The ease of operation of the proposed model will increase efficiency by reducing effort and hence the fatigue on the operator. The revolutionary changes that are proposed to be incorporated in the new model are as simple as replacing steel with aluminum where ever necessary, yet having a significant impact on the overall ergonomics. Other such pivotal changes are equipping the cart with an economic motor and a battery to provide assistance in maneuvering the cart on challenging terrain. Also, a braking system is proposed to be integrated into the cart to prevent undue movement of the cart. A turntable to make the bins instantly accessible is also added which reduces the time while loading and unloading of garbage.

**Keywords** Ergonomic design · Pushcart · Modeling · Fabrication

## 1 Introduction

The survey study for the development of the product was conducted in Bangalore, India. Bangalore generates about 3000–3500 tons of solid waste daily. The city corporations carry out the collection, transportation, processing, and disposal of municipal solid waste, with a workforce of around 14,300 women pourakarmikas using 11,000 pushcarts. The primary issues with the pushcarts are the outdated design, inadequate capacity, non-adaptability to bad road conditions, difficult to operate, demands a high amount of manual labor. These drawbacks lead to a lot of health

---

P. Jayesh · A. Gopala Krishna · M. Vishal · A. Mohan (✉) · S. Afridhi  
MVJ College of Engineering, Bangalore, India  
e-mail: [abhaymohan789@gmail.com](mailto:abhaymohan789@gmail.com)

© Springer Nature Singapore Pte Ltd. 2020  
H. K. Voruganti et al. (eds.), *Advances in Applied Mechanical Engineering*,  
Lecture Notes in Mechanical Engineering,  
[https://doi.org/10.1007/978-981-15-1201-8\\_123](https://doi.org/10.1007/978-981-15-1201-8_123)

1169

problems, especially the overexertion of the musculoskeletal system. The aim of the effort is to prepare an ergonomically designed pushcart for the pourakarmikas, so as to make the carriage of waste easy and comfortable. The adoption of a wheeled cart for enabling the pushing of multiple units is discussed by Spindel et al. [1]. A latching device mechanism for the pushcart system is proposed by Krummel et al. [2]. Latching mechanism for a push-back cart storage system includes an outer side member having a notch. Eberlein et al. [3] presented a motor-assisted hand-movable cart; it has drive chassis with two front casters, two back casters, and an electromotor drive unit connected to a running wheel located in between the front and back casters. A system for motorizing a shopping cart or the like is designed by Losego [4]. Taylor [5] proposed a low-pressure operating liquid spring and shock absorber. The work involved developing a design for pushcarts considering the Occupational Safety and Health Administration (OSHA) standards and ergonomic standard charts Rapid Upper Body Assessment (RULA) and Rapid Entire Body Assessment (REBA).

## 2 Ergonomic Analysis of the Existing System

In ergonomic analyses, employers are required to assess the health and safety risks of employees resulting from working tasks and activities, including manual handling. It is a technique that focuses on job tasks as a way to identify hazards before they occur and focuses on the relationship between the worker, the task, the tools, and the work environment. To identify the problem faced by the pourakarmikas with the existing system (shown in Fig. 1), standard charts such as RULA and REBA charts were used for the risk assessment and a comparison survey was conducted for 10 pourakarmikas who collect garbage across the different regions of Bangalore city.



**Fig. 1** Existing traditional pushcart

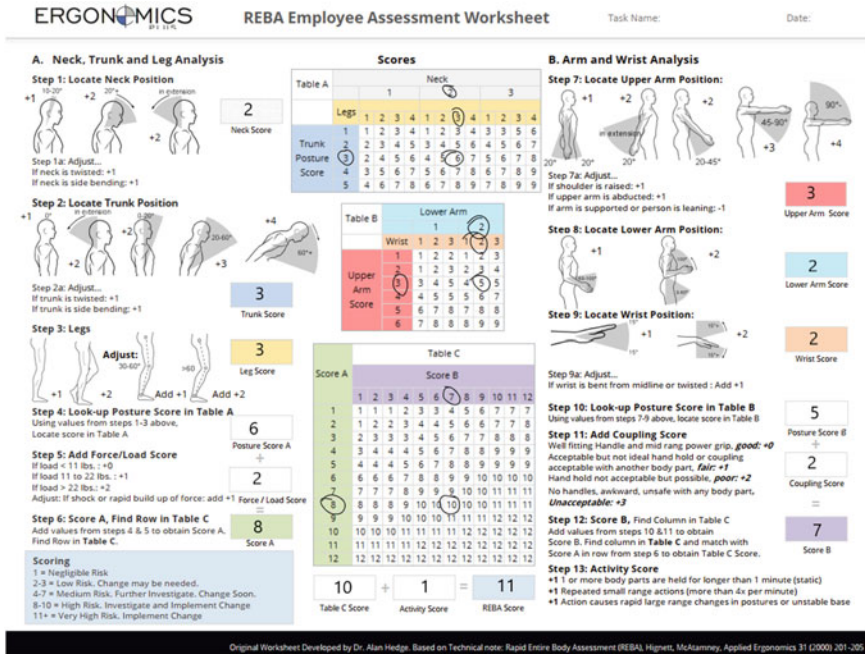


Fig. 2 Existing cart REBA

### 2.1 Rapid Entire Body Assessment (REBA)

This ergonomic assessment tool uses a systematic process to evaluate whole-body postural musculoskeletal disorders (MSDs) and the risks associated with job tasks. A single-page worksheet is used to evaluate required or selected body posture, forceful exertions, type of movement or action, repetition, and coupling [6]. The traditional, less adaptable existing pushcart system underwent a detailed study conducted from across Bangalore city. The case study system is shown in Fig. 2. The scorecard sheet of the REBA assessment is shown in Fig. 2 and the score is reached at a magnitude of 11. The REBA score of 11 indicates that there is a very high amount of risk involved and needs a change, which has been tried to implement in the current project.

### 2.2 Rapid Upper Limb Assessment (RULA)

The RULA assessment tool was developed to evaluate the exposure of individual workers to ergonomic risk factors associated with upper extremity MSD. The RULA ergonomic assessment tool considers biomechanical and postural load requirements of job tasks/demands on the neck, trunk, and upper extremities. Using the RULA





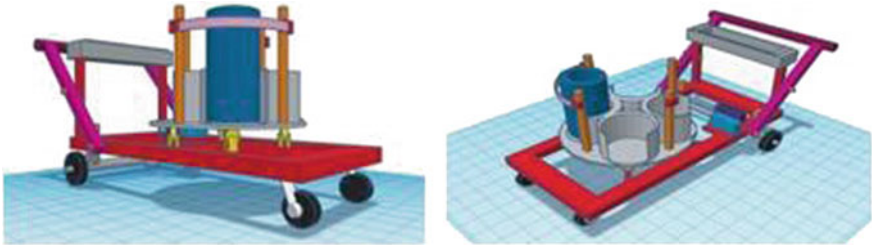


Fig. 4 Right-hand side and diametric view of the model (TinkerCAD)

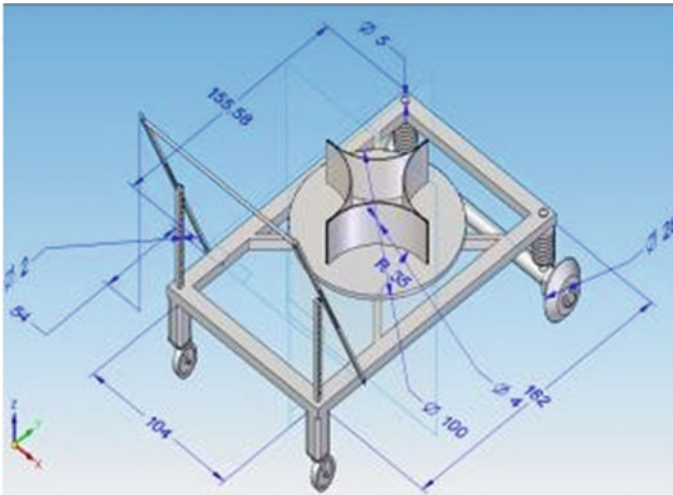
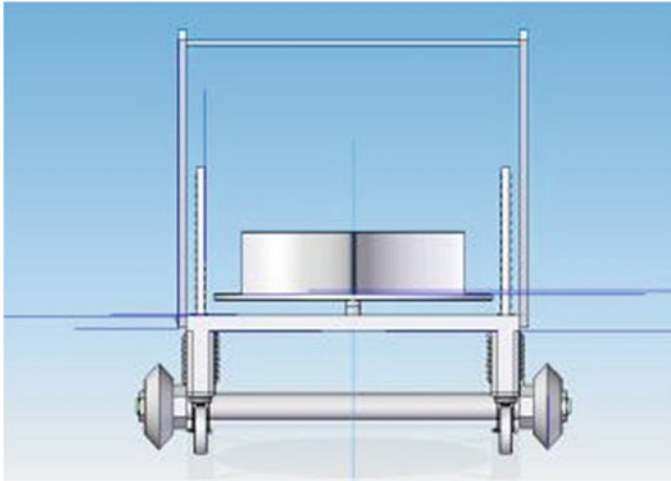


Fig. 5 Isometric view of the model

### 3.1 Fabrication

The fabrication of the cart was made in-house on the campus. Before fabrication, the materials with the best quality were procured from the local suppliers. The fabrication process includes cutting, welding, and fitting of the material to form the individual components. After the fabrication is completed, the components are assembled and the quality is checked. The component or part of the systems is explained in Table 1.



**Fig. 6** Front view of the model

**Table 1** List of components of the cart

Sl. No	Parts and Components	Material	Specifications
1	Frame of the cart	Mild steel	1.7 m × 1 m
2	X-Cross section on the frame	Mild steel	Length = 1.12 m
3	Handle	Mild steel	Four different posture height according to requirement
4	Turntable	Aluminum	Diameter 0.98 m
5	Journal bearing	–	Inner diameter = 28 mm, Outer diameter = 32 mm
6	Storage Bins	Polyethylene FDA	75 liters each
7	Small sprocket	steel	4915 15T
8	Motor	DC Type	1.6 Nm, 100 rpm
9	Solar panel	–	12 W output, charging time 5 h
10	Solar panel charger controller	–	3A current, 14.8 V maximum; Lithium battery cells
11	Shaft to mount bearing	Mild steel	25 mm length, 29 mm diameter
12	Battery to store energy	–	12 V DC
13	Swiveling casters	polypropylene	150 mm diameter (2)
14	Front axle casters	polypropylene	150 mm diameter (2)
15	Spring for suspension	Mild steel	Offset of 5 cm, 5 cm diameter, 15 cm length

### 4 Result

After the fabrication of the proposed model, the obtained results are compared with the existing model and tabulated, shown in Table 2 (Fig. 7).

The standard RULA and REBA assessment charts have been used for the ergonomic analysis. The survey is conducted for ten workers in Bangalore city. A sample of the case study chart shown in Fig. 8 for the reference of REBA score calculation and analysis. The assessment result and average RULA and REBA score for the ten workers are shown in Table 3.

A sample of the case study chart shown in Fig. 9 for the reference of RULA score calculation and analysis. A comparison of the proposed system with the existing system reveals a performance improvement with the proposed cart scoring 6.2 on the REBA chart, as compared to the previous score of 11. The RULA chart also shows a performance improvement with a new score of 3.8 against the score of 8 of the existing pushcart. The consistency of the proposed system is checked for an average of ten workers using both the charts. Approximately, 80% of workers score between 4 and 7 on the REBA score, with the remaining 20% scoring in the range of 8–10. A similar result for the RULA assessment was obtained, with approximately 90%

**Table 2** Features comparison of existing and proposed systems

Sl. No	Features	Existing System	Proposed System
1	Assistance to tread elevations	No	Yes
2	Turntable	No	Yes
3	Capacity	215–240 kg	330–350 kg
4	Manual labor	High	Medium
5	Suspension system	No	Yes
6	Number of wheels	3	4
7	Handling conditions	Poor	Good



**Fig. 7** Different views of the assembled cart

**ERGONOMICS PLUS** REBA Employee Assessment Worksheet Task Name: \_\_\_\_\_ Date: \_\_\_\_\_

**A. Neck, Trunk and Leg Analysis**

**Step 1: Locate Neck Position**  
 19-20° +2 20° +2  
 Neck Score: 1  
 Step 1a: Adjust...  
 If neck is twisted: +1  
 If neck is side bending: +1

**Step 2: Locate Trunk Position**  
 19° +2 20° +2 20-45° +3 45-90° +4  
 Trunk Score: 1  
 Step 2a: Adjust...  
 If trunk is twisted: +1  
 If trunk is side bending: +1

**Step 3: Legs**  
 Adjust: 30-40° +0 40° +2  
 Leg Score: 2  
 Add +1 Add +2

**Step 4: Look-up Posture Score in Table A**  
 Using values from steps 1-3 above. Locate score in Table A.  
 Posture Score A: 2

**Step 5: Add Force/Load Score**  
 If load < 11 lbs.: +0  
 If load 11 to 22 lbs.: +1  
 If load > 22 lbs.: +2  
 Adjust: If shock or rapid build up of force: add +1  
 Force / Load Score: 2

**Step 6: Score A, Find Row in Table C**  
 Add values from steps 4 & 5 to obtain Score A. Find Row in Table C.  
 Score A: 4

**Scoring**  
 1 = Negligible Risk  
 2-3 = Low Risk. Change may be needed.  
 4-7 = Medium Risk. Further Investigate. Change Soon.  
 8-10 = High Risk. Investigate and Implement Change  
 11+ = Very High Risk. Implement Change

**Scores**

**Table A Neck**

		Neck		
Legs	Trunk Posture	1	2	3
1	1	3	4	1
1	2	3	4	1
2	2	4	5	3
2	3	4	5	3
3	2	4	5	6
3	3	5	6	7
4	3	5	6	7
4	4	6	7	8
5	4	6	7	8
5	5	7	8	9
6	5	7	8	9
6	6	8	9	9
7	6	8	9	9
7	7	9	9	9
8	7	9	9	9
8	8	9	9	9
9	8	9	9	9
9	9	9	9	9
10	9	9	9	9
10	10	10	10	10
11	10	10	10	10
11	11	11	11	11
12	11	11	11	11
12	12	12	12	12
12	12	12	12	12

**Table B Lower Arm**

		Lower Arm		
Wrist	Upper Arm	1	2	3
1	1	2	1	2
1	2	3	2	3
2	2	3	3	4
2	3	4	4	5
3	2	4	5	6
3	3	5	6	7
4	3	5	6	7
4	4	6	7	8
5	4	6	7	8
5	5	7	8	9
6	5	7	8	9
6	6	8	8	9
7	6	8	8	9
7	7	9	9	9
8	7	9	9	9
8	8	9	9	9
9	8	9	9	9
9	9	9	9	9
10	9	9	9	9
10	10	10	10	10
11	10	10	10	10
11	11	11	11	11
12	11	11	11	11
12	12	12	12	12
12	12	12	12	12

**Table C**

		Score B											
Score A	1	2	3	4	5	6	7	8	9	10	11	12	
1	1	1	2	3	4	5	6	7	7	7	7	7	
2	1	2	3	4	4	5	6	6	7	7	7	8	
3	2	3	3	4	5	6	7	7	8	8	8	8	
4	3	4	4	5	6	7	8	8	9	9	9	9	
5	4	4	5	6	7	8	8	9	9	9	9	9	
6	6	6	7	8	8	9	9	10	10	10	10	10	
7	7	7	8	9	9	10	10	10	11	11	11	11	
8	8	8	9	10	10	10	10	10	11	11	11	11	
9	9	9	10	10	10	11	11	11	12	12	12	12	
10	10	10	10	11	11	11	12	12	12	12	12	12	
11	11	11	11	12	12	12	12	12	12	12	12	12	
12	12	12	12	12	12	12	12	12	12	12	12	12	

**B. Arm and Wrist Analysis**

**Step 7: Locate Upper Arm Position:**  
 20° +1 20° +2 20° +2 20-45° +3 45-90° +4 90° +4  
 Upper Arm Score: 2  
 Step 7a: Adjust...  
 If upper arm is abducted: +1  
 If arm is supported or person is leaning: -1

**Step 8: Locate Lower Arm Position:**  
 +1 +2  
 Lower Arm Score: 1

**Step 9: Locate Wrist Position:**  
 +1 +2  
 Wrist Score: 2  
 Step 9a: Adjust...  
 If wrist is bent from midline or twisted: +Add +1

**Step 10: Look-up Posture Score in Table B**  
 Using values from steps 7-9 above. Locate score in Table B.  
 Posture Score B: 2

**Step 11: Add Coupling Score**  
 Well fitting handle and mid range power grip. **good: +0**  
 Acceptable but not ideal hand hold or coupling acceptable with another body part. **fair: +1**  
 Hand hold not acceptable but possible. **poor: +2**  
 No handles, awkward, unsafe with any body part. **Unacceptable: +3**  
 Coupling Score: 1

**Step 12: Score B, Find Column in Table C**  
 Add values from steps 10 & 11 to obtain Score B. Find column in Table C and match with Score A in row from step 6 to obtain Table C Score.  
 Score B: 3

**Step 13: Activity Score**  
 +1 = 1 or more body parts are held for longer than 1 minute (static)  
 +1 Repeated small range actions (more than 4x per minute)  
 +1 Action causes rapid large range changes in postures or unstable base  
 Activity Score: 2

**Table C Score** 4 + **Activity Score** 2 = **REBA Score** 6

Original Worksheet Developed by Dr. Alan Hedge. Based on Technical note: Rapid Entire Body Assessment (REBA), Hignett, McAtamney, Applied Ergonomics 31 (2000) 201-205

Fig. 8 REBA sample for case study 3

Table 3 REBA and RULA case study for ten workers

Worker Number	REBA score	RULA score
1	5	4
2	7	3
3	6	4
4	8	5
5	8	4
6	5	4
7	5	3
8	6	4
9	6	4
10	6	3
Average	6.2	3.8

of workers under a score of 3–4 and the remaining 10% with a score in the range of 5–6.

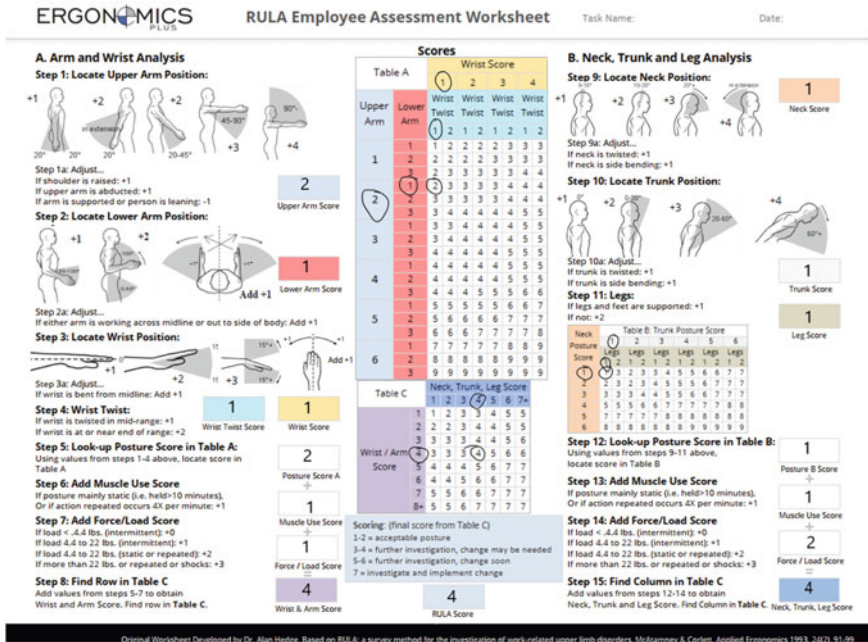


Fig. 9 RULA sample for case study 1

## 5 Conclusion

As a societal commitment, the existing cart in the Bangalore city used by the BBMP workers was analyzed, their ergonomic issues were addressed using standard process and procedures, and finally, the cart was developed to sort out the challenges effectively. The technological advancements were made within the cost-effective ranges. Ergonomic charts' scores suggest that the existing system has a high amount of risk and needs immediate change. Based on the results, a new design is proposed, which has better features compared to the existing system. With the new design, posture correction can be done, avoiding musculoskeletal disorders in the workers. There are a lot of improvements that can be incorporated into this project that make it more complete and feature rich. The chance of theft could be the major issue on the cart. For addressing energy conservation, further improvements could be made on automation, braking system, etc. to the cart.

## References

1. Spindel M, Cino N (2003) Adaptation to wheeled cart to enable pushing of multiple units, US 6550794 B1, 23 Apr
2. Krummel JVR, Davison KE (1994) Latching mechanism for push-cart, US 5312004, 17 May
3. Eberlein H, Kriz P (2002) Motor assisted hand moveable cart, US6343665, 5 Feb
4. Losego M (1989) System for motorizing a shopping cart or trolley, or the like. US5064012A
5. Taylor PH (1971) Low pressure operating shock absorber, US3698521, 9 Nov
6. Ansari NA, Sheikh MJ (2014) Evaluation of work posture by RULA and REBA: a case study. *J Mech Civil Eng* 11(4):18–23. ISSN 2320-334X
7. Peterson GJ (1970) Brake mechanism for grocery carts, US3501164 A, 17 Mar

# Redesigning of Electric Plug for Assembly Time Reduction Using DFA



V. Naga Malleswari, B. SurendraBabu and Ch. Praneeth

**Abstract** The important element to meet today's competitive market during the development of any product is the reduction of assembling time. The industries which use a variety of component geometry Design For Manufacturing and Assembly (DFMA) play a vital role in product development. Design for Assembly (DFA) is one of the principles in DFMA. The principle concept of DFA is to reduce the number of parts used and to maximize the use of existing parts and to eliminate or redesign the parts which take more assembly time. Many of the companies successfully used this technique for product design improvement. The aim of the present work is to propose a new design of electric plug assembly that is better in design efficiency, total assembly time. The analysis is done by using Boothroyd Dewhurst DFA method. There is a reduction in the number of parts from 16 to 11 after redesign of electric plug assembly and assembly time is reduced from 87.4 to 33.9 s. Design efficiency is improved from 36 to 64.89%. In product development, reducing assembly time is one of the important tasks because it reduces labor time. Simple design with least number of components makes assembly easy and fast.

**Keywords** DFA · Redesign · Product development · Assembly time

## 1 Introduction

Design for Assembly (DFA) has many benefits in addition to cost of assembly. When a product contains minimum number of parts, assembly procedure becomes easier. Inventory levels of each part can be reduced. Storage and maintenance cost of the components can be reduced and which in turn reduces the production time and cost. While designing a product DFA can be considered. Design team can show alternative designs and give more consideration to make the assembly or sub-assembly easy

---

V. Naga Malleswari (✉) · B. SurendraBabu · Ch. Praneeth  
Industrial Engineering, GITAM Institute of Technology, Visakhapatnam, A.P, India  
e-mail: [nagamalleswari.vangipurapu@gitam.edu](mailto:nagamalleswari.vangipurapu@gitam.edu)



during production and also service time. The developed concepts are analyzed over selected cost and performance. A systematic analysis of product assembly should be performed. If cost or performance analyses require a concept to be changed or redesigned, then the efficiency of assembly of the reconceived design should be analyzed before the final design is approved. During the design components, assemblies, subassemblies, its features, and corresponding dimensions should be verified so that it indicates the findings of the DFA analysis. The analysis of product design for ease of assembly depends on whether the product is to be assembled manually, with special-purpose automation, or a combination of these.

## 2 Literature Review

Lefever and Wood [1] used a technique to reduce the number of components in an assembly. This technique consists of a component elimination procedure, component combination analysis and lastly established a logical approach for the abstract component elimination or combination opportunities technique to redesign an auxiliary automobile visor. Ismail et al. [2] have used DFMA methodology for redesigning a pressure vessel. The existing design of the pressure vessel was modified by incorporating the design for manufacture and assembly requirements. Using DFMA Technique manual assembly efficiency is improved. Geren et al. [3] have studied the design of intensifier used in the prototype of a Water Jet Machining system. Suresh et al. [4] have done research for determining environmental impact sustainability analysis and engineering analysis. A case study using charge alternator pulley is redesigned using DFMA technology. CAD modeling, stress analysis and sustainability analysis of pulley model done for reducing the product cost and minimal impact on the environment. Emmatty and Sarmah [5] have presented a framework for modular product development by integrating function-based modular product architecture, platform-based design, and design for manufacture and assembly. It reduces product manufacturing cost and throughput time for product development. A case study of a watch mechanism was used by them. Naiju et al. [6] have used DFMA technique in reducing the time and cost in the development of a new product. Food processor was taken as a case study and overall manufacturing cost was reduced. Till now many DFMA studies are published. However, very few studies have addressed the consumer durables of Indian market. No such study has been published on electric plug assembly. Not many studies were done to detail the DFMA methodology with respect to Indian consumer products. The main task of this research paper is to show that assembly time reduction is possible for a product and provides significant time benefits to the manufacturing industry.

### 3 Methodology

The initial step of the present work is existing product assembly design is analyzed. Then, each part functionality is recognized. Material used for each part is also recognized. The symmetry of the product design is found based on the Alpha and Beta symmetry. Worksheet analysis is done based on the Boothroyd Dewhurst manual handling and manual insertion coding system. From that total operation, time is calculated as

$$\text{Total operation time} = (\text{part handling time} + \text{insertion time}) * \text{number of parts.} \quad (1)$$

Without affecting the functionality, each part has to study based on the criteria wherever elimination or redesign of part is required. If the component meets the minimum part criteria two different parts are combined into a single part otherwise it is eliminated. The minimum part criteria are taken as specified by Boothroyd et al. [7].

An important element of DFA method is to calculate the efficiency of the product assembly time. The two important elements that impact the assembly time of a product are

- (a) The total number of components in a product and the easiness of handling each component.
- (b) Insertion of the component and fastening of the components with another component.

Finally, assembly efficiency is measured. The assembly efficiency,  $E_{ma}$  is calculated using the following formula.

$$E_{ma} = N_{\min} t_a / t_{ma} \quad (2)$$

where

$N_{\min}$ —theoretically minimum number of components

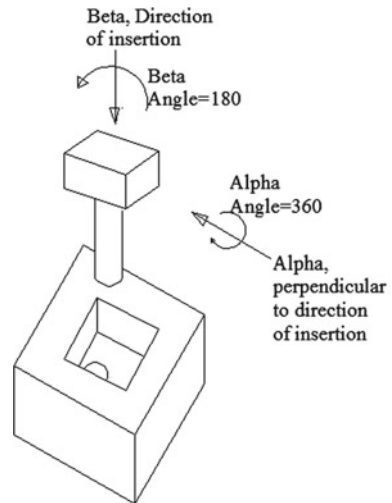
$t_a$ —basic assembly time for each component

$t_{ma}$ —estimated time to complete the assembly of the actual product.

#### 3.1 Effect of Part Symmetry on Handling Time

Part symmetry is one of the geometrical design features which impacts the assembly time needed to pick up and positioning of a part. At least two components are required for assembly operation. Positioning of a part means exact alignment of the part to the inserted part. As per these two operations are performed (i) the axis of one component

**Fig. 1** Alpha and beta symmetry



is aligned with the axis of another inserted component. (ii) Rotating the component about the axis of the insertion part. The symmetry of a part can be classified as Alpha symmetry is the angle through which a part must be rotated about an axis perpendicular to the axis of insertion and to repeat its orientation. Beta symmetry is the angle through which a part must be rotated about the axis of insertion and to repeat its orientation [7]. It is shown Fig. 1.

## 4 Case Study

In the present work electric plug (Anchor, 3 pin Top deluxe) is taken as a case study. Exploded view of the product is shown in Fig. 2. Analysis of each part based on the DFA technique is shown in Table 1.

### 4.1 Work Sheet Analysis for Top Frame

The insertion axis for the top frame is vertical and the top frame can only be inserted one way along this axis so the alpha angle of symmetry is  $360^\circ$ . If the top frame is rotated about the axis of insertion, it will repeat its orientation every  $360^\circ$  so, this is beta angle of symmetry. The total angle of symmetry is  $360 + 360 = 720^\circ$ . Next step is to find the handling code and estimated times from Fig. 3.15 [7]. Top frame can be grasped and manipulated with one hand without the aid of grasping tools. Thickness of the top frame is greater than 2 mm and size is greater than 15 mm so, the code is “3” and corresponding time is 1.95 s. Next step is to find the insertion

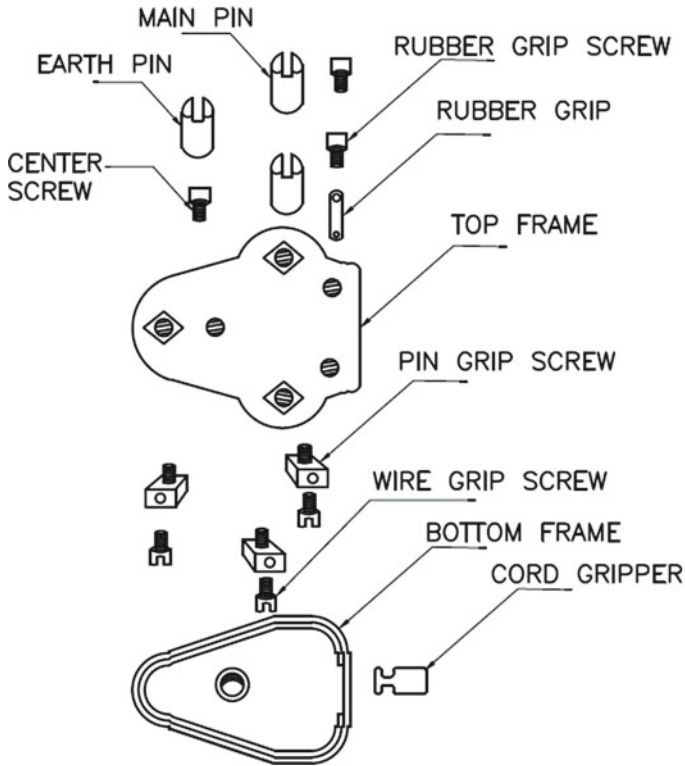


**Fig. 2** Exploded view of electric plug assembly

code and estimated time from Fig. 3.16 [7]. Top frame does not require any other part for assembly immediate to place the part securely. After this part, no holding is required to maintain the orientation and location of the part. The top frame is easy to align and position during assembly and does not require any resistance to hold the part. So, the manual insertion code is “00” and corresponding time is 1.5 s. From the above data total operation time is calculated using Eq. (1) that is  $(1.95 + 1.5) * 1 = 3.45$  s.

#### **4.2 Component Elimination and Redesign of Electric Plug Using DFA Technique**

In DFMA analysis the first step is to analyze the existing assembly design with DFA analysis. Each component functions and materials are studied next. Third step is to identify a part for elimination or redesign based on the minimum part criteria. Any part not meeting the criteria is a part for elimination or redesign. By reducing

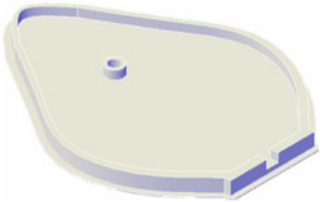
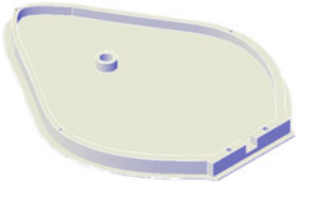
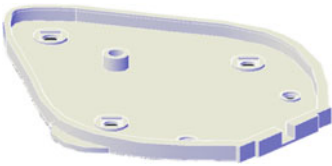
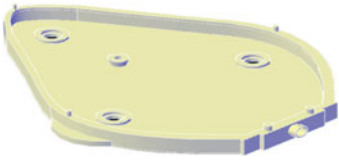




the number of components in a product assembly or sub-assembly design, assembly time efficiency can be increased. In the present work electric plug is taken as a case study. Existing design is studied with DFA analysis. The following redesign steps were identified during the analysis: (a) Integration of cord gripper to bottom frame, (b) replacement of center the screw with transition fit joint, (c) elimination of rubber grip and screws and redesign and (d) redesign of pin grip screw. Redesign steps a, b and c are the most significant redesign changes as these eliminate the need for a separate part altogether. Due to usage of lesser number of components, activities like parts fabrication, storage, stock verification and maintenance, quality assurances can be avoided. The production cost can be further reduced by removing the component which consumes more assembly time.

- (a) Integration of cord gripper to bottom frame: In the existing design of the electric plug, the cord gripper and bottom frame are separate parts. The minimum criteria are not met by the cord gripper component hence it is eliminated. To accommodate this bottom frame is redesigned.
- (b) Replacement of the center screw with transition fit joint: Threaded joints take more assembly time. In place of threaded joints, fit joints can be selected. In the present case study threaded joint is replaced with transition fit. Threaded joints take more assembly time and material cost is increased because of separate screws. In electric plug assembly while fastening the center screw to bottom frame obstructed the part and restricted the vision. By replacing this center screw with a fit saves the assembly time, cost and improves the easiness of assembly.
- (c) Elimination of rubber grip and screws and redesign: Main function of this rubber grip is to provide guidance to the card. In the original design, it is taking major assembly time. Eliminating the rubber grip and screws based on the minimum part criteria, it is integrated with the top frame.
- (d) Redesign of pin grip screw: Orientation of the pin grip screw is consuming more time during assembly. Based on the concept of part symmetry on handling time pin grip screw is redesigned. Eliminated the square seating into circular seating. While assembling, more concentration and care is not required. In turn, it reduces operation time from 27 to 9 s.

$t_a = 2$  s (handling and insertion time for each part is taken as 2 s on average). The original design consists of  $N_{\min} = 16$  parts and estimated assembly time is  $t_{ma} = 87.4$  s. Then design efficiency from the Eq. (2) obtained as 36%. After implementing DFA analysis, minimum number of parts is reduced to  $N_{\min} = 11$  parts and estimated assembly time is  $t_{ma} = 33.9$  s. Finally design efficiency has improved to 64.89%. Further, prototype has to be prepared by using the Rapid Prototyping Technique (RPT) and the results have to verify (Table 2).

**Table 2** Redesign of electric plug assembly

Name of the part	Before DFA	After DFA
Bottom frame		
Top frame		
Pin grip screw		

## 5 Conclusion

In the present work, DFA rules are considered to reduce the assembly time of electric plug. This electric plug consists of 16 components. According to the minimum part criteria two components are eliminated without affecting the functionality and also two components are redesigned so that assembly time is reduced by 53.5 s. Finally, the total number of components is reduced by 5 units. Using DFA methodology assembly efficiency is improved from 36 to 64.89%. Because of reducing assembly time, assembly cost and then in turn production cost can be reduced and profitability of the industry can be increased. Reducing the assembly time of a product is significant change in the production cost of the product. This work can be extended to other consumer products which consist of more components and also cost analysis can be done.

## References

1. Lefever DD, Wood KL (1996) Design for assembly techniques in reverse engineering and redesign. In: ASME design theory and methodology conference, pp 1–28
2. Ismail AR, Abdullah SC, Manap AHAA, Sopian K, Tahir MM, Usman IMS, Wahab DA (2008) DFM and DFA approach on designing pressure vessel. In: Proceedings of the 7th WSEAS

international conference on system science and simulation in engineering (ICOSSSE), pp 147–151

3. Geren N, Bayramoglu M, Esme U (2007) Improvement of a low-cost water jet machining intensifier using reverse engineering and redesign methodology. *J Eng Des* 18(1):13–37
4. Suresh P, Ramabalan S, Natarajan U (2016) Integration of DFE and DFMA for the sustainable development of an automotive component. *Int J Sustain Eng* 9(2):107–118
5. Emmatty FJ, Sarmah SP (2012) Modular product development through platform based design and DFMA. *J Eng Des* 23(9):696–714
6. Harlalka A, Naiju CD, Janardhanan MN, Nielsen I (2016) Redesign of an in-market food processor for manufacturing cost reduction using DFMA methodology. *Prod Manufact Res* 4(1):209–227
7. Boothroyd Geoffrey, Dewhurst Peter, Knight Winston (2010) *Product design for manufacture and assembly*, 3rd edn. CRC Press, New York



# Analysis and Optimization of Queuing Systems in Airports—Discrete Event Simulation



Rishabh Jain, Hrishikesh Bedekar, K. Jayakrishna, K. E. K. Vimal  
and M. Vijaya Kumar

**Abstract** The objective of this paper is to present an authentic queuing scenario for airports both international and domestic including transit passengers in constant efforts to create a uniform flow of passengers and baggage. This study aims also at the simulation that can be used to identify bottlenecks in the systems as well as to gain insight into the whole process. Similarly, the study suggests multiple modified scenarios that provide a solution to the challenges in existing systems that can be adopted by the industry in the near future. More specifically, these scenarios are rearrangements and modifications to the existing system. As security checkpoints are points in the system which can cause severe delays and are notorious for separation of individuals in a group. Therefore, scenarios are considered wherein the number of checkpoints can be increased such that the total number of individuals waiting gets distributed effectively. Lastly, another scenario in which gate specific checkpoints are considered has been modeled for reference and can be seen on a few busy airports, it was also observed that the waiting times at security checkpoints reduced by 0.10 out of 0.43, 0.07 and 0.33. Though a longer queue time was observed at the last scenario than the second scenario, the third scenario would be a better replacement as it yields an optimum performance time without increasing the load on other points such as immigration, check-in and baggage claim unlike the second scenario wherein the queuing at security check point is reduced but pressure builds up on other parts of the system.

**Keywords** Supply chain · Airports · Optimization · Logistics · Queuing · ARENA

---

R. Jain · H. Bedekar · K. Jayakrishna (✉)  
School of Mechanical Engineering,  
Vellore Institute Technology, Vellore 632014, India  
e-mail: [mail2jaikrish@gmail.com](mailto:mail2jaikrish@gmail.com)

K. E. K. Vimal  
Department of Mechanical Engineering, NIT Patna, Patna, Bihar 800005, India

M. Vijaya Kumar  
Department of Mechanical Engineering, NIT Warangal, Hanamkonda,  
Telangana 506004, India

## 1 Introduction

The identification of bottlenecks at the airport and their rectification would definitely make it a better and efficient system. The overall improvement of the system can be a critical factor influencing the success and efficiency of management at the airport [1]. Improved systems will reduce the time wasted unnecessarily due to stoppages at certain levels. Moreover, it will reduce the load on a single system and happy passengers would indeed be a key measure to organizational success [2]. The optimum utilization of resources would be an easier task if the system is well planned thereby reducing unnecessary expenditure and wasted capital.

The objective of this paper is to develop innovative methods of analyzing and optimizing queuing systems in a system with a special focus on airports. Principles of data collection, data interpretation by data fitting and modelling and simulation methodologies have been proposed. Different scenarios with varying arrangements of entities at the airport have been observed. The different scenarios to perform iterations towards improved results have contributed by depicting a unique solution. Using these methodologies, a novel structure of airports has been proposed. Major part of this research has been focused on modelling and simulation of systems in the manufacturing and production domains. This work, however, aims to use these methodologies in the airports which have been rarely discussed. Moreover, the literature emphasises on minor optimizations in the already established structure. However, this work tries to present an unconventional arrangement of queuing systems to achieve similar objectives.

## 2 Methodology

This part of the study mainly deals with developing innovative methods of modelling and simulating supply chains to minimize queuing times with an emphasis on airports. Data collection, interpretation, fitting coupled with modelling and simulation methodologies have been discussed in detail. The queueing theory forms a basis of this simulation and can be used for further calculations by considering the arrival time of passengers. The main equation derived is shown below,

$$P_0 = \frac{1}{1 + \sum_{n=1}^{\infty} \prod_{i=0}^{n-1} \frac{\lambda_i}{\mu_{i+1}}} [4] \quad (1)$$

where

$\mu$ : Average service rate of a single service

$\lambda$ : Average arrival rate

$P$ : Probability of  $n$  customers in the system

$n$ : Number of people in the system

It is best to start with a simple model and build toward greater complexity and it is not a necessity to have a one-to-one mapping between the model and the real system [3]. In our case study, large amounts of relevant data was collected in order to determine the probability distribution of the various processes involved. The logic of the system is converted to a computer understandable format using modules offered by the used application [4]. For example, the security check can be easily translated into a queuing module following “first come first serve” rule and the entities being served one by one by each module. Verification pertains to the computer program prepared for the simulation model [5]. Is the computer program performing properly or not? [6]. For example, increasing the number of people arriving level of the model must correspond to increase in the waiting times. If, however, a decrease in waiting times is seen, a fallacy of the model is exposed which must then be rectified. Validation usually is achieved through the calibration of the model, an iterative process of comparing the model against actual system behaviour and using the discrepancies [4]. The alternatives that are to be simulated must be determined. Often, the decision concerning which alternatives to simulate will be a function of runs that have been completed and analyzed [3].

### **3 Analysis**

An in-depth analysis of a few airports revealed the airports with widely varying structures. In this case study a traditional model is adapted and improved upon to reduce queuing times. Here, real case data is collected from Chatrapati Shivaji International Airport to carry out simulations.

### **4 Model Conceptualization**

In order to translate the system into a discrete event simulation model in the arena an extensive analysis of the system was done. Various points of queuing and delays were investigated. Data was collected and the appropriate probability distributions were estimated for the data to be input into the simulation [6].

#### ***4.1 Data Fitting***

In order to simulate the model using DIS fitting the data obtained into the appropriate distribution of probability was carried out in a systematic method [6]. Random number generating methods were used in order to simulate the inter-arrival times of the PAX [4]. Triangular distribution of data was used in cases wherein the maximum amount of population completed the given task in a given amount of time.

## 4.2 Models

Table 1 illustrates the different modules being used in the ARENA simulation each representing an entity. These entities represent the actual component involved in the system of queueing at the airport. Further details of the representation and their significance are mentioned in Table 1. Using the following modules coupled with sets queues in ARENA a comprehensive and realistic model was developed of the airport system. Using this system three scenarios (A, B and C) were considered for which simulations were run. Scenario B and C eventually evolved as a viable solution that could help mitigate the current problems faced by conventional queueing systems today. The three scenarios encompassing three types of airport systems are [6]:

**Table 1** Model description

Module	Explanation
Gate security check	Simulated the inter-arrival times of the patients intended to depart from the airport
Check-in counter	Checking of documents followed by issue of tickets
Incorrect passenger detail failure	Case checking for failure of details to comply
Dispose 1	Passengers leave the system due to incorrect details
Check if international passenger	To check if the passenger in the system is flying international or not
Immigration	Immigration facility for international passengers
Immigration check	Immigration check
Immigration fail	Case checking the failure of immigration
Security check	Security check for airport
Gate international	International gates
Aircraft international	Boarding an international aircraft
Security check domestic	Security check for domestically flying passengers
Gate domestic	Domestic gates
Aircraft domestic	Boarding a domestic aircraft
Arrival	Simulating the inter-arrival times for passenger arrival to the airport
If international	Checks if arrived passenger is an international passenger
Immigration arrival	Immigration for arriving patients in transit
Immigration check arrival	Immigration check for arriving passenger in transit
Quarantine or held back	Passenger held back on immigration failure
Baggage claim	Baggage claim for passengers
Customs arrival	Customs for international passengers
Customs pass	Check if the passenger passed customs
Confiscated fined	Passenger fined on custom failure
International exit	International passengers leave the system



## 6 Conclusions

As observed in the study, modifications can be made to the layout to make it more flexible leading to less crowding in the bottlenecks especially the security check channel, immigration desks and the baggage counters [8, 9]. Modifications such as having separate security gateways at each gate instead of a common gateway reduce the burden on the system and also the total lead time involved in the formalities. The total cost to make this layout flexible and add the modifications is less when compared to the cost after incurring losses in the long run as customers-passengers are directly affected thereby holding the reputation of the Airport at stake. Similarly, such simulations can also be applied to the planning of other industries as it is easier and faster to analyze scenarios and identify pitfalls before developing the model into a defective entity thereby saving a lot of time and capital which can otherwise be used for more important things or where it is most required.

## References

1. Ju Y, Wang A, Che H (2007) Simulation and optimization for the airport passenger flow. In: 2007 International conference on wireless communications, networking and mobile computing. IEEE, pp 6605–6608
2. Brown JR, Madhavan P (2011) Examining passenger flow choke points at airports using discrete event simulation
3. Prinz R, Väättäinen K, Laitila J, Sikanen L, Asikainen A (2019) Analysis of energy efficiency of forest chip supply systems using discrete-event simulation. *Appl Energy* 235:1369–1380
4. Banks J, Carson II, Nelson BL, Nicol DM (2005) *Discrete-event system simulation*. Pearson
5. Kleijnen JP (1998) Experimental design for sensitivity analysis, optimization, and validation of simulation models. In: *Handbook of simulation: principles, methodology, advances, applications, and practice*, pp 173–223
6. De Neufville R, Budd L, Ison S (2016) Airport systems planning and design. In: *Air transport management: an international perspective*, p 61
7. Joustra PE, Van Dijk NM (2001) Simulation of check-in at airports. In: *Proceedings of the 33rd conference on winter simulation*. IEEE, pp 1023–1028
8. Pritsker AAB (1979) Compilation of definitions of simulation. *Simulation* 33(2):61–63
9. Szymanczyk O, Dickinson P, Duckett T (2011) Towards agent-based crowd simulation in airports using games technology. In: *KES international symposium on agent and multi-agent systems: technologies and applications*. Springer, Berlin, Heidelberg, pp 524–533

# An Extensive Study of Multi-level Inventory Lot Sizing Optimization Problem



V. V. D. Sahithi, C. S. P. Rao and M. Srinivasa Rao

**Abstract** Inventory management is the heart of manufacturing industry because proper inventory management leads to major cut back in the operating costs. Several researchers had focused on this issue because of its importance in cost reductions. Lot of traditional, nontraditional and heuristic algorithms were developed to solve this problem with good solution efficiency and computational effectiveness. In this paper authors are trying to explain about the research in the area of inventory management especially in the Lot sizing of inventory techniques from 1913 to 2018 and different soft computing techniques Like Particle swarm optimization and Harmonic Search were applied to Multi-Level Capacitated Lot sizing problem and they were compared with the different algorithms from the previous literature.

**Keywords** Lot sizing · Optimization · Evolutionary algorithms · MRP

## 1 First Section

Inventory Lot sizing optimization gained the attention of researchers because of its efficient impact on the reduction of total variable cost. Lot sizing problem helps in determining the order quantities of different items in the Bill of materials structure in the given planning horizon. If the order quantity  $Q$  is increasing, it reduces the ordering cost but at the same time, this increases the carrying cost.

However, if we reduce the order quantity size it reduces the carrying cost and increases the ordering cost. Therefore, minimizing the total variable cost by finding the correct Lot size is always a trade of between ordering cost and the carrying cost of inventory. In this paper, the objective is to find out the efficient algorithms by

---

V. V. D. Sahithi (✉)

Mechanical Engineering Department, VNRVJIET, Hyderabad, Telangana 500090, India  
e-mail: [Sahithi.hai@gmail.com](mailto:Sahithi.hai@gmail.com)

C. S. P. Rao

National Institute of Technology Andhra Pradesh, Tadepalligudem, Andhra Pradesh 534102, India

M. Srinivasa Rao

JNTU Hyderabad, Hyderabad, Telangana 500090, India

© Springer Nature Singapore Pte Ltd. 2020

H. K. Voruganti et al. (eds.), *Advances in Applied Mechanical Engineering*,

Lecture Notes in Mechanical Engineering,

[https://doi.org/10.1007/978-981-15-1201-8\\_126](https://doi.org/10.1007/978-981-15-1201-8_126)

comparing different evolutionary algorithms for multi-level lot sizing problem and also to know about the behaviour of different algorithms in case of Multi-Level Lot sizing Optimization.

## 2 Lot Sizing Optimization: Literature Review

Inventory Lot sizing rules were the feature of inventory optimization for several decades. The inventory Lot sizing optimization problem is a traditional issue in inventory management. Even though it is treated as an important problem since industrial revolution, the main research started in this Lot sizing area when Harris [1] first developed his Economic Order Quantity (EOQ) model for his article "How Many Parts To Make At Once" in the year 1913 for simple Lot sizing problem with study demand rate. After that Wagner and Whitin [2] developed a Dynamic version of Lot sizing in 1958. Clark [3] developed an inventory model for Dynamic Lot sizing with single item and Multi echelon environment for U.S. Air Force supply systems in 1958. J. J. DeMatteis developed a part-period algorithm for economic Lot sizing optimization problem. In 1968 [4]. Willard I. Zangwill introduced backlogging into uncapacitated Lot sizing model in 1969 [5]. Silver E. A., Meal H. C. developed a heuristic algorithm for deterministic time-varying demand rate and discrete opportunities for replenishment in 1973 [6]. Panayotis Afentakis et al. developed a computationally efficient heuristic technique for multi-stage assembly structures in 1984 [7]. R. Kuik and M. Salomon applied Simulation annealing heuristic technique for solving multi-level Lot sizing (MLLS) problems in 1990 [8]. Horst Tempelmeier, Stefan Helber developed a heuristic technique for solving Dynamic Multi-item and Multi-level capacitated lot sizing (MLCLS) for general product structures in 1994 [9] and then Tempelmeier along with Matthias Destroff developed a Lagrangian-based heuristic for solving same kind of problems in 1996 [10]. William Hernandez and Gursel A. Suer developed Genetic Algorithms (GA) to solve simple Lot Sizing problems in 1999 [11] and then N. Dellaert et al. Extended this work to multi-level lot sizing problems in 2000 [12]. Xie, J. and Dong, J. applied GA for most complex Capacitated lot sizing problems in 2002 [13]. N. P. Dellaert and J. Jeunet developed a randomized heuristic technique for simple multi-level lot sizing problems. In 2004 [14]. Juan J. Gonzalez and Raydel Tullous Extended Wagner Whitin algorithm for Lot sizing problem with back-ordering in 2004 [15]. July Jeunet, Nicolas Jonardb developed a stochastic search algorithm for MLLS problems in 2005 [16]. Lotfi Gaafar Applied GA to dynamic lot sizing problem with batch ordering in 2006 [17]. Tobias Schulz developed a new silver meal based heuristic for dynamic lot sizing problem with return and remanufacturing in 2009 [18]. Yi Hana et al. developed a particle swarm optimization algorithm for MLLS problem in 2009 [19]. Christian Almeder developed a new heuristic algorithm by combining ant colony algorithm with an exact solver for linear programs in 2010 [20]. Klorklear Wajanawichakon<sup>1</sup>, Rapeepan Pitakaso<sup>2</sup> extends PSO technique for MLLS problems [21]. Vahid Hajipour applied



A hybrid ant colony heuristic algorithm to MLCLS problem in 2014 [22]. Abdolreza Roshani et al. developed a simulated annealing heuristic for MLCLS problem in closed manufacturing systems [23]. Jörg Homberger applied a Parallel Genetic Algorithm for simple MLLS problem without capacity constraints in 2016 [24]. Amit Gupta et al. Worked on Evaluation and Selection of Lot Sizing Techniques using SAW Approach in 2017 [25].

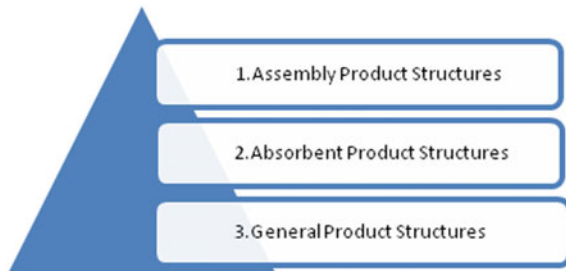
### 3 Mathematical Formulation

In the manufacturing systems, most of the end items are made up of number of sub-items. All these are represented by bill of material structure. Generally bill of material (BOM) structure is hierarchical in its nature, with all the finished products at the top, i.e. called zeroth level. BOM includes different product codes, descriptions of parts, quantities, parts costs and also the additional specifications. In multi-level lot sizing problem product structures are mainly divided into 3 types as shown in Fig. 1.

For mathematical formulation, we assume that all the end item demands are independent, no backlogging or shortages are allowed. Lead times of all the items are zero. For the sake of simplicity, no positive inventories or scheduled receipts are introduced in the first period. This multi-level capacity-constrained lot sizing problem is a mixed-integer programming problem. Following are the notations to describe the problem

- $N$  = total number of items,
- $T$  = total number of periods in planning horizon
- $C_{it}$  = unit production price of item  $i$  in period  $t$
- $h_{it}$  = unit holding cost of item  $I$  in period  $t$
- $S_{it}$  = setup cost of item  $i$  and period  $t$
- $d_{it}$  = he demand for item  $I$  in period  $t$
- $V_{ikt}$  = the amount of resource  $k$  necessary to produce item  $i$  in period  $t$
- $b_{kt}$  = the amount of resource  $k$  available in period  $t$
- $M$  = the upper bound on  $X_{it}$

**Fig. 1** Major types of product structures



$S(i)$  = the set of immediate successor items to item  $I$

$r_{ij}$  = the number of units of item  $i$  needed by one unit of item  $j$ , where  $j \in S(i)$

Decision variables are

$x_{ij}$  = the lot size of item  $i$  in period  $t$

$y_{it}$  = '1' if item is produced in period  $t$  and zero otherwise

$I$  is the inventory of item  $i$  in period  $t$ .

$$\text{Min(Total cost)} = \sum_{i=1}^N \sum_{t=1}^T (C_{it}X_{it} + h_{it}I_{it} + S_{it}Y_{it}) \tag{1}$$

$$\text{Min(total Variable cost)} = \sum_{i=1}^N \sum_{t=1}^T (h_{it}I_{it} + S_{it}Y_{it}) \tag{2}$$

$$I_{i,t-1} + X_{it} - I_{it} = d_{it} + \sum_{j \in S(i)} r_{ij}X_{jt}$$

$$i = 1, 2, \dots, N; \quad T = 1, 2, \dots, T \tag{3}$$

$$\sum_{i=1}^N (V_{ikt}X_{it} + f_{ikt}y_{it}) \leq b_{kt}$$

$$k = 1, 2, 3, \dots, K; \quad t = 1, 2, 3, \dots, T \tag{4}$$

$$X_{it} \leq My_{it}$$

$$i = 1, \dots, N; \quad t = 1, \dots, T \tag{5}$$

$$X_{it}, I_{it} \geq 0 \quad i = 1, \dots, N; \quad t = 1, \dots, T \tag{6}$$

$$y_{it} \in \{0, 1\} \quad i = 1, \dots, N; \quad t = 1, \dots, T \tag{7}$$

Equation (1) is to minimize the sum of production, inventory holding and setup cost. Equation (2) is to minimize the total variable cost which is our objective for the current problem, Eq. (3) is the inventory balance constraint (4) represents the capacity constraints. Constraint (5) ensure that the solution will have setup when it has production. The last two constraints (6) and (7) require that variables must be positive and setup variables must be binary.

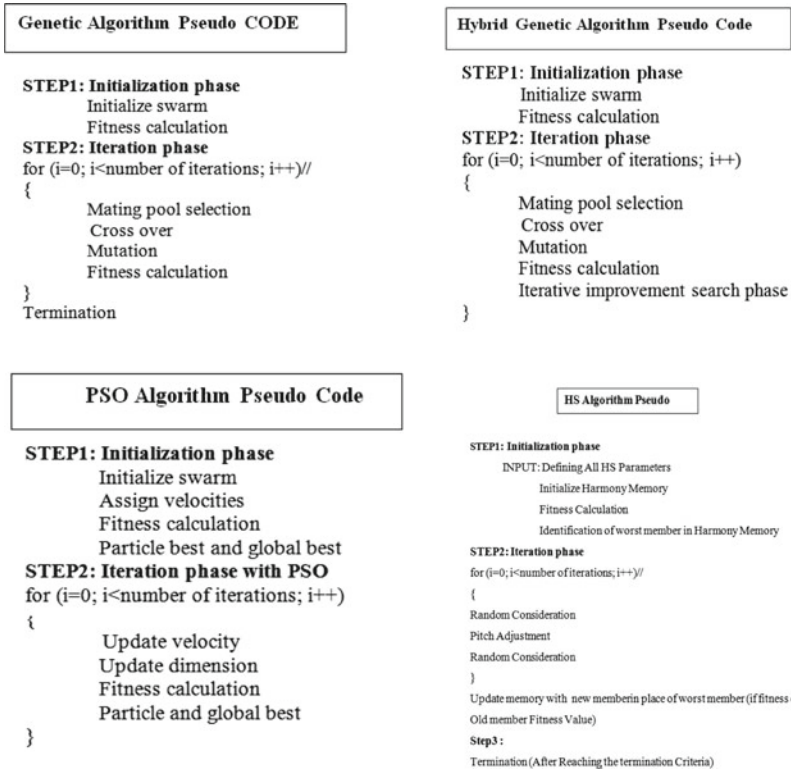


Fig. 2 Pseudo codes of different algorithms

## 4 Implementation of Different Algorithms for Multi-Level Lot Sizing Problem

Inventory Lot sizing optimization gained the attention of researchers because of its efficient impact on the reduction of total variable cost. Lot sizing problem helps in determining the order (Fig. 2).

## 5 Results and Discussions

From the literature, here we are going to observe the performance of the different algorithms like Simulated Annealing (SA), Taboo Search (TS), Lagrangean relaxation algorithm (LA), Hybrid Ant Colony Optimization Algorithm (HACO), Genetic

**Fig. 3**  $7 \times 6$  problem lot sizing problem

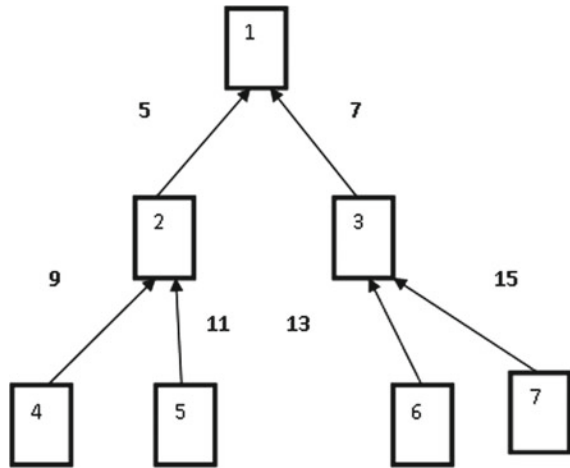


**Table 1** Optimum results of different algorithms for  $7 \times 6$  lot sizing problem

Algorithm	SA	TS	GA	HACO	LR	Hybrid GA	PSO	HSA
Total variable cost	10,740	9620	9245	9241	9239	8320	8320	8320

Algorithm(GA), Hybrid Genetic Algorithm (HGA), Harmonic Search Algorithm (HS) [13, 22].

**Problem 1: Single item multi-level Capacitated Lot Sizing Problem ( $7 \times 6$ )**

In order to apply HAS for capacitated multi-level lot sizing problem, the reference problem is taken from work done by **Jinxing Xie and Jiefang Dong** on Heuristic genetic algorithms for general capacitated lot-sizing problems [13]. Here Fig. 3 shows the BOM structure of  $7 \times 6$  problem.

Table 1 shows the results obtained by different algorithms including HSA for the above-discussed problem, Fig. 4 shows the comparison graph of results when different optimization algorithms were applied for the above-discussed problem (Fig. 5, 6, 7, 8 and 9).

**6 Results and Discussions**

In this paper, the authors implemented different algorithms for Multi-level Bill of Material structures to optimize the total Variable cost. Behaviour of the different algorithms was compared in case of different assembly structures.

1. Authors successfully implemented GA, HGA, PSO, HS algorithms for different product structures.

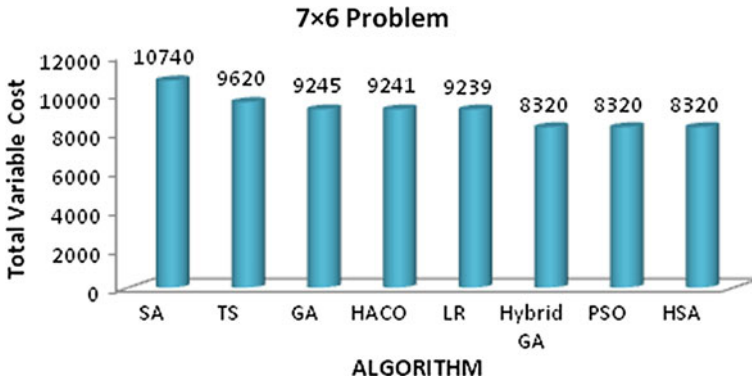


Fig. 4 Comparison optimum total variable cost different algorithms for 7 × 6 lot-sizing problem

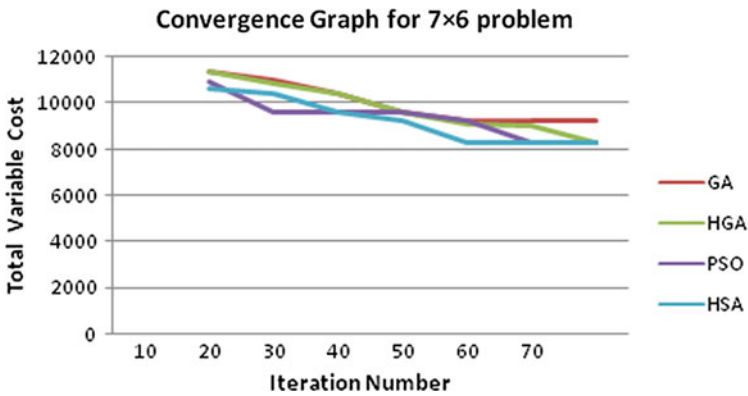


Fig. 5 Convergence graph for 7 × 6 problem

2. Results are compared with the previous works and obtained the best results with these algorithms.
3. Among these algorithms PSO and HS algorithms are giving the best results in all scenarios.
4. The convergence is faster in HS, PSO algorithms when compared to the other algorithms like GA and Hybrid GA.
5. HS algorithms convergence is more promising in all scenarios.
6. With HS and PSO algorithms within very number of iterations optimum solutions are obtained.
7. Even though the initially selected solution is bad the algorithm is performance is reasonably good in faster convergence.

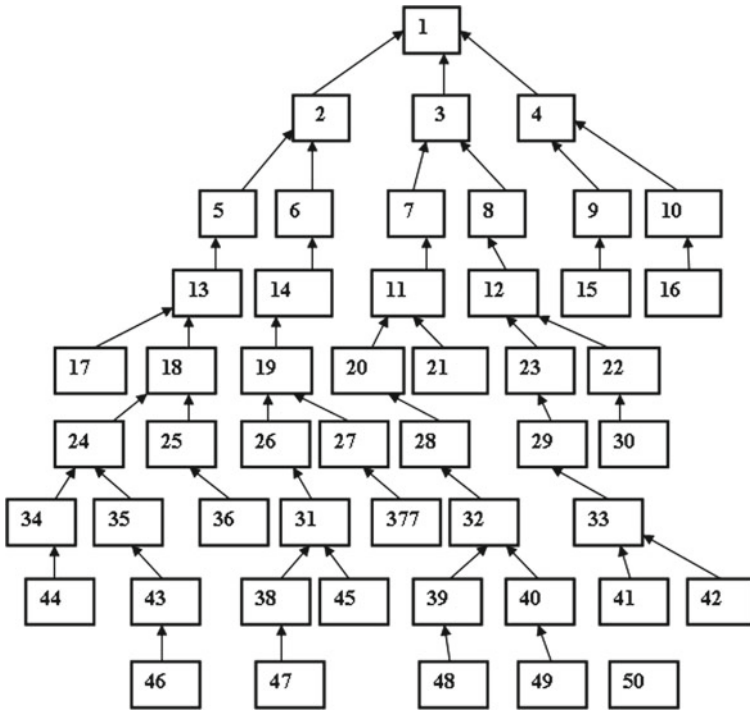


Fig. 6 BOM structure of  $50 \times 12$  problem

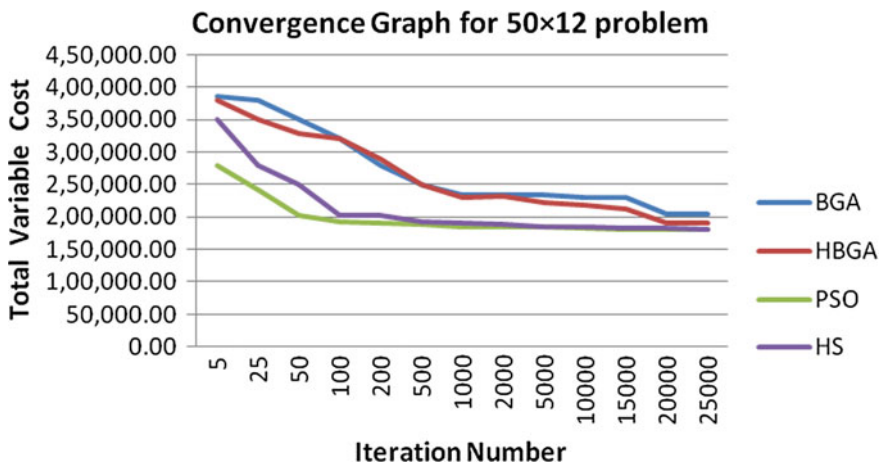


Fig. 7 Convergence Graph for  $50 \times 12$  problem

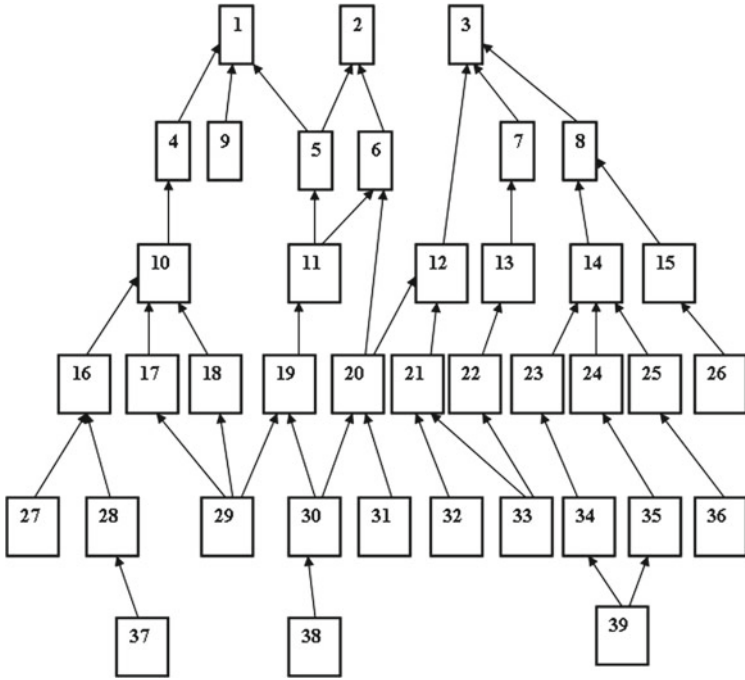


Fig. 8 BOM Structure of  $39 \times 12$  problem

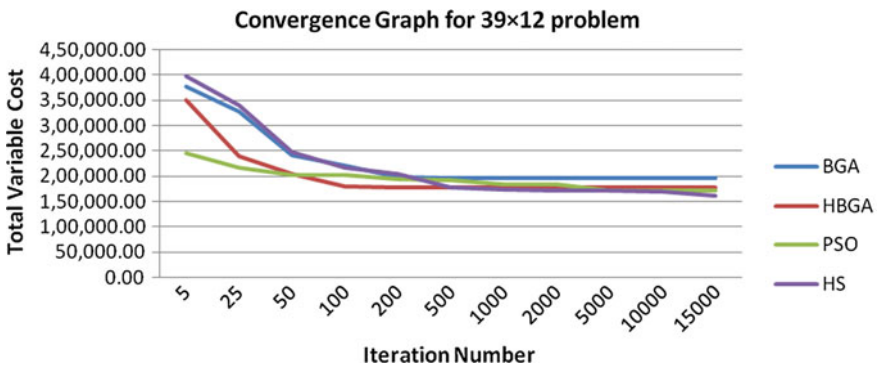


Fig. 9 Convergence graph for  $39 \times 12$  problem

## References

1. Harris FW (1913) How many parts to make at once. *Mag Manage* 10:135–136
2. Wagner HM, Whitin TM (1958) Dynamic version of the economic lot size mode. *Manage Sci* 5(1):89–96
3. Clark AJ (ed) (1958) U.S. airforce, project rand, research memorandum. ASTIA document number AD 209538
4. DeMatteis JJ (ed) (1968) An economic lot-sizing technique: the part-period algorithm. *IBM Syst J* 7:30–38
5. Zangwill WI (ed) (1969) A backlogging model and a multi-echelon model of a dynamic economic lot size production system—a network approach. *Manage Sci* 15(9):506–527. JSTOR. <https://www.jstor.org/stable/2628386>
6. Silver EA, Meal HC (eds) (1973) A heuristic selecting lot size requirements for the case of a deterministic time-varying demand rate and discrete opportunities for replenishment. *Prod Inventory Manage* 14(2):64–74
7. Panayotis Afentakis P, Gavisht B, Karmarkari U (1984) Computationally efficient optimal solutions to the lot-sizing problem in multistage assembly systems. *Manage Sci* 30(2). Printed in U.S.A
8. Kuik R, Salomon M (1990) Multi level lot sizing problem: evaluation of a simulation annealing heuristic. *Eur J Oper Res*
9. Tempelmeier H, Helber S (1994) A heuristic for dynamic multi item multi level capacitated lot sizing for general product structures. *Eur J Oper Res* 75:296–311. North-Holland
10. Tempelmier H, Destroff M (1996) A lagrangean-based heuristic for dynamic multilevel multiitem constrained lotsizing with setup times. *Manage Sci* 42(5). ABI/INFORM Collection, p 738
11. Hernandez W, Suer GA (1999) Genetic algorithms in lot sizing decisions. In: *Proceedings of the 1999 congress on evolutionary computation*. ISBN 0-7803-5536-9
12. Dellaert N, Jeune J, Jonard N (2000) A genetic algorithm to solve the general multi-level lot-sizing problem with time-varying costs. *Int J Prod Econ* 68:241–257
13. Xie J, Dong J (2002) Heuristic genetic algorithms for general capacitated lot sizing problems. *Comput Math Appl* 44:263–276
14. Dellaert NP, Jeunet J (2003) Randomized multi-level lot-sizing heuristics for general product structures. *Eur J Oper Res* 148:211–228
15. Gonzalez JJ, Tullous R (2004) Optimal lot size decisions using the Wagner-Whitin model with backorders: a spreadsheet version. In: *Second world conference on POM and 15th annual POM conference*, Cancun, Mexico, April 30–May 3
16. Jeuneta J, Jonard N (2005) Single-point stochastic search algorithms for the multi-level lot-sizing problem. *Comput Oper Res* 32:985–1006
17. Gaafar L (2006) Applying genetic algorithms to dynamic lot sizing with batch ordering. *Comput Ind Eng* 51:433–444
18. Schulz T (2009) A new silver meal based heuristic algorithm for the single-item dynamic lot sizing problem with returns and remanufacturing. *FEMM working papers*, vol 49. *Fac Econ Manage*. <https://doi.org/10.1080/00207543.2010.532916>
19. Hana Y, Tanga J, Kakub I, Mua L (2009) Solving uncapacitated multilevel lot-sizing problems using a particle swarm optimization with flexible inertial weight. *Comput Math Appl* 57:1748–1755
20. Almeder C (2010) A hybrid optimization approach for multi-level capacitated lot-sizing problems. *Eur J Oper Res* 200:599–606
21. Wajanawichakon K, Pitakaso R (2011) Solving large unconstrained multi level lot-sizing problem by a binary particle swarm optimization. ISSN 1750-9653, England, UK. *Int J Manage Sci Eng Manage* 6(2):134–141
22. Hajipour V, Fattahi P, Nobari A (2014) Hybrid ant colony optimization algorithm to optimize capacitated lot-sizing problem. *J Ind Sys Eng* 7(1):1–20. Autumn 2014



23. Roshani A, Giglio D, Paolucci M (2016) A simulated annealing approach for the capacitated dynamic lot sizing problem in a closed remanufacturing system. *IFAC-PapersOnLine* 49–12:1496–1501
24. Homberger J (2016) A parallel genetic algorithm for the multilevel unconstrained lot-sizing problem. [129.219.247.33] On: 18 Aug 2016, At: 01:01, *INFORMS*
25. Gupta A, Singha M, Jindala S, Chahalb V (2017) Evaluation and selection of lot sizing techniques using SAW approach for Indian automobile industries. *Int J Theor Appl Mech* 12(2):311–318, ISSN 0973-6085